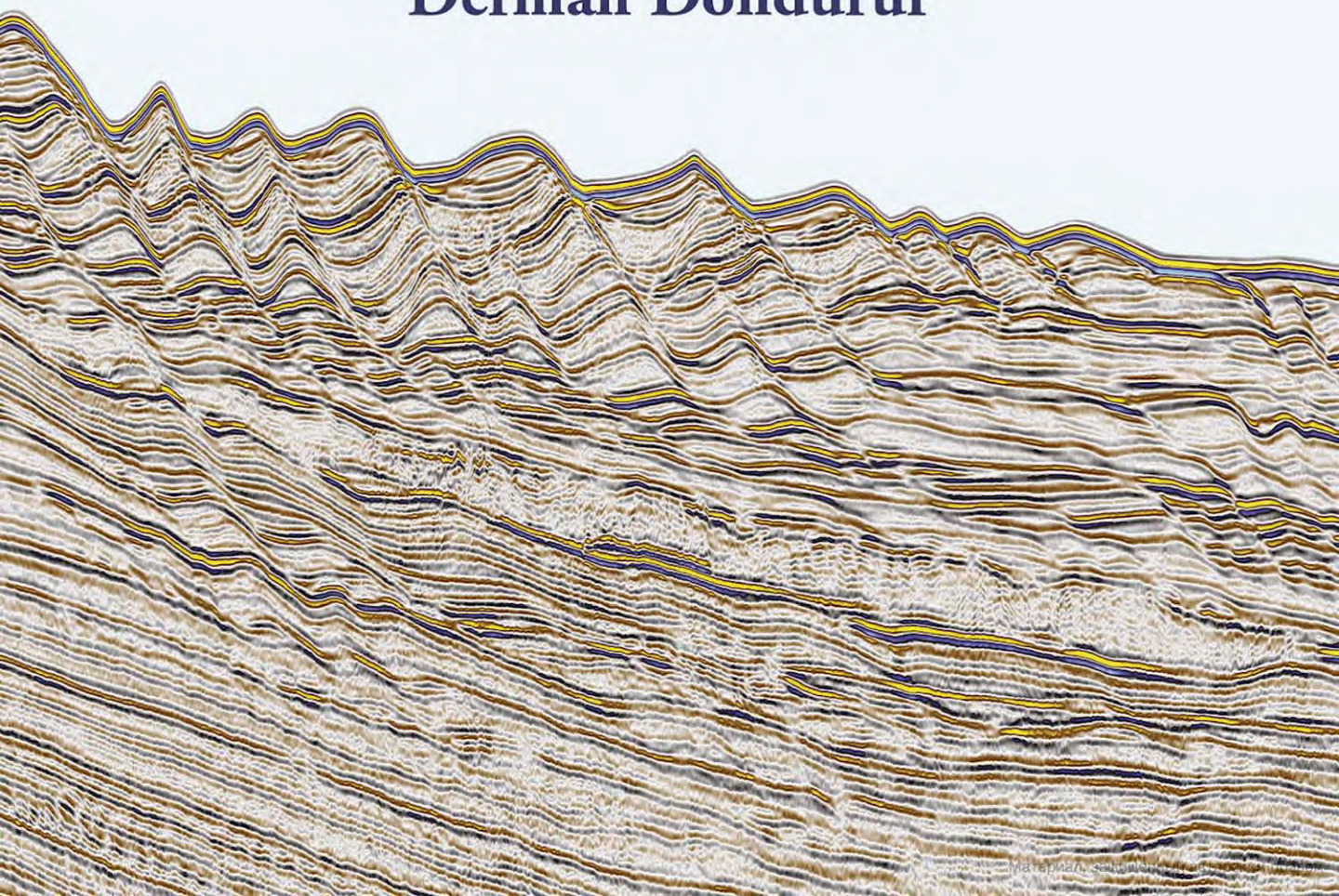
Acquisition and Processing of Marine Seismic Data

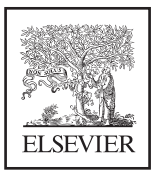
Derman Dondurur



ACQUISITION AND PROCESSING OF MARINE SEISMIC DATA

ACQUISITION AND PROCESSING OF MARINE SEISMIC DATA

DERMAN DONDURUR



Elsevier
Radarweg 29, PO Box 211, 1000 AE Amsterdam, Netherlands
The Boulevard, Langford Lane, Kidlington, Oxford OX5 1GB, United Kingdom
50 Hampshire Street, 5th Floor, Cambridge, MA 02139, United States

© 2018 Elsevier Inc. All rights reserved.

No part of this publication may be reproduced or transmitted in any form or by any means, electronic or mechanical, including photocopying, recording, or any information storage and retrieval system, without permission in writing from the publisher. Details on how to seek permission, further information about the Publisher's permissions policies and our arrangements with organizations such as the Copyright Clearance Center and the Copyright Licensing Agency, can be found at our website: www.elsevier.com/permissions.

This book and the individual contributions contained in it are protected under copyright by the Publisher (other than as may be noted herein).

Notices
Knowledge and best practice in this field are constantly changing. As new research and experience broaden our understanding, changes in research methods, professional practices, or medical treatment may become necessary.

Practitioners and researchers must always rely on their own experience and knowledge in evaluating and using any information, methods, compounds, or experiments described herein. In using such information or methods they should be mindful of their own safety and the safety of others, including parties for whom they have a professional responsibility.

To the fullest extent of the law, neither the Publisher nor the authors, contributors, or editors, assume any liability for any injury and/or damage to persons or property as a matter of products liability, negligence or otherwise, or from any use or operation of any methods, products, instructions, or ideas contained in the material herein.

Library of Congress Cataloging-in-Publication Data
A catalog record for this book is available from the Library of Congress

British Library Cataloguing-in-Publication Data
A catalogue record for this book is available from the British Library

ISBN: 978-0-12-811490-2

For information on all Elsevier publications visit our website at https://www.elsevier.com/books-and-journals



Publisher: Candice Janco
Acquisition Editor: Marisa LaFleur
Editorial Project Manager: Katerina Zalvia
Production Project Manager: Maria Bernard
Cover Designer: Mark Rogers

Typeset by SPi Global, India

To my son, A. Batuhan Dondurur…

CHAPTER

1

Introduction

OUTLINE

1.1 Underwater Acoustics 7

1.2 Marine Acoustic Methods 9

1.2.1 Bathymetric Systems 12

1.2.2 Side-Scan Sonar 14

1.2.3 Subbottom Profiler 17

1.2.4 Single Channel and Multichannel Seismics 19

1.2.5 Yesterday/Today/Future of Seismic Exploration at Sea 22

1.3 Fundamentals of Marine Seismics 25

1.3.1 Seismic Waves 25

1.3.2 Reflection From an Interface 27

1.3.3 Shot Gathers 29

1.3.4 Reflection Hyperbolas 31

Seismic reflection exploration today is, obviously, used extensively by the oil and gas industry. Indeed, the increase in new hydrocarbon discoveries over the last 50 years almost parallels the advancements in data processing and acquisition techniques. Following the digital recording of seismic data, incorporating the common midpoint (CMP) acquisition technique, powerful workstations are now used to process large amounts of digital data using sophisticated processing applications. This has led to a considerable increase in discovery and production (Fisher, 1991), since these developments have provided many quality subsurface images at relatively higher resolution, especially in complex geological environments such as areas of salt intrusions, where subsalt imaging today has become a challenging phenomenon. Continuous development of acquisition and processing techniques of seismic data, after their first introduction in the early 1920s, has resulted in very high-resolution subsurface images, which have enabled us to discover much smaller hydrocarbon traps, and it is now possible to map the target levels in much higher detail.

Raw seismic data should be processed using several complex data-processing steps in order to obtain a subsurface image from 2D or 3D multichannel seismic datasets. This procedure, consisting of a number of sequential mathematical processes, is known as seismic data processing. Data-processing applications commenced

https://doi.org/10.1016/B978-0-12-811490-2.00001-3

© 2018 Elsevier Inc. All rights reserved.

following the digital recording of seismic data in the mid-1960s, resulting in a considerable increase in the final seismic image quality after proper processing. Thenceforward, the basic goal of the processing has not changed and it is still quite simple: increasing the seismic resolution, and enhancement of the signal level while suppressing the noise amplitudes – in other words, increasing the signal-to-noise (S/N) ratio of the seismic data. If the noise embedded in the data can be separated by one of its specific characteristics, such as its frequency band, propagation velocity and/or direction, its amplitude with respect to the primary reflection amplitudes, etc., then it may be possible to remove most of the noise components from the data.

Early noise-suppression applications, when digital recording and processing techniques were not available, were accomplished by grouping geophones to suppress the coherent noise, such as ground roll in land seismic acquisitions. The technological revolution caused by World War II also resulted in significant developments related to seismic data-processing methodology. The practices used in communication technology during wartime were later applied to seismic data by the researchers at the Massachusetts Institute of Technology in the 1950s, which ultimately advanced the methodology and approaches utilized in seismic exploration and processing (Flinn et al., 1967). Today, seismic data is digitally recorded and processed before interpretation. Several different data-processing steps can be applied to the seismic data in different domains, such as time-distance, frequency, frequency-distance, etc. The selection of suitable domain for the application is dependent on which domain provides the best separation of signal from the noise.

Seismic data processing consists of several processing steps that are consecutively applied to the input data. Such a complete procedure composed of different processing steps is termed a processing flow. A basic processing flow consists of loading the dataset from disk, applying one or more processing step(s) sequentially, and then writing the processed data back to the disk (Fig. 1.1). The effectiveness of many processing steps strongly depends on the parameters used in the previous steps. For instance, if a band-pass filter is not properly applied before the deconvolution, we will not obtain satisfactory results from the deconvolution step. Therefore, a processor is responsible for proper selection of each data-processing parameter and testing of the results of each step to ensure the quality of the output.

Both for 2D and 3D projects, a whole seismic reflection study consists of data acquisition,

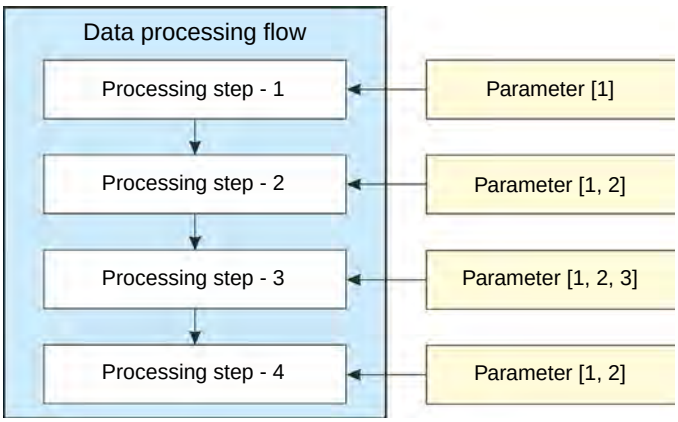


FIG. 1.1 Schematical illustration of a typical processing flow and the parameters of the processing steps.

processing, and interpretation stages (Fig. 1.2). Data acquisition parameters generally strongly affect the structure of the processing flows as well as the parameters of each processing step in the flow. For instance, depths of the seismic streamer or gun array play the most important role in the frequency content of marine seismic data. If a wider frequency band with relatively higher frequency content is required, then the streamer and/or gun array must be towed at shallower depths. This situation also controls the band-pass filter cut-off frequency values during the processing steps later on.

Yılmaz (2001) defines the primary steps of the processing as (i) deconvolution, (ii) stacking, and (iii) migration (Fig. 1.2). Other processing steps can substantially be considered as contributory methods used to prepare suitable inputs for these three major processing steps, to increase their efficiency. For instance, almost all of the preprocessing steps are used to prepare a noise-free input to deconvolution; velocity analysis is needed to obtain velocities as input to normal moveout (NMO) correction and then stacking, as well as subsequent migration steps, etc.

On the other hand, even these primary processes strongly need some important prerequisites. For instance, deconvolution requires a normal incidence stationary minimum phase wavelet, as well as a noise-free reflectivity series. While an accurate stacking in 2D seismic data needs perfect hyperbolic reflection curves on common depth point (CDP) gathers, 2D poststack time migration algorithms need zero-offset sections consisting of only primary reflections generated by wave fields in-plane to the seismic survey. Today, stacking itself is the most effective noise-suppression method that significantly removes both random and coherent noise, such as multiple reflections. This process, however, produces a stack section, but the oil and gas industry also needs noise-free prestack seismic data in order to analyze amplitude versus offset (AVO) anomalies, which may indicate possible hydrocarbon reservoirs. Likewise, seismic data as clean as possible is also required for some other prestack

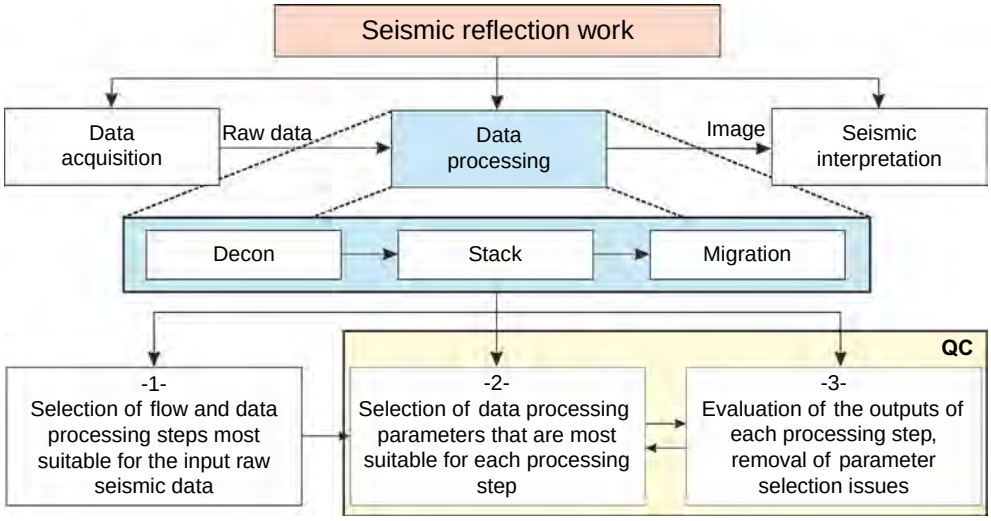


FIG. 1.2 Basic stages of a conventional seismic reflection project, consisting of data acquisition, processing and interpretation, and primary steps of data processing along with the quality control (QC) recurrence in processing.

processing steps, such as velocity analysis or prestack migration.

During the processing, some of the processing steps and their orders of application may differ from one dataset to another, depending on the selection of the processor. For instance, while a strong tail buoy noise in a marine seismic survey may require an application of a suitable frequency-wavenumber (*f-k*) filter, this may not be necessary for another line. While some data processors apply deconvolution to the shot gathers, the others prefer an application to CDPs.

A strict quality control (QC) system must be applied to the outputs of each processing step to ensure that the specific processing application produced acceptable results. These QC analyses are schematically illustrated in Fig. 1.2:

- At first, processor should determine the most appropriate data processing flow for the input dataset, which consists of proper processing steps.
- Then, the suitable parameters for each processing step is determined, such as cut-off frequency values for band-pass filtering, deconvolution operator length, etc. These processing steps with initially determined parameters are then applied to the input data one at a time.
- After each application, the quality and acceptability of the outputs are analyzed in different domains and with different tools. For instance, output of a band-pass filter can be analyzed by checking the power spectrum of the band-pass filter output, while the success of a spiking deconvolution can be assured by controlling the auto-correlograms of the deconvolution output. Whenever a processing step produces an unacceptable result, its parameters are updated and the step is re-applied to the data with new parameters to adjust the mistakes arising from inappropriate parameter selections. This recurrence can be done on shots, CDPs, brute stack sections or a near trace section, and is known as quality control in data processing (QC).

An almost conventional seismic data-processing flow used to process marine seismic data is shown in Fig. 1.3. However, since the data-processing flows are dependent on the data and the data processor, any particular noise in the seismic data may require additional processing steps and/or application of the steps in a different order. The data is processed as gathers or ensembles, termed prestack data until it is stacked. Following the stacking process, the data is called poststack data.

Because the data-processing flow, steps and the parameters are determined by the processing specialists, and hence are operator-dependent, the final product of the same raw input dataset processed by different operators may have a different appearance. The output images may have discrepancies by means of their frequency content, S/N ratio, resolution and trace-by-trace consistency. The factors affecting the quality of the output of the seismic data-processing sequence are

- S/N ratio of the input dataset
- environment of the data collected (e.g., land data almost always has a lower resolution than marine data)
- algorithm and software used
- data-processing flow
- experience of the processor (especially in determining the parameters and QC implications)

The data processor should apply a series of parameter tests to the input data for each step to determine the suitable parameters, and the results are carefully analyzed after each test attempt. However, only a specific part of the seismic data is generally extracted for parameter testing, since using the whole seismic line for a parameter test is time consuming and is not practical. For instance, to determine the cut-off frequencies for a band-pass filter, tests can be

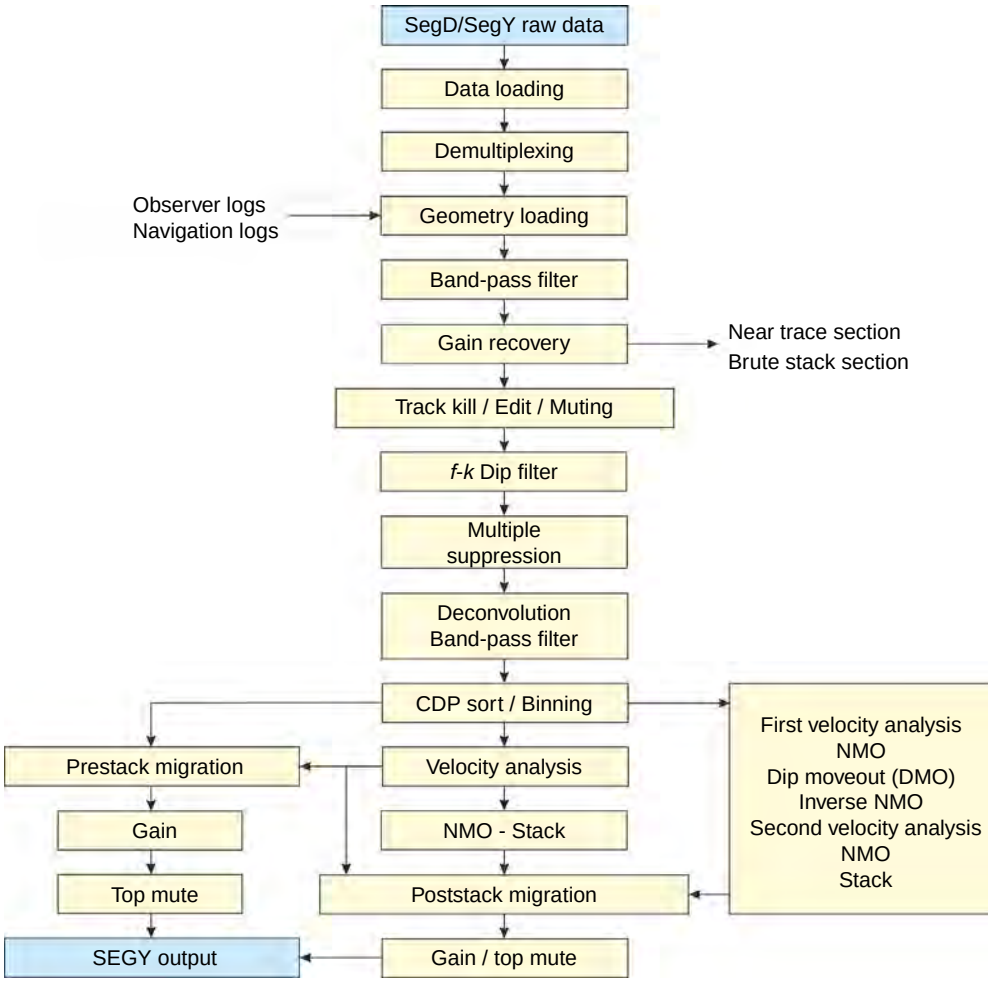


FIG. 1.3 A conventional seismic data-processing flow for marine seismic data.

performed on the very first shots of the line instead of applying the filter to the whole seismic line. After determination of all parameters for each step, the flow is run for the whole line using approved parameters, which is known as production processing.

Each of these steps is of a specific run time controlled by data volume, processing hardware, and the algorithm implemented. As an example, necessary rendering times in seconds for different steps for the same 2D seismic dataset are shown in Fig. 1.4. Here, the dataset used has 500 shots with 480 recording channels, resulting in a total of 240,000 traces and 120-fold seismic data. Sampling rate and maximum recording time are 1 ms and 6 s, respectively. Apart from the hardware specifications used to prepare this illustration, the relative time span for each processing step is remarkable. In general, the processes performed on prestack data require much more run time than those applied to poststack data, because the data volume is significantly reduced after

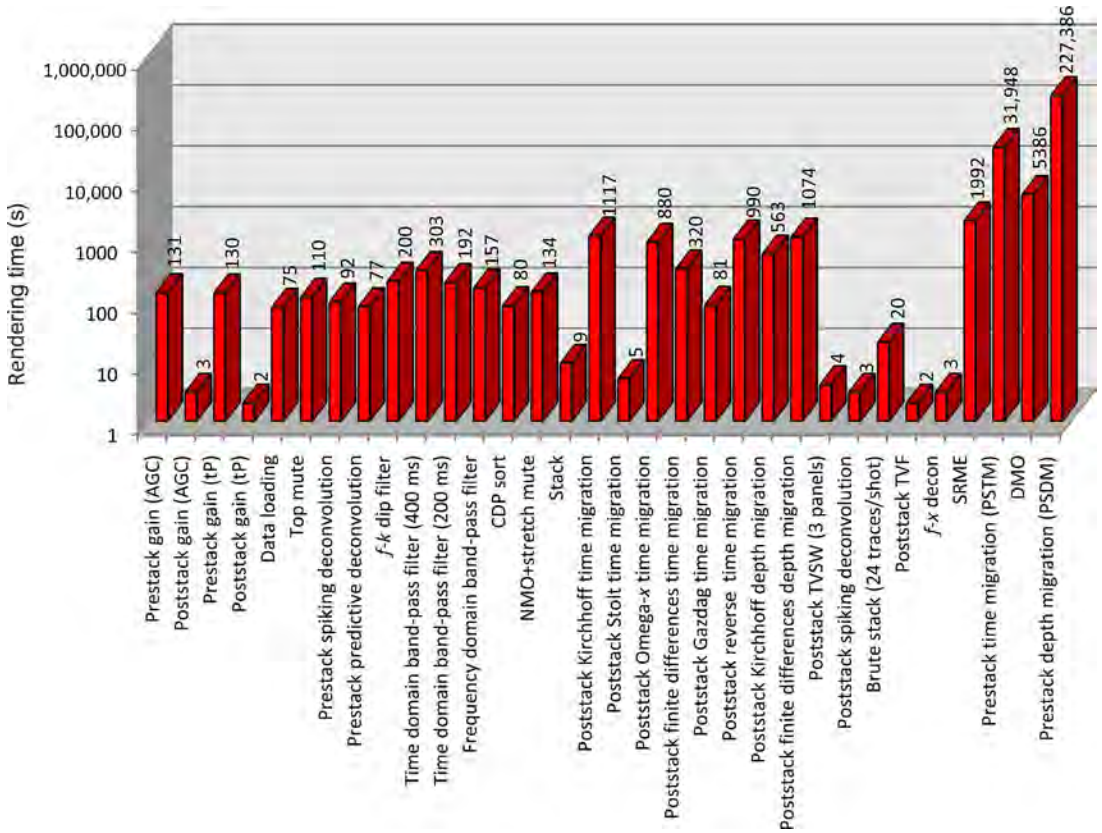


FIG. 1.4 Run times in seconds for different processing steps for the same 2D dataset. Note that the vertical axis is set to logarithmic so that the small rendering times of some particular steps also become evident. *AGC*, automatic gain control; *NMO*, normal moveout correction; *TVSW*, time variant spectral whitening; *TVF*, time variant filter; *SRME*, surface related multiple elimination; *DMO*, dip moveout.

stacking. The most costly processes are the prestack migration algorithms.

Today, several sophisticated commercial software packages exist in the market. In addition to the dedicated private software developers, most of the seismic survey companies also develop their own seismic processing software. The most distinguished software suites commercially available today, especially for the petroleum industry, are:

- Omega (©Western Geco)
- Echos, previously Disco Focus (©Paradigm)
- SeisSpace/Promax (©Landmark)
- Geovation, previously Geovecteur (©CGG Veritas)
- GeoThrust (©GeoTomo LLC)
- Globe Claritas (©GNS Science)
- RadExPro (©DECO Geophysical)
- Vista (©Gedco)
- Seismic Processing Workshop (SPW) (©Parallel Geoscience)

Apart from the commercial software listed here, a couple of freeware processing codes are also available, generally used by academia:

- Stanford Exploration Project, SEPlib (Stanford University)
- Seismic Un*x (SU) (Colorado School of Mines)
- FreeUSP (BP America Inc.)

1.1 UNDERWATER ACOUSTICS

Since we use sound waves to explore the ocean bottom and subsurface sediments, we should know the velocity of the sound waves in seawater and the parameters affecting the velocity and other properties of our acoustic signal. Behavior of the sound waves is the study area of ocean acoustics. In marine seismic exploration, the seismic signal is always produced in seawater, and once it is created, it is no longer under our control. When we apply an impact in the water, it creates pressure waves that successively compress and decompress the water molecules, resulting in the traveling of the sound wave in all directions in three dimensions away from the source through the seawater. Sound in the oceans travels as pressure variations as compressions and decompressions and can be detected by specific pressure sensors, termed hydrophones. In this section, brief definitions of the factors affecting the sound velocity in the water column as well as the fundamental physical characteristics of the seawater are discussed.

Sound waves within the frequency band of the seismic signal can travel large distances due to the relatively low signal attenuation characteristics of the oceans. This makes the sound waves excellent tools for acoustic exploration of the sea. The sound velocity in the water column (approximately 1500 m/s) is determined by the physical properties of the ocean water, such as salinity, temperature, and density (hence the pressure). Table 1.1 shows the influences of these parameters on the sound velocity. Salinity in a specific region generally does not change significantly, except in the areas of river mouths, seabed freshwater discharge areas, and glacial melting zones. In practice, the most important agent that affects the sound velocity in the oceans is the temperature. Although the temperature at the ocean floor is very stable, rapid temperature changes in both vertical and horizontal directions can occur in the surficial waters due to climatic conditions.

TABLE 1.1 Effects of the Seawater Physical Parameters on the Sound Velocity

Parameter	Effect on the Sound Velocity
Temperature (T)	2.7 (m/s)/°C
Salinity (S)	1.2 (m/s)/ppt
Pressure or depth (P)	0.017 (m/s)/m

There are specific types of layers within the water column, termed clines, which have different physical properties from the surrounding water. The physical properties of seawater, such as density, temperature and salinity, may change with depth at a particular location, creating well-established specific zones just below the surficial water layer within the water column. These zones are known as pycnocline, thermocline, and halocline, respectively (Fig. 1.5).

Warm water is less dense than cold water, and therefore it remains along the sea surface and gets warmer and warmer because of solar heating. This situation results in the formation of a relatively warmer surficial water zone, termed the surficial water layer or mixed layer. The thermocline is a transition zone from the mixed layer at the surface to the deep water layer (Fig. 1.5A). In the thermocline zone, the temperature rapidly decreases from the surficial layer temperature to a relatively colder deep water temperature. The depth and thickness of the thermocline zone are affected by climatic variations, latitude and local tide and current conditions. The halocline is a layer within the seawater column, where salinity changes

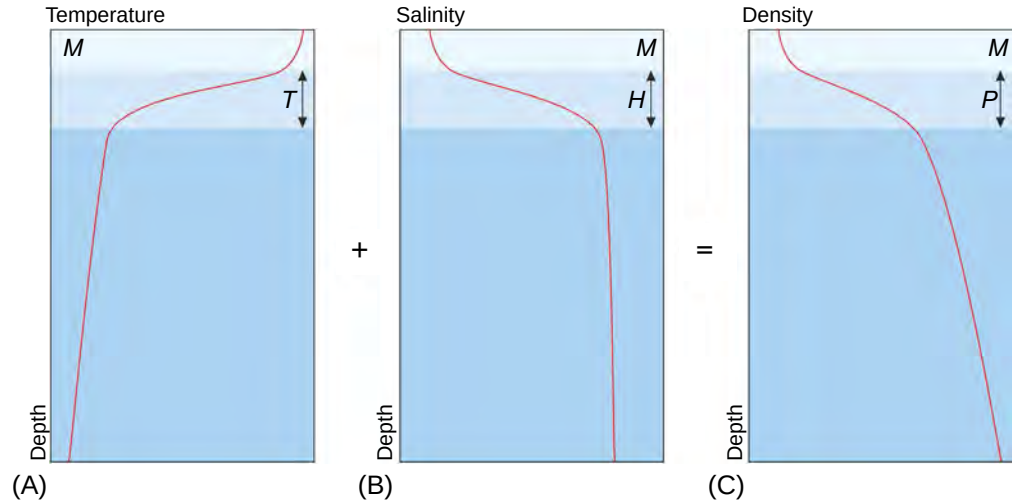


FIG. 1.5 Physical zones, or clines, within the water column. (A) Thermocline (*T*), (B) halocline (*H*), and (C) pycnocline (*P*) layers. *M* represents the surficial, or mixed, water layer.

rapidly with depth (Fig. 1.5B). It is located below the uniformly saline surface water layer and is characterized by a strong, vertical salinity gradient. Below the halocline, salinity remains high. Below the mixed layer, there is a horizontal layer within the water column where the density gradient is greatest due to the rapid change in temperature or salinity (Fig. 1.5C). This layer is the pycnocline, where a large density contrast is therefore observed between the surficial water layer and deep oceanic waters, which prevents the formation of vertical currents. Except for the arctic zones, where no pycnocline layer exists, this layer is quite stable and separates the surficial layer from deep ocean waters where variations in salinity and temperature are very small.

Clines in the seawater extend almost horizontally for large distances. The vertical stratification at a specific location due to the temperature and salinity variations as a function of depth creates "channeling" for sound waves in the water column. This channel is located at a depth where the effects of temperature and pressure create a layer of minimum sound velocity in the water column. It is termed the Sound Fixing and Ranging (SOFAR) channel, where the sound waves in the seawater are trapped and travel for long distances without losing their energy significantly. The depth where the minimum sound velocity occurs is the axis of the channel. Velocity increases above and below the axis because of the temperature and pressure increases, respectively. Although the location of the SOFAR channel axis varies with the temperature and water depth, it commonly lies between 600 and 1200 m below the sea surface in open oceans.

Sound velocity information in marine acoustic applications is vital, especially in some specific marine geophysical applications. For instance, we definitely need sound velocity in seawater in sufficient detail for multibeam bathymetric surveys to convert the arrival times of the signals reflected back from the seafloor into the water depths. In 3D seismic surveys, the distances between the streamers are maintained by acoustic communications among the

sensors using the specific instruments in the seawater regularly positioned along the spread. Therefore, the sound velocity in the water column must be continuously measured in real time during 3D surveys, since it may change with time and location in the survey area.

Variation of the sound velocity in seawater can be obtained using velocimeters, which directly measure the velocity, or the specific sensors termed CTDs (conductivity-transmission-depth), which measure the physical parameters used to calculate the sound velocity. In addition, an expendable bathythermograph (XBT) probe can be used to measure the temperature of the upper kilometer of the ocean, and the data is then used to calculate the sound velocity profile. CTD measurements used to determine the conductivity and temperature as a function of depth of the ocean are more common in obtaining the velocity. There are several empirical approximations to obtain the sound velocity from measured physical parameters. A more recent international standard algorithm has been developed by Chen and Millero (1977) and later modified by Wong and Zhu (1995). It is also known as the UNESCO algorithm today and is expressed as

$$V(S,T,P) = A + B \times S + C \times S^{3/2} + D \times S^2 \quad (1.1)$$

where velocity (V) is in meters per second, temperature (T) is between 0 and 40°C, salinity (S) is between 0 and 40 ppt, and pressure (P) is between 0 and 1000 bars, and the coefficients A, B, C, and D are given by

$$\begin{aligned} A = {} & (1402.388 + 5.03830T - 5.81090\text{E-}2T^2 \\ & + 3.3432\text{E-}4T^3 - 1.47797\text{E-}6T^4 + 3.1419\text{E-}9T^5) \\ & + (0.153563 + 6.8999\text{E-}4T - 8.1829\text{E-}6T^2 \\ & + 1.3632\text{E-}7T^3 - 6.1260\text{E-}10T^4)P \\ & + (3.1260\text{E-}5 - 1.7111\text{E-}6T + 2.5986\text{E-}8T^2 \\ & - 2.5353\text{E-}10T^3 + 1.0415\text{E-}12T^4)P^2 \\ & + (-9.7729\text{E-}9 + 3.8513\text{E-}10T \\ & - 2.3654\text{E-}12T^2)P^3 \end{aligned}$$

$$\begin{aligned} B = {} & (1.389 - 1.262\text{E-}2T + 7.166\text{E-}5T^2 \\ & + 2.008\text{E-}6T^3 - 3.21\text{E-}8T^4) \\ & + (9.4742\text{E-}5 - 1.2583\text{E-}5T - 6.4928\text{E-}8T^2 \\ & + 1.0515\text{E-}8T^3 - 2.0142\text{E-}10T^4)P \\ & + (-3.9064\text{E-}7 + 9.1061\text{E-}9T \\ & - 1.6009\text{E-}10T^2 + 7.994\text{E-}12T^3)P^2 \\ & + (1.100\text{E-}10 + 6.651\text{E-}12T \\ & - 3.391\text{E-}13T^2)P^3 \end{aligned}$$

$$\begin{aligned} C = {} & -1.922\text{E-}2 - 4.42\text{E-}5T \\ & + (7.3637\text{E-}5 + 1.7950\text{E-}7T)P \end{aligned}$$

$$D = 1.727\text{E-}3 - 7.9836\text{E-}6P$$

Fig. 1.6 shows a CTD cast from deep waters of the Black Sea. The thermocline (T) is between 15 and 80 m depth, where the seawater temperature decreases significantly. There is an approximately 130-m thick halocline (H) layer below the surficial mixed water layer (M). Until the bottom of the thermocline, the sound velocity is predominantly controlled by the temperature variations in the water column. At greater depths, however, the effect of pressure on the sound velocity value becomes increasingly dominant, resulting in a linear velocity increase since the pressure increases almost linearly with depth. As a result, velocity is relatively high both in surficial and deep waters because of the higher temperature in surficial waters and linearly increasing pressure in deeper waters, respectively.

1.2 MARINE ACOUSTIC METHODS

Marine geophysics studies are performed to understand the structure and morphology of the seafloor and subsurface sediments and monitor their short- and long-term behaviors, to safely settle the offshore geo-engineering structures such as pipelines and platforms, and to explore the offshore mineral and energy sources. The methodology and equipment used

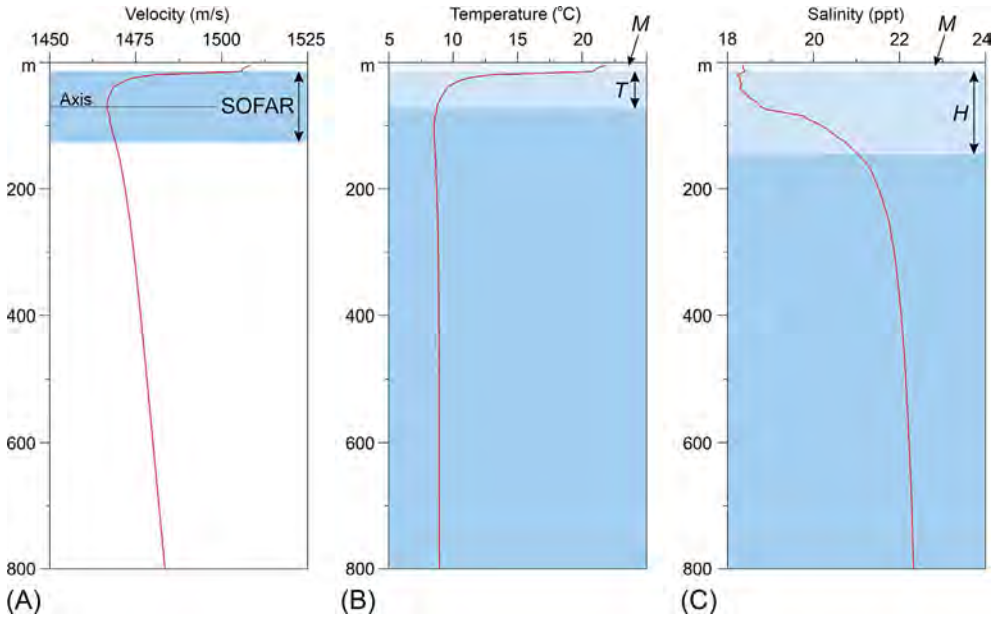


FIG. 1.6 Physical properties of seawater and sound velocity obtained from a CTD profile. (A) Calculated sound velocity, (B) temperature, and (C) salinity as a function of depth. *M*, *T*, and *H* represent mixed water, halocline and thermocline layers, respectively.

in marine acoustic exploration are different from those used in onshore surveys. Discrepancies arise from the purposes of the surveys, the penetration depths and resolution differences, the working principles of the equipment, and the information obtained.

Marine geophysical surveys have been conducted since the 1960s utilizing several different acoustic and nonacoustic methods. Among these, gravity and magnetic surveys, seismic methods, heat flow measurements, and other high-resolution acoustic methods such as bathymetric, side-scan sonar and subbottom profiler surveys are the most common techniques. In this section, the marine geophysical methods employing acoustic signals in different frequency, amplitude and signal forms are discussed briefly. Excluding the conventional marine seismics, these methods are generally known as high-resolution marine geophysical techniques, and are commonly used to solve geo-engineering problems or to map geo-hazards encountered during shallow marine installations.

Before drilling an offshore well, there is a need to define the surficial morphology as well as the subsurface sediments in the area surrounding the well location in detail. This operation is often termed a site survey. Since the resolution of conventional 2D and 3D seismic data is not sufficient to provide detailed subsurface information on the shallow stratigraphy, high-resolution techniques employing much higher frequency signals are used to map the geo-hazards, such as slides, excessive seafloor inclinations, shallow gas and gas hydrates, active faulting, etc. Although single channel or multichannel short spread sparker seismic reflection surveys are also used for the shallow geo-engineering problems, 2D and 3D conventional multichannel seismic surveys are mostly used for hydrocarbon exploration by dedicated survey companies, as well as by academia for

scientific purposes worldwide, and are not included in the site surveys.

The marine geophysical methods for high-resolution site surveys use different sensors to produce acoustic signals within a significantly wide frequency spectrum. Table 1.2 shows general information on the frequency band of the most common marine acoustic systems. The most suitable method with an appropriate frequency is selected by factors such as required information, resolution and penetration purposes. Relatively low-frequency signals used in seismic surveys are produced by air guns (generally between 10 and 200 Hz) or spark arrays (between 50 and 800 Hz), while higher-frequency acoustic signals from approximately 3 to 800 kHz are produced in the water column by specific instruments called transducers. These instruments convert one type of energy (e.g., the electric signal) into another (e.g., the acoustic signal), or vice versa. Transducers use piezoelectric crystals made by ceramic material, which vibrate when they are excited by an electric pulse. These vibrations are transmitted into the water column as pressure (P) waves to generate the acoustic signal. The same transducer is also used to receive the reflected signals, and

TABLE 1.2 Frequency Ranges of Major Marine Geophysical Survey Systems

Acoustic System\Frequency (kHz)	0.05				0.5				5				50				500			
Side-scan sonar																				
• Short-range sonar																				
• Medium-range sonar																				
• Long-range sonar																				
Multibeam bathymetry																				
• Shallow water																				
• Deep water																				
Subbottom profiler																				
• Pinger																				
• Boomer																				
• Parametric system																				
• Chirp																				
Sparker seismic exploration																				
• 500 J array																				
• 2000 J array																				
• 6000 J array																				
Air gun seismic exploration																				
• 45 in^3 air gun																				
• 200 in^3 air gun																				
• 2000 in^3 air gun array																				

converts them into an electric signal for subsequent processing and plotting.

The most important acquisition parameter for such high-resolution marine geophysical systems is the signal frequency. The resolution power and penetration depth of these different types of acoustic methods strongly depend on the signal frequency they employ. Even though their penetration depths are limited, the systems that use higher frequency signals generally provide higher resolution data for the same seafloor morphology and subsurface sediments than that of low-frequency systems.

1.2.1 Bathymetric Systems

Acoustic systems used to measure the depth of the oceans (bathymetry) are known as echosounder systems. Measurement of bathymetry is one of the fundamental offshore observations and is required during installations of offshore platforms (even temporary ones) and submarine pipelines, as well as for offshore excavation studies. Water depth can also be used in seismic data processing by some specific multiple suppression techniques to eliminate the multiple reflections. Echosounders can be classified as single-beam and multibeam systems depending on the number of acoustic beams they utilize. Table 1.3 shows the general specifications of both systems.

Single-beam echosounders emit only one vertical beam toward the seafloor and use the arrival time of the beam to calculate the water depth profile just beneath the keel along the vessel route. Fig. 1.7A schematically illustrates the beam used in single-beam echosounders. A conventional single-beam echosounder records the travel time of a beam originated from a hull-mounted transducer, and generally a single averaged water column velocity is used to convert arrival time of the beam into the water depth. The same transducer used to generate the acoustic signal is also used to receive the returned echo. In analog recorders, calculated water depth is plotted on a thermal printer after amplification, or digitally recorded into the disks in digital systems.

Multibeam echosounders are state-of-the-art bathymetric systems that utilize more than one beam to map not only the depth below the keel, but also the bathymetry along both sides of the vessel. They use several beams for a single swath emitted at different angles from the transducers, termed a ping. Fig. 1.7B schematically illustrates the beams used in multibeam echosounders and the example data obtained. Modern multibeam echosounders employ more than 500 beams per ping, which constitute a fan-shaped sweep area extending to both sides of the vessel. Fig. 1.8A schematically shows the beams, pings and the

TABLE 1.3 Specifications of Single- and Multibeam Echosounder Systems Used to Obtain Bathymetry of the Seafloor

System	Frequency (kHz)	Penetration Depth (m)	Applications
Single-beam echosounder	10–40	None	• Water depth below the keel • Gas bubbles on 1D profile • 2D bathymetry
Multibeam echosounder	10–500	None	• Water depth from a swath area • Gas bubbles on 2D surface • 3D bathymetry • Reflectivity of the seafloor • Geological mapping • Underwater archaeology • Pipeline inspection

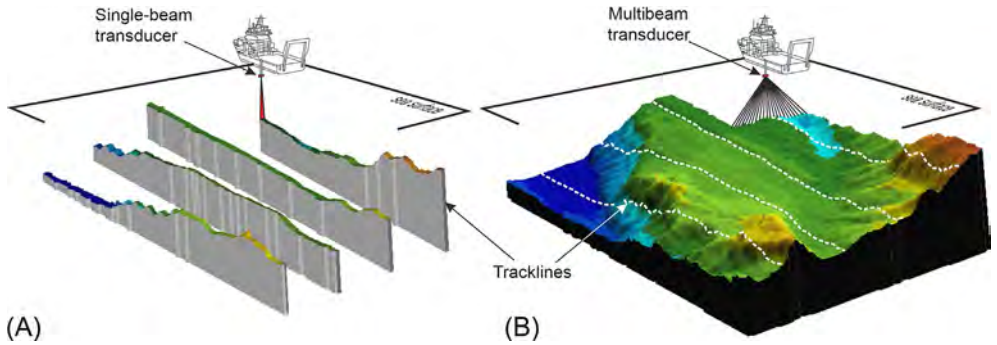


FIG. 1.7 Schematic display of the applications of (A) single-beam and (B) multibeam echosounders and the data obtained.

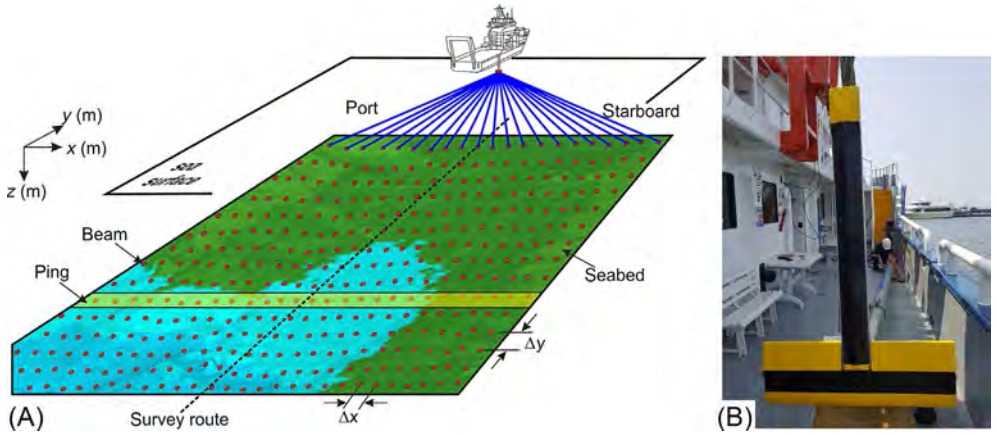


FIG. 1.8 (A) Schematical illustration of beams *(blue lines)*, pings *(the group of beams in the yellow rectangle)* and the points where the bathymetry of the seafloor is obtained *(red dots)* during the multibeam survey. (B) Transducer of SeaBat 7160 multibeam echosounder.

sampled seafloor from a multibeam echosounder. Pings consist of a certain number of beams, each of which carries depth information from a particular point on the seafloor. The emission angle of the beams is quite critical and should be corrected for the movements of the vessel (and hence the transducer). Therefore, 3D movements of the vessel obtained from motion sensors in real time are considered in the beam-forming process for each beam at each ping. Some systems use separate transducers for transmitting and receiving the beams (Fig. 1.8B).

Vertical (depth) resolution of the multibeam echosounders is very high, on the order of a few centimeters. Horizontal resolution is defined in along-track (parallel to the survey line) and across-track (perpendicular to the survey line) directions. In modern equidistal multibeam echosounders, the distance between the beams at the seafloor is kept constant, resulting in a very high-resolution image of the seafloor sampled at quite regular intervals in 2D. Fig. 1.9 compares bathymetric maps obtained by an interpolated single-beam and a multibeam

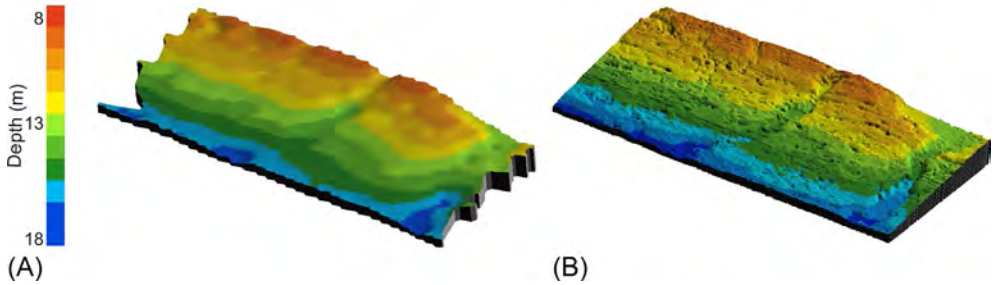


FIG. 1.9 An example bathymetric map obtained by (A) single-beam and (B) multibeam echosounder. Single-beam data is interpolated to obtain a complete map of the seafloor.

echosounder. Both vertical and horizontal resolutions are superior in multibeam bathymetric maps.

In addition to the depth information, multibeam systems can also provide a morphological display of the seafloor sediments, a similar display to that obtained by a side-scan sonar survey (Section 1.2.2), known as a reflectivity map. The basic concept of the reflectivity is to measure and record the amplitude of the reflected beam in addition to the arrival time in order to discriminate seafloor sediment types of different reflectivity characteristics. Reflectivity maps can therefore be used to distinguish variations in the seafloor sediment types and provide seabed sediment classification of large areas by mapping the low- and high-reflectivity zones.

Contemporary multibeam echosounders record not only the amplitudes of the beams reflected back from the seafloor, but also the amplitudes possibly reflected from the targets within the water column. Such water column sampling attributes provide spectacular views of the active gas seeps from the sediments into the seawater. Mapping and monitoring such hot spots provide crucial information for the oil and gas industry about the hydrocarbon potential of the survey area.

1.2.2 Side-Scan Sonar

Side-scan sonar is the system that provides high-resolution seafloor morphology from both sides of the vessel track. The sonar data, often called sonographs, are acquired using a transducer pair mounted on a deep-towed tow-fish, one for the port side and the other for the starboard side. Table 1.4 shows the general specifications of side-scan sonar systems. A sonar record is used for various purposes, mainly to identify the morphological changes (such as large- or small-scale slides) and natural or

TABLE 1.4 Specifications of Side-Scan Sonar Systems Used to Obtain Morphology of the Seafloor

System	Frequency (kHz)	Penetration Depth (m)	Applications
Side-scan sonar	10–1000	None	• Seafloor morphology • Gas bubbles in 2D • Reflectivity of the seafloor • Geological mapping • Underwater archaeology • Targets within the water column • Pipeline inspection

man-made targets (like gas seeps or pipelines) on the seabed.

Fig. 1.10 schematically illustrates the principle of side-scan sonar data acquisition. Both transducers utilize one single beam, which is very narrow in the horizontal plane (approximately 1 degree), and wide in the vertical plane (approximately 40 degrees). Side-scan sonar provides very high-resolution morphologic data from the seafloor. Since it utilizes a high-frequency acoustic signal, it is compulsory to deploy the transducers on a deep-towed tow-fish independent from the 3D movements of the survey vessel, which considerably increases the data quality. Towing of the transducers at a certain altitude from the seafloor also ensures that the signal is less affected by the heterogeneities within the water column. The altitude of the tow-fish from the seafloor is kept constant by the operation of a side-scan sonar winch used to adjust the length of the tow-cable in real time during the acquisition. The total length of the cable paid out depends on the water depth and survey speed. The altitude of the tow-fish is kept between 10% and 20% of the total sonar range, and the cable pay-out is adjusted accordingly during the survey as the water depth changes along the route.

Both port and starboard transducers emit a narrow beam to each side at time zero and then the system starts to record all the amplitudes that arrive at both transducers immediately after

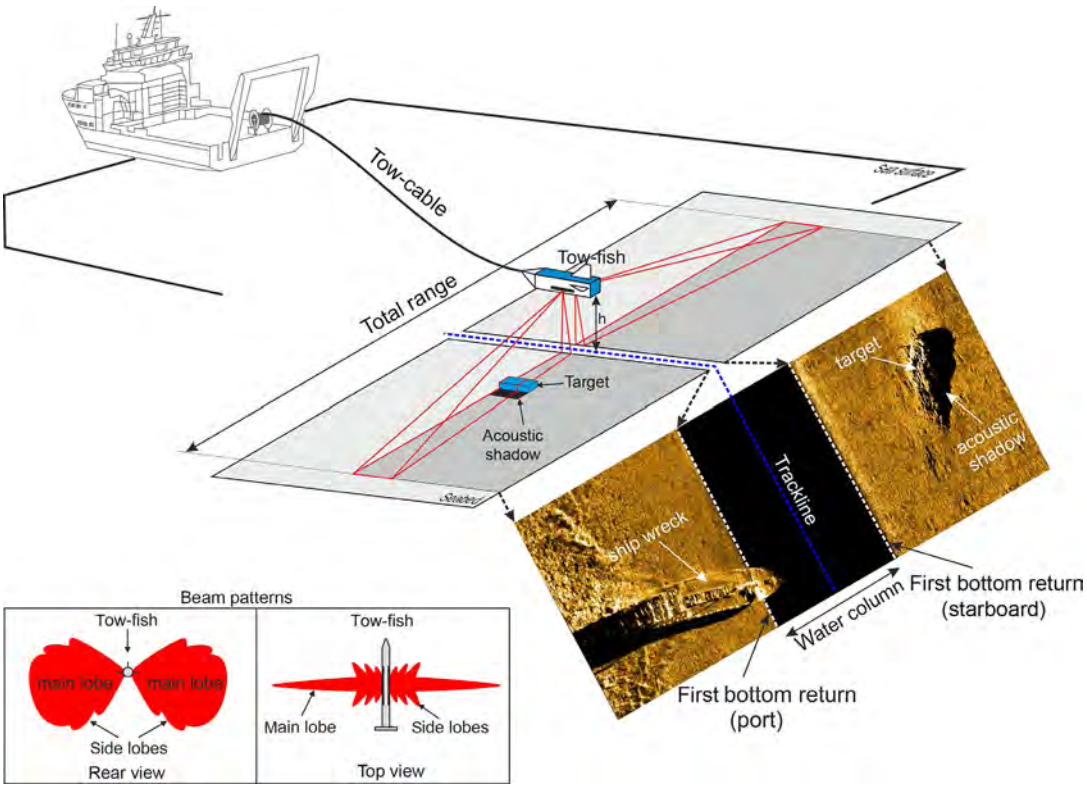


FIG. 1.10 Schematical illustration of the side-scan sonar data acquisition and conceptual beam patterns of a sonar transducer; *h* is tow-fish altitude. *Sonar data example (sonograph) is from Özdaş, H., Kızıldağ, N., Baydan, C., 2016. Shipwreck Inventory Project of Turkey (SHIPT), Special Project Supported by Ministry of Development of Turkey.*

transmission. Each emitted beam is also perceived by the transducers during the recording, and forms an extremely high-amplitude input at the zero time, called the output signal. Then the beams start to travel at both sides of the tow-fish away from the transducers. The first meaningful return is generally from the seafloor close to the tow-fish. Since the travel of the signal to and from the seafloor will take some time, depending on the tow-fish altitude, and since almost no signal amplitude is transmitted in a vertical direction due to the directional pattern of the emitted signal, there will be a blank zone between the output signal and the seabed return, which corresponds to the time span for the sonar signal to travel through the water column to the seafloor and back to the tow-fish. This blank zone is indicated by the water column in Fig. 1.10. Subsequent to this blank (and in most cases, amplitude free) zone, the seafloor return will arrive at the transducers. After that, returns from progressively distal ranges of the seafloor are successively received by the transducers. Returned amplitudes are recorded into the disk files starting from time zero to the end of the recording for both sides, after converting their arrival time to one-way distance from the tow-fish. Fig. 1.11 shows a sonar tow-fish and a shallow water sonograph with small-scale boulders on a sandy seafloor.

The beginning time of the recording, the time zero, is the time that the transducers emit the beams at both sides of the tow-fish. The maximum recording distance is termed the sonar range. The distances are normally measured along a slanted range from the transducers and do not correspond to horizontal distances, but can be converted into horizontal distances after a specific correction, termed the slant-range correction.

The returned signal to the sonar tow-fish is termed backscatter, not the reflection, and is composed of backscattered energy because of the roughness of the sediment particles on the seafloor. This roughness acts as a diffractor, which scatters the energy in all directions, including the tow-fish direction. Most of the emitted energy from the transducers is reflected away from the tow-fish direction, since the reflection angle equals to the incidence angle. However, there will always be some amount of backscattered energy, which returns to the tow-fish, is perceived by the transducers, and is recorded by the sonar recording unit. The amplitude of the backscatter is the main information received and recorded by the sonar system, and is used to discriminate different types of seafloor sediments, since the backscatter amplitudes (in addition to the seafloor topography) are directly associated with the particle sizes (roughness) and composition of the seabed sediments. For instance, a common order of sediment roughness from low to high may be clay, silty clay, silt, silty sand, fine sand, and coarse sand. Therefore, each

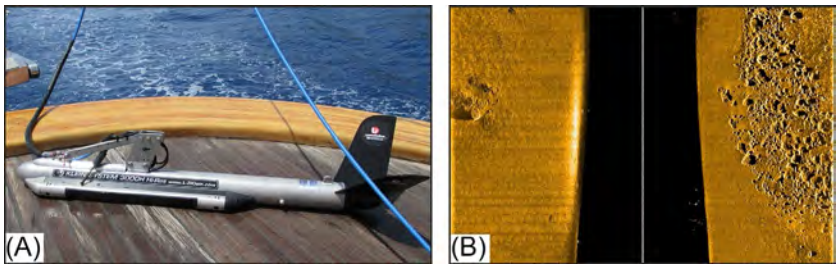


FIG. 1.11 (A) A sonar tow-fish and (B) a shallow water side-scan sonar record showing small-scale boulders on a sandy seafloor. Sonar frequency is 455 kHz and the range is 50 m per side. *Data is from Özdaş, H., Kızıldağ, N., Baydan, C., 2016. Shipwreck Inventory Project of Turkey (SHIPT), Special Project Supported by Ministry of Development of Turkey.*

of these different sediment compositions scatters a different amount of energy back to the tow-fish unit and hence they appear in different gray shades in the sonographs.

Each signal emission is termed a ping. Sonographs consist of several successive pings along the route of the tow-fish, and seafloor reflectivity is demonstrated as the maps of gray shades, which are proportional to the amplitude of the returned signal. Generally 8-bit grayscale mapping is used, which allows the use of 256 different gray tones between black and white. In general, a high-amplitude return (i.e., high backscatter) is shown as black, or vice versa. Modern acquisition and processing software offers the use of different color patterns to display the sonographs for a better analysis of the small-scale targets. The targets with a positive relief on the seafloor prevent the signal from penetrating back of the targets, constituting an amplitude-free shadow zone, which enables us to discriminate targets as well as their heights from the seafloor. In practice, sonar data is collected along several parallel lines with a certain amount of overlap (e.g., 10% of the sonar range). At the end of the survey, these parallel lines are merged to produce one large reflectivity map of the seafloor, termed the sonar mosaic.

As is the case in multibeam echosounders, the horizontal resolution of the side-scan sonar system is defined in along- and across-track directions. Along-track resolution is the minimum distance in which two parallel targets on the seafloor lying along the survey line can be distinguished as two separate objects. Similarly, across-track resolution is defined as the minimum distance in which two parallel targets on the seafloor lying perpendicular to the survey line can be detected as two separate objects. Across-track resolution is a function of beam width, signal frequency and pulse length, while along-track resolution depends on ping rate and survey speed.

We can classify side-scan sonar systems into three categories based on their maximum ranges as short-, medium- and long-range sonars. As a general rule for the sonar systems, maximum range decreases as the operating frequency increases. The long-range systems are towed at shallower depths close to the sea surface, whereas short- and mid-range systems are of higher resolution and must be towed at small altitudes close to the seafloor. General properties of these systems are as follows:

- Short-range side-scan sonar systems employ beams with a relatively high frequency range between 250 and 1000 kHz and are generally used to map an area of approximately maximum 250 m per side. They are generally operated at shallow waters in continental shelves and provide very high-resolution seabed images, generally delineating the small natural structures and man-made small-scale targets.
- Medium-range systems operate at a 50–250 kHz frequency band and generally have a maximum range of approximately 1 km per side. These systems are used to map continental slopes and relatively deep water areas.
- Long-range sonar systems use relatively low-frequency signals (generally around 10 kHz) and provide morphologic data up to 20 km range per side. They are used in reconnaissance surveys to quickly map relatively large areas in considerably lower resolution.

1.2.3 Subbottom Profiler

Subbottom profilers are basically single channel seismic systems operating at 1–10 kHz frequency band (generally 3.5 kHz), which provides a high-resolution stratigraphic display of the uppermost sediments. Depending on the system frequency, the vertical resolution of many subbottom profiler systems is better than 50 cm. Although their penetration depth reaches 200 m below the seabed depending on the

geology and the power of the system used, it is generally limited to 60 m. Table 1.5 shows the general specifications of subbottom profiler systems. A typical system consists of a transmitter/receiver (together termed a transceiver) unit, a transducer array and a recording unit. They are very similar to single-beam echosounders, but their operating frequency is much lower and the output power is much higher than the echosounders.

Transducer arrays of subbottom profilers are either mounted to the hull or over-the-side of the survey vessel, although there are also deep-tow subbottom profilers mounted on a tow-fish. The signal transmitted from transducers penetrates into the shallow subsurface sediments and is reflected back from the interfaces. The reflected signal is received by the same transducers, amplified and digitally recorded into the disks. Some side-scan sonars also have subbottom profiler transducers mounted on the tow-fish to collect subbottom profiler seismic data along the tow-fish tracklines along with the sonar data, known as a combined system. When properly calibrated, a subbottom profiler system is also used to obtain bathymetric profiles along the survey route.

Depending on the signal shape and the equipment used to generate the signal, subbottom profilers can be classified into four categories:

TABLE 1.5 Specifications of Subbottom Profiler Systems Used to Obtain Shallow Stratigraphy of the Uppermost Sediments

System	Frequency (kHz)	Penetration Depth (m)	Applications
Subbottom profiler	1–10	10–60	• Very shallow stratigraphy • Gas bubbles in 1D profile • Gassy sediments • Pipeline inspection

- Single frequency (pinger) systems
- Chirp systems
- Boomer
- Parametric systems

Single frequency subbottom profilers emit single frequency signals as sinuous wave trains into the water column and are known as linear systems. The signal frequency depends on the resonance frequency of the transducer array and is generally 3.5 or 5 kHz. Penetration depths of the single frequency subbottom profilers are relatively low and change from 2 to 30 m. The main advantages of these systems are their ease of use and maintenance, fast ping rates and portability, whereas their shortcomings are their narrow frequency bands, too long pulse lengths consisting of several oscillations resulting in low-resolution data, and their relatively low output power preventing higher subsurface penetration.

Chirp (acronym for Compressed High Intensity Radar Pulse) systems use sweep signals very similar to those used in land VibroSeis systems. They use frequency-modulated (FM) sweep signals generated by the computers using predetermined signal parameters such as the amplitude, frequency band, etc. They operate at frequencies between 1 and 10 kHz (generally 2–7 kHz) and their penetration depth is commonly limited to 60 m. The theoretical vertical resolution of a Chirp signal of 2–7 kHz for 1500 m/s water velocity is approximately 12.5 cm. Since it is a controlled-source signal, its source signature generated by computers is well known. Reflection signals are commonly cross-correlated with the known source signature before recording the data onto the disks to obtain Klauder wavelets of relatively higher resolution and S/N ratio. Therefore, among the other high-resolution seismic equipment, Chirp subbottom profilers are the systems that have the highest possibility of recovering the signal from the noise. Fig. 1.12 shows the transducer array of a 3.5 kHz Chirp system and an example of Chirp data.

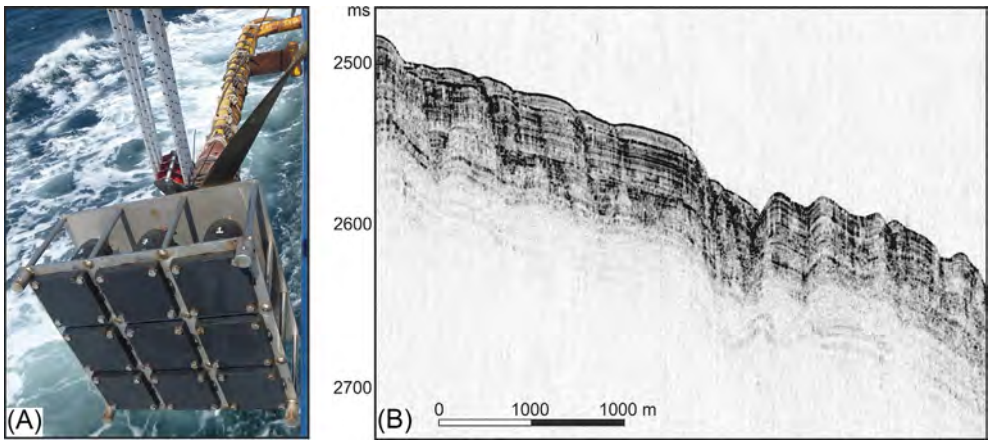


FIG. 1.12 (A) A 3.5 kHz Chirp transducer array ready for an over-the-side mounting; (B) an example Chirp record. The penetration of Chirp data is approximately 50 m.

Boomers generate an acoustic signal between approximately 1 and 6 kHz. They have capacitors to store the energy until shooting, and at each shot point, the stored energy is discharged through a spiral coil, which flexes a copper plate attached to the coil to produce a stable high-frequency seismic signal. Boomer sources are mounted either on a catamaran towed behind the vessel, or on a tow-fish.

Normally, large transducer arrays are required to produce a narrow beam in subbottom profiler frequency bands of 1–10 kHz. To overcome this issue, nonlinear acoustic systems, termed parametric systems, are used. Parametric systems enable us to produce a narrow source signal using relatively small-size transducers. In parametric sounding, two different high-frequency acoustic signals (f_1 and f_2), called primary frequencies, are emitted into the water column simultaneously. Nonlinear interference of these two signals produces a third one with a new frequency band, called a secondary frequency, which equals the difference between primary frequencies ($f_3 = |f_1 - f_2|$). For instance, using a primary frequency pair of 100 and 104 kHz or 100 and 112 kHz, it is possible to obtain 4 and 12 kHz secondary frequency signals, respectively. Since a narrow secondary signal has no side lobes and does not oscillate, its resolution is quite high.

1.2.4 Single Channel and Multichannel Seismics

Conventional single- and multichannel seismic methods utilize much higher amplitude acoustic signals at relatively lower frequency bands. Therefore, they have much more penetration depth than subbottom profilers, although their resolution is relatively lower. Today, the conventional seismic method is the primary tool for offshore hydrocarbon exploration, mapping of shallow and deep stratigraphy, and structural setting (Table 1.6).

If we put a receiver next to the seismic source and start recording at that receiver after each shot, we can obtain true zero-offset seismic data when we move this system along a straight survey line. Acquisition geometry very similar to this configuration is still used in marine exploration and is known as single-channel seismic reflection. As its name indicates, seismic data is collected using a very short streamer consisting of only one single recording channel and a single-channel seismic recorder. Although it is supposed to be zero-offset acquisition, there is

TABLE 1.6 Specifications of Conventional Single- and Multichannel Seismic Systems Used to Obtain Relatively Deep Stratigraphy and Tectonic Setting

System	Frequency (kHz)	Penetration Depth (m)	Applications
Single-channel seismics	0.05–1	10–500	• Shallow stratigraphy • Gassy sediments • Shallow structural setting • Offshore engineering settlements
Multichannel seismics	0.01–0.2	10–10,000	• Deep stratigraphy • Oil and gas exploration • Shallow and deep structural setting

always some offset between the source and streamer because of the safety conditions, since the source energy may damage the streamer. After each shot, the amplitudes of the reflected signals received by the single-channel streamer are transmitted to the recorder. These amplitudes are digitized at the recorder and plotted side by side for each shot to constitute a zero-offset section (Fig. 1.13A). For single-channel acquisition, it is possible to obtain a preliminary display of the subbottom stratigraphy during the recording since plotting of the recorded traces is done in real time.

Different seismic sources with different frequency and amplitude characteristics can be used for single-channel acquisition. Although a single air gun (mostly a GI gun) or a water gun can be deployed, the most common single-channel seismic source is the sparker array, which uses extremely high electric voltage discharge to produce an impulsive source signal in the water column (Section 2.1.3).

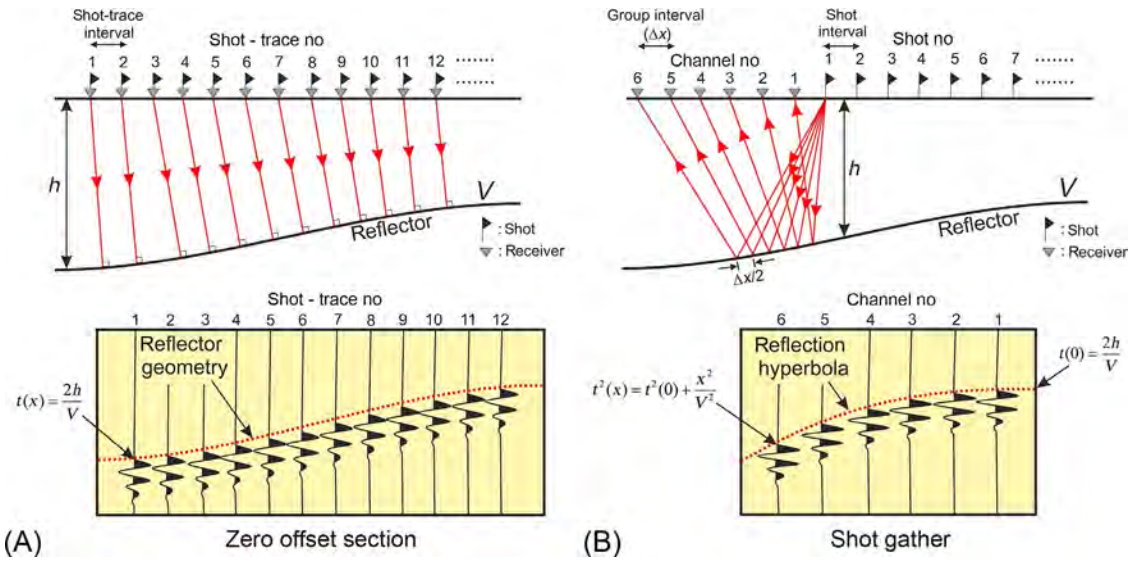


FIG. 1.13 Schematic illustration of (A) single- and (B) multichannel seismic data acquisition. Even though it is possible to obtain subbottom reflector geometry during single-channel acquisition, multichannel seismic data require several additional processing steps to obtain the subsurface geology; $t(x)$ indicates the arrival time of each specific reflection event.

Single-channel acquisition is relatively simple and more economical in terms of equipment deployed and the data acquisition methodology, as compared to multichannel data acquisition. Processing of single-channel data is also less complex. However, it does not allow us to obtain the subsurface velocity distribution in 1D or 2D since we only have the information of arrival times of the reflections shown by $t(x)$ in Fig. 1.13A. Because the arrival time of a specific reflection is a function of reflector depth and the propagation velocity, and because we cannot know the depth of the reflectors originating the recorded reflections, we cannot obtain the seismic velocities of the subsurface sediments by single-channel seismics.

Applications of single-channel acquisition are limited to the engineering surveys before the settlements of offshore geo-engineering structures. Today, modern marine seismic data is acquired with some offset between source and several recording channels located within a single (2D acquisition) or multi (3D acquisition) receiver cables (streamers). The term offset is the distance between source location and each recording channel. In multichannel acquisition, offset distances of each recording channel are different, and in general, it is regularly increasing as we move away from the source location along the streamer. Utilization of multichannel acquisition with different offsets provides several advantages, such as:

- It is possible to obtain subsurface velocity model from multichannel seismic data after velocity analysis.
- Stacking process suppresses most of the random and significant amount of coherent noise.
- Multiples can be suppressed using different approaches using prestack seismic data.
- Amplitude variations with increasing offsets may indicate subsurface hydrocarbon accumulations.

In multichannel seismic acquisition, specific trace groups, called shot gathers, are obtained as raw seismic data, and therefore, it is not possible to obtain subbottom stratigraphy during the acquisition because multichannel seismic data requires various additional data-processing steps to obtain the subsurface structure (Fig. 1.13B).

After NMO correction and stacking (Chapter 10), multichannel seismic data also becomes zero offset since NMO correction removes the offsets between the source and receivers in CDP gathers. The effect of stacking on the data quality is spectacular and the seismic image is of a much higher S/N ratio. As an example, Fig. 1.14 compares two zero-offset sections along the same 2D survey line: One is single-channel seismic data (Fig. 1.14A), and the other is 48-fold stacked multichannel seismic data (Fig. 1.14B). The data quality of the stack section is superior with a better trace-by-trace consistency and higher S/N ratio.

Before the introduction of 3D seismics, the data were collected along straight lines to record 2D data. In 2D acquisition, a number of closely spaced parallel (as well as crossing) lines are necessary to reliably map the survey area. In any case, the gaps between the 2D survey lines are interpolated during mapping. Today, multichannel marine seismic data is collected by several receiver cables (multistreamers) lying parallel to each other to obtain 3D seismic data without any gaps in the survey area. A 2D survey provides subsurface information with data coverage limited to survey line locations, whereas it is possible to explore each specific point independently from the survey line locations in 3D seismic data, which provides a better image of the subsurface that is very close to the real world (Fig. 1.15). Advantages and disadvantages of 2D and 3D conventional seismic surveys are summarized in Table 1.7.

The output of a 2D survey consists of sparsely located seismic lines, whereas the output of a 3D survey is a seismic data volume, which covers both inline and crossline directions of the survey area (Fig. 1.16A). We can extract 2D

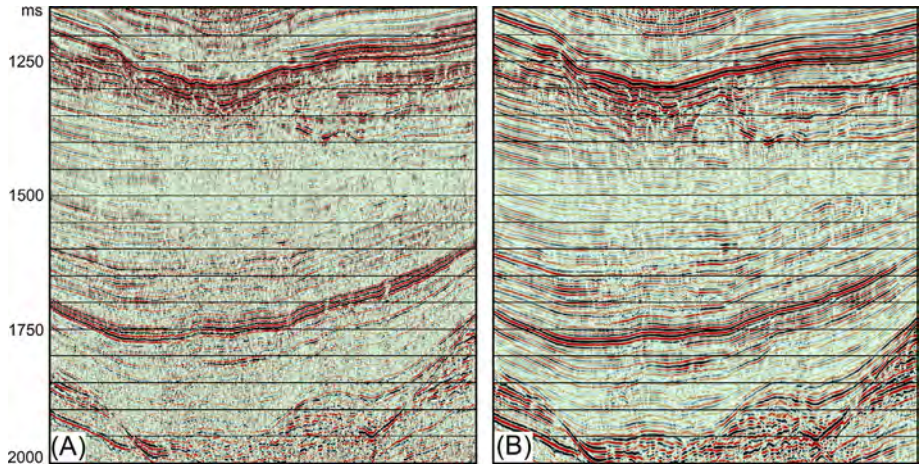


FIG. 1.14 (A) A single-channel seismic section, and (B) a 48-fold stacked multichannel seismic section collected along the same 2D survey line.

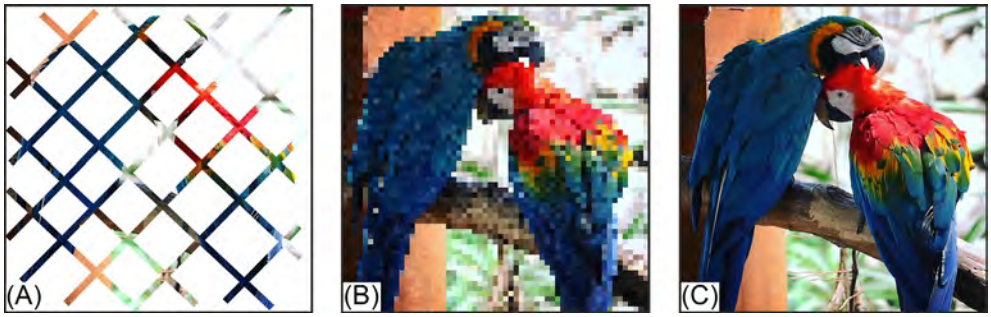


FIG. 1.15 Schematic illustration for the illumination of subsurface using (A) 2D survey, (B) 3D survey, and (C) actual image.

sections from this data volume in any direction (Fig. 1.16B): inline sections (vertical slices parallel to the shooting direction), crossline sections (vertical slices perpendicular to the shooting direction), diagonal sections (vertical slices at any azimuth), random sections (vertical slices of zig-zag lines, typically crosscutting the well locations) and time slices (horizontal maps prepared for constant time values). Horizontal time slices are the essential parts of 3D data volumes, which provide distribution of seismic reflection amplitudes in 2D at any constant recording time. Fault traces, 2D traps, meandering channels, etc., can easily be traced on time slices.

1.2.5 Yesterday/Today/Future of Seismic Exploration at Sea

The seismic reflection method can be considered to be the most important geophysical technique by means of the number of surveying operations, the details and accuracy in the information obtained, and the amount of the

TABLE 1.7 Applications, Advantages and Shortcomings of 2D and 3D Conventional Seismic Surveys

2D seismic	Advantages
	• Equipment and applications are much more economical
	• Data processing is less complicated and relatively faster
	• Acquisition is relatively less complicated
	Shortcomings
	• It provides data only along the 2D survey lines
	• It is used today for academical and reconnaissance purposes only
	• It is not possible to collect data from more than one single azimuth angle
	• 3D effects are considered as significant noise
3D seismic	Advantages
	• It is possible to obtain 3D image of the sub-surface
	• It is used for detailed exploration especially before drilling
	• It is possible to collect data in different azimuth angles
	• 3D effects are the data itself
	Shortcomings
	• Data processing is more complicated and less economical
	• Navigation of the vessel and in-sea equipment is extremely important
	• Equipment and applications are more complicated and expensive

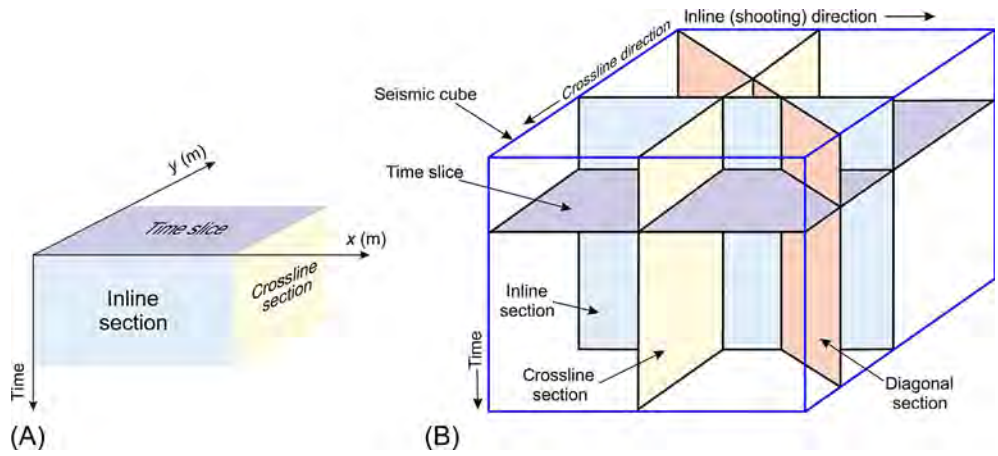


FIG. 1.16 (A) Schematic representation of a 3D data volume, and (B) extracted sections from a 3D volume in any direction.

investment. What makes the seismic reflection the most effective geophysical method is that the final image obtained by the reflection work is of great detail and spectacular resolution as compared to the information obtained from any other geophysical technique. Seismic sections are quite similar to subsurface geological cross-sections in appearance. This is also the most widely used and well-known geophysical method, which is mainly because of the excessive investment, especially that made by the hydrocarbon industry on the development of new acquisition techniques and equipment, as well as modern and sophisticated processing technology. Due to the continuous investment both for acquisition and processing, new developments in the theoretical basis as well as applications of the seismic reflection method proceed uninterruptedly over the years.

The first applications of the method took place in the early 1920s, to discover the possible oil reservoirs around the salt domes in Texas using single-fold or fan-shooting seismic data. Its theoretical development was based on the theory of earthquake seismology, since both methods use elastic waves to understand the earth's interior. The milestones in marine seismic reflection exploration can be summarized as follows:

- 1920. John Evans and Bevan Whitney applied for a patent for the reflection method.
- 1924. Discovery of oil field beneath the Nash salt dome in Texas.
- 1932. First analog filters, initiation of seismic data processing.
- 1937. First seismic survey in Gulf of Mexico.
- 1944. Initiation of widespread marine seismic surveys.
- 1956. CDP acquisition technique.
- 1958. Digital recording and processing.
- 1965. Air gun seismic source.
- 1971. Streamer depth control.
- 1972. Bright spot technology.
- 1976. First 3D seismic acquisition.
- 1976. First multistreamer acquisition.
- 1985. First AVO analysis.
- 1989. 4D time-lapse seismic.
- 1990. DGPS and acoustic ranging, widespread 3D seismic acquisition.
- 1995. First 4C ocean bottom cable (OBC) acquisition in Gulf of Mexico.
- 2000. Seismic acquisition with 14 streamers.
- 2003. Development of converted wave-processing techniques.
- 2005. New technology solid streamers.
- 2007. Dual-sensor towed streamer.
- 2013. Variable depth streamer acquisition.
- 2014. Full azimuth survey.

2D seismic lines may provide valuable information about the basins under exploration if no other information about the subsurface structure and stratigraphy is available. However, mapping relatively complex structures and reconstructing the fault pattern of the basin, even with a dense grid of 2D seismic lines, may have uncertainties in the interpretation stage. Today, 3D seismic is applied in the exploration, development, and production stages to reduce the uncertainties. In addition to the precise determination of well locations over the pay zones, 3D seismic provides monitoring of the fluid movement in the existing reservoirs as the production continues (which is the basics of time-lapse or 4D seismics).

The reduced acquisition time of 3D data makes marine 3D surveys more economical and widespread. Onboard QC applications and reliable instrumentation ensure high-quality 3D seismic data, which has become the industry standard, especially for the hydrocarbon exploration in the last two decades, and no drilling is done without a 3D seismic survey in the petroleum industry today, using at least 4 streamers with a minimum length of 4–6 km. In processing, 3D depth migration has become almost a standard interpretive data-processing method. Today's limits of the

marine seismic reflection exploration can be listed as follows:

- 3D acquisition up to 24 streamers, each 12 km long
- 50 m streamer separation
- Two synchronized seismic source arrays at different depths
- Two synchronized streamers at different depths
- Fan mode acquisition
- Slanted streamer acquisition
- Shooting over the seismic spread (TopSeis)

The petroleum industry will lead in the development of new sophisticated instruments and acquisition as well as data-processing techniques in seismic exploration in forthcoming years. The most important advancements will possibly be in the production and monitoring of existing reservoirs, utilizing time-lapse 4D seismics. Incorporating shear waves with multicomponent acquisition using ocean-bottom cables or permanently positioned nodes will provide a better imaging of structures with different fluid types, such as gas chimneys or reservoir evaluations, to reduce uncertainties. In forthcoming years, marine seismic exploration will possibly involve the following new developments:

- Full azimuth acquisition with permanent nodes
- Increasing number of time-lapse or 4D acquisition
- Widespread multicomponent towed streamer technology for ghost-free data
- Commercial use of converted wave acquisition and processing
- Increasing number of multiazimuth data acquisition
- Longer streamers (12 km), deeper penetration
- Much smaller streamer separation
- Use of synchronized multisources
- New processing methods for 3D, 4D, and 4C data to increase the resolution and better suppress the noise
- Widespread incorporation of anisotropy

1.3 FUNDAMENTALS OF MARINE SEISMICS

1.3.1 Seismic Waves

Seismic waves are often termed elastic waves, which can be described as the energy caused by a sudden breaking of rock within the earth, such as from earthquakes, or explosions, such as from the sources in seismic surveys. They can travel in air and in solid or liquid materials, e.g., through the earth's interior or within the oceans. The particles during the wave energy passage are successively compressed (termed compressions) and pulled apart (termed rarefactions), or they perform a lateral movement (termed shear), depending on the elastic wave type they are affected by.

Seismic waves propagate in an expanding spherical shape in a homogeneous medium after they are generated by an explosive source in seismic surveys, such as the expanding spherical waves formed by a pebble thrown into calm water. This frontal energy is termed the wave front. The direction perpendicular to any point on the wave front is named the ray path. There are two main seismic waves generated by seismic sources as well as earthquakes, termed body waves and surface waves. Body waves are of higher frequency and propagation velocity than surface waves.

There are two types of body waves, termed primary (*P*) waves and secondary (*S*) waves; both can penetrate into the earth through the deeper layers. *P* waves are faster than *S* waves and arrive at the seismometers first, followed by *S* waves, during an earthquake. That is why we call them primary and secondary waves,

respectively. *P* waves express compression (therefore, they are also known as compressional waves), while *S* waves create shear (hence, they are also known as shear waves) through the particles during the wave passage. *P* waves can travel in solids such as rocks and sediments of the subsurface, liquids such as the water column of the oceans, and gasses. Particles affected by *P* waves move in the same direction, parallel to the ray path that the wave propagates on (Fig. 1.17). The velocity of the *P* waves can be expressed by elastic constants of the propagating medium, as

$$V_P = \sqrt{\frac{k + \frac{4}{3}\mu}{\rho}} \tag{1.2}$$

where k is bulk modulus, μ is rigidity or shear modulus, and ρ is density of the medium.

S waves propagate only in solids, and particles affected by *S* waves move in a perpendicular direction to the ray path that the wave propagates along. This may be in two directions: up and down or vertical transverse vibration (which is the vertical shear or *SV* wave), or side-to-side or horizontal transverse vibration (which is the horizontal shear or *SH* wave). The movements of the particles affected by *SV* and *SH* waves are schematically shown in Fig. 1.17. The velocity of the *S* waves can be expressed by elastic constants of the propagating medium as

$$V_S = \sqrt{\frac{\mu}{\rho}} \tag{1.3}$$

where μ is rigidity or shear modulus and ρ is density. Velocity of *S* waves is always slower than *P* waves.

The second type of seismic wave is the surface wave, which propagates at the free surface of a medium such as the earth's surface. They can be divided into two types, called Rayleigh (*R*) waves and Love (*L*) waves, which are distinguished by their different types of particle motions. Particle movement of Love waves is similar to *SH* waves, which show an entirely horizontal polarization, whereas Rayleigh waves exhibit a retrograde elliptical particle motion near the surface, which moves the particle up and down and side-to-side in the same

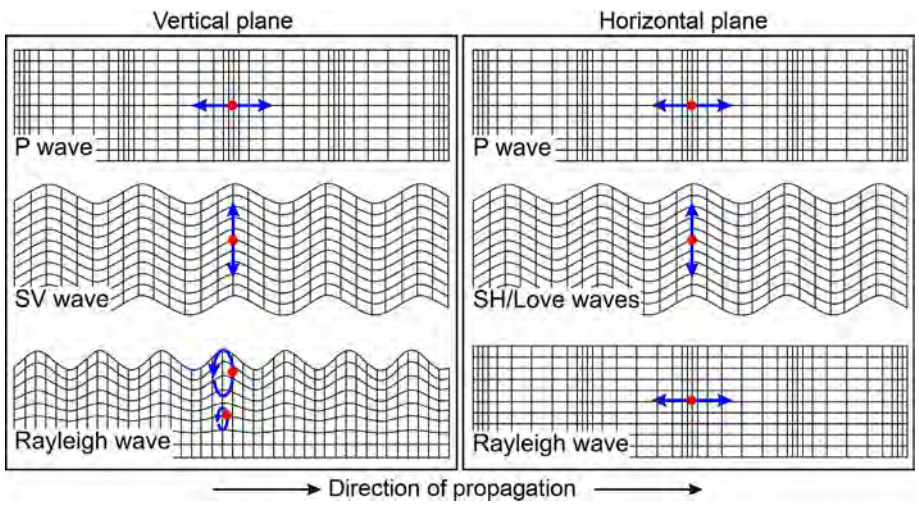


FIG. 1.17 Particle movements affected by *P* waves, *S* waves, Love waves, and Rayleigh wave in vertical and horizontal planes.

direction parallel to the ray path that the wave propagates on (Fig. 1.17), but it changes into prograde motion at some depth (e.g., Sheriff and Geldart, 1995). The Rayleigh waves produce a well-known noise type, termed ground roll in land seismics.

P waves are the major seismic wave type used in seismic exploration both in land and marine seismic acquisition. According to Eq. (1.3), *S* wave velocity depends on rigidity modulus and the density of the propagating medium. Since rigidity is zero in liquids, *S* waves do not propagate in water, and therefore explorations by *S* waves are not common in marine seismics. However, it is possible to record *S* waves using ocean bottom cables (OBCs), ocean bottom seismometers (OBSs), or seabed nodes in marine surveys, which can provide four-component (4C) seismic data (Section 2.4.1). Although still not common, *S* wave surveys in marine exploration can also be done by using converted wave surveys, in which *S* waves converted from *P* waves at the reflecting interfaces by phase conversion are recorded and specifically processed to obtain converted *S* wave seismic sections, which are then interpreted along with the regular *P* wave sections. Because the surface waves are considered to be a combination of *P* and *S* waves, they are not observed in marine seismic data since *S* waves in marine seismic surveys are nonexistent.

1.3.2 Reflection From an Interface

When the compressional wave strikes an interface separating two media with different propagation velocities and densities, some certain part of the incident energy is reflected from the boundary back into the upper medium, while the remaining part is transmitted into the underlying media (Fig. 1.18A). A reflecting interface in seismic methods is determined by the differences in velocity and density values of both layers it separates. Seismic waves are reflected from the interfaces that separate two media of different acoustic impedances defined by

$$Z = \rho V \tag{1.4}$$

where Z is the acoustic impedance, ρ is density, and V is velocity of the medium.

If the incidence angle is not 90 degrees, which is the case for nonnormal incidence, reflected and transmitted *SV* waves are also generated from incident *P* waves, which is known as phase conversion. In case of nonnormal incidence, the

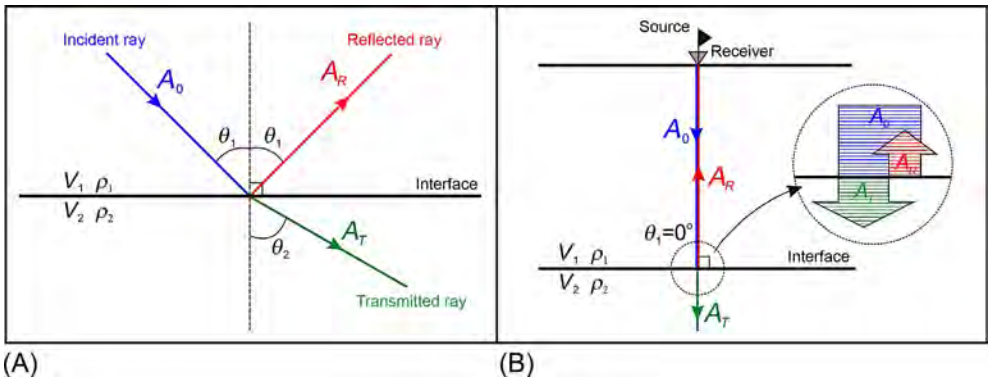


FIG. 1.18 (A) Energy partitioning at an interface for a nonnormal angle of incidence (θ_1) case. A_0, A_R, and A_T are the amplitudes of incident, reflected and transmitted waves, respectively. V_1, V_2, and ρ_1, ρ_2 are velocity and densities of upper- and underlying media, respectively. Converted waves are not included. (B) Energy partitioning at an interface for vertical incidence case ($\theta_1 = 90$ degrees).

amplitudes of reflected and transmitted waves can be calculated by Zoeppritz equations given by Eq. (12.8). In the case of vertical incidence as shown in Fig. 1.18B, Zoeppritz equations can be simplified in such a way that the reflected and transmitted wave amplitudes relative to the incident wave amplitude are associated with the reflection and transmission coefficients, respectively. The reflection coefficient of a given interface is

$$k_R = \frac{Z_2 - Z_1}{Z_2 + Z_1} \tag{1.5}$$

and the transmission coefficient is

$$k_T = \frac{2Z_1}{Z_2 + Z_1} \tag{1.6}$$

where Z_1 and Z_2 are the acoustic impedances of the upper- and underlying medium, respectively. The amplitude of the reflected portion of the incident wave is

$$A_R = k_R A_0 \tag{1.7}$$

and the transmitted wave amplitude is

$$A_T = k_T A_0 \tag{1.8}$$

where A_0 is the amplitude of the incident wave. The sum of the reflected and transmitted amplitudes equals to the incident wave amplitude.

According to Eq. (1.7), amplitude and polarity of the reflected wave depend only on acoustic impedances of both media, Z_1 and Z_2. If the difference between acoustic impedances is high, then it will produce a high reflection coefficient value, and hence a large reflected wave amplitude. In addition, if $Z_2 < Z_1$, the reflection coefficient is negative, resulting in a reverse polarity reflection with respect to the incident wave polarity. The changes in acoustic impedance are predominantly caused by velocity variations within the upper- and underlying medium, since the changes in medium densities are negligible as compared to the variations in velocity.

The relationship between the incidence and reflection angles is governed by Snell's Law, which states that the incidence angle is equal to the reflection angle. The transmitted ray also changes direction with respect to the normal vector of the interface for nonnormal incidence angles. The direction of the transmitted ray is determined by the ratio of the velocities: If the velocity of the underlying medium is faster than that of the upperlying medium, the transmitted ray is bent toward the horizontal, which is the most common case. The opposite occurs in the case of a higher velocity upperlying medium. The relationship between the incidence and transmission angles based on the geometry and parameters in Fig. 1.18A is given by

$$\frac{\sin\theta_1}{V_1} = \frac{\sin\theta_2}{V_2} \tag{1.9}$$

Specifically, the transmitted wave travels along the interface with the propagation velocity of underlying medium when $\theta_2 = 90$ degees. In this case, $\sin(\theta_2) = 1$ and Eq. (1.9) becomes

$$\sin\theta_C = \frac{V_1}{V_2} \tag{1.10}$$

where the incidence angle θ_1 is termed the critical angle and usually denoted by θ_C. The incident P wave with the incidence angle of θ_C traveling along the boundary with a velocity of V_2 is known as a refracted wave, or a head wave.

The ray paths and appearance of the reflected signal, direct wave and head wave on the synthetic seismograms are schematically illustrated in Fig. 1.19. By a certain distance, indicated by X_K in Fig. 1.19, direct waves arrive first at the receivers because the ray path they travel is the shortest. After crossing distance X_K, the head waves catch the direct arrivals and become the waves that arrive first at the receivers because they travel at the velocity of the underlying medium V_2, and hence they are faster, since $V_2 > V_1$. By the critical distance X_C in Fig. 1.19, we cannot observe head waves on the

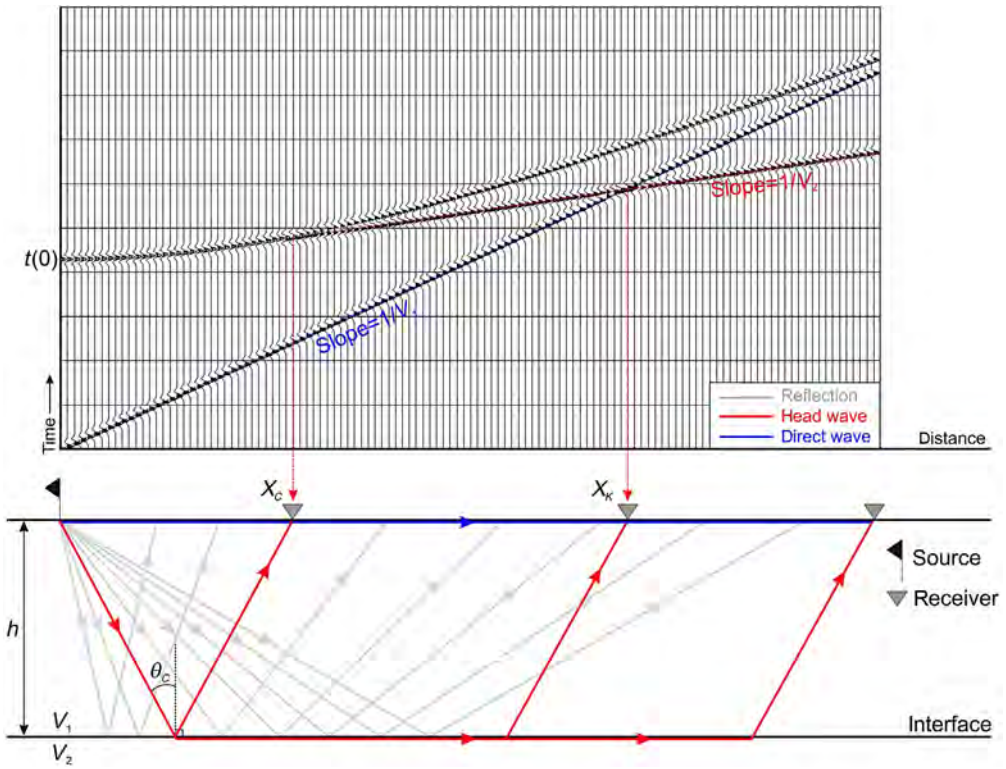


FIG. 1.19 Schematic illustration of ray paths of reflected signal, direct and head waves (bottom), and appearance of these specific waves on the synthetic seismograms (top). θ_C is the critical angle, which is the incidence angle when the transmission angle is 90 degrees. X_C is the critical distance where the head wave and reflections arrive at the same time, and X_K is the crossing distance where the head wave and direct wave arrive at the same time at the receivers. Here, $t(0)$ stands for the zero offset arrival time of the reflections. Until the critical distance, head waves cannot be formed.

seismograms because the incidence angle must reach the critical angle value for head waves to form. At this distance, the reflection signal and head waves arrive at the same time. We can calculate the velocities of the upperlying and underlying media by using the slopes of the direct and head waves on the seismograms.

1.3.3 Shot Gathers

Ensembles, or gathers, are the specific group of traces constructed from recorded seismic data. In the different stages of processing, recorded traces can be grouped by considering their different attributes. For instance, many processing applications are performed on shot gathers, such as band-pass filtering, *f-k* filtering or deconvolution, and then the data is sorted into CDP gathers for further analysis, such as velocity analysis, NMO correction or stacking. There are several different trace gather types used in the different stages of processing, and the most common ones are defined in Section 5.4.

Shot gathers are the specific group of seismic traces originated from the same shot but recorded at different receivers (Fig. 1.20). The number of traces involved in a shot gather equals the total number of recording channels plus auxiliary channels, if available. The distance between each

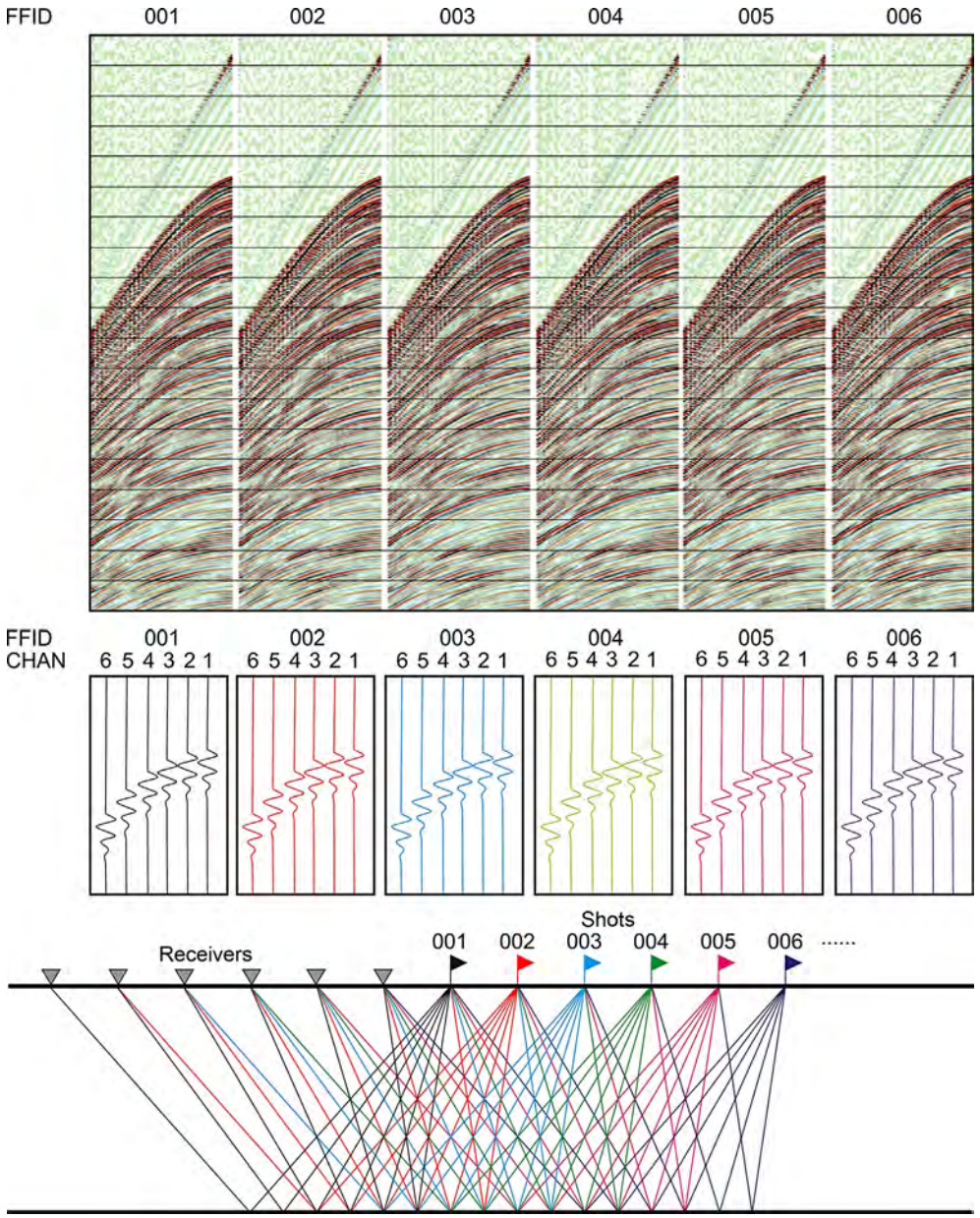


FIG. 1.20 Ray paths of six successive shots over a single horizontal reflector (bottom) and schematic display of these shots recorded at six receivers (middle). Real shot gathers have several reflections in hyperbolic form (top). FFID is Field File ID number.

recording channels and their corresponding shot location is termed the offset distance for each trace in a shot gather. As a specific case, the distance from the first channel to the shot point is called the minimum offset. Reflection events appear as hyperbolas, termed reflection hyperbolas on the shot gathers.

Both for 2D and 3D seismic acquisition, the raw seismic data is collected as shot gathers. Recording starts at the exact time that the source is fired. The recorder receives the seismic amplitudes perceived by all channels along the spread and constitutes a shot gather by sorting them with an increasing order of channel number or corresponding offset value. This is repeated for each shot and a shot gather is reproduced and recorded into the disks for each shot location. Each shot gather has a unique and regularly increasing (or decreasing, according to the settings of the acquisition parameters) shot number termed the Field File ID Number (FFID) and used to discriminate the successive shots (Fig. 1.20). The existence of FFID and recording channel numbers in the seismic trace headers is of vital importance in the processing stage (Section 5.2).

Both land and offshore seismic reflection data is collected as shot gathers. However, there are strict distinctions between land and marine shot gathers in terms of the seismic events they contain, types of noise, resolution, etc. These distinctions arise due to the differences in acquisition geometry, seismic source types, the noise components in land and marine environments, and the presence of a water column in marine surveys. In land seismics, the acquisition geometry is more flexible and can be modified based on the requirements of the survey area: It is possible to collect data along the crooked lines; shots can be located at any location along the survey line (the split-spread surveys) or off the survey line (which provides a better azimuth distribution for 3D surveys). For split-spread surveys, it is possible to record whole reflection hyperbolas along both sides of the shot point (Fig. 1.21A). This flexibility is not possible for marine surveys (except a quite new acquisition method termed TopSeis applied by CGG) since the shot must be fired at the front end (the vessel side) of the spread, which results in recording only half of the reflection hyperbolas (Fig. 1.21B). Noise types involved in land and marine seismics are also different. For instance, Rayleigh waves or ground roll is an important type of noise in land seismics, but it does not exist in marine seismic surveys. In addition, we do not observe air blast in the marine surveys, since the streamer is towed at a certain depth below the sea surface. However, there are several different types of noise encountered in marine surveys and these are discussed in Chapter 3 in detail.

1.3.4 Reflection Hyperbolas

Reflections recorded at different receivers constitute hyperbolas on the shot gathers when the traces are sorted in increasing order regarding the channel number or their offset distance. Fig. 1.22A shows a reflection hyperbola from a single horizontal reflector model. The shot point is located at the center of the spread and the recorded hyperbola is symmetrical about the shot location. As a specific case, the reflected signal reaches the receiver first at $x = 0$ m (the shot location) and the arrival time of the reflected energy at $x = 0$ m receiver is known as zero-offset time, often designated with $t(0)$ and expressed by

$$t(0) = \frac{2h}{V} \tag{1.11}$$

where h is depth of the reflector and V is velocity of the upperlying medium. In such an earth model consisting of a single horizontal interface, the arrival time of the reflected signal at a receiver at offset x can be calculated by

$$t^2(x) = t^2(0) + \frac{x^2}{V^2} \tag{1.12}$$

If the interface is inclined with an inclination angle of ϕ, the situation is somewhat different: The recorded reflection hyperbola is asymmetrical about the shot location and the zero-offset time

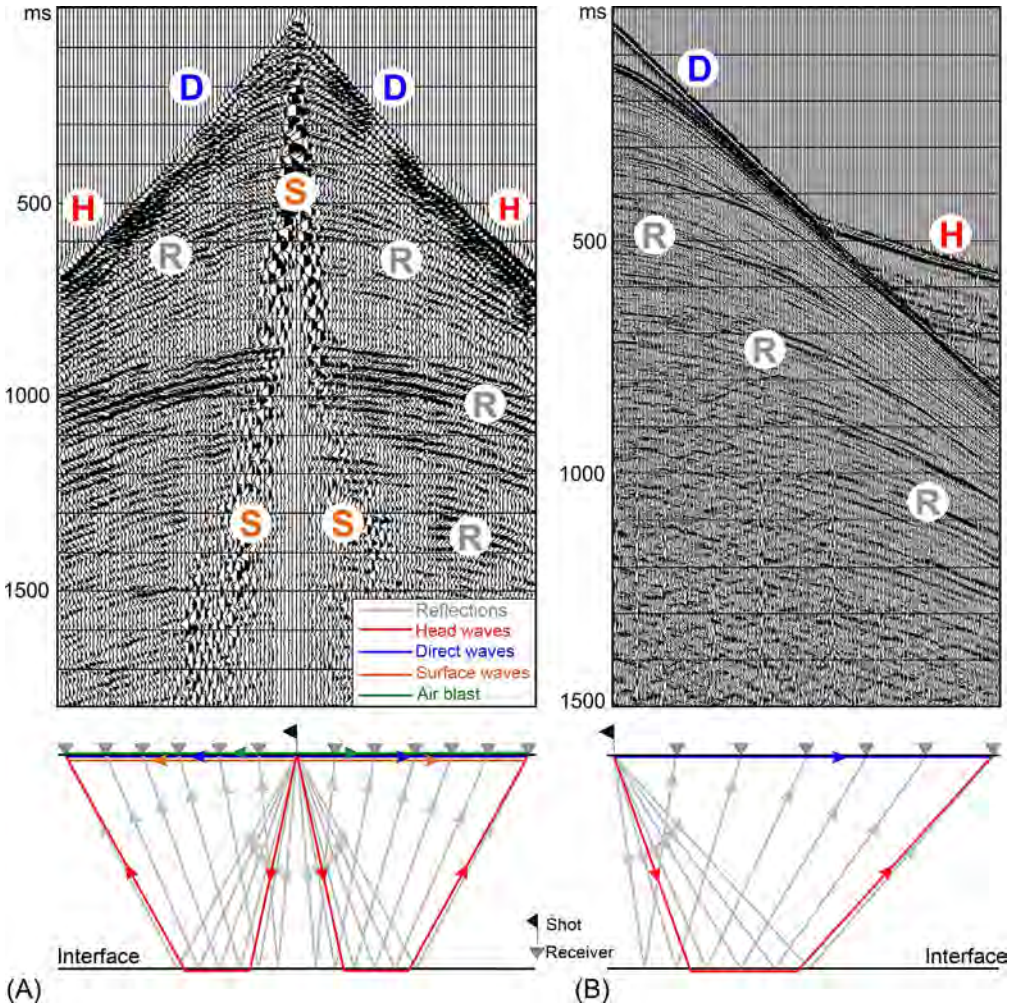


FIG. 1.21 Shot gathers (top) and corresponding ray paths (bottom) from (A) land and (B) marine seismic survey. *R*, primary reflection; *H*, head wave; *S*, surface (Rayleigh) wave; *D*, direct wave.

moves in an updip direction (Fig. 1.22B). In this case, the arrival time of the reflected signal at a receiver at offset x can be calculated by the Levin equation (Levin, 1971)

$$t^2(x) = t^2(0) + \frac{x^2\cos^2\phi}{V^2} \tag{1.13}$$

The difference between the arrival time of a reflection event at a receiver at offset x calculated by Eq. (1.12) or Eq. (1.13) and zero-offset time calculated by Eq. (1.11) is termed normal moveout (NMO). Specifications of NMO are explained in detail in Section 10.1. Maximum NMO time of any reflection hyperbola is of key importance in velocity analysis. The higher the maximum NMO time, or the curvature, of a recorded reflection hyperbola, the better the resolution and accuracy in the final velocity field is. In addition, some of the multiple suppression methods, such as stacking or Radon transform,

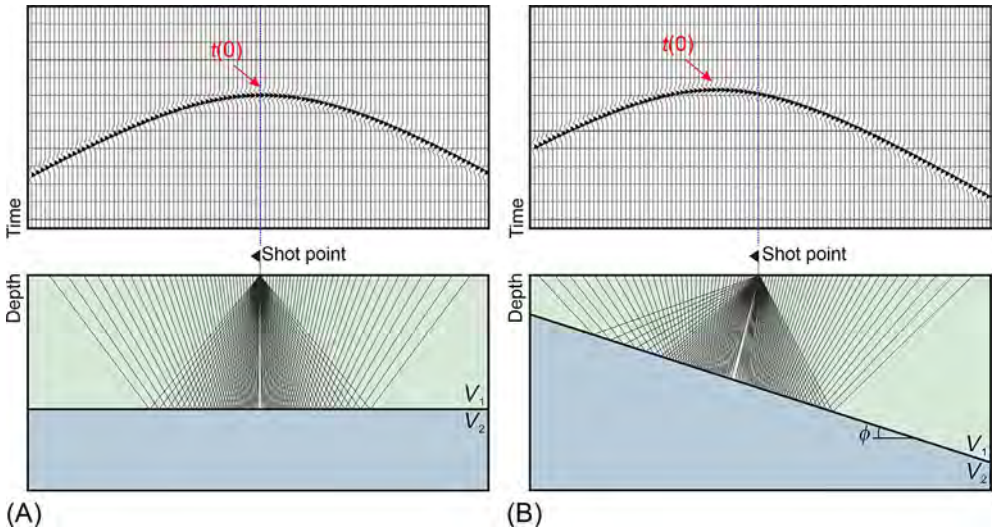


FIG. 1.22 Theoretical reflection hyperbolas obtained from (A) a single horizontal reflector model and (B) a single inclined reflector model. If the interface is horizontal, the recorded hyperbolas are symmetrical about the shot location, whereas it is asymmetrical in the case of an inclined interface and zero-offset time moves in an updip direction.

require NMO times as high as possible to work properly.

The NMO time of a specific reflection hyperbola increases with offset distance. Since long offsets provide higher NMO times for the reflection hyperbolas, longer streamer cables are preferred during the acquisition of marine seismic data. Maximum NMO time is also larger for shallow reflections, and it decreases with increasing reflector depth (Fig. 1.23A). In addition, NMO time decreases as the propagation velocity increases (Fig. 1.23B). In the real world, the velocity of the subbottom sediments commonly increases with increasing reflector depth, and therefore, as a combined effect of reflector depth and velocity, we can expect an overall decrease in the maximum NMO time for deeper reflection hyperbolas (Fig. 1.23C). These consequences restrict the quality of the velocity field obtained from seismic data by velocity analysis, which is discussed in Chapter 9.

In seismic data processing, some crucial processing steps, such as NMO correction or velocity analysis, assume perfectly hyperbolic reflection events in the prestack data. In some cases in marine seismics, however, reflections do not display hyperbolic moveout, especially in areas of rapid morphological changes. Fig. 1.24 shows a migrated section through a steeply dipping continental slope crosscutting several morphological structures of submarine canyons in different scales with steeply dipping walls, which constitute morphological variations both on the seafloor and within the subbottom sediments. Example shot gathers from different locations along the seismic line are also provided in Fig. 1.24 to analyze the effect of morphological variations on the shape of the reflection hyperbolas. Especially in areas where the rough seafloor exists, reflection hyperbolas on the shot gathers are distorted due to the multivalued reflections from steep walls of the submarine channels. In these areas, velocity analysis does not provide accurate results and the quality of the stacking output is degraded since it is impossible to flatten such reflection hyperbolas with an imperfect moveout during NMO correction.

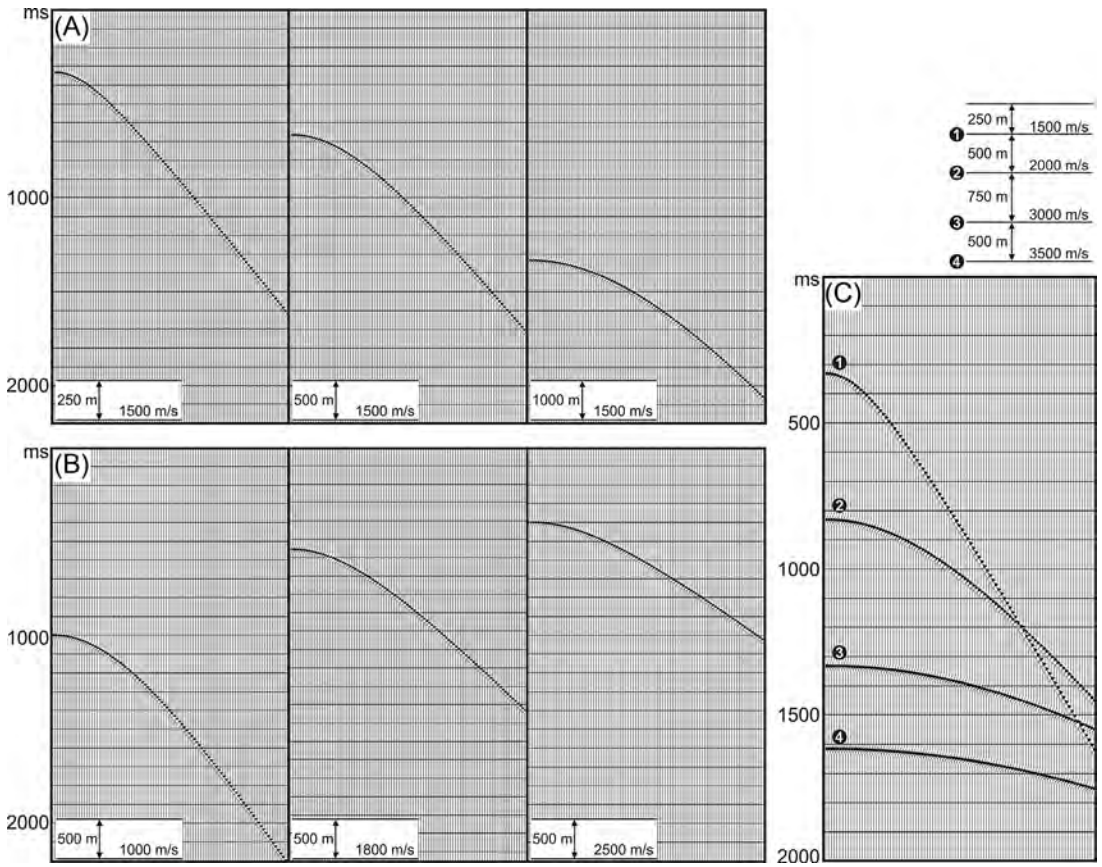


FIG. 1.23 Synthetic shot gathers illustrating how the NMO time or curvature of a theoretical reflection hyperbola changes with (A) increasing reflector depth for a constant velocity and (B) increasing velocity for a constant reflector depth. (C) Combined effects of reflector depth and velocity on the NMO time for four different reflector depths with increasing velocities.

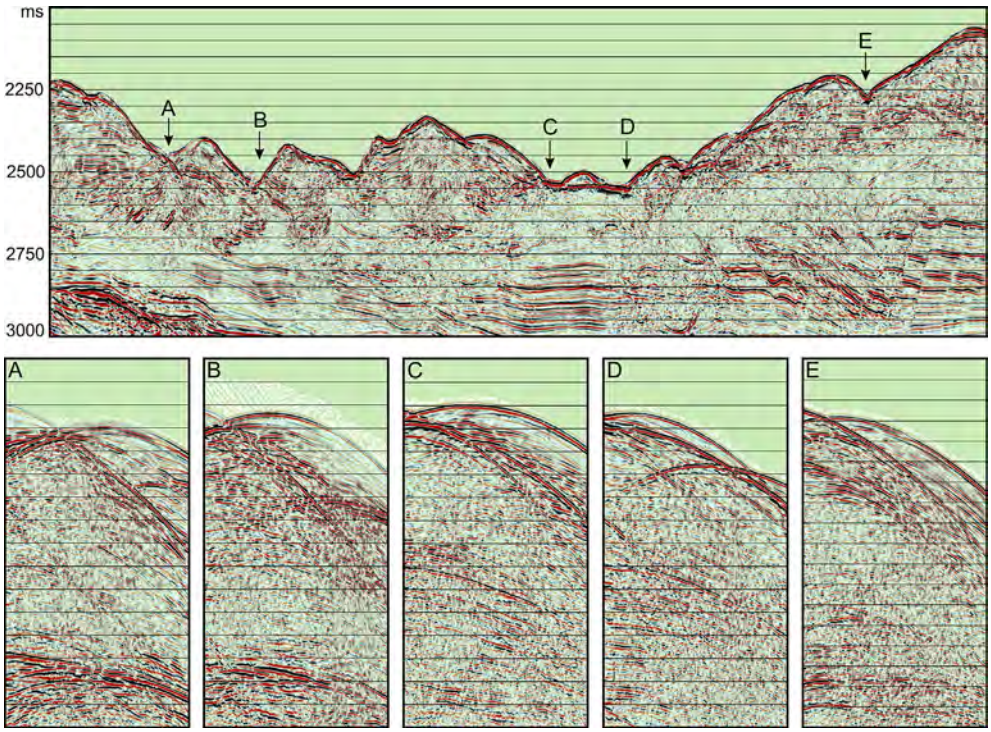


FIG. 1.24 Examples for reflections of nonhyperbolic moveout (bottom) from a migrated section crosscutting a number of submarine canyons through the continental slope (top). Locations of the shot gathers are indicated by letters A to E on the migration section.

CHAPTER

2

Marine Seismic Data Acquisition

OUTLINE

2.1 Components of Marine Seismic Acquisition 40
- *2.1.1* Seismic Vessels 41
- *2.1.2* Hydrophones and Streamer 44
- *2.1.3* Marine Seismic Energy Sources 53
- *2.1.4* Gun Control Systems 55
- *2.1.5* Streamer Depth Controllers 57
- *2.1.6* Seismic Recorder 58
- *2.1.7* Integrated Navigation System 59
- *2.1.8* Tail Buoys, Dilt Floats and Paravanes 60
- *2.1.9* Lead-in and Deck Cables 62

2.2 Air Gun Arrays 62
- *2.2.1* Air Gun Principles 63
- *2.2.2* Air Gun Bubble Effect 65
- *2.2.3* Ghost Reflection 68
- *2.2.4* Near-/Far-Field Source Signatures 69
- *2.2.5* Cluster/String/Array 72
- *2.2.6* Tuning and Array Performance 76

2.3 3D Marine Seismic Acquisition 81
- *2.3.1* Acquisition Patterns 82
- *2.3.2* Streamer Steering 84
- *2.3.3* Streamer Layout 85
- *2.3.4* Acoustic Network 88
- *2.3.5* Flip-Flop Shooting 91
- *2.3.6* Slant Streamer Acquisition 92
- *2.3.7* Fan Mode Acquisition 93
- *2.3.8* Multiazimuth Surveys 94

2.4 Specific Acquisition Techniques 100
- *2.4.1* Ocean Bottom Seismic Acquisition 100
- *2.4.2* Time-Lapse (4D) Seismic 108
- *2.4.3* Transition Zone Acquisition 109
- *2.4.4* P-Cable Acquisition 110

2.5 Data Acquisition Parameters 112
- *2.5.1* Parameters for Survey Geometry, Sources, and Receivers 114
- *2.5.2* Parameters for Data Recording 127

2.6 QC in Data Acquisition 131
- *2.6.1* Preacquisition Instrument Tests 134
- *2.6.2* Analysis of Seismic Data 140
- *2.6.3* Analysis of Navigation Data 146
- *2.6.4* Analysis of Seismic Source 154
- *2.6.5* QC Reporting 158

https://doi.org/10.1016/B978-0-12-811490-2.00002-5

© 2018 Elsevier Inc. All rights reserved.

Seismic surveys use elastic waves generated by artificial explosions or vibrations on land, and commonly high-pressure air discharges in marine surveys. Some of the generated waves are reflected back from the interfaces separating the different stratigraphic units in the earth, and we receive and record the amplitudes as well as arrival times of this reflected energy on the earth or ocean surface using specific sensors, called geophones for land acquisition and hydrophones for marine surveys. All types of marine seismic surveys consist of one or two source arrays and a specific configuration of several hydrophones assembled in a receiver cable, termed a streamer. The configuration varies based on the purpose of the survey: it may be one single cable (for 2D acquisition), several parallel cables (for 3D and 4D acquisition), or receivers lying onto the seafloor (for 4C acquisition), etc.

Coherent and random events observed in the seismic data determine the characteristic specifications of the data recorded. Most of the coherent noise components are generated by the acquisition components; for instance, operational noise is produced by the survey vessel, or bird noise arises from the movements of the wings of depth levelers mounted at regular intervals along the streamer (Chapter 3). Data processors should be familiar with the nature and origin of these specific noise types originating from the nature of the seismic acquisition, to suitably determine the data-processing steps and required processing parameters. In general, parameters and outputs of some specific data-processing steps strongly depend on the data acquisition parameters. Therefore, a processor should be aware of the basic concepts of acquisition to design the most suitable processing flow with optimum processing parameters. This section includes basic principles of marine seismic data acquisition as well as the equipment used in 2D and 3D surveys in addition to some specific types of surveys, like P-cable and 4C acquisitions, in order to provide a complete source from the acquisition to the end of data processing.

Offshore seismic surveys are conducted both for academic purposes, to understand the structure and dynamics of the continental margins and deep basins, and for exploration, production and development of offshore oil and gas fields. Seismic acquisition is a very specific area of expertise that requires professional field teams to conduct the surveys and collect the data in required quality limits without any complications. Although it may vary according to the requirements of the specific project, Fig. 2.1 shows a general offshore seismic survey crew list and structure. The HSE (Health, Safety and Environment) team ensures that all the operations onboard are conducted in accordance with the safety regulations based on the implementations determined and declared in the project's

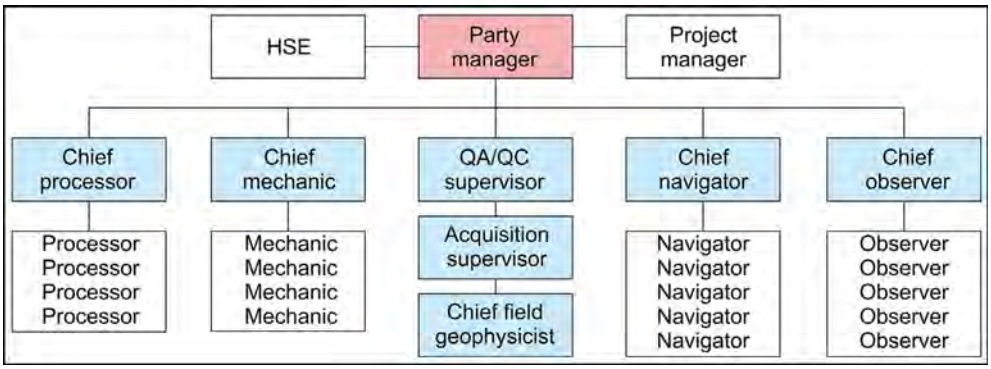


FIG. 2.1 A general crew structure for an offshore seismic survey.

HSE plan specifically prepared for each survey. The project manager, as a general description, is responsible for ensuring the overall project objectives according to the requirements of the client, to maintain the budget and timelines of the project, and to prepare necessary project reports to demonstrate that the project proceeds in accordance with the client's needs. The head of the crew is the party manager or party chief, who is responsible for overall seismic operations, and preparing daily reports for the survey. Processing related to the data quality and quality assurance/quality control (QA/QC) issues, as well as onboard processing applications, are handled by the processors under the supervision of QA/QC supervisor. Observers set up the initial shot and recording parameters and analyze the bubble level. They watch and check the data during recording and perform some initial online quality controls of the raw data in addition to the handling of the issues of streamers and other components of the acquisition system. Mechanics deploy and retrieve gun arrays and performs the maintenance and repair of the air guns and air compressors. Navigators watch and check navigation data from in-sea equipment during the acquisition. They also check the data logging of the required navigation information, real-time binning, and the depths and feathering of the streamers in real-time.

Since the seismic data acquisition requires comprehensive work, including professionals from different areas of expertise, there are several private seismic survey companies that acquire 2D/3D/4D seismic, ocean bottom cable (OBC), ocean bottom node (OBN) and ocean bottom seismometer (OBS) data all over the world, operating their own dedicated fleets. These well-known operators are

- Western Geco (2D, 3D, 4D towed streamer and OBC acquisition; Western Geco stopped seismic acquisition in early 2018)
- CGG Veritas (2D, 3D, 4D towed streamer, OBC and OBN acquisition)
- PGS (2D, 3D, 4D towed streamer acquisition)
- Dolphin Geophysical (2D, 3D, 4D towed streamer acquisition)
- Polarcus (2D, 3D, 4D towed streamer acquisition)
- Fugro (2D, 3D, 4D and high resolution towed streamer acquisition)
- SeaBird Exploration (2D towed streamer acquisition)
- Seabed Geosolutions (OBC, OBN acquisition)
- Geospace Technologies (OBC, OBN manufacturer)
- Fairfield Nodal (OBN acquisition)
- OceanGeo (OBC, OBS acquisition)
- RXT ASA (OBC acquisition)
- SAExploration (OBN acquisition)
- Geokinetics (OBC acquisition)

In addition to academia, which performs marine acoustic surveys mostly for scientific purposes, commercial surveys are conducted by the private survey companies listed here, which act as service companies for oil and gas industry worldwide. They conduct several different types of seismic surveys, mainly for reservoir exploration and development, as well as reservoir characterization and monitoring over an existing reservoir (Table 2.1). Among these, 2D and especially 3D towed streamer surveys are the most common commercial activities. Academic environments generally perform 2D towed seismic operations, except that Columbia University carries out 3D seismic operations onboard of research vessel R/V Marcus G. Langseth. OBS deployments are commonly used by academia for research purposes in addition to long-term monitoring of active submarine fault zones. OBN and OBC are specific survey techniques mostly used for monitoring and characterization of existing reservoirs conducted by oil and gas industry around the offshore production platforms. Ocean bottom acquisition systems generally collect 2- or 4-component (2C or 4C) data, one being pressure data from a hydrophone and the others from a three-component geophone. Monitoring of an existing reservoir is done by repeated 3D surveys over the same area,

TABLE 2.1 Different Types of Marine Seismic Surveys, Components of Recorded Data, and General Applications of the Techniques

Method	Dimension	Component	Area of Application
Towed streamer acquisition	2D, 3D, 4D	1C, 2C, 3C	Exploration and development, used by academia and oil and gas industry
Transition zone acquisition	2D, 3D, 4D	1C, 2C	Exploration and development, commonly used by oil and gas industry
Ocean bottom seismometer (OBS)	2D, 3D	4C	Mainly for exploration, commonly used by academia
Ocean bottom nodes (OBN)	3D, 4D	4C	Reservoir characterization and monitoring, used by oil and gas industry
Ocean bottom cables (OBC)	3D, 4D	2C, 4C	Reservoir characterization and monitoring, used by oil and gas industry

1C: one hydrophone, 2C: one hydrophone and one velocimeter, 4C: one hydrophone and three accelerometers for x, y, and z components.

with a time period of several months to several years. This operation is known as time-lapse or 4D seismic.

2.1 COMPONENTS OF MARINE SEISMIC ACQUISITION

Acquisition of marine seismic data requires several different systems and software packages to compatibly work simultaneously, which are in communication with each other in real-time during the acquisition. Fig. 2.2 shows a general block diagram of a marine seismic acquisition system. These specific systems and equipment are introduced and their basic specifications are described in this section.

Before starting the survey, navigation sensors, including the gyrocompass (the electronic compass device) and motion sensor (for heave, roll and pitch data) as well as the single-beam echosounder must be calibrated. DGPS (differential GPS) signal verification must be performed to

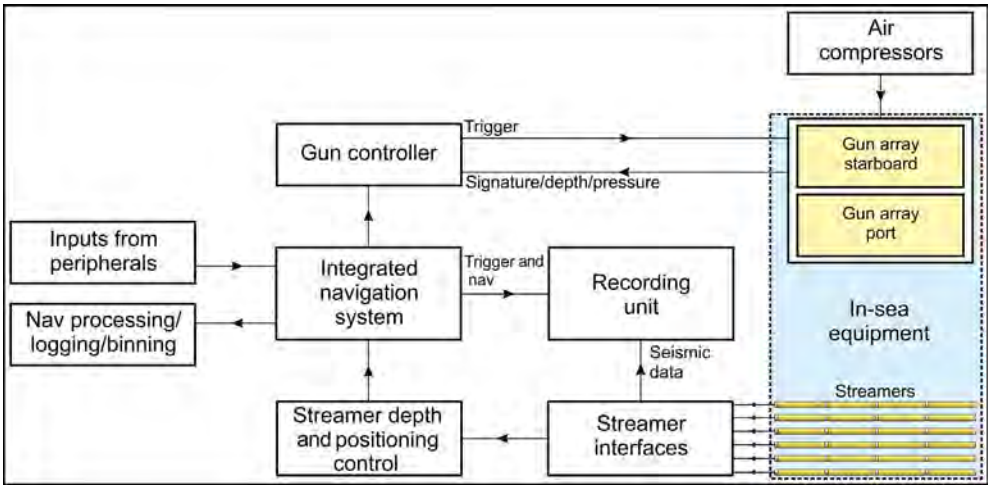


FIG. 2.2 General block diagram and components of a basic towed streamer marine seismic acquisition system.

ensure that the standard deviation of the GPS error is within the acceptable limits of the survey. The rGPS (relative GPS) system must be checked and calibrated. All other static offsets around the vessel, such as the locations of the aforementioned sensors must be verified and accurately set into the integrated navigation system. All these measurements, calibrations and verifications are fulfilled when the vessel is at the dock.

Several experts must work together to keep the all the seismic system components fully operational during the recording. First, data acquisition parameters such as sampling rate, record length, shot interval, etc. are correctly set in the navigation and recording units by navigators and observers. The vessel is kept at a constant speed of approximately 4–4.5 knots and then tail buoys and streamers are deployed first, along with the necessary navigational units attached, such as depth levelers (birds), acoustic rangers and streamer positioning or steering equipment. After deploying the dilt floats (streamer front buoys) and paravanes, observers watch the positions of all the in-sea equipment to settle using rGPS and acoustic ranger inputs. Finally, the air compressors are started and air gun arrays are deployed. After positioning of all the equipment, several tests for streamers and guns are carried out to ensure that all systems are functioning properly before the data recording is initiated. Gun mechanics assure that all air guns are working properly, with no air leakage within the pressurized components, and that gun timing for all guns of all strings is in required tolerance limits. Navigators check that all the streamer cables are at their predetermined positions, all the acoustic ranging systems are properly functioning, and depth and lateral positions of all streamers are correct. Observers get some noise records without firing the guns to analyze the static noise level on the streamers, and then check the test shots and visually inspect the data and noise levels on all streamers before the recording.

If all systems are working properly, then the vessel is ready to run into the first sail line. The shooting and recording starts at a certain distance before the actual line start position, which is termed the run-in distance. At every shot point location determined by the integrated navigation system as the vessel proceeds along the line, the shooting is repeated and data is recorded. The shooting and recording stops at a certain distance after the actual line end position, which is termed the run-out distance. The seismic vessels need a large turning area to run into the next line, which is planned by the navigators and generally controlled and carefully monitored by the navigation system. During the line change, vessel speed is generally kept constant at acquisition speed.

Typically, the following equipment is mobilized for a 2D seismic survey (Fig. 2.3A):

- Seismic vessel
- Seismic recorder
- Onboard processing/QC system
- Streamer
- Seismic sources
- Gun controller
- Streamer depth controller
- Air compressors
- Integrated navigation system
- DGPS/rGPS systems
- Tail buoy
- Lead-in and deck cables

The following additional equipment is also required for 3D surveys (Fig. 2.3B):

- Paravanes
- Dilt floats
- Lateral streamer positioning equipment
- Acoustic rangers
- Other equipment (velocimeters, separation ropes, etc.)

2.1.1 Seismic Vessels

Seismic vessels are specific ships dedicated to use solely for 2D or 3D seismic data acquisition in the ocean. Since in-sea equipment deployed during the acquisition consists of large spreads, commonly up to 16 streamers each 8–10 km

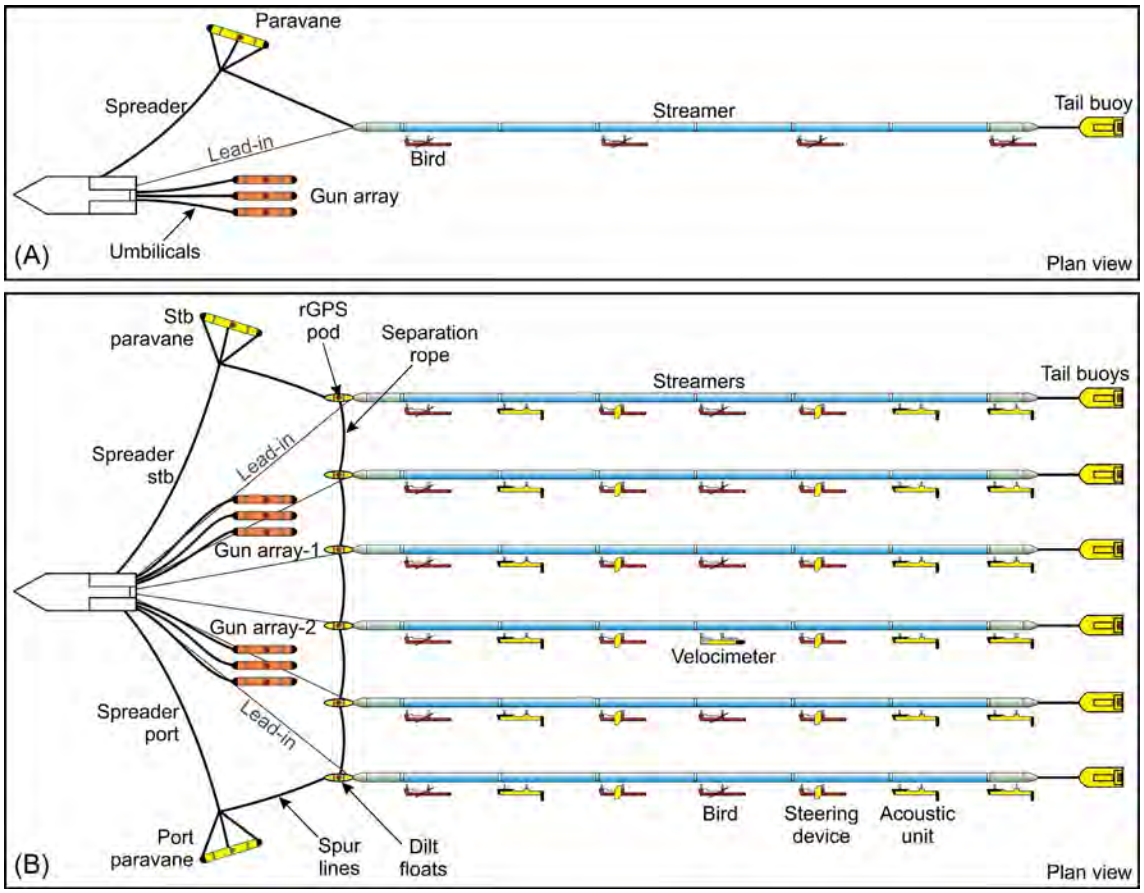


FIG. 2.3 Plan view of general in-sea equipment for (A) 2D and (B) 3D conventional towed streamer seismic survey.

long, the vessels used to manage this equipment must have very specific characteristics. Although some fishing ships were converted into 2D seismic vessels after the 1980s, seismic acquisition is maintained by operating modern 3D seismic vessels dedicated to acquire seismic data all over the world. They are commonly designed as powerful diesel-electric vessels with at least two drivelines to operate on a 24/7 basis for the acquisition of 2D and 3D seismic data.

Since the deployment and recovery of the in-sea equipment, especially the streamers, are quite time-consuming processes, all shipping operations as well as crew changes are done during the acquisition without any interruption of data recording. All modern seismic vessels have a helicopter deck to use for emergency situations and crew change. In addition, acquisition is accompanied by at least one chase boat, which provides connection to the land for transferring data or replenishing supplies and tries to keep all the spread safe from shipping activities of other nearby vessels. Even bunkering is done as the vessel tows the streamers. Damaged or defective streamer sections are repaired or replaced by work boats when the streamers are still in the water.

Although 2D seismic vessels may be smaller, overall lengths of contemporary seismic vessels

range between 90 and 120 m and they provide accommodations for 50–60 people onboard, including ship's crew, seismic team, and client representatives. When it is taken into account that a survey may take several months, depending on the size of the working area, the vessels must also contain some recreational facilities such as a TV room, a sauna, gym and sometimes a swimming pool, or even a basketball court.

These vessels have a unique back deck design to accommodate all required in-sea equipment such as guns, streamers, birds, etc. 2D and 3D seismic vessels have two separate back decks: the streamer deck (which is the upper deck used to store and deploy the streamers and related devices such as tail buoys or birds), and the gun deck (which is the lower deck used to store and deploy the guns and their peripherals). Fig. 2.4A shows the stern photo of the Sanco Sword seismic vessel of Dolphin Geophysical. The Sanco Sword can handle up to 16 streamers, each of which is deployed through its own fairleads at the towpoints (Fig. 2.4B). Gun decks host the air gun arrays (Fig. 2.4C). 2D vessels have one single array while 3D vessels generally have two identical source arrays for flip-flop acquisition. There are also a gun shack and an air gun control room in the gun deck. Back decks also involve the tail and head buoys with their specific rGPS navigation equipment mounted.

Both 2D and 3D vessels also have a central hydraulic system and several different winches and reels to store, deploy and retrieve the streamers, buoys, gun umbilicals, paravanes and other necessary towing ropes and cables. Streamer decks also have a shack for birds and

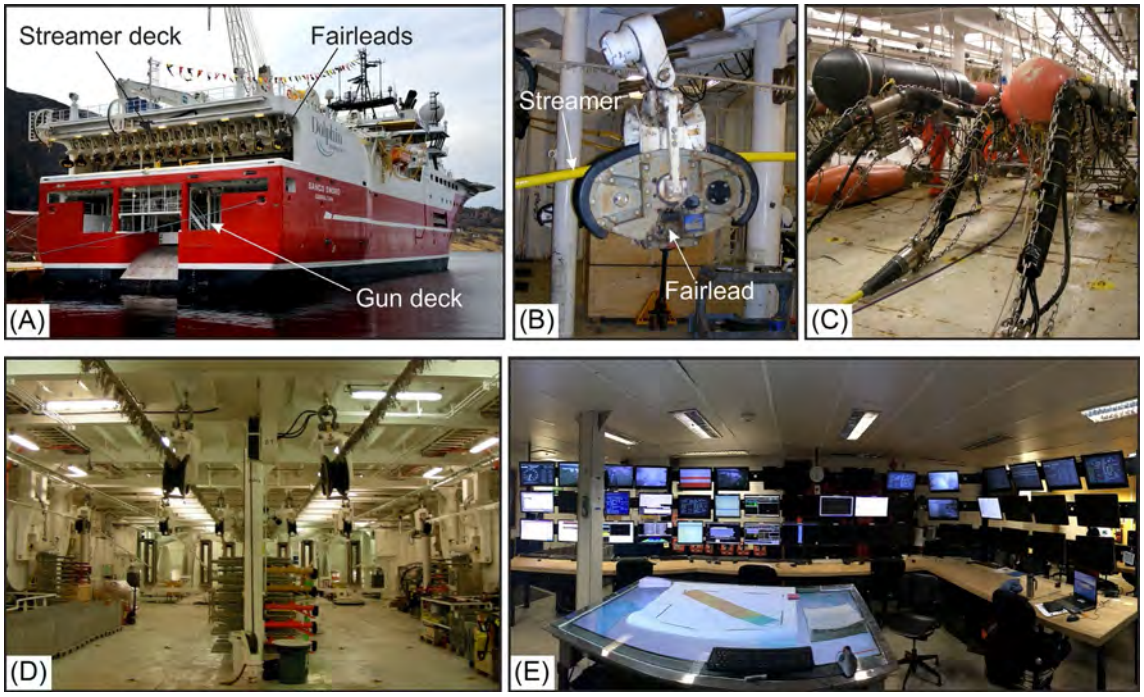


FIG. 2.4 (A) Stern photo of Sanco Sword 3D seismic vessel of Dolphin Geophysical, (B) fairleads used to deploy the streamers, (C) gun deck, (D) streamer deck, and (E) instrument room of R/V Marcus Langseth operated by Columbia University.

acoustic devices, tail buoy storage and workshop, and a streamer repair room (Fig. 2.4D). All of the seismic operations related to the data recording, onboard processing, QC, navigation, etc., are conducted from seismic instrument room (Fig. 2.4E). Navigators and observers all work together in the instrument room to ensure data quality. Generally, seismic QC processes and onboard processing applications are performed on the specific processing servers in the instrument room. Seismic data is acquired and stored on the tapes located in the instrument room after a fast-track processing.

Seismic vessels have several precise navigation sensors connected to a sophisticated navigation software located in the instrument room. Generally, two independent DGPS receivers simultaneously provide precise coordinate information with less than 1 m horizontal accuracy. Today, the most modern seismic vessels are navigated by a dynamic positioning (DP) system, which is a fully computer controlled system controlling the vessel's propellers and thrusters to maintain the vessel position and heading, analyzing the data from the available sensors of DGPS, motion sensor and gyrocompass. The DP system also provides a precise survey speed to the vessel during the data acquisition and deployment of the in-sea equipment.

2.1.2 Hydrophones and Streamer

In land seismics, reflection signals are perceived by geophones and transmitted to the recorder following a conversion into electrical signals. In marine seismics, reflection amplitudes are detected by specific sensors termed hydrophones which respond to pressure variations in the water column. They are made by ceramic piezoelectric elements which are bent when exposed to a pressure wave, and hence generates an electric voltage between the surfaces of the ceramic elements (Fig. 2.5A). This voltage is actually the seismic signal itself, to be recorded in the seismic recorder.

Since the hydrophones are sensitive to pressure variations in the water column, they also receive the effect of acceleration of the streamer during the tow, because the movement of the streamer in the ocean also induces a constant pressure onto the hydrophones. This is a one-way effect and it is only towards to the tow direction. In order to cancel the effect of streamer acceleration, two identical piezoelectric elements are coupled in reverse directions to form a single hydrophone (Fig. 2.5B). Since the acceleration is a one-way pressure field, it generates positive voltage on one piezoelectric element and vice versa for the other element because they are reversely conjoined to each other. This

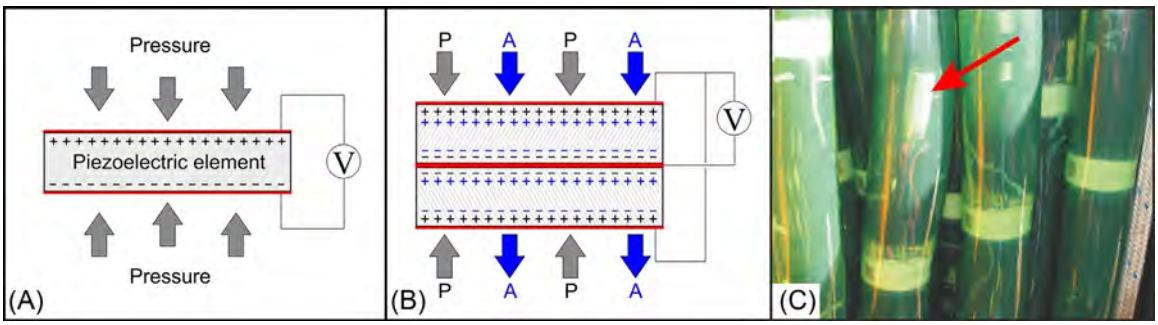


FIG. 2.5 (A) Formation of the voltage (seismic amplitude) between the surfaces of a piezoelectric element under the impact of a pressure wave. (B) Use of two identical elements to form a hydrophone to cancel out the acceleration (A) of the streamer while strengthening the pressure signal (P). (C) Photo of a hydrophone in a fluid-filled streamer *(arrow)*.

form is known as acceleration canceling hydrophone, and it ultimately cancels out the streamer acceleration when the voltage wirings are connected in parallel. The pressure waves from reflected signals, however, generate a positive voltage on the surfaces of both elements, and hence strengthen each other. Fig. 2.5C shows a hydrophone placed in a fluid-filled streamer.

Several hydrophones are located at regular intervals along the length of a long tow cable termed a streamer. The diameter of modern streamers is approximately 2 in., and their total length ranges from a few meters for single-channel acquisition to 12 km for conventional hydrocarbon exploration. Lengths of the streamers have gradually increased over time depending on the type and depth of the subsurface target. Considering the total length of the streamers for one single spread, a typical 3D vessel can tow more than 100 km of active streamer section for a single 3D survey.

Streamers are manufactured as appendable bidirectional sections of 75, 100, or 150 m, known as active sections so that repair, maintenance and replacement of a damaged streamer section can easily be managed. Several active sections are conjoined end-to-end to form a complete seismic streamer of many kilometers. During data recording, streamers are towed at a predetermined depth in the water, typically at 7–15 m below the sea surface for conventional acquisition for hydrocarbons, and at 3–5 m for high-resolution surveys. Once deployed, it is quite common for the streamers to remain in the water for several weeks to several months, depending on the size of the project.

Streamers end up with dead sections, generally 50–100 m long, termed stretch sections, which have the same structure as the active sections but host no hydrophones. Stretch sections isolate the active streamer sections from the strum noise originating from the movement of the water around the lead-in cables, mechanical cable noise from the fluctuations in tow speed, operational noise from the vessel machinery, and vibrations from the tail buoys. A stretch section is basically very similar to an active streamer section, but the strength members of the stretch sections are generally constructed from a more elastic material. Even though they are quite efficient to suppress the aforementioned noise types, especially those lower than 8 Hz, they may exhibit issues regarding environmental and safety situations since they are produced as fluid-filled sections. In addition to the active and stretch sections, modern streamer layouts contain several other components such as lead-in cables, digitizing modules, interconnects, tail buoy power units, auxiliary channel box, etc. They also include several external devices mostly for positioning purposes, such as depth controller birds, streamer steering units, acoustic rangers, etc. Power required for the operation of these systems is provided by the wirings inside of the streamer or the batteries included in the external devices.

The manufacturing of streamers and hydrophones is quite complex work, and there are several innovative companies that produce low-noise streamers and hydrophones worldwide today:

- Sercel (1C and 3C Digital solid streamers)
- ION Geophysical (Digital solid streamers)
- HydroScience Technologies Inc. (Digital solid streamers)
- Geometrics (Analog fluid-filled/solid streamers)
- Teledyne (Hydrophones, digital/analog fluid-filled streamers)

Fig. 2.6 shows configurations of the most widely used digital streamers in the market: the Sentinel streamer of Sercel, DigiStreamer of ION Geophysical, and SSCT streamer of HydroScience Technologies Inc.

Fig. 2.7 shows a sketch of the contents and a photo of a typical solid streamer section. An active section consists of hydrophones, an external jacket, wiring and connectors, buoyancy spacers, bird communication coils commonly

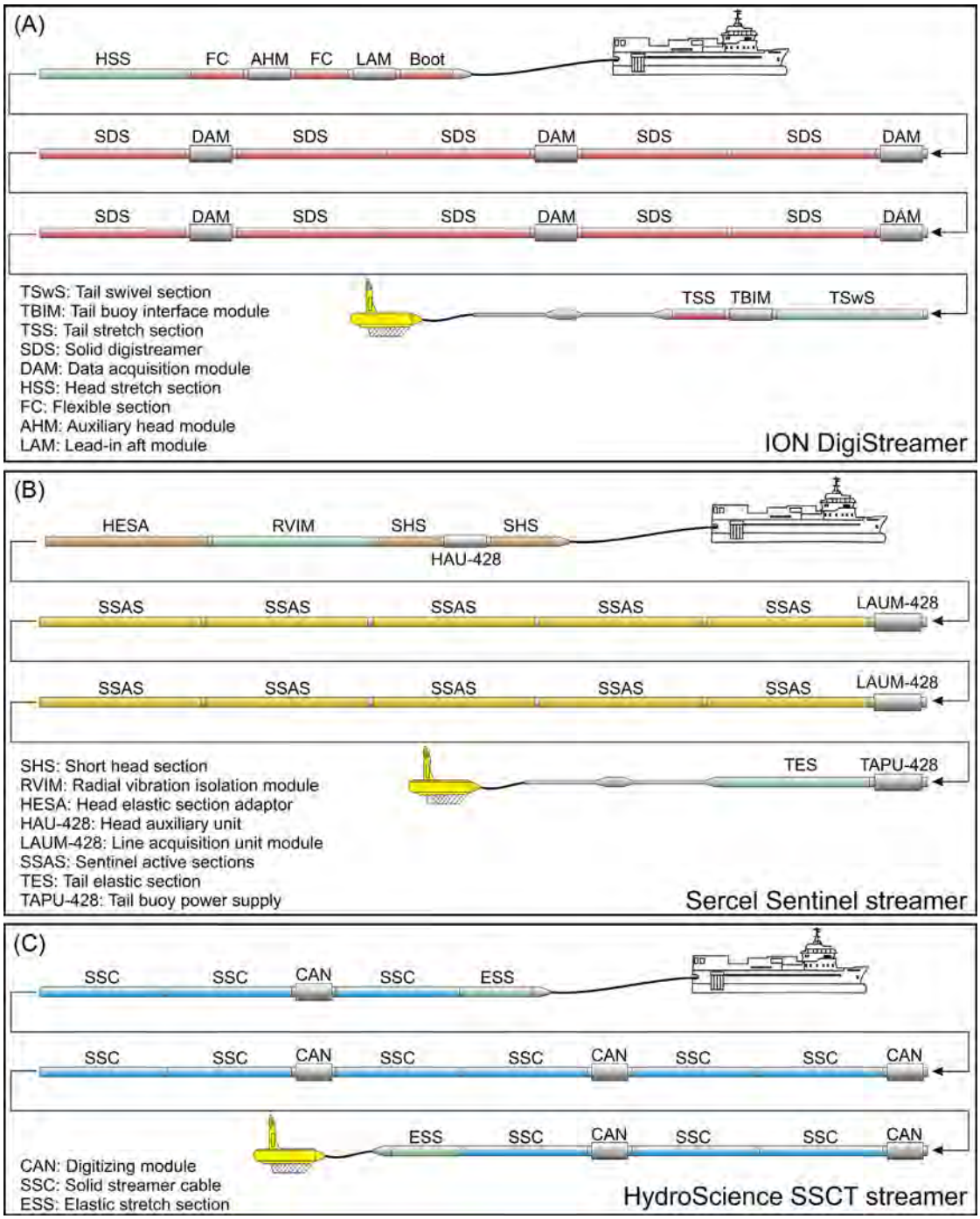


FIG. 2.6 Basic layouts of the streamers manufactured by (A) ION Geophysical, (B) Sercel, and (C) HydroScience Technologies Inc.

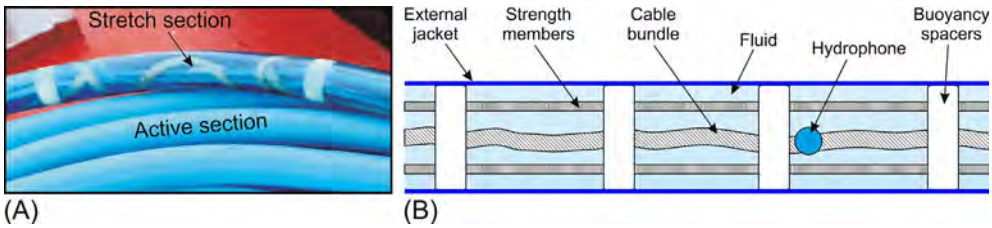


FIG. 2.7 (A) A photo of a small part of the fluid-filled stretch section (transparent segment) and solid active sections (opaque blue segments), and (B) sketch of the contents of a typical fluid-filled streamer section.

located one or two per section close to the end points, and strength members. The external jacket covering the whole exterior surface of the streamer is commonly produced from 3 mm thick polyurethane, which protects the hydrophones and wirings in the streamer section from sea water intrusion. Each section has typically two or three strength members extending from one end to another, which carry and transmit the tension load along the streamer due to the towing of the vessel. Each fluid-filled streamer section contains buoyancy spacers located at regular intervals along the streamer cable, which ensures that the sections are of the same average density as the surrounding ocean water to make the streamer neutrally buoyant when it is in the water. Inside the sections, there is also a cable bundle extending along the whole streamer, which consists of necessary wirings for electrical power transmission for streamer and digitizers as well as bird coils, and up- and down-link data communication to and from the recorder in the instrument room.

Outputs of 8–16 adjacent hydrophones are grouped with an electrical connection in parallel to form a single recording channel (Fig. 2.8) which enhances the low-frequency response of the hydrophone array. The hydrophone groups are formed by combining either equally or unequally spaced hydrophones with equivalent sensitivity. This is a similar configuration to the receiver arrays used in land seismics to attenuate ground roll and enhance the reflection amplitudes. By grouping the hydrophones, reflected signal amplitudes are enhanced since they are all in-phase while out-of-phase random noise is suppressed. Channels composed of only one single hydrophone in fluid-filled streamers are excessively noisy. Therefore, suitable design of the hydrophone groups may also attenuate the effect of bulge waves, and hence, reduce the mechanical cable noise amplitudes in fluid-filled

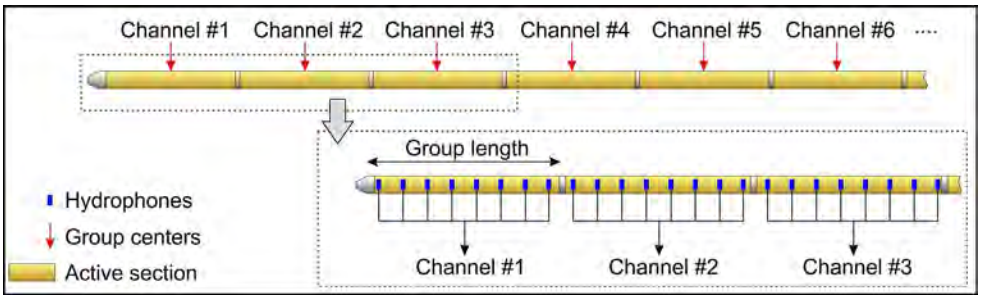


FIG. 2.8 Schematic sketch of hydrophone groups within the active streamer sections: Outputs of eight neighboring hydrophones are grouped to form one recording channel.

streamers. Modern seismic systems have 480–960 active channels per streamer. The center of each hydrophone group is appointed as the exact location of that specific recording channel, and the term group interval, instead of channel interval, denotes the distance between channels in marine seismic acquisition. Group intervals of modern streamers are typically 3.125 or 6.25 m for high-resolution surveys, and it is generally 12.5 m in case of a conventional 2D or 3D seismic survey for hydrocarbon exploration. Thus, a streamer section of 100 m consists of 16 or 8 channels for 6.25 and 12.5 m group intervals, respectively. In practice, smaller group intervals are preferred to keep the horizontal resolution higher and to prevent the spatial aliasing.

Streamers can be grouped as analog and digital types. Analog streamers transmit the seismic amplitudes as electric signals to the recorders, and the data is digitized by a 24-bit analog-to-digital (A/D) converter in the recording equipment. Today, small-size analog streamers are still in common use to acquire commonly single trace high-resolution seismic data for site survey purposes. Modern streamers used for exploration and reservoir development purposes by the hydrocarbon industry and academia are digital streamers in which the perceived signal is digitized within the streamer and transmitted to the recorder in digital form. The digitizing process is maintained by digitizers or modules mounted between the active streamer sections at regular intervals, and there is no need for an additional A/D converter at the recorder. Depending on the streamer configuration used, one digitizer per 16–60 channels is located on the streamer. These are placed between two active sections so that they digitize the analog signals from the hydrophones of both sections, and set up a two-way telemetry along the streamer by transmitting the digitized signal to the recorder.

Digital streamers have several advantages as compared to the analog ones. The diameter of digital streamers is much smaller, since, in transferring the digital data to the recorder, there is no need to place a separate transmission line within the streamer for each recording channel as is the case for analog streamers. This allows us to manufacture streamers with significantly reduced diameters, and it has become possible to spool longer streamers onto the reels of the vessels. Increasing the overall length of a digital streamer is quite easy: It is generally sufficient to append new active sections and digitizers to the tail of an existing spread, in some cases, along with an update in the recording software. Furthermore, digital streamers allow us to redesign the group interval of the streamer according to the requirements of the survey by an option termed trace summing. With this option, it is possible to increase the group interval of the digital streamer by a suitable channel setting in the recording software without physically modifying the existing streamer configuration. Trace summing can be performed in the order of 1:2, 1:3, or 1:4. For the 1:2 case for instance, two neighboring channels are grouped to form a single combined channel simply by adding the outputs of the adjacent channels. Similarly, in order to form 1:3 and 1:4 order trace summing, three and four neighboring channels are grouped into a single channel, respectively. Consequently, group interval and the number of channels involved in the streamer change accordingly. For instance, in the case of a 960-channel digital streamer with a 6.25 m group interval, the number of total recording traces is reduced to 480, and the group interval is increased to 12.5 m when a trace summing of 1:2 is used.

Today, three types of streamers are used in seismic exploration:

- Fluid-filled streamers
- Gel-filled streamers
- Solid streamers

Fluid-filled streamers are considered to be the traditional seismic streamers, having been used in the seismic industry for more than 50 years (Fig. 2.9A). These streamers are filled with a nonconductive buoyant fluid, generally low-density

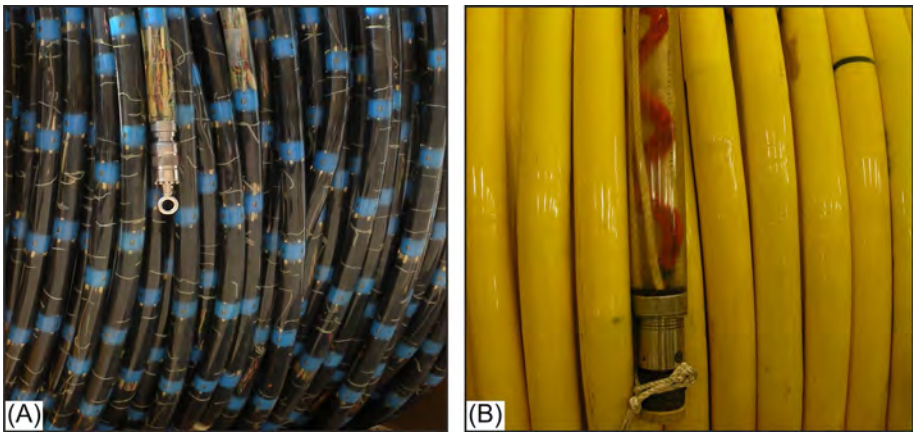


FIG. 2.9 Photos of (A) fluid-filled digital, (B) solid digital streamers.

kerosene, to enable cable buoyancy in the seawater. Although fluid-filled streamers are outdated today, they are still in use, especially along with small-scale seismic systems used by academia and with the single-channel acquisitions for site surveys. This kind of streamers suffers from several significant issues. One of the most important problems with the fluid-filled streamers is safety, since the kerosene is toxic and easily flammable, which may cause environmental hazards and safety or health issues onboard in case of possible damage in the jacket of the streamer encountered during the tow and deployment. Furthermore, such damage to the skin results in salty seawater intrusion into the housing, which may result in serious issues with the electronic components of the streamer and typically results in a spike-like noise appearing as extreme amplitude bursts distributed randomly along the channels within the damaged streamer sections. Therefore, fluid-filled streamers require frequent maintenance, which may ultimately cause downtimes during the acquisition.

Fluid-filled streamers also suffer from noise originated by bulge waves, which are formed by the interactions among the members in the streamer housing, such as kerosene itself, wiring, buoyancy spacers, or strength members, and the streamer skin. Axial vibrations of the streamer travel along the cable as pressure fluctuations resulting in the streamer jacket contracting and bulging out. The bulge waves induce noise into the hydrophones of the fluid-filled streamers. Moreover, these streamers are also quite sensitive to the ripples at the surface of the ocean. High-amplitude acoustic noise at the low-frequency band originating from the ocean surface ripples radiates along the fluid filling the streamer, which ultimately means that the fluid-filled streamers must be towed at relatively higher depths to avoid the ocean surface noise. This situation, however, adversely affects the seismic data resolution, resulting in the collection of seismic data with much narrower frequency band, since the depth of the streamer is an important parameter directly affecting the resolution of the seismic data due to the ghost signal interference (Section 2.5.1.2).

An approach to overcoming the aforementioned shortcomings of the fluid-filled streamers is to use a soft and flexible gel material produced from polyurethane to fill in the streamer housing. Gel-filled streamers have several advantages as compared to fluid-filled streamers. First of all, they are more durable than fluid-filled streamers and they do not induce environmental, safety and health issues. Since the gel is not liquid, no

water invasion occurs if the outer skin is ruptured. In addition, gel-filled streamers do not suffer from bulge waves as do fluid-filled streamers. However, they are sensitive to the noise occurring along the streamer skin due to the turbulent flow, and the hydrophones are mounted into specific cells to isolate them from the noise originating from the cable motion in the water.

The total lifetime of the gel-filled streamers was not very long in the industry, and they have been quickly replaced by solid streamers over the last decade (Fig. 2.9B). Today, almost all of the seismic acquisition service companies use the new technology solid streamers in hydrocarbon exploration, since they have significant advantages over both the fluid- and gel-filled streamers. The filling fluid is replaced by flexible polymer foam in solid streamers (Fig. 2.10A), and therefore they are more robust and resistant to external damage; they require smaller maintenance costs; and they do not present environmental, safety and health issues due to the rupture of the outer streamer skin. Their buoyancy is much more consistent between the active sections as compared to the fluid-filled streamers. In addition, one of the most important advantages of solid streamers is that they are less sensitive to the noise originating from sea swell (Fig. 2.10B). This enables us to tow the solid streamers at shallower depths, resulting in a relatively wider frequency band and hence much higher-resolution seismic data, and acquisition can continue at relatively rough seas. In solid streamers, generally one strength member is located at the center of the cable and the hydrophone is isolated from strength member to reduce the noise. In addition, they are not affected by the bulge waves and also less sensitive to bird noise during the tow. They require less maintenance and they are environmentally friendly since they do not contain kerosene.

In towed streamer acquisition, downgoing energy reflected back from the sea surface is termed ghost and it occurs both at the source and receiver sides (Section 2.2.3). Ghost reflections cause constructive and destructive interference at the reflected signals, and results in the attenuation of the amplitudes of certain frequency bands of the spectrum. These narrow bands in the spectrum are termed ghost notches and they significantly limit the higher frequency end of the amplitude spectrum and severely reduce the resolution of the data, thus reducing the available bandwidth. Removal of ghost signals from the recorded data provides higher

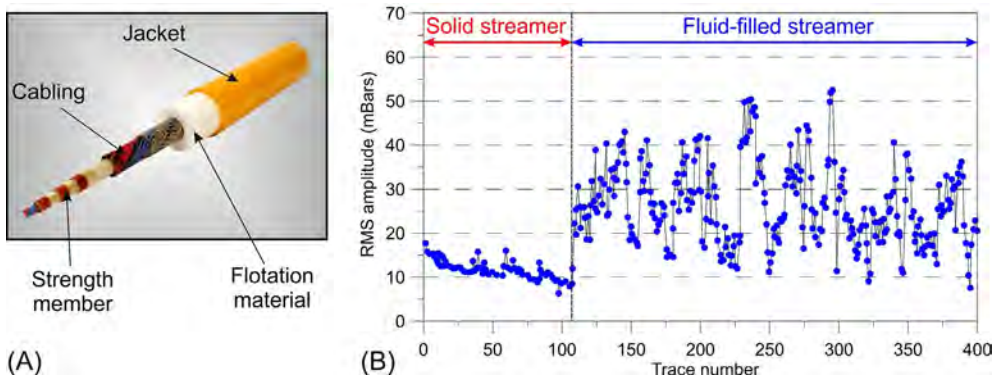


FIG. 2.10 (A) Internal structure of Sercel Sentinel solid streamer, and (B) RMS noise amplitudes for solid and fluid-filled streamers in moderate sea conditions measured using a fluid-solid combined streamer. *After Dowle, R., 2006. Solid streamer noise reduction principles. SEG Technical Program Expanded Abstracts 2006, pp. 85–89.*

resolution, enhancing the amplitude spectrum. A much higher-resolution data termed broadband seismic data can be obtained by assembling extra sensors into the towed streamers in addition to the conventional pressure hydrophones to cancel the ghost signal. In the last decade, multisensor towing streamer technology has been under development. Currently, there are three types of multisensor recording systems on the market:

- GeoStreamer (PGS)
- Sentinel MS (Sercel)
- IsoMetrix (Schlumberger)

These systems record pressure data using a hydrophone and one or two additional acceleration components for both crossline and vertical wave fronts to obtain the measurement of full upgoing and downgoing seismic wave field. The result with a 3D deghosting is an enhanced broadband subsurface image used for high resolution mapping and reservoir monitoring. This technology was actually developed by PGS in 2007 when they introduced their first multisensor solid streamer with hydrophones and motion sensors, called GeoStreamer, which uses a dual-component technology to measure both pressure and vertical component of the particle velocity simultaneously (Tenghamn et al., 2007). The particle velocity measurements along with the pressure fields are used to decompose the seismic wave field into the upgoing and downgoing pressure and velocity wave fields (Carlson et al., 2007). The ultimate goal is to eliminate the effect of ghost reflections to obtain broadband seismic data, and using multiple sensor measurements, the approach is quite simple: The upgoing pressure and velocity wave fields are of the same polarity. Since the downgoing pressure field, the ghost signal, is reflected from the sea surface (Fig. 2.11A), its polarity is reversed in the hydrophone output, whereas it has the same polarity as the upgoing velocity wave field in the particle velocity sensor (Fig. 2.11B). After a careful processing, much higher resolution data consisted of only the upgoing pressure field with a relatively wider spectrum is obtained if the measurements of pressure and velocity wave fields are summed up (Fig. 2.11C). Fig. 2.12 shows data examples for pressure and velocity sensors and their amplitude spectra.

Following the success of the GeoStreamer, similar multi component solid streamers have been developed in recent years. Sentinel MS is a radially symmetrical three-component (3C) solid streamer with a strength member at the core. It contains a hydrophone to measure the pressure field, and two orthogonally mounted analog accelerometers to directionally measure the crossline and vertical wave fronts, as well

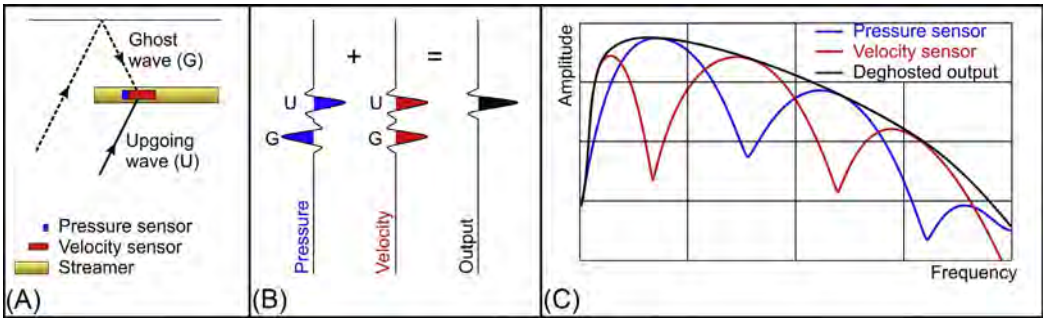


FIG. 2.11 (A) Up- and downgoing signal ray paths measured by the pressure (hydrophone) and velocity sensors, (B) corresponding schematic measurements for upgoing (U) and ghost (G) signals, and (C) comparison of amplitude spectra from pressure and velocity fields as well as the final upgoing pressure field.

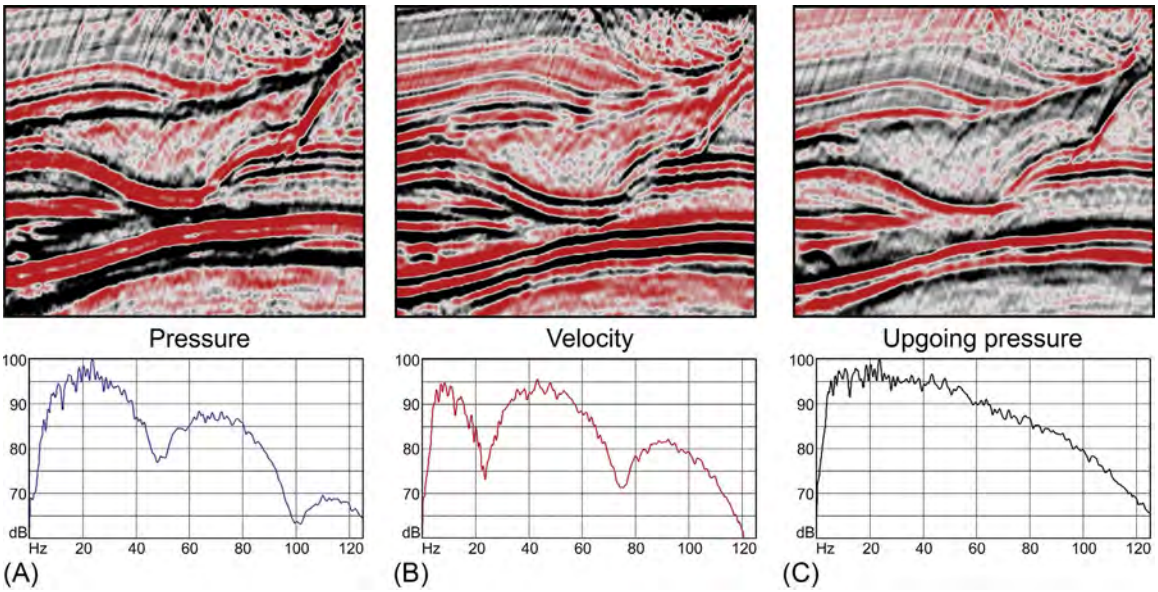


FIG. 2.12 Comparison of (A) pressure, (B) velocity sensor measurements, and (C) computed final upgoing pressure field data. Corresponding amplitude spectra are shown in the bottom panels. *After Carlson, D., Long, A., Söllner, W., Tabti, H., Tenghamn, R., Lunde, N., 2007. Increased resolution and penetration from a towed dual'sensor streamer. First Break 25, 71–77.*

as a separate tilt sensor to correct the orientation of the sensors for each recording channel to obtain a true vertical and horizontal measurement. Mellier et al. (2014) have shown that hydrophone data separates the signal and noise at very low frequencies, whereas the accelerometer data is quite noisy at frequencies up to 24 Hz. Therefore, the accelerometer signal is used to reconstruct higher frequency components, especially those lost at the ghost notches, for a careful summation process between hydrophone and vertical accelerometer data.

The IsoMetrix system utilizes a single-sensor triaxial microelectromechanical accelerometer technology on Nessie-6 (Western Geco) point receiver seismic streamer, which measures pressure and accelerations related to the vertical and crossline gradients of the pressure field. The acceleration measurements are used to obtain pressure gradients for recovering the missing frequency components at the ghost notches and for dealiasing in crossline direction (Bunting et al., 2013). Since the ghost effect is eliminated by IsoMetrix technology, it becomes possible to tow the streamer at higher depths, which provides more low frequencies and widens the overall frequency band (Breistøl, 2015).

Dual sensor data needs some specific preprocessing applications. The velocity sensor data is incorporated only for the frequencies typically higher than 20 Hz since it is too noisy at lower frequencies. Therefore, velocity sensor data for low frequencies must be predicted from hydrophone record. The data is separated into up- and downgoing pressure and velocity wave fields, where both sets of data can be extrapolated to any desired recording depth, and then a conventional processing flow can be applied (Carlson et al., 2007).

Recording with dual sensor streamers has several significant advantages. First, the bandwidth of the data is considerably extended by

removing the ghost notches from the amplitude spectrum, which ultimately provides much higher resolution and imaging of the smaller traps in relatively complex stratigraphic environments. The streamers can be towed at any depth and restriction of the available frequency band depending on the streamer depth is not an issue. Therefore, utilizing the collocated pressure and motion sensor technology also allows the operators to tow the streamers deeper at a quieter and more stable environment to prevent the noise from the sea surface, which provides longer operating times, even during the rough seas, resulting in less downtime. Deeper towing also provides better recording of low-frequency amplitudes, which ensures a better illumination of deeper stratigraphy.

2.1.3 Marine Seismic Energy Sources

The seismic sources used in conventional marine seismic surveys produce high-amplitude acoustic signals by a positive shock wave due to the sudden pressure increase. The signal generated is of a wide frequency band with a dominant frequency of approximately 60 Hz for conventional surveys, and can penetrate into the subsurface sediments up to 10 km deep. Even though explosive sources were used for seismic signal generation in marine acquisition until the 1950s, they have been replaced by repeatable sources because of their environmental and safety issues. Different marine seismic energy sources are used for various purposes in offshore surveys today; each has its own advantages and shortcomings:

- Sparker sources (GeoMarine Survey Systems, SIG France and Applied Acoustics)
- Air guns
  - Water gun (Sercel)
  - GI gun (Sercel)
  - Sleeve gun (Seamap)
  - G gun II (Sercel)
  - LongLife (LL) gun (Teledyne Bolt)

Sparkers are high-resolution seismic sources generally used with single-channel surveys, or with short analogue streamers with 24- to 48-channel acquisitions. The seismic signal is produced by a sudden discharge of several thousand volts of electrical voltage into the water. Electric discharge is done via specific cables, termed electrodes mounted on a catamaran-type carrier (Fig. 2.13A). Today, modern sparker systems use several electrodes known as multitip sparker sources, which produce a seismic energy typically between 160 and 16,000 J. Sparker electrodes are used for high-resolution seismic studies, generally for site survey purposes, to map shallow stratigraphy as well as active tectonism in continental margins, and geo-hazards before drilling. Although the penetration of the signal is relatively low, ranging from a few tens of meters to approximately 500 m depending on the power level of the source, resolution of these systems is considerably high since the multitip arrays produce narrow wavelets with a significantly wide amplitude spectrum, between 50 and 2000 Hz.

The standard seismic source used in marine seismic exploration today is the air gun, which produces seismic signal by a sudden discharge of high pressure air into the water. The pressurized air generated by seismic compressors is supplied to the air guns via high pressure hoses, and released into the water column initiated by a time break signal from the gun controller at each shot point. High-capacity air compressors supply the compressed air, typically at 2000 psi, and they can recharge the air guns during the shooting at every 10–15 s. The most important disadvantage of the air guns is their bubble noise (Sections 2.2.2 and 3.2) and several air guns with different volumes should be used to suppress the bubble noise, which is known as array tuning. A single air gun can be used for high-resolution shallow surveys, whereas an air gun array consisting of several air guns within the subarrays is utilized at 4–10 m depth during the conventional seismic operations by the oil

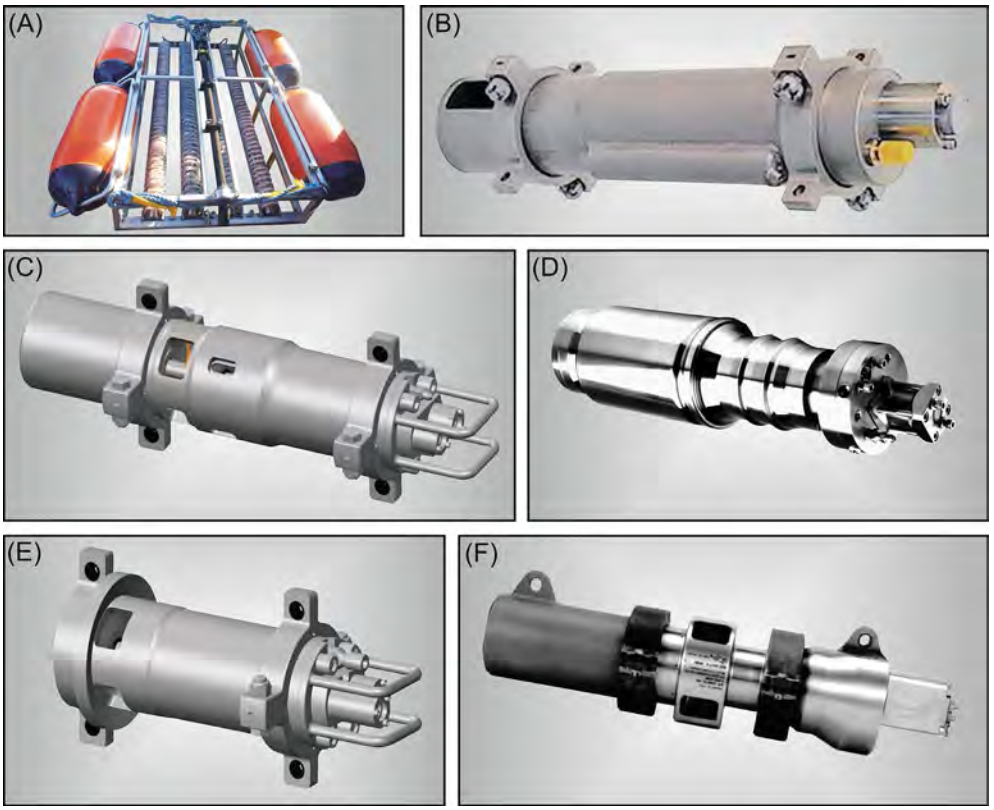


FIG. 2.13 Common marine seismic energy sources. (A) GeoMarine 6000-J sparker array, (B) water gun (Sercel), (C) GI gun (Sercel), (D) sleeve gun (Seamap), (E) G gun (Sercel), and (F) LL gun (Teledyne Bolt).

and gas industry. The volume of each air gun typically ranges from 10 to 250 in^3 and total gun volume within an air gun array varies from 1000 to 8000 in^3 for a modern 2D or 3D seismic vessel. For most air gun types available in the market, it is also possible to create different size volume chambers during the operation using dedicated plastic volume reducers for a better array tuning. A detailed explanation of the air gun source signals and signatures, gun arrays and their performance parameters, etc., is given in Section 2.2.

The basic operation of a water gun is similar to that of the air gun, but a shuttle is used to discharge the water, instead of compressed air, into the water column to produce a vacuum bubble (Fig. 2.13B), and the seismic signal is generated during the collapse of this bubble. Water gun source signatures need a signature deconvolution process since it has pressure variations, termed precursors, due to the initial acceleration of the water from the gun chamber appearing before the main pressure signal is formed, which makes the source signal of the water gun a mixed-phase wavelet (Lee et al., 2000). The main advantage of the water guns is that they do not have bubble oscillations since they do not discharge air, and therefore, there is no need to perform an array tuning to suppress the bubble noise. They can generate relatively high frequencies, and hence are suitable for high-resolution surveys while their low-frequency components

are rather limited, which results in the low penetration of the seismic signal. Although they are still in use commonly by academia today, the production line of water guns stopped in 2014 and they are no longer manufactured.

The GI (generator/injector) gun is a specific air gun type that suppresses its own bubble effect (Fig. 2.13C). Its working principle is given in Section 2.2.2. A GI gun has two independent air chambers termed the generator and injector chambers, which are fired independently. The generator chamber generates the main seismic pulse, while the injector chamber is fired a few milliseconds later to prevent the collapsing of the air bubble produced by the generator chamber to eliminate the bubble noise. GI guns are manufactured as three types: 210 in^3 (105 + 105), 255 in^3 (150 + 105), and 355 in^3 (250 + 105). A specific type of GI gun with 60 in^3 (30 + 30) is known as mini GI. GI guns can be designed either as true GI mode (where the generator volume is much smaller than the injector volume), or as harmonic mode (where generator and injector volumes are equal). The true GI mode configuration should be used for a complete suppression of the bubble. Even though the maximum output signal amplitude of the GI guns is lower as compared to the conventional air guns, the primary-to-bubble (PBR) ratio of the generated signature is significantly increased since it can suppress its own bubble. A properly designed GI gun, therefore, can be used as a single gun instead of an air gun array and is generally preferred for high-resolution seismic surveys because of its high PBR value and wide amplitude spectrum. GI guns have their own hydrophones to observe and record the near-field source signatures and bubble amplitudes.

Sleeve guns are specific type of the conventional air gun, which use single 360-degree discharge ports to release the compressed air into the water column instead of the smaller multiple ports used by traditional air guns (Fig. 2.13D). This design provides a complete spherical air bubble. When they were first introduced to the market in 1984, the largest available volume was 40 in^3, which caused issues in the design of large arrays since it was required to use several sleeve guns to form an array of 3000 in^3 volume in total. Today, sleeve guns are manufactured as two series, sleeve gun-IC (10, 20, and 40 in^3) and sleeve gun-IIC (70, 100, 150, 210, and 300 in^3). Sleeve guns are relatively safe to operate since they can be deployed into the water and retrieved onboard without being pressurized.

One of two industry standard air gun types used by the hydrocarbon industry is the G gun II, which provides recoilless shooting with a reliable acoustic performance (Fig. 2.13E). G guns can also be deployed into the water and retrieved onboard without being pressurized. They are manufactured in a single consistent base design and various configurations can be achieved by a suitable replacement of different casings, which allows creating different volume sizes. Today, G guns are manufactured in four different sizes as 150, 250, 380, and 520 in^3. It is also possible to form different chamber sizes with various volumes using plastic volume reducers except for 520 in^3. Specific types of G guns with 12, 20, 24, 40, and 60 in^3 also exist for high-resolution studies and are known as mini G guns.

The other industry standard air gun is the Long Life (LL) gun, which produces stable source signature with a considerably high peak signal output (Fig. 2.13F). They are quite reliable and require significantly low maintenance during operations. Today, there are three LL gun models with different volume ranges: 1500LL (from 70 to 2000 in^3), 1900LLX-T (from 10 to 250 in^3), and 2800LLX (from 5 to 120 in^3).

2.1.4 Gun Control Systems

Gun controllers are used to control firing of the air guns within the gun array at each shot point. They transmit electrical signals to solenoid valves of each individual air gun to fire exactly at the same time, termed the air gun aim point. Gun control units of modern gun

controllers are mounted onto the gun strings and are known as distributed gun control systems. There must be exact time synchronization between the integrated navigation system, gun controller and seismic recorder (Fig. 2.14A) to synchronize the actual gun firing time and start of the data recording. The need for this accurate timing is due to the fact that it is necessary to align the peaks from primary bubble pressures of each specific air gun in an array at each shot location.

Gun controllers also have hydrophone inputs to record near-field source signatures of the air guns in the arrays. The gun signatures are recorded for each shot and analyzed to ensure that the guns are working properly and there is no misfire, auto fire or air leaks. The signatures are also used to ensure that the time-break signals are aligned at the aim point (Fig. 2.14B). Commonly, there is an offset (generally less than 2 ms) between the time break and actual gun fire. Recorded near-field signatures can be used to incorporate further signature processing to increase the temporal resolution of the seismic data. Modern gun controllers also have inputs for gun array depth and air pressure for each string provided by depth and pressure sensors, respectively (Fig. 2.14C).

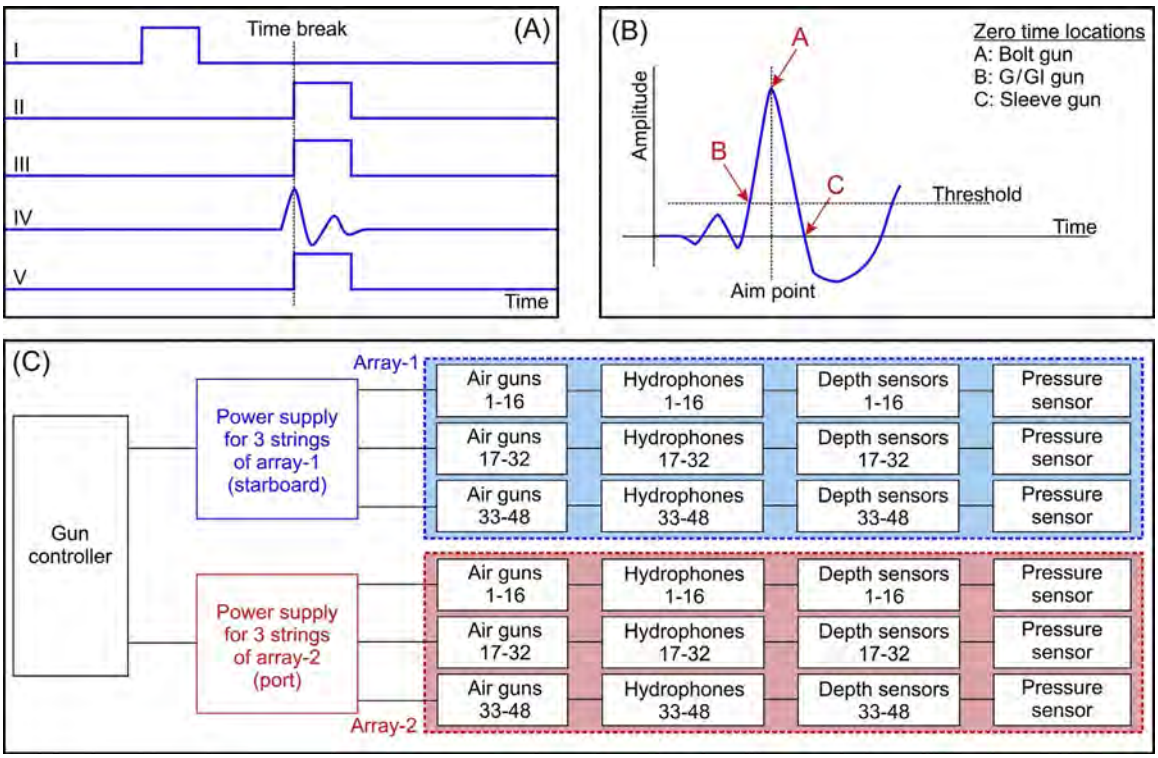


FIG. 2.14 (A) A schematic display of timing signals between the integrated navigation system (INS), gun controller and recorder. I: fire command from INS to gun controller to initiate the firing sequence, II: trigger from INS to recorder to initiate the recording, III: recording starts at the recorder, IV: guns are fired by the gun controller, V: confirmation from the gun controller to INS when the guns are fired. (B) Schematic display of the near-field signature hydrophone output with the specific time offsets to locate the zero time alignments for different gun types. (C) Block diagram of an example gun system with two arrays, each consisting of three strings with 16 air guns.

2.1.5 Streamer Depth Controllers

In practice, the streamer is towed at a depth range between 3 and 10 m to prevent the noise interference from the sea surface. During the data acquisition, depth of the streamer can be controlled by the movements of the wings of specific external devices called birds attached to the streamer cable. Depth leveler birds are mounted at regular intervals along the streamer cable commonly with a maximum separation of 300 m. Only streamer depth control units are required for 2D seismics. In 3D surveys, however, streamer positioning or steering equipment used to maintain the depth and lateral position of the streamers are also required (Section 2.3.2). Currently, there are two types of streamer depth control units on the market (Fig. 2.15A and B):

- DigiBird (ION Geophysical)
- Navigator bird (OYO Geospace)

Birds have no electrical connection with the streamer internal components and the power required for bird units is provided by their own internal battery pack. The communication with the birds is maintained via electromagnetic communication coils located within each active and stretch section of the streamer (Fig. 2.15C), where the birds are attached as close as possible using specific collar pairs. All communications between the birds and bird control units in the instrument room are handled electromagnetically via communication coils within the streamer and the birds.

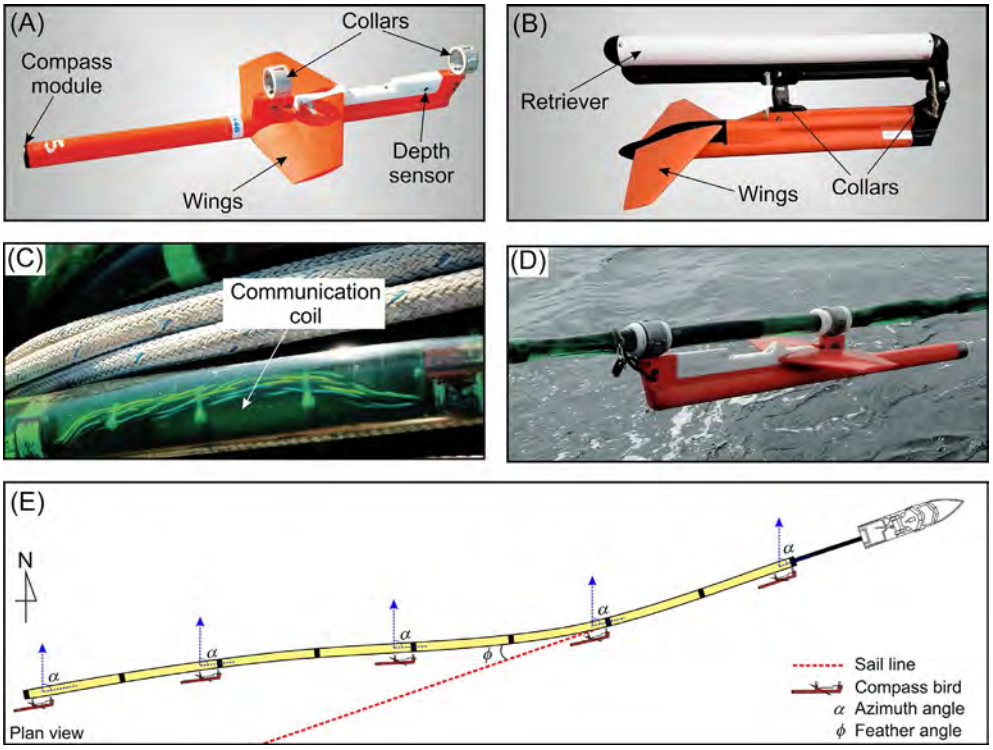


FIG. 2.15 (A) ION 5011 CompassBird, (B) OYO Navigator bird and retriever, (C) electromagnetic communication coil within the fluid-filled streamer, (D) ION 5010 DigiBird attached to the streamer. (E) Compass birds are used to monitor the azimuth angle (α) of the streamer during the survey to calculate the possible cable feathering (ϕ).

Each bird transmits its depth information obtained from its depth sensor to the control unit. The wing angles of the birds are modified during the acquisition to maintain the depth of the streamer generally within a depth range of ±1 m. This process is done automatically: A target depth to each bird unit is assigned, and control software keeps the birds at the desired depth range during the survey by modifying the wing angles automatically. Depths and wing angles of each bird are read by the software normally at each shot position and graphically displayed on the screen, fed into the navigation system and logged into the disk files for further offline QC processes after the survey.

Some birds are equipped with a fluxgate magnetometer, termed compass birds, which measures and transmits the azimuth angle of the birds in addition to the depth information (Fig. 2.15A). If the compass birds are mounted on the streamer at regular intervals, then it becomes possible to observe the feathering angle of the streamer in areas of strong surficial currents and streamer bending at each line change (Fig. 2.15E). Furthermore, a specific inflatable device can also be mounted onto the birds, termed streamer recovery device or retriever, which recovers the streamer sections in case of an accidental failure during the acquisition (Fig. 2.15B). The retrievers are placed above the cable leveling devices and are automatically activated to inflate when the streamer sinks to a depth of 48 m.

2.1.6 Seismic Recorder

The seismic recorder is the system that receives all the seismic amplitudes at each time sample from all available streamers at each shot, and stores the raw seismic data into its internal hard disk drivers or external storage devices. In analog seismic systems, the recording unit also has an analog-to-digital (A/D) conversion unit. In modern digital systems, there is no need to have an A/D converter since the incoming data is already digitized by modules mounted to the streamer(s). Seismic recorders control the initialization of the streamers and digitizing modules, and analyze some specific information from the streamer cables, such as temperature and pressure information on the digitizers or the tension on the streamers if a tension sensor is available. Some important data acquisition parameters such as trace summing, record length and sampling rate are set in the recorder.

Modern seismic recorders are of low instrument noise, harmonic distortion and power line interference. They are capable of recording tens of thousands of channels from several streamers as well as automated analyzing and QC methods (Lansley, 2006), and also recording and managing the auxiliary channels. They are expected to have a dynamic range as high as possible. The dynamic range is defined as the ratio of largest signal amplitude that can be recorded to the smallest amplitude above the system noise (Section 2.5.2.4). Seismic recorders may commonly have various frequency filters. The most common filter types are specific low-pass antialiasing and 50- or 60-Hz notch filters to prevent recording of the aliased signal and power line interference, respectively.

Starting with a trigger signal from the integrated navigation system, the seismic recorder immediately initiates data logging from all available active and auxiliary channels into the disk and/or magnetic tape units for a predetermined time span, that is, the recording length. It also opens the navigation port and receives the shot and channel positions from navigation system to record into the seismic data headers. Modern recorders perform demultiplexing and DC offset removal on the seismic data before constructing the raw shot gathers. The raw seismic data is recorded in a specific format, as binary coded data files. A number of sophisticated seismic data formats are defined by the Society of Exploration Geophysicists (SEG). The most common format types are known as SegD for raw data and SegY for data exchange between the different processing and interpretation platforms (Section 5.2).

2.1.7 Integrated Navigation System

Modern 2D and 3D seismic acquisition systems use complex navigation software systems which integrate the inputs from several different sensors to calculate the positions for vessel reference location, streamers, gun arrays, paravanes, tail buoys, etc. (Fig. 2.16). Currently there are four different integrated navigation software packages available on the market to use with 2D and 3D seismic surveys used by hydrocarbon industry:

- SeaPro (Sercel)
- Orca (ION Geophysical)
- Spectra (Concept Systems)
- TRINAV (Western Geco)

Normally more than one differential GPS (DGPS) receiver, each of which provides navigation information with less than 1-m accuracy, is used to determine the vessel position in real-time. Generally, a global DGPS correction service is used to apply DGPS correction to the received GPS signal. For a complete solution, output of a digital gyrocompass is also used to obtain the vessel azimuth, or heading. Water depth information below the keel is used for some specific processing stages, such as suppression of multiples, and is provided into the integrated navigation system (INS) from a hull mounted single-beam echosounder. INS calculates the position of the next shot point and issues a trigger signal to the gun controller and seismic recorder to fire the guns and to initiate the recording simultaneously. Modern INS software packages allow autopilot option to control the vessel from instrument room, which provides efficient maneuvering during the line changes.

Relative GPS (rGPS) systems are used to determine the positions of the moving objects, such as buoys, relative to another object, such as a survey vessel. rGPS transponders are mounted onto the buoys of source arrays, tail buoys and paravanes. The INS also receives the rGPS information from the transponders and computes the positions of the dynamic

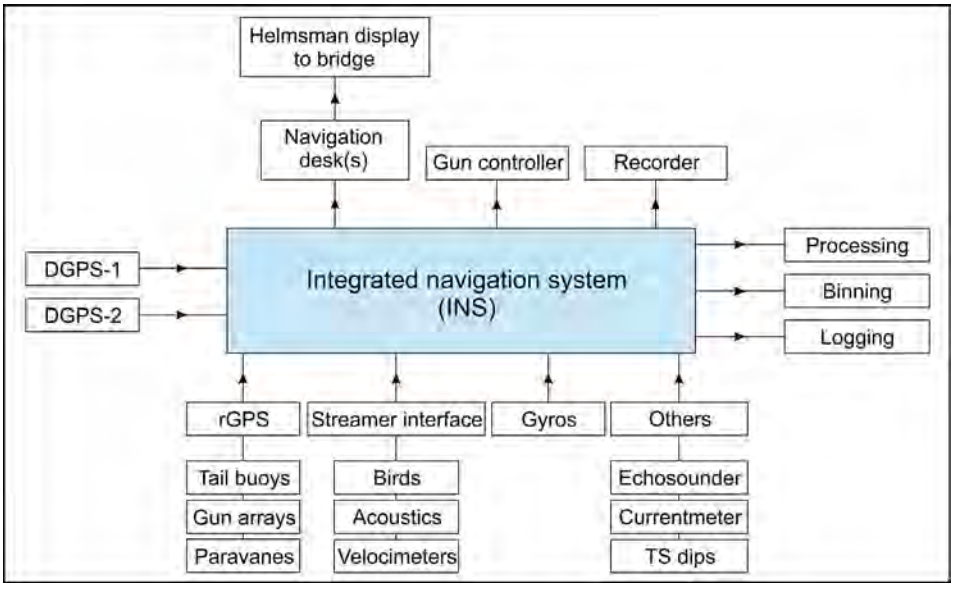


FIG. 2.16 Main components and peripheral systems of an integrated navigation system (INS) used for 2D and 3D seismic acquisition.

buoys relative to the vessel reference position. The accuracy of rGPS systems is commonly less than 1 m.

INS software has also an interface to the acoustic ranging system to display and log the positions of the streamers. Acoustic ranging instruments (Section 2.3.4) use acoustic signals to communicate with each other in order to keep the streamer separation in the determined lateral range. Since the communication is done in through acoustical means, we definitely need to know the sound velocity in the sea water during the survey, since it varies with location and time (Section 1.1). Therefore, a couple of velocimeters are generally attached to the head and tail of one or two streamers for 3D surveys to measure the sound velocity in real-time as an input to INS to accurately compute the acoustic ranges between the streamers. In some cases, specific sensors may be used to measure temperature (T) and salinity (S) as a function of water depth, which is termed TS dips. These measurements are used to compute the sound velocity in the water column, which is entered into the INS for acoustic ranging computations in real-time. In some cases, vessels also have acoustic Doppler current profiler (ADCP) inputs to the INS to obtain the local surficial currents to predict the streamer feathering.

A GPS receiver provides only the position of its antenna location. A seismic vessel, however, has several offset positions for various sensors, such as gyrocompass or motion sensor, or specific locations on and around the vessel superstructure, such as the location of vessel reference position, location of vessel stern, transducer of the single-beam echosounder or center of source arrays, etc. (Fig. 2.17). Lateral and vertical separations between the equipment are termed nominal offsets, which define the predetermined towing and acquisition configuration of the seismic spread with respect to the center of navigation or vessel reference point. These offsets are set into the INS to calculate their exact positions during the survey for logging. INS software receives the positioning information from the aforementioned peripheral systems to compute the navigation for the vessel reference position (VRP), as well as the exact positions of predefined offsets around the vessel with respect to the VRP. INS also computes the source and all available receiver positions in real-time.

INS software packages perform navigation data logging during the acquisition for further navigation processing, offline QC and binning purposes. The log data files are generally in a specific format termed UKOAA files. Raw and processed navigation data files are commonly distributed in UKOAA P2/94 and UKOAA P1/90 format, respectively. While raw P2 files contain raw survey observations of navigation, generally in range and bearing format such as heading, rGPS or acoustic ranging data, processed P1 files comprise source and receiver positions as well as common midpoint (CMP) coordinates. The information logged by INS may vary for each specific survey and for each specific seismic system. However, it commonly includes positions of the vessel reference position, shot and receiver locations, center of source (COS), heading, streamer depths from birds, locations of the CDPs, vessel speed, system timing information, lateral separations of source and streamers, etc. Using the navigation logs, fold distribution is computed in regular intervals in 3D surveys.

2.1.8 Tail Buoys, Dilt Floats and Paravanes

Each streamer ends up with a tail buoy (Fig. 2.18A and B), which is equipped with a flashing beacon for night time vision, a radar reflector to be easily detected by the nearby vessels, and an rGPS transponder (Fig. 2.18C) to monitor the location and direction of streamers during the acquisition. Some tail buoys are powered from specific tail buoy power modules mounted at the tail of the streamers, while others have their own power generator from a small-

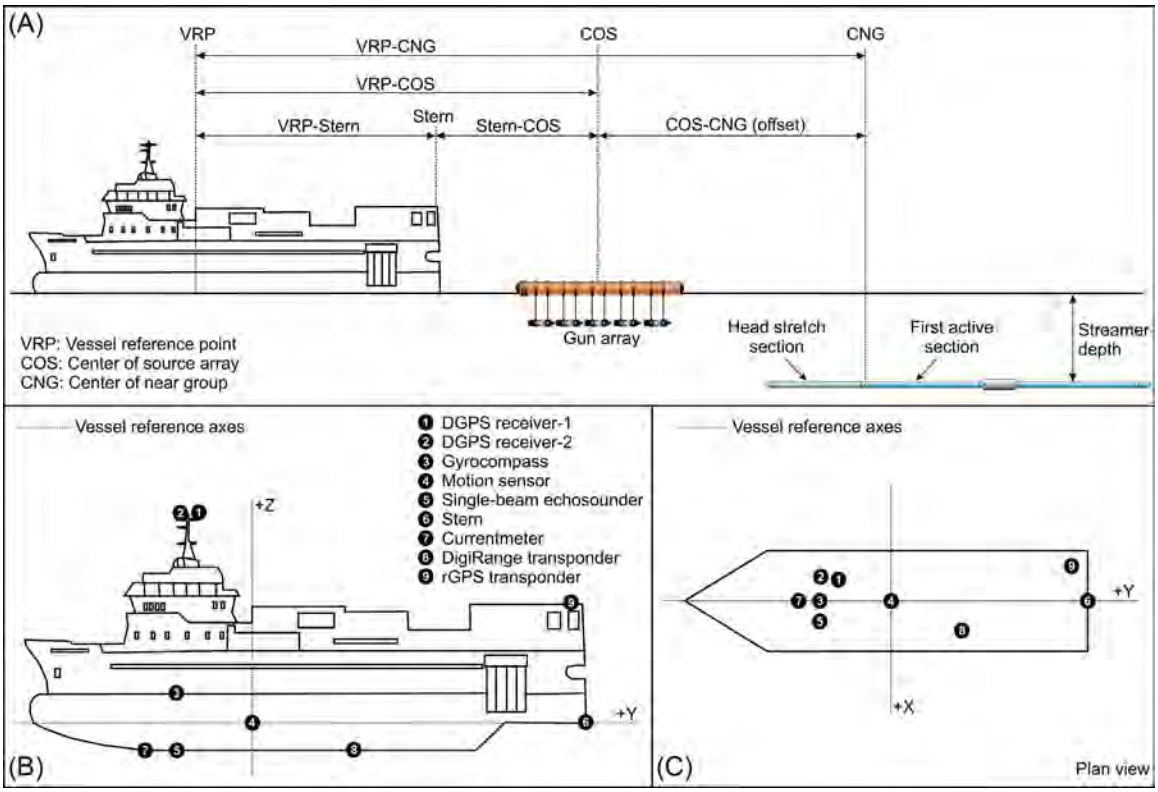


FIG. 2.17 (A) Side view of general vessel offsets analyzed by INS; (B) side view and (C) plan view of example static offset locations of a seismic survey vessel.

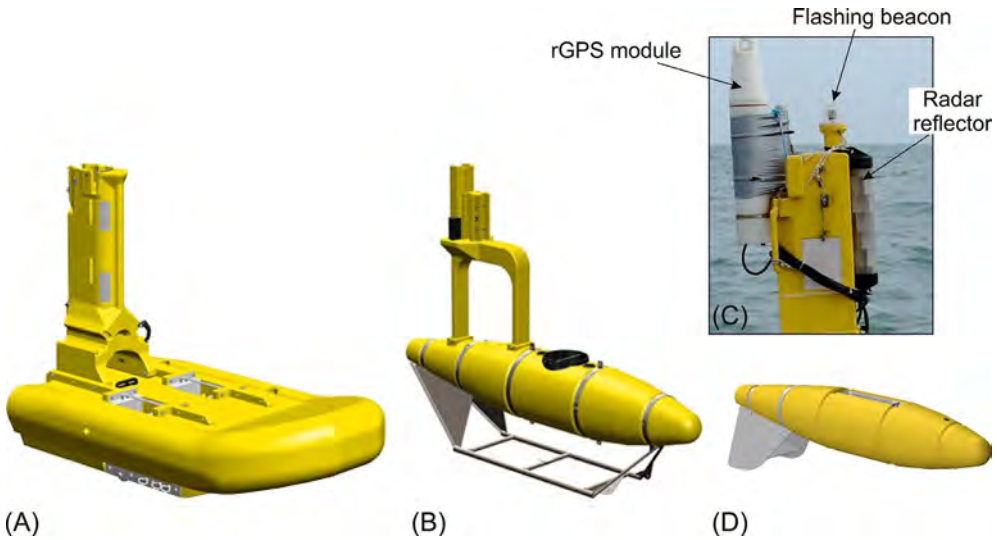


FIG. 2.18 (A) 900- and (B) 1000-liter tail buoys produced by PartnerPlast, and (C) additional equipment typically attached on a tail buoy. (D) 1000-liter dilt float produced by PartnerPlast.

scale propeller at the bottom. The front end of each streamer is located with a specific buoy termed a dilt float or front buoy (Fig. 2.18D). In some dilt float models, the depth of the streamer can be arranged with an adjustable steel cable. Both tail buoys and dilt floats are made from polyethylene material.

The lateral distance between the streamers is fixed by deploying a specific cable called a spreader or super wide cable. There is only one spreader cable in 2D vessels, while two identical spreader cables are used in 3D surveys, one for each side of the vessel (Fig. 2.3). Spreader cable is dragged from the vessel by paravanes at both sides of the vessel, which provide correct tension to the spreader cables to extend from the vessel during the deployment. A paravane includes a cylindrical float and a frame with deflectors attached to the float, and is generally suspended at each side of the survey vessel when not deployed (Fig. 2.19A). The deflectors produce lateral force applied to the spreader cable, which directly depends on the shape of the paravanes and tow speed. Since the lateral forces applied to the outermost paravane in 3D surveys may be excessive when the vessel turns, it may be necessary to lower the vessel speed during the line change. In order to determine the accurate position of the paravanes, they are also equipped with rGPS transponders (Fig. 2.19B).

2.1.9 Lead-in and Deck Cables

Streamers are coupled to the seismic vessels by strong lead-in cables, which are used to deploy the streamers from the vessel and to maintain the tow distance of the streamers from the stern of the vessel. Lead-in cables connect the front end of the streamer to the deck cable via a slip-ring mounted on the axial part of the streamer reel (Fig. 2.20A). It includes electrical or optical conductors that transmit the seismic and other streamer data from the sensors on the streamers. The signal is transmitted from lead-in to streamer interface unit located in the instrument room, via a specific cable known as the deck cable (Fig. 2.20A). Signal transmission wires within the lead-in cable are surrounded by several layers of helically wound steel wires, termed armor, to protect the conductors. Lead-in cables are usually deployed with cable fairing, which is required to streamline the flow around the cable (Fig. 2.20B). Cable fairing also reduces the cable vibration, known as cable strum, due to the vortex shedding during the tow.

2.2 AIR GUN ARRAYS

Air guns are mechanical devices that store and rapidly release the compressed air from their internal air chambers through four small

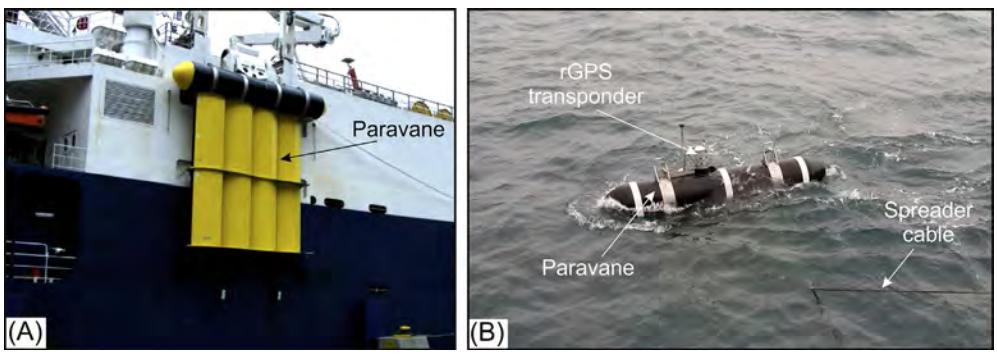


FIG. 2.19 (A) A paravane suspended at the port side of the survey vessel when it is at the dock, and (B) a paravane during deployment.

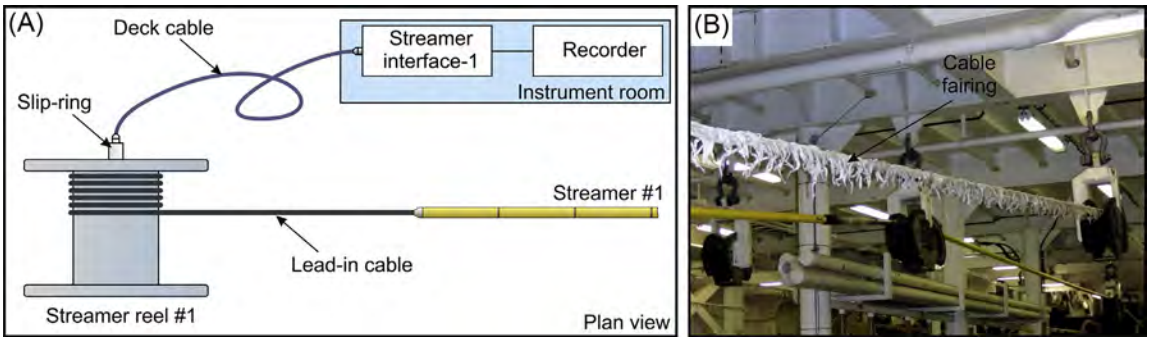


FIG. 2.20 (A) Schematic illustration of lead-in, deck cable and slip-ring assembly for streamer number 1. (B) Cable fairing on the lead-in cable to reduce the strum noise.

ports whenever a shot point is reached during the survey. When it is fired, the energy in the released air is converted into sound waves, which generate the seismic signal (Dragoset, 2000). The capacity of an air gun is expressed by the volume of its internal air chamber in liters, or more commonly, in cubic inches. Typical air reservoirs of conventional air guns range from 20 to 300 in^3.

Air guns today are conventional seismic sources for seismic exploration at sea. Although it is possible to use one single air gun for shallow surveys, especially for academical or site survey purposes, in the surveys for the hydrocarbon industry, several air guns are combined to form gun arrays, which typically consist of 18–48 air guns of different volumes with a total volume of approximately 3000–4500 in^3 towed at 4–10 m depths, usually at 6 m. These arrays are capable of producing seismic signals >50 bar-m pressure pulses, which have a frequency band of approximately 5–120 Hz. The operating air pressure of the air gun arrays is typically 2000 psi (approximately 140 bars), and the output signal amplitude is directly proportional to the air pressure applied. Air guns have significant advantages as compared to the other seismic sources used in marine seismic exploration, including:

- The source signature of air guns can be modeled.
- They are repeatable sources which can easily be controlled from the instrument room.
- They are relatively cheap and require little maintenance.
- They have almost no negative effect on marine life.

2.2.1 Air Gun Principles

Each air gun has two air chambers, shown by I and II in Fig. 2.21A. In its armed or charged position, both chambers are filled with compressed air supplied by air compressors via high-pressure air hoses. The major chamber that produces the main seismic signal is the lower one. Chamber I is fed from air inlet at the top, and chamber II is filled with the air passing through the small orifice in the shank of the shuttle. The air gun is sealed, or armed, since the area of upper flange of the shuttle is larger than that of the lower flange, which ultimately produces a downward or holding force when it is pressurized.

The gun is fired with an electrical signal sent to the solenoid valve that allows the compressed air in chamber I passes underside of the upper flange (Fig. 2.21B) via a small orifice (shown by A in Fig. 2.21A) through the solenoid valve. This results in an upward force applied to the shuttle which suddenly moves up to discharge

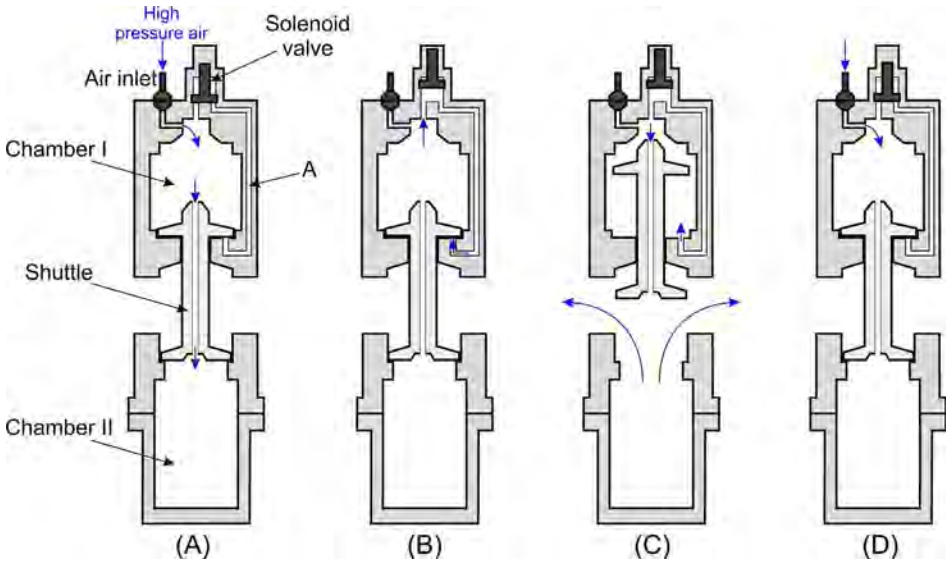


FIG. 2.21 Schematic drawing of an air gun (A) in armed position, (B) solenoid valve is open and the air is fed beneath the upper flange of the shuttle via orifice A, (C) shuttle moves up and the gun is fired, and (D) air gun reverts to its initial armed position.

the compressed air in chamber II into the water rapidly (typically in 1–4 ms) through the four discharge ports (Fig. 2.21C). Since the air in chamber II is released into the water, the air pressure in chamber I increases again to produce a downward force on the shuttle, and it returns to its initial or armed position, which allows the chamber II to fill with the compressed air again (Fig. 2.21D).

The bubble discharged into the surrounding water expands rapidly because the pressure within the exhausted air bubble far exceeds the ambient hydrostatic pressure at the beginning. However, it suddenly starts to shrink soon after the initial discharge since its surficial area extends during the expansion, which produces an additional acoustic signal, termed bubble effect (Section 2.2.2). The air can only escape from an air gun's ports at a certain limited rate, and this throttling effect diminishes the amount of air that can be discharged during the rise time of the first impulse (J. Diebold, pers. comm.). When we put a hydrophone close to a discharge port of an air gun, we get the typical near-field source signature. When the ghost interference is incorporated, the output signal from the air gun changes into a far-field signature (Section 2.2.4).

The maximum output signal amplitude of an air gun is directly proportional to the cubic root of the gun chamber volume. The reason for this is that the expanding bubble is pushing the water radially away from its center, and the volume depends on the radius cubed. In practice, an air gun of 250 in^3 (cubic root is 6.3) produces only 2.3 times higher amplitude than an air gun of 20 in^3 (cubic root is 2.7) although it has 12.5 times larger air chamber volume. This is also true for the gun arrays: the signal amplitude generated by a larger volume array is not much higher than a small volume array. For instance, an 8000 in^3 array produces only twice the amplitude of a 1000 in^3 array, although the total volume ratio between them is 8. This situation leads us to increase the number of guns within the array instead of increasing the volumes of

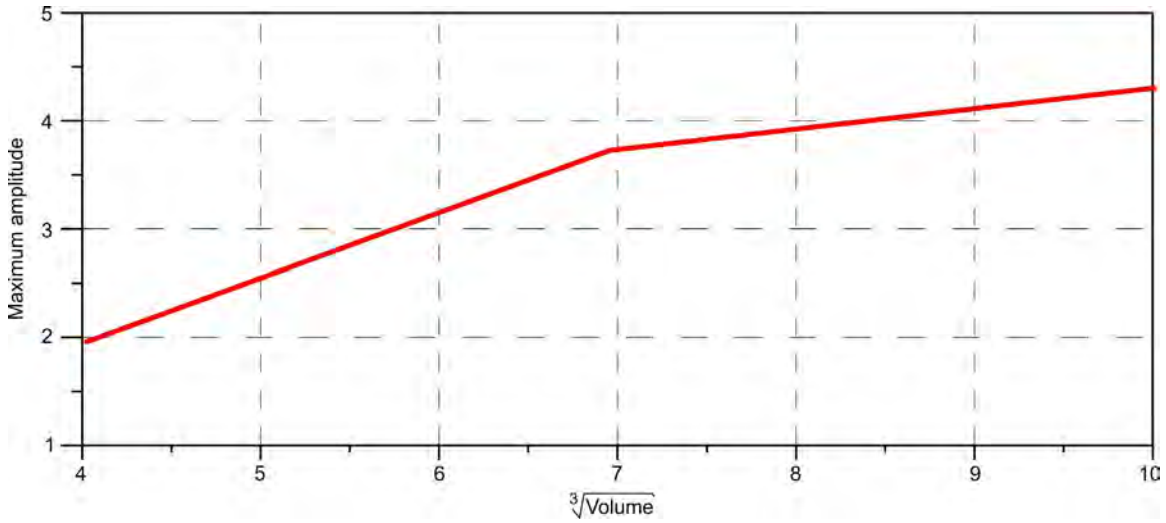


FIG. 2.22 Variation of peak amplitude with the cubic root of total air gun volume obtained from the gun array tests of R/V Ewing (J. Diebold, pers. comm.).

the individual air guns to increase the signal amplitude generated by the array. Fig. 2.22 shows the results of air gun tests performed onboard of R/V Ewing by Lamont Doherty Earth Observatory in 1990. For this gun array, the cubic root rule fails for the gun volume above 350 in^3.

2.2.2 Air Gun Bubble Effect

The released compressed air from an air gun into the water column tends to consecutively expand and collapse, ultimately resulting in an oscillating seismic source signature. This is known as bubble effect and may be an important issue if a single ordinary air gun is used as a seismic source. When the air gun is fired, it suddenly discharges high-pressure air from its air chamber into the water, and this generates the desired pressure spike: the seismic signal (Fig. 2.23A). At the beginning, the pressure inside this initial air discharge, namely the air bubble, is much higher than the ambient pressure at the air gun's depth; hence the bubble immediately starts to expand. At a certain point during this expansion, the internal pressure of the bubble becomes lower than the ambient pressure because of its excessively increased volume. This is the point where the bubble reaches its maximum size, and it starts to shrink after this point because of the higher ambient pressure, which ultimately produces a secondary seismic signal in the water. This is the first bubble effect (Fig. 2.23B), which is known as rarefaction, expressed by positive numbers on the seismic records. This second signal, however, has reverse polarity with respect to the primary seismic signal generated during the first expansion because it is produced during the collapse of the air bubble. The collapsing bubble then reaches its minimum size and it starts to expand again since its internal pressure exceeds the ambient pressure again, because of its reduced volume in the water, which produces another seismic signal with the same polarity as the primary signal since it is generated during the expansion. This is the second bubble effect (Fig. 2.23C), which is known as compression, expressed by negative numbers on the seismic records. This behavior of the bubble in the water

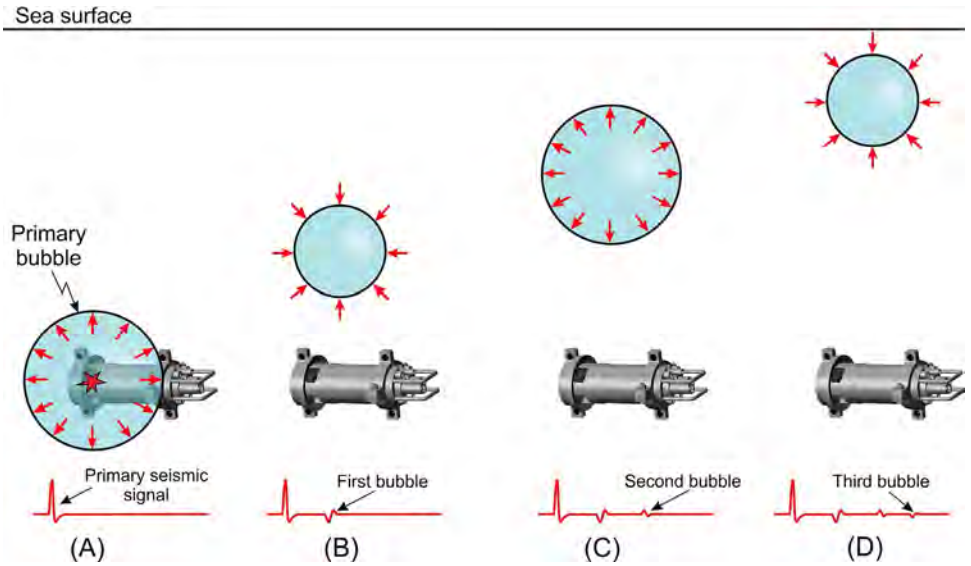


FIG. 2.23 Schematic illustration of bubble effect formation from an air gun source. (A) An air gun provides a sudden air discharge into the water as an expanding bubble, which produces the primary seismic signal. (B) A certain time later, the bubble suddenly shrinks (termed rarefaction) because of the higher ambient pressure than internal pressure of the bubble, which produces the first bubble signal on the signature. (C) Then bubble expands again (termed compression) because of its higher internal pressure than ambient pressure, which produces the second bubble signal on the signature. (D) The expansion and shrinkage of the bubble continues until it breaks at the sea surface.

column continues in that way and each individual expansion and collapse produces a new signal (Fig. 2.23D) until frictional losses damp out the bubble oscillations, or the bubble breaks at the surface when it reaches to the sea surface. Polarities of each bubble signal generated by the expansion and collapse of the air bubble are reversed and the amplitudes are reduced with respect to the previous bubble signal polarity and amplitude.

The signal shape produced by an air gun can be observed via near-field hydrophone located close to a discharge port of the air gun, that is, the near-field signature. Fig. 2.24A shows a typical near-field signature of an air gun, which consists of the primary seismic signal generated during the first expansion of the air bubble and the amplitudes from the bubble effects resulting from the successive collapse and expansion of the initial air bubble within the water. The amplitude generated by the bubble oscillation decreases with increasing time. The bubble oscillation period is not constant from one cycle to another and depends on the temperature and volume of the air discharged into the water, initial air pressure, and the ambient pressure (i.e., depth of the air gun). The bubble effect causes oscillations in the low-frequency components of the amplitude spectrum of the far-field source signature (Fig. 2.24B) typically between 4 and 50 Hz. The effect of bubble oscillations can be suppressed by using several air guns with different volumes instead of deploying single gun or instead of using a number of guns with the same volume (Section 2.2.6).

A specific air gun type, the GI (generator/injector) gun, first introduced by Pascouet (1991), can eliminate its own bubble effect by taking advantage of its two independent air chambers (termed generator and injector chambers)

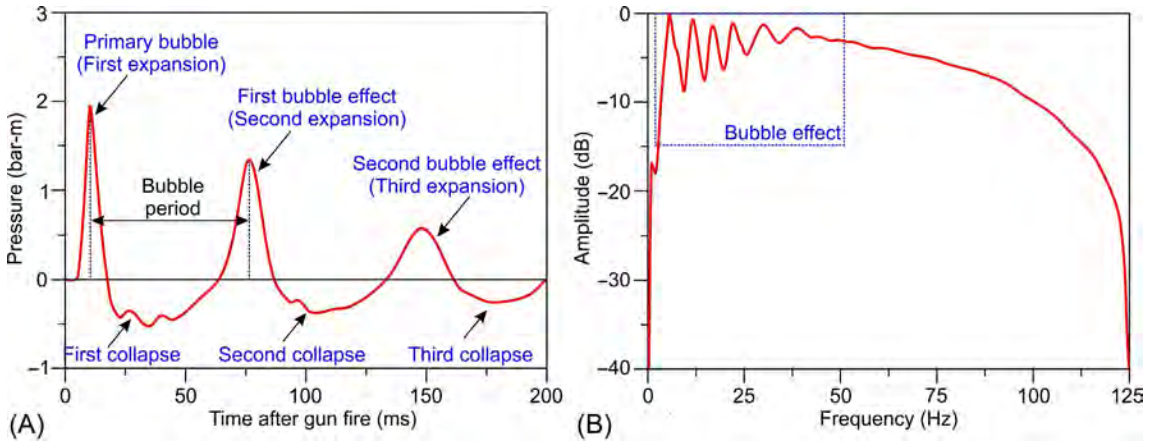


FIG. 2.24 (A) Typical near-field signature of a single air gun. (B) Amplitude spectrum of the far-field signature of an air gun signal fired at 6 m depth.

fired with a small time interval via two dedicated discharge ports (Fig. 2.25). A GI gun basically works as two independent conventional air guns. When a shot point is reached, the generator chamber is fired first at the air gun aim point, which produces the air bubble and the primary seismic signal (Fig. 2.25A). Then the bubble starts to expand and, whenever it reaches its maximum size, the injector chamber is fired directly into the existing air bubble just before it starts to

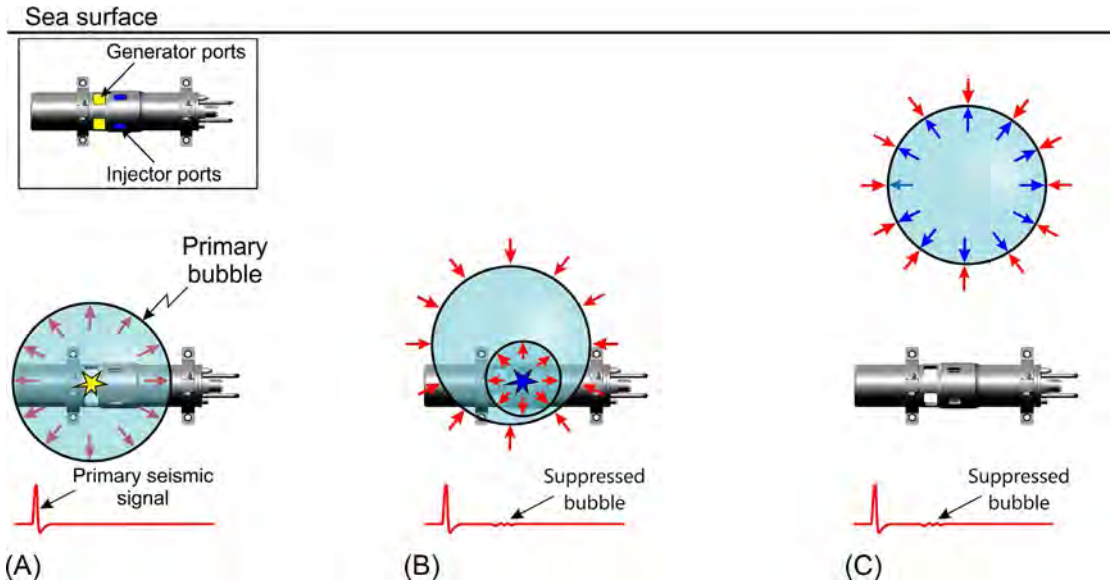


FIG. 2.25 Schematic illustration of the working principle of a GI gun. (A) Generator chamber is fired first to generate the air bubble and seismic signal. (B) During the expansion of bubble, the injector chamber is fired directly into the air bubble when it reaches its maximum size. (C) Firing of the injector increases the internal pressure of the bubble and prevents shrinking.

shrink (Fig. 2.25B). This increases the internal pressure of the bubble again and prevents it from collapse (Fig. 2.25C). The time span between firing of the generator and injector chambers is on the order of a few milliseconds and is known as injector time delay, which depends on the depth of the GI gun and application pressure. It is important to determine this parameter correctly for a complete suppression of the bubble effect.

2.2.3 Ghost Reflection

The reflection coefficient of the sea surface is approximately 1.0, and the upgoing signal emitted from an air gun below the sea surface is almost completely reflected back into the water column at all reflection angles. This signal is termed the ghost reflection and is a delayed version of the primary seismic signal with an opposite polarity. Since we cannot separate the ghost signal from the primary signal, it is considered to be a part of the source signature. Therefore, the far-field signature of the air guns consists of the combination of both signals (Fig. 2.26). The time separation between the primary and source ghost is $\Delta t = 2h/V_W$, where V_W is the water velocity and h is the gun depth (Fig. 2.27A). This time separation is normally quite small: the ghost signal arrives at the receivers only 8 ms later than the primary signal for a source fired at 6 m depth. The ghost signal occurs both at the source and receiver sides (Fig. 2.27B), which are respectively termed the source and receiver ghosts. Interference of the ghost signal significantly restricts the frequency band of the seismic data: It results in periodic notches in the spectrum (Fig. 2.27C), and the available frequency band becomes limited between 0 and the first ghost notch frequency, which decreases as the gun depth increases. For instance, the first notch frequency is 250 Hz for a 3 m source depth, whereas it is 125 and 82.5 Hz for 6 and 9 m source depth, respectively.

Elimination of ghost interference from the source signature widens the amplitude spectrum of the data since it removes the ghost notches and hence we can obtain a much higher resolution seismic data. There are a number of developments which aim to deghost the data during the acquisition stage:

- *Variable-depth or slant streamers*: The method was introduced by CGG Veritas and known as BroadSeis acquisition technology (Soubaras, 2010). The streamer is configured to have variable receiver depths so that the receiver ghost notches occur at different frequencies along the offset, which is then exploited to deghost the data (Section 2.3.6).
- *Over-under streamers*: The method was first introduced by Western Geco in the early 1980s. It comprises two streamers on top of each other at depths of approximately 20 and

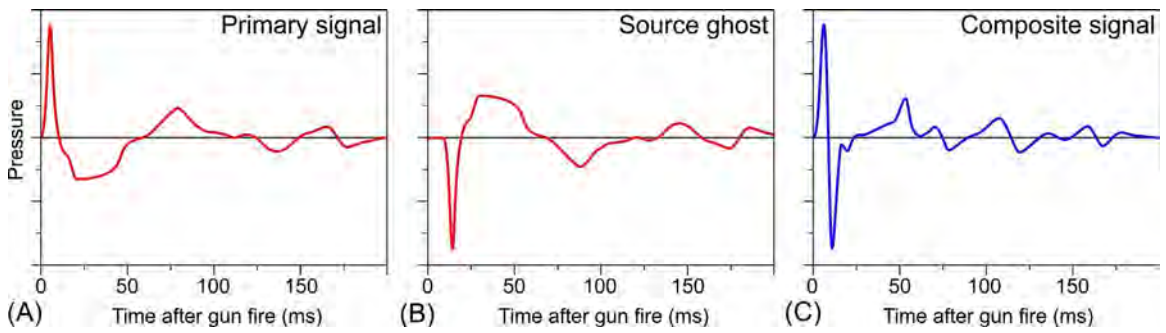


FIG. 2.26 (A) Primary signal produced by an air gun, (B) source ghost, which is the polarity reversed version of the primary signal, and (C) the signature of an air gun is the combination of the primary signal and the ghost interference.

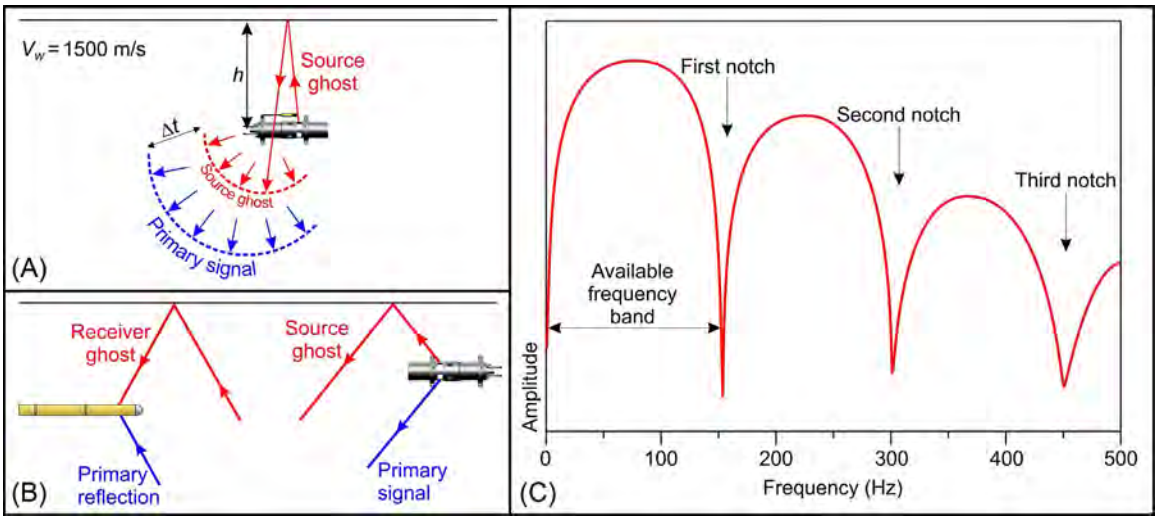


FIG. 2.27 (A) Ghost reflection is of opposite polarity of the primary signal with a time delay of $\Delta t = 2h/V_W$. (B) Ghost reflections occur both at the source and receiver sides and both are included in the far-field source signature. (C) Ghost interference causes periodic notches on the amplitude spectrum of the data appearing at certain frequencies.

25 m. The idea is that the ghost notches of the overstreamer are filled out by the data from the understreamer (Özdemir et al., 2008).

- *Dual-sensor (2C) streamers*: The method was introduced by PGS in 2007 and known as GeoStreamer technology. The GeoStreamer records the pressure field by a hydrophone and vertical component of the particle velocity field by a motion sensor to separate up- and downgoing energy (Carlson et al., 2007). A suitable combination of both wave fields provides ghost-free broadband seismic data (Section 2.1.2).
- *Multicomponent (4C) streamers*: Multicomponent (4C) streamer technology was introduced by Western Geco in the early 2010s. The method uses microelectromechanical systems (MEMS) to measure the particle acceleration in three dimensions, in addition to the pressure field measured by a hydrophone. Both measurements are then used for up- and downgoing wave field separation (Robertsson et al., 2008).

2.2.4 Near-/Far-Field Source Signatures

The characteristic pressure shape as a function of time produced by an air gun or a gun array is termed the pressure signature, expressed in bar-m. There are two types of source signatures of an air gun:

- Near-field signature
- Far-field signature

The near-field signature is the measurement of the pressure, or amplitude, produced by the discharged high-pressure air in the vicinity of the discharge ports of an air gun, or within the air bubble (Fig. 2.28A). The near-field is defined as the distance between the physical size of the source (or array) and wavelength of the signal. For instance, the near-field is between 1 and 15 m for a 1-m long air gun and for a signal with 100 Hz frequency propagating in the water with 1500 m/s velocity. Far-field means the depth below the source with respect to the array size and measurement bandwidth, which, in practice, is the distance that the signals from

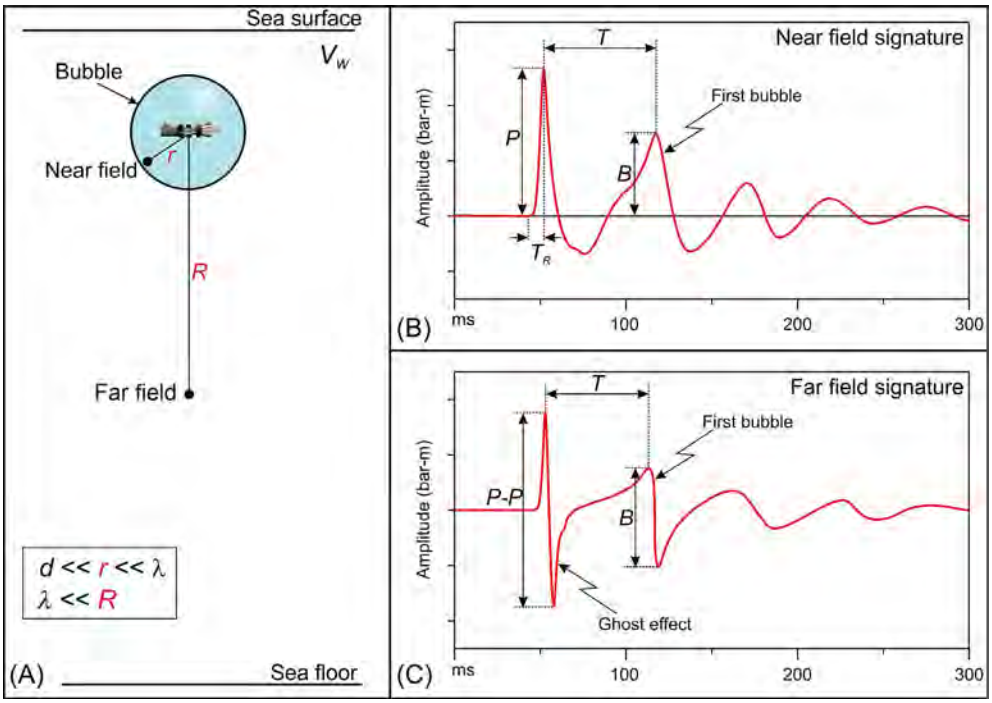


FIG. 2.28 (A) Near- and far-field zones of a marine seismic source. Near-field signature is measured in the zone between the physical dimensions of the source array (d) and the dominant wavelength of the signal (λ) while the far-field signature is measured with a hydrophone located approximately 300 m below the source array. (B) Typical near-field signature. P is peak amplitude of initial pressure, B is amplitude of the first bubble effect, T is bubble period, and T_R is the rise time. (C) Typical far-field signature. P-P is peak-to-peak amplitude of initial pressure.

individual guns of a gun array interfere constructively and arrive at a distant hydrophone within one sampling interval (Dragoset, 2000). The far-field signature is measured with a hydrophone typically located 300 m below the array (Fig. 2.28a) so that the signal appears as if it is emitted from a point source. If we locate the hydrophone to the aft or side of a gun array, the signatures change from one location to another due to the array effect, so the far-field hydrophone must be directly below the array so that the pressure pulses from each individual gun arrive at the hydrophone at the same time.

Near- and far-field signatures are commonly used to delineate the source strength (maximum acoustic pressure radiated by the source) and peak-to-bubble ratio (the ratio of maximum acoustic pressure to maximum bubble pressure). Both parameters are measured from zero-to-peak value for near-field signatures and peak-to-peak value for far-field signatures. Near-field signatures have an initial high pressure pulse, which then falls to negative pressure values below the hydrostatic pressure followed by oscillating amplitudes due to the successive collapse and expansion of the air bubble (Fig. 2.28B). This initial pressure creates the highest amplitude of the signature, which then gradually decreases with time. The effect of the source ghost is very small on the near-field signature because of the location of the near-field hydrophone. The important parameters that can be obtained from the near-field signature are the bubble period (T) and peak-to-bubble ratio (PBR),

where P and B are the peak primary and bubble amplitudes, respectively (Fig. 2.28B).

A near-field hydrophone located close to the air gun discharge ports can provide the following information which then can be used to evaluate the performance and reliability of the gun's operation by a careful observation and analysis during the data acquisition in terms of online or real-time quality control applications:

- The accuracy of air gun aim point
- Primary signal shape and amplitude (P)
- Bubble period
- Amplitude and the ratio of P-P to bubble amplitude (PBR)
- Possible air leakage or other malfunctions of the gun

The far-field signature incorporates the source ghost on the near-field signature in addition to the primary and bubble amplitudes (Fig. 2.28C). It is measured with a hydrophone directly below the gun array, and defines the nominal source strength: that is, the amount of pressure at 1 m away from the source center in bar-m. Far-field signatures are characterized by their three components:

- The initial high pressure pulse produced when the air gun is fired
- The source ghost produced by the reflection of the initial pulse from the water surface
- The bubble pulse train produced by the successive collapse and expansion of the initial air bubble

A far-field signal can provide the following information which can be used to evaluate the overall performance and reliability of the gun array:

- Peak-to-peak (P-P) amplitude of the primary signal
- The ratio of P-P to bubble amplitude (PBR)

P-P amplitude is the distance between the primary positive peak amplitude and the ghost's negative peak amplitude. Normally, the pressure value measured at a certain depth below the array is multiplied by the source-hydrophone distance to obtain the source strength. For instance, a source strength of 50 bar-m implies that 0.5 bar pressure is measured at a distance of 100 m from the array center. In practice, higher P-P amplitude is preferred for a better signal penetration into the subsurface. The PBR parameter determines how the bubble is suppressed by the overall design of the whole air gun array. A PBR value as high as possible is desired so that the array signature is close to an ideal spike with no side oscillations, with a wide frequency band. Both parameters depend on the number of guns and total gun array volume, the air pressure applied, and the gun array depth. Near- and far-field signatures of an air gun array can be computed by dedicated software packages to evaluate the performance of the designed arrays before the surveys.

In towed streamer acquisition, four signals with different ray paths arrive at the receivers for a single reflection event. In Fig. 2.29, these individual signals are schematically shown along with their ray paths:

- A single reflection with no ghost from a tuned air gun array consists of a wavelet, which would be recorded if the source and receivers were located within an infinite half space (Fig. 2.29A).
- The recorded reflection signal shape changes when the source ghost from the water surface is incorporated. The source ghost occurs since the source is located below the sea surface (Fig. 2.29B).
- The effect of only receiver ghost on the recorded reflection signal shape is similar to that of the source ghost. The receiver ghost occurs since the receiver is located below the sea surface (Fig. 2.29C).
- The recorded reflection signal shape is further modified if we incorporate the receiver and source ghost signals together

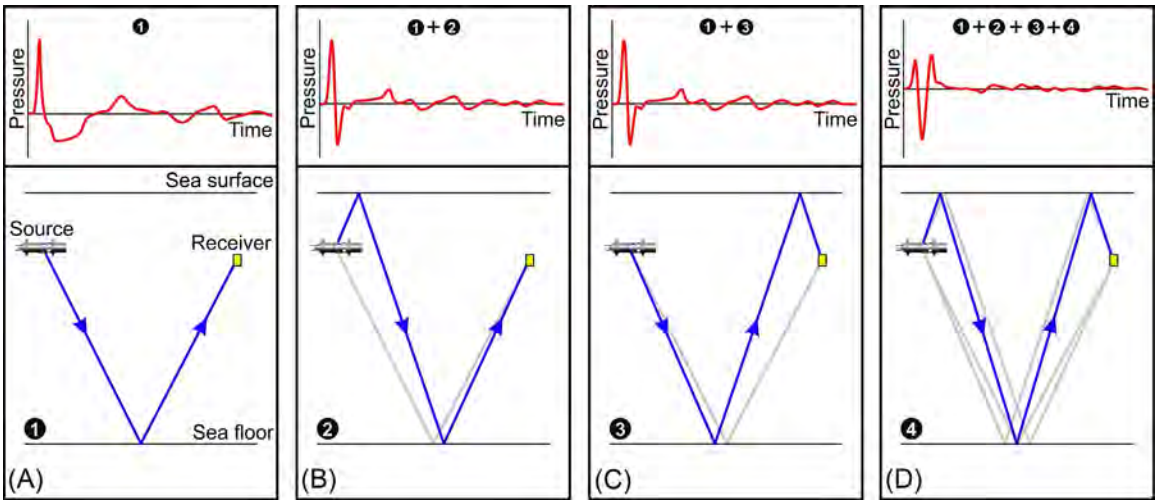


FIG. 2.29 Schematic illustration of four different signals (top) received from a single shot and their ray paths (bottom). (A) A single reflection with no ghost, (B) reflection signal plus source ghost, (C) reflection signal plus receiver ghost, and (D) reflection signal plus receiver ghost plus source ghost, that is what actually samples the subsurface. When source and ghost notches are incorporated, the recorded reflection signal becomes a Ricker wavelet.

(Fig. 2.29D). This is what we record as a single reflection signal in conjunction with both source and receiver ghost interferences. This signal actually samples the earth.

Fig. 2.30 shows this situation on a far-field signal of a 3190 in^3 air gun array. In practice, streamers are towed deeper than the source arrays, and the far-field signatures become much more complicated when we incorporate the receiver ghost: The source signature becomes a Ricker wavelet with a large negative peak between two relatively small positive peaks, as is the case in Fig. 2.29D. Another notch appears in the amplitude spectrum of the far-field signal in addition to the source ghost. For the example spectrum in Fig. 2.30D, there are two receiver (R_1 and R_2) and two source (S_1 and S_2) ghost notches in the amplitude spectrum. Receiver ghost notches arise at 107.5 and 215 Hz, while the source notches appear at 125 and 250 Hz, depending on their tow depths of 7 and 6 m, respectively.

In order to remove the residual bubble amplitudes and the interference of ghost reflections, sometimes signature deconvolution is applied to the data to convert the source signature into its zero phase equivalent (dephasing) or to remove the source signature from the data (designature) as an early step in wavelet processing (Section 6.8) for a possible preconditioning of the data for subsequent predictive deconvolution. However, it is normally not possible to obtain the entire signature (including the bubbles) for every shot to use with the deterministic deconvolution. Furthermore, a regular recording of the far-field signatures is impossible, which leads us to use conventional predictive deconvolution to suppress the residual bubble effects in later processing steps (Larner et al., 1982).

2.2.5 Cluster/String/Array

In conventional marine seismic operations, air gun arrays are used as seismic sources, where several air guns with different volumes are fired simultaneously. The amplitude produced by an air gun array depends on the number of

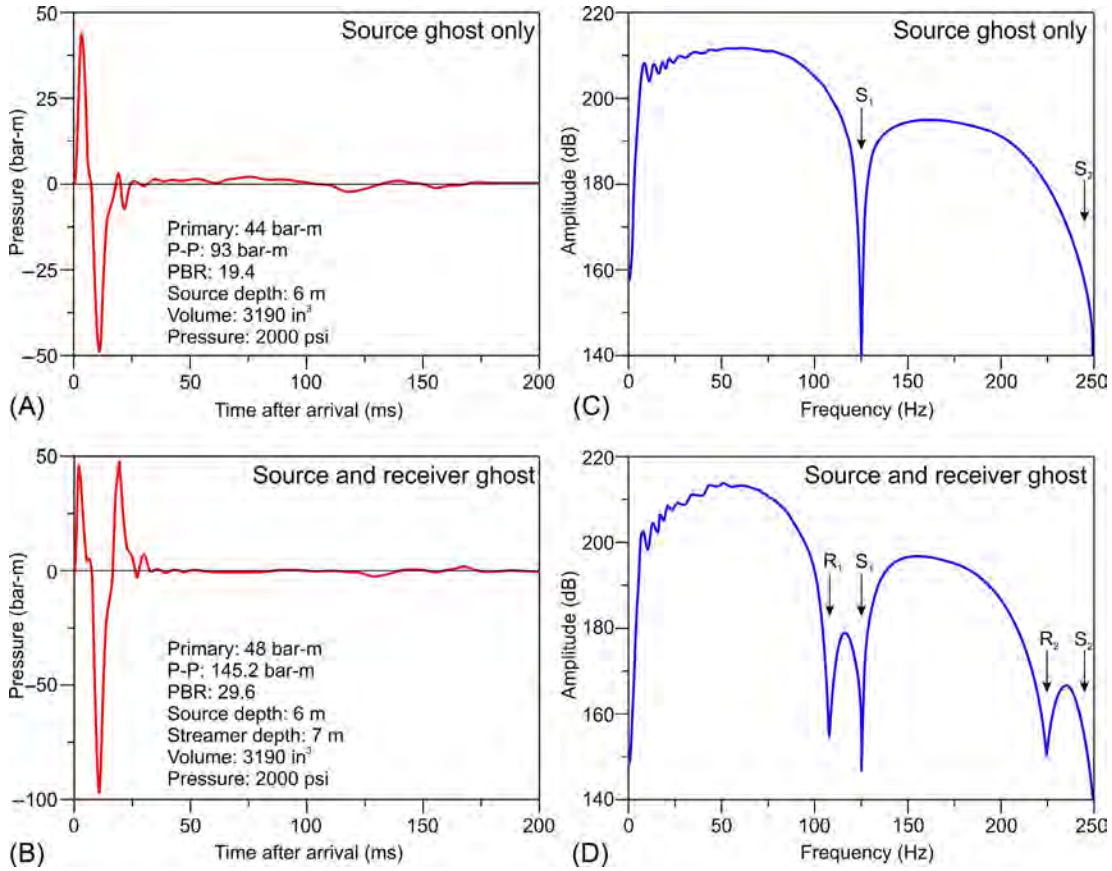


FIG. 2.30 Far-field signatures of a 3190 in^3 array with (A) only source ghost and (B) source and receiver ghost interference. Their corresponding amplitude spectra are given in (C) and (D), respectively. Since source and receivers are towed at different depths, they have their own ghost notches appearing at different frequencies in the amplitude spectrum. R_1 and R_2 are the receiver notches, while S_1 and S_2 represent the source notches.

elements in the array, the air pressure applied to the guns, and the total gun volume of the array. An array with 20 guns produces two times larger amplitude than an array with 10 air guns. In practice, the number of guns in the array is the most efficient parameter on the resultant primary amplitude. The output amplitude is almost directly proportional to the operation pressure, and an array with 3000 psi pressure produces almost 1.5 times larger amplitude than an array operating at 2000 psi pressure. Finally, the amplitude is directly proportional to the cubic root of the total gun volume of the array.

In an air gun array, individual guns are in weakly or strongly interacting positions based on the distance between them. If two or more guns are positioned with a lateral distance slightly less than or equal to one meter, the array is termed strongly interacting. If the separation is more than approximately 1 m between two successive guns, then the array is termed weakly interacting. The gun groups with a lateral separation of approximately 1 m are named clusters. In the last two decades, array designs with several strongly interacting guns or gun clusters have become very popular and a modern gun

array consists of a combination of both strongly and weakly interacting guns.

Basically there are two main reasons for using gun arrays in seismic surveys:

- to increase the primary signal strength, since the signature of a single air gun is too weak to penetrate deeper layers and signal-to-noise (S/N) ratio is poor even for moderate subsurface depths. Signal amplitude is directly proportional to the number of guns within the gun array.
- to suppress the bubble amplitudes, since the signature of a single gun is contaminated by undesired amplitudes from the bubble effect, which can be eliminated by carefully tuned air gun arrays.

In petroleum industry, guns of different sizes are grouped in clusters, strings and arrays (Fig. 2.31). Clusters are gun groups consisting of two or three closely spaced guns and they are more effective with regard to the peak amplitude they produce and suppression of bubble amplitudes. The advantage of the gun clusters is that their *P-P* amplitude and PBR is higher than one single gun of equal volume. The horizontal distance between the guns in a cluster is typically 1 m. If we set a cluster of two guns with the same volume, we observe that the primary signal amplitude increases and the bubble amplitude and period decrease as the distance between the two guns decreases.

Gun arrays are composed of gun strings, which are subarrays consisting of several air guns of different volumes, or gun clusters. They typically involve six to eight individual guns or gun pairs grouped and hung by chains from their harnesses suspended from large flotation tubes (Fig. 2.31). Each string is hung from a rail on the back deck to easily deploy the guns. In specifically designed gun strings, all of the components may consist of gun clusters.

An air gun array is generally composed of three to six strings in total with a maximum of 48 guns. In 2D surveys, typically one array with three strings is used, whereas two identical arrays, each consisting of three strings, are used in 3D surveys to perform a flip-flop shooting,

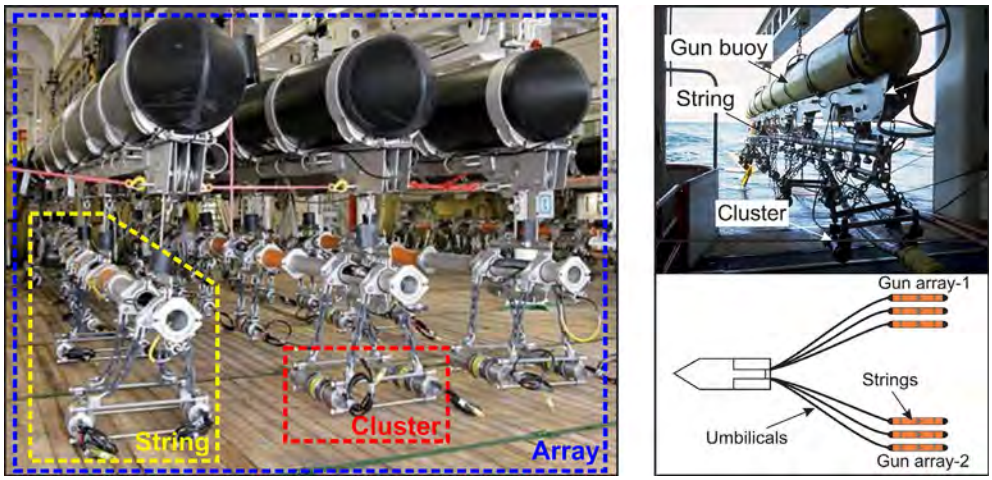


FIG. 2.31 Clusters, strings and gun arrays. Clusters are gun groups generally consisting of two closely spaced air guns. Gun strings are composed of several air guns or gun clusters. An air gun array is formed by three to six strings with a maximum of 48 air guns. One array of three strings is used in 2D surveys while two identical independent arrays, each consisting of three strings are used in 3D surveys.

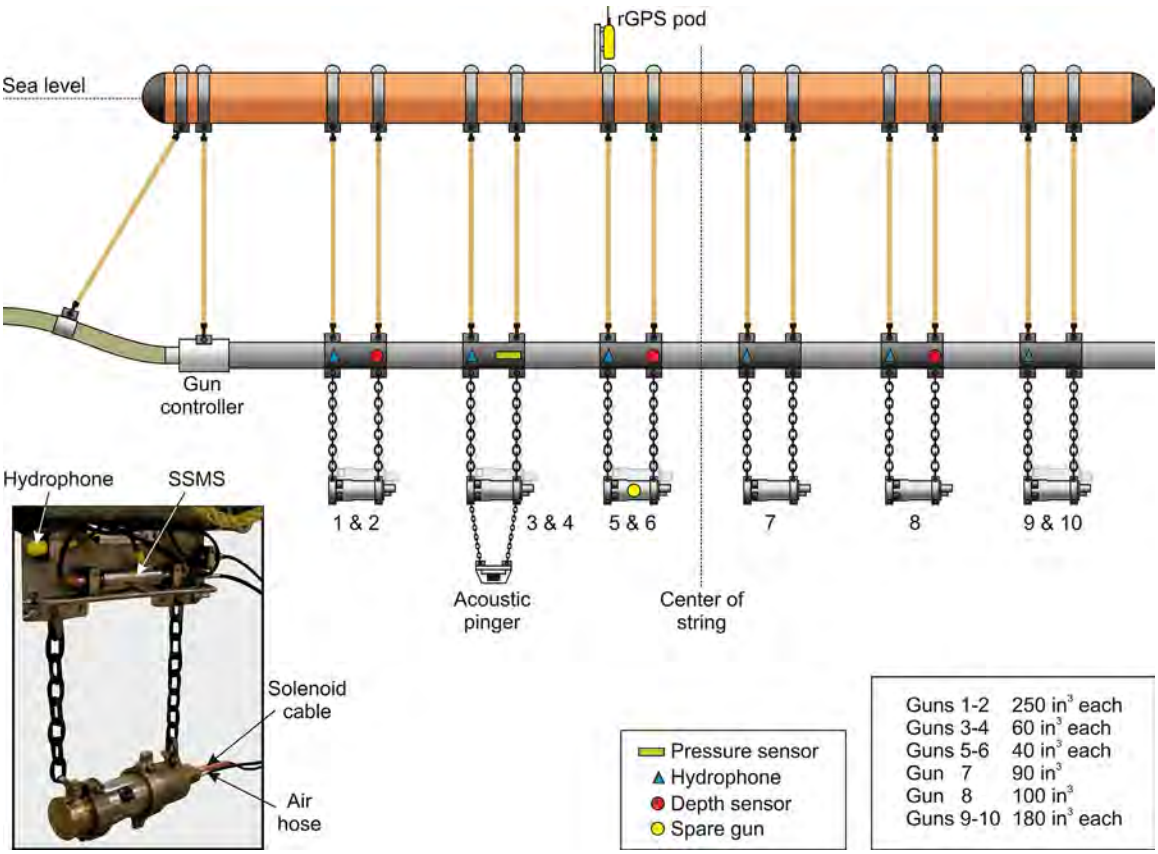


FIG. 2.32 Side view of a typical gun string. Inset shows a photo of a real air gun hung from its harness by chains. SSMS is seismic source management system, which consists of a pressure sensor, a digitizer for near-field hydrophone data, a depth sensor, and a distributed firing system.

where arrays are fired alternatively at each successive shot points (Section 2.3.5). Dimension of each gun array is typically 15 m × 20 m.

A common layout of a gun string with a total of 10 guns is shown in Fig. 2.32. This example string has four clusters with a lateral separation of 0.75 m and two single guns, and one of the cluster guns is used as a spare. The inactive or spare guns are used to immediately replace the malfunctioning guns without interrupting the acquisition in case of gun failures. Strings have rGPS pods on the flotation tubes to accurately locate each string during the acquisition. The depth of the guns within the strings is important in terms of frequency content of the generated signal, and therefore strings are also equipped with depth transducers, or sometimes a pinger, to ensure the operating depths of the guns. Each gun or cluster in the string has its own near-field hydrophone located close to the discharge ports, to obtain the near-field signature of each gun for real-time and offline quality control implications.

Fig. 2.33 shows a plan view of an example layout of a gun array with three gun strings. Each string has 12 guns with two spares and three clusters distributed at the frontal and rear positions, forming a total gun volume of 3130 in^3.

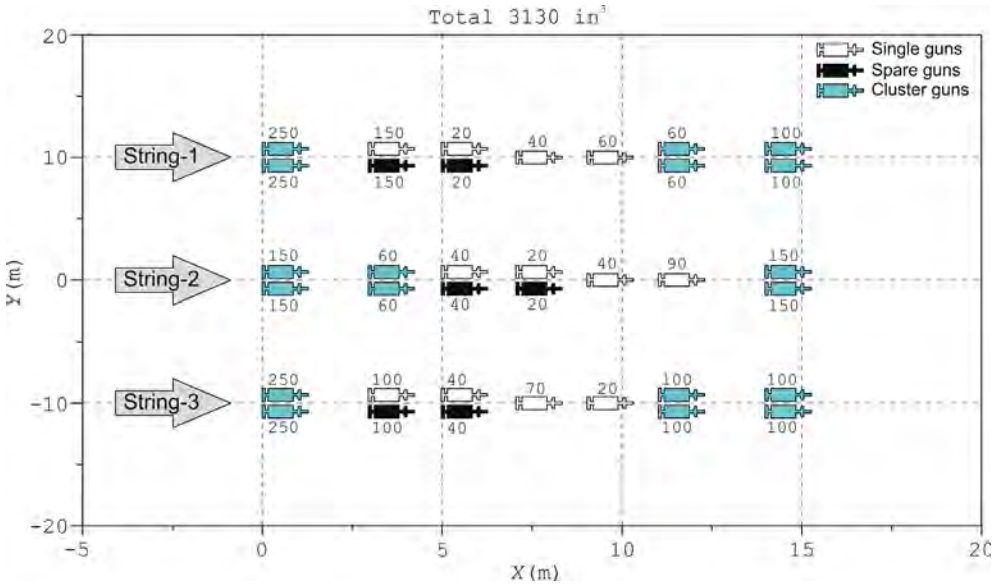


FIG. 2.33 Plan view of an example air gun array layout consisting of three gun strings with a total volume of 3130 in^3. Numbers indicate the gun volume in cubic inches.

The lateral distance between the strings is 10 m while the separations between the guns in each string are variable, slightly larger for outer guns of larger volume, which makes the overall array dimension 15 m × 20 m. Using specific software simulations, it is possible to calculate the *P-P* and PBR amplitudes of such a gun array to test the performance of the array during the array design. It should be noted that this simulation produces a *P-P* pressure termed back calculated pressure, which is the pressure level obtained if all the guns in the array are consolidated into the center of the array with no physical dimensions.

2.2.6 Tuning and Array Performance

Array tuning is the process to optimally suppress the bubble amplitude, or to maximize the PBR, while increasing the *P-P* primary signal amplitude by a proper design of the gun array. The bubble effect can be significantly attenuated by suitably tuned arrays composed of air guns with different volumes. The theoretical basis is that the guns with different volumes produce bubbles with different oscillation periods: Bubble periods of larger gun volumes are higher because expansion of the bubble takes much more time until it collapses, since the volume of the air discharged into the water column is larger when compared to that of small guns. Therefore, the bubble amplitudes of the guns with different volumes are summed destructively, whereas we obtain large primary amplitude because of the constructive summation of the primary pulses from each individual gun.

Fig. 2.34 shows the superposition of the far-field signatures of individual guns to strengthen the primary signal amplitude, since they are all in-phase. If a proper design can be achieved with suitable volumes of guns, then the bubbles cancel out each other in the far-field signature since they are out-of-phase. When primary signal amplitudes are synchronized, the bubble amplitudes can be suppressed by taking advantage of the variation of bubble period with respect to the gun size (Larner et al., 1982).

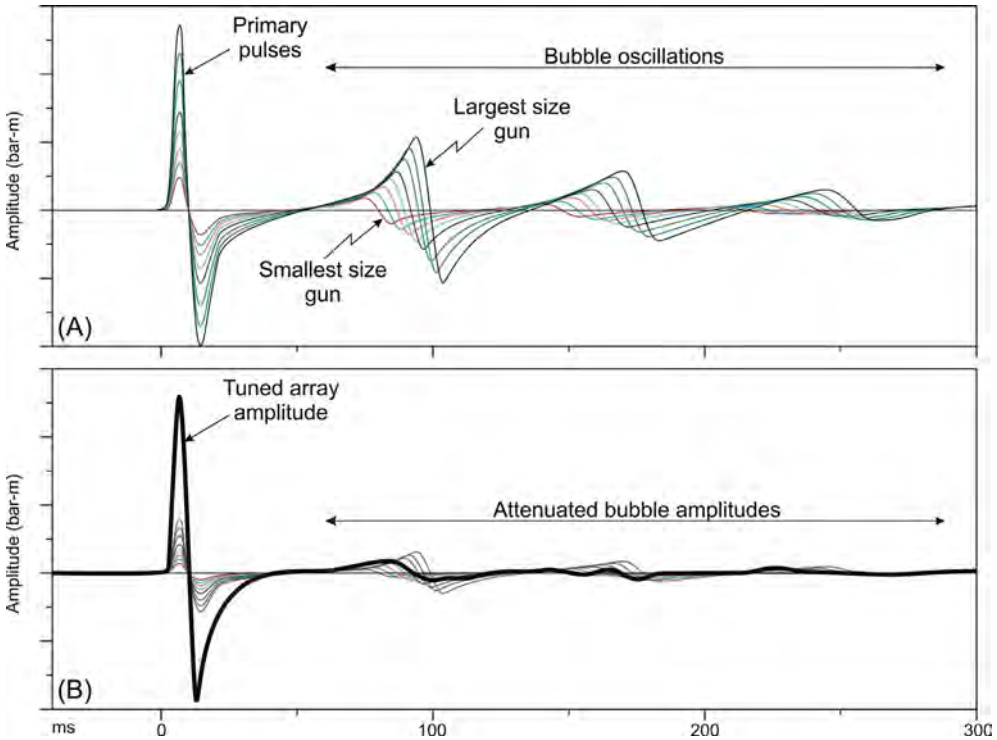


FIG. 2.34 Schematic illustration of bubble suppression using a number of air guns with different sizes. (A) Far-field signatures of individual guns, and (B) tuned array output.

In the far-field signature, all positive peaks are followed by a negative peak, due to the ghost reflection interference for both primary and bubble pulses. In a suitably tuned array, the gun volumes are determined to realize that the bubble amplitude of one larger gun is cancelled by the ghost of the bubble of a smaller gun, since the ghosts arise at the same time following the positive peaks because all guns are at the same depth.

The performance of an array is evaluated by three parameters deduced from the far-field signature of the array (Fig. 2.35):

- *Peak-to-peak (P-P) amplitude of the primary signal*: It is the amplitude of the main seismic signal and is the measure of the total energy produced by the array (Fig. 2.35A).
- *Peak to bubble amplitude ratio (PBR)*: It demonstrates how the bubble amplitude is suppressed by the array and indicates how good the array tuning is. In a properly designed array, PBR must be higher than approximately 15 (Fig. 2.35A).
- *Amplitude spectrum*: It shows the locations of the ghost notches, and hence the width of the effective frequency band of the seismic signal (Fig. 2.35B).

The effective far-field signature of an air gun array designed with different size of air guns can be simulated to obtain the most suitable design of the gun array to suppress the bubble and increase the primary signal amplitude. The inputs for the simulation are the number of guns and their positions within the array, air

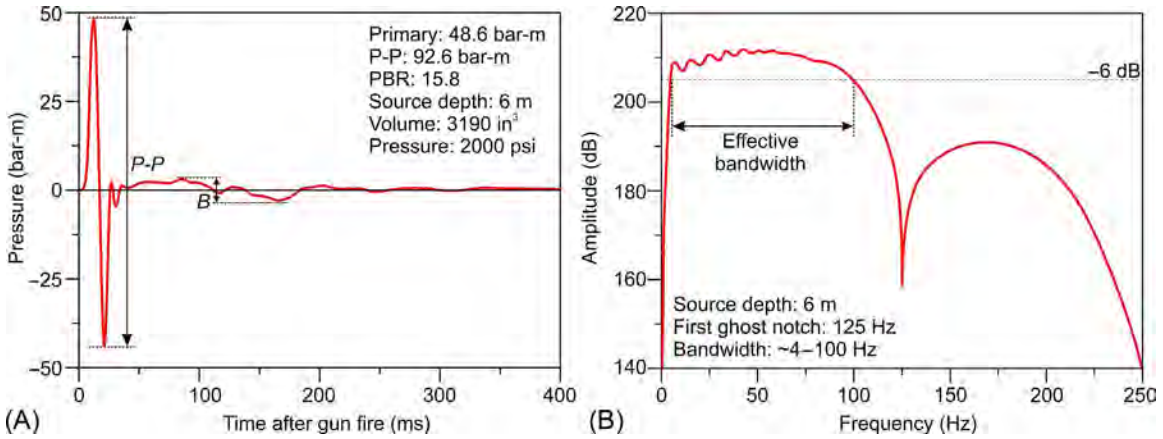


FIG. 2.35 (A) A typical far-field signature of a 3190 in^3 air gun array, and (B) its amplitude spectrum. The performance of an array can be evaluated by *P-P*, PBR and effective frequency bandwidth, where the signal amplitude drops 6 dB below its maximum value.

pressure, size of each gun, and operating depth to obtain the far-field signature output of the whole array to compute the preceding three parameters, and pressure radiation pattern, or source directivity of the array. However, when we record the far-field signature of an array to verify the simulation results, we observe that the actual *P-P* amplitude of a gun array is always approximately 20 dB less than the back calculated value. This occurs due to the partial destructive interference between the signals of each individual gun in a weakly interacting array, and is termed the array effect.

Towing depth of the gun arrays has a fundamental effect on tuning performance since the ghost time delay depends on the operating depth. Fig. 2.36 shows three example far-field signatures of the 6600 in^3 gun array of the R/V Marcus Langseth computed for three different tow depths, along with their corresponding amplitude spectra. It is clear that the PBR significantly decreases as the depth increases, although *P-P* amplitude of the primary pulse is not seriously affected by the tow depth. That is because the array is tuned for an optimum deployment at 6 m, which has become a conventional standard for operation depth today.

The amplitude spectra of the far-field signatures in Fig. 2.36D indicate that the ghost notch moves to higher frequency band as the towing depth is decreased. The first notch appears at 125 Hz for 6 m tow depth, which defines the upper frequency band of the spectrum for most conventional surveys. Typically, a gun array is towed at shallower depths for higher resolution seismic data with a wider spectral bandwidth, such as those for site surveys. *P-P* and PBR values are dependent upon the frequency band of the far-field signatures of the array: Both values decrease when the array signature is of low-frequency bandwidth, such as for the case of deeper tow.

Far-field signature tests are also important to observe the source stability from one shot to another. It is important for a suitably designed array to produce a stable source signature all over the survey. Source stability depends on several factors, including the weather, gun specifications, and stability of operating air pressure, etc., although the most important factor is the design of the array components. Degradation in the predetermined or simulated *P-P* and/or PBR value may result in down times during the acquisition.

Modern 3D seismic vessels used in the hydrocarbon industry deploy gun arrays with

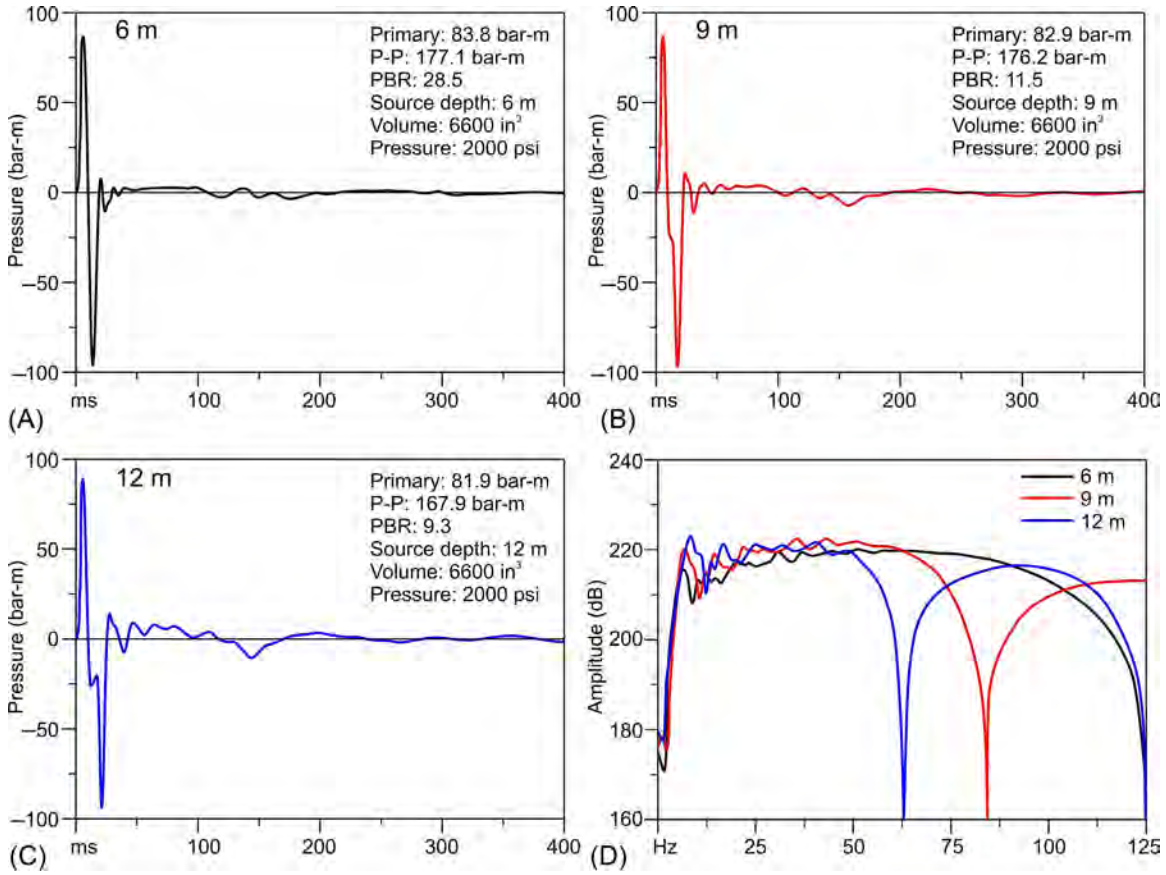


FIG. 2.36 Far-field signatures of gun array of R/V Marcus Langseth for (A) 6 m, (B) 9 m, (C) 12 m source depth, and (D) their corresponding amplitude spectra (J. Diebold, pers. comm.).

3000–4500 in^3 total volumes, typically towed at 6 m depth. They produce primary signals with *P-P* amplitude larger than 100 bar-m with a PBR value larger than 20. Table 2.2 shows example gun arrays and their performances from industry standard 3D seismic vessels.

During the array design, the pressure radiation pattern, so-called source directivity of the array, can be computed to analyze how the produced source energy propagates in three dimensions. Fig. 2.37 shows a typical radiation pattern from a 3090 in^3 array of three strings towed at 6 m depth. These plots show the energy distribution along a vertical plane for inline and crossline directions. Gun arrays are designed to concentrate the primary energy downwards directly to the seafloor approximately between 0 and 45 degrees for inline and 0 and 30 degrees for crossline directions. Signal directivity is a function of frequency, and there is more energy at relatively higher frequencies. In addition, side lobes appear at higher frequencies, especially for energy distribution in crossline directions, and their propagation direction is also a function of frequency.

As deduced from the radiation patterns in Fig. 2.37, the energy does not radiate in a symmetrical and uniform way in all three

TABLE 2.2 Example Gun Array Specifications of Modern 3D Survey Vessels

	R/V Marcus Langseth (NSF)	M/V Pacific Explorer (PGS)	M/V Geo Challenger (CGG)	M/V Bergen Surveyor (CGG)
Gun type	1500LL and 1900LL	1900LL	G gun II	1500LL and 1900LL
Array volume (in^3)	6600	3090	4480	4100
Pressure (psi)	2000	2000	2000	2000
Number of strings	2 × 2	2 × 3	2 × 3	2 × 3
Tow depth (m)	6	6	7	6
String separation (m)	8	10	10	8
Array length (m)	16	14	17	16
Gun separation (m)	2.4 (inner) 3.2 (outer)	2 (inner) 3 (outer)	3 (inner) 3 (outer)	3 (inner) 3 (outer)
P-P amplitude (bar-m)	177.1	122.7	125.8	111.1
PBR value	28.5	34	28.3	21.9

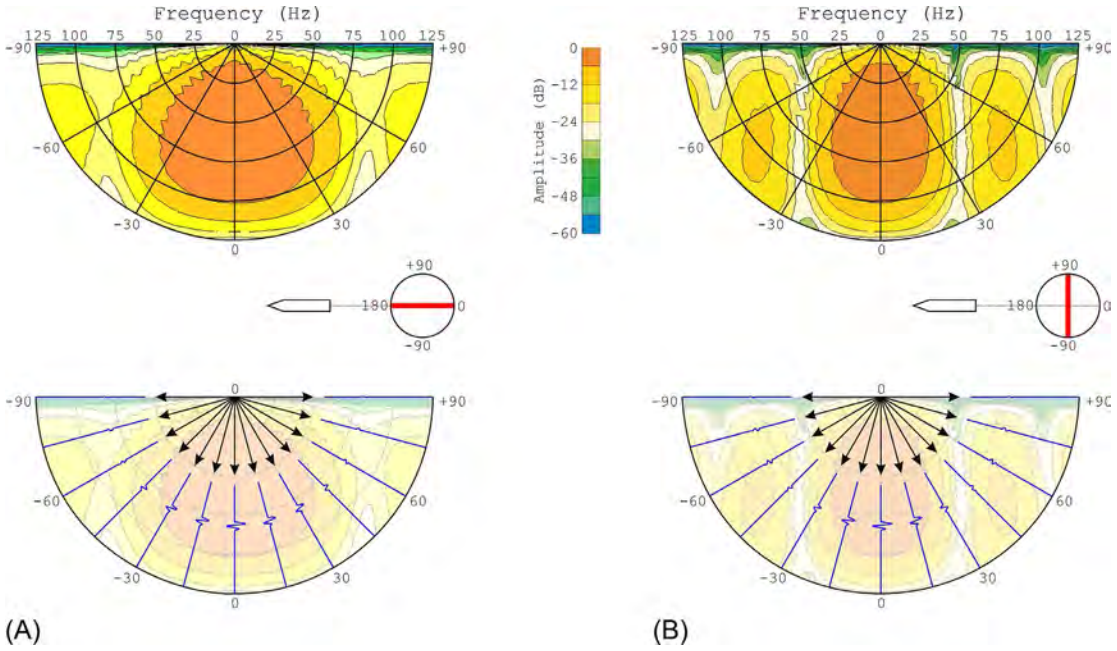


FIG. 2.37 Example source directivity of an air gun array. Amplitude distributions for (A) inline and (B) crossline directions (top) and schematic illustration of emitted signal signatures with respect to the radiation angle (bottom).

dimensions from the array center, and in general, horizontally radiating amplitude levels are approximately 20 dB lower than the vertically radiating amplitudes. The simulated amplitudes vary with the frequency of the emitted signal and tow depth, and there is less amplitude difference between the horizontally and vertically radiating signals at low frequencies. The difference arises from a number of factors: the array dimensions and horizontal design of the guns, irregular distribution of gun volumes within the array, and other oceanographic conditions such as variations in water temperature and salinity both in the vertical and horizontal planes.

2.3 3D MARINE SEISMIC ACQUISITION

In the last two decades, 3D seismic exploration has become a standard tool for the hydrocarbon industry following the introduction of sophisticated streamer steering and positioning systems, and it has replaced 2D surveys, which are commonly still used for academic research purposes and site surveys for engineering purposes, in addition to the reconnaissance surveys prior to a detailed 3D survey today. Although the equipment, data acquisition and data processing in 3D exploration are much more costly than in 2D seismic surveys, the information and data quality provided are not comparable to those of 2D acquisition. Since 3D acquisition covers the entire survey area with no gaps between the subsurface bins, the results and interpretations are much more correct and accurate than those deduced from 2D seismic data. In particular, the development of real-time and offline QC and QA applications during and after 3D surveys has provided more reliable and accurate 3D seismic datasets. In this section, the components of 3D surveys, especially the steering and positioning devices dedicated to 3D acquisition, are introduced. Some specific acquisition techniques, such as slant streamer or fan mode acquisition, as well as multiazimuth surveys, are also explained.

Conventional 3D acquisition has become standard for hydrocarbon exploration before an offshore drilling decision has been made. In the very first applications of 3D acquisition, only one single streamer and two identical source arrays (Fig. 2.38A), or two parallel streamers with one source array (Fig. 2.38B), were used, which doubled the number of acquisition lines for each sail line at the beginning of 1980s. Then the introduction of twin source and flip-flop acquisition concepts increased the number of acquisition lines to four in the case of two-streamer acquisition (Fig. 2.38C). Since then, the number of towed streamers and their overall lengths have increased consistently. Today, modern seismic vessels tow 8–16 parallel streamers, each 6–10 km long with a 100 m streamer separation shooting with dual-source design to achieve 16–32 acquisition lines per sail line. Typically, array separation is half of the streamer separation, which enables a crossline bin size that equals to one-quarter of the streamer separation. Total crossline coverage is directly proportional to the number of streamers in the spread. For instance, the total lateral distance of an 8-streamer spread with 100 m separation is 700 m, and the total crossline coverage achieved is 350 m. Today, up to 960 recording channels per streamer are used to record seismic data in 3D surveys. Unlike 2D acquisitions, which provide one single shot gather for each shot, 3D seismic provides several shot gathers recorded from each individual streamer for every shot. Fig. 2.39 shows an example shot gather group from a 3D dataset recorded with eight streamers and 480 channels per streamer.

Marine seismic contractors develop complete acquisition systems to provide solutions to the issues of the conventional 3D acquisition and to improve seismic data quality, especially in challenging areas such as the regions of salt

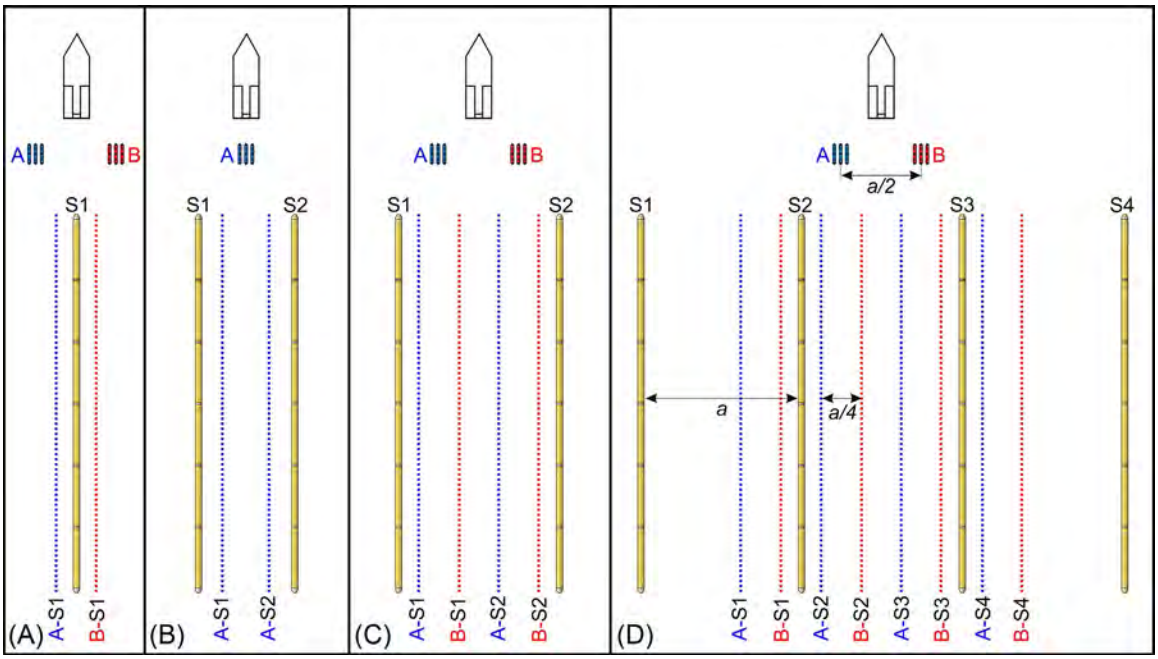


FIG. 2.38 Example of conventional 3D source and streamer layouts. (A) Dual source (A and B) and a single streamer (S1), (B) single source (A) and two streamers (S1 and S2), (C) dual source and two streamers, (D) dual source with four streamers. *Dashed lines* correspond to CMP lines associated with specific source-streamer pairs.

tectonism, as is the case in the Gulf of Mexico. The common purpose is to obtain seismic data with improved S/N ratio, greater bandwidth and better resolution to obtain a more reliable illumination and mapping of the target. For instance, Western Geco employs the Q-Marine acquisition system in towed streamer acquisitions, which utilizes point-receivers to record the data using calibrated receivers and a calibrated seismic source. The Q-Marine system also uses fully braced acoustic positioning for better streamer steering. PGS employs GeoStreamer and GeoSource technology in their fleet to eliminate the ghost and acquire higher resolution data along with steerable seismic source arrays for a better repeatability of 4D time-lapse seismic surveys. CGG Veritas utilizes BroadSeis and BroadSource technology to completely remove the source and receiver ghosts, to acquire data with a superior resolution mainly incorporating the marine seismic products of Sercel.

2.3.1 Acquisition Patterns

In a conventional 3D survey, seismic data is acquired along several parallel preplot lines with the same azimuth over predetermined target zones determined from vintage seismic data of previous 2D surveys. The typical sail line spacing for 3D surveys changes between 400 and 800 m depending on the number of streamers deployed and the separation between the streamers. The acquisition template for 3D surveys is termed a racetrack pattern, which significantly reduces the dead times required for line changes during the turns, where the vessel skips over several parallel sail lines when it

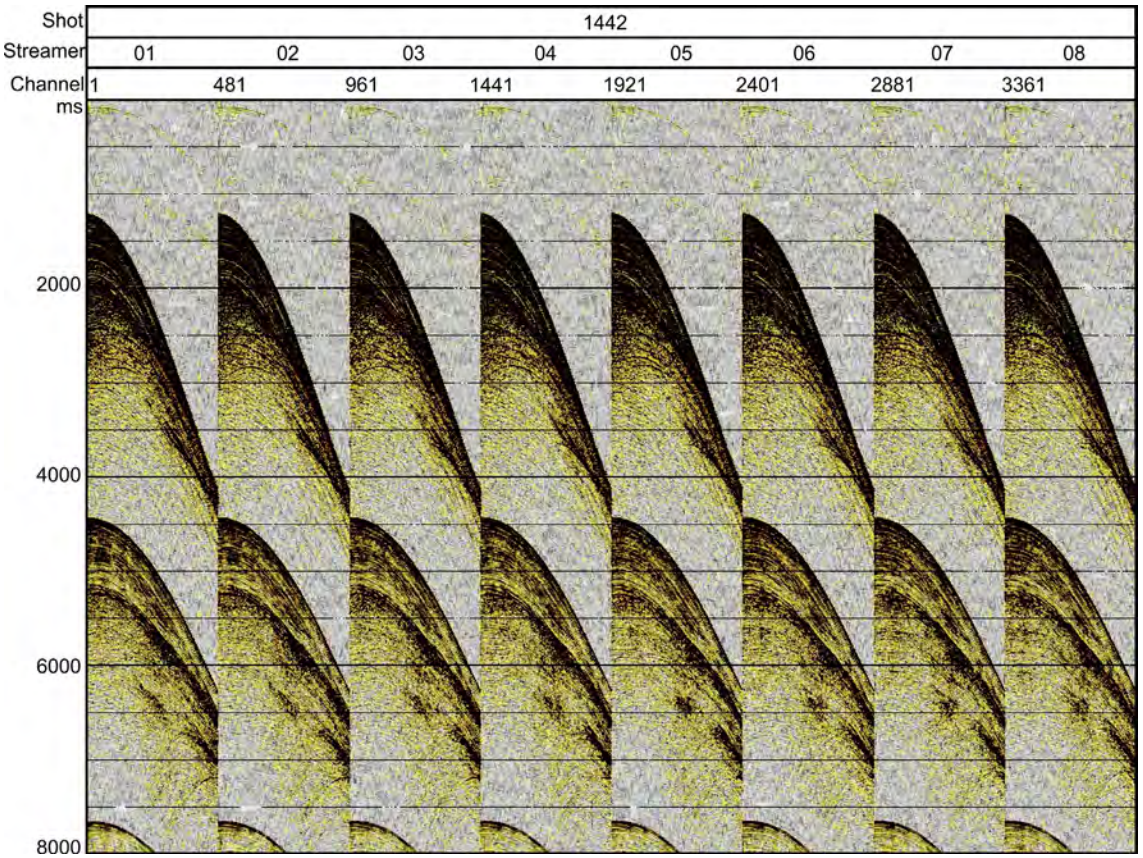


FIG. 2.39 An example 3D shot gather group acquired using eight streamers with 480 channels per streamer.

finishes shooting a sail line (Fig. 2.40A). In the case of antiparallel acquisition geometry, the vessel runs into the adjacent survey line when it finishes acquiring a sail line after a large circular line turn (Fig. 2.40B). The advantage of the racetrack pattern is that it requires less line change time with respect to the antiparallel acquisition pattern.

The vessel continues firing and recording for one-half the length of the streamer, which is the run-out distance, whenever it reaches the edge of the 3D survey area. Then the vessel starts turning to another parallel sail line at a certain distance away from the first one. Firing is initiated at a certain distance before the edge of the survey area, usually one-half the length of the streamer, which is the run-in distance. Except for a specific acquisition geometry, termed coil shooting (Section 2.3.8), generally no data is recorded between run-in and run-out zones, because, during the turns, steering devices may not properly handle the streamer separation, hindering the precise calculation of the receiver positions. Furthermore, increasing lateral drag, especially for the outer streamers, causes excessive swell noise induced on these streamers. The nonproductive time spent during the line changes for conventional 3D surveys may reach 50% of the total survey time. In order to reduce the number of turns during the survey,

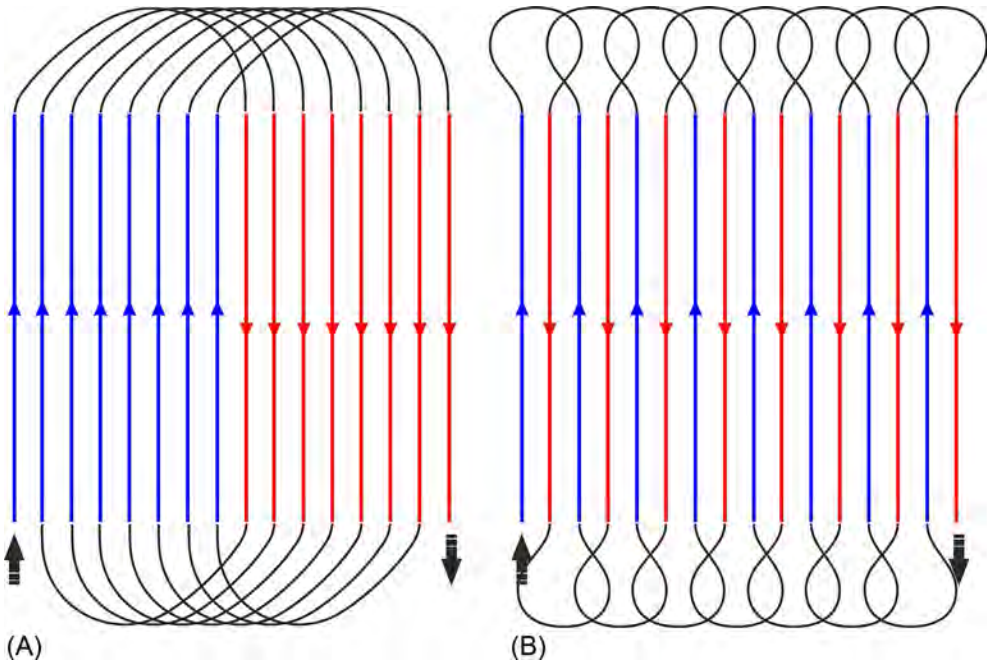


FIG. 2.40 Typical acquisition patterns for conventional 3D surveys. (A) Racetrack and (B) antiparallel survey patterns.

it is always preferred to shoot along the long sail lines. If the survey area is rectangular, then it is more feasible to collect the data along the sail lines lying parallel to the longer borderline of the survey area.

Line naming of the seismic profiles is usually in the following format:

AABBYY-LLLLCSSSS

AA: Client code
BB: Survey area code
YY: Year of acquisition
LLLL: Line number
C: Code for line type
- P: Prime line
- R: Reshoot line
- F: Infill line
- T: Test line

SSSS: Line sequence number

The sequence number starts from 0001 and regularly increases for each line with respect to the acquisition order of the seismic lines.

2.3.2 Streamer Steering

3D towed seismic acquisition simply requires several streamers to be deployed and towed by the vessel in parallel. Typically, the lateral separation between the streamers is 100 m even though it is 50 m for high-resolution 3D surveys. In 2D acquisition, only the depth of the streamer is an issue and we deploy bird units at regular intervals of approximately 300 m along the streamer to maintain the streamer depth along the sail lines. In 3D surveys, specific steering equipment is also required to maintain both vertical and lateral positions of several streamers. Operation of these steering units is controlled by an integrated navigation system, which automatically controls the wings of the devices, and required streamer separation is obtained and maintained in minutes following the activation of the streamer steering system. The steering system usually fails to keep the streamers straight behind the vessel in the case of strong

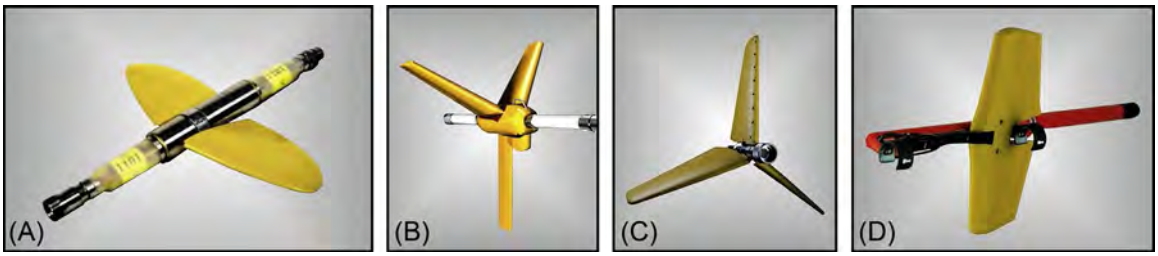


FIG. 2.41 Different 3D streamer steering devices. (A) Q-Fin (Schlumberger), (B) Nautilus (Sercel), (C) eBird (Kongsberg), and (D) DigiFIN (ION Geophysical).

surface currents, although it perfectly preserves the separation between the streamers.

Today, there are four different 3D streamer steering devices available in the market (Fig. 2.41):

- Q-fin (Schlumberger)
- Nautilus (Sercel)
- eBird (Kongsberg)
- DigiFIN (ION Geophysical)

Q-Fin, Nautilus and eBird devices allow streamer steering in addition to depth control, while DigiFIN provides only steering and the 3D spreads that use DigiFINs also need regular depth leveler birds to maintain the streamer depth. Nautilus is a 3D steering device specifically designed and developed to use with the Sercel's Sentinel streamers. Nautilus units do not require an internal battery pack to operate, since the power is supplied by the wiring within the streamer, which means fewer workboat operations to replace the internal batteries of the steering devices.

Constant streamer separation during the deployment and retrieval of the streamers, recording and line changes, even in the rough sea states and strong currents, is achieved by deploying these devices at regular intervals along the streamers. They also provide improvement in crossline sampling, a better subsurface coverage, and more uniform offset and azimuth distribution in the crossline direction, reducing the infill acquisition. This technology also allows us to apply different streamer layouts, such as fan mode acquisition (Section 2.3.7) by automatic steering using sophisticated computer algorithms. Steering devices also provide more reliable 4D data acquisition with a better replicating streamer shape for subsequent surveys for reservoir monitoring.

2.3.3 Streamer Layout

In a typical 3D seismic acquisition layout, there are 8–16 streamers, two paravanes, 8–16 tail and front buoys, and two identical gun arrays generally consisting of three strings. The distance between the streamers is not more than 100 m to achieve the required crossline sampling. An example 3D tow layout with eight streamers and two gun arrays is shown in Fig. 2.42. In this example, the vessel tows 8 streamers, each with 8000 m overall length. The separation between the streamers and gun arrays is 100 and 50 m, respectively, which provides 25 m crossline bin size. Minimum offset is 300 m and the total crossline coverage is 700 m. In order to accurately calculate the relative and actual geographical positions of each in-sea component, some of the surficial equipment such as gun floats, front buoys and tail buoys is equipped with rGPS transponders.

In 3D seismic acquisition, it is crucial to maintain the geometry of the in-sea equipment in the predetermined offset positions relative to each other. It is also quite important to precisely determine the positions of each source array as

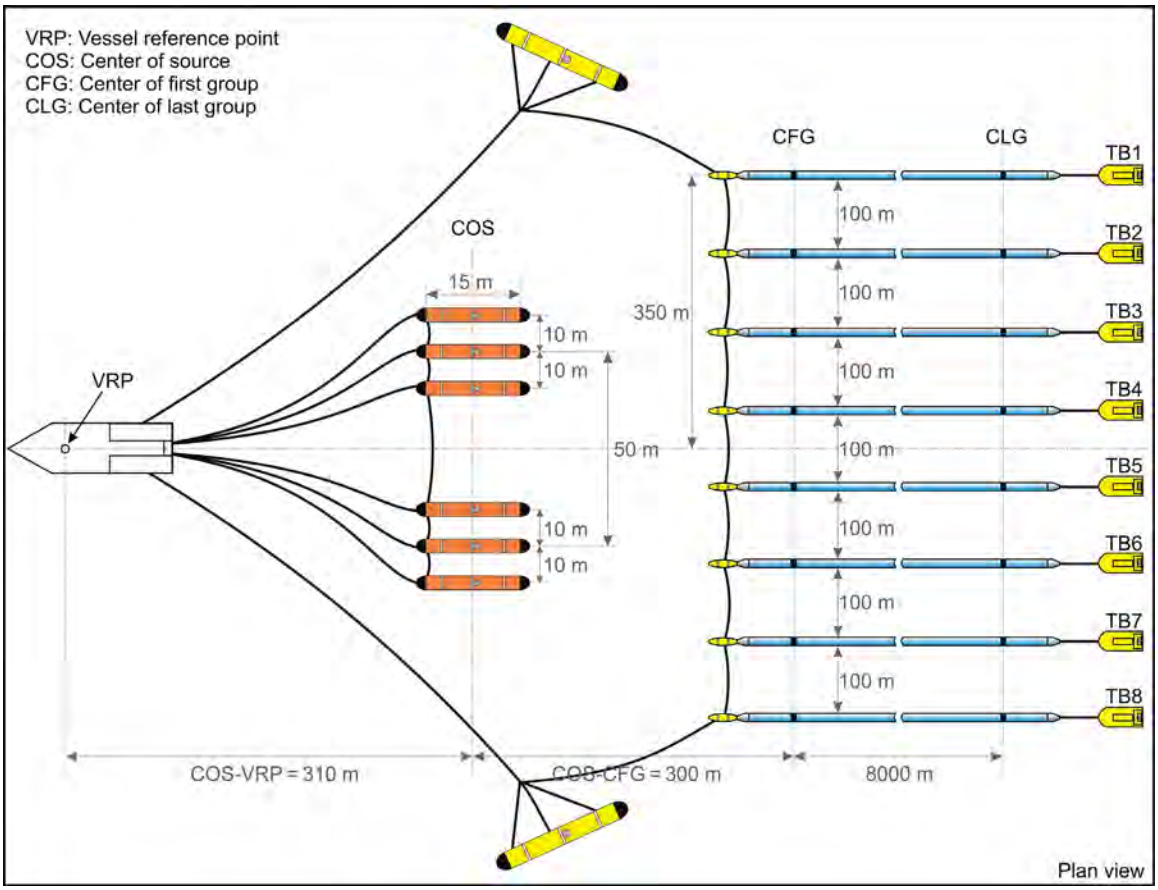


FIG. 2.42 Schematic illustration of a conventional 3D seismic tow layout with eight streamers and two identical gun arrays. TBs represent tail buoys.

well as the recording channels relative to the shot location at each shot point. These are accomplished by deploying specific instruments mounted onto the streamers and source arrays. These secondary navigation instruments are streamer steering devices, acoustic ranging devices, velocimeters, speed logs and compass birds.

A typical configuration example for one of the 6000 m-long streamers of a 3D layout is shown in Fig. 2.43. It consists of 80 active sections; each is 75 m long. The data is digitized by 40 digitizing modules, each of which handles the data from two active sections. In order to maintain the depth of the streamer, a total of 22 compass birds are attached to the streamer at regular intervals, approximately at every 300 m. Acoustic ranging is achieved by 10 acoustic units mounted at the frontal, middle and tail sections of the streamer to establish the front, mid, and tail acoustic ranging networks. In general, one of the gun strings in each array and some of the tail buoys also have acoustic transceivers to arrive at a solution in the acoustic ranging to obtain the positions of the streamers in the water. A total of 15 DigiFIN streamer steering units are used to maintain the lateral streamer separation, based on the information from the

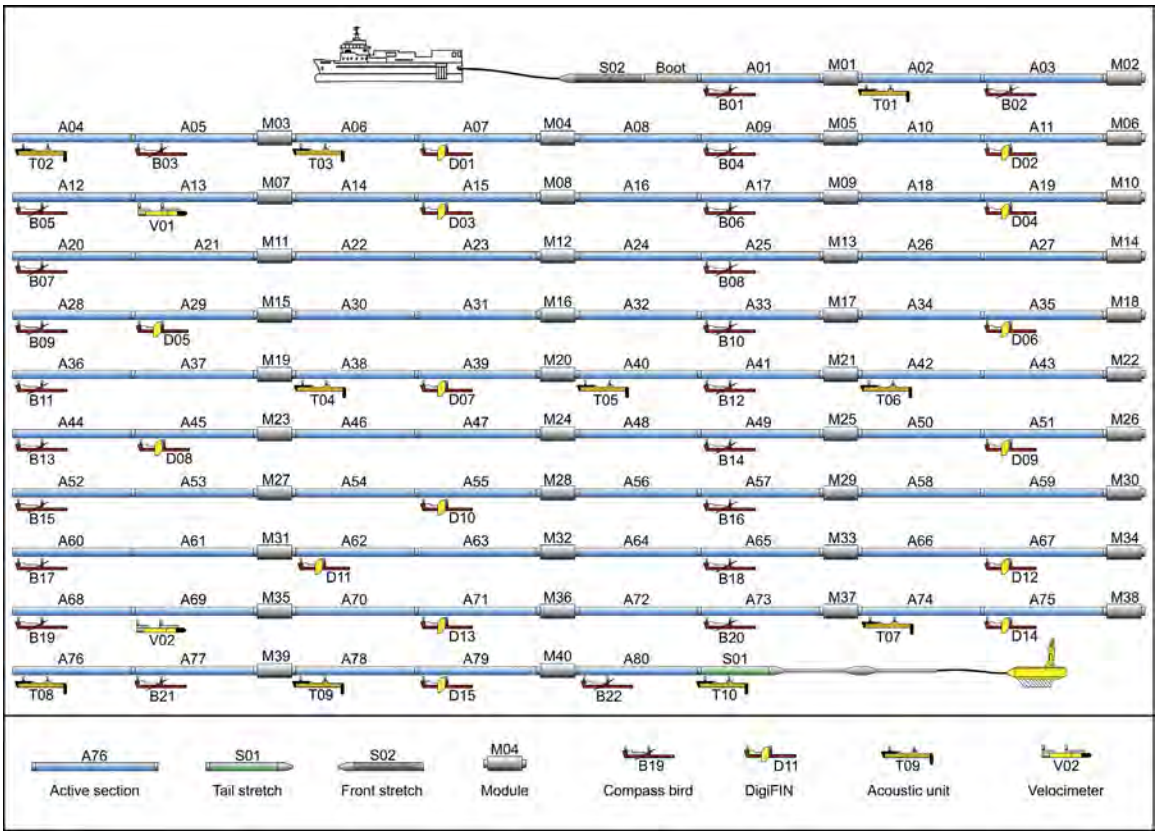


FIG. 2.43 An example configuration of a 6000-m streamer for a 3D spread including several acoustic positioning units, steering devices, depth levelers (birds) and velocity sensors attached directly to the streamer.

acoustic ranging units. Finally, two separate velocity sensors are attached to the streamer to obtain the real-time velocity variations along the surficial waters of the survey area. All of these sensors send and receive data via the streamers using specific communication coils and their internal battery packages, except for the acoustic ranging system IRMA (Western Geco) and steering system Nautilus (Sercel), both of which use power transported by the wiring within the streamers.

Fig. 2.44 shows the plan view of an example navigation configuration for an 8000-m spread with 10 streamers. Each streamer of this spread consists of 19 depth levelers, 15 acoustic units (three for front-, three for mid-, and three for tail-nets as well as one unit for each gun string), 18 rGPS units located on gun strings, paravanes and tail buoys. The spread also has three velocity sensors to measure the real-time water velocity for acoustic networking. In addition to these devices, two specific sensors termed speed logs are also attached to the central parts of the outermost streamers of the spread. During the line change, the shooting and recording cannot be done, and it is always preferred to perform a fast line change since there is no production during this dead time. When the vessel starts turning, however, the outermost streamers are exposed to extra stress since they move faster.

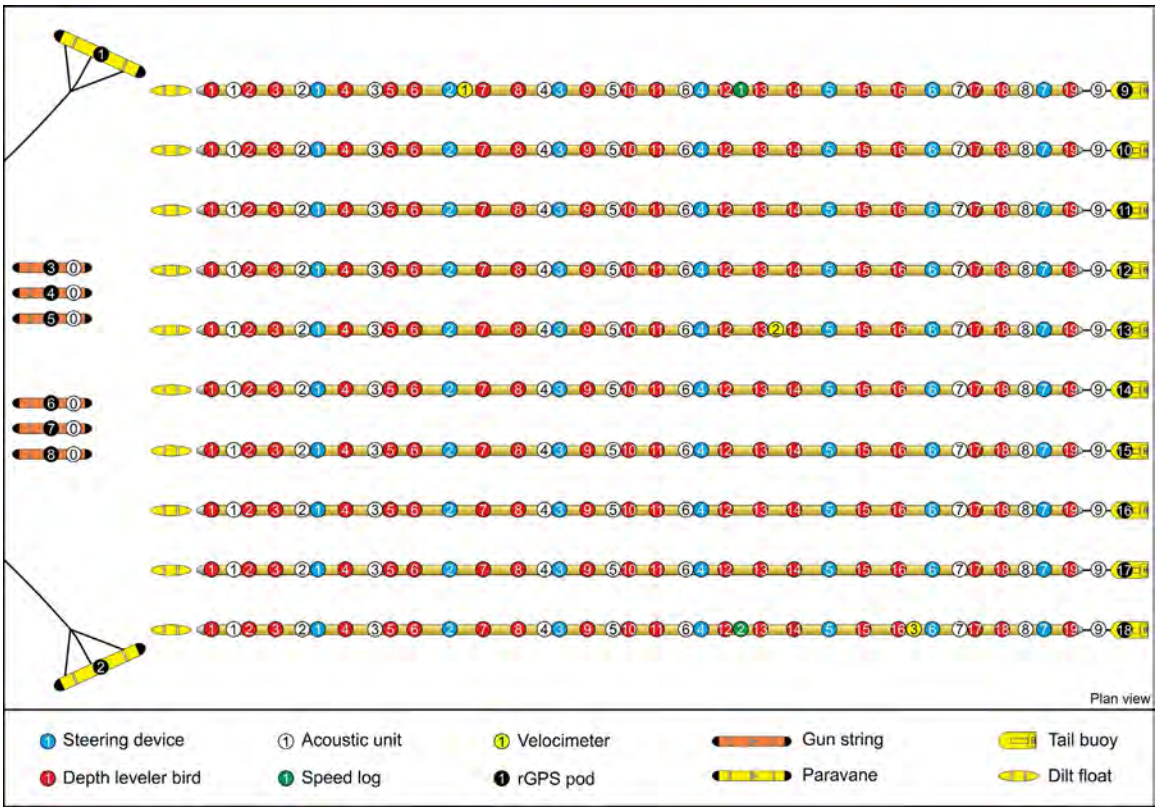


FIG. 2.44 An example navigation configuration of a spread with 10 streamers including several acoustic ranging units, steering devices, depth levelers (birds), rGPS pods, speed logs and velocity sensors.

The velocity information from these speed sensors attached to the outermost streamers enables us to perform a line change as fast as possible without exceeding the strength limitations of the streamers.

2.3.4 Acoustic Network

The separation between the streamers is measured with specific acoustic transceivers which utilize high-frequency acoustic signals to communicate with other acoustic devices in their vicinity and calculate the one-way slant range distances to adjacent units mounted on different positions on the nearby streamers in real-time. These devices enable us to observe and modify the shape of the streamers relative to the towed array in the case of strong surficial currents and rough weather conditions as well as during the line changes, and the positions of all available recording channels can be precisely determined. Apart from mounting directly on the streamers, these acoustic units are also attached to the hull of the vessel, front and tail buoys, and gun strings to communicate with each other for the determination of the positions of all in-sea equipment within the spread.

They work between the 50 and 100 kHz frequency band with an acoustic range resolution of 5 mm. The acoustic ranging units are typically spaced at 100 m intervals along the streamers, specifically located at front, middle and tail

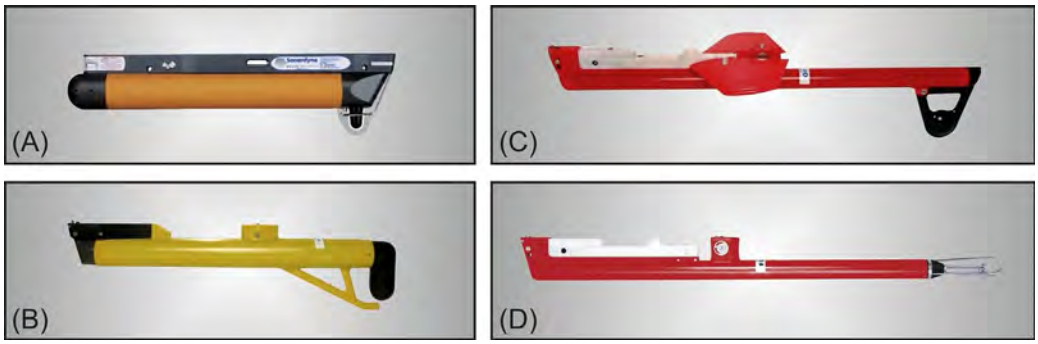


FIG. 2.45 Different external devices attached to the streamers for acoustic networking. (A) Sips 2 XSRS (Sonardyne), (B) CMX (ION Geophysical), (C) acoustic bird (ION Geophysical), and (D) velocimeter model 7000 (ION Geophysical).

sections of the spreads, and can both transmit and receive acoustic pulses for range determination. Fig. 2.45 shows the most common acoustic positioning devices on the market today. SIPS 2 XSRS (Sonardyne) and DigiRANGE-II CMX (ION Geophysical) are the most widely used positioning units. Each XSRS has four receive channels and one transmit channel, and as an example configuration, a typical layout of 6 streamers of 8 km long requires 42 units to derive the acoustic ranging solution. In addition to the aforementioned systems, Western Geco has developed a digital acoustic positioning system known as IRMA (Intrinsic Ranging by Modulated Acoustics) to work with their streamer steering system Q-Fin for a fully braced acoustic solution. In addition, the Nautilus system developed by Sercel also has its own acoustic positioning module to operate with the Sercel's Sentinel streamer. ION Geophysical produces a device called the acoustic bird which combines a conventional depth leveler bird and a CMX device to operate with ION's DigiFIN lateral streamer steering device (Fig. 2.45C).

Since all the communications between the acoustic positioning devices are performed by high-frequency sound pulses, it is necessary to know the sound velocity in the water column to precisely convert the arrival times of the acoustic pulses to distance ranges. Since the seismic spread has very large dimensions, the inner and outer streamers as well as front and tail sections may expose different sound velocities. The velocity information is obtained in real-time during the survey by velocimeters or speed sensors mounted on the front and tail sections of one or two selected streamers in the spread. Fig. 2.45D shows the model 7000 velocimeter of ION Geophysical. Sips 2 XSRS transceivers and Nautilus devices also offer an option to include sound velocity sensors.

All acoustic positioning devices attached to the streamers, vessel's hull, the gun strings, and the front and tail buoys form acoustic nodes. These nodes compose an acoustic network among the streamers and other in-sea equipment, which enable us to measure the ranges. The acoustic network of a 3D spread may be quite complex consisting of several hundred nodes. Fig. 2.46 illustrates an example 3D acoustic network and the ranges between the nodes for a four streamer case. The network consists of three subnetworks of front-, mid- and tail-net. In addition to the acoustic ranging units on the streamer, each gun string has also its own acoustic transponder to incorporate the ranging network. The main purpose is to find out the positions of each individual node within the network by incorporating the specific nodes whose positions are already known by some external measurements, such as rGPS observations. These specific nodes are termed fixed nodes.

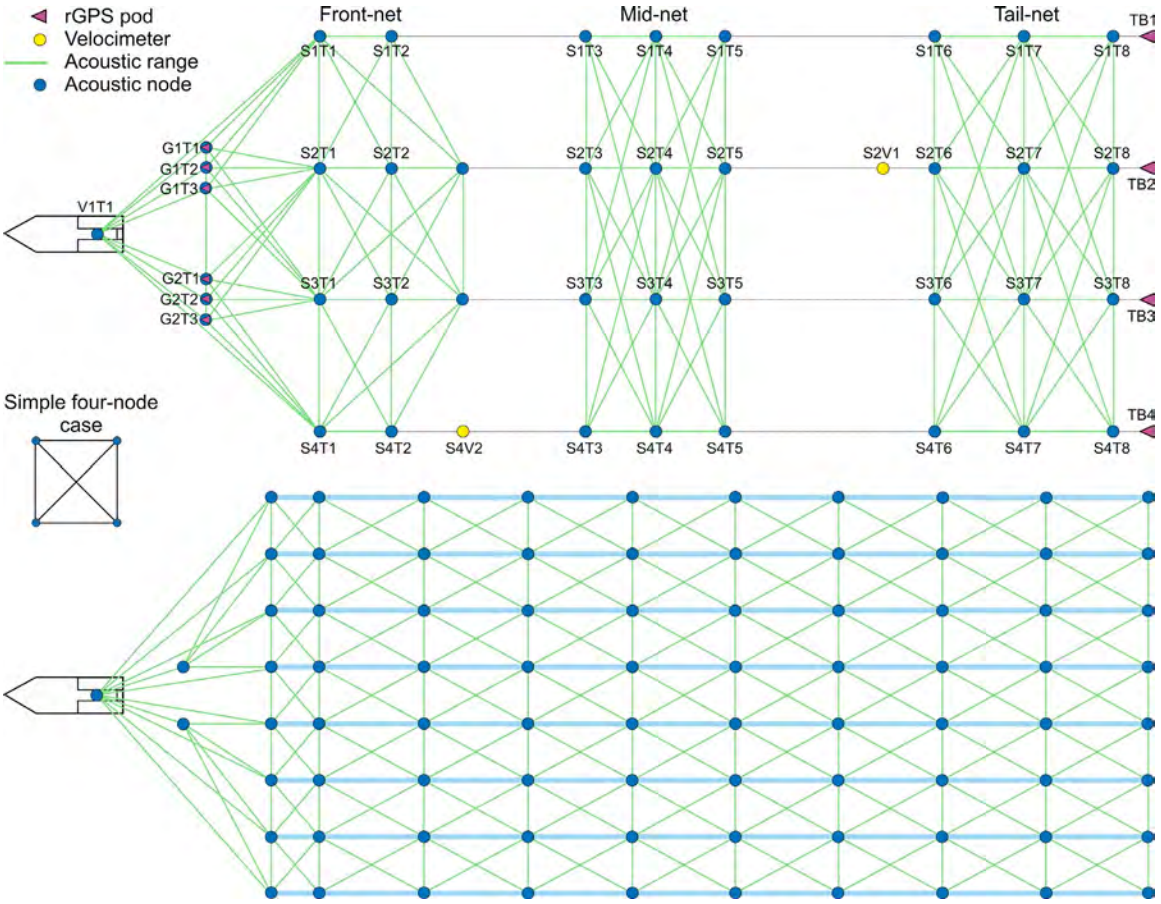


FIG. 2.46 An example 3D acoustic network and the ranges between the nodes along with the rGPS transponders and velocimeter locations for a typical four-streamer acquisition spread (top), and a schematic fully braced acoustic network (bottom).

The solution is accomplished by the least squares approach. In this method, a node must have at least two ranges to determine its position. In a simple four-node case, there are six possible ranges between the nodes despite the four unknown node positions, which makes the system mathematically overdetermined in terms of least squares method. Overdetermined systems are termed redundant networks, with the difference between the observations and the unknowns called redundancy. In a 3D acoustic network, one can arrive at a reliable solution simply if there is redundancy. Fixed nodes for the frontal part of the streamers are typically the front buoy nodes or the gun strings if they are incorporated into the solution. The networks are designed and the acoustic positioning devices are located over the spread so that it becomes an over determined network over which a positioning solution is obtained for the entire network to compute the positions of the nodes, and hence, each receiver group.

Today, most seismic vessels utilize three individual networks along the spread (Fig. 2.46): front-net (incorporates the nodes at gun strings, paravanes, front buoys and the specific nodes on

the head sections of the streamers), mid-net (incorporates only the specific nodes on the middle sections of the streamers), and tail-net (incorporates the nodes at tail buoys and the specific nodes on the tail sections of the streamers). As a specific case, if the network runs the overall length of all available streamers within the spread, then it is termed a fully braced acoustic network, which provides a complete solution without deploying the compass birds to arrive at a solution (Fig. 2.46). The IRMA acoustic positioning system of Western Geco and the complete Nautilus streamer steering solutions, along with the Sentinel streamers of Sercel, provide fully braced acoustic networks.

Separation between the streamers is automatically maintained by dedicated software, which integrates the data from streamer steering devices and acoustic positioning units in the areas of moderate surficial currents. These systems can compensate streamer feathering up to 3 degrees and they can assure to maintain the zero feathering soon after activation of the real-time streamer steering control system (Fig. 2.47A). For higher feathering angles, the separation between the streamers can be assured by steering systems, although straightness of the streamers behind the vessel cannot be retained parallel to the sail line (Fig. 2.47B). Without automatic steering systems, however, it is not possible to maintain the streamer separation along the crossline offset (Fig. 2.47C).

2.3.5 Flip-Flop Shooting

Conventional 3D seismic acquisition is performed by firing two identical air gun arrays alternately termed flip-flop acquisition. The separation between the arrays is generally half of the streamer separation of the spread, which doubles the crossline sampling and reduces the acquisition footprint. In flip-flop acquisition, the

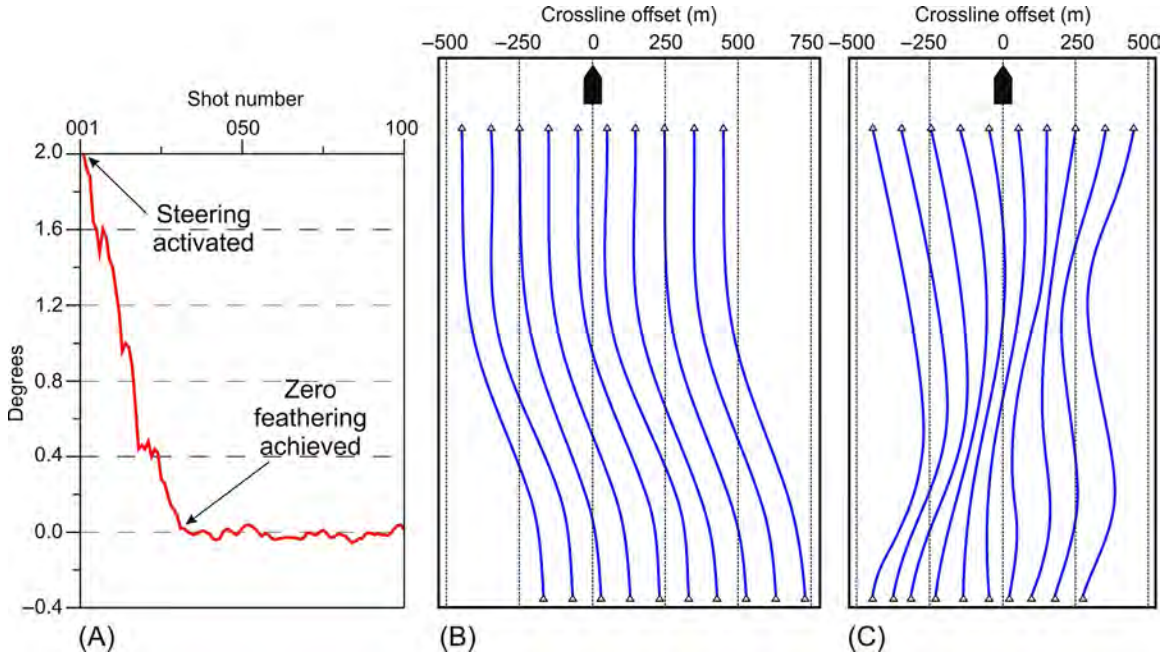


FIG. 2.47 (A) Feather angles after the activation of automated streamer steering control. Schematic illustrations of streamers (B) with and (C) without automatic steering system.

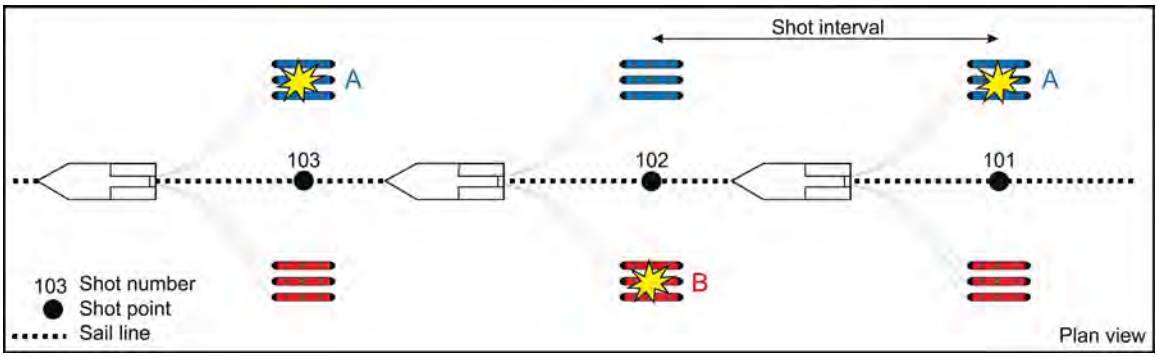


FIG. 2.48 Schematic illustration of flip-flop shooting technique in 3D surveys. Starboard array (A) is fired at odd-numbered shot points while port array (B) is fired at even-numbered shot points.

starboard array (A) is fired at odd-numbered shot points while the port array (B) is recharged by compressed air; and array B is fired at even-numbered shot point locations while array A is recharged (Fig. 2.48). Flip-flop technique is standard for 3D towed streamer acquisition today and it provides 12 CMP lines for six parallel streamers and a better coverage of the subsurface.

Fig. 2.49 shows the ray paths of the seismic energy radiating from each source array in crossline and plan views for the six-streamer case. In flip-flop shooting, the shot interval for each individual CMP line is twice the firing interval. For instance, at the first shot point, odd CMP lines in Fig. 2.49A have traces of the reflections from source S1. At the second shot point, source S2 will be fired (Fig. 2.49B) and there will be no trace contribution from this shot to odd-numbered CMP lines. The third shot will provide again traces reflected from odd-numbered CMP lines. As a result, the reflections from every second shot belong to the same CMP line for flip-flop acquisition. If each gun array is fired every 25 m, then the shooting interval for each CMP line is 50 m.

2.3.6 Slant Streamer Acquisition

In conventional 3D acquisition, all streamers are towed horizontally at a constant depth, which also determines the available bandwidth of the recorded data due to the receiver ghost interference. As the streamer gets closer to the sea surface, the ghost notch arises at higher frequencies resulting in a wider frequency bandwidth (Section 2.2.3), although it causes attenuation of lower frequencies and increases the noise in the recorded data. When we tow the streamers deeper, on the other hand, the ghost notch occurs at lower frequencies limiting the high-frequency end of the spectrum although it provides better low-frequency content.

In 2010, CGG Veritas developed a simple methodology to completely remove the receiver ghost interference, which is named variable depth or slanted streamer technology, or BroadSeis. Using an optimally curved streamer configuration, it is possible to record both low and high frequencies based on the notch diversity: Combining the data from different receivers located at different depths along a variable depth streamer (Fig. 2.50), the resultant data has no notches since each receiver has a different notch frequency because of their varying depths, following an advanced joint deconvolution algorithm (Soubaras and Lafet, 2011). This algorithm is based on the application of two sections. The first one is conventional migrated section applied to the data from variable depth streamer. The second one is the mirror migration output, which treats the data as if it is recorded

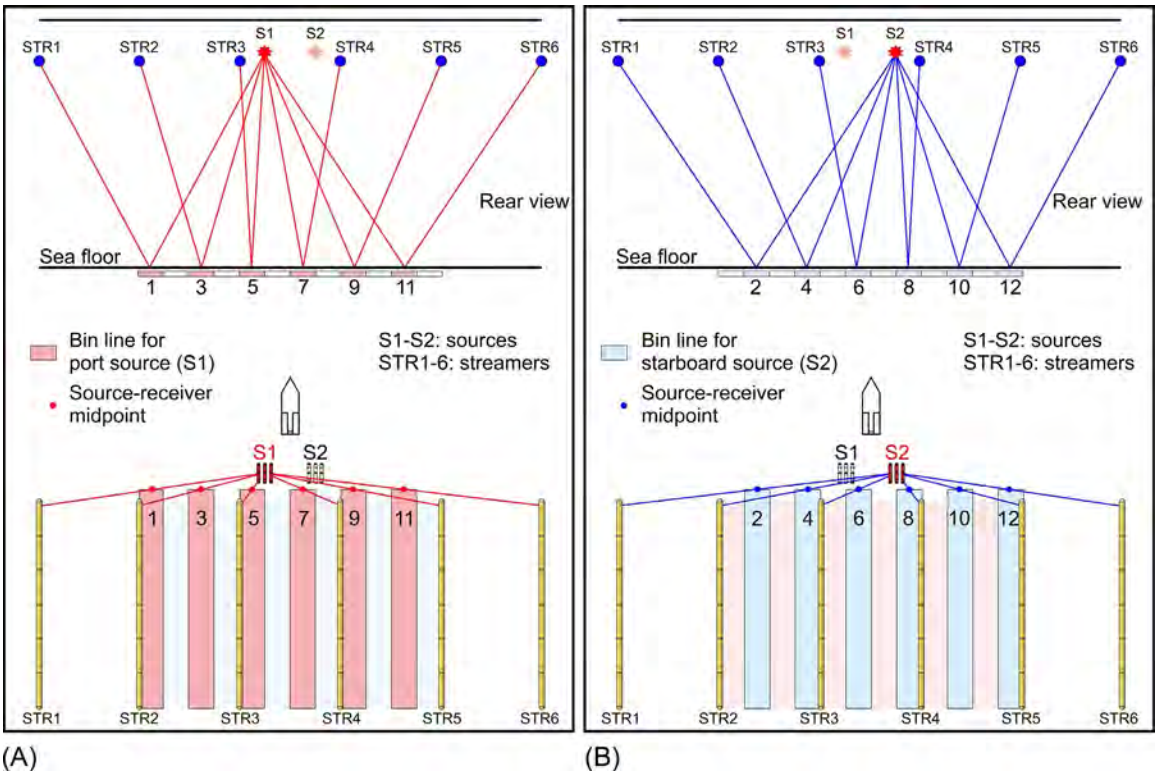


FIG. 2.49 Schematic illustration of flip-flop acquisition geometry for dual sources (S1 and S2) and six streamers (STR1 to STR6). (A) When the first source (S1) is fired, the signals following the red ray paths form red bin lines along the sail line. (B) When the second source (S2) is fired, the signals following the blue ray paths constitute blue bin lines.

by a mirror cable located above the sea level as the real slanted cable below the sea surface. The joint deconvolution algorithm combines two migrated sections to provide a broadband section without receiver ghost interference.

In variable depth streamer acquisition, the depth of the streamer does not linearly increase over its offset, but a curved streamer layout is applied. The shape and curvature of the slanted streamer can be configured according to the target depth. The slope of the streamer is larger for the frontal sections and the remaining portion of the streamer is simply flat (Fig. 2.50), which ultimately provides a receiver ghost-free seismic data, since the receiver ghost notch varies along the slanted cable. Therefore, it allows us to record seismic data with a wider spectral bandwidth from the ultra-low frequencies of 2.5 Hz to source notch frequency. Fig. 2.51 compares conventional and slant streamer data along with their corresponding amplitude spectra.

2.3.7 Fan Mode Acquisition

Conventional 3D towed streamer acquisition is performed to acquire a uniform surface coverage using 8–16 parallel streamers with typical overall streamer lengths of 6–12 km. In the case of 8 × 12 km streamers with 100 m separation, the overall spread covers an area of 700 m × 12,000 m. Although precise positioning systems for in-sea equipment are utilized for accurate positioning and to compensate streamer feathering during the acquisition,

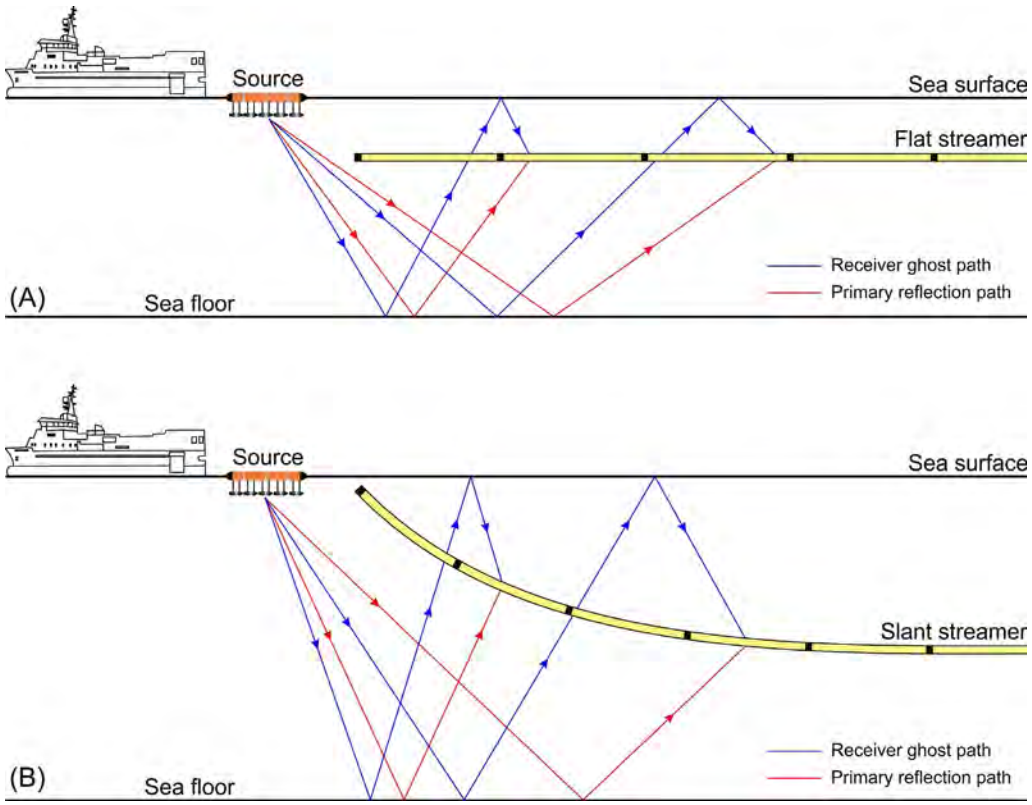


FIG. 2.50 (A) Conventional flat streamer acquisition and (B) variable depth (slant) streamer acquisition.

strong surficial currents divert the streamers from the preplot lines, which reduces the coverage or results in gaps in various sizes in the final fold coverage distribution. In such cases, an infill acquisition program is planned to acquire extra data to fill in these gaps. However, the extra infill lines are costly and increase the total survey time, sometimes amounting to 15% of the entire survey.

In order to minimize the infill time, modern seismic vessels deploy fan mode acquisition configurations for 3D acquisition, where the streamer separation is increased with offset progressively from the head to tail with the real-time benefit of streamer steering devices. The final spread has a fan-like shape in plan view. The main purpose of a fan mode spread is to obtain a regular coverage distribution, especially for far offsets and to reduce infill up to 5%, especially in areas of extreme cable feathering due to the surface currents and rough weather conditions. In the example configuration in Fig. 2.52, the streamer separation for head and tail sections are 100 and 200 m, respectively.

2.3.8 Multiazimuth Surveys

The azimuth of each individual trace can be defined as the angle between the vector line from center of the source to receiver location that it is recorded, and the survey sail line. For instance, the azimuth of a trace recorded at the nearest channel of the first streamer for the signal emitted from source S1 in Fig. 2.53A is α_1;

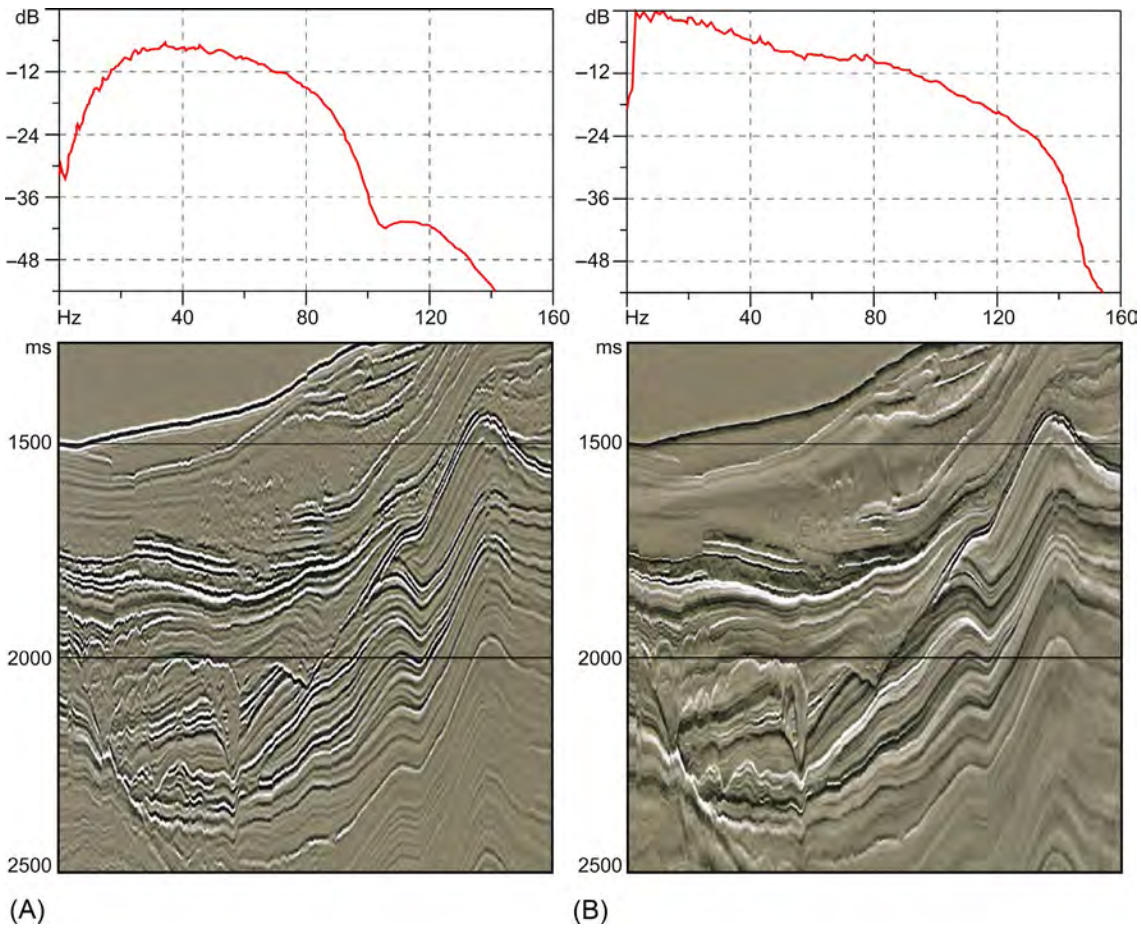


FIG. 2.51 (A) Conventional and (B) variable depth streamer (BroadSeis) data. Corresponding average amplitude spectra are given in the upper panels. *After Lin, D., Sablon, R., Gao, Y., Russier, D., Hardouin, D., Gratacos, B., Soubaras, R., Whiting, P., 2011. Optimizing the processing flow for variable-depth streamer data. First Break 29, 89–95.*

while it is α_2 for the farthest channel of the same streamer and source pair. As the vessel sails through the survey line, several reflections are recorded for the same bin on the sea floor. Each of these reflections within the same bin has different offsets and azimuths (Fig. 2.53B). We can map these azimuths as an azimuth distribution map (Fig. 2.53C) or as a rose diagram (Fig. 2.53D) for each bin. In addition, it is also possible to map the distribution of all offsets within the bins as a histogram display (Fig. 2.53E).

In conventional 3D recording with a racetrack shooting pattern by a single vessel, however, relatively long and narrow streamer spreads provide a range of different azimuths only in areas of the frontal part of the streamers. Therefore, a single vessel 3D acquisition allows us to collect data only a narrow-azimuth range, which is thus termed narrow-azimuth (NAZ) surveys. Fig. 2.53D shows a typical rose diagram of azimuth distribution from a NAZ survey. The offset increases from zero at the center of the circles to the outside, and each radial line

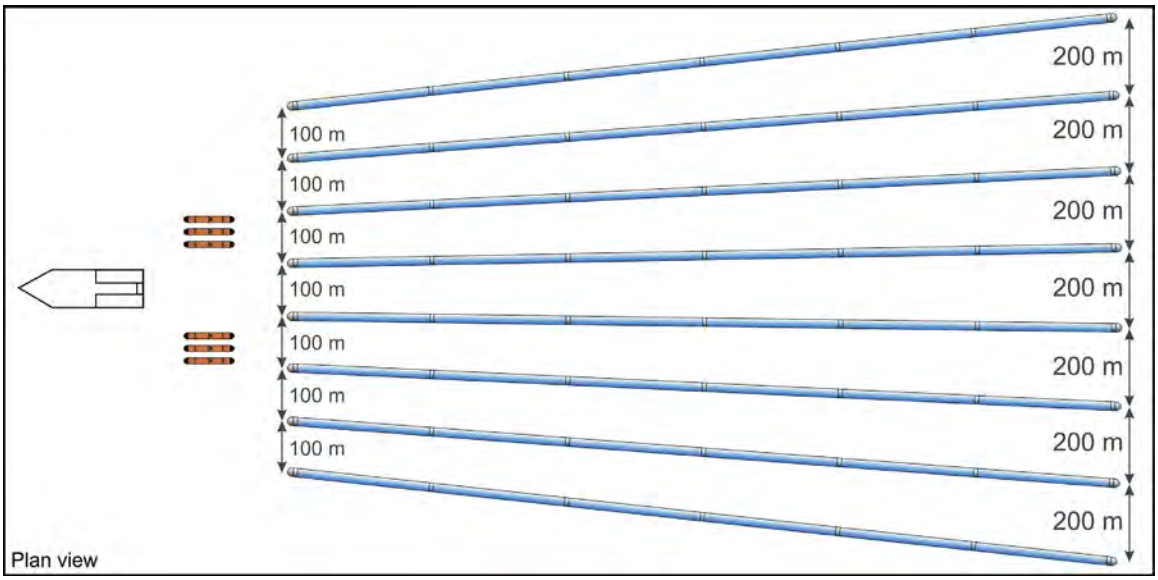


FIG. 2.52 Schematic illustration of fan mode acquisition with eight streamers. The separation between the streamers is linearly increased with offset from head to tail for a better coverage for far offsets to minimize the infill time.

represents a source-receiver azimuth. Although short offset traces have a variety of azimuths, generally within ±60 degrees, long offset traces are of poor azimuth distribution, typically within ±10 degrees.

While 2D acquisition provides only one constant azimuth, 3D acquisition enables us to record seismic data from different azimuths for each shot. It is always preferred to record data rich in azimuth to illuminate the subsurface geology in different shooting directions (survey azimuths), which can provide a complementary target illumination (Long, 2009). Incorporating different azimuths provides visualization of the target from different directions, which ensures a better imaging of all sides of the target structure. Fig. 2.54 compares a narrow azimuth and multiazimuth (three surveys) 3D data from the same survey line. The multiazimuth data has a better S/N ratio and trace-by-trace consistency, or lateral resolution both for shallow and deep parts.

The term illumination indicates that the energy reflected from everywhere at the target has uniform distribution by means of offsets and azimuths, which ultimately provides a high-quality seismic image of the target. In conventional NAZ surveys, however, target illumination is not uniform and specific acquisition patterns, termed multiazimuth acquisition, are performed to resolve the target illumination problems in 3D exploration. We can classify these specific techniques into different categories. Fig. 2.55 shows the rose diagrams of azimuth distributions along the offsets for each of the following different acquisition patterns:

- *Narrow-azimuth surveys (NAZ)*: One single vessel tows all the streamers and source arrays along a single azimuth sail line (Fig. 2.55A).
- *Multiazimuth surveys (MAZ)*: Several NAZ surveys are performed by one single vessel in different sail line azimuths over the same target zone (Fig. 2.55B).

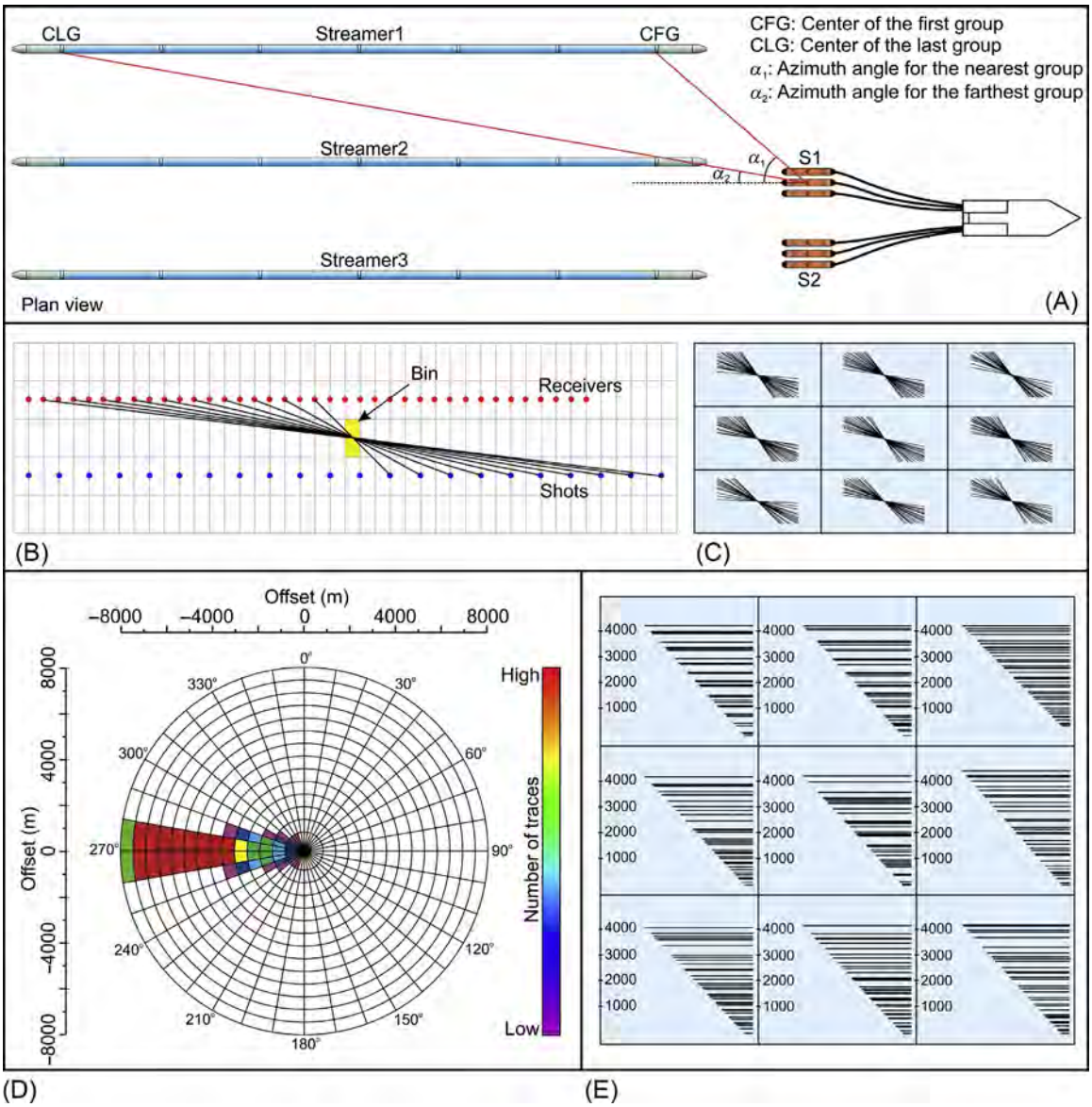


FIG. 2.53 (A) Azimuth angles for the nearest (α_1) and farthest (α_2) channels of the first streamer for the signals emitted from source array-1 (S1). (B) Schematic illustration of the rays with different azimuth and offset ranges in a selected bin. (C) Azimuth distribution of nine neighboring bins. (D) Rose diagram for a narrow-azimuth survey. Distance from the center of the circles is the offset, and the angles correspond to azimuth. Color codes indicate the number of traces recorded for each offset-azimuth pair. (E) Distribution of all offsets within nine neighboring bins as a histogram display where the vertical axis is source-receiver offset of each trace in each individual bin.

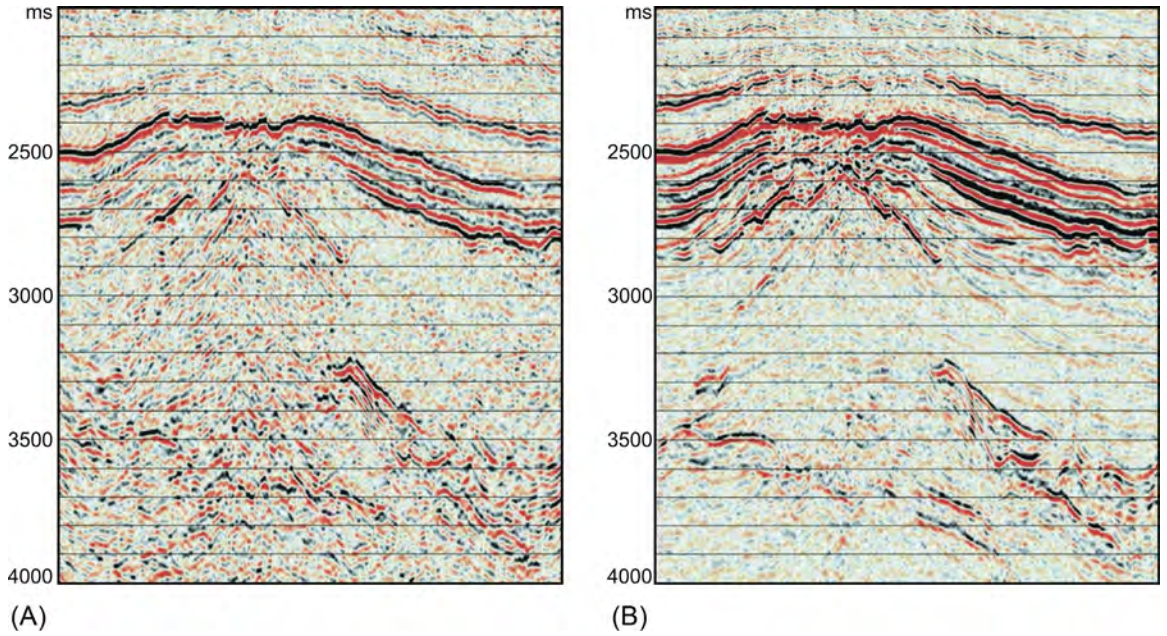


FIG. 2.54 Prestack migration comparison of (A) single azimuth data from a NAZ survey and (B) three-azimuth data from a MAZ cube. *After Long, A., 2009. Evolutions in seismic azimuth: past, present and future. Geohorizons 4–13.*

- *Wide-azimuth surveys (WAZ)*: One or two shooting vessels accompany the single NAZ vessel along a single azimuth sail line (Fig. 2.55C).
- *Rich-azimuth surveys (RAZ)*: A combination of MAZ and WAZ surveys provides the most regular azimuth distribution in the survey area (Fig. 2.55D).
- *Coil shooting*: One single vessel tows the streamers and a source array along a circular path (Fig. 2.55E). An extra shooting vessel may also be used (Fig. 2.55F).

Recently, CGG Veritas has tested a specific acquisition technique called TopSeis, where the seismic sources are towed from a second vessel, positioned above the middle of the streamer spread towed by the streamer vessel, which is an innovative source-over-spread acquisition configuration (Whaley, 2017). The streamers are towed at approximately 50 m at the center of the spread, where the sources are located. This configuration provides an increased near-offset coverage from a split spread layout with zero and negative offsets. TopSeis provides a better azimuth distribution and notch diversity, enabling a higher-resolution data with no ghost reflection.

Although they are more costly than conventional 3D NAZ acquisitions, the main benefits of wide-azimuth seismic data are an improved target illumination, a better S/N ratio due to the contributions from different azimuths during the stacking of each 3D azimuth cube, and a better multiple attenuation (Moldoveanu, 2006). As the world's hydrocarbon exploration strategy moves into more challenging areas such as the areas of salt tectonism, or the regions covered by volcanic rocks or carbonates, different types of unconventional surveys which provide extra azimuths become more and more popular to image complex subsurface targets, particularly beneath the large salt bodies. MAZ surveys can be performed as complementary surveys to

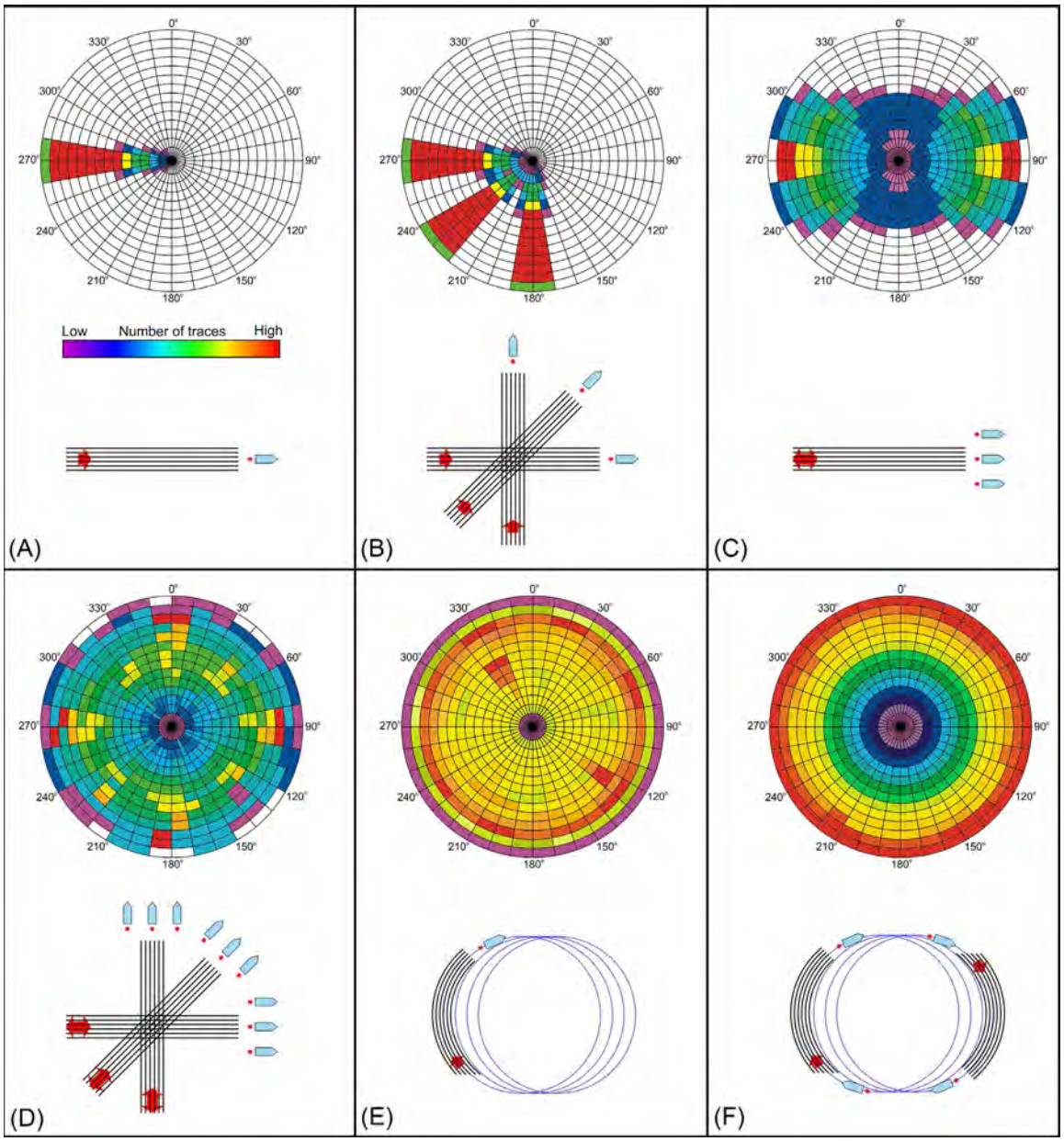


FIG. 2.55 Azimuth-offset distributions as rose diagrams for different acquisition geometries. (A) Narrow-azimuth (NAZ), (B) multiazimuth (MAZ), (C) wide-azimuth (WAZ), (D) rich-azimuth (RAZ), (E) full-azimuth (coil shooting), (F) full-azimuth (dual coil shooting). Single and dual coil shooting surveys are done by Western Geco.

an existing NAZ data, typically over a relatively small-scale target, to improve the image of that specific target instead of being applied to a whole 3D survey area. WAZ surveys assure significant improvements in azimuth distribution, especially for near offsets: While they can provide almost a full range of azimuths for near offsets, it is only ±30 degrees for far offsets. RAZ surveys use WAZ vessel configuration with a MAZ shooting design, and acquires the most regular azimuth distribution for all shots within the survey. A full-azimuth (FAZ) survey was conducted in 2014 by PGS using five vessels (Long et al., 2014). During the survey performed in the Gulf of Mexico, all five vessels towed source arrays, two vessels tow 10×8100 m streamers with 120 m separation, and 30-degree, 90-degree, and 150-degree survey azimuths were applied. The result is a uniform full-azimuth sampling for all source-receiver offsets.

Coil shooting is another approach for full-azimuth (FAZ) surveys. It was not realized that the circular acquisition for rich azimuth data was practical for 3D surveys until it was successfully tested in 2006 by Western Geco. In coil shooting surveys, only one single vessel tows both source array and streamers and the vessel sails in closely spaced circles in the area to acquire FAZ data for the whole survey. The technique provides narrow azimuths for near offsets, while the far offsets are acquired with much larger azimuths. The main advantages of the method are that a better illumination of the target is obtained with higher S/N ratio along with a more complete suppression of the multiples. Furthermore, a proper sorting of coil shooting data based on the different azimuth ranges promises anisotropic analysis, such as anisotropic fracture detection or velocity analysis.

A recent acquisition method is known as FreeSeis which provides full-azimuth seismic data using several parallel submerged streamer cables, while the seismic source is towed by a source vessel (Haumonté, 2017). Each streamer, floating in the mid-water, are independent and autonomous, controlled by a pair of small vessels which regulate the position and record the seismic data. Streamers have 4C sensors every 25 m, each with a hydrophone and geophone measuring the wave pressure and velocity to cancel out the ghost reflection, which provides a broadband high-resolution seismic image of the subsurface. Since the streamers are not towed, the swell noise from water flow and mechanical cable noise are completely eliminated.

2.4 SPECIFIC ACQUISITION TECHNIQUES

Today, both 2D and 3D towed streamer acquisitions have been employed worldwide to map shallow and deep reservoirs, shallow gas and gas hydrates, faults or small scale fractures and stratigraphic character of the subsurface. The towed streamer surveys are considered to be conventional marine seismic acquisitions. Apart from narrow- or rich-azimuth towed streamer surveys, there are a couple of unconventional or specific seismic acquisition techniques which are used based on the requirements of the acquisition environment or necessities of the project. In this section, unconventional acquisition methods, such as four-component (4C) ocean bottom seismic recording by ocean bottom cables or nodes, time-lapse (4D) acquisition for reservoir monitoring, transition zone acquisition and P-cable acquisition, are briefly introduced.

2.4.1 Ocean Bottom Seismic Acquisition

Although two-component (2C) with a hydrophone and an accelerometer and four-component (4C) with a hydrophone and three-component motion sensor technologies have been successfully utilized for towed streamer acquisition in recent years, today single sensor 2D and 3D towed streamers are still widely used

to record pressure fields produced by the source arrays and perceived by suitably configured hydrophone groups. Technological developments in the last decade have allowed us to record 4C data using different sensors directly in contact with the sea floor. These multicomponent recording systems include three orthogonally oriented geophones or accelerometers for 3C recording as well as a hydrophone for pressure. Since S waves cannot propagate through water, S wave exploration at sea can only be achieved by 4C ocean bottom sensor recording. While P waves are recorded by vertical component geophones/accelerometers and the hydrophone, the mode converted S waves are recorded by horizontal (X and Y) component geophones/accelerometers (Fig. 2.56).

The primary purpose of 4C acquisition is to obtain a more detailed and accurate subsurface image at the reservoir level by recording both acoustic and elastic wave field components, including mode converted S waves generated by incident P waves at nonnormal incidence angles along the interfaces.

There are three techniques which are used to record ocean bottom seismic data:

- Ocean bottom cable (OBC)
- Ocean bottom seismometer (OBS)
- Ocean bottom nodes (OBN)

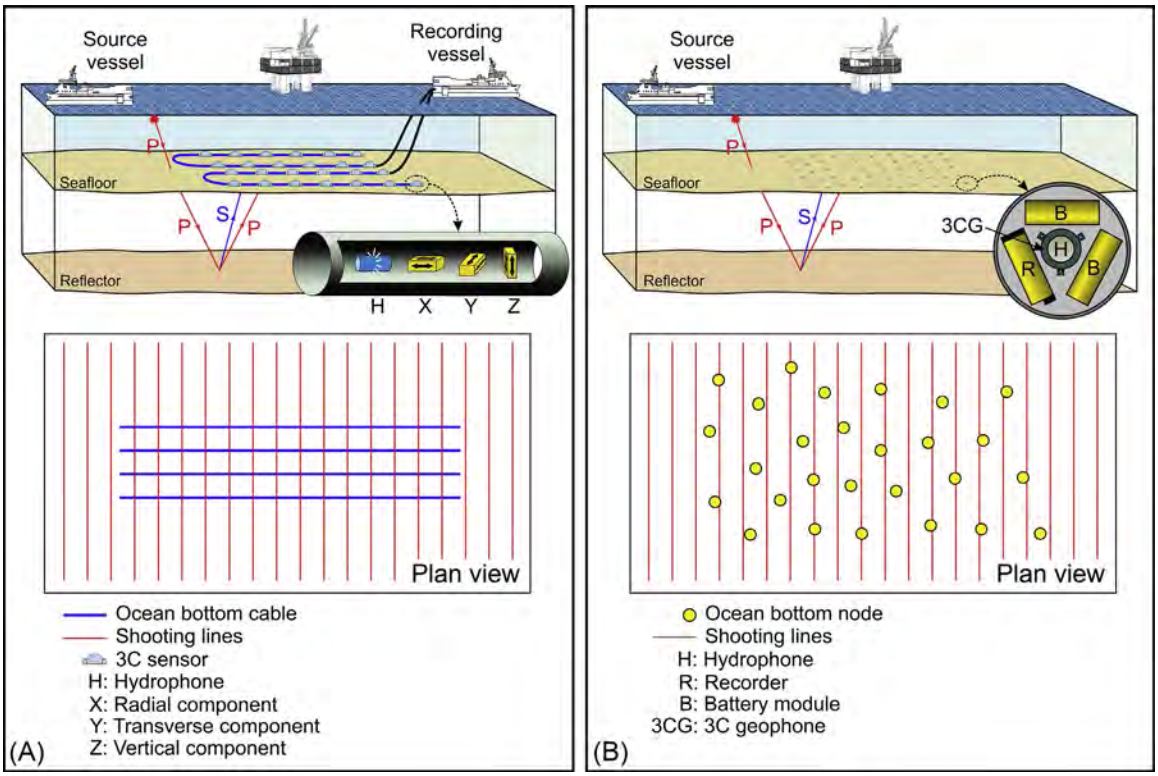


FIG. 2.56 Schematic illustration of (A) ocean bottom cable (OBC) and (B) ocean bottom node (OBN) for 4C data acquisition. In OBC surveys, an additional recording vessel or recorder buoy is necessary. Nodes may have either regular or irregular distribution around the vicinity of a production well, and the shooting lines may be linear or circular.

Ocean bottom cables and nodes are not used for exploration purposes, but are the methods to monitor the existing reservoirs during their production period in order to understand ways to enhance the hydrocarbon recovery (Fig. 2.56). Ocean bottom seismometers, however, are typically used to understand the crustal structure of the earth using earthquake waves, mostly utilized by academia. Today, there are OBS applications to obtain long offset seismic data for reservoir mapping, especially by amplitude versus offset (AVO) analyses. In each case, the sensors are located on the sea floor and a separate source vessel is used to generate seismic signal. The separation of the sensors and the seismic source provides data acquisition in different azimuths with different shooting geometries.

There are several advantages of ocean bottom recording:

- Ocean bottom seismic acquisition provides S wave data, which allows us to obtain important supplementary information about the reservoir, such as the V_P/V_S ratio or attenuation characteristics of the reservoir, etc.
- It becomes possible to record full-azimuth seismic data in different offsets since the source and receivers are separated, which provides better target illumination due to a wider diversity of ray paths, especially for complex geological environments such as salt intrusions and long offset data for deeper reservoirs.
- 4D repeatability is increased since the source and receiver repositioning can be done more accurately.
- Design flexibility makes it possible to acquire data where the towed streamers fail due to the different obstructions at the sea surface, such as production platforms.
- S/N ratio is improved because the sensors are located in a quieter environment, away from the surface noise. Downtimes because of bad weather conditions are reduced.
- Acquisition of data with virtually unlimited far offsets as well as very close to zero-offset can be achieved, which is not possible in conventional surface seismic acquisition except for TopSeis and FreeSeis techniques (Section 2.3.8).
- A better inversion of seismic data can be obtained by using ocean bottom data with a more complete far offsets, low frequency amplitudes, as well as S wave information.
- Bandwidth of the seismic data is improved because the receiver ghost is eliminated, which provides much higher resolution seismic data.
- It is possible to separate up- and downgoing wave fields by ocean bottom recording, which provides a better attenuation of multiples.

The main shortcomings of the ocean bottom recording techniques are their relatively higher cost with respect to the towed streamer acquisition and more difficult processing of the data. Since elastic wave field recording of S waves in a marine environment requires the sensors to be located on the seabed, coupling of the receivers to the sea floor is important, especially in OBC and OBN surveys. Inconsistent coupling can cause poor vector fidelity (equivalent component response to the same ground motion) and can degrade the data quality of horizontal components.

S waves produced by a mode conversion of incoming P waves are termed C-waves or PS waves. PS wave data used in conjunction with the conventional P wave data from towed streamers provides important additional interpretive information about the reservoir properties. Both types of data can be used to determine rock properties such as V_P/V_S or Poisson's ratio of the subsurface, which is sensitive to the changes of some specific rock characteristics, such as lithology, porosity or reservoir fluid type, since V_S is more sensitive to pore content than V_P and can provide a correlation with

lithology variations and prediction of rock type (Allouche et al., 2011).

S wave velocity is almost insensitive to the pore fluid content such that the reflectivity and velocity of S waves do not change in the case of gas, oil or water saturation. It is possible to distinguish lithology variations and fluid changes along a given interface by analyzing the lateral changes in reflection amplitudes of P and S waves: P wave amplitude variations along the boundaries may be due to both lithology or fluid change, however, if the S wave reflection amplitude also changes along the boundary, then it possibly indicates a lithology change (Barkved et al., 2004). These characteristics are used to define and interpret the direct hydrocarbon indicators (DHI) in the seismic data. The S wave data typically do not show any indication of gas and/or oil contact, fluid saturation effects, etc., while these factors affect the amplitude, phase and frequency characteristics of P waves, which may result in distinctive anomalies on the seismic data. Fig. 2.57 shows an example comparison of P and PS wave seismic data from a gas cloud through an anticline structure. Although the P wave data is affected by attenuation due to the gas charged sediments, PS wave data provides a clearer subsurface image.

2.4.1.1 Ocean Bottom Cable

In ocean bottom cable (OBC) surveys, a single cable (for 2D surveys) or several parallel cables (for 3D or 4D surveys) containing 2C or 4C sensors, typically located at every 25 or 50 m along the cable, are deployed on the ocean bottom. The cables are connected to the recording vessel by an electrical only or electrofiber optic umbilical cable for long-distance data transmission and cable control. A source vessel towing an air

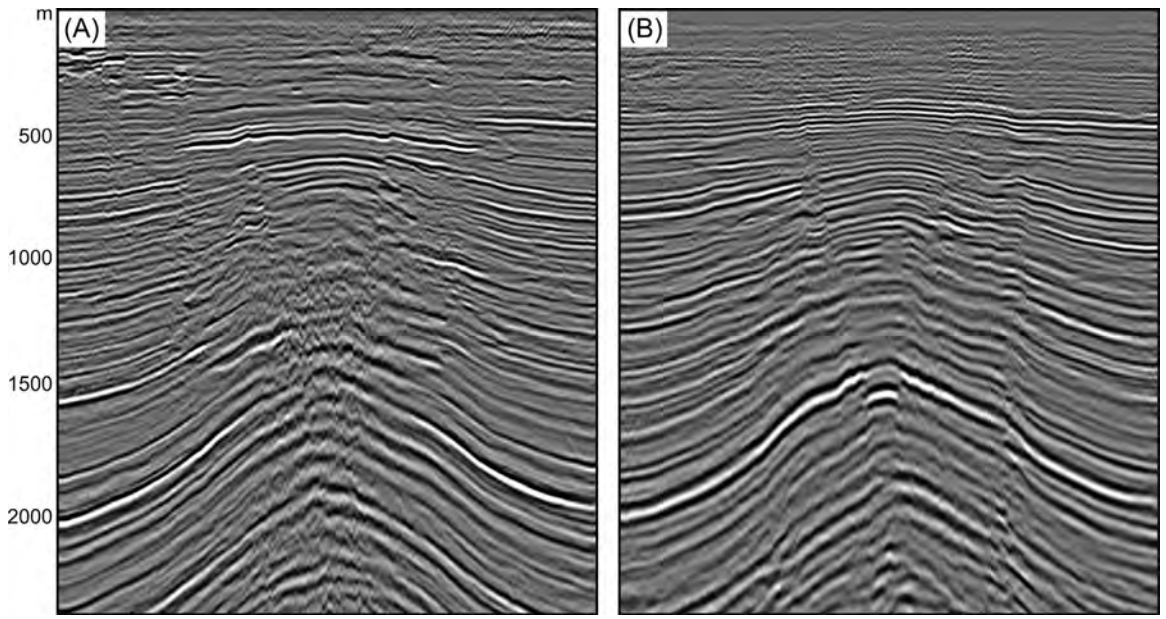


FIG. 2.57 Comparison of (A) P wave and (B) PS wave prestack depth migration data in depth domain. *From Akalin, M.F., Muhamad, A.A., Tan, Y.C., Yusoff, Y.B.M., Radzi, N.A.M., Zohdi, S.F.M., Hashim, M.H., Ghazali, M., Maitra, S., Wardoyo, A., Ghazali, M.L., Murthy, J.V.S., Wang, G., Miao, X.G., 2014. 3D-PS converted waves—solving 3D-imaging challenges under gas clouds—offshore Malaysia. In: 76th EAGE Conference and Exhibition, Amsterdam; Data courtesy of PETRONAS Carigali Sdn. Bhd.*

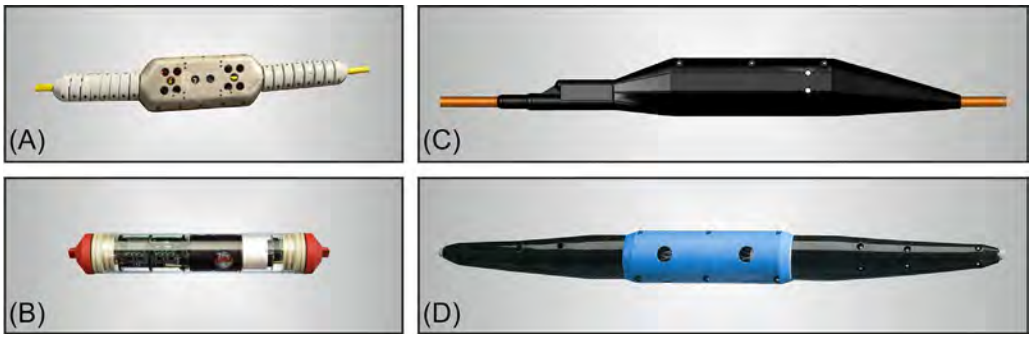


FIG. 2.58 Photos of different ocean bottom cable sensors. (A) SeaRay (Sercel), (B) 4C sensor module of GeoRes (OYO), (C) shallow, and (D) deep water OBC sensors of GeoRes (OYO).

gun array generates the seismic signal on the sea surface. The OBC survey can also be applied in shallow water areas, lakes and even in rivers. There are several different OBC systems available worldwide today (Fig. 2.58):

- Q-Seabed (Western Geco)
- SeaRay (Sercel)
- VectorSeis Ocean (ION Geophysical)
- GeoRes (OYO)

The Q-Seabed system employs a maximum of four cables in water depths up to 1500 m. Each cable has a maximum active length of 30 km, with 25-m sensor intervals. The Q-Seabed system also uses an acoustic ranging system termed IRMA, similar to that used for the Q-marine 3D towed streamer acquisition of Western Geco. The IRMA system in connection with the transponders on the hull of the vessel provides precise cable positioning. SeaRay is Sercel's omnidirectional 3C ocean bottom cable system capable of recording seismic data up to 500-m water depths. It has a maximum of 37-km cable length capability with 3C sensors, which are insensitive to tilting when coupled on the sea floor. VectorSeis Ocean is ION's redeployable OBC acquisition system, which utilizes three identical microelectromechanical systems (MEMS) along with a hydrophone to record 4C data. It can be operated at water depths up to 2000 m. It has a buoy-based recording system that does not require a separate recording vessel, which significantly reduces the operating cost. The GeoRes system employs OMNI series geophones, which are also insensitive to tilt angle. Its 4C sensors include an internal inclinometer that measures the vertical orientation of all three orthogonal axes of the geophones. The cable length of GeoRes system is typically 3.6 km with a custom sensor spacing of 25–200 m. Fig. 2.59 compares the seismic sections from a conventional streamer and OBC P wave data from Valhall Field in the North Sea.

Some production fields have been equipped with permanent installations of cables with fiber optic data transmission technology for time-lapse monitoring of the reservoir for hydrocarbon recovery and injection processes in order to optimize the production at periodic intervals, such as a couple of months. Such permanent seismic installations are for time-lapse or 4D seismic surveys and are termed Life of Field Seismic (LoFS), which significantly reduces the repeating survey costs as compared to conventional time-lapse seismics. Although the source and receiver positions cannot be repeated precisely during each consecutive survey for conventional 4D surveys, permanently installed cables provide the highest repeatability, since the receivers are in fixed positions at the sea floor, and hence provide superior image quality to evaluate the small changes in the reservoir

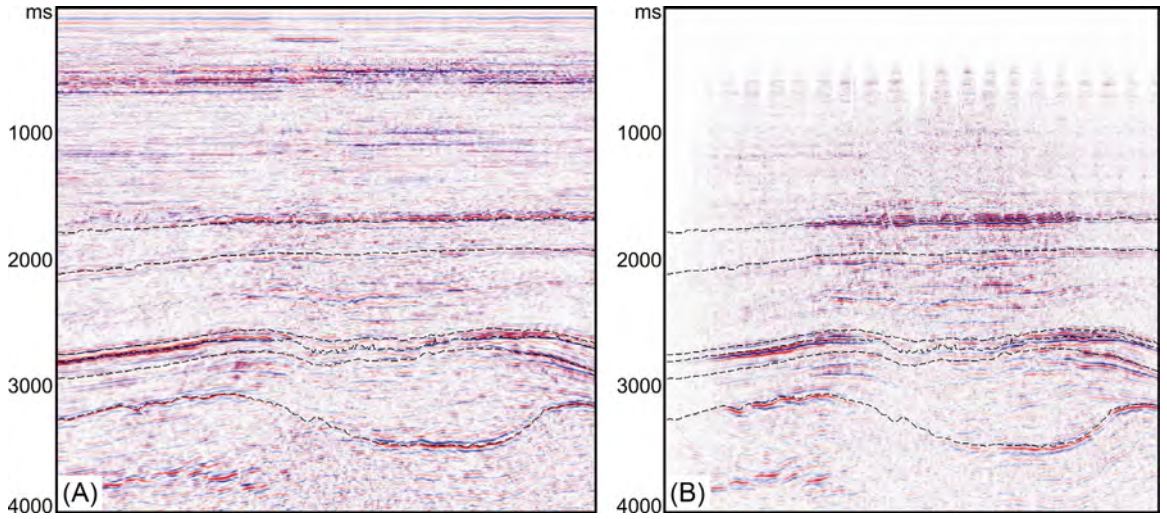


FIG. 2.59 Comparison of (A) conventional streamer and (B) ocean bottom cable P wave seismic sections. *After Hall, S.A., MacBeth, C., Barkved, O.I., Wild, P., 2005. Crossmatching with interpreted warping of 3D streamer and 3D ocean-bottom-cable data at Valhall for time-lapse assessment. Geophys. Prospect. 53, 283–297.*

characteristics due to the more consistent source and receiver positioning (Eriksrud, 2014).

2.4.1.2 *Ocean Bottom Seismometer*

Ocean bottom seismometers (OBS) are devices that contain a 3C seismometer and a hydrophone to record long offset seismic or seismological data. They are not permanent devices located on the sea floor, and are typically designed to work down to 6000 m water depths for a maximum operational period of approximately 3 months. The OBS system is buoyant in the water and is attached onto an iron frame or anchor (Fig. 2.60). It is recovered with an acoustic release system: On completion of the survey, the device is separated from the anchor by an acoustic release and ascends to the surface by sending a coded acoustic signal emitted by the ship's transducer to the transponder of the OBS. The instrument also has a radio beacon to be detected by the ship's radar, as well as a flash light and a flag for an easy detection and retrieval onboard.

OBS systems are commonly used for seismological research by academia and oceanographic

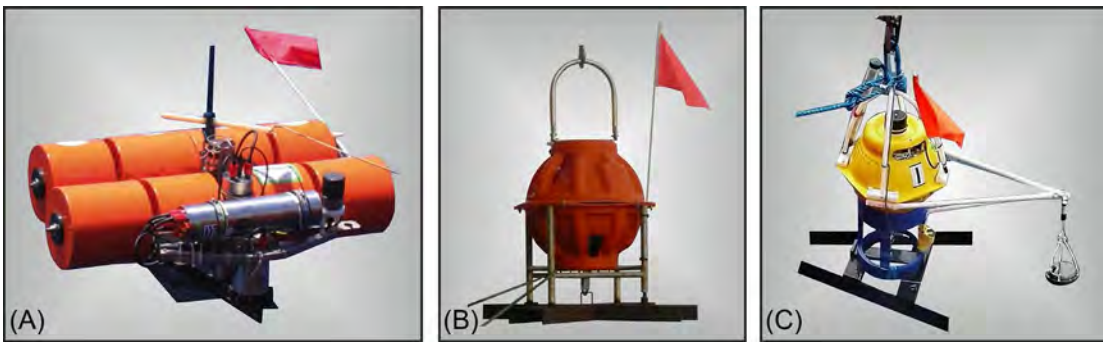


FIG. 2.60 (A) Geomar, (B) Sercel, and (C) USGS ocean bottom seismometers.

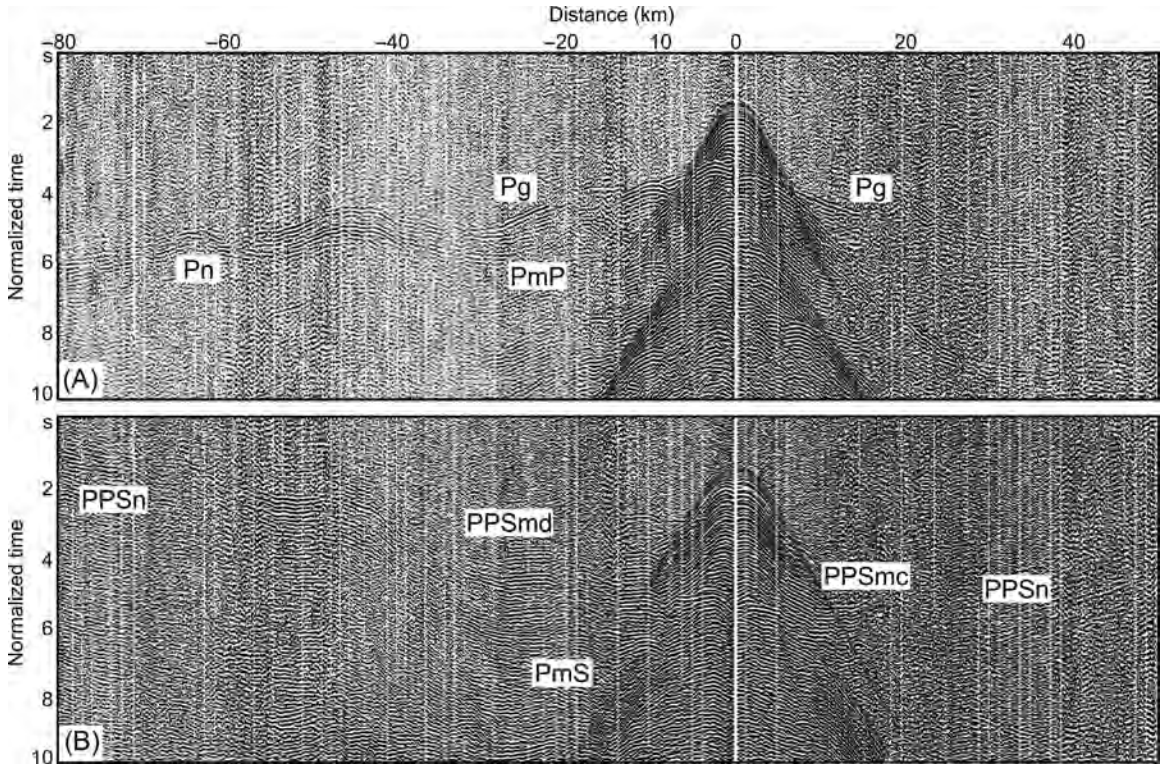


FIG. 2.61 An example (A) vertical and (B) horizontal component OBS data from south China Sea. Different arrivals from crustal structures are also indicated. *After Zhao, M., Qiu, X., Xia, S., Xu, H., Wang, P., Wang, T.K., et al., 2010. Seismic structure in the northeastern South China Sea: S-wave velocity and V_p/V_s ratios derived from three-component OBS data. Tectonophysics 480, 183–197.*

research groups to obtain information about the upper crust using earthquake waves (Fig. 2.61). Recorded data is generally interpreted along with the ray tracing modeling results to obtain a reliable model of the upper crust and Moho. They are also used to record microearthquakes and monitor the active faults offshore. In such large-scale observations, several OBS devices are deployed several kilometers apart within the research zone. For hydrocarbon-related exploration, however, much more dense OBS spacing, sometimes as close as 100 m, is used and a source vessel at the sea surface generates the seismic signal. For reservoir-related surveys, OBS data is typically used for AVO analyses, since it may provide very long offset seismic data. In the case of using a source vessel at the surface, the only reference to match the recorded data with shooting events is the time. Each OBS has an accurate internal clock calibrated by GPS time to minimize the timing drifts between the surface equipment and the recorded data within the OBS.

The OBS devices for seismological research and seismic exploration have different instrumentations. Generally, much heavier and larger sensors are used for seismological OBS systems because the earthquake signals have a relatively lower frequency band of 0.01–30 Hz. These types of OBS devices also have larger battery packages to supply power for much longer operating time periods. Short period OBSs can record

high-frequency events and smaller earthquakes, and their deployment periods are relatively shorter. Long period OBSs can record a broader range of frequencies and mid-range earthquakes, and their deployment periods are relatively longer.

2.4.1.3 Ocean Bottom Nodes

In the last decade, autonomous and cable-connected ocean bottom nodes (OBN) directly beneath the production platforms have been introduced. These nodes are either connected to each other and to the recording vessel by a transmission cable, or record the data into their internal recording units. Cabled systems can stay at the sea floor for a longer period than autonomous nodes, which have less endurance due to their limited internal power supply, with a typical battery life of more than 30 days. Remotely operated vehicles (ROVs) are used to accurately locate and retrieve the nodes on the seabed, which also enables a visual inspection of the nodes during the deployment and it becomes possible to locate the nodes very close to the platforms or seabed pipelines.

Since the deployment requires costly ROV operations and takes considerable time, the nodes are deployed in a relatively sparse grid with a separation between the neighboring nodes of approximately 400 m, and a source vessel generates the seismic signal at the sea surface. The recording within the nodes is continuous, and passive seismic monitoring is done before and after shooting. This requires the shot data to be extracted from node's continuous data record. The reference between the shot and recording is the shot time, which should be precisely synchronized with the node's internal time.

There are a number of different OBN systems available worldwide today manufactured by different vendors (Fig. 2.62):

- Trilobit (CGG Veritas)
- Z100, Z700 and Z3000 (Fairfield Nodal)
- CASE Abyss and Manta (Seabed Geosolutions)
- OBX (OYO GeoSpace)

Trilobit nodes from CGG Veritas have been successfully used for surveys in the North Sea and Gulf of Mexico. They are in operation with continuous data recording up to 104 days at a maximum operating depth of 3000 m. Fairfield Nodal offers three different node models for shallow, mid and deep waters, Z100, Z700, and Z3000, which have maximum operating depths of 100, 700, and 3000 m, respectively. The Z100 and Z700 model nodes can record data for 30 and 60 days, respectively, while the Z3000 can be fully operational for 180 days. The OBX system from OYO GeoSpace is an autonomous node for 4C acquisition, offering 500 h of continuous recording at a maximum depth of 3500 m. Seabed Geosolutions, a joint venture between Fugro and CGG, produces CASE Abyss and Manta nodes, both of which are operational at 3000 m maximum water depths.

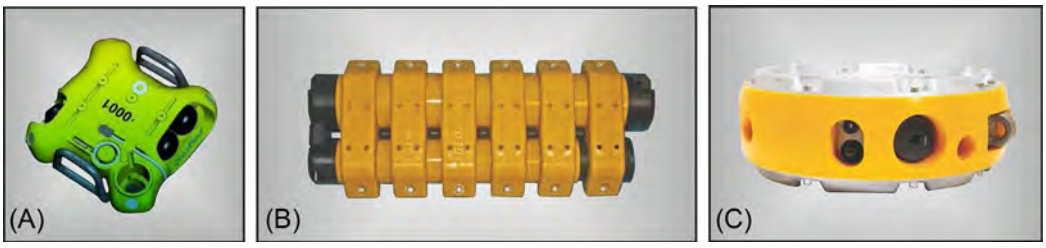


FIG. 2.62 Different ocean bottom node devices. (A) CASE Abyss (Seabed Geosolutions), (B) OBX (OYO GeoSpace), and (C) Z700 (Fairfield Nodal).

Since the nodes can be operated in surveys in congested areas with obstacles such as production platforms and ROVs can precisely reposition the devices to their previous locations for each repeated survey, autonomous nodes are successfully used for 4D reservoir monitoring, which requires a high level of repeatability. Acquisition by OBNs provides very ample fold distributions around the platforms and provides better subsurface images as compared to towed streamer NAZ seismic data, especially beneath the complex geological structures such as salt intrusions. One disadvantage of autonomous nodes is that, unlike the towed streamer or OBC surveys, the data can only be retrieved upon retrieval, since it is not practical to harvest the data in real-time. This results in blind shooting whilst the nodes are on the seabed for all the survey time, and no real-time QC analyses can be done on the recorded data until the nodes are recovered.

2.4.2 Time-Lapse (4D) Seismic

Time-lapse (4D) seismic surveys have been performed since mid-1990s for monitoring of the existing reservoirs during their production period. They involve repeated 3D seismic surveys in the same area over predetermined time periods to observe the changes in the reservoir with time due to the oil or gas production. The elapsed time between the base survey and subsequent surveys, which is actually considered the fourth dimension, is typically a few months for permanent OBC installations to a few years for conventional 3D towed streamer acquisition. The primary purpose is to obtain the differences between consecutively recorded data, which indicates the variations in pressure, fluid content or saturation distributions within the reservoir due to the production, away from the well location. Fig. 2.63 shows the time-lapse seismic survey results from Gullfaks oil field to predict the waterfront movements within the existing reservoirs. The 4D seismic concept is simply based on the fact that the properties of seismic reflections change as fluid saturations and pressures in the reservoir change during production. The difference images of sub-sequent 3D surveys are obtained, which do not include subsurface geology since it is time-invariant, to produce time-variant fluid-flow changes within the reservoir (Lumley, 2001).

Time-lapse seismic data is the subtraction of two seismic datasets from successive surveys to analyze the variations in the reservoir between the two surveys (Eriksrud, 2014). These changes, however, are very subtle in most cases

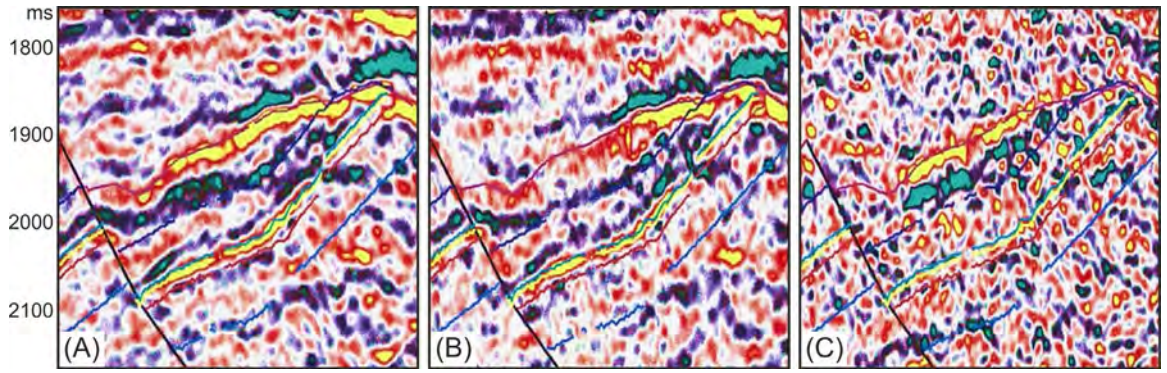


FIG. 2.63 Results of a time-lapse seismic study. (A) Base survey in 1985, (B) repeat survey in 1996, and (C) difference between 1985 and 1996 surveys. *After Landrø, M., Strønen, L.K., Digranes, P., Solheim, O.A., Hilde, E., 2001. Time-lapse seismic as a complementary tool for in-fill drilling. J. Pet. Sci. Eng. 31, 81–92.*

and require careful analyses, since they may easily be masked by differences in the acquisition properties, parameters and geometry of both datasets, as well as the noise level embedded in the data. Therefore, the reliability of 4D data strongly depends on the accuracy and repeatability of the sensor and shot positions between two successive surveys.

4D seismic surveys can provide valuable information for the management of the reservoir, and monitoring of the dynamic structure of the reservoir may lead to higher production and a better estimate of the reserves while it minimizes the further infill drilling costs. 4D seismic can also be used in monitoring the injection fluids, such as water, gas, steam, CO_2, etc., into the existing reservoir during the development stage, and can reduce costs by optimizing well injection programs (Lumley, 2001).

2.4.3 Transition Zone Acquisition

Transition zones are the most challenging regions of very shallow marine, lake and river environments where the acquisition of seismic data can be quite complex and problematic. Since these are the regions where the conventional land or marine acquisition techniques are not applicable, generally mixed source and receiver types are involved in the acquisition. Logistics, operational and geographical difficulties as well as near surface conditions often affect the quality of the acquired data, because the working environments involve different surficial conditions, such as land, swamps, reefs, beaches, marsh zones with fresh or salt water intrusions, etc.

Although different types of seismic sources (dynamite, Vibroseis or air guns) and receivers (geophones or hydrophones) can be used (Fig. 2.64), it is preferred to utilize one type of source and receiver for the entire survey to prevent the phase changes in the seismic wavelet from one type of source to another and to obtain a stationary source signature for the whole dataset. Dynamite detonated in shallow holes both on land and shallow marine areas can be used as a suitable seismic source when the safety issues are not concerned.

A hydrophone cable is often used to receive the signals. However, placing the hydrophone cables in correct position without dynamic depth levelers (birds) is very difficult and the cable is typically anchored to the sea floor. OBC or OBN acquisition can often be suitable choice for transition zone acquisition up to 30 m water depths. In addition, dedicated receiver cables and receivers compatible to the existing land

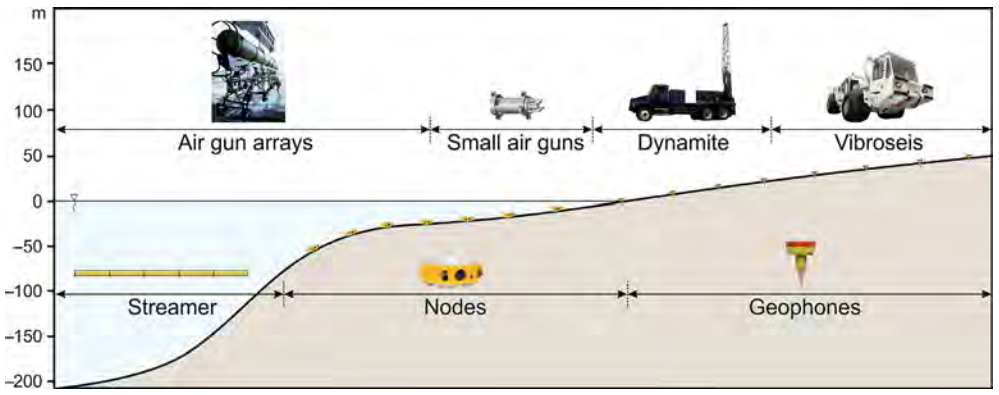


FIG. 2.64 Schematic illustration of different types of sources (top) and receivers (bottom) used for transition zone surveys. Vertical scale is arbitrary.

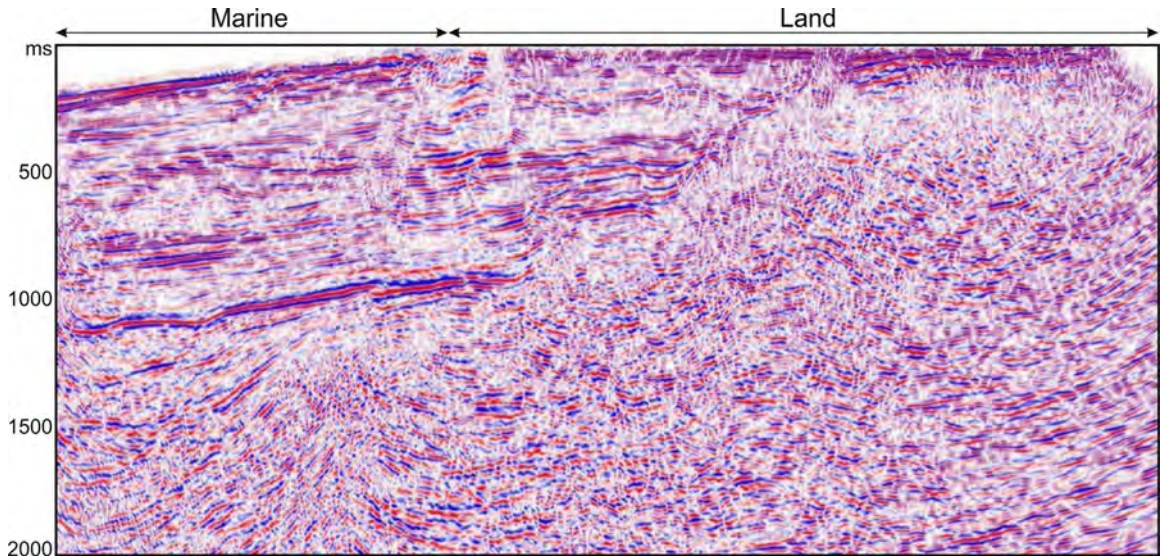


FIG. 2.65 An example seismic line from a land-to-marine transition zone. Three different sources (air gun, Vibroseis and dynamite) were used to generate the seismic signal, while four different types of receivers (land/marsh geophones, hydrophones and OBNs) were used to record seismic data. *After Roberts, D., Fitzpatrick, J.P., 2016. Planning and operating a transition zone 2D seismic survey on Lake Tanganyika, Search and Discovery Article No. 41765.*

recording systems for shallow water operations down to 50-m water depths are also commercially available today. Fig. 2.65 shows an example seismic line acquired during a 2D transition zone seismic survey on Lake Tanganyika, where three different types of sources (air gun, Vibroseis and dynamite) and four different types of receivers (land/marsh geophones, hydrophones and ocean bottom nodes) are used to produce and receive the seismic signal.

2.4.4 P-Cable Acquisition

P-cable is a low-cost, high-resolution 3D seismic data acquisition system in relatively deep-water areas. It consists of an acquisition cable towed perpendicularly to the sail line direction and several short streamers attached to this cross cable (Fig. 2.66). It was first conceived in 2001 by Geometrics and its design has been continuously improved in the last decade by incorporation of several research institutions and seismic service companies, and a fully digital P-cable system was introduced to the seismic market in 2010.

Twelve to twenty-four streamers up to 300 m length are towed on the cross-cable. Typical group intervals of the streamers are 1.6–12.5 m. The cross-cable, which provides power and data telemetry for a maximum of 24 streamers in the spread, is separated by two small paravanes typically 150–300 m apart, depending on the number of streamers deployed. The active streamer sections are attached to the cross-cable by a watertight junction box at every 6.25 or 12.5 m intervals. This geometry provides a maximum of 150 m crossline coverage for each sail line. Navigation information is obtained from rGPS modules located on the paravanes and gun buoy. Generally high-resolution seismic sources, such as GI guns, are used to obtain high temporal resolution.

The P-cable system is a very high-resolution 3D seismic system and is used by both the

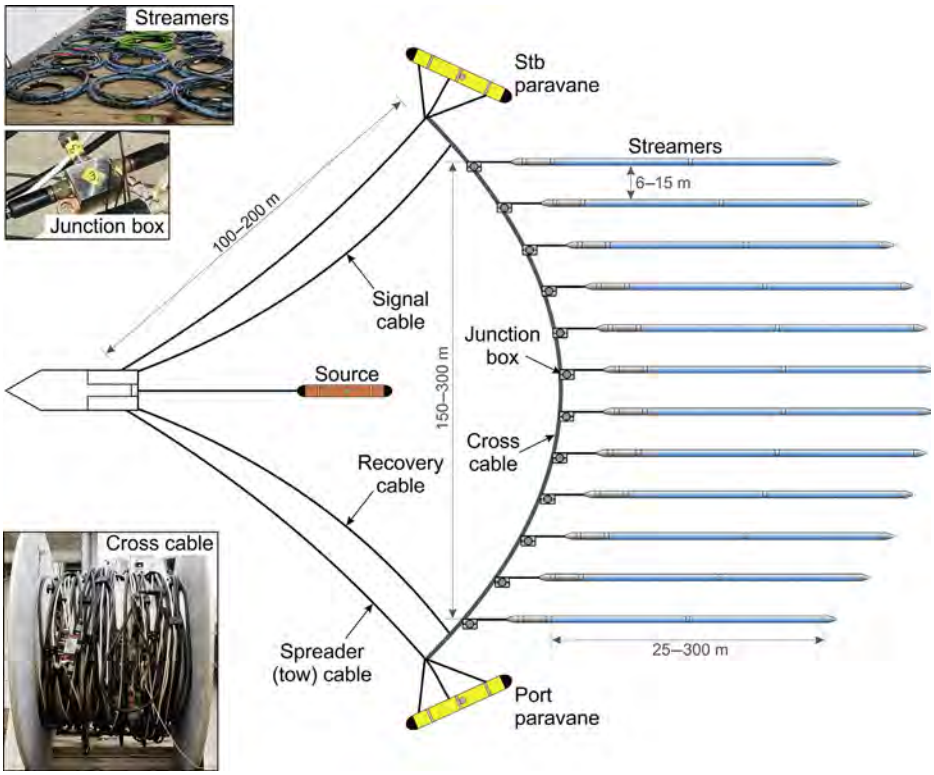


FIG. 2.66 Schematic illustration of P-cable layout with twelve streamers, each 25–300 m long. Separation between the streamers is typically between 6 and 15 m, which provides a 3–7.5 m crossline bin size.

hydrocarbon industry and academia for mapping the reservoirs in more detail, detection of seeps, shallow gas chimneys, gas hydrates and other shallow gas anomalies, mapping of small-scale faults and fractures, and understanding the character of the shallow stratigraphic sequences. It may also be preferred for site surveys to map the possible geohazards before the drilling of offshore wells.

P-cable 3D acquisition has several advantages. Short offset distances and significantly smaller streamer spacing provide for acquisition a very high-resolution 3D seismic data cube with a typical bin size of 3.125×6.25 m, when compared to conventional 3D towed streamer data. Fig. 2.67 shows a comparison of conventional seismic and P-cable data from the same survey area. Its lightweight design also enables a quick deployment and retrieval of the whole spread, typically in 1.5–2 h, on a medium-size research vessel. Instead of mapping large areas, the P-cable is especially preferable for detail surveys of relatively smaller areas from 10 to 50 km^2.

Inconsistent streamer depths during the acquisition, however, lead to degradation of data and distortion of the acquisition footprint, since generally no depth levelers are deployed along with the streamers. In addition, lack of long offsets prevents obtaining correct and accurate 3D subsurface velocity distributions and makes it difficult to eliminate the multiples in relatively shallow water surveys.

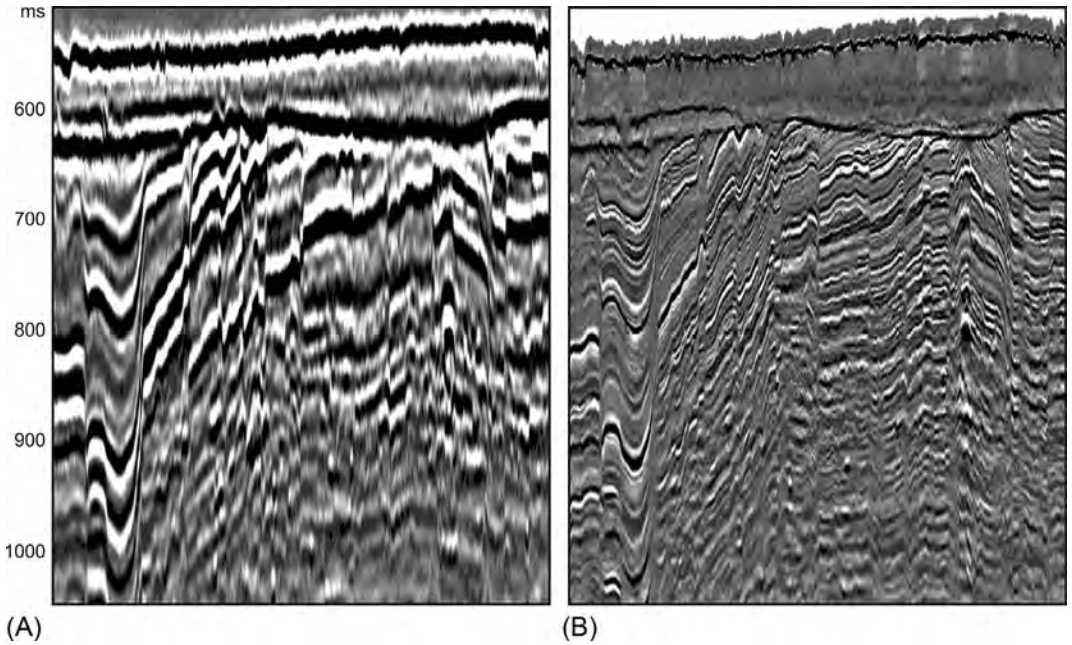


FIG. 2.67 A comparison of (A) conventional and (B) P-cable seismic data. *Data Courtesy of TGS.*

2.5 DATA ACQUISITION PARAMETERS

The suitable selection of data acquisition parameters both in 2D and 3D seismics widely affects the quality of the collected data. The determination process of acquisition parameters is termed seismic survey design, the main purpose of which is to optimize the survey to obtain the most suitable seismic data that matches the requirements of the survey. In practice, these parameters are determined in conjunction with the requirements of the survey, and in general they are selected to produce a suitable source signal and to record the best quality data with a minimal noise component, providing that they suit the cost and HSE (health, safety, and environment) requirements for the entire survey.

Good seismic data can be defined by its three specific characteristics (Ashton et al., 1994):

- High S/N ratio
- Good temporal and spatial resolution
- Good spatial coverage for 3D

A high S/N ratio can be achieved by increasing the signal level while trying to reduce the noise amplitudes. A proper determination of source and receiver geometry may reduce the source-generated noise amplitudes as well as spatial aliasing. A good temporal resolution is achieved by recording seismic data with a wide frequency bandwidth, which involves both low- and high-frequency components at the same time to resolve the upper and lower boundaries of the target. The bandwidth of the data at its higher frequency end is limited by the source and receiver ghost notches, and different acquisition geometries are introduced to eliminate the negative effect of, especially, receiver ghosts to improve the seismic signal bandwidth (Section 2.2.3). A good data coverage requires a suitable definition of inline and crossline receiver spacing to avoid spatial aliasing.

A successful seismic survey design provides for obtaining the goals of the conducted seismic survey in a cost-effective manner, within the predetermined time schedule of the survey. In the selection of suitable survey parameters, the

following agents should be considered, which are generally obtained from 2D vintage seismic data:

- Depth, size, type and other characteristics of the target
- Maximum expected subsurface dip
- Depths of shallowest and deepest target levels
- Two-way arrival time of target reflections
- Appropriate fold for a high-quality dataset
- V_{RMS} distribution down to the deepest target level
- Desired temporal and spatial resolution
- Specific noise types, if exist
- Area for a complete image
- Maximum and dominant frequency at the target level
- HSE regulations for the survey and working environment

The acquisition parameters that should be predetermined before the survey can be classified into two groups:

(i) Acquisition parameters directly related to the seismic spread geometry, and some specific characteristics of sources and receivers (Table 2.3). The nominal offsets and general geometrical parameters for 2D

TABLE 2.3 Acquisition Parameters Associated With the Survey Geometry, and Characteristics of Sources and Receivers

Parameter	Specification/Relevance/Effect
Shot interval	Optimal fold number of the data and record length
Streamer/source depth	Frequency content and bandwidth of the data
Group interval	Spatial sampling and inline bin size
Minimum offset	Frequency content and bandwidth in shallow waters
Maximum offset	Optimal fold number of the data and inline coverage
Sail line azimuth	Optimization of the survey
Streamer separation (3D)	Spatial sampling and crossline bin size
Number of streamers (3D)	Crossline coverage
Number of source arrays (3D)	Spatial sampling and crossline bin size
Number of recording channels	Optimal fold number of the data and inline coverage
Sail line interval	2D and 3D coverage
Bin size	Spatial sampling
Line interval and reshooting	Regular fold distribution (3D) and lateral resolution (2D)
Run-in/run-out distance	Inline coverage
Gun array volume	Seismic signal amplitude and overall signal penetration
Gun number	Seismic signal amplitude and overall signal penetration
Gun array design	Source directivity and bubble suppression
Gun pressure	Seismic signal amplitude and overall signal penetration
Source separation (3D)	Crossline sampling
Tow distance	Operational noise level
Vessel speed	Shot interval and operational noise level

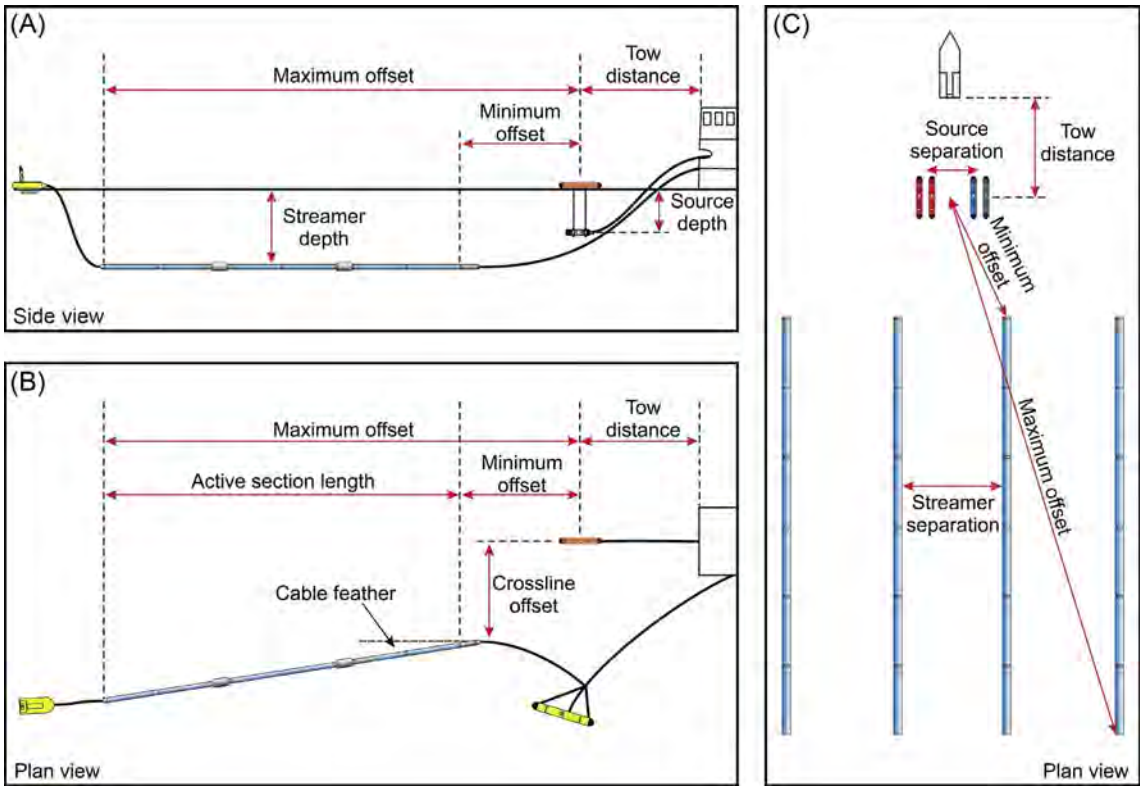


FIG. 2.68 Geometrical acquisition parameters in (A) side view and (B) plan view for 2D surveys, and (C) for a conventional 3D towed streamer, dual source acquisition.

and 3D survey spreads are illustrated in Fig. 2.68.

(ii) Acquisition parameters associated with the data recording or characteristics of the recorded seismic data (Table 2.4).

2.5.1 Parameters for Survey Geometry, Sources, and Receivers

2.5.1.1 Shot Interval

Shot interval is the horizontal distance between two successive shot points along the seismic lines. In marine seismic acquisition, recording process continues while the vessel sails along the seismic profiles with a constant speed as far as possible. Shooting is done at

TABLE 2.4 Acquisition Parameters Associated With the Characteristics of the Recorded Seismic Data

Parameter	Specification/Relevance/Effect
Record length	Target depth and migration aperture
Sampling rate	Nyquist frequency of the recorded data
Antialias cut-off frequencies	Frequency aliasing
Sample format/dynamic range	Overall bandwidth of the recorded data
Fold	Quality and S/N ratio of the data

every shot point whenever the vessel reaches a shot location. On time break at a shot point, recording immediately starts and continues until the last time sample of the record length is received and recorded. The key parameter here is the time period that the vessel travels between two consecutive shot points. This time period should exceed the recording length; otherwise the vessel reaches the next shot location before the recording of the previous shot is completed. This situation is termed overlapped shot points, in which the time between two consecutive shot points is less than the record length, which appears whenever the vessel speed is too fast during the acquisition.

In the case of overlapped shot points, the late arrivals of previous shot record are contaminated by the signals of overlapping (next) fire. This situation is indicated in the acquisition logs and quality control reports to remove the next shot's interference by a suitable muting or editing during the processing. Therefore, vessel speed, shot interval and record length should be selected accordingly to prevent overlapped shots. In practice, vessel speed is kept constant, typically at 4–4.5 knots with a minimum of 3.5 knots to keep the streamers stable during the tow. Then the recording length is determined based on the target depth and average velocity of the subsurface by a careful analyzing of the vintage seismic data. Then the minimum shot interval which is larger than the recording length is calculated so that it is an exact multiple of group interval (for instance, shot interval can be 12.5, 25, 37.5 m, etc., for a 12.5 m group interval).

Shot interval directly affects the optimum fold of the data: The smaller the shot interval, the higher the optimum fold, and hence, the higher the S/N ratio of the seismic data. Therefore, it is always preferable to shot at regular intervals as small as possible. In practice, a safe time is set between the end of recording of the previous shot and the time of the forthcoming shot. That is, the vessel should arrive to the next shot point at a certain time later after the recording of the previous shot is completed. This time period is generally about 2 s. Table 2.5 shows typical shot interval and record length relations for 4.0 and 4.5 knots vessel speeds. In 3D flip-flop surveys, a 50-m shot interval for each gun array with 25-m overall shot interval for the data, which provides a recording length of approximately 8–10 s, is typical.

In the hydrocarbon industry, distance-based shooting is considered, where the guns are fired at regular distance intervals along the line to obtain a more uniform fold distribution for the whole survey. In some specific cases, especially

TABLE 2.5 Typical Shot Intervals in Meters and Their Corresponding Shot Interval Times for 4.0 and 4.5 Knot Vessel Speeds

Vessel Speed (knot)	Shot Interval (m)	Shot Interval (s)	Suitable Record Length (s)	Vessel Speed (knot)	Shot Interval (m)	Shot Interval (s)	Suitable Record Length (s)
4.0	12.50	6.1	4.0	4.5	12.50	5.4	3.0
	18.75	9.1	7.0		18.75	8.1	6.0
	25.00	12.1	10.0		25.00	10.8	8.0
	37.50	18.2	16.0		37.50	16.2	14.0
	50.00	24.3	22.0		50.00	21.6	18.0

Maximum feasible record lengths deduced from the shot interval times are also provided. The time difference between maximum feasible record length and shot interval in seconds is the "safe time" to prevent the overlapped shots.

for the surveys of academic purposes, time based shooting may be preferred, where the guns are fired at specific time periods without considering the exact shot locations. This results in an irregular shot interval distribution along the line depending on the speed of the vessel. When the capacity of the air compressors is limited to supply compressed air to the source array, time-based shooting provides more regular air supply to the guns.

2.5.1.2 Streamer/Source Depth

Depth of the seismic streamer and source array is the most effective parameter on the recorded data bandwidth. Since both the source and receivers are towed below the sea surface, the bandwidth of towed streamer data is determined by the tow depth of the source and streamers because the source and receiver ghost interference results in notches at specific frequencies in the amplitude spectrum and limits the frequency band of the signal (Section 2.2.3).

Source and streamer immersion have exactly the same effect on the seismic data bandwidth. In practice, it is always preferred to tow the streamer as deep as possible, which minimizes the effect of sea surface waves and operational noise, makes the streamers more stable, and optimizes the penetration of low frequencies (Carlson et al., 2007). However, as the immersion increases, the bandwidth of the recorded data becomes narrower. Solid streamer design allows us to tow the streamers at relatively shallower depths and hence provides higher bandwidth, since they are less affected by the noise arising from the rough weather conditions at the sea surface (Section 2.1.2). However, it should be considered that the ghost interference at shallower tow depths also attenuates low frequencies.

The first ghost notch frequency is given by

$$f_n = \frac{V}{2h} \tag{2.1}$$

where V is the water velocity and h is the immersion depth. Fig. 2.69A shows the theoretical amplitude spectra of the far-field source signatures generated by a source at 4, 6, and 8 m depth and recorded by a streamer at the sea surface, where only source ghost is incorporated. Fig. 2.69B shows the same spectra with a receiver ghost included from a streamer at 6 m depth. For shallow high-resolution seismic acquisition, such as that for site surveys, the operating depth is typically 3–5 m, where the

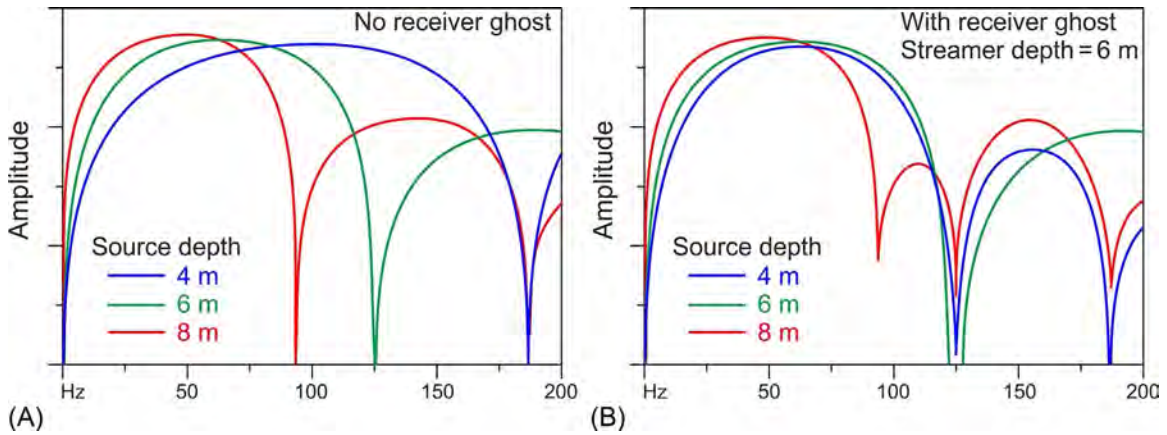


FIG. 2.69 (A) Theoretical amplitude spectra of source signatures from a source fired at 4, 6, and 8 m depths. No receiver ghost is incorporated since the streamer is at the sea surface. (B) The same spectra as in (A) but a receiver ghost is incorporated from a streamer at 6 m depth.

ghost notch is located between 150 and 250 Hz. For hydrocarbon exploration, most of the signal amplitude is between 4 and 100 Hz. Therefore, the streamer depth is kept at approximately 6–8 m below the sea surface for conventional oil and gas exploration.

Resolution of the seismic data is governed by the depth of the gun and streamer. Fig. 2.70 shows example average amplitude spectra and stack sections of high-resolution seismic data to demonstrate the effect of gun and streamer depth on the spectral bandwidth and data resolution. The sampling rate was 2 ms, which corresponds to a 250 Hz Nyquist frequency. The amplitude spectra illustrate the bandwidth of the raw data recorded with a streamer at 6 and 10 m depth for a constant source depth of 4.5 m. The ghost notch of the source appears approximately at 160 Hz constant frequency for both spectra. The maximum usable frequency is approximately 125 and 75 Hz for 6 and 10 m streamer depth, respectively. The processed seismic data clearly illustrates the difference in resolution, which is lost in deeper parts first for the data collected with the streamer at 10 m depth.

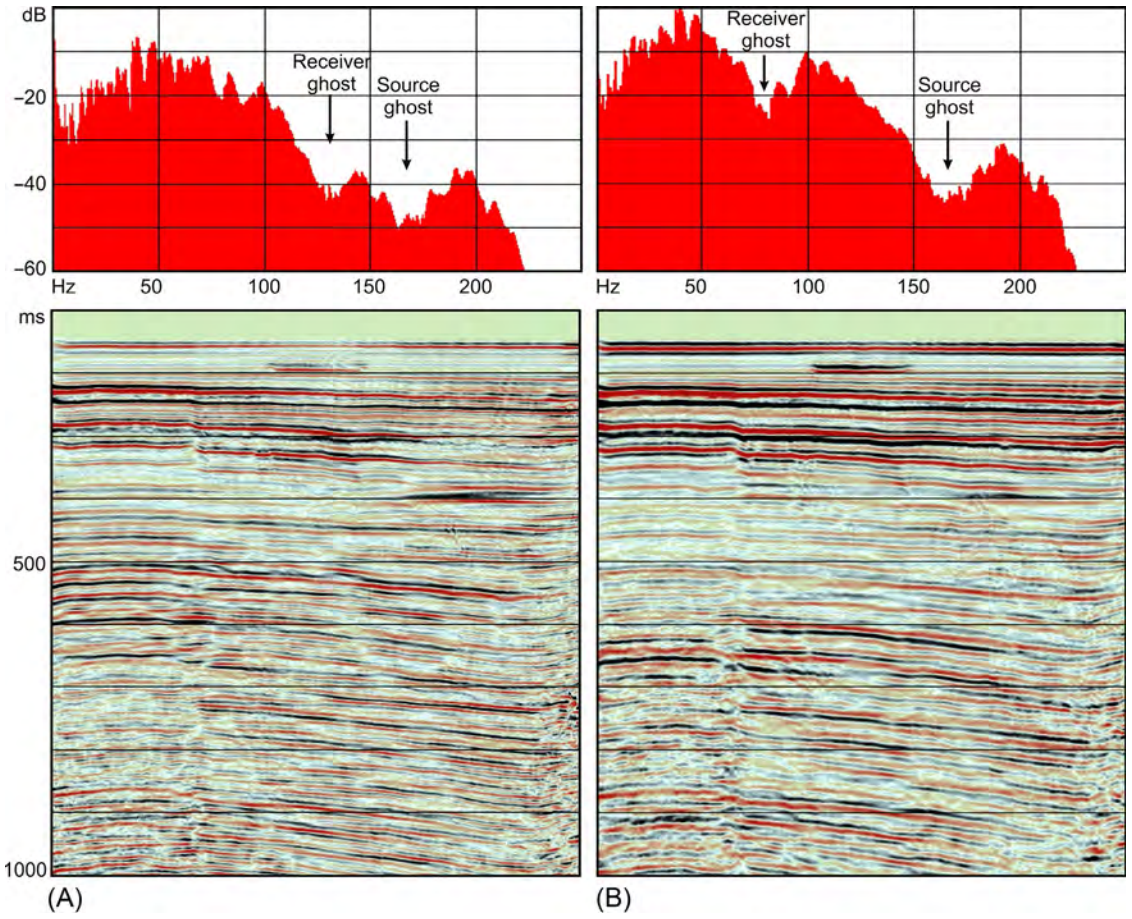


FIG. 2.70 Comparison of two stack sections of high-resolution seismic data collected by (A) 6 m and (B) 10 m streamer depth for a 4.5 m constant source depth. Corresponding average amplitude spectra of both sections are given on upper panels.

Depth of the streamer(s) should be controlled carefully, especially for high-resolution surveys where the streamer is towed at relatively shallow depths. In high-salinity warmer waters, streamer trimming with specific weights may be necessary. If some sections of the streamer are shallower than the remaining sections, then the channels in shallow sections record too much swell noise. If they are deeper, however, this results in distinct phase distortions along the reflections. Fig. 2.71 shows an interesting example shot gather for this situation. The tail sections of the streamer, which involve approximately last 64 channels, are much deeper than the remaining frontal part of the cable. This causes significant phase distortions, both on the sea floor and subsurface reflections, which cannot be handled during the processing.

2.5.1.3 *Group Interval*

Group interval is the distance between the centers of two adjacent recording channels. In marine seismic equipment, the group interval is designed during production and cannot be modified later except that it can be increased by trace summing option provided by digital seismic streamers. Since a smaller interval provides a smaller inline bin size (which always equals the half group interval, as shown in Fig. 2.72), and hence better inline resolution, it is always preferred to use a group interval as small as possible. Today, a 6.25 or 12.5 m group interval is typical for conventional 2D or 3D exploration, while a 3.125 m interval is used for high-resolution seismic systems.

Group interval defines the largest spatial sampling that prevents aliasing during the migration process. According to sampling theory, a

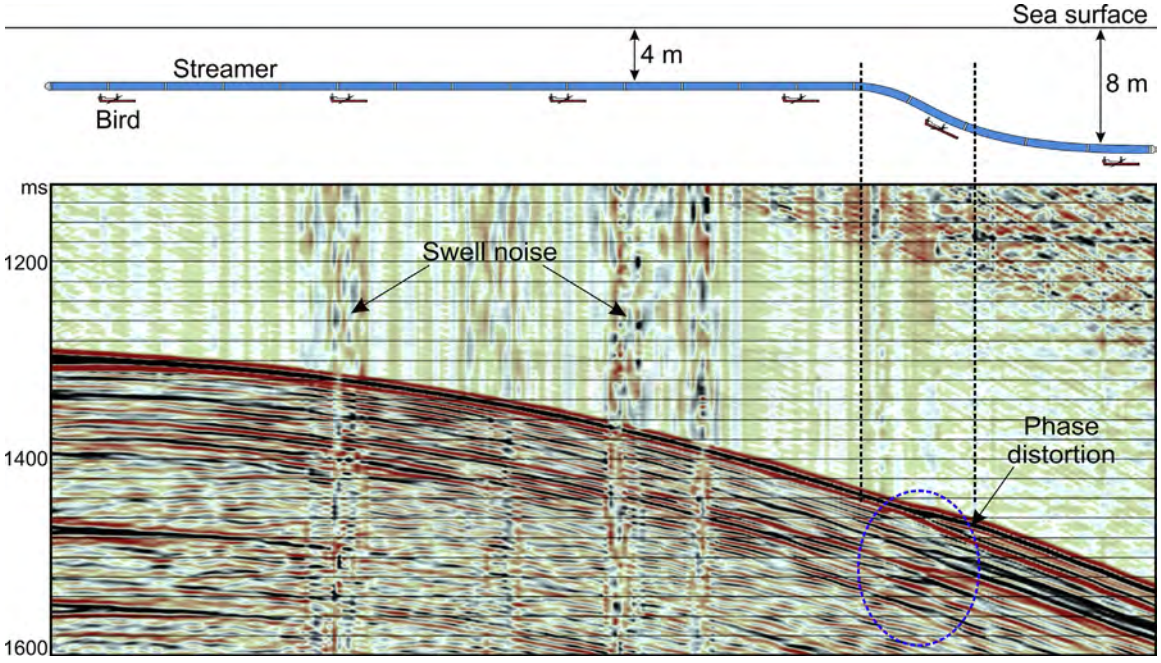


FIG. 2.71 An example shot gather illustrating the effect of depth variations along the streamer on the recorded data. Depth of the last 64 channels is twice the rest of the streamer depth, which results in distinct phase distortions in the area, shown by a dashed ellipse.

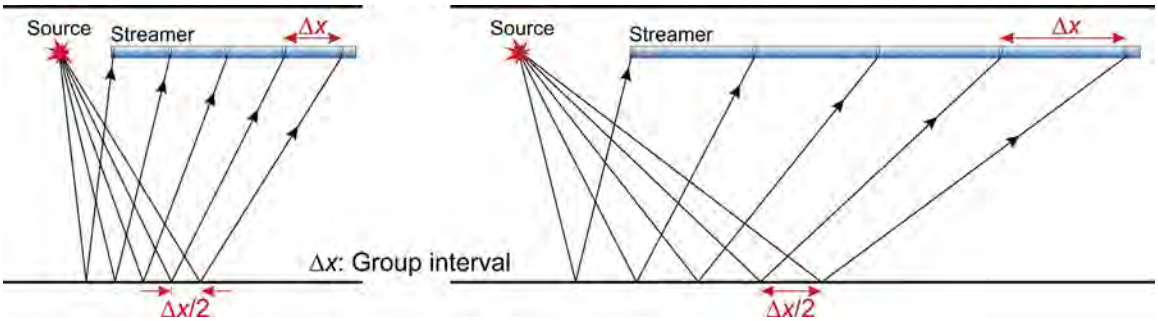


FIG. 2.72 Inline bin size equals the half group interval (Δx).

function can be reconstructed from its discrete samples, providing that at least two amplitude values per period have been sampled. In seismic acquisition, the subsurface is sampled at discrete intervals of the half group interval, which allows us to retrieve the minimum wavelength as equal to the group interval. In other words, data should be spatially sampled at least two points per wavelength. For a proper migration application, horizontal wavelengths of the reflections should be suitably and regularly sampled so that the group interval provides an adequate number of horizontal samples to prevent spatial aliasing during the migration.

Spatial aliasing occurs in the case of insufficient sampling of the data along the space axis using a large trace interval, especially for high frequencies and steeply dipping reflectors. The trace interval for a stack or zero offset section without spatial aliasing is given by (Yılmaz, 1987)

$$\Delta x \leq \frac{\lambda_{app}}{2} = \frac{V}{4 f_{\max} \sin\theta} \tag{2.2}$$

where λ_{app} is apparent wavelength, V is the RMS velocity at target depth, θ is the dip of the target reflector, and $f_{\max}$ is the maximum frequency at the target reflector.

2.5.1.4 *Offset Distance*

The term "offset" of each trace is the distance between each individual recording channel and the center of the source. As a specific case, the distance between the first (or the nearest) channel and the source center is termed minimum offset, which affects the frequency content of the recorded data in shallow water surveys because the receiving channels of the streamers are designed to form hydrophone arrays or groups. The output of each recording channel within the seismic streamer consists of individual outputs of several hydrophones connected in parallel to form hydrophone arrays, positioned along the cable with a certain separation between each particular hydrophone (Section 2.1.2). As a result, hydrophones forming the array spread the overall group length along the streamer. For such a composite receiver system, the reflected wave front arriving at a 0-degree incidence angle (vertical) arrives at all hydrophone components approximately at the same time. On the other hand, hydrophone arrays suppress the horizontally propagating noise amplitudes such as operational noise. As the incidence angle increases, each hydrophone receives the reflection signal with a certain time delay (Fig. 2.73). These time delays filter the signal amplitude depending on the signal frequency, group length and number of hydrophones forming the group, which is known as the directivity effect. The filtering effect is frequency dependent and decreases with the decreasing incidence angle and no filtering occurs for 0 degrees. For instance, the amplitude attenuation for a 50-Hz signal with

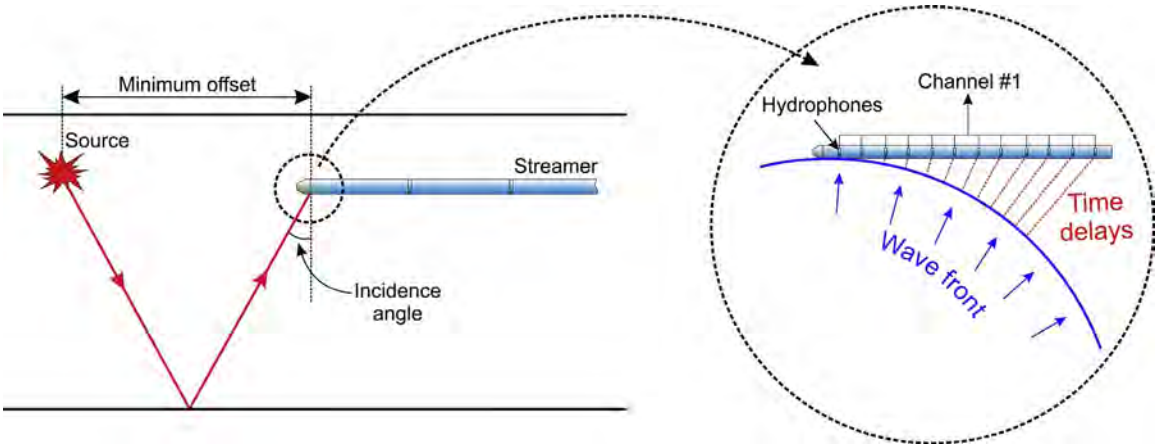


FIG. 2.73 Several hydrophones are connected in parallel to form hydrophone arrays for each recording channel, which results in each hydrophone receiving the reflected energy with a time delay. When summing up the outputs of the hydrophones, this causes a specific filtering termed the directivity effect, the influence of which decreases with decreasing incidence angle.

an incidence angle of 45 degrees is 7 dB, whereas it is 14 dB for a 100-Hz signal.

In seismic streamers, group interval and number of hydrophones forming the group is fixed. Therefore, the only way to reduce the amplitude decrease is to lower the incidence angle of the incoming signal. For a constant target depth, the incidence angle depends on the source-receiver distance, that is, the offset. Small offset corresponds to small incidence angle, which means that less amplitude attenuation occurs for high-frequency components. The effect of minimum offset distance may be significant in shallow water surveys. In relatively deep waters, such as two times the streamer length, high-frequency amplitudes are not significantly decreased since the incidence angles are already small.

The distance between the last (or the farthest) channel and the source center is termed the maximum offset. For a constant group interval, increasing the number of recording channels increases the maximum offset distance of the data. As a general rule, maximum offset distance should approximately equal to the target depth. For several reasons, long offsets are required to obtain better quality data, which include:

- Increasing the number of channels also increases the nominal fold of the data.
- Long offsets are crucial for amplitude versus offset (AVO) analyses for hydrocarbon exploration.
- Some of the multiple reflection elimination techniques require long offset data.
- Seismic velocities of deeper layers can be more precisely resolved if long offsets are available.
- Longer streamers provide higher inline coverage and slightly better azimuth distribution.

2.5.1.5 *Sail Line Azimuth*

Sail line azimuths should be chosen in parallel to the structural dip of the subsurface if there is vintage seismic data for the planning of the acquisition. This also ensures a more reliable migration and prevents recording side-sweeps. If the purpose of the survey is to map the faults, then the sail lines should be perpendicular to the fault strikes.

The azimuth of the seismic profiles is important in the optimization of the survey. In a rectangular working area, it is always preferred to shoot on the line parallel to the longer border of the area for a cost-effective survey, if the structural dip permits. This allows running of longer profiles with respect to the orthogonal direction with a smaller number of line changes, which cause significant dead times during the turns, especially with long spreads. In addition, sail lines should be sufficiently long to obtain full-fold data from target depth and a reliable migration result.

2.5.1.6 2D and 3D Coverage

Coverage is the subsurface area where the seismic data is recorded, depending on the size of the seismic spread. Only inline coverage is pronounced for 2D surveys, while 3D surveys provide both inline and crossline coverage. Total coverage for one single shot depends on different factors, such as

- Streamer separation (3D)
- Number of streamers (3D)
- Number of sources (3D)
- Number of recording channels (2D and 3D)

For 2D surveys, the seismic data is recorded only from the zone just beneath the seismic line, and the total inline coverage area is always half of the total streamer length of the active sections (Fig. 2.74). If the number of recording channels or length of the streamer(s) increase, inline coverage also increases.

In 3D surveys, multistreamer acquisition provides a wide coverage area for a single sail line. Inline coverage is the same as that for 2D surveys; however, increased number of streamers simply extends the total crossline coverage. An eight-streamer acquisition yields two times wider coverage area than that from a four-streamer acquisition (Fig. 2.75), which, therefore, results in a more optimized operation time, since the sail line interval can be increased. The number of total sail lines in 3D surveys is inversely proportional to the number of streamers deployed. Acquisition with higher number of streamers also provides better azimuth distribution.

Lateral distance between the streamers in 3D surveys determines the distance between CMP lines from which the seismic traces are actually reflected. For a single source array, the distance between CMP lines is half of the streamer separation (Fig. 2.76A). In a flip-flop acquisition with two identical source arrays, it is reduced to one quarter of the streamer separation (Fig. 2.76B) if the source separation is half of the streamer separation as a common survey layout in 3D towed streamer acquisition. As a result, smaller

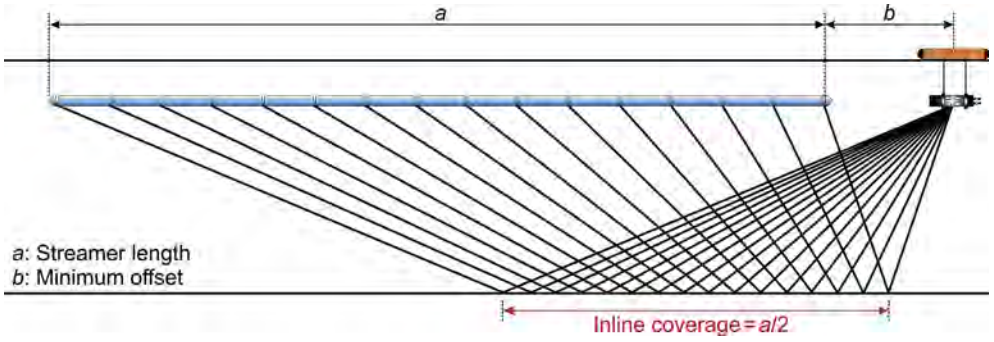


FIG. 2.74 Coverage area for one single shot in a 2D case. For 2D surveys, only inline coverage is pronounced, which equals to the half of the overall streamer length (*a*).

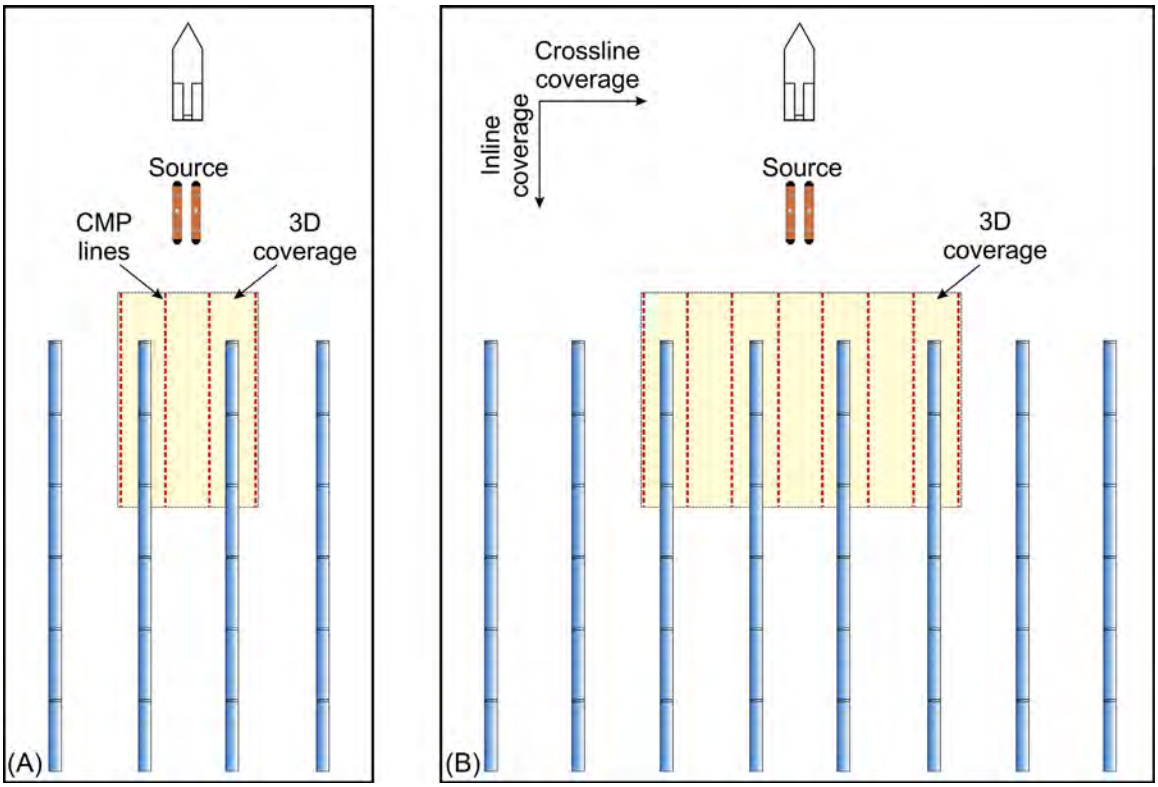


FIG. 2.75 Coverage area for one single shot in 3D case. Coverage areas for (A) four- and (B) eight-streamer acquisitions. *Red dashed lines* correspond to CMP lines obtained from each streamer.

streamer separations result in a smaller bin size, and therefore provide a better spatial resolution. Acquisition with a fan mode shooting layout (Section 2.3.7) can further increase the crossline coverage, especially for long offsets, which can reduce the shooting times for additional infill areas.

2.5.1.7 Bin Size

A CDP bin is a square or rectangular area containing several traces radiated from different sources and recorded at different receivers, but all of which have the same midpoints (Chapter 8). Bin size represents the length and width of the rectangular or square-shaped CDP bin, and depends on the target size, spatial resolution needed, and the cost of the survey. In the early 1980s, 12.5 m $\times$ 50 m inline and crossline bin sizes were typical. By the introduction of dual source flip-flop acquisition and smaller streamer separations, inline and crossline bin sizes were reduced to 6.25 m $\times$ 12.5 m, respectively.

In 3D marine surveys, bin size is governed by the geometry of the spread. Inline bin size is typically chosen as one-half of the group interval both for 2D and 3D acquisition. Crossline bin size is, however, controlled by a number of factors, such as number of streamers, streamer separation, and number of sources. Incorporation of dual source doubles the number of CDP lines and reduces the crossline bin size by half. In conventional dual source 3D acquisition, source separation is half of the streamer separation,

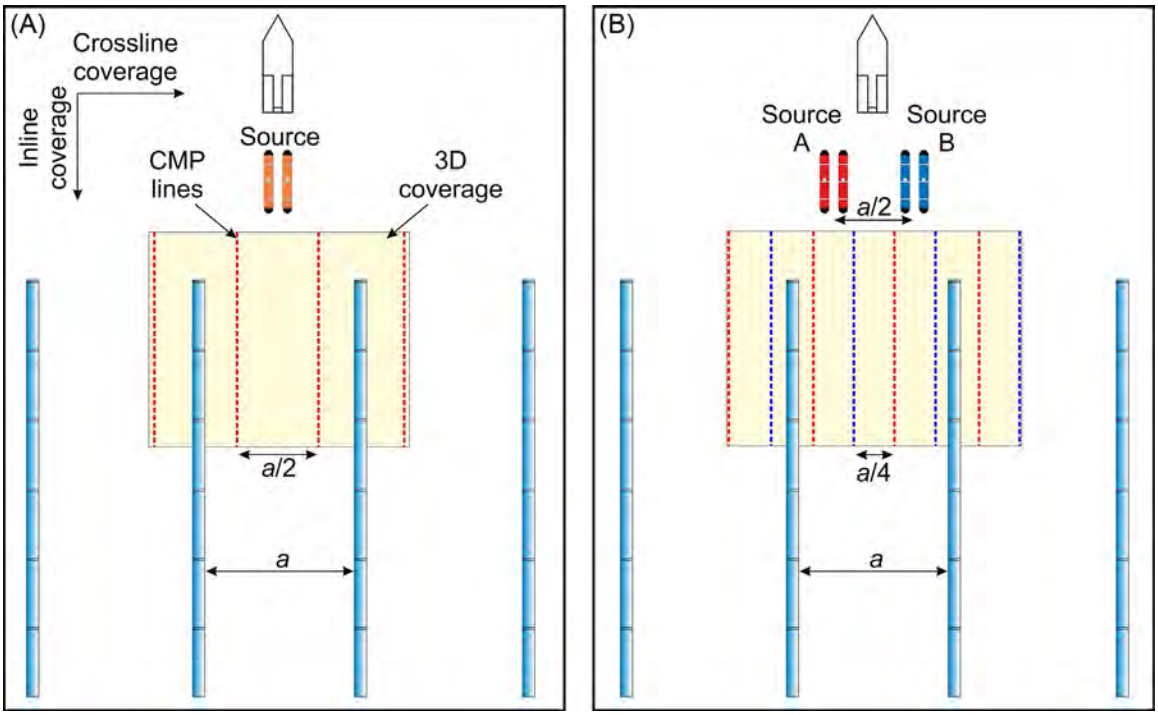


FIG. 2.76 (A) The separation between the CMP lines is one-half of the streamer separation for single source 3D acquisition. (B) In dual source flip-flop acquisition, the separation between the CMP lines is one-quarter of the streamer separation.

so that the crossline bin size is one-quarter of the streamer interval. In a theoretical sense, the length of the bin may equal to the radius of the Fresnel zone, which is defined as the area on a subsurface reflector that reflects the energy arriving at the receiver within a time delay equal to half the dominant period. The radius of the Fresnel zone is expressed by

$$r = \frac{V_{RMS}}{2}\sqrt{\frac{t_0}{f}} \tag{2.3}$$

where V_{RMS} is the average RMS velocity down to the target depth, f is the dominant frequency of the seismic signal, and t_0 is the two-way travel time.

The bin size will affect the spatial resolution of the survey: it should be small enough to avoid spatial aliasing during the processing stage, especially for the migration process. If the bin size is too large, the subsurface is too coarsely sampled, which ultimately results in aliasing of the higher frequencies. In practice, bin size should be small to ensure the high lateral resolution, which significantly improves the seismic image quality. Widely spaced streamers in 3D surveys result in larger bin sizes, while smaller spacing between the hydrophone group centers and between the streamers provides denser trace spacing and higher resolution data, although it will reduce the total swath width or spatial coverage, which requires more closely spaced sail lines and increases the overall survey time.

Fig. 2.77 shows a comparison of two 3D seismic datasets with different bin sizes. The line in Fig. 2.77A was collected with four streamers of 53.3 m separation and a single

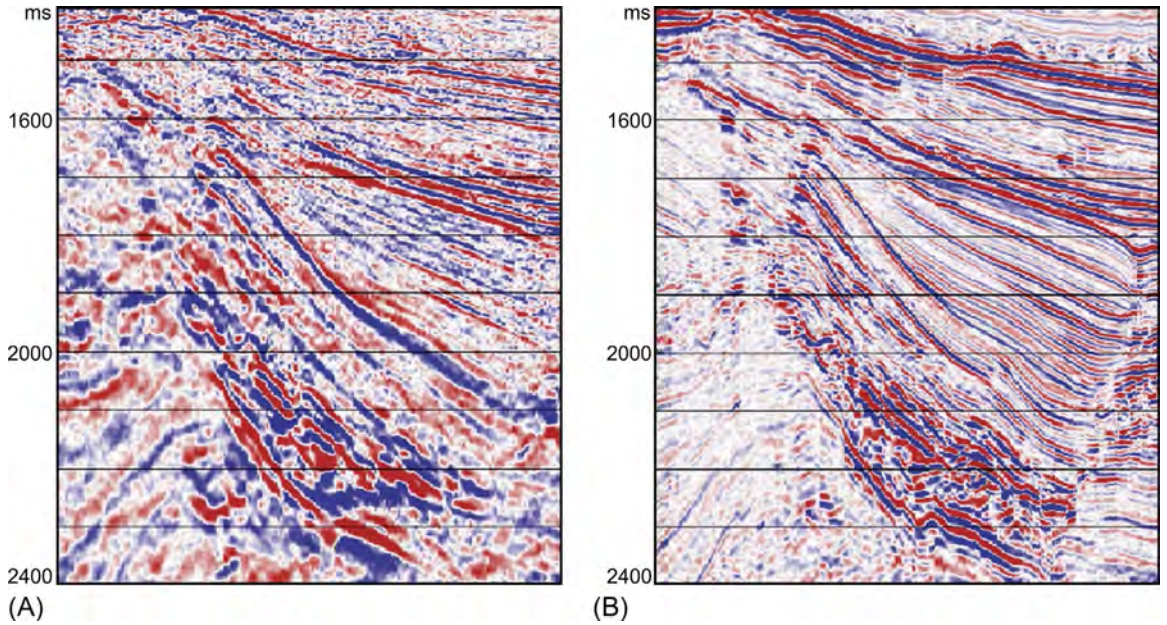


FIG. 2.77 Comparison of two 3D seismic datasets with (A) 13.3 m × 26 m and (B) 12.5 m × 12.5 m bin sizes. *After Chopra, S., 2004. Expert answers. Theatr. Rec. 29, 1–20.*

source array, and processed at 13.3 m × 26 m bin size. The data in Fig. 2.77B, however, was collected with eight streamers of 100 m separation and dual source arrays, and processed at 12.5m × 12.5 m bin size. Although some of the acquisition and processing parameters are different, the resolution difference between the sections due to the different bin sizes is significant.

2.5.1.8 *Line Interval and Infill*

Separation between the sail lines is commonly determined by considering the lateral resolution required for mapping the subsurface structures in a lateral direction in 2D surveys. However, it is a function of the number of streamers and streamer separation in 3D case. In 2D surveys, seismic profiles are several kilometers apart depending on the requirements and purpose of the survey. For a regional 2D seismic acquisition for reconnaissance purposes, the line interval is typically not less than 5 km. For denser line spacing, crossline mapping of the structures can be more reliably achieved. In 2D surveys, line ties with vintage data as well as a nearby well are also important.

In 3D acquisition, however, the study area is fully covered with a line interval of one-half the crossline width of the whole spread. For instance, a 400-m sail line interval is required for 8 streamer acquisition with 100 m streamer separation. It is critically important to cover the whole target zone within the survey area by evenly distributed bin fold and source-receiver offset without any data gaps in 3D surveys. In some cases, high feathering angles of the streamers exceeding 10 degrees due to the strong ocean currents and data gaps caused by bad weather conditions, marine traffic and technical down times induce local gaps or irregular fold distribution in the 3D seismic datasets. Streamer feathering becomes a serious issue in the case of the ocean currents that change direction within the 3D survey area, which causes

significant gaps across the contiguous sail lines since the feathering angles may change by means of amplitude and direction in such cases.

In order to compensate the uneven fold distributions or to fill in the gaps within the survey area, the vessel reshoots some of the lines after primary 3D acquisition is completed. This additional shooting is termed infill and it requires an additional survey design and sometimes significantly increases the survey costs, since they may cover 15% of the total production time. Fig. 2.78 shows an example 3D fold distribution map before and after infill shots from a 3D survey conducted in Eastern Pacific Rise in 2008 by the R/V Marcus Langseth of Columbia University.

To reduce the infill shots, streamer positioning and surficial weather conditions as well as the direction and strength of the local currents with respect to the sail line azimuth should be carefully observed, and the survey should be optimized by a rigorous analysis of real-time binning of the data during the acquisition. Running the infill lines may become challenging for far offsets since they are much more affected by the ocean currents and hence feathering is more pronounced for the tail sections of the streamers. Acquisition with the fan mode layout (Section 2.3.7) may significantly reduce the infill times for 3D surveys and hence reduces the overall cost of the survey.

2.5.1.9 Run-In and Run-Out Distances

In 2D and 3D surveys, shooting is initiated at a certain distance before the preplot profiles; similarly, it is stopped at a certain distance after than the actual end positions of preplot lines. These distances are termed run-in and run-out distances, respectively (Fig. 2.79), and they allow the streamer cable(s) to straighten after each turn. Because of the shooting geometry, nominal fold decreases towards both ends of the survey line in 2D acquisition and in the regions close to the borders of 3D survey area, which are termed fold taper zones. Run-in is defined as the additional distance required for

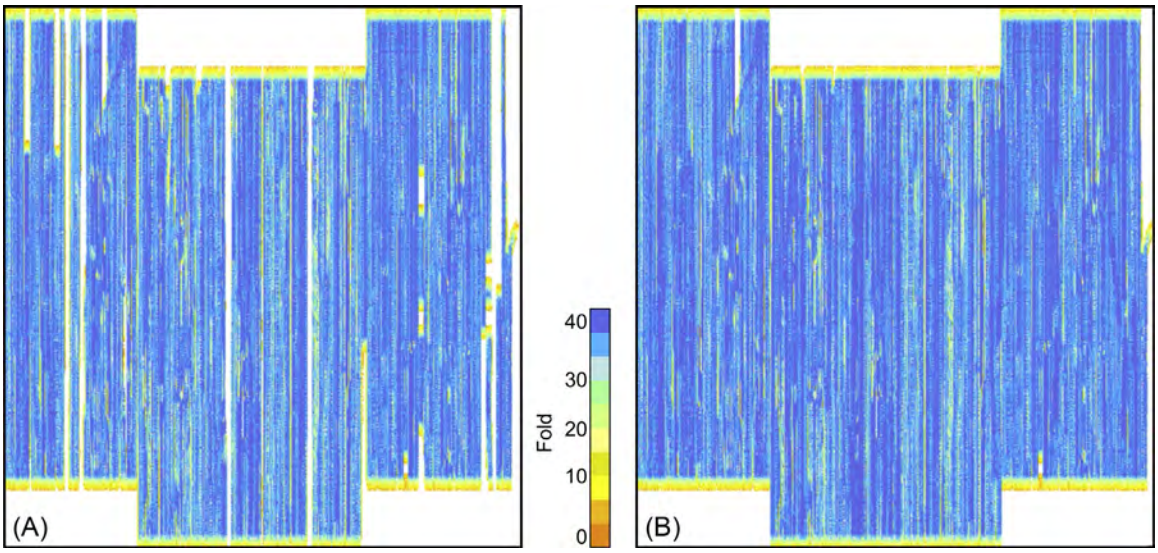


FIG. 2.78 Fold distribution (A) before and (B) after infill shots from a 3D survey in Eastern Pacific Rise conducted by the R/V Marcus Langseth. *After Mutter, J.C., Carbotte, S.M., Canales, J.P., Nedimovic, M., 2008. A 3D MCS investigation of the magmatic-hydrothermal system at the East Pacific Rise 9°50′N, MGL0812 Cruise Report.*

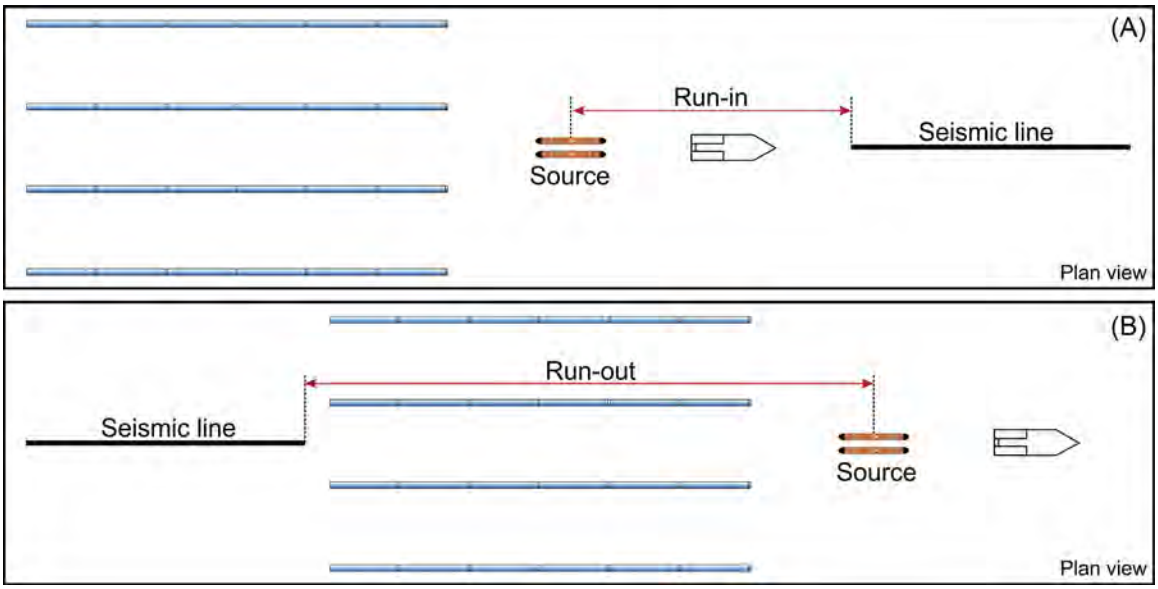


FIG. 2.79 (A) Run-in and (B) run-out distances used to keep the streamers straight before and after each line change. Shooting starts at run-in distance before, and stops at run-out distance after the seismic profile to collect full-fold data along the actual preplot line.

taking the acquisition fold from its minimum value in the fold taper zones to its nominal of full-fold value in the shooting direction, and generally equals to the streamer length. Similarly, run-out is defined as the distance required for taking the acquisition fold from its nominal value to minimum in the fold taper zone, and generally equals to one half of the streamer length.

2.5.1.10 *Air Gun and Array Parameters*

Effect of the air gun array parameters on the quality of the acquired data is explained in Section 2.2 in detail. The volume of each individual air gun is inversely proportional to the frequency content of the generated signal. Small-size air guns produce higher frequency seismic signals, which provide higher resolution, but lower penetration. As a general rule, the resultant seismic signal amplitude is approximately proportional to the cubic root of the total volume of an air gun array, which means that an air gun array of 1000 in^3 generates only 10 times higher signal amplitude than an air gun of only 1 in^3 volume. Therefore, the most effective way to increase the signal amplitude, and hence the overall signal penetration, is to use several air guns simultaneously instead of increasing the volume of each single air gun.

Air gun array design is important to obtain a proper seismic signal of high amplitude and peak-to-bubble ratio (PBR) by suitably designing the volumes and positions of each individual air gun or gun cluster within the array (Section 2.2.6). PBR increases as the volume of the gun and air pressure increase. Signal amplitude is directly proportional to the air pressure applied to the guns, and 2000 $\pm$ 100 psi air pressure is standard for the seismic acquisition industry today. Capacity of the air compressors is also important. The compressors should deliver compressed air to the gun array(s) of specified total volume at time periods determined by the shot interval and vessel speed

(Table 2.5). If not, it may require a decrease in the vessel speed to supply more time for compressors to fill in the guns between two successive shots, which ultimately affects the overall time schedule of the survey.

In 3D acquisition of flip-flop shooting, separation between the two air gun arrays affects the crossline bin size and hence spatial resolution of the seismic data. In general, the lateral distance between two arrays is half of the streamer separation to obtain a regular CMP line distribution.

2.5.1.11 Tow Distance and Vessel Speed

Tow distance states the distance between the stern and towed equipment, such as gun arrays and streamers. It is not related to the resolution or frequency content of the data, but is directly associated with the operational noise level of the data. If smaller, operational noise level increases. Distant tow requires additional umbilicals and lead-in cables with appropriate length, as well as extra data telemetry units for long-distance data transmission.

Speed of the seismic vessels is expressed as nautical miles per hour, or knots: 1 knot equals 1 mile/h and is 1853 m/h. Vessel speed during the survey affects the total survey program, and is closely related to the record length and shot interval (Table 2.5). In addition, higher tow speeds induce higher noise on the recorded data and decrease the overall S/N ratio. In 2D and 3D seismic acquisition, vessel speed is kept constant between 4.0 and 4.5 knots, even though it can be increased during the line changes depending on the strength limitations of the towed equipment.

2.5.2 Parameters for Data Recording

2.5.2.1 Record Length

Record length is the time span that the reflection amplitudes arriving at the receivers immediately after a time break signal are perceived by the hydrophones and recorded to the tapes or disks by the seismic recorder. Record length is a function of depth and seismic velocity of the deepest horizon and is directly proportional to the target depth. It should be selected long enough to record the reflections from the deepest horizon of interest and to collapse the diffractions from the deepest reflector for a reliable migration.

As a general convention, the record length, t_r, should satisfy

$$t_r \geq t_d + 2 \times t_{FL} + 1.5 \text{ s} \tag{2.4}$$

where t_d is two-way time to the deepest horizon of interest at maximum offset, and t_{FL} is the time length of the longest filter to be applied (e.g., 400 ms for frequency filtering). An additional 1.5 s is for NMO/DMO correction and migration.

In practice, record length is also related to the source strength or maximum penetration depth of the signal. If it is selected too long, then it causes recording of an unnecessarily large volume of useless data beyond the penetration depth of the source signal, which may significantly increase the processing time and hence the overall cost of the survey.

2.5.2.2 Sampling Rate

The amplitudes of reflected energy are perceived by the hydrophones and are digitized at regular time intervals before recording to the tapes or disks. This time interval is constant for all traces of all shots along the seismic line and is termed the sampling rate. Based on the sampling theory given in Section 4.10, sampling rate directly affects the maximum frequency value that can be recorded, termed the Nyquist frequency, f_N, which is

$$f_N = \frac{1}{2\Delta t} \tag{2.5}$$

where Δt is the sampling rate. As the sampling rate increases, the Nyquist frequency decreases. Even if the source produces high-frequency components, these cannot be recorded. For

instance, up to 250 and 500 Hz frequencies can be recorded with 2- and 1-ms sampling rates, respectively. Normally, ghost notches determine the upper frequency limit of the seismic signal spectrum, and it is 125 Hz for a 6-m depth streamer (Fig. 2.36). If we use a sample rate of 1 ms with a 500-Hz Nyquist frequency, then we have an oversampled dataset between 125 and 500 Hz, which considerably increases the processing time since sampling rate directly affects the total volume of the recorded data.

In conventional 2D or 3D acquisition, the sampling rate is selected at either 2 or 4 ms depending on the resolution required. For most seismic surveys, 2 ms is preferred. In high-resolution surveys, however, 1-ms sampling is typical since higher frequencies can be recorded by towing the source and streamer at shallower depths.

2.5.2.3 Recording Filter Cut-Off Frequencies

The maximum signal frequency that can be reconstructed after digitizing the reflected seismic signal is determined by the Nyquist frequency (Section 4.10). In other words, we cannot record the frequency components higher than Nyquist. However, this does not imply that there are no higher frequency amplitude components in the water. Indeed, there is always a static noise component, which spreads all over the available spectral bandwidth, including the frequencies beyond the Nyquist frequency. Our sampling rate is always high for these higher frequency random noise components, since these noise amplitudes are of frequencies higher than our Nyquist value. As a result, our predetermined sample rate downsamples these noise components, which ultimately results in them being aliased onto the amplitudes of lower frequency components in the spectrum.

In order to prevent aliasing of the high-frequency noise amplitudes beyond the Nyquist frequency during the recording, wideband filters, termed antialiasing filters or recording filters, are applied to the data before digitizing. Their low cut frequency is approximately 3–4 Hz, while high-frequency cut-off is generally 80% of the Nyquist frequency. In conventional seismic surveys, 4–200 Hz (18–300 dB/Oct) cut-off values are typical, whereas a wider pass-band is designed for high resolution acquisition, such as 5–412 Hz (12–300 dB/Oct).

2.5.2.4 Dynamic Range and Seismic Sample Format

Dynamic range is defined as the ratio between the highest and the lowest amplitude that can be recorded by an instrument without any distortion and is usually expressed as decibel units (dB). For instance, if a recording system can receive and convert analog data between 1 and 100 amplitude units, then the dynamic range of this system is $20 \times \log(100/1) = 40$ dB. For a seismic recording system, dynamic range is important since it defines the range of the input signal amplitude (maximum and minimum signal amplitude values) that can be reliably converted to the digital form during sampling. If the dynamic range of the recording system does not satisfy the amplitude range of the seismic signals, then the high signal amplitudes are clipped, as in the case in Fig. 2.80.

A seismic system with a high dynamic range can record both extremely small and excessively high signal amplitudes at the same time without distortion. Direct arrivals and sea floor reflections in relatively shallow water surveys, especially in the case of hard sea bottom, can generate high amplitude arrivals. The amplitude difference between the largest signal amplitude and the ambient noise level may be more than 100 dB, which indicates an amplitude ratio of 100,000/1 (Shirley et al., 1985). In 1991, delta-sigma type analogue-to-digital (A/D) converters introduced 24-bit recording systems into the seismic industry, which provides a 144.48 dB dynamic range.

Received and digitized seismic amplitude samples are recorded onto the tape drives or

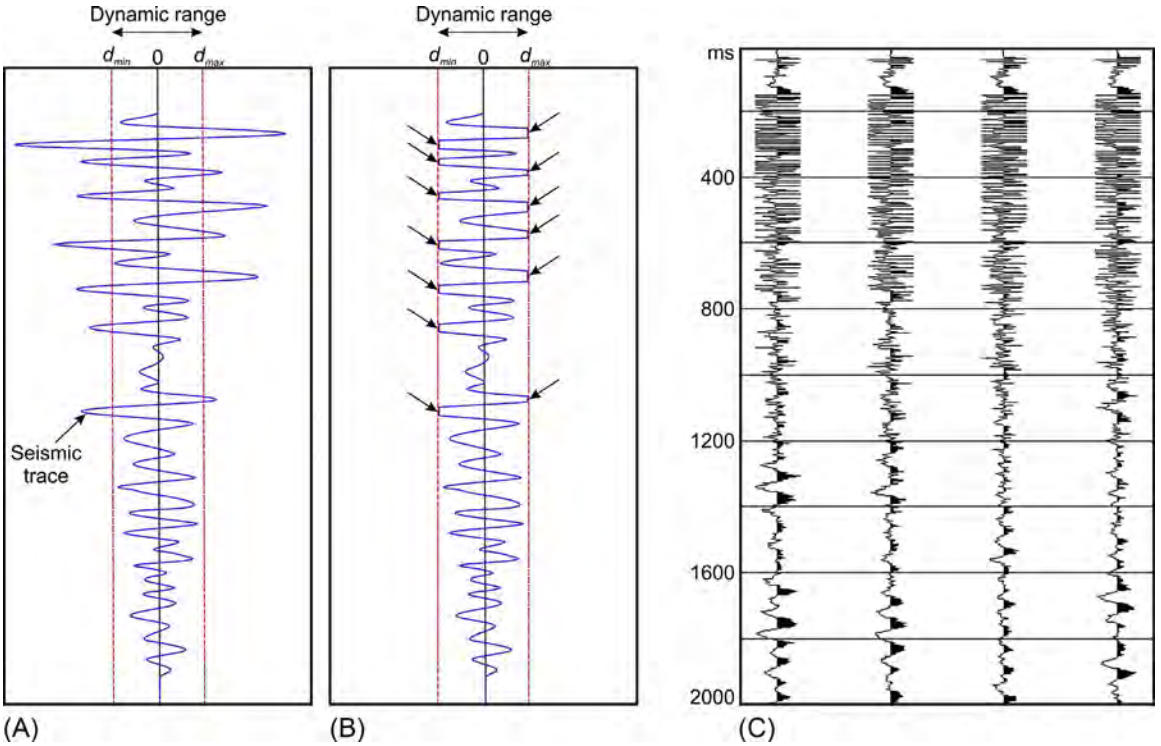


FIG. 2.80 (A) Schematic illustration of seismic trace amplitudes and dynamic range limits of a recording system. (B) In such a narrow dynamic range recording, higher amplitudes of the reflections are clipped *(arrows)*. (C) Four example traces with high amplitudes at their early arrivals, which are outside the dynamic range of the recording system.

hard disks in specific BINARY data formats (Section 5.2). These seismic data samples can be recorded in different sample formats represented by different numbers of bytes (Table 2.6). These formats define how precisely the amplitude samples will be stored in the recording media. Since the capacity of computer hardware is limited, it is not possible to store and process these numbers with an extremely high precision. Today, seismic data is acquired in 32-bit floating point format which uses four successive bytes to record each seismic amplitude sample. In some cases, it is converted, or compressed, into 8-bit integer format during the interpretation, known as scaling, to reduce disk and/or memory consumption, since the

TABLE 2.6 Different Sample Formats Used to Store the Seismic Data

Data Format	Bits	Bytes	Signed Limits
IBM floating point	32 Bit	4 Byte	$\pm 5.4 \times 10^{-79}$ to 7.2×10^{75}
IEEE floating point	32 Bit	4 Byte	$\pm 1.18 \times 10^{-38}$ to 3.37×10^{38}
Integer	32 Bit	4 Byte	−2,147,483,648 to +2,147,483,647
Integer	16 Bit	2 Byte	−32,768 to +32,767
Integer	8 Bit	1 Byte	−128 to +127

Data is normally recorded as 32-bit floating point. From top the bottom, the recorded data have lower resolution and dynamic range, but occupies smaller disk space.

volume of the large seismic datasets may be huge and sometimes pushes the hardware limits of the interpretation computers. This process, however, reduces the dynamic range of the data.

2.5.2.5 Optimum Fold

Fold is defined as the number of traces in a CMP bin. The S/N ratio of the seismic data increases with the square root of the number of traces within the bins. As a general rule, 3D data fold is selected as being larger than half the nominal 2D fold of the vintage data. In conventional 3D NAZ acquisition, the data is collected by one single vessel towing all the streamers and the data is recorded by only one pass for each sail line. The distance between parallel sail lines in the 3D survey area is determined by the total crossline coverage depending on the number of streamers and streamer separation, and typically there is no overlap between the parallel lines. Therefore, crossline fold in 3D marine NAZ surveys is normally 1 and nominal inline fold is given by Eq. (8.1).

Since the fold number has a significant effect on the data quality, it is always preferred to acquire high fold seismic data. In order to increase the fold, either the length of the streamer(s) should be increased or the shot interval should be decreased according to Eq. (8.1). The latter is more practical even though it may require the record length to be decreased. If not, vessel speed should be decreased to keep the record length longer.

In conventional 3D acquisitions, the survey area is not constrained by the extensions of the target structure. It should be extended in both inline and crossline directions to comprise a full-fold zone and a fold taper zone (Fig. 2.81). Fold taper zone, or halo distance, is the area around the two edges of the full-fold zone in the acquisition direction, where the optimum fold value increases from its minimum to full-fold value. The fully migrated area is the central part of the whole 3D acquisition area, that is, the green zone in Fig. 2.81. The main purpose is to collect full-fold seismic data within this

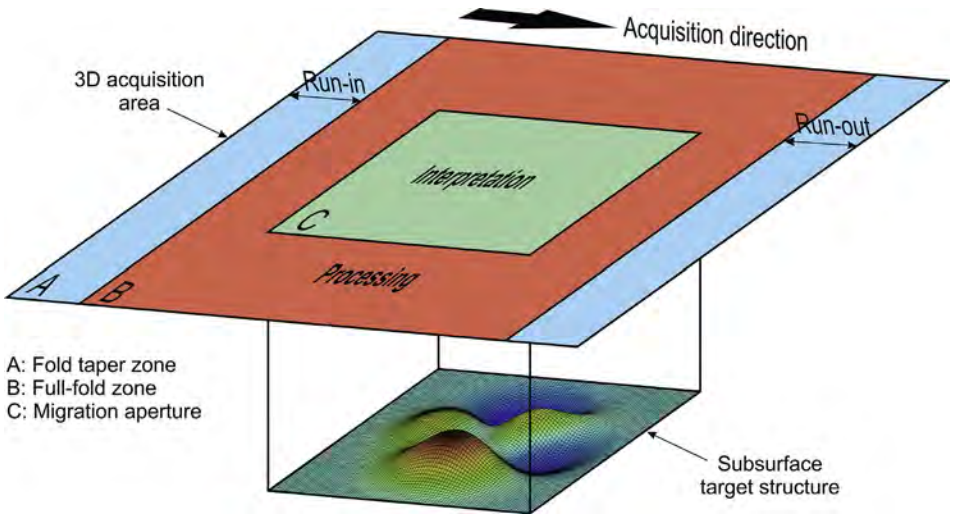


FIG. 2.81 The 3D survey area is not limited to the zone comprising only the target structure, but is extended in both directions to include the red full-fold zone and blue fold taper zone. In order to fully migrate the data within the green (target) zone, all the data in the red and green areas is required.

interpretation zone, which typically covers the target structure in the subsurface. The whole 3D area is planned by the field geophysicists who actually design the complete survey and determines the acquisition parameters, depending on the requirements of the survey. Full-fold zone is handled by seismic processors to properly migrate the data that involves the target structure. Finally, the data in the target zone is ready for interpreters.

2.6 QC IN DATA ACQUISITION

By its general definition, quality control (QC) is the process that defines how well the solution of a problem is known, or how well the methodology used to solve the problem is applied. QC work is often pronounced with quality assurance (QA) implementations, which include a documented and certificated management system of the systematic control process to prevent faults and mistakes during production and to check whether the product meets the specified requirements of the work. As a general approach, QC applications aim to detect and eliminate the errors and defects in the final product or data, while QA implementations intend to remove the effects or any agents that may cause QC issues in the product and to take the necessary precautions.

The quality control term in seismic surveys comprises procedures and applications for analysis and evaluation of the seismic data quality in each specific step, from data acquisition to interpretation, to ensure the quality of the seismic data. It is classified as QC in data acquisition and in data processing, and comprises a comprehensive documentation and reporting procedure. QC analyses of seismic data acquisition can be done in real-time and offline following the acquisition. In this section, offline quality control applications used on the seismic data after it is acquired as well as documentation and reporting in QC processes are discussed.

QC assessments in seismic data acquisition comprise not only the analysis of the seismic data itself but also the navigation data, as well as the evaluation/analysis/recalibration of mobilized instruments and seismic source performance tests, and periodic reporting of the QC analyses and results (Fig. 2.82). The main purpose of the QC implementations in seismic data acquisition is to evaluate the data quality onboard during the acquisition, even in real-time if possible, to

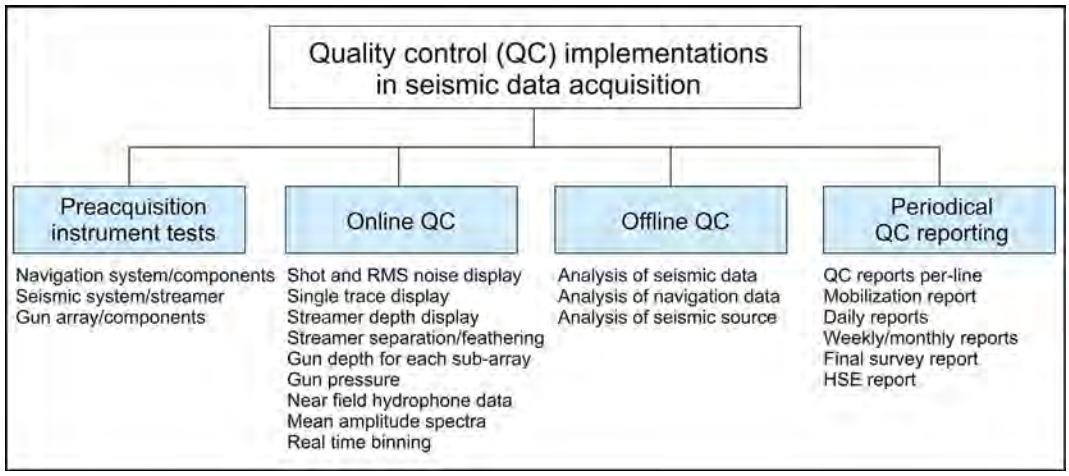


FIG. 2.82 Responsibilities of onboard seismic survey crew in terms of QC applications for data acquisition.

ensure that the quality, accuracy and resolution of the acquired data meet the predetermined requirements and are within the specified limits. QC procedures enable us to identify any issues during the acquisition as soon as they occur, which may result in reshooting some of the lines or a temporary suspension of the whole survey. Identifying acquisition problems arising from the instruments or weather conditions as well as software specifications such as bad records, misfires, defective or dead channels, air leakages, specific strong noise interferences, etc., early in the data collection minimizes the technical downtimes during the acquisition.

QC in data acquisition is fulfilled as real-time (or online) and offline implementations (Fig. 2.82). Online QC involves analyzing the data as it is collected. Today, online QC applications to document the quality of the acquired seismic data are widespread in the seismic industry. Online QC can be performed on seismic, source and navigation data as soon as the data is received during the acquisition, and typically contains

- Shot displays of all streamers (bad records, misfires, noisy channels, etc.)
- Near trace displays (data quality, static time shift between the shots, etc.)
- Near-field hydrophone data (gun timing, bubble level and period, air leakage)
- Sum of all channels of each streamer per shot (electrical noise and cross feed)
- RMS noise display of all channels (ambient and operational noise level)
- Mean amplitude spectra
- Depth display of the streamers
- Gun depth for each subarray
- Gun pressure for each subarray
- Real-time fold distribution
- Checking the data header values
- Separation and feathering of the streamers

After a seismic line is acquired and recorded, offline QC processing is initiated. Each member of the survey crew in Fig. 2.1 has different responsibilities in terms of QC applications just before, during and after the data acquisition. A typical quality control management system for marine seismic surveys consists of three different levels of control and quality management (Fig. 2.83). At the first level QC applications, several standard data and instrument analyses are performed by observers (for seismic data), navigators (for navigation and streamer steering data) and mechanics (source signal data), and their QC reports are approved by the chief observer, chief navigator and chief mechanic (Table 2.7). These reports are further approved by the chief field geophysicist at the second level of the QC applications, in addition to the other assessments such as preparing of daily reports

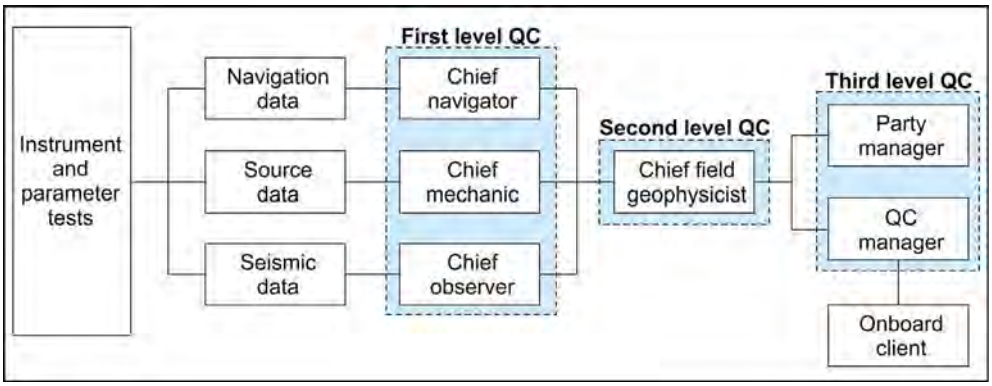


FIG. 2.83 A typical three-level onboard QC management system for marine seismic surveys.

TABLE 2.7 Level-1 Quality Control Assessments for Marine Seismic Surveys

Approved by	Duty
Chief mechanic	Tests of guns, compressors, gun controller
	Verification of source array layout
	Performing the bubble tests
	Checking the near-field signatures of all air guns
	Checking the gun pressures
	Verification of source depth
	Checking the air leakage
Chief navigator	Tests of navigation system and related devices
	Verification of navigation parameters
	DGPS verification and gyro calibration
	Preparing streamer layout
	Verification of shooting parameters
	Real-time checking the positions of in-sea equipment
	Controlling the vessel speed
	Checking the feather angles of all streamers
	Checking the bird/acoustics/steering devices status
	Preparing the preplots
	Preparing real-time binning and fold map
Chief observer	Tests of recording unit, tape drives, data transmission
	Verification of recording parameters
	Real-time checking the seismic shot data
	Checking the RMS noise level
	Analyzing the specific noise types and overall data quality
	Checking the missed shots
	Checking the static shifts between recorder and gun controller
	Checking the amplitude spectra of the selected shots
	Preparing near trace gathers and brute stacks
	Hydrophone polarity and sensitivity tests
	Collecting the noise records
	Collecting the test record, if required

Continued

(Table 2.8). The party manager and onboard QC manager perform the third level of QC assessments by verifying all the QC procedures and reports, and checking of overall data quality (Table 2.9). All available QC reports, related data and other QC-related products are then submitted to the onboard client for a final approval.

TABLE 2.8 Level-2 Quality Control Assessments for Marine Seismic Surveys

Approved by	Duty
Chief field geophysicist	Checking and approval of level-1 quality control assessments
	Project start-up report
	Project daily reports
	Checking and improvement of onboard processing flow

TABLE 2.9 Level-3 Quality Control Assessments for Marine Seismic Surveys

Approved by	Duty
Party manager	Checking and approval of level-2 quality control assessments
	Project final report
	Checking of overall data quality
Onboard QC manager	Checking and approval of level-2 quality control assessments
	Coordination with onboard client about QC issues
	Checking of overall data quality

2.6.1 Preacquisition Instrument Tests

Several tests and calibrations are performed before the survey to ensure that all mobilized equipment is functioning properly. These tests are termed start-up tests and include testing and calibration of navigation units, seismic recorder and streamer, and air gun array. Some of the instrument tests are repeated regularly in a daily or monthly basis, depending on the requirements of the survey and client demands. An instrument mobilization checklist for streamers and recording system as well as seismic source is prepared by the chief observer and approved by the party manager before each survey. These checklists are used to assure that the parameters for the source, navigation devices, recording system and survey geometry are complete and properly set. An example checklist for source, streamer, navigation devices, and recording system is shown in Table 2.10.

Preacquisition implementations may also include the acquisition of a test line close to the study area just before the survey is initiated to ensure that all the equipment deployed is operational in a predefined manner, if requested by the client. Usually, one or more noise records is collected before start-of-line (SOL) and after end-of-line (EOL) for each survey profile, to understand the ambient noise level in the survey area.

TABLE 2.10 An Example Parameter Checklist for the Mobilized Instruments (Streamers, Recording System and Seismic Source) Controlled Before the Survey

	Parameter	Planned	Configured	☑
Streamers	Number of streamers	6	6	☐
	Total length of active channels	8000 m	8000 m	☐
	Streamer depth	8 m	8 m	☐
	Streamer separation	100 m	100 m	☐
	Total number of channels per streamer	640	640	☐
	Group interval	12.5 m	12.5 m	☐
	Number of depth leveler bird per streamer	10	10	☐
	Number of compass bird per streamer	16	16	☐
	Number of steering devices per streamer	16	16	☐
	Total number of acoustics per streamer	14	14	☐
	Total number of velocimeters for spread	2	2	☐
	Minimum offset	120 m	120 m	☐
Recording system	Record length	10 s	10 s	☐
	Sample rate	2 ms	2 ms	☐
	Shot interval	25 m	25 m	☐
	Data format	SegD 8036	SegD 8036	☐
	Array forming	N/A	N/A	☐

Continued

	Parameter	Planned	Configured	☑
	Low cut filter	3 Hz/18 dB	3 Hz/18 dB	□
	High cut filter	200 Hz/210 dB	200 Hz/210 dB	□
	Auxiliary channels	60	60	□
Sources	Number of sources	2	2	□
	Total gun volume per source	3090 in^3	3090 in^3	□
	Number of subarrays	3	3	□
	Number of guns per subarray	8	8	□
	Number of hydrophones per subarray	8	8	□
	Number of depth transducers per subarray	4	4	□
	Number of pressure sensors per subarray	1	1	□
	Source depth	6 m	6 m	□
	Source separation	50 m	50 m	□
	Nominal air pressure	2000 psi	2000 psi	□
Verifications				
Checking of recording system/streamer telemetry				□
Performing a full recording system/streamer test				□
Checking of trace polarity				□
Checking of near-field hydrophones (tap test)				□
Checking of string depth ropes				□
Checking of string depth sensors				□
Checking of birds/acoustics communications during and after deployment				□
Checking of bird depth sensors before deployment				□
Checking of acoustic network and offsets				□
Checking of data gain				□
Checking of echosounder velocity				□
Checking of DGPS/rGPS systems				□
Performing a test line				□
Checking of external SegD data header after test line				□
Performing bubble period tests for each individual gun				□
Checking of gun line integrity				□

2.6.1.1 Tests for Navigation System and Components

The navigation system and all existing components and sensors are checked and controlled before the survey. Health checks of the navigation system and its components are carried out onshore to verify that the installation of all the equipment including DGPS receivers, gyros, motion sensor, echosounder, ADCP, etc., is completed accurately in terms of data receiving, transmission, and data logging, with the correct operational settings. Most of the calibrations and verifications are based on the elimination of possible differences between accurately computed (C) and observed (O) values of the device readings, which are then entered into the controlling software of the devices to correct the errors between computed and observed values (C-O).

Preacquisition assessments also include preparing the plots of all sail lines on the integrated navigation system (INS) known as preplot lines; assessing the possible major difficulties, such as weather conditions and local currents in the area; and checking the navigation parameters and datum shifting. Typically, following controls, calibrations and verifications of the navigation system and components are executed before the initialization of the survey:

- Setting up the navigation parameters
- Preparing streamer layout
- Gyro calibration
- DGPS verification
- rGPS check
- Echosounder depth data verification
- Control of the streamer steering and acoustic devices

a. *Navigation parameters*: All the navigation parameters of the study area including ellipsoid, projection, UTM zone parameters and datum shifting are entered into the INS. Preplots are prepared based on the predetermined line name format and sail line coordinates. Fig. 2.84 shows two example preplot maps for 2D and 3D surveys. Offsets of the vessel and all other navigation units as well as in-sea equipment with respect to the

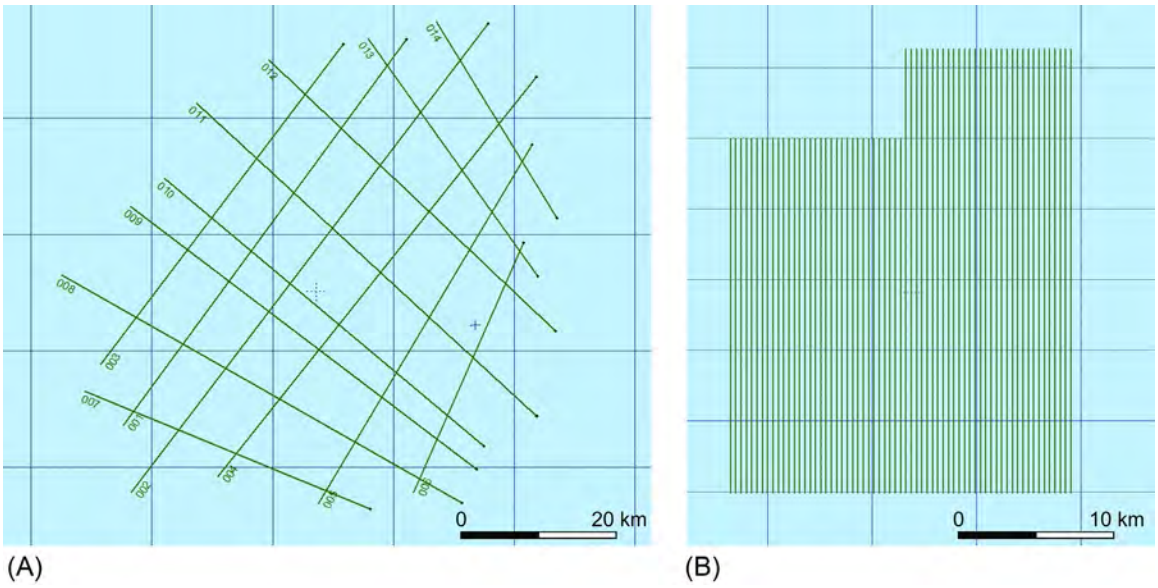


FIG. 2.84 Example preplot maps for (A) 2D and (B) 3D seismic survey.

reference axes of the vessel are defined in the INS (Section 2.1.7).

b. *Streamer layout*: Preparing the layout of the streamer(s) is a time-consuming process and should be done correctly to maintain all the streamers in the desired positions. Proper streamer steering is achieved by attaching specific navigation instruments to the streamers (Section 2.3.2). These include 3D steering devices, devices for acoustic ranging, velocimeters, speed logs and compass birds. The positions of these devices should be accurately determined for a complete solution of the streamer positioning during the surveys (Figs. 2.43 and 2.44).

c. *Gyro calibration*: Seismic vessels commonly have two simultaneous gyros, which should be calibrated before the survey when the vessel is at dock using two survey prisms located at the bow and stern, aligned along the centerline of the vessel. The purpose of gyro calibration is to find out the differences in mounting angles between gyro heading and vessel's centerline. The true vessel heading is computed by surveying the prisms using a Total Station and the obtained heading is compared to the gyro's readings. Any differences between computed and observed values are applied to the INS to correct the gyro alignment error (Table 2.11). In some cases, two calibration surveys in opposite directions are performed, if required. The data from the gyro(s) is then logged for a certain time period and the differences are evaluated.

TABLE 2.11 Computed (C) and Observed (O) Values of Vessel Heading for Gyro Calibration

	C (°)	O (°)	C-O (°)
Gyro1	240.15	241.03	−0.88
Gyro2	241.53	241.03	0.50

d. *DGPS verification*: At least two simultaneous DGPS receivers are installed on the seismic vessels. DGPS verification is done when the vessel is at dock to observe the error in the GPS solution. For DGPS receivers, normally the horizontal positioning error is less than 1 m. In order to determine the accurate coordinates of the DGPS antennas, range and bearings to the GPS antennas are calculated using a Total Station located on a survey point on the quay whose coordinates are precisely known, while the vessel's navigation system logs the antenna coordinates. The computed coordinates of the antennas are compared to the vessel's readings to derive the differences in the computed and observed coordinates (Table 2.12). The antenna coordinate of the DGPS is then logged for a certain time period and the scattering in the positioning is evaluated.

e. *rGPS check*: The purpose of the rGPS check is to find out the positioning errors and standard deviation in the rGPS system. All existing rGPS pods are located on the quay when the vessel is at the dock. Range and bearings from each rGPS pod to DGPS antenna are calculated using a Total Station. The computed coordinates of the pods are compared to the rGPS system readings for a couple of minutes to derive the differences in the computed and observed coordinates as well as the standard deviations (Table 2.13).

f. *Echosounder verification*: The accuracy of water bottom depth measurements from single-beam echosounders are controlled when the vessel is at dock. The purpose is to find out the accurate draught of the echosounder transducer from the sea level. Seismic vessels have dual transducer echosounders operating at two different frequencies, typically 38 and 200 kHz, to obtain the depth information for deep and shallow waters, respectively; 1500 m/s constant sound speed for sea water is used, and a draught correction of zero is entered in the echosounder. Depth

TABLE 2.12 Computed (C) and Observed (O) Values of DGPS Antennas for DGPS Verification

	C		O		C-O	
	Easting	**Northing**	**Easting**	**Northing**	**Easting**	**Northing**
DGPS1	359385.42	4534585.65	359385.14	4534585.42	0.28 m	0.23 m
DGPS2	359384.03	4534586.05	359384.72	4534586.89	−0.69 m	−0.84 m

TABLE 2.13 Computed (C) and Observed (O) Values of rGPS Pods for rGPS Check

	C		C-O		SD	
	Easting	**Northing**	**Easting**	**Northing**	**Easting**	**Northing**
T101 pod	359375.23	4534580.55	0.18 m	0.28 m	0.10	0.16
T102 pod	359378.56	4534586.72	−0.24 m	−0.14 m	0.14	0.21
T103 pod	359377.86	4534585.46	0.07 m	0.18 m	0.08	0.09
T104 pod	359374.34	4534584.17	0.19 m	0.34 m	0.23	0.17
A201 pod	359380.14	4534582.13	0.28 m	0.11 m	0.08	0.10
A202 pod	359381.43	4534585.25	−0.11 m	−0.24 m	0.15	0.16
D301 pod	359379.24	4534581.73	−0.18 m	0.14 m	0.18	0.20
D302 pod	359377.33	4534584.66	−0.22 m	0.21 m	0.16	0.11

SD represents the calculated standard deviations.

measurement errors of both transducers are calculated separately and entered as correct draught value (C-O) into the dedicated bathymetry software (Table 2.14).

g. *Control of streamer steering and acoustic devices*: A complete control and check of the navigation instruments attached to the streamers for steering and positioning, such as streamer steering devices, acoustic ranging units, velocimeters, speed logs and compass birds, are performed to ensure that they are all functioning properly. Most of these devices use their internal battery packs, and they must be checked and replaced before the survey, if necessary. Wing reset and compass read tests, as well as depth readings, are performed on the external steering devices and depth levelers. In some cases, depth sensors need to be recalibrated before the survey.

TABLE 2.14 Computed (C) and Observed (O) Values of Depth Measurement for Echosounder Verification

	C	O	C-O
38 kHz echosounder	15.05 m	8.13 m	6.92 m
200 kHz echosounder	15.45 m	7.80 m	7.65 m

2.6.1.2 Tests for Seismic System and Streamer

Several tests on the seismic system, and especially on the circuitry of A/D converters or digitizing modules, data telemetry and the hydrophone elements, are performed before the survey. Results of the seismic system and

streamer tests are reported in the final acquisition report in daily, monthly and end-of-job test results, separately. In each specific report, the channel numbers and corresponding test(s) that they fail as well as the dead channels are listed accordingly. Although several other tests are also possible depending on the specifications of the seismic system employed, typically the following controls on the recording system and components are executed before the initialization of the survey:

- Verification of recording parameters, recording format and headers
- Control of the recording unit, streamer and telemetry
- Hydrophone and digitizers' A/D tests
- RMS noise (typically 5 μV, maximum 8 μV)
- DC offset (typically 6 μV, maximum 10.0 μV)
- Harmonic distortion (typically ≤ -100.0 dB)
- Gain accuracy (typically 0.02%, maximum 0.05%)
- Crosstalk (≤ -95.0 dB)
- Hydrophone discharge/leakage (typically 5 MΩ, minimum 1 MΩ)
- Impulse response (± 0.08 dB)

a. *Recording parameters, recording format and headers*: Data recording parameters including recording length, sampling rate, seismic data and sample formats, recording filter cut-off frequencies and trace summing parameters if required, are entered into the seismic recorder (Section 2.5.2). The information written into the EBCDIC headers of the seismic data is prepared.

b. *Control of the recording unit, streamer and telemetry*: This step comprises testing of all available digital components of the recorder and streamer including telemetry, digitizer, lead-in connections, etc.

c. *A/D tests for hydrophones and digitizers*: Modern seismic recording systems automatically perform several tests on the hydrophone and digitizing modules before the survey. The main purpose of RMS noise and DC offset tests is to measure the noise generated by the internal circuitry and A/D converter of the digitizers. A harmonic distortion test is done by sending a sine wave with −3 dB amplitude generally at 31.25 Hz frequency to the input circuitry and A/D converter to measure the harmonic distortion level generated by the input circuitry. An instrument gain and phase test is used to find out the deviation of the gain and phase of the digitizers' A/D converters from 0 to the high-frequency cut-off value. A hydrophone discharge/leakage test reveals the timing and slope of the response to a pulse sent to the hydrophones. A crosstalk test is performed to check the unwanted signals within the neighboring channels in the digitizing modules. The test is achieved in two stages using a sine wave with −3 dB amplitude generally at 31.25 Hz frequency: first, all even channels and then all odd channels are tested separately. An impulse response test is used to obtain the response of each individual channel to a one sample-long pulse.

2.6.1.3 Tests for Gun Array and Components

A couple of start-up tests before the survey are also performed on the air gun array(s) and related equipment to ensure that all the individual guns as well as the whole gun array system is working properly. These simple tests include

- Control of the gun line integrity and triggering
- Array leakage test
- Gun signature tests
- Drop-out modeling/tests

a. *Gun line integrity and triggering tests*: All the connections between the guns, near-field hydrophones, array depth sensors and the gun controller, as well as the high pressure hoses from air compressors to each air gun via

gun umbilicals, are checked and verified. Manual triggering, termed solenoid click test, is performed for each gun in the array to ensure that all the signal connections and solenoid valves are functional.

b. *Array leakage test*: Air leakage can occur from loosely connected or damaged air hoses or directly from the inside of the air guns if the o-rings are corroded or not properly emplaced. The whole system can be pressurized before the survey to observe if any air leakage exists within the array. The strings must maintain the applied pressure at 90% of the full 2000 psi at least for 15 min with all valves closed. Defective components should be replaced or repaired before the survey.

c. *Gun signature tests*: When the gun array is in water before the regular shooting is initiated, each gun is fired individually to observe and record its near-field signature. PBR values, signal amplitudes and bubble periods of the guns with the same volume are compared to understand if the signal from each gun is consistent. Array far-field signature modeling and radiation patterns in along- and across-side directions are calculated by array modeling to analyze if the source signature of the whole array is acceptable.

d. *Drop-out tests*: Consistency of seismic source is one of the key factors affecting the overall data quality and repeatability for 4D studies. Before the survey, modeling of the seismic source (and field tests, if possible) is performed to understand if the spare guns can compensate the gun drop-outs during the shooting. This provides gun drop-out specifications for each string, which shows how the generated peak-to-peak (*P-P*) signal amplitude and the ratio of *P-P* to bubble amplitude (PBR) deviate from its nominal source signature in case of gun failures. Drop-out specifications document when a spare gun is turned on, and when a specific gun needs maintenance.

2.6.2 Analysis of Seismic Data

One of the fundamental processes performed during the offline QC applications is the detailed analysis of the collected seismic data, which consists of analyzing the data itself by a fast-track processing, analyzing the specific noise types embedded in the data, and evaluating the spectral content. The basic purpose is to assess the impact of noise in the seismic data being collected and to document the probable acquisition issues in order to take the necessary precautions associated with acquisition and recording to prevent any agents that degrade the overall data quality and decrease the S/N ratio of the data, typically by evaluating the data in a line-by-line basis. Definitions of shot/trace issues associated with the seismic data are determined before the survey. For instance, a trace will be defined as a dead (or bad) or noisy trace if it falls into any of the categories given in Table 2.15, and a shot record is considered a bad record or misfire if it meets the specifications given in Table 2.16.

Analysis of the acquired data is done by an onboard processing application, termed fast-track processing. Modern seismic vessels have processing systems and hardware to fully process 2D and 3D seismic data onboard to provide a full onboard processing if claimed by the client at an extra cost. Onboard processing is usually performed for quality control purposes and it typically comprises basic processing steps, such as

- SegD data loading
- Resampling from 2 to 4 ms (if necessary)
- Seismic and navigation merge
- Removal of recording delay (if necessary)
- Gun and streamer static correction
- Shot and channel edit
- Low-cut filter for swell noise attenuation (typically 4–8 Hz, 18 dB/Oct)
- Spherical divergence correction
- Near trace section/single fold cube/ brute stack

TABLE 2.15 Example Definitions or Characteristics of Dead and Noisy Traces Typically Encountered During the Acquisition

Dead traces	• If trace polarity is reversed or partly reversed • If trace has continuous spikes or spike-like noise • If trace amplitude is significantly low compared to an adjacent group (weak trace) • If trace amplitude is significantly high compared to an adjacent group (wild trace) • If trace amplitude range is over the dynamic range (saturation) • If RMS noise limits exceed the specifications • If trace does not pass from daily tests • If trace sensitivity is not within the range of manufacturer's specifications
Noisy traces	• If trace has a noticeable noise over the source signal • If trace has a noticeable noise under strong weather or terrestrial conditions (storms, thunders, waves, tides, earthquake, etc.) • If trace has strong seismic interference noise • If trace has a noticeable noise from man-made sources (shipping, fisheries, vessel's machinery, etc.) • If trace has noise at a specific frequency

TABLE 2.16 Example Definitions or Characteristics of Bad Records and Misfires Typically Encountered During the Acquisition

Bad records	• If seismic data or positioning information is lost for any reason • If acquisition/source/recording/streamer/navigation parameters do not meet the specifications • If source misfires/auto-fires, or if there is no fire • If source separations do not meet the specifications • If source and/or streamer positioning is outside the specified criteria • If the shot is recorded during air leaks • If extended header or navigation header of the shot is not correctly recorded • If shot numbers or file numbers on digital records do not correspond to shot numbers on data sheet • If unrecoverable errors or a complete loss of magnetic tape recording occur • If number of dead traces in a shot exceeds 5% of the total number of channels • If more than 5 consecutive channels are defined as bad traces • If total number of dead and noisy traces exceeds 10% of total number of channels
Misfires	• If an auto firing of any gun within the array occurs • If the performance of a string is below the drop-out specifications • If source depth/separation/configuration is different from specifications • If one or more guns has timing errors more than ± 1 ms • If air pressure of an air gun drops below 90% of the normal pressure level • If source signature does not meet the specifications • If total source volume does not meet the specifications • If signature recording of near-field hydrophone is lost • If shooting time of a record is not clearly indicated

The following additional processing steps can also be applied to seismic data onboard if specifically requested by the client to obtain a fully migrated 3D seismic data at the end of the survey:

- Linear noise attenuation
- Q compensation
- Velocity analysis (typically at 1.0 km $\times$ 1.0 km grid)
- Radon multiple attenuation
- Binning and trace interpolation
- 3D stack (typically 12.5 m $\times$ 25 m grid)
- Post stack Kirchhoff time migration

The purpose of the onboard processing is actually not to eliminate noise embedded in the data but to analyze the data during the recording and to document the possible issues for a comprehensive processing in the processing center. Auxiliary channel data (up to 60 channels) which record the system time breaks and signatures of each air gun from their individual near-field hydrophones mounted on the gun strings are

also analyzed along with the seismic data. After the offline QC processes of the seismic data, the following deliverables are produced in addition to the other client-specific requests:

- QC reports per line
- SegY header map
- Brute stack plots
- Brute stacks in SegY format with navigation in the headers
- Near trace plots
- Single trace or near trace cube
- Velocity files in specified format (if necessary)
- Migrated fast-track cube (if necessary)

In addition to the visual inspection of the shot records, the near trace sections, brute stack sections and single fold cube are the main products of the QC analysis for the seismic data. Preparing near trace sections is the best way for a quick determination of possible acquisition errors, such as bad records, misfires, auto fires, overlapping shot points, array amplitude issues, time-break problems, etc. These sections also provide an initial opinion about the strength of the multiples and front-end noise level including swell and operational noise. A single fold 3D cube without flex binning is prepared using a single velocity function for NMO correction to verify the navigation and seismic merge as well as the survey coverage. Single fold cubes are not used for interpretation purposes, but they provide time slice maps as well as inline and crossline displays of the seismic data. They are also used to verify the navigation and seismic merge, where incorrect navigation merge results in jumps in the crossline traces and striping effects in the time slices. Common channel stacks and common shot stacks can be generated for every sequence (Fig. 2.85) to check for abnormally high amplitudes, such as cross-feed, leakage or other electrical problems of a potential faulty streamer section.

Determination of bad or noisy traces, dead traces, auto-fires, misfires, and lost records for each completed seismic line is an important QC implementation, and is performed by a visual inspection of all or selected shot gathers along the line after a suitable band-pass filter

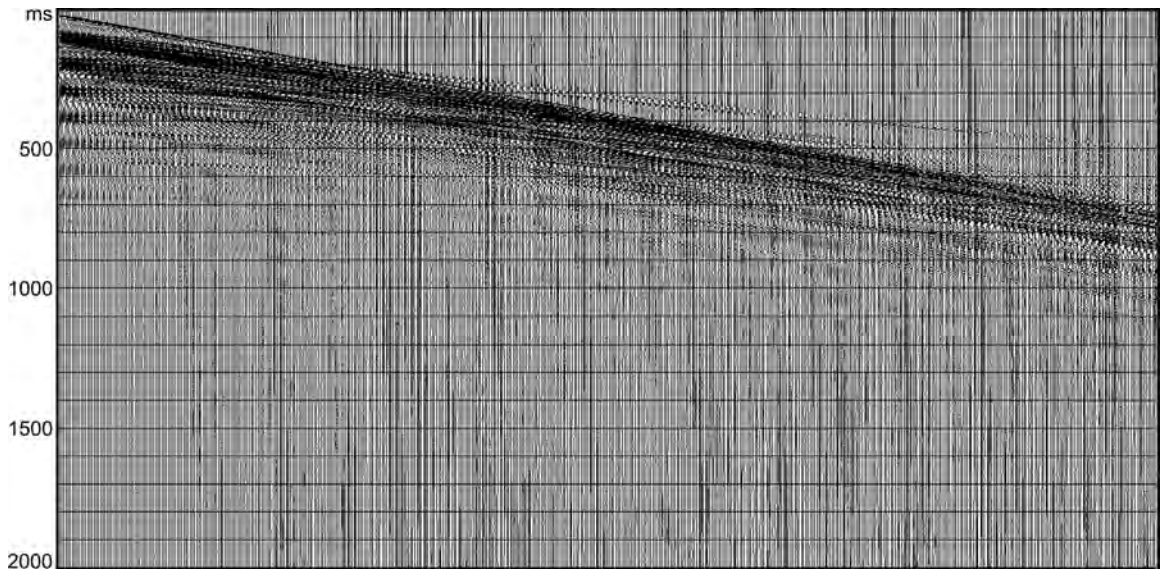


FIG. 2.85 Common channel stack computed for the first 400 shots of the line.

and an optional gain application. RMS amplitude displays of all available channels for each shot can be used to locate suspicious shots, which can be then individually investigated. Various QC applications, including raw/filtered data displays, RMS noise displays, power and *f-k* spectra of the data and producing brute stacks, are performed to identify noise problems and to assess the compliance of the data based on various acceptance criteria.

Analyzing of seismic data by an onboard processing for QC implementations reveals if the data contains unacceptable problems. This is done by a simple comparison of the observed issues with the tolerance values determined before the survey. Tolerance standards may change from one service provider to another. The following are example acceptance tolerances for seismic data:

- Maximum acceptable bad records are 5% of total shots for a line or for a segment.
- A maximum of 10 bad records in 50 consecutive shots is acceptable.
- Maximum three consecutive bad records are allowable.
- Maximum allowable bad records are 5% of total shots per line.
- Maximum acceptable dead traces are 4% of the total channels per streamer.
- Maximum 5 consecutive dead traces are acceptable for a shot record.
- Maximum acceptable dead traces are 2 for 20 front channels of each streamer.
- ± 1 m streamer depth variation is acceptable for maximum 30 consecutive shots.
- ± 1.5 m streamer depth variation is acceptable for maximum 20 consecutive shots.
- Maximum allowed positioning error for front of the streamers is 2 m.
- Maximum allowed positioning error for gun strings is 2 m.
- Maximum allowed positioning error for tail buoys is 5 m.
- Maximum acceptable gun timing error is ± 1 ms.
- Maximum acceptable air pressure variation for each string is 2000 psi $\pm$ 100 psi.
- Maximum allowable gun array drop-out tolerance is ± 1.5 dB.
- A minimum of three depth sensors per string must be operational during the recording.
- Maximum allowable source depth variation averaged over the sequences is ± 0.5 m.
- Maximum allowable variation in source separation is ± 4 m.
- Maximum allowable variation in string (subarray) separation is ± 2 m.
- Maximum allowable variation in streamer separation is $\pm 10\%$.
- Maximum acceptable feather angle value for any of the streamers is 10 degrees.

In some specific cases, reshooting of an initially collected line is necessary depending on the offline QC results. Reshooting is done by collecting the data in the same direction as the initial survey, generally with a 10 shot points overlap, and is performed anytime during the survey. In addition, if a seismic line is aborted within 10 km of the line start, it is totally reshot. Reshooting of a line takes place whenever the previous example situations are observed during QC analyses.

Analyzing the amount and specific types of noise embedded in the seismic data is a crucial part of the online and offline QC implementations. At the start and end of each line, at least one noise record is acquired and analyzed in terms of ambient background and operational noise levels both on shot records and RMS amplitude plots, which allows us to identify noisy traces for further evaluations. An example noise record analysis is given in Fig. 3.2. During the offline QC analyses, the following noise types are specifically reported in the per-line QC reports:

- Streamer bend noise
- Operational noise

- Tug and strum noise
- Swell noise
- Seismic interference
- Cross-feed or spike-like noise
- Bird noise
- Guided waves
- Noise from other marine vehicles

Displaying the data as raw or filtered shot gathers provides consistently noisy or dead channels, which are also indicated in the observer logs. A fast and efficient way to evaluate the noise levels in the data is to prepare RMS noise analysis plots, which are produced on a line-by-line basis during the offline QC analysis. The RMS noise analysis is done by calculating an RMS amplitude value over a number of specified time windows along the traces. It is done by calculating either an RMS value of each channel, or an average RMS value for each shot along the line. Displaying channel RMS plots reveals the dead or noisy channels and the consistency of the noise for each shot, while average RMS plots of shot gathers show the bad records, misfires, and noisy areas along the lines (Fig. 2.86).

Separate RMS noise plots are also computed over the desired time window(s): The first window is from the water column before the seabed arrival to reveal the RMS ambient noise, the second window covers the target area to understand the RMS signal value if necessary, and a third window is selected over the last 0.5 s of the trace to target the swell noise. The scale bar to plot the RMS amplitudes is typically in microbars × 10. In ideal cases, the average RMS of random noise must typically not exceed 8 μbar. Fig. 2.87 shows the RMS noise level on the streamers recorded before the shooting is initiated. 3D distribution of RMS noise along the

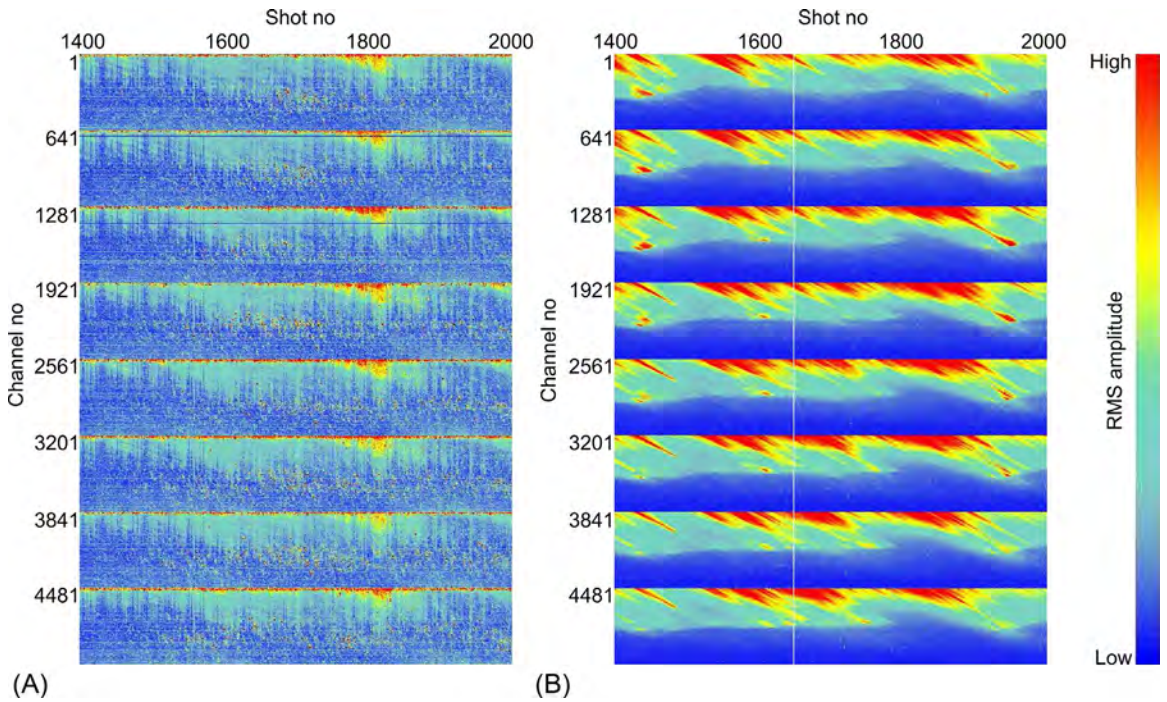


FIG. 2.86 Average RMS amplitude of each recording channel for all shot gathers ranging from 1400 to 2000 along the line computed for (A) water column and (B) a window with 1000-ms length starting from the seafloor reflection.

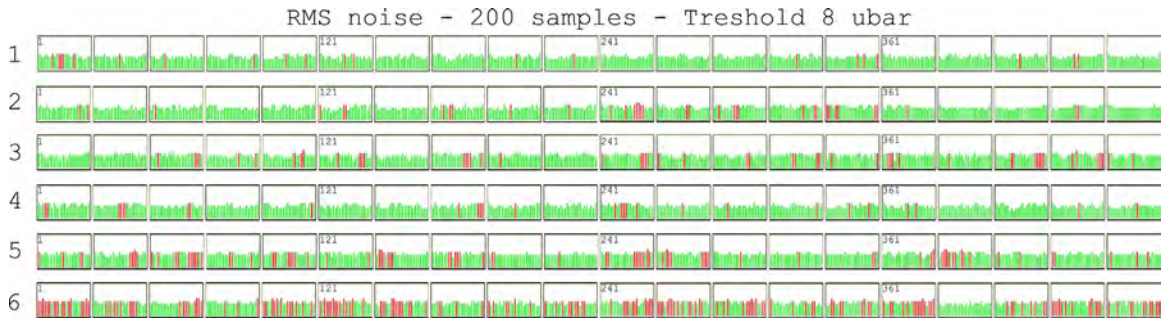


FIG. 2.87 Real-time display of the RMS noise level on the six streamers recorded before the shooting is initiated. Green to red threshold is 8 μbar.

survey area can also be produced to show the regional variations of noise and signal for different time windows.

Spectral content of the selected shots along the line is analyzed during online and offline QC implementations. Average power (Fig. 2.88A) and *f-x* spectra (if required) of a number of consecutive shots are computed and displayed to ensure that the frequency content of the generated signal is appropriate and comprises both

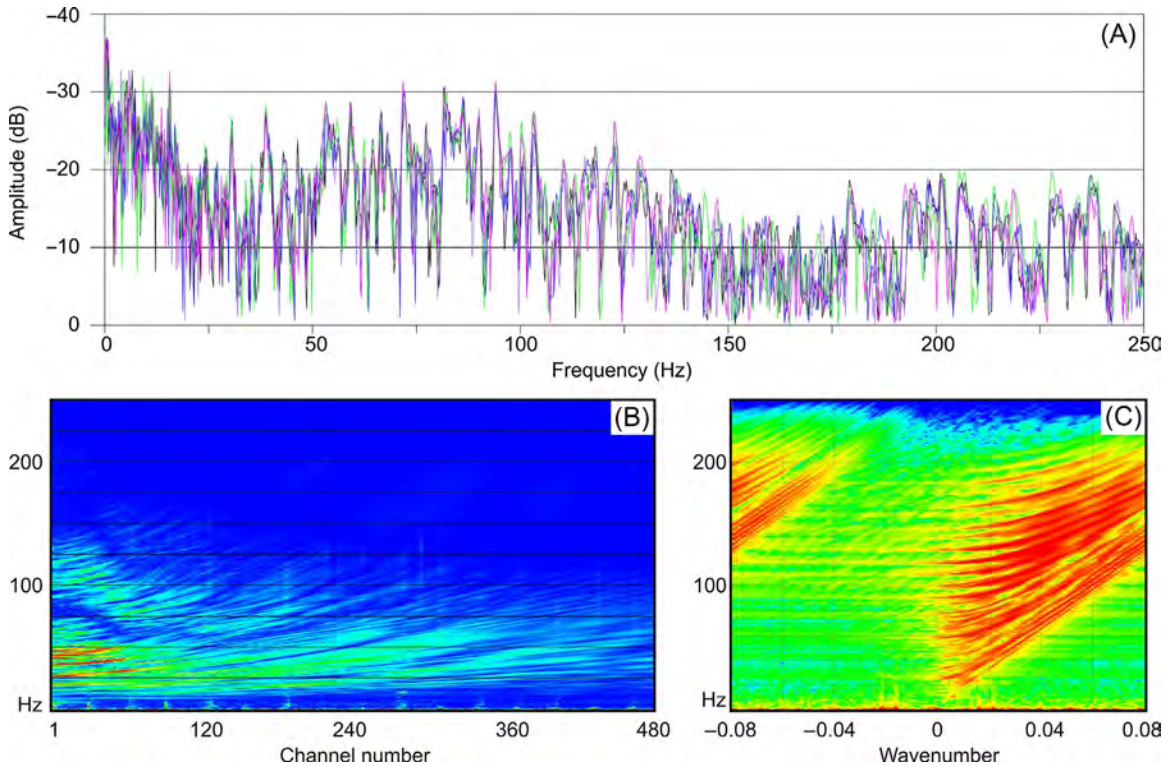


FIG. 2.88 (A) Average power spectrum of five successive shots, (B) *f-x* spectrum, and (C) *f-k* spectrum of a selected shot.

low- and high-frequency components from approximately 3 Hz to the first ghost notch. The spectrum can also be computed over different time windows, such as the water column, shallow subsurface, target depth and deep window to compare the frequency content of the data from early to late arrivals.

Spectral analysis is sometimes performed for the first and last shot groups of the seismic line, and *f-x* and *f-k* spectra of the selected shots can also be computed whenever a specific type of noise is observed (Fig. 2.88B and C). The *f-x* spectrum can indicate the variations of spectral content of the data from near to far offsets along the streamer(s), and it can also be used to evaluate the local noise amplitudes, such as the noise arising from the wing motions of the depth levelers, or streamer bending noise, etc. The *f-k* spectrum can be used to analyze the possible seismic interference or other types of linear noise as well as the amplitudes of spatially aliased data.

2.6.3 Analysis of Navigation Data

Offline analysis on the navigation data for all dynamic offsets, rGPS data, and streamer acoustics is completed using UKOAA navigation files and other specific navigation logs (if available) recorded during the acquisition. Most of the navigation data analysis is done online and then a detailed analyses and plotting of specific parameters are also performed during the offline QC analyses. The only coordinate computed in real-time by a global positioning within the whole spread is the vessel's reference position, tied to the DGPS antenna offsets. Inline and crossline offsets of the other equipments/components are all nominal values determined before the survey. Sources and streamers are towed behind the vessel at these predetermined nominal layback distances. However, actual locations of source centers, head and tails of the streamers and crossline distances such as source/subarray and streamer separations during the acquisition must be determined, to analyze whether the survey geometry is maintained with respect to the nominal parameters. Navigation QC for in-sea equipment to document the nominal predetermined geometry typically comprises the following analyses:

- Vessel navigation/DGPS accuracy/gyro data information
- Vessel speed and shot interval plots
- Streamer depth/bird data/feathering information
- Minimum offset check
- Acoustic network analysis
- Streamer separation plots
- rGPS data
- Array and string separations
- Source depth plots
- Echosounder/TS dip/currentmeter data
- Line deviations/coverage maps/fold distribution

Accuracy in the vessel positioning is important since all the positions of in-sea equipment are tied to the vessel reference position, which is the only position determined directly from a GPS system via satellite connection. Each seismic vessel is equipped with at least two DGPS receivers and two independent gyros; each is calibrated carefully before the survey. Modern INSs provide error ellipses or scatter plots (Fig. 2.89A) for DGPS quality checks and online control of dilution of precision (DOP) during the acquisition. Today, horizontal error in determining positions of the antenna locations of a DGPS system is less than 1 m. For vessel positioning QC, readings for each gyro are plotted against shot point for each line (Fig. 2.89B).

Shot interval is one of the most important parameters that must be maintained according to the predetermined survey parameters since it affects the fold distribution. Variations in the shot interval result in a nonuniform inline fold distribution along the line. In order to document that the shot intervals are within the survey acceptance limits, shot intervals for each sail line

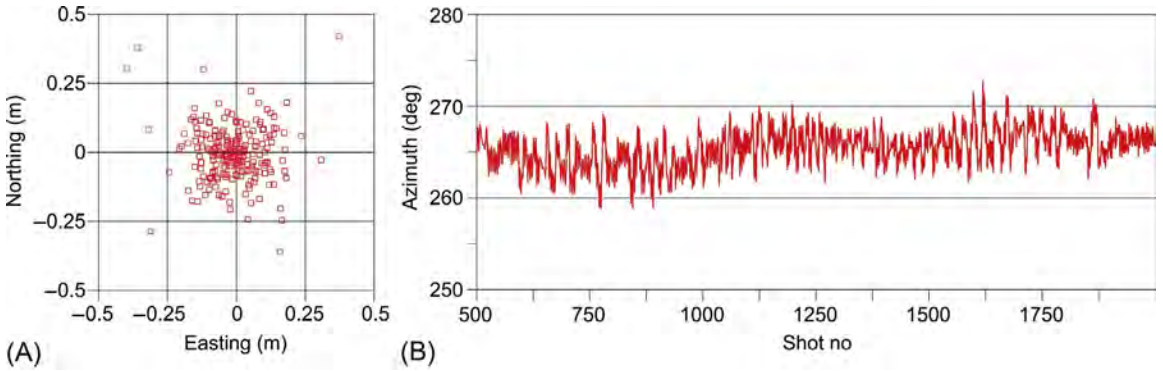


FIG. 2.89 (A) Scatter plot of a DGPS receiver and (B) gyro headings for each shot point along the line.

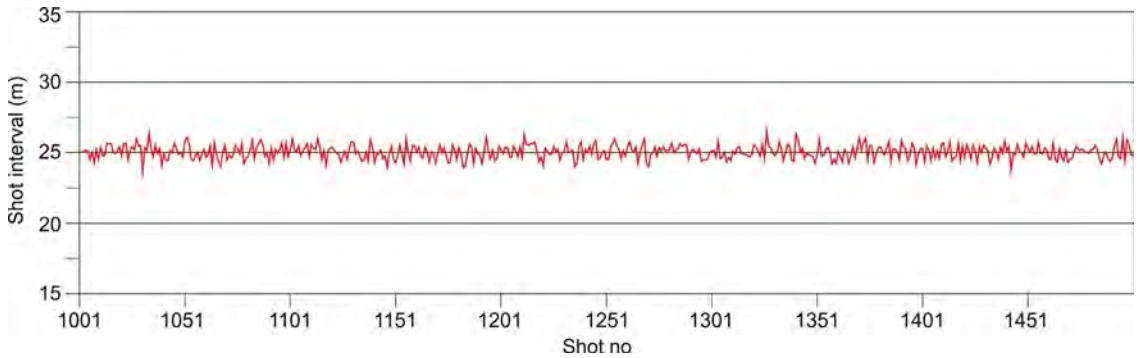


FIG. 2.90 Shot interval for each shot point along the line.

are plotted against the shot point either in time or distance (Fig. 2.90).

Vessel speed is proportional to shot interval and affects the operational noise level in the data. Increasing of the tow speed induces more bird and strum noise and decreases overall S/N ratio of the recorded data. In any type of seismic surveys, vessel speed is kept constant between 4.0 and 4.5 knots so that there are no overlapping shots. It is documented in the offline QC reports by plotting the vessel speed versus shot point for each survey line (Fig. 2.91A). The average/minimum/maximum vessel speed plot is also prepared for all sequences within the survey to document the consistency of the acquisition speed for all the sail lines (Fig. 2.91B).

Depths of the streamers are maintained by depth levelers or 3D steering devices attached to the streamers at regular intervals, commonly at every 300 m. Depending on the survey requirements, depths of all streamers are kept constant to achieve data consistency in terms of ghost interference and available effective frequency band of the recorded traces. In broadband acquisitions, however, depth of the streamers gradually increases with offset to arrange the slant streamer design (Section 2.3.6). In any case, depths of all deployed streamers are plotted for each shot point to ensure that the depths of all streamers are within the survey specifications and within the predetermined depth limits. This is done by plotting the depth sensor data from

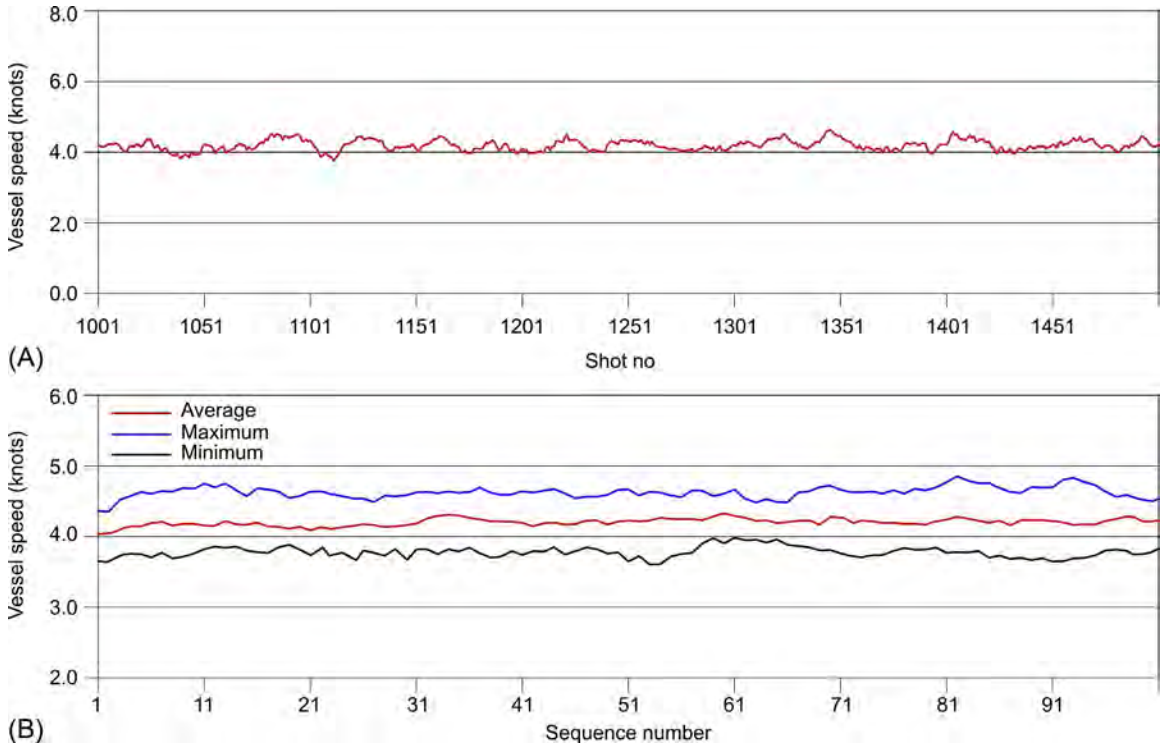


FIG. 2.91 (A) Vessel speed for each shot point along the line, and (B) average, minimum and maximum vessel speed plots for all sequences in the survey to show the consistency of the acquisition speed for all sequences.

each bird along the streamers for each shot. In addition to the depth information, azimuth angles from compass birds and wing angles of all birds can also be plotted and analyzed for each shot point (Fig. 2.92). Comparing the bird compass values from each streamer with the sail line azimuth from vessel's gyro provides streamer feathering information for each streamer.

Minimum offset distance for each streamer is also an important QC parameter. These values are obtained and plotted either from acoustic networking data or from rGPS pods if they are mounted on the dilt floats (Fig. 2.93) to ensure that the offsets for all streamers are within the survey acceptance limits. Checking of the near offset distances can also be done by merging the processed navigation files with the near trace data. After a linear moveout (LMO) correction applied to the seismic data, direct arrivals are moved to a common time so that it can be compared to the predicted first break arrival times derived from UKOAA P1 navigation data. This plot can be prepared for each gun and streamer pair in the spread (Fig. 2.94). The limit between predicted and near trace first break times is typically ± 3 ms (± 4.5 m for 1500 m/s water velocity).

Acoustic networks between the streamers and source arrays are the main tool to determine the lateral offsets of the in-sea equipment, and its geometric configuration is critically important to arrive at a network solution in terms of the least squares approach in determining the positions of the receiver groups for all streamers (Section 2.3.4). As the redundancy of each node increases, the reliability of the network solution

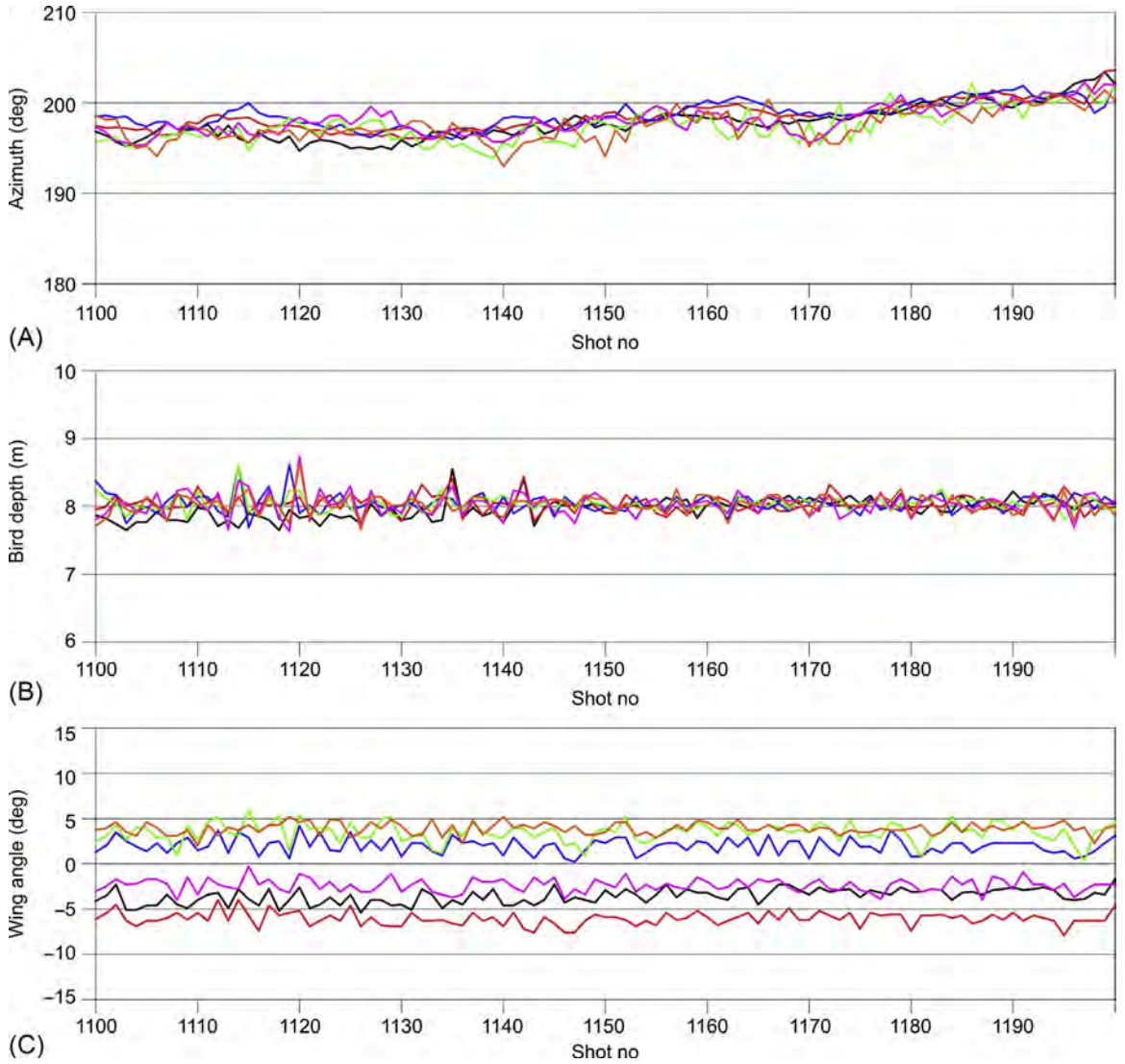


FIG. 2.92 (A) Azimuth angle, (B) depth, and (C) wing angle plots of first six compass birds attached to the fourth streamer of the spread for each shot along the line.

also increases. QC of the acoustic network should be performed online during the acquisition, and nodes producing erroneous range values are statistically determined and excluded from the network solution computations in real-time. In general, crossline nodes are noisier than inline nodes, and longer ranges contain more error than shorter ones. Furthermore, the nodes close to the rGPS pods, such as those nearby the source arrays or tail buoys, will provide more reliable range data, which makes the mid-net ranges less reliable.

Crossline separation between the streamers is maintained by streamer steering devices

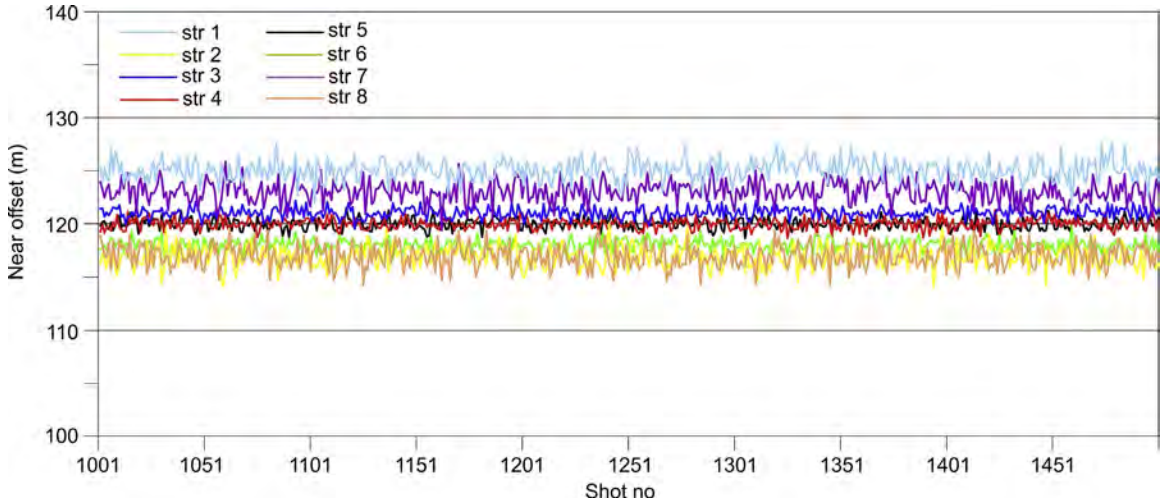


FIG. 2.93 Minimum offset plot from rGPS data for all eight streamers for each shot along the line.

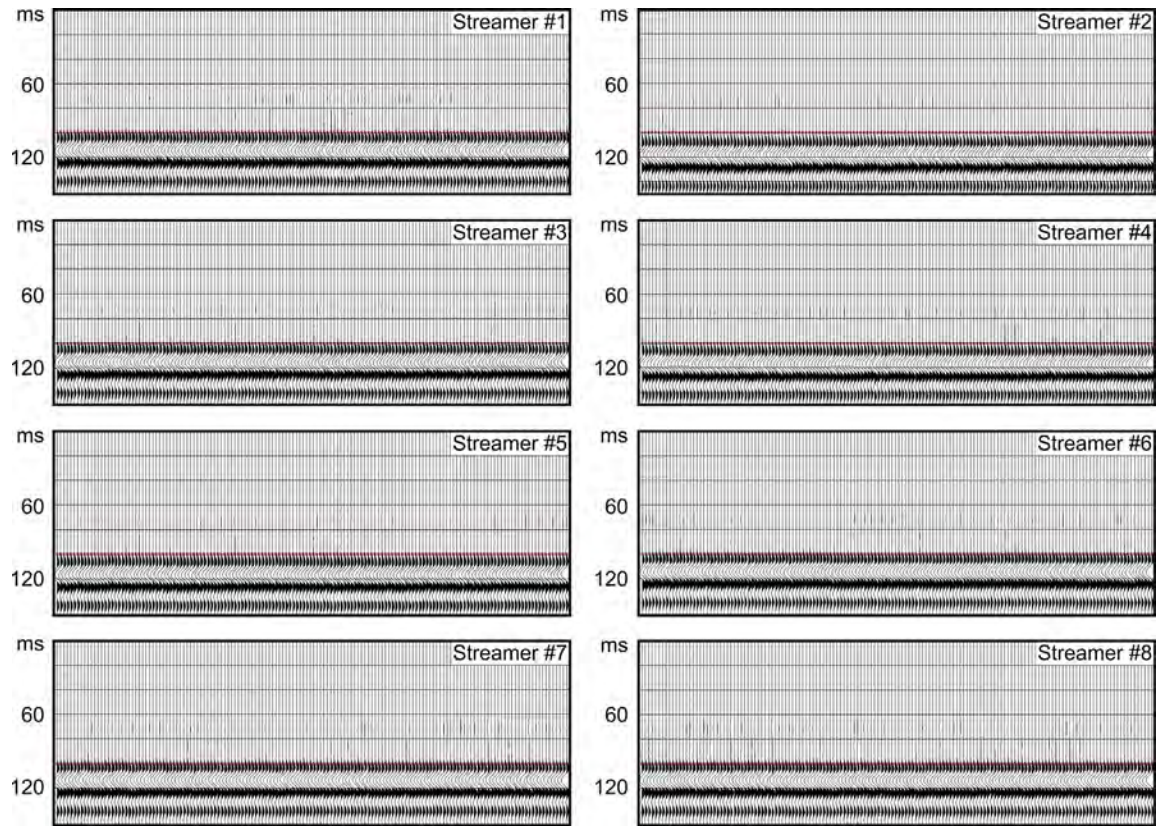


FIG. 2.94 Comparison of navigation first break arrival times *(red crosses)* and linear moveout corrected direct arrivals for the first 150 shots of each streamer to ensure that the minimum offset value (150 m) is within the survey limits.

attached to the streamers. They cooperate with the acoustic ranging to maintain the nominal streamer separation, typically 100 m, within the specified survey tolerances. The crossline separation between the streamers must be well analyzed during online QC work, and are documented in offline QC implementations to ensure that the lateral offsets between the streamers are within the survey acceptance limits for near, middle and far offset ranges (Fig. 2.95). The separation between the outermost streamers is specifically important since it describes the total crossline coverage for 3D surveys. Near offset separations are important to maintain nominal source-near trace (minimum offset) parameter, while far offsets become also critical in the case of fan mode acquisition. In addition, radial distances of the heads of each streamer with respect to the vessel reference point can also be prepared.

The geometry of the whole seismic spread must be under control during the acquisition. Positioning of the source strings, paravanes, tail buoys and dilt floats (if necessary) are achieved by rGPS pods, which enable us to calculate the range and bearing of these buoys to the vessel reference position. Reliable operation of the rGPS system during the entire survey is critical since it is used not only to determine the layback distances of sources, paravanes or tail buoys, but also to derive the receiver positions for each streamer via acoustic network ranging, because the nodes on the buoys with rGPS pods are termed fixed nodes and are used to solve all acoustic networking between the streamers (Section 2.3.4). During the offline QC analysis, ranges obtained from each rGPS pod are plotted for each shot to ensure that the entire rGPS system has been properly worked out within specified survey tolerances. Fig. 2.96 shows an example range plot of six rGPS pods.

Maintaining source and string (subarray) separations is an important part of the overall spread geometry. An effective acquisition of each CMP line with a regular fold distribution depends on the consistency of source geometry. In conventional 3D towed streamer acquisition, a nominal source separation of 50 m between the centers of source arrays is typical for flip-flop acquisitions, and tolerance value in source separation is usually ±10% of the nominal separation.

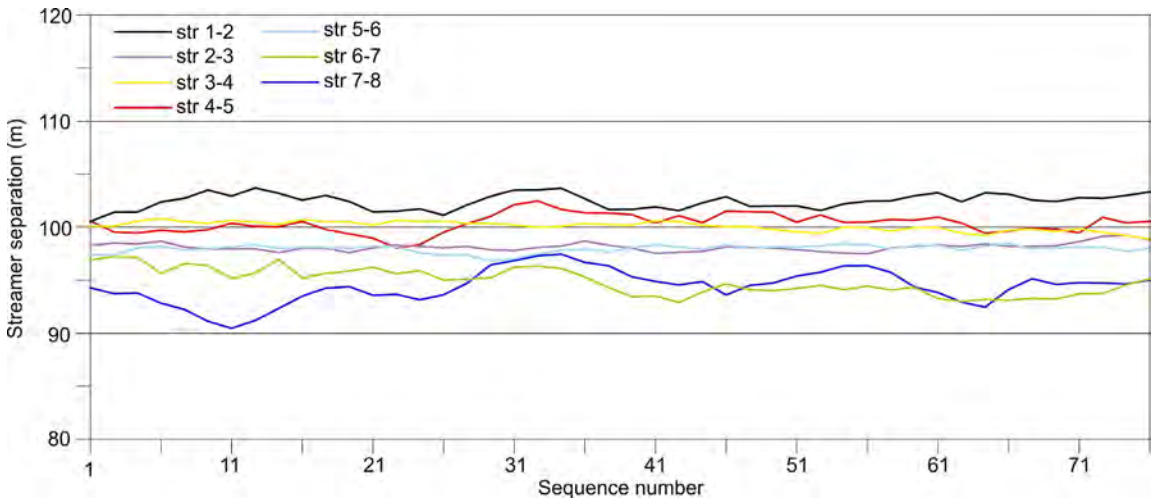


FIG. 2.95 Average streamer separations at mid offsets for all sequences. Nominal crossline separation for the spread is 100 m.

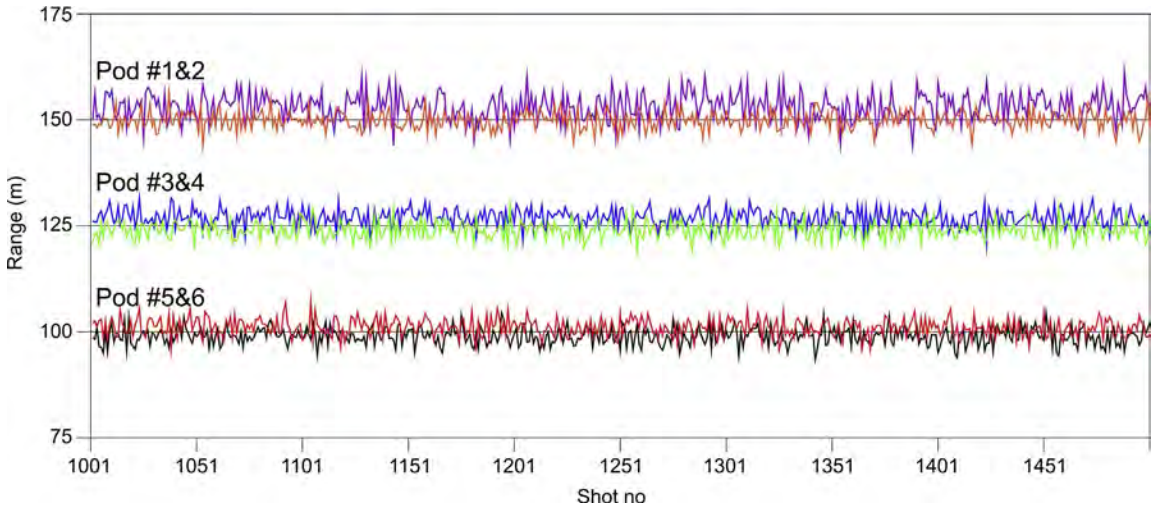


FIG. 2.96 Example rGPS ranges obtained from six pods.

Each gun array typically consists of three strings or subarrays. Crossline separation of the strings is also a critical parameter to be maintained during the survey since it affects the source signature produced by the array. The lateral distance between the strings is generally 7–10 m with a survey tolerance of ±10%. If the separation between the strings exceeds the survey limits, it will affect the far-field signature and hence may degrade the overall data quality, resolution and signal consistency from one shot to another. Each string of each source array includes an rGPS pod attached on the gun floats and the array geometry is controlled real-time, and the positions are logged during the acquisition. In offline QC analysis, source and string separations are plotted for each shot to determine the possible issues on the source geometry variations. The average source separation plot is also prepared for all sequences to document the consistency of the crossline source separation for all sail lines (Fig. 2.97). Furthermore, radial distances of source positions with respect to the vessel reference point can also be prepared and plotted.

Water depth below the keel of the vessel is determined with a single-beam echosounder and the collected data is used to prepare 2D depth contours of the survey area at the end of the survey. In offline QC analysis, a water depth profile is obtained for each survey line (Fig. 2.98A). The suitable frequency of the echosounder signal is selected depending on the water depth (Section 1.2.1). In some cases, a tidal correction is needed to reduce the data to a common datum surface. Either a global water velocity of typically 1500 m/s is used to convert the echosounder data into the depth, or the velocity is obtained from an average of TS dip (temperature-salinity dip) measurement (Fig. 2.98B), which is primarily used for acoustic ranging. Depth information below the keel from a single-beam echosounder is stored in the UKOAA navigation files. In addition to this auxiliary equipment, all modern seismic vessels are equipped with acoustic Doppler current profilers (ADCPs) to obtain the amplitude and direction of local ocean currents. The ADCP continuously measures surficial current magnitude and direction during the surveys and computes

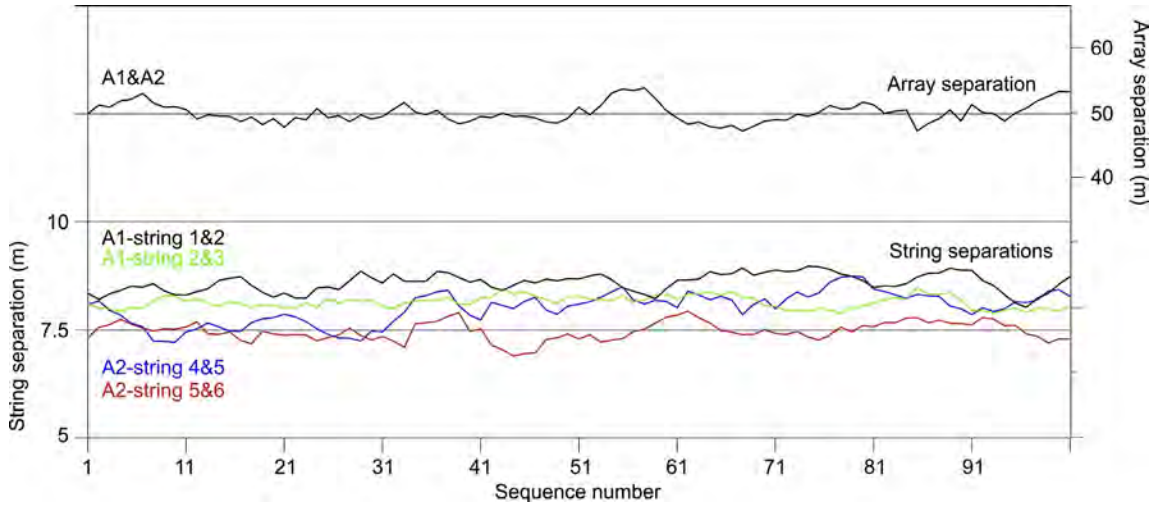


FIG. 2.97 Average distance between the sources (A1 and A2) and strings for all sequences.

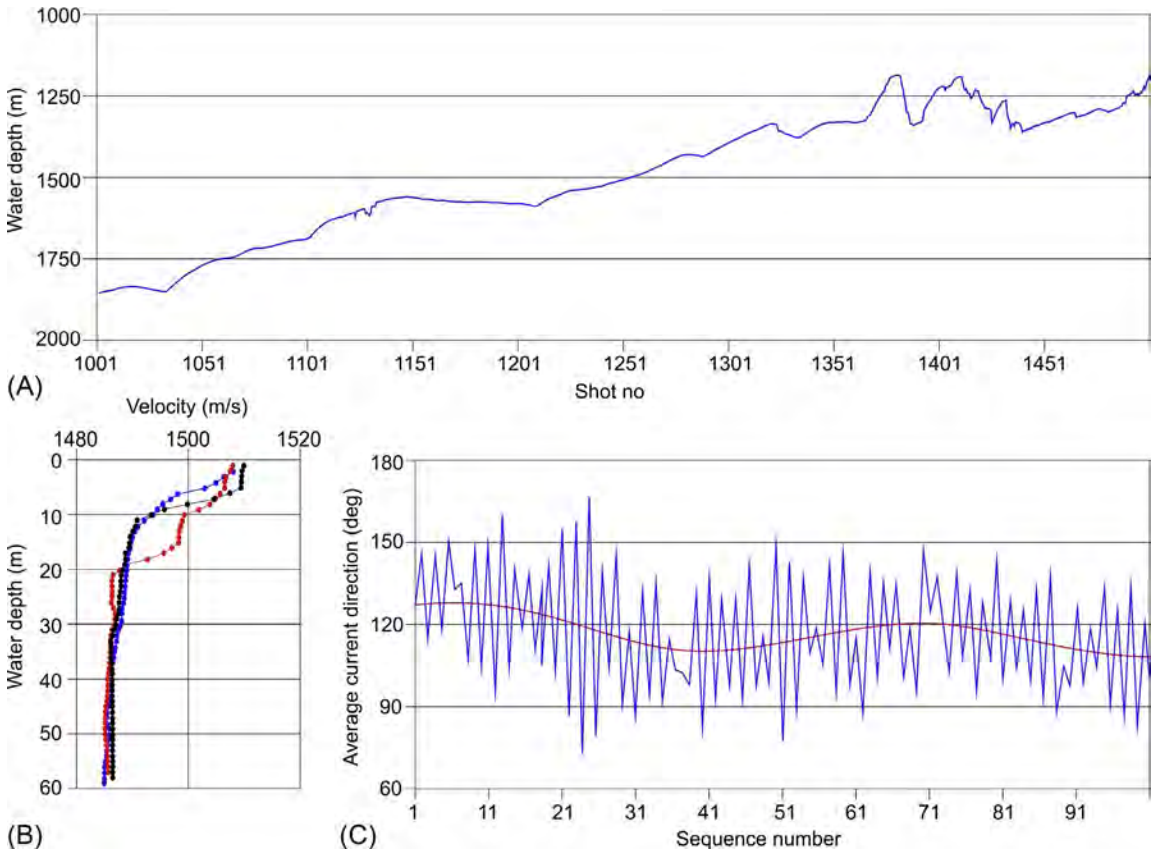


FIG. 2.98 (A) Water depth profile along the line, (B) three TS dip profiles obtained during the survey, and (C) average current direction of the survey area for each sequence obtained from ADCP measurements.

the vessel's water speed. Periodical analysis of ADCP data in 2D along the acquisition area as it is collected during the survey can provide information to predict the predominated current direction and streamer feathering, and hence, can be used to improve the survey design and parameters. Fig. 2.98C shows an example of an average current direction plot from ADCP data on a sequence-by-sequence basis.

The seismic sail line plot (the preplot lines) prepared before the survey is entered into the INS for line steering. However, it is commonly not possible to steer the vessel along the preplot lines perfectly because of the local weather and current situations. Radial deviations between the preplot and realized (postplot) lines are computed for each shot location and plotted for each shot point (Fig. 2.99) to ensure that all the shot points are in the survey tolerance (e.g., typically ±5 m).

Today, real-time binning is standard for 3D surveys, providing the fold coverage of the surveyed part of the whole area. Typically, periodic hardcopy coverage plots are produced to discuss the fold distribution, especially over the target zone, and fold gaps that require additional infill shots at the end of the survey. Fold coverage maps are generally prepared separately for near, mid and far offset ranges with and without bin flexing, which is an interpolation approach to fill in the missing offsets within the bins with data gaps using neighboring bins to obtain a more regular fold distribution (Section 8.3). At the end of the survey, a complete map of coverage is obtained and the gaps in fold distribution due to the acquisition problems such as rough weather conditions or obstacles in the survey area are determined. Such gaps need additional work, termed infill shots, which affect the overall time schedule of the survey (Section 2.5.1.8). Final fold distribution is analyzed in terms of required infill shots after bin-flexing to fill the missing offsets in adjacent crossline bins in a constrained manner. Several tests to determine the suitable amount of flexing are performed on near, mid and far ranges, separately. After flex binning, final fold coverage of 3D data becomes much more uniform.

2.6.4 Analysis of Seismic Source

A number of real-time and offline analyses on the source data are performed in terms of source QC. These analyses basically are carried out in order to understand if all the air guns within the array(s) are working properly. Offline source QC applications typically include

- Checking the near-field signature for all guns
- Controlling the near-field hydrophone data

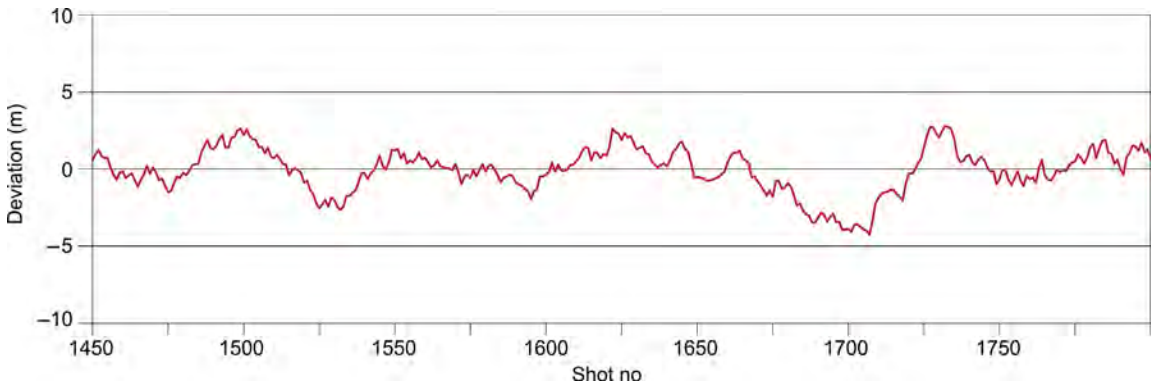


FIG. 2.99 Example plot for the deviations from the sail lines obtained from preplot minus postplot lines for each shot point.

- Plotting the depths of each individual array
- Plotting the gun timing error for each array
- Controlling the pressure for each subarray
- Plotting the total gun volume in the array along the line
- Plotting source RMS amplitudes from near trace data
- Verifying the gun flag for flip-flop operations

An important source QC application is the comparison of recorded signal strength between port and starboard source outputs (Fig. 2.100). An RMS average amplitude value is computed for each shot from the signal within a specified window for all the streamers separately for each array, and then the average RMS amplitudes are compared. Plotting of both amplitude values provides the performance and issues of each individual source array.

Gun timing issues result in degradation of source signal. *P-P* amplitudes and PBR values may change depending on the timing errors and gun size. During the offline QC analyses, gun timing errors for each shot can be plotted to ensure that the timing for both sources are within the survey tolerance limits. Depth and pressure applied to the source arrays should be stable within the specified minimum and maximum limits since both affect the bubble suppression performance of the array. Depth of seismic source is an important QC parameter

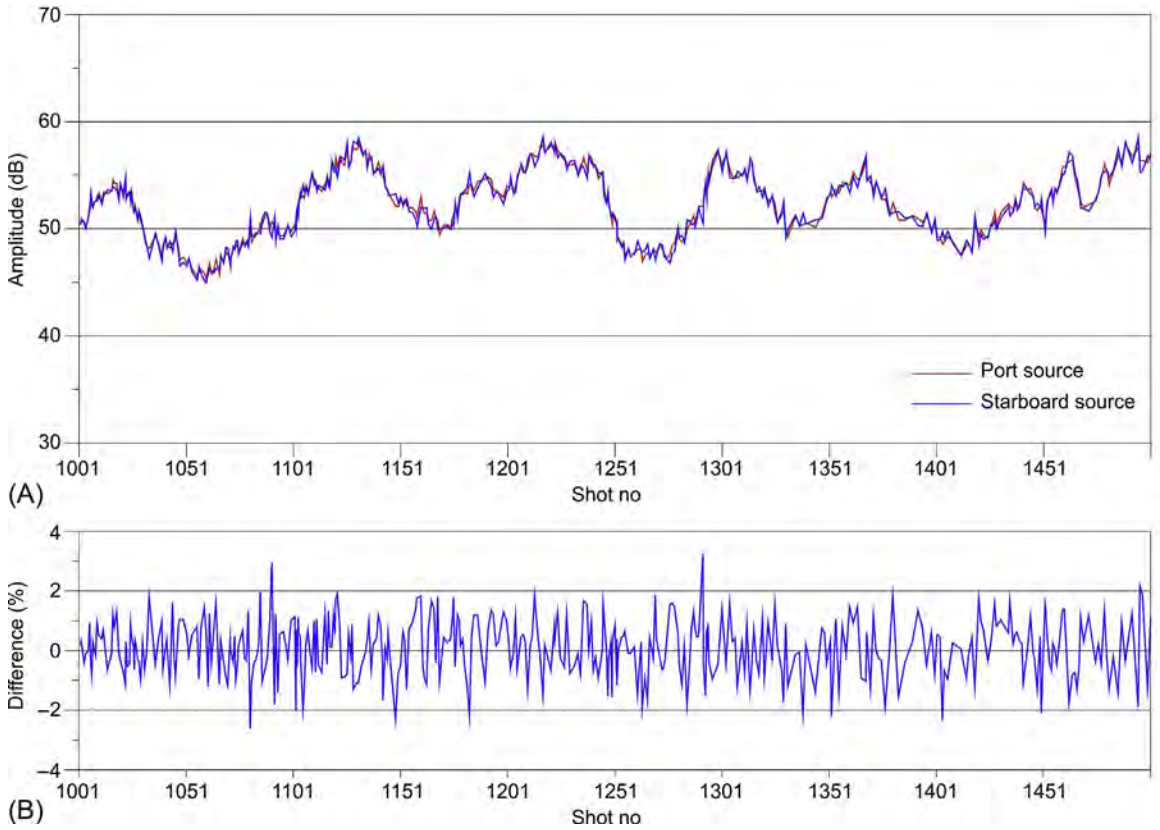


FIG. 2.100 (A) An example comparison of *P-P* signal strength for port and starboard sources computed for a window of 1000 ms length below the sea floor. (B) Amplitude difference graph for port and starboard arrays.

since it affects the frequency content of the far-field seismic signature depending on the ghost notch interference (Section 2.2.3), which determines the high-frequency content of the source signal. Consistency in the source depth is crucial to maintain the frequency content of the seismic signal shot-by-shot for each sequence (Fig. 2.101A). In order to ensure that the source depth is in survey limits, at least one depth sensor is attached to each gun string to measure the depth of the guns from gun float to the depth sensors. Pressure variations also affect the amplitude and frequency content of the seismic signal. Plotting of the array pressure with respect to the shot number provides information on the gun drop-outs and problematic shot records due to the abnormal pressure variations (Fig. 2.101B). In addition to the shot number versus pressure or array depth plots, aerial maps showing the depth and pressure variations in whole survey area can be prepared to evaluate the areas of source problems and overall performance of the source arrays.

QC of auxiliary channels is also important since the near-field hydrophone signatures are recorded into the auxiliary channels for each shot together with the time break, gun aim point, and 1pps GPS time synchronization pulses for every second. For each completed line, near-field signatures are displayed side by side for all guns along the line to ensure that each gun generates a consistent seismic signal for each shot as well as to identify air leaks and gun timing errors (Fig. 2.102). Plotting and analysis of auxiliary channels are done online and offline during the acquisition to reveal the possible bubble period changes that may be the indication of air leaks. Plotting of the auxiliary channels in stacked form shows the gun firing errors and auto-fires.

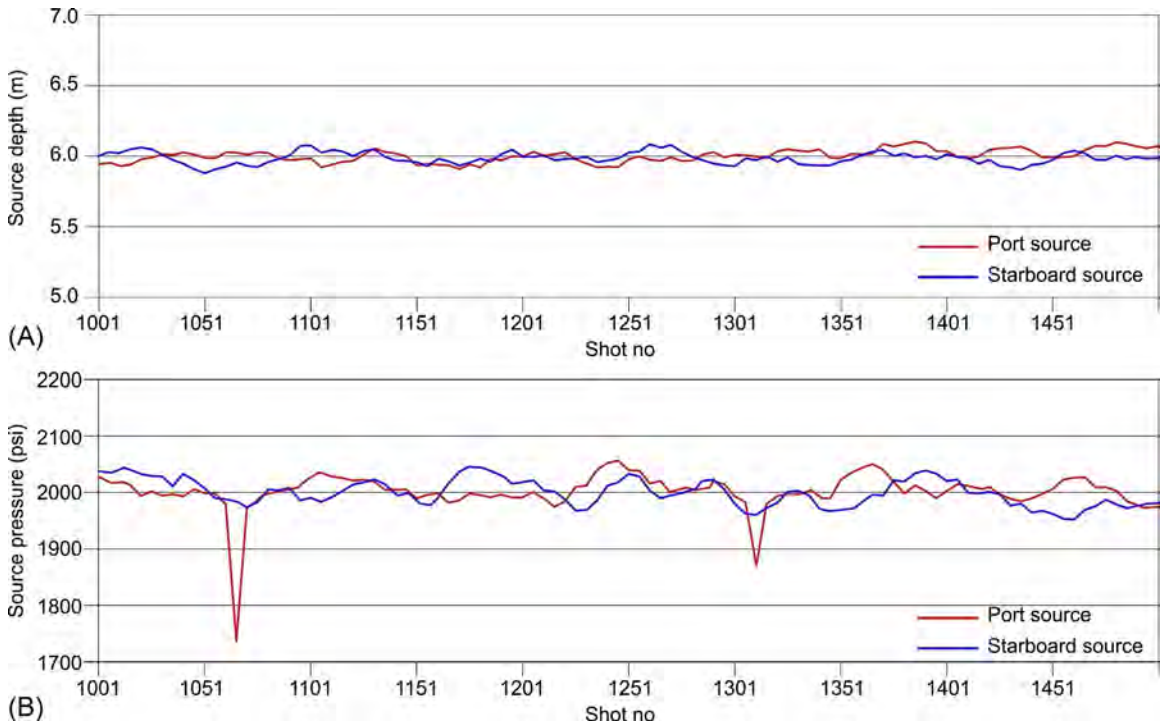


FIG. 2.101 (A) Depth of port and starboard arrays along the line and (B) air pressure applied to both arrays for each shot point.

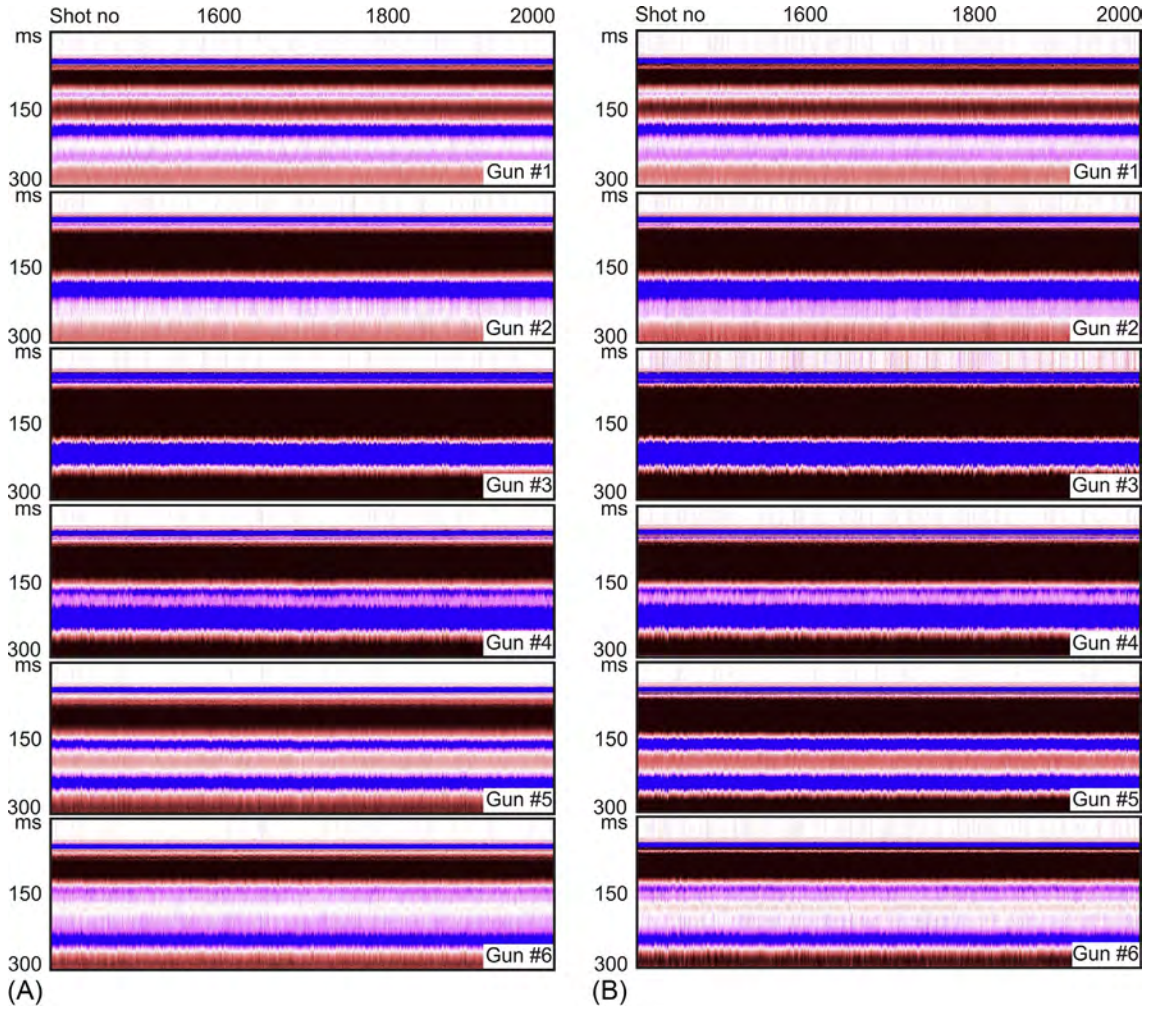


FIG. 2.102 Near-field hydrophone outputs of two identical strings, (A) string number-1 and (B) string number-6, both consisting of six guns.

Another QC implementation for seismic source is to verify the gun flag in case of flip-flop acquisition which is standard operation for 3D NAZ surveys today. In flip-flop acquisition, port and starboard source arrays are fired alternately, in which port array is fired at odd numbered shot points, while starboard array is fired at even numbered shot points (Section 2.3.5). The gun flag states the number of the individual source array firing alternatively, e.g., 1 for port array and 2 for starboard array. As the acquisition continues, the gun flag is stored in the navigation log file to signify which array is fired at which shot point. Log files are checked for each line to ensure that the firing of the sources is consistent for whole line. Alternatively, coordinates of all shot points are plotted to verify the flip-flop shooting (Fig. 2.103).

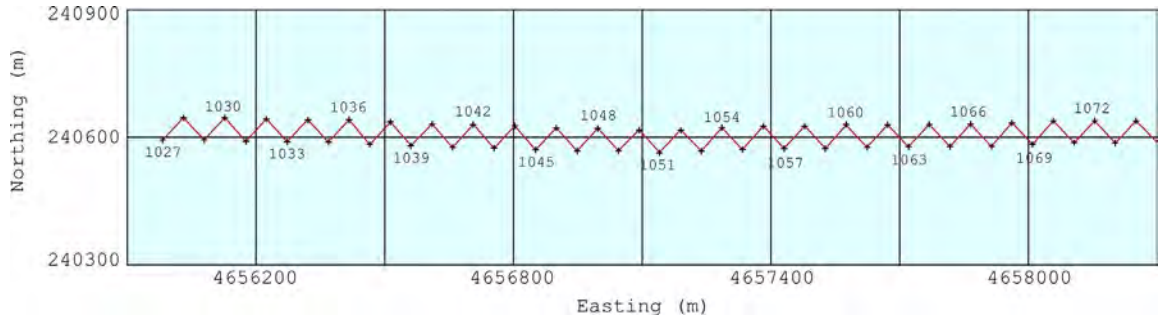


FIG. 2.103 Checking for the gun flag in case of flip-flop shooting by plotting the shot coordinates of both arrays for all shot points.

2.6.5 QC Reporting

An integral part of the QC processes is to document and reporting of the quality control products and results. Several digital and hardcopy deliverables are produced during offline QC analyses and are delivered to the client periodically during the survey. In addition, a final report consisting of the necessary information on the data acquisition, processing, and QC results are prepared at the end of the survey.

2.6.5.1 Mobilization Report

A mobilization report mainly describing the project plans such as, methodology, equipment, documentation, predicted survey schedule and acquisition parameters, is prepared just before the survey and submitted to the client for approval. In general, a mobilization report contains a detailed description of the following items:

a. *Description of the survey and scope of the work*: Definition of the survey area, corner coordinates and maps of the whole survey zone, and overall bathymetry.

b. *Environmental implications*: Possible obstructions that may cause undershooting, such as production or drilling platforms, fishing activities, marine traffic, permanent buoys, etc., regional tides and magnitude and direction of surface currents, expected weather conditions within the survey period with minimum and maximum expected wave heights, to predict overall stand-by percentage caused by bad weather conditions.

c. *Acquisition pattern and survey plan*: Preplot maps of the sail lines, start and end coordinates, total number of predicted shot points, length and bearing information of each prime line, proposed line acquisition pattern, definition of turning radius, vessel speed during the line changes, run-in/run-out distances to estimate the approximate line change times, total kilometers of prime lines, and estimated size of the survey area.

d. *Logistics*: Information about the agents, shipments before/during/after the survey, periods and procedures for crew change, chase boat(s), procedure for fuel supply during the survey period.

e. *Data acquisition parameters*: Description of the survey, geodesy, source and streamer as well as binning parameters optimally determined by the survey design process, and tolerance values of each parameter. An example acquisition parameter list, including the tolerance values for a conventional 3D survey is shown in Table 2.17.

f. *Equipment and software*: Vessel information, a complete list of model/brand of all

TABLE 2.17 Example of General Acquisition Parameters List and Tolerance Values for a 3D Survey

	Parameter	Nominal Value	Tolerance
General	Survey size	2412.60 km^2	N/A
	Total prime line length	4810.60 km	N/A
	Estimated survey time	80–90 days	N/A
	Acquisition speed	4–4.5 knot	N/A
	Shooting azimuth	45.16°	N/A
	Distance between sail lines	400 m	N/A
	Number of sail lines	172	N/A
	Number of total CMP lines	2752	N/A
	Run-in	4000 m	N/A
	Run-out	4000 m	N/A
	Bin size	6.25 m × 25 m	N/A
	Optimum fold	80	N/A
Geodesy	Ellipsoid	WGS84	N/A
	Semi major axis	6,378,137.0000	N/A
	Inverse flattening	298.2572235630	N/A
	Eccentricity	0.081819190843	N/A
	Projection	UTM	N/A
	Scale factor	0.999600000000	N/A
	Central meridian	063°00′0.0000″	N/A
	False easting	500,000.0000	N/A
	False northing	10,000,000.0000	N/A
	UTM zone	41S	N/A
Layout	Type of streamers	Solid	N/A
	Number of streamers	8 × 8000 m	N/A
	Streamer separation	100 m	N/A
	Number of channels	640 per streamer	N/A
	Group interval	12.5 m	N/A
	Streamer depth	8 m	±1 m
	Minimum offset	120 m	±10 m
	Number of birds per streamer	12 × acoustic bird 16 × compass bird	N/A
	Number of acoustic units per streamer	12 × acoustic bird 8 × CMX	N/A
	Number of steering devices per streamer	16 (every 500 m)	N/A
	Number of rGPS pods	2 × paravanes 6 × source strings 8 × tail buoys	N/A
Recording	Record length	10,000 ms	N/A
	Sample rate	2 ms	N/A
	Total number of shot points	192,424	N/A
	Data format	SegD rev01	N/A
	Trace summing	N/A	N/A
Source	Number of source arrays	2	N/A
	Number of strings	3 per source	N/A
	Total volume	3200 in^3 per array	N/A
	Source separation	50 m (25 m flip-flop)	±10%
	String separation	8 m	±10%
	Source dimension	16 m × 8 m	±10%
	Source depth	6 m	±0.5 m
	P-P pressure	112.5 bar-m	±5%
	PBR ratio	28.6	±5%
	Air pressure	2000 psi	±10%
	Gun timing	N/A	±1 ms

Continued

mobilized equipment, hardware and software lists, streamer configuration plots (Figs. 2.43 and 2.44), source drawings (Figs. 2.32 and 2.33), gun drop-out specifications, misfire and bad record descriptions (Table 2.16), presurvey calibration results of the navigation equipment (Section 2.6.1.1), vessel offsets diagram (Fig. 2.17), and towing diagram (Fig. 2.42).

g. *QC applications*: Fast-track processing sequence description, online and offline QC implementations for navigation, seismic data and source.

h. *HSE plan for the survey*: Vessel and company regularizations for potential issues on health, safety and environmental situations, HSE management plan, permissions for the operations, procedures for training and safety drills (fire alarms, man overboard, blackout vessel, abandon ship, oil spill), overall risk assessments for the survey, emergency response plans and procedures.

i. *Other topics*: Key persons for the survey and their contact information (vessel management, data processing supervisor onboard and on land, party manager, fleet and HSE manager, etc.), data formats, data storage implementations, deliverables, etc.

2.6.5.2 QC Reports Per-Line

An offline quality control report specific to each sail line, termed the per-line QC, for each completed survey line is produced after a careful analysis of the seismic, navigation and source data. These reports contain information specific to one single seismic line, and they are approved by the onboard client at the end of each sequence to decide if the line is acquired within the quality tolerances of the survey. If not, the client may decide to reshoot the complete or a specific part of the line. In close connection with the online QC analysis, per-line QC reports typically consist of the following items:

a. *Information on the line and survey*: Line name/sequence number, data recording parameters (start/end time, average vessel speed, number of shots, record length, average gun/streamer depth, shot and sampling interval, offsets, number of channels per streamer), production statistics, observer log of the line, etc.

b. *Visual inspection*: Checking of the shots from all cables along the line to define the specific noise types such as strum/tug noise, seismic interference, strong swell noise, etc. (Chapter 3) as well as auto-fires and misfires. This is usually done during the real-time QC and reported in the per-line documents to indicate shots/traces that must be edited during the processing. A detailed and complete listing of the shots/channels for editing is provided after a visual inspection of the data.

c. *Noise evaluation*: Noise records and RMS noise displays (Fig. 2.86) for each streamer at the beginning and end of the line.

d. *Data spectrum*: Display of raw/filtered first and last shots with their corresponding amplitude spectra (Fig. 2.88).

e. *Fast-track processing results*: Near offset gather and brute stack.

f. *Navigation information/plots*: Line direction plot, fold coverage map after the line, additional plots of shot interval (Fig. 2.90), gyro data (Fig. 2.89B), vessel speed (Fig. 2.91), water depth plot (Fig. 2.98A) against the shot point.

2.6.5.3 Daily Reports

Daily progress reports are prepared by the party manager onboard and submitted to the client until the next work day at 08:00. These reports simply indicate what has been done during the last operation day of the survey, statistical details of overall production and operations, meetings and other HSE implications, and comments for the next day. A daily report typically contains the following information:

a. *Project information*: Project and vessel name, study area, work day, contact name and addresses, total survey area, total sail line of the survey in kilometers, estimated completion date of the survey, crossline coverage per sail line, basic acquisition parameters such as shot interval, minimum offset, number of streamers, streamer separation, total array volume, streamer length and depth, record length, sampling rate, total number of recording channels, etc.

b. *Daily production details*: A list of daily completed or ongoing lines consisting of sequence number and line name(s), line direction, FSP (first shot point), LSP (last shot point), TSP (total shot point along the line), sail line length in kilometers, prime/infill/reshoot areas in square kilometers and total full fold (FF), daily production in square kilometers (Table 2.18), remaining prime lines in kilometers overall project progress in percentage and completed and remaining works (Fig. 2.104), statistical information on the cumulative details of daily, weekly, monthly and overall project production times in terms of mobilization/demobilization (mob/demob), production, stand-by and downtimes (Table 2.19), brute

TABLE 2.19 Statistical Information About the Overall Project Progress in Hours and in Percentage Prepared for Daily Reports

	Today		Cumulative	
	Hours	**%**	**Hours**	**%**
Mobilization	00.00	00.00	186.00	28.50
Demobilization	00.00	00.00	00.00	00.00
Stand-by	00.00	00.00	140.40	21.50
Downtime	02.45	11.46	16.20	2.50
Production-prime	04.30	18.76	216.10	33.10
Production-infill	10.25	43.39	26.45	4.20
Line change	06.20	26.39	66.25	10.20
Total	24.00	100.00	652.20	100.00

TABLE 2.18 Example List of Daily Production Details Prepared for Daily Activities Report

Seq.	Line	FSP	LSP	TSP	Length (km)	Infill (km^2)	Prime (km^2)	Total FF (km^2)
042	DEG16-1442P1042	1511	3261	1751	43.775	0	21.8875	21.8875
043	DEG16-1418P1043	1210	3423	2214	55.350	0	27.6750	27.6750
044	DEG16-1388F1044	3220	3907	688	17.200	8.60	0	8.6000
Total daily production				4653	116.325	8.60	49.5625	58.1625

FSP is first shot point, LSP is last shot point, TSP is total shot point along the line, and FF is full fold.

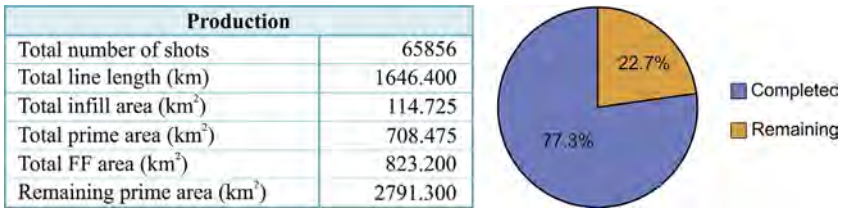


FIG. 2.104 Completed and remaining works prepared for daily reports. FF is full fold.

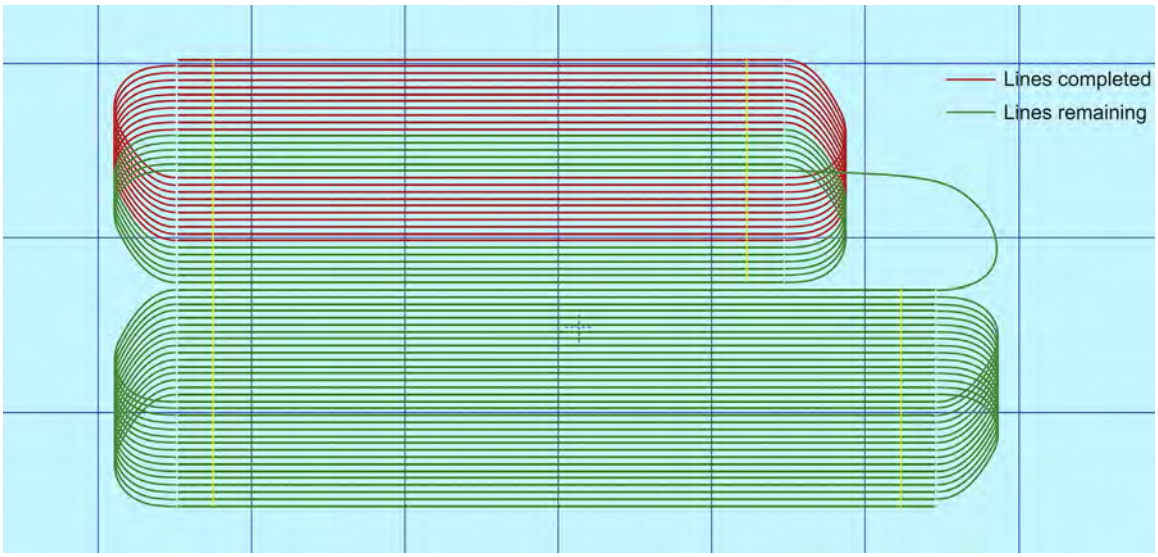


FIG. 2.105 Example map of completed and remaining lines in cumulative display prepared for daily reports. *Yellow lines* define the FF area.

stack of the daily completed lines (if required), and map of daily and cumulative completed lines (Fig. 2.105). Daily progress information contains the time rates that are spent for the different operations during the survey. These operations are specifically termed as

- *Mob/demob*: Time spent for mobilization and demobilization of the vessel, including deployment and retrieval of the in-sea equipment.
- *Production*: Time spent for recording the data for prime, infill or reshoot lines.
- *Line change*: Time for the sailing from a completed line to the next sail line.
- *Downtime*: Time spent for repairing the seismic, navigation, source or other survey equipment as well as the seismic vessel itself.
- *Stand-by*: Downtime due to the weather conditions, obstructions, fishing activity, marine traffic, or seismic activity of other vessels.

c. *Weather conditions*: Wind speed and direction, wave height and direction, overall weather conditions in Beaufort scale, weather forecast for the next survey day.

d. *HSE implications and personnel*: Cumulative listing of HSE meetings, safety drills, toolbox meetings, possible injures, number of personnel and crew onboard (Table 2.20).

e. *Equipment*: Information on the equipment conditions, damage, failure and maintenance implications.

f. *Comments*: Plans for the forthcoming day, and any other information that must be conveyed to client.

2.6.5.4 Weekly and Monthly Reports

Weekly reports contain simple production information for the last week of the survey and are submitted to the client at the day after the last day of every week. These reports list the line information completed during the whole week, including sequence number and line name(s), FSP (first shot point), LSP (last shot

TABLE 2.20 Cumulative Listing of HSE Events Prepared for Daily Reports

HSE Event	Today	Cumulative
Safety drills	0	2
Fire drills	0	2
Man overboard	0	1
Safety/HSE meetings	1	5
Safety audit	0	6
Toolbox meeting	2	26
Vessel induction	0	3
Crew change	0	2
Workboat operations	0	2
Bunkering	0	2
Helicopter landing	0	0
First aid case	0	1
Injures	0	1

point), TSP (total shot point along the line), sail line length in kilometers, prime/infill/reshoot areas in square kilometers and total full fold (FF) weekly production in square kilometers (Table 2.21). Weekly reports may also contain statistical information on the weekly progress of the survey (Fig. 2.106).

Monthly reports submitted to the client after the last day of the month primarily consist of statistical information on the operations within the last month of the survey. They include monthly production statistics of the completed prime, infill and reshoot lines for a cumulative demonstration of operational times, stand-by, downtimes, and mob/demob periods.

2.6.5.5 *Final Survey Report*

After completion of a survey, a final survey report is prepared usually within the following 60 days. These reports are quite comprehensive and include all the necessary information about the survey, such as statistical details of the survey, equipment mobilized, vessel, acquisition details, calibrations, collected data, onboard processing, QC and HSE procedures, etc. A final acquisition report of a 2D or 3D marine seismic survey typically consists of the following items:

a. *Survey information*: Study area and location maps, objectives, survey description, survey program, seismic vessel, chase and support vessels.
b. *Personnel*: Key personnel onboard, office support personnel, contact person information for client and company.
c. *Survey parameters*: Data acquisition parameters applied to whole survey (Table 2.17).
d. *Operational factors*: General information on the weather conditions during the survey, current and tides, obstructions and water depth, fisheries and shipping traffic, seismic interference, etc.
e. *Instrument tests*: Calibrations and verifications of all equipment, echosounder verification, gyro monitoring, GPS monitoring, currentmeter monitoring, acoustic range system, rGPS verification, compass calibrations, start-up tests, daily and monthly tests, end of job test (Section 2.6.1).
f. *Towing configuration and offsets*: General plot of all towed systems and in-sea equipment, inline and crossline offsets (Fig. 2.42).
g. *Streamer configuration*: Streamer system description, streamer layout (Figs. 2.43 and 2.44).
h. *Source configuration*: Source system description, source layout (Figs. 2.32 and 2.33), gun array performance (Section 2.2.6), far-field signature modeling results (Section 2.2.4), array directivity maps (Fig. 2.37), gun drop-out specifications, gun timing (Fig. 2.14).
i. *Recording system configuration*: Recording system description, seismic data flow, overall system timing.

TABLE 2.21 Example List of Weekly Production Details

Date	Seq.	Line	FSP	LSP	TSP	Length (km)	Infill (km^2)	Prime (km^2)	Total FF (km^2)
01.08.2016	042	DEG16-1442P1042	1511	3261	1751	43.775	0.00	21.88	21.88
	043	DEG16-1418P1043	1210	3423	2214	55.350	0.00	27.67	27.67
	044	DEG16-1388F1044	3220	3907	688	17.200	8.60	0.00	8.60
02.08.2016	045	DEG16-1243P1045	1124	3268	2145	53.625	0.00	26.81	26.81
	046	DEG16-1189P1046	1652	3106	1455	36.375	0.00	18.18	18.18
03.08.2016	046	DEG16-1189P1046	3107	1809	703	17.575	0.00	8.78	8.78
	047	DEG16-1145P1047	1853	3507	1655	41.375	0.00	20.68	20.68
	048	DEG16-1014P1048	2314	2755	442	11.050	0.00	5.52	5.52
04.08.2016	049	DEG16-1512F1049	3568	4153	586	14.650	7.32	0.00	7.32
	050	DEG16-1546F1050	2536	3793	1258	31.450	15.72	0.00	15.72
	051	DEG16-1635F1051	1965	3440	1476	36.900	18.45	0.00	18.45
05.08.2016	052	DEG16-1693F1052	1645	2507	863	21.575	10.78	0.00	10.78
	053	DEG16-1726F1053	2687	3054	368	9.200	4.60	0.00	4.60
	054	DEG16-1204P1054	1235	2076	842	21.500	0.00	10.75	10.75
06.08.2016	054	DEG16-1267P1054	2077	3180	1104	27.600	0.00	13.80	13.80
	055	DEG16-1296P1055	1456	3110	1655	41.375	0.00	20.68	20.68
07.08.2016	056	DEG16-1314P1056	1024	1780	757	18.925	0.00	9.46	9.46
	057	DEG16-1388P1057	1227	1546	320	8.000	0.00	4.00	4.00
Total weekly production					20,282	507,500	65.47	188.21	253.68

FSP is first shot point, LSP is last shot point, TSP is total shot point along the line, and FF is full fold.

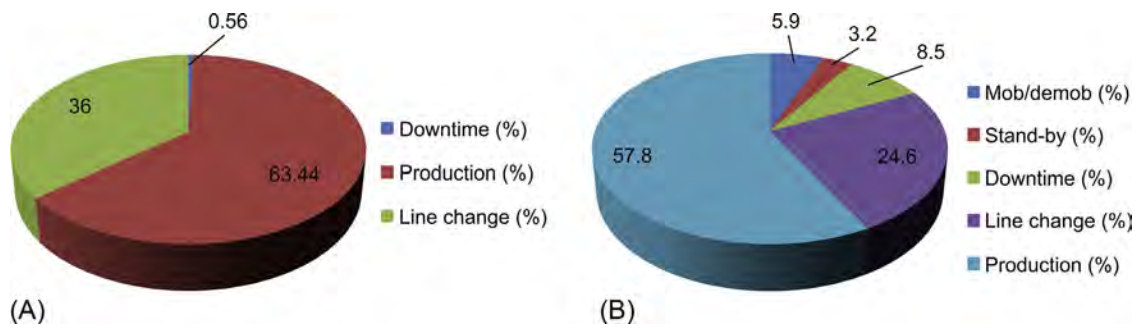


FIG. 2.106 Statistical information of (A) weekly and (B) cumulative progress of the survey.

j. *Navigation and positioning system*: Navigation system description and components (Fig. 2.16), system configuration, surface positioning/DGPS and rGPS system (Section 2.1.7), streamer and source positioning (Section 2.3.2), acoustic ranging (Section 2.3.4), echosounder/gyro/currentmeter/ADCP.

k. *Production summary*: Primary time use of the survey (Fig. 2.107), daily production lengths (Fig. 2.108), cumulative production lengths (Fig. 2.109), average vessel speed (Fig. 2.110), line change times (Fig. 2.111), daily operations summary (Table 2.22), postplot map, fold distribution maps (flexed and unflexed).

l. *HSE implementations*: Meetings and drills, vessel induction, safety events, incident reporting, internal and external audits, helideck operations, work boat operations, marine mammal observations.

m. *Acquisition QC*: Online QC monitoring, offline QC analysis, analysis of seismic data, navigation analysis and processing, analysis of source signal, acoustic ranging data analysis, rGPS data analysis.

n. *Onboard processing*: Software and hardware systems available for onboard processing, flow and parameter tests, final deliverables.

o. *Data and shipments*: Seismic data format description, navigation data format description, list of original data tapes and contents.

2.6.5.6 HSE Report

Health, safety and environment (HSE) management is an integral part of marine seismic operations today. Each service company develops its own safety management and crew education/audit system to minimize the injuries onboard, especially during deck operations. They periodically inform and educate the employees in terms of HSE implications, their personal responsibilities, precautions that they must take before the geophysical operations, procedures and instructions for emergency situations, safety procedures for onboard activities and operations to reduce possible hazards based

Production	
Prime	3086.750 km
Infill	680.125 km
Total	3766.875 km

Time distribution		
Activity	**Hour**	**%**
Production	446.24	41.66
Line change	340.56	31.79
Mob/demob	124.33	11.60
Downtime	96.14	8.97
Stand-by	64.12	5.98
Total	1071.39	100.00

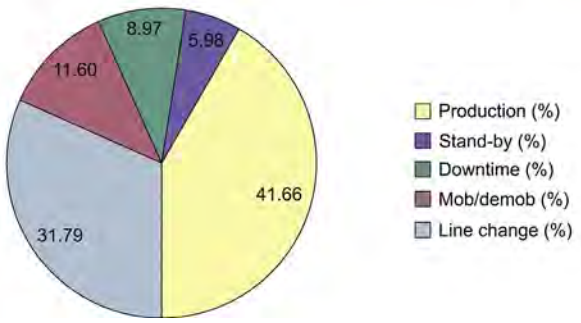


FIG. 2.107 Primary time use of the survey in hours and percentage, and overall production in kilometers.

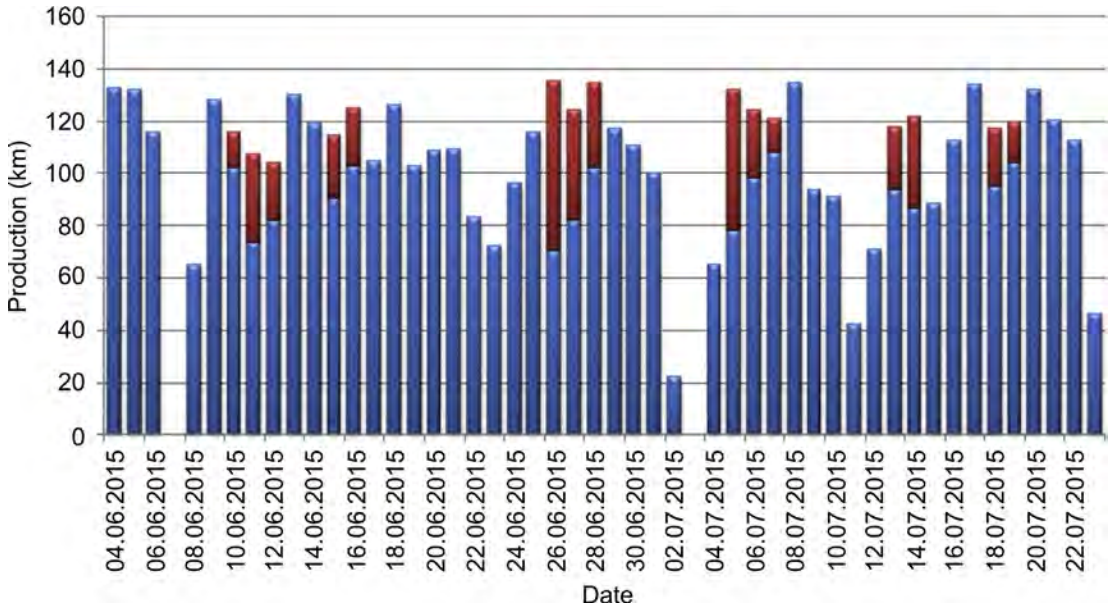


FIG. 2.108 Daily production for prime *(blue)* and infill *(red)* lines.

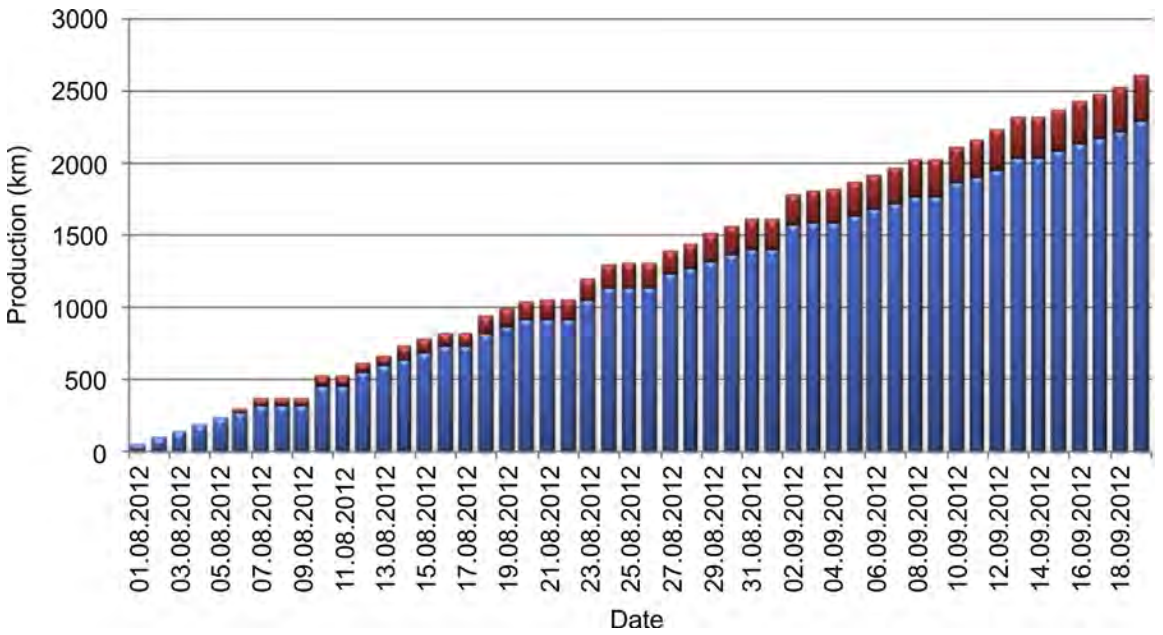


FIG. 2.109 Cumulative production for prime *(blue)* and infill *(red)* lines.

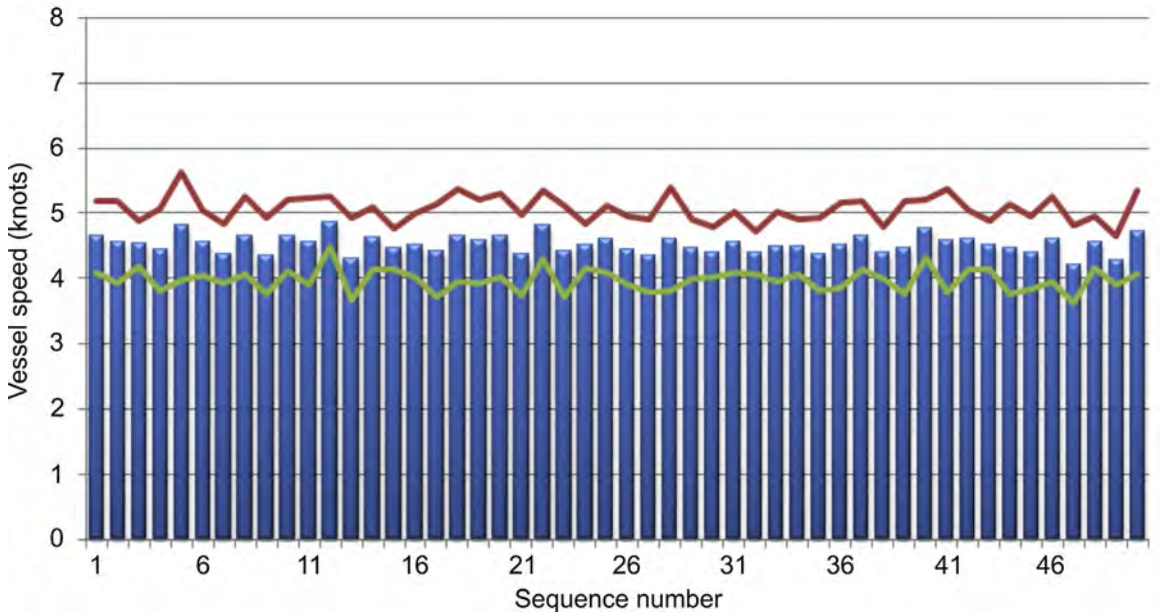


FIG. 2.110 Average, maximum *(red)* and minimum *(green)* vessel speed for every sequence.

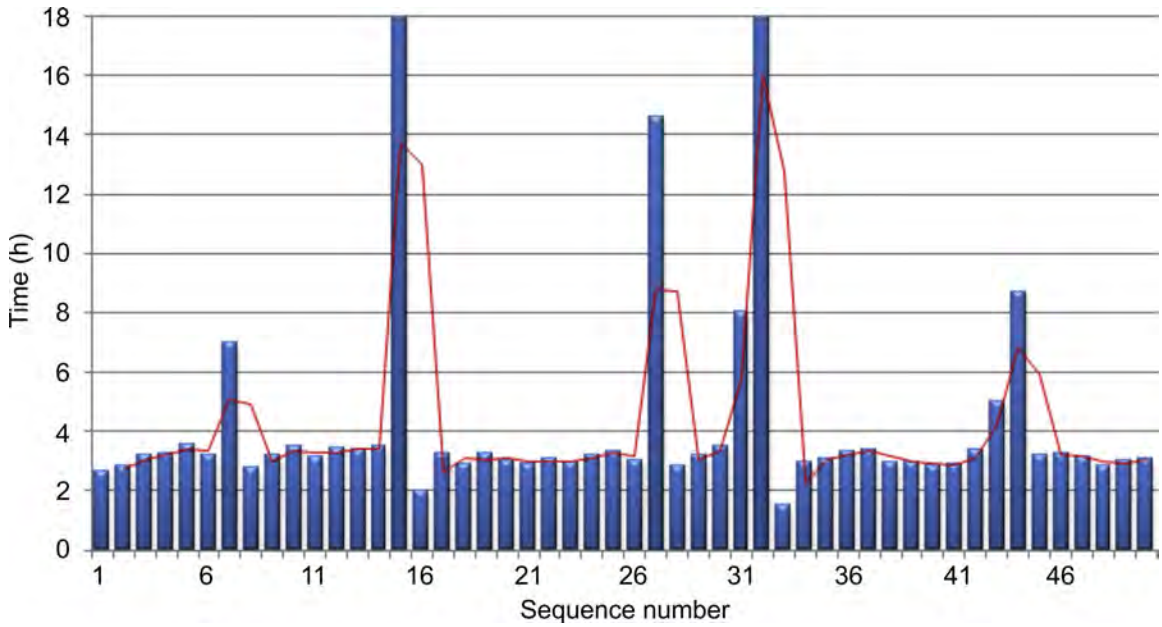


FIG. 2.111 Line change times for every sequence. *Red line* represents the daily average.

TABLE 2.22 An Example List of Daily Operations Summary for First 10 Days of the Survey Prepared for the Final Survey Report

Date	Time	Total Time	Activities
18.08.2012	00:00-22:00	22:00	Mob-all cables/sources deployed
18.08.2012	22:00-24:00	02:00	Production-Test line seq.-01
19.08.2012	00:00-01:14	01:14	Downtime d/t air leaks
19.08.2012	01:14-24:00	01:14	Production- seq.-02-03
20.08.2012	00:00-24:00	24:00	Production- seq.-04-05-06
21.08.2012	00:00-24:00	24:00	Production- seq.-06-07
22.08.2012	00:00-16:12	16:12	Production- seq.-07
22.08.2012	16:12-24:00	08:48	Stand-by d/t bad weather
23.08.2012	00:00-10:40	00:40	Stand-by d/t bad weather
23.08.2012	10:40-14:45	04:05	Downtime d/t main engine fuel leakage
23.08.2012	14:45-24:00	09:15	Production- seq.-08-09
24.08.2012	00:00-24:00	24:00	Production- seq.-09-10-11
25.08.2012	00:00-24:00	24:00	Production- seq.-11-12-13
26.08.2012	00:00-24:00	24:00	Production- seq.-13-14
27.08.2012	00:00-13:10	13:10	Production- seq.-14-15
27.08.2012	13:10-21:25	08:15	Downtime d/t a failure section#15/streamer#4
27.08.2012	21:25-24:00	02:35	Production- infill seq.-15
28.08.2012	00:00-24:00	24:00	Production- seq.-16-17-18

on the standard safety instructions in the project HSE plan.

Safety drills and crew safety meetings are the crucial parts of the HSE plan and are performed periodically. In addition, task-specific meetings, termed toolbox meetings, are called just before the task, in which the task is defined and possible hazards are identified. HSE reports also include total exposure hours for the seismic crew onboard. HSE statistics also have a cetacean log to evaluate the potential impact of seismic operations on marine mammals and to take the necessary precautions to minimize any effects on marine biological life.

HSE analysis and statistics of a seismic survey are usually involved in the final survey report. HSE reports typically involves the statistical information on the safety events occurred during the survey period, such as crew change, bunkering, safety meetings, drills, etc. (Table 2.23), statistical information on injuries (Table 2.24), and the explanations of the incidents.

2.6.5.7 Final Deliverables

Several deliverables are produced before, during and after the seismic survey. A mobilization report is prepared and submitted to the client after a kick-off meeting to discuss the technical details of the survey, and periodic

TABLE 2.23 Example HSE Events for the Whole Survey

HSE Event	Count
Port calls	2
Safety drills	6
Fire drills	4
Man overboard drills	2
Oil spill drills	2
Abandon ship drills	3
Blackout vessel drills	0
Emergency steering	0
Emergency towing	0
Safety/HSE meetings	13
Safety audit	14
Cross inspections	12
Toolbox meetings	186
Vessel induction	8
Crew change	5
Workboat operations	9
Bunkering	4
Helicopter landing	1
First aid case	2
Injures	4
Exposure hours (vessel crew)	11,474
Exposure hours (seismic crew)	12,350
Exposure hours (third party crew)	3,614

TABLE 2.24 Example Statistical Information List on Injuries for Whole Survey

HSE Event	Count
Fatality	0
Restricted work case	0
Lost time case	1
Medical treatment	0
First aid treatment	2
Not work-related injuries	0
Not work-related illnesses	0
Onboard hazard observations	0
Improvement suggestions	6
Environmental hazard observations	0
Near-miss reports	16
Material loss	6
Marine mammal observations	8

items are delivered as the acquisition proceeds. These typically include

- Daily reports
- Weekly reports
- Monthly reports
- Daily instrument test results
- QC reports per-line
- Observer logs

Final products are prepared and delivered after the survey, and are completed with a signed protocol for the following data transfer:

- Raw seismic field tapes in SegD format
- Seismic field tapes with the navigation loaded into the headers in SegY format
- All observer logs and the other records in digital and paper copy
- Raw navigation files in UKOOA P2/94 format
- Processed navigation files in UKOOA P1/90 format
- Processed gravity and magnetic data
- Onboard processing tapes (velocity fields, stack and migrated data) in SegY format
- A final survey report that includes a detailed description of seismic data acquisition, QC applications and analyses, HSE events and statistics.

CHAPTER

3

Noise in Marine Seismics

OUTLINE

3.1 Operational Noise 174
3.2 Bubble Effect of the Air Gun 175
3.3 Multiple Reflections 177
3.4 Swell Noise 180
3.5 Bird Noise 183
3.6 Inline Waves 185
3.6.1 Tail Buoy Noise 185
3.6.2 Mechanical Cable Noise 188
3.6.3 Direct Waves 190
3.6.4 Refracted Waves 191
3.7 Diffractions 193
3.8 Guided Waves 193
3.9 Seismic Interference 196
3.10 Other Noise Types 200
3.10.1 Powerline Harmonic Noise 200
3.10.2 Spikelike Noise 202
3.10.3 Side-Sweep 204
3.10.4 Noise From Other Marine Vehicles 206
3.10.5 Marine Mammals 208
3.10.6 Streamer Ballasts 208

Recorded traces during the seismic survey consist of a linear summation of reflected signal and noise amplitudes. The "noise" can be defined as all kind of events or amplitudes appearing on the seismic data other than genuine reflections. Recorded noise is sometimes generated by the seismic system components themselves (e.g., air gun bubble, bird noise, etc.), and sometimes it arises because of the specifications of the working environment (e.g., marine mammals, propellers, marine traffic, etc.). The first noise type is termed source-generated noise whereas the second type is known as ambient noise.

The noise in the seismic data is classified either as coherent noise, which has trace-by-trace consistency and can be traced over several seismic traces, or random noise, which does not have a systematic consistency from one trace to another (Fig. 3.1). Coherent noise, such as multiple reflections or powerline harmonic noise, can be modeled and subtracted from the data by a

https://doi.org/10.1016/B978-0-12-811490-2.00003-7

© 2018 Elsevier Inc. All rights reserved.

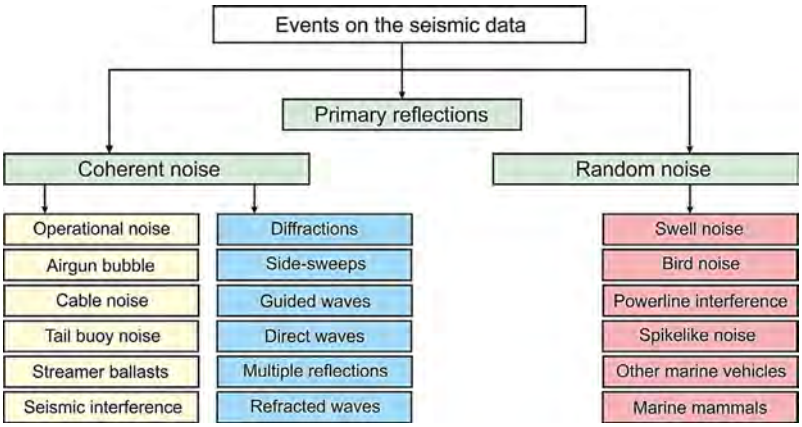


FIG. 3.1 Different coherent and random noise types specifically observed in marine seismic data. *Yellow boxes* in coherent noise types encompass the noise generated by technical components of the survey system, while *blue boxes* indicate the noise from geological environment.

suitable match filter application. Random noise can be attenuated if it can be separated from signal by one of its specific characteristics, such as frequency band. Today, stacking of multichannel seismic data is the most effective noise attenuation technique both for random and coherent noise types.

Whenever the reflection amplitudes are weak, all these different noise types become problematic and some of them require specific techniques with properly determined parameters to suppress. For instance, high- or low-frequency random noise, swell noise or inline waves all can be attenuated by a simple frequency-wavenumber (*f-k*) filter; however, suppression of multiples requires very specific techniques.

Detailed studies performed on the design of seismic streamers in 1960s and 1970s ensured important advances in suppressing noise during the acquisition. Double-sided hydrophones eliminated the effect of acceleration due to the towing of streamers (Section 2.1.2); group forming with several hydrophones suppressed the bulge waves in fluid-filled streamers; stretch sections were attached at both ends of the streamer to suppress mechanical cable noise as well as operational and tail buoy noises; and dynamic ranges of the receiving and recording systems were increased. At any rate, the seismic data is contaminated by random and coherent noise amplitudes extending from one trace to another. In order to suppress different noise types, we need to know which specific property of the noise separates it from the signal. For instance, reflection hyperbolas and mechanical cable noise seem to interfere on shot records; in the frequency-wavenumber (*f-k*) domain, however, they can easily be discriminated in accordance with their different dips on the shot gathers. The effectiveness of the noise suppression is strongly dependent on the proper selection of the suppression method and the domain (e.g., frequency domain, *f-k* domain, time domain, etc.) in which the methodology will be carried out.

Characteristics and level of the ambient noise, such as its frequency band or amplitude can be investigated by collecting noise records before and after shooting. Noise records are collected as an ordinary shot gather is recorded but without firing the guns, in order to obtain only ambient noise in the operational environment, which provides information especially on the characteristics of swell noise, operational noise, bird

noise, strum and tug noise, etc. Fig. 3.2A shows first 48 traces of a noise record and its mean amplitude spectrum. Low frequency (less than approximately 10 Hz) swell noise amplitudes (S) are dominant on the record. When the record is filtered with a 14-Hz low-cut filter to remove the swell noise (Fig. 3.2B), the linear operational noise from vessel's propeller (O) at approximately a 20-Hz frequency dominates. Finally, if we again filter the record with a 24-Hz low-cut filter to remove the operational noise, other high frequency noise components (such as powerline harmonic noise interference (E) appeared at 50 Hz and its multiples and high-frequency random noise amplitudes between 140 and 180 Hz) and tug noise from tail buoy (T) become visible on the data and on the amplitude spectrum (Fig. 3.2C).

As the noise record indicates, seismic data contain different types of noise generally interfering with the reflections in the time domain. Some of them are masked by relatively higher amplitudes of other noise components. For instance, when the swell noise is removed from the record, the noise

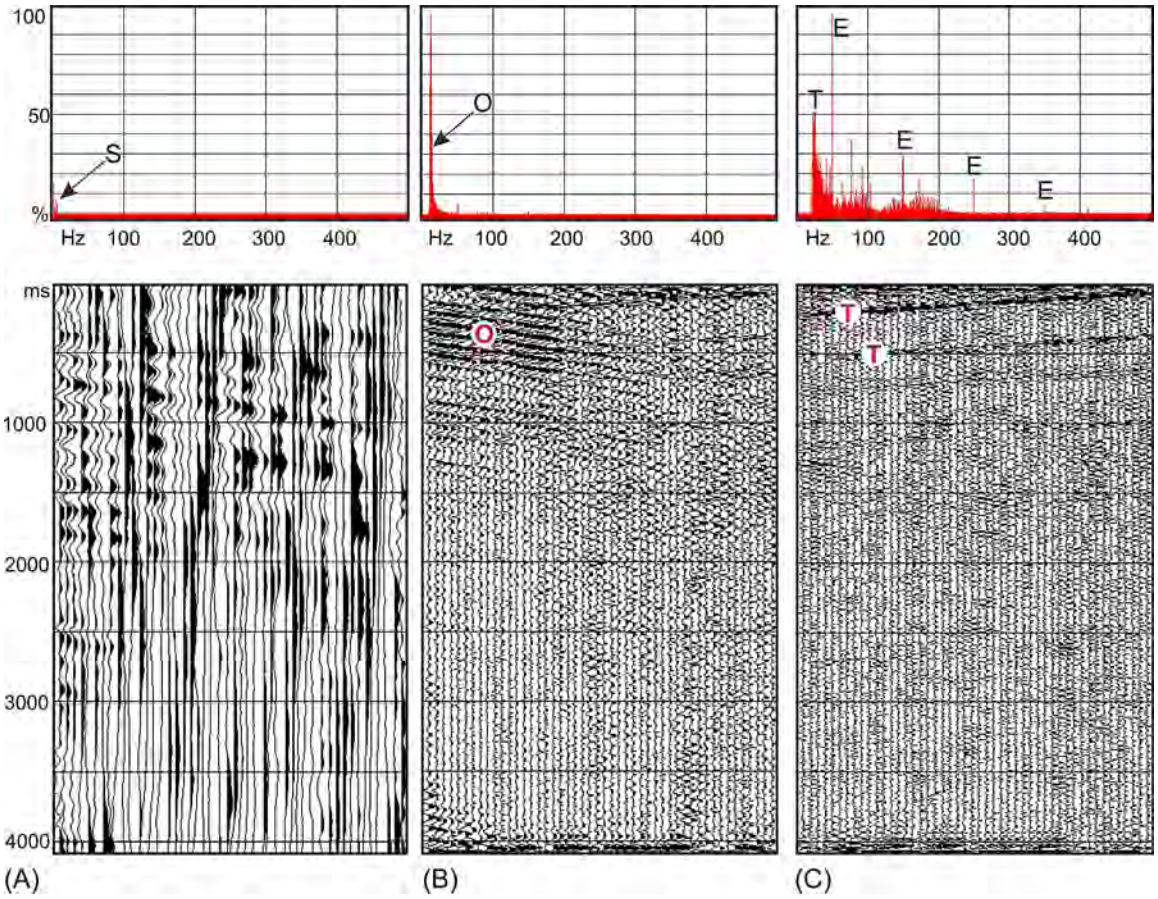


FIG. 3.2 (A) A noise record and its filtered versions with (B) 14 Hz and (C) 24 Hz high-pass filter. Their mean amplitude spectra are given in the upper panel. *S*, swell noise; *O*, operational noise; *E*, powerline harmonic noise; *T*, tug noise from tail buoy.

from vessel's propeller shows up, and, if we remove this operational noise, then powerline interference becomes visible. Sometimes it is not possible to completely remove all of these noise amplitudes of different dip, amplitude or frequency characteristics from the data using the conventional processing techniques.

Marine seismic data contain individual noise types that are quite different from those observed on land records. Understanding the source and physical specifications of noise has key importance in the determination of processing steps and the parameters in removing the particular noise types. Main purpose of seismic data processing is simple: to suppress the noise and make genuine reflections more prominent: in other words, to increase the signal/noise ratio (S/N). Definition of the noise embedded in the data and investigation of its characteristics are important for the processors to determine the suitable processing steps to remove a particular noise type. The main characteristic features of the noise components are their trace-by-trace consistency and dip on the shot/CDP gathers or on the stack sections, and their frequency and amplitude specifications. In this section, most of the noise types encountered in marine seismic data are defined and discussed in detail by means of their appearance and dip on the shot records as well as on stack sections, and their amplitude and frequency characteristics. Several noise examples from real seismic data are introduced and analyzed. In most cases, before/after representations are also included.

3.1 OPERATIONAL NOISE

Operational noise originates directly from a seismic vessel's hydrodynamic movement, its engine(s), machinery, and propeller(s). The shape, amplitude and frequency characteristics of operational noise primarily depend on the dimensions, tow speed and construction form of the vessel. Operational noise from onboard machinery occurs due to the transformation of vibrations from the main engine(s), power generators, or air compressors into the water column. These vibrations appear on the data spectrum as narrow bands proportional to the speed and revolution of the main engines, and their amplitudes depend on several agents such as specifications, mounting and stability of the engines. Hydrodynamic noise arises from the movement of the vessel and may be effective on the near offset traces, since it is not transmitted for long distances.

The noise from propeller is important for seismic data because the propellers directly operate in the water and they produce a continuous low amplitude noise in the water column, which creates linear events at near-offset traces. This noise can be distinguished as periodic high amplitudes in the amplitude spectrum, which are proportional to the propeller's rotation speed. The peak frequency of the propeller noise can be calculated using $f = nR/60$, where n is the number of propeller blades and R is the rotation speed of the propeller in rpm. For instance, a propeller with three blades rotating at 300 rpm produces an operational noise at approximately 15 Hz center frequency. Fig. 3.3 shows linear operational noise and its mean amplitude spectrum, prominent at the water column, and late arrivals of near traces. The noise repeats itself periodically relative to the rotation of the propeller and has a dominant frequency of approximately 20 Hz. Although it is not possible to completely avoid recording this noise, hydrophone arrays along the streamer and long tow distances from the vessel may reduce the noise level. In practice, reflection amplitudes in near traces are strong enough to suppress operational noise and relatively weak amplitudes of the noise are masked under strong amplitudes of genuine reflections. The operational noise, however, becomes evident for late arrivals where reflection amplitudes cease, and amplitude restoration processes such as automated gain control (AGC) increases the noise amplitude.

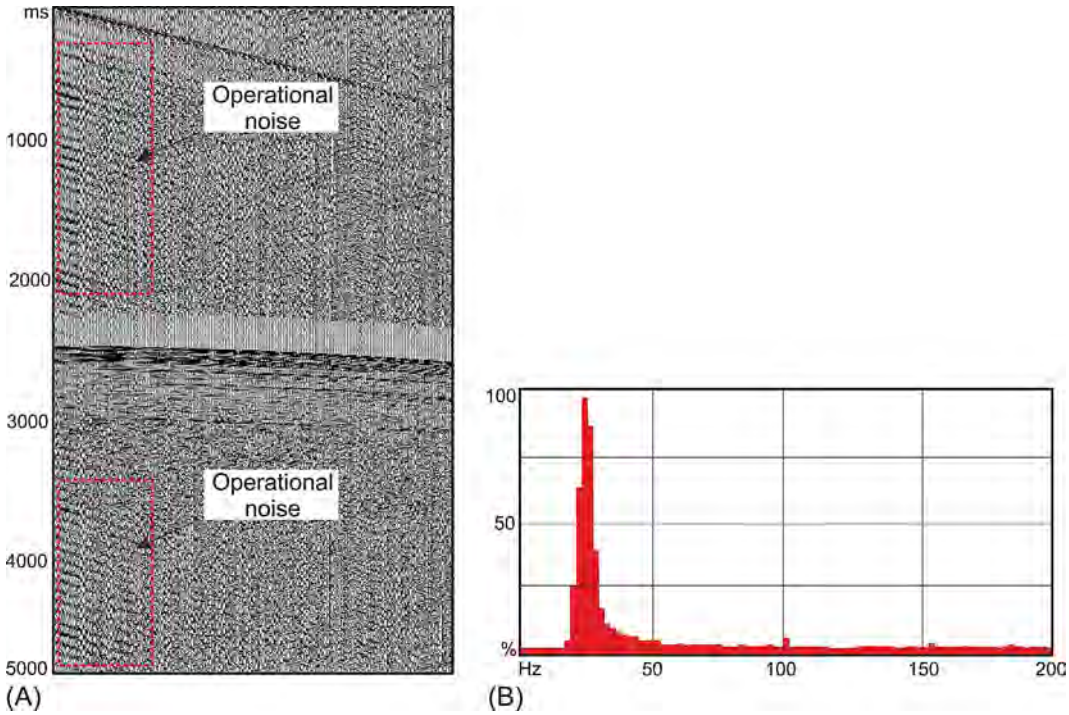


FIG. 3.3 (A) Linear operational noise at near traces on a shot gather, and (B) mean amplitude spectrum of the *dashed rectangles* in (A).

Because the operational noise is linear on the shot records and propagates in the water column with a water velocity of 1500 m/s along the streamer, it can be removed by a suitable frequency-wavenumber (*f-k*) filter. Fig. 3.4 shows an application of *f-k* filter designed to effectively eliminate the operational noise.

3.2 BUBBLE EFFECT OF THE AIR GUN

Air guns are standard seismic sources for conventional 2D and 3D seismic surveys today. When a single air gun is fired at a certain depth in the water column, it discharges high-pressure air from its air chamber into the water to generate the primary seismic signal. Interactions between the internal pressure of the air bubble generated by this sudden air discharge and the ambient pressure result in periodic expansion and collapse of the air bubble as it ascends towards the sea surface. Each individual expansion and collapse produces a new signal with opposite polarity until it reaches to the sea surface, which is termed bubble noise. Occurrence of the air gun bubble and its characteristics are discussed in Section 2.2.2 in detail.

The bubble effect of the seismic sources becomes an important issue if a single ordinary air gun is used as the seismic source. To overcome the bubble noise problem, a specific air gun type known as generator/injector (GI) gun (Section 2.2.2) can be preferred, especially for high resolution seismic acquisition such as site surveys. In addition, large air gun arrays consisting of several gun strings with large number of air guns, each with different chamber

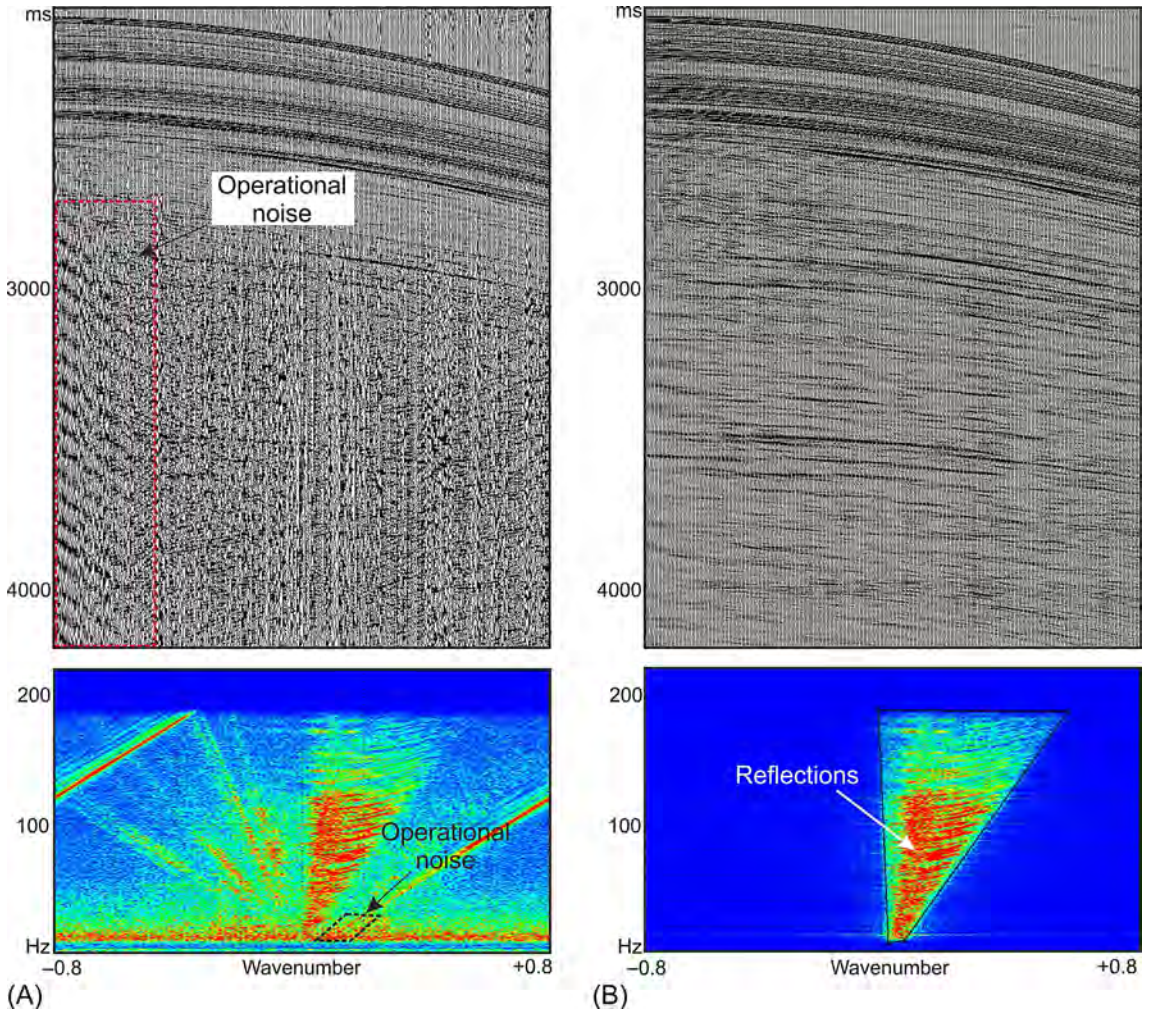


FIG. 3.4 (A) A filtered shot record with distinctive linear operational noise at near traces, and (B) same shot after application of an *f-k* filter. Corresponding *f-k* domain representations are given in the lower panels.

sizes used for hydrocarbon exploration, are suitably tuned to suppress the bubble amplitude of the resultant seismic signal (Section 2.2.6).

The bubble effect occurs as reversed polarity recurrent amplitudes on the seismic data (Fig. 3.5A). It appears a certain time later after the seabed reflection, which mimics the seabed with a good trace-by-trace consistency and generally cross-cuts the primary reflections (Fig. 3.5B). The first bubble with the largest amplitude can be seen on the final stack sections when a single air gun is used. In some cases, the amplitude of the first bubble is so strong that even its multiple reflection can be visible on the stack data. Although bubble effect can be suppressed by air gun arrays or by using a GI gun, it can also be attenuated during the processing stage by a suitable deconvolution application (Fig. 3.6). Selection of suitable parameters for predictive deconvolution is explained in detail in Section 6.4.

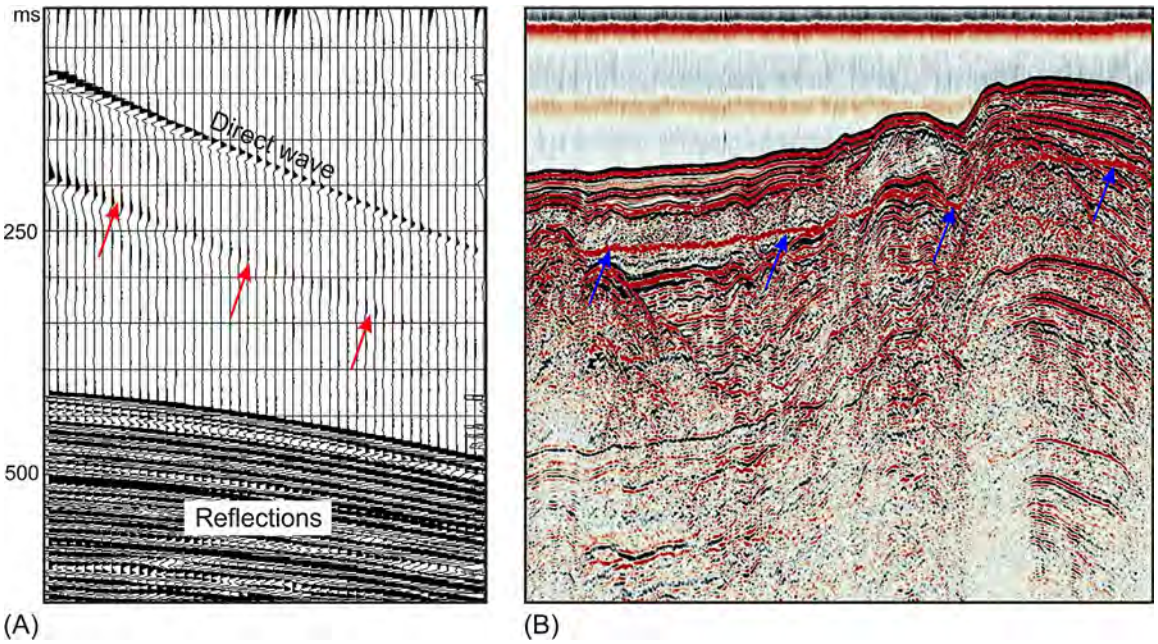


FIG. 3.5 (A) Bubble effect *(red arrows)* of a 105 in^3 single air gun on a shot gather. (B) Bubble effect *(blue arrows)* mimics the seabed on the near trace sections with as a reversed-polarity continuous event.

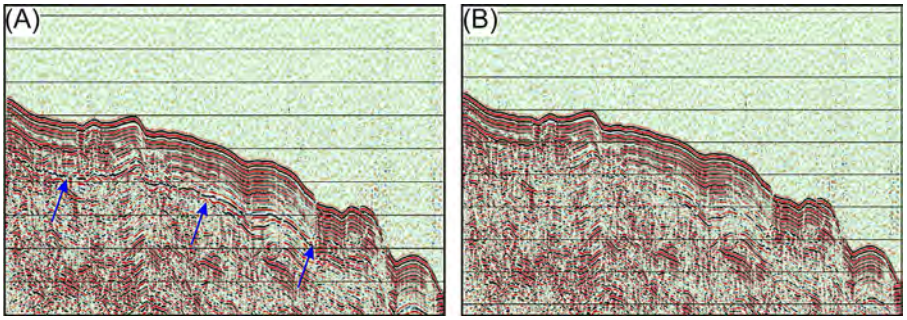


FIG. 3.6 Attenuation of bubble amplitudes *(blue arrows)* by a predictive deconvolution application. (A) Before and (B) after deconvolution of the section obtained by a single 45 in^3 ordinary air gun source.

3.3 MULTIPLE REFLECTIONS

Multiple reflections occur when the seismic signal travels along the same ray path more than one time, and they produce reflection arrivals that repeat themselves on the shot records and stack sections. These reflections may constitute significant issues especially in shallow water surveys. Because the seabed is a good reflector with relatively high reflection coefficient, it reflects back an important portion of incoming seismic energy towards to sea surface, recorded

as a strong seabed reflection. This reflection energy then passes through the streamer, reaching to the sea surface, and reflected back towards the seabed since air-sea surface boundary is also a very good reflector. This signal will act as a secondary seismic source, producing its own reflections from seabed and shallow subsurface sediments. This reflection process may repeat itself on the data several times depending on the water depth, source strength and recording length, and all of these reflections are received by the hydrophones and recorded in the seismic data.

The arrival time of the first multiple reflection from seabed is exactly twice the seabed reflection arrival time (Fig. 3.7). If the sea bed is inclined, the inclination of multiple reflections increases on the stack sections (Fig. 3.8). In most cases, the repeating amplitudes are not only the energy from the seabed, but also the reflected energy from subbottom sediments repeats itself as a complete reflection packet. Sometimes the amplitudes of multiple reflections are so strong that primary reflection amplitudes are completely masked.

One of the most common multiple reflection types is peg-leg multiple, originating from a high amplitude reflection from a strongly reflective deeper boundary, such as an acoustic basement, and the reflection repeats itself in the water column (Fig. 3.9). Hence, a phantom interface that mimics the real reflector occurs, and the time interval between the two reflections always equals to the water depth, since the peg-leg reflection has an additional travel time from its propagation in the water column.

Multiple reflections propagate mostly in the water column and in shallow subsurface sediments; hence their propagation velocity is

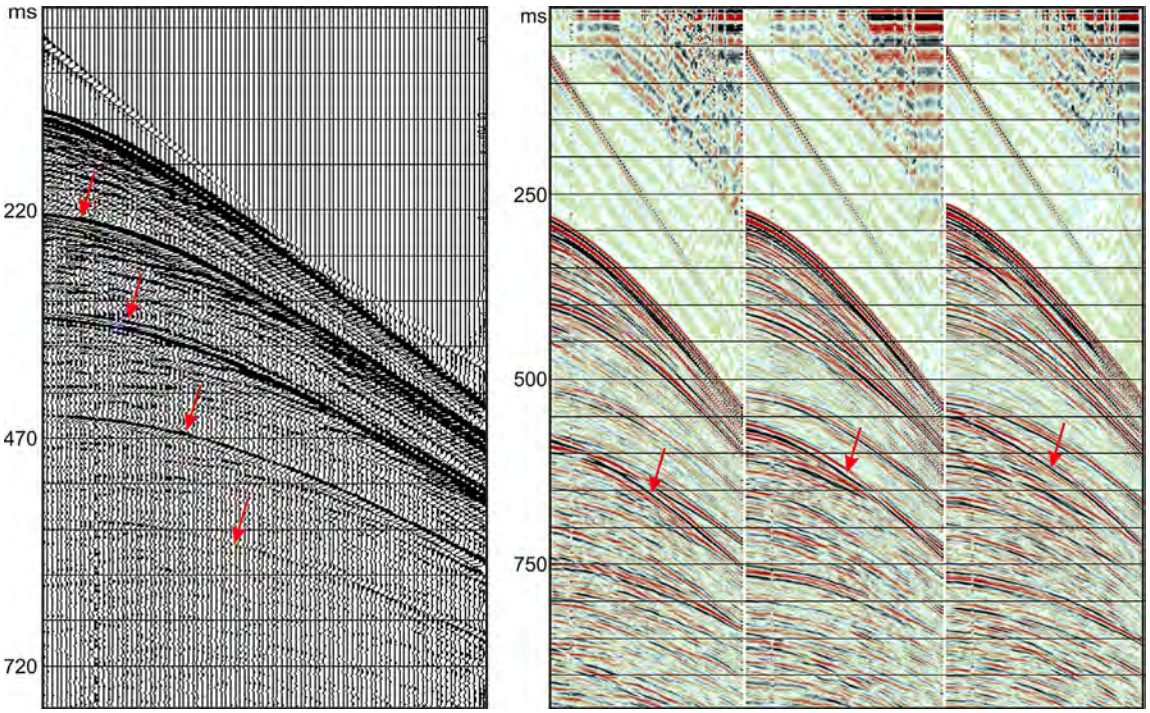


FIG. 3.7 Multiple reflection hyperbolas *(red arrows)* on shot gathers.

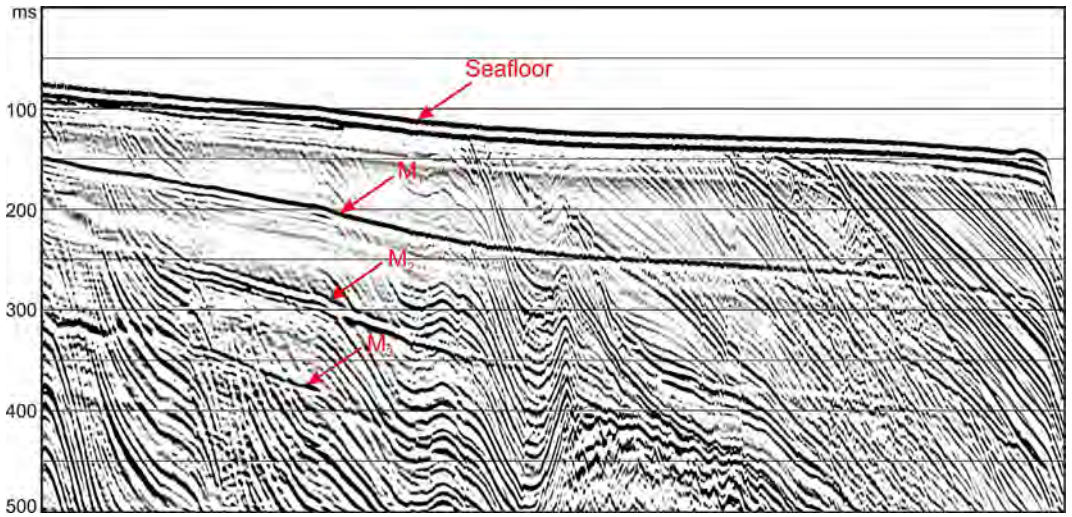


FIG. 3.8 Inclinations of successive multiple reflections (M_1, M_2, and M_3) increase on the stack sections in case of a dipping seafloor.

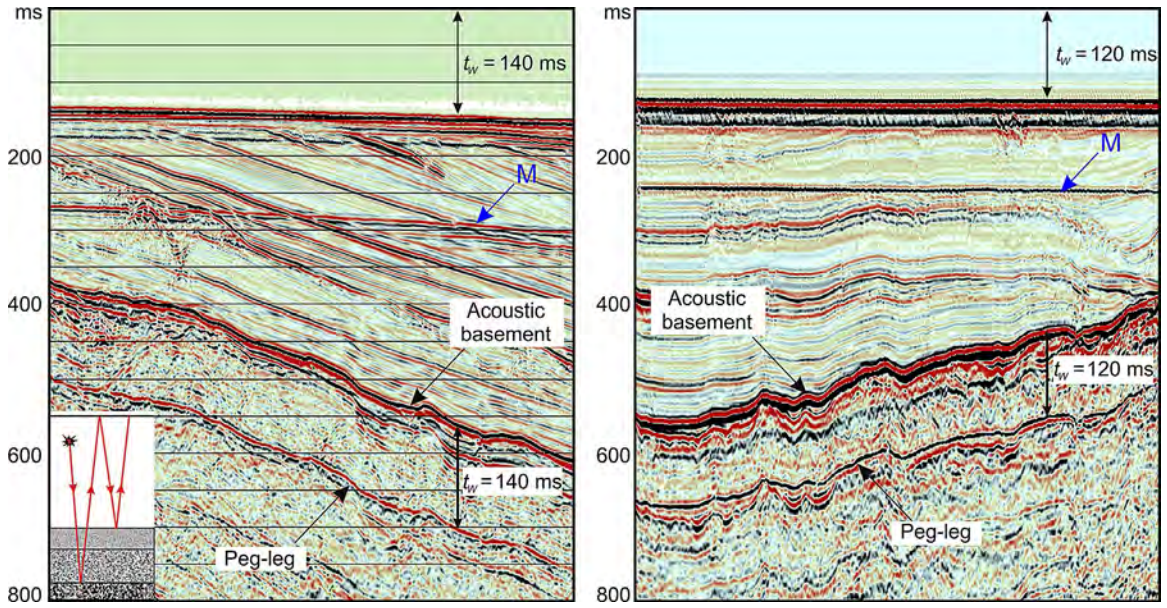


FIG. 3.9 Two examples of peg-leg reflections from a strongly reflective acoustic basement. t_W is the time for the seafloor reflection, and M is first bounce seafloor multiple.

approximately 1500 m/s. The primaries arrive at the same recording time as multiples; however, they almost always have higher velocities than multiples. Multiple reflection hyperbolas cross-cut the primary reflection hyperbolas on shot and CDP gathers, because the propagation velocity of the signal directly affects the curvature of the reflection hyperbolas (Section 1.3.4).

It is not possible to avoid recording of the multiples during acquisition, and therefore a number of specific processing methods have been developed to remove the multiple amplitudes, such as surface-related multiple elimination (SRME), wave equation multiple rejection (WEMR), predictive deconvolution, etc. The theoretical basis and application restrictions of these methods along with their specific characteristics are explained in detail in Chapter 7.

3.4 SWELL NOISE

Swell noise is the most dominant noise type in raw marine seismic data. The main characteristics of the swell noise are its large amplitude and low-frequency content, and it sometimes induces delays or temporary suspension of data acquisition in marine surveys (Dondurur and Karslı, 2012). It occurs either from (i) wind-driven longitudinal sea surface waves (which cause hydrostatic pressure fluctuations due to the vertical motion of the ocean), and (ii) dynamic pressure variations along the streamer (turbulence effect of hydrostatic pressure fluctuations due to a turbulent layer surrounding the streamer) when the streamer bends in the water. Both agents produce significantly large amplitude variations on the seismic data (Fig. 3.10). The first type is seen as positive and negative low frequency noise bands with high amplitudes. This is because the hydrophones are sensitive to pressure changes, including the ambient pressure, which is continuously modified by surface wind-driven wave activity (Fig. 3.10A). While wave troughs cause low ambient pressure, wave peaks result in high pressure on the hydrophones, which ultimately creates successive positive and negative high amplitude bands on the shot records during the surface wave passage. The noise amplitude becomes significant during rough weather conditions, especially when the streamer is towed at relatively shallow depths for high-resolution surveys.

Swell noise generally obscures underlying primary reflection amplitudes on the raw shots because of its relatively higher amplitudes with respect to the reflections, and degrades overall data quality. Although this type of noise is extremely dominant due to its higher amplitude, we can easily discriminate swell noise and reflection amplitudes in terms of their different frequency contents. Amplitude and the frequency band of the swell noise increases as the weather conditions become rough (Berdenbender et al., 1970), and most of the noise amplitudes are below 10 Hz, which allows us to remove almost all swell noise using a suitable band-pass filter. Elboth et al. (2009) suggested that noise amplitudes in the 0–2 Hz range are from wind-driven surface waves, whereas those above 2 Hz originate from hydrostatic pressure fluctuations.

Fig. 3.11A illustrates a raw shot gather and its amplitude and *f-k* spectra, while Fig. 3.11B shows its 14 Hz low-pass filtered version which has only amplitudes lower than 14 Hz. This frequency band almost completely contains only swell noise amplitudes, especially for the shallow parts of the data.

The turbulence effect along the streamer becomes significant if shooting is initiated before turning of the streamer is not completed during the line change. This type of noise is distinguished on shots as vertical high-amplitude stripes. Fig. 3.12 shows a number of successive shots with prominent swell noise from the turbulence effect formed by streamer turning at the beginning of a survey line, which produced

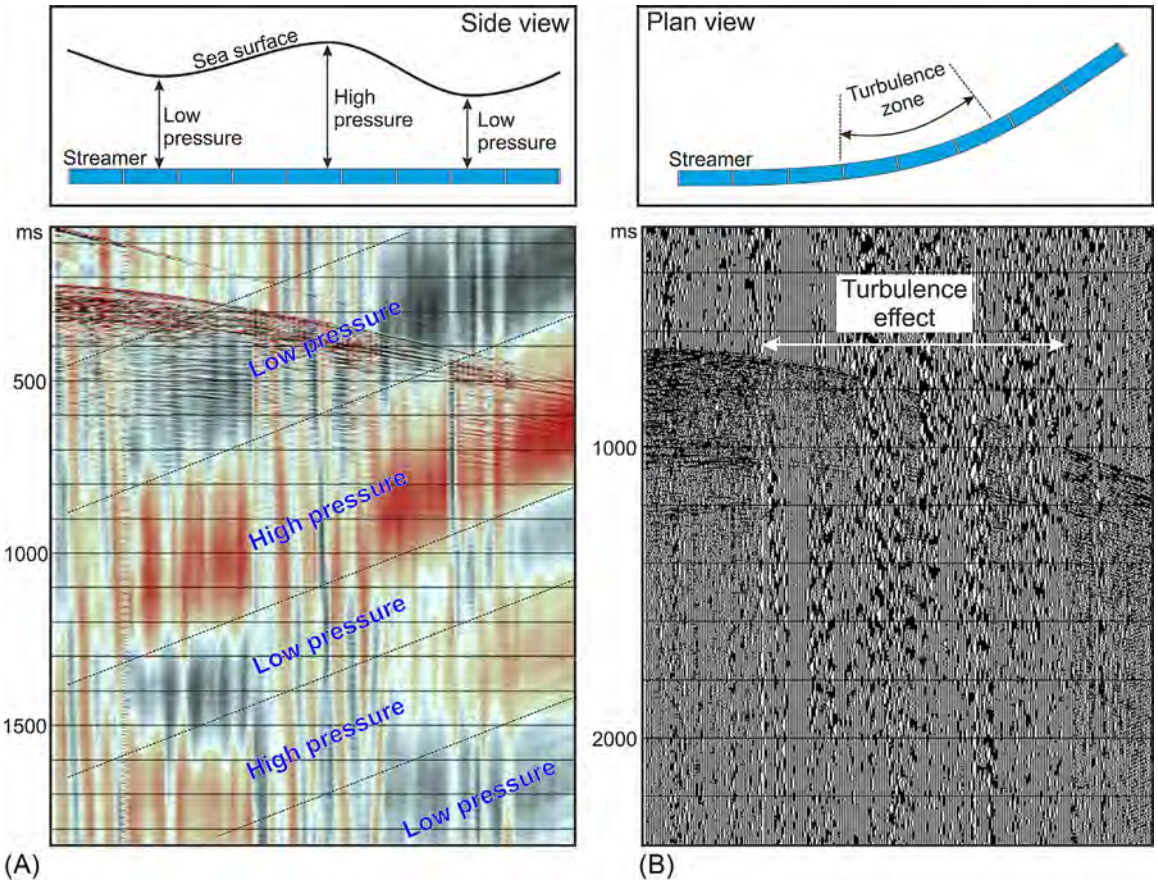


FIG. 3.10 Swell noise is formed by (A) wind-driven sea surface waves, and (B) turbulence effect of dynamic pressure fluctuations along the streamer. Their formation mechanisms are schematically illustrated in the upper panels.

a vertical high-amplitude noise band exactly at the recording channels where the streamer bends. As the vessel proceeds along the line, the channels with the swell noise band move gradually to the far offsets.

It is possible to reduce swell noise amplitudes by selecting suitable acquisition parameters. For instance, tow depth of the streamer can significantly affect the swell noise level in the data, because a deeper tow ensures acquisition in a quieter environment, since wind-driven swell noise activity is much stronger close to the surface. However, the frequency band of the recorded data is strongly dependent on the streamer tow depth because of the ghost signal interference producing notches in the amplitude spectrum (Section 2.5.1.2). The lower the tow depth, the wider the frequency band, and hence the higher the resolution, although this will induce higher swell noise in the data. Therefore, high-resolution seismic surveys are exposed more swell noise interference because of shallower streamer tow depths. In order to avoid turbulence effect of hydrostatic pressure

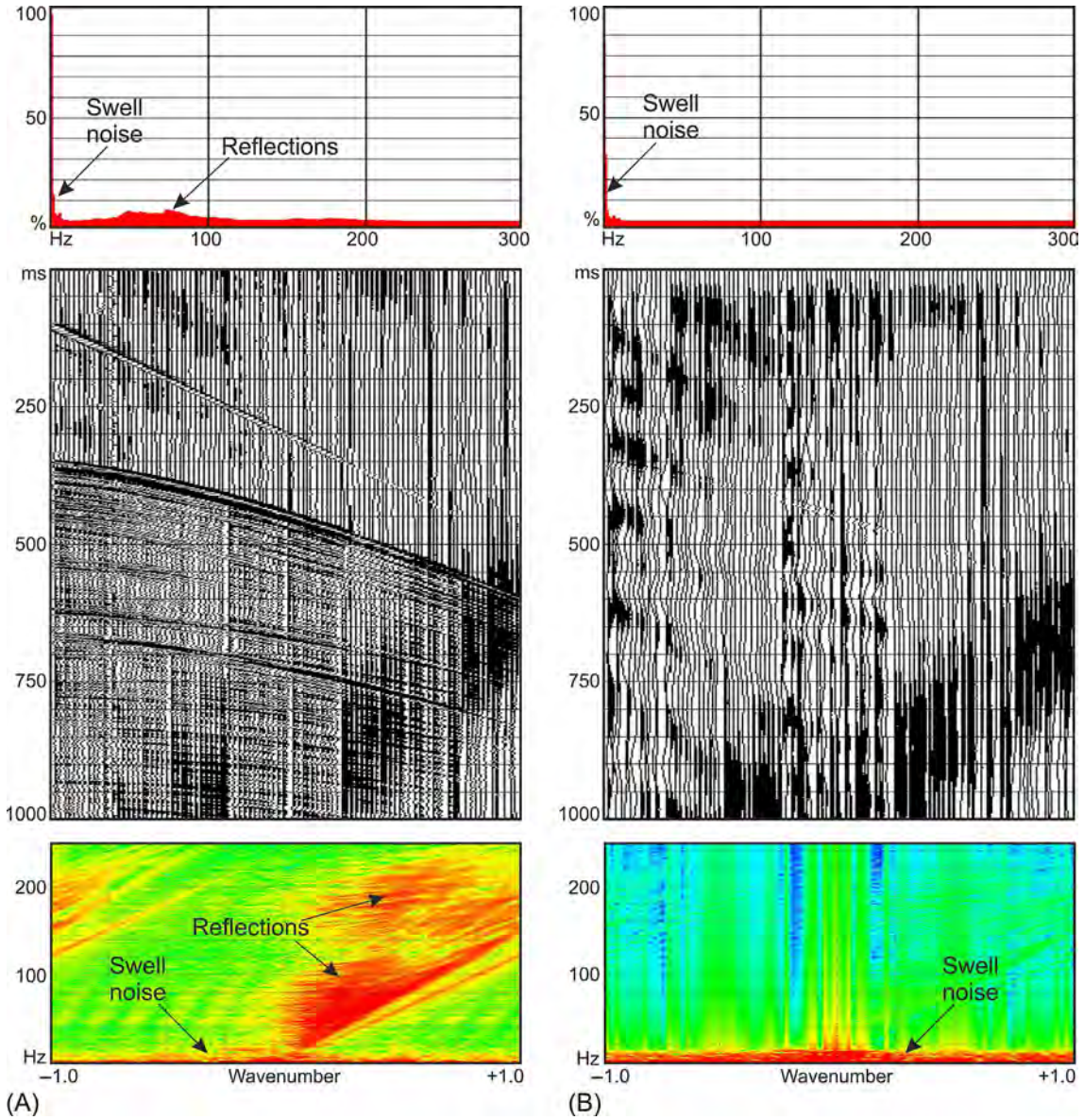


FIG. 3.11 (A) A raw shot gather with strong swell noise, and (B) its 14-Hz low-pass filtered version. Mean amplitude and *f-k* spectra are given in upper and lower panels, respectively.

fluctuations along the streamer, recording is not performed when streamer turns during the line changes, and run-in and run-out distance restrictions are applied (Section 2.5.1.9).

The conventional method to remove swell noise at the processing stage is the frequency domain discrimination of swell noise and reflections, which is based on the rejection of low

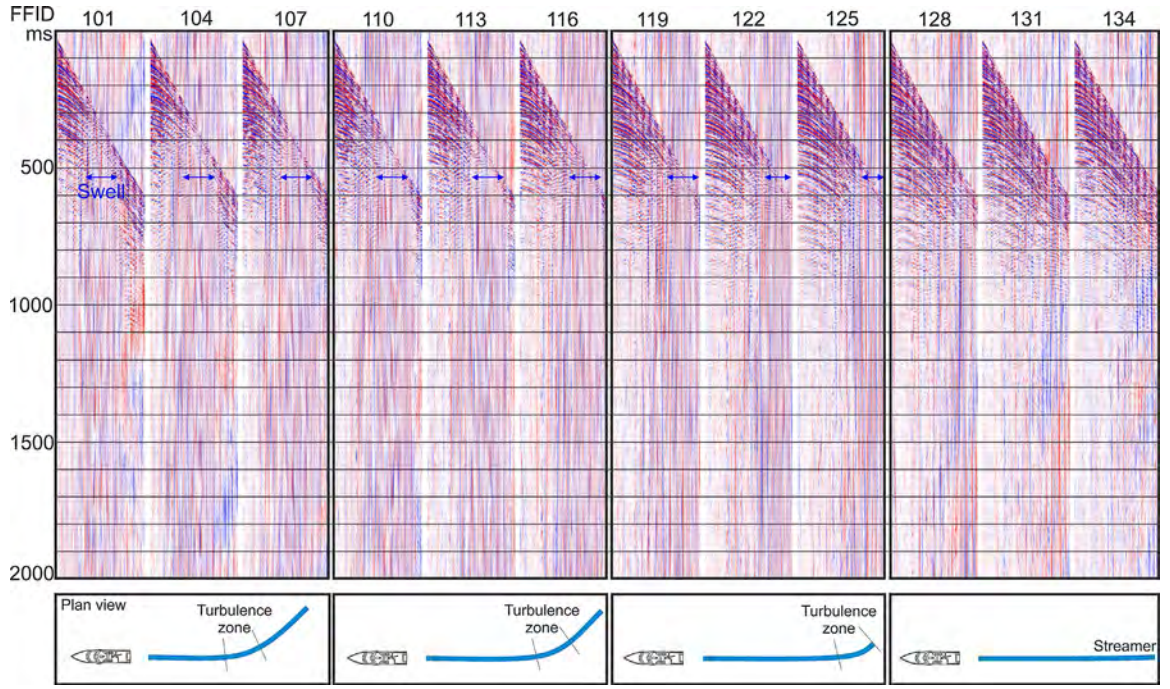


FIG. 3.12 Turbulence effect along the streamer formed by streamer turning during the line change. Bending of the streamer during the turn is schematically shown in the lower panels.

frequency band of the data by suppressing the amplitudes at approximately 0–15 Hz frequency band by applying a band-pass or an *f-k* filter. Fig. 3.13 shows application of a 14–180 Hz band-pass filter to remove swell noise on two successive shot records. Although band-pass filtering is very successful in swell noise suppression, it also results in a total loss of amplitudes from low frequency reflections which contain the amplitudes of deeper reflections. This issue becomes more important for high-resolution seismic surveys in which the seismic penetration is generally low, and low frequencies carry valuable information from deeper reflectors. Furthermore, a shallower streamer depth is preferred to keep the available frequency band wider, which ultimately causes higher swell noise induced in the data (Dondurur and Karslı, 2012).

3.5 BIRD NOISE

Devices known as birds are mounted onto the streamer at regular intervals (Section 2.1.5) to maintain the depth (for 2D surveys) and lateral positions (for 3D surveys) of the streamer. Fin angles of the birds are automatically modified by the control software whenever the depth of the streamer changes during the acquisition, to maintain the streamer at target depth level. The motion of the fins and the effect of water turbulence surrounding the birds during recording may induce noise on the shot records. Low frequency (approximately 30 Hz) bird noise appears at channels close to the birds along the streamer and it arises as high amplitude vertical bands on the shot records.

Fig. 3.14 schematically shows the RMS noise along the streamer, indicating that the noise levels

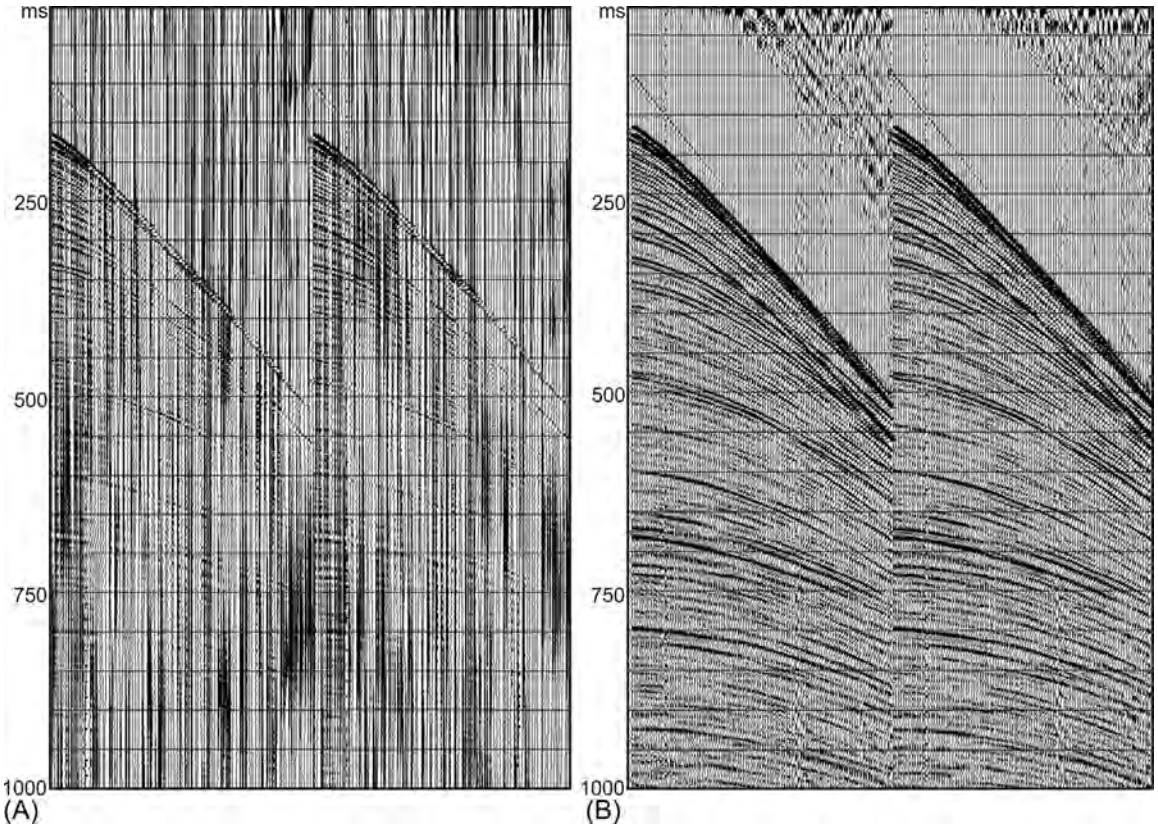


FIG. 3.13 (A) Two successive raw shot gathers with significant swell noise, and (B) after removal of the swell noise using a 14–180 Hz band-pass filter.

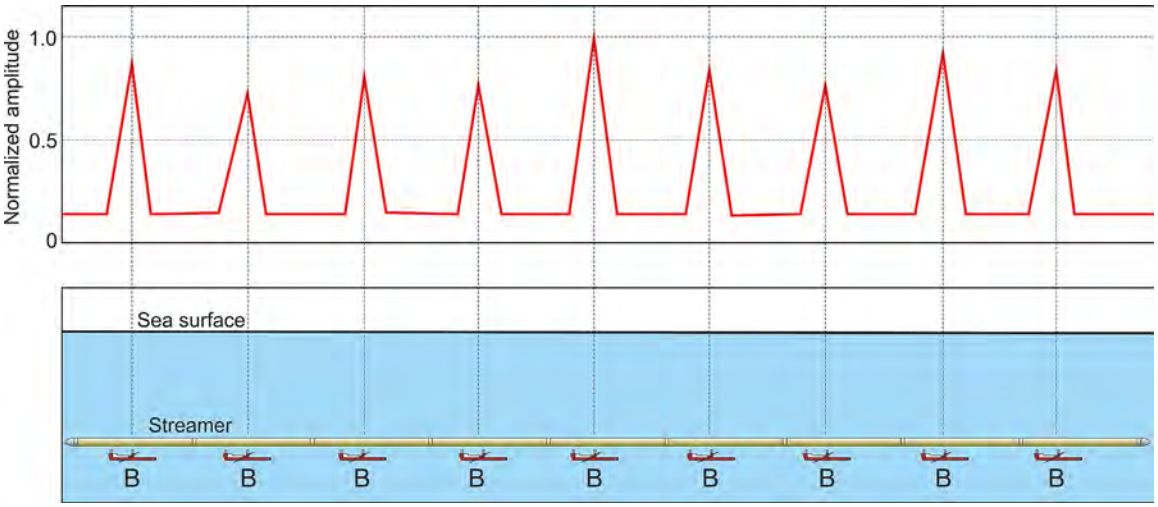


FIG. 3.14 Schematical illustration of the noise level along the streamer. RMS noise significantly increases at channels close to the bird (B) locations.

close to the bird locations are obviously three or four times higher than those at channels off the birds. Schoenberger and Mifsud (1974) manufactured a special streamer section with 20 hydrophones located 2.4 m apart and mounted a bird at the center of the section in order to observe how the bird noise spreads along the streamer. The result indicates that the bird noise is apparent only at nearby channels and is almost symmetrical. While close hydrophones (1.2 m apart) are quite noisy, they observed almost no noise amplitudes at the hydrophones located farther than 3.6 m from the bird location. Their analysis also provided information about the mechanism of the bird noise: Symmetry and rapid decay are not the characteristics of the turbulence effect from the water flow around the bird fins, which suggests that the bird noise is transferred onto the streamer and hydrophones by mechanical means.

Fig. 3.15A shows an example shot record with distinct bird noise appearing as vertical high-amplitude bands at the channels close to the bird locations indicated by arrows. Amplitude restoration processes, especially AGC, may significantly increase the amplitudes of the bird noise. Fig. 3.15B illustrates a shot gather filtered with an *f-k* filter to make the bird noise much more prominent. Bird noise can easily be recognized on *f-k* spectrum: The amplitudes come up as horizontal bands on the 2D Fourier spectra because they are seen as vertical bands on time sections (B in Fig. 3.15B).

Fig. 3.16A shows a shot gather with bird noise as vertical high-amplitude stripes. The *f-k* spectrum of the shot indicates that the bird noise has approximately 20-Hz frequency and it is seen as a horizontal band along the wavenumber axis. The *f-x* spectrum, which illustrates the frequency content of each trace separately, shows high amplitude vertical bands indicated by arrows around the dominant bird noise frequency. A suitable *f-k* polygon that accepts only reflection amplitudes in the *f-k* panel removes most of the noise arising from the birds (Fig. 3.16B). In addition to the band-pass or *f-k* filters, the most important contribution to eliminate the bird noise is supplied by the stacking process, which can remove almost all of the remnant bird noise from the data.

3.6 INLINE WAVES

The noise appearing as linear events with trace-by-trace consistency on the raw shot records is classified as inline waves. Raw seismic data may contain several linear events from different sources, such as

- Tail buoy noise
- Mechanical cable noise (tug and strum)
- Direct waves
- Refracted waves

3.6.1 Tail Buoy Noise

The far end of the streamers is determined by a tail buoy, generally with an rGPS transmitter (Section 2.1.8). Depending on the weather conditions, movement of the tail buoy may generate low-amplitude linear noise around the far offsets of the shot gathers. Its amplitude depends on the ocean surface conditions, and if the sea conditions are rough, the tail buoy may act as a seismic source, such that the generated signal propagates from far to near offsets along the streamer. Therefore, tail buoy noise is observed at far offsets as events with linear but reverse-dip continuous amplitudes on the shot records (Fig. 3.17). Its form does not change with the tow speed for 4–8 knots range, and its frequency band is rather low and is around 20 Hz.

A reasonable way to avoid tail buoy noise during the acquisition is to tow the buoy as far as possible from the last active section of the streamer. The tail buoy noise has reverse dip on the shots, hence its amplitudes appear in negative panel on the *f-k* spectrum, and therefore it is generally easy to remove this noise using a suitable *f-k* filter.

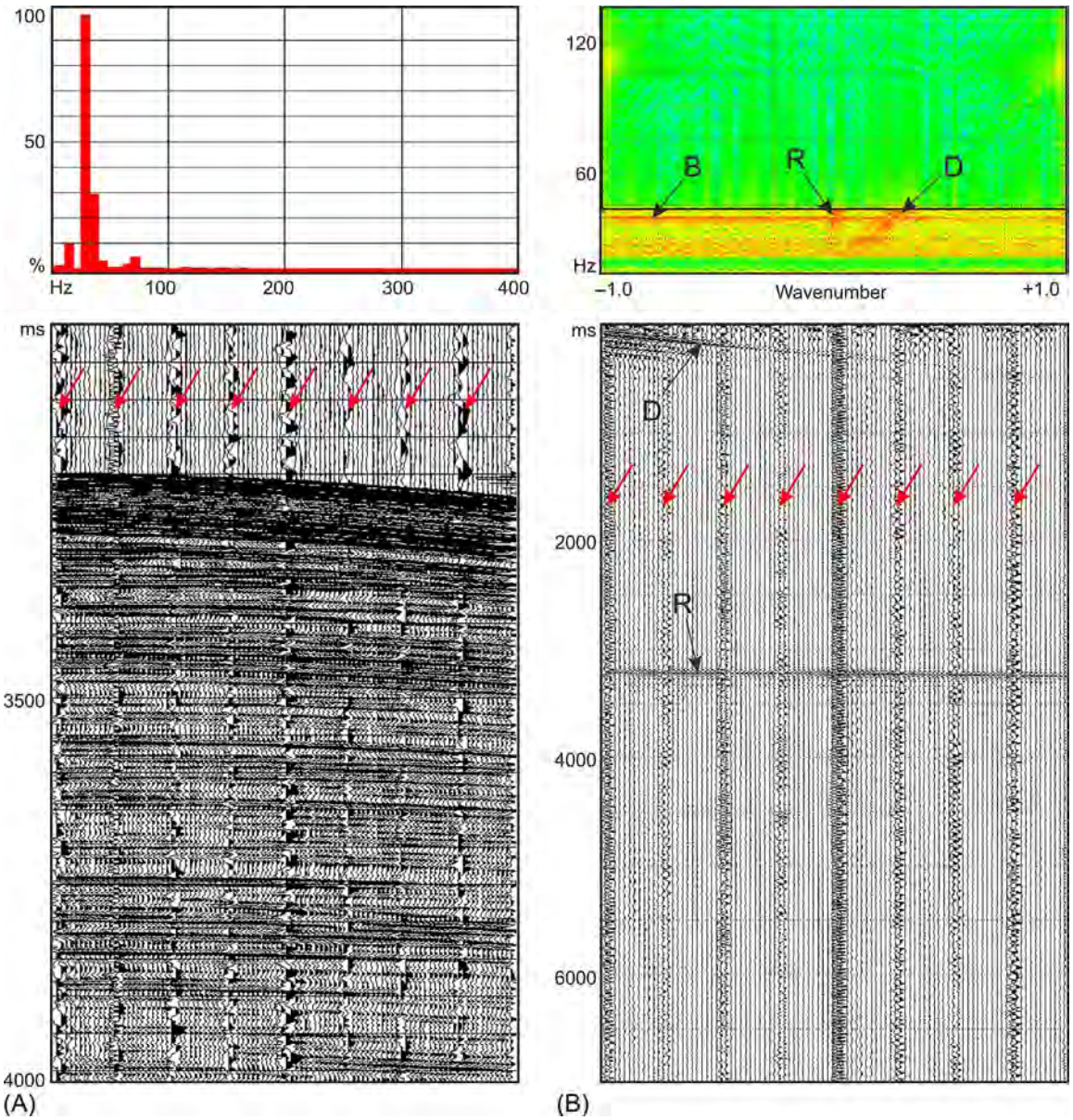


FIG. 3.15 (A) Bird noise *(red arrows)* on a band-pass filtered shot gather along with its amplitude spectrum (upper panel). (B) An example shot gather filtered with an *f-k* filter to make the bird noise *(red arrows)* more clear (upper panel is its *f-k* spectrum after filtering). *R*, seabed reflection; *D*, direct wave; *B*, bird noise.

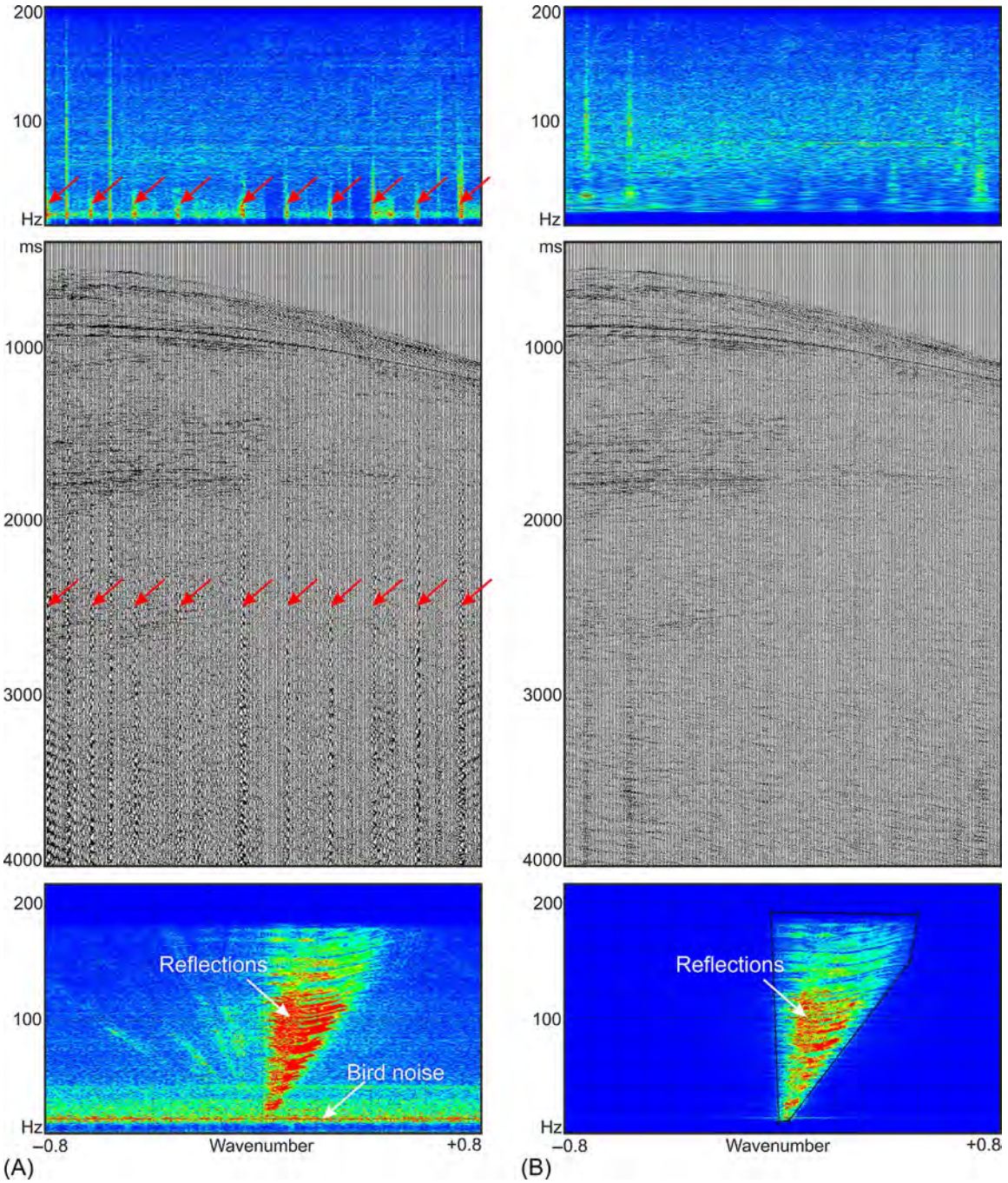


FIG. 3.16 A filtered shot gather with significant bird noise *(red arrows)*. (A) Before and (B) after application of an *f-k* filter. The *f-x* and *f-k* spectra of the input and output shots are given in the upper and lower panels, respectively.

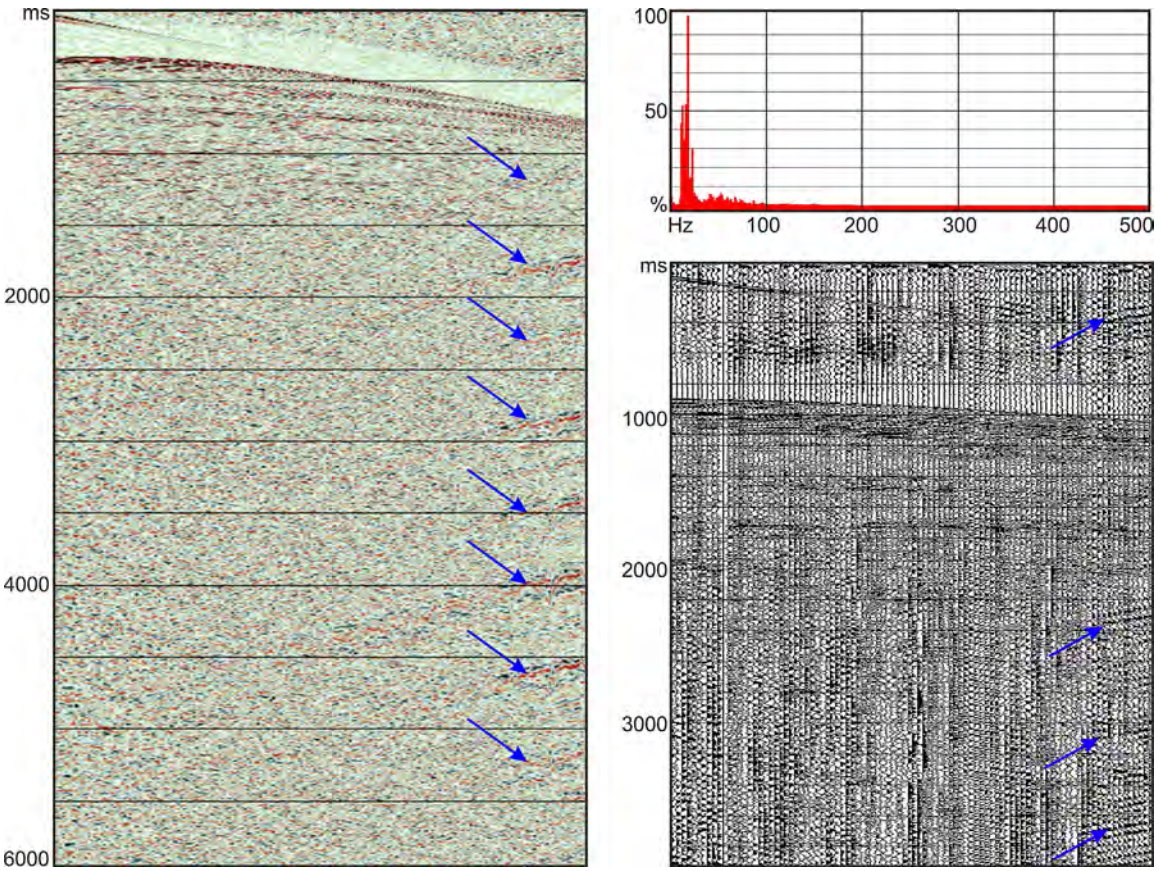


FIG. 3.17 Tail buoy noise at the far offsets of two different shot gathers *(blue arrows)* and amplitude spectrum of the noise.

3.6.2 Mechanical Cable Noise

Towing of the streamer behind the seismic vessel during the acquisition induces a specific linear noise on the data termed mechanical cable noise. It occurs due to the effect of stretch tensile of both vessel and tail buoy on the streamer during the tow, and is linear coherent noise with moderate to high amplitudes on the raw shot gathers. The cable noise becomes more distinctive at the late arrivals where the amplitudes of the primary reflections are relatively low.

Mechanical cable noise is typically considered tug and strum noise, for far-to-near offset and near-to-far offset directions, respectively. These arise from the vibrations of lead-in cables in 2D surveys and spreader cables used for lateral separation of the streamers in 3D surveys, because of the tugging and strumming from the survey vessel, paravanes, lead-in cables or tail buoys. Their amplitude and frequency are relatively low as compared to the genuine reflections, typically in the range of 3–10 Hz. In order to reduce the amplitudes of tug and strum noise, fairings are used on all lead-in and spreader cables (Section 2.1.9), which are the structures attached to the tow cables to streamline the flow around the cable during the tow. Tug and strum noise amplitudes are 3–9 dB lower in case of faired lead-in cables for whole frequency range.

Fig. 3.18 shows two filtered shots with linear cable noise and amplitude spectrum of the noise, which appears at a dominant frequency of approximately 20 Hz. Directions of these events on the shot gathers are from near to far offsets for tensile originating from the vessel, and vice versa from the tail buoy. Both events may form a diagonal cross appearance with several parallel events on the shot gathers (Fig. 3.18B).

The propagation velocity of linear mechanical cable noise, calculated from the seismic data, ranges from 1200 to 2400 m/s. The velocity of the events in Fig. 3.18B is approximately 1900 and 2200 m/s for positive (from near to far

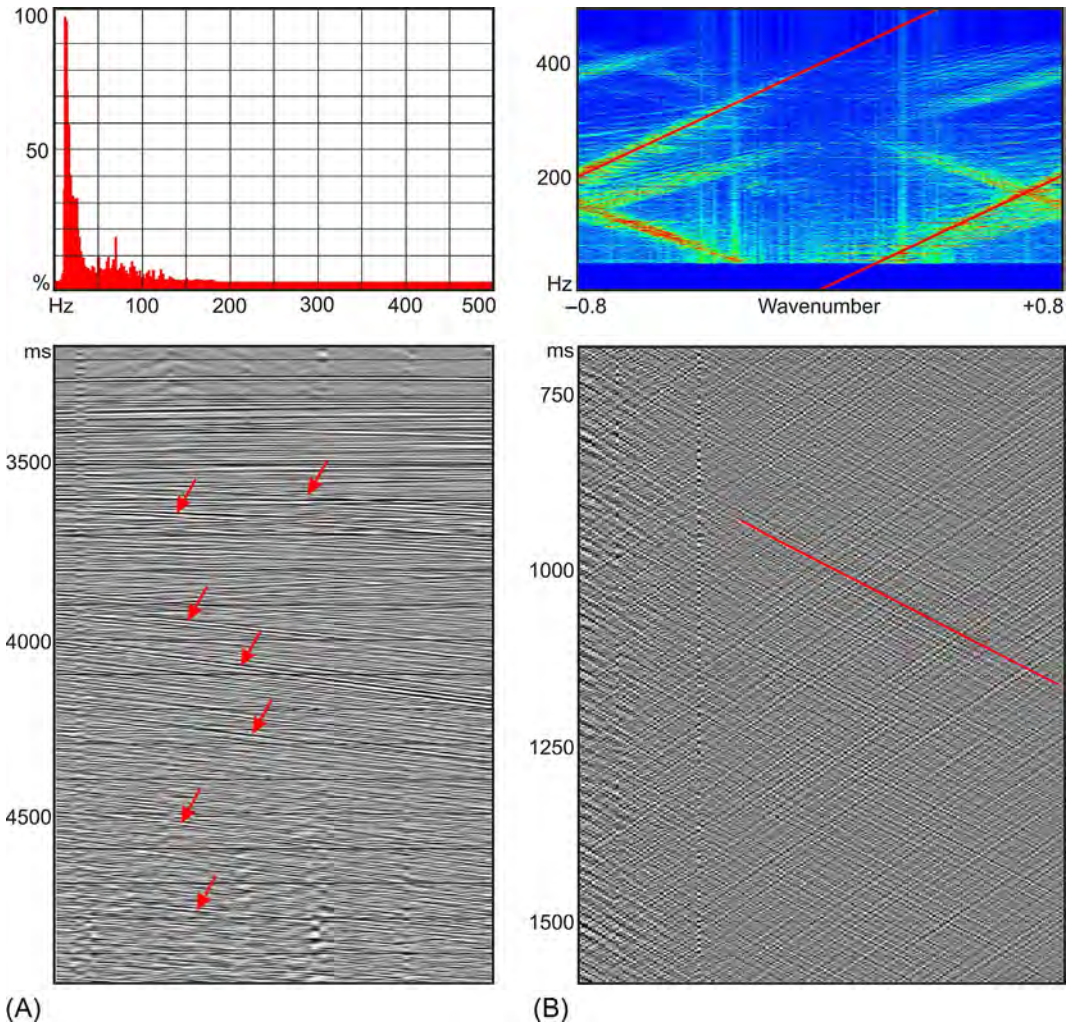


FIG. 3.18 (A) A filtered shot gather with linear cable noise *(arrows)* with its amplitude spectrum (upper panel), (B) late arrivals of another example shot and its *f-k* spectrum (upper panel). The *red line* indicates a selected linear event on the shot gather and its corresponding amplitudes on the *f-k* spectrum.

offset) and negative (from far to near offset) dips, respectively. The amplitude of the cable noise is dependent on the weather conditions, tow speed, balance of the streamer in the water, efficiency of the stretch sections at both ends of the streamer, and concordance between lead-in cable and active sections (Larner et al., 1983). Application of too much gain or usage of unnecessarily low AGC operator lengths may increase the amplitudes of the cable noise.

The amplitude of the noise is proportional to the third order of the vessel speed, and if the vessel speed is doubled, S/N decreases with a ratio of 1/11. On the contrary, if we decrease the tow speed on the order of 18%, then the S/N will be doubled (Schoenberger and Mifsud, 1974), which indicates that high tow speeds are not practical for seismic acquisition. Noise test results obtained at 5.3 and 8.6 knot speeds using a streamer with no birds deployed show that noise amplitudes do not increase or decrease with the distance to the tow point, but they exhibit rather regular distribution along the streamer, which suggests that the noise is produced in a continuous manner within the streamer. In addition, the frequency content of the noise does not change significantly with the tow speed and only absolute amplitude increases (Schoenberger and Mifsud, 1974).

The amplitude of the cable noise depends strongly on the vessel speed and it is significantly reduced by collecting the data with an optimum tow speed. One can use *f-k* filters to remove the cable noise during the processing stage, because they are linear on the raw shot records, especially those with negative dip on the shots. During the *f-k* filtering for the positive dip cable noise, however, extra attention should be paid since their dip may coincide with those of the primary reflection amplitudes, particularly at far offsets where the reflection hyperbolas becomes relatively linear. Fig. 3.19 shows an example removal of the mechanical cable noise by an *f-k* filter. The *f-k* panel in Fig. 3.19A indicates that the shot involves moderate amplitude cable noise in negative dip and relatively low amplitude in positive dip. An application of an *f-k* filter with a suitable *f-k* polygon almost completely removes cable noise from the data (Fig. 3.19B).

3.6.3 Direct Waves

Direct waves propagate horizontally along the sea surface from the source to hydrophones and are recorded by whole available channels, and they are always the first arrivals at each channel. Because they travel only in the water column, their propagation velocity always equals to the P wave velocity in the sea water (approximately 1500 m/s). Their amplitude diminishes with increasing offset: It is maximum for the very first recording channel while minimum amplitude is recorded at the farthest one.

Fig. 3.20 shows direct waves on two filtered shot gathers recorded at water depths of 90 and 180 m, respectively. As the water depth increases, the time between seabed reflection and the direct wave increases at all offsets. In fact, direct wave is an asymptote to the seabed reflection merging at infinite offset. Minimum offset distance in the source-streamer layout can be verified using the arrival time of the direct wave at the first channel of the streamer. By using the inclination of direct waves on the shot or CDP gathers, it is possible to obtain P wave velocity along the surficial waters, which is a crucial parameter for some multiple elimination methods.

It is not possible to avoid recording direct waves during the acquisition. However, they always appear before the seabed reflection hyperbola, which is the first meaningful signal carrying primary reflection information from the seabed, and since direct wave is an asymptote to the seabed reflection, they theoretically never interfere. Therefore, the direct waves are generally not problematic for reflection seismic studies and they can be eliminated using a

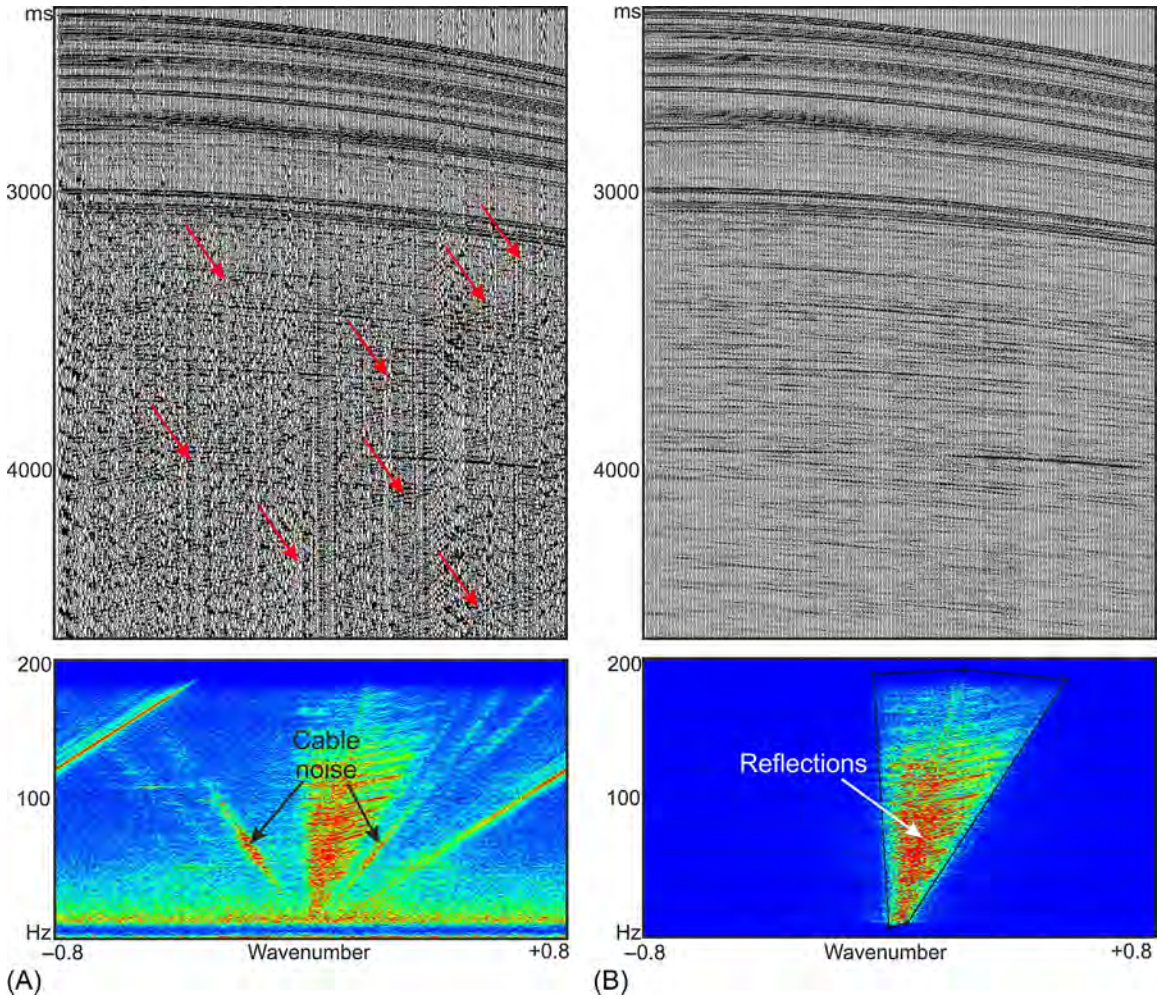


FIG. 3.19 Example *f-k* filter application to remove mechanical cable noise. (A) A filtered shot with cable noise in both positive and negative dip *(arrows)*, and (B) shot record after *f-k* filter. Corresponding *f-k* domain representations are given in the lower panels.

simple top mute, which zeroes out all amplitudes before the seabed arrival time (Section 5.8). If not muted out, they may complicate the velocity semblance contours and it may not be easy to determine seabed reflection velocity, especially in shallow waters. In addition, an effective method, SRME (Section 7.7) requires direct waves to be removed from the shots by muting to efficiently suppress the multiples.

3.6.4 Refracted Waves

Refractions or head waves travel horizontally in the subsurface sediments and reach the receivers after they are refracted. They travel with the velocity of subsurface sediment units and hence they always have higher velocity and lower dip than direct waves on the shot records (Fig. 3.21), and they carry velocity

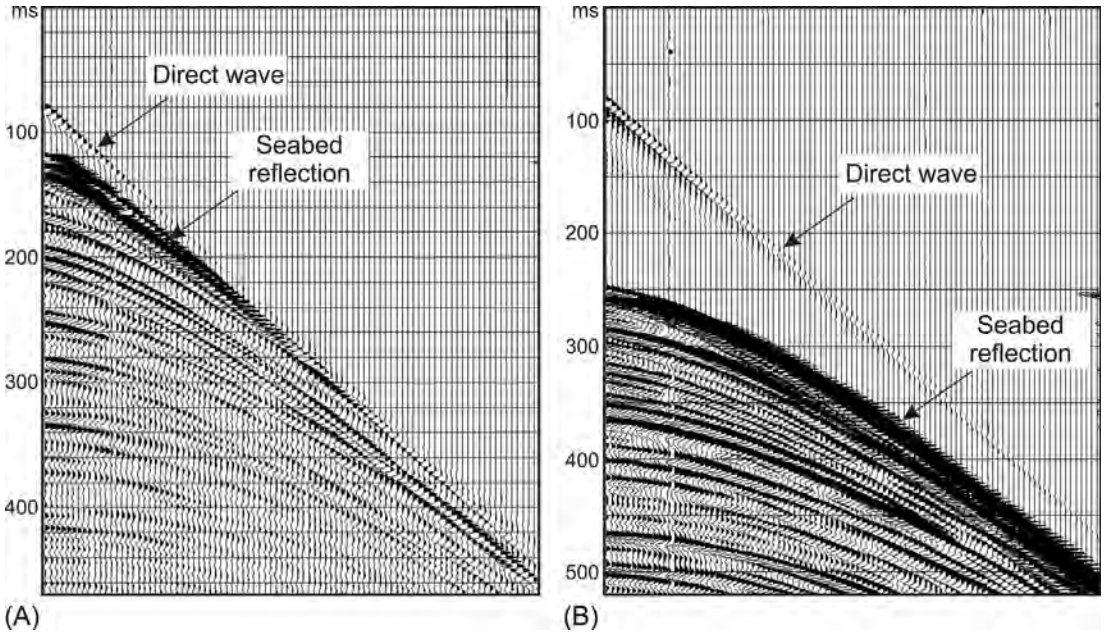


FIG. 3.20 Direct waves on two filtered shot gathers recorded at water depths of (A) 90 m and (B) 180 m.

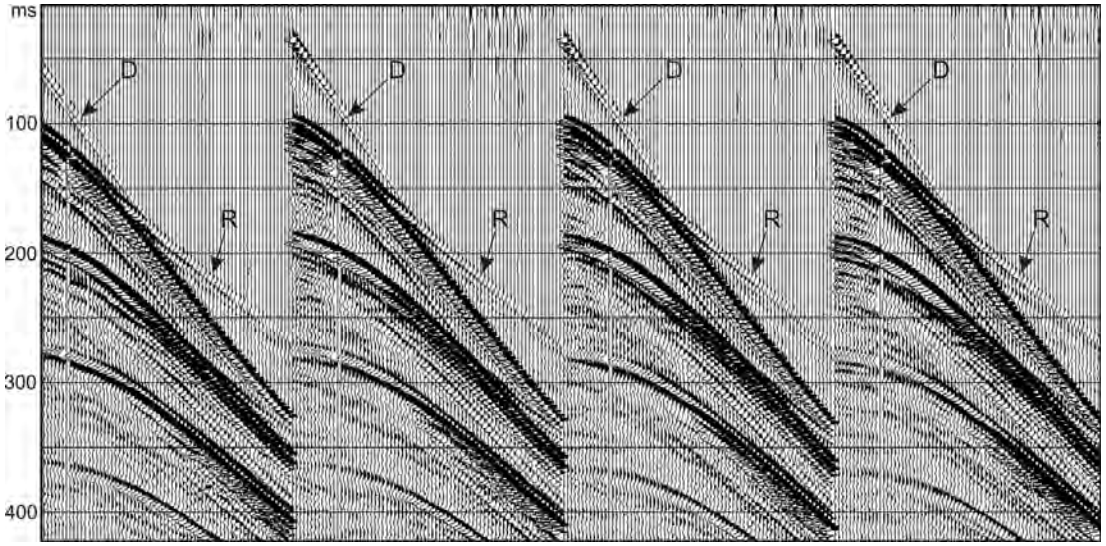


FIG. 3.21 Example of successive shot records showing direct (D) and refracted (R) waves.

information of the topmost sedimentary unit. Relatively long offsets are required to record refracted waves, since it is necessary for them to refract, to travel horizontally, and to refract again to arrive at the streamer (Section 1.3.3). Therefore, they can be observed at relatively shallower waters with longer streamers. They always appear before the seabed reflection hyperbola like direct waves and can be removed by a top mute (Section 5.8).

3.7 DIFFRACTIONS

Diffractions occur either from irregular seafloor morphology or suddenly terminated subbottom layers. These irregularities act as point diffractors with various sizes and the waves diffracted from these points produce diffraction hyperbolas on the shot records and stack sections (Fig. 3.22). These hyperbolas have extremely high normal moveout times on the shot and CDP gathers. Similar diffraction hyperbolas are also obtained from suddenly terminated layers, such as at fault planes or pinch-outs. Therefore, fault planes on the nonmigrated stack sections are characterized by a series of diffraction hyperbolas. These hyperbolas can be completely removed by a suitable migration algorithm, which sums up the diffraction energy to the apex point providing that a correct velocity field for whole seismic line is known (Chapter 11).

3.8 GUIDED WAVES

Guided waves travel horizontally in the subsurface sediments like refracted waves and reach to the receivers after they are reflected repeatedly in the water column; therefore, they are also termed refracted reflections. This type of wave has dispersive character such that different frequency components propagate with different velocities. Low-frequency components

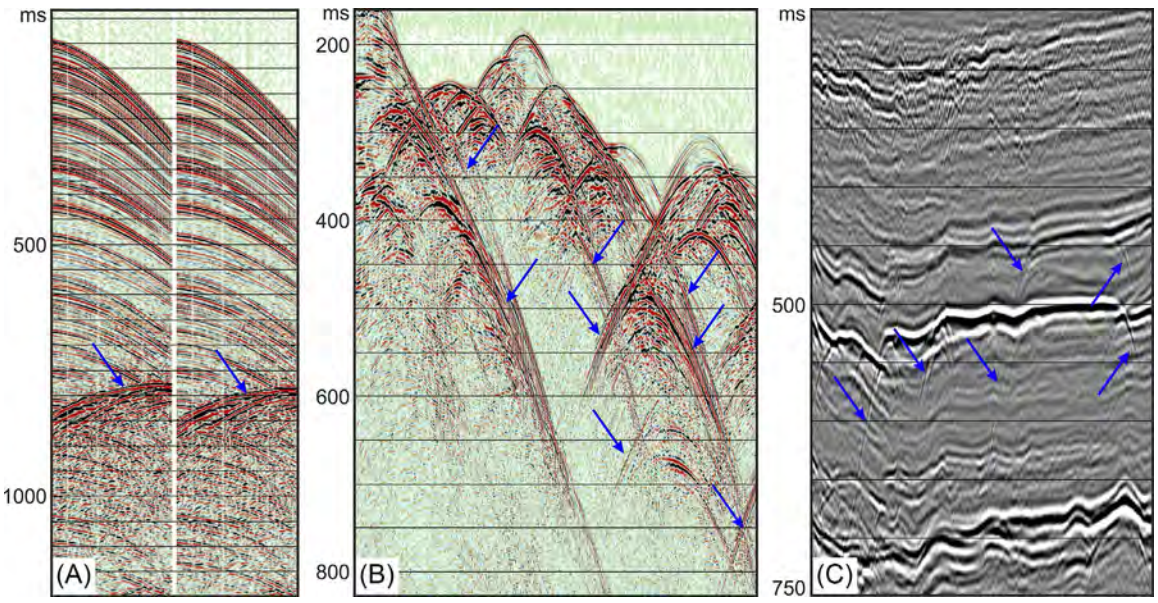


FIG. 3.22 Diffraction hyperbolas *(blue arrows)* on (A) a shot gather, and stack sections originating from (B) gullies and (C) faults.

typically have higher velocities, and therefore they arrive at the receivers much earlier than high frequency components, hence, they exhibit lower dips on the shot records.

Guided waves generally arise at shallow waters where a hard seafloor exists, and are sometimes very strong at early arrivals of far offset traces lying parallel to the head waves. Fig. 3.23 shows an example shot record with extremely strong guided wave interference and its ray path. In this case, the noise makes the far offsets of early arrivals completely useless. Fig. 3.24 shows an *f-k* analysis of a shot record contaminated by strong guided wave amplitudes. The *f-k* panel in Fig. 3.24A suggests that the guided waves have a frequency band between 20 and 150 Hz, which is clearly in the frequency band of the primary reflections. This situation implies that it is not possible to suppress the guided waves by a simple band-pass filtering.

Guided waves can be significantly attenuated during stacking, and because they are linear on the shot gathers, a τ-p transform (slant stacking, Section 4.9) can be applied to discriminate and suppress their amplitudes. Fig. 3.25 shows an analysis of guided waves in τ-p domain. On τ-p gathers, guided waves are aligned along a narrow vertical band around the p value determined by their dip on the time section (Fig. 3.25B). If this narrow zone is muted out in the τ-p domain (Fig. 3.25C), guided wave amplitudes are significantly removed in the time domain after an inverse τ-p transform (Fig. 3.25D). Although τ-p transform, trace mixing and *f-k* filters may be effective in suppressing the guided waves, sometimes it is not possible to completely remove them from the seismic data

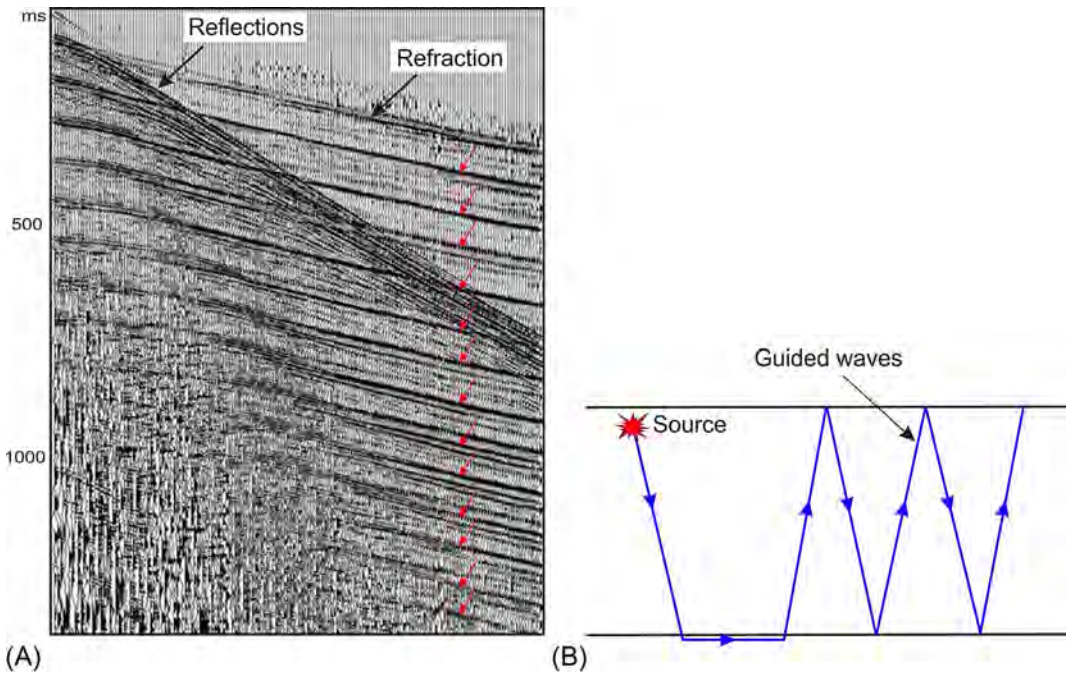


FIG. 3.23 (A) An example shot record with strong guided wave interference *(red arrows)* in early arrivals of far offsets, and (B) the ray path of a guided wave.

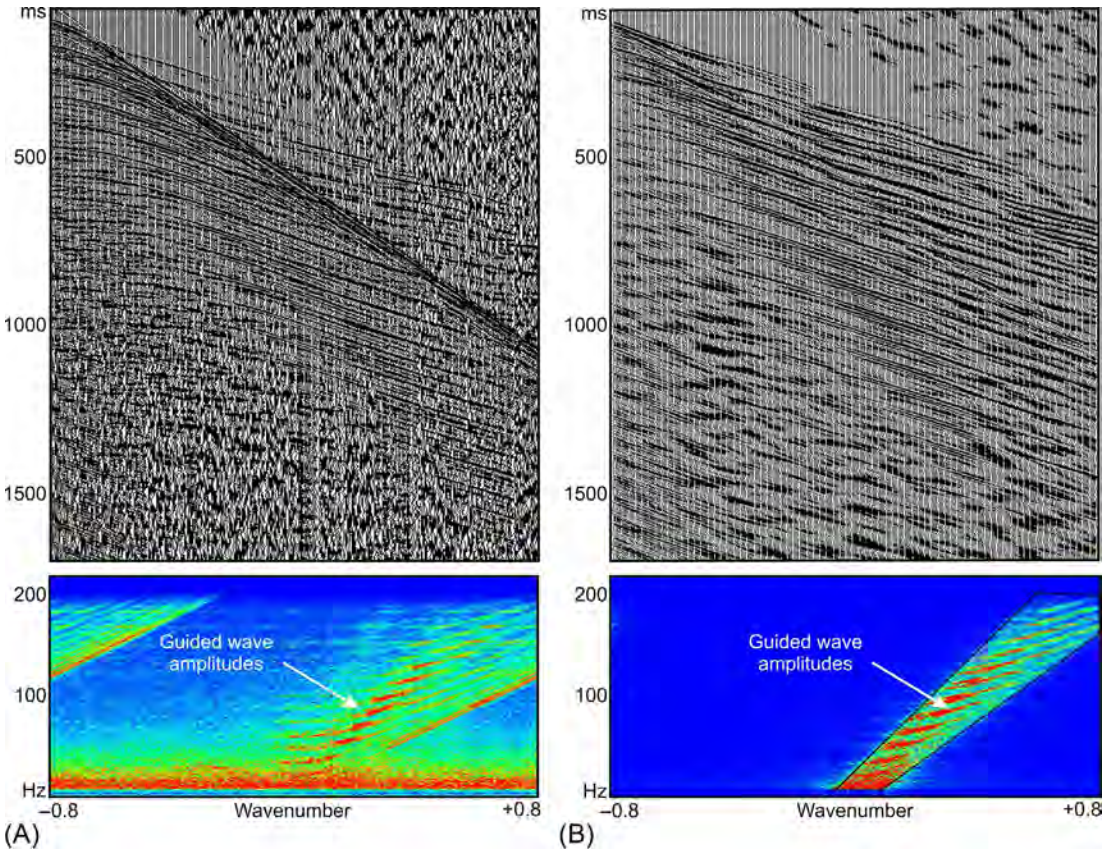


FIG. 3.24 (A) A shot record with strong guided wave amplitudes along with its *f-k* spectrum (lower panel), and (B) same shot after *f-k* filter to make the guided waves clearer.

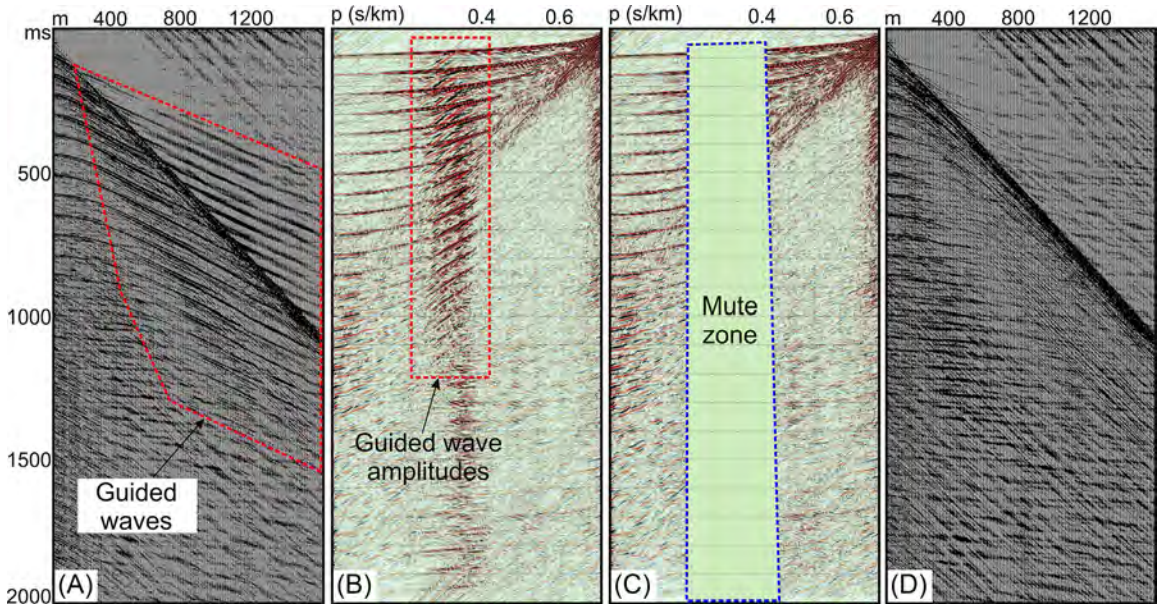


FIG. 3.25 Analysis and suppression of guided waves by τ-p transform. (A) A band-pass filtered shot gather with guided waves, (B) τ-p transform of the shot gather, (C) muting out of guide wave amplitudes, and (D) same shot gather after inverse τ-p transform.

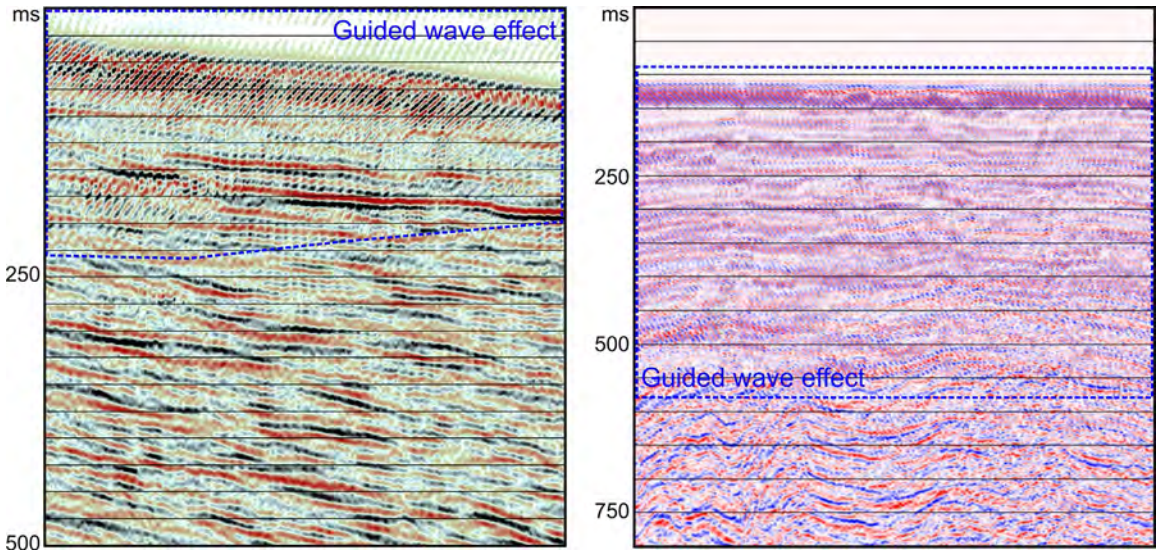


FIG. 3.26 Two stack sections with guided wave effects (*dashed blue polygons*).

using these prestack processing techniques. Fig. 3.26 shows two different stack sections contaminated with strong guided wave effect in their shallow parts, consisting of very steep discontinuous line segments. In such cases, the only way to remove them is to mute out the guided waves from shots using a surgical mute.

3.9 SEISMIC INTERFERENCE

Seismic interference from other seismic vessels shooting close to the survey area may be an important issue during the acquisition. Since seawater is a very good conductor for elastic waves, the echoes from large air gun arrays used by the oil and gas industry today can be perceived by the hydrophones from several tens of miles away from the seismic source. This type of seismic interference has very good trace-by-trace consistency on the shot records, and appears at regular time intervals on the shot records, depending on the shooting rate at the source of noise. Its shape varies with the distance between receiving streamer and source of interference. If the source is close enough to the receiving streamer, the interference signal has a hyperbolic moveout. If it is located at a long distance, then we observe the interfering signal as linear events. In shot gathers in Fig. 3.27, the interference, possibly originating from a boomer source, has a linear moveout since source is located at a very long distance away from the receiving streamer. The time between the successive interference signals is 1.6 s. After shot number 109, shooting at the recording vessel was stopped because of the strong interference, but the recording continued to see the character of the interfering noise. Between shots 110 and 114, records show only the interference signal.

In tectonically active regions, such as at subduction zones, a special case of seismic interference may be local earthquakes, appearing as strong coherent events on the shot records; they are usually removed by muting. Fig. 3.28, shows an interesting example of an earthquake interference on a 3D shot record group consisting of eight streamers. The interference is so strong that the records are considered to be bad shots and should be edited during the processing stage.

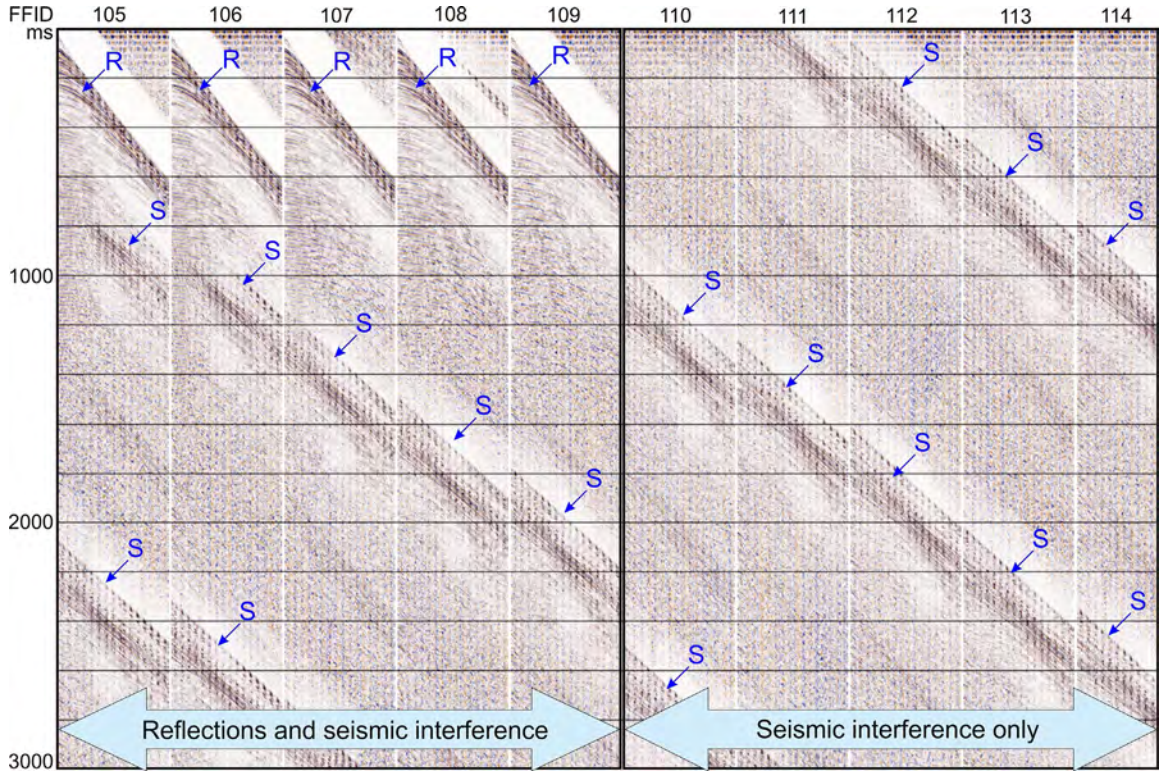


FIG. 3.27 A number of successive shot gathers including extreme seismic interference with linear moveout. Between the shot numbers 105 and 109, the records consist of both primary reflections (R) and interference noise (S), whereas records show only the interference signal between shots 110 and 114.

Fig. 3.29 shows spectral analysis of an example shot record with strong linear seismic interference in positive dip (from near to far offset traces). The mean amplitude spectrum of the input shot in Fig. 3.29A indicates that the data with primary reflections and seismic interference have a spectral bandwidth between 10 and 160 Hz. According to the *f-k* panel of the input shot record, we are lucky enough to discriminate the genuine reflections and seismic interference amplitudes in the *f-k* domain, because the gather is from relatively deep waters and the curvatures of the primary reflection hyperbolas are quite low with respect to the dip of the interference signal, which ultimately results in the amplitudes from reflections and interference being accumulated in different parts of the *f-k* panel since they both have different dips in the shot gather. Fig. 3.29B shows the same shot with application of an *f-k* filter to cause the shot has only interference signal. Fig. 3.29C illustrates the same shot after an *f-k* filter applied to remove the interference, and its mean amplitude spectrum indicates that the frequency band of primary reflections perfectly coincides with that of the interference signal shown in the upper panel of Fig. 3.29B.

Depending on the strength of the source array, sometimes it may not be possible to

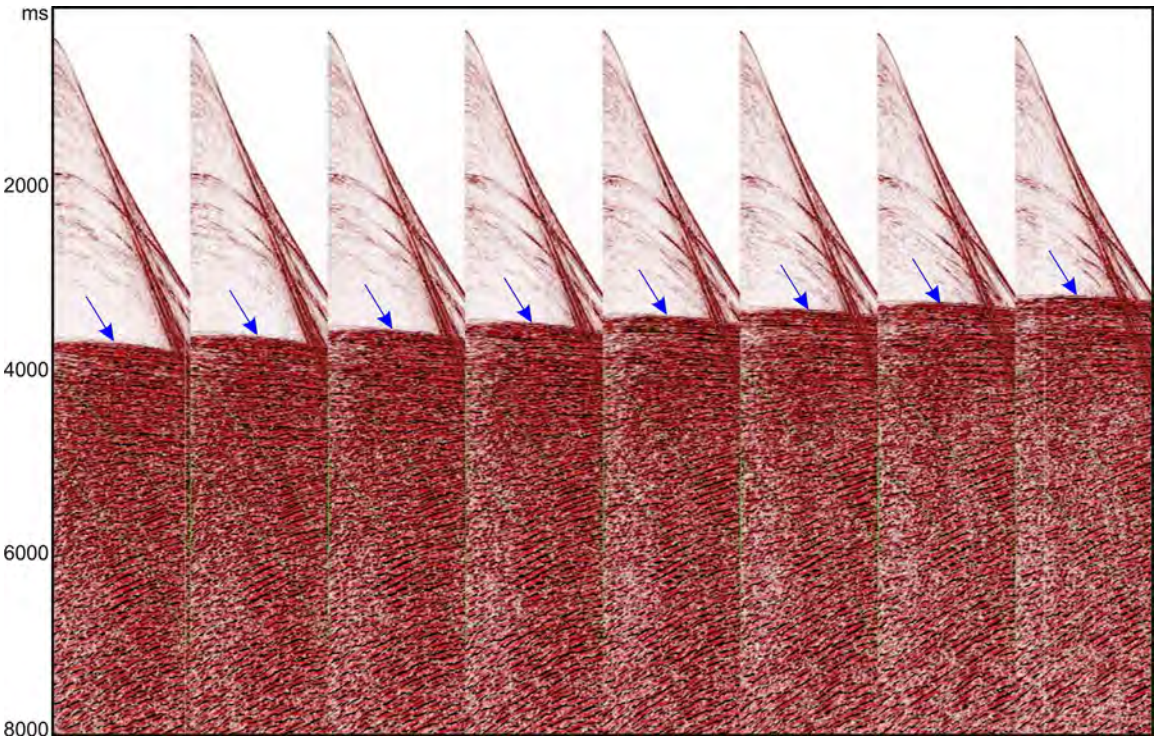


FIG. 3.28 An example 3D shot record group of eight streamers with strong earthquake interference *(blue arrows)*.

remove the seismic interference from the data completely. If the stack section is obtained without applying a suitable prestack technique for the seismic interference suppression, its effect cannot be removed by stacking itself and the interference appears as linear stripes with extremely high inclination on the stack sections (Fig. 3.30). They are much clearer in deeper parts of the section where the amplitudes of the genuine reflections are relatively weaker.

The direction where the interference signal is transmitted has remarkable importance in the removing process of the noise. Fig. 3.31 shows three possible situations for the source location responsible from the interference with respect to the receiving streamer:

(i) The noise source is behind the receiving streamer (Fig. 3.31A). The interference signal extends from far to near offset traces. This is the most favorable situation in a removal process because the reflection hyperbolas and the interference signal have opposite dips on the shot gathers, which allows us to eliminate the interference with a suitable *f-k* filter or a τ-p filter.

(ii) The noise source is at one side of the receiving streamer (Fig. 3.31B). The interference signal is of generally hyperbolic moveout depending on the length of the receiving streamer and extends to all offsets. According to the shape and moveout of the interference, it may or may not be possible to remove the noise using conventional processing techniques.

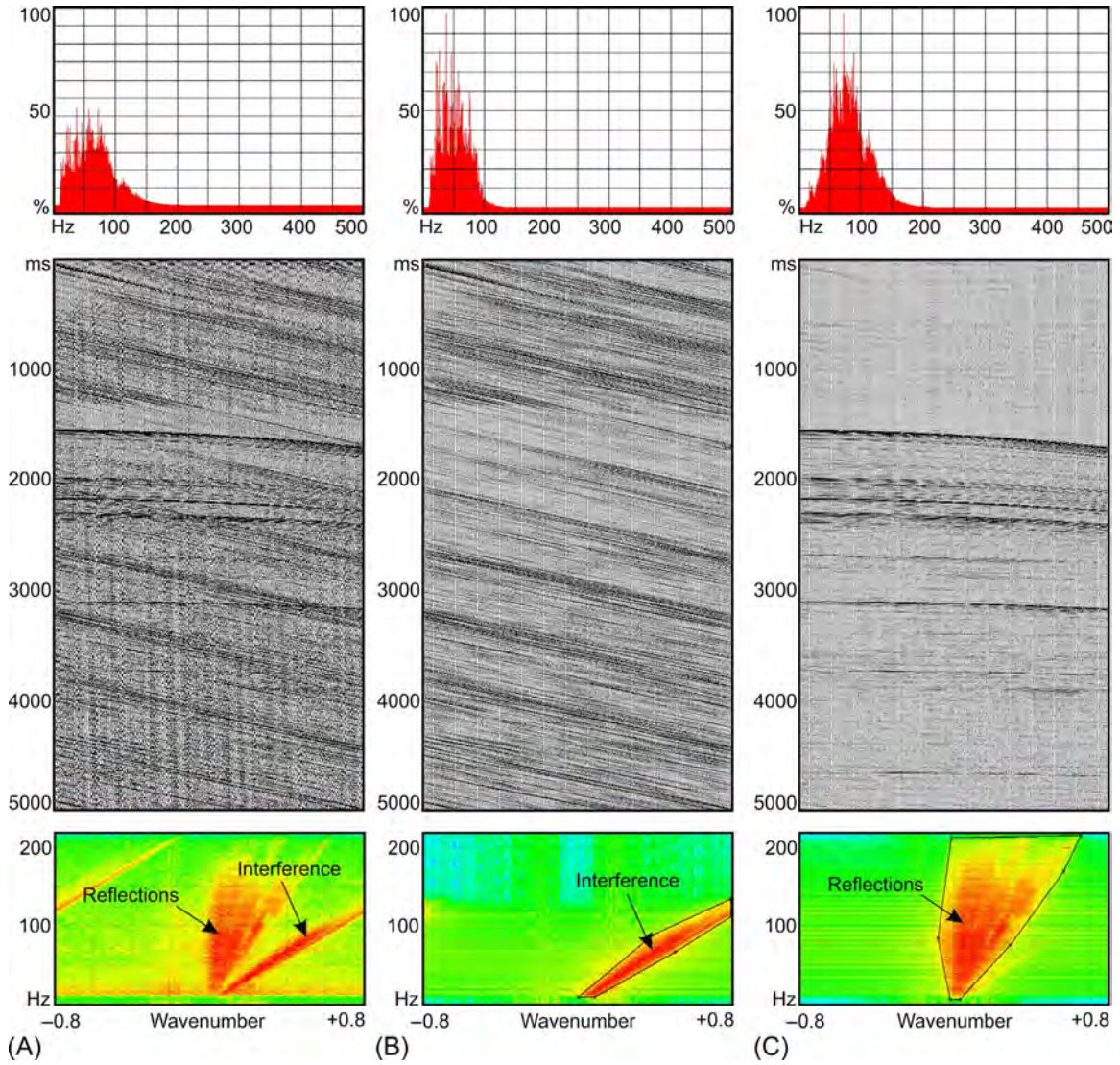


FIG. 3.29 Spectral analysis of a shot with seismic interference. (A) Filtered shot gather together with interference and primary reflections, (B) *f-k* filtered shot to indicate only the interference signal, and (C) primary reflections after removal of the interference with an appropriate *f-k* filter. Mean amplitude and *f-k* spectra of each gather are given in the top and bottom panels, respectively.

(iii) The noise source is in front of the receiving streamer (Fig. 3.31C). The interference signal extends from near to far offset traces. This is the worst situation in a removal process because the reflection hyperbolas and the interference signal have the same dip on the shot gathers. In this case, it may not be possible to filter out the interference completely.

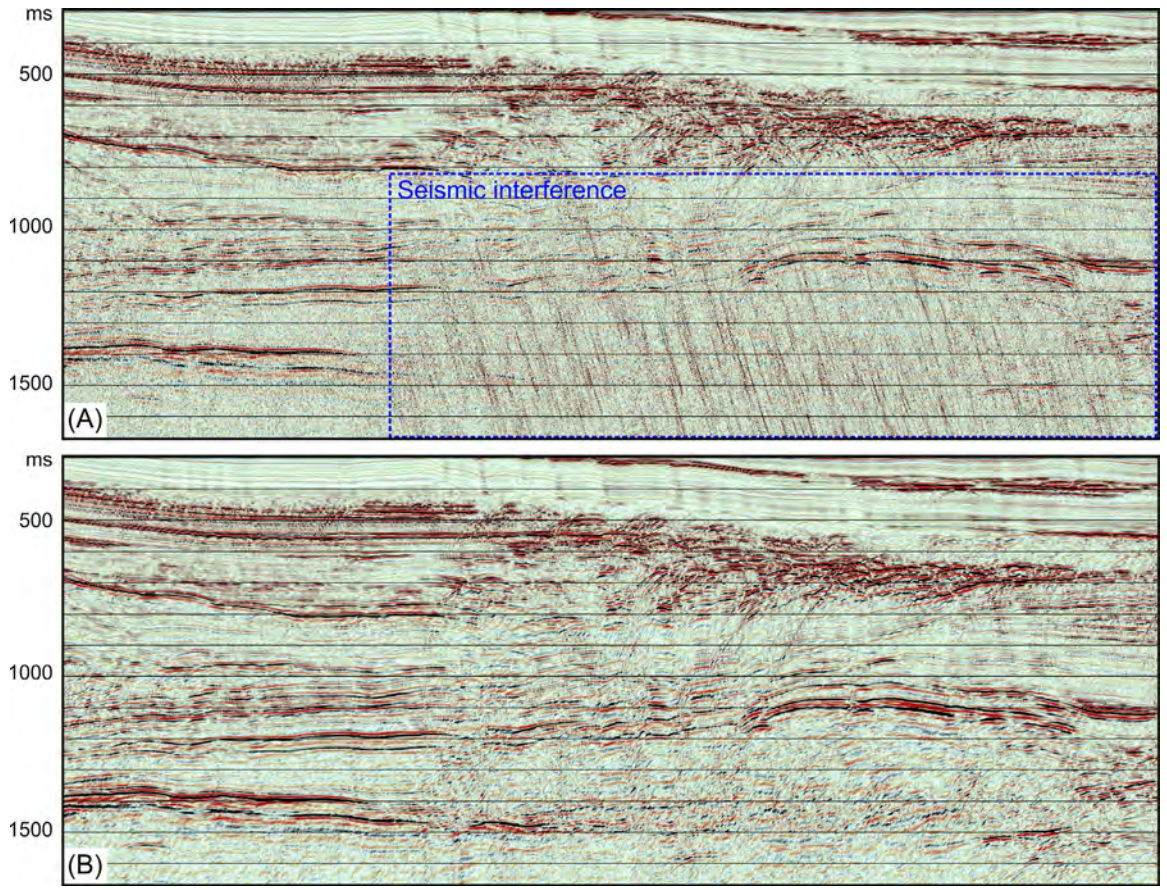


FIG. 3.30 (A) A stack section obtained without seismic interference removal, and (B) the same section after prestack suppression of the interference using *f-k* filtering.

3.10 OTHER NOISE TYPES

3.10.1 Powerline Harmonic Noise

Single frequency harmonic noise with 50 or 60 Hz frequency in prestack marine seismic data arises from various sources at the fundamental frequency of the power transmission line and its harmonics. Electrical interference can originate from the amplifier in the recording instrument, thermal noise due to the electrical resistance of the streamer, and the 50-Hz powerline of the seismic vessel, which is the most important electrical interference (Berdenbender et al., 1970).

During the marine seismic data acquisition, on-board generators produce powerline noise, which is in the available spectral band of the data and is seen as spikelike characteristics at 50-Hz frequency or its multipliers in the amplitude spectrum. Since the signal frequencies in a high-resolution marine seismic survey generally range from 10 to 200 Hz, the harmonic noise and

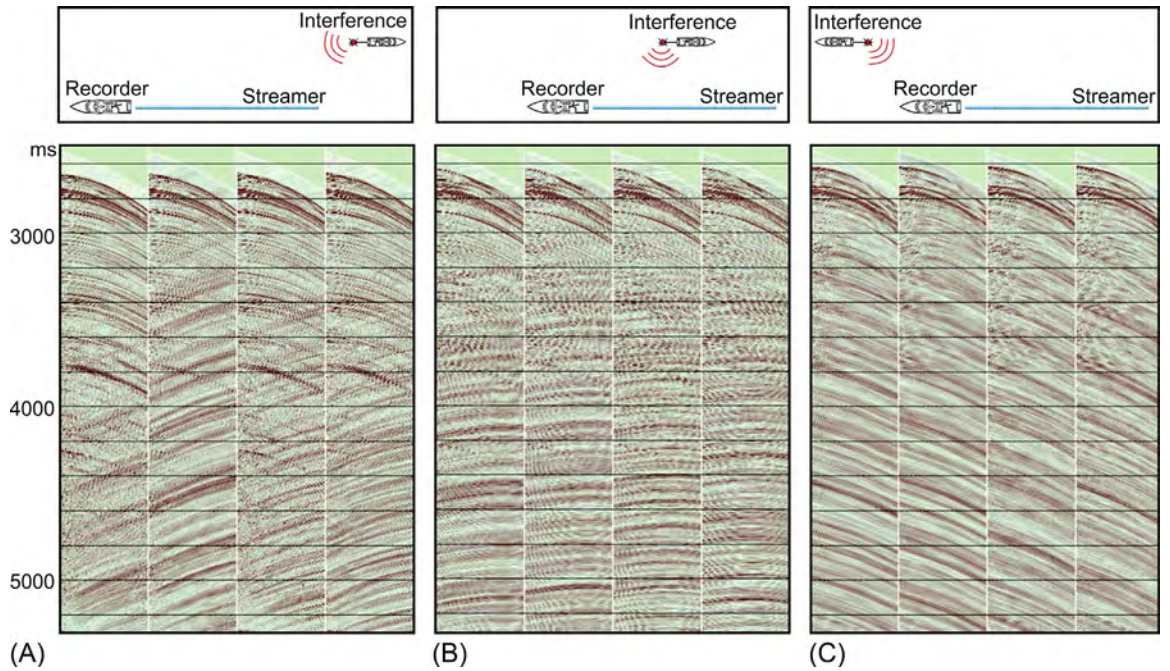


FIG. 3.31 Schematic illustration of three possible situations for the interfering source location (upper panel) and corresponding real data examples for the interference. The source is located (A) behind, (B) at one side, and (C) in front of the receiving streamer.

its multipliers (100, 150, 200 Hz, etc.) are within the available frequency band. The main specification of this noise is that its amplitude is relatively constant with recording time, whereas the amplitudes of seismic reflections decay with time. Fig. 3.32 shows a dead channel of a shot gather because of the strong powerline interference and its amplitude spectrum. The spectrum indicates anomalously high amplitude bursts at 50 Hz and its multipliers. The highest amplitude resides at 50 Hz and the amplitude of the bursts decays with increasing frequency.

Single-frequency harmonic noise of electrical powerline interference can be removed using very narrow bandstop (notch) filters, which cut out a very narrow frequency band (e.g., between 48 and 52 Hz to remove 50-Hz interference) from the data, or the channels with high-amplitude harmonic noise interference are killed or muted out. Fig. 3.33 shows a notch filter application to a single trace section constructed using a channel with severe harmonic noise interference. The amplitude spectrum indicates anomalously high-amplitude harmonic noise bursts at 50 Hz and its multipliers. At first, the section is 12–180 Hz band-pass filtered to remove the swell and high-frequency random noise. Then a notch filter is used to remove the harmonic noise amplitudes (Fig. 3.33B). Although the notch filter removes most of the powerline interference from the data, it also produces "notches" in the amplitude spectrum, which may cause issues during deconvolution in later steps.

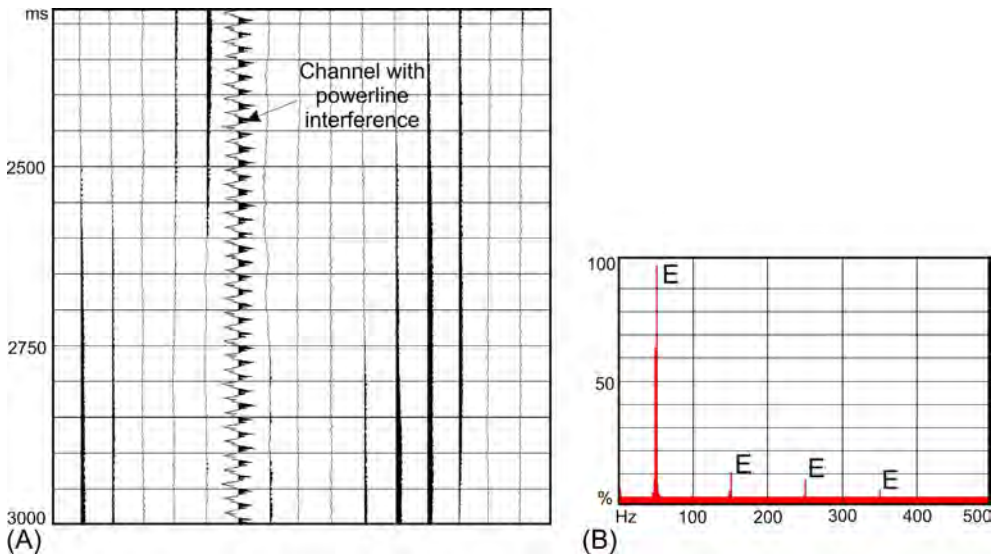


FIG. 3.32 (A) A dead channel of a shot gather because of the strong powerline interference, and (B) its amplitude spectrum. Monofrequency powerline interference (E) appears at 50 Hz and its multipliers in the amplitude spectrum.

3.10.2 Spikelike Noise

Seismic data may contain extremely high-amplitude transient noise bursts. These can be classified into two different groups:

(i) high-amplitude spikelike noise distributed randomly among the recording channels (Fig. 3.34A)

(ii) high-amplitude noise appearing at several consecutive channels with exactly the same onset time, known as cross-feed (Fig. 3.34B)

The first type occurs because of the current leakage in the recorder and even in the streamer, which causes random current interference in the analog-to-digital (A/D) converter or in the streamer electronics. In digital streamers, bad data links or improper coupling of the connectors between active streamer sections may also result in spikelike noise. In fluid-filled streamers, seawater leakage into the streamer active sections cause serious spike noise in the data, as is the case in Fig. 3.34A. The amplitude spectrum of the noisy parts of the data indicate that the noise has amplitudes distributed across almost all available frequency bands, and its character indicates harmonic distortions related to current leakage or shortcuts inside of the streamer fluid (Fig. 3.34C and D). In this case, the fluid in the streamer sections should be completely replaced.

The second type high-amplitude noise appears as horizontal events on shot records and has trace-by-trace consistency. This noise is generally formed by defective A/D converters, and in the case of digital streamers, a possible defect in a digitizing module results in cross-feed noise along the whole recording channels digitized by that module. In Fig. 3.34B, a module digitizing 24 active channels is defective and produces recurrent high-amplitude cross-feed along these 24 channels.

Since they have amplitudes several orders higher than those of primary reflections, even

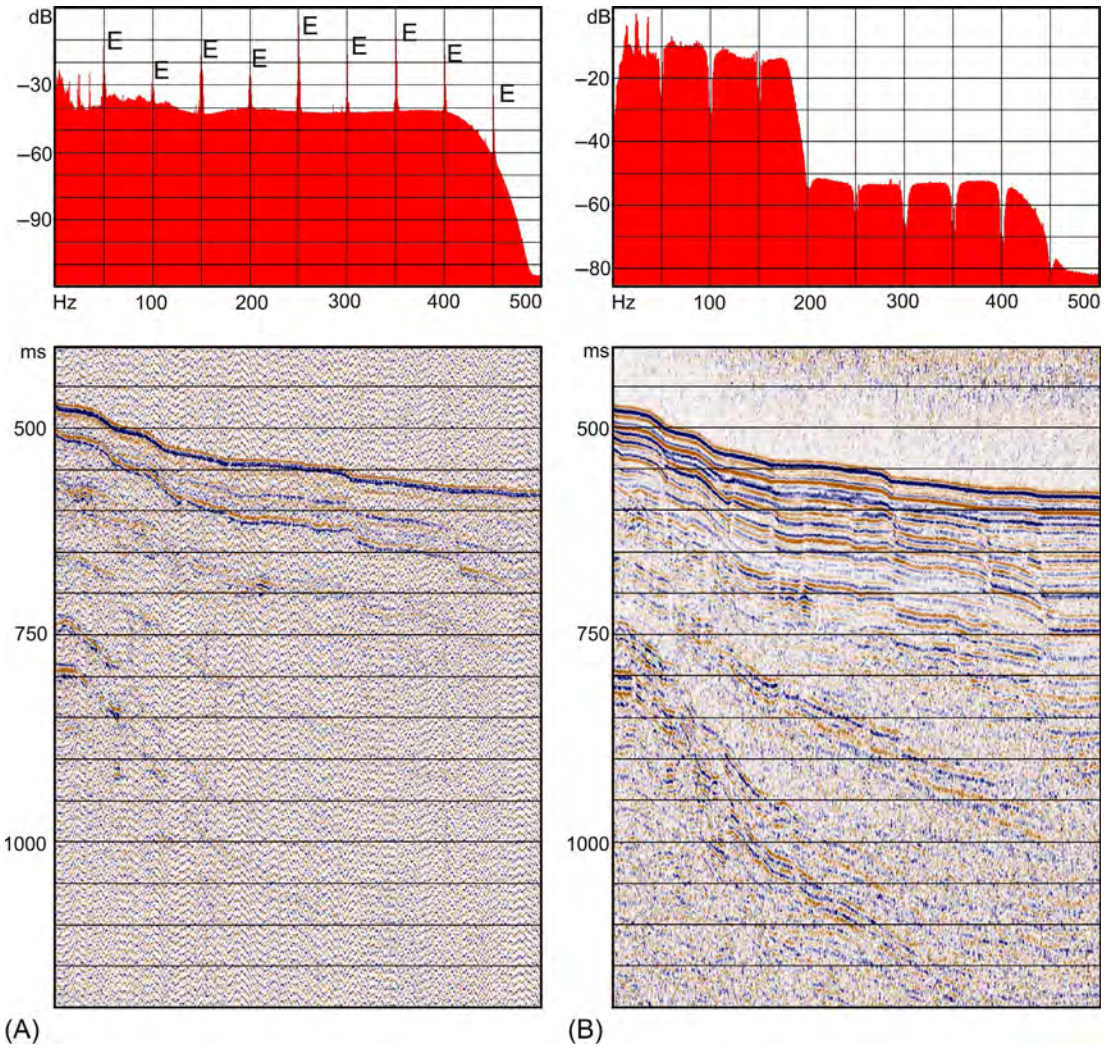


FIG. 3.33 (A) A raw common offset section with strong harmonic noise interference (E) and its amplitude spectrum (upper panel), and (B) after application of a notch filter to remove the harmonic noise at 50 Hz and its multipliers followed by a 12–180 Hz band-pass filter.

higher than correlated and un-correlated noise embedded in the data, they cannot be suppressed by stacking and spikes also exist on the stack sections as localized noise bursts (Fig. 3.35A). The *f-k* filters may increase their amplitudes and make them much clearer on the stack data. If not removed, this type of noise causes deadly issues during the migration: the spikes create semicircular artifacts (so called "smiles") after migration, which may completely corrupt the data (Fig. 3.35B); this makes it important to remove them before stacking. Although there are some specific algorithms to automatically search and remove spikelike

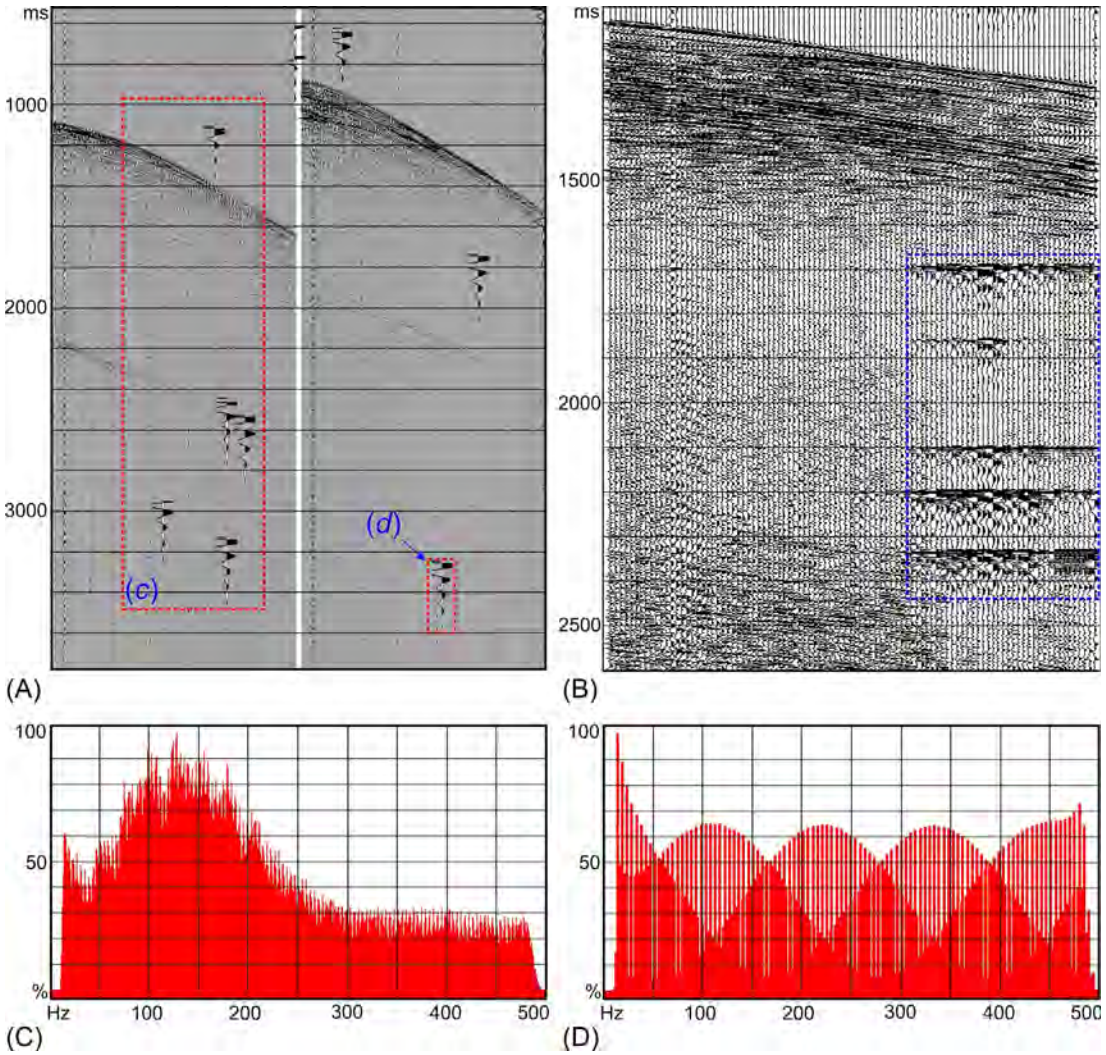


FIG. 3.34 (A) Randomly distributed high-amplitude spikelike noise, (B) high-amplitude cross-feed noise *(dashed blue rectangle)* on shot records, (C) and (D) amplitude spectra of the zones indicated by *dashed red rectangles* in (A).

noise from the data, they often fail because the amplitudes, onset times, phase and frequency characteristics, even the time lengths of the noise are not stable along the data for each shot and may vary significantly from one trace to another. Therefore, they are generally muted out by a surgical mute.

3.10.3 Side-Sweep

Sources of the diffractions are not necessarily located in-line with the seismic profile. The signal generated by the seismic source propagates in all directions and it may also be reflected or diffracted back from both sides of the survey

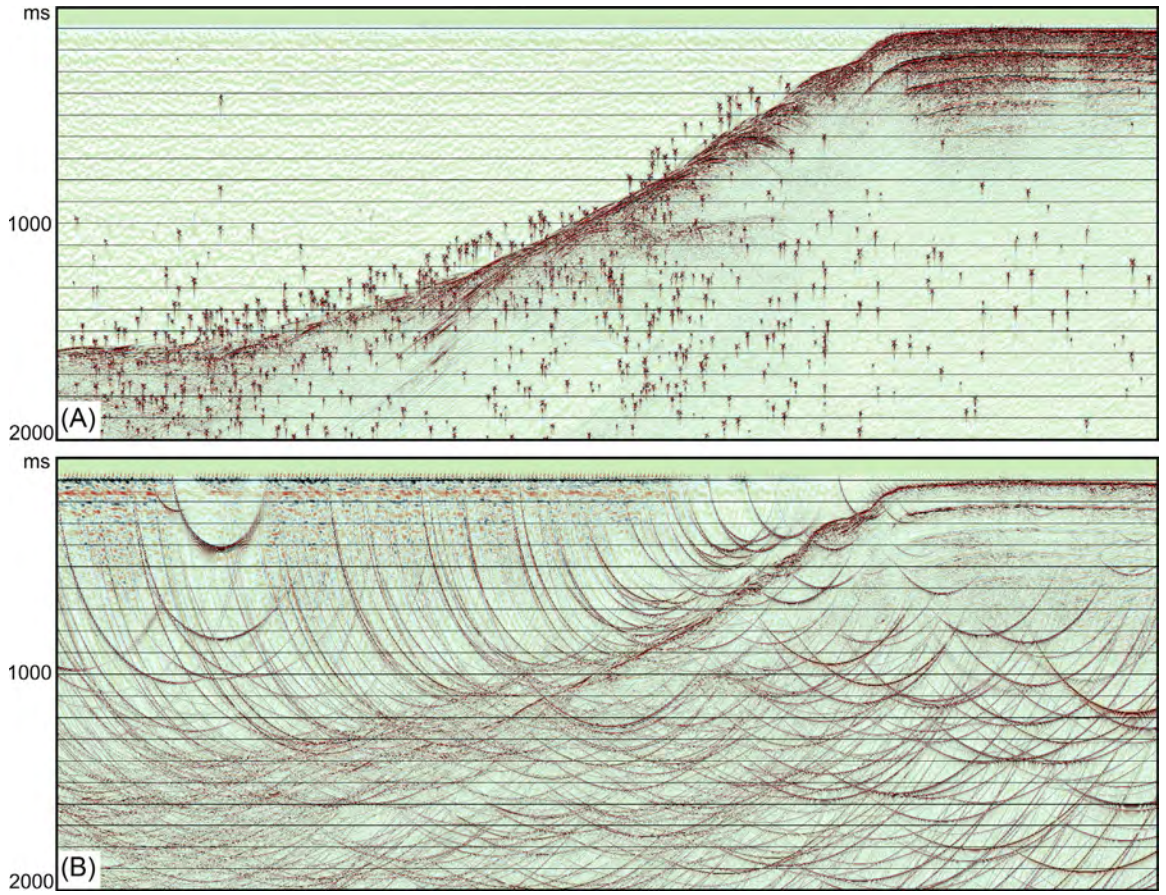


FIG. 3.35 (A) High-amplitude spikelike noise on a stack section. (B) If not removed before stacking, they cause smiles after migration process.

line, which is schematically shown by the inset in Fig. 3.36, whenever there is sufficient inclination on the seabed in the crossline direction. The diffractions coming from out-of-plane (or from the third dimension) are considered as noise and known as side effects or side-sweeps in 2D seismic surveys, whereas they do constitute seismic data itself in 3D surveys.

Side-sweeps need anomalously high NMO velocities during the NMO correction to flatten on the CDP gathers. Particularly mounds, canyon walls, slab-type slide material, and mud volcanoes may generate distinctive side-sweep reflections. They are generally seen as weak to moderate amplitude dome-shaped structures located over the seabed reflection. Fig. 3.36 shows an example side-sweep from a small-scale mound just above the seafloor reflection. Although in-line (2D) diffractions can be eliminated by a 2D migration completely, side-sweeps are not easy to remove from 2D seismic data since 2D migration is not sufficient to remove the 3D effects from the data.

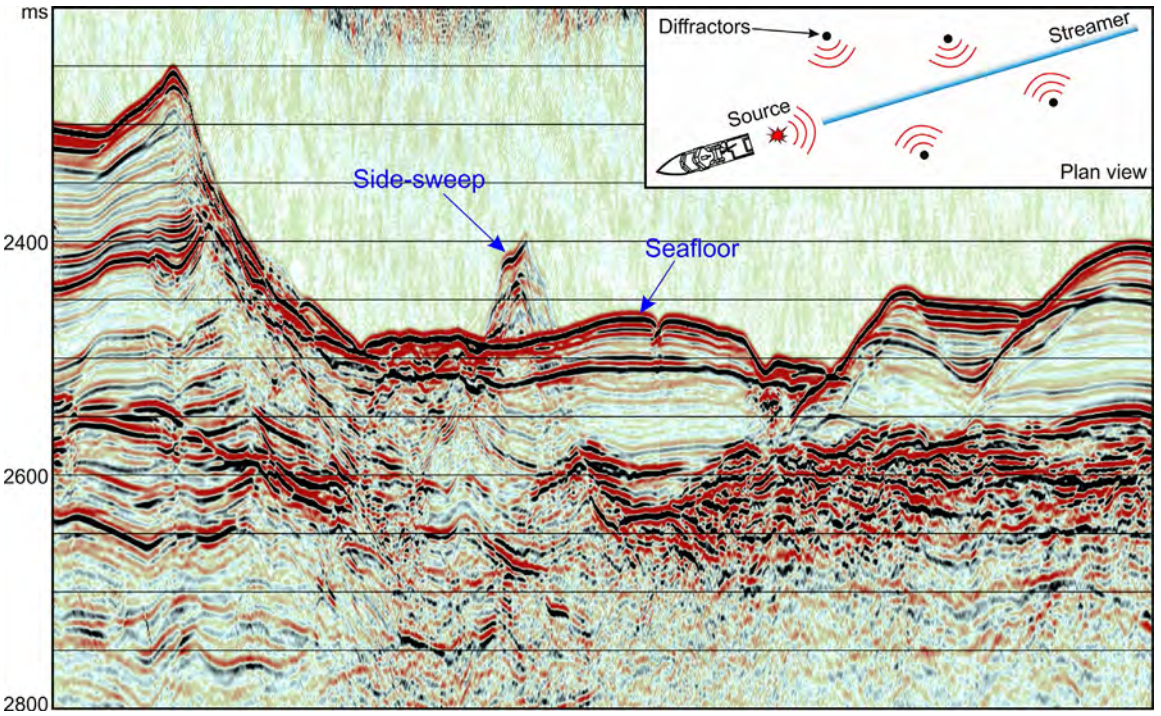


FIG. 3.36 An example stack section with side-sweep reflection above the seabed. Inset schematically shows diffractions from out-of-plane scattering points.

3.10.4 Noise From Other Marine Vehicles

Hydrophones are so sensitive that they can perceive the signal propagating from nearby vessels' propellers. Experience has shown that this noise can be received from long distances from the vessel, e.g., at approximately 5 miles away from the propeller. Their amplitude is rather low with respect to the amplitudes of the genuine reflections, so the noise from other marine vessels is generally visible at early times of the shots corresponding to the water column before the seabed arrival.

These appear as semisymmetrical continuous hyperbolas on the shot gathers if the propeller is close enough (Fig. 3.37). However, its character changes with the distance to the noise source. Fig. 3.38 shows a number of successive shots with propeller noise interference from an oil tanker approaching from the aft of the seismic vessel and passing through one side towards the bow. At first, the propeller noise of the tanker is linear from far to near traces, indicating that the tanker is far behind the seismic vessel. Then it approaches to the sideward of the streamer and the propeller noise appears as symmetrical hyperbolas on the shot records at the center in Fig. 3.38. As the tanker moves away to the bow of the seismic vessel, the propeller noise becomes linear again from near to far traces, indicating that the tanker is far ahead of the streamer.

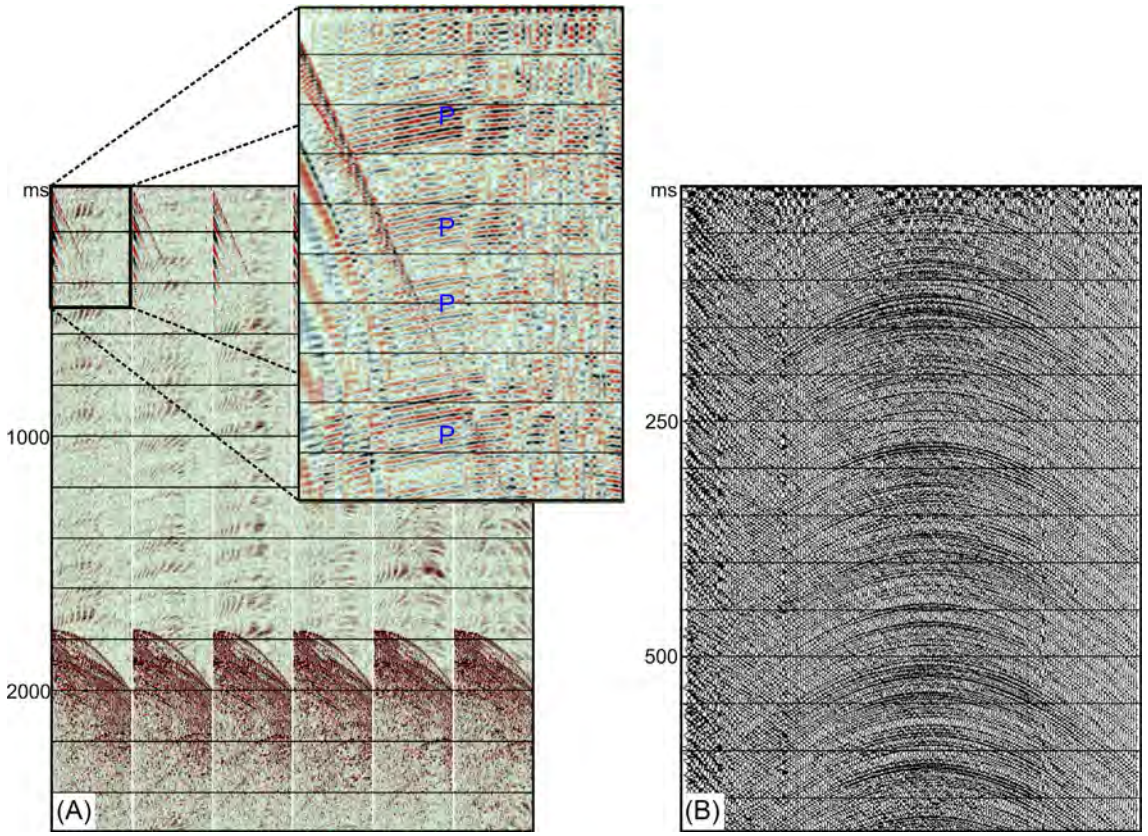


FIG. 3.37 (A) Propeller noise (P) from a nearby container vessel, and (B) noise record showing the propeller noise of the seismic ship's support vessel.

Transport ships do not transmit signals into the water column, and their propellers are the only source of noise for seismic surveys. Navy vessels, especially minesweepers, and submarines, however, can use different sonar systems, which transmit acoustic pulses into the ocean with various frequency and amplitude ranges. These pulses may constitute serious noise on the seismic data. Fig. 3.39A shows extremely high-amplitude linear noise interference from the sonar signal of a possible submarine located at the bow side of the vessel. The *f-k* spectrum of the interference indicates that the noise is not a single or narrow frequency pulse, but has a frequency band (e.g., from 40 to 180 Hz) which almost coincides with the seismic bandwidth (Fig. 3.39B). The linear noise is periodic and there are approximately 80 ms between the consecutive pulses.

Excessive gain applications or AGC may increase their amplitudes, and the propeller noise from other vessels can be mostly attenuated during the stacking process. In this case, because the noise is linear and its dip is quite different from those of primary reflection amplitudes, one can easily remove this type of

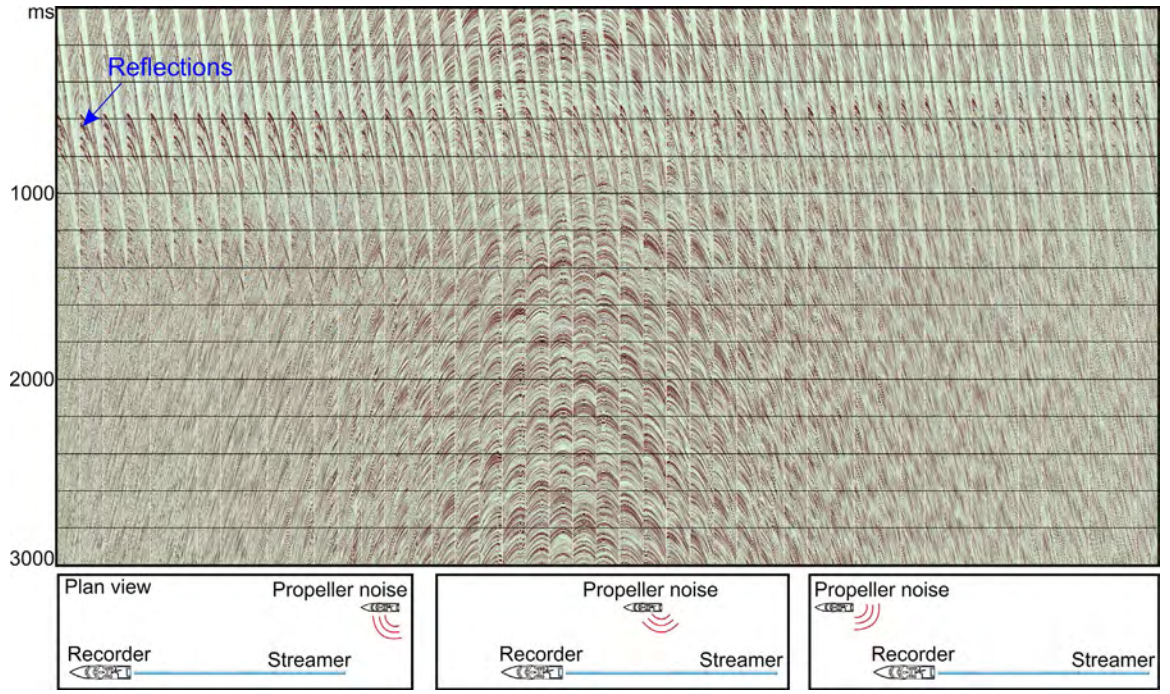


FIG. 3.38 A number of successive shot gathers contaminated with distinctive propeller noise interference from an oil tanker approaching from the aft. A schematic illustration of three possible situations for the source location of the propeller noise is given in the lower panels.

interference with a properly designed *f-k* filter or muting out of the noise amplitudes in τ-p domain.

3.10.5 Marine Mammals

Marine mammals, particularly dolphins, are sometimes curious and can approach to the streamer during the acquisition. The birds on the streamer may draw their attention. When they are too close to the streamer, their movement in the water and even contact with the streamer result in a localized noise on the data. It appears as specific reverse *V* shape transient events at the channels close to the mammal's movement (Fig. 3.40). The dip of the linear flank of this reverse V-shaped noise is parallel to the direct wave, indicating a propagation velocity in the water column of approximately 1500 m/s. The frequency of the noise is rather low and changes from 10 to 20 Hz, and because they are linear, it is possible to suppress them using *f-k* filters unless their positive dip flank does not interfere with the dip of the primary reflection hyperbolas, especially at far offsets. In this case, it may be preferable to mute out these zones by a suitable surgical mute.

3.10.6 Streamer Ballasts

The depth of the streamer(s) from the sea surface is maintained by depth levelers, or birds, attached on the streamers at regular intervals, typically at every 300 m. Especially in warm

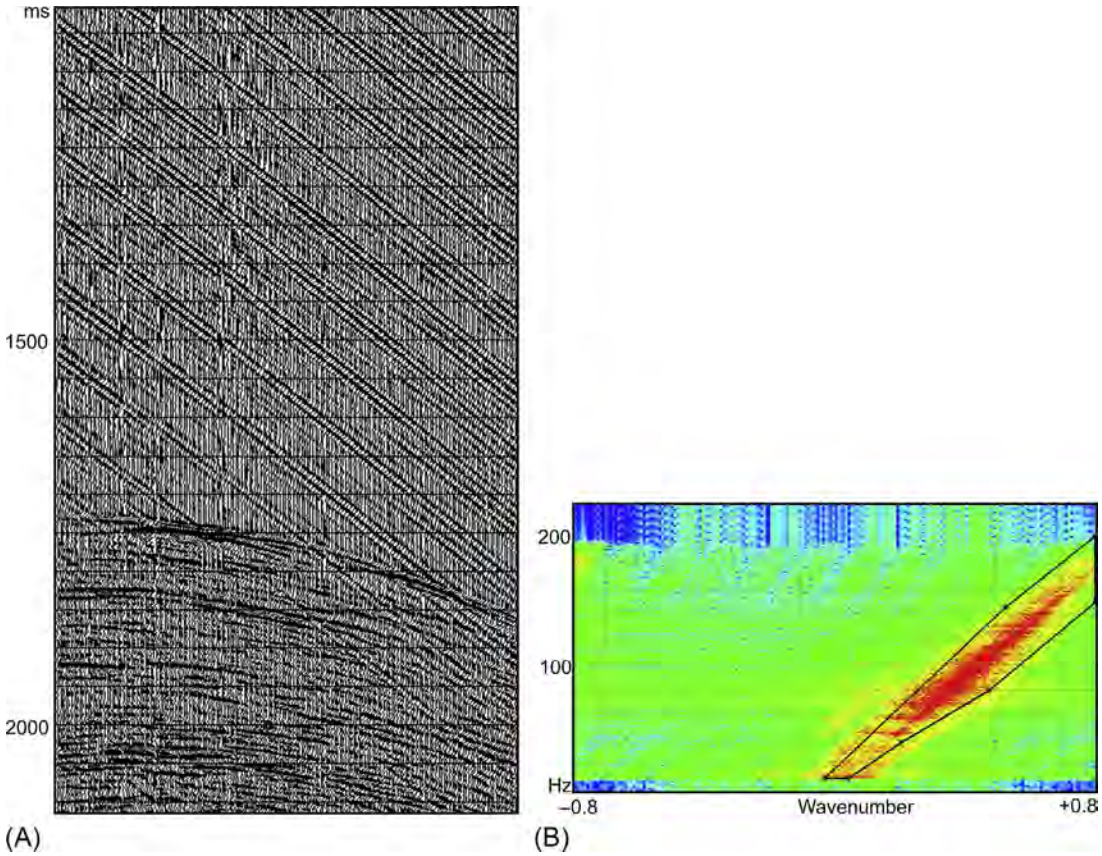


FIG. 3.39 (A) High-amplitude linear noise interference from a possible submarine located at the bow side of the vessel, and (B) *f-k* spectrum of the interference shows that its frequency band coincides with the seismic bandwidth.

and saline waters, sometimes it may be necessary to use streamer ballasts in addition to the birds to maintain the stability of the streamer in the water. This may be required especially in marine environments of relatively high salinity and hence high density, such as Mediterranean waters, which forces the streamer to float. This process is termed streamer trimming and may take significant survey design and planning time.

Even though the streamer ballasts are specifically designed weights to reduce the turbulence effect during their movement in the water, they can induce localized noise at channels in their vicinity. The ballast noise appears as reverse V shape linear events similar to the noise from marine mammals. However, unlike the marine mammal noise, the noise from streamer ballast emanates on shot gathers for full recording time from 0 ms to end of the recording. Fig. 3.41 shows three shot gathers with a distinctive noise from streamer ballast attached at the location of channel 148.

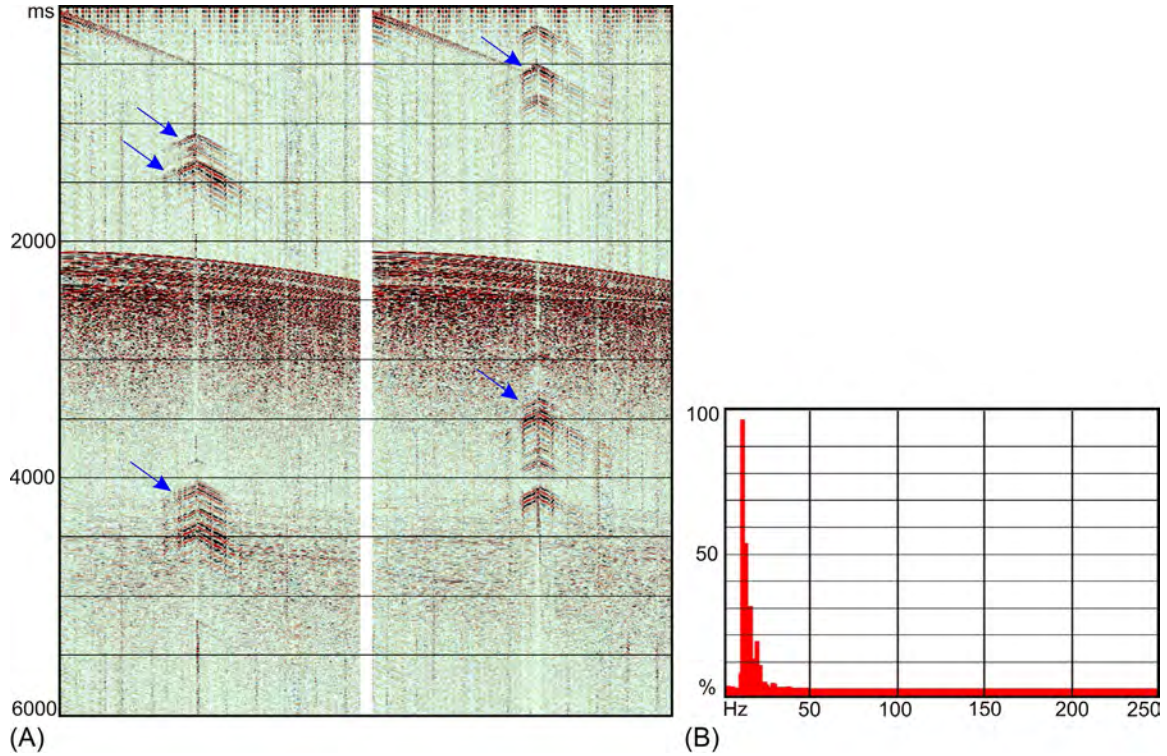


FIG. 3.40 (A) Noise from marine mammals *(blue arrows)* on two filtered shot gathers, and (B) amplitude spectrum of the noise.

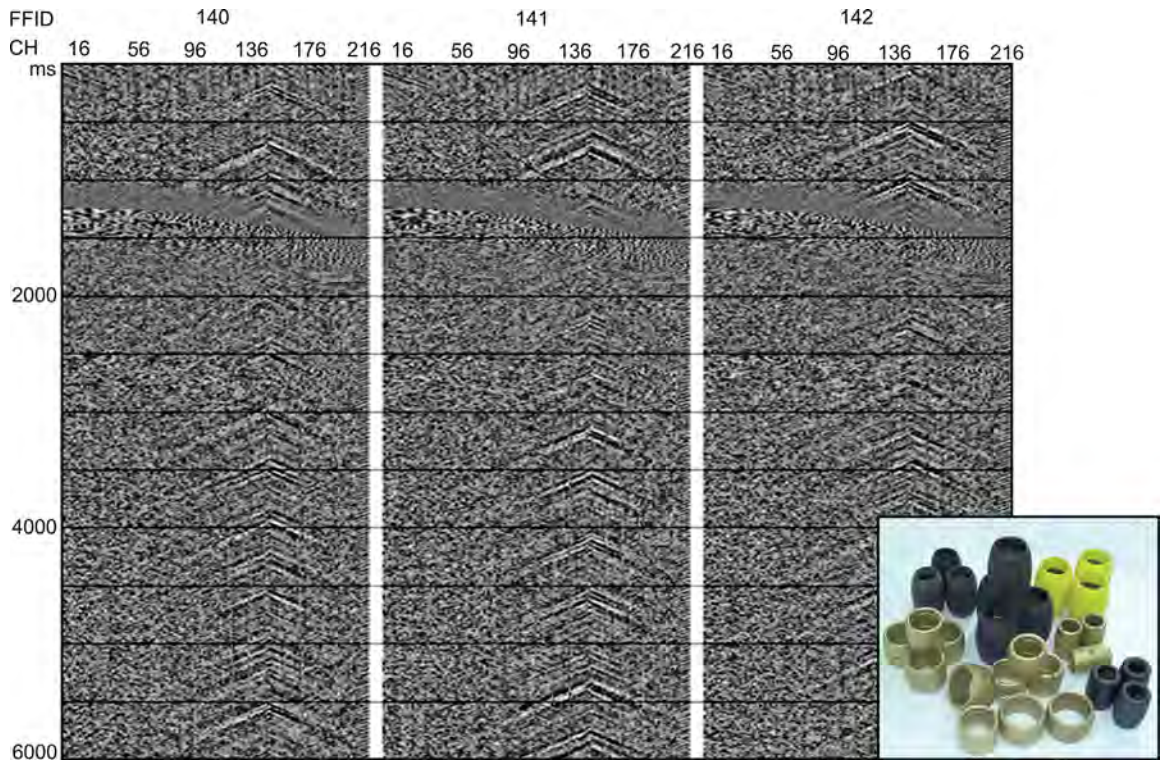


FIG. 3.41 Three shot gathers contaminated by reverse V-shaped noise from streamer ballast attached at the location of channel 148. Inset shows different size ballasts used to trim streamer in order to maintain the streamer stability. *Photo courtesy Seamap Inc.*

CHAPTER

4

Fundamentals of Data Processing

OUTLINE

4.1 Autocorrelation	213	4.6 2D Fourier Transform	222
4.2 Crosscorrelation	215	4.7 z Transform	230
4.3 Convolution	215	4.8 Hilbert Transform	231
4.4 Fourier Series	216	4.9 τ-p Transform (Slant Stack)	232
4.5 1D Fourier Transform	219	4.10 Sampling Theory	235

In seismic data processing, some fundamental processes and the determination of processing parameters are accomplished by analyzing specific correlation functions and frequency components of the input seismic data. Correlation can be handled by computing auto- or cross-correlation functions, while the frequency characteristics of the data are investigated by computing the Fourier transform, which moves the data from the time to the frequency domain. In addition, some of the processing steps such as bandpass filtering or deconvolution in the time domain are implemented by convolution. Since these applications are the main tools of data processing, their fundamental concepts and basic properties have significant importance for a seismic processor. In this section, some of the basic mathematical processes such as auto- and cross-correlations and convolution, some generalized functions such as the Dirac Delta or unit impulse, box-car or sinc function, and some of the most common transforms such as the Fourier, Hilbert or τ-p transforms and their characteristics, as well as application fields, are explained.

Signal processing in geophysics is generally achieved by carrying out a number of mathematical processes applied to the geophysical signal, which is generally in the form of discrete time series. Based on the environment where the signal is observed, the data is a function of either time or space: that is, the data is defined in time or distance domains, respectively. If the observed signal is a function of frequency, then the frequency domain is considered. It is

© 2018 Elsevier Inc. All rights reserved.

possible to transform the data from the time or distance domain to the frequency domain by spectral analysis. Because some of the mathematical processes can be performed much more easily on the frequency components of a time domain signal, time and frequency domains are sometimes mentioned together.

A periodic signal in the time or space domain is defined by a number of specific parameters. The magnitude of the signal is amplitude, defined as maximum deviation from zero or its mean value. If measured from zero to maximum, it is known as zero-to-peak (0-p) amplitude, and if measured as an absolute value between minimum and maximum, then it is termed peak-to-peak (p-p) amplitude (Fig. 4.1A and B). For seismic data, it is the maximum deviation of an event in the seismic data from the zero magnitude axis. Period is defined as recurrence time of a continuous signal observed in the time domain. In seismic exploration, the unit of the period is seconds. It is represented by T, and is inversely proportional to the frequency as $T = f^{-1}$ (Fig. 4.1A). Signal frequency is the number of recurrences of a periodic signal in a unit time span, observed in the time domain. Unit time in seismic exploration is always 1 s. Frequency is represented by f, and its unit is cycle/s or hertz (Hz). The phase of the signal is its onset angle at origin time, generally expressed as radians, and changes between $\pm 180°$ (if it is in degrees) or $\pm\pi$ (if it is in radians). It is also expressed as the relative displacement between the signals with the same frequency (Fig. 4.1C).

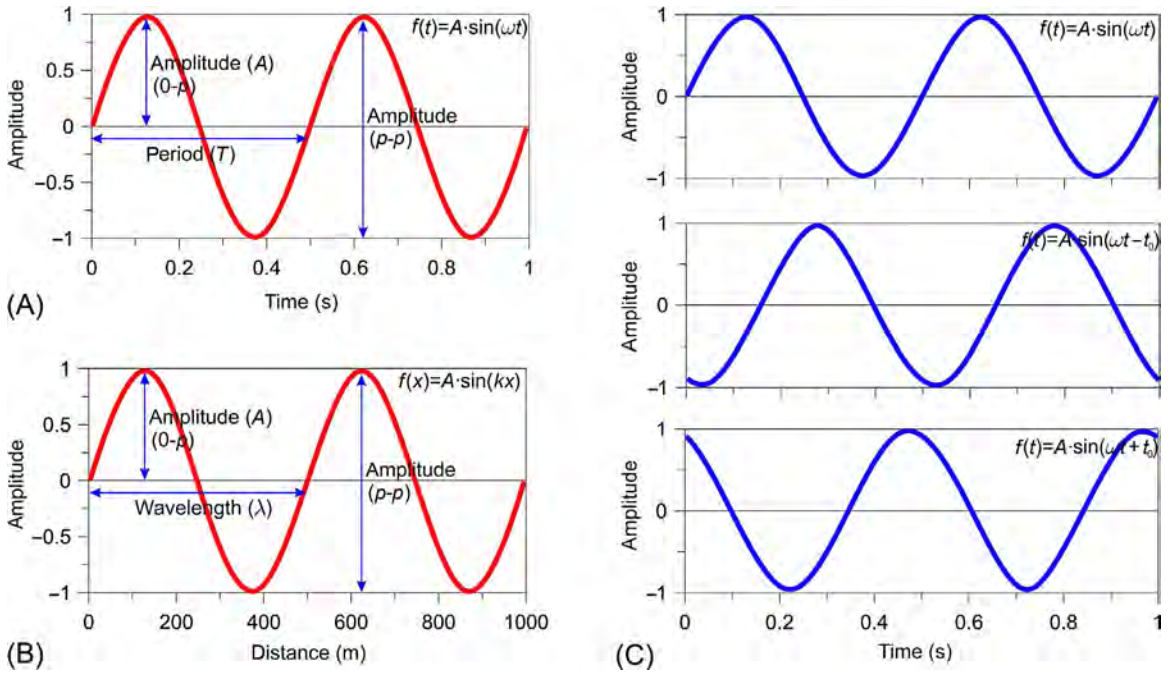


FIG. 4.1 Amplitude, period and wavelength of a periodic sinus function observed in (A) time, and (B) space domains. k is wavenumber, ω is angular frequency, 0-p and p-p are zero-to-peak and peak-to-peak amplitudes, respectively. (C) Effect of phase shift on the periodic signal. A phase shift of $-t_0$ moves the signal along the positive time axis, while vice versa for $+t_0$.

Angular frequency is defined as recurrence speed of the signal in radians/s and is expressed as $\omega = 2\pi f$, where f is the frequency.

For the signals observed in the space domain, however, wavelength and wavenumber terms are used instead of period and frequency parameters. Wavelength is the recurrence distance of a periodic signal observed in the space domain and expressed as $\lambda = V/f$, where V and f are signal propagation velocity and frequency, respectively. Vertical resolution of seismic data depends on the wavelength of the recorded signal (Fig. 4.1B). Wavenumber is defined as the number of recurrence of a periodic signal in a unit distance. It is represented by k, and its unit is m^{-1}.

Using the parameters defined here, a periodic sinusoid in the time domain can be mathematically expressed as

$$f(t) = A \cdot \sin(\omega_0 t + \phi) = A \cdot \sin(2\pi f_0 t + \phi) \quad (4.1)$$

where A is the amplitude, ω_0 is the angular frequency ($\omega_0 = 2\pi f_0$), and f_0 and ϕ are the fundamental frequency and phase angle of the sinusoid, respectively. These terms are illustrated on a periodical signal in Fig. 4.1. When the signal is in time domain, we define the signal using its period and frequency (Fig. 4.1A), whereas for a space domain signal, these parameters correspond to wavelength and wavenumber, respectively (Fig. 4.1B). Phase is defined as the negative of the phase shift, and a negative time shift corresponds to a positive phase value (Fig. 4.1C).

There are some specific functions termed "generalized functions" which are often used during the processing or to derive theoretical implications of the processing methodology. For instance, odd and even functions are used to compute the Fourier series approximation of a given function; box-car and sinc functions are important in designing the band-pass filter operators; and Signum function is used to obtain Hilbert transform of the signal, which is then used to compute complex trace attributes of the seismic data. The mathematical and graphical expressions of these functions, as well as their graphics and important properties are provided in Table 4.1.

4.1 AUTOCORRELATION

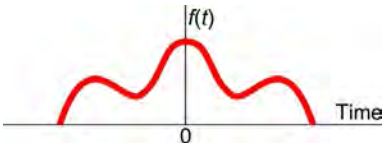
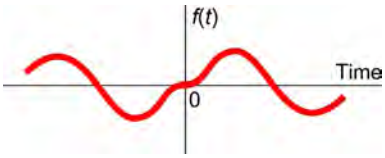
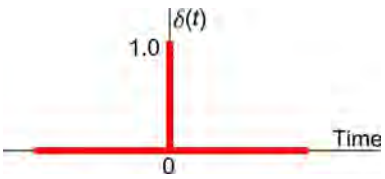
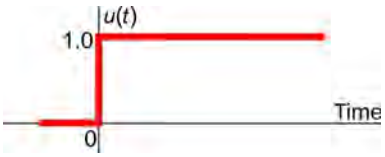
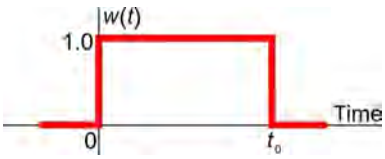
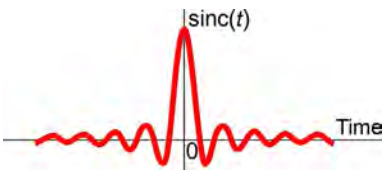
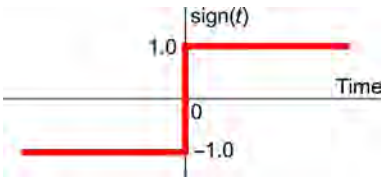
Autocorrelation is used to obtain the degree of similarity of a time series with itself, which provides to obtain periodical components embedded in the data. Autocorrelation of an $x(t)$ series is expressed analytically as

$$R_{xx}(\tau) = \int_{-\infty}^{\infty} x(t)x(t+\tau)dt \quad (4.2)$$

where τ is the time lag. According to Eq. (4.2), $x(t)$ analytical function is lagged by an amount of τ, multiplied by $x(t)$, and summed up via integration. Autocorrelation function is even, which is expressed as $R_{xx}(-\tau) = R_{xx}(\tau)$. When $\tau = 0$ (lag 0), autocorrelation value is always maximum, which corresponds to the total energy of the input function. If function $x(t)$ is periodic, then its autocorrelation function $R_{xx}(\tau)$ is also periodic, and we can determine the periodic components of the input by examining its autocorrelation. Hence, autocorrelation function is used to determine the required parameters of the deconvolution process. Furthermore, deconvolution operator is obtained by calculating the autocorrelation of the input seismic trace (Chapter 6). In addition, quality control and effectiveness of the deconvolution output involves analyzing the autocorrelation of deconvolved output.

Calculation of autocorrelation of an $x(t)$ series in time domain means squaring the amplitude spectrum in frequency domain. Phase spectrum of the autocorrelation output becomes zero, which implies that autocorrelation function $R_{xx}(\tau)$ is not reversible. That is, we cannot recover $x(t)$ function if we only know $R_{xx}(\tau)$. Because a time domain autocorrelation calculation equals squaring of the amplitude spectrum, time domain counterpart of the power spectrum is autocorrelation function, which is known as

TABLE 4.1 Mathematical and Graphical Expressions and Important Properties of Generalized Functions Used in Signal Processing, Where * Denotes Convolution, $\Im\{\}$ is Fourier Transform, a_n and b_n are Fourier Series Coefficients, ω is Angular Frequency, T is Period, and i is $(-1)^{1/2}$

Function	Graphic	Specifications
Even functions $f(t)=f(-t)$		$\int_{-T/2}^{T/2} f(t)dt = 2\int_{0}^{T/2} f(t)dt$ In Fourier series summation $b_n = 0$
Odd functions $f(-t)=-f(t)$		$\int_{-T/2}^{T/2} f(t)dt = 0$ $f(0) = 0$ In Fourier series summation $a_n = 0$
Dirac Delta Function $\delta(t)=\begin{cases}1 & t=0\\ 0 & t\neq 0\end{cases}$		$\int_{-\infty}^{\infty} \delta(t)dt = 1$ $\delta(-t)=\delta(t)$ $f(t)^{*}\delta(t)=f(t)$ $f(t)\delta(t)=f(0)\delta(t)$
Unit step function $u(t)=\begin{cases}1 & t\geq 0\\ 0 & t<0\end{cases}$		$\int_{-\infty}^{\infty} u(t)\phi(t)dt = \int_{0}^{\infty} \phi(t)dt$ $\frac{du(t)}{dt}=\delta(t)$
Box-Car function $w(t)=\begin{cases}1 & 0\leq t<t_0\\ 0 & \text{other}\end{cases}$		$\Im\{w(t)\}=\sin c(\omega)$
Sinc function $\text{sinc}(t)=\frac{\sin(t)}{t}$		$\Im\{\text{sinc}(t)\}=w(\omega)$ $\text{sinc}(0)=1$
Signum function $\text{sign}(t)=\frac{1}{\lvert t\rvert}=\begin{cases}-1 & t\leq 0\\ 1 & t>0\end{cases}$		$\text{sign}(-t)=-\text{sign}(t)$ $\Im\{\text{sign}(t)\}=\frac{2}{i\omega}$

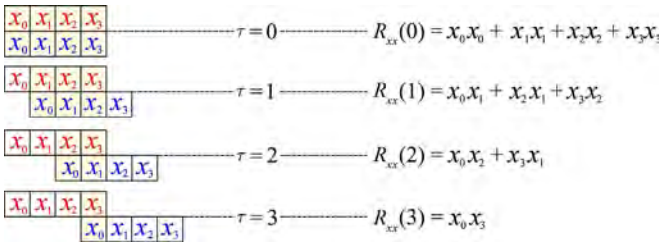


FIG. 4.2 Schematical illustration of autocorrelation calculation of a time series $x(t)$ consisting of four discrete elements. Mutual elements of the series in *yellow boxes* are multiplied and the results are summed. τ is the autocorrelation lag.

Wiener-Khintchine Theorem and can be expressed as

$$\Im\{R_{xx}(\tau)\} = R_{xx}(\omega) = X(\omega) \cdot X(\omega) = |X(\omega)|^2 \tag{4.3}$$

Eq. (4.3) indicates that taking the autocorrelation of an $x(t)$ function in time domain corresponds to calculating the power spectrum of $x(t)$ in frequency domain.

Fig. 4.2 schematically shows the autocorrelation calculation of discrete time series. Corresponding elements of the input series are multiplied and the results are summed ($\tau = 0$). Then one of the series is lagged one time sample ($\tau = 1$) and the process is repeated, and calculations continue until the last sample of the series is reached.

4.2 CROSSCORRELATION

Crosscorrelation is used to obtain the degree of the similarity between two different time series. The crosscorrelation of $x(t)$ and $y(t)$ series is expressed analytically as

$$R_{xy}(\tau) = \int_{-\infty}^{\infty} x(t)y(t+\tau)dt = \int_{-\infty}^{\infty} x(t-\tau)y(t)dt$$
$$R_{yx}(\tau) = \int_{-\infty}^{\infty} y(t)x(t+\tau)dt = \int_{-\infty}^{\infty} y(t-\tau)x(t)dt \tag{4.4}$$

where τ is the time lag. According to Eq. (4.4), $y(t)$ analytical function is lagged by an amount of τ, multiplied by $x(t)$, and summed up via integration. If $x(t)$ and $y(t)$ functions are of different time lengths, then the length of $R_{xy}(\tau)$ will equal to the length of $x(t)$. Calculation of crosscorrelation of $x(t)$ and $y(t)$ time series in time domain corresponds to the multiplying of amplitude spectra of both functions in frequency domain, and the phase spectra of both functions are subtracted. Order of the functions in crosscorrelation calculation is important, and $R_{xy}(\tau) = R_{yx}(-\tau)$.

If both functions are similar, then the crosscorrelation calculation produces a large positive number, while smaller correlation values are obtained if the functions are not alike. In practice, two time series have similarities if one is the time-lagged version of another. Hence, crosscorrelation actually indicates the amount of time shift of a function relative to other, and is used to obtain deconvolution operator in predictive deconvolution (Section 6.4). Fig. 4.3 schematically shows the crosscorrelation calculation of discrete time series. Calculations are performed as for the autocorrelation calculations.

4.3 CONVOLUTION

Convolution is the mathematical process between input and output of a linear system. That is, there is a convolution process between input and output of a stationary system. For $x(t)$ and $y(t)$ time series, it is analytically expressed as

$$f(t) = \int_{-\infty}^{\infty} x(\tau)y(t-\tau)d\tau \tag{4.5}$$

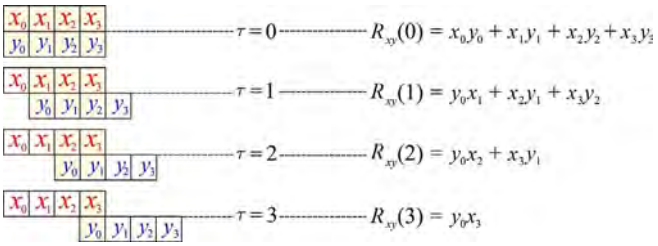


FIG. 4.3 Schematical illustration of crosscorrelation calculation of discrete time series $x(t)$ and $y(t)$ consisting of four discrete elements. Mutual elements of both series in shaded areas are multiplied and the results are summed. τ is the crosscorrelation lag.

TABLE 4.2 Mathematical Properties of Convolution Process, Where * Denotes Convolution, $\Im\{\}$ is Fourier Transform, k is a Scalar, and δ is the Dirac Delta Function

Property	Mathematical Expression
Commutative	$x(t)^* y(t) = y(t)^* x(t)$
Distributive	$x(t)^*[f(t)+y(t)] = x(t)^* f(t) + x(t)^* y(t)$
Associative	$[x(t)^* f(t)]^* y(t) = x(t)^*[f(t)^* y(t)]$
Identity for convolution	$x(t)^* \delta(t) = x(t)$ and $x(t)^* k\delta(t) = kx(t)$
Time shift	$x(t)^* \delta(t+T) = x(t+T)$
Fourier transform	$\Im\{x(t)^* y(t)\} = X(\omega)\cdot Y(\omega)$ $\Im^{-1}\{X(\omega)^* Y(\omega)\} = x(t)\cdot y(t)$

where τ is the time lag. According to Eq. (4.5), $y(t)$ analytical function is reversed and lagged by an amount of τ, multiplied by $x(t)$, and summed up via integration. When two functions are convolved in time domain, amplitude components of the same frequencies of both functions are multiplied in the frequency domain, while their phase spectra are summed. The amplitudes at different frequency values do not interfere during the multiplication. Some of the mathematical properties of convolution are given in Table 4.2.

Convolution is of great importance in seismic exploration and data processing. Recorded seismic trace is composed of the convolution of source signal and reflection coefficients of the subsurface interfaces. In this case, earth itself represents the linear system, which is known as convolutional model and is explained in detail in Section 6.1. Convolutional model also constitutes the theoretical background of the calculation of synthetic seismic trace. Furthermore, several processing steps are fulfilled by convolution in seismic processing. For instance, the filter operator in time domain is convolved with the seismic trace to obtain the filtered trace. Even deconvolution is achieved by convolution: the deconvolution operator in time domain is also convolved with the seismic data by a trace-by-trace basis to obtain the deconvolution output. Fig. 4.4 schematically shows the convolution computation of discrete time series. Calculations are performed as for autocorrelation calculations, with only one difference that the second time series is reversed. Convolution output of two series with M and N discrete elements consists of $M + N - 1$ elements.

4.4 FOURIER SERIES

Periodic functions can be represented by summation of amplitudes at increasing frequency values of two orthogonal functions. Jean Baptiste Joseph Fourier (1768–1830) accomplished this summation by using sine and cosine functions. Periodic functions can be decomposed into sinusoidal harmonics, which means that any kind of periodic function can be expressed as weighted summation of infinite number of sine and cosine functions with different amplitude, phase and frequency values using Fourier series summation approximation in such a way that, using orthogonal sine and

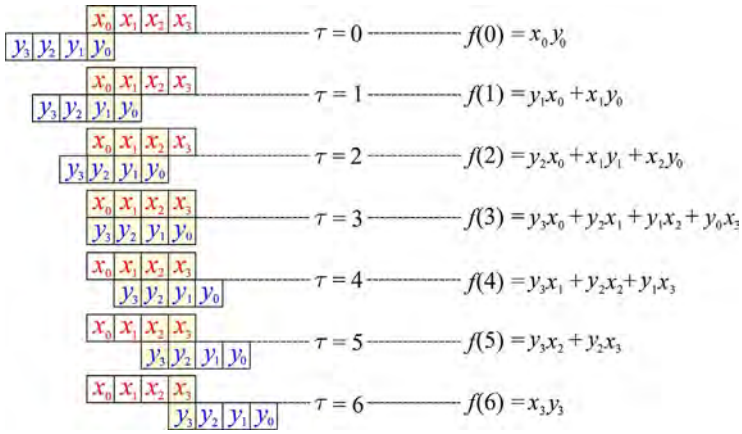


FIG. 4.4 Schematical illustration of convolution calculation of discrete time series $x(t)$ and $y(t)$ consisting of four discrete elements. τ is the convolution lag.

cosine function summations, a periodic $f(t)$ function is approached by

$$f(t) = \frac{1}{2}a_0 + \sum_{n=1}^{\infty}[a_n \cos(n\omega_0 t) + b_n \sin(n\omega_0 t)] \tag{4.6}$$

The basis of Fourier series expansion is to find out a_0, a_n, and b_n coefficients and substitute them into Eq. (4.6). These three coefficients are obtained by following integral equations

$$\begin{aligned} a_0 &= \frac{2}{T}\int_{-T/2}^{T/2} f(t)dt \\ a_n &= \frac{2}{T}\int_{-T/2}^{T/2} f(t)\cos(n\omega_0 t)dt \quad (n = 0, 1, 2, \ldots) \\ b_n &= \frac{2}{T}\int_{-T/2}^{T/2} f(t)\sin(n\omega_0 t)dt \quad (n = 0, 1, 2, \ldots) \end{aligned} \tag{4.7}$$

where a_0 is the mean value of $f(t)$ function and is known as DC component for $n = 0$, which determines how much the summed harmonics are shifted along the y axis. For odd functions, $a_n = 0$, while $b_n = 0$ for even functions in Fourier series summation (Table 4.1). Fourier series expansion is an approximation to the original periodic function and it allows us to express the periodic function with several (in theory, infinite number of) summed amplitudes of sine and cosine functions with different frequency and phase characteristics. Although it is practically unfeasible, a perfect approximation to $f(t)$ function is obtained if the summation is done over infinite number of n values.

For the Fourier series analysis, $f(t)$ function should satisfy some specific conditions known as Dirichlet conditions:

(i) $f(t)$ function must be periodic and integrable over a period, e.g., the power of the function is limited over one period.
(ii) $f(t)$ function must have a finite number of discontinuities and a finite number of extrema (finite number of maxima and minima) in a given time interval.

As an example, let's express a box-car (a square wave) function as an infinite series summation of sine and cosine functions using Fourier series expansion. Mathematical expression of a box-car defined in the $(-\pi, \pi)$ interval is given by

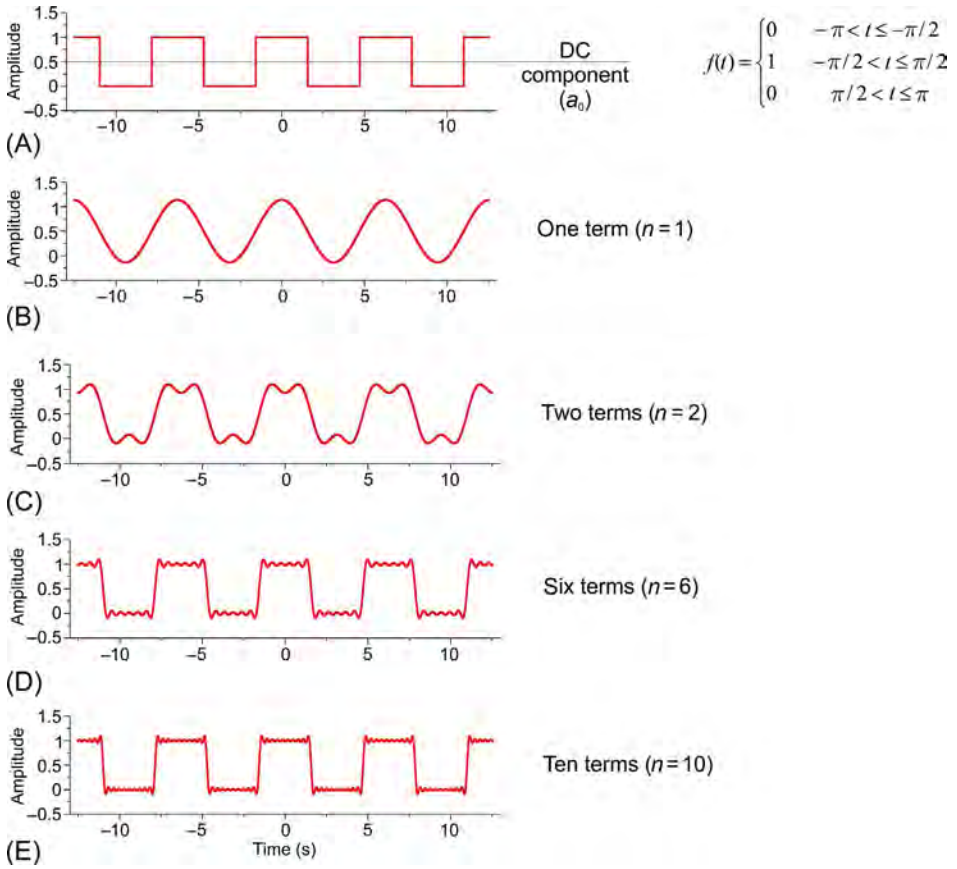


FIG. 4.5 Approximation to a box-car function using Fourier series expansion. (A) The box-car function given by Eq. (4.8), and its Fourier series expansion for (B) 1 term ($n=1$), (C) first 2 terms ($n=2$), (D) first 6 terms ($n=6$), and (E) first 10 terms ($n=10$) of Eq. (4.10). DC component, a_0 for $n=0$, is 1/2.

$$f(t)=\begin{cases}0 & -\pi<t\le-\pi/2\\ 1 & -\pi/2<t\le\pi/2\\ 0 & \pi/2<t\le\pi\end{cases} \tag{4.8}$$

The period of this function is 2π and its angular frequency is $\omega=2\pi/T=2\pi/2\pi=1$. Since $f(-t)=f(t)$, box-car is an even function (Fig. 4.5A), and therefore, all b_n coefficients are zero. Using Eq. (4.7), a_0 and a_n can be obtained as

$$a_0=1/2$$
$$a_n=\frac{2}{n\pi}\sin\left(n\frac{\pi}{2}\right)=\begin{cases}0 & n\text{ even}\\ \dfrac{2(-1)^k}{\pi(2k+1)} & n=2k+1,\quad k=0,1,2,\ldots\end{cases} \tag{4.9}$$

Substituting Eq. (4.9) into Eq. (4.6), we get.

$$f(t)=\frac{1}{2}+\frac{2}{\pi}\left(\cos(t)-\frac{\cos(3t)}{3}+\frac{\cos(5t)}{5}-\frac{\cos(7t)}{7}+\frac{\cos(9t)}{9}-\ldots\right) \tag{4.10}$$

Eq. (4.10) is actually an approximation to the periodic box-car function given in Eq. (4.8) by summing infinite number of sinusoids with different phase, amplitude and frequency values. In practice, the more terms are included in the summation (i.e., the higher the maximum n value is incorporated), the closer the result to

$f(t)$ function is (Fig. 4.5). However, n should be infinite for an exact approximation.

4.5 1D FOURIER TRANSFORM

Although the periodic functions can be approximated by Fourier series expansion, non-periodic functions cannot be expressed as the summation of sine and cosine functions using Fourier series. In that case, non-periodic functions are regarded as periodic that their period is infinitely large. When the period is infinite, then the frequency becomes infinitely small, and the frequency components of such functions can be obtained directly by Fourier transform using Fourier integral instead of Fourier series expansion.

The spectrum of a time series of a sequence of amplitudes as a function of time is obtained by calculating the amplitude and phase spectra. The basis of taking the spectrum of a time function is to find out the amplitudes and phase values of the sinusoids which constitute the original function when summed up. The amplitudes of these sinusoids as a function of their corresponding frequency forms the amplitude spectrum, while plotting the phase values as a function of frequency constitutes the phase spectrum. In amplitude spectrum, amplitudes of the sinusoids are lined up with respect to their corresponding frequency. Square of the amplitude spectrum denotes power spectrum which equals the Fourier transform of autocorrelation function.

Fourier transform $F(\omega)$ of a non-periodic $f(t)$ time signal is analytically obtained by Fourier integral as

$$\Im\{f(t)\} = F(\omega) = \int_{-\infty}^{\infty} f(t)e^{-i\omega t}dt \qquad (4.11)$$

where $i = \sqrt{-1}$ and $\omega = 2\pi f$ is angular frequency. Fourier transform is reversible, and for a given Fourier transform $F(\omega)$, original time signal $f(t)$ can be reconstructed by inverse Fourier transform by

$$\Im^{-1}\{F(\omega)\} = f(t) = \frac{1}{2\pi}\int_{-\infty}^{\infty} F(\omega)e^{i\omega t}d\omega \qquad (4.12)$$

Here, $f(t)$ and $F(\omega)$ are termed Fourier transform pair and represented by $f(t) \leftrightarrow F(\omega)$. Fourier transform $F(\omega)$ is a complex function of frequency and expressed as

$$F(\omega) = a(\omega) - ib(\omega) \qquad (4.13)$$

or

$$F(\omega) = |F(\omega)|e^{i\phi(\omega)} \qquad (4.14)$$

where $a(\omega)$ and $b(\omega)$ are real and imaginary components, and $|F(\omega)|$ and $\phi(\omega)$ are amplitude and phase spectra, respectively, which can be obtained by

$$\begin{aligned} |F(\omega)| &= \sqrt{a(\omega)^2 + b(\omega)^2} \\ \phi(\omega) &= a\tan\left[-\frac{b(\omega)}{a(\omega)}\right] \end{aligned} \qquad (4.15)$$

Fourier transform is the mathematical process which allows us to analyze frequency contents of the time series represented by a series of amplitude values as a function of time in the time domain as like seismic traces. Some of the mathematical properties of Fourier transform are given in Table 4.3.

The seismic traces typically consist of billions of discrete time samples on millions of traces, which make the Fourier transform computationally expensive because it takes excessive time for huge data volumes such as seismic datasets. Today, discrete Fourier transform is computed much faster by using a specific algorithm known as fast Fourier transform (FFT). FFT algorithm works only for time series whose number of time samples are on the order of 2^n (where n is an integer). If the input time series do not exactly contain 2^n discrete amplitude samples, then the data is extended by appending additional zeroes at the end of the series so that it has time

TABLE 4.3 Mathematical Properties of Fourier Transform, Where * Denotes Convolution, a and b are Scalars, n is an Integer, and $Y^*(\omega)$ is Complex Conjugate of $Y(\omega)$

Property	Mathematical Expression
Linearity	$af(t) + bg(t) \leftrightarrow aF(\omega) + bG(\omega)$
Scaling	$f(at) \leftrightarrow \frac{1}{\lvert a\rvert}F\left(\frac{\omega}{a}\right)$ $\frac{1}{\lvert a\rvert}f\left(\frac{t}{a}\right) \leftrightarrow F(a\omega)$
Time shift	$f(t \pm a) \leftrightarrow e^{\pm i\omega a}F(\omega)$
Frequency shift	$e^{-ita}f(t) \leftrightarrow F(\omega + a)$
Symmetry	$f(\omega) \leftrightarrow F(t)$
Time reversal	$f(-t) \leftrightarrow F(-\omega)$
Differentiation (nth order)	$\frac{df^n(t)}{dt^n} \leftrightarrow (i\omega)^n F(\omega)$ $(-it)^n f(t) \leftrightarrow \frac{d^n F(\omega)}{d\omega^n}$
Integration	$\int_{-\infty}^{\infty} f(t)dt \leftrightarrow \frac{F(\omega)}{i\omega}$ $\frac{f(t)}{it} \leftrightarrow \int_{-\omega}^{\omega} F(\omega)d\omega$
Convolution	$f(t)\cdot g(t) \leftrightarrow F(\omega)*G(\omega)$ $f(t)*g(t) \leftrightarrow F(\omega)\cdot G(\omega)$
Crosscorrelation	$R_{xy}(\tau) \leftrightarrow X(\omega)\cdot Y^*(\omega)$
Autocorrelation	$R_{xx}(\tau) \leftrightarrow X(\omega)\cdot$ $X^*(\omega) = \lvert X(\omega)\rvert^2 = R_{xx}(\omega)$

samples exactly equals to an order of the closest 2^n. This process is termed zero padding.

If we compute Fourier transform of a monochromatic sinusoid, we get only one amplitude value in the amplitude spectrum appeared exactly at the frequency value of the input mono-frequency sinusoid. Fig. 4.6A and B show amplitude spectra of two sinusoids with 40 and 100 Hz frequencies, respectively. Their amplitude spectra consist of only two amplitude values at 40 and 100 Hz, respectively. Similarly, the amplitude spectrum of a time signal obtained by the superposition of two sinusoids with 40 and 80 Hz frequency consists of two successive amplitudes at 40 and 80 Hz (Fig. 4.6C). Because the real seismic traces are composed of amplitudes at all frequency components, amplitude spectra of actual seismic traces are continuous and contain a combination of several successive amplitudes which exist at every frequency values.

Fig. 4.7 graphically shows a Fourier analysis of an input time signal. The signal, indicated by (*), is expanded into Fourier series to obtain several sinusoids with different phase and amplitudes. The analysis in Fig. 4.7 is obtained by plotting these sinusoids side-by-side on a horizontal axis of their corresponding frequencies in increasing order. Hence, the horizontal axis of the plot is frequency of the sinusoids. The signal marked by (*) can be reconstructed if all these sinusoids are simply summed up. It can be observed that amplitudes of the sinusoids with approximately 40, 80 and 150 Hz frequency (marked with *A*, *B*, and *C*) are relatively higher than the others.

Fig. 4.8 shows the same information in spectrum display form. Considering the analysis in Fig. 4.7, the amplitude spectrum of (*) signal can be obtained by plotting the amplitudes of each individual sinusoids with respect to their corresponding frequencies (Fig. 4.8B), whereas the phase spectrum of the (*) signal is achieved by plotting the phase angles (Fig. 4.8C) as a function of frequency of the sinusoids. Every single point on the amplitude spectrum corresponds to the amplitude of that component shown in Fig. 4.7, and each point on the phase spectrum indicates the phase of the component at that frequency. Amplitude values in the amplitude spectrum in Fig. 4.8B are also higher at the specific frequency values of approximately 40, 80 and 150 Hz (around A, B, and C).

As a specific case, if the peak amplitudes of all sinusoids constituting the time signal are aligned to time zero ($t = 0$), the signal has a zero phase spectrum, and is termed a zero phase signal. In Fourier analysis of a zero phase signal, amplitudes of the harmonics are constructively summed up and a maximal peak amplitude

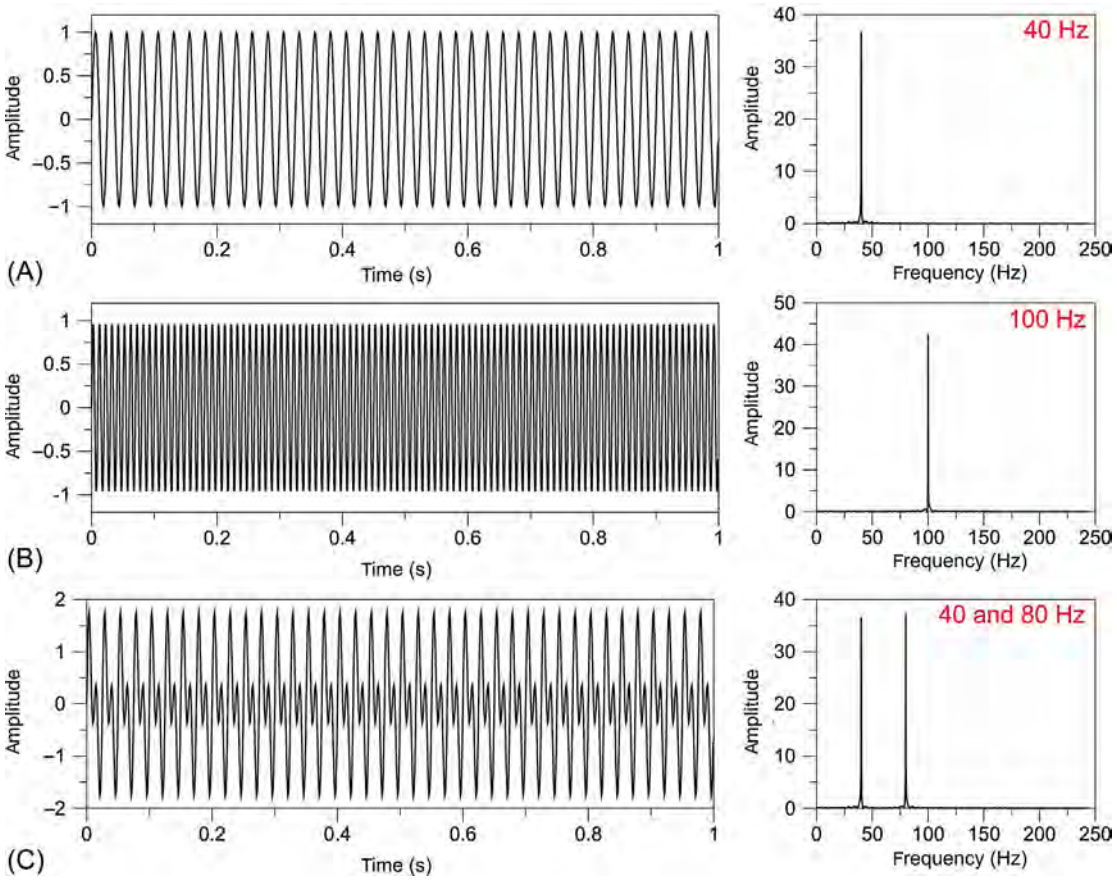


FIG. 4.6 (A) 40 Hz and (B) 100 Hz monochromatic sinusoids, and (C) a time signal obtained by a superposition of 40 and 80 Hz sinusoids. The amplitude spectra of time signals are provided in right panels.

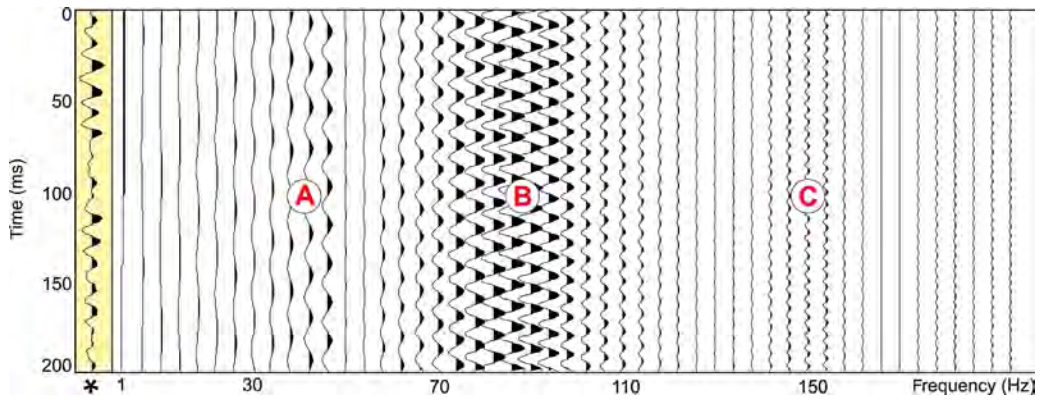


FIG. 4.7 Fourier analysis of a time signal (*) illustrates sinusoids with different amplitudes at different frequency values. Amplitudes marked with A, B, and C around 40, 80, and 150 Hz are relatively higher.

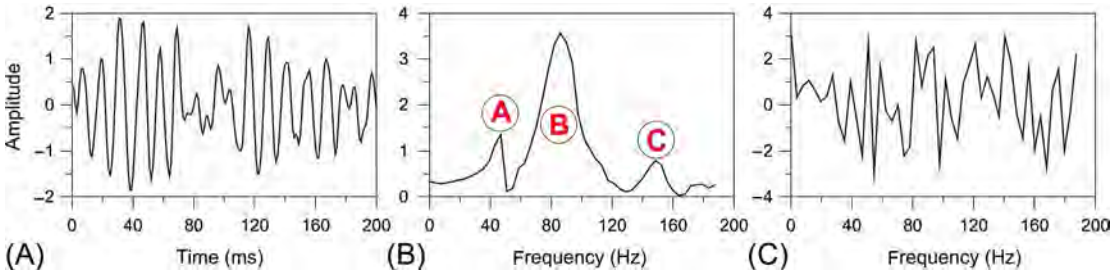


FIG. 4.8 Illustrating the same information in Fig. 4.7 as spectrum display. (A) Same time signal indicated with (*) in Fig. 4.7, and its (B) amplitude and (C) phase spectra. Amplitudes marked with A, B, and C around 40, 80, and 150 Hz are relatively higher as in Fig. 4.7.

occurs at $t = 0$. Adding components with higher frequencies into the series expansion causes narrowing of the time signal; and if we include all the frequency components in the summation, the reconstructed time signal becomes a spike. This implies that a spike, or Dirac delta function, is an in-phase summation of all frequencies with unit amplitudes from 0 to the Nyquist frequency. Therefore, the amplitude spectrum of the Dirac delta function is 1 for all frequencies and its phase spectrum is 0.

Modification of the phase spectrum of a given wavelet changes the form of the wavelet in the time domain. For instance, Fig. 4.9A shows a 40-Hz zero phase Ricker wavelet and its amplitude and phase spectra. If the phase spectrum is modified to increase (Fig. 4.9B) or decrease (Fig. 4.9C) linearly, this induces a time shift to the wavelet along the time axis, but the shape of the wavelet does not change. The inclination of the line is directly proportional to the amount of time shift: a positive dip results in a time shift in the $-t$ direction, while a negative dip causes a time shift in the opposite direction. If the phase spectrum is modified to become a positive (Fig. 4.9D) or negative (Fig. 4.9E) constant value, then the shape of the wavelet changes. Finally, it is possible to change the form of the wavelet completely by modifying the phase spectrum arbitrarily (Fig. 4.9F). The amplitude spectra of all wavelets in Fig. 4.9 are, however, exactly the same, because they all have the same frequency content, and the only difference is their phase spectra.

Understanding the effects of modifications on the phase spectrum of a time signal is more difficult than the effects of amplitude spectrum modification. The phase content of the signal may be quite complex in reality, and any interference to the phase may completely change the signal shape. In practice, generally the amplitude spectrum is modified during seismic processing and the signal frequency bandwidth may be modified. The phase spectrum is, however, generally kept untouched.

4.6 2D FOURIER TRANSFORM

In a 1D Fourier transform, the input wavelet is only a function of time. In practice, however, the seismic data is time and space (offset or common midpoint) dependent, which allows us to apply a 2D Fourier transform to the seismic data. The Fourier transform pair for the time dimension is frequency, while it is wavenumber for the space dimension. Forward and inverse Fourier transforms of two-dimensional $f(x, t)$ wave fields are expressed as

$$\Im\{f(x,t)\} = F(k,\omega) = \iint f(x,t)e^{i(kx-\omega t)}dxdt \quad (4.16)$$

$$\Im^{-1}\{F(k,\omega)\} = f(x,t) = \iint F(k,\omega)e^{i(-kx+\omega t)}dkd\omega \quad (4.17)$$

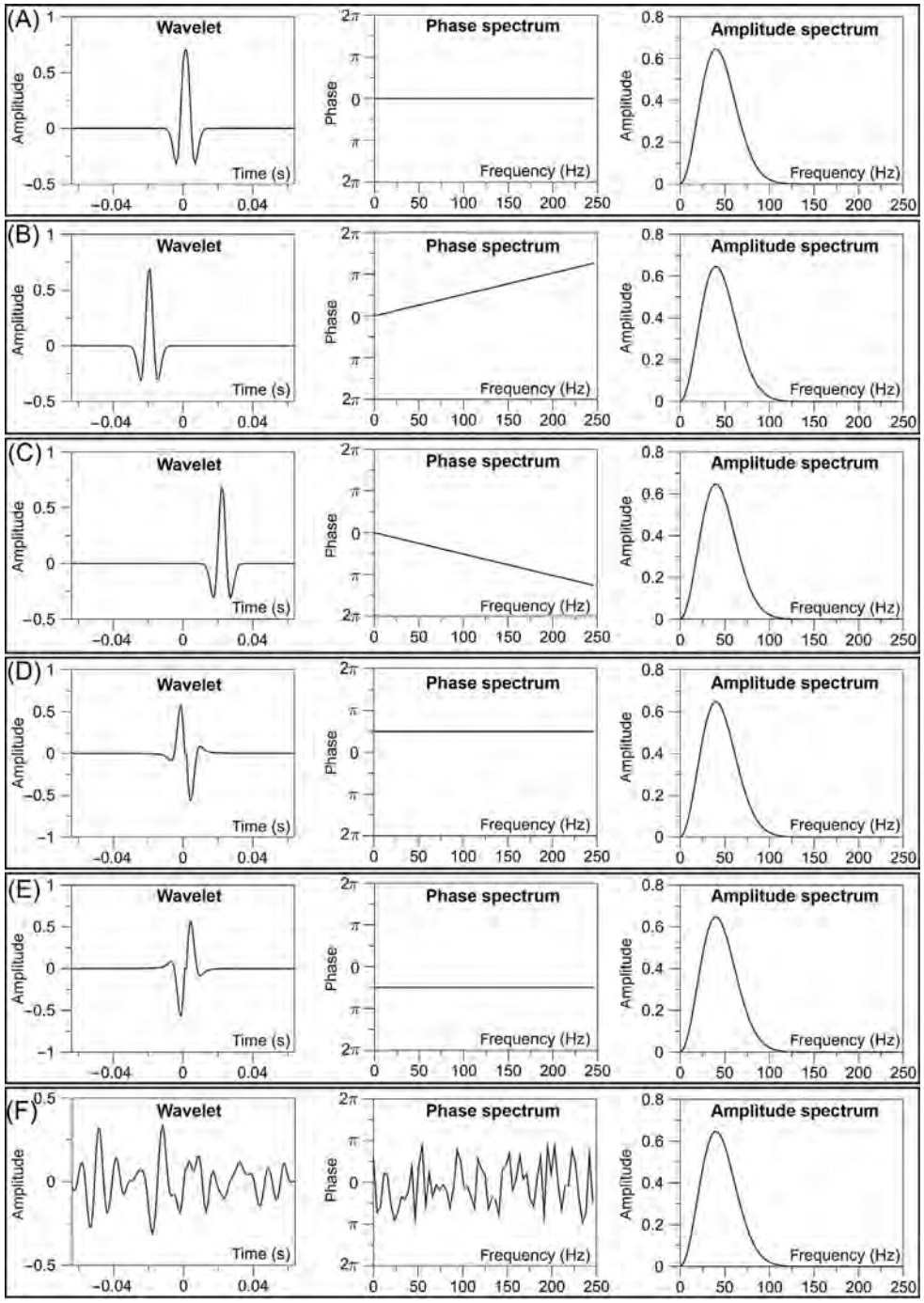


FIG. 4.9 (A) 40-Hz zero phase Ricker wavelet (left) and its phase (middle) and amplitude (right) spectra. Wavelet shape changes if the phase spectrum becomes (B) linearly increasing with the frequency, (C) linearly decreasing with the frequency, (D) a positive constant value, (E) a negative constant value. (F) Random modification of the phase spectrum while keeping the amplitude spectrum untouched changes the shape of the wavelet completely.

Using a 2D Fourier transform, the signal observed in the time-distance (t-x) domain is transferred into the frequency-wavenumber (f-k) domain. Hence, the obtained spectrum is also known as the f-k spectrum. A 2D Fourier transform of discrete signals is achieved by successive application of the 1D Fourier transform: the first one is along the time axis, which transforms the data from the (t, x) to (f, x) domain. Then a second 1D Fourier transform is performed along the distance axis, which transforms the data from the (f, x) to (f, k) domain. In practice, the events with different dips in the time domain can be discriminated in the f-k domain: the amplitudes of events with positive dip (from near to far offset) appear at the positive panel, whereas the amplitudes of events with negative dip (from far to near offset) are grouped in the negative panel (Fig. 4.10) of the f-k panel. For a constant frequency, high inclination of the seismic data corresponds to high wavenumber.

The events with different dips in the t-x domain are located at different parts of the f-k panel in the frequency domain. For a certain dip value, amplitudes of all frequency components are aligned on a straight line passing through the origin of the f-k panel. The amplitudes of 0° dip (horizontal events) on the seismic data appear at $k = 0$ axis (e.g., along the vertical frequency axis). The line on which the amplitudes are aligned approaches to the horizontal wavenumber axis in the f-k panel as the dip of the event in the time domain increases (Fig. 4.11).

Fig. 4.12 shows zero offset synthetic seismograms formed by 20-Hz monochromatic sinusoids consisting of linear events with increasing dips. Because the sections have monofrequency sinusoids with a unique positive dip, their amplitudes appear at their corresponding single frequency and wavenumber values in the f-k spectra. A 0° dip corresponds to 0 wavenumber and its amplitude, being equal to the amplitude of a single-frequency sinusoid, is plotted at a point along the 20-Hz frequency on the f-k panel. As the dip increases in the time domain, the amplitudes of the sinusoids move towards the positive wavenumber axis. Regardless of the dips of the events in the time domain, the amplitudes of the sinusoids appear at their 20-Hz frequency value in the f-k domain as expected.

Fig. 4.13 illustrates similar seismograms with their f-k spectra, this time, however, calculated with 60-Hz sinusoids. Only amplitudes of seismograms for 5 ms/trace dips appear at the correct wavenumber value in the positive panel in the f-k spectrum, whereas for seismograms of 8 ms/trace dip, the amplitudes arise at both positive and negative panels. This suggests that the section includes events with both positive and negative inclinations, which are observed as

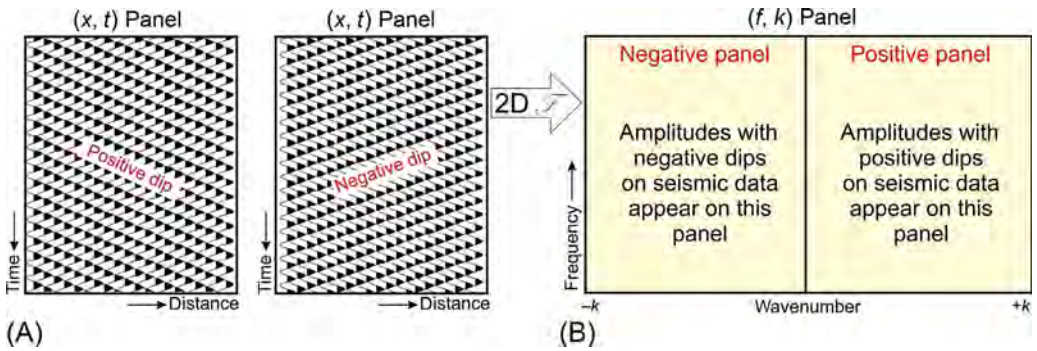


FIG. 4.10 Schematic illustration of events with different dips in (A) time, (B) f-k domains.

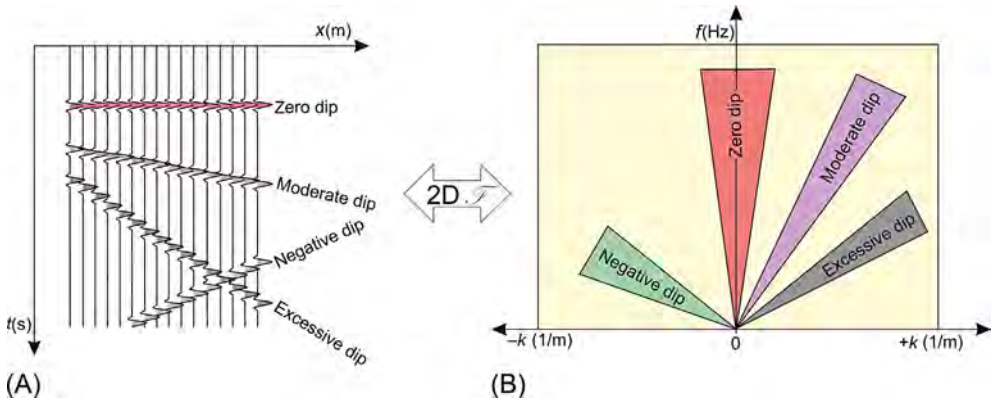


FIG. 4.11 Schematic illustration of the *f-k* domain display of events with different dips in the time domain. (A) Time-distance (*t-x*) domain, and (B) frequency-wavenumber (*f-k*) domain.

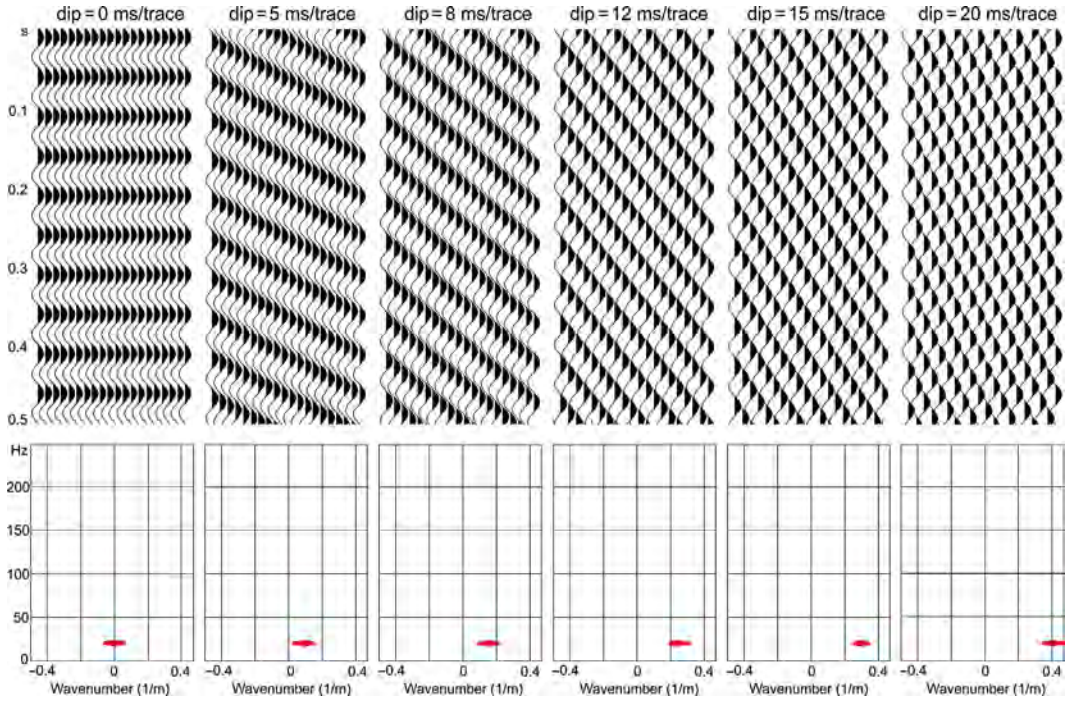


FIG. 4.12 Zero offset synthetic sections consisting of linear events with increasing dips formed by monochromatic sinusoids of 20 Hz and their corresponding *f-k* spectra (lower panels).

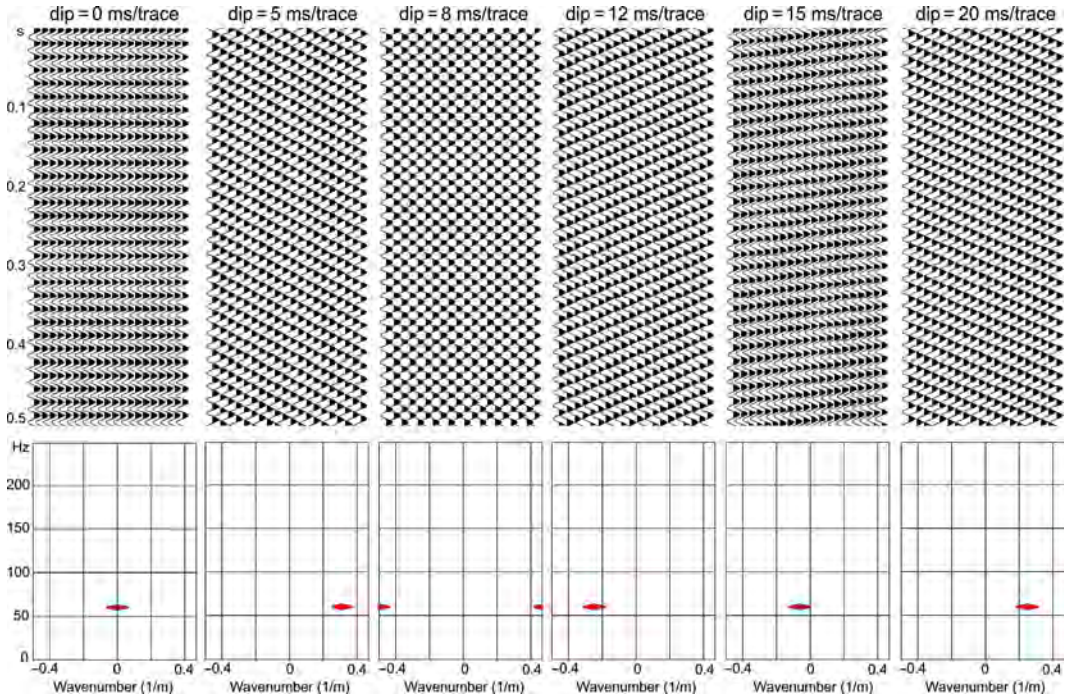


FIG. 4.13 Zero offset synthetic sections consisting of linear events with increasing dips formed by monochromatic sinusoids of 60 Hz and their corresponding *f-k* spectra (lower panels).

crisscross events in the time section. The amplitudes of the events with 12 and 15 ms/trace dip are located at negative panels in the *f-k* spectra, indicating that 60-Hz monochromatic events with 12 and 15 ms/trace dip are spatially aliased. This is also evident at the synthetic sections where the dip of the events is incorrect in the negative direction. Furthermore, the events with 20 ms/trace dip appear at the positive panel, indicating that they are aliased twice, and therefore their dips on the time sections are again in a positive direction.

Let's assume that we have seismograms composed of linear summation of several sinusoids with different frequencies but the same dip. Fig. 4.14 shows zero offset synthetic seismograms consisting of linear events with increasing dips formed by superposition of 20-, 60-, 80- and 140-Hz sinusoids, and their corresponding *f-k* spectra. The amplitudes of all frequency components with 0° dip appear at their corresponding frequency value along the $k = 0$ axis in the *f-k* panel, indicating that there is no spatial aliasing. Each dipping event seems to be aligned on the dashed blue line passing through the origin of the *f-k* panel. As the dip of linear events in the time domain increases, the inclination of this line also increases, approaching the horizontal wavenumber axis, which ultimately results in spatial aliasing in the *f-k* domain. Aliasing occurs at higher frequency components first. For instance, although the amplitudes of events with 20, 60 and 80 Hz appears exactly at their expected wavenumber value on the *f-k* panel for the seismograms with 5 ms/trace dip, the amplitude of the 140-Hz event is located at the negative *f-k* panel, that is, only the amplitudes of 140-Hz events are spatially aliased for 5 ms/trace dip.

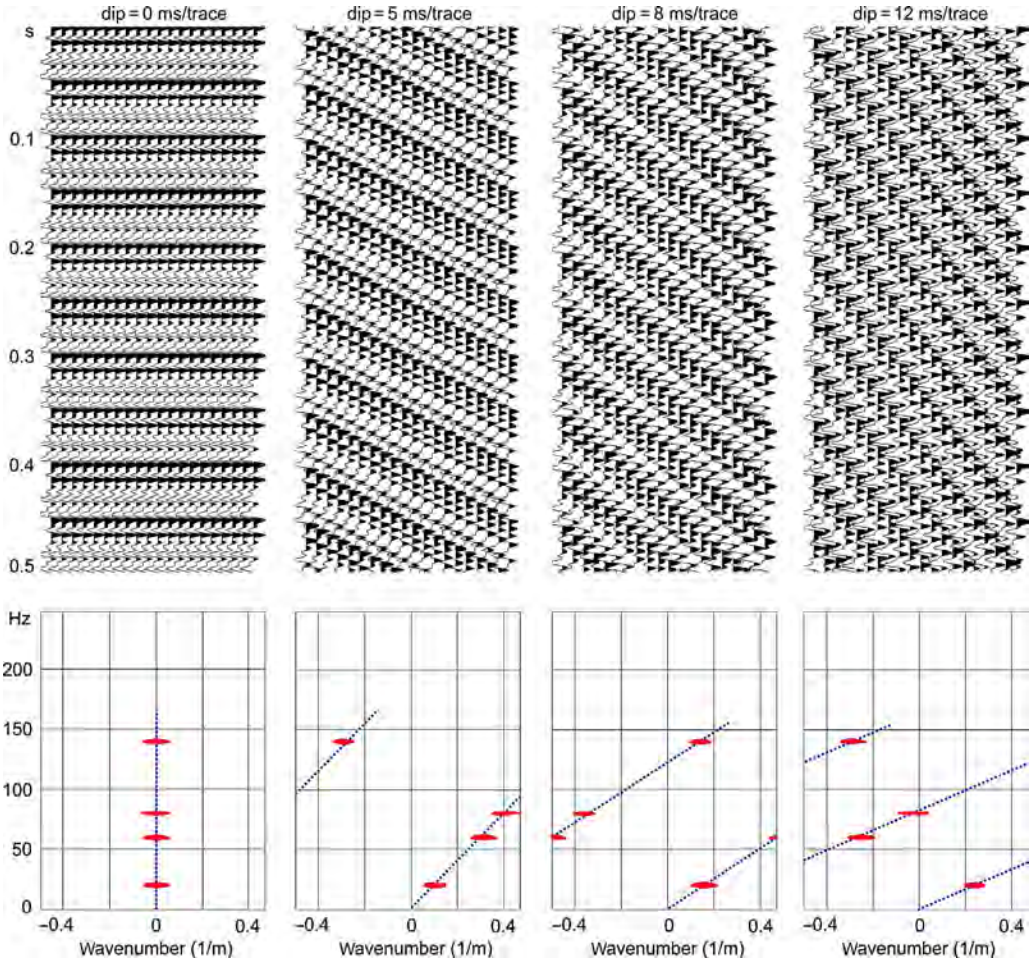


FIG. 4.14 Zero offset synthetic seismograms consisting of a linear superposition of sinusoids with 20-, 60-, 80- and 140-Hz frequencies with different dips in the time domain, and their corresponding *f-k* spectra (lower panels).

For 8 ms/trace dip events, the amplitudes of 60-, 80- and 140-Hz components are aliased. Furthermore, the amplitude of the 140-Hz component is aliased twice for 12 ms/trace dip.

These seismograms of monochromatic sinusoids are represented by a single point in the *f-k* domain, and they can be considered as monochromatic plane waves propagating at a certain angle from the vertical. Because the seismic wave field is a combination of several dips and frequencies, it can be considered to be the summation of several different plane wave fields. The 2D Fourier transform decomposes the spherical wave field recorded during the seismic surveys into its plane wave components. A similar plane wave decomposition method is known as slant stack or τ-p transform, explained in Section 4.9.

Fig. 4.15A shows zero offset synthetic seismograms with 2-m trace interval consisting of dipping events in opposite directions, indicated by A, B, C, and D, computed using a 100-Hz Ricker

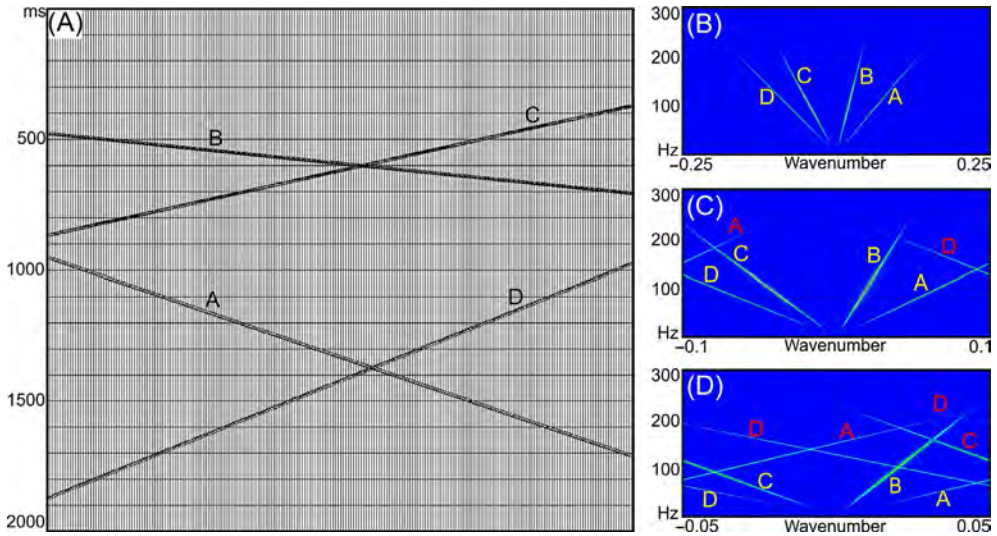


FIG. 4.15 (A) A synthetic zero offset section with four dipping events indicated by A, B, C, and D, and its *f-k* spectra for (B) 2 m, (C) 5 m, and (D) 10 m trace interval. Spatially aliased event amplitudes are indicated in *red* on the *f-k* spectra.

wavelet. In the *f-k* panel for the section of the 2-m trace interval in Fig. 4.15B, amplitudes of all dipping events appear as straight lines passing through the origin and there is no spatial aliasing in the *f-k* spectrum. If we recompute the time section with a 5-m trace interval, inclinations of all straight lines increase and the amplitudes of the events A and D with extreme dip are spatially aliased in the *f-k* spectrum (Fig. 4.15C). For a 10-m trace interval, only the amplitudes of event B with the smoothest dip are not aliased in the *f-k* spectrum, while the amplitudes of event D are aliased twice (Fig. 4.15D).

In the 2D Fourier spectrum of the seismic data, spatial aliasing is often pronounced, depending on the trace interval of the input data. The Nyquist wavenumber, k_N, determines the aliasing wavenumber, which is

$$k_N = \frac{1}{2\Delta x} \tag{4.18}$$

where Δx is the spatial sampling interval (or trace interval of the input). Wavenumbers larger than the Nyquist wavenumber will simply alias in the *f-k* domain. An aliased signal is undesired since it represents incorrect dips in the time domain. The maximum unaliased frequency on an *f-k* spectrum F_u can be calculated by

$$F_u = \frac{V}{2\Delta x \sin\theta} \tag{4.19}$$

where Δx is the trace interval, V is the velocity of the medium, and θ is the inclination of the event in the time domain. Eq. (4.19) suggests that the higher the dip on time sections, the lower the aliasing frequency in the *f-k* domain. Similarly, the higher the trace interval in the time domain, the lower the aliasing frequency in the *f-k* domain.

Fig. 4.16A shows a real shot gather with its *f-k* spectrum. The data has 96 traces with 6.25 m trace interval. The *f-k* spectrum of the shot indicates that the components higher than approximately 120 Hz are spatially aliased. Fig. 4.16B and C show the same shot but decimated to obtain shot records with 48 (12.5 m group interval) and 32 (18.75 m group interval) traces, respectively. The aliasing frequency of the *f-k* spectra decreases to 60 Hz for the shot with 12.5 m and 40 Hz for the shot with 18.75 m group interval. Furthermore, the amplitudes of the

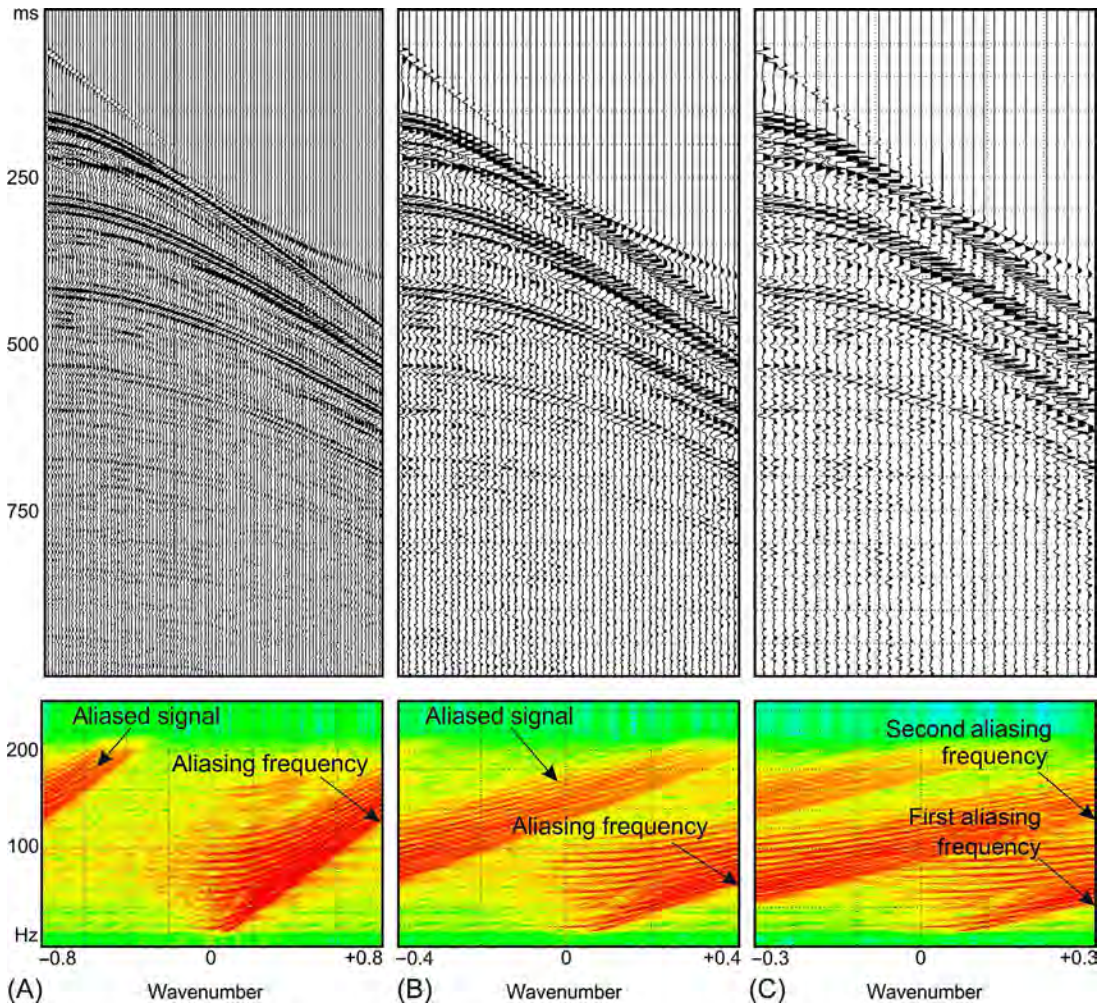


FIG. 4.16 (A) A real shot gather consisting of 96 channels with 6.25 m group interval, and its decimated versions for (B) 48 channels (12.5 m group interval), and (C) 32 channels (18.75 m group interval). The *f-k* spectra of each gather are illustrated in the lower panels. The aliasing frequency decreases with the increasing trace interval of the input.

shot with 18.75 m group interval in Fig. 4.16C seem to be aliased twice approximately at 130 Hz in the *f-k* panel. The analysis suggests that the aliasing frequency significantly decreases as the trace interval of the input data increases.

The aliased energy is typically filtered out by an *f-k* filter during the conventional seismic processing. Spatial aliasing has negative effects on the performance of some seismic processing applications, such as migration. Migration algorithms recognize aliased energy incorrectly and migrate it in the opposite updip direction. Theoretical approaches to avoid the spatial aliasing might be

(i) decreasing the dips of the events in the input data

(ii) cutting out the high-frequency components with a low-pass filter
(iii) decreasing the group interval

The first two approaches are practically infeasible, since the first one will change the inclination of the events in the data, and the second will remove the high-frequency information. The third approach requires increasing the total number of recording channels for a standard streamer length during the acquisition. If this is not possible, the group interval can be reduced by using a data-dependent interpolation method, which provides extra synthetic traces between the successive channels.

4.7 Z TRANSFORM

The z transform converts discrete time series into a polynomial expressed by the powers of the variable z. That is, the z transform of a time series is a polynomial of z, and the coefficients of z are the discrete samples of the input series. The discrete Fourier spectrum of $x(t)$ is given by

$$x(\omega) = \sum_{-\infty}^{\infty} x_n e^{-i\omega n \Delta t} \tag{4.20}$$

and if we expand the summation, we get

$$x(\omega) = x_0 + x_1 e^{-i\omega\Delta t} + x_2 e^{-i\omega 2\Delta t} + \cdots \tag{4.21}$$

Substituting $z = e^{-i\omega\Delta t}$ into Eq. (4.20), we get

$$x(z) = \sum_{-\infty}^{\infty} x_n z^n \tag{4.22}$$

If the elements of the discrete x_n series are

$$x_n = x_0, x_1, x_2, x_3, x_4, \ldots \tag{4.23}$$

then its z transform is expressed as

$$x(z) = x_0 + x_1 z + x_2 z^2 + x_3 z^3 + \ldots. \tag{4.24}$$

The power of the variable z corresponds to the time lag of the discrete time samples of the x_n series. Therefore, if we multiply the transformation by z^{-1}, we shift the time series one sampling rate along the time axis.

The z transform has several applications in signal processing. The Fourier transform can be done using the z transform. The convolution process can be performed with a multiplication process by the z transform. The multiplication of the z transforms of two time series equals the z transform of their convolution. Let's consider two series as $x(t) = (2, -1)$ and $y(t) = (3, 2, -1)$. Their convolution is $x(t)^* y(t) = (6, 1, -4, 1)$. The z transforms of both series are $x(z) = (2 - z)$ and $y(z) = (3 + 2z - z^2)$. The multiplication of both z transforms gives $x(z)\cdot y(z) = (6 + z - 4z^2 + z^3)$, and the coefficients of the resultant polynomial define the inverse z transform, $z\{x(z)\cdot y(z)\}^{-1} = (6, 1, -4, 1)$, which corresponds to the convolution of the $x(t)$ and $y(t)$ series.

The z transform is also used in wavelet processing. The inverse of the seismic wavelet, which is used in deterministic deconvolution applications (Section 6.3), can be obtained by the z transform. The relation between the wavelet $w(t)$ and its inverse $\overline{w}(t)$ is given by

$$w(t)^* \overline{w}(t) = \delta(t) \tag{4.25}$$

where $\delta(t)$ is the Dirac delta function and its z transform is $z\{\delta(t)\} = 1$. Hence, we get the inverse

$$w(z)\cdot \overline{w}(z) = 1 \tag{4.26}$$

$$\overline{w}(z) = 1/w(z) \tag{4.27}$$

The inverse of the z transform of any function can be obtained by Taylor's series expansion. Taylor's series approximation of an $f(x)$ function in the neighborhood of zero is known as the MacLaurin series and can be found in the following form of infinite series expansion:

$$f(x) = f(0) + \frac{f'(0)}{1!}x + \frac{f''(0)}{2!}x^2 + \frac{f'''(0)}{3!}x^3 + \cdots \tag{4.28}$$

where $f'(0)$ denotes the first derivative of $f(x)$ around zero, $f''(0)$ denotes the second derivative,

etc. For example, let's find out the inverse of the wavelet $w(t) = (2,\ 1)$. The z transform of the wavelet is $w(z) = (2 + z)$ and its inverse is $\overline{w}(z) = 1/(2+z)$. In order to determine the inverse $\overline{w}(z)$, derivatives of $1/(2 + z)$ are calculated. The first four derivatives of $\overline{w}(z) = 1/(2+z)$ are

$$\overline{w}'(z) = -\frac{1}{(2+z)^2} \quad \overline{w}''(z) = \frac{2}{(2+z)^3} \quad \overline{w}'''(z) = -\frac{6}{(2+z)^4} \quad \overline{w}''''(z) = \frac{24}{(2+z)^5}$$

Substituting $z = 0$ into the derivatives of $\overline{w}(z)$, we can obtain the coefficients in Eq. (4.28). Using a MacLaurin series expansion, the z transform of the inverse of wavelet $w(t) = (2,\ 1)$ can be obtained as

$$\overline{w}(z) = \frac{1}{2} - \frac{1}{4}z + \frac{1}{8}z^2 - \frac{1}{16}z^3 + \frac{1}{32}z^4 - \cdots$$

Getting the coefficients of z, the inverse of the wavelet $w(t) = (2,\ 1)$ can be found as $\overline{w}(t) = (1/2,\ -1/4, 1/8,\ -1/16, 1/32, \ldots)$.

4.8 HILBERT TRANSFORM

The Hilbert transform is a useful tool to obtain extra information from the seismic data, known as complex trace attributes, explained in Section 12.5. It is a mathematical process applying a $\pi/2$ rad phase difference to each frequency component of the input function. The theoretical basis of the transform depends on the definition of analytical function. The time-dependent analytical function $u(t)$ is a complex function and can be defined as

$$u(t) = x(t) + iy(t) \tag{4.29}$$

where $x(t)$ and $y(t)$ are real and imaginary components, respectively, and are known as the Hilbert transform pair (Fig. 4.17A). Bracewell (1965) suggested that the imaginary component $y(t)$ is obtained by the Hilbert transform of the real component $x(t)$ by

$$y(t) = h(t)^* x(t) \tag{4.30}$$

where * denotes convolution, $h(t)$ is the Hilbert transform operator (Fig. 4.17B) defined by

$$h(t) = \frac{1}{\pi t} \tag{4.31}$$

and its Fourier transform $H(\omega)$ is described as (Fig. 4.17C):

$$H(\omega) = -i\,\mathrm{sgn}(\omega) = \begin{cases} -i & \omega > 0 \\ +i & \omega < 0 \\ 0 & \omega = 0 \end{cases} \tag{4.32}$$

where $\mathrm{sgn}(\omega)$ is the signum function. Substituting Eq. (4.31) into Eq. (4.29), we get (Barnes, 2007):

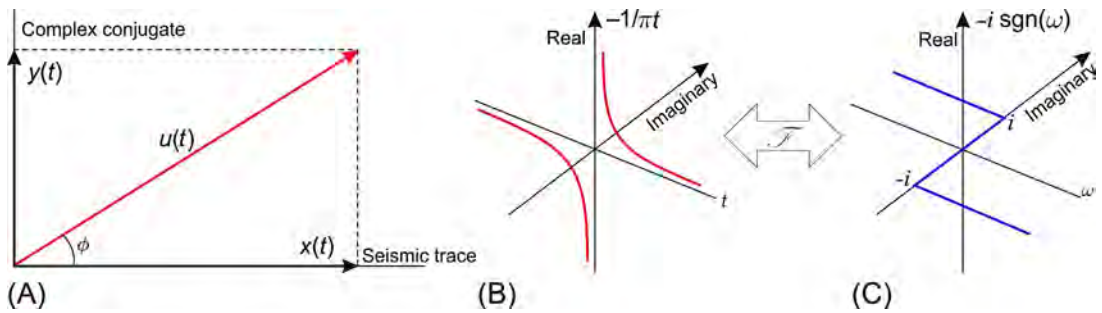


FIG. 4.17 (A) Analytical signal, (B) Hilbert transform operator, (C) Fourier transform of (B).

$$u(t) = x(t) + i\frac{1}{\pi t} * x(t)$$
$$u(t) = \left[\delta(t) + i\frac{1}{\pi t}\right] * x(t) \tag{4.33}$$

The Hilbert transform of an analytical signal provides its complex conjugate. As related to seismic exploration, the real component $x(t)$ corresponds to the recorded seismic trace and $y(t)$ is the imaginary component calculated by the Hilbert transform of $x(t)$. Hence, the analytical signal can be obtained by applying the expression in brackets in Eq. (4.33) to the seismic trace. The complex analytical function consisting of real and imaginary components is schematically illustrated in Fig. 4.18.

4.9 τ-P TRANSFORM (SLANT STACK)

The τ-p transform, also known as the Radon transform or slant stack, is a plane wave decomposition method and is used in suppression of multiple reflections, time-variant dip filtering, trace interpolation, velocity analysis and prestack migration applications. Shot or CDP gathers, which are normally formed by spherical wave fields, can be decomposed into plane wave components. This decomposition process is achieved by applying a linear time shift to the data and then summing the amplitudes along the offset axis.

The τ-p transform converts the offset axis of the seismic data into a ray parameter (p) axis, which represents the horizontal phase velocity, and the time axis into zero offset time, $\tau = t(0)$. The trace gather formed by several traces for different p values is termed the τ-p gather, or slant stack gather. Each trace in this gather corresponds to a plane wave propagating with a certain angle from vertical. The seismic signal generated by the seismic source propagates in all directions in a spherical manner, and the reflected signals reach each receiver at a different angle of incidence. This angle increases as the offset increases or the depth of the reflective interface decreases.

Considering the variable p as a ray parameter, Snell's law proposes

$$\frac{\sin\theta_1}{V_1} = \frac{\sin\theta_2}{V_2} = \frac{\sin\theta_3}{V_3} = \cdots\cdots = p \tag{4.34}$$

where θ_i are the incidence angles of the reflected waves for each interface, and V_i are the velocities of each layer. The parameter $(\sin\theta)/V$ in

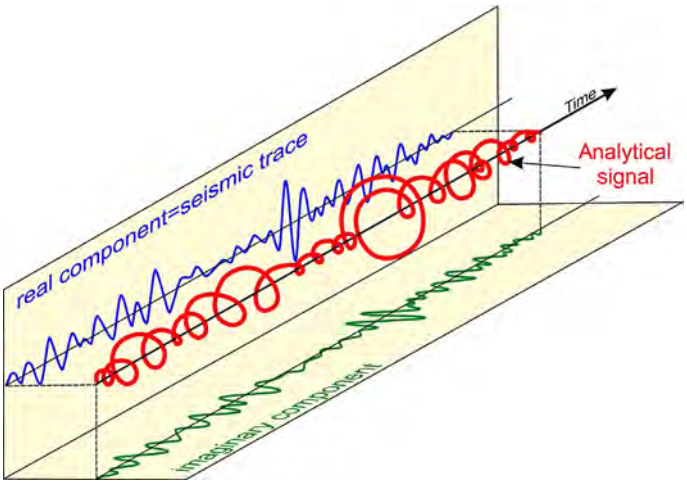


FIG. 4.18 Analytical signal and its real and imaginary components (Taner et al., 1979).

Eq. (4.34) is constant along the ray path in a layered media.

For a plane wave decomposition of a shot or CDP gather, the amplitudes of all traces in the gather must be summed up along several slanted lines, each having a time lag of the sampling rate (Δt). Fig. 4.19 schematically shows plane wave decomposition of a reflection hyperbola on a CDP gather. Let's assume that the CDP contains only one reflection hyperbola. A single reflection hyperbola on shot or CDP gathers becomes an elliptical hyperbola on τ-p gathers. First, the amplitudes on the CDP gather are summed along the horizontal line ($p = 0$) indicated by 1 in Fig. 4.19. This horizontal line is tangential to the reflection hyperbola around the point A, and point A is moved to a point A' in the τ-p gather. Then the line is inclined, and this new line, indicated by 2, is tangential to the reflection hyperbola at point B, which is transformed to point B' in the τ-p gather. The process continues in this manner; each time after increasing the inclination of the line, the amplitudes on the CDP gather along the line are summed up, and the obtained sum is assigned to the corresponding point on the τ-p gather. The line with the $p = 1/V$ dip has the largest inclination, indicated by number 5 in Fig. 4.19, and is asymptotical to the reflection hyperbola on the CDP gather. This line corresponds to a plane wave propagating horizontally (e.g., at a 90-degree angle from vertical), and the sum of the amplitudes along this line is assigned to point E' on the τ-p gather. The process of summation of the amplitudes along straight lines is known as a linear τ-p transform. Amplitudes,

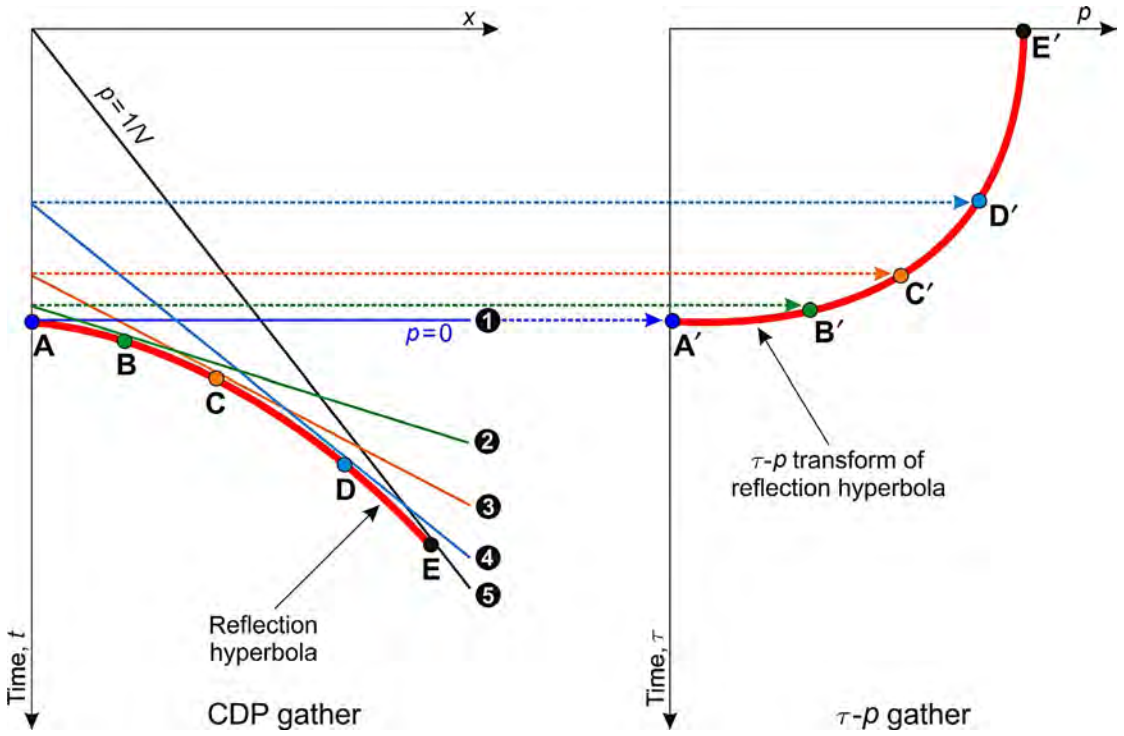


FIG. 4.19 Schematic representation of plane wave decomposition of a single reflection hyperbola on a CDP gather by τ-p transform.

however, can be summed along the hyperbolas or parabolas instead of the lines, which are termed the hyperbolic and parabolic τ-p transform, respectively.

A linear event on the CDP or shot gather (e.g., refractions, guided waves or direct waves) appears as a single point on the τ-p gather at its corresponding p trace determined by its inclination in the time domain (Fig. 4.20A). Similarly, a linear event on a τ-p gather becomes a single point in the CDP or shot gathers. Hyperbolic events such as reflections on CDP or shot gathers are transformed into semielliptical events on τ-p gathers with a specific appearance, determined by their curvature and zero offset time $t(0)$ on the shot gathers (Fig. 4.20B).

In theory, far offset flanks of reflection and diffraction hyperbolas extend to infinite offsets along the distance axis. This means that, in practice, all of the reflection hyperbolas on shot gathers are incomplete because the seismic streamers are of finite length. Therefore, amplitudes of reflection hyperbolas at long offsets on shot records are lacking, and their counterparts on τ-p gathers are also incomplete and do not appear as perfect semielliptical events. Their amplitudes close to the higher p values on the τ-p gathers are always lacking.

Fig. 4.21 shows the τ-p transform of a real shot gather, which consists of a number of reflection hyperbolas as well as refracted and direct waves. While linear events like refracted and direct waves appear as single points on a τ-p gather, reflection hyperbolas can be observed as semielliptical events approaching the p value of 1/1500 s/m (e.g., the inverse of P wave velocity in seawater).

After carrying out a processing application (generally muting or filtering) in the τ-p domain, for instance zeroing out the amplitudes of multiple reflections, it is possible to reconstruct a time signal in the time-offset domain via the inverse τ-p transform. The point here is that the total trace number after the inverse transform is not necessarily the same as the number of traces in the input shot gather. That is, we can obtain extra traces during the inverse transform, which means that it is possible to perform

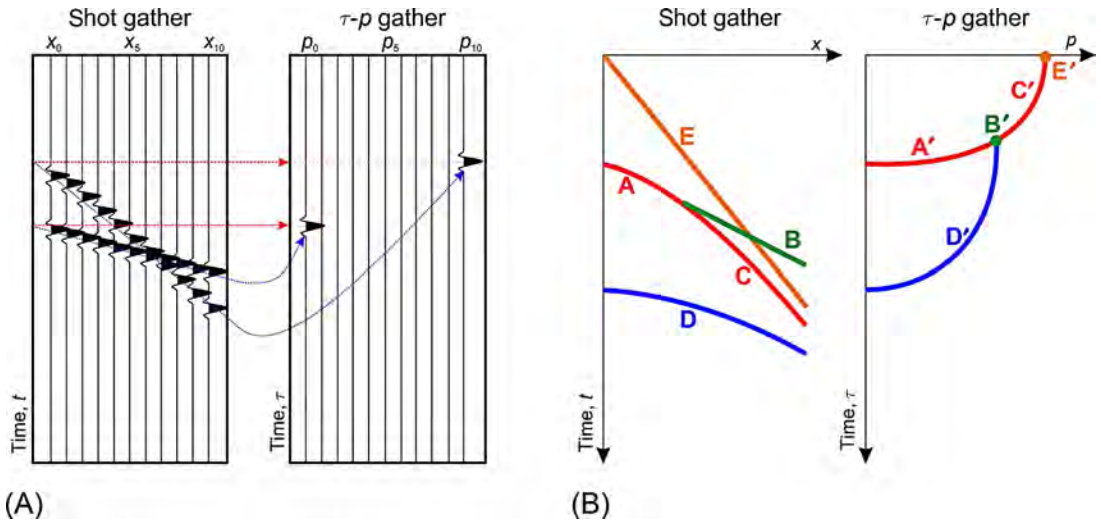


FIG. 4.20 (A) Schematic display of linear events on the shot and τ-p gathers, (B) schematic τ-p domain representation of different events on a shot gather. (A and D) subcritical reflections (reflected with an angle smaller than critical angle), (B) head wave, (E) direct wave, (C) supercritical reflection (reflected with an angle higher than critical angle).

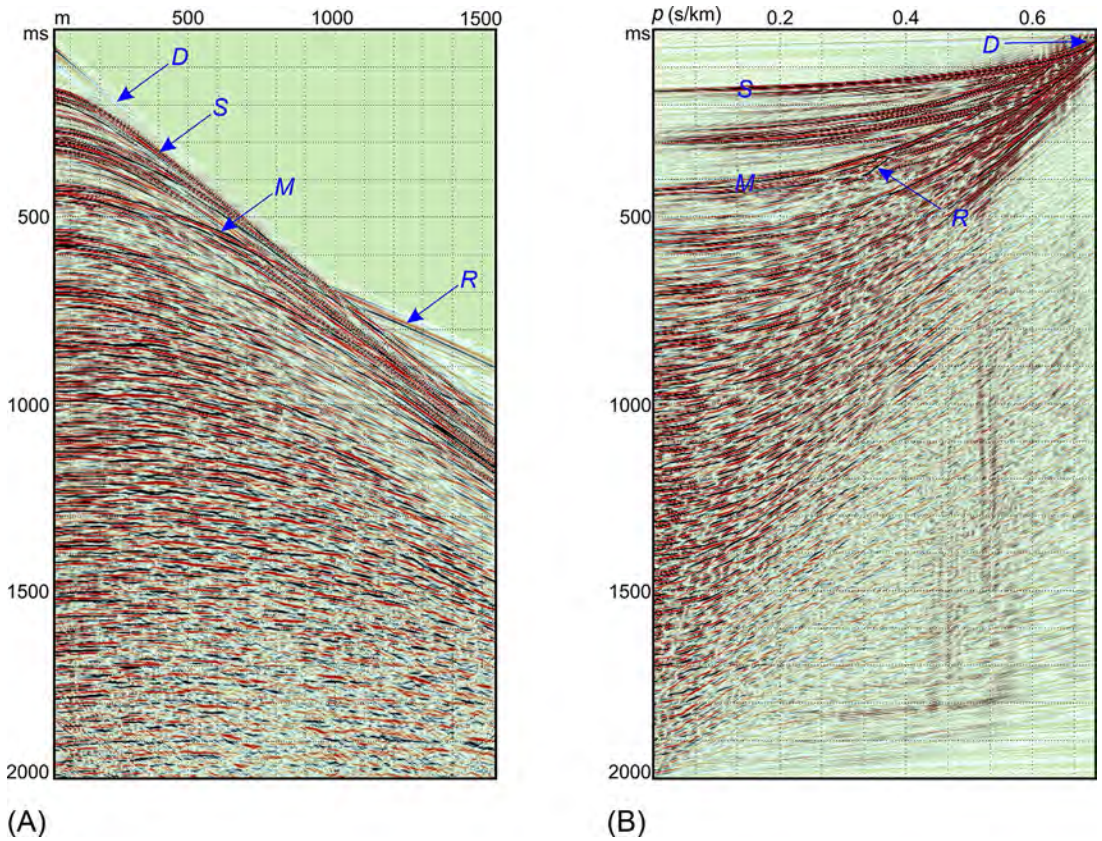


FIG. 4.21 (A) A real shot gather, and (B) its τ-p transform. *S*, seabed reflection; *M*, multiple reflection; *D*, direct wave; *R*, refracted wave.

trace interpolation by the τ-p transform. This allows us to reduce the trace interval in a CDP or shot gather, and spatial sampling can be increased. This is particularly useful in prevention of spatial aliasing during *f*-*k* filtering.

4.10 SAMPLING THEORY

Digitizing of a continuously observed analog signal in regular time intervals for further digital processing is termed sampling. If the continuous signal observed between $0 \leq t \leq T$ is digitized at Δt time intervals, discrete data will consist of $N = (T/\Delta t) + 1$ discrete amplitude samples. The maximum available frequency after digitization at regular Δt intervals is known as the Nyquist frequency (f_N) and is determined only by the sampling interval. The Nyquist frequency is expressed as

$$f_N = \frac{1}{2\Delta t} \tag{4.35}$$

$$\Delta f = \frac{2f_N}{N} = \frac{1}{N\Delta t} \tag{4.36}$$

where Δf is the frequency sampling interval. The higher the sampling interval Δt chosen, the smoother the digitized signal that is obtained, which results in a complete loss of high

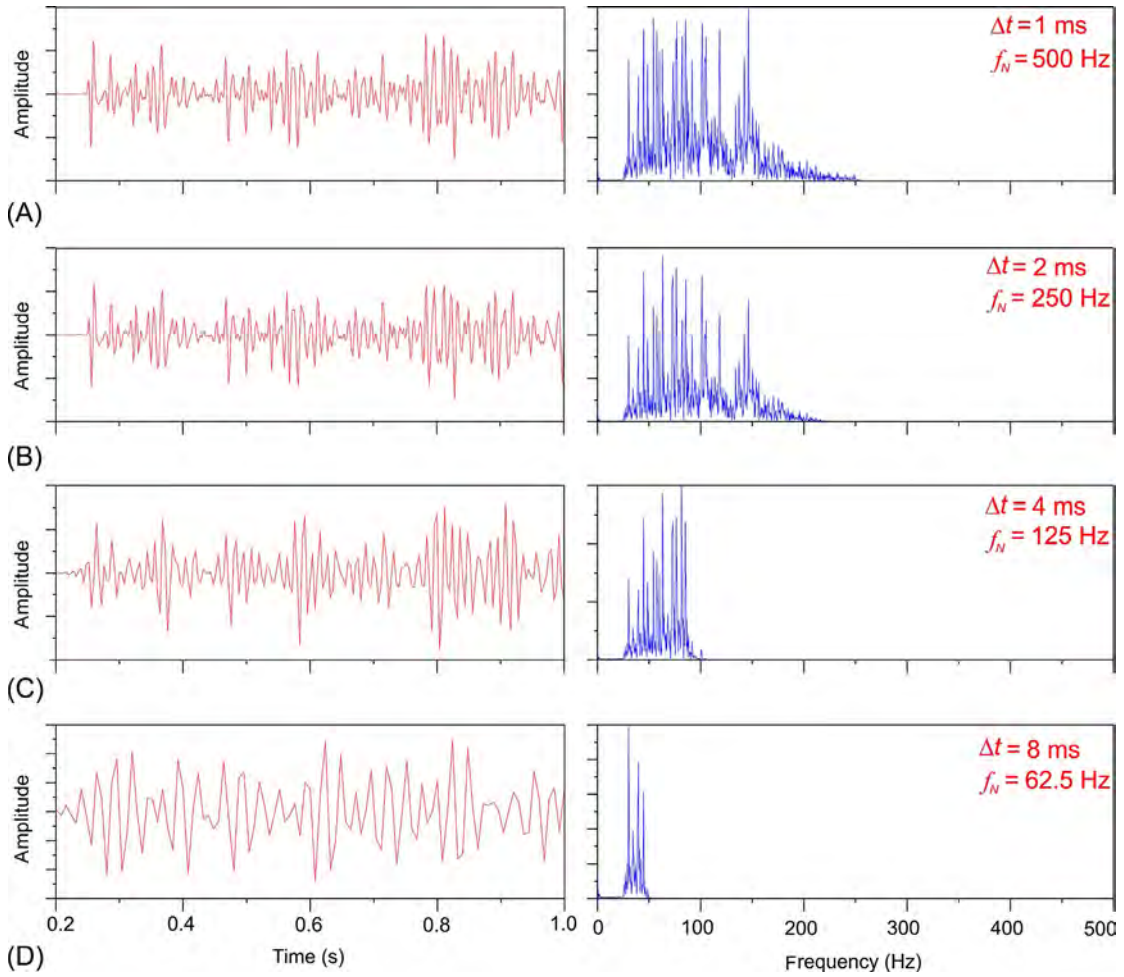


FIG. 4.22 A real seismic trace sampled at (A) 1 ms, (B) 2 ms, (C) 4 ms, and (D) 8 ms sampling rates (left) and their corresponding amplitude spectra (right). Δt is sampling interval and f_N represents Nyquist frequency.

frequencies. Fig. 4.22 shows a real seismic trace sampled at 1, 2, 4 and 8 ms sampling rates and their respective amplitude spectra. The signal loses its details when sampled at high sampling intervals. These missing details correspond to high-frequency components.

In digital recording, the frequency components higher than the Nyquist frequency are not recorded and these components cannot be recovered after digitization. If the maximum frequency of the signal propagating in the subsurface is 150 Hz, the components between 125 and 150 Hz are lost (cannot be recorded) when the sampling rate is 4 ms ($f_N = 125$ Hz), and these components cannot be recovered during the following processing stages. In practice, these missing amplitudes actually do not vanish and they reappear at low frequencies. For instance, the amplitude spectrum of the 100-Hz sinusoid sampled at $\Delta t = 2$ ms ($f_N = 250$ Hz) in Fig. 4.23A contains only one amplitude at the 100-Hz frequency, as expected. If we digitize the same signal using a

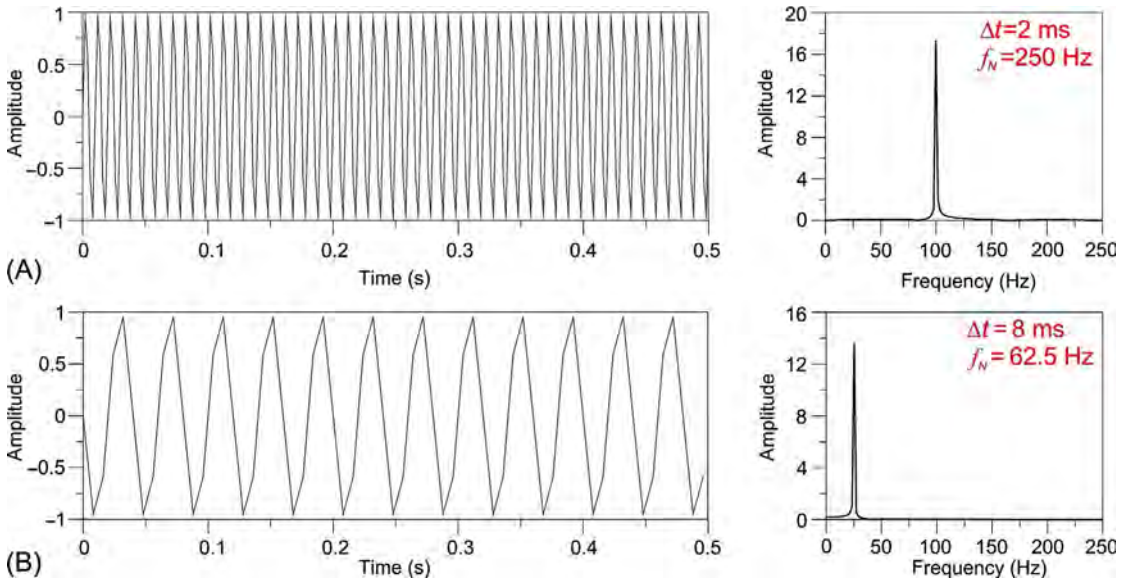


FIG. 4.23 Sinusoid with a 100-Hz frequency sampled at (A) 2 ms, and (B) 8 ms sampling rate (left) and their corresponding amplitude spectra (right). Δt is the sampling interval and f_N represents the Nyquist frequency.

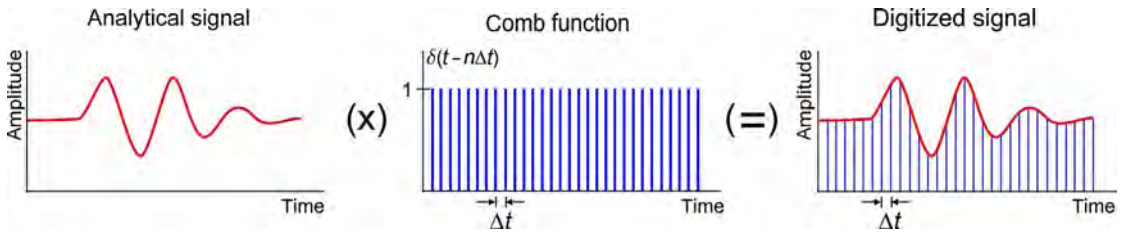


FIG. 4.24 Digitization of a time series at regular Δt time intervals equals the multiplication of the time signal with a comb function sampled at Δt.

$\Delta t = 8$ ms ($f_N = 62.5$ Hz) sampling rate, frequency aliasing occurs and the amplitude of the input signal appears at 25-Hz frequency (Fig. 4.23B).

Disruption of the spectrum because of the sparse sampling of a time signal is termed aliasing. If the time sampling interval Δt is not specified sufficiently small, the digitized signal cannot represent the original analog signal accurately and high-frequency components are missed. These missing components, however, do not simply disappear, but they are aliased onto the lower frequency part of the amplitude spectrum. Aliasing occurs because: when digitized at Δt intervals, the analog $f(t)$ signal is multiplied by a unit-amplitude comb function $\delta(t - n\Delta t)$ in the time domain (Fig. 4.24). This multiplication produces a discrete time series f_r, which consists of a series of amplitude values, mathematically expressed as

$$f_r = f(n\Delta t) = f(t) \cdot \delta(t - n\Delta t) = \sum_{n=-\infty}^{\infty} f_n(n\Delta t) \cdot \delta(t - n\Delta t) \tag{4.37}$$

The digitized signal is multiplied by $\delta(t - n\Delta t)$, and multiplication in the time domain corresponds to their amplitude spectra being convolved in the frequency domain. The amplitude spectrum of a comb function is also a comb function sampled at Δf intervals (Fig. 4.25). When the observed signal $f(t)$ is digitized, this results in its amplitude spectrum $F(\omega)$ being convolved with a comb function. As a consequence, $F(\omega)$ becomes periodic along the frequency axis with a period of Δf, and periodic recurrences of the discrete spectrum line up at $\pm n/\Delta t$ intervals. Because the widening in the frequency domain causes narrowing in the time domain, Δf becomes smaller as Δt gets larger. Therefore, high- and low-frequency components of the periodic spectrum superimpose (Fig. 4.25). Consequently, if we take

$$\Delta t > \frac{1}{2f_N} \tag{4.38}$$

then aliasing occurs in the digitized time series. As a general rule, if the time sampling interval

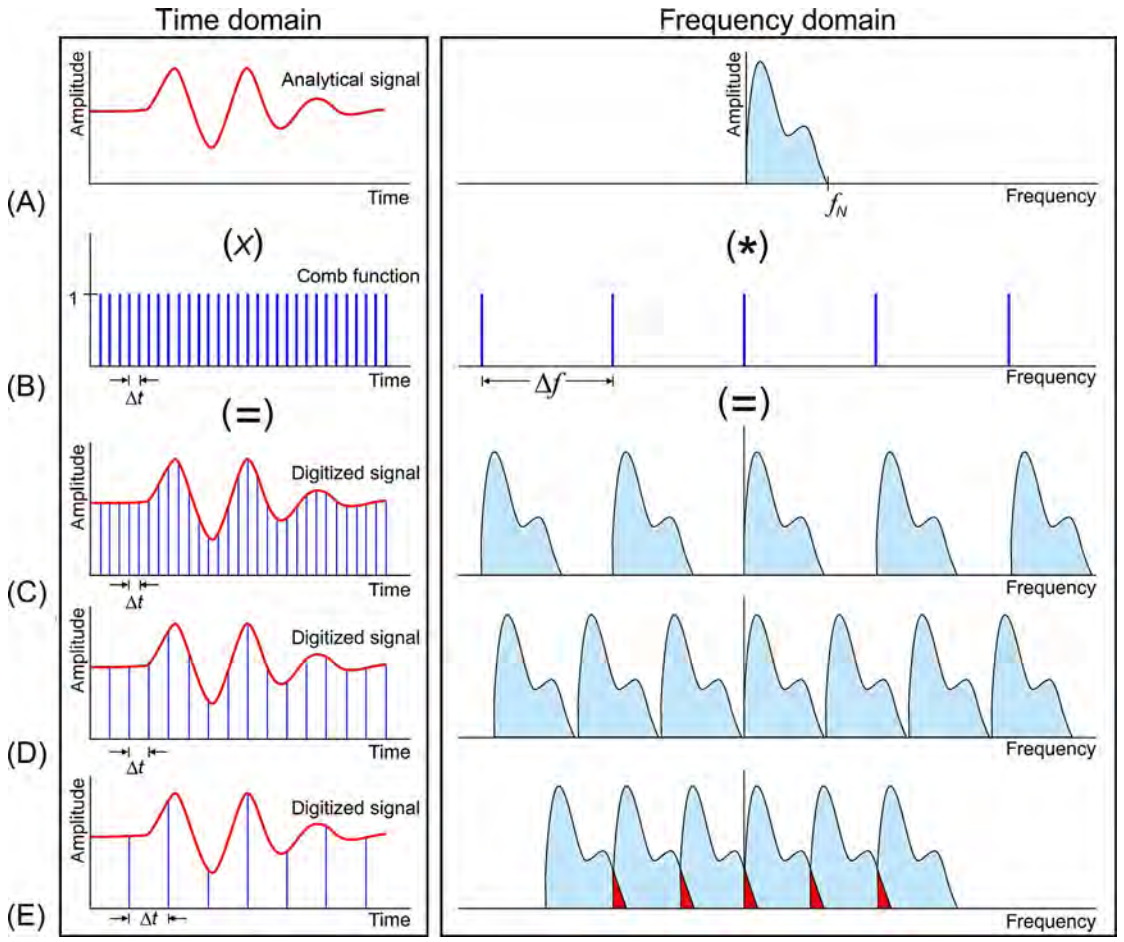


FIG. 4.25 Schematic illustration of sampling and aliasing in time (left) and frequency (right) domains. (A) Analog function, (B) comb function, (C) dense sampling, (D) sampling at Nyquist frequency (f_N), and (E) sparse sampling, which results in frequency aliasing *(red areas)*. * denotes convolution, Δt and Δf are time and frequency sampling intervals, respectively.

Δt is determined to be equal to or smaller than half of the smallest period present in the observed signal $f(t)$, aliasing does not occur in the digitized signal.

Degradation of the spectrum due to low-frequency sampling using a sparse sampling interval presents practical issues. When $f(t)$ is band limited, that is, when its maximum frequency is finite, the analog $f(t)$ signal can be reconstructed from a digitized discrete signal $f_r(t)$ without any information loss. In practice, however, such band-limited signals are rarely observed. In addition, the sampling rate must be determined before recording during seismic acquisition. Yet, it is not practically possible to determine the appropriate sampling rate that is sufficiently small to prevent aliasing, because we do not know the highest frequency we record before shooting. Therefore, electronically designed low-pass and wide-band filter circuits, termed anti-aliasing filters, are designed (Section 2.5.2.3). These are specific bandpass filters of wide passband and their higher frequency cutoff is generally 80% of the Nyquist frequency. A sufficiently small sampling rate is decided on during the acquisition, and the frequency components higher than the Nyquist frequency of the determined sampling rate are filtered out by anti-aliasing filters so that the data becomes band limited. Thus, no data with frequency components beyond the Nyquist frequency is digitized.

CHAPTER

5

Preprocessing

OUTLINE

5.1 Demultiplexing 242

5.2 Data Loading 243

5.3 Single Trace Section 244

5.4 Geometry Definition 246
5.4.1 QC in Geometry Loading 251

5.5 Band-Pass Filter 253
5.5.1 Filter Operator 256
5.5.2 Band-Pass Filtering of Marine Seismic Data 260
5.5.3 Time Varying Filtering 264
5.5.4 QC in Band-Pass Filtering 268

5.6 Gain Recovery 272
5.6.1 Spherical Divergence Correction 276
5.6.2 Time Raised to a Power Correction (t^p) 277
5.6.3 Automatic Gain Control 279
5.6.4 QC in Gain Recovery 284

5.7 Trace Edit 287

5.8 Muting 294
5.8.1 QC in Muting 295

5.9 f-k Dip Filters 299
5.9.1 f-k Filtering of Marine Seismic Data 302
5.9.2 QC in f-k Filtering 307

5.10 Brute Stack 310

Preprocessing involves the processing steps known as data preconditioning, since they are mainly used to prepare raw seismic data for the main seismic data processing steps, such as deconvolution, stacking, or migration. The main goal is to increase the signal-to-noise (S/N) ratio by removing the different coherent and incoherent noise types, as well as loading the geometry, applying the statics corrections (if necessary), etc. Typical preprocessing steps are illustrated in Fig. 5.1. Although normally all of the processing steps in Fig. 5.1 are

https://doi.org/10.1016/B978-0-12-811490-2.00005-0

© 2018 Elsevier Inc. All rights reserved.

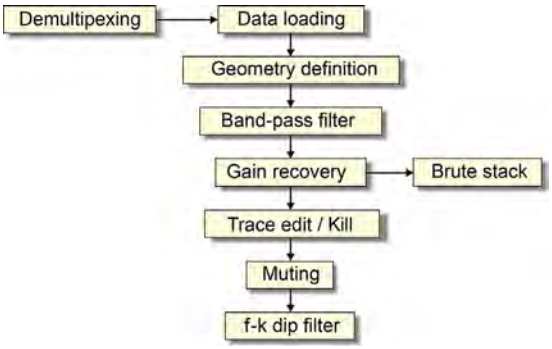


FIG. 5.1 Preprocessing steps for prestack seismic data conditioning.

routinely applied to raw seismic data, demultiplexing, *f-k* dip filter or shot-channel edit may not be needed, according to the specifications, quality and the noise content of the input seismic dataset. In addition, the application order may also differ from one processor to another, depending on the requirements of the input data.

5.1 DEMULTIPLEXING

Raw seismic data is recorded as samples in rows, in which the amplitude samples digitized at the same recording time at each individual channel are recorded in the same data row into the tapes or hard disks. This results in a data volume consisting of the first sample of first channel, first sample of second channel, first sample of third channel, etc. (Fig. 5.2A). Seismic data should be rearranged so that it consists of data columns: all amplitude samples of first channel, all amplitude samples of second channel, etc. This arrangement is known as demultiplexing and mathematically it is a transpose process in which each row is transposed individually so that the data volume consists of data columns, each containing amplitude samples of one particular channel (Fig. 5.2B). Today, modern seismic data recording systems perform demultiplexing before storing the data onto the disk or tape drives, and therefore, depending on the specifications of the recording unit, demultiplexing may not be required during data processing.

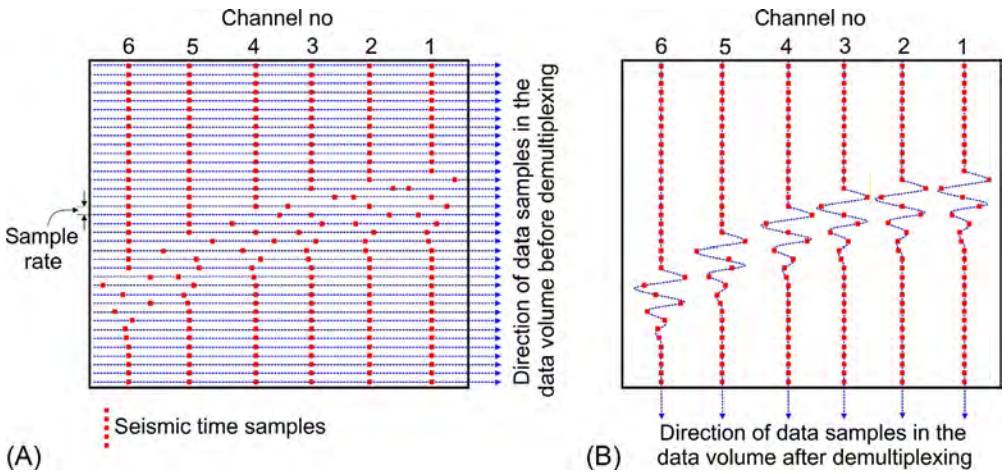


FIG. 5.2 Schematic representation of demultiplexing on a shot gather with six traces. (A) Sorting of the amplitude samples of raw seismic data set during acquisition, and (B) amplitude samples after demultiplexing.

5.2 DATA LOADING

The input process of the raw field data volume into the processing system is termed data loading. Raw seismic data is recorded in specific binary data formats defined by the Society of Exploration Geophysicists (SEG). This specific format is read by the processing system and the data becomes ready to process after the data loading step. This specific data format includes not only the digitized seismic reflection amplitude samples, but also vital information related to the data, such as shot number (FFID), sampling rate, number of samples per trace, number of channels, etc., and the blocks of these subsidiary areas inside of the data are termed headers.

Various seismic data format types used for different purposes are defined by SEG today. For instance, seismic data for engineering purposes collected by engineering seismographs are generally recorded using a format known as Seg2, while raw seismic reflection data both from land and marine surveys are commonly recorded in SegD format. However, the most common seismic data format is known as the SegY data format, which can be recognized by any kind of seismic data processing as well as interpretation software on the market. SegY is a seismic data exchange format that allows seismic data to circulate among data processing systems of different contractors. The SegY format has three different header blocks of different sizes to record the subsidiary information along with the seismic amplitude samples.

Fig. 5.3A shows a schematic diagram of a SegY file structure consisting of only three seismic traces. The file structure can be grouped into four blocks: (i) EBCDIC header, (ii) BINARY header, (iii) TRACE headers, and (iv) amplitude values of the seismic data. The first block is a 3200 byte–long EBCDIC header consisting of 80 columns and 40 rows, which stores either field parameters if it is raw SegY data or processing sequence and parameters if it is processed SegY data. This header is in ASCII format and is filled by field engineers during the data acquisition or by data processors at the end of the processing. The second block is a 400 byte–long binary header and consists of general information of identical parameters for all channels, such as number of channels per shot, sampling rate, number of samples per trace, etc. The last header block is known as the TRACE header, which is located just before the very first samples of each recording channel. Each TRACE header is 240 bytes long and every single trace in a SegY seismic data volume has its own TRACE header, which stores trace-specific substantial information about the trace it belongs to, such as channel number of the trace, shot number that the trace resides in, offset distance or coordinates of the trace, etc. (Fig. 5.3A).

On the seismic market today, the SegD format is preferred for raw seismic data recording during the acquisition because it has huge header spaces to store the field data parameters. Fig. 5.3B shows a schematic diagram of a SegD file structure consisting of only three seismic traces. The SegD format can be grouped into six blocks including the headers: (i) GENERAL header(s), (ii) CHANNEL SET header, (iii) EXTENDED header(s), (iv) EXTERNAL header(s), (v) TRACE headers, and (vi) amplitude values of the seismic data. Unlike the SegY file format, the number of EXTENDED and EXTERNAL headers in SegD format can be extended up to 1000 header blocks, 32 bytes each, which ultimately makes the SegD format suitable for acquisition.

Seismic data is normally recorded either in SegD or in the internal format of the seismic acquisition system. However, seismic data processing software commonly has proprietary seismic data formats, known as internal format, which is normally much more practical to use during the processing. Therefore, data loading also includes a format conversion from raw data format into the processing software's internal

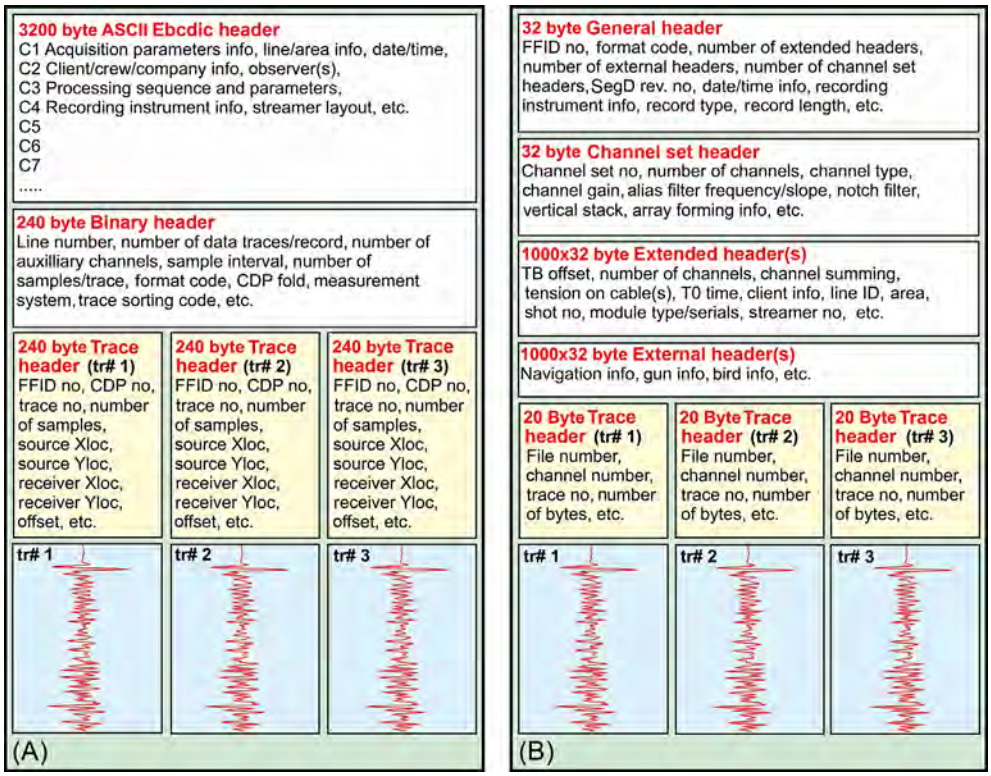


FIG. 5.3 Schematic representation of (A) SegY and (B) SegD seismic data format structures for only three seismic traces.

format. Today, the data is generally collected in SegD or a proprietary seismic data format, and then converted into the internal format of the processing system during the processing, and finally exported in SegY format after processing for the interactive interpretation or visualization systems.

5.3 SINGLE TRACE SECTION

It is possible to obtain single trace (common offset) sections from multichannel seismic data. A single trace section is almost identical with single channel data, except that the offset value between the shot and receiver is nonzero. Fig. 5.4 schematically shows constructing the single trace sections: Shot gathers are band-pass filtered and a gain function is applied. Then the single trace section is simply formed by plotting the traces of the same offset value for each shot gather. Generally, one of the very first channels of each shot is selected because the arrival times of the reflections increase with increasing offset due to the normal moveout time (Section 10.1), and the single trace sections are prepared generally from one of the channels close to the source location. Fig. 5.4 schematically shows the formation of a single trace section by selecting the first (minimum offset) channel.

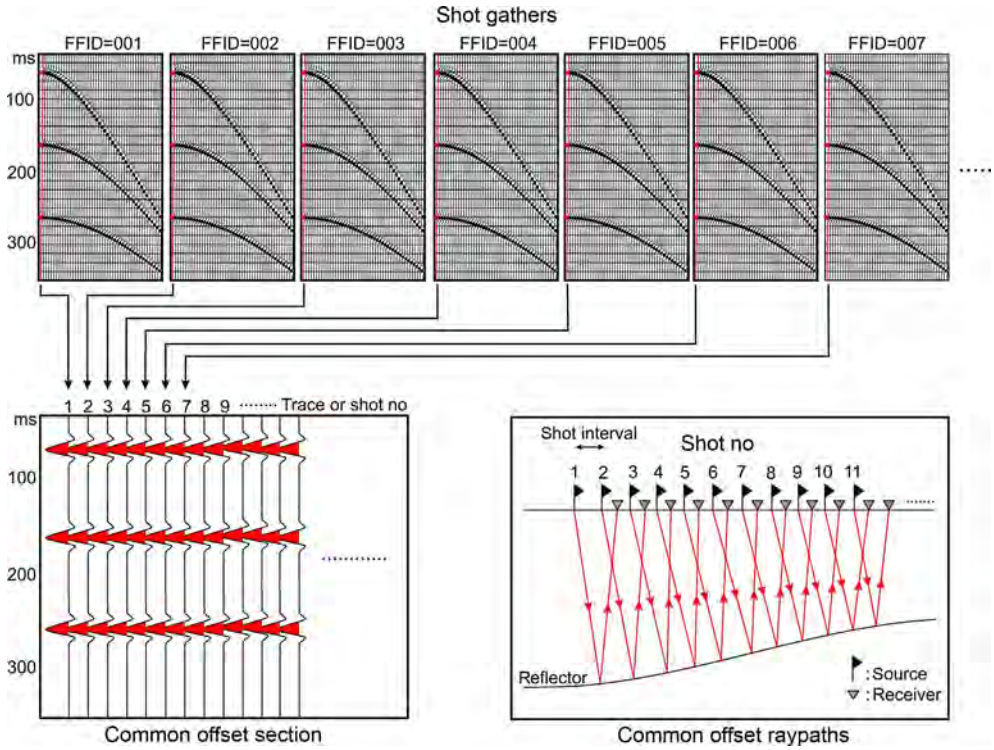


FIG. 5.4 Schematic illustration of single trace (common offset) section construction using first channels (minimum offset) of each shot *(red traces)*, and the theoretical ray paths of the common offset reflection(s).

Fig. 5.5A shows an example single trace section formed by every first trace of each shot. The full stack section of the same line is also provided in Fig. 5.5B to compare the data quality for single trace and full stack sections. Although the S/N ratio of a single trace section is significantly low when compared to stack sections, band-pass filtered single trace sections with a suitable gain can be used for a quick display of subsurface structure immediately after the acquisition of the seismic line is completed. In addition, some of the acquisition software supplies a real-time display of single trace sections during the acquisition, which allows the observer to perform real-time acquisition QC or visually check the data quality issues. During the processing, the outputs of some specific processing steps, such as band-pass filtering, deconvolution, or gain applications, can be analyzed on single trace sections. Processing QC applications can be done more correctly by analyzing the results on a single trace section instead of displaying the shot gathers before and after a processing step.

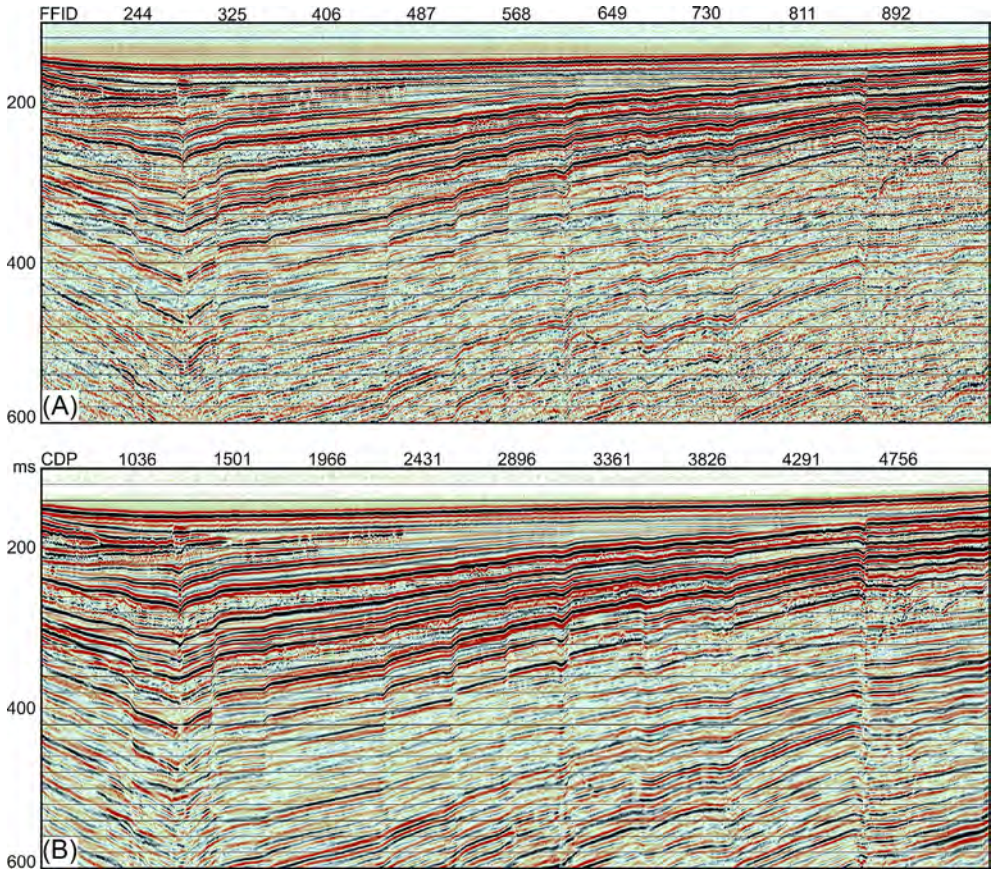


FIG. 5.5 (A) An example single trace section formed by plotting every first trace of the shot gathers. The traces were band-pass filtered and a gain function was applied. (B) Full stack of the same data for a comparison by means of the data quality and resolution.

5.4 GEOMETRY DEFINITION

Geometry definition is based on the designation of source-receiver geometry and generally done by using real geographical coordinates of the sources and group centers of each channel for each shot position. The most important geometric parameters are the shot and group intervals, shot and streamer depths, and the absolute distance of each individual trace from the shot point. Geometry definition needs acquisition geometry information and these parameters are recorded in the observer logs prepared for each sail line during the acquisition. These logs involve the recording parameters for the streamer layout, seismic source, and navigation as well as survey notes taken by the observers, and the accuracy of these parameters is vital for a proper processing later on. Observer logs for 2D seismic surveys are simple and consist of basic information on the recording, streamer, seismic source, and navigation parameters (Fig. 5.6). For 3D surveys, however, a standard observer log involves extra information on

AREA:	LINE NAME:	CLIENT:	DATE:	SEA CONDITION: ☐ SMOOTH ☐ CHOPPY ☐ ROUGH	RAIN: ☐ YES ☐ NO

STREAMER PARAMETERS	
LENGHT (m)	
DEPTH (m)	
GROUP INT. (m)	
# OF MODULES	
# OF SECTIONS	
LEVELER BIRDS	
COMPASS BIRDS	

GUN PARAMETERS	
# OF GUNS	
TYPE OF GUNS	
PRESSURE (psi)	
TOW DEPTH (m)	
VOLUME (in^3)	

RECORDING PARAMETERS		
RECORDER		
DEVICE and S/N		
DATA FORMAT		
NUMBER OF CHANNELS		
SHOT INTERVAL	☐ m	☐ s
REC. LENGTH (ms)		
SAMPLE RATE (ms)		
MINIMUM OFFSET (m)		
FIRST SHOT (FFID)		
LAST SHOT (FFID)		
FIRST SegY FILE TAPE		
LAST SegY FILE TAPE		
LOW-CUT / SLOPE		
HIGH-CUT / SLOPE		

NAVIGATION PARAMETERS			
SEQUENCE NO			
LINE TYPE			
LINE LENGTH / BEARING (m / °)			
NOMINAL VESSEL SPEED (knots)			
CUSTOM LOG FILE NAME			
UKOAA P1/90 LOG FILE NAME			
LINE START TIME			
LINE END TIME			
COORDINATES		LATITUDE & LONGITUDE	UTM (Zone:)
	START	Lat:	Easting (m):
		Lon:	Northing (m):
	END	Lat:	Easting (m):
		Lon:	Northing (m):
	DATUM	☐ WGS84 ☐ ED 50	☐ Other:.....

OPERATORS	
NAME(s)	SHIFT TIME

DELAYS	
FFID to FFID	Delay (ms)

SURVEY NOTES

FIG. 5.6 An example observer log for 2D multichannel seismic surveys.

channel distribution for all available streamers, a detailed description of auxiliary channels, streamer/gun array separation, information on the real-time QC results (shot and channel edits), gun array timing and drop out issues, and rGPS information.

In addition to the observer logs, coordinates of gun array center(s), all available sensors such as bird locations or acoustic rangers, and offsets such as dilt floats, tail buoys or paravane locations from rGPS pods are logged for each shot point into the navigation logs. Although an industry standard navigation file format known as UKOOA P1/90 is common on the market today (Section 2.1.7), these navigation logs can also be in free ASCII format. Depending on the recording system and the seismic data format that the recorder generates, some of these navigation parameters can also be stored in the header blocks of the raw seismic data.

Geometry definition of a seismic line is achieved using both streamer layout information (the geometry) and real coordinates of each shot and receiver locations (the navigation). Geometry information includes the information about the number of shots, number of channels, minimum inline and lateral offset(s), number of streamers, depths of gun array(s) and streamer(s), and streamer group interval, while navigation information includes the coordinates of gun arrays for each shot as well as calculated locations of each recording channel for each shot point. In addition, water depth information from the single beam echo-sounder is also entered into the system, since some multiple reflection removal methods need water depth information below the keel. Commonly, the geometry is constructed and recorded in the database first, and then it is matched with the traces and loaded into the trace headers of the seismic data.

In seismic exploration, all of these geometrical and navigational parameters should be in the metric system and are expressed as absolute distances, not degrees-minutes-seconds of geographical coordinates. The problem here is that the world's shape is like an ellipsoid and the exact location of an arbitrary point on this surface can be given by a latitude and longitude pair (Fig. 5.7A). The solution is to convert geographical coordinates into metric (projected) coordinates using a suitable coordinate projection transform. The idea is that a particular surficial area on an ellipsoid can be regarded as a flat surface providing the surface is small enough. Let this area be the red rectangular surface in Fig. 5.7A, which is then considered to be a flat rectangle containing seismic survey lines in Cartesian coordinates in which both axes are in meters (Fig. 5.7B). The issue is to define the origin of this Cartesian coordinate system, since the distances between the meridians simply decrease towards the poles, which forces us to

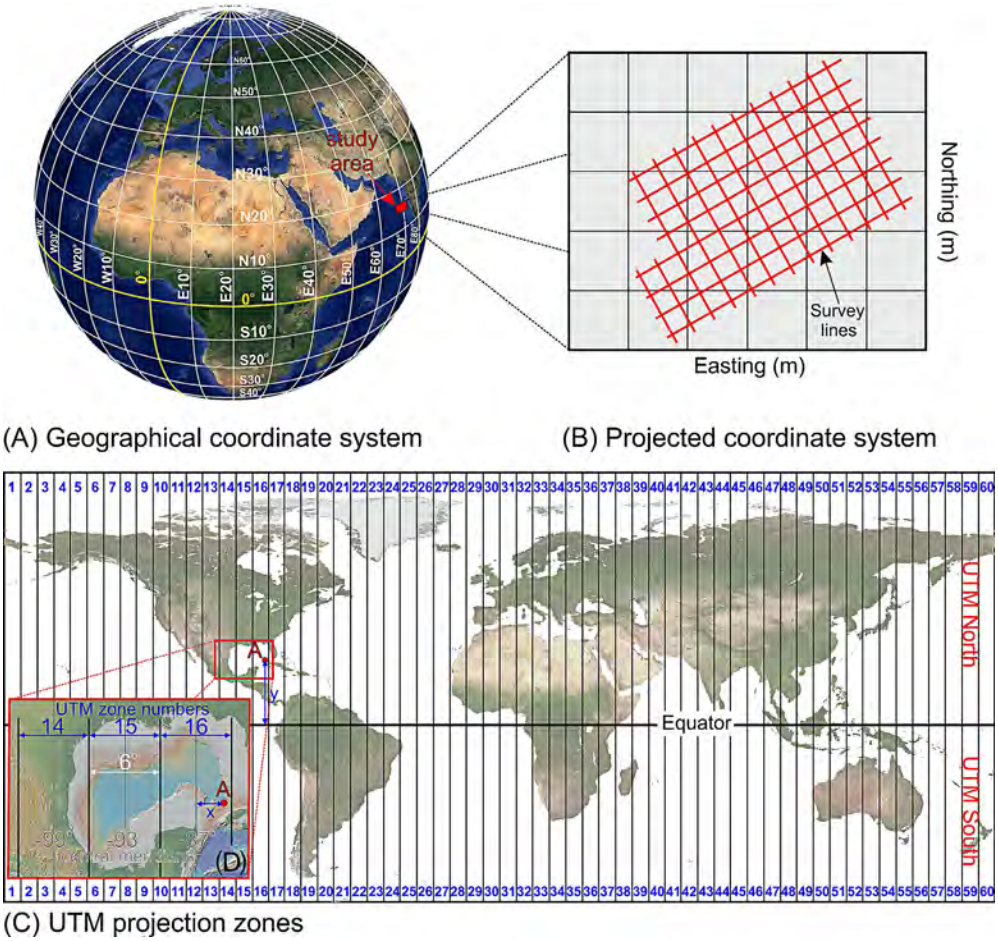


FIG. 5.7 (A) Geographical coordinate system, and (B) a small area on earth's surface as the working site for seismic surveys can be regarded as a flat area so that the metric coordinates can be applied. (C) Universal Transverse Mercator (UTM) projection zones to systematically convert geographical coordinates into metric (projected) coordinates. (D) Definition of the UTM zone details on the Gulf of Mexico as an example study area.

define a generalized approach describing the reference latitude and longitudes or origin of the metric coordinate system. This can be achieved using map projections that transform the geographical coordinates (e.g., latitude and longitude in degrees-minutes-seconds) into metric coordinates (e.g., easting and northing in meters).

Although a number of projection systems are used today, the most common one is known as the Universal Transverse Mercator (UTM), which provides systematic representation of geographical coordinates as metric coordinates all over the world. In UTM projection, the world is divided into 60 segments (named UTM zones) in the north to south direction, where each zone is 6° wide (Fig. 5.7C) and has a central meridian located at the center of each segment. Fig. 5.7D shows an example of this segmentation for the Gulf of Mexico which extends through three successive UTM zones: Zone 14, 15, and 16 North. Each UTM zone has its own central meridian: for instance, it is W99° for Zone 14, W93° for Zone 15, and W87° for Zone 16. Based on this layout, easting (x) and northing (y) values of any point in the survey area, like point A in Fig. 5.7C and D, can be obtained in meters as

x(m) = [Horizontal distance from the central meridian to point A] + [False easting/2].

y(m) = [Vertical distance from Equator].

Here, false easting is a constant to prevent negative x coordinate values in areas close to the western border of any UTM zone and is taken as 500,000.

After loading the geometry into the database and trace headers of the data, seismic traces can be grouped and processed/displayed as different trace groups. These different trace groups sorted by different geometric criterion are known as trace gathers, or ensembles. Constructing such different trace gathers commonly changes the domain of the data, such as from shot to the CDP domain, or to common offset domain, etc. Sorting the traces into different gathers requires the use of the geometry and other information stored in the trace headers prepared during the acquisition or processing stages. The main purpose in reconstructing the different trace gathers is to apply the different processing steps in different domains where the noise is best separated from the signal.

The ray paths and schematic displays of the most common trace gathers are shown in Fig. 5.8A. In addition, if we plot the shot coordinates against the receiver coordinates using the geometrical relationships given in Fig. 5.8B, we get a specific source/receiver location chart, termed the stacking chart, schematically represented in Fig. 5.8C for the end-on spread, which is standard for marine surveys. Each blue point on this chart represents a seismic trace from a 2D survey with a time axis perpendicular to the paper plain. Definitions of the trace groups indicated by the numbers from 1 to 5 are as follows:

1. *Common-shot gather* is the group of traces propagated from a single shot and recorded by all available receivers. It is also known as a shot gather, and raw seismic field data is recorded as shot gathers. The number of traces it contains equals the number of channels available on each streamer. Trace spacing between the successive traces in a shot gather equals the group interval. In the shot gathers, receiver coordinates change while the shot coordinate is fixed. 3D seismic data consists of several shot gathers even for one single shot, termed shot groups, which consist of the traces from one shot and recorded at different streamers.
2. *Common-receiver gather* is the group of traces propagated from different shots but recorded at a common receiver located exactly at the same station point along the seismic line. According to the reciprocity theory (i.e., interchanging source and receivers reveals exactly the same data), a common-receiver gather contains exactly the same information as that in a shot gather with the same geometry. In offshore seismic refraction

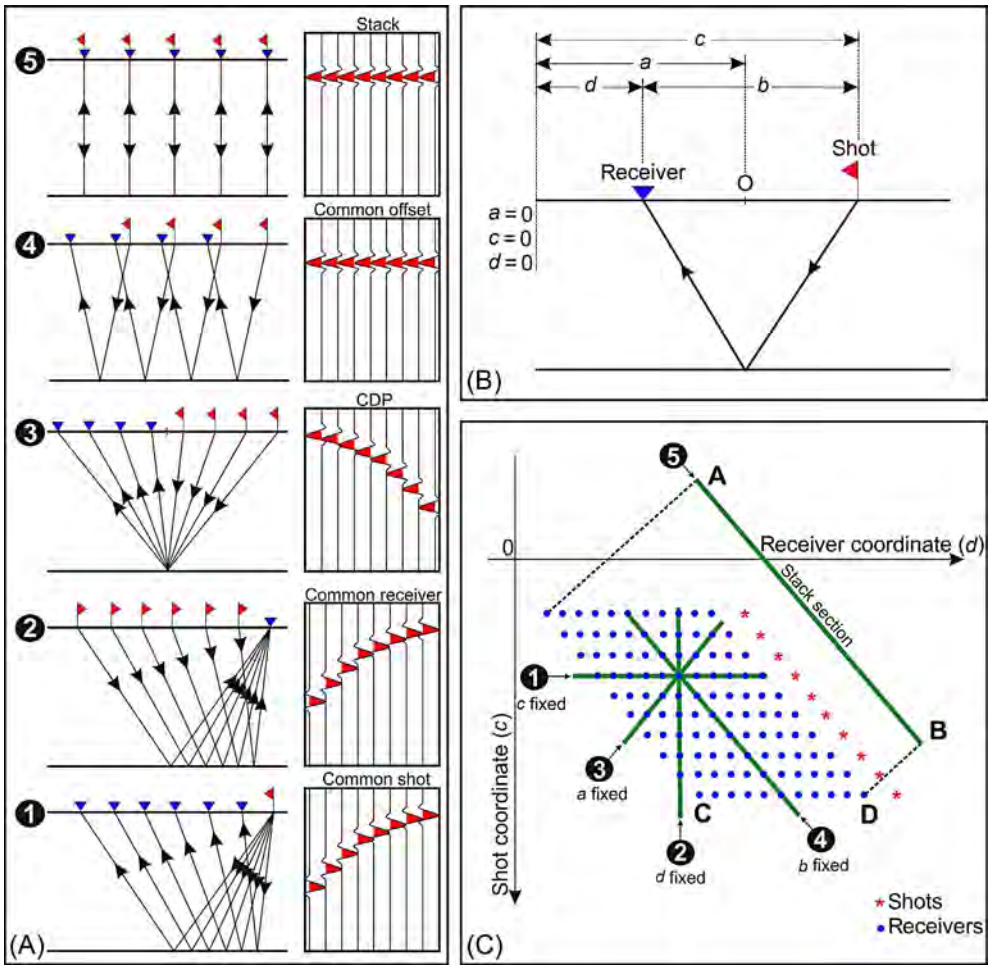


FIG. 5.8 (A) Ray paths and schematic displays of different trace gathers commonly encountered in seismic surveys. (B) Schematic representation of the geometrical relationships constituting the stacking chart in (C) for a 2D survey. Each blue point represents a receiver or a seismic trace with a time axis perpendicular to the paper plain. C-D corresponds to streamer length and A-B is the total length of the seismic line.

surveys, the data is commonly collected as common-receiver gathers, since it allows us to record extremely long offset arrivals required for refraction work without deploying a very long streamer cable. In common-receiver gathers, shot coordinates change while the receiver coordinate is fixed. Trace spacing between the successive traces in a common receiver gather equals the shot interval.

3. *Common depth point gather* is the group of traces propagated from different shots and recorded at different receivers, but reflected at the same subsurface reflection point, the common depth point (CDP). Considering a horizontal earth model, a CDP point lies exactly below the midpoint of the respective shot and receiver pairs. Following the preprocessing steps, the seismic data is "sorted" from shot gathers to

CDP gathers so that we can apply velocity analysis and stacking. In the CDP gathers, midpoint coordinates of each shot and receiver pair are fixed, while both shot and receiver coordinates change. Trace spacing between the successive traces in a CDP gather equals the double of the shot or receiver spacing, depending on which of these is larger.

4. *Common-offset section* is the group of traces from exactly the same recording channel (and hence with the same offset) of all shots along the line. It is also known as a single trace section and is generally prepared using the first or second channel of each shot gather (Section 5.3). A common-offset section resembles the final stack section, but its S/N ratio and resolution are quite poor (Fig. 5.5). In the common-offset sections, the offset value between shot and receivers is fixed while both shot and receiver coordinates change. Trace spacing between the successive traces in a common-offset section equals the shot interval and the trace-by-trace consistency of the reflections on the common-offset sections demonstrates the subsurface geology.
5. *Stack section* is a group of traces obtained by stacking all traces in each CDP gather following the normal moveout (NMO) correction. The traces in a stack section are reduced to the zero-offset time since the required propagation time of the signals from shots to receivers along the subsurface is removed by NMO correction. After stacking, each CDP gather produces only one single "stacked trace" and stack sections are prepared plotting these stacked traces side by side (Section 10.3). Trace spacing between the successive traces in a stack section equals half of the group interval and the reflections on the stack sections reveal the subsurface geology. Although a number of additional processing steps can be applied to the data after stacking, such as migration, scaling, or time variant filtering, a stack section is the ultimate objective of the seismic surveys.

5.4.1 QC in Geometry Loading

Several data processing steps such as NMO correction, CDP sort, or velocity analysis require that the geometry of the seismic data be already defined in the database and in the trace headers before the application of these steps, and incorrect geometry definition results in incorrect outputs from forthcoming processing steps. Even simple mistakes during the geometry loading may result in deadly errors on the final stack sections. Therefore, quality control implications are always necessary after loading the geometry into the trace headers, and this can be achieved in different ways:

i. *Checking the trace headers*: Trace headers of randomly selected traces from raw shot gathers can be displayed and some specific header words can be analyzed to ensure that they all have the correct geometry and navigation information, such as offset, shot/receiver x coordinate, shot/receiver y coordinate, CDP numbers, and CDP fold. Fig. 5.9A shows the first 90 bytes of an example seismic trace in SegY format (the first channel from shot number 101) before the definition of geometry. After geometry loading, some specific headers such as CDP number at byte 21, offset value at byte 37, shot and receiver coordinates in meters between bytes 73 and 88, etc., are correctly filled in (Fig. 5.9B).
ii. *Calculating the propagation velocities from shot gathers*: After loading the geometry, seismic velocities can be computed on the shot gathers, since the offset values of each trace are defined by the geometry loading. Checking the propagation velocities of well-known arrivals, such as direct wave and seabed reflection, can provide information about the accuracy of the geometry loading. For this purpose, seismic traces of the filtered shot gathers can be displayed and the propagation velocity of direct wave as well as seabed and subsurface reflections can be computed (Fig. 5.10) to ensure that

Value	Description	Bytes
1	Trace index	
1	* Trace sequence number withing line	1- 4
1	Trace sequence number withing reel	5- 8
101	* FFID - Original field record number	9-12
1	* Trace number withing field record	13-16
101	SP - Energy source point number	17-20
0	CDP ensemble number	21-24
0	Trace number	25-28
1	* Trace identification code	29-30
0	Number of vertically summed traces	31-32
0	Number of horizontally stacked traces	33-34
0	Data use (1-production, 2-test)	35-36
0	Distance from source point to receiv grp	37-40
0	Receiver group elevation	41-44
0	Surface elevation at source	45-48
0	Surface depth below source	49-52
0	Datum elevation at reciever group	53-56
0	Datum elevation at source	57-60
0	Water depth at source	61-64
0	Water depth at group	65-68
-10000	Scaler to all elevations & depths	69-70
-10000	Scaler to all coordinates	71-72
0	Source X coordinate	73-76
0	Source Y coordinate	77-80
0	Group X coordinate	81-84
0	Group Y coordinate	85-88
3	Coordinate units (1-lenm/lt 2-secarc)	89-90

(A)

Value	Description	Bytes
1	Trace index	
1	* Trace sequence number withing line	1- 4
1	Trace sequence number withing reel	5- 8
101	* FFID - Original field record number	9-12
1	* Trace number withing field record	13-16
101	SP - Energy source point number	17-20
4110	CDP ensemble number	21-24
0	Trace number	25-28
1	* Trace identification code	29-30
0	Number of vertically summed traces	31-32
0	Number of horizontally stacked traces	33-34
0	Data use (1-production, 2-test)	35-36
-1244	Distance from source point to receiv grp	37-40
0	Receiver group elevation	41-44
0	Surface elevation at source	45-48
30000	Surface depth below source	49-52
0	Datum elevation at reciever group	53-56
0	Datum elevation at source	57-60
0	Water depth at source	61-64
0	Water depth at group	65-68
-10000	Scaler to all elevations & depths	69-70
-100	Scaler to all coordinates	71-72
468197	Source X coordinate	73-76
4363555	Source Y coordinate	77-80
468305	Group X coordinate	81-84
4362316	Group Y coordinate	85-88
3	Coordinate units (1-lenm/lt 2-secarc)	89-90

(B)

FIG. 5.9 First 90 bytes of trace headers of raw seismic data (the first trace of shot number 101). (A) Before loading the geometry information in the headers, and (B) after geometry loading.

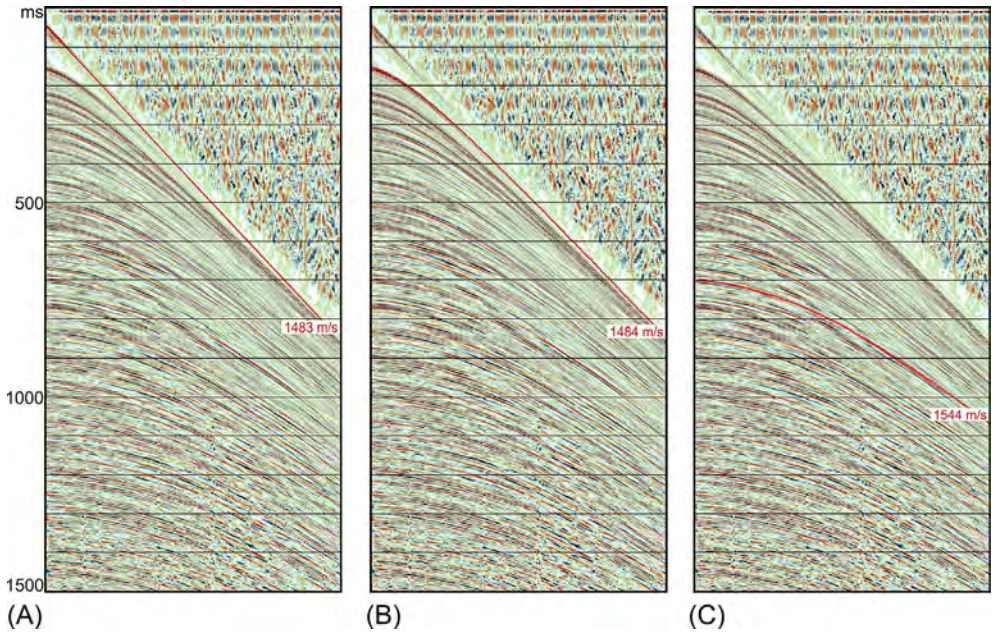


FIG. 5.10 Calculation of propagation velocities of (A) direct wave, (B) seabed reflection, and (C) a subsurface reflection on a filtered shot gather. Here, calculated velocities of direct wave, seabed reflection and a subsurface reflection are 1483, 1484, and 1544 m/s, respectively.

the velocities of direct wave and seabed reflection are approximately between 1480 and 1520 m/s, although higher and lower velocity values can be obtained in areas of inclined seafloor. Slightly higher velocity values are expected for subsurface reflection hyperbolas, since the wave velocity generally increases with depth.

iii. *Checking the database*: Some specific information in the database such as fold map, stacking chart, and direction of the survey line constructed by plotting x and y coordinate pairs for each CDP or shot gather can be analyzed (Fig. 5.11) to ensure that the database has correct entries after geometry loading.

iv. *Analyzing the brute stack*: The brute stack of the seismic line can be prepared to check whether the data after loading the geometry seems normal. Fig. 5.12 shows the result of a wrong channel order definition. In this example, the processor incorrectly supposes that the channel numbers decrease along the offset.

5.5 BAND-PASS FILTER

Frequency filtering is the process of directly modifying the amplitude spectrum of the seismic data. The main motivation for frequency filtering is that the signal and noise amplitudes appear at different frequency components in the seismic data. If noise frequencies are close to the signal frequencies, then the reflection signals may also be removed along with the noise by frequency filtering.

As expressed in Section 4.5, seismic traces are composed of the summation of several sinusoids with different phase, amplitude and frequency characteristics. We can decompose the traces into their different sinusoidal components of different frequencies using spectral analysis, and then we can remove the undesired amplitude components of a specified frequency band by applying a suitable filter operator. The frequency band that a frequency filter keeps is termed the pass-band, defined by low (f_1) and high (f_2) frequency cut-off values. Frequency filters are typically classified according to the characteristics of their pass-band regions.

Several different filter designs exist to properly modify the amplitude spectrum of the input data:

- Low-pass filters (Fig. 5.13A) remove the frequencies higher than a specified cut-off frequency value. Low-frequency cut-off (f_1) is zero.
- High-pass filters (Fig. 5.13B) remove the frequency band lower than a specified cut-off frequency value (f_1). High-frequency cut-off (f_2) is the Nyquist frequency.
- Band-pass filters (Fig. 5.13C) keep the specified frequency band between a low- and a high-frequency cut-off value (f_1 and f_2, respectively).
- Notch filters (Fig. 5.13D) remove only one specified frequency value or a very narrow frequency band typically used to filter out specific monofrequency noise components, such as 50- or 60-Hz powerline interference.

Not all of the amplitudes from different frequency components of a seismic trace may be useful, because the seismic record contains both signal and noise components with different frequency bands. In general, raw marine seismic data contains both high-frequency random noise and low-frequency swell noise components embedded in the data (Fig. 5.14). Therefore, it is generally required to remove both high- and low-frequency amplitudes, and such a filtering is generally achieved by applying a band-pass filter designed to keep the amplitude components within a frequency band while removing the amplitudes outside this band of the input amplitude spectrum. The pass-band of a band-pass filter is schematically defined as a rectangular window in the frequency

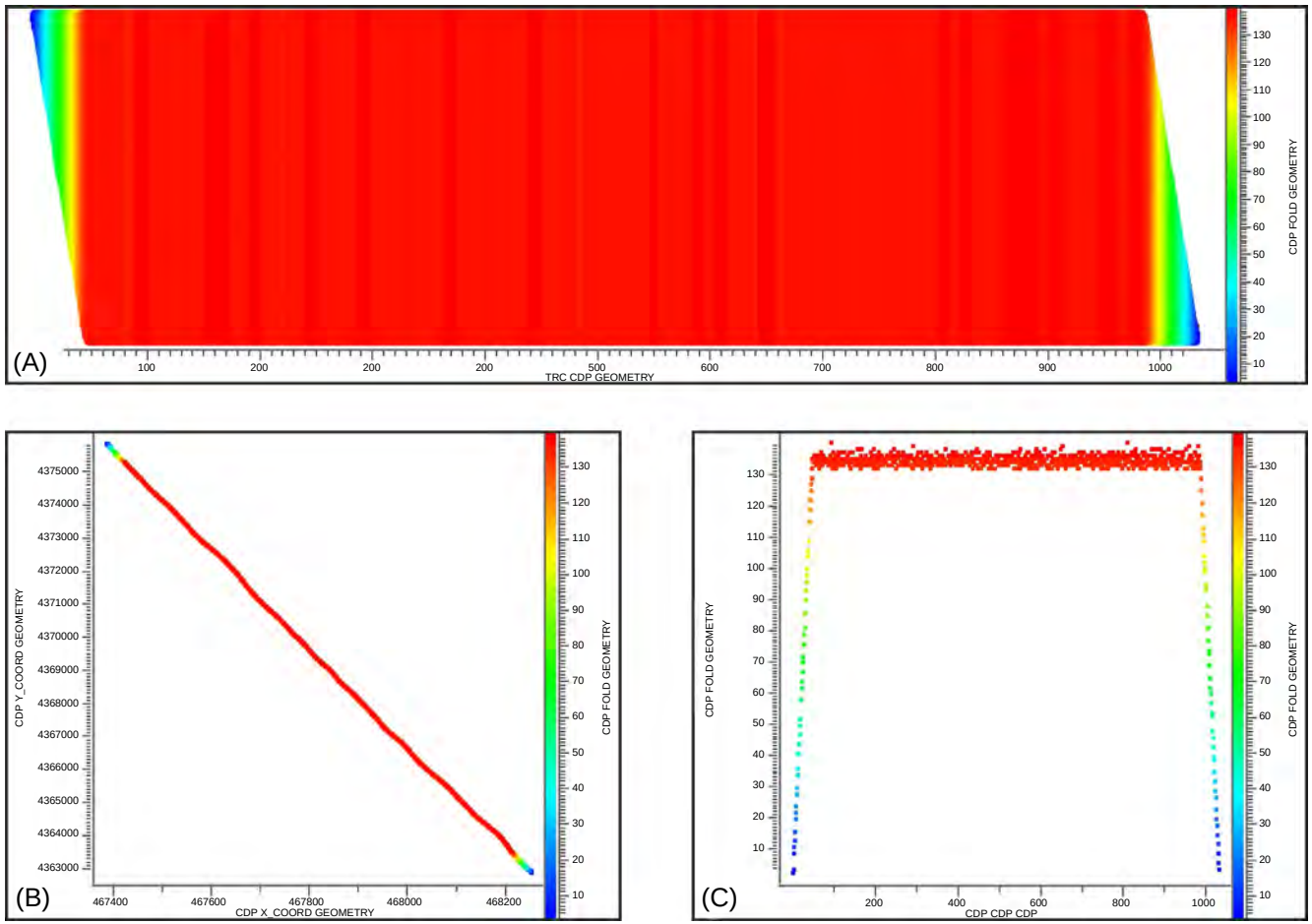


FIG. 5.11 Plotting of geometry information in the database after geometry loading for a 2D seismic line. (A) Stacking chart, (B) line direction, and (C) CDP fold map.

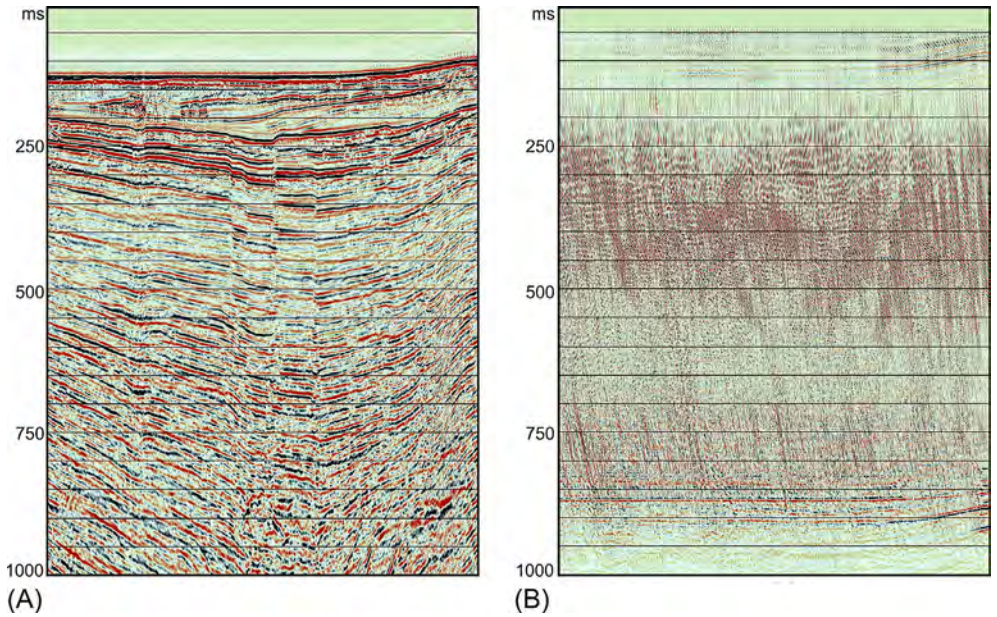


FIG. 5.12 Result of an incorrect channel order definition along the offset during the geometry loading. (A) Brute stack with correct geometry definition (channel numbers increase along the offset), and (B) brute stack with incorrect channel order definition (channel numbers decrease along the offset).

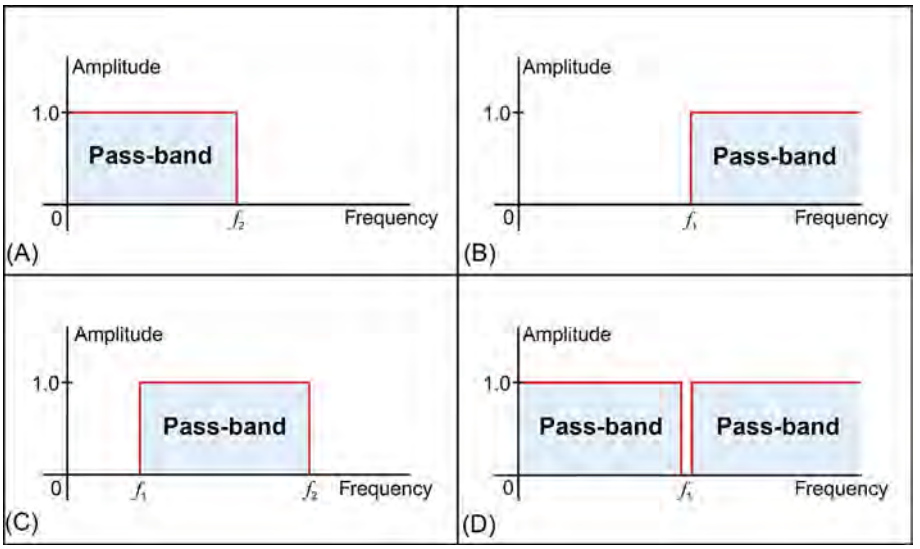


FIG. 5.13 Schematic illustration of pass-bands of different filter designs in the frequency domain. (A) Low-pass, (B) high-pass, (C) band-pass, and (D) notch filters. f_1 and f_2 represent cut-off frequencies.

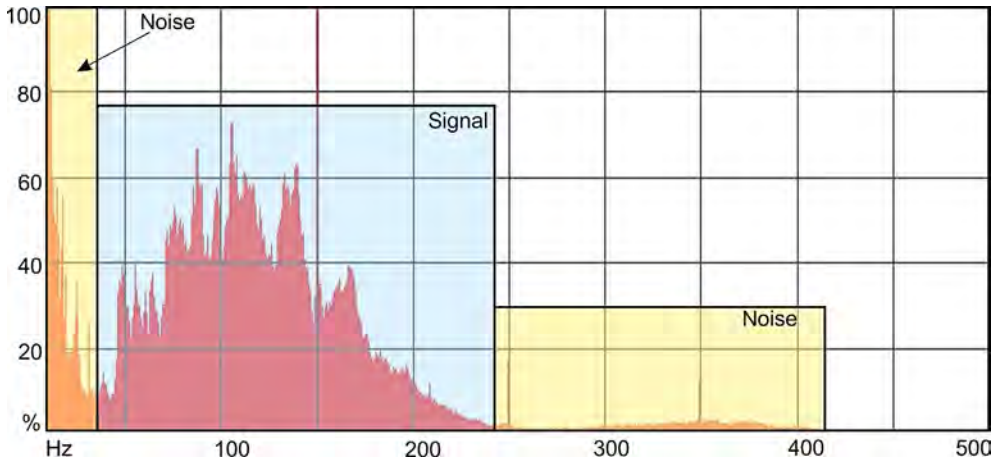


FIG. 5.14 An example mean amplitude spectrum of a marine shot gather showing the signal frequency band as well as low- and high-frequency noise zones.

domain (Fig. 5.13C). When applied to seismic data, a band-pass filter will cut out the amplitude components with frequencies lower and higher than cut-off frequency values, f_1 and f_2, respectively. The output data then becomes band-limited.

Raw seismic data have amplitudes with the entire frequency band between 0 and Nyquist frequency, f_N. While some of these amplitudes correspond to reflection signals, the others constitute noise components. The frequencies of the desired amplitude components of the reflected signals are generally limited to the frequency bandwidth of the input data, depending on the seismic source type and source/streamer depth (Section 2.5.1.2). For instance, if the effective bandwidth of the data is between 10 and 140 Hz, and if the sampling rate is 1 ms ($f_N = 500$ Hz), this means that the amplitude components between 140 and 500 Hz consist of high-frequency noise. Using suitable digital filters, undesired frequency components of the seismic data can be filtered out while the desired frequency components are preserved. A high-frequency random noise interference (with frequencies higher than approximately 90 Hz) on a land shot record is shown in Fig. 5.15A, and this noise is completely removed by a 10–90 Hz band-pass filter (Fig. 5.15B).

5.5.1 Filter Operator

In practice, band-limited wavelets are used to filter the seismic data, which are known as filter operators in the time domain, and amplitude samples of this operator are termed filter coefficients. The most practical filter operator to be used for frequency filtering is determined by the Fourier transform theory. The main purpose in band-pass filter operator design is that the filter operator must pass the amplitudes within the pass-band without any amplitude distortion, while suppressing the amplitudes outside of this frequency band. The amplitude spectrum of the most suitable filter operator to implement this purpose could be defined as a box-car shaped spectrum

$$A(f) = \begin{cases} 1 & f_1 < f < f_2 \\ 0 & \text{other} \end{cases} \tag{5.1}$$

where f represents the frequency, and f_1 and f_2 are the cut-off frequencies. Indeed, this is an ideal spectrum that we could use to filter our seismic data when we simply multiply it by

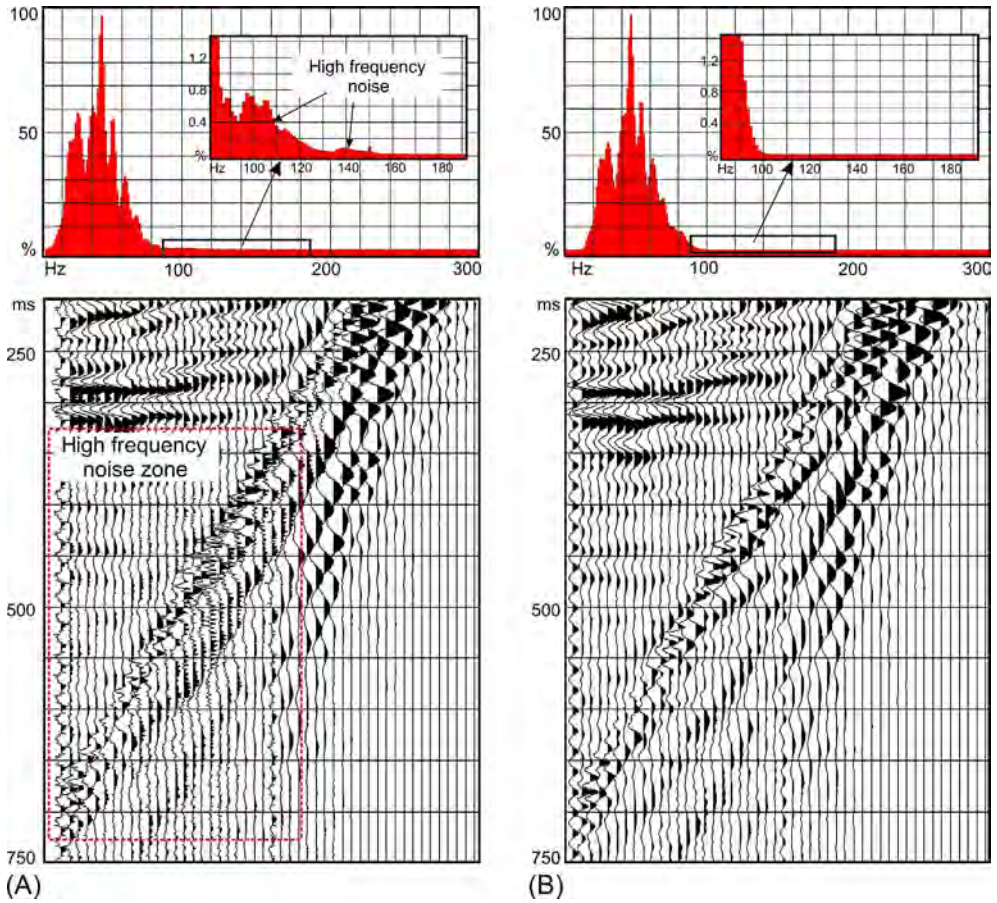


FIG. 5.15 (A) High-frequency noise amplitudes observed on a land shot record. (B) A 10–90 Hz band-pass filter removes high-frequency noise completely. Mean amplitude spectra of the records are shown in the upper panels.

our data spectrum since it will never affect the amplitudes in the pass-band (since we multiply them by 1) and it will completely remove the amplitudes off the pass-band (since we multiply them by 0). However, we have a critical issue in using such a band-pass filter operator spectrum in practice. The function given in Eq. (5.1) is known as a box-car spectrum and its time domain counterpart is a sinc function (Table 4.1), expressed by (Fig. 5.16)

$$A(t) = \mathrm{sinc}(t) = \frac{\sin(t)}{t} \tag{5.2}$$

The issue with this function is that it has amplitudes in $\pm\infty$ time interval (Fig. 5.16B). In practice, a filter operator cannot have an infinite number of filter coefficients lying along a $\pm\infty$ time interval. Therefore, in practice it should be truncated at both ends to obtain a finite time series before applying the seismic data. On the other hand, a sinc function truncated in the time domain will no longer represent a box-car spectrum in the frequency domain, and its real amplitude spectrum becomes ringy. This phenomenon is known as the Gibbs effect and it arises because of an approximation to a box

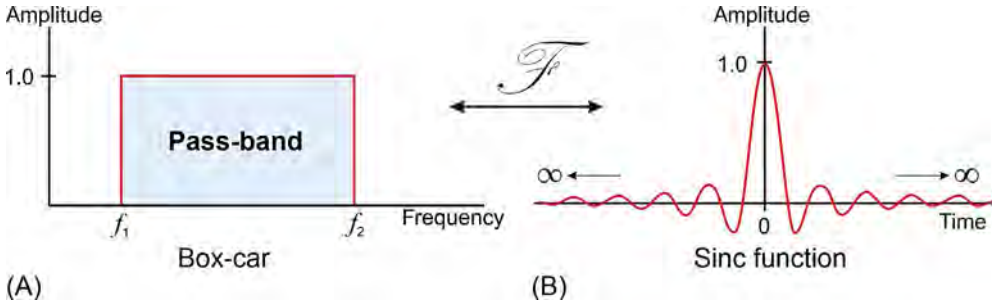


FIG. 5.16 (A) A box-car shaped amplitude spectrum in the frequency domain, and (B) its time domain counterpart, the sinc function.

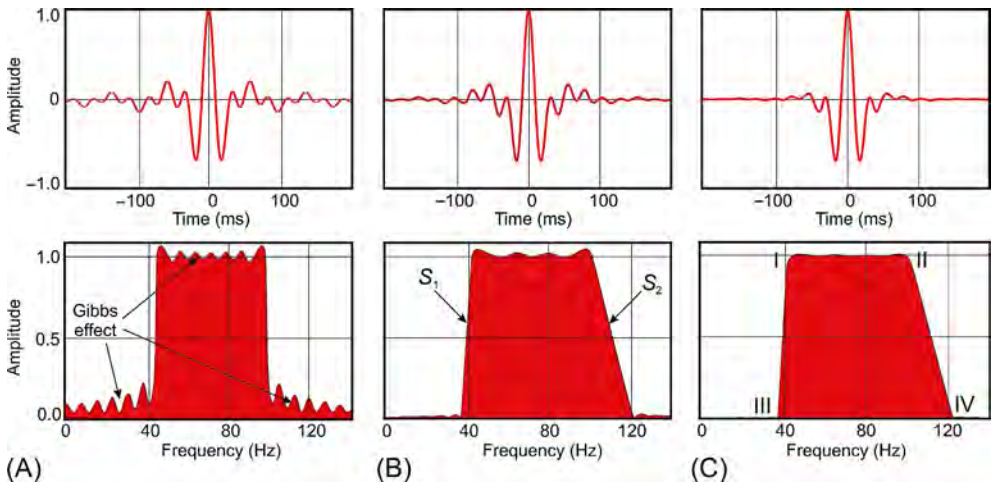


FIG. 5.17 (A) A truncated sinc function (upper panel) and its real amplitude spectrum (lower panel). (B) If both flanks of the pass-band region are inclined (indicated by S_1 and S_2), and (C) the edges indicated by I, II, III, and IV are smoothed, a narrower filter operator can be obtained in the time domain, and the Gibbs effects are eliminated in the frequency domain.

car using a finite number of coefficients in the time domain (Fig. 5.17A). These oscillations are normally undesired, since some of the amplitudes are weakened while some others are strengthened during the filtering. Furthermore, these oscillations also result in passing of amplitudes in the reject band. In order to avoid the Gibbs effect in the frequency domain, instead of defining a rectangular pass-band region, both flanks of the box-car are inclined (Fig. 5.17B) so that the pass-band becomes a trapezoid, which makes the operator much narrower in the time domain with fewer nonzero filter coefficients. These inclined parts in the pass-band region are known as the transition band. In practice, the slope at the higher frequency side of the trapezoid is suggested to be larger than that at the lower frequency side. In addition, since the Fourier transform is valid only for continuous functions, a smoothing is applied to the edge points I, II, III, and IV in Fig. 5.17C in order to avoid sharp edges in the spectrum.

Based on such a frequency domain operator, a proper band-pass filter operator design is achieved in the following way (Fig. 5.18):

i. Define the box-car spectrum and its cut-off frequency values in the frequency domain (Fig. 5.18A). Set the phase spectrum to zero.
ii. Obtain the filter operator in the time domain by an inverse Fourier transform. This spectrum is represented by a sinc function extending to infinite time in both directions along the time axis (Fig. 5.18A).
iii. Truncate the operator at both ends in the time domain, which results in an amplitude spectrum with severe ripples in the frequency domain. Take the forward Fourier transform to examine the real amplitude spectrum of the truncated filter operator.
iv. Define the cut-off slopes in the frequency domain, which results in a trapezoid shaped pass-band region. In practice, it is suggested to use a higher slope at the low-frequency side of the trapezoid (Fig. 5.18B). Because higher frequencies primarily cause ripples, a smoother transition is required for the high-frequency end. This will provide a narrower filter operator with fewer amplitude samples in the time domain.
v. Smooth the edges of the trapezoid to remove the hard transition from pass-band to reject bands at both high- and low-frequency sides in the frequency domain. This will provide a

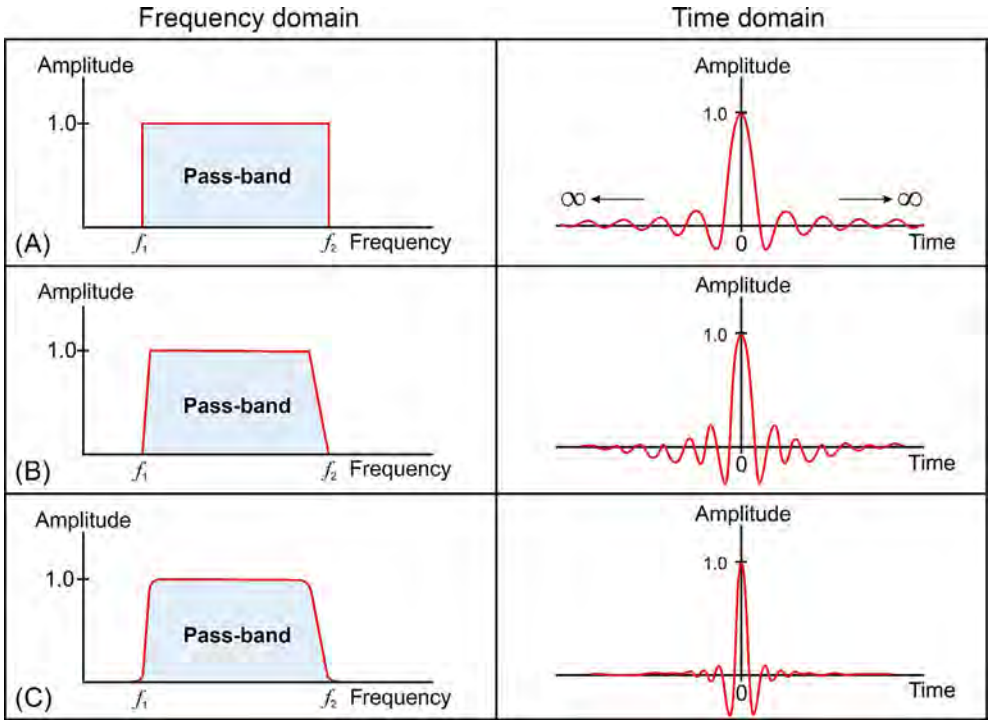


FIG. 5.18 Schematic representation of a band-pass filter operator design. (A) Starting with a box-car shaped amplitude spectrum to define the pass-band region. (B) Setting the slopes around the cut-off frequencies resulting in a trapezoid shaped pass-band region. This ensures a narrower filter operator in the time domain. (C) Smoothing the edges of the trapezoid in the frequency domain ensures a much narrower filter operator in the time domain. f_1 and f_2 represent the cut-off frequencies. Possible Gibbs effects are not included to simplify the illustration.

much narrower filter operator in the time domain. Take the inverse Fourier transform to obtain the final filter operator in the time domain (Fig. 5.18C).

Using the filter operator obtained as shown in Fig. 5.18, filtering of the seismic data can be done either in the time or frequency domain. In the frequency domain application, the amplitude spectra of the input seismic trace and the filter operator are multiplied (Fig. 5.19A). In the time domain, however, a convolution process is performed and coefficients of the filter operator are convolved by seismic trace amplitudes (Fig. 5.19B). Even though both applications produce the same results (Fig. 5.19C), the time domain application is preferred in practice since the convolution process is more economical than computing the forward and then inverse Fourier transform before and after filtering.

After the application, the filtered output trace will contain amplitudes only in the frequency band of the filter operator. Filtering does not affect the phase spectrum; only the amplitude spectrum becomes band limited. If the pass-band widens in the frequency domain, the filter operator in the time domain narrows, and hence contains a fewer number of nonzero filter coefficients, which makes the filter operation computationally faster. The time domain length of the operator is also important. Fig. 5.20 shows filter operators of different lengths and their corresponding amplitude spectra, that is, the pass-band in the frequency domain. The computations in Fig. 5.20 indicate that increasing the operator length makes the desired and actual operator spectra similar. The operator lengths shorter than 400 ms leave some residual ripples in the pass-band region, while operator lengths longer than 400 ms do not provide further improvement on the spectral shape of the pass-band. When the operator is truncated too much, the amplitude spectrum of the operator degrades, although the slopes of the spectrum are not affected from the truncation process. In practice, however, shorter operator lengths are preferred because they require less computational time during the applications and hence they are more economical.

Frequency filtering is generally used to improve the vertical resolution of the seismic data. It is generally believed that high frequencies ensure vertical resolution. On the other hand, Yılmaz (1987) showed that both low- and high-frequency components are required to enhance the vertical resolution. Therefore, it is desired that the seismic data have a wide frequency band involving both low and high frequencies. In the interpretation stage, the frequency content of any particular reflection is important by means of its continuity on the intersecting seismic lines when the sections are tied. Therefore, application of a band-pass filter with similar pass-bands for all vintages of a particular prospect is important to correlate different seismic datasets.

5.5.2 Band-Pass Filtering of Marine Seismic Data

A spectral analysis of the raw seismic data is required for a correct determination of the cut-off frequency and transition band slope parameters before filtering the marine seismic data. In general, very high-amplitude swell noise dominates in the low-frequency band of the spectrum of raw marine shots records. Fig. 5.21A shows a schematic illustration of an amplitude spectrum of a shot gather from a high-resolution marine seismic survey visualized between 0 and the Nyquist frequency (here, 500 Hz for 1 ms sampling rate). In addition to its high amplitude content, the most significant characteristic of this noise is its low-frequency content. The frequency band of the swell noise is generally limited to a 0–10 Hz band and the noise can easily be removed by application of a band-pass filter with an approximately 10-Hz low-frequency cut-off. The 0–10 Hz frequency band, however, may also contain signal amplitudes from deeper

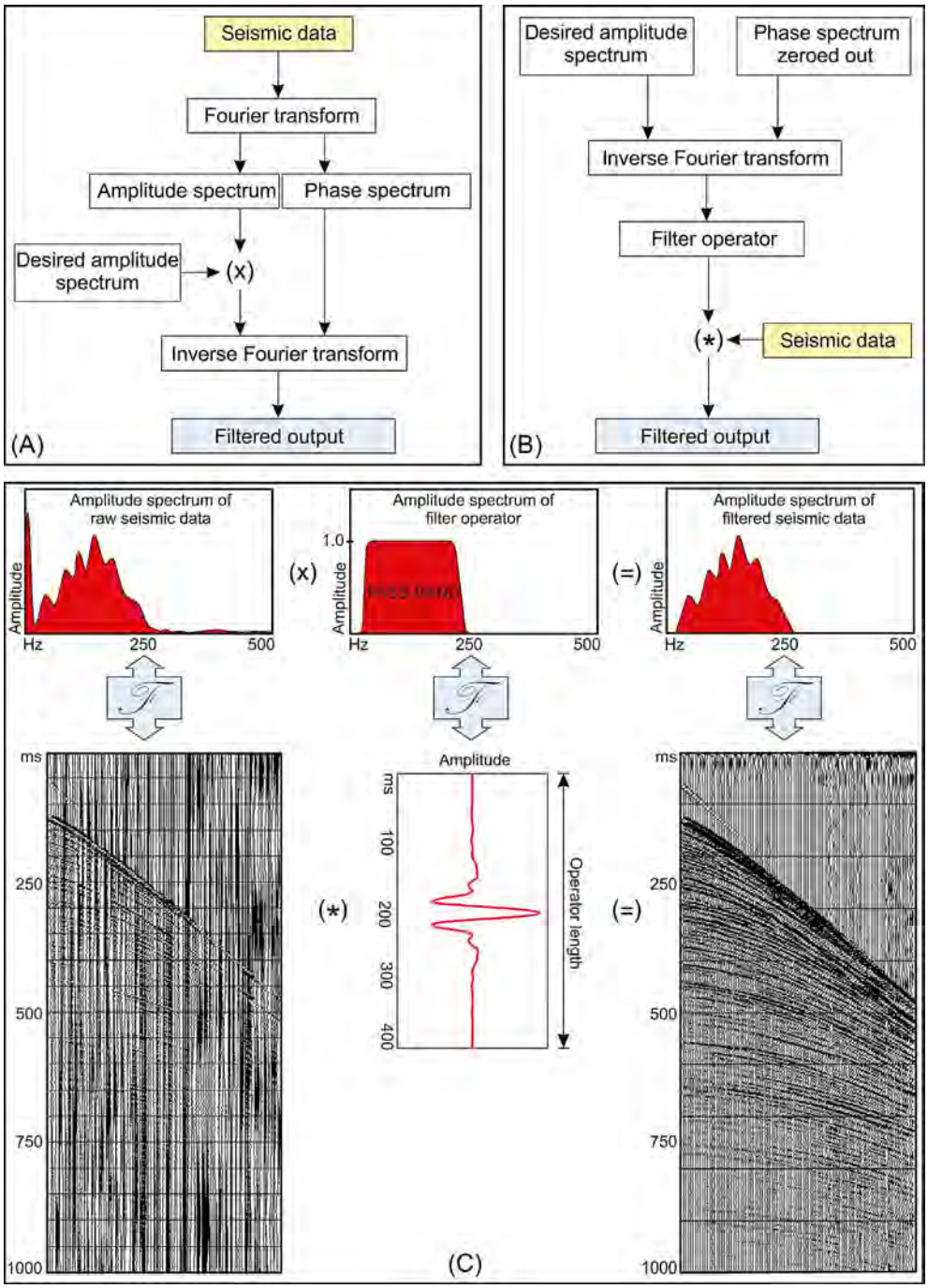


FIG. 5.19 Workflow for band-pass filtering process in (A) frequency and (B) time domains. (C) Filtering is performed either using multiplication (×) of the amplitude spectra of the raw seismic and filter operator in the frequency domain (upper panel), or by a convolution (*) of the seismic data itself with the filter operator in the time domain (lower panel).

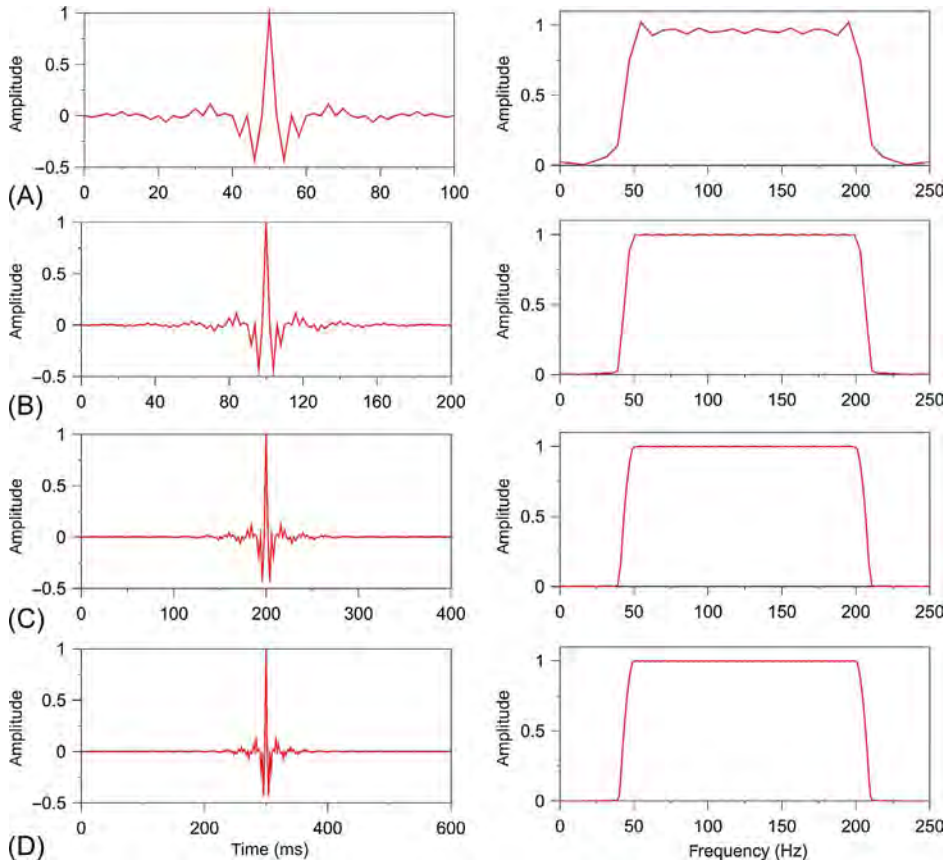


FIG. 5.20 Effect of time domain length of the filter operator on the shape of the pass-band region in the frequency domain for the filter operators of (A) 100 ms, (B) 200 ms, (C) 400 ms, and (D) 600 ms lengths (left panels) and their corresponding amplitude spectra (right panels). The operator is designed as a 40–210 Hz band-pass filter with 10-Hz transition bands.

reflections and filtering out this frequency band can degrade the low-frequency deeper reflection amplitudes. Although some recent studies exist in the literature to remove swell noise without degrading the low-frequency signal amplitudes (e.g., Dondurur and Karslı, 2012), band-pass filtering is widely used today to remove the swell noise from raw marine shots.

It is practically not possible to designate an estimation of the frequency components of the recorded signal because the data spectrum is formed by both noise (which sometimes has a systematic appearance) and reflection signal amplitudes at the same time. In marine seismic applications, the most effective factors determining the data frequency band are the source frequency and the source and/or streamer depths (Section 2.5.1.2). When we omit the effects of source and streamer depths and hence the effect of ghost reflection interference, normally the larger the source signal spectrum, the wider the recorded data frequency band. The Nyquist frequency determined by the sampling rate controls the maximum frequency

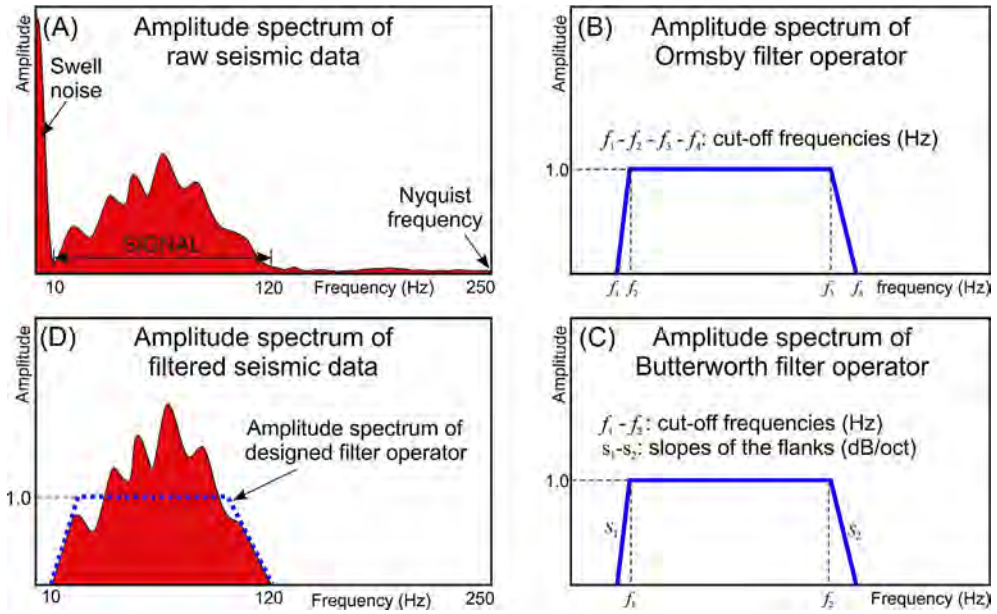


FIG. 5.21 Schematic illustration of modification of the amplitude spectrum in the frequency domain. (A) A schematic amplitude spectrum of a raw shot. Theoretical amplitude spectra of (B) Ormsby, and (C) Butterworth filter operators. (D) Schematical amplitude spectrum of a filtered shot. The amplitude spectrum of either Ormsby or Butterworth operators is multiplied by the spectrum of a raw shot in (A) to obtain the filtered spectrum in (D).

value that can be recorded by the preferred sampling rate, and hence limits the high-frequency end of the spectrum. When the streamer depth is involved, the frequency spectrum of the recorded data becomes band limited from both high and low frequency ends of the frequency axis. In the schematic illustration in Fig. 5.21A, this band is suggested to be 10–120 Hz. Amplitude components corresponding to the frequencies higher than this frequency band are mainly high frequency random noise.

In practice, either Butterworth or Ormsby filter operators can be used to filter amplitudes outside of the effective bandwidth of the seismic data (Fig. 5.21B and C). Although both operators normally have the same frequency domain appearance, the difference is in the way to define the cut-off frequencies in the frequency domain. For the definition of the Ormsby operator, four different frequency values are used to constitute the trapezoid-shaped pass-band and transition regions (Fig. 5.21B). The Butterworth operator, on the other hand, requires two frequencies for low- and high-frequency cut-off values and two slope values for the transition band definition of the trapezoid (Fig. 5.21C). One of the filter operator spectra shown either in Fig. 5.21B or C is multiplied by the raw data spectrum in the frequency domain, or the time domain representations of the operator can be convolved with the input raw data to obtain the band-pass filtered output. In both cases, the spectrum of filtered data (Fig. 5.21D) will only have the amplitudes at those frequencies defined by the operator's frequency band (here between 10 and 120 Hz).

The dominant swell noise can be analyzed using noise records obtained before the shooting starts. These records are useful in analyzing the static noise levels in the ocean as well as their frequency content. Fig. 5.22A shows a noise record

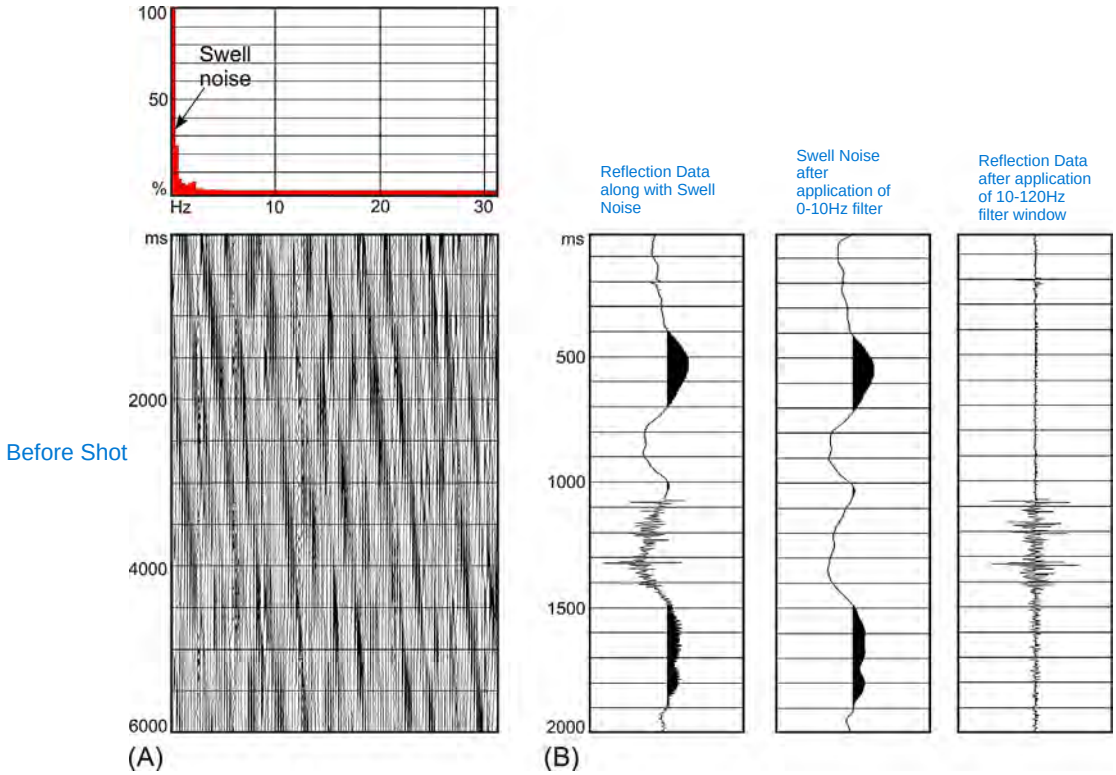


FIG. 5.22 (A) An example noise record (bottom) and its corresponding amplitude spectrum (top) with low-frequency swell noise. (B) A raw seismic trace contains strong swell noise and relatively high-frequency reflections after approximately 1080 ms (left), while its 0–10 Hz filtered version consists of only swell noise amplitudes (middle), and a 10–120 Hz band-pass filter completely removes swell noise and reveals the reflection amplitudes (right).

and its mean amplitude spectrum, indicating that the frequency band of the swell noise is between 0 and 10 Hz. Fig. 5.22B shows an example raw seismic trace of a first channel from a marine shot gather with relatively high amplitude swell noise along with reflection amplitudes appearing after approximately 1080 ms. When we filter this trace with a 0–10 Hz low-pass filter, we get a trace comprising only swell noise amplitudes. An application of the 10–120 Hz band-pass filter, however, almost completely filters out the dominant swell noise amplitudes and uncovers the primary reflections (Fig. 5.22B). After a band-pass filter application, the amplitude spectrum of the data becomes band limited and both high- and low-frequency amplitudes are suppressed. Fig. 5.23 shows a number of example raw and band-pass filtered shots (between 12 and 220 Hz) to remove the swell noise. The reflection hyperbolas of the primary reflections become visible after removal of the swell noise.

5.5.3 Time Varying Filtering

Because of the attenuation effect of the earth on the seismic signal, especially high-frequency components of the source signal are absorbed quickly. Therefore, its dominant frequency band decreases when the signal propagates into the

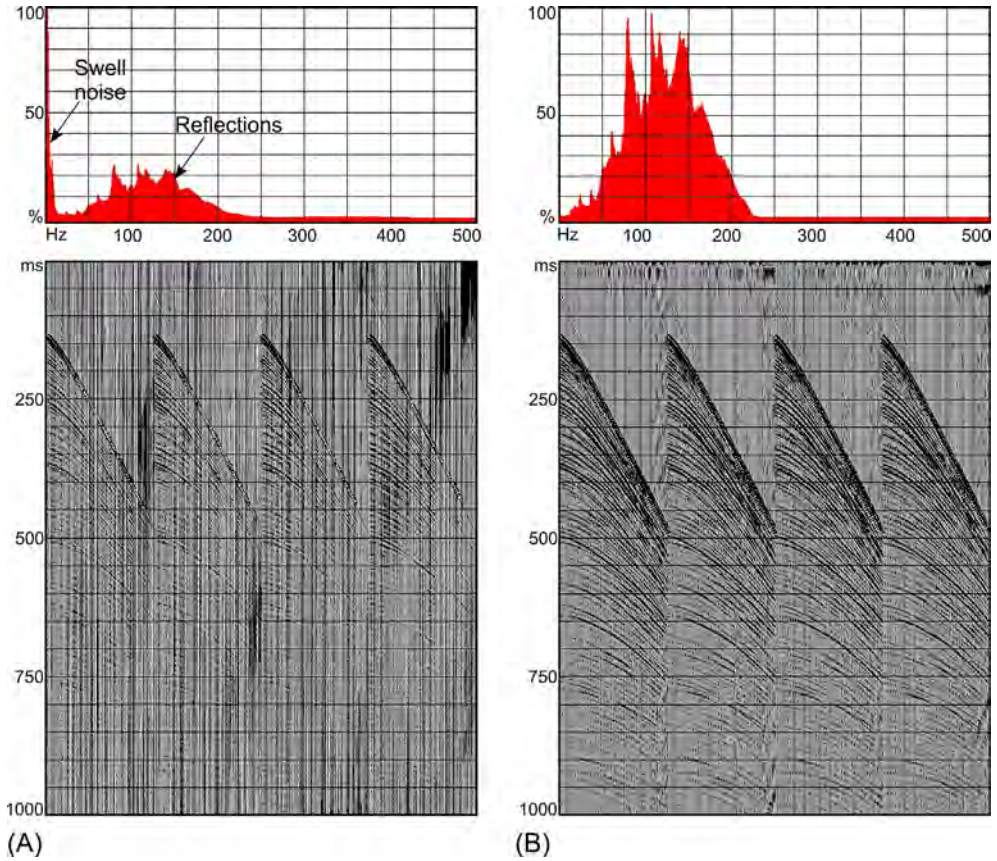


FIG. 5.23 (A) Sample raw marine shot gathers, and (B) their 12–220 Hz band-pass filtered versions. Their corresponding average amplitude spectra are given in the upper panels.

earth (Section 5.6), and the higher frequency signal is present only in the shallow parts of the seismic sections, while the deeper parts (the late arrivals) contain only relatively lower frequency reflections since they need to travel longer distances and hence they are exposed to severe absorption effects. These lower frequencies simply result in lower resolution in the deeper parts of the data.

An example stack section that shows this significant decrease in the frequency content of late arrivals is illustrated in Fig. 5.24. From shallow to deep parts, the frequency spectra of different portions of the section indicated by A, B, C, and D are computed to illustrate the attenuation effects along the temporal axis. The section has frequency components higher than 200 Hz and the dominant frequency is approximately 120 Hz for the first 150 ms from the seabed in part A. In the deeper parts, however, high-frequency content of the data gradually decreases and the dominant frequency becomes approximately 40 Hz for the last 500 ms of the section in part D. This depth dependence of the available frequency band of a seismic signal may require time-dependent application of frequency filters. In time varying filtering (TVF) applications, the cut-off frequency values

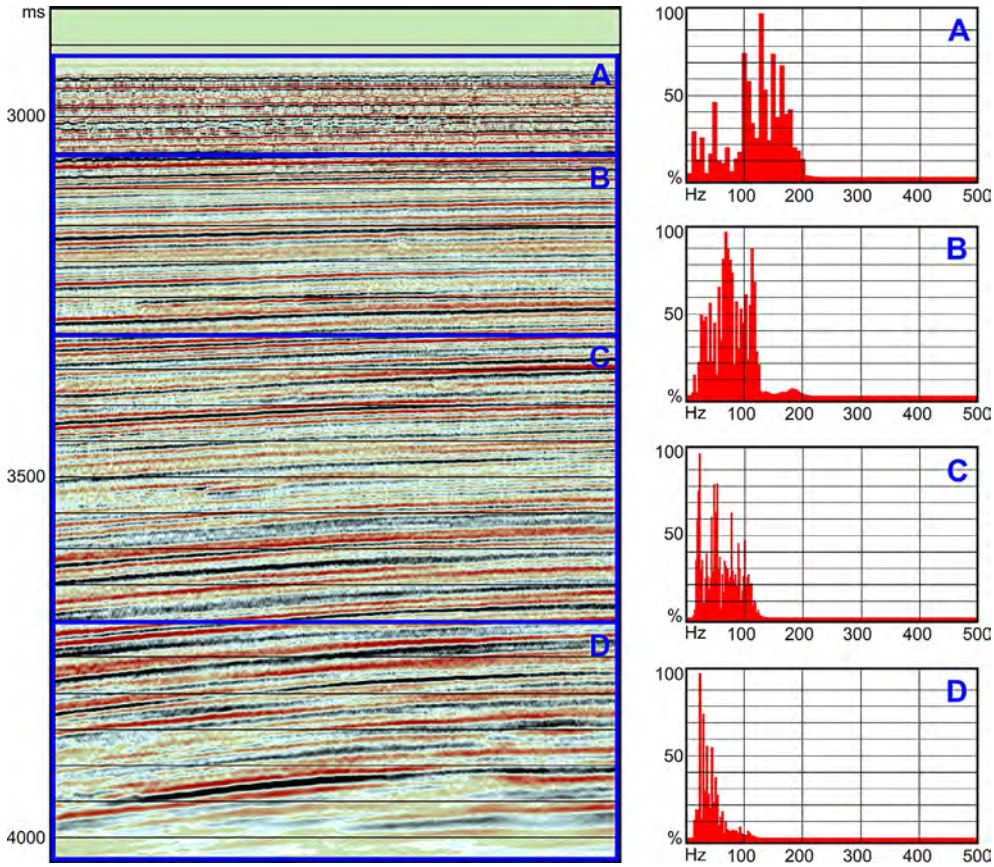


FIG. 5.24 An example stack section and amplitude spectra of its different parts from shallow to deep zones (from A to D), illustrating the dramatic decrease in the frequency content in the late arrivals.
TVF - Time varying Filtering

change along the time axis of the seismic sections. TVF is generally applied to stack sections which are first divided into different time windows, and then band-pass filters with different cut-off frequency values are applied to each time window. Normally, wider pass-bands are used for the shallow zones while the high-frequency cut-off value is gradually decreased for deeper windows.

Fig. 5.25 shows an application of TVF to a stack section using three time windows, indicated by A, B and C in Fig. 5.25A. Since the frequency band decreases at late arrivals, high-frequency random noise becomes more distinct in deeper parts of the seismic section. The average amplitude spectra for each window are also provided. The frequency bandwidths of the input section in Fig. 5.25A are approximately 6–200 Hz, 4–80 Hz, and 4–40 Hz for windows A, B and C, respectively. Applying a TVF using these frequency bands for three time windows removes most of the high-frequency random noise amplitudes for the deeper parts, and hence the low amplitude deeper reflections become much more visible (Fig. 5.25B). Time windows must be determined by considering the dominant frequency characteristics and the structural style of the geological formations, as in

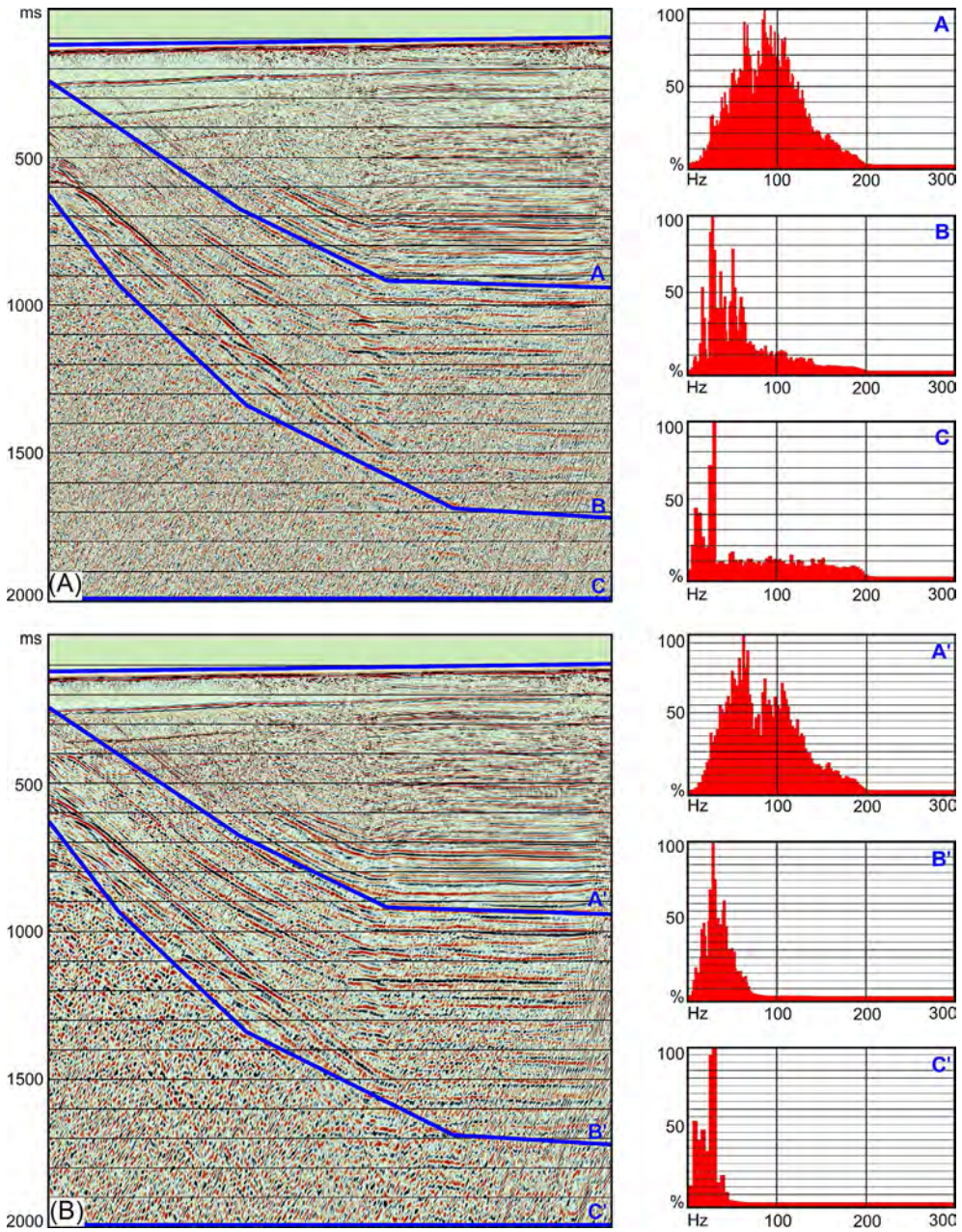


FIG. 5.25 (A) A migrated stack section with three time windows, indicated by A, B and C, and their corresponding amplitude spectra. (B) TVF output of the section in (A) using 6–200 Hz, 4–80 Hz, and 4–40 Hz frequency bands for windows A′, B′ and C′, respectively.

Fig. 5.25A. In addition, windows may overlap if required. However, if the high-frequency cut-off values for each window are not close to each other, amplitude artifacts with abnormally low amplitudes may arise along the overlap zones after gain application.

5.5.4 QC in Band-Pass Filtering

Quality control of a frequency filtering application is generally done by visually analyzing the filtered shot gathers and by a visual comparison of amplitude spectra of raw and filtered shots. A successful band-pass filter application must remove most of the undesired noise amplitudes of both high- and low-frequency components. Especially in rough weather conditions during high-resolution surveys, where the streamer is towed at shallow water to enhance the resolution, the reflection amplitudes are quite weak and are covered by high amplitudes of swell noise. After a successful band-pass filtering either in the time or frequency domain, reflection hyperbolas must become visible on the shot gathers, and the amplitude spectrum must have almost no frequency components of swell and high-frequency random noise amplitudes (Fig. 5.23).

The following parameters are predetermined before frequency filtering:

i. Cut-off frequency values
ii. Time domain operator length
iii. Domain of application (time or frequency)
iv. Type of filter (Ormsby or Butterworth)
v. Phase of the filter (minimum or zero)

The cut-off frequency values can easily be determined by analyzing the average amplitude spectra of the raw shot gathers, and this spectral analysis must be done on a number of successive shots to determine an optimum cut-off frequency pair. In marine seismic data, the low-pass cut-off frequency is typically determined to exclude the low-frequency swell noise amplitudes from the pass-band. The cut-off frequency at the high-frequency end determines the bandwidth of the seismic data and must be chosen carefully. Because the usable frequency band is limited by the ghost notches, the high-frequency cut-off is normally determined by the frequency of the first ghost notch in the spectrum. The appearance of the first notch is controlled by the depth of the gun array(s) and the streamer(s), and hence it determines the upper limit of the available spectrum (Sections 2.2.3 and 2.2.4). Fig. 5.26 shows the mean amplitude

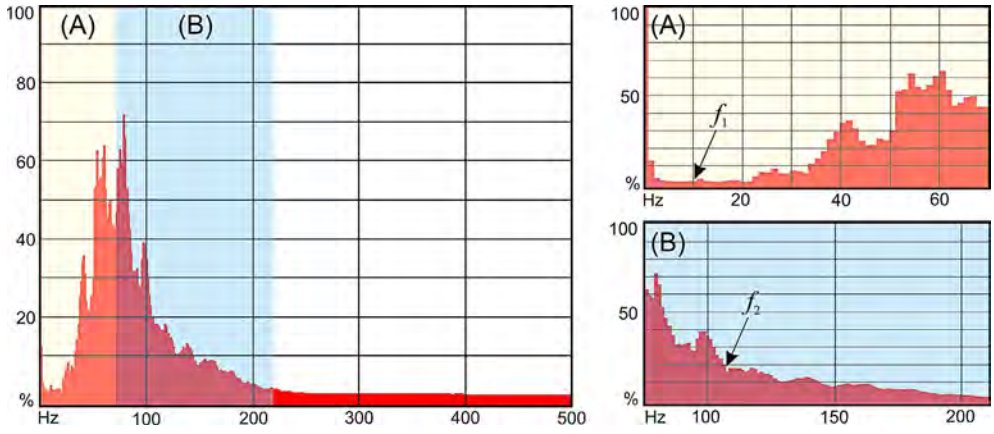


FIG. 5.26 Mean amplitude spectrum of a raw shot gather, and its close-ups for (A) low- and (B) high-frequency zones. f_1 and f_2 are suitable cut-off values for low and high frequencies of the band-pass filter, respectively.

spectrum of a raw shot gather along with two close-ups for low (0–70 Hz) and high (70–220 Hz) frequency ends of the available frequency band, illustrating the areas where low-cut and high-cut frequencies can be determined. Based on an amplitude spectrum as in Fig. 5.26, a possible cut-off frequency pair for low and high frequencies is 10 and 120 Hz, respectively. Below 10 Hz, swell noise dominates, while predominantly random noise amplitudes exist above 120 Hz.

Before the application of a band-pass filter with determined parameters, different filter panels can be prepared to specify the most suitable parameters for the filtering on a brute stack or single trace sections. Fig. 5.27 shows example filter panels to designate the high-frequency cut-off value, which is obtained by several band-pass filters with different high-frequency cut-off values ranging from 50 to 400 Hz for a constant 6-Hz low-frequency cut-off applied to a small portion of a brute stack section. Higher frequency components apparently increase the resolution of the seismic data. However, random noise becomes more visible, especially at deeper parts, if unnecessarily higher frequencies are incorporated in the pass-band (Fig. 5.27F and G). According to the filter panels in Fig. 5.27, the suitable high-frequency cut-off can be selected as 100 Hz.

Fig. 5.28 shows similar test panels obtained by applying the same portion of the same brute stack section in Fig. 5.27, this time, however, with a varying low-frequency cut-off value for a constant 250-Hz high-frequency cut-off. An excessive removal of low-frequency components from the seismic data causes much more dramatic results: details in the filtered output section are immediately lost (compare Fig. 5.28A and C), the data becomes ringier, and deeper reflections die out as the frequency band narrows (e.g., in Fig. 5.28E). When we compare the analysis in Figs. 5.27 and 5.28, we also conclude that the low-frequency components exist both in the deep and shallow parts of the seismic data, whereas the high frequencies can only be found in shallow parts because of the attenuation effects.

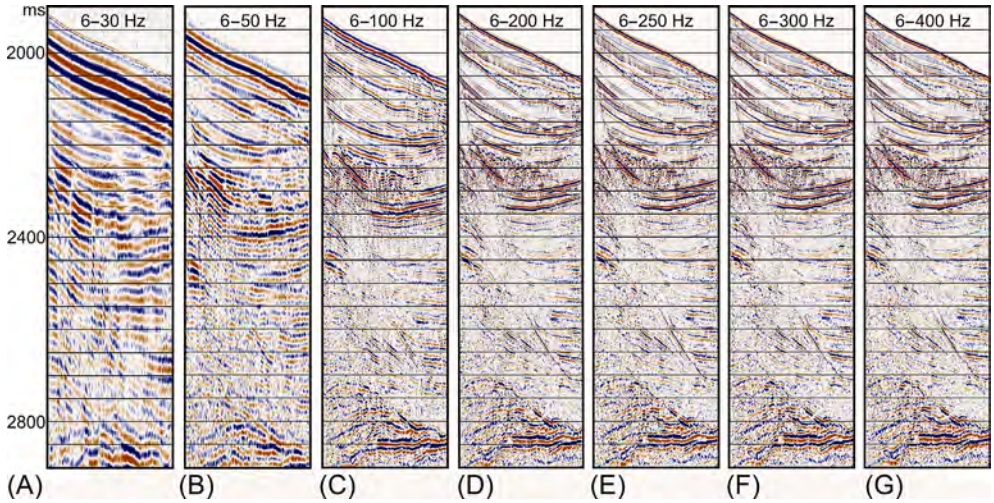


FIG. 5.27 Example filter panels for a stack strip with variable high-frequency cut-off value. Band-pass filter outputs for (A) 6–30 Hz, (B) 6–50 Hz, (C) 6–100 Hz, (D) 6–200 Hz, (E) 6–250 Hz, (F) 6–300 Hz, and (G) 6–400 Hz pass-bands.

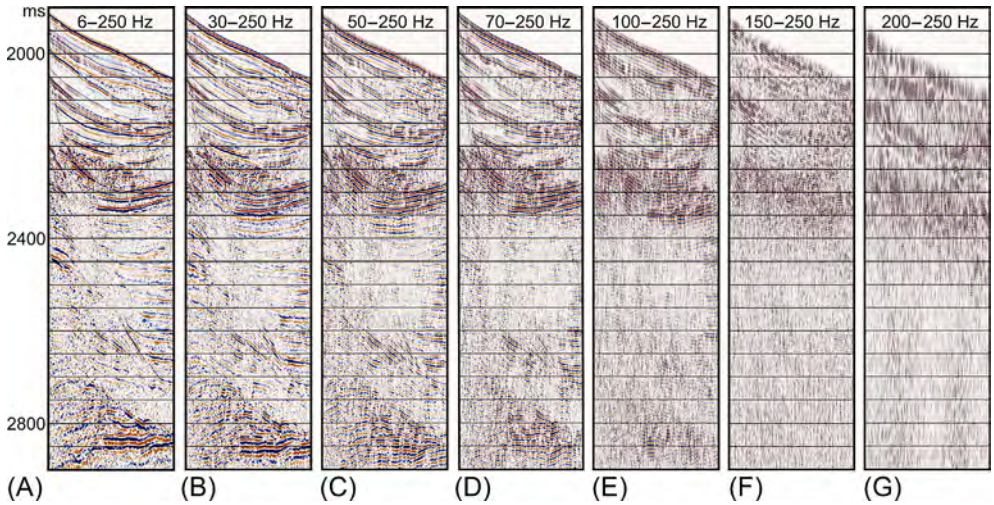


FIG. 5.28 Example filter panels for a stack strip with variable low-frequency cut-off value. Band-pass filter outputs for (A) 6–250 Hz, (B) 30–250 Hz, (C) 50–250 Hz, (D) 70–250 Hz, (E) 100–250 Hz, (F) 150–250 Hz, and (G) 200–250 Hz pass-bands.

The time domain length of the filter operator is one of the most important factors affecting the filter performance. Operators with smaller time lengths do not have an amplitude spectrum of ideal trapezoid shape (Fig. 5.20), so the length of the operator should be long enough to properly suppress undesired frequency components. Fig. 5.29 shows outputs of the filtering applications using filter operators with different time lengths and their mean amplitude spectra. Short filter operators fail in removing all of the swell noise, leaving some residual undesired swell noise amplitudes around 0 Hz in the output amplitude spectra. These residual amplitudes, however, vanish with increasing filter operator length and completely disappear in the output shot filtered with 400-ms operator length. If the swell noise cannot be removed by a band-pass filter, longer operator lengths must be considered. An effective *f-k* filter, or two successive band-pass filters with the same parameters, can also be used.

Because narrowing in the frequency domain results in widening in the time domain (Section 4.5), definition of a narrow pass-band in the frequency domain requires a significantly wide filter operator in the time domain, consisting of several nonzero time samples (Bracewell, 1965). Application of such a filter operator after truncating both ends will significantly reduce the filter performance since several nonzero samples of the operator are excluded. In order to avoid this, much longer time domain filter operator length should be considered when the required pass-band of the filter is narrow, e.g., when applying a single frequency notch filter. Longer operator lengths, however, require more computational time, and they may not be economical, especially for large data volumes. Fig. 5.30 schematically shows the relationship between the width of the pass-band in the frequency domain and the operator length in the time domain. Wider pass-bands always correspond to narrow time series (the filter operator)

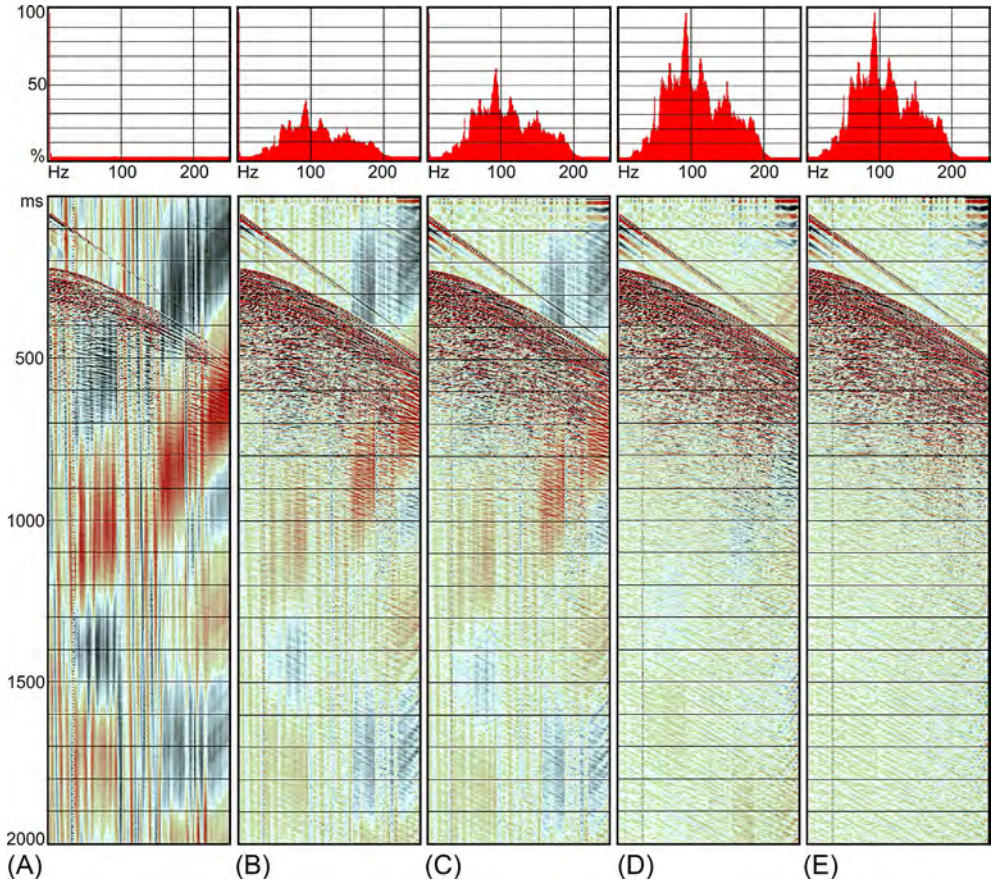


FIG. 5.29 Test of the filter operator length on a shot gather filtered between 30 and 200 Hz. (A) Raw shot gather and its 12–200 Hz band-pass filtered outputs for (B) 50 ms, (C) 100 ms, (D) 200 ms, and (E) 400 ms operator lengths (lower panels), and their corresponding mean amplitude spectra (upper panels).

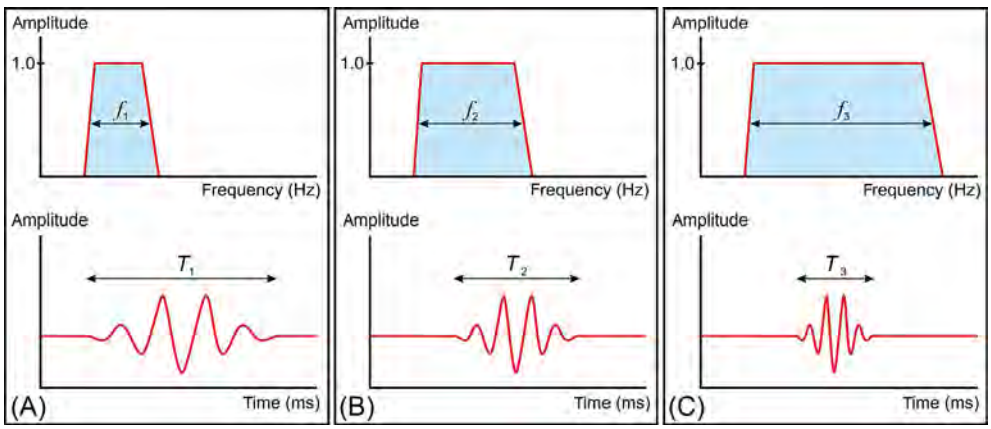


FIG. 5.30 Schematic illustration of the relationship between the width of the pass-band in the frequency domain (top) and the operator length in the time domain (bottom). (A) Narrow, (B) moderate, and (C) wide pass-bands in frequency domain and their corresponding filter operators in time domain. Here f_i are the widths of the pass-bands and T_i are the operator lengths. When $f_1 < f_2 < f_3$, then $T_1 > T_2 > T_3$.

in the time domain. Processors must take extra care with band-pass filters to filter out a narrow frequency band, and several tests on the selected shots may be required to determine the optimum operator length.

Normally the filter operators are designed as zero phase wavelets, which have amplitudes before zero time since they are not causal (Yılmaz, 1987). After the convolution of this operator with a minimum phase input signal during filtering, this noncausality results in side oscillations in the filtered output before the onset of the signal itself (Fig. 5.31). If the seismic data is composed of a minimum phase source signal, as is the case for impulsive sources like an air gun array or dynamite, then a minimum phase filter operator produces better results. In this case, the operator is again designed as zero phase, and then its minimum phase equivalent is calculated and applied to the data.

5.6 GAIN RECOVERY

Amplitude distribution along the time axis of raw seismic data is not uniform, since the late arrivals have much lower amplitudes while the amplitudes of early arrivals from shallow reflectors are relatively higher. Gain recovery basically causes the data to have much more uniform amplitude distribution in both the shallow and deep portions by increasing the lower amplitude values of the late arrivals while decreasing the higher amplitudes of the shallow reflections.

Several factors affect the amplitude of the seismic signal generated by the seismic source, most of which depend on the physical characteristics of the medium in which the signal propagates. These effects tend to decrease the seismic signal amplitude as it travels away from the source location. Fig. 5.32 schematically illustrates some

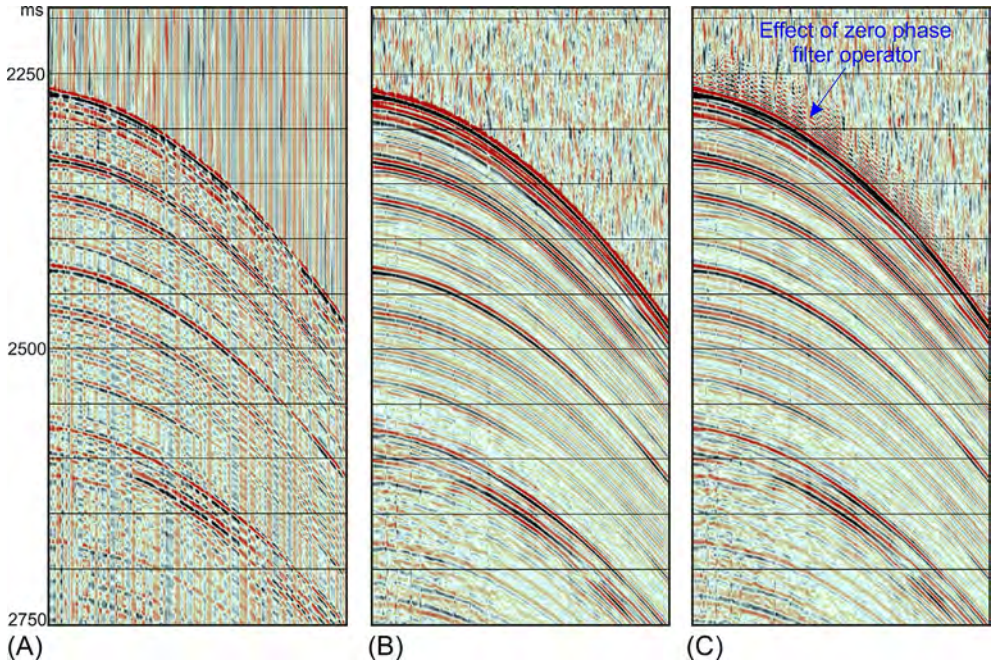


FIG. 5.31 (A) A sample raw shot, and its 10–140 Hz band-pass filtered versions using 400-ms operator length with (B) minimum phase and (C) zero phase filter.

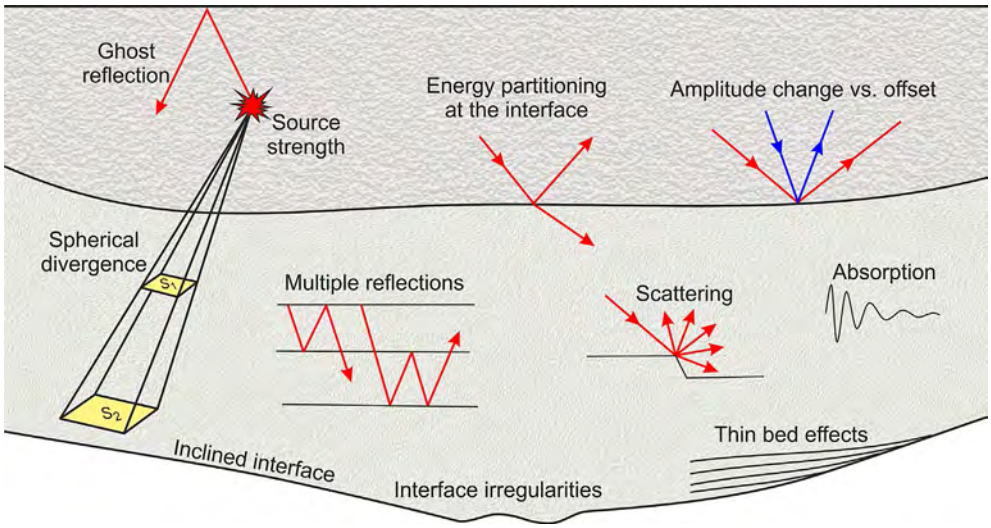


FIG. 5.32 Schematic illustration of various factors affecting the seismic signal amplitude during its propagation. Among these, spherical divergence and absorption are of primary importance.

of these factors affecting the signal amplitude. Although the existence of irregularities along the reflective interface, multiple reflections, energy partition at the interface, and diffractions decrease the amplitude, the spherical divergence and absorption have a primary effect on the amplitude.

A shot gather is composed of the wave field generated by a single shot, and in a constant velocity medium, this point source produces a spherical wave field. Two principal agents affect the characteristics of the signal amplitude. The first one is termed spherical divergence and only results in amplitude decay and other characteristics of the signal, such as phase or frequency content, are not affected (Fig. 5.33B). Since the acoustic waves propagate as spherical wave fronts, the total energy in small surficial areas indicated by S_1 and S_2 in Fig. 5.32 is equal. However, because S_1 is smaller than S_2, the energy density is lower in area S_2. Energy density decreases proportionally to $1/r^2$ in a homogenous medium, where r is the radius of the wave field, while wave amplitude is proportional to the square root of energy density, and hence it will decrease proportionally to $1/r$. If $A(0)$ is the amplitude at the source and $A(r)$ is the amplitude at a distance (r) away from the source, then the spherical divergence effect can be expressed as

$$A(r) = A(0)\frac{1}{r} \tag{5.3}$$

The other principal effect, absorption, on the other hand not only reduces the amplitude but also modifies the frequency content of the signal, and the dominant frequency decays as the signal propagates (Fig. 5.33C). The effect of absorption can be expressed as

$$A(r) = A(0)e^{-\alpha r} \tag{5.4}$$

where α is the absorption coefficient and equals

$$\alpha = \frac{\pi f}{QV} \tag{5.5}$$

where f is the dominant frequency of the signal, Q is the rock quality designation (RQD), and V is the wave velocity of the medium. The spherical divergence and absorption effects together are known as attenuation and can be expressed as

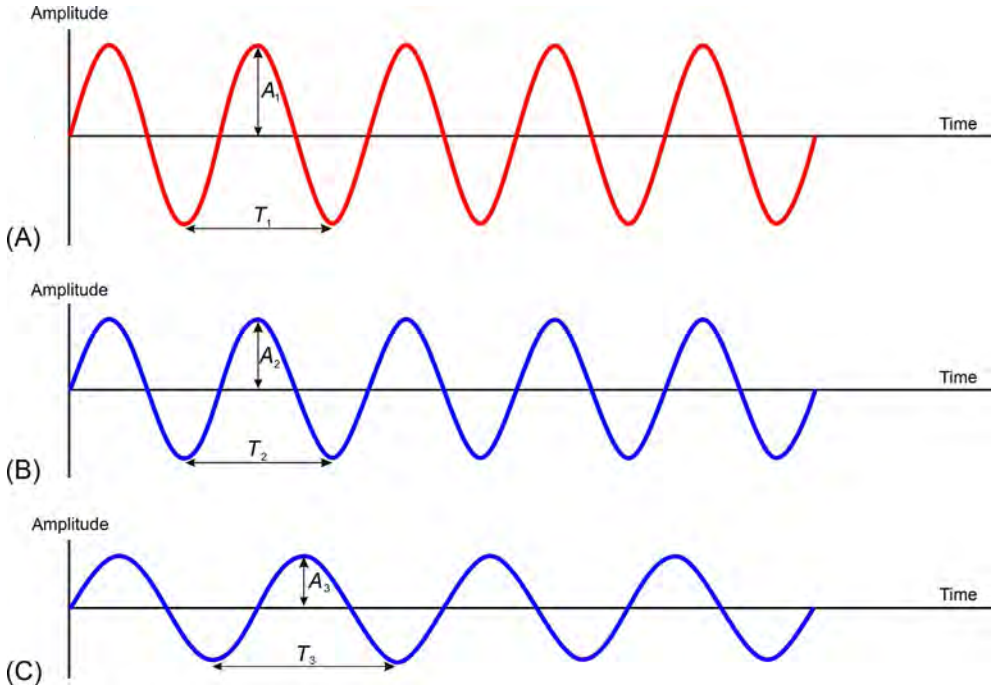


FIG. 5.33 Schematic illustration of the attenuation effect on a sine wave. (A) Input monofrequency sinusoid, after (B) spherical divergence and (C) absorption effects. T and A represent period and amplitude of the sinusoid, respectively. Only amplitude decay occurs in the case of the spherical divergence effect, while both amplitude decay and frequency decrease occur due to the absorption effect. Here, $T_1 = T_2 < T_3$ and $A_1 > A_2 > A_3$.

$$A(r) = A(0)\frac{e^{-\alpha r}}{r} \tag{5.6}$$

Eq. (5.6) suggests several implications: first, higher frequency components are absorbed more quickly with respect to the lower frequency components of the signal. Therefore, higher frequency amplitudes of the propagating signal die rapidly, the period (and hence the wavelength) of the signal increases and the dominant frequency decreases. In addition, the absorption of the signal becomes higher as the absorption coefficient increases. For a constant velocity subsurface, the absorption coefficient of the medium is mainly controlled by the rock quality factor, Q, which has a relatively small value for weathered layers while it is larger for massive and compact media. Weathered layers absorb the signal quickly, and this causes serious issues in land seismic surveys because the surficial weathered soil layer does not only absorb the signal, but also creates lateral velocity variations. To overcome this issue, dynamite is located into the shallow bore holes penetrating the base of the surficial weathered layer.

Although fluid saturation and free gas content of the pore spaces contribute to absorption, the primary reason is the transformation of the kinetic energy into heat energy due to the friction of the rock particles during the wave passage. The heat emerging during the compression when the acoustic wave travels through a medium is consumed during the dilatation and cannot be recovered. The longer the signal travels, the higher the effect of the absorption is, and therefore reflections from deeper

reflectors almost always have much lower amplitudes and frequency content when compared to the shallow reflections. Assuming a constant velocity medium, a lower dominant frequency implies a higher signal period and hence a longer wavelength, which ultimately causes much lower resolution in the deeper parts of a seismic section.

Although we can compensate for the spherical divergence effect by applying a suitable gain function to the seismic traces, the effect of absorption cannot be completely eliminated by existing processing techniques, since we cannot model the subsurface distribution of Q values in three dimensions along the entire survey area. Today, there are several inverse Q filtering approaches (e.g., Wang, 2002; Nunes et al., 2011) in the literature to compensate for the absorption effects, but most of them consider a constant Q value for the whole survey area since the distribution of the Q value in three dimensions cannot be obtained from the seismic data in sufficient resolution.

Because of these effects, amplitudes of the late arrivals in raw seismic data are not visible on the raw data although they do exist. These invisibly small amplitudes are boosted by gain recovery, which is actually a time variant scaling of the seismic traces. There are various methods to recover the low amplitudes of the seismic data. The most common techniques are known as true amplitude recovery (TAR), which is applied as either spherical divergence correction or t^P correction, and automatic gain control (AGC). In principle, a proper gain function is defined for a specific time gate along the time axis, and the amplitudes within this gate are multiplied by the gain function (Fig. 5.34) as

$$s(t) = g(t) \times a(t) \tag{5.7}$$

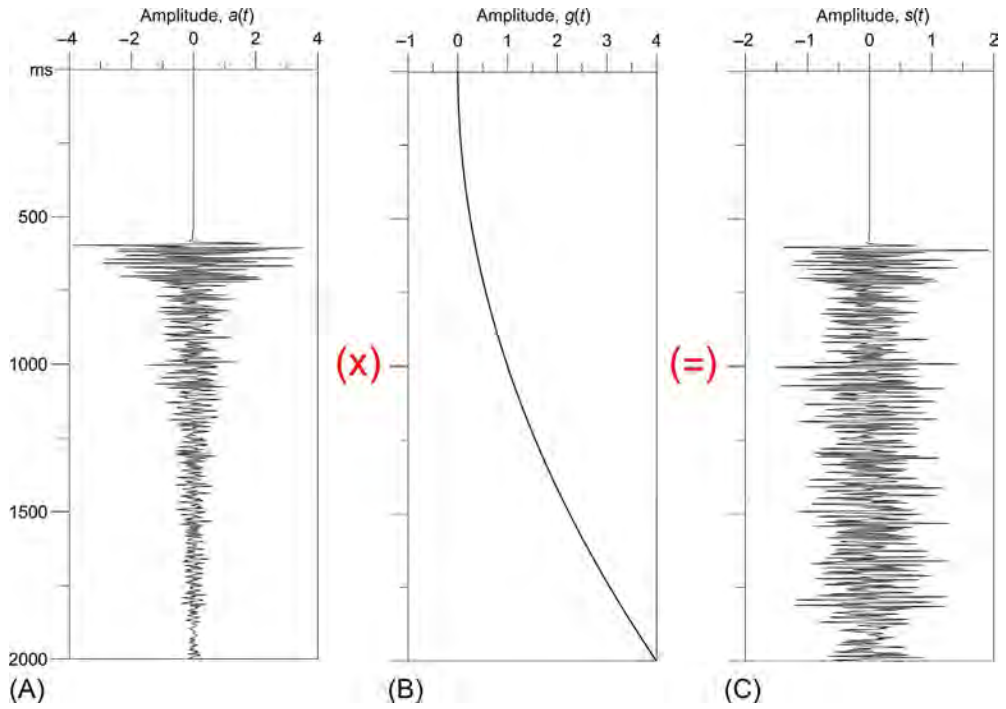


FIG. 5.34 (A) A filtered seismic trace, (B) gain function, and (C) trace after gain recovery.

where $g(t)$ is the gain function, $a(t)$ is the input seismic trace, and $s(t)$ is the output data after gain recovery.

Fig. 5.35 shows a gain application to a number of marine seismic shots. After the gain application, lower amplitudes of the late arrivals increase while higher amplitudes of early arrivals are suppressed to obtain a more regular amplitude distribution along the time axis. The disadvantage of the gain applications is that the amplitudes of both random and coherent noise, especially at the deeper parts where the reflection amplitudes are small, may also be boosted.

5.6.1 Spherical Divergence Correction

Amplitude decay due to the spherical divergence is proportional to $1/r$ and $1/(V^2t)$ in the case of a homogenous medium and a layered subsurface, respectively. Here, V is the velocity of the medium, r is the distance to the source point, and t is the time. Thus, the spherical divergence effect can be compensated for in a homogenous medium by using a gain function of

$$g(t) = V \cdot t \tag{5.8}$$

and for a layered subsurface, the gain function can be expressed as

$$g(t) = \left[\frac{V(t)}{V(0)}\right]^2 \left[\frac{t}{t(0)}\right] \tag{5.9}$$

where $V(t)$ is the root-mean-square (RMS) velocity (Section 9.1), and $V(0)$ is the velocity at time $t(0)$. According to Eqs. (5.8) and (5.9), spherical divergence correction requires seismic velocity which is, however, unknown at the very beginning of the processing. Therefore, spherical divergence correction is applied to the data with

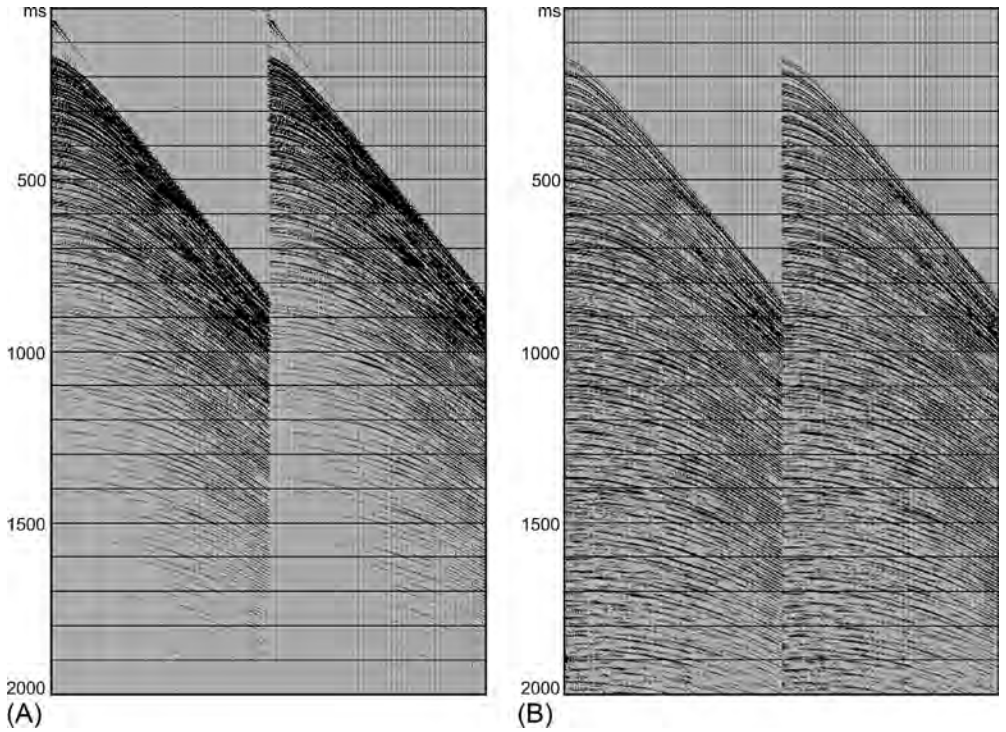


FIG. 5.35 An example gain correction for two filtered marine shots gathers. (A) Before, and (B) after gain application.

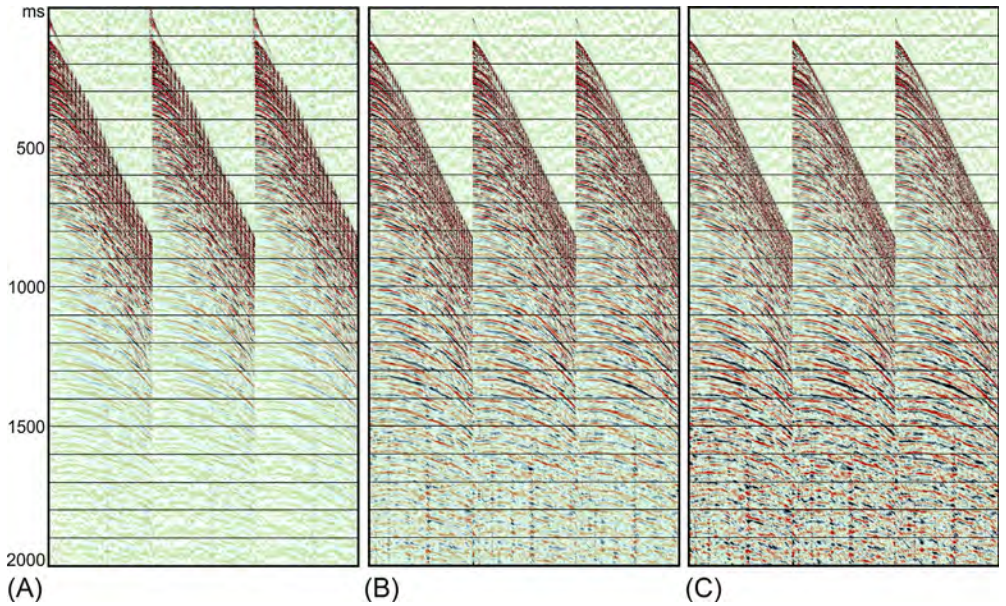


FIG. 5.36 (A) Filtered input shot gathers with no gain, and spherical divergence correction results for (B) homogenous, (C) layered media.

approximate velocities first, and then after the velocity analysis, the correction is removed and reapplied with the correct velocity distribution obtained from a velocity analysis. Fig. 5.36 shows example shot gathers with and without a spherical divergence correction, using correct velocities for both homogenous and layered subsurfaces.

Amplitudes of late arrivals become visible after removal of the spherical divergence effect from the seismic data. This type of gain recovery, however, does not contain any correction for the absorption effect and the amplitudes of high-frequency components consumed by the absorption cannot be recovered at all. The most important advantage of spherical divergence correction is that it preserves relative amplitudes of the seismic data, termed relative amplitude processing. Therefore, it is preferred for data collected for oil and gas exploration, where relative amplitude changes are critically important since they may indicate the subsurface hydrocarbon accumulations.

5.6.2 Time Raised to a Power Correction (t^P)

Gain correction based on a power of arrival time of seismic amplitudes is one of the most common gain recovery methods in processing. It consists of trace-by-trace multiplication of seismic amplitudes by a gain function, defined as

$$g(t) = t^P \tag{5.10}$$

where t is the recording time of the seismic sample and P is a constant typically between 0.5 and 4.0. The method does not require velocity information on the subsurface, is easy to apply, and also preserves the relative amplitude changes in the seismic data.

t^P is a gain function that decreases the amplitudes of early arrivals for $t < 1.0$ s and increases the amplitudes of late arrivals for $t > 1.0$ s. Fig. 5.37 shows t^P gain functions for different P values. The efficiency of time raised to a power correction is directly proportional to the value of P:

shallow amplitudes are suppressed while the deeper amplitudes are boosted for larger P values. As the P value decreases, the effectiveness of the t^P correction also decreases: amplitudes of early arrivals are less suppressed while the amplitudes of late arrivals are insufficiently amplified. Figs. 5.38 and 5.39 show two applications of the t^P correction for different P values on two different marine shot

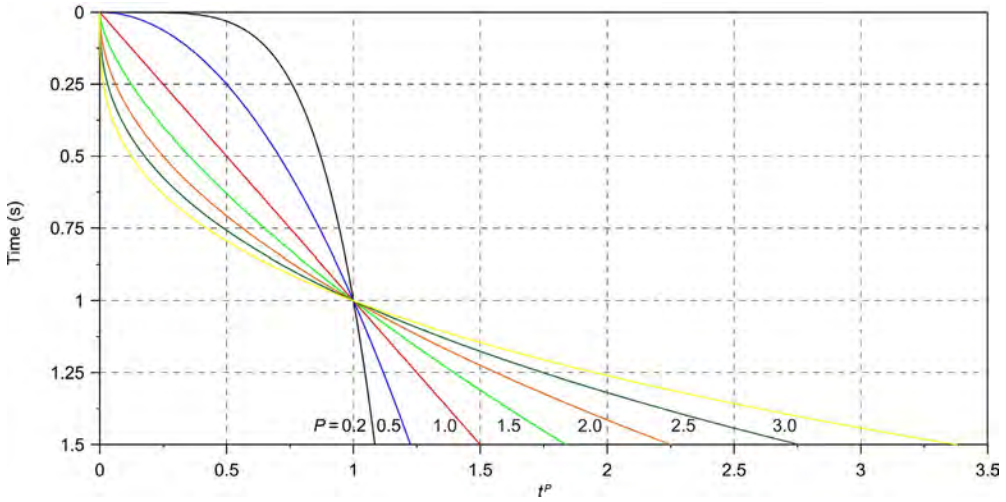


FIG. 5.37 t^P gain for different P values. The efficiency of t^P correction depends on P value.

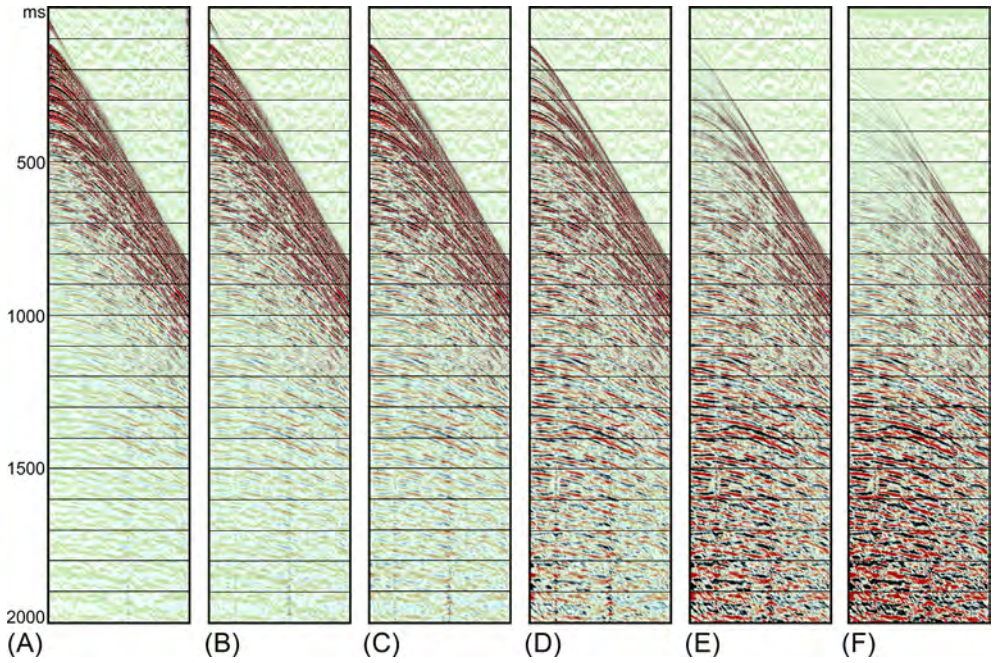


FIG. 5.38 t^P corrections for different P values on a marine shot gather from relatively shallow waters. (A) Filtered shot with no gain, and its t^P corrected versions for (B) $P = 0.5$, (C) $P = 1.0$, (D) $P = 2.0$, (E) $P = 3.0$, and (F) $P = 4.0$.

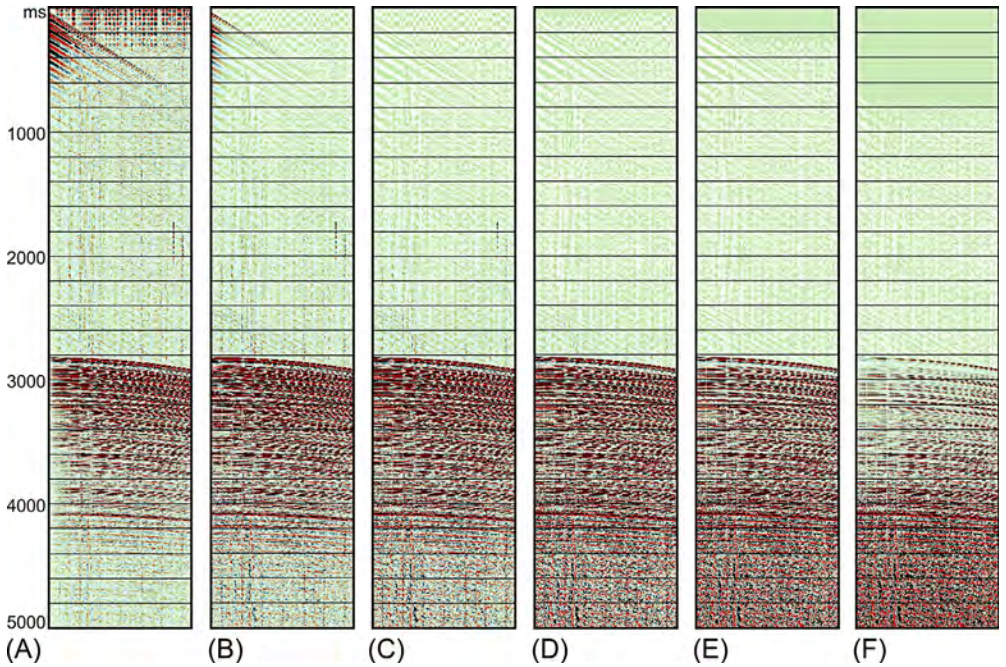


FIG. 5.39 t^P corrections for different P values on a marine shot gather from relatively deeper waters. (A) Filtered shot with no gain, and its t^P corrected versions for (B) $P = 1.0$, (C) $P = 2.0$, (D) $P = 4.0$, (E) $P = 6.0$, and (F) $P = 10.0$.

gathers from a shallow continental shelf and a relatively deep basin area, respectively. Selection of the proper P value depends on the recording length and seabed depth. In general, smaller P values are appropriate for the seismic data from shallow shelf areas while higher values are required for seismic data from deeper waters, to properly recover the amplitudes of late arrivals. For instance, $P = 2.0$ is suitable for the shot in Fig. 5.38, but $P = 4$ or even $P = 6$ can be selected for the shot in Fig. 5.39. In general, if a lower P value is selected, then the amplitudes of deep reflections are not sufficiently recovered. On the contrary, if an unnecessarily high P value is used, then the amplitudes of early arrivals almost die (Fig. 5.38F).

5.6.3 Automatic Gain Control

Automatic gain control (AGC) is one of the most common gain recovery methods in seismic processing. AGC is applied to the seismic data on a trace-by-trace basis using a sliding time window. Fig. 5.40 shows the principle of AGC application. A window with a length of Δt is selected (Fig. 5.40A), and this window is progressively moved down along the time axis sample-by-sample (e.g., Fig. 5.40B and C). Here, Δt is also known as AGC operator length. Each time, a scale factor is calculated using the amplitudes within the specified time window. This scalar may equal to the inverse of root mean square (RMS), mean or median amplitude value of the time window. Although the scalar can be multiplied by the sample value located at the center, beginning or end of the AGC window, generally the amplitude value at the center of the window is preferred, as is the case in Fig. 5.40. Then the window is moved one sample and a new scalar is calculated and applied to the central sample of the window. The AGC operation continues in this fashion along the time axis from the beginning to the end of the time samples within the trace. At the beginning and end of the trace, however, there will not be

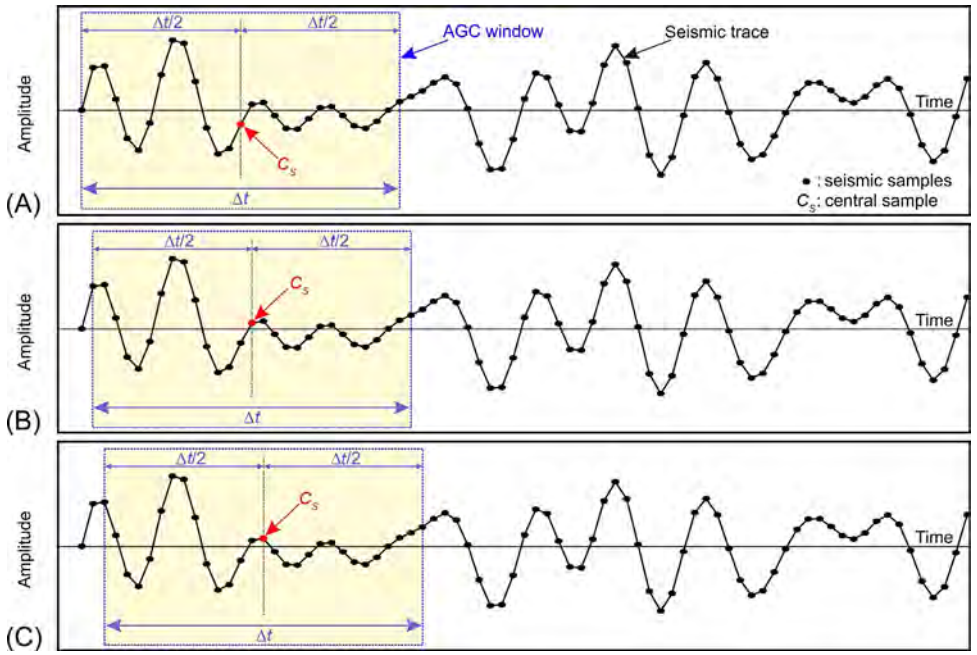


FIG. 5.40 Schematic illustration of how AGC is applied using a sliding time window. (A) A time window of Δt ms length (also known as the AGC operator length) is selected *(yellow window)*, and a scale factor is calculated using the amplitudes within this time window, which equals to the inverse of RMS, mean, or median value of the amplitudes in the window. Then it is multiplied by the sample value at the center, beginning or end of the time window (here by the sample at the center, c_s). As in (B) and (C) the window is moved one sample down along the time axis, and each time, a new scalar is calculated and applied to the central sample of the window, and the operation continues until end of the samples in the trace is reached.

enough amplitude samples to meet the AGC window length. Therefore, the operator length starts with a small value at the beginning and increases as it is moved down along the trace, until the full window length is reached, it remains constant at this full operator length until it reaches to the end of the trace, and then starts progressively decreasing to smaller lengths at the end of the trace.

Depending on the calculation method of the scalar, the AGC type is named mean, RMS, or median AGC. Fig. 5.41 shows an example application of three different AGC applications based on the AGC scalar calculation types. Although the outputs are quite similar, the mean AGC is preferred in seismic data processing applications. Fig. 5.42 shows an application of the AGC to a marine shot gather with a gain scalar applied to central, trailing, and leading samples of the AGC window. Based on the location of time sample within the AGC window that the scalar is applied, effectiveness of the AGC operation varies: Application to the trailing sample reduces the amplitudes of early arrivals; however it does not adequately recover the amplitudes of the late arrivals (Fig. 5.42B). Application of the scalar value to the central or leading samples of the AGC window produces a much more regular amplitude distribution along both the time and offset axes (Fig. 5.42C and D). Using the leading sample also does not produce a quiet zone just above the seabed.

The most important parameter to be selected properly in AGC gain correction is the AGC window (or AGC operator) length which is represented by time length in milliseconds.

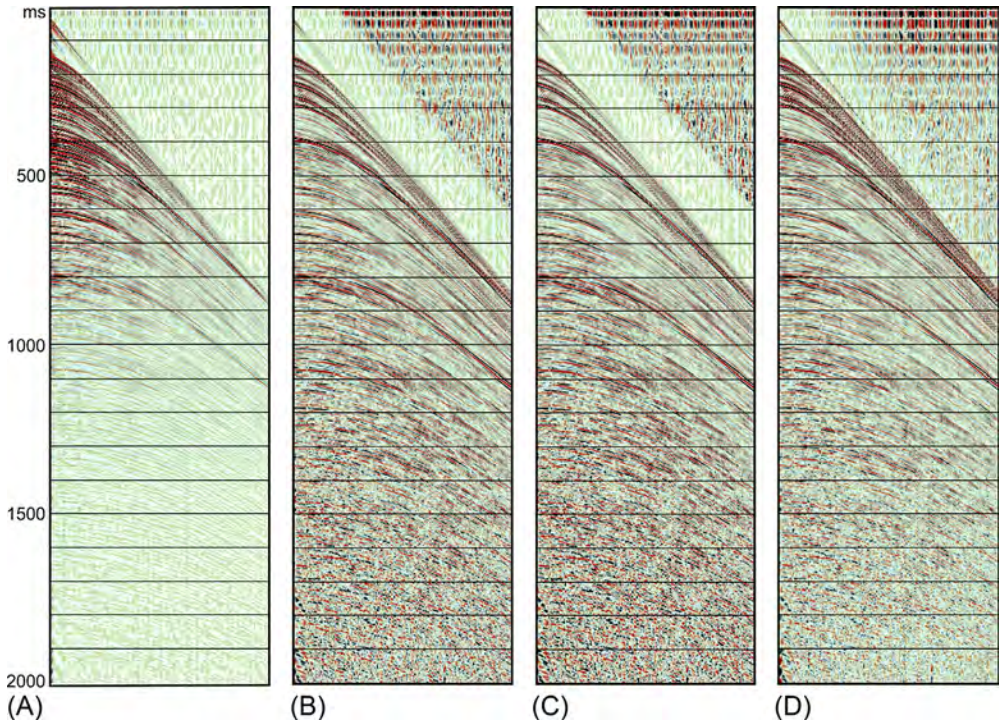


FIG. 5.41 AGC gain corrections for different AGC scalar calculation methods on a marine shot gather. (A) Filtered shot with no gain, and its AGC corrected versions using 500 ms operator length calculated by using (B) mean, (C) RMS, and (D) median values of the amplitudes samples within the AGC window.

Fig. 5.43 illustrates the effect of AGC operator length on the efficiency of the application. AGC operation is much more effective for smaller operator lengths, and the amplitudes of both in shallow and deeper parts of the data become much more balanced. AGC application becomes progressively ineffective as the operator length increases. In practice, the suitable operator length is selected by considering the recording length of the input data. Operator lengths between 250 and 1000 ms generally produce acceptable results; however, depending on the record length, the most suitable operator length can be determined by trying several different values and visually checking the results after each trial.

AGC blows up the noise in the water column and produces a relatively high-amplitude noise zone just above the seabed (Fig. 5.43), which is termed the shadow zone. In the case of using AGC scalar applications on the central samples of the AGC window, there will be a low amplitude "quiet" zone just before the seabed reflection on the shot gathers, the length of which exactly equals half of the AGC operator length ($\Delta t/2$) in the case of the application to the central samples of the AGC window. If a smaller AGC operator is used, this quiet zone will be narrow. Above this zone is the shadow zone in the water column on the shot gathers. This quiet zone is not only observed on shot gathers, but also evident on the final stack sections if an AGC is applied after stacking (Fig. 5.44A). When there is a strong reflection on the stack data, there may be a low amplitude band of $\Delta t/2$ milliseconds width just below the high amplitude reflection after AGC (Fig. 5.44B).

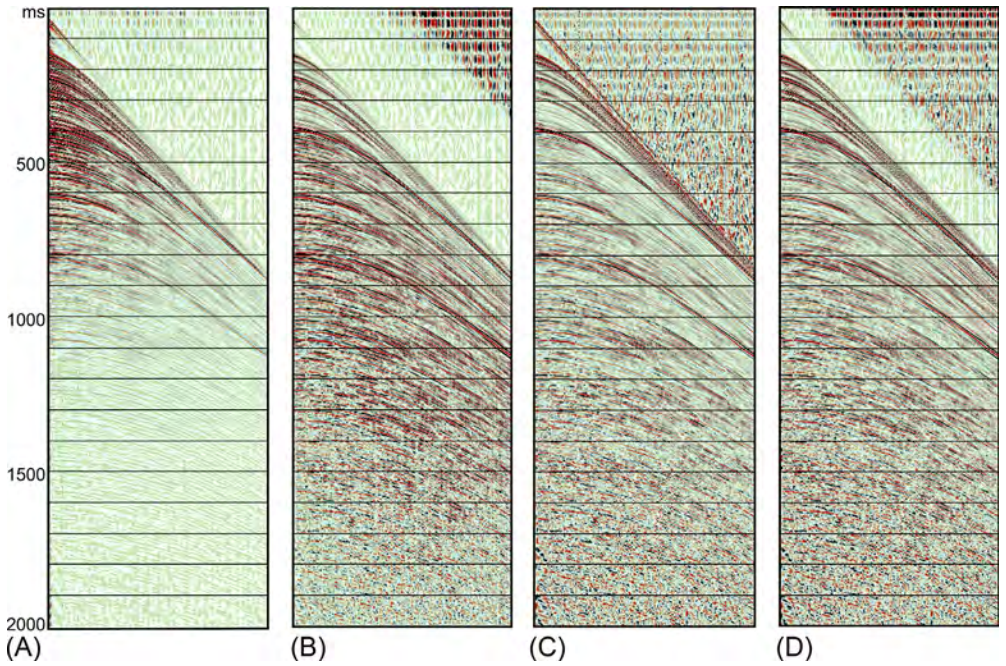


FIG. 5.42 AGC gain corrections for applications of the scalar to different samples on a marine shot gather. (A) Filtered shot with no gain, and its AGC corrected versions using 500 ms operator length for applications of the scalar to (B) trailing, (C) leading, and (D) central samples of the AGC window.

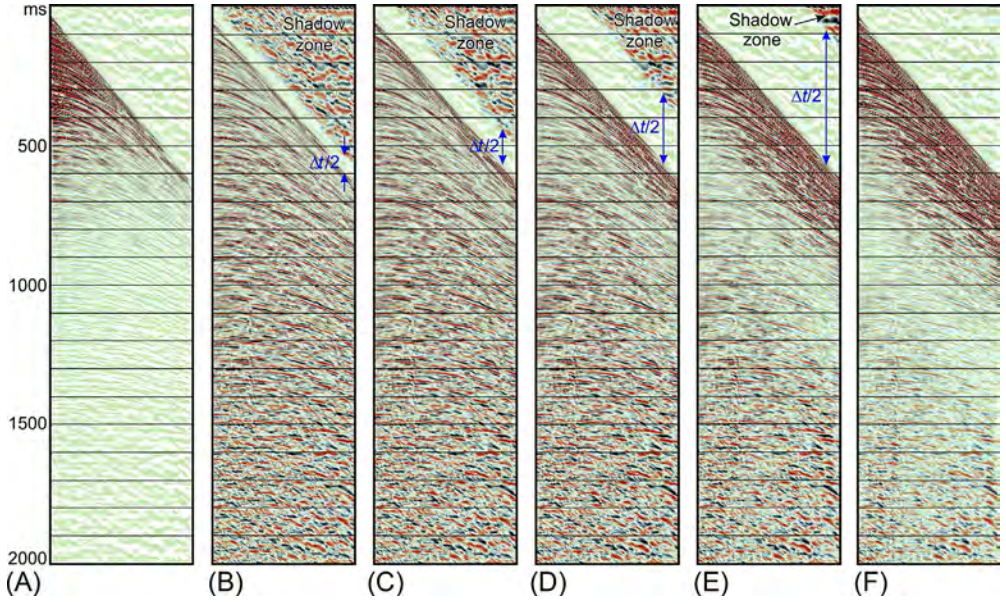


FIG. 5.43 AGC corrections for different AGC operator lengths (Δt) on a marine shot gather. (A) Filtered shot with no gain, and its AGC applied versions for (B) $\Delta t = 100$ ms, (C) $\Delta t = 250$ ms, (D) $\Delta t = 500$ ms, (E) $\Delta t = 1000$ ms, and (F) $\Delta t = 2000$ ms window lengths. There is a low-amplitude band just before the seabed reflection with a length of $\Delta t/2$ after AGC applied to the central sample of the AGC window. The length of this quiet zone, however, is Δt if the AGC is applied to the leading sample.

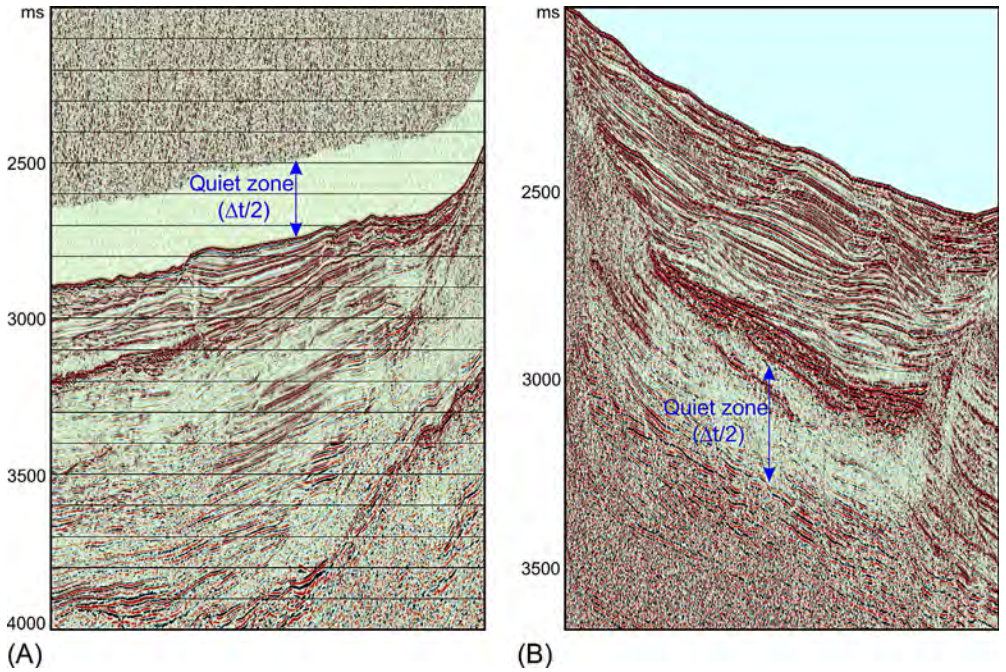


FIG. 5.44 Example stack sections after 500 ms AGC indicating low amplitude "quiet" zones located (A) just above the seabed, and (B) just below a strong subsurface reflection. Width of this quiet zone always equals half of the AGC operator length ($\Delta t/2$ ms) for an application to the central samples of the AGC window, here 250 ms for both sections.

The most important advantage of AGC is that it is very fast to apply and does not require complicated processing parameters to be selected accurately. However, it also has a very substantial disadvantage: it completely removes relative amplitude information embedded in the seismic data. On the other hand, trace-by-trace amplitude variations sometimes indicate subsurface stratigraphic transitions within the seismic data. For instance, gas accumulations in a reservoir or oil-gas interfaces produce high-amplitude local reflections on the seismic data. In order to delineate such high-amplitude reflections, trace-by-trace amplitude consistency must be preserved during the gain recovery. Fig. 5.45A shows a stack section with no gain containing a mud volcano at the central part. A common characteristic of underwater mud volcanoes is that they have an almost completely transparent feeder channel filled with mud breccia reaching from seabed to considerable depths. Since the mud breccia has no reflective internal composition for seismic waves, the feeder channel appears as a vertical chimney with no internal amplitudes with respect to the surrounding stratigraphy, which makes the mud volcanoes easily distinguishable on the seismic data. Fig. 5.45B shows the section after the t^P correction, in which the mud volcano is still quite distinct and the feeder channel is still transparent with almost no internal amplitudes. In addition, the amplitudes of the relatively deeper reflections are slightly increased while the shallow amplitudes are diminished as expected. In Fig. 5.45C, however, the minor amplitudes, possibly from high-frequency random noise, in the

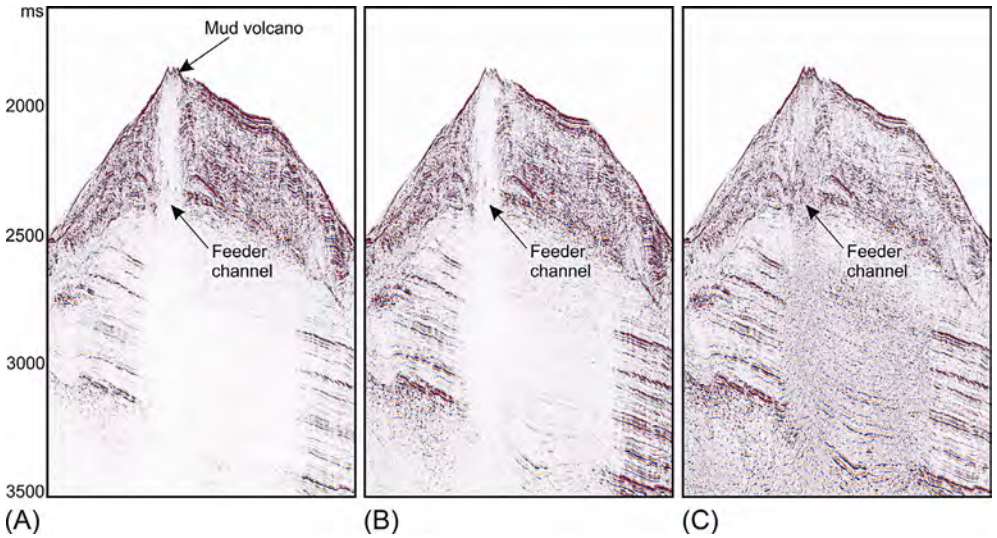


FIG. 5.45 A comparison of t^P correction and AGC to represent the relative amplitude preservation by t^P correction. (A) Stack section with no gain containing a mud volcano with a transparent feeder channel. The same section after (B) t^P correction, and (C) 500 ms AGC correction.

feeder channel are boosted by AGC and they become almost as high as the amplitudes of adjacent stratigraphic reflections, which ultimately makes the feeder channel less distinct and recognizable. Fig. 5.46 shows another example for relative amplitude processing. Several gas chimneys exist in the stack section in Fig. 5.46A, which are recognized as narrow transparent vertical columns. Since they are formed by ascending gas from deeper sediments to the seabed, we have almost no amplitudes within these columnar structures because of the extreme absorption effect of the shallow gas on the seismic signal. After AGC, the transparency characteristics of the gas chimneys are completely lost (Fig. 5.46B) although their disruptions in the sediments are still visible.

AGC is commonly used for display purposes of the seismic data in hydrocarbon exploration. In addition, if the main objective of the seismic survey is to obtain structural information such as mapping faults or preparing the isopach maps, AGC produces seismic sections with much better trace-by-trace consistency and, hence, easier structural interpretation. If the purpose of the seismic survey is oil and gas exploration, however, relative amplitude information is extremely important, and spherical divergence or t^P corrections must be preferred instead of an AGC correction. Before applying a quantitative interpretation method like amplitude vs. offset (AVO) or seismic amplitude inversion, AGC must be strongly avoided. In practice, preparing both true amplitude and an AGC scaled version of the same seismic line after processing might be useful for both structural and seismic amplitude interpretation.

5.6.4 QC in Gain Recovery

QC tests after gain recovery can be done on shot gathers as well as on the brute stack sections. After a successful gain application, a regular amplitude distribution both for shallow and deep arrivals must be achieved (Fig. 5.47B). Simply, if the amplitudes of the early arrivals are

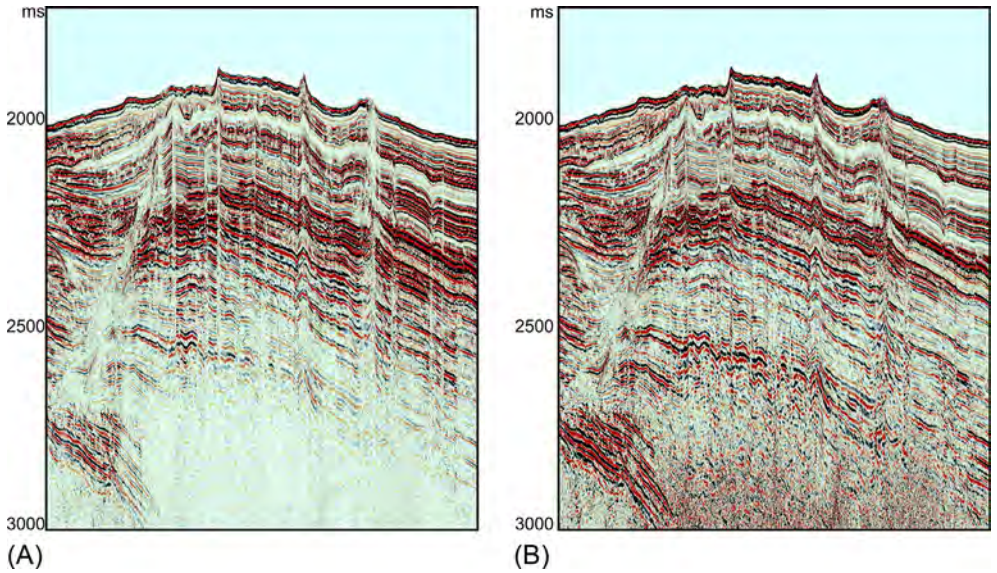


FIG. 5.46 A comparison of t^P correction and AGC to represent the relative amplitude preservation by t^P correction. (A) Stack section with t^P correction containing several gas chimneys as narrow transparent columns. (B) After AGC correction, the transparency characteristics of the chimneys are completely destroyed.

higher than the late arrivals, this means that the gain is too low, or the AGC window is too long (Fig. 5.47C). On the contrary, if the amplitudes over the whole line are absolutely too close to each other, then the AGC window is too short (Fig. 5.47D), which may result in loss of resolution in the final stack data.

In the case of t^P correction, values for P between 1.5 and 4 produce acceptable results for most seismic data, yet several tests may be required to determine the most suitable P value for each seismic line. If the amplitudes of the early arrivals are low with respect to the late arrivals, then the P value is too high and should be reduced (Fig. 5.48). Since a suitable P value is a function of recording time, seabed depth and the total recording time affect the optimal P. Furthermore, a number of different P values may be required in the case of a variable seabed depth along the seismic line. This is particularly required for those seismic lines from shallow continental shelves to deep abyssal plains via steep continental slopes along the continental margins. Fig. 5.49 shows an example seismic line that requires variable P values according to the variable water depth for t^P correction to keep the relative amplitude information. In Fig. 5.49A, $P = 3$ is used for whole line; although this is suitable for deeper parts of the section, it excessively suppresses the amplitudes in the shallow parts. Slightly increasing P values along the downslope solves the problem and produces a more regular amplitude distribution along the line while preserving the relative amplitudes.

In high-resolution seismic surveys like single or multichannel sparker surveys, the recording length may be considerably smaller when compared to the conventional multichannel surveys, e.g., between 100 and 300 ms. A relatively small AGC window length must be selected in the case of small recording lengths to recover the deeper amplitudes properly.

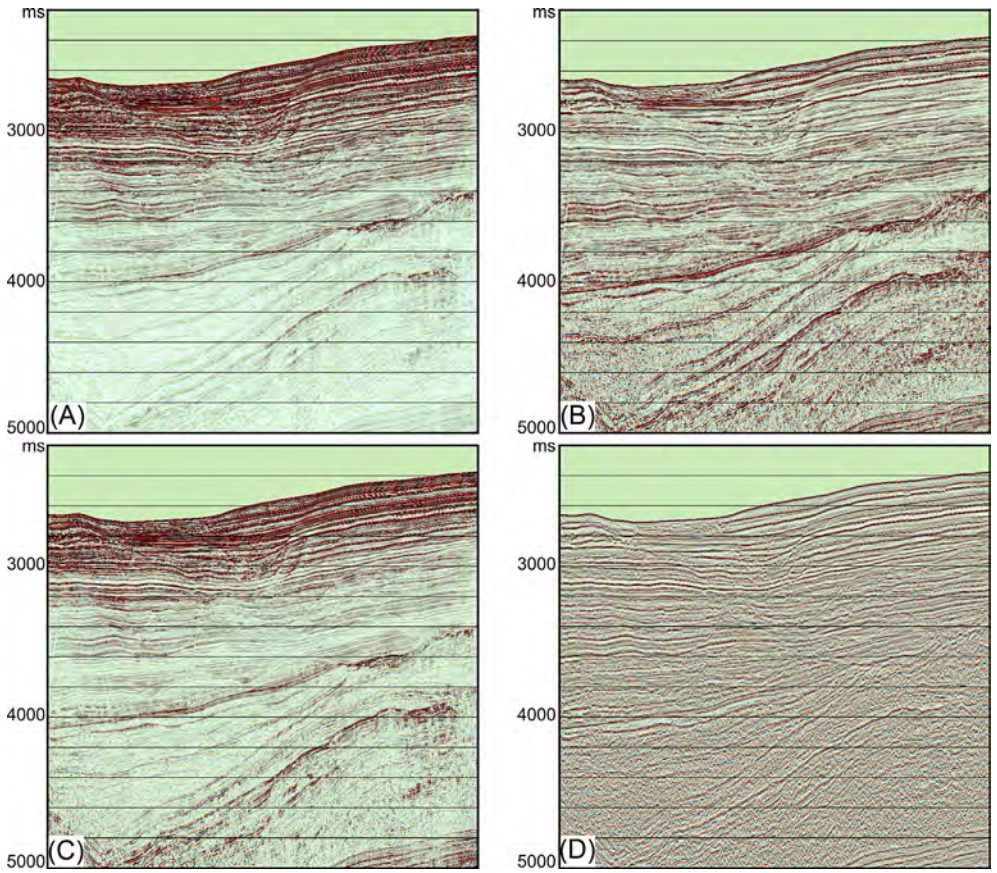


FIG. 5.47 Effect of AGC operator length on a final stack section with (A) no gain, (B) suitable gain with 500 ms AGC, (C) too low gain due to a long AGC window (2000 ms), and (D) too high gain due to a short AGC window (50 ms).

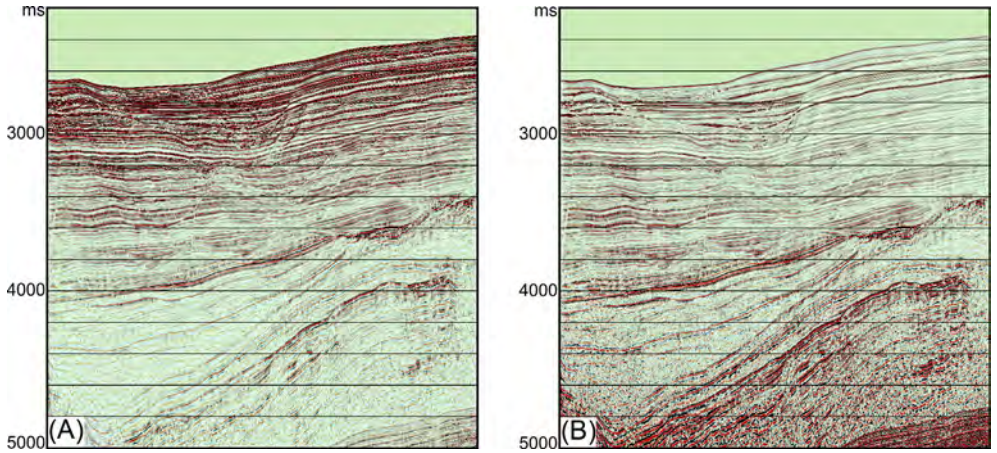


FIG. 5.48 Effect of P value for t^P correction on the final stack section. (A) Gain using $P = 2$ is too low to increase the amplitudes of deep arrivals, and (B) gain using $P = 7$ is too high, such that the amplitudes of early arrivals are significantly reduced.

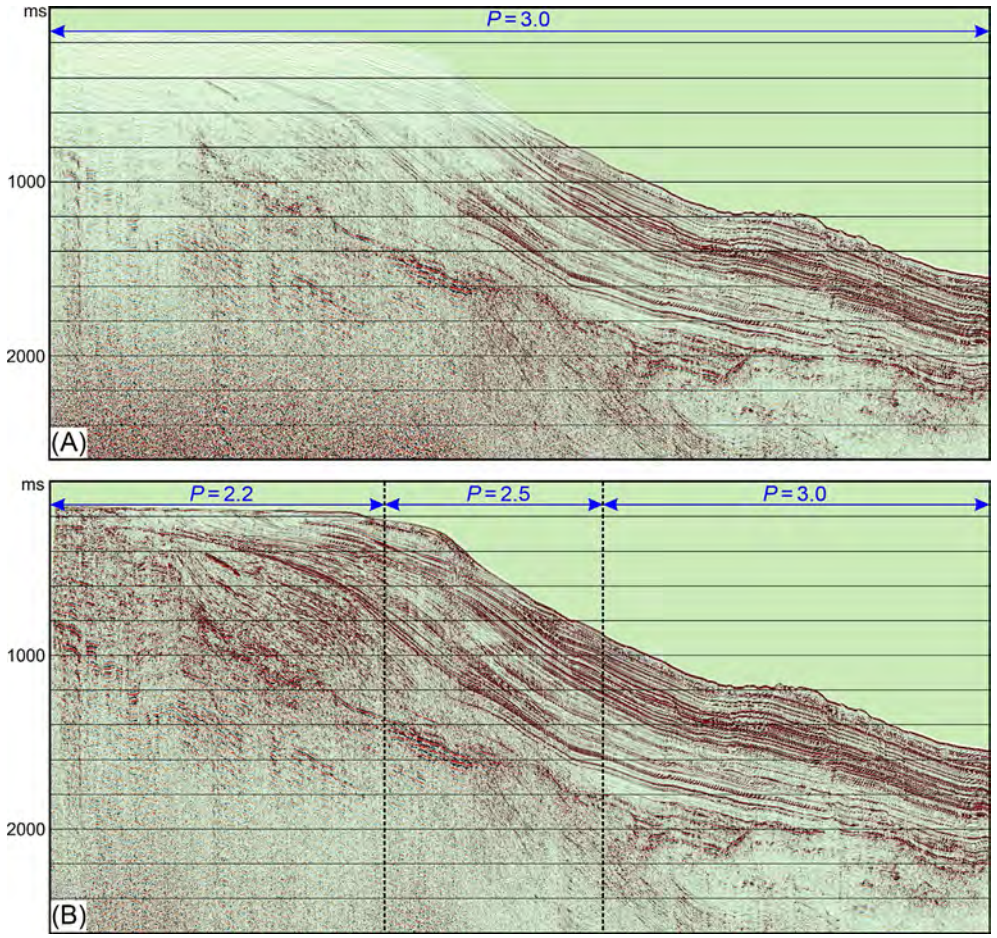


FIG. 5.49 (A) An example seismic line extending from the shallow continental shelf to deep abyssal plain with t^P gain of constant P value ($P = 3$) applied to whole data. (B) Same line with t^P gain with slightly increasing P values downslope from 2.2 to 3.0.

5.7 TRACE EDIT

Trace edit is one of the earliest methods for removing noise from the data. Commonly, not all of the recorded traces are usable. If the noise level on a specific trace, or on a number of traces, is dramatically high and it is not possible to remove it using available processing techniques, then the trace is killed: that is, the amplitudes of the trace are simply zeroed out. This operation is termed trace kill, and it is generally applied to the channels which

- contain powerline harmonic noise interference (Fig. 5.50),
- are completely nonfunctional (Fig. 5.51),
- have very distinctive spike-like noise (Fig. 5.52),
- belong to missed shots or autofires (Fig. 5.53),
- have uncertain static time shifts (Fig. 5.54),
- are contaminated by extreme swell noise (Fig. 5.55),
- have acquisition issues such as streamer bending (Fig. 5.56),
- have other issues, such as gun timing errors specified as bad channels or shots.

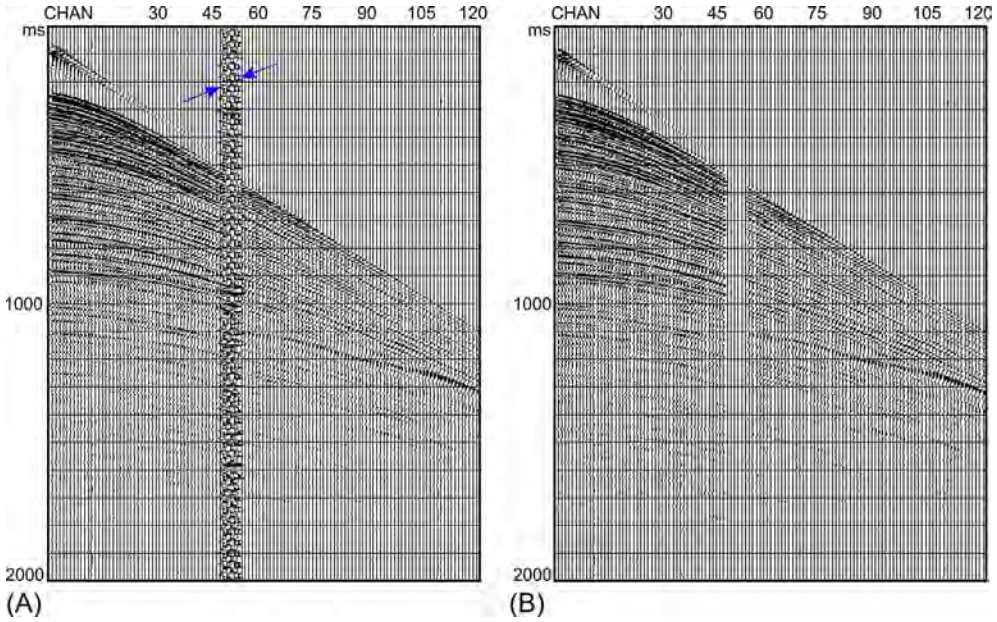


FIG. 5.50 (A) A raw shot gather with strong power-line harmonic noise interference between the channel numbers 48 and 52. (B) Same shot after killing the traces containing the interference.

Fig. 5.50 shows an example trace kill application on a shot gather which has strong powerline harmonic noise interference at six traces between channel numbers 48 and 52. Although these channels may have data as well, the interference is so strong that the reflection amplitudes are concealed behind the noise. The noise has monofrequency amplitudes appearing at 50 Hz and its multipliers; therefore it is necessary to apply a notch filter to remove the interference. However, applying a monofrequency notch filter is generally avoided because it produces amplitude notches in the spectrum, which may ultimately cause issues during deconvolution. Therefore, killing these traces is generally the easiest and most convenient way to remove powerline harmonic noise (Fig. 5.50B).

If one or more channels of the recording instrument are nonfunctional, then the amplitudes recorded at those traces cannot be used, since they may corrupt the quality of the final stack section after stacking. In two successive shot gathers in Fig. 5.51, the first six and last three channels of the recording system are dead and are recording only noise. Fig. 5.51B shows the same shots after the dead channels are killed. Normally, the channel numbers of those dead traces do not change for a specific survey; therefore, a regular channel number definition is generally sufficient to apply the trace kill to the whole seismic dataset, to remove the dead channels.

As mentioned in Section 3.10.2, seismic data may contain extremely high-amplitude transient noise bursts, or spikes, with amplitudes distributed on almost all the available frequency band. Spikes may not be suppressed by simple stacking because they may have extremely higher amplitudes than those of primary reflections. In some cases, such as seawater leakage into the fluid-filled streamer sections, there may be several spikes randomly distributed

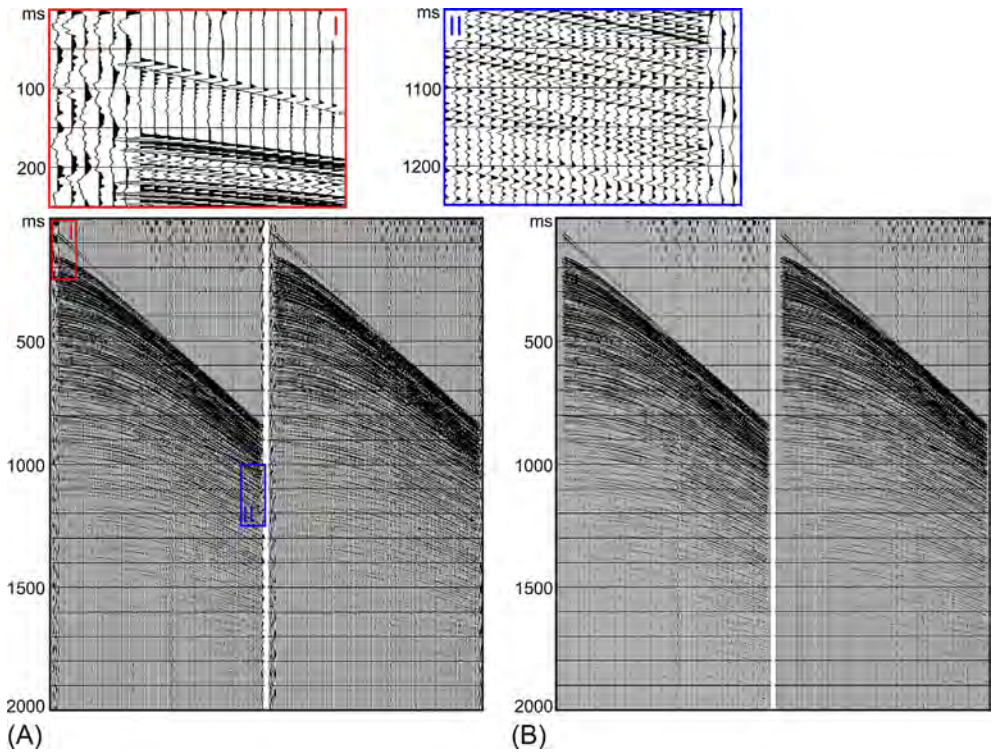


FIG. 5.51 (A) Two filtered successive shots in which the first six and last three channels are dead. (B) Same shots after removing the amplitudes of dead channels. The *red* and *blue* boxes correspond to close-ups from the very first and last channels of the shot, indicated by I and II before the trace kill, respectively.

over the channels of each shot gather, as is the case in Fig. 5.52A. Although it is also possible to remove them with a surgical mute (Section 5.8), it will take too much time when the number of spikes is excessive and it may be much more practical to use trace kill. Fig. 5.52B shows the spiky shot after the trace kill in which six traces containing extremely high-amplitude spike noise are edited and killed.

In marine seismic acquisition, a precise timing for firing the source and starting the recording is necessary. In the case of timing issues, the seismic recorder may be triggered and recording starts although the gun array is not fired. In these cases, the recorded data contains only noise and is termed a missed shot. The problem may be the gun control unit or communication/triggering issues between the gun controller and triggering system, and the recording unit. All traces of the missed shots are killed completely from the dataset; if not, these traces corrupt the stack section after stacking and reduce the S/N ratio of the final seismic section. Fig. 5.53A shows a number of successive shots with a missed shot (shot number 113) containing only noise, and the shots after removing the traces of shot 113 by trace kill are shown in Fig. 5.53B.

Triggering problems not only create missed shots, but may also constitute static time shifts in shot gathers if a triggering delay occurs between the recording unit and the gun

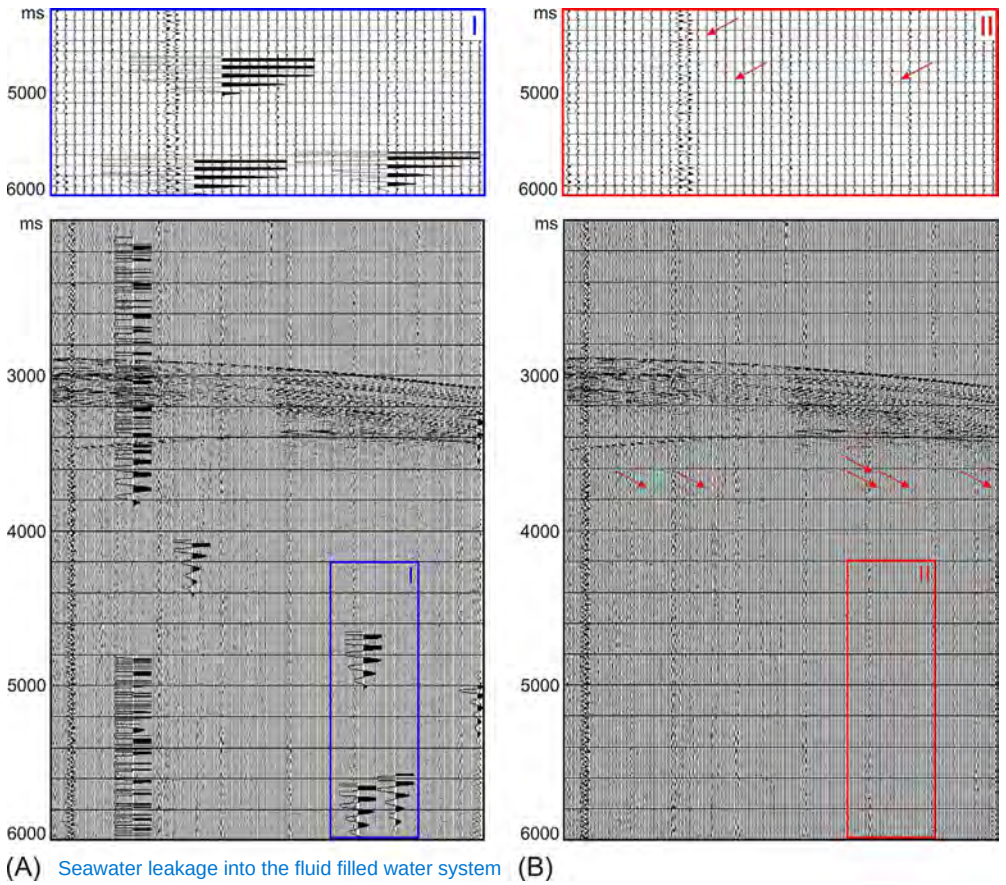


FIG. 5.52 (A) A filtered shot with very high-amplitude spike-like noise bursts. (B) Same shot after killing the channels *(red arrows)* that contain the spikes. *Red* and *blue* close-ups show a small area from the noisy zone before and after the trace kill, respectively.

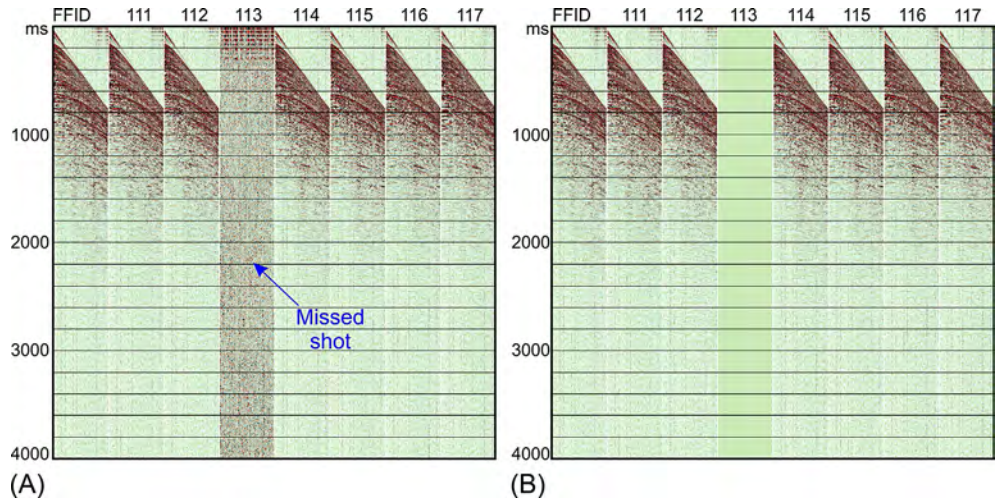


FIG. 5.53 (A) A number of successive filtered shot gathers, including one missed shot (FFID 113), and (B) same shots after killing the traces of shot 113.

Autofire

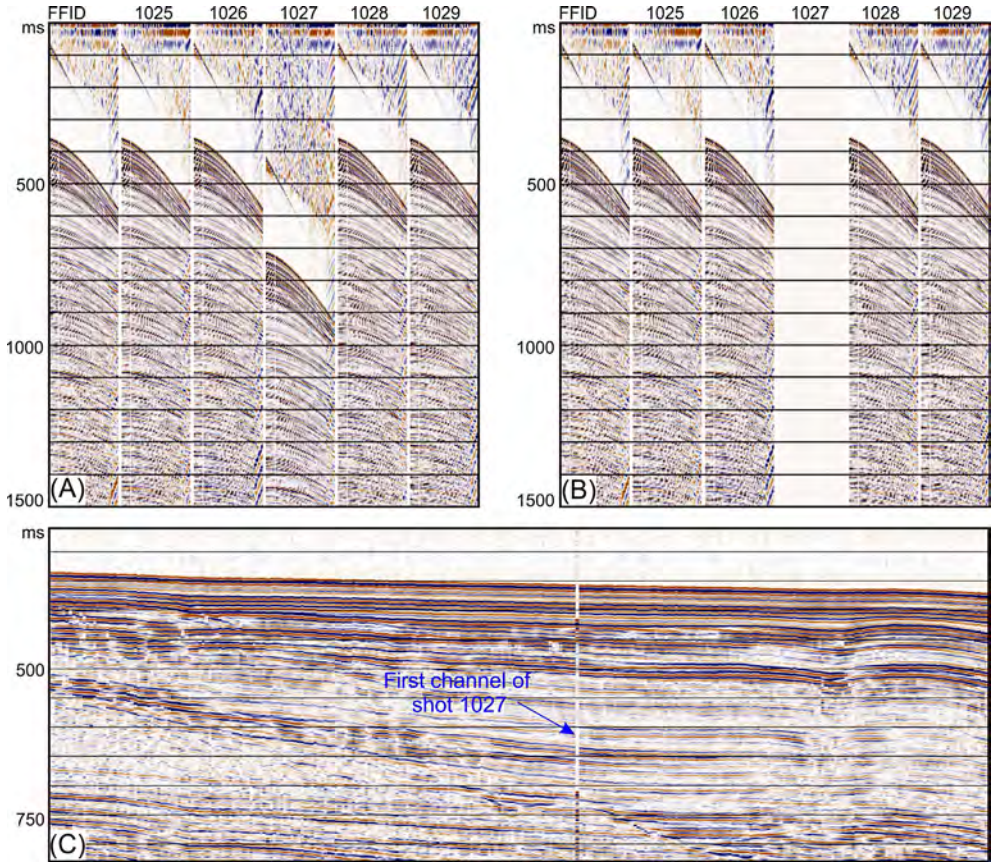


FIG. 5.54 An example filtered shot with timing issues. (A) Shot number 1027 is delayed approximately 350 ms, possibly due to a triggering delay between the recording unit and the gun controller. (B) After the trace kill, shot 1027 is removed from the dataset. (C) Shots with static time delays can be distinguished by their odd appearance on the common offset sections.

controller. Because this time delay is generally arbitrary, it may not be possible to determine the exact timing of the delayed shot to correct the time delay by a manual static time shift. Fig. 5.54A shows an example shot gather for the delayed shot issue. Here, shot 1027 is delayed approximately 350 ms, which means that either the recording unit is triggered 350 ms before the guns are fired, or the gun array is fired 350 ms later than its expected aim point for this shot. Because the determined delay is approximate, this shot is removed from the dataset by killing all traces of the shot (Fig. 5.54B). Missed shots and the shots with timing issues can easily be determined by inspecting odd traces on single trace sections (Fig. 5.54C), which appear as traces inconsistent with the neighboring traces.

Sometimes swell noise is extremely effective on a number of successive channels and induces very high-amplitude noise, appearing as narrow vertical stripes extending from zero time to the end of the recording on the shot gathers. In most cases, the issue is that a small part of the

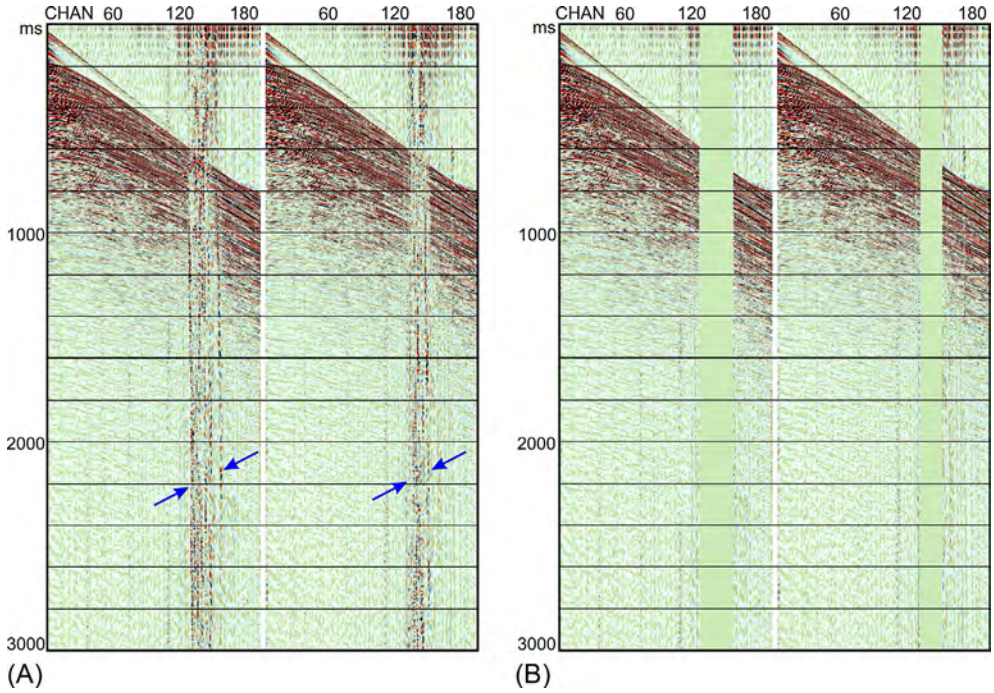


FIG. 5.55 (A) Two filtered shots with dominant swell noise between channels 130 and 160 (indicated by *blue arrows*). (B) After killing the traces with high amplitude swell noise.

streamer approaches to the sea surface, possibly because of a nonfunctional or miscalibrated bird, and the hydrophones on this part of the streamer receive a large amount of swell noise. Fig. 5.55A shows two filtered shot gathers contaminated by swell noise between channel numbers 130 and 160. Their amplitudes are so high that it is sometimes impossible to recover reflection amplitudes behind the swell noise. In such cases, the most appropriate way to remove the swell noise is to kill the traces dominated by swell noise amplitudes, as in Fig. 5.55B.

When the vessel maneuvers from one line to another during the line changes, streamers bend behind the vessel and, depending on the length of the streamer(s), it takes a considerable time for streamers to become straight again, even if the vessel itself is already on the survey line. That is why we use run-in distance when entering a new line during the acquisition (Section 2.5.1.9). However, if the line is too close to the land, or if there is an obstruction in the maneuvering area such as marine traffic or production platforms, then it may not be possible to fulfill the entire run-in distance, and in this case, recording can be initiated before the streamer finishes its turn completely. This results in recording with far channels that are still turning behind the vessel. During their turn, these channels will be closer to the gun array than they normally should be, which means that these channels will record the reflections earlier than their expected arrival times. That is, a curved zone of the reflection amplitudes occurs at far offsets of the shot gathers. Fig. 5.56A shows a number of shots from the beginning of a 2D seismic line with such curved zones indicated by blue arrows. This zone appears at the very first shots of the survey lines,

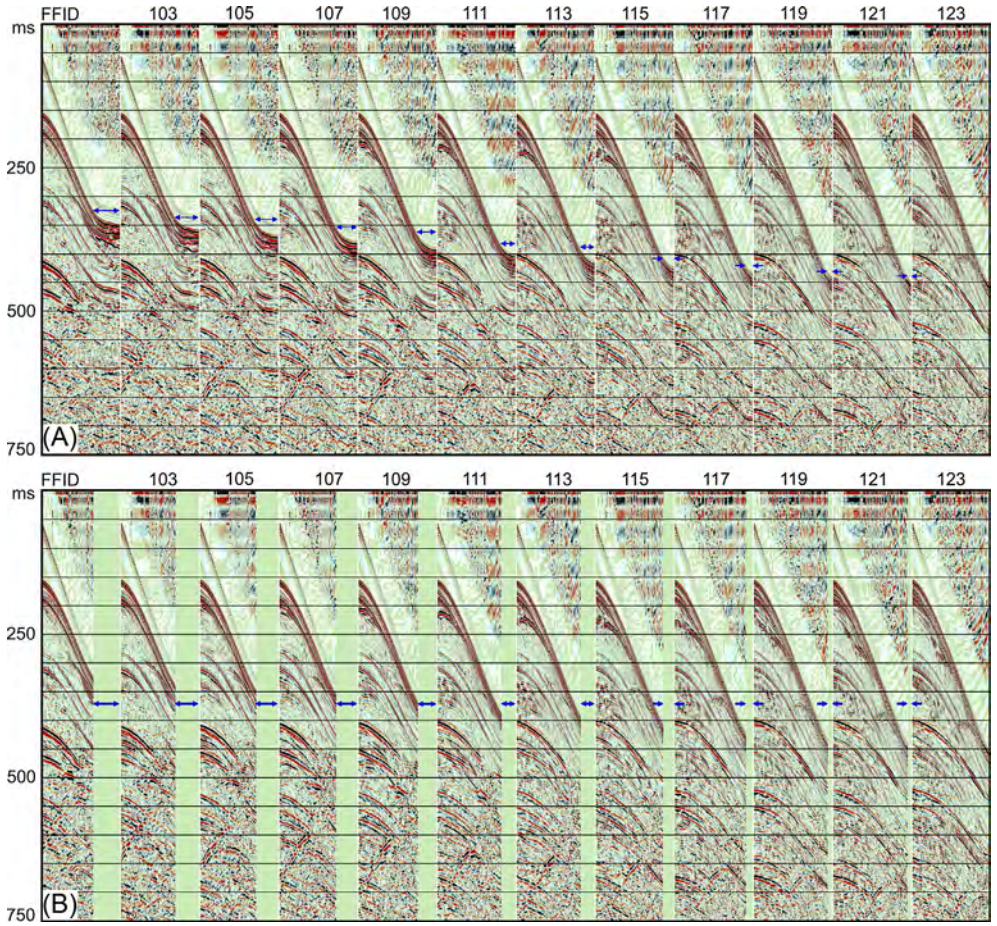


FIG. 5.56 The effect of turning of the streamer behind the vessel when entering a survey line. (A) A number of shots from the beginning of a seismic line, recorded in the course of a streamer's turn, which result in curved disruption zones, indicated by *blue arrows*. (B) Same shots after killing the far offsets with curved arrival times *(blue arrows)*. After shot number 123, the streamer finishes its turning and becomes straight.

and narrows with increasing shot number, since the streamer becomes straighter and straighter along the line. After shot number 123 in Fig. 5.56A, it seems that the streamer becomes straight again. These curved areas have incorrect reflection arrival times and should be completely removed from the data. Fig. 5.56B shows the shot gathers after killing the far offset traces with incorrect arrival times. These disruption zones may also occur at the end of the survey lines if the run-out distances are not fully considered and shooting proceeds during the vessel's turn at the end of the line.

In modern seismic data processing, manual editing of the traces and shots is definitely impractical since the large seismic datasets, especially 3D data volumes, contain thousands of shots and millions of traces, and it is impossible to examine all available traces of such datasets manually in a feasible time period, even for an experienced processor. Therefore, specific algorithms are developed that automatically

scan whole datasets, generally based on a proper amplitude criterion, and then kill the traces that do not satisfy the criterion. If not applied automatically, trace kill does not have any parameter to be determined. Therefore, the only QC application for trace kill is to check the traces/shots after trace kill to make sure that the process is being applied correctly.

5.8 MUTING

Muting is used to remove the amplitudes of some noisy areas in the seismic data. The difference from trace kill is that the muting zones may not necessarily comprise the whole sample of a specific seismic trace. These specific areas are the zones of coherent noise, such as the amplitudes in the water column, direct waves, refractions, or the areas with abnormally low S/N ratio on the shot gathers. That is, the amplitudes in these undesired areas are simply multiplied by zero. This process is known as muting and it can be applied to the seismic data in three different implementations:

- *Top Mute:* Since the first meaningful signal is seabed reflection, the amplitudes or arrivals appearing in the water column section before the seabed reflection hyperbola, such as direct or refracted waves, are muted out (Fig. 5.57A). Generally, it is applied to filtered shot gathers.
- *Surgical Mute:* The noisy area inside the dataset is muted out (Fig. 5.57B). Generally, this is applied to filtered shots or CDP gathers.
- *Normal Moveout (NMO) Stretch Mute:* The frequency disruption zone occurred at the early arrivals of far offsets after NMO correction is muted out (Fig. 5.57C). This is automatically applied to CDP gathers after NMO correction, and will be discussed in detail in Section 10.2.

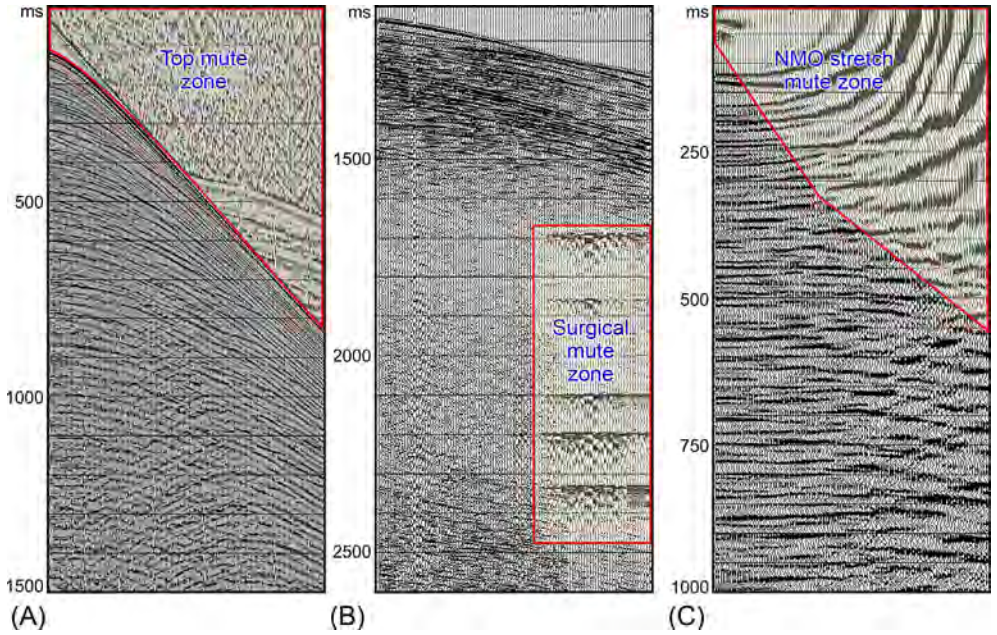


FIG. 5.57 (A) Top mute area on a filtered shot gather, (B) surgical mute area of a cross-feed noise on a shot gather, and (C) NMO stretch mute area of a very low-frequency disruption zone on a CDP gather after NMO correction.

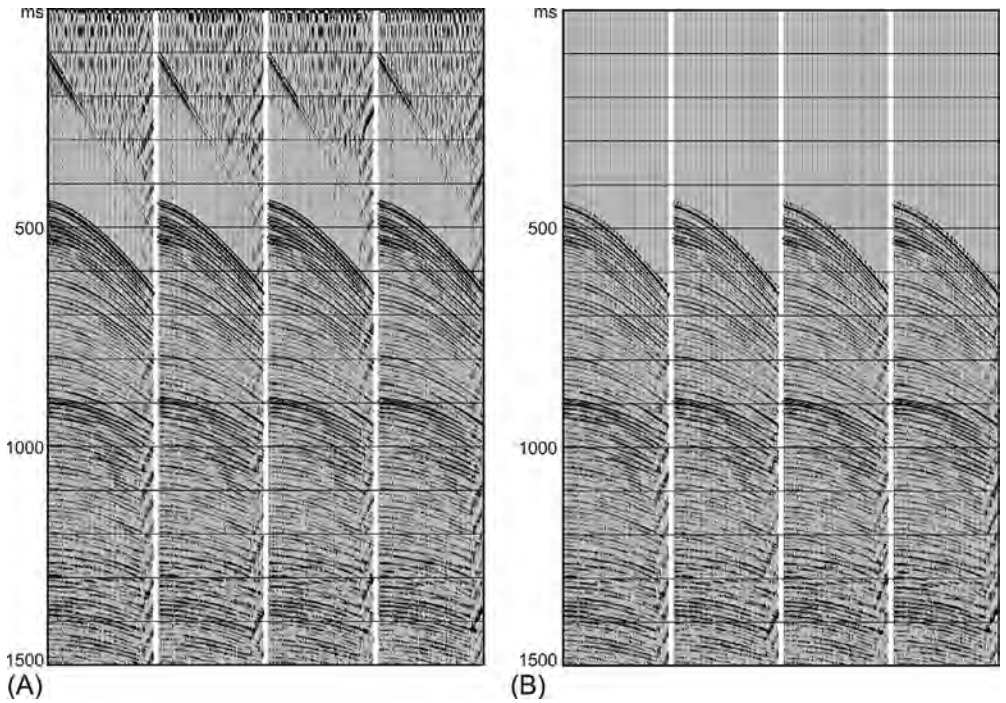


FIG. 5.58 Application of top mute. (A) Filtered shot gathers, and (B) after top mute.

Fig. 5.58 shows a top mute application on a number of successive filtered shot gathers. Especially in shallow waters, the top muting process prevents the occurrence of apparent closures in the shallow parts of the semblance contours during the velocity analysis later on. In addition, removing the direct wave and refracted arrivals makes the *f-k* spectrum less complicated and provides an easy and more correct selection of the *f-k* polygon. Top mute is also applied to final seismic sections after migration as a final step of the processing sequence, to remove the noisy area just above the seabed reflection produced by some specific processing steps, such as *f-k* filter or migration. In particular, migration may produce semihyperbolas with upward flanks aligned on the seabed reflection. Just before the presentation of the data, or before the interpretation step, this noisy water column zone is muted out with a suitable top mute process, known as final top mute, which produces a clearer final seismic section (Fig. 5.59).

Fig. 5.60A shows an example application of surgical mute on two filtered successive shot gathers with 500 ms AGC; both have distinctive high-frequency harmonic noise in a triangular zone along the near offset channels. It is not easy to remove this type of noise using conventional processing methodology, and the most effective way to eliminate this noise is to apply a surgical mute (Fig. 5.60B).

5.8.1 QC in Muting

Muting is the process used to zero out the amplitudes of specific areas on the seismic data. Therefore, QC is particularly important after a muting process. A visual inspection of the output gather is necessary after muting. A brute stack section must be prepared after mute to

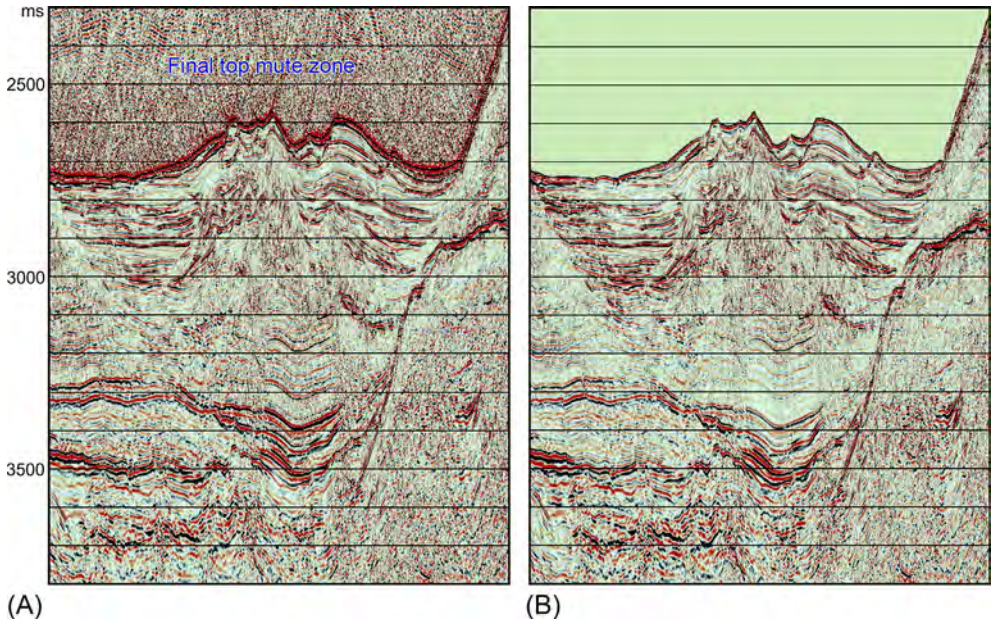


FIG. 5.59 Application of a final top mute. (A) Final migrated seismic section, and (B) after final top mute to remove the noisy zone above the seabed reflection.

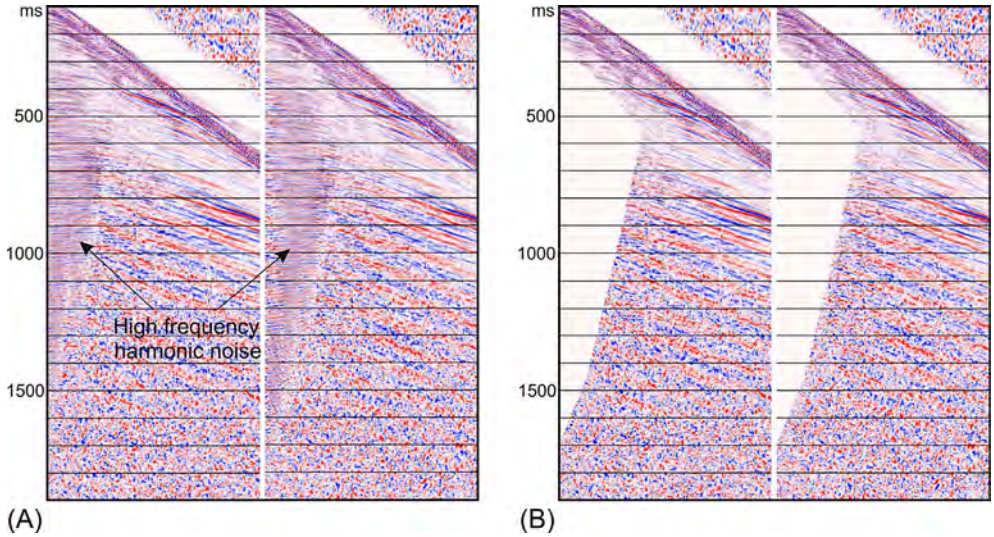


FIG. 5.60 (A) Two successive shot gathers contaminated by harmonic noise, and (B) after surgical mute.

ensure that the muting is applied to the data properly. This is especially important in the case of top muting, because it is not feasible to pick top mute polygons on every single shot along the line, and generally top mute polygons are picked on every 50 or 100 shots, depending on the number of shots in the data (Fig. 5.61A). Between these shots, mute polygons are automatically interpolated. However, water depth along the line can be erratic, especially in the areas of continental margins, which requires definition of a rapidly changing top mute zone, depending on the water depth along the line. Since the polygon interpolation is performed automatically, the processor must be sure that any areas of the erratic seabed are not accidentally muted out. Fig. 5.61B shows an example stack section with a mound structure on the sea floor. After stacking followed by a top mute, a significant amount of data is also muted out

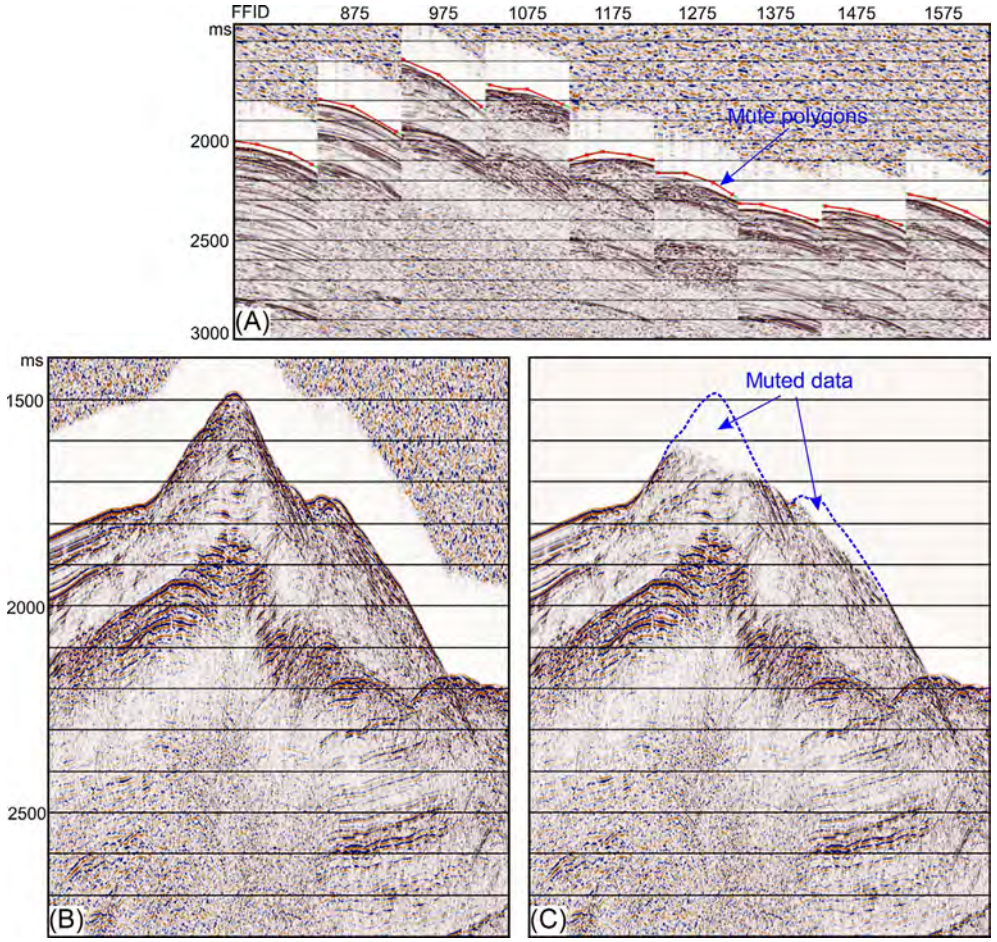


FIG. 5.61 (A) Top mute polygons *(red curves)* manually picked on every 100 shots. (B) An example stack section including a mound structure without top mute, and (C) the same stack followed by an incorrect top mute application. A significant amount of data is improperly muted out around the mound (data shown by *dashed lines*) because of the sparse picking of the top mute polygons on the shot gathers.

around the mound (Fig. 5.61C) because of the sparse picking of the top mute polygons on the shot gathers.

The only parameter that must be selected before muting is the mute ramp value, in milliseconds. During the mute process, undesired portions of the trace(s) are simply multiplied by zero, whereas the areas of genuine reflections are multiplied by 1.0, which means that the seismic data is actually multiplied by a unit step function on a trace-by-trace basis, as indicated in Fig. 5.62A. This multiplication zeroes out the undesired part of the data and does not affect the signal zone. However, the sharp transitions in the time domain signal, such as the edges of a box-car function, create the Gibbs effect in the frequency domain, as explained in Section 5.5.1 in detail. In the case where a frequency domain operation is performed on these trace(s) later on after muting, a ramp zone is defined instead of using a unit step function in multiplication during the muting process (Fig. 5.62B). This ramp zone provides a slight transition from zero to the maximum amplitude of the trace, to prevent the Gibbs effect in the forthcoming frequency domain operations.

The amplitudes in the ramp zone are not directly transferred into the mute output; they are multiplied by a scaling factor gradually changing from 0 to 1. This makes the edge of the mute zone not as sharp, but constitutes a smooth transition zone. The time length of this ramp zone is important for an effective muting, especially for the top mute process, because the amplitudes within the ramp zone are slightly suppressed. In the case of top mute applications, these amplitudes correspond to seabed reflections. Fig. 5.63 shows several example stack sections before and after a top mute process using different ramp zones to demonstrate the effect

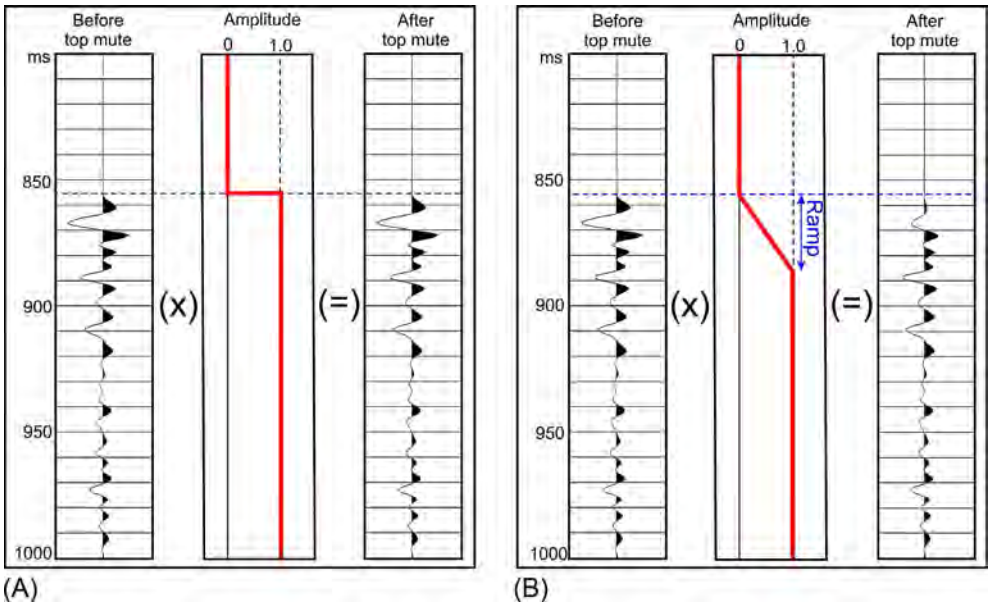


FIG. 5.62 Schematic explanation of top muting on a seismic trace. (A) Each seismic trace is basically multiplied by a unit step function (indicated by the *red line*) in a trace-by-trace basis for top muting. (B) In practice, a transition or ramp zone is defined to multiply with the seismic data instead of using a unit step function to avoid the Gibbs effect in subsequent frequency domain applications.

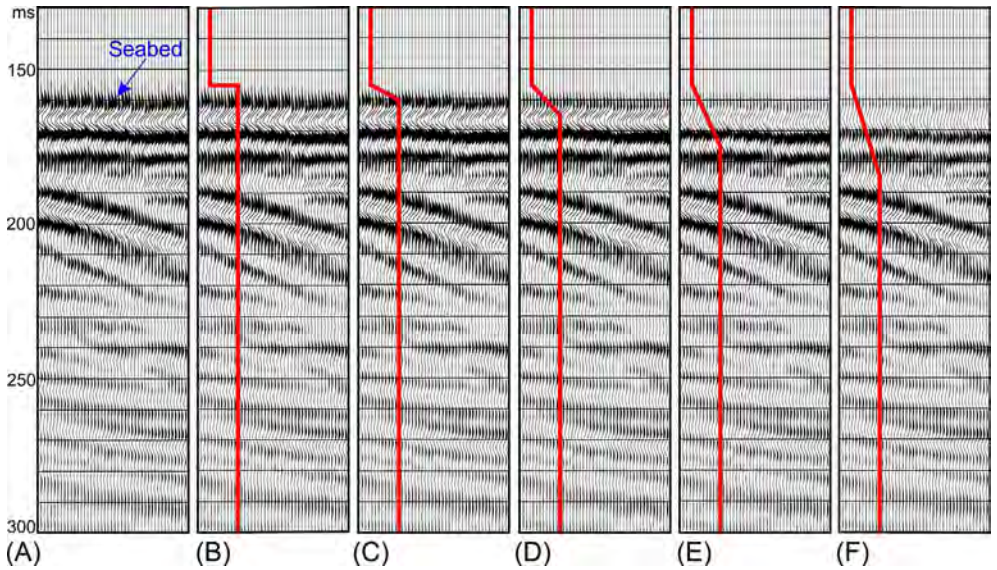


FIG. 5.63 Effect of top mute ramp on the seabed reflection. (A) Example stack section with no top mute. Same section after top muting with ramp values of (B) 0 ms, (C) 5 ms, (D) 10 ms, (E) 20 ms, and (F) 30 ms. The ramped unit step functions multiplied by the seismic data are indicated by heavy *red lines*. The longer the mute ramp length, the higher the suppression of the seabed reflection amplitudes.

of the ramp length on the seabed reflection amplitudes. As the ramp value increases, the amplitudes of the seabed reflections are increasingly suppressed after muting, which can result in issues in autopicking during the interpretation stage. As a rule of thumb, the ramp value should not exceed one-third of the dominant period of the seismic wavelet, to avoid excessive amplitude reduction along the seafloor reflection.

5.9 *f-k* DIP FILTERS

Shot gathers and stack sections have correlated events of different dips consisting of coherent noise and primary reflections. For instance, direct waves and refractions appear as linear correlated events extending from near to far offsets on the shot records, whereas primary reflections and their multiples are in the form of hyperbolic events of relatively lower dip. Dip filtering uses a 2D Fourier transform to remove certain types of correlated noise propagating with different velocities, which appear as events with different dips on the seismic data.

As explained in Section 4.6, a 2D forward Fourier transform converts the seismic data from the time-distance (*t-x*) domain into the frequency-wavenumber (*f-k*) domain, and thus the result of a 2D Fourier transform of the seismic data is known as the *f-k* spectrum. The amplitudes of certain correlated events in the time domain appear at specific points on the corresponding *f-k* spectrum. This may allow us to discriminate the noise and signal amplitudes in the *f-k* domain. Fig. 5.64 shows the schematic illustration of the common events that can be observed on a marine shot gather and their frequency domain appearance after a 2D Fourier transform.

The *f-k* spectrum is a powerful tool to discriminate the correlated events with different

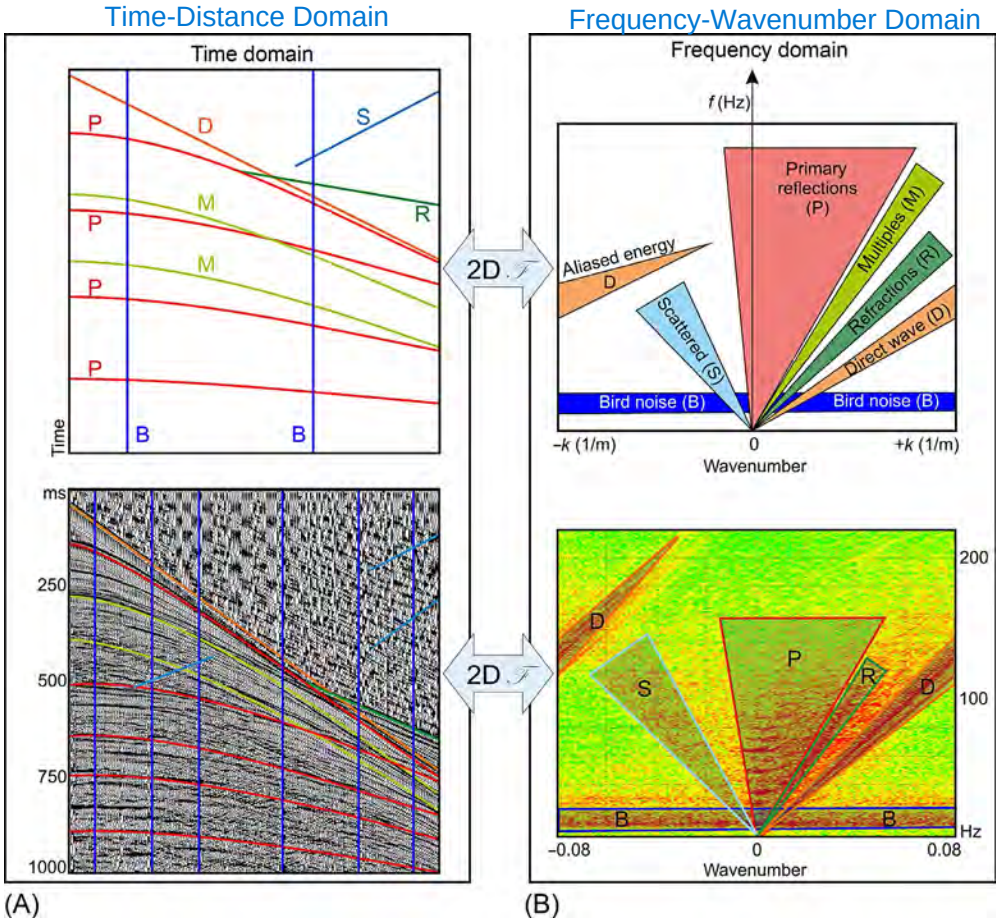


FIG. 5.64 (A) Schematic illustration of the common events on a marine shot gather (top) and corresponding displays of the same events on a real marine shot gather (bottom). (B) Schematic (top) and real (bottom) *f-k* spectra of the example shot gathers in (A). *P*, primary reflection; *R*, refracted (head) wave; *D*, direct wave; *B*, bird noise; *M*, multiple reflections; *S*, scattered or negative dip events.

dips appearing in time domain seismic data. In the time domain, complicated events of several different dips can easily be differentiated in the *f-k* domain, since the amplitudes of each correlated event arise at different portions of the *f-k* spectrum depending on their dips in the seismic data. If the dip is from near to far offset on the shot gather, this means that the event has a positive dip and its amplitudes arise in the positive wavenumber panel of the *f-k* spectrum. If the dip is from far to near offset, then the opposite situation occurs. As the inclination of an event increases in the time domain, the amplitudes of this event in the frequency domain become closer to the horizontal wavenumber axis. Amplitudes of horizontal events in the time-distance domain are grouped close to the vertical frequency axis in the *f-k* domain. A vertical event in the time domain, such as the bird noise on the shot gathers, appears completely horizontal in the *f-k* domain (Fig. 5.64).

As explained in Section 4.6, the *f-k* spectrum consists of two panels: one is negative and other is a positive panel, represented by negative and positive wavenumbers against the frequency, respectively (Fig. 5.65). In marine shot gathers, the positive panel involves the amplitudes of primary and multiple reflections, direct wave and refractions, while the negative panel comprises spatially aliased signals, back-scattered amplitudes and the events with negative dip, such as tail buoy noise. Bird noise and mechanical cable noise amplitudes are located in both panels. In general, it is not possible to recognize the amplitudes of multiple reflections as an isolated amplitude package in the *f-k* spectra. In land seismic shot gathers, however, direct and refracted wave amplitudes, as well as air waves, appear in both panels of the *f-k* spectrum. In addition, surface waves, known as ground-roll, are quite dominant on the *f-k* spectra, and their respective amplitudes are prominent packages isolated from the primary reflections close to the wavenumber axis of both panels in the *f-k* spectrum. Essentially, the *f-k* filter is one of the most efficient and commonly used methods in removing the ground-roll noise from land shot gathers.

The 2D Fourier transform enables us to filter the seismic data in 2D and to suppress some specific correlated noise types. Basically, the process is as follows (Fig. 5.66): the *f-k* spectrum is calculated by computing the 2D Fourier transform of the input seismic data. Amplitudes of the events with different dips (or different propagation velocities) accumulate in different areas on the *f-k* panel according to their wavenumbers and frequencies. In order to remove a particular event in the time domain data, for instance the ground-roll in land seismic data, the area in the *f-k* domain that contains the amplitudes of that particular event is multiplied by a small coefficient close to zero. The reason that the amplitudes are not multiplied by zero is based on the Fourier theory: If we multiply the amplitude spectrum by a constant in the frequency domain, this means that the function is scaled

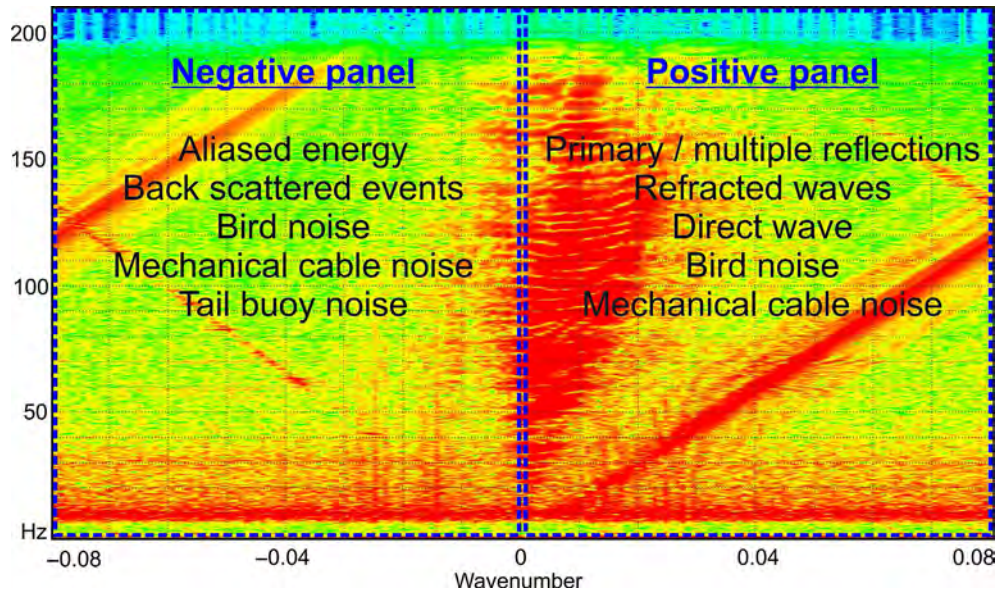


FIG. 5.65 Negative and positive panels of an *f-k* spectrum and *f-k* domain appearance of common events encountered in marine shot gathers.

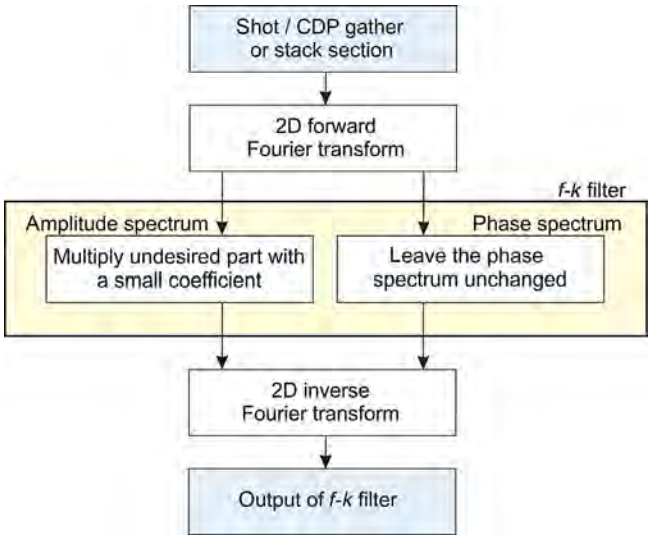


FIG. 5.66 Schematic illustration of the steps involved in *f-k* filter application. The area containing undesired amplitudes in the amplitude spectrum is multiplied by a small coefficient in the *f-k* domain, and then a 2D inverse Fourier transform converts the filtered data back into the time domain.

by the inverse of that constant in the time domain (Table 4.3), and the inverse of zero is simply infinite. In practice, the area of undesired amplitudes is selected by a polygon, termed the *f-k* polygon. Then the data is transferred back into the time domain by a 2D inverse Fourier transform after the amplitudes in the *f-k* polygon are multiplied by a small coefficient value close to zero. The filtered data does not contain the amplitudes of the undesired events in the time domain.

Since the reflections are hyperbolic, their amplitudes are grouped in a fan-shaped region around the frequency axis in the positive panel. In an *f-k* filtering application, we need only the amplitudes of primary reflections to be passed by the filter, while all other events are simply filtered out. This can be achieved by two different types of polygons in the *f-k* spectrum: either an accept or a reject polygon is defined to discriminate the signal and noise zones in the *f-k* domain (Fig. 5.67). An accept polygon encloses the signal amplitudes that are supposed to be passed by the *f-k* filter, whereas a reject polygon surrounds the noise area, which is filtered out by the *f-k* filter. In the case of the accept polygon, the amplitudes outside of the polygon are multiplied by the small coefficient, while for the reject polygon, it is the opposite. Although both approaches normally produce the same results, accept polygons are preferred in practice because it is easier to enclose the signal zone in the *f-k* domain.

5.9.1 *f-k* Filtering of Marine Seismic Data

The primary purpose of the application of an *f-k* filter to marine shot gathers is generally to remove the linear correlated events, such as tail buoy noise, bird noise, or mechanical cable noise. Primary reflection amplitudes generally appear in the positive panel of the *f-k* spectrum close to the frequency axis. The negative panel, however, contains the amplitudes of negative dip events, such as tail buoy noise, aliased signal, and diffracted energy due to the existence

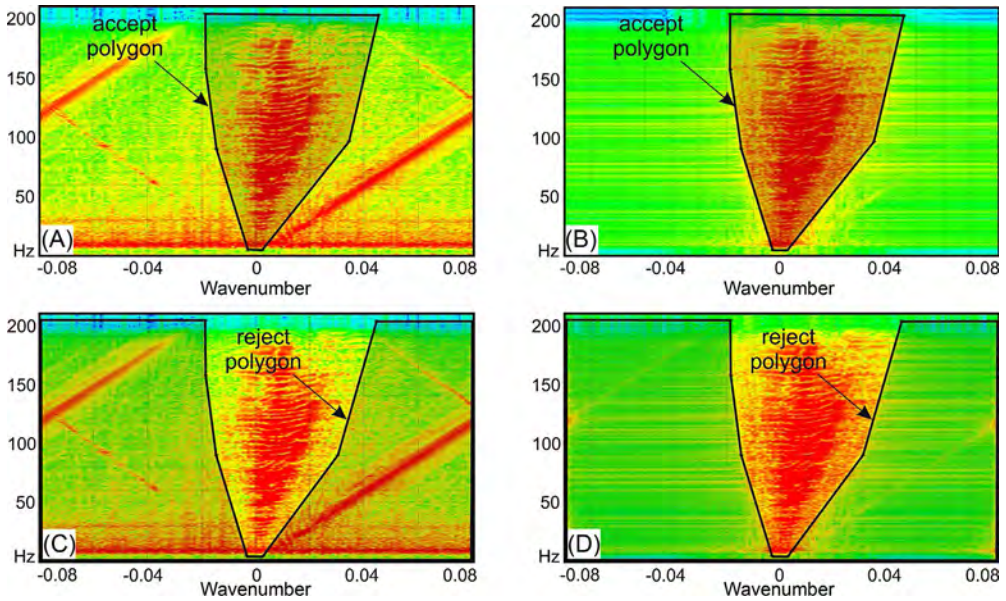


FIG. 5.67 Either an accept (encloses the signal amplitudes) or a reject (encloses the noise amplitudes) polygon can be defined to discriminate the signal and noise zones in the *f-k* domain. (A) Accept polygon and (B) its *f-k* filter output. (C) Reject polygon and (D) its *f-k* filter output.

of subsurface faults or irregular seafloor morphology, possibly because of the existence of canyon systems on the seafloor. Mechanical cable noise can be observed as linear strong amplitudes in both panels, since this kind of noise may occur in the near to far channel (positive dip), or vice versa (negative dip). Bird noise is vertical in shot gathers and effective on the channels close to the bird locations, and thus, their amplitudes arise in a narrow frequency band in both positive and negative panels parallel to the wavenumber axis. Therefore, in practice, generally the amplitudes in a triangular area close to the wavenumber axis in the positive panel, and almost all amplitudes in the negative panel, are removed in the *f-k* spectra. The remaining part contains the amplitudes of the primary reflections.

Fig. 5.68A shows a marine shot gather and its *f-k* spectrum with some significant events superimposed. Before the *f-k* filter, a band-pass filter of 8–180 Hz was used to remove low-frequency swell noise and high-frequency random noise amplitudes. Primary reflections (R) are located in a fan-shaped zone in the positive panel close to the frequency axis in the *f-k* spectrum. There is very distinctive horizontal bird noise (B) in both panels, and linear tail buoy noise (T) in the negative panel in the *f-k* spectrum. In some cases, especially for data collected in rough weather conditions, swell noise amplitudes are so strong that a band-pass filter may not completely remove them. Although a band-pass filter was applied prior to the *f-k* filter to the shot gather in Fig. 5.68A, the data still has residual swell noise (S) components in a very low-frequency band (e.g., between 0 and 4 Hz) along the whole wavenumber axis. The direct wave is indicated by D, which appears as a linear event in the positive panel. Since its propagation velocity is relatively low with respect to the primary reflections, and it is the linear event with the highest inclination on the shot gather, its amplitudes appear very close to the horizontal

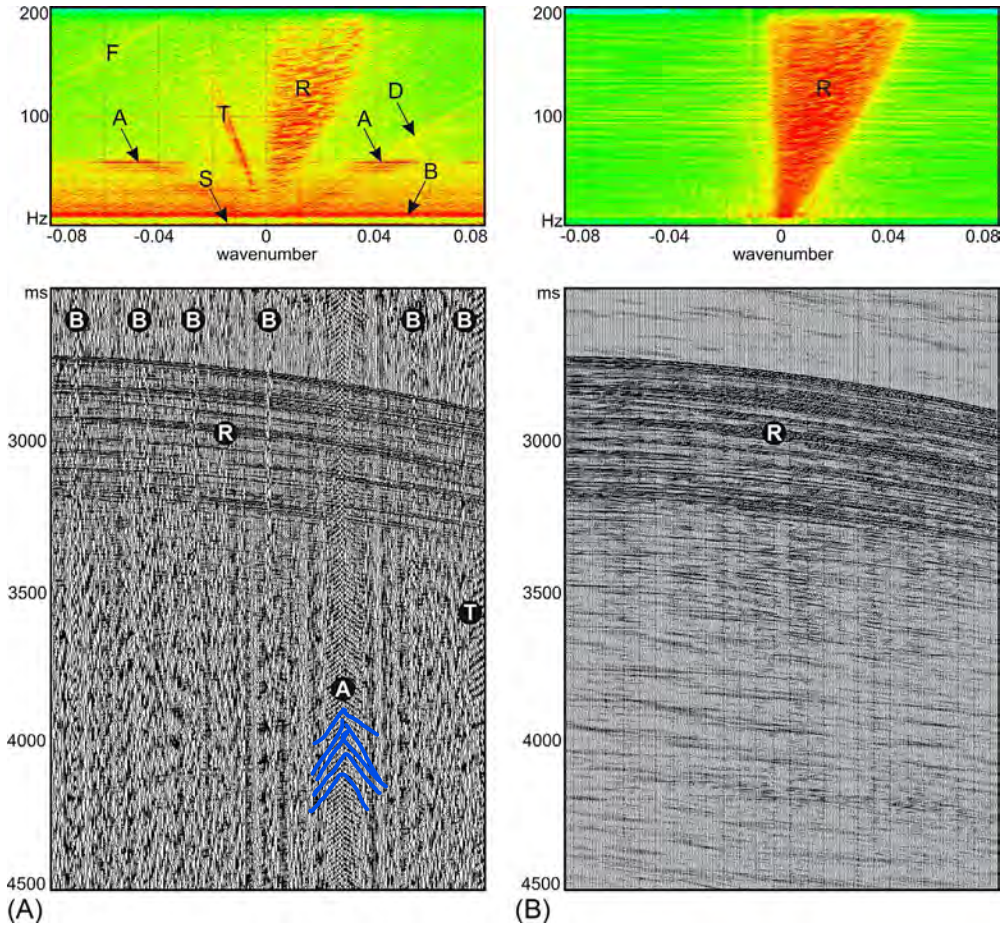


FIG. 5.68 (A) A marine shot gather (bottom) and its *f-k* spectrum (top). (B) Output of an *f-k* filter designed to pass only reflection amplitudes. *R*, primary reflections; *A*, streamer ballast noise; *T*, tail buoy noise; *S*, residual swell noise; *D*, direct wave; *F*, aliased direct wave energy; *B*, bird noise.

wavenumber axis in the *f-k* spectrum. Also, it is folded approximately at 120 Hz and the amplitudes with frequencies larger than the aliasing frequency appear in the negative panel (F). What is interesting on this shot gather is the streamer ballast noise (A), which appears as reverse V-shaped linear events on the shot. Because this noise has amplitudes in both positive and negative directions on the time section, it has amplitudes in both the positive and negative panels in the *f-k* spectrum (Fig. 5.68A), with a dominant frequency between the 50 and 60 Hz band according to the *f-k* spectrum.

The amplitudes of different events in the shot record in Fig. 5.68A are mixed up on the shot gather, and it is not possible to discriminate the amplitudes of only one specific event in the time domain. In the frequency domain, however, most of the amplitudes of these events are grouped in different parts of the *f-k* panel, enabling us to suppress most of this correlated noise. The primary reflection amplitudes (R) in

particular seem to be isolated from most of the linear correlated noise components. Fig. 5.68B shows the output of the *f-k* filter applied to the shot in Fig. 5.68A, which is designed to pass only reflection amplitudes while suppressing all other types of amplitudes. The *f-k* spectrum involves almost only amplitudes of primary reflections and the S/N ratio is significantly increased in the output shot gather (Fig. 5.68B).

Fig. 5.69 shows an analysis of mechanical cable noise using the *f-k* spectrum of the deep portion of a noise record. Cable noise may be in both directions from near to far or far to near channels (Section 3.6.2); the former produces positive dip linear events on the *f-k* spectrum, while the latter creates negative dip. Although these events form a checkerboard appearance in time domain data (Fig. 5.69A), they can easily be discriminated in the *f-k* domain according to their different dips (Fig. 5.69B and C).

Guided waves and seismic interference can also be analyzed in the *f-k* domain. Fig. 5.70A

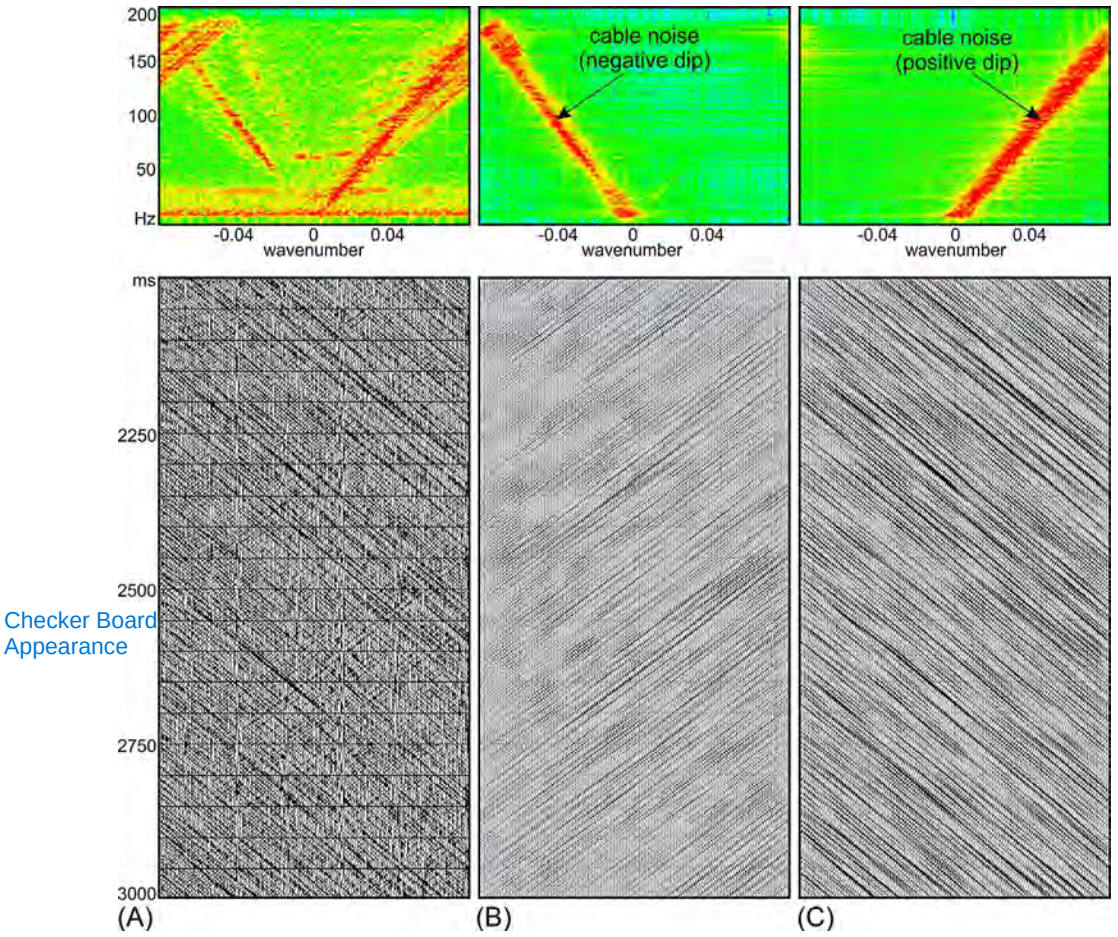


FIG. 5.69 Analysis of mechanical cable noise using the *f-k* spectrum of a noise record. (A) Deep portion of a filtered noise record (bottom) with significant cable noise in both directions and its *f-k* spectrum (top), after an *f-k* filter to make (B) negative dip and (C) positive dip cable noise clearer.

In seismic, guided waves are a type of trapped wave that are generated by multiple reflections in low-velocity layers. They are characterized by high amplitude and shingling, and are often observed in field seismic data

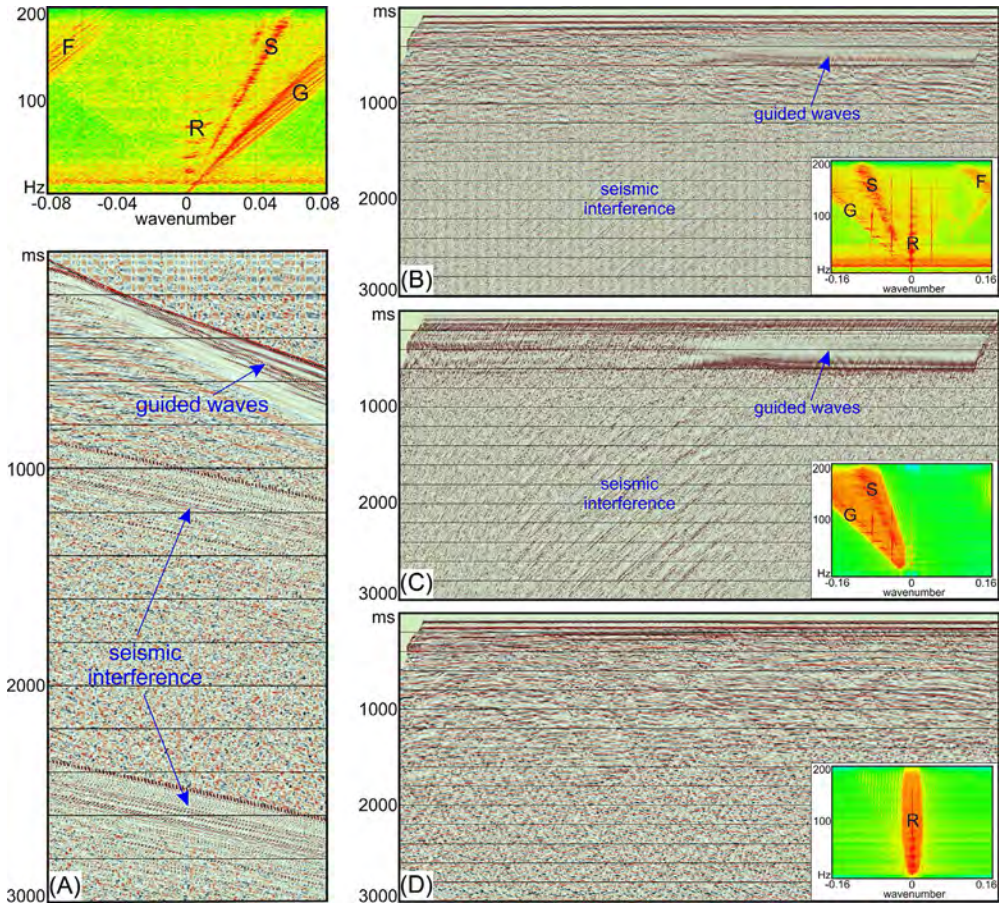


FIG. 5.70 (A) An example shot gather with guided waves and linear seismic interference (bottom) and its corresponding *f-k* spectrum (top). (B) An example stack section contaminated by residual guided waves and highly inclined seismic interference. (C) Since the guided waves and seismic interference have negative dip, their amplitudes appear in the negative panel of the *f-k* spectrum. (D) Removal of the residual guided wave energy and seismic interference by a suitable *f-k* filter. *S*, seismic interference; *G*, guided waves; *R*, primary reflections; *F*, spatially aliased guided wave energy. Insets show the corresponding *f-k* spectra of the stack sections.

Different Frequencies with different velocities

shows a shot gather with strong guided waves and linear seismic interference. Since the guided waves are dispersive, they do not have a single propagation velocity and they exhibit a fan-shaped appearance on the shot gathers around the far offsets. Their amplitudes also cover a fan-shaped area in the positive panel of the *f-k* spectrum (indicated by G). In the example shot shown in Fig. 5.70A, the seismic interference is linear and has higher propagation velocity than guided waves. Therefore, its amplitudes appear as an isolated package in the *f-k* spectrum (indicated by S). Although the *f-k* filter is generally applied to filtered shot gathers in marine seismic data processing, in some specific cases it is also possible to apply it to stack sections to remove residual mechanical cable noise, seismic interference, or guided wave energy. Fig. 5.70B shows an example stack section contaminated by residual guided waves and seismic interference. In accordance with their dip direction on the stack section, their amplitudes are located

in the negative panel of the *f-k* spectrum (Fig. 5.70C). Because the reflections in this section are almost horizontal, their amplitudes arise around the frequency axis (indicated by R). A suitable *f-k* filter removes almost all of the residual guided wave energy as well as seismic interference from the stack section (Fig. 5.70D).

5.9.2 QC in *f-k* Filtering

The most important QC application in *f-k* filtering is to check the shots/CDPs/brute stack data after the filter to ensure that there is no problem in the application. Brute stacks are substantial in QC implementation since the application of an *f-k* filter produces extremely high-amplitude X-shaped noise on the brute stack sections, if the data contains high-amplitude spikes. Fig. 5.71 shows a small part of an interesting example stack section which suffers from extremely dense spike noise. If this noise is not removed by a surgical mute or trace kill prior to the *f-k* filter, then the stack sections are excessively contaminated by crisscross-shaped noise bursts after the *f-k* filter.

For an efficient *f-k* filter application, the reject zone must not be defined as a narrow band. In addition, almost all of the negative panel (except the areas close to the vertical frequency axis) must always be in the reject zone since the folded energy reduces the effectiveness of the *f-k* filter if a spatially aliasing area exists. The most important point in an *f-k* filtering application is to discriminate signal and noise amplitudes in the *f-k* panels. Since reflections are mainly in the positive panel, noise amplitudes with positive dip appearing in the positive panel of the *f-k* spectrum along with the reflection amplitudes, such as the one in Fig. 5.69C, may not be completely removed and some noise components with positive dip may still remain in the filtered data after the *f-k* filter.

In addition, especially in areas of complex seafloor morphology, this separation may be difficult because a high amount of back scattered energy, particularly from large-scale seafloor

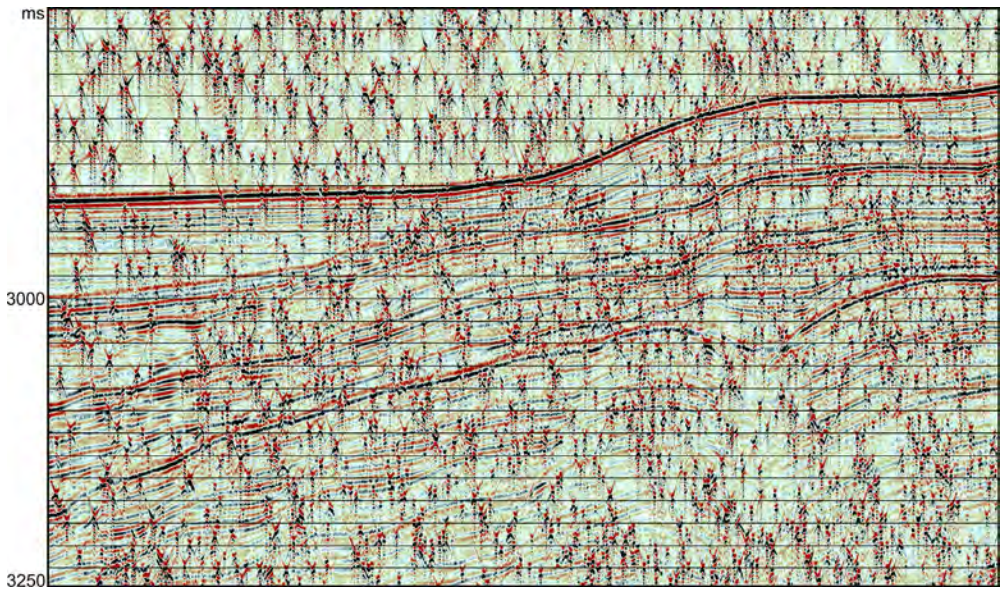


FIG. 5.71 An example stack section with extreme spike noise, which is transformed into X-shaped high-amplitude bursts by the *f-k* filter.

structures such as canyon walls along the seismic line, may exist in the seismic data (Fig. 5.72A). In this case, a reject zone comprising a whole negative panel of the *f-k* spectrum may not be appropriate, because it will completely remove the scattered energy from the canyon walls or extreme dipping morphology on the seabed (Fig. 5.72B). Actually, it is preferable to keep these amplitudes in the accept zone since they will later be moved to their correct locations on the seismic section by migration (Chapter 11). Therefore, in such cases, it is suggested to define a larger accept polygon including the scattered amplitudes in the negative panel, as in Fig. 5.72C.

Related to the picking of an accept polygon including the amplitudes in the negative panel of the *f-k* spectrum, another issue arises from the deeper reflection amplitudes. Normal move-out times of primary reflections are so small in near offset traces of the shot gathers that they appear as horizontal instead of hyperbolic events (Fig. 5.73A). This situation is especially

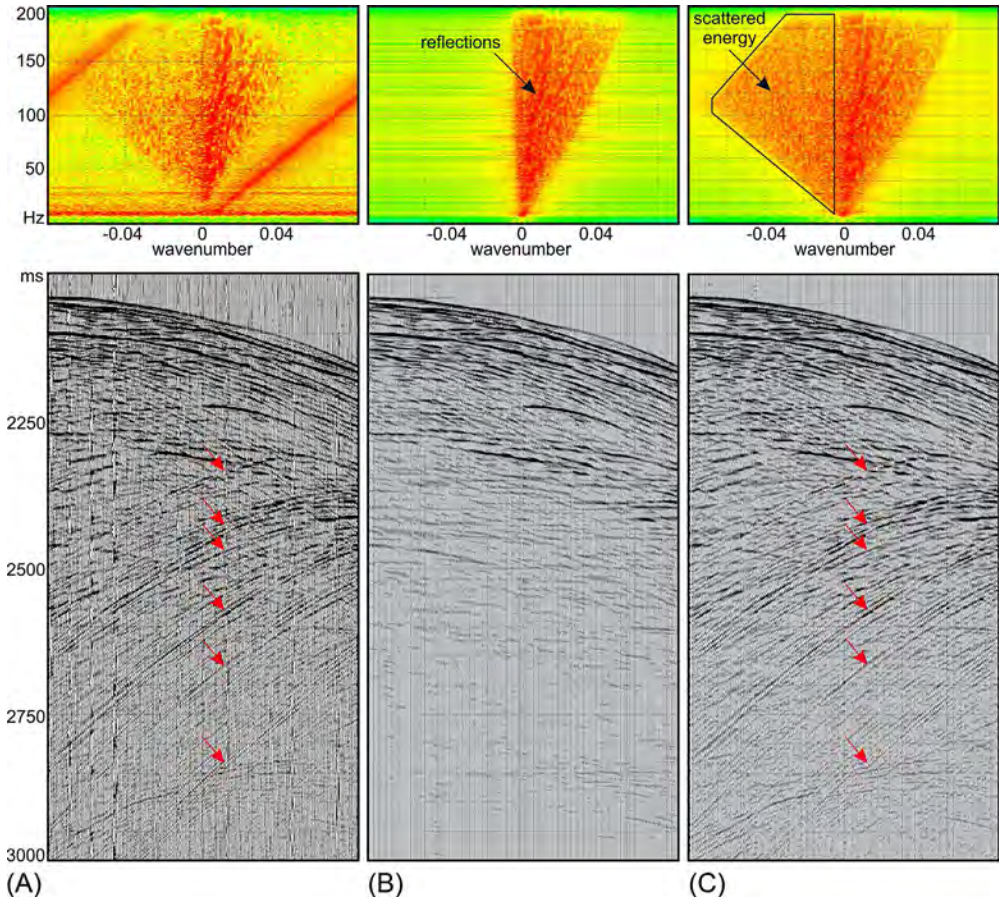


FIG. 5.72 An example shot gather (bottom) and its *f-k* spectrum (top) to illustrate the importance of amplitudes in the negative panel of an *f-k* spectrum in the case of complex seafloor morphology. (A) Back-scattered energy from seafloor canyon walls are observed as reverse hyperbolas on shot gathers *(red arrows)*. (B) Rejecting the entire negative panel of the *f-k* spectrum completely removes the scattered energy, which can be moved to its correct location after migration. (C) A larger accept polygon including the scattered amplitudes in the negative panel will keep this scattered energy *(red arrows)* while removing the other types of noise.

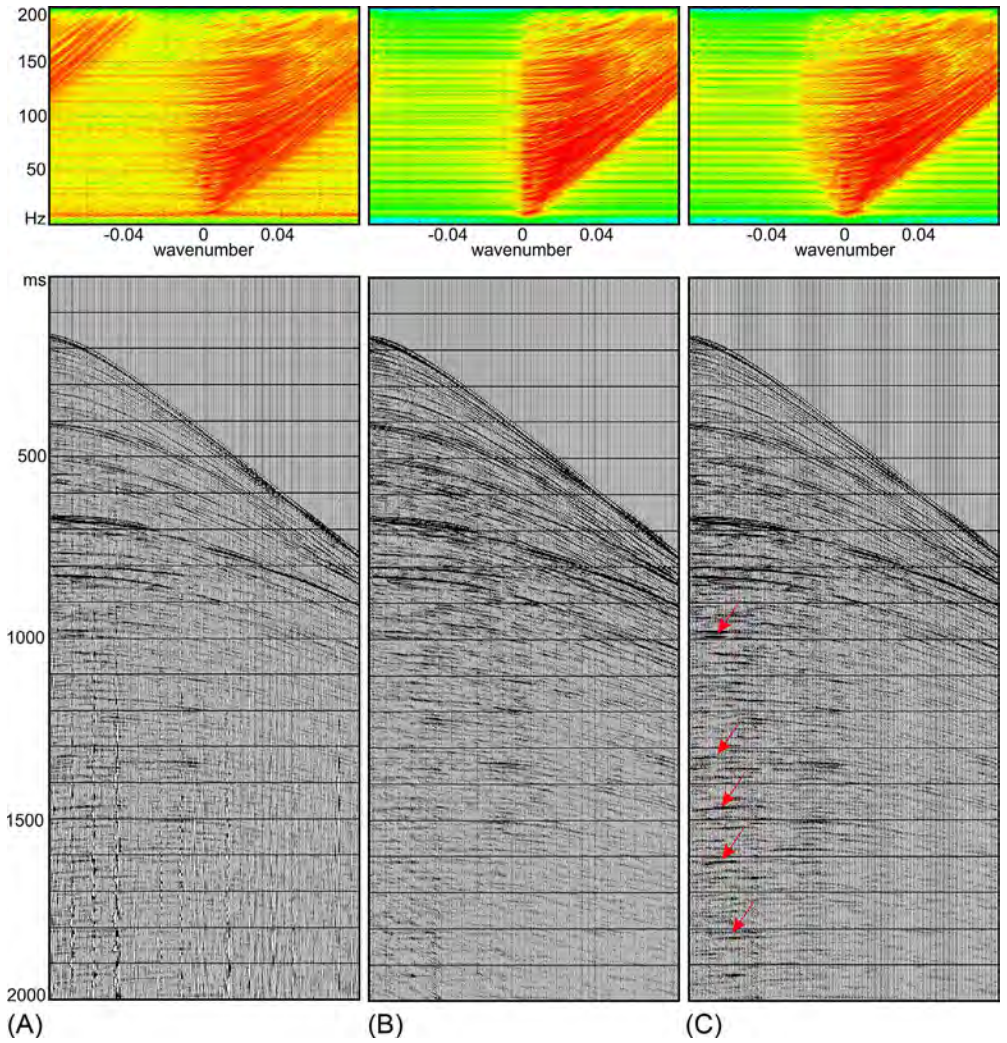


FIG. 5.73 An example shot gather (bottom) and its *f-k* spectra (top) to illustrate the importance of amplitudes in the negative panel of an *f-k* spectrum for deep reflection events. (A) Deep reflections appear almost horizontal instead of hyperbolic events in near offset traces of the shot gathers and small parts of their amplitudes may arise in the negative panel. (B) Rejecting all amplitudes in the negative panel of the *f-k* spectrum causes amplitude reduction in the late arrivals of deep reflections in the near-channel traces. (C) Accepting the amplitudes close to the frequency axis in the negative panel restores these amplitudes *(red arrows)*.

distinct on the late arrivals of the traces from very near channels in deep water seismic data. These are the tips of the reflection hyperbolas, and since they are almost horizontal in time domain data, their amplitudes accumulate around the vertical frequency axis of the *f-k* spectrum close to the zero wavenumber value. Some parts of these amplitudes may extend into the negative panel, and rejecting the entire negative panel of the *f-k* spectrum removes these signal amplitudes, which ultimately results in amplitude reduction in the late arrivals of deep reflections in the near-channel traces (Fig. 5.73B). In this case, accepting the negative panel amplitudes close

to the vertical frequency axis recovers the amplitudes of deeper reflections in near offsets and produces better *f-k* filter results (Fig. 5.73C).

5.10 BRUTE STACK

Brute stacks are the sections prepared by applying only essential processing steps to raw seismic data. They are used for several reasons:

- Brute stacks provide subsurface geological information immediately after a survey line is completed.
- Several acquisition QC tests can be performed on the brute stacks instead of applying them to shot or CDP gathers, which can provide a better understanding of acquisition issues.
- Preparing brute stack sections also ensures effective QC analysis of processing applications. For instance, quality of a deconvolution or band-pass filter output can be better guaranteed by analyzing the results on the brute stacks instead of shot gathers.
- If the survey line contains extensive seabed morphology variations, or large-scale subsurface geological structures such as salt domes, diapirs, or potential reservoirs, extra velocity analysis locations may be preferred in the vicinity to delineate the possible lateral velocity variations around these structures. Such specific velocity analysis locations along the seismic line can be precisely determined on the brute stacks.
- Some of the multiple suppression algorithms require water bottom arrival time to be entered into the database and into the headers of the seismic data. Water bottom time along the survey line can be picked on the brute stack sections if no single-beam echo-sounder data is available.
- Some data processing software enables us to perform an automatic application of top mutes using water bottom times picked from the brute stack sections.
- Calculations of some processing steps, implemented on a trace-by-trace basis, such as band-pass filtering or deconvolution, can be initiated from seabed arrival time instead of applying them to whole time samples of the data. This prevents us from processing the water column noise and may significantly save data processing time, especially for large data volumes.

During the preparation of brute stacks, only essential steps are applied and time-consuming processing applications such as deconvolution, muting, velocity analysis, or migration are omitted. Basically, a brute stack can be obtained using the steps given in Fig. 5.74. In data loading, it is not necessary to include all available channels in shot gathers, and in general, the first 24 channels are sufficient for a proper brute stack. One of the most important points is that a constant velocity of approximately 1500 m/s is used for NMO correction for an entire line. In some cases, a single velocity function linearly increasing with recording time is preferred instead of a constant velocity. In each case, velocity analysis is ignored. If necessary, a fast migration algorithm, such as Stolt migration (Section 11.4), can also be applied to brute stack sections. In 3D seismic data, brute stack cubes

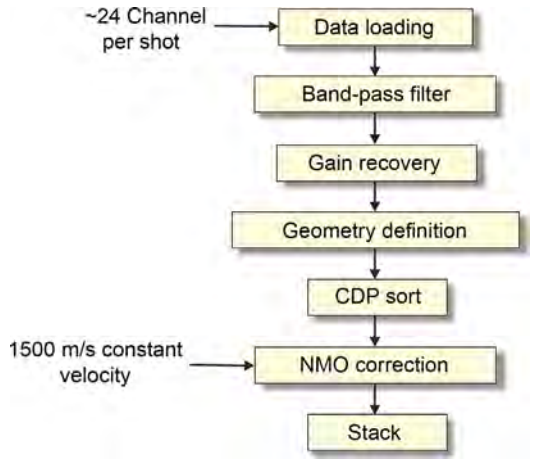


FIG. 5.74 Basic processing steps used to obtain a brute stack section. Complex steps such as velocity analysis or migration are omitted in brute stack flows.

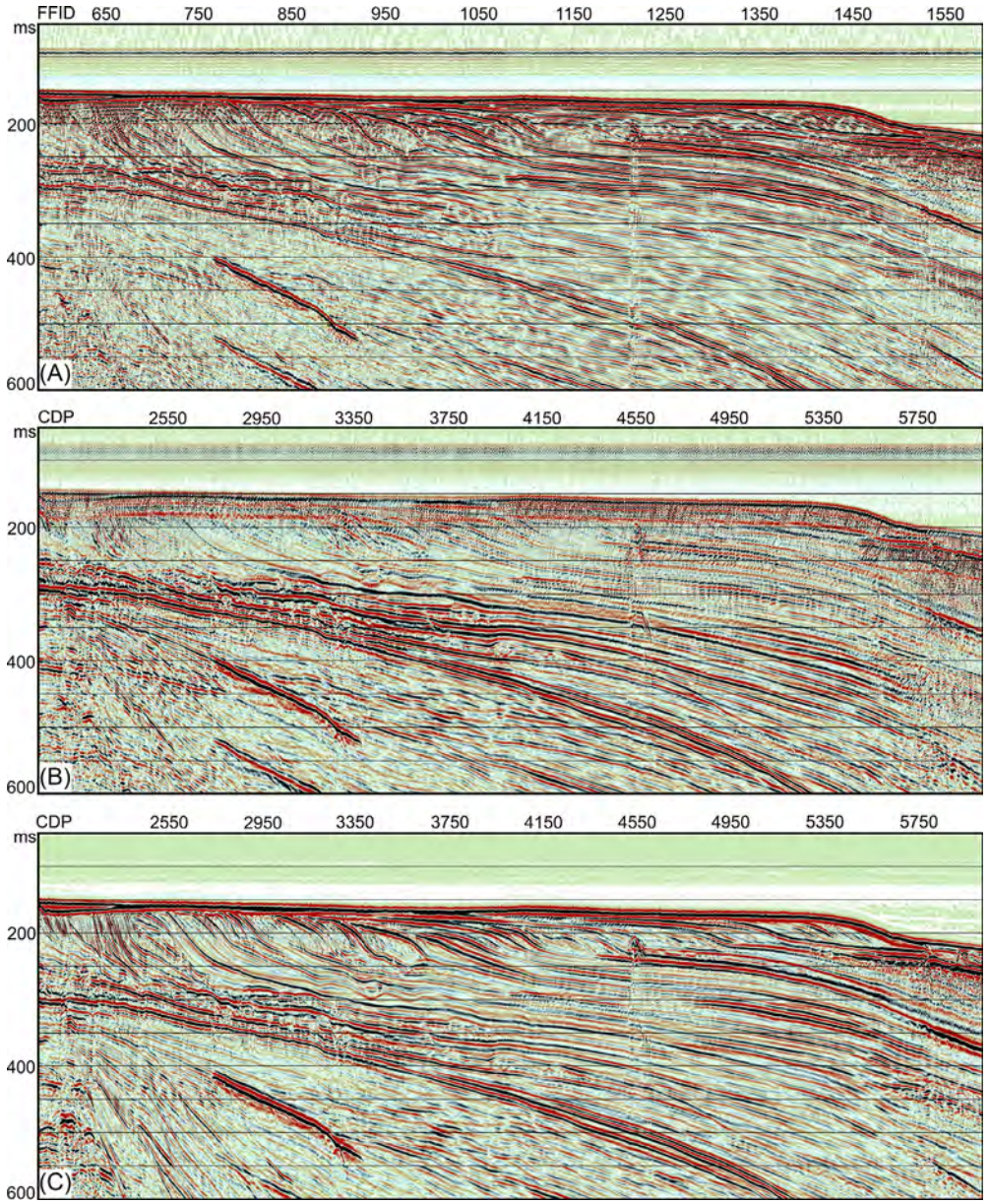


FIG. 5.75 Comparison of (A) common offset, (B) brute stack, and (C) full stack sections of a marine seismic line. 1500 m/s constant velocity was used to compute the brute stack. The horizontal axis of the brute stack and full stack is CDP number, whereas it is FFID number for the common offset section.

can be obtained in certain periods during the acquisition for QC and visualization purposes.

Fig. 5.75 compares the common offset (Fig. 5.75A), brute stack (Fig. 5.75B), and full stack (Fig. 5.75C) sections of a marine seismic line. Although all three sections are quite similar in appearance, substantial differences exist among the sections such as:

- Common offset sections are obtained by displaying the first channel of every shot, and thus, their horizontal axis is shot (or FFID) number, because each shot contributes one single trace to the common offset section. Brute and full stacks, however, are obtained by stacking after a CDP sort process; therefore, they have the order of CDP as the horizontal axis.
- The *S/N* ratio of the sections is quite different: The quality of the common offset section is relatively low since it is single trace data and does not benefit from stacking. Although the *S/N* ratio is better for deeper parts of the brute stack, it is considerably low for shallow areas; this is because the shallow parts of a section need a precise velocity field for an accurate NMO correction, yet we use a single velocity function for an entire section, which seems not to represent the correct velocity of shallow subsurface sediments in sufficient accuracy. As expected, the full stack section has the highest S/N ratio and resolution both in shallow and deeper parts.
- The reflections are not located at their correct horizontal locations in the common offset sections because each trace in the common offset section is assigned at a shot point location for each shot. However, assuming a horizontal subsurface reflector, the reflections are recorded from the midpoints of the source-receiver pairs, and this is ensured by the CDP sort process in brute stack and full stack sections.
- The number of traces in a common offset section is relatively low when compared to brute and full stack sections. Since each shot gather provides one trace, the number of traces in the common offset section exactly equals the number of shots along the line, and the distance between these traces equals the shot interval. However, the number of traces in a full stack section is [(2 × shot interval)/receiver interval] times higher than those in a common offset section, and the distance between these traces equals half of the group interval. This indicates that the lateral resolution of a common offset section is considerably lower than that of a brute stack or a full stack section.
- Common offset and brute stack sections generally suffer from multiple reflections. This is because the common offset sections do not benefit from the advantage of stacking in eliminating the multiple reflections. In brute stack sections, multiples may also be quite distinct since there is no velocity analysis and typically water velocity is used in NMO correction. Multiples are of relatively high amplitudes on the brute stacks because they also propagate mainly with water velocity (Chapter 7), which results in the flattening of multiple reflection hyperbolas during the NMO correction. However, stacking itself is a powerful method to suppress multiples, and full stack sections benefit from this property of the stacking.

CHAPTER

6

Deconvolution

OUTLINE

6.1 Convolutional Model 316

6.2 Assumptions for Deconvolution 319
- *6.2.1 Assumption 1: A Simple Earth Model* 320
- *6.2.2 Assumption 2: Stationary Wavelet* 320
- *6.2.3 Assumption 3: Noise Component* 320
- *6.2.4 Assumption 4: Source Waveform* 320
- *6.2.5 Assumption 5: Wavelet Causality* 320
- *6.2.6 Assumption 6: Random Reflectivity* 321

6.3 Spiking Deconvolution 324
- *6.3.1 Deconvolution With Inverse Filter* 325
- *6.3.2 Inverse Filtering With Least Squares* 328
- *6.3.3 Optimum Wiener Filters* 330
- *6.3.4 Prewhitening* 334

6.4 Predictive Deconvolution 335

6.5 Determination of Deconvolution Parameters 337
- *6.5.1 Autocorrelation Time Gate* 339
- *6.5.2 Deconvolution Design Gate* 340
- *6.5.3 Operator Length* 341
- *6.5.4 Prediction Lag* 341

6.6 Poststack Deconvolution 349

6.7 Maximum Entropy (Burg) Deconvolution 349

6.8 Shaping Filters 350

6.9 Surface Consistent Deconvolution 356

6.10 QC in Deconvolution 357

By its simplest definition, deconvolution is the inverse of the convolution process. In the convolutional model theory explained in Section 6.1, the seismic trace is formed by a simple convolution of the source signal and the earth's reflectivity series in depth. Deconvolution tries to remove the source signal from the seismic trace. In seismic data processing, it is widely used for improving the temporal resolution of the seismic data, since it is always preferred to work with seismic data having a broad amplitude spectrum, including frequencies both low and as high as possible,

© 2018 Elsevier Inc. All rights reserved.

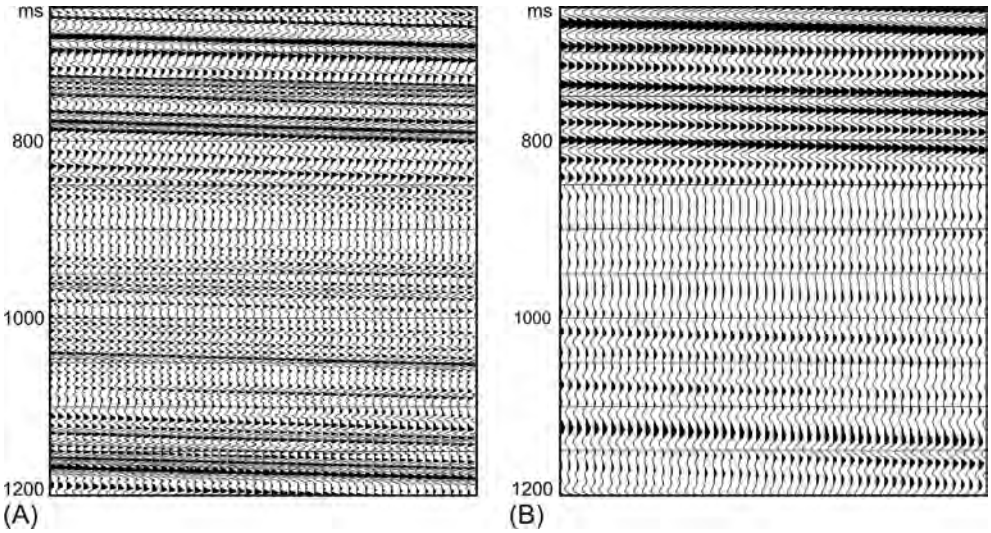


FIG. 6.1 Effect of the bandwidth on the resolution of seismic data. (A) Wide band (4–140 Hz), and (B) narrow band (4–60 Hz) seismic data.

because a wide spectral band always corresponds to a better temporal resolution. As an example, Fig. 6.1 compares small portions of wide (4–140 Hz, Fig. 6.1A) and narrow band (4–60 Hz, Fig. 6.1B) seismic sections, where the resolution is much better in the case of wide bandwidth. That is, the dominant frequency of broadband data is relatively higher, which ultimately results in a smaller wavelength, increasing the resolution of the seismic signal.

Deconvolution has a number of significant effects on seismic data, as shown schematically in Fig. 6.2. In ideal conditions, the deconvolution

- improves temporal (vertical) resolution
- removes or compresses the seismic wavelet from the data
- removes the ringy character of the reflections
- eliminates multiple reflections
- whitens the amplitude spectrum to obtain broad-band data

The recorded seismic data is band limited at both high- and low-frequency ends of the spectrum because of the ghost reflection notches and the high swell noise amplitudes, respectively.

Low Freq

High Freq

Deconvolution broadens the band-limited spectrum, and even tries to convert it into a white spectrum consisting of a balanced amplitude distribution for the whole available frequency band. The theoretical basis underlying the use of deconvolution to achieve these goals is basically to remove (at least, to compress) the source wavelet embedded in the seismic data. The time length of the wavelet before deconvolution is much larger than that of the wavelet after deconvolution (Fig. 6.2).

Although deconvolution is generally applied to preprocessed shot or common depth point (CDP) gathers, it can also be applied to stack sections, which is known as deconvolution after stack (DAS). If applied to prestack data, the shots or CDPs must be properly preconditioned and the coherent and random noise components must be removed as far as possible, since the quality of deconvolution output is quite sensitive to noise in the data. Figs. 6.3 and 6.4 compare the preprocessed shots and stack sections before and after a spiking deconvolution, respectively. The deconvolution is especially effective on the early arrivals and removes the

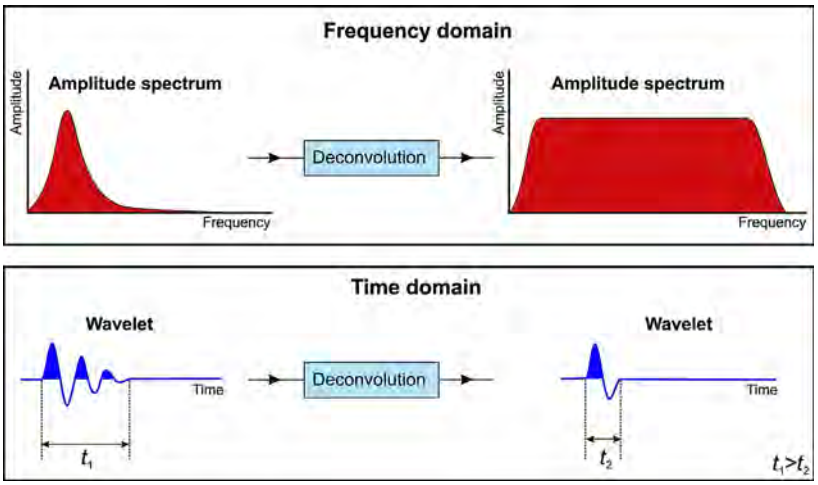


FIG. 6.2 Schematic illustration of the main effects of deconvolution on a simple wavelet in frequency (top) and time (bottom) domains. Deconvolution tries to widen the amplitude spectrum and compresses the seismic wavelet.

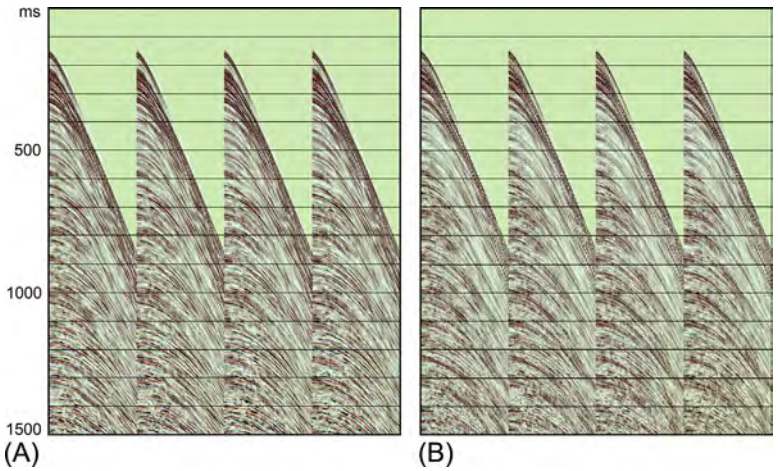


FIG. 6.3 Example preprocessed shot gathers (A) before, and (B) after deconvolution. Deconvolution compresses the seismic wavelet and enhances vertical resolution.

ringy character of the reflections and improves the vertical resolution of the data. The mean amplitude spectra of both sections in Fig. 6.4 indicate that deconvolution increases the amplitudes of high-frequency components and tries to whiten the amplitude spectrum.

Several different deconvolution techniques have been developed for different purposes. Table 6.1 summarizes the deconvolution approaches available in the seismic industry. One of the most common deconvolution techniques is spiking deconvolution, which tries to remove source wavelets from the recorded data by converting them into a spike. The purpose is to obtain the earth's impulse response, or the reflectivity series. In other words, spiking deconvolution tries to convert an input seismic trace into the earth's reflectivity series. Another

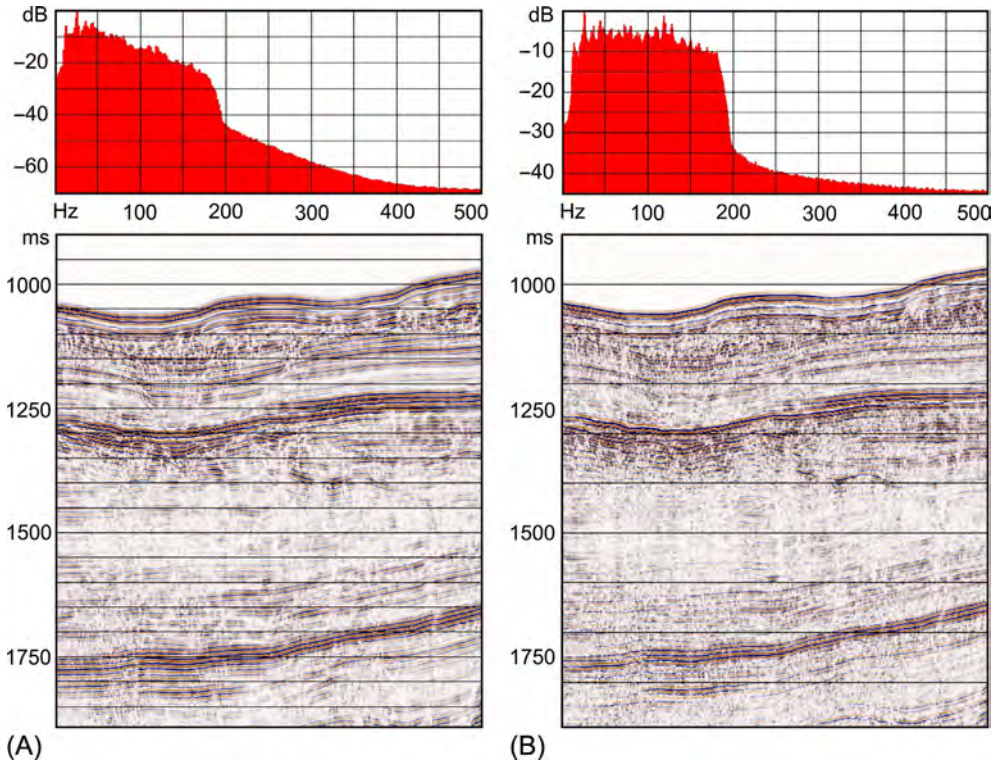


FIG. 6.4 An example stack section (A) before, and (B) after deconvolution and its corresponding mean amplitude spectra (top). Deconvolution removes the ringy character of the reflections, which is especially evident for the strong reflections at 1300 and 1750 ms.

well-known deconvolution method is predictive deconvolution, which tries to estimate and remove the multiple reflections from the data. Among these numerous deconvolution methods available, spiking and predictive deconvolutions are the most common techniques and have widespread applications in the seismic industry today.

6.1 CONVOLUTIONAL MODEL

In order to comprehend the theoretical basis of deconvolution, one must consider the 1D convolutional model which underlies 1D seismic modeling and is used to compute zero-offset synthetic sections. Reflections are acquired from the interfaces defined by the acoustic impedance contrasts of the subsurface layers. Although the acoustic impedance equals the multiplication of velocity and density for a specific layer (Section 1.3.2), the densities of the subsurface layers are not generally considered in acoustic impedance calculations in the case where there is no well log information in the area, because the variations of the density values are quite small with respect to the velocity changes across the interfaces. Therefore, it is generally thought that the subsurface interfaces separate the mediums of different wave velocities, and a reflection coefficient can be calculated for each individual interface using only the velocities of the media it

TABLE 6.1 Different Deconvolution Techniques and Their Application Areas

Deconvolution Method	Application
Spiking deconvolution	Converts the source wavelet in the seismic data into a spike and improves the temporal resolution
Predictive deconvolution	Predicts and removes multiple reflections from the seismic data
Waveform deconvolution	Transforms one waveform into another (generally converts a mixed phase wavelet into the minimum phase)
Adaptive deconvolution	Deconvolution parameters are automatically updated during the application
Homomorphic deconvolution	Transforms the data into cepstrum domain where the wavelet and reflectivity series can be decomposed
Maximum entropy (Burg) deconvolution	Uses entropy approach to obtain random and predictable components in the data
Minimum entropy deconvolution	Tries to reduce the disorder of the signal in order to improve the vertical resolution
Surface consistent deconvolution	Decomposes the signal into source, receiver, offset, and reflectivity coefficients, generally used for amplitude vs. offset (AVO) studies
Frequency domain deconvolution	Deconvolution filter operator is determined in frequency domain

separates. Fig. 6.5A shows a simple earth model of four horizontal layers to calculate the reflection coefficients using layer velocities. The series consisting of the earth's reflection coefficients from several successive interfaces is termed the impulse response or reflectivity series. Theoretically, this is the series obtained as the earth's seismic response if an impulse could be used as the source signal, which is why we call it the impulse response. Fig. 6.5B schematically shows the reflectivity series obtained from the earth model given in Fig. 6.5A. In reality, the reflectivity series of the earth's interior is much more complicated and can be obtained from sonic and density logs from nearby wells for computations of 1D synthetic sections.

The convolutional model suggests that the recorded seismogram is obtained by convolving the reflection coefficients of the interfaces with the source wavelet. Fig. 6.6A shows a minimum phase source wavelet which is convolved by reflection coefficients or the earth's reflectivity series (Fig. 6.6B) to obtain the synthetic seismic trace (Fig. 6.6C) where each interface is represented by an individual source wavelet after convolution. If there is sufficient distance between the interfaces (e.g., if they are thick enough) – in other words, if there is enough time span between the successive reflection coefficients in the reflectivity series – then it is possible to discriminate each individual reflection from every interface on the trace. However, as in the seismogram shown in Fig. 6.6C, the events from closely spaced interfaces overlap, since the source wavelet has a time length determined by its dominant frequency, and this phenomenon is known as interference. Attaining the reflectivity series from seismic data by decomposing the interfered events is actually the inverse of the convolution process and is termed deconvolution.

The convolutional model implies that the recorded seismogram involves the source wavelet reappearing at every individual reflection event. As a simple approach, if we can remove the effect of the source wavelet from the seismic traces, then what we have is the earth's reflectivity series, which is the ultimate goal to acoustically define the subsurface. Deconvolution tries to derive the reflectivity series (or impulse response) of the subsurface by eliminating the source wavelet from the recorded seismogram, in ideal conditions converting it into a spike. By means of the convolutional model, the

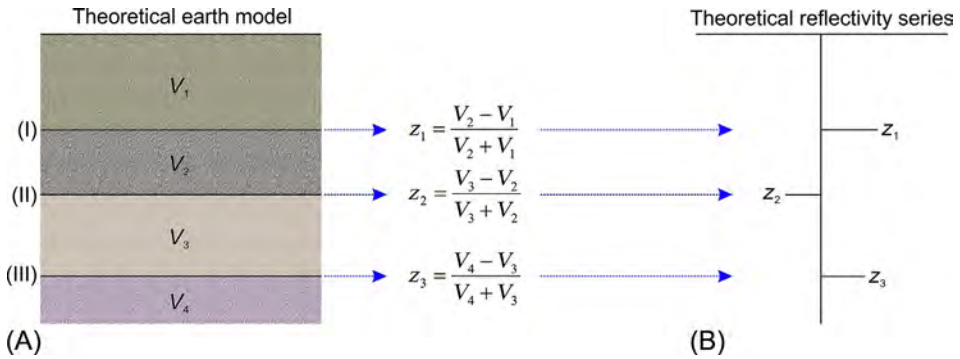


FIG. 6.5 (A) A simple earth model with four horizontal constant velocity (V_i) layers (separated by the interfaces indicated by I–III). The reflection coefficients (z_i) are calculated individually for each interface. (B) These reflection coefficients constitute a series termed a reflectivity series. Here, z_2 is negative since V_3 is a low-velocity layer ($V_4 > V_3 < V_2 > V_1$).

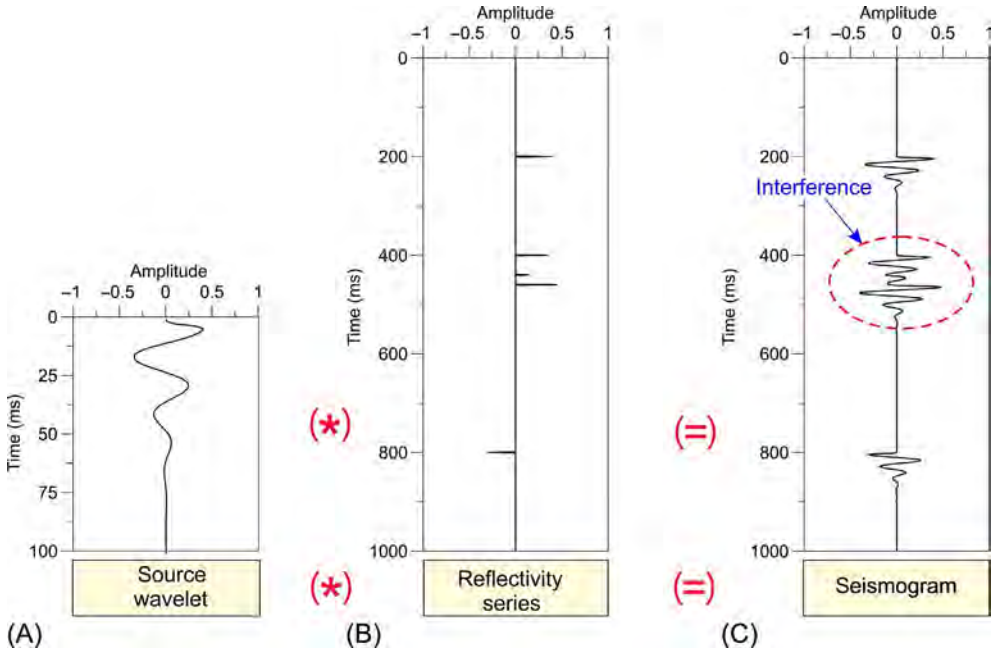


FIG. 6.6 Schematic illustration of how the synthetic seismogram is obtained by the convolutional model. (A) A minimum phase source wavelet, (B) theoretical reflection coefficients or reflectivity series, and (C) synthetic seismic trace obtained by convolving the reflection coefficients with the source wavelet. If the reflection coefficients are too close to each other, then the individual wavelets representing each interface overlap, which is known as interference. (*) denotes convolution.

recorded seismogram can mathematically be expressed as

$$s(t) = w(t)^* r(t) + n(t) \tag{6.1}$$

where $s(t)$ is the recorded seismogram, $w(t)$ is the source wavelet, $r(t)$ is the reflectivity series, and $n(t)$ is random noise. Fig. 6.7 shows the schematic display of the expression given in Eq. (6.1). In practice, the reflectivity series $r(t)$ is not known and is expected to be revealed by deconvolution; the source wavelet $w(t)$ is also not known, and the noise component $n(t)$ cannot be estimated since it is random. That is, the only known quantity in Eq. (6.1) is the recorded seismogram $s(t)$. This implies that a convolutional model consists of an equation with one known and three unknown parameters, and under these circumstances, Eq. (6.1) can only be solved by considering a number of critical assumptions to accomplish the deconvolution process.

6.2 ASSUMPTIONS FOR DECONVOLUTION

Eq. (6.1) expresses how a seismic trace is constructed by a simple convolutional model. In the deconvolution process, we simply try to solve this equation to obtain the earth's reflectivity series, and to achieve this six substantial assumptions must be considered, since Eq. (6.1) involves only one known and three unknown parameters. Here, we discuss these assumptions and their importance to the deconvolution. Although most

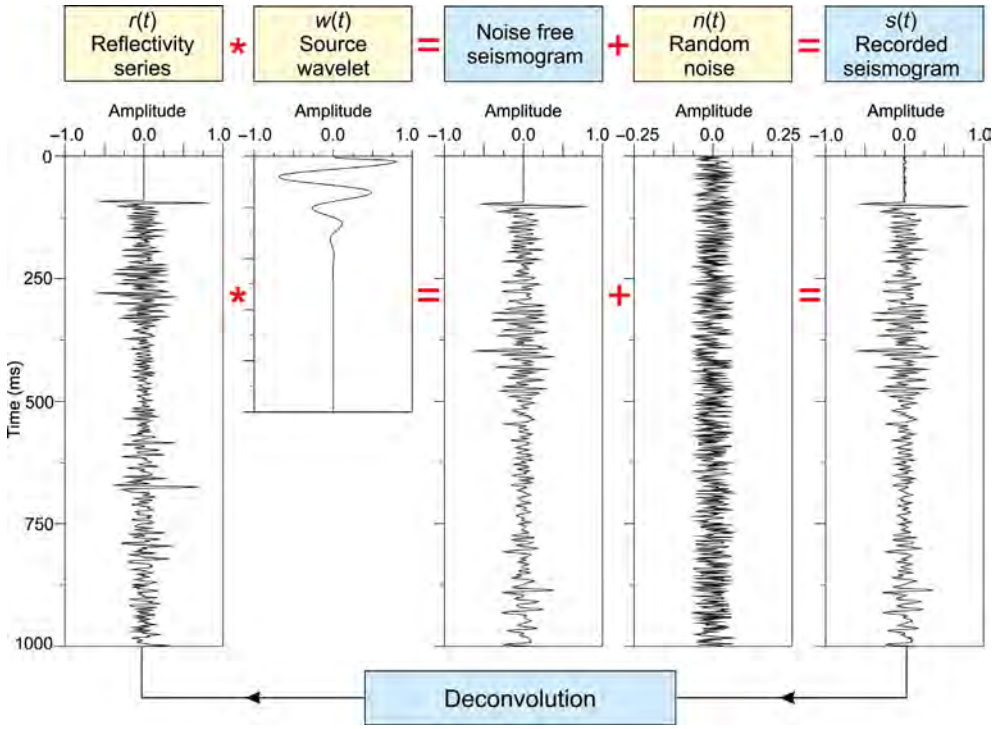


FIG. 6.7 Schematic display of the mathematical expression of the convolutional model given by Eq. (6.1). According to the convolutional model, the recorded seismogram is obtained by convolving the earth's reflectivity series with the source wavelet. Deconvolution aims to extract the reflectivity series from the recorded seismic traces by removing the source wavelet. (*) denotes convolution.

of them are not realistic and cannot be tolerated due to the nature of the seismic methodology, the deconvolution algorithms still produce satisfactory results since they have a robust theoretical and mathematical basis.

6.2.1 Assumption 1: A Simple Earth Model

According to this assumption, the earth is composed of horizontal layers and no lateral velocity variations exist within these constant velocity layers. This assumption is violated in areas of anisotropy and complex geology with strong lateral velocity changes. It is also assumed that the source generates only compressional (P) plane waves of vertical incidence, which anticipates a zero-offset data acquisition geometry in which no shear (S) waves are generated at the interface by phase conversion. Except for some specific marine seismic surveys, such as shallow sparker seismic acquisition, zero-offset seismic data is not collected. However, if the reflector is too deep with respect to the source-receiver separation, the incidence angle can be regarded as small enough. In addition, the plane wave assumption is also invalid since the seismic sources generate spherical waves, not plane waves.

6.2.2 Assumption 2: Stationary Wavelet

This assumption suggests that the source waveform is stationary and does not change while it is propagating through the earth. The pressure wave generated by an explosive source, such as dynamite or an air gun, is known as the source signature, and its amplitude decreases and high-frequency components are absorbed during its propagation. A certain time after its onset, the source waveform becomes quite different from when it was generated. Furthermore, the waveform in the shallow parts of the recorded traces is also quite different from that in the deeper parts of the seismic data, due to absorption effects. The time-dependent change in the source waveform is termed nonstationarity, and attempts are made at compensating for it before the deconvolution process, by use of a suitable gain recovery application.

6.2.3 Assumption 3: Noise Component

Since the noise component in Eq. (6.1) is not known, this assumption supposes that the noise component in the seismogram is zero, or that it can be reduced to zero during the preprocessing. However, recorded seismic traces always include random and several different types of coherent noise amplitudes, and they are added to the data both in the time and frequency domains. The random noise components cannot be predicted beforehand and are variable both in time and space.

6.2.4 Assumption 4: Source Waveform

Deconvolution needs the source waveform to be known. Based on this assumption, the $w(t)$ term in Eq. (6.1) is supposed to be known. However, for explosive sources the source waveform is normally not known. Although the waveform from air gun arrays can be recorded in marine surveys, this gives the waveform at the onset time, known as the near-field signature. But the signal is exposed to different influences during its propagation and its shape becomes quite different after ghost interference (Section 2.2.4). If the source waveform is known, then the applied deconvolution is termed deterministic deconvolution, and if it is unknown (which is the common case), then a statistical deconvolution is used.

6.2.5 Assumption 5: Wavelet Causality

A wavelet is a transient waveform of finite length. Based on the phase specifications or their maximum energy distributions, there may be four types of wavelets: minimum, mixed, zero,

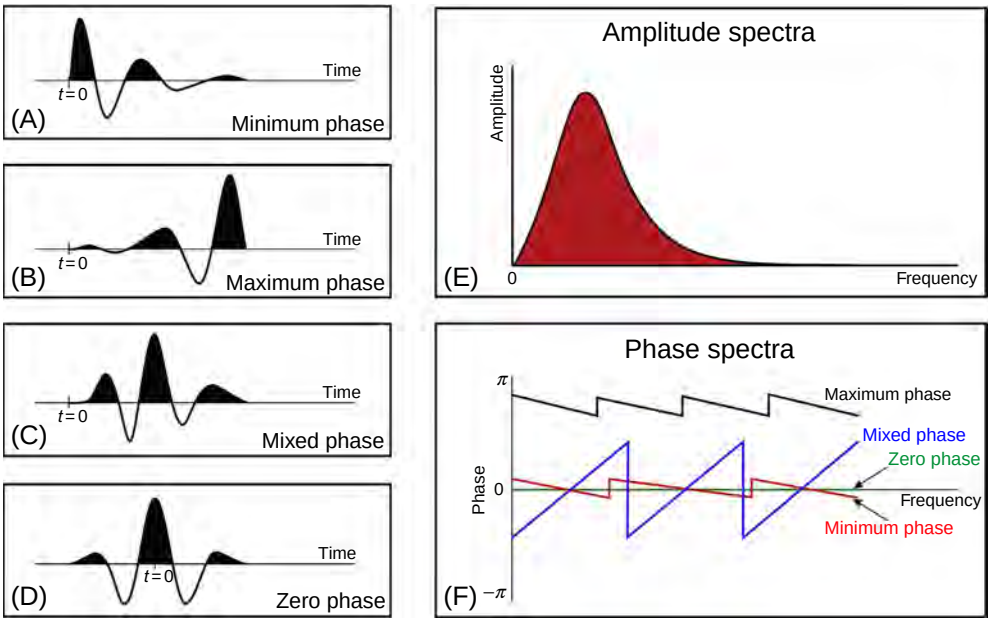


FIG. 6.8 Schematic illustration of (A) minimum, (B) maximum, (C) mixed, and (D) zero phase wavelets. (E) All of these wavelets have the same amplitude spectrum, and (F) the only difference in frequency domain is their phase spectra.

and maximum phase. Fig. 6.8 shows their schematic displays with corresponding amplitude and phase spectra. The wavelet energy is front-loaded, middle-loaded, and back-loaded for minimum phase, mixed phase, and maximum phase wavelets, respectively. A zero phase wavelet is symmetrical with a maximum at time zero. Zero phase wavelets have energy before time zero, which makes them noncausal, and therefore they are not physically realizable. A zero phase wavelet has a shorter duration than its minimum phase equivalent, which makes it a wavelet with higher resolving power. All of the wavelets in Fig. 6.8 are of the same amplitude spectrum; the only difference is their phase spectra.

The phase characteristics of the source wavelet embedded in the seismic traces have great importance in the deconvolution process. According to Assumption 5, the seismic wavelet is always minimum phase, which is a causal signal and its energy is zero before time zero. If the source wavelet in the seismic trace is not minimum phase, the deconvolution produces unstable results. In such cases, it is necessary to convert the source wavelet into its minimum phase equivalent. Although Vibroseis data in land surveys is zero phase, and water gun data is maximum or mixed phase, fortunately the remaining land and marine impulsive sources generally produce minimum phase source signals.

6.2.6 Assumption 6: Random Reflectivity

This assumption suggests that the reflectivity series is random. Although it is commonly not easy to understand the yields of this simple assumption, it is one of the most important prerequisites that enable us to perform deconvolution. The importance of this assumption arises for the calculation of the deconvolution operator. As will be explained in Section 6.3.3, autocorrelation of the source wavelet, not the

source wavelet itself, is required to obtain the deconvolution operator. Yet, how can we obtain the autocorrelation of the source wavelet when we do not know the wavelet itself? The answer lies in Figs. 6.9 and 6.10. The upper panel of Fig. 6.9 shows the components used to obtain the convolutional model, in which the source wavelet is convolved with the earth's reflectivity series in a noise-free environment to obtain the seismograms, or seismic traces, while the lower panel is composed of corresponding autocorrelation traces of each component in the convolutional model. When a convolution process is performed to obtain the seismogram, autocorrelations of the source wavelet and reflectivity series are also convolved to reveal the autocorrelation of the seismogram, which is maximum at the zero lag and has small values for the remaining lags. In addition, autocorrelations of the seismogram and wavelet are similar for the initial parts of the seismogram's autocorrelation.

At this point, the importance of Assumption 6 arises: If the reflectivity series is random, then it has characteristics of white noise. The autocorrelations of random functions such as white noise have a maximum value at zero lag, and they exactly equal zero for all other lags. Such an autocorrelation function is actually a Dirac delta or unit impulse function (Table 4.1), and the convolution of the wavelet's autocorrelation with a Dirac delta function yields the wavelet's autocorrelation (middle panel in Fig. 6.10), and this exactly equals the autocorrelation of the seismogram, expressed as

$$R\{r(t)\}^{*}R\{w(t)\} = R\{s(t)\} \tag{6.2}$$

where $R\{r(t)\}$, $R\{w(t)\}$, and $R\{s(t)\}$ are the autocorrelations of the reflectivity series, source wavelet, and the seismogram, respectively. If the reflectivity series is random, then its autocorrelation is a Dirac delta, and Eq. (6.2) becomes

$$\delta(t)^{*}R\{w(t)\} = R\{s(t)\} \tag{6.3}$$

where $\delta(t)$ is the Dirac delta function, and since $\delta(t)$ is the identity element for the convolution process, we get

$$R\{w(t)\} = R\{s(t)\} \tag{6.4}$$

Eq. (6.4) indicates that autocorrelation of the recorded seismogram can be used in lieu of

lieu = place

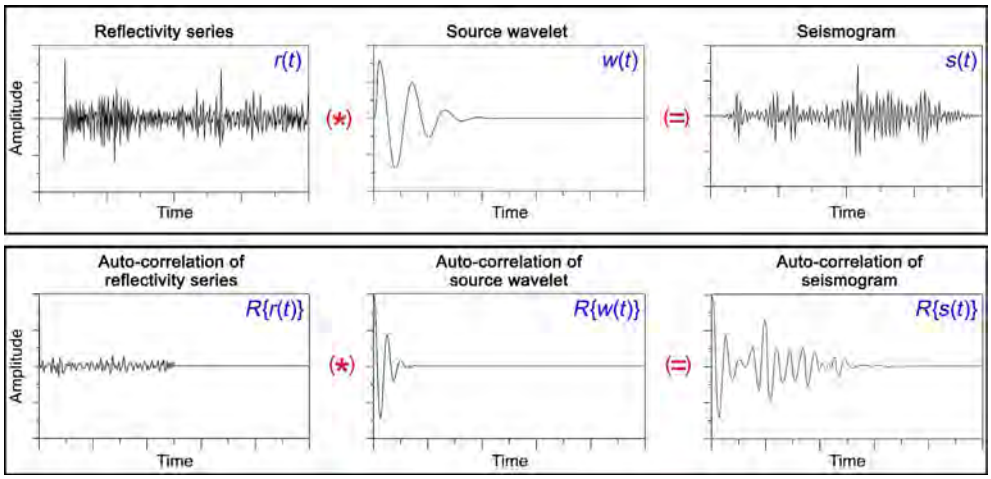


FIG. 6.9 Schematic display of the components for the convolutional model. Convolution of the source wavelet with the reflectivity series produces the seismogram (upper panel). The lower panel shows the corresponding autocorrelation traces. (*) and $R\{\}$ denote convolution and autocorrelation, respectively; $r(t)$ is reflectivity series, $w(t)$ is source wavelet, and $s(t)$ is recorded seismogram.

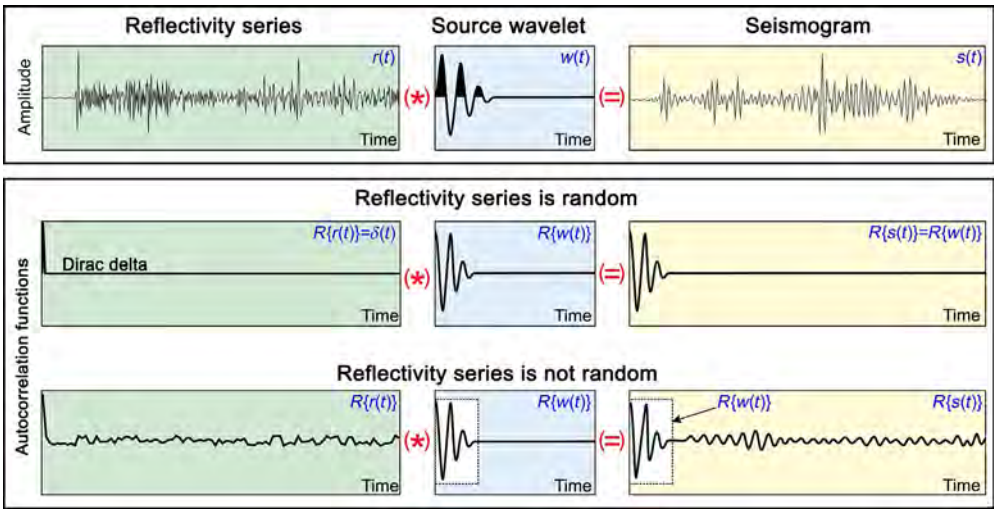


FIG. 6.10 Schematic display of the importance of Assumption 6. Components for the convolutional model to obtain the seismogram are shown in the upper panel. Autocorrelation of a random function is the Dirac delta ($\delta(t)$), and convolving it with the wavelet's autocorrelation yields again the wavelet's autocorrelation (middle panel) since $\delta(t)$ is the identity element for the convolution process. In this case, autocorrelation of the seismogram directly equals the autocorrelation of the wavelet. In reality, autocorrelation of the reflectivity series does not equal to $\delta(t)$, and therefore only the initial parts of the autocorrelation of the seismogram resemble the characteristics of the autocorrelation of the source wavelet (white section in lower panel). (*) and $R\{\}$ denote convolution and autocorrelation, respectively; $r(t)$ is reflectivity series, $w(t)$ is source wavelet, and $s(t)$ is recorded seismogram.

autocorrelation of the wavelet, providing that the reflectivity series is random. However, this is not the case in reality: autocorrelation of the reflectivity series does not equal to the Dirac delta because the earth's reflectivity series does not have the characteristics of a random series (lower panel in Fig. 6.10). Even though it has a maximum value at zero lag, it is actually nonzero at the remaining lags and has small amplitudes distributed along the whole axis, most of which arise from short and long path multiples. The autocorrelation of the seismogram obtained by convolving the autocorrelation of the wavelet with this function does not exactly equal to the autocorrelation of the source wavelet. In fact, only the initial part of this resultant autocorrelation function reflects the characteristics of the autocorrelation of the source wavelet (lower panel in Fig. 6.10).

In order to perform deconvolution, we definitely need Assumption 6 and it has key importance in the theoretical foundation of deconvolution, because it enables us to use the known autocorrelation function of the recorded seismogram instead of the unknown autocorrelation of the source wavelet as shown in Fig. 6.11. As a result of this assumption, an inverse filter or deconvolution operator can be obtained directly from the autocorrelation of the seismogram. For such a deconvolution procedure, we do not necessarily need to know the source waveform to obtain its autocorrelation for the deconvolution operator, and therefore Assumption 4 is no longer required.

Furthermore, the amplitude spectra of the recorded seismogram and the source wavelet display a general similarity (Fig. 6.12). According to the convolutional model, the

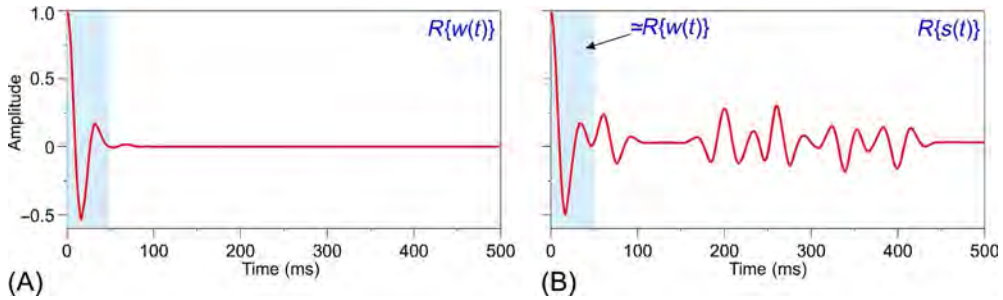


FIG. 6.11 Autocorrelation functions of (A) minimum phase wavelet $w(t)$, and (B) minimum phase seismogram $s(t)$. Autocorrelations of both source wavelet and seismogram show similar characteristics for the initial parts *(blue shaded areas)*.

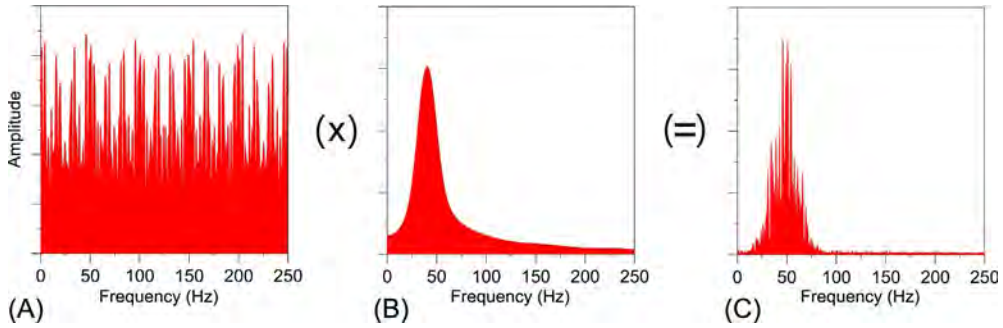


FIG. 6.12 Amplitude spectra of (A) reflectivity series, (B) source wavelet, and (C) recorded seismogram. The amplitude spectrum of the wavelet is quite similar to the smoothened version of the seismogram's amplitude spectrum.

amplitude spectrum of the seismogram equals the multiplication of the amplitude spectra of the source wavelet and earth's reflectivity series. In fact, the smoothened version of the seismogram's amplitude spectrum is almost the same as the wavelet's amplitude spectrum. This is actually the theoretical basis of a wavelet extraction method: compute the forward Fourier transform of the seismogram, smooth the amplitude spectrum, and take the inverse Fourier transform to obtain the wavelet embedded in the data in the time domain. In general, the overall shape of the seismogram's amplitude spectrum is formed by the source wavelet, and its rapidly fluctuating components originate from the reflectivity series (Fig. 6.12).

6.3 SPIKING DECONVOLUTION

Compressing the source wavelet into a zero-lag spike is termed spiking deconvolution, which aims to remove the effect of the source wavelet from the seismic data. According to the convolutional model, the remaining part for a noise-free environment is the earth's reflectivity series. The problem of spiking deconvolution is to find out the filter operator coefficients, known as the deconvolution operator, which remove the source wavelet from the data. The process is achieved by convolving the filter coefficients with the seismic trace in the time domain (Fig. 6.13). Spiking deconvolution can be done either as inverse filtering or as optimum Wiener filters, the latter using the least-squares

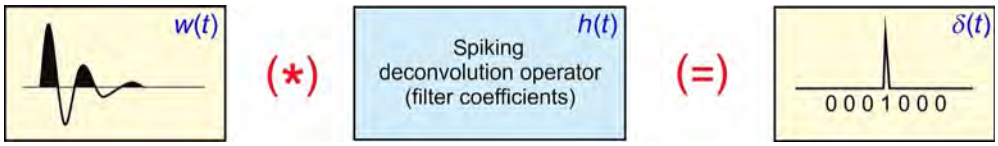


FIG. 6.13 Schematic illustration of spiking deconvolution in the time domain. The process is used to convert the minimum phase source wavelet $w(t)$ embedded in the seismic data into a zero-lag spike $\delta(t)$ by convolving the seismogram or input wavelet with the deconvolution operator $h(t)$. (*) denotes convolution.

approach to obtain the deconvolution operator. If the autocorrelation of the source wavelet is directly obtained from a known source waveform, then the process is termed deterministic deconvolution; otherwise, if it is obtained from the seismic trace itself, then a statistical deconvolution is performed. Inverse filtering is a deterministic approach and requires the source wavelet to be known. In most seismic surveys, normally the source waveform is not known and the considered deconvolution type is statistical, which is mathematically implemented using an optimum Wiener filtering approach.

6.3.1 Deconvolution With Inverse Filter

Inverse filtering is a deconvolution process performed using the inverse of a known source wavelet, and hence it is deterministic. An inverse filter operator $h(t)$ provides the earth's estimated reflectivity series $r(t)$ when convolved with the recorded seismogram $s(t)$, which is

$$r(t) = h(t)^* s(t) \tag{6.5}$$

Substituting Eq. (6.5) into the noise-free convolutional model in Eq. (6.1), we get

$$s(t) = w(t)^* r(t) = s(t) = w(t)^* h(t)^* s(t) \tag{6.6}$$

The point here is that this equality is valid only if

$$w(t)^* h(t) = \delta(t) \tag{6.7}$$

where $\delta(t)$ is the Dirac delta function. When we solve the deconvolution operator $h(t)$ from Eq. (6.7), we get

$$h(t) = \delta(t)^* \widetilde{w}(t) \tag{6.8}$$

where $\widetilde{w}(t)$ is the inverse of the input wavelet and is assumed to be known at this stage. Because $\delta(t)$ is the identity element for convolution, we finally get

$$h(t) = \widetilde{w}(t) \tag{6.9}$$

The deconvolution operator $h(t)$ obtained directly from the inverse of the input wavelet converts the wavelet into a spike at $t = 0$ (here, this spike is supposed to correspond to a reflection coefficient). Once we obtain the deconvolution operator by the inverse filtering approach, we can calculate the deconvolved trace by convolving the operator with the recorded seismic trace (Fig. 6.14) as

$$d(t) = h(t)^* s(t) \tag{6.10}$$

where $d(t)$ is the deconvolved output. This operation corresponds to a multiplication in the frequency domain: the amplitude spectrum of the recorded seismogram is multiplied by its inverse to obtain a flat amplitude spectrum (Fig. 6.15) as

$$D(\omega) = H(\omega) \times S(\omega) = 1 \tag{6.11}$$

where $D(\omega)$, $H(\omega)$, and $S(\omega)$ represent the amplitude spectra of deconvolved output, deconvolution operator, and input seismogram, respectively.

The inverse of the known source wavelet is not a simple mathematical division process; it can be calculated by a z transform (Section 4.7). For instance, if the minimum phase wavelet is $w(t) = (2, -1)$, its z transform is

$$w(z) = 2 - z$$

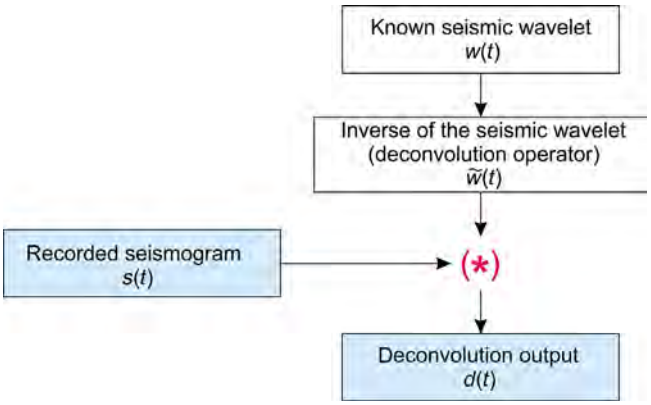


FIG. 6.14 Block diagram of spiking deconvolution application in the time domain by inverse filtering. (*) denotes convolution.

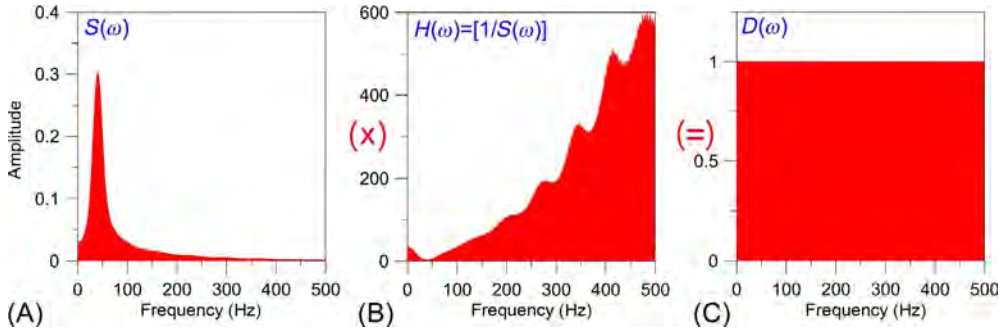


FIG. 6.15 Application of deconvolution with inverse filtering in the time domain corresponds to multiplication in the frequency domain. (A) Amplitude spectrum of the recorded seismogram, (B) inverse of (A), and (C) amplitude spectrum of deconvolved output.

The inverse of this wavelet $\tilde{w}(z)$ can then be obtained by a MacLaurin series expansion as a summation of an infinite number of terms

$$\tilde{w}(z) = \frac{1}{2-z} = \frac{1}{2} + \frac{1}{4}z + \frac{1}{8}z^2 + \frac{1}{16}z^3 + \frac{1}{32}z^4 + \cdots\cdots.$$

Here, the coefficients of the variable z (1/2, 1/4, 1/8, 1/16, 1/32,…) give the deconvolution operator $h(t)$. Even though the operator is of an infinite number of samples, they rapidly decay to zero, and in practice the number of samples in the operator is truncated. If we consider the first three terms $h(t) = (1/2, 1/4, 1/8)$ and convolve them with the input wavelet $w(t)=(2, -1)$, we get the deconvolved output shown in Table 6.2. Although the result is not a perfect spike, it is closer to a zero-lag spike than the input wavelet. If we continue attempts by considering the first four terms (1/2, 1/4, 1/8, 1/16) of the operator to determine whether we get a

TABLE 6.2 Deconvolution Output Obtained by Convolving the Input Minimum Phase Wavelet $w(t) = (2, -1)$ With the First Three Terms of the Inverse Filter Operator $h(t) = (1/2, 1/4, 1/8)$

		2	−1			Output
1/8	1/4	1/2				1
	1/8	1/4	1/2			0
		1/8	1/4	1/2		0
			1/8	1/4	1/2	−0.125

TABLE 6.3 Deconvolution Output Obtained by Convolving Input Minimum Phase Wavelet $w(t) = (2, -1)$ With the First Four Terms of the Inverse Filter Operator $h(t) = (1/2, 1/4, 1/8, 1/16)$

			2	**−1**				**Output**
1/16	1/8	1/4	1/2					1
	1/16	1/8	1/4	1/2				0
		1/16	1/8	1/4	1/2			0
			1/16	1/8	1/4	1/2		0
				1/16	1/8	1/4	1/2	−0.0625

better result, we obtain the output in Table 6.3, which is much closer to a spike. As the number of involved terms increases, the output approaches to an ideal spike. However, the resultant wavelet will never be an exact spike, because the operator must always be truncated to make a finite length time series.

The energy of the wavelet in these examples is front-loaded, that is, the wavelet is minimum phase, and therefore it has a stable and convergent inverse and the inverse filtering is successful in converting this wavelet into a spike. What if the wavelet is not minimum phase? If we consider a maximum phase wavelet w(t)=(−1, 2), its z transform is

$$w(z) = -1 + 2z$$

The inverse of this wavelet $\widetilde{w}(z)$ obtained again by a MacLaurin series expansion is

$$\widetilde{w}(z) = \frac{1}{-1+2z} = -1 - 2z - 4z^2 - 8z^3 - 16z^4 + \cdots\cdots.$$

The coefficients of variable z (−1, −2, −4, −8, −16,…) provide the deconvolution operator $h(t)$. However, this time we get a divergent series of an infinite number of samples. When we convolve them with the input wavelet $w(t)$=(−1, 2) after truncating to use the first three terms $h(t)$= (−1, −2, −4), we get the deconvolved output shown in Table 6.4. The result is quite different from an ideal spike, even though it is less spiky than the input. Furthermore, incorporating the higher filter coefficients of the operator into the deconvolution process, such as the first four terms, makes the output much more unfavorable (Table 6.5). The reason for this is that the filter coefficient values increase with time, and if we apply them to the input after truncation, larger terms are excluded since it is a divergent

TABLE 6.4 Deconvolution Output Obtained by Convolving Maximum Phase Input Wavelet $w(t) = (-1, 2)$ With First Three Terms $h(t) = (-1, -2, -4)$ of the Inverse Filter Operator

		−1	**2**			**Output**
−4	−2	−1				1
	−4	−2	−1			0
		−4	−2	−1		0
			−4	−2	−1	−8

TABLE 6.5 Deconvolution Output Obtained by Convolving Maximum Phase Input Wavelet $w(t) = (-1, 2)$ With First Four Terms $h(t) = (-1, -2, -4, -8)$ of the Inverse Filter Operator

			−1	**2**				**Output**
−8	−4	−2	−1					1
	−8	−4	−2	−1				0
		−8	−4	−2	−1			0
			−8	−4	−2	−1		0
				−8	−4	−2	−1	−16

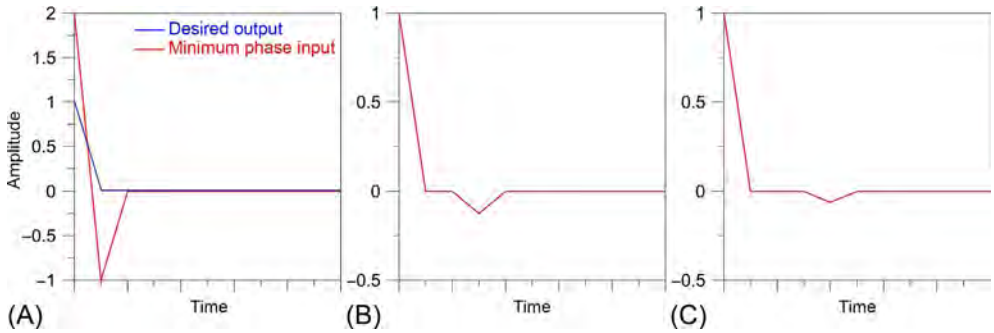


FIG. 6.16 Comparison of the performance of inverse filtering in spiking deconvolution for a minimum phase source wavelet. (A) Input wavelet $w(t) = (2, -1)$ with the desired zero lag spike output, and its inverse filter outputs using deconvolution operators (B) $h(t) = (1/2, 1/4, 1/8)$, (C) $h(t) = (1/2, 1/4, 1/8, 1/16)$.

series. Because the wavelet is not minimum phase, its energy is not front-loaded and Assumption 5 is violated. Therefore, increasing the number of terms will not provide a further improvement in the deconvolution output. Comparisons of the results of deconvolution with inverse filtering for the minimum phase and maximum phase source wavelets are shown in Figs. 6.16 and 6.17.

6.3.2 Inverse Filtering With Least Squares

A better result in converting a source wavelet into a spike can be obtained by incorporating the least-squares approximation in the calculation of the deconvolution operator. Recalling the same example as in inverse filtering, the least-squares problem can be described in such a way that one can find a two-term filter series of (a, b) so that, after application to the minimum phase input wavelet $w(t)=(2, -1)$, the error between desired output $(1, 0, 0)$ and actual output is minimum by means of the least-squares approach. In order to obtain filter coefficients (a, b), we convolve these filter coefficients $h(t) = (a, b)$ with input wavelet $w(t) = (2, -1)$. The output is given in Table 6.6.

Cumulative error energy E is defined as the sum of the squares of the differences between actual and desired outputs, and according to the results in Table 6.6, we get

$$E = [(2a) - 1]^2 + [(2b - a) - 0]^2 + [(-b) - 0]^2 \tag{6.12}$$

Now the purpose is to determine the optimum coefficients (a, b) that minimize the cumulative error energy E. By means of a least-squares approximation, taking the partial derivatives of E with respect to a and b, and setting them to zero, we get two equations with two unknowns as

$$\begin{aligned} \frac{\partial E}{\partial a} &= 10a - 4b - 4 = 0 \quad \Rightarrow 5a - 2b = 2 \\ \frac{\partial E}{\partial b} &= 10b - 4a = 0 \quad \Rightarrow -2a + 5b = 0 \end{aligned} \tag{6.13}$$

When we rearrange these equations into a matrix form, and solve them for a and b coefficients, we get

$$\begin{bmatrix} 5 & -2 \\ -2 & 5 \end{bmatrix} \begin{bmatrix} a \\ b \end{bmatrix} = \begin{bmatrix} 2 \\ 0 \end{bmatrix} \tag{6.14}$$

$$a = \frac{10}{21} \quad \text{and} \quad b = \frac{4}{21}$$

Convolving these coefficients with input wavelet $w(t) = (2, -1)$ to obtain the deconvolved output, we get the result given in Table 6.7, which is

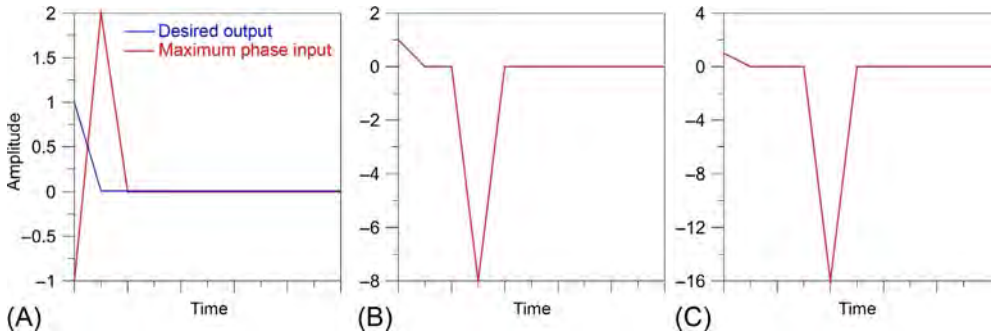


FIG. 6.17 Comparison of the performance of inverse filtering in spiking deconvolution for a maximum phase wavelet. (A) Input wavelet $w(t) = (-1, 2)$ with the desired zero lag spike output, and its inverse filter outputs using deconvolution operators (B) $h(t) = (-1, -2, -4)$, (C) $h(t) = (-1, -2, -4, -8)$.

TABLE 6.6 Convolution of Minimum Phase Input Wavelet $w(t) = (2, -1)$ with a Two-Term Deconvolution Operator $h(t) = (a, b)$

	2	−1		Actual Output	Desired Output
b	a			2a	1
	b	a		2b − a	0
		b	a	−b	0

Desired output is a zero-lag spike (1, 0, 0).

TABLE 6.7 Deconvolution Output by Convolving Minimum Phase Input Wavelet $w(t) = (2, -1)$ With Filter Coefficients $h(t) = (10/21, 4/21)$ Obtained by a Least Squares Approximation

	2	−1		Actual Output
4/21	10/21			0.95
	4/21	10/21		−0.095
		4/21	10/21	−0.19

much closer to a zero-lag spike than the result obtained by inverse filtering.

A least-squares approximation in inverse filtering produces a suitable result in converting a minimum phase input into a zero-lag spike. What if the input wavelet is not minimum phase? We can perform the same analysis using the maximum phase wavelet $w(t) = (-1, 2)$ on

TABLE 6.8 Convolution of Maximum Phase Input Wavelet $w(t) = (-1, 2)$ with a Two-Term Deconvolution Operator $h(t) = (a, b)$

	−1	2		Actual Output	Desired Output
b	*a*			$-a$	1
	b	*a*		$-b+2a$	0
		b	*a*	$2b$	0

Desired output is a zero-lag spike (1, 0, 0).

which the inverse filter produces unacceptable results. After convolving the filter coefficients $h(t) = (a, b)$ with the input maximum phase wavelet $w(t) = (-1, 2)$, the actual output is shown in Table 6.8.

The cumulative error energy E based on the results in Table 6.8 is

$$E = [(-a) - 1]^2 + [(-b + 2a) - 0]^2 + [(2b) - 0]^2 \tag{6.15}$$

By taking the partial derivatives of error energy E with respect to a and b, and setting them to zero, we get

$$\begin{aligned} \frac{\partial E}{\partial a} &= 10a - 4b + 2 = 0 \quad \Rightarrow 5a - 2b = -1 \\ \frac{\partial E}{\partial b} &= 10b - 4a = 0 \quad\quad\;\; \Rightarrow -2a + 5b = 0 \end{aligned} \tag{6.16}$$

Rearranging Eq. (6.16) into a matrix form, and solving it for filter coefficients a and b, we obtain

$$\begin{bmatrix} 5 & -2 \\ -2 & 5 \end{bmatrix} \begin{bmatrix} a \\ b \end{bmatrix} = \begin{bmatrix} -1 \\ 0 \end{bmatrix} \tag{6.17}$$

$$a = -\frac{5}{21} \quad \text{and} \quad b = -\frac{2}{21}$$

Convolving these coefficients with the input wavelet $w(t) = (-1, 2)$ to obtain the deconvolved output, we obtain the results in Table 6.9. Although the deconvolved output is closer to a spike as compared to the inverse filter output for the maximum phase wavelet, it does not match the desired deconvolution output because of the violation of Assumption 5. The results of the deconvolution with a least-squares approximation for minimum and maximum phase wavelets are compared in Fig. 6.18.

TABLE 6.9 Deconvolution Output by Convolving Maximum Phase Input Wavelet $w(t) = (-1, 2)$ With Filter Coefficients $h(t) = (-5/21, -2/21)$ Obtained by a Least-Squares Approximation

	−1	2		Actual Output
−2/21	−5/21			0.238
	−2/21	−5/21		−0.38
		−2/21	−5/21	−0.19

As a result, the spiking deconvolution operator is exactly the inverse of the input source wavelet. If the wavelet is of minimum phase and its energy is front-loaded, then it has a stable inverse. Its inverse is also minimum phase because its coefficients constitute a convergent series so that the energy of the wavelet inverse is also front-loaded. This inverse is used as a stable filter operator for the deconvolution process. On the other hand, if the wavelet is of maximum or mixed phase, then it has an unstable inverse which is not favorable to use as a spiking deconvolution operator.

6.3.3 Optimum Wiener Filters

Recalling Eq. (6.14) to convert minimum phase input wavelet $w(t) = (2, -1)$ into a zero-lag spike (1, 0, 0), we observe that the lefthand side of Eq. (6.14) consists of autocorrelation of the input wavelet (Table 6.10), while the righthand side is composed of cross-correlation of the desired output and input wavelet (Table 6.11).

For an operator consisting of n terms, we get the following general equation system for

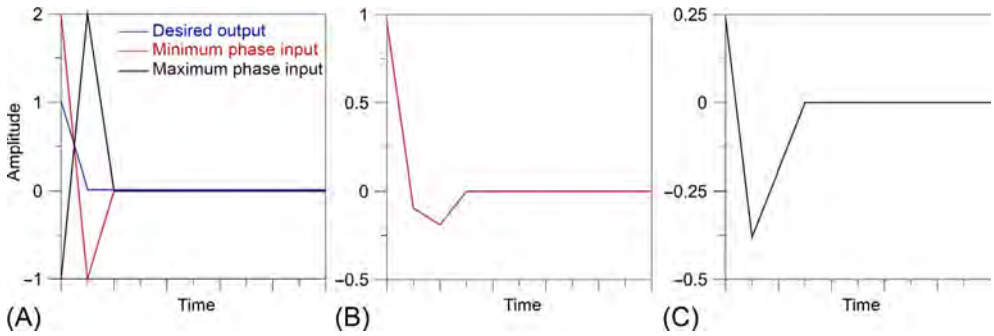


FIG. 6.18 Comparison of the performance of inverse filtering with a least-squares approximation. (A) Input minimum phase $w(t) = (2, -1)$ and maximum phase $w(t) = (-1, 2)$ wavelets with desired zero-lag spike output. Least-squares inverse filter outputs for (B) minimum phase wavelet with deconvolution operator $h(t) = (10/21, 4/21)$, and (C) maximum phase wavelet with deconvolution operator $h(t) = (-5/21, -2/21)$.

TABLE 6.10 Autocorrelation of the Input Wavelet $w(t) = (2, -1)$

2	−1		Output
2	−1		5
	2	−1	−2

TABLE 6.11 Cross-Correlation of the Desired Output (1, 0, 0) and Input Wavelet $w(t) = (2, -1)$

1	0	0		Output
2	−1			2
	2	−1		0
		2	−1	0

the deconvolution operator (Peacock and Treitel, 1969)

$$\begin{bmatrix} a_0 & a_1 & a_2 & \dots & a_{n-1} \\ a_1 & a_0 & a_1 & \dots & a_{n-2} \\ a_2 & a_1 & a_0 & \dots & a_{n-3} \\ . & . & . & \dots & . \\ . & . & . & \dots & . \\ . & . & . & \dots & . \\ a_{n-1} & a_{n-2} & a_{n-3} & \dots & a_0 \end{bmatrix} \begin{bmatrix} h_0 \\ h_1 \\ h_2 \\ . \\ . \\ . \\ h_{n-1} \end{bmatrix} = \begin{bmatrix} c_0 \\ c_1 \\ c_2 \\ . \\ . \\ . \\ c_{n-1} \end{bmatrix} \tag{6.18}$$

where a_i is autocorrelation of the input wavelet, h_i is the filter coefficients (deconvolution operator) to be solved, and c_i is the cross-correlation of the desired output and input wavelet. The expression in Eq. (6.18) is known as the normal equations (Robinson and Treitel, 1967). This symmetrical autocorrelation matrix is termed the Toeplitz matrix, and it can be solved by a Levinson algorithm. In practice, the algorithms based on Wiener filter theory are known as Wiener-Levinson algorithms. The deconvolution operator is obtained by solving Eq. (6.18) for filter coefficients h_i, and then the deconvolution is performed by convolving the filter coefficients with the input seismic trace as schematically shown in Fig. 6.19. The issue here is how to find the autocorrelation of the seismic wavelet. As explained in Section 6.2.6, if the reflectivity series is random, the autocorrelation of the seismic wavelet can be obtained from the recorded seismic trace itself (Assumption 6). That is, the initial parts of the autocorrelation of the seismogram resemble the characteristics of the autocorrelation of the source wavelet, and these parts can be used to set the normal equations in Eq. (6.18). In practice, the time duration along which the autocorrelation of the seismogram approximately corresponds to the autocorrelation of the source wavelet is an important processing parameter termed the operator length, and it must be properly chosen for a suitable deconvolution application. Determination of optimum operator length from the autocorrelation of the recorded seismogram and practical analysis of different examples will be discussed in Section 6.5.

Wiener filters are optimal by means of a least-squares approach, such that the least-squares error between the desired and actual outputs is minimal. These filters can further be designed for any sort of output shape, such as zero-lag spike, a time-shifted version of the input (predictive deconvolution), a spike with an arbitrary time delay, or a zero phase wavelet (Yılmaz, 2001). As a specific case, if the desired output is a zero-lag spike as (1, 0, 0, 0,…), the Wiener filter is equivalent to a least-squares inverse filter.

Normal equations can be generalized for Wiener spiking deconvolution: cross-correlation of the desired output (1, 0, 0,…) and input wavelet (w_0, w_1, w_2, …, w_{n-1}) generates a series of (w_0, 0, 0,…). Hence, we obtain the normal equations normalized with $1/w_0$ as

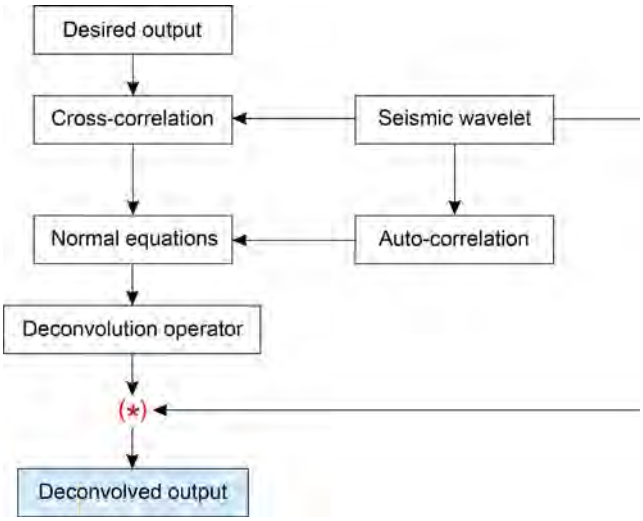


FIG. 6.19 Schematic illustration of calculation and application of deconvolution with optimum Wiener filters. (*) denotes convolution.

$$\begin{bmatrix} a_0 & a_1 & a_2 & \dots & a_{n-1} \\ a_1 & a_0 & a_1 & \dots & a_{n-2} \\ a_2 & a_1 & a_0 & \dots & a_{n-3} \\ . & . & . & \dots & . \\ . & . & . & \dots & . \\ . & . & . & \dots & . \\ a_{n-1} & a_{n-2} & a_{n-3} & \dots & a_0 \end{bmatrix} \begin{bmatrix} h_0 \\ h_1 \\ h_2 \\ . \\ . \\ . \\ h_{n-1} \end{bmatrix} = \begin{bmatrix} 1 \\ 0 \\ 0 \\ . \\ . \\ . \\ 0 \end{bmatrix} \tag{6.19}$$

In fact, Wiener spiking deconvolution mathematically equals to least-squares inverse filtering. The difference between them is that a known source wavelet is used in the calculation of the autocorrelation matrix of normal equations in the case of least-squares inverse filtering (implying a deterministic deconvolution), whereas this matrix is obtained from the seismic trace itself in the case of Wiener spiking deconvolution (implying a statistical deconvolution). The amplitude spectrum of the Wiener spiking deconvolution operator is approximately the inverse of the amplitude spectrum of the source wavelet. This type of deconvolution can also be used to derive the minimum phase equivalent of a mixed, maximum or zero phase wavelet. The method to calculate the minimum phase equivalent of a wavelet is to compute the inverse of its spiking deconvolution operator (Yılmaz, 2001).

Fig. 6.20 shows an application of statistical and deterministic Wiener spiking deconvolution to a synthetic seismic trace consisting of a minimum phase wavelet. Although deterministic deconvolution produces almost perfect results, as expected (Fig. 6.20C), it has very limited application in seismic exploration because it requires the source waveform to be known. Statistical deconvolution today is a common technique in seismic processing and it produces satisfactory results, even if the source wavelet is not known, providing that the seismogram is composed of a minimum phase wavelet (Fig. 6.20D). A similar analysis is shown in Fig. 6.21, this time for a seismogram composed of a mixed phase wavelet. For both statistical and deterministic approaches, Wiener spiking deconvolution yields unacceptable results for mixed phase wavelets.

As a result, if the source waveform is not minimum phase, spiking deconvolution cannot convert it into a zero-lag spike. For instance, wavelet $w(t)=(-1, 2)$ cannot be converted into a zero-lag spike (1, 0, 0) by spiking

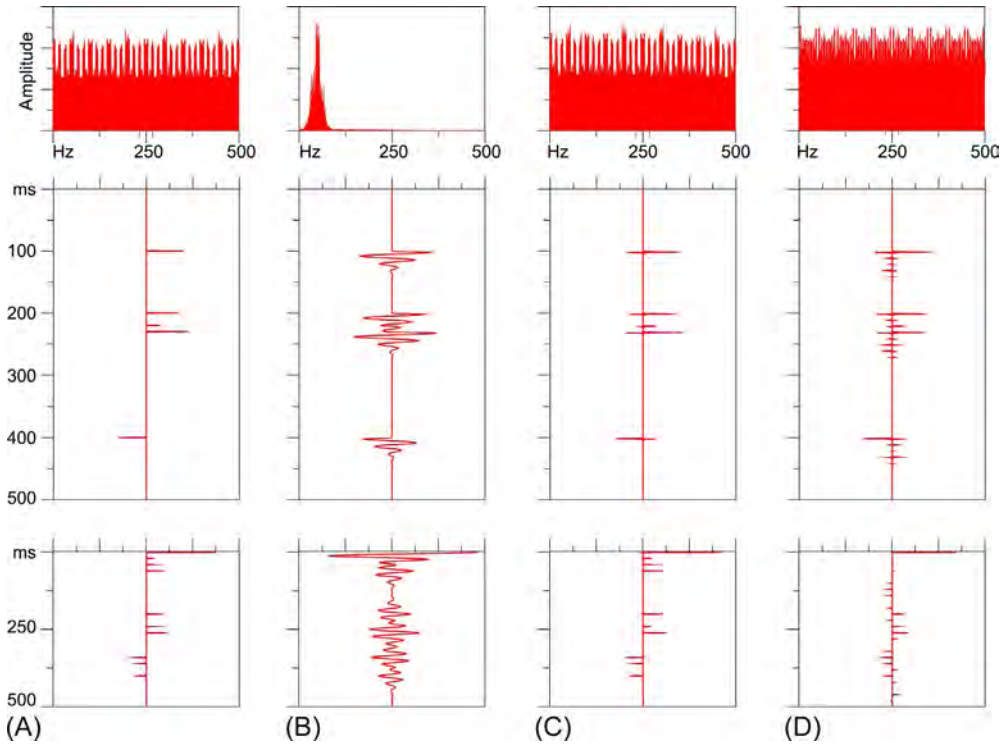


FIG. 6.20 Application of Wiener spiking deconvolution to a minimum phase synthetic trace. (A) Reflectivity series, (B) minimum phase seismogram, (C) deterministic, and (D) statistical deconvolution results. Corresponding amplitude spectra and autocorrelograms are given in the top and bottom panels, respectively.

deconvolution because its energy distribution is more appropriate for a delayed spike, such as (0, 1, 0). For this reason, mixed or maximum phase wavelets can be converted into delayed spikes instead of zero-lag spikes. If the desired output is an arbitrary shape, applied deconvolution is termed wavelet shaping (Section 6.8). In seismic data processing, shaping filters are commonly applied to convert the input wavelet into delayed spikes, or convert the source wavelets into zero phase wavelets. In general, the optimum delay is zero if the input is minimum phase, while it generally equals the length of the wavelet for maximum phase.

Minimum phase spiking deconvolution can also be implemented in the frequency domain, which produces the same results as Wiener spiking deconvolution in the time domain. As a specific case, if only the amplitude spectrum is whitened, it is termed zero phase frequency domain deconvolution, and if applied through different time gates along the time axis, it is actually equivalent to time variant spectral whitening (Section 12.4). Since we assume that the reflectivity is random, based on Assumption 6, the general shape of the spectrum of the recorded seismogram is formed by the wavelet, not the earth's reflectivity series, and therefore the shape of the source wavelet's amplitude spectrum can be estimated from the smoothed version of the spectrum of the recorded seismogram. At this stage, the unknown wavelet phase is assumed to be minimum.

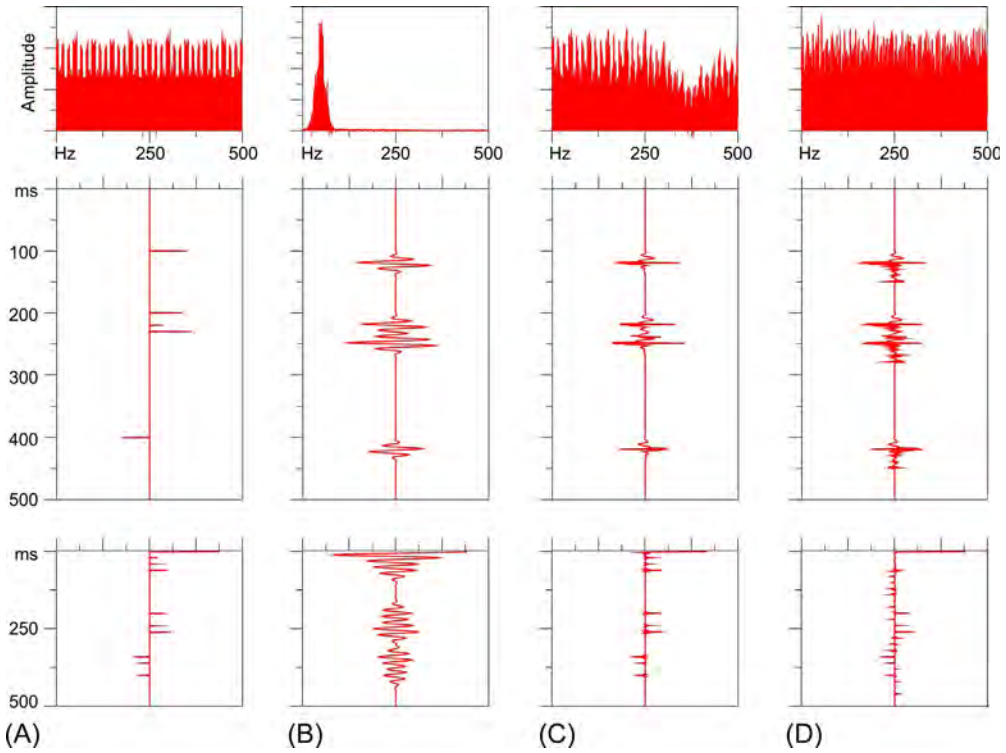


FIG. 6.21 Application of Wiener spiking deconvolution to a mixed phase synthetic trace. (A) Reflectivity series, (B) mixed phase seismogram, (C) deterministic, and (D) statistical deconvolution results. Corresponding amplitude spectra and autocorrelograms are given in the top and bottom panels, respectively.

6.3.4 Prewhitening

The amplitude spectrum of the spiking deconvolution operator approximately equals the inverse of the input wavelet's amplitude spectrum. The convolution process in the time domain during the deconvolution becomes multiplication of the corresponding amplitude spectra in the frequency domain, so that the spectrum of the deconvolution output is exactly a white spectrum, including amplitudes along the whole available frequency band. If zeroes or extremely small amplitudes close to zero exist in the wavelet's amplitude spectrum (Fig. 6.22A), this causes enormous amplitude bursts in the inverse spectrum (Fig. 6.22B). These bursts may produce unstable deconvolution results in the time domain, because the deconvolution process also tries to boost extremely small amplitudes.

Zeroes or notches in the amplitude spectrum rarely occur since random noise amplitudes always exist and are incorporated into the data, in both the time and frequency domains (Yılmaz, 1987). However, a small amount of white noise is added onto the amplitude spectrum (Fig. 6.22C) to prevent enormous amplitude values for computational stability (Fig. 6.22D). This process is termed prewhitening and can be applied by adding a constant value to the zero-lag value of the

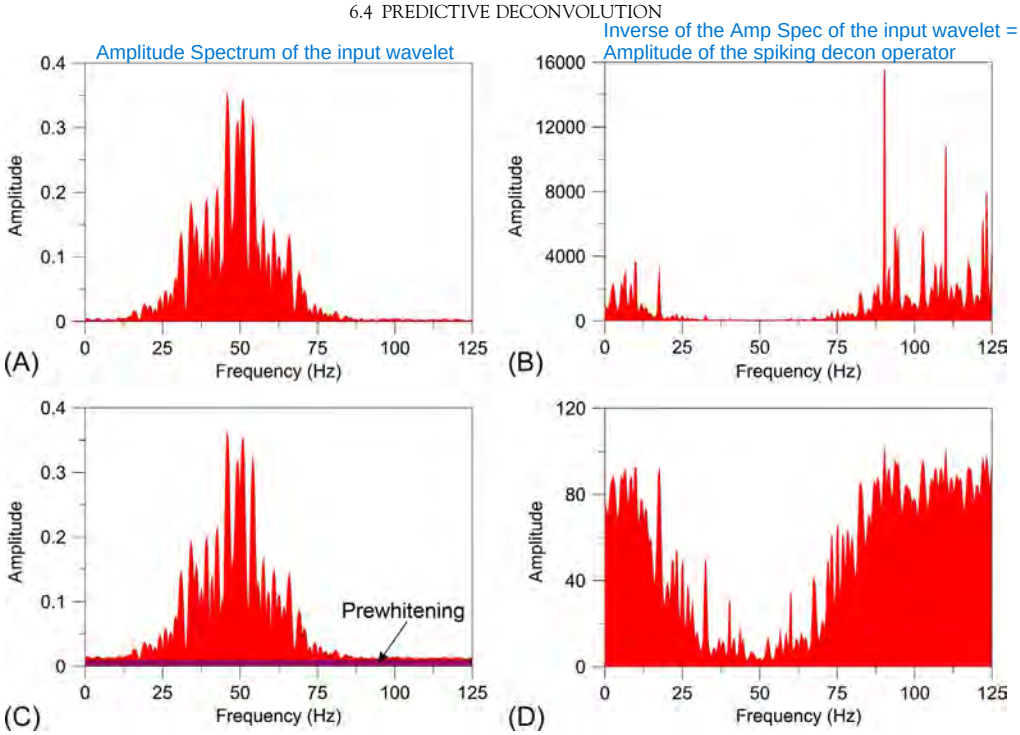


FIG. 6.22 (A) An example amplitude spectrum of a seismogram, (B) inverse of the spectrum in (A) with enormous amplitude bursts because of the extremely small amplitudes in (A). (C) A small amount of white noise *(shaded zone)* is added to the amplitude spectrum in (A) for computational stability which is termed prewhitening, (D) inverse of the prewhitened spectrum in (C).

autocorrelation function of the seismogram, or to the diagonal elements of a Toeplitz matrix. In practice, a constant value between 0.1% and 1.0% produces satisfactory results.

6.4 PREDICTIVE DECONVOLUTION

Predictive deconvolution is used to obtain a time-advanced version of the input trace and consists of a prediction process. A time-advanced version of an $f(t)$ series, which is $f(t+\alpha)$, is predicted, where α is called the prediction lag. $f(t+\alpha)$ can be obtained by a specific design of normal equations given in Eq. (6.18). Let's consider a six-term f_i series ($i = 0, 1, 2, 3, 4, 5$), and let α be 3. Autocorrelation of the f_i series, and cross-correlation of the desired output $f(t+\alpha)$ and $f(t)$ for $\alpha = 3$ are shown in Tables 6.12 and 6.13, respectively.

When we compare Tables 6.12 and 6.13, we observe that $c_i = a_{i+\alpha}$, and the normal equations for $\alpha = 3$ can be rearranged to get

$$\begin{bmatrix} a_0 & a_1 & a_2 & a_3 & a_4 & a_5 \\ a_1 & a_0 & a_1 & a_2 & a_3 & a_4 \\ a_2 & a_1 & a_0 & a_1 & a_2 & a_3 \\ a_3 & a_2 & a_1 & a_0 & a_1 & a_2 \\ a_4 & a_3 & a_2 & a_1 & a_0 & a_1 \\ a_5 & a_4 & a_3 & a_2 & a_1 & a_0 \end{bmatrix} \begin{bmatrix} h_0 \\ h_1 \\ h_2 \\ h_3 \\ h_4 \\ h_5 \end{bmatrix} = \begin{bmatrix} a_3 \\ a_4 \\ a_5 \\ a_6 \\ a_7 \\ a_8 \end{bmatrix} \tag{6.20}$$

TABLE 6.12 Autocorrelation of an Arbitrary f_i Series ($i = 0, 1, 2, 3, 4, 5$)

f_0	f_1	f_2	f_3	f_4	f_5							Output
f_0	f_1	f_2	f_3	f_4	f_5							$a_0 = f_0^2 + f_1^2 + f_2^2 + f_3^2 + f_4^2 + f_5^2$
	f_0	f_1	f_2	f_3	f_4	f_5						$a_1 = f_0f_1 + f_1f_2 + f_2f_3 + f_3f_4 + f_4f_5$
		f_0	f_1	f_2	f_3	f_4	f_5					$a_2 = f_0f_2 + f_1f_3 + f_2f_4 + f_3f_5$
			f_0	f_1	f_2	f_3	f_4	f_5				$a_3 = f_0f_3 + f_1f_4 + f_2f_5$
				f_0	f_1	f_2	f_3	f_4	f_5			$a_4 = f_0f_4 + f_1f_5$
					f_0	f_1	f_2	f_3	f_4	f_5		$a_5 = f_0f_5$
						f_0	f_1	f_2	f_3	f_4	f_5	$a_6 = 0$
							f_0	f_1	f_2	f_3	f_4	$a_7 = 0$
								f_0	f_1	f_2	f_3	$a_8 = 0$

TABLE 6.13 Cross-Correlation of Desired Output $f(t + \alpha)$ and $f(t)$ for $\alpha = 3$

f_3	f_4	f_5									Output
f_0	f_1	f_2	f_3	f_4	f_5						$c_0 = f_0f_3 + f_1f_4 + f_2f_5$
	f_0	f_1	f_2	f_3	f_4	f_5					$c_1 = f_0f_4 + f_1f_5$
		f_0	f_1	f_2	f_3	f_4	f_5				$c_2 = f_0f_5$
			f_0	f_1	f_2	f_3	f_4	f_5			$c_3 = 0$
				f_0	f_1	f_2	f_3	f_4	f_5		$c_4 = 0$
					f_0	f_1	f_2	f_3	f_4	f_5	$c_5 = 0$

TABLE 6.14 The Actual Deconvolution Output Obtained by Convolving h_i Filter Coefficients With Input f_i Series

					f_0	f_1	f_2	f_3	f_4	f_5	Deconvolution output
h_5	h_4	h_3	h_2	h_1	h_0						$d_0 = h_0f_0$
	h_5	h_4	h_3	h_2	h_1	h_0					$d_1 = h_1f_0 + h_0f_1$
		h_5	h_4	h_3	h_2	h_1	h_0				$d_2 = h_2f_0 + h_1f_1 + h_0f_2$
			h_5	h_4	h_3	h_2	h_1	h_0			$d_3 = h_3f_0 + h_2f_1 + h_1f_2 + h_0f_3$
				h_5	h_4	h_3	h_2	h_1	h_0		$d_4 = h_4f_0 + h_3f_1 + h_2f_2 + h_1f_3 + h_0f_4$
					h_5	h_4	h_3	h_2	h_1	h_0	$d_5 = h_5f_0 + h_4f_1 + h_3f_2 + h_2f_3 + h_1f_4 + h_0f_5$
						h_5	h_4	h_3	h_2	h_1	$d_6 = h_5f_1 + h_4f_2 + h_3f_3 + h_2f_4 + h_1f_5$
							h_5	h_4	h_3	h_2	$d_7 = h_5f_2 + h_4f_3 + h_3f_4 + h_2f_5$
								h_5	h_4	h_3	$d_8 = h_5f_3 + h_4f_4 + h_3f_5$
									h_5	h_4	$d_9 = h_5f_4 + h_4f_5$
										h_5	$d_{10} = h_5f_5$

The term on the righthand side of Eq. (6.20) is the α units advanced version of the autocorrelation function. The actual predictive deconvolution output calculated by convolving the h_i coefficients with the f_i input series is given in Table 6.14. The output is a prediction of the input f_i series for $\alpha = 3$ units. Here, the (h_0, h_1, h_2, h_3, h_4, h_5) series is termed a prediction filter, which yields the predictable components in the seismic trace corresponding to multiple reflections, whereas the (1, 0, 0, $-h_0$, $-h_1$, $-h_2$, $-h_3$, $-h_4$) series is known as a prediction error filter, which yields the error in the prediction process corresponding to primary reflections.

In a generalized form, the normal equations for prediction lag of α and prediction filter length of n can be rewritten as (Peacock and Treitel, 1969)

$$\begin{bmatrix} a_0 & a_1 & a_2 & \dots & a_{n-1} \\ a_1 & a_0 & a_1 & \dots & a_{n-2} \\ a_2 & a_1 & a_0 & \dots & a_{n-3} \\ . & . & . & \dots & . \\ . & . & . & \dots & . \\ . & . & . & \dots & . \\ a_{n-1} & a_{n-2} & a_{n-3} & \dots & a_0 \end{bmatrix} \begin{bmatrix} h_0 \\ h_1 \\ h_2 \\ . \\ . \\ . \\ h_{n-1} \end{bmatrix} = \begin{bmatrix} a_\alpha \\ a_{\alpha+1} \\ a_{\alpha+2} \\ . \\ . \\ . \\ a_{\alpha+n-1} \end{bmatrix} \tag{6.21}$$

The design of a prediction filter needs only the autocorrelation of the input. According to Assumption 6, the reflectivity series is random, and therefore everything in the seismic data (such as primary reflections) except the multiples cannot be predicted. In fact, a predictive deconvolution is a general technique that also involves the spiking deconvolution.

In summary, a prediction error filter shortens the input wavelet with a length of ($n + \alpha$) into an output wavelet with a length of α. Therefore, predictive deconvolution is a general approach that can control how shortened the wavelet is, and thus it also controls the improvement in the temporal resolution (Peacock and Treitel, 1969). For $\alpha =$ unity (the sampling rate), the process is equivalent to a spiking deconvolution.

In general, predictive deconvolution has two applications:

i. Application for a spiking deconvolution using a unit (or close to unit) prediction lag: used for temporal resolution improvement.
ii. Prediction of the input trace in a future time period defined by the prediction lag: used to predict and suppress multiples.

The effects of the spiking and predictive deconvolution approaches on the whitening of the amplitude spectrum, and hence improving the resolution of the seismic data, are different. In Fig. 6.23, a stack section without deconvolution is compared to its versions with spiking and predictive deconvolution applications, along with their corresponding amplitude spectra and autocorrelograms. In general, spiking deconvolution strengthens the high-frequency components in the seismic data and provides a higher resolution output.

6.5 DETERMINATION OF DECONVOLUTION PARAMETERS

Before digital seismic recording, the aim of prestack deconvolution applied to marine seismic data was to remove the multiple reflections rather than enhance the resolution. In practice, deconvolution is applied to prestack marine seismic data on a trace-by-trace basis on the shot or CDP gathers. Since deconvolution is very sensitive to the noise, data must be properly preconditioned to remove the random and coherent noise during preprocessing.

Before the application, the parameters that should be properly designated are the deconvolution operator length and prediction lag. In fact, there is no exact mathematical rule that restricts the prediction lag and/or operator length, and these are commonly determined by several tests based on user experience with the autocorrelograms of seismic traces. In addition, the

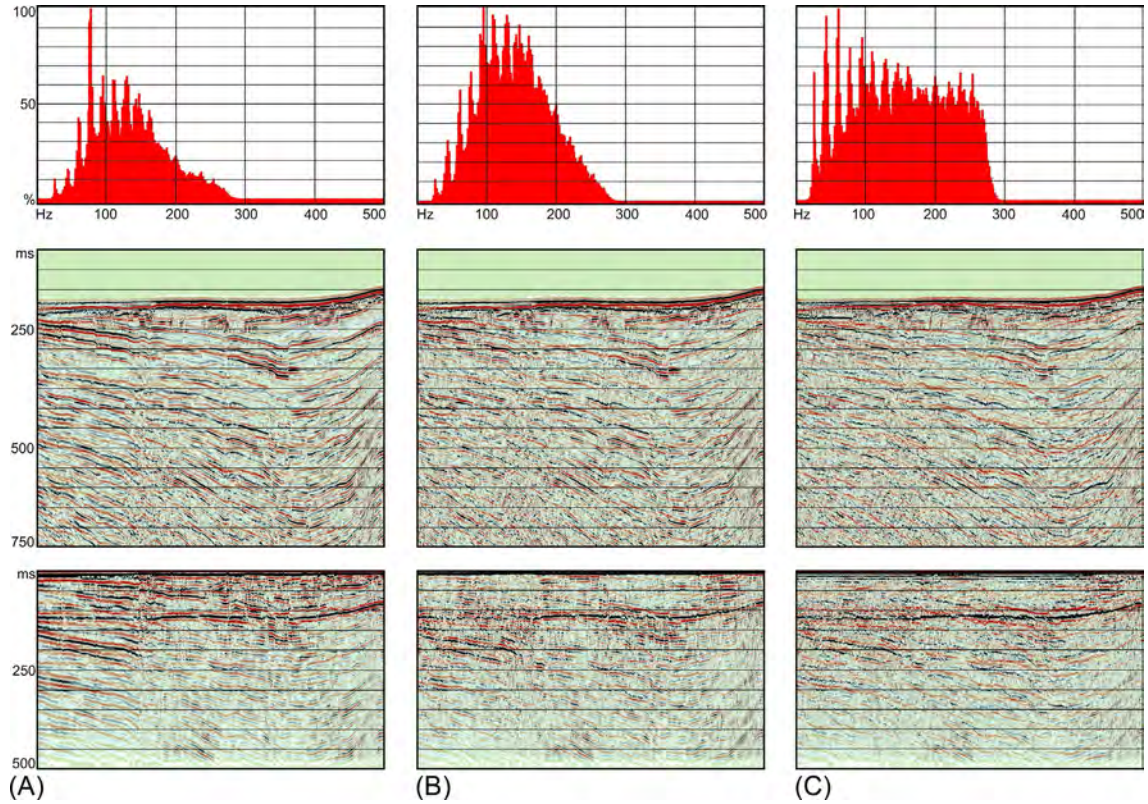


FIG. 6.23 Comparison of stack sections (A) without deconvolution, (B) with predictive deconvolution ($n = 80$ ms and $\alpha = 12$ ms), and (C) with spiking deconvolution ($n = 80$ ms), and their corresponding mean amplitude spectra (top) and autocorrelograms (bottom).

autocorrelation time gate and deconvolution design gate must be suitably defined.

6.5.1 Autocorrelation Time Gate

Autocorrelation of the input seismic trace provides substantial information used to determine the deconvolution parameters and to evaluate the quality of deconvolution outputs. Analyzing the autocorrelation function, recurring events, such as long- or short-period reverberations, in the seismic data can be determined. Long-period reverberations appear as isolated amplitude packages in the autocorrelation series, and, in ideal conditions, it is separated from other amplitudes with an amplitude-free zone. Fig. 6.24 shows an example brute stack section from a shallow continental shelf and its autocorrelation section. Since 1500 m/s water velocity is used in NMO correction during the preparation of the brute stack, multiple reflections are quite distinct both on the brute stack and autocorrelation sections.

The autocorrelation time gate corresponds to the window over which the autocorrelations of the traces are calculated. It is selected from the zones of usable reflections and the noisy areas should be avoided. On the shot gathers, the gate generally starts just above the seafloor reflection and typically has a length of 500–1000 ms. Length of the autocorrelation gate is another aspect and its effects are illustrated on the shot gather and its autocorrelograms in Fig. 6.25. If the gate is too short, it may not be possible to determine the length of the first transient zone on the autocorrelograms (Fig. 6.25B). The time

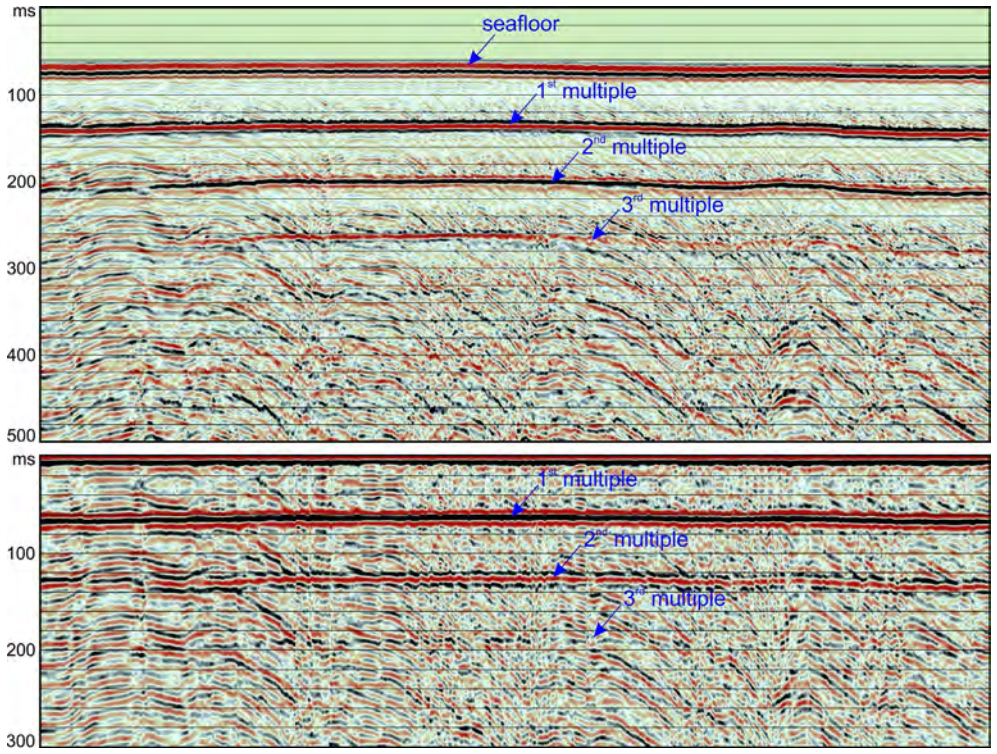


FIG. 6.24 A shallow brute stack section (top) with several seafloor multiples and its autocorrelation traces (bottom).

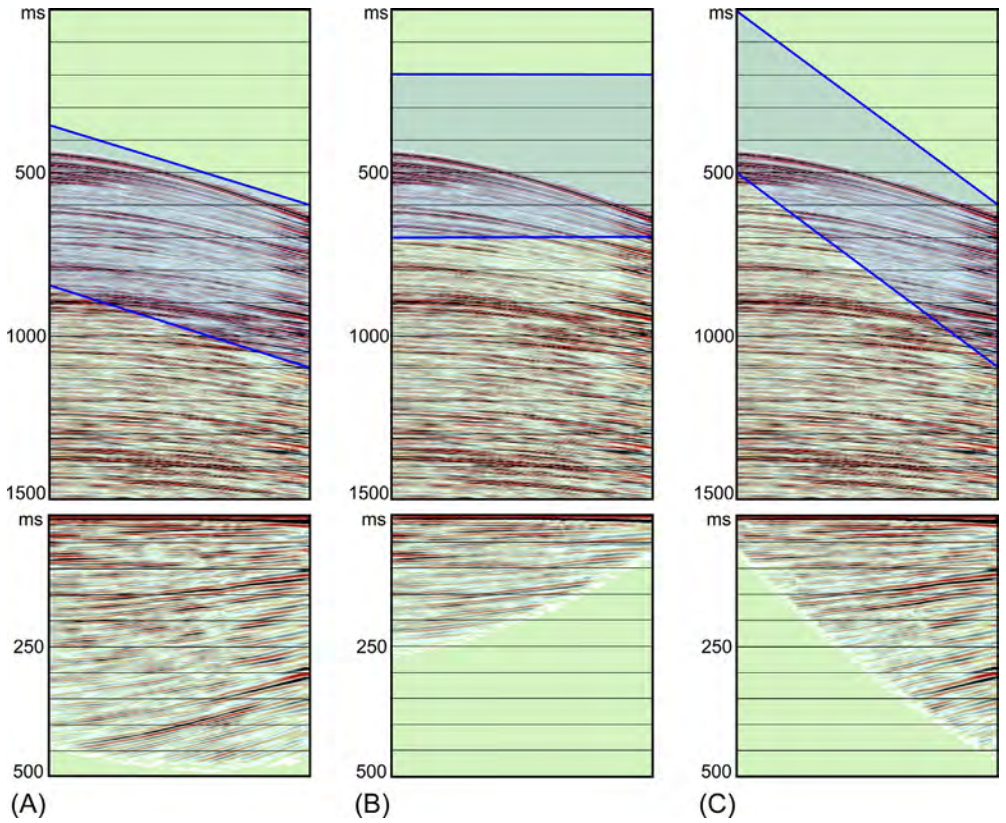


FIG. 6.25 A shot gather (top) and its autocorrelograms (bottom) for different time gates *(shaded areas)* of 500 ms over (A) a proper time gate. (B) and (C) improper autocorrelation time gates, resulting in amplitude loss in autocorrelograms of near or far offset traces.

length of nonzero data samples in the gate also has an important effect on the autocorrelation output. For instance, the autocorrelations for the near offset traces in Fig. 6.25C are calculated from a too-short time gate, resulting in too-few nonzero amplitude samples involved in the calculation of the autocorrelation to obtain a full-length autocorrelogram.

6.5.2 Deconvolution Design Gate

In statistical deconvolution, autocorrelation of the input seismic trace is used in the calculation of the deconvolution operator using normal equations given by Eq. (6.18). The deconvolution design gate determines which part of the input trace is considered in order to calculate the autocorrelograms in setting up the normal equations. In practice, the design gate is selected over the target zone, and any kind of random and coherent noise zones are avoided. Typically, it is initiated just above the seafloor reflection and should be as long as possible, up to ten times the preferred operator length. Fig. 6.26 shows an analysis of the deconvolution outputs for different design gates along with their corresponding amplitude spectra and autocorrelograms. In deconvolution calculations, the operator length $n = 140$ ms and a prediction lag $\alpha = 8$ ms are used. The most suitable gate that widens the

amplitude spectrum and suppresses the amplitudes in the autocorrelograms is indicated by (*) in Fig. 6.26.

6.5.3 Operator Length

The time span over which the autocorrelation of the input seismic trace approximately equals the wavelet's autocorrelation is defined as the deconvolution operator length. In practice, the operator length is one of the most crucial parameters of the deconvolution application and must be properly determined, since it controls the efficiency of the deconvolution. The suitable operator length for the seismic data is obtained from the analysis of autocorrelations of input seismic traces.

Figs. 6.27 and 6.28 show a minimum phase seismogram sampled at 1 ms and its deterministic and statistical spiking deconvolution results for different operator lengths, respectively. In both deconvolution outputs, the effect of the seismic wavelet seems to be removed and the major reflectivity peaks are properly located. In the case of deterministic deconvolution, the analysis shows that better results are obtained as the operator length increases (Fig. 6.27). For statistical deconvolution, however, some minor noise amplitudes as spikes trailing the major reflectivity peaks occur in the deconvolution output, and do not diminish as the operator length increases (Fig. 6.28). Similar spiky noise amplitudes are also visible in the deterministic deconvolution output for small operator lengths. In both cases, the best deconvolution result is obtained for $n = 100$ ms operator length. This is because the first transient zone of 100-ms length in the autocorrelograms in Figs. 6.27B and 6.28B resembles the autocorrelation of the source wavelet.

The suitable operator length approximately equals the length of the wavelet's autocorrelation. Since we normally do not know the source wavelet embedded in the seismic trace, we can use the initial parts of the autocorrelation of the recorded seismogram, which represent the general characteristics of the wavelet's autocorrelation (Fig. 6.11). The deconvolution operator length can be determined from the autocorrelation of the input seismogram, and must be chosen as close as possible to the time length of the first isolated amplitude package of the autocorrelogram (Fig. 6.29A). In practice, it may not be easy to determine the proper operator length by analyzing only one trace from one shot, and therefore it is a general approach to include several traces from successive shots in the analysis (Fig. 6.29B).

Fig. 6.30 shows an analysis of the deconvolution outputs for different operator lengths along with their corresponding amplitude spectra and autocorrelograms on a marine shot gather. Too-short operator lengths leave some residual energy in the autocorrelograms corresponding to the source wavelet and reverberations, whereas operator lengths longer than 100 ms do not provide further improvement on the deconvolution output. For the example shot gather in Fig. 6.30, the most suitable operator length can be considered to be 80 ms.

6.5.4 Prediction Lag

Prediction lag is definitely the most important parameter for predictive deconvolution. It controls the resolution of the deconvolution output, and the multiple reflections can also be suppressed using properly determined prediction lag values (Section 7.2). Shorter prediction lags cause much more compression of the source wavelet, and hence increase the bandwidth of the output; however, they may also boost the low- and high-frequency noise amplitudes. As the prediction lag increases, the effectiveness of the deconvolution on the whitening of the spectrum is reduced and the output autocorrelograms include more energy in nonzero lags. If it equals the sampling rate, the process becomes a spiking deconvolution. Although the prediction lag can have any value, selection of the first or

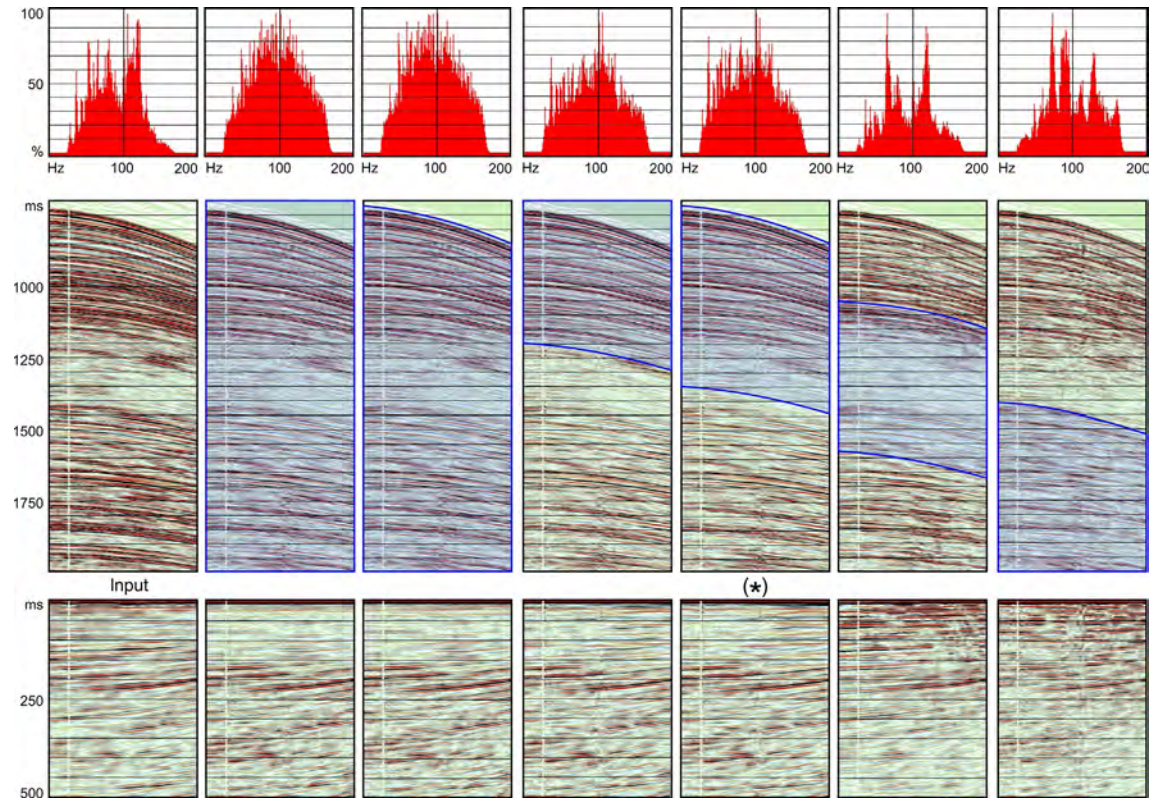


FIG. 6.26 Deconvolution outputs for different deconvolution design gates *(shaded areas)* and their corresponding amplitude spectra (top) and autocorrelograms (bottom). $n = 140$ ms and $\alpha = 8$ ms is used for deconvolution calculations. Suitable time gate is indicated by (*).

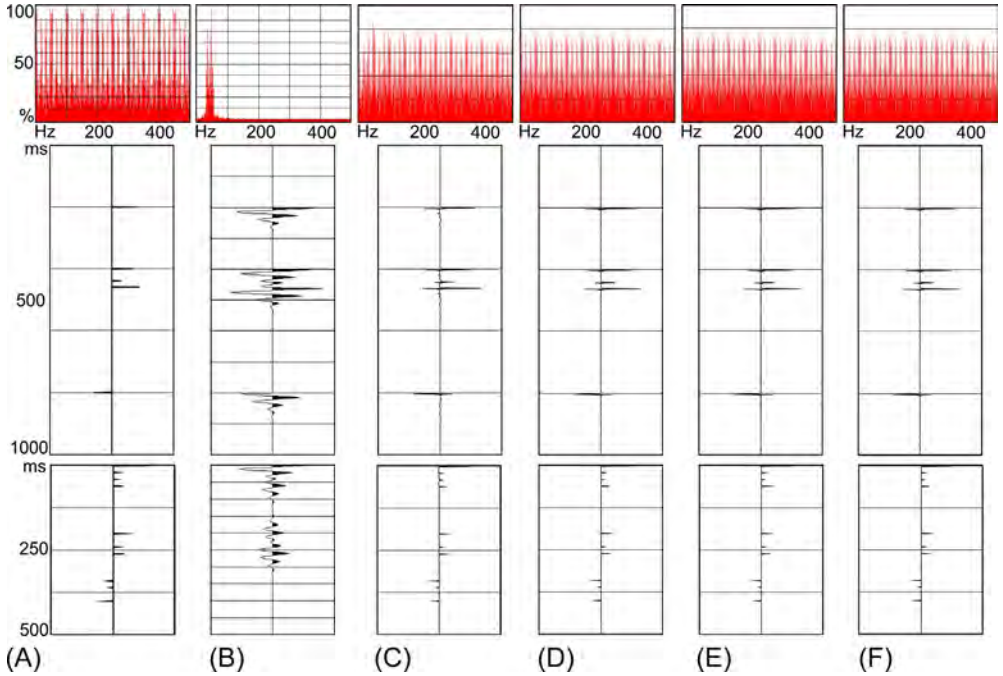


FIG. 6.27 Deterministic deconvolution results of a minimum phase synthetic seismogram for different operator lengths. (A) Reflectivity series, (B) minimum phase synthetic seismogram, and its deterministic deconvolution results for (C) $n = 20$ ms, (D) $n = 40$ ms, (E) $n = 80$ ms and (F) $n = 100$ ms operator lengths. Corresponding amplitude spectra and autocorrelograms are given in the top and bottom panels, respectively.

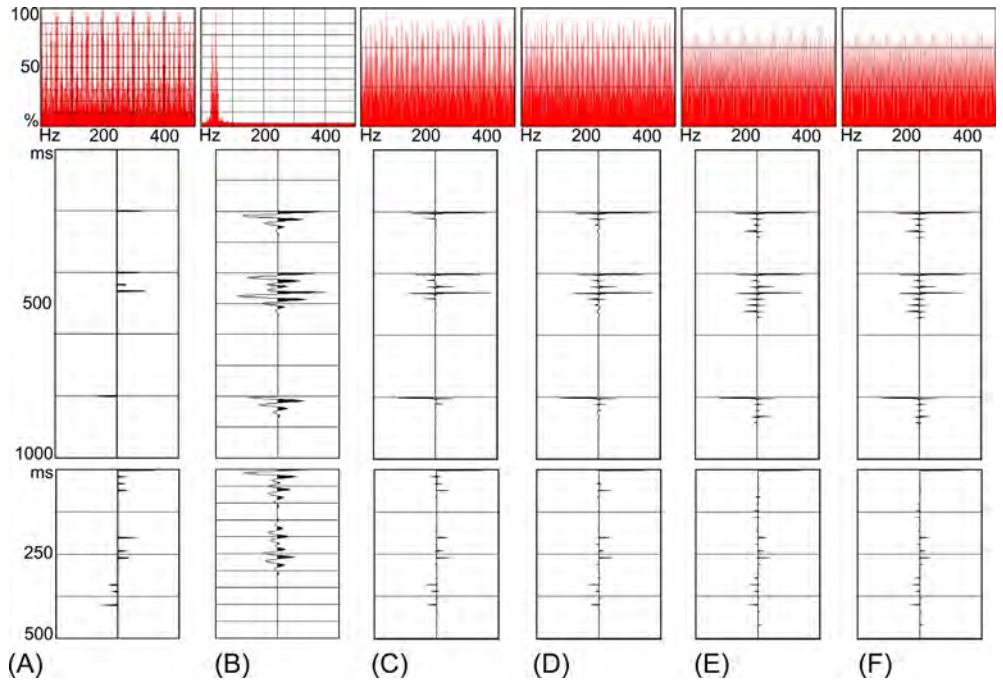


FIG. 6.28 Statistical deconvolution results of a minimum phase synthetic seismogram for different operator lengths. (A) Reflectivity series, (B) minimum phase synthetic seismogram, and its deterministic deconvolution results for (C) $n = 20$ ms, (D) $n = 40$ ms, (E) $n = 80$ ms and (F) $n = 100$ ms operator lengths. Corresponding amplitude spectra and autocorrelograms are given in the top and bottom panels, respectively.

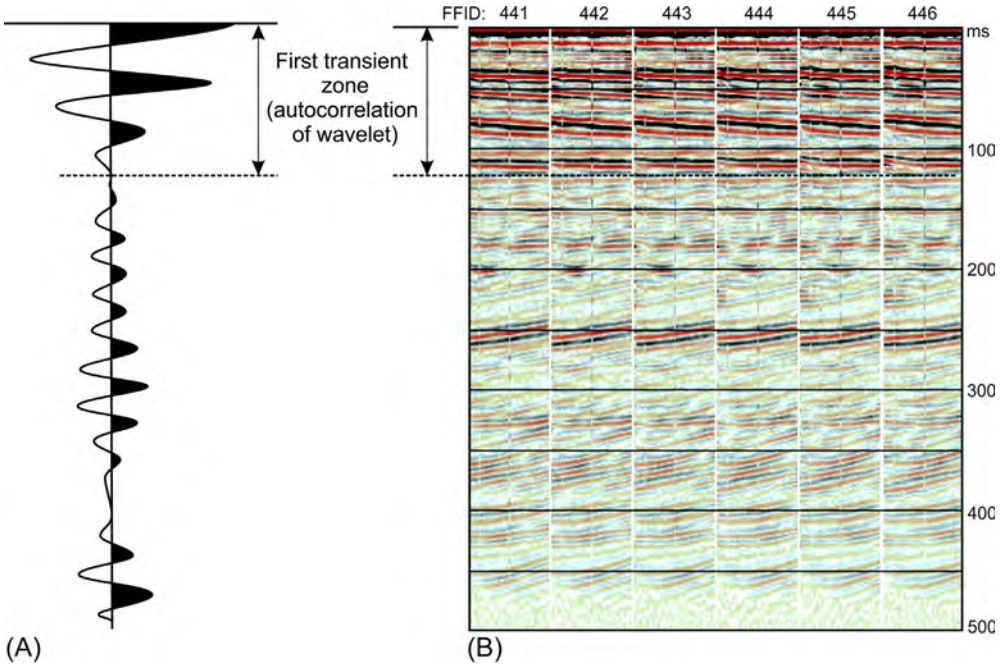


FIG. 6.29 Determination of suitable deconvolution operator length from the autocorrelation of an input seismogram. (A) Schematic display of a trace's autocorrelogram indicating the length of the first isolated amplitude package (suitable deconvolution operator length). (B) Generally, autocorrelations of a number of successive shot gathers are analyzed together to determine the operator length more precisely. The first transient zone on the autocorrelation traces is expected to have almost similar characteristics for all seismic traces of the shots, representing the autocorrelation of the source wavelet.

second zero crossing point of the autocorrelogram of the input seismogram is a general convention. Fig. 6.31 shows statistical deconvolution results with an operator length of $n = 100$ ms applied to a minimum phase wavelet for different prediction lags. Specifically, $\alpha = 6$ ms and $\alpha = 18$ ms correspond to the first and the second zero crossing times of the autocorrelation in Fig. 6.31, respectively.

If the prediction lag is not unity, the predictive deconvolution produces a wavelet of finite length instead of a zero-lag spike. As a general implication, for a given input wavelet with a length of $(\alpha + n)$, a deconvolution operator with a length of n and a prediction lag of α truncates the wavelet in the deconvolved output into a compressed wavelet of α ms length. The first α lags of the autocorrelation are passed, while the remaining n lags are zeroed out. Furthermore, as the α increases, the amplitude spectra of the input and deconvolution outputs become similar. In the example in Fig. 6.31, the deconvolution is ineffective on the wavelet after $\alpha = 86$ ms because all lags of the autocorrelation are passed to output. Fig. 6.32 shows statistical deconvolution results with an operator length of $n = 100$ ms applied to a minimum phase seismogram for different prediction lag values. Resolution of the deconvolution output is inversely proportional to the prediction lag value.

Resolution power of a predictive deconvolution output in a noise-free environment can be controlled by prediction lag. A unit prediction lag ($\alpha =$ sampling rate) corresponds to spiking deconvolution and represents the maximum

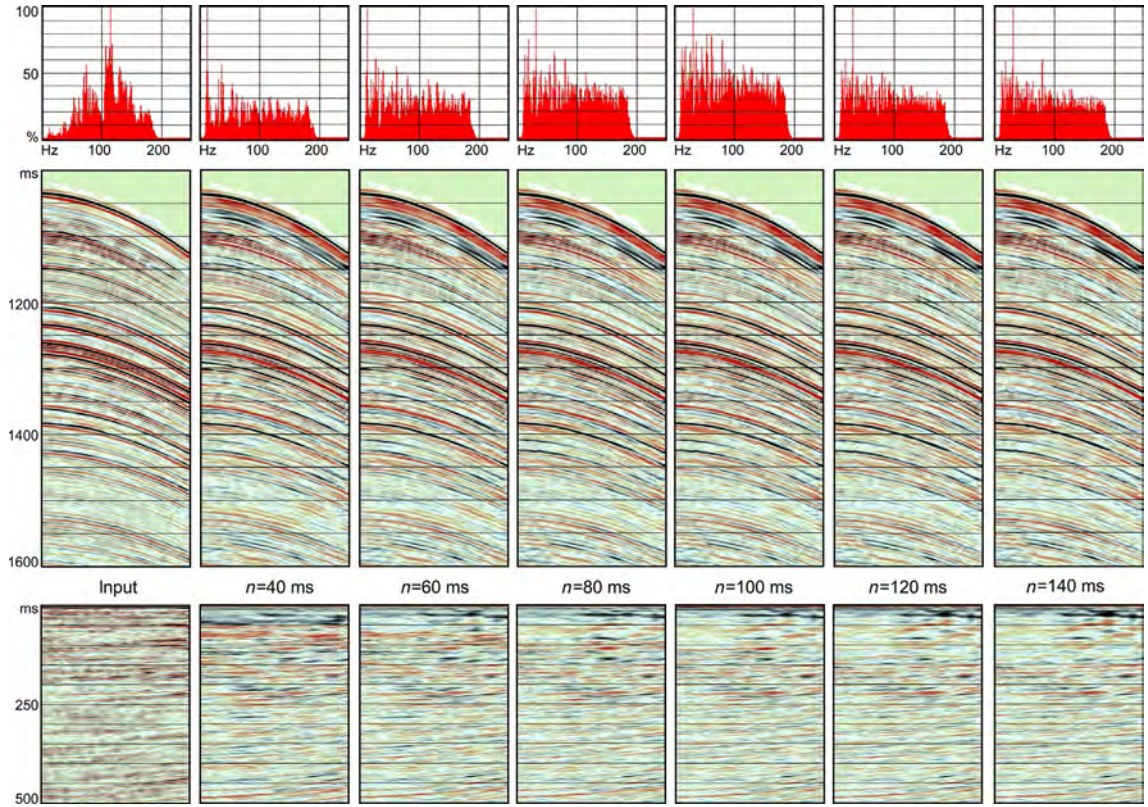


FIG. 6.30 Predictive deconvolution outputs for different operator lengths for a marine shot gather and their corresponding amplitude spectra (top) and autocorrelograms (bottom). $\alpha = 8$ ms is used for deconvolution calculations. $n = 80$ ms is suitable for this dataset.

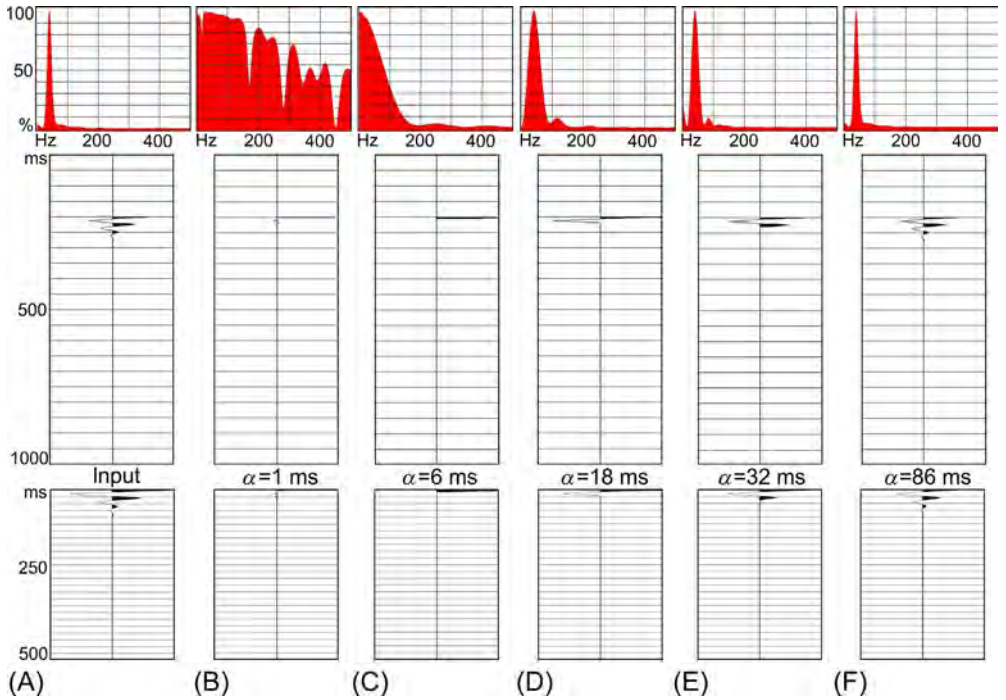


FIG. 6.31 Statistical predictive deconvolution results of a minimum phase wavelet with an operator length of $n = 100$ ms for different prediction lag values. (A) Minimum phase wavelet, and its deconvolution results for (B) $\alpha = 1$ ms, (C) $\alpha = 6$ ms, (D) $\alpha = 18$ ms, (E) $\alpha = 32$ ms, and (F) $\alpha = 86$ ms prediction lags. Corresponding amplitude spectra and autocorrelograms are given in the top and bottom panels, respectively.

resolution, and the output contains a wider frequency bandwidth with much higher frequency content. Deconvolution is commonly used for resolution improvement to transform the amplitude spectrum of the seismic data into a white spectrum. However, the resolution may be poor again if these higher frequencies consist of random noise amplitudes. Increasing the prediction lag makes the spectrum band limited, implying a colored spectrum. As a consequence, the following implications hold for the operator length and prediction lag parameters, which are also schematically shown on an autocorrelation function in Fig. 6.33:

- Operator length must be chosen as close as possible to the time length of the first transient package of the autocorrelation (❶in Fig. 6.33).
- Prediction lag can be chosen as the first or second zero crossing points of the autocorrelation for resolution improvement (❷in Fig. 6.33).
- If the prediction lag equals unity (the sampling rate), the process becomes a spiking deconvolution (❸in Fig. 6.33).

In practice, a second zero crossing point is generally preferred as the prediction lag, since selecting the second crossing produces an output wavelet with one positive and one negative lobe, which resembles a minimum phase wavelet, although the second crossing of the wavelet autocorrelogram does not necessarily coincide with the second zero crossing of the wavelet itself.

Fig. 6.34 shows an analysis of the deconvolution outputs for different prediction lags.

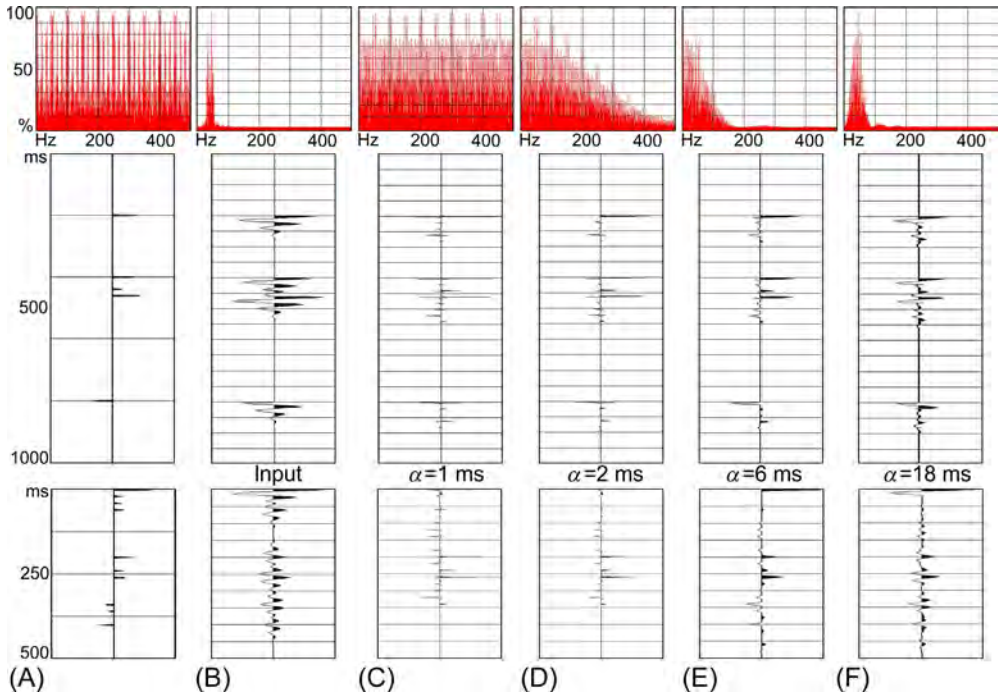


FIG. 6.32 Statistical predictive deconvolution results of a minimum phase seismogram with an operator length of n = 100 ms for different prediction lag values. (A) Reflectivity series, (B) minimum phase seismogram, and its deconvolution results for (C) $\alpha = 1$ ms, (D) $\alpha = 2$ ms, (E) $\alpha = 6$ ms, and (F) $\alpha = 18$ ms prediction lags. Corresponding amplitude spectra and autocorrelograms are given in the top and bottom panels, respectively.

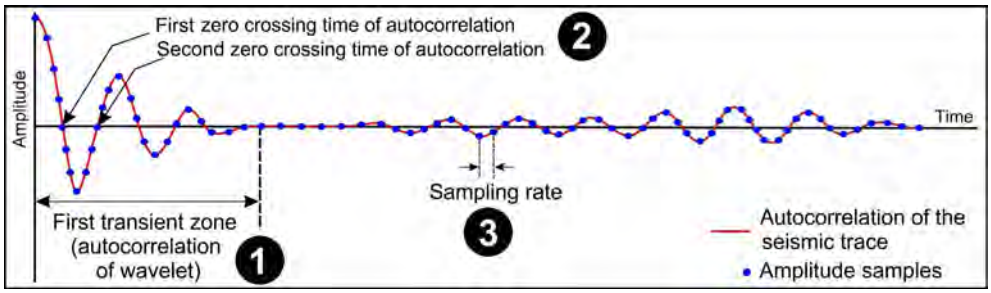


FIG. 6.33 Operator length must be close to the length of the first transient package of the autocorrelogram (1). Prediction lag is commonly chosen as either the first or second zero crossing points of the autocorrelation for resolution improvement (2). If the prediction lag equals the sampling rate, then a spiking deconvolution is performed (3).

A prediction lag of $\alpha = 1$ ms corresponds to spiking deconvolution, and $\alpha = 4$ and $\alpha = 8$ ms lags represent the first and second zero crossing times of the autocorrelograms, respectively. For smaller prediction lags, high-frequency components are much more strengthened, and the spectrum becomes more whitened. For the example shot gather in Fig. 6.34, the suitable

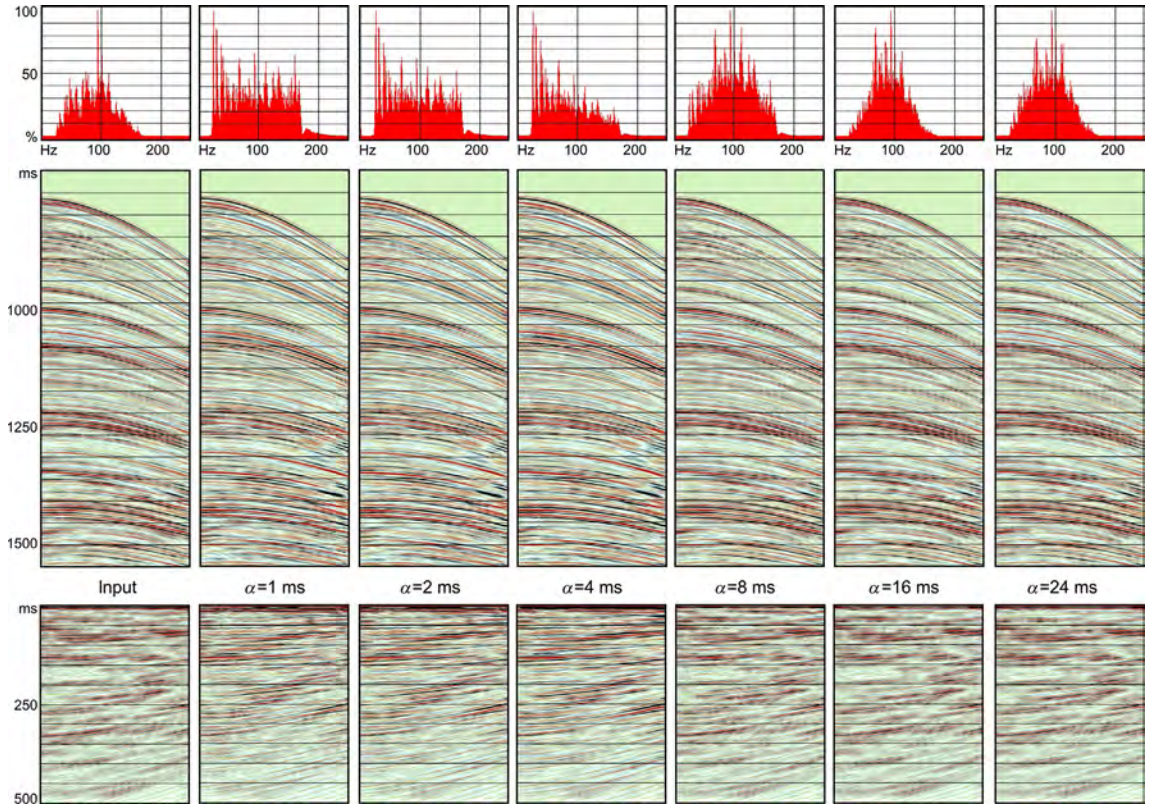


FIG. 6.34 Deconvolution outputs for different prediction lags and their corresponding amplitude spectra (top) and autocorrelograms (bottom) for a shot gather. Computations are done for an operator length of $n = 100$ ms, and $\alpha = 8$ ms is suitable for this dataset.

prediction lag is $\alpha = 8$ ms, which both widens the amplitude spectrum and suppresses the amplitudes in the autocorrelograms.

6.6 POSTSTACK DECONVOLUTION

Although it is a general convention to apply the deconvolution to prestack data, due to a number of practical reasons, deconvolution can also be applied to stack sections, which is known as deconvolution after stack (DAS). These reasons include

- After prestack deconvolution, a minor wavelet effect remains in the seismic data because almost none of the deconvolution assumptions are entirely satisfied, and this residual wavelet effect can be removed by a poststack deconvolution.
- Because the stack section is an approximation to a zero-offset section, predictive deconvolution can be successful in suppressing the multiples on the stack data.

Fig. 6.35 shows an example application of poststack deconvolution. After deconvolution, the amplitude spectrum widens to include both high- and low-frequency amplitudes, indicating a significant temporal resolution improvement. Since migration may change the period of the multiples, DAS is generally applied before migration. DAS parameters are determined as in the parameter determination for prestack deconvolution: A new autocorrelation gate and a deconvolution design gate are picked, and the operator length and prediction lag parameters can be determined from autocorrelograms of the stack section.

6.7 MAXIMUM ENTROPY (BURG) DECONVOLUTION

The term *entropy* determines the amount of disorder in a given system. Maximum entropy is an alternative spectral estimation approach aiming to improve the spectral content of the seismic data based on the maximum entropy concept. The basic principle is to select a spectrum corresponding to the most unpredictable series that has an autocorrelogram conforming the known series. It was first applied to seismic data by Burg (1967) to improve resolution using the power spectrum estimation algorithm, which was indeed a different approach to the power spectrum calculation.

If the Fourier transform of a given $f(t)$ series is $F(\omega)$, an $H(\omega)$ transfer function whitening the $f(t)$ series is defined as (Ulrych, 1972)

$$F(\omega)H(\omega) = k \tag{6.22}$$

where k is given by

$$|F(\omega)|^2 = k^2/|H(\omega)|^2 \tag{6.23}$$

where the absolute value sign means amplitude spectrum. The righthand side of Eq. (6.23) is an estimation of the power of the $f(t)$ function. Accordingly, this approach can also be used to widen the amplitude spectrum of the seismic data based on a prediction-error filter. Burg (1967) calculated the autocorrelation function in normal equations given by Eq. (6.18), minimizing the power of a prediction filter applied to the data both in forward and backward directions. This method is today known as the Burg algorithm, based on the maximum entropy theory, and it is a powerful spectral balancing technique (Ulrych, 1972).

The only parameter to be determined for Burg deconvolution is the operator length. Fig. 6.36 shows an analysis of Burg deconvolution on a minimum phase synthetic seismogram for different operator lengths. Shorter operator lengths leave some residual noise, the amplitudes of which decrease as the operator length increases. For this synthetic trace, $n = 100$ ms is suitable. Fig. 6.37 shows a similar analysis on a marine shot gather for different operator lengths. As the operator length increases, the amplitudes in the autocorrelation series are diminished, and the amplitude spectrum becomes broader after deconvolution, indicating a significant improvement in the

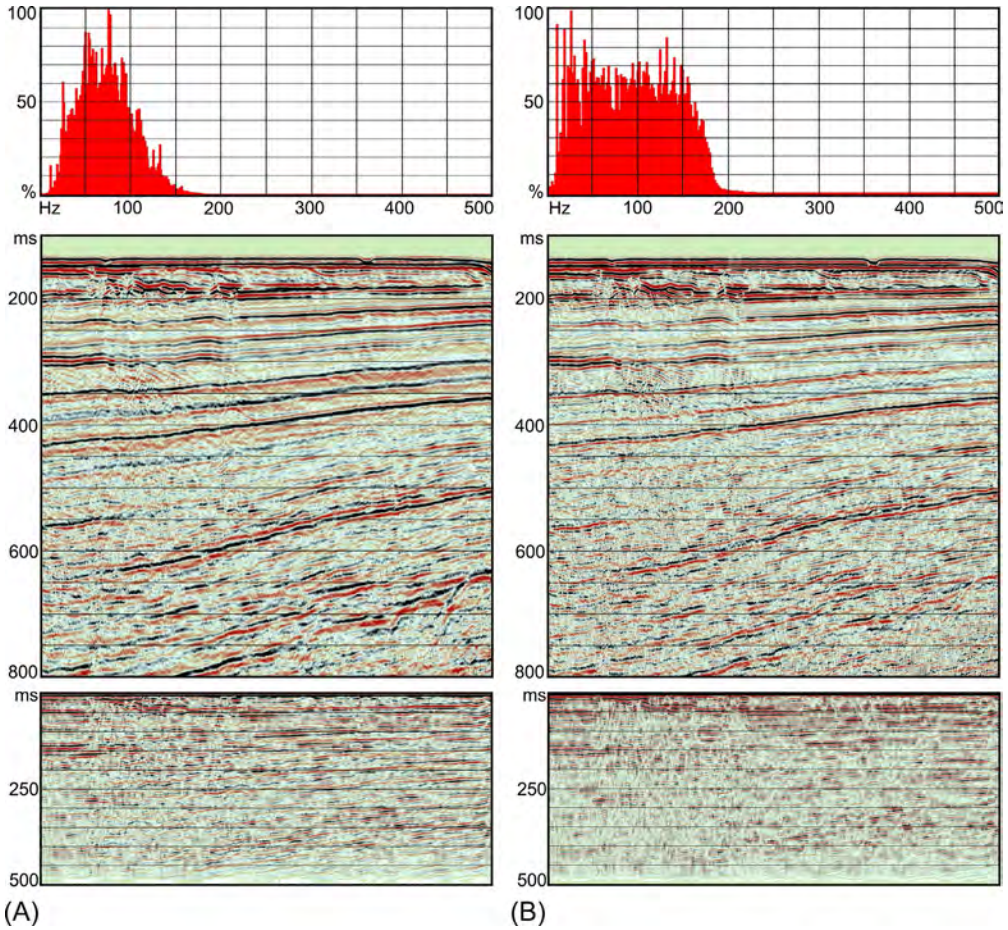


FIG. 6.35 An example poststack deconvolution (DAS). A stack section (A) before and (B) after DAS and its corresponding amplitude spectra (top) and autocorrelograms (bottom).

temporal resolution. The most balanced amplitude distribution in the amplitude spectrum is obtained for $n = 60$ ms for this shot gather. Since extreme low- and high-frequency bands may include relatively high noise amplitudes, a bandpass filter is generally required following the Burg deconvolution.

Burg deconvolution can also be applied to stack seismic data as a poststack deconvolution. Fig. 6.38 shows a stack section before and after Burg deconvolution for $n = 40$ ms, along with their corresponding autocorrelograms and mean amplitude spectra. The Burg deconvolution significantly improved the temporal resolution of the section, and it also whitens the amplitude spectrum in the available frequency band between approximately 15 and 170 Hz.

6.8 SHAPING FILTERS

Wiener deconvolution is successful for minimum phase wavelets and seismograms composed of a minimum phase wavelet. However,

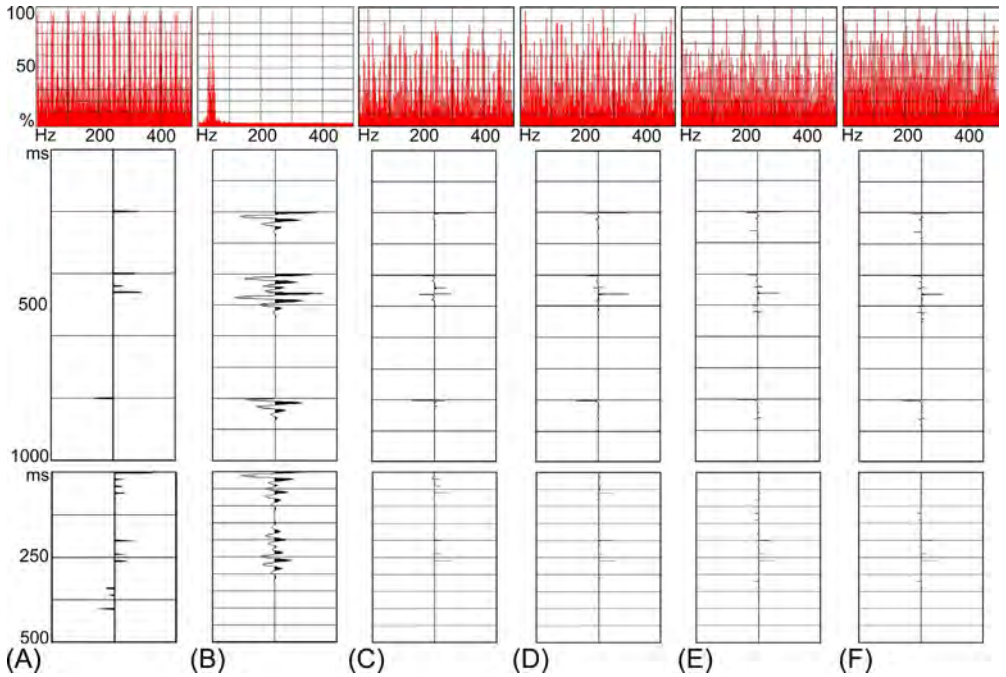


FIG. 6.36 Burg deconvolution results of a minimum phase synthetic seismogram for different operator lengths. (A) Reflectivity series, (B) minimum phase synthetic seismogram, and its Burg deconvolution results for (C) $n = 20$ ms, (D) $n = 40$ ms, (E) $n = 80$ ms and (F) $n = 100$ ms operator lengths. Corresponding amplitude spectra and autocorrelograms are given in the top and bottom panels, respectively.

the methodology can also be used successfully if the output of the deconvolution is any desired wavelet shape. In that case, the process is termed wavelet shaping and generally is applied in three forms:

i. Converting a mixed or maximum phase wavelet into a delayed spike
ii. Converting the minimum phase wavelet into a zero phase wavelet (dephasing)
iii. Removal of the source signature from the data (designature)

Maximum Phase

If the input wavelet is not minimum phase, it cannot be converted into a zero-delayed spike by spiking deconvolution. For instance, the wavelet $w(t) = (-1, 2)$ considered in deconvolution with inverse filtering cannot be converted to a zero-delay spike of (1, 0, 0) since its energy distribution is more suitable to a delayed spike like (0, 1, 0). Therefore, mixed or maximum phase wavelets can be converted into delayed spikes instead of zero phase spikes. Fig. 6.39 shows an example application of Wiener deconvolution to a mixed phase wavelet. Because the wavelet is not minimum phase, deconvolution converting the wavelet into a 0-ms delayed spike fails. In this example, the deconvolution application to convert an 8-ms delayed spike produces the optimum result.

In general, the wavelet embedded in the seismic data is minimum phase except the Vibroseis data from land surveys and watergun data from marine seismics. Although they are not physically realizable since they are not causal, zero phase wavelets have two major advantages over minimum phase wavelets:

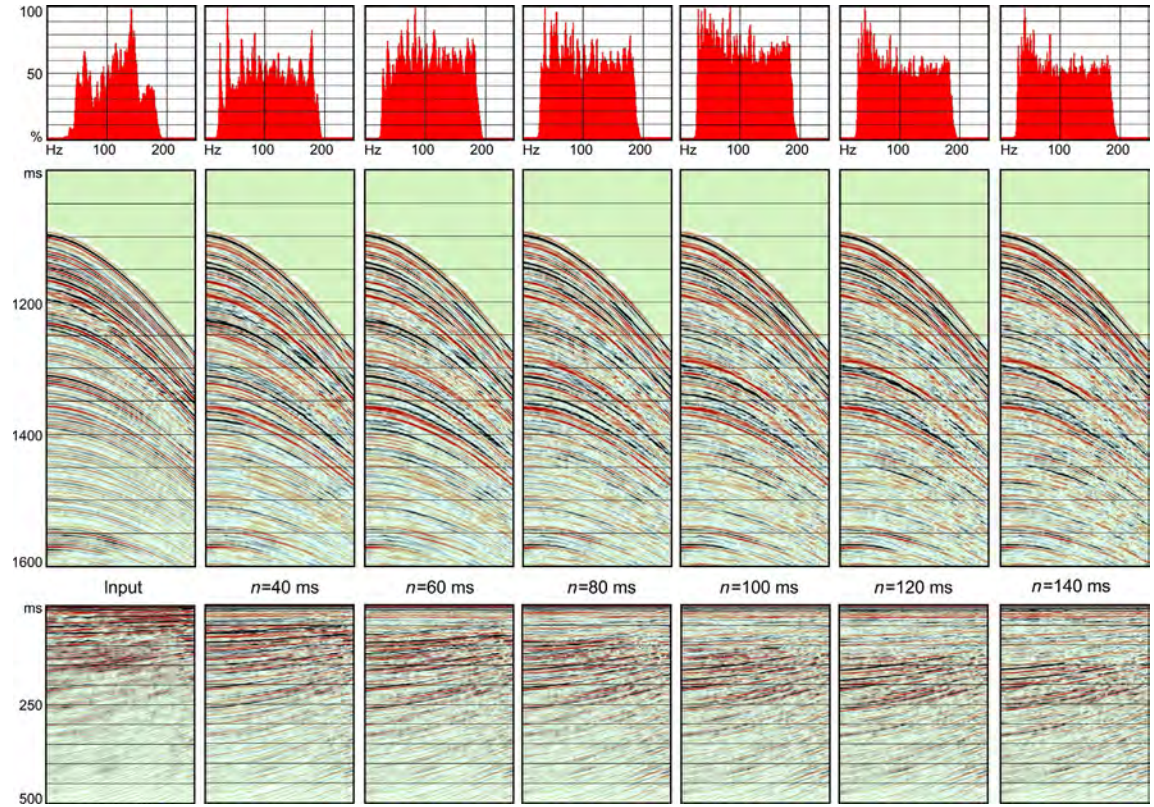


FIG. 6.37 Burg deconvolution outputs of a marine shot gather for different operator lengths and their corresponding amplitude spectra (top) and autocorrelograms (bottom). $n = 60$ ms is suitable for this shot.

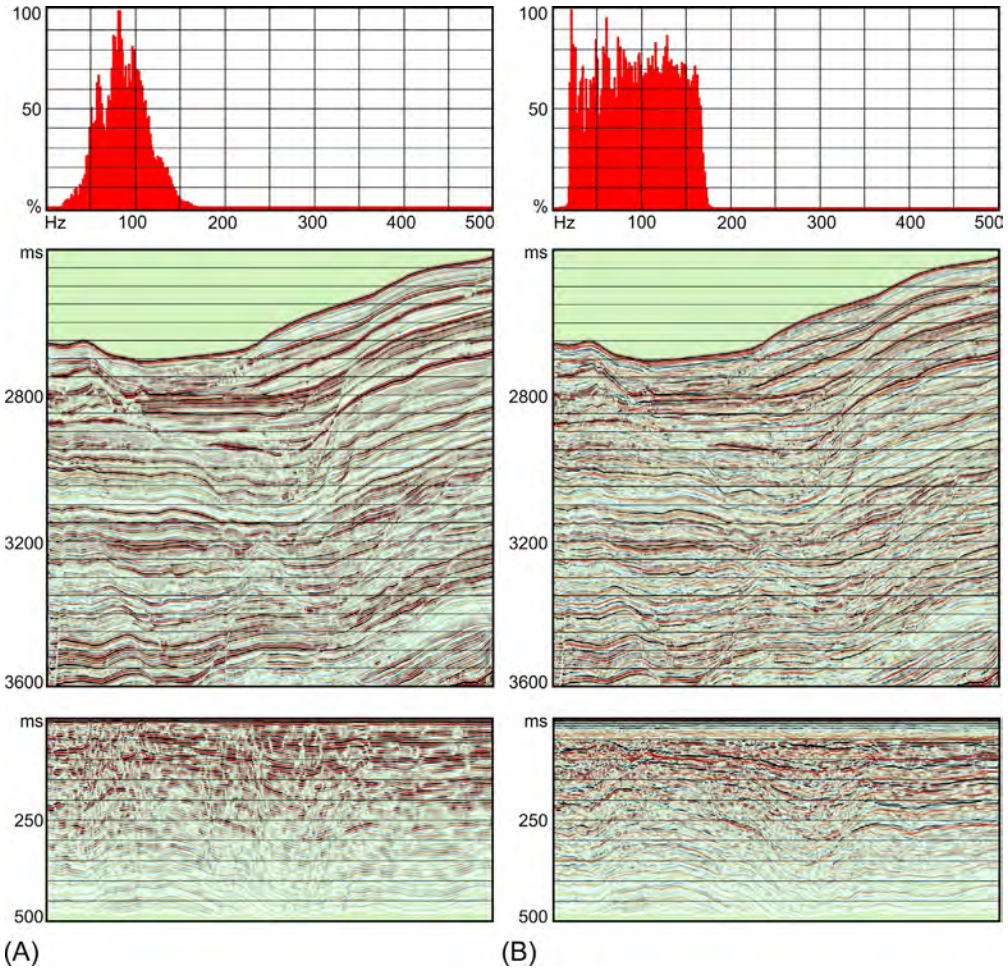


FIG. 6.38 Poststack Burg deconvolution application. Stack sections (A) before, and (B) after Burg deconvolution ($n = 40$ ms). Corresponding amplitude spectra and autocorrelograms are given in the top and bottom panels, respectively.

i. Time durations of zero phase wavelets are shorter than their minimum phase equivalents of the same amplitude spectra. This property causes the zero phase wavelets to have higher resolving power.
ii. While the onset of a minimum phase wavelet coincides with the horizon, the main positive lobe of a zero phase wavelet exactly coincides with the stratigraphic interface, which makes the horizon picking easier and more convenient if the data is zero phase.

Therefore, a conversion from minimum phase to zero phase is commonly applied to the marine seismic data during data processing and is known as dephasing. The wavelet in the seismic data is converted to a zero phase wavelet with an amplitude spectrum the same as that of the input wavelet. Fig. 6.40 shows an example application to zero phase conversion of a minimum phase stack section. Note that the seabed reflection is located at 170 ms, which corresponds to the onset time of the minimum phase wavelet and the main lobe is located at

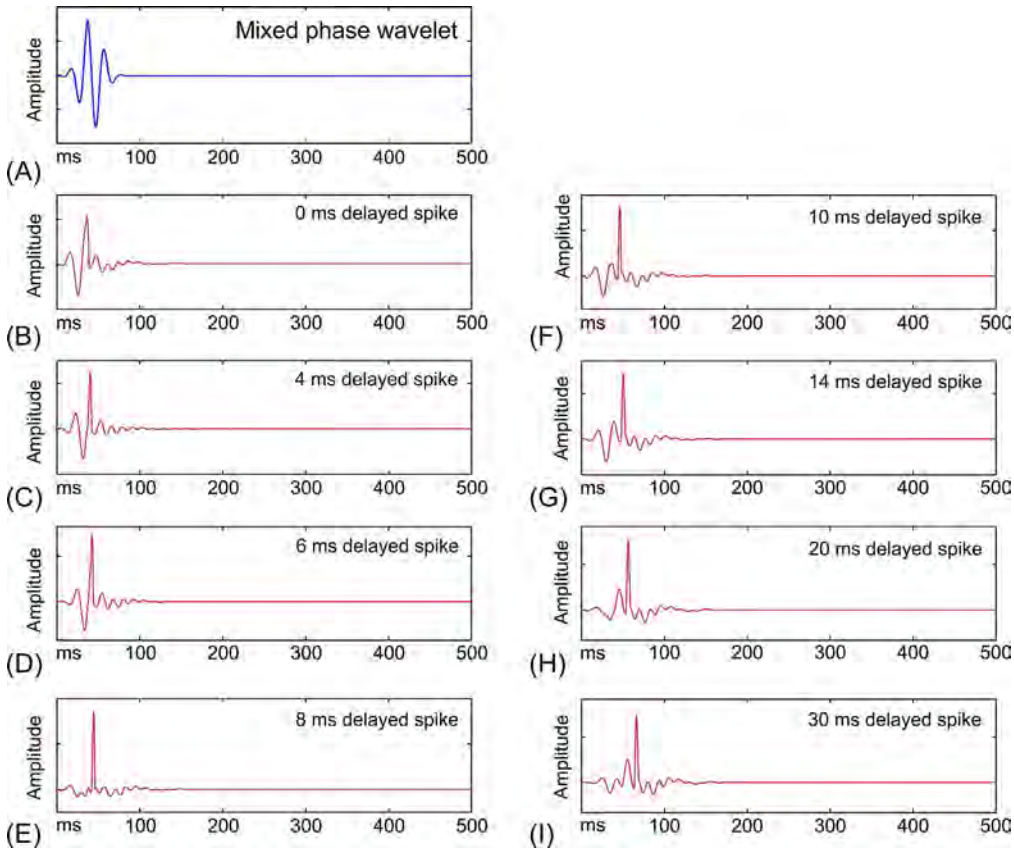


FIG. 6.39 Wiener spiking deconvolution application of a nonminimum phase wavelet. (A) Input of a mixed phase wavelet, and its spiking deconvolution results for (B) 0 ms, (C) 4 ms, (D) 6 ms, (E) 8 ms, (F) 10 ms, (G) 14 ms, (H) 20 ms, and (I) 30 ms delayed spike. The optimum result is obtained for 8-ms delay.

approximately 180 ms with a 10-ms delay in Fig. 6.40A, whereas the seafloor appears at 170 ms, which exactly coincides with the main lobe of the reflections composed of zero phase wavelets in Fig. 6.40B.

If we have the source signature, the wavelet shaping is known as signature processing, and the removal of the source signature effect from the recorded seismograms is termed designature. Generally, the source wavelet embedded in the data is estimated, and a filter is designed to convert this wavelet into a desired shape, and then this filter is applied to the seismic data. Designature requires knowledge of the source wavelet. Although several techniques exist to estimate the source wavelet from recorded seismic traces, the most common approach is known as the Kolmogorov spectral factorization method, described in detail by Claerbout (1976). Its practical application involves the natural logarithm of the recorded seismogram to be computed in the frequency domain, and then in the time domain a Hilbert transform is calculated, in which the positive time amplitudes

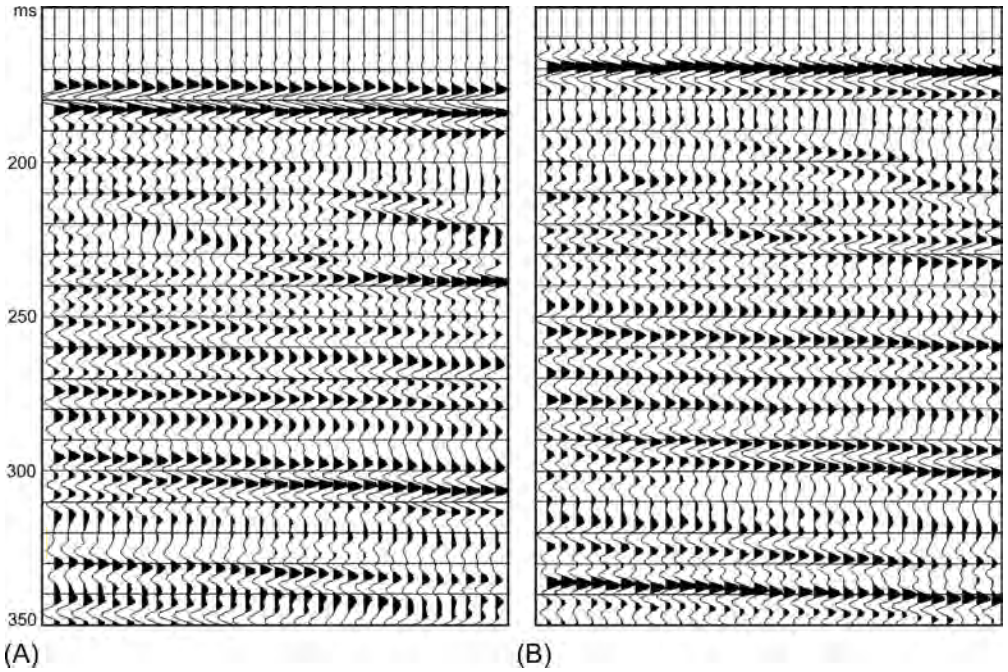


FIG. 6.40 An application of dephasing. (A) A minimum phase stack section, and (B) its zero phase conversion.

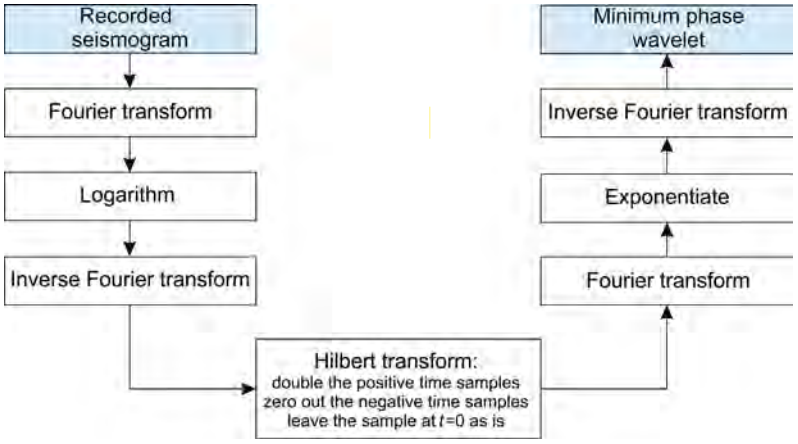


FIG. 6.41 Flow of the processing steps to obtain minimum phase wavelet for signature processing.

are doubled while negative time amplitudes are zeroed out (Yılmaz, 1987). In the frequency domain, the exponential of the spectrum is calculated and the minimum phase wavelet is obtained in the time domain after an inverse Fourier transform (Fig. 6.41). Fig. 6.42 shows an example application of designature to a shot gather. In this example, designature also converts input seismograms into zero phase equivalents.

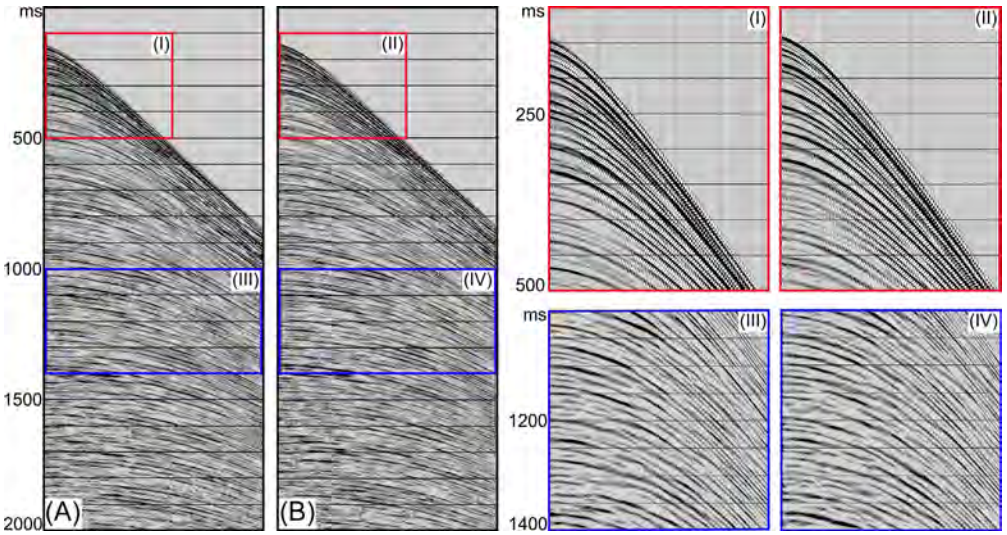


FIG. 6.42 An example application of designature to a shot gather. (A) Input shot, and (B) after designature. *Blue* and *red* insets show corresponding zoom-in areas.

6.9 SURFACE CONSISTENT DECONVOLUTION

Surface consistent deconvolution is an effective resolution improvement method generally used in land seismic data processing. The seismic trace is decomposed into the convolution effects of source, receiver, reflectivity series, and offset by surface consistent deconvolution, which accounts for the weathering effects just below the source and/or receiver locations, and the effect of offset. The deconvolution is then applied as an inverse filter after decomposition. Surface consistent deconvolution is used to correct amplitude, phase and frequency variations caused by geophone responses, poor coupling, and near-surface seismic transmission properties for land seismic data. The most important advantage of this method is its stability and effectiveness on data with poor quality and low S/N ratio in the presence of high noise amplitudes.

In practice, it is assumed that the shape of the wavelet embedded in the data depends on the source and receiver locations. A surface consistent convolutional model for the recorded seismogram $x(t)$, source wavelet $w(t)$, and reflectivity at source-receiver midpoint $r(t)$ in a noise-free environment is given by

$$x(t) = s_i(t)^* h_{(i-j)/2}(t)^* r_{(i+j)/2}(t)^* e_j(t) \tag{6.24}$$

where $s_i(t)$ is the effect of the source at location i, $e_j(t)$ is the effect of the receiver at location j, and $h(t)$ is the effect of the offset. Taking the Fourier transform of Eq. (6.24), we get

$$X(\omega) = S(\omega)H(\omega)R(\omega)E(\omega) \tag{6.25}$$

and taking the natural logarithm of the amplitude spectra for linearity, we obtain

$$\ln[|X(\omega)|] = \ln[|S(\omega)|]\ \ln[|H(\omega)|]\ \ln[|R(\omega)|]\ \ln[|E(\omega)|] \tag{6.26}$$

$\ln[|S(\omega)|]$ and $\ln[|E(\omega)|]$ for source and receivers can be solved by a least-squares iterative approach, finally to obtain the inverse filter operator as (Yılmaz, 1987)

$$s_i^{-1}(t)s_i(t) = e_j^{-1}(t)e_j(t) = \delta(t) \tag{6.27}$$

Surface consistent deconvolution also assumes a minimum phase source wavelet and noise-free seismograms. It is recommended to be applied to the datasets before the AVO analysis. Although the method is widely used in onshore seismic processing, the most reasonable application in marine seismic processing is decomposition only for source location. On the receiver and offset functions, imperfect geophone coupling or localized soil conditions and the variations in near-surface conditions are accounted for in the decomposition of the land survey data. In marine seismic, however, a poor receiver coupling or the effect of a weathered surficial layer is not pronounced; the most important part is the repeatability of the source or the stability of the source signal. Therefore, a decomposition accounting for the source function for marine seismic data can provide the necessary whitening in the amplitude spectrum.

As an example application, Fig. 6.43 shows a number of stack sections, each of which is decomposed for the convolution effects of different components as source, receiver, CDP, and offset locations, as well as the effects of all components together. Although the decompositions based on offset, CDP, or receiver functions do not ensure any whitening in the amplitude spectra of the deconvolution output, decomposition based only on the source locations yields a significantly whitened amplitude spectrum. Fig. 6.44 compares a small portion of a shot gather from a conventional marine seismic dataset before and after surface consistent deconvolution, in which the decomposition was performed only for source location.

6.10 QC IN DECONVOLUTION

Application of a Wiener deconvolution process consists of the following steps, which are generally applied to the shot gathers:

i. Picking the autocorrelation gate
ii. Picking the deconvolution design gate
iii. Calculation of the autocorrelations of selected shots
iv. Determination of deconvolution parameters from autocorrelograms
v. Application of the deconvolution
vi. Checking the results to ensure the quality of deconvolution output

Autocorrelations are generally calculated and displayed for a number of shots. It is recommended to select shot records at different shot locations along the seismic line so that the autocorrelation characteristics of the seismic data from beginning to the end of line can be analyzed together. This enables us to identify whether the autocorrelation of the source wavelet is stable for all shots in the line, which is particularly important when the geology varies laterally in the survey area. Fig. 6.45 shows an example common offset section of a regional seismic line and autocorrelograms of its selected shots from four different locations on the line. Locations are selected from the points where the geology tends to change laterally, to analyze its effect on the shape of the source wavelet embedded in the seismic data. Indeed, the appearances of the autocorrelograms do change along the line, including the length of the first transient zone. In areas of complex geology, especially on the continental margins of steep slopes, it may not be easy to reliably determine the operator length from the autocorrelograms. Although some of the commercial processing software allows us to use variable deconvolution operator lengths along the seismic lines, generally one single operator length that optimally represents the whole seismic line is determined from computed autocorrelograms.

Deconvolution tries to whiten the amplitude spectrum to yield a broader-band data, and this widening is also achieved both for extreme low- and high-frequency components of the spectrum, which are sometimes dominated by the

Spectral Whitening occurring in marine data only for spectral decomposition for the effect of Source

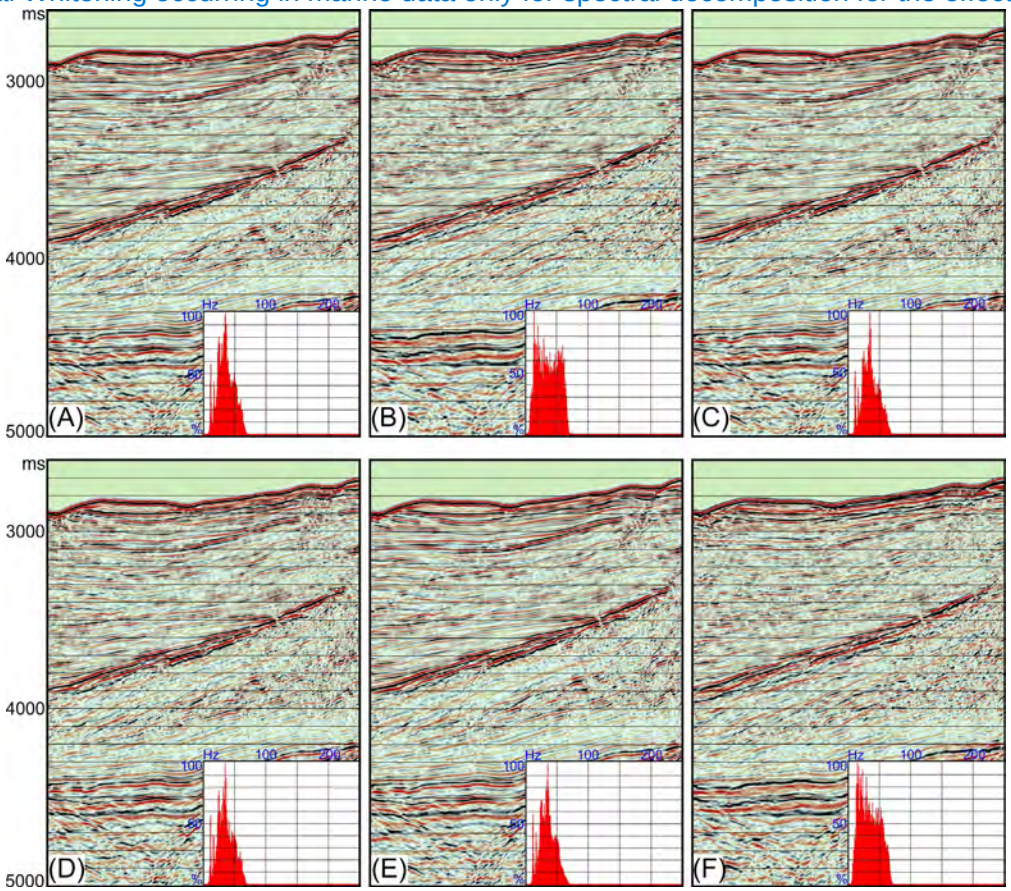


FIG. 6.43 (A) Example stack section before surface consistent deconvolution, and its surface consistent deconvolution outputs decomposed for the effects of different components of (B) source, (C) receiver, (D) CDP, (E) offset, and (F) all components together. Insets show the corresponding amplitude spectra of the deconvolution outputs.

noise amplitudes. As a result, the amplitudes of the noise may also be boosted after deconvolution. This is particularly significant for the high-frequency end of the spectrum, where relatively low amplitude random noise, especially at the late arrivals of the seismic data, becomes clearly visible after deconvolution. Therefore, the deconvolution is generally followed by a band-pass filter to suppress the boosted noise amplitudes. Fig. 6.46 shows an example noise analysis after deconvolution, which boosted both low- and high-frequency noise amplitudes, and are almost completely removed by a 10–120 Hz band-pass filter following the deconvolution (Fig. 6.46C). The noise boost of deconvolution is also evident for poststack deconvolution, which created especially high-frequency noise at the deeper parts of the stack sections (Fig. 6.46D), and after a suitable band-pass filter following the deconvolution makes the deeper reflections much clearer (Fig. 6.46E).

Deconvolution output must be checked to ensure whether it worked properly and the determined parameters were appropriate. This

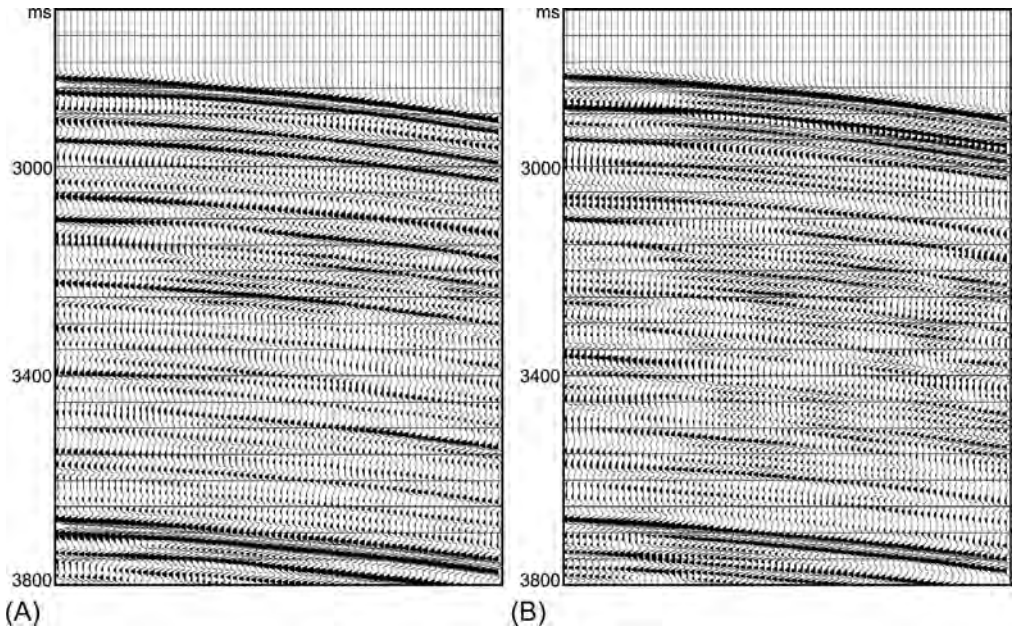


FIG. 6.44 An example marine shot gather (A) before, and (B) after surface consistent deconvolution. Decomposition is done only for shot location.

can be done by use of the following analysis before and after deconvolution:

i. Displaying the selected shot gathers
ii. Preparing the common offset/brute stack sections
iii. Analyzing the amplitude spectra of the selected shots
iv. Analyzing the autocorrelograms of the selected shots

Selected shot gathers (Fig. 6.47) as well as brute stacks (Fig. 6.48) or common offset sections (Fig. 6.49) before and after deconvolution application must be visually compared to analyze if the resolution is improved after deconvolution. The ringy character of the reflections must be removed and the primary reflections should be clearer after deconvolution, especially at the deeper parts of the data where the seismic resolution is relatively low due to the severe attenuation effects. In addition, random and coherent noise must be checked to ensure that the noise amplitudes are not revived by deconvolution. Late arrivals of the shot and brute stacks are particularly important in terms of boosted noise amplitudes, since the reflection amplitudes at the deeper parts of the data are relatively low and the noise amplitudes may easily become dominant to genuine reflections at late arrivals. Phase and polarity of the output data may also be checked on the seabed reflection to see if the correct phase information is preserved after the deconvolution. If a zero phase conversion is aimed for, then the effectiveness of the phase conversion can be analyzed by comparing the seabed reflections of input and output data.

In order to obtain the optimum Wiener deconvolution output, several tests may be needed to select the operator length and

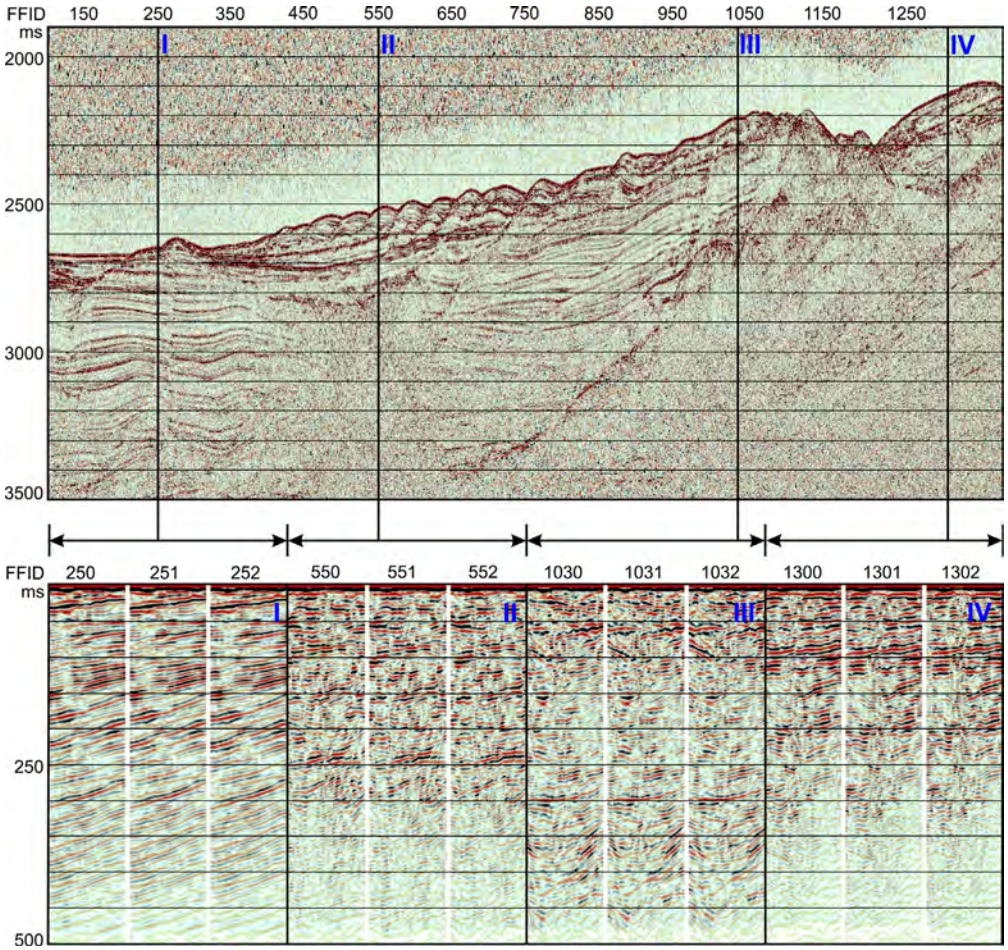


FIG. 6.45 An example common offset section (top) and autocorrelograms of the shots from its selected locations calculated for three successive shots for each determined location (bottom): between FFID 250 and 252 (location I), between FFID 550 and 552 (location II), between FFID 1030 and 1032 (location III), between FFID 1300 and 1302 (location IV).

prediction distance. It is faster, and hence cheaper, to apply these tests on the shot gathers or common offset sections. Immediately after each test with a different parameter, it is strongly recommended to compute the amplitude spectrum (Fig. 6.50) and the autocorrelogram (Fig. 6.51) of the deconvolution output to ensure that the application yields satisfactory results. The most suitable parameters are those that whiten the amplitude spectrum as much as possible, and at the same time transform the autocorrelograms into a zero lag spike representing the autocorrelogram of a random reflectivity series, which is actually regarded as the ultimate goal of the deconvolution application.

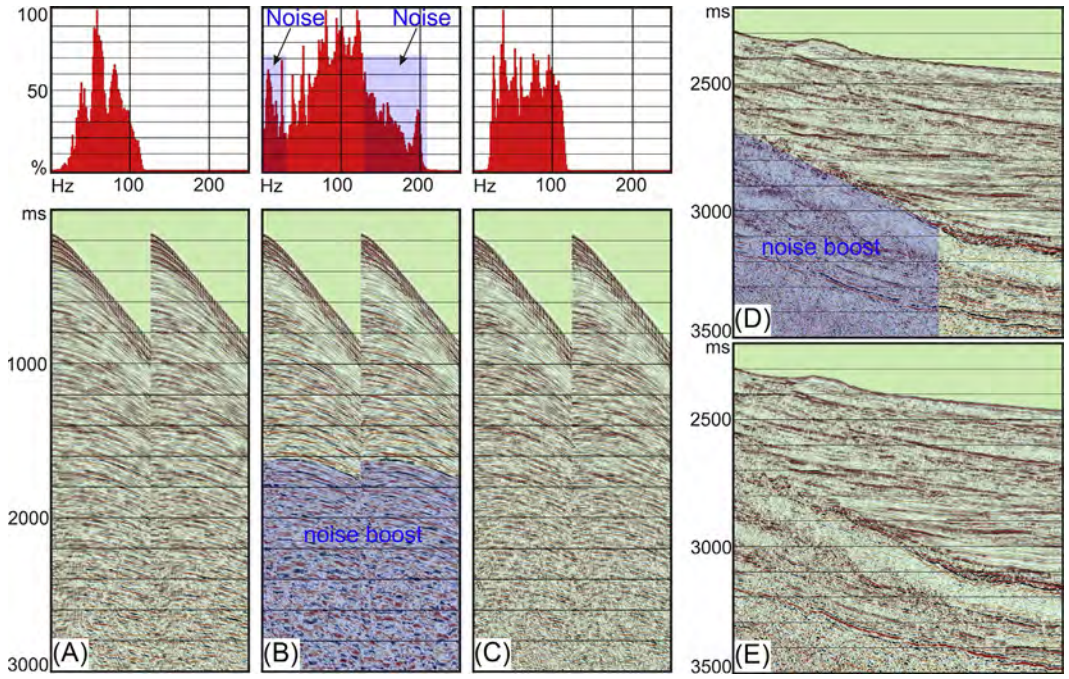


FIG. 6.46 Example noise analysis after deconvolution. (A) Two example input shots before deconvolution, (B) shots after deconvolution with boosted noise amplitudes at late arrivals *(shaded area)*, and (C) shots after a 10–120 Hz band-pass filter following the deconvolution to remove the noise. Their corresponding amplitude spectra are given on top. (D) Poststack deconvolution also induces noise, especially at the late arrivals *(shaded area)*, and (E) deeper reflections become more distinct after a suitable band-pass filter following the deconvolution.

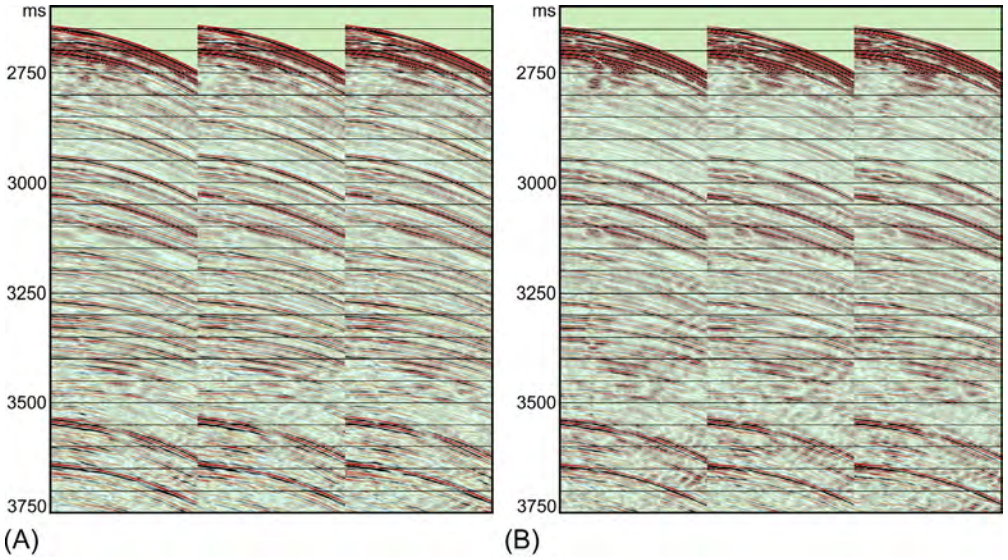


FIG. 6.47 Selected shots gathers (A) before and (B) after deconvolution for quality control purposes.

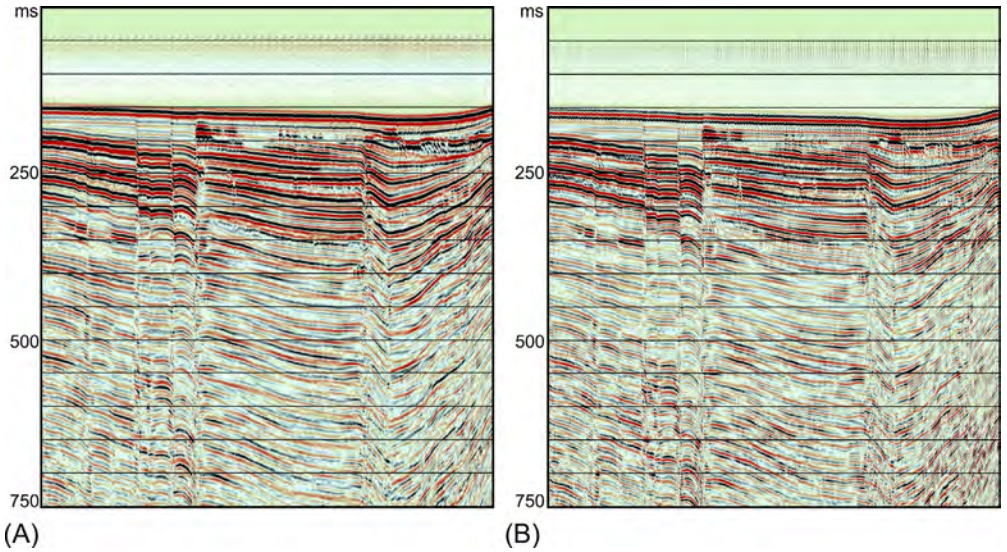


FIG. 6.48 Brute stacks obtained (A) without and (B) with deconvolution for quality control purposes.

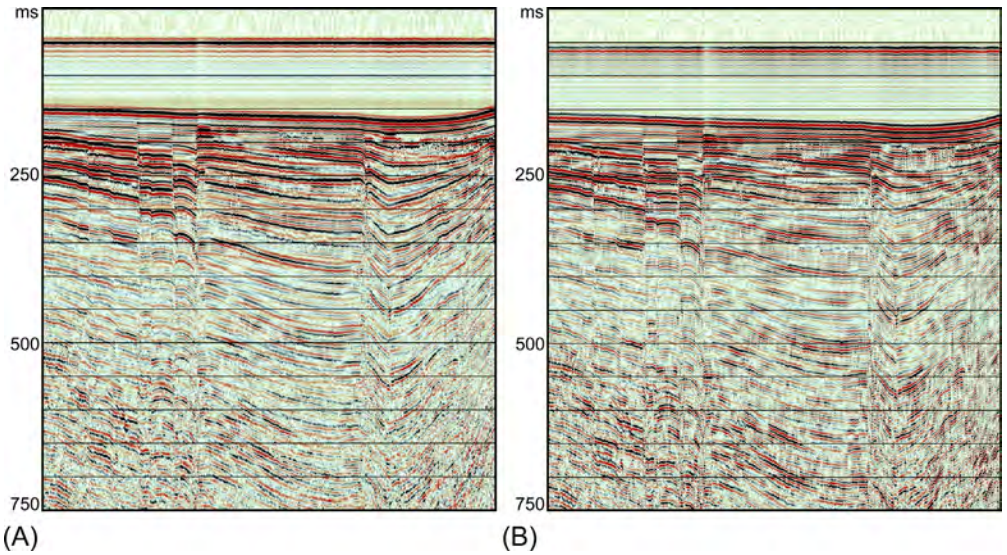


FIG. 6.49 Common offset sections obtained (A) without and (B) with deconvolution for quality control purposes.

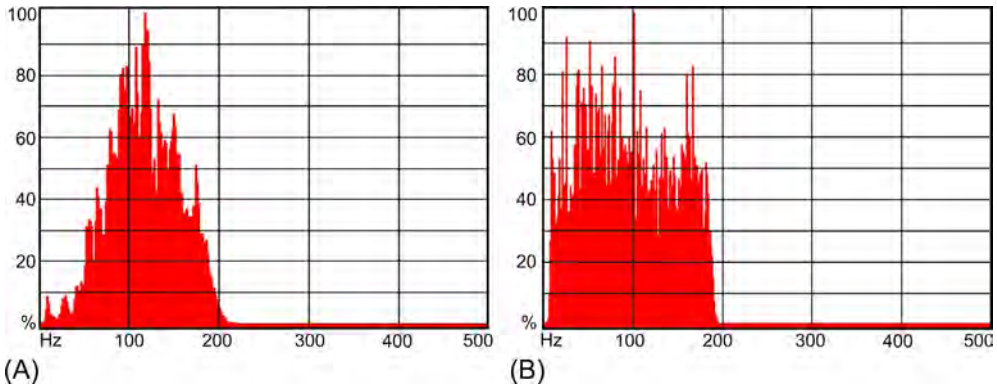


FIG. 6.50 Mean amplitude spectrum of the selected shot gathers (A) before and (B) after deconvolution for quality control purposes.

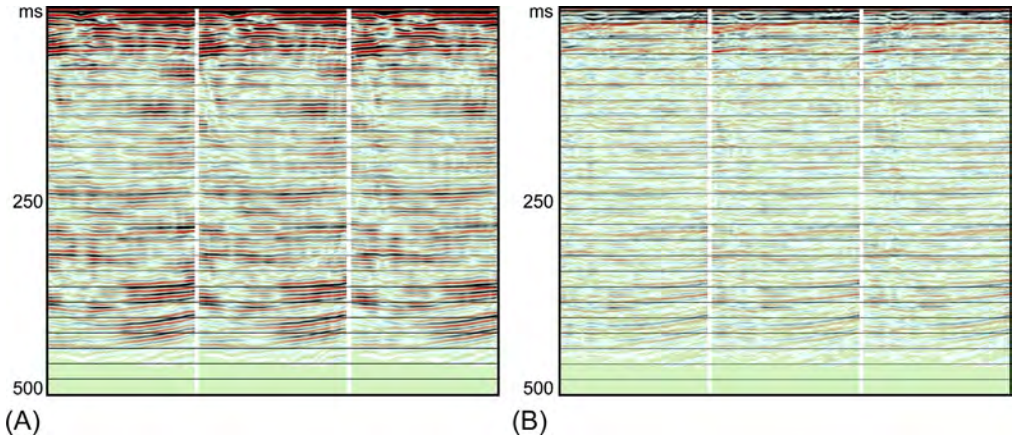


FIG. 6.51 Autocorrelograms of three successive shot gathers (A) before and (B) after deconvolution for quality control purposes.

CHAPTER

7

Suppression of Multiple Reflections

OUTLINE

7.1 CDP Stack	368	7.5 Wave Equation Multiple Rejection	388
7.2 Predictive Deconvolution	372	7.6 *f-k* Filtering	391
7.3 Deconvolution in τ-p Domain	382	7.7 Surface-Related Multiple Elimination	394
7.4 Radon Velocity Filter	383	7.8 QC in Multiple Suppression	400

Multiple reflections occur when the seismic signal travels along the same ray path more than once, commonly within the water column. In marine seismic acquisition, these are generally referred to as reverberations, and they may induce significant issues during the processing of data collected with short streamers in relatively shallow waters (Section 3.3). Multiples are one of the most serious noise problems in marine seismic surveys, since they generally occur in the frequency band of the primary reflections and their arrival times generally also coincide with those of the primary reflections.

Two different types of multiples are observed in marine surveys (Fig. 7.1). The first type is directly related to the sea surface and they are known as long period or surface-related multiples, which have at least one downward reflection initiated at the sea surface. The other type is the short period or interbed multiples, which have their downward reflections initiated at the seafloor or subsurface interfaces (Dragoset and Jeričević, 1998). In addition to these common multiple types, peg-leg multiples, which are reflected from a strongly reflective interface in the subsurface, commonly from the acoustic basement, and then downward reflected from the sea surface, can create recurring phantom interfaces that mimic the actual reflector. Since their first recognition on the seismic records in the late 1940s, considerable efforts have been made on the suppression of multiple reflections. The first dedicated attempt to attack multiples was inverse filtering or predictive deconvolution, and several different techniques were developed later with different specific assumptions. In this section,

© 2018 Elsevier Inc. All rights reserved.

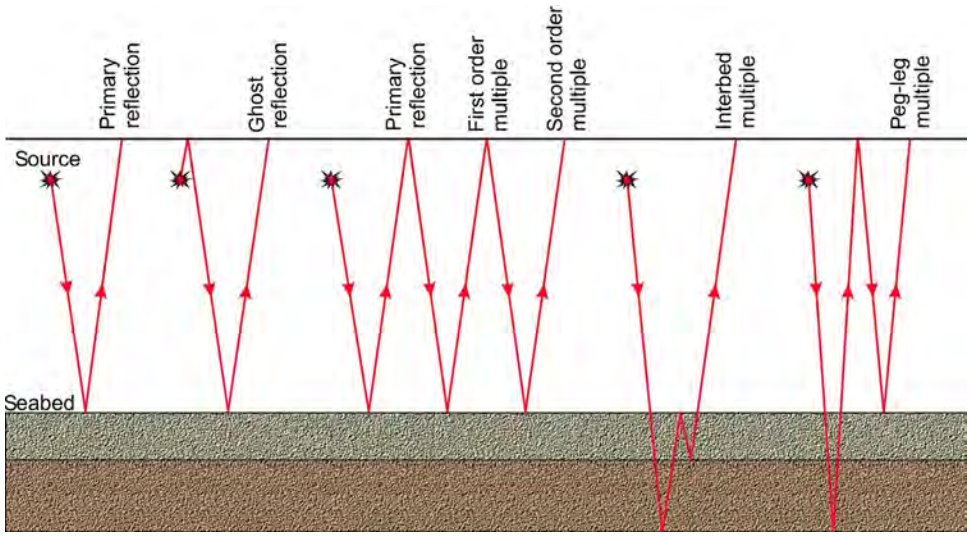


FIG. 7.1 Ray paths of different types of multiple reflections. Multiples related to the seafloor are known as long period or surface-related multiples while those arising from the trapping of the energy in a subsurface layer are termed short period multiples.

the most common demultiple methods are analyzed regarding their underlying theory and practical applications, assumptions, advantages and disadvantages, as well as their limitations.

Primary reflections may be misinterpreted when they interfere with the multiples. The interference may also affect the amplitudes of the primaries: a possible constructive interference boosts the amplitudes of the primaries whereas a destructive interference reduces the amplitudes. Removal of the multiples in the early stages of processing is crucial since prestack migration or inversion processes assume a seismic section composed of primary reflections only.

Multiples appear as recurring reflections both on shot records and stack sections. For long period multiples, seabed and shallow subsurface reflections repeat themselves as a whole reflection package. Their relative amplitudes depend on the seafloor reflectivity characteristics. In the case of a horizontal seafloor, seabed reflection and its multiples lie horizontal and parallel to each other. The time between the two is constant and the arrival time of the first multiple is exactly double the seabed reflection time. If the seabed is inclined, however, the inclination of the multiples on the stack sections progressively increases (Fig. 7.2). Multiples originating from the seabed can be regarded as primary reflections produced by apparent reflectors at the subsurface, and hence they have all the characteristics of primaries. Travel time expression of a seabed multiple of mth order for a horizontal seafloor is given by

$$t^2(x) = \frac{x^2 + 4(m+1)^2 z^2}{V^2} \tag{7.1}$$

where z is the perpendicular distance from source to seafloor, V is the propagation velocity, and x is source-receiver distance. For $m = 0$, Eq. (7.1) becomes the travel time equation of a source-receiver pair for a horizontal reflector. The inclinations of the multiples originated from an inclined seabed are not constant and increase with the increasing order of multiples. According to the geometry in Fig. 7.2A, the travel time

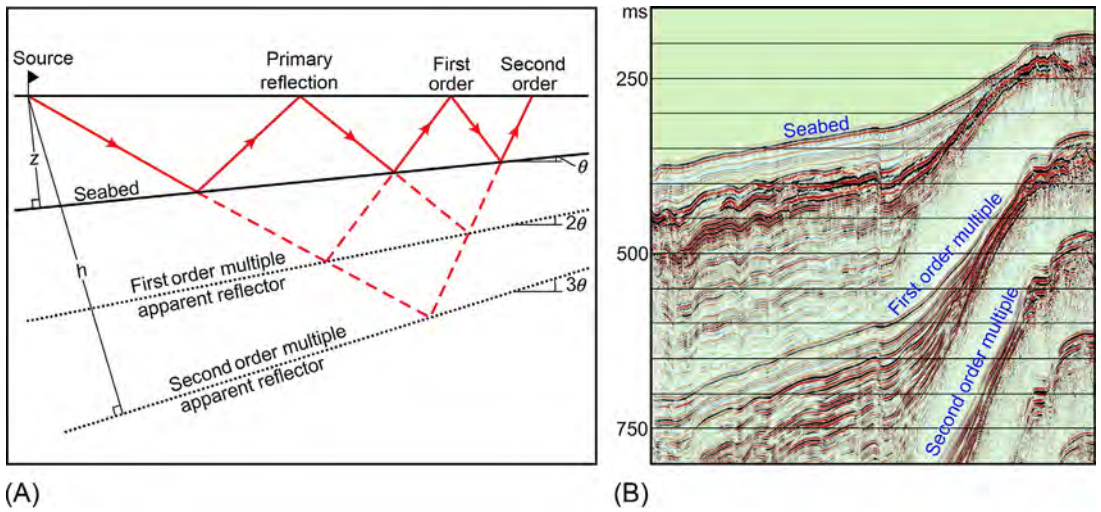


FIG. 7.2 (A) Schematic display of multiple reflection ray paths in the case of an inclined seabed; (B) an example marine stack section from an inclined seafloor. Multiples can be regarded as primary reflections from apparent reflectors lying at the subsurface in the case of an inclined seafloor.

expression of a seabed multiple of mth order for a seafloor with an inclination angle of θ is given by

$$t^2(x) = \frac{x^2 + 4h^2 - 4hx\sin(m+1)\theta}{V^2} \qquad (7.2)$$

where h is the perpendicular distance from source to the specific apparent multiple reflector (Fig. 7.2A). Eq. (7.2) indicates that the inclination of each consecutive multiple increases on the zero offset sections. If the inclination of the seafloor is θ, then the inclination of the mth order multiple will be $m\theta$. This situation prevents the complete success of most demultiple approaches.

The multiples can be suppressed if one of their characteristics, such as velocity or periodicity, meets the theoretical basis of the existing multiple removal approaches. Some of the demultiple methods are based on specific differentiations between primaries and multiples, such as moveout differences, while the others try to model or predict the multiples and then subtract from the input data. These differences between primaries and multiples regarding their main specifications are as follows:

- Multiples are predictable, yet primaries are not.
- Multiples appear at regular time intervals, at least for near offsets on shot gathers.
- Multiples always have higher moveout times than the primary reflections of the same zero offset arrival time.
- Lower velocities are required to flatten the multiple reflection hyperbolas during normal moveout (NMO) correction.
- The inclination of a multiple reflection produced by an inclined reflector is higher than the inclination of the primary reflection from the same reflector.
- Amplitudes of primary and multiple reflections with same zero-offset time are generally different.
- Polarity of seabed multiple reflections is reversed with respect to the polarity of the seafloor reflection.

Several different methods to predict and remove multiple reflections have been developed based on their characteristics given in the preceding list. For instance, predictive

deconvolution is based on the predictability of the multiples; stacking, *f-k* filtering, or Radon velocity filtering in the τ-p domain is based on the moveout time, dip, or velocity differences. In addition, the wave equation multiple rejection (WEMR) method uses wave equation modeling and subtraction, and surface-related multiple elimination (SRME) employs the autoconvolution approach. Most of these methods, except common depth point (CDP) stacking, are applied to prestack data, commonly to the preconditioned shot or CDP gathers.

7.1 CDP STACK

Because of the moveout time differences between primary and multiple reflections after NMO correction, most of the multiple amplitudes are suppressed during stacking. CDP stacking is the earliest technique which successfully suppresses the multiples based on the residual moveout differences. Fig. 7.3 schematically shows this process on a schematic CDP gather containing three primary reflections (*P*) and a seabed multiple reflection (*M*). Because the surface-related multiples propagate in the water column and in the uppermost sediments, their propagation velocity generally equals the average water velocity (approximately 1500 m/s). This velocity is considerably low when compared to the velocities obtained from the primary reflections with the same zero offset time on CDP gathers, which makes the curvatures of the multiple reflections, or their moveout times, higher than those of the genuine reflections (Fig. 7.3A). This difference is particularly pronounced for far offset traces. Since the velocities of primary reflections are used during the NMO correction, which is higher than the velocity of multiples (Fig. 7.3B), the reflection hyperbolas of multiples are not perfectly flattened after NMO correction (Fig. 7.3C).

While in-phase amplitudes of primaries are strengthened in the stacked trace, out-of-phase amplitudes of the multiples tend to diminish

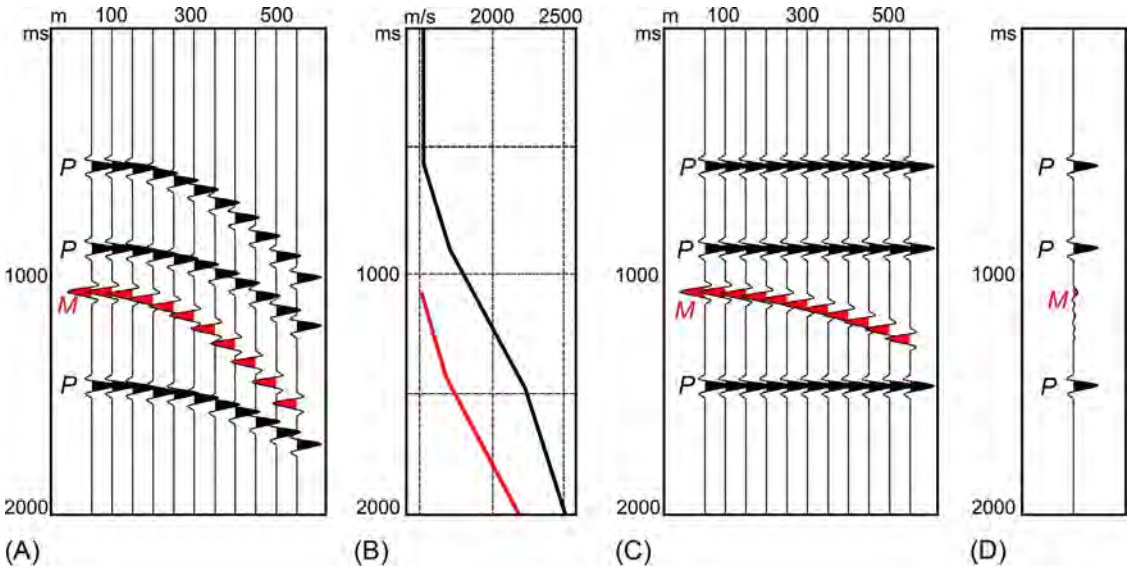


FIG. 7.3 (A) A schematic CDP gather involving three primary (*P*) and one multiple (*M*) reflections, (B) schematic NMO velocity functions for primary *(black)* and multiple *(red)* reflections, (C) same schematic CDP gather after NMO correction using the velocity function of primary reflections, and (D) suppressed multiple energy on the stacked trace.

when the traces in the CDP gather are summed up during stacking (Fig. 7.3D). As a real data example, two successive CDP gathers with three distinct seabed multiples are shown in Fig. 7.4. After NMO correction with the primary reflections' velocities (Fig. 7.4B), the multiples still remain hyperbolic and out-of-phase while the primary reflection hyperbolas are flattened to become in-phase (Fig. 7.4C).

Fig. 7.5 shows an example marine seismic line to illustrate the suppression of multiples during stacking. The brute stack section in Fig. 7.5A is obtained for 1500 m/s constant velocity and has quite distinct multiple amplitudes since the velocity used for NMO correction is also the velocity of multiple reflections, resulting in the flattening of the multiples as well as the primaries. Fig. 7.5B illustrates the full stack section obtained using the velocities of primary reflections. Almost all of the second-order multiple and most of the first-order multiple amplitudes are suppressed after stacking.

The efficiency of stacking in suppression of the multiples is directly proportional to the number of traces included in the stacking, that is, the fold number. In general, the higher the fold of the data, the better the suppression of the multiples by stacking. Fig. 7.6 compares 24 and 48 fold stack sections. As the maximum fold increases, a better suppression of the multiples by stacking is obtained.

In practice, amplitudes in far offsets tend to suppress the multiples after stacking, whereas the amplitudes in near offset traces contribute multiple amplitudes on stack sections (Fig. 7.7). This is because the moveout times between multiples and primaries are significantly low for near offset traces after NMO correction, which makes them almost in-phase and, when stacked, their amplitudes strengthen each other, resulting in

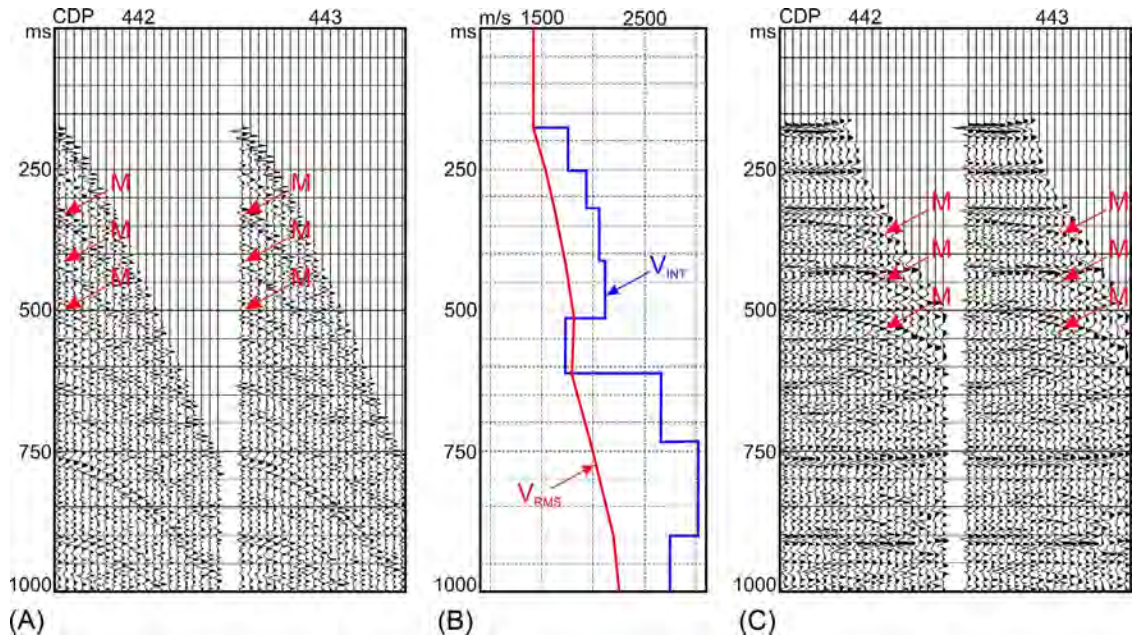


FIG. 7.4 (A) Two example CDP gathers with three multiple (*M*) reflections, (B) RMS *(red)* and interval *(blue)* velocity functions of the primary reflections from the location of CDP 442, (C) multiples are still hyperbolic whereas the primary reflections are flattened after NMO correction.

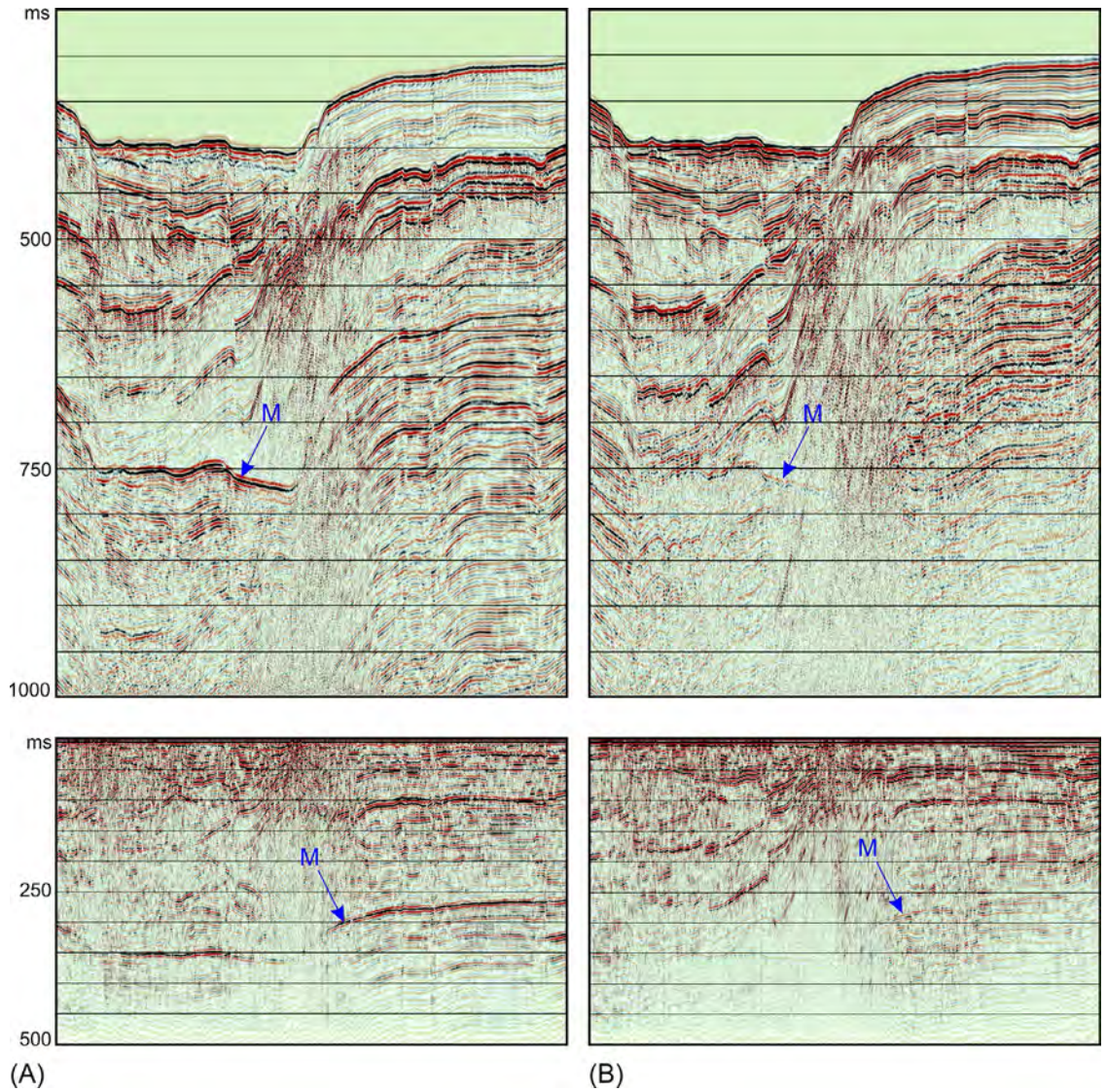


FIG. 7.5 (A) A brute stack with an NMO correction using 1500 m/s constant velocity, and (B) full stack with the velocities of primary reflections. *M* denotes the multiple energy. Autocorrelograms of each section are given in the bottom panels.

relatively high amplitude multiples on the stack data. To prevent the amplitudes of the multiples in near offset traces from increasing the multiple energy after stacking, one can mute out the specific zones of near offset traces where the multiple amplitudes are distinct. This is known as inner mute, and it can provide a better stack section with lower multiple energy. Fig. 7.8 shows an example application of inner mute. In Fig. 7.8B, the near offset parts of the multiple reflection amplitudes are muted out and a better stack section is obtained in which most of the first-order

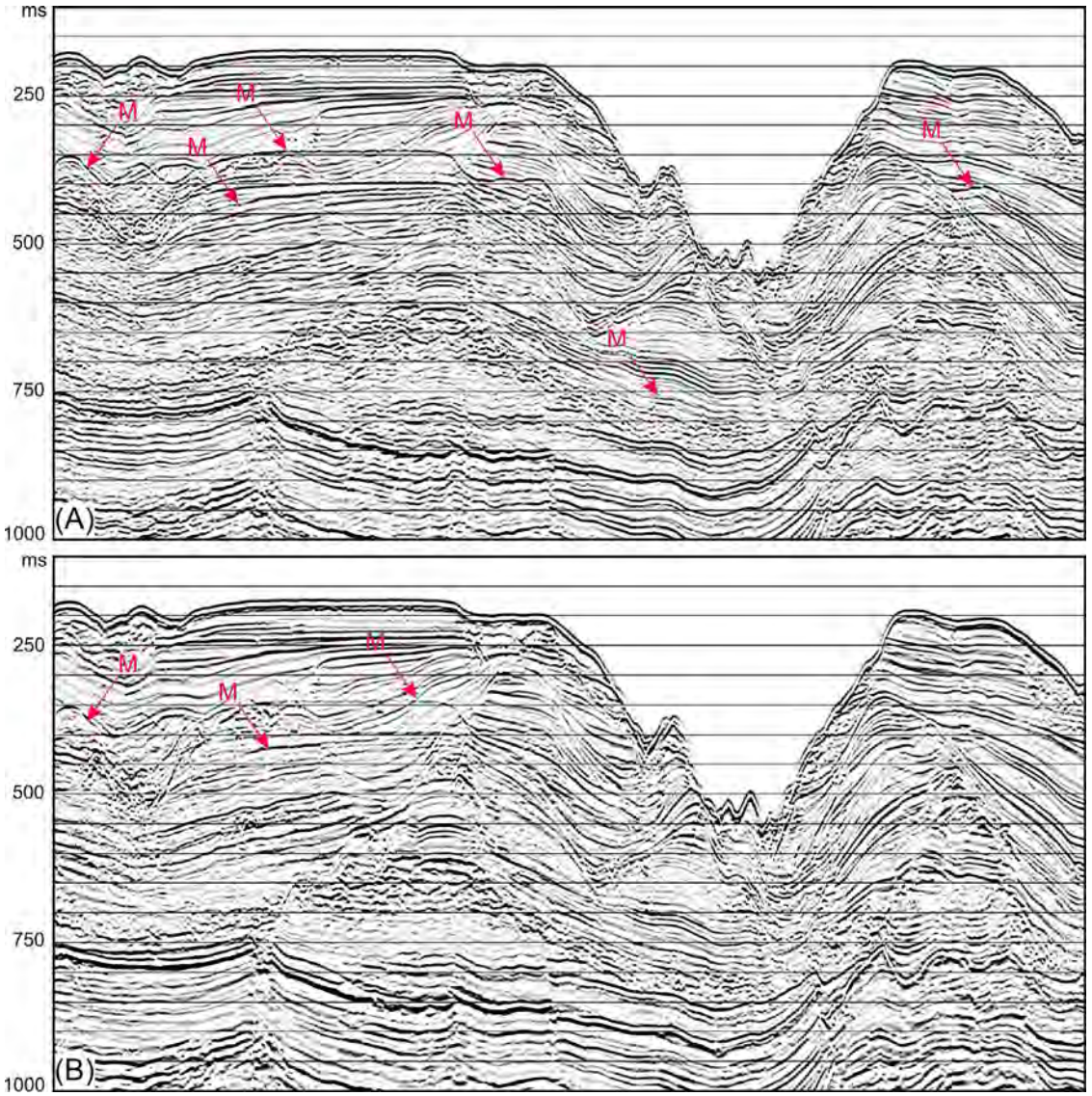


FIG. 7.6 (A) 24, and (B) 48 fold stack sections. As the maximum fold increases, a better removal of the multiples is achieved.

and almost all of the second-order multiple amplitudes are diminished (Fig. 7.8D), as compared with the conventional stack (Fig. 7.8C).

In the conventional stacking process (Section 10.3), all the traces in a CDP gather are simply summed up and the resultant amplitude values are divided by the number of traces involved in the summation. Since this is an averaging process, the approach is known as mean stack. In this case, all the traces in the stacking process are equally weighted using a constant weighting coefficient, and if the

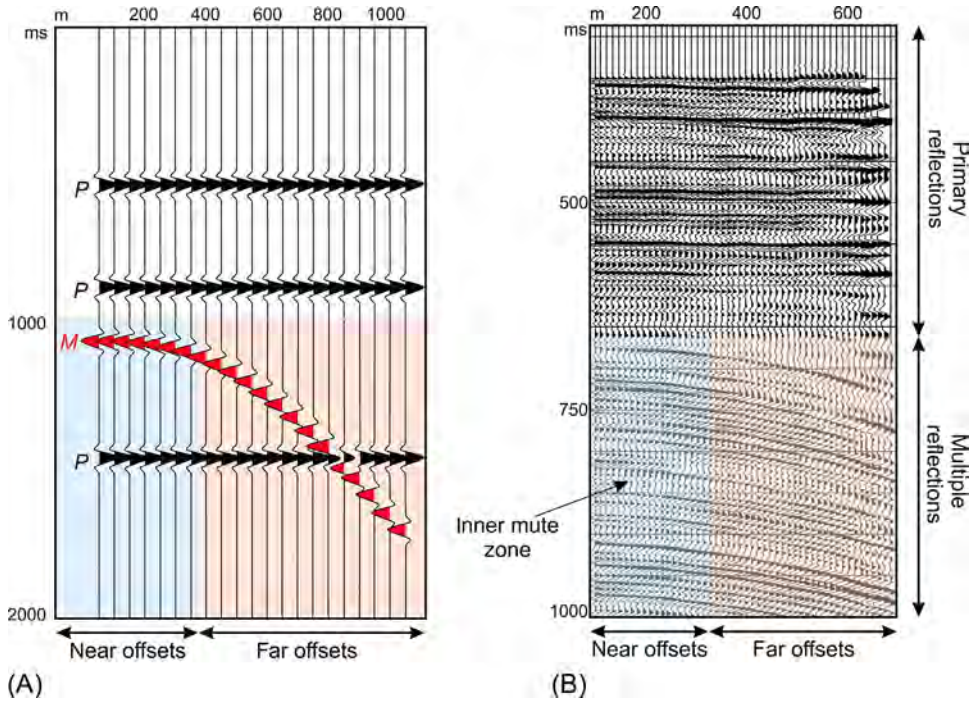


FIG. 7.7 (A) A schematic CDP gather after NMO correction, in which the primary reflections (*P*) are flattened whereas the multiple reflection (*M*) is still hyperbolic. In areas of near offsets, multiple amplitudes are almost in-phase *(blue area)*, and after stacking, their amplitudes strengthen each other. In the far offset areas, however, multiple amplitudes are out-of-phase *(red area)*, and after stacking, their amplitudes tend to diminish. (B) A real CDP gather example after NMO correction indicating a proper inner mute zone *(blue area)* to remove the in-phase multiple amplitudes.

number of traces involved is N, then the amplitude of the multiples will be decreased by an order of $1/N$ (Schoenberger, 1996). Observations indicate that the amplitudes of the multiples, however, change with the offset in CDP gathers in such a way that the multiple amplitudes are slightly higher than the primary reflection amplitudes for far offset traces, and lower for near offsets. Using this information, one can analyze the amplitudes in a CDP gather to obtain the most suitable weighting coefficients from near to far offsets by means of a least-squares approach. Then using these optimum weighting coefficients in stacking, a better suppression of multiples can be accomplished. This process is termed weighted stack.

Stacking is one of the most effective processes to suppress multiples, providing that the seismic data involves long offsets. However, it removes a significant amount of multiple energy only in the stack sections, and no improvement by means of multiple removal for prestack data is achieved by stacking. Therefore, in practice, the effect of stacking could be regarded as an additional contribution to multiple suppression, which removes the residual multiple energy remaining after the specific multiple removal techniques.

7.2 PREDICTIVE DECONVOLUTION

Suppression of multiple reflections by predictive deconvolution is based on the periodicity of the multiples in the seismic data. A prediction

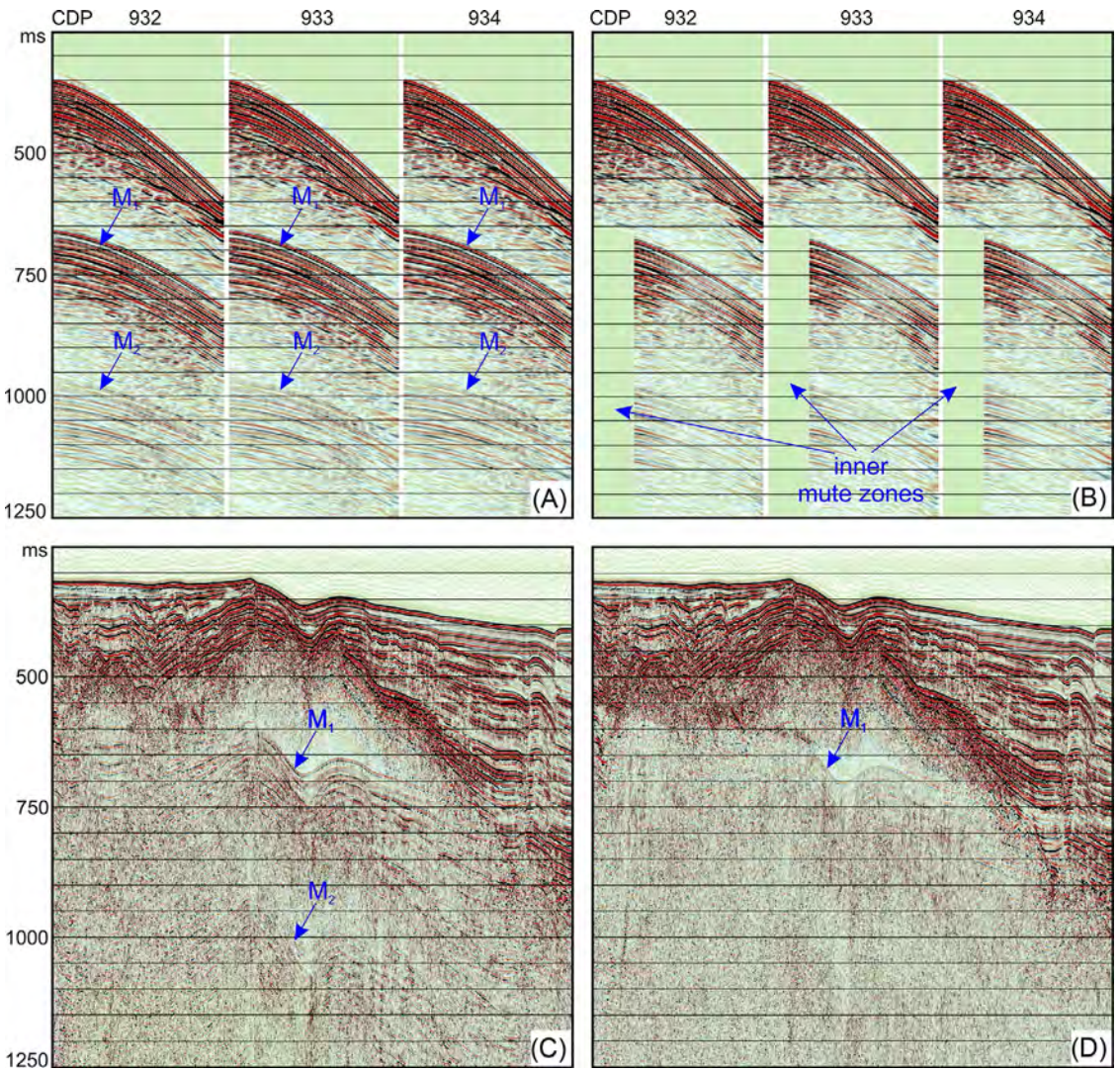


FIG. 7.8 Application of inner mute. (A) Four successive CDPs with first- and second-order multiples (M_1 and M_2), (B) inner mute zones *(shaded areas)* to remove in-phase multiple amplitudes, (C) full offset stack, and (D) stack with inner mute.

lag close to the sampling rate of input seismic data in predictive deconvolution can be used to improve the temporal resolution, while a higher lag value results in the suppression of multiple reflections. The prediction filter in the deconvolution process obtained by Eq. (6.21) predicts the periodic events in the seismogram, such as multiples, and the prediction error filter reveals the unpredictable components, such as primary reflections (Peacock and Treitel, 1969). Considering the long period multiples related to the seafloor, if the reflection coefficient of the seafloor is R_S, then the recorded time series will be $\{R_S, 0, 0, \ldots, 0, -R_S, 0, \ldots, 0, R_S^2, 0, \ldots, 0, -R_S^3, \ldots.\}$. This periodicity in the time series appears as periodic peaks (or notches) in the

amplitude spectrum of the seismogram (Fig. 6.12). As the time span between the multiple reflections in the time series increases, the notches in the spectrum get closer to each other.

Predictive deconvolution can be used to remove the multiple energy from the seismic data by predicting and suppressing the multiple reflection series. A successful predictive deconvolution can remove the complete multiple energy from the seismic data, provided that all of the assumptions listed in Section 6.2 are satisfied. Deconvolution is particularly efficient on short period multiples, and almost ineffective on the multiples with a period larger than approximately 200 ms. This is because the periodicity of the multiples varies with increasing offset due to the normal moveout of the reflection hyperbolas, as schematically shown in Fig. 7.9A and on a real marine shot gather in Fig. 7.9B. Although the time span between the successive multiples is almost constant in near offset traces, it progressively increases for far offsets. This is also evident on the autocorrelograms of the shot gather in Fig. 7.9C, in which the multiple energy is not horizontal but curved towards the far offsets, indicating that the periods of the multiples decrease at far offsets.

In deconvolution application, an optimal selection of prediction lag and operator length parameters is crucial. Fig. 7.10A shows the attenuation rates of the multiple amplitudes by predictive deconvolution for a range of prediction lag and operator length values. In this example, a synthetic seismic trace with one primary reflection and its multiple is used (Fig. 7.10B), and the amplitude suppression rate of the multiple after each application of predictive deconvolution for different prediction lag and operator length parameters is recorded. According to the autocorrelogram of the input synthetic trace shown

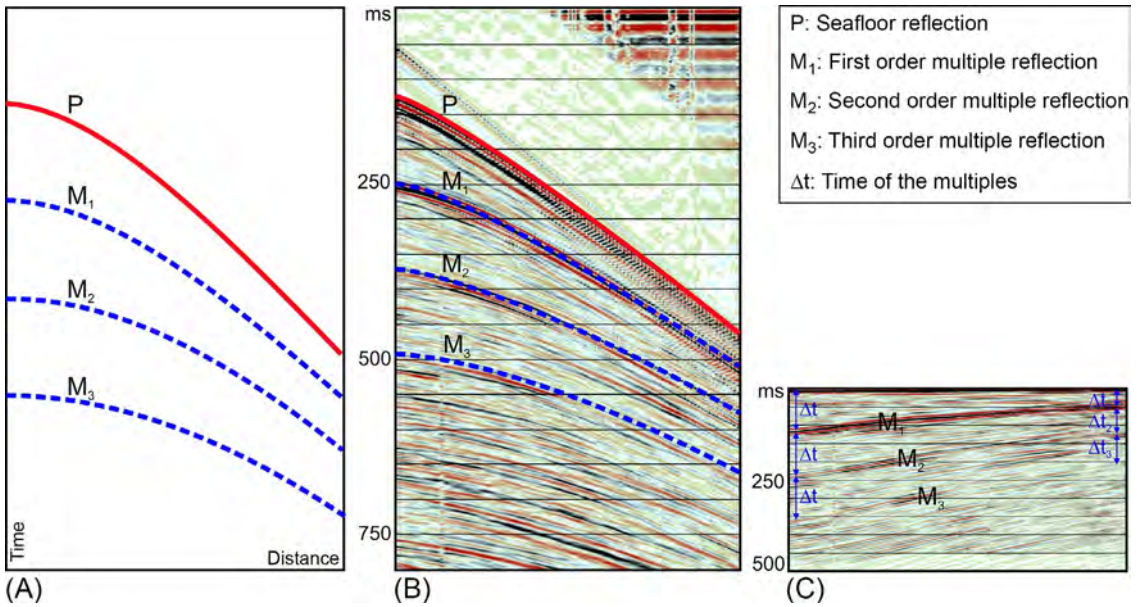


FIG. 7.9 Illustration of the variations in periodicity of multiples (M_1, M_2, and M_3) with increasing offset on (A) a schematic and (B) a real marine shot gather. (C) Autocorrelograms of the shot in (B) indicating the offset dependency of the multiple periods.

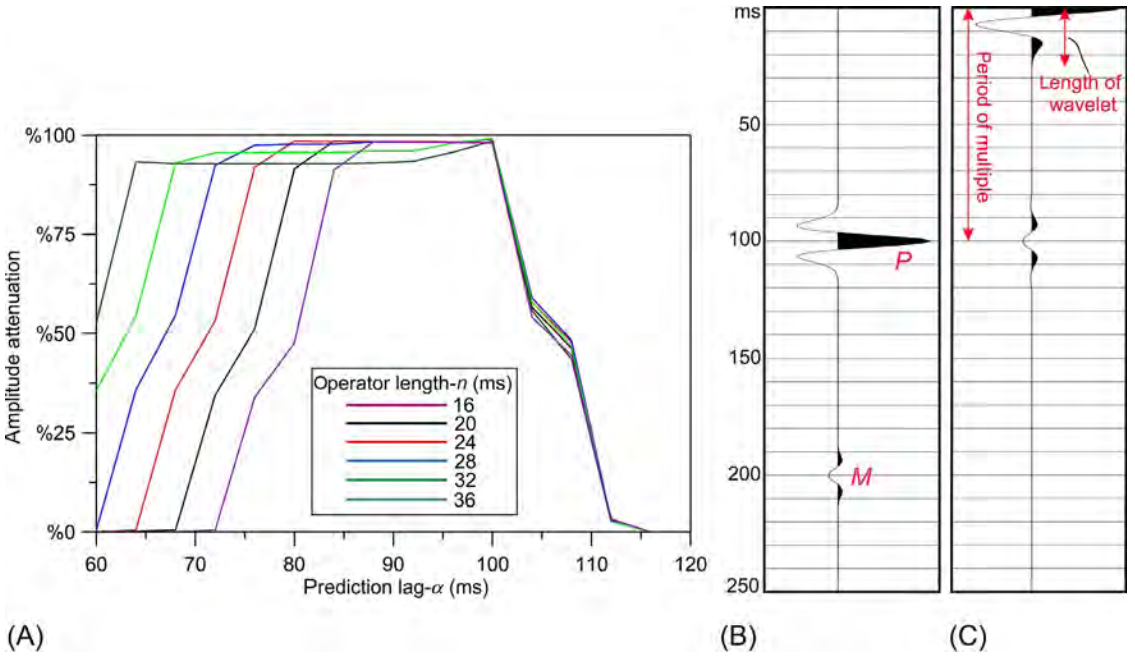


FIG. 7.10 (A) Amplitude attenuation rates of multiples for a range of prediction lag and operator length values. (B) A synthetic trace with one primary reflection (*P*) and its multiple (*M*) used for the analysis in (A). (C) The autocorrelogram of the synthetic trace in (B), indicating that the multiple period and time length of the wavelet are 100 and 28 ms, respectively.

in Fig. 7.10C, the multiple period and time length of the wavelet are 100 and 28 ms, respectively.

Based on the analysis in Fig. 7.10A, the maximum attenuation in multiple amplitude is obtained when the prediction lag equals the multiple period (100 ms) regardless of the operator length. Although the attenuation is not widely affected by operator length, the decay in the multiple amplitude slightly decreases for higher operator lengths if the prediction lag is small (e.g., compare the decay curve of 36-ms operator length for a prediction lag range between 60 and 95 ms). In any case, the multiple suppression is maximum when the prediction lag exactly equals the multiple period. The multiple period is the time span between the multiples in the seismogram and can be obtained by analyzing the autocorrelogram of the input trace. Practically, the multiple period equals the onset time of the first-order multiple in the autocorrelation series. When the prediction lag exceeds the multiple period, multiple attenuation simply fails regardless of the operator length (Fig. 7.10A). As a result, operator length must be selected as close as possible to the length of the source wavelet embedded in the data, and the prediction lag must equal to the multiple period which it is intended to suppress. The time length of the source wavelet is the length of the first isolated energy package in the autocorrelogram (Fig. 7.10C). If smaller, it progressively corresponds to a deconvolution application for the temporal resolution improvement (Section 6.5). In any case, the prediction lag must not exceed the multiple period for a successful multiple elimination.

Fig. 7.11 shows an analysis of multiple suppression by predictive deconvolution on a synthetic minimum phase trace consisting of a

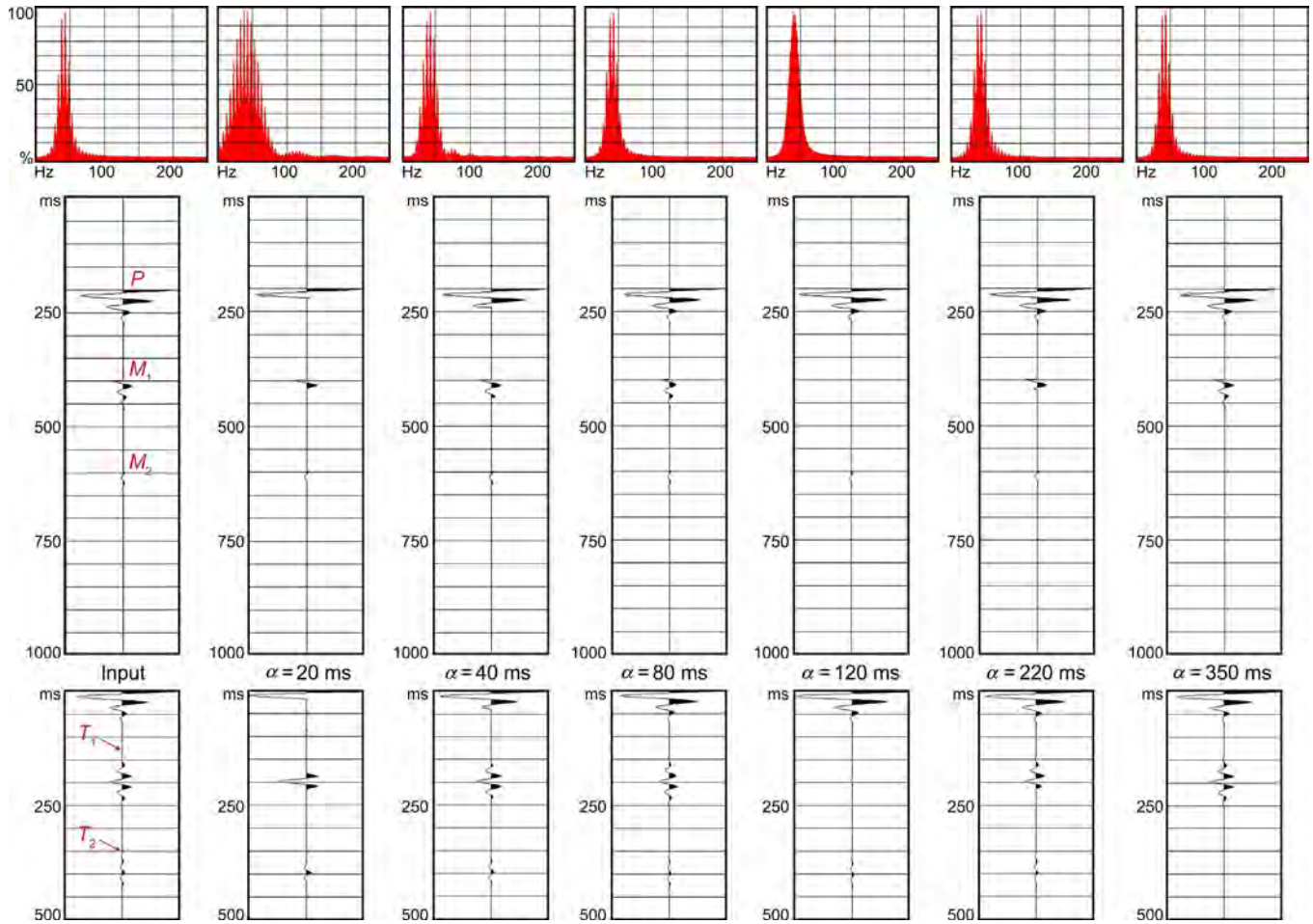


FIG. 7.11 Predictive deconvolution outputs for different prediction lags with a constant operator length of $n = 100$ ms on a synthetic trace with one primary (P) and its two multiples (M_1 and M_2) with their corresponding amplitude spectra (top) and autocorrelation traces (bottom). T_1 and T_2 represent the periods of the multiples M_1 and M_2, respectively.

primary reflection (P) at 200 ms and its two successive multiples (M_1 and M_2) at 400 and 600 ms. Outputs of the predictive deconvolution with corresponding amplitude spectra and autocorrelation traces are computed for a range of prediction lag values for a constant operator length of $n = 100$ ms. The periodic events such as multiples in the input time series result in notches in the amplitude spectrum of the seismogram. Small prediction lags, such as $\alpha = 20$ ms, shorten the seismic wavelet and hence improve the resolution, yet do not contribute to the suppression of multiple amplitudes (Fig. 7.11). However, deconvolution outputs for $\alpha = 120$ ms and $\alpha = 350$ ms indicate interesting results. For $\alpha = 120$ ms, the first-order multiple M_1 is completely removed by deconvolution, and there are almost no amplitudes for M_1 in the autocorrelogram. For $\alpha = 350$ ms, on the other hand, second-order multiple M_2 is completely suppressed. That is because the periods of the first- and second-order multiples are 120 and 350 ms, respectively, indicated by T_1 and T_2 in the autocorrelogram of the input seismogram. If there are more than one order of multiples in the data, periods of each individual multiples in the autocorrelogram are used as prediction lag values and more than one predictive deconvolution can be applied successively to the data, each of which can suppress one individual multiple.

In order to remove a source wavelet from the seismic trace, a spiking deconvolution can also be applied following the predictive deconvolution. Fig. 7.12A shows the same synthetic seismogram as in Fig. 7.11A. Fig. 7.12B illustrates its predictive deconvolution output for $n = 100$ ms and $\alpha = 120$ ms. Only primary and second-order multiple amplitudes exist in the seismogram since the first-order multiple is completely removed after predictive deconvolution. Amplitudes associated with the first-order multiple in the autocorrelogram are diminished, and the periodic notches in the amplitude spectrum disappear. If desired, predictive deconvolution can be applied one more time to remove the second-order multiple using a prediction lag of $\alpha = 350$ ms. In Fig. 7.12C, a spiking deconvolution using $n = 100$ ms and $\alpha = 2$ ms is applied to the seismogram following the predictive deconvolution to improve the temporal resolution. Specifically, the first zero crossing time of the autocorrelogram ($\alpha = 6$ ms) can also be used to improve the resolution, which makes the data more band-limited (Fig. 7.12D). The application order of predictive and spiking deconvolutions is changeable and either predictive or spiking deconvolution can be applied first.

Fig. 7.13 shows the effects of different operator lengths and prediction lags on a preconditioned real marine shot gather. Predictive deconvolution suppresses the amplitudes in the autocorrelograms in a specific gate between (α) and ($\alpha + n\Delta t$), where Δt is the sampling interval, and n is the operator length in time samples. The time length of these gates is $n\Delta t$, indicated by double arrows in Fig. 7.13. For instance, in the autocorrelograms of the predictive deconvolution output for $n = 40$ ms and $\alpha = 100$ ms in Fig. 7.13, the amplitudes between 100 and 140 ms are significantly suppressed. If the amplitudes corresponding to the multiple reflections coincide with this gate, then almost all of the multiple reflections are removed from the shots. For the example shot in Fig. 7.13, $n = 80$ ms and $\alpha = 60$ ms produce the best deconvolution result, since most of the multiple energy (except that at the far offsets) are within the gate.

In summary, prediction lag (α) must be longer than the time length of the first isolated energy in the input trace's autocorrelogram. If not, some of the amplitudes in the autocorrelation corresponding to the seismic wavelet will be zeroed out by deconvolution. In practice, the optimal output is obtained when prediction lag equals the multiple period. Predictive deconvolution suppresses the amplitudes between (α) and ($\alpha + n\Delta t$), and therefore it is preferred to set

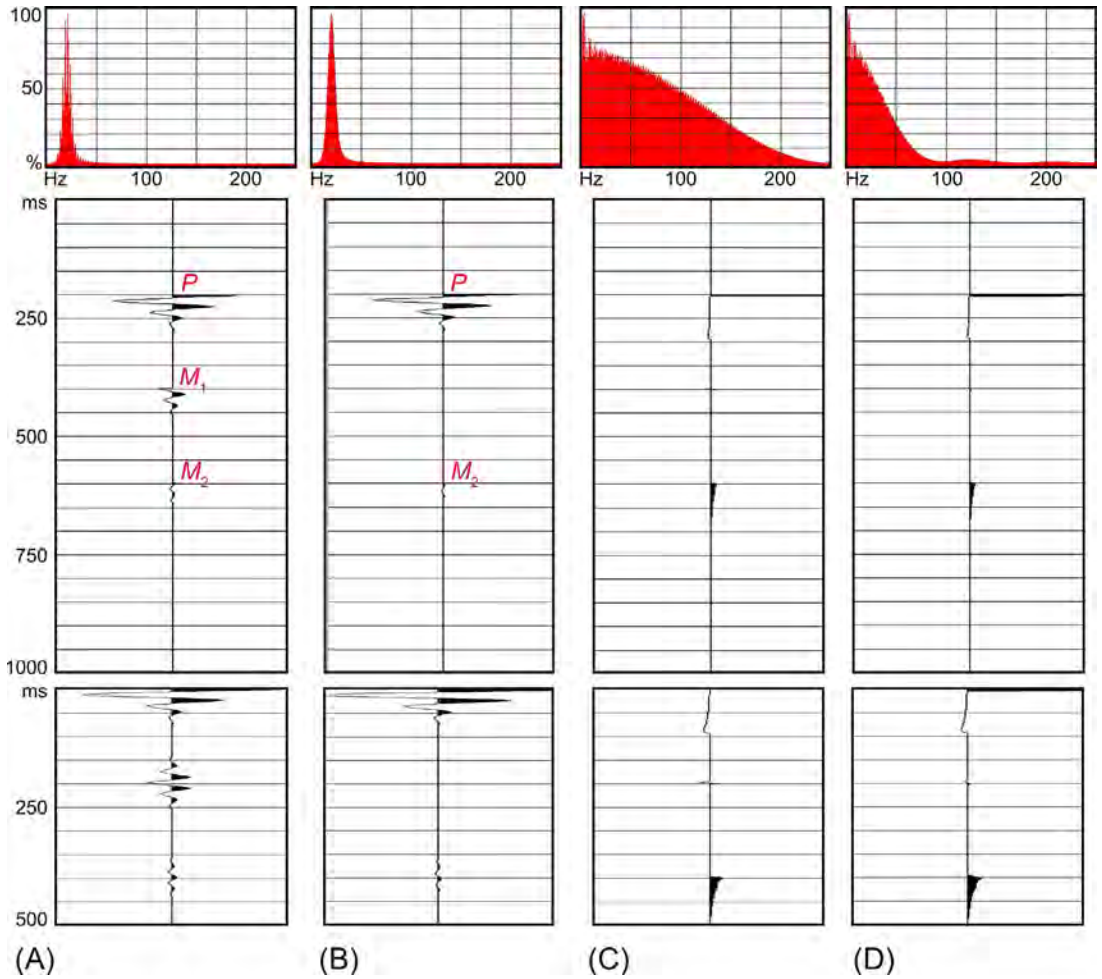


FIG. 7.12 Application of spiking deconvolution after predictive deconvolution to remove the source wavelet. (A) A synthetic trace with one primary (P) and its two successive multiples (M_1 and M_2), (B) predictive deconvolution output to remove M_1 for $\alpha = 120$ ms, (C) spiking deconvolution output for $\alpha = 2$ ms, and (D) predictive deconvolution output for $\alpha = 6$ ms (first zero crossing time of autocorrelogram). The operator length is $n = 100$ ms for all outputs. Corresponding amplitude spectra and autocorrelograms are given in the top and bottom panels, respectively.

the operator length (n) as the time length that the multiple energy extends in the autocorrelograms. In most cases, water depth changes along the seismic line, which means that the period of the multiples also changes along the line. In this case, it is recommended to use a water depth–dependent prediction lag value, which accounts for the variations in the period of the multiples.

Fig. 7.14 shows the selection of optimum values for α and n parameters on a schematic autocorrelation trace. If α is set to the multiple period, then n can be easily determined after a number of tests. This approach is illustrated on a marine shot gather in Fig. 7.15, which shows predictive deconvolution outputs with different operator lengths for a constant

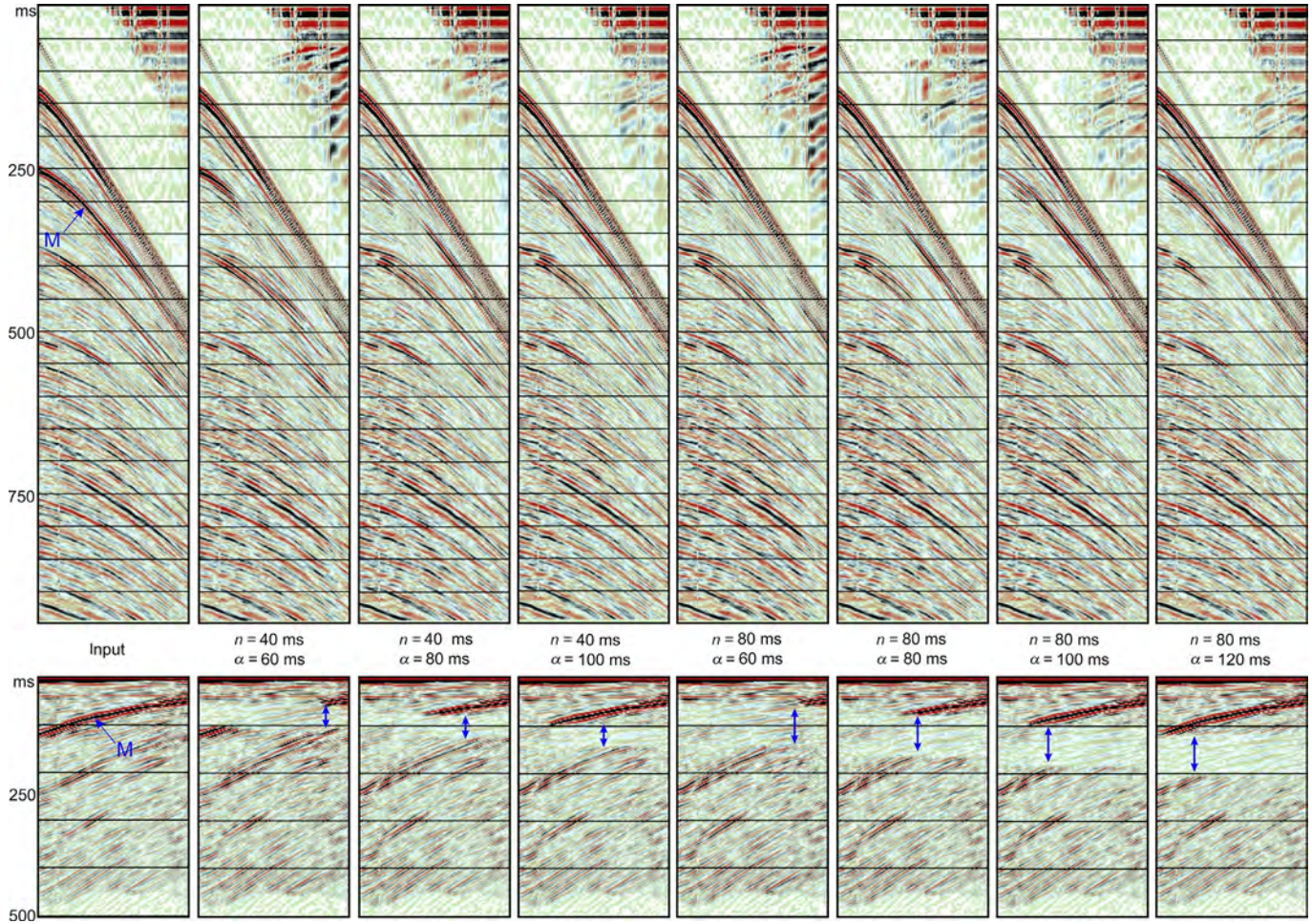


FIG. 7.13 Effect of different operator lengths and prediction lags on a real shot gather (top) and its autocorrelograms (bottom). *Double arrows* indicate the time gates where the amplitudes in the autocorrelograms are suppressed by predictive deconvolution. First-order long period multiple reflection is indicated by *M*.

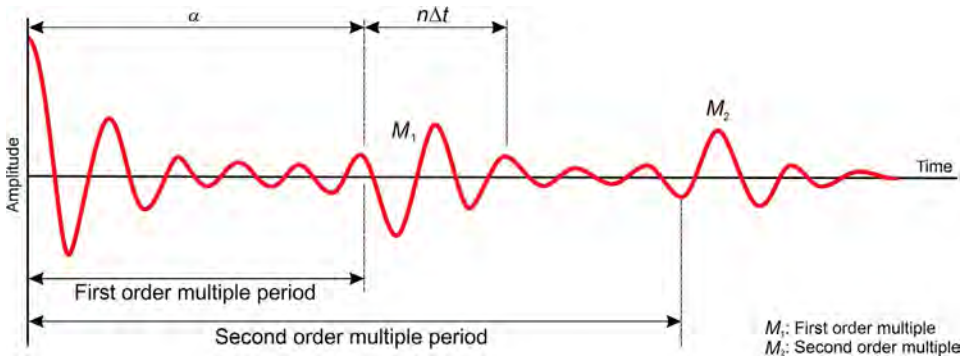


FIG. 7.14 Determination of operator length and prediction lag parameters on a schematic autocorrelation trace with reflection energy of two multiples (M_1 and M_2). Optimum deconvolution parameters (α and $n\Delta t$) are shown only for the first-order multiple M_1.

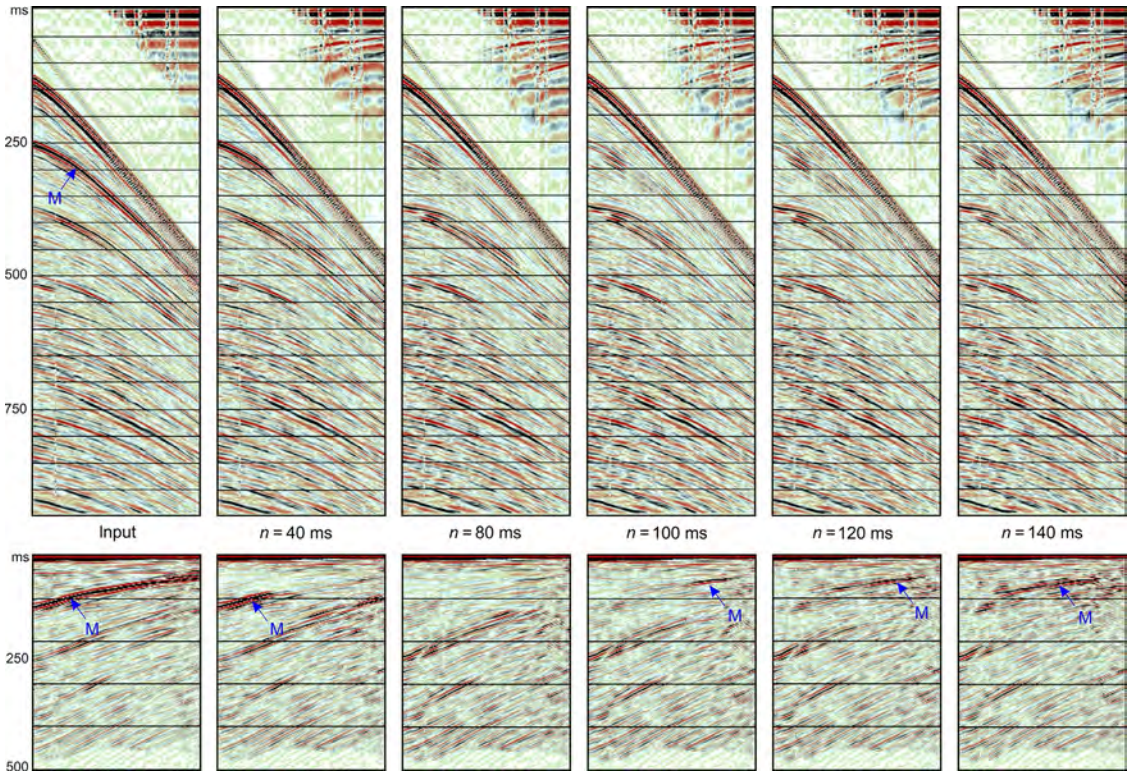


FIG. 7.15 Predictive deconvolution outputs of a shot gather (top) and its autocorrelograms (bottom) with different operator lengths for a constant prediction lag of $\alpha = 40$ ms.

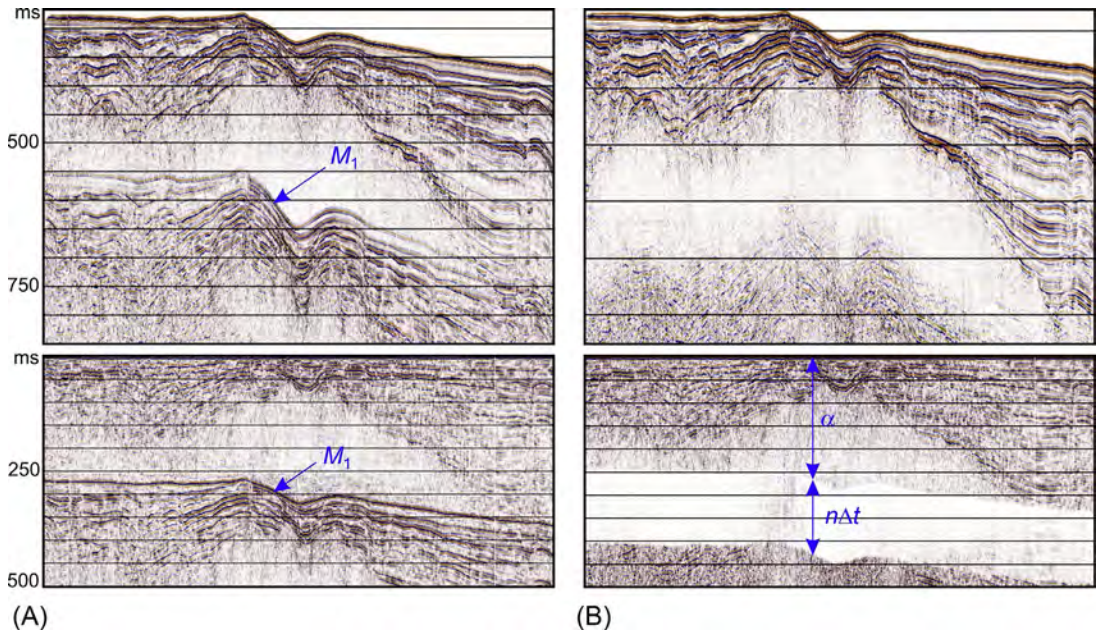


FIG. 7.16 (A) A high-resolution shallow seismic line with a first-order multiple (M_1), and (B) output of the predictive deconvolution for $n = 160$ ms with a water depth-dependent prediction lag. Autocorrelograms of the sections are given in the bottom panels.

prediction lag of $\alpha = 40$ ms. The most suitable operator length for the shot in Fig. 7.15 is $n = 80$ ms, which removes almost all of the multiple energy from autocorrelograms of the deconvolution output.

Fig. 7.16A shows a shallow seismic line along which the water depth slightly changes. Uplifting of the acoustic basement results in a transparent and reflection-free zone at the center, in which the first-order multiple (M_1) is clearly visible. Autocorrelograms of the input section indicate that the period of the multiple also changes as the water depth increases. Therefore, a prediction lag varying from 240 to 340 ms depending on the water depth is used with an operator length of 160 ms. The output of predictive deconvolution shows that most of the first-order multiple energy is suppressed (Fig. 7.16B), and the primary reflections of the deeper parts of the righthand side of the section, where the multiples and primaries interfere, become much more distinct.

The theoretical foundation of predictive deconvolution is based on the periodicity of the multiples in shot gathers or CDPs. The periodicity, however, is only completely preserved in zero-offset sections, and therefore predictive deconvolution may not be perfectly successful on nonzero offset data, such as shot or CDP gathers. In some cases, predictive deconvolution is applied to the stack sections. On the other hand, a suitable result may not be achieved since the stacking modifies the amplitude relations between the primaries and the multiples. In fact, the only domain where the periodicity and amplitude relationships are preserved is the slant stack (τ-p) domain, and the multiples can be better suppressed by predictive deconvolution applied in the slant stack domain. In the following section, the theory and practice of the

application of predictive deconvolution in the τ-p domain after transforming the data by Radon or τ-p transform is described.

7.3 DECONVOLUTION IN τ-P DOMAIN

It is possible to suppress the multiples by predictive deconvolution in the τ-p domain (Treitel et al., 1982). The theoretical basis of the slant stack or τ-p transform, which is a method of plane wave decomposition, is explained in Section 4.9. Since plane waves do not have spherical divergence effects, a spherical divergence correction must not be applied to input data before the deconvolution in the τ-p domain.

As described in Fig. 7.9, the multiples in nonzero offset data are not periodic, and the time span among the successive multiples is not constant and decreases with offset. In the τ-p domain, however, the situation is somewhat different. Fig. 7.17 shows the arrival time curves of a schematic shot gather with a primary (P) and its two multiple reflections (M_1 and M_2), and its τ-p transform. In arrival time curves in Fig. 7.17A, the time between the multiples is constant only for the $x = 0$ m offset. However, in the same shot gather, the time between the multiples is also constant along the radial lines cross-cutting the reflection and multiple hyperbolas, such as the A-A' line in Fig. 7.17A. Since amplitudes are summed up along these radial lines during the τ-p transform, the time difference between multiples is also constant for a certain p value in the τ-p gather, such as p_0 in Fig. 7.17B, and hence they are periodic in the τ-p domain.

Taner (1980) suggested that, based on the periodicity of the multiples after the τ-p transform, predictive deconvolution can be applied in the τ-p domain to suppress the multiples. In this approach, a predictive deconvolution operator can be computed for each p value from the autocorrelation of the τ-p gather. α and n values can be determined from the trace of the minimum p value in this autocorrelation. According to Yılmaz (1987), α decreases as the p value

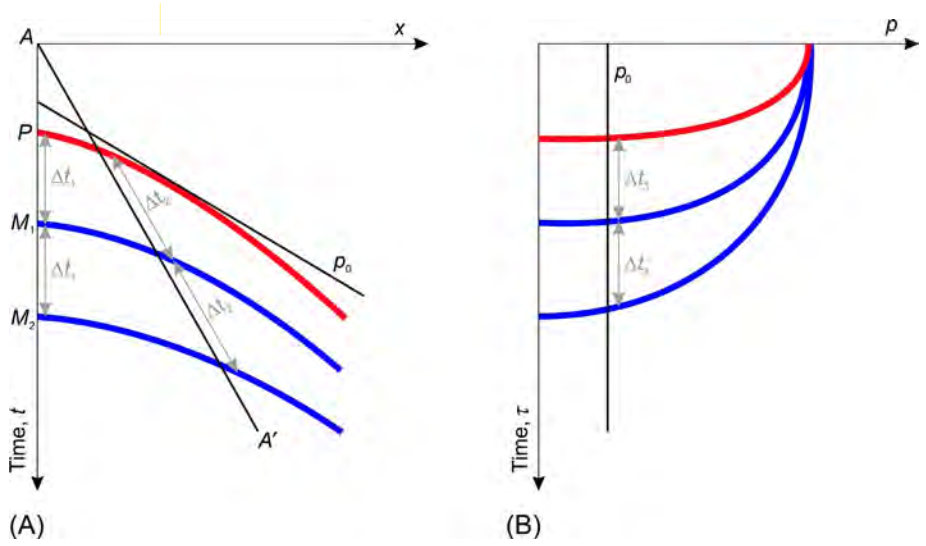


FIG. 7.17 Schematic illustration of arrival time curves of shot gather with a primary (P) and its two multiple reflections (M_1 and M_2) in (A) time domain and (B) slant stack domain after a τ-p transform. Multiples are periodic with a period of Δt for $x = 0$ m offset, along the radial line, like A-A', and along any constant (vertical) p value in τ-p gather, like p_0.

increases, and therefore α must be modified as the p value changes during the computations, while n is kept constant. The α value as a function of p is given by

$$\alpha_p = \alpha_0 \sqrt{1 - p^2 V_M^2} \tag{7.3}$$

where α_0 is the prediction distance at $p = 0$, and V_M is the propagation velocity of the multiples. The data examples given here, however, are computed for constant α and n parameters.

Fig. 7.18 shows an application of the τ-p domain predictive deconvolution to a marine shot gather. Prediction lag is determined as 160 ms, being equal to the length of the first transient package in the autocorrelograms, and then different operator lengths are tested. Deconvolution with an operator length smaller than $n = 100$ ms cannot suppress the multiple, and the efficiency of the deconvolution increases as the operator length increases. The optimal parameters for this shot are $\alpha = 160$ ms and $n = 240$ ms. Fig. 7.19 shows the τ-p domain predictive deconvolution results on a brute stack section using the parameters given here.

7.4 RADON VELOCITY FILTER

Long period multiples can be suppressed by parabolic Radon transform based on the moveout differences between primary and multiple reflection hyperbolas in CDP gathers. The method was first proposed by Hampson (1986) and it is accomplished by an application of the τ-p transform to NMO-corrected CDPs. The most important advantage of the method is that it does not require information on the formation mechanism of the multiples. Practical applications indicate that the Radon velocity filters are effective in suppressing the long period multiples, especially at far offsets. However, for complete success, the residual moveout between primary and multiple reflections after NMO correction should be at least 30 ms. In practice, the higher the residual moveout, the more effective the method in multiple elimination. This prerequisite requires long offset seismic data to be collected, and therefore the method is generally almost ineffective on the data collected with a short streamer cable. In addition, since the method is based on the moveout differences after NMO correction, it also requires a careful velocity analysis.

The amplitudes in the CDP gathers are mapped into different areas in the τ-p domain, depending on their curvature controlled by their residual moveout times since the horizontal axis of the τ-p gather corresponds to residual moveouts. Providing an accurate velocity field, the multiple reflections are still hyperbolic while the primary reflections are flattened following the NMO correction. This difference results in the amplitudes of primaries and the multiples being mapped in different areas in the τ-p domain, in which the amplitudes of the multiples are muted out (Landa et al., 1999). The important point here is the correct picking of this mute zone, which discriminates the primary and multiple amplitudes in the τ-p domain. The method involves following steps which are schematically shown in Fig. 7.20.

i. NMO correction with velocities of primary reflections is applied to input CDP.
ii. CDP gather is transferred into the τ-p domain by Radon transform.
iii. The area comprising the multiple amplitudes in τ-p domain is muted out.
iv. CDP is transferred back into the time-distance domain by inverse Radon transform.
v. If required, an inverse NMO is applied to obtain original CDP gather.

Fig. 7.20A schematically shows reflection hyperbolas representing the arrival times of five primary and three multiple reflections. If we apply an NMO correction to this CDP gather using primary reflection velocities, hyperbolas of the primary reflections are flattened.

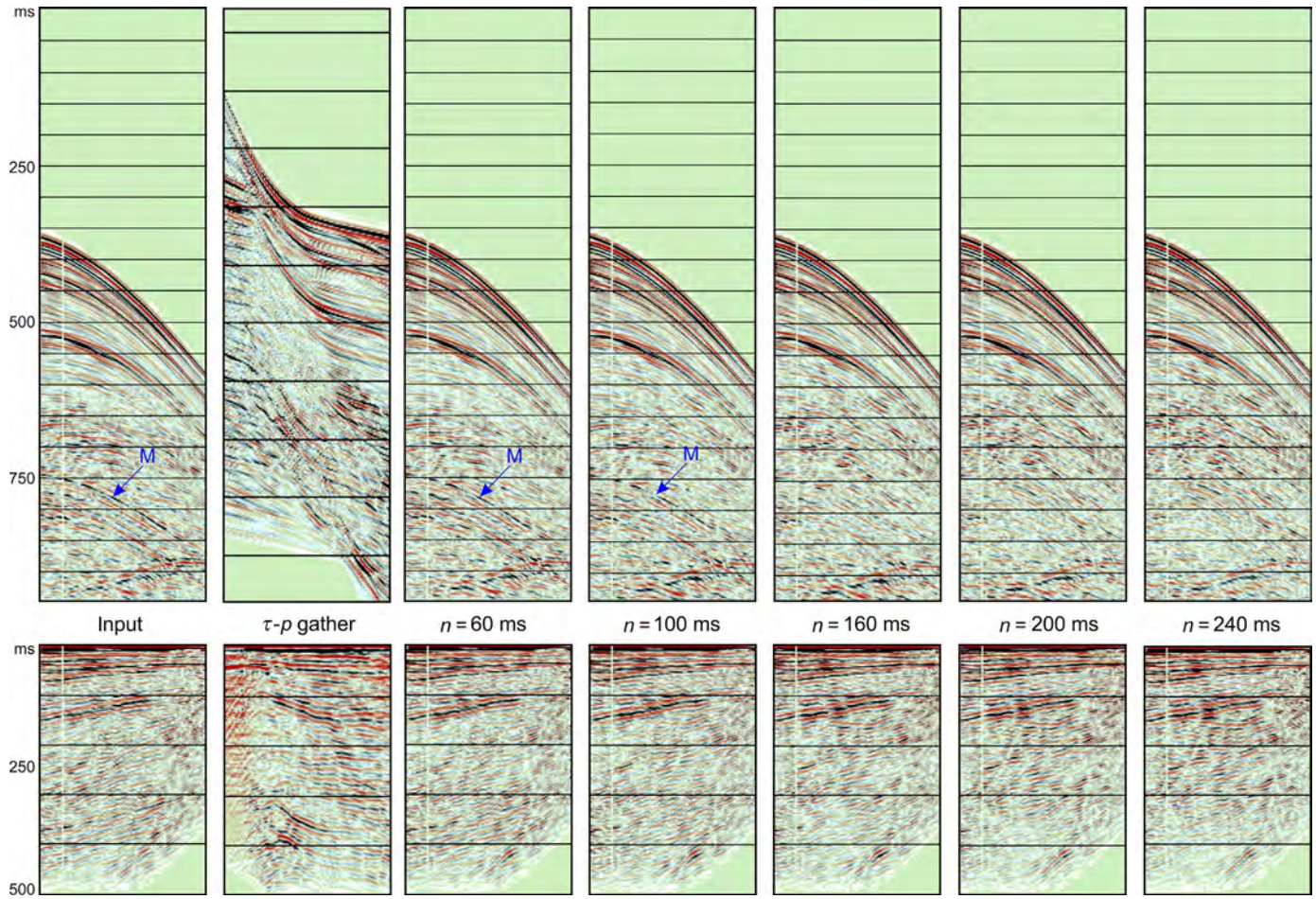


FIG. 7.18 The τ-p domain predictive deconvolution application to a shot gather (top) for different operator lengths with $\alpha = 160$ ms, and corresponding autocorrelograms (bottom).

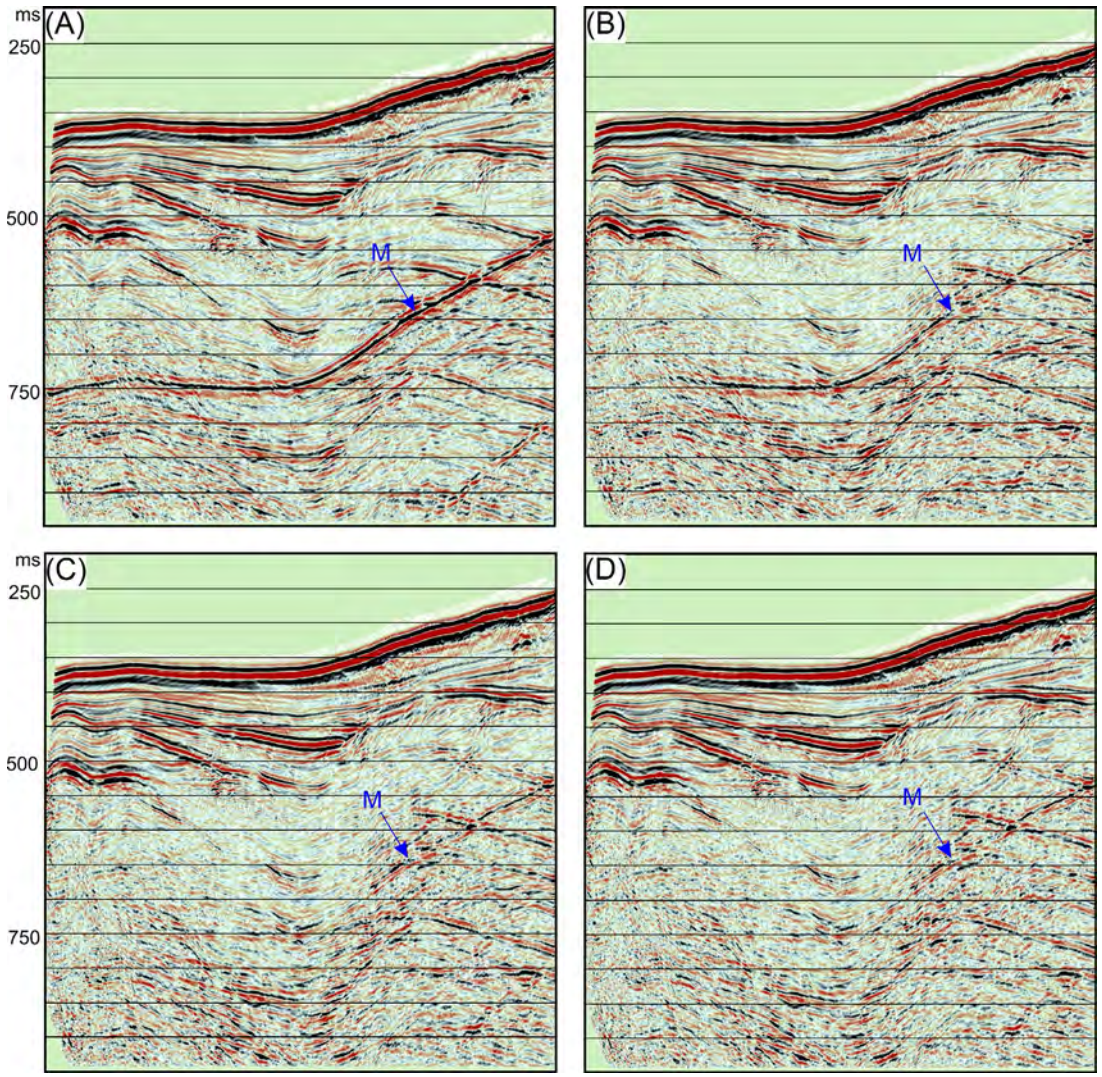


FIG. 7.19 (A) A brute stack section, and its τ-p domain predictive deconvolution results with a constant prediction lag of $\alpha = 160$ ms for different operator lengths of (B) $n = 160$ ms, (C) $n = 200$ ms, and (D) $n = 240$ ms. M represents the first-order seabed multiple.

Because the velocity used in NMO correction is almost always higher than the velocity of the multiples, multiple reflection hyperbolas cannot be completely flattened and they exhibit a residual moveout shown by Δt_1, Δt_2, and Δt_3 in Fig. 7.20B. An overcorrected reflection hyperbola produces negative residual moveout, while an undercorrected one (like the hyperbolas of multiple reflections) exhibits positive residual moveout value. If the hyperbola is exactly flattened after NMO correction, as expected for primary reflections, then there will be no residual moveout in the τ-p domain. Therefore, when we transfer the NMO corrected gather in

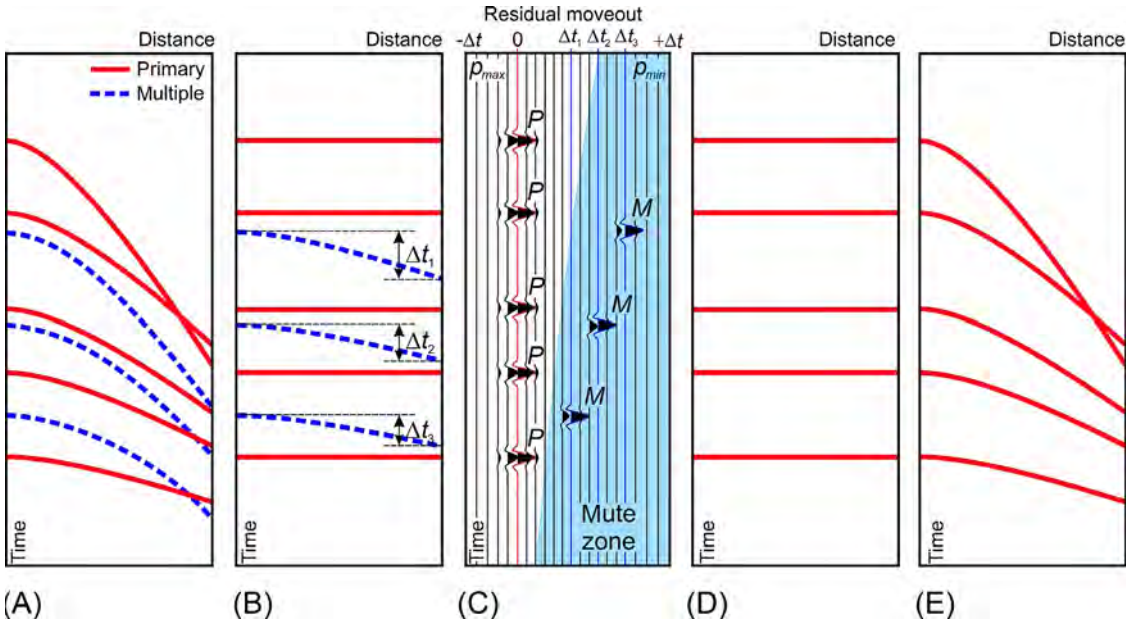


FIG. 7.20 Schematic illustration of Radon velocity filter application. (A) A CDP gather with primary *(red)* and multiple *(dashed blue)* reflections. (B) NMO correction with the velocities of primary reflections leaves a certain amount of residual moveout (shown by Δt_1, Δt_2, and Δt_3) on the reflection hyperbolas of multiples, while the primaries are flattened. (C) CDP gather in the τ-p domain after Radon transform and the mute zone *(blue shaded area)* involving the multiple amplitudes. (D) CDP gather after muting and inverse Radon transform, and (E) original CDP gather after inverse NMO correction with no multiple amplitudes.

Fig. 7.20B into the τ-p domain, the primary amplitudes (P) are aligned onto the zero residual moveout axis, whereas multiple amplitudes (M) are still hyperbolic and are mapped onto the positive panel in the τ-p domain (Fig. 7.20C). The higher the residual moveout of the multiples, the more distant their amplitudes from the zero moveout axis in τ-p domain. When the area of multiple amplitudes indicated by shaded area in Fig. 7.20C are muted out, a CDP gather without multiples is obtained after an inverse Radon transform (Fig. 7.20D). This gather is still in NMO corrected form, and if required, the original CDP is reconstructed after an inverse NMO correction using primary reflection velocities (Fig. 7.20E).

Fig. 7.21 shows an example application of muting in the τ-p domain on a real CDP gather. Fig. 7.21A illustrates an input NMO corrected CDP gather in which the primary reflections are flattened while the multiples are still hyperbolic and have a certain amount of residual moveout. Its τ-p domain representation is shown in Fig. 7.21B, computed for a residual moveout range from −100 to 200 ms. The amplitudes of the primary reflections between approximately 250 and 500 ms are located along the zero moveout axis, whereas the amplitudes of the multiples between 500 and 1000 ms are mapped in the positive moveout panel. This differentiation in the amplitudes based on their residual moveout times allows us to easily discriminate the multiple and primary amplitudes in the τ-p domain. As in Fig. 7.21C, we can mute out the amplitudes of the multiples to obtain multiple-free CDPs. Alternatively, one can also mute

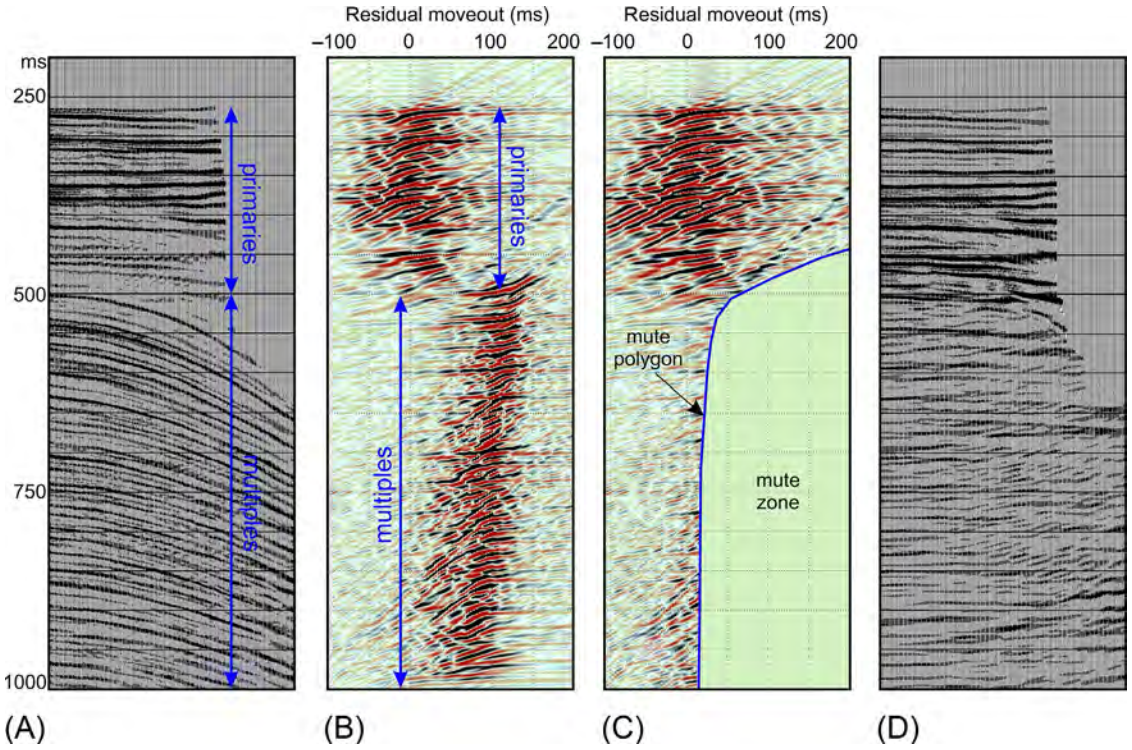


FIG. 7.21 (A) An NMO corrected CDP gather, (B) its τ-p domain representation after Radon transform, (C) muting out of the multiple reflection amplitudes in the τ-p domain, and (D) multiple-free CDP gather after inverse Radon transform.

out the zone of primary reflection amplitudes to get the multiples-only CDPs, as in Fig. 7.22. In this case, the multiple amplitudes are subtracted from input CDPs to get the multiple-free CDPs. Although the applications indicate that both approaches produce quite similar results, it is practically more straightforward to apply a mute zone for multiple amplitudes in the τ-p domain.

Fig. 7.23 shows a CDP gather before and after a Radon velocity filter. The multiple hyperbolas between approximately 500 and 1000 ms are almost completely eliminated after filtering. Fig. 7.24 compares a brute stack section with and without the Radon filter. Trace-by-trace consistent amplitudes below the acoustic basement are interbed multiples removed by the Radon velocity filter.

In addition to the enhancement in the CDPs, removing of the multiples substantially improves the quality of the semblance plots in velocity analysis. Fig. 7.25A and B compare two semblance plots of the same CDP gather before and after a Radon filter, respectively. In Fig. 7.25A, the velocity of the primary reflections slightly increases from approximately 1500 to 1600 m/s between 250 and 500 ms for shallow subsurface sediments. Between 500 and 1000 ms, however, two velocity trends quite similar to each other exist: one from 500 to 750 ms, and the other from 750 to 1000 ms. These two individual trends correspond to the semblance contours formed by the first- and second-order multiple reflections, respectively. These contours dominate the semblance plot in deeper parts between 500 and 1000 ms

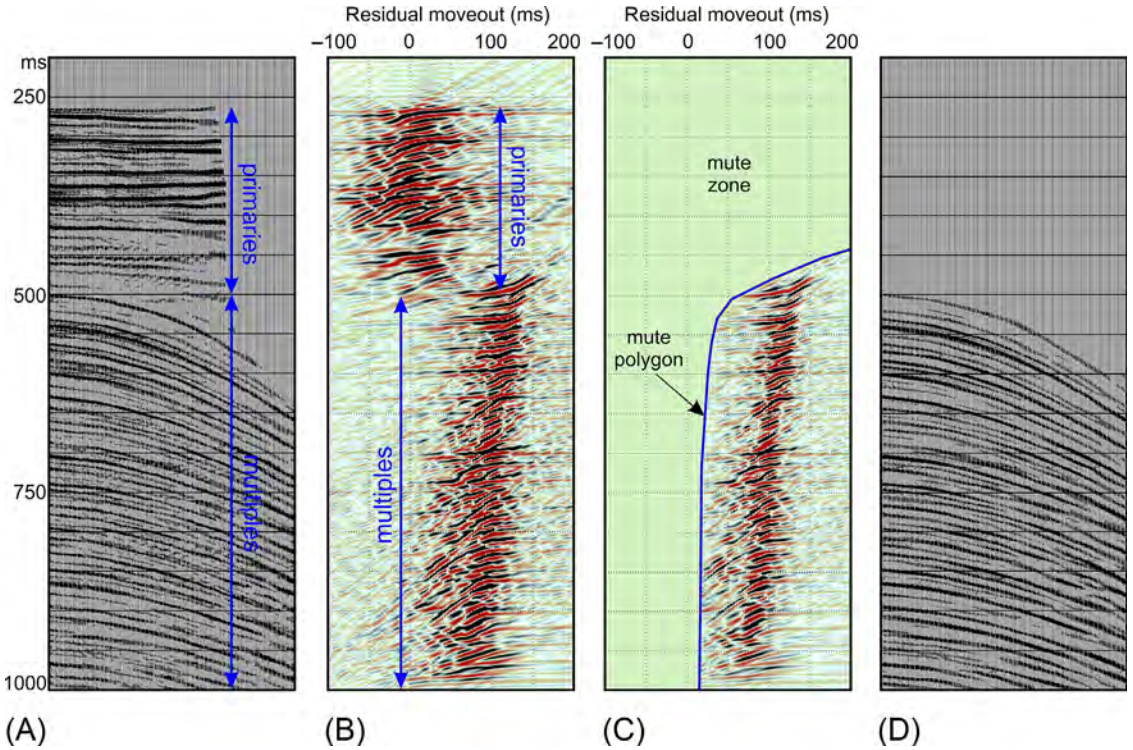


FIG. 7.22 (A) An NMO corrected CDP gather, (B) its τ-p domain representation after Radon transform, (C) muting out of the primary reflection amplitudes in the τ-p domain to keep the multiple amplitudes, and (D) output CDP gather consisting of only multiple reflections after inverse Radon transform.

preventing us from picking the velocities of primary reflections for late arrivals, where the amplitudes of the primaries are all hidden behind the multiples. In Fig. 7.25B, however, there are no contours and enclosures connected to the multiple energy on the semblance: correctly picking the primary velocities is possible after a Radon velocity filter.

In practice, a first-pass velocity analysis is performed before the Radon velocity filter to use during the Radon transform. After application of a Radon filter in the τ-p domain, a second-pass velocity analysis is done to accurately pick the velocities of the deeper primaries buried under the dominant multiple amplitudes.

7.5 WAVE EQUATION MULTIPLE REJECTION

Generation of multiple reflections in the water column can be approached by wave field modeling. Using seafloor topography and acoustic wave equation modeling, it is actually possible to estimate all multiples via surface seismic data. The method is known as wave equation multiple rejection (WEMR) and was first proposed by Wiggins (1988), who suggested that once the long period multiples are modeled, then they can be subtracted from the input seismic data by an adaptive subtraction. Short period multiples cannot be eliminated by WEMR, but their amplitudes are reduced.

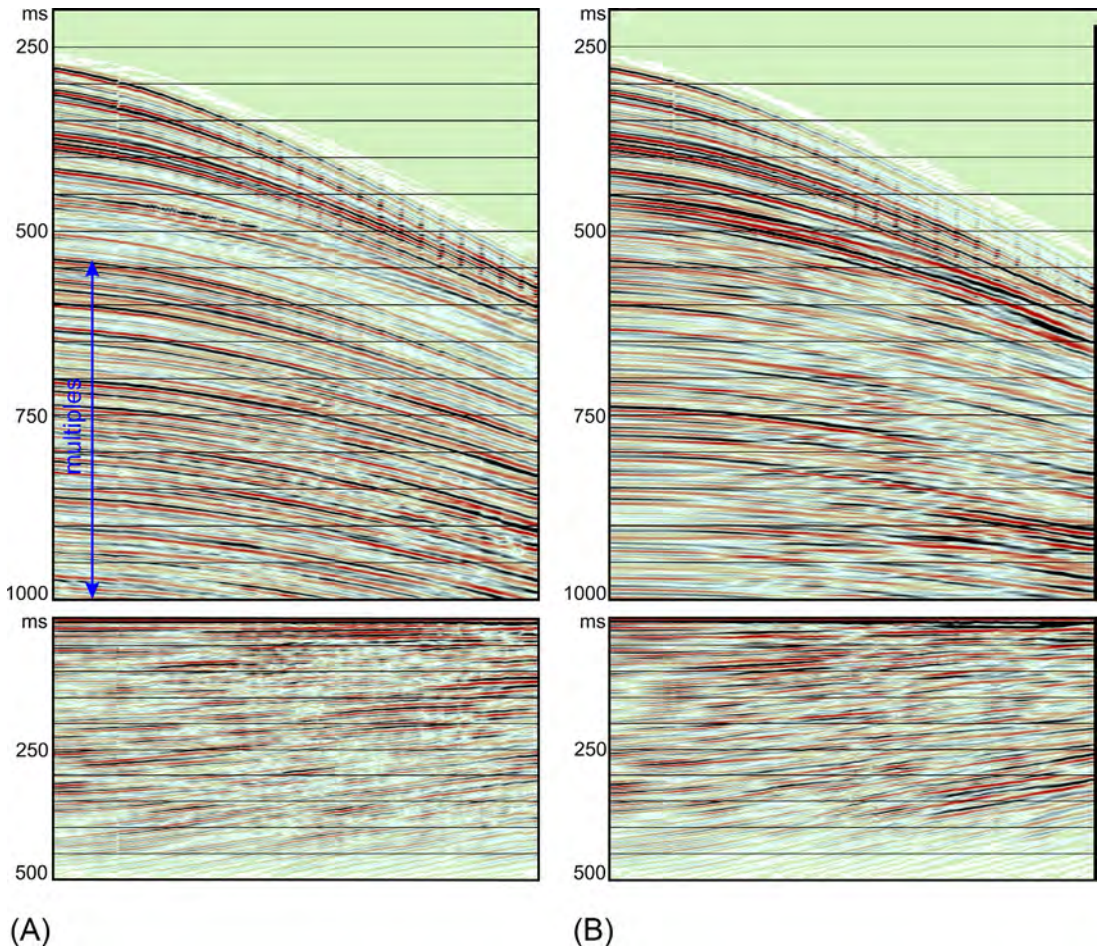


FIG. 7.23 A CDP gather (A) before and (B) after Radon velocity filter (top), and their corresponding autocorrelograms (bottom). Multiples between 500 and 1000 ms in (A) are removed after filtering in (B).

WEMR is a method that models the wave field propagated in the water column by a wave equation modeling approach that considers the streamer and seafloor geometry. It is accomplished in two steps. First, the propagation time differences between the multiples are obtained using acoustic wave equation modeling. Second, the reflection coefficient of the seafloor is estimated. The most important points in suppressing the multiples using WEMR are to determine the form and the amplitudes of the multiples accurately (Lu et al., 1999).

To explain the theoretical basis of WEMR, let's assume a seismic signal produced by the seismic source in the water column, reflected from the seabed and recorded at receiver R_3. The same signal continues its propagation towards the sea surface, where it is reflected back towards the seabed. It is then reflected from the seabed and recorded at the receiver, for instance, R_6. Similarly, it is again reflected from the sea surface and then the seabed to be recorded at receiver R_8, and the signal propagation continues within the water column in this

Ghost Reflection

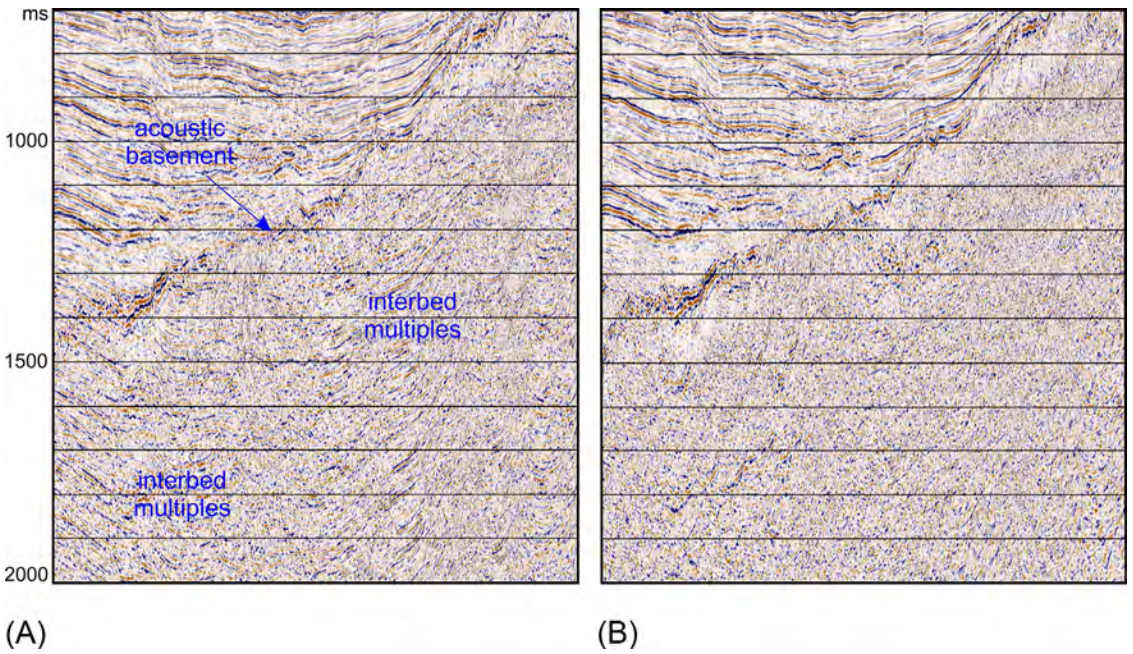


FIG. 7.24 A brute stack section (A) before and (B) after Radon velocity filter. Amplitudes below the acoustic basement in (A) represent interbed multiples.

manner. According to this signal propagation geometry, the signal recorded at receiver R_3 can be used to estimate the record at R_6, and similarly, the record at receiver R_6 can be used to estimate the record at R_8, and so on. The following information can then be deduced from this signal propagation geometry (Wiggins, 1988):

i. Reflection from sea surface: used to determine surface reflection coefficient.
ii. Propagation to the seabed: used to obtain travel time to the seafloor, and amplitude loss due to the spherical divergence.
iii. Reflection from seabed: used to calculate seabed reflection coefficient statistically.
iv. Propagation to the receiver: used to obtain travel time to the receiver, and amplitude loss due to the spherical divergence.

Reflection from the seabed and propagation to a receiver require that the seabed already be defined in time and distance dimensions along the line. For simplicity in computations, it is assumed that the seafloor is horizontal for each individual shot. Seabed reflection is picked from brute stack sections and the arrival time of this reflection is converted into depth using average wave velocity in the water. If the seabed is inclined, the data can be migrated using a fast migration algorithm, such as the Stolt *f-k* migration using a constant velocity. In addition, since the reflection coefficient of the seabed cannot be obtained from the seismic data, it is calculated in a statistical fashion.

Fig. 7.26A shows a stack section from a shallow continental shelf with a horizontal seafloor consisting of a nice stratigraphy over a regional basement high. The section also includes both long period and peg-leg multiples indicated by *M*, which are especially distinct below the basement high at the lefthand side where there are no primary reflections. Fig. 7.26B shows the multiple energy modeled by WEMR, which is then subtracted from the input data to obtain the output section in Fig. 7.26C. The output stack

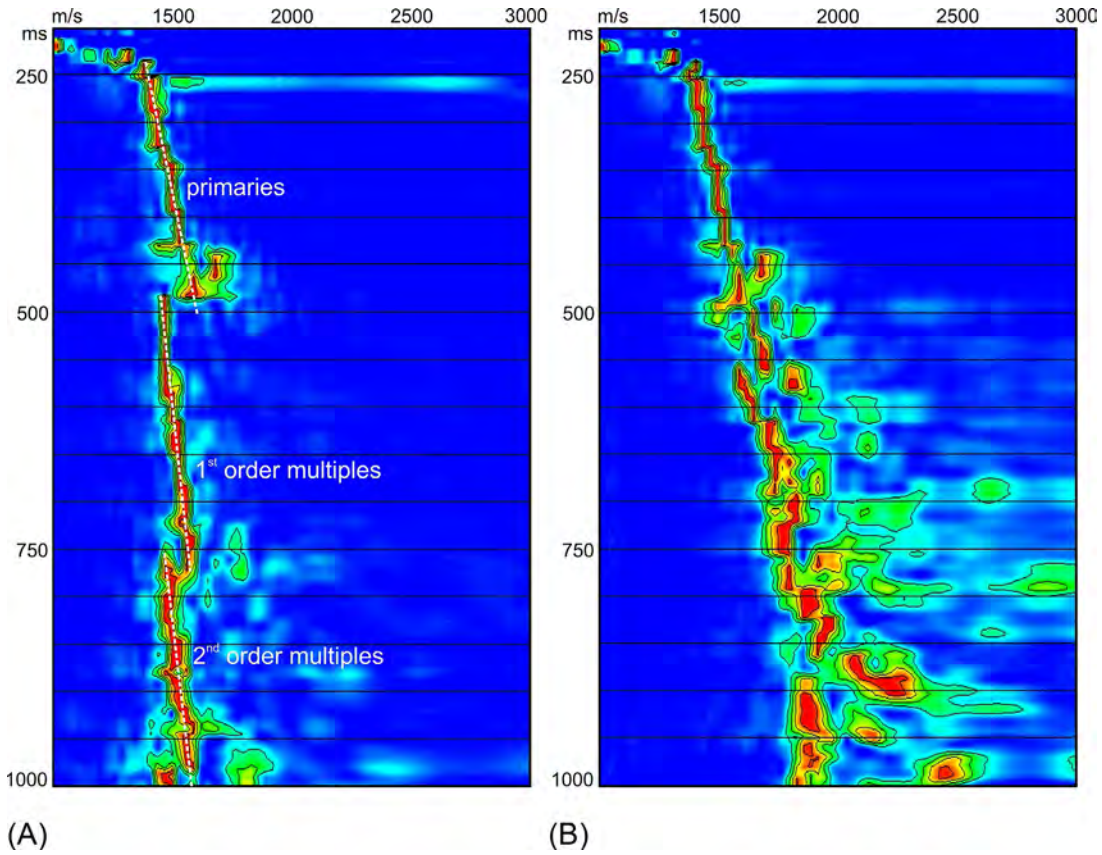


FIG. 7.25 Two semblance plots calculated from the same CDP gather (A) before and (B) after Radon velocity filter. In (A), enclosures from first- and second-order multiple reflection amplitudes dominate the semblance plot in deeper parts, preventing the picking of primary reflection velocities. After removal of the multiples, semblance contours of primary reflections hidden behind the multiples become visible.

section of WEMR is almost multiple free and, in particular, the long period multiples are completely removed.

WEMR is an effective multiple removal technique that can be successfully applied even in the areas of complex geology. Correct picking of the seafloor arrival times and converting them into the depth using accurate water column velocity is crucial in the efficiency of the method. It is generally applied to shot gathers, and it is one of the most appropriate methods for AVO analysis in which the relative amplitudes are of significant importance. Processes such as trace balancing, deconvolution, true amplitude recovery (TAR) or automatic gain control (AGC) must not be applied before WEMR, since these processes modify the amplitudes of the seismic data and result in issues during the modeling of the multiples by WEMR.

7.6 *f-k* FILTERING

Multiples can arrive at the receivers at the same time as the primary reflections. However, moveouts of the reflection hyperbolas of both arrivals will be different since they propagate with different velocities, and the curvature of

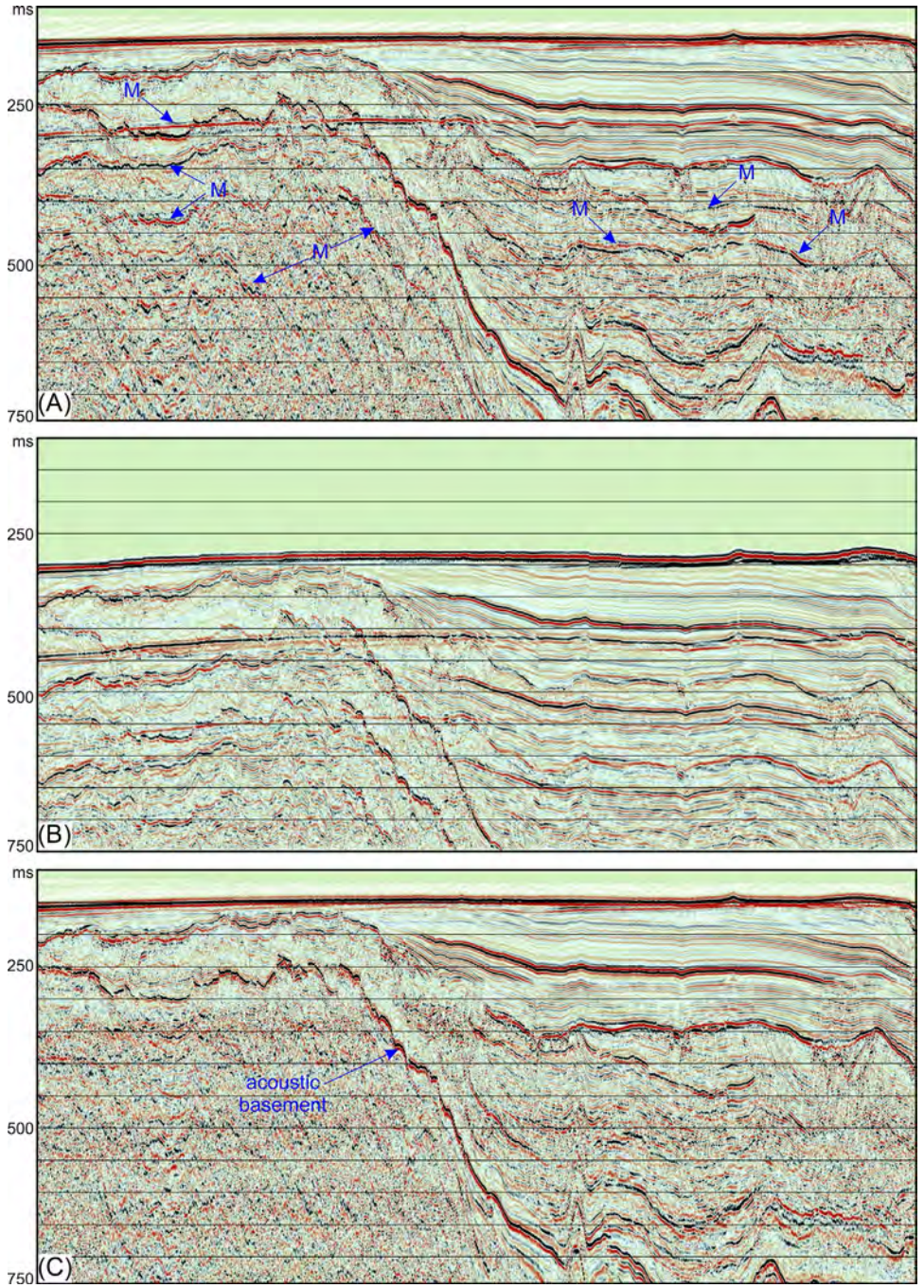


FIG. 7.26 (A) A stack section from a shallow continental shelf with both long period and peg-leg multiples (*M*), (B) multiples modeled by WEMR, and (C) the same stack section obtained after adaptive subtraction of the multiples in (B). Amplitudes in (B) are not proportional to those in (A) and (C).

the hyperbolas from multiples is higher than the curvature of primary reflections for an identical zero-offset time. Genuine reflections almost always have higher velocities than multiple reflections. Although we cannot know the exact and accurate propagation velocities of the primaries because of the limitations and resolution restrictions of the velocity analysis techniques applied to the seismic data (Chapter 9), we can assume the velocity of long period multiples being approximately 1480–1500 m/s since they travel only in the water column and uppermost sediments. This difference in primary and multiple reflection velocities allows us to discriminate amplitudes of primary and multiples in the *f-k* domain.

Let's consider that NMO correction is applied to the CDP gathers using multiple velocities of 1500 m/s, which results in the flattening of the multiple reflection hyperbolas. Since this velocity is considerably low for primary reflections, they are overcorrected after NMO correction. Fig. 7.27A schematically shows reflection hyperbolas representing the arrival times of five primary and three multiple reflections. If we apply an NMO correction to this CDP gather using multiple velocities, hyperbolas of multiple reflections are flattened and primary reflection hyperbolas are overcorrected (Fig. 7.27B). The *f-k* domain representation of this CDP gather is schematically shown in Fig. 7.27C, in which almost all of the multiple reflection amplitudes are aligned onto the vertical zero wavenumber ($k = 0$) axis since they are flattened and horizontal in the *t-x* domain. The amplitudes of primary reflections, however, are mapped onto the negative *f-k* panel since they have negative dip in the *t-x* domain after NMO correction with multiple velocities. The narrow vertical area around the zero wavenumber axis consisting of the

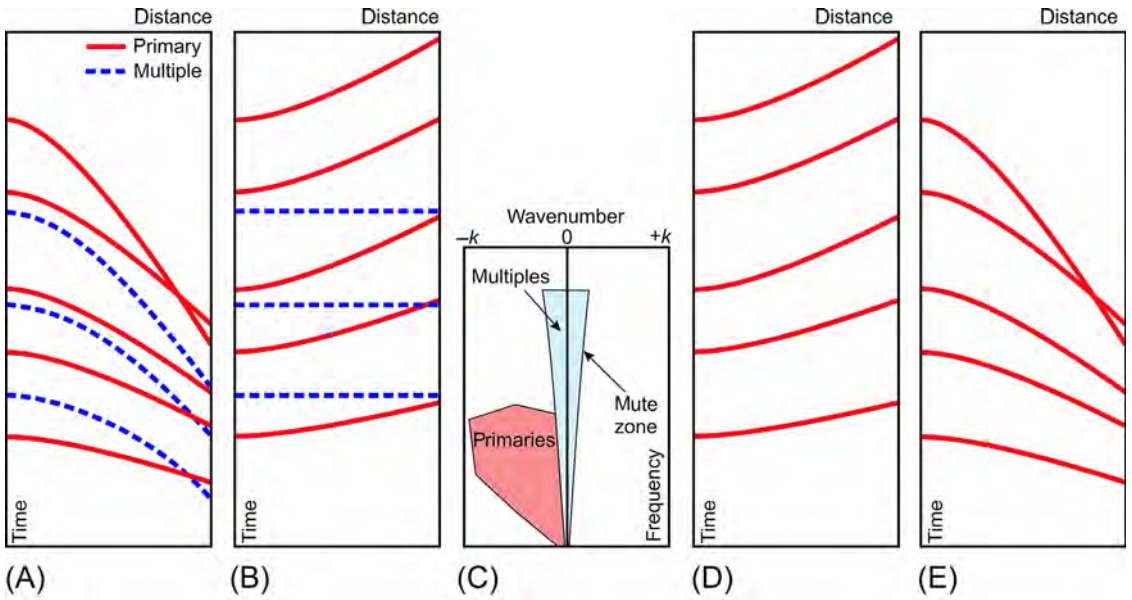


FIG. 7.27 Schematic illustration of multiple elimination with *f-k* filtering. (A) A CDP gather with primary *(red)* and multiple *(dashed blue)* reflections, (B) after NMO correction of multiple velocities and flattening of multiple reflection hyperbolas, (C) *f-k* domain representation of CDP gather in (B) and the vertical mute zone *(blue shaded area)* involving the multiple amplitudes, (D) CDP gather after inverse 2D Fourier transform, and (E) original CDP gather without multiple amplitudes after inverse NMO correction.

multiple amplitudes is muted out in the *f-k* domain (Fig. 7.27C) and the data is transferred back into the time domain (Fig. 7.27D) by an inverse 2D Fourier transform. This gather is still in NMO corrected form and the primaries are still overcorrected. An inverse NMO correction with multiple velocities must then be applied to obtain the multiple free original CDP gather (Fig. 7.27E). These steps are summarized in the block diagram in Fig. 7.28.

Fig. 7.29 shows an application of multiple elimination by *f-k* filtering. An NMO corrected CDP gather using 1500 m/s NMO velocity with its corresponding *f-k* spectrum is given in Fig. 7.29A, in which the multiple hyperbolas (*M*) are flattened whereas the primary reflections are overcorrected. Fig. 7.29B shows the output CDP gather with its *f-k* spectrum after muting out the narrow zone along the zero wavenumber axis. Flattened multiple reflection amplitudes do not exist in the output gather. Fig. 7.30 compares three successive CDPs before and after *f-k* filtering for multiple removal. Most of the first-order (M_1) and all of the second-order (M_2) multiples are removed from the data. Fig. 7.31 shows the stack section before and after an *f-k* filter, indicating that the long period multiple is removed from the stack.

In multiple removal by *f-k* filtering, the mute zone in the *f-k* domain must be selected carefully around the low-frequency zone where the primary and multiple amplitudes overlap. Practical applications indicate that especially near-offset amplitudes of the multiples can be effectively removed by the *f-k* filtering technique, which is also evident in the example CDPs in Fig. 7.30. However, the near offsets of the primaries where there is no enough residual moveout after NMO correction may also be removed by use of an *f-k* filter. In addition, the automatic muting zone due to the NMO stretch cannot be recovered after the inverse NMO correction; therefore, it is suggested to toggle off automated NMO stretch mute to prevent data loss in long offsets of early arrivals.

7.7 SURFACE-RELATED MULTIPLE ELIMINATION

The surface related multiple elimination (SRME) technique has become quite popular in recent years to predict and iteratively subtract the multiples from seismic data. Surface-related multiples are formed through a reflection against a free surface, which is the topmost surface for seismic surveys, such as the sea surface for marine seismics. They are generated by the waves downgoing from a seismic source, reflecting from the seafloor or subsurface sediments, having at least one downward reflection from a free surface, reflecting one more time from

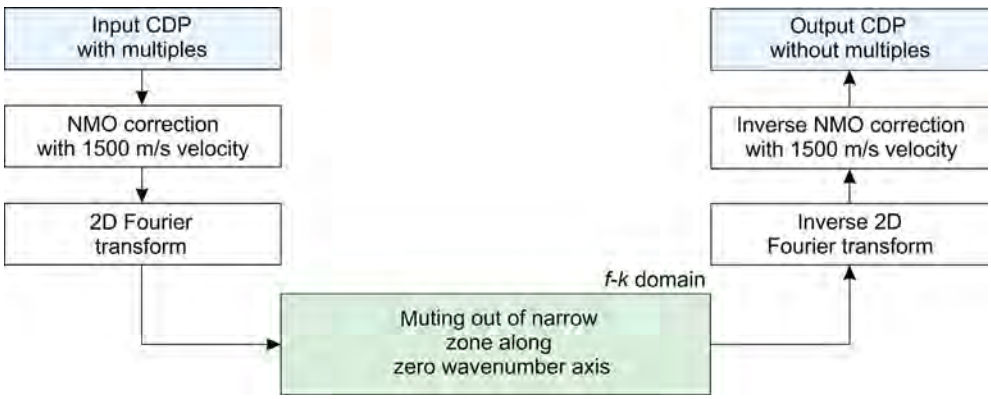


FIG. 7.28 Block diagram illustrating the steps of the multiple elimination with *f-k* filtering.

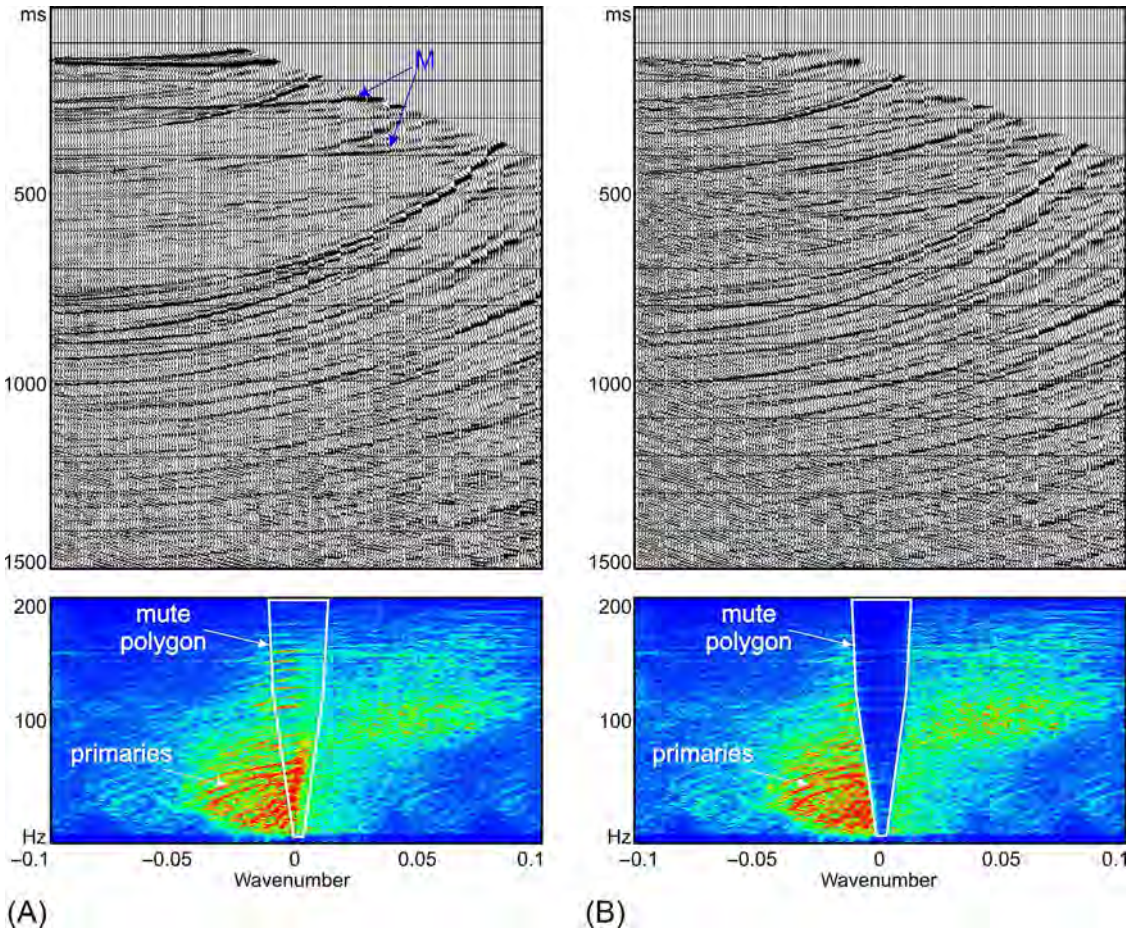


FIG. 7.29 Application of *f-k* filtering for multiple elimination. (A) NMO corrected CDP gather with 1500 m/s multiple reflection velocity, which flattens the multiples (*M*) and overcorrects the primary reflections. (B) The same CDP after muting out the narrow vertical zone in the *f-k* domain. Corresponding *f-k* spectra of the CDP gathers are given in the bottom panels.

the seafloor or subsurface sediments, and then being recorded at the receivers. SRME is one of the most effective multiple elimination methods today in the seismic industry, and it can deal with any kind of surface-related multiples, such as long period and peg-leg multiples, or multiple energy at near offset traces, as well as the multiples of very little differential moveout. The key advantage of SRME is that it is entirely data driven and needs no subsurface or any other extra information, since the multiples are completely predicted from the data itself, which is accomplished by 2D autoconvolutions of the input data in time and space directions (Verschuur et al., 1992). In order to remove the multiples from one single shot by the SRME method, all other shot records in the line are also required.

In the application, only reflection coefficient of the sea surface (generally assumed to be −1 for marine seismic surveys) and the recorded seismic data is required to define a surface

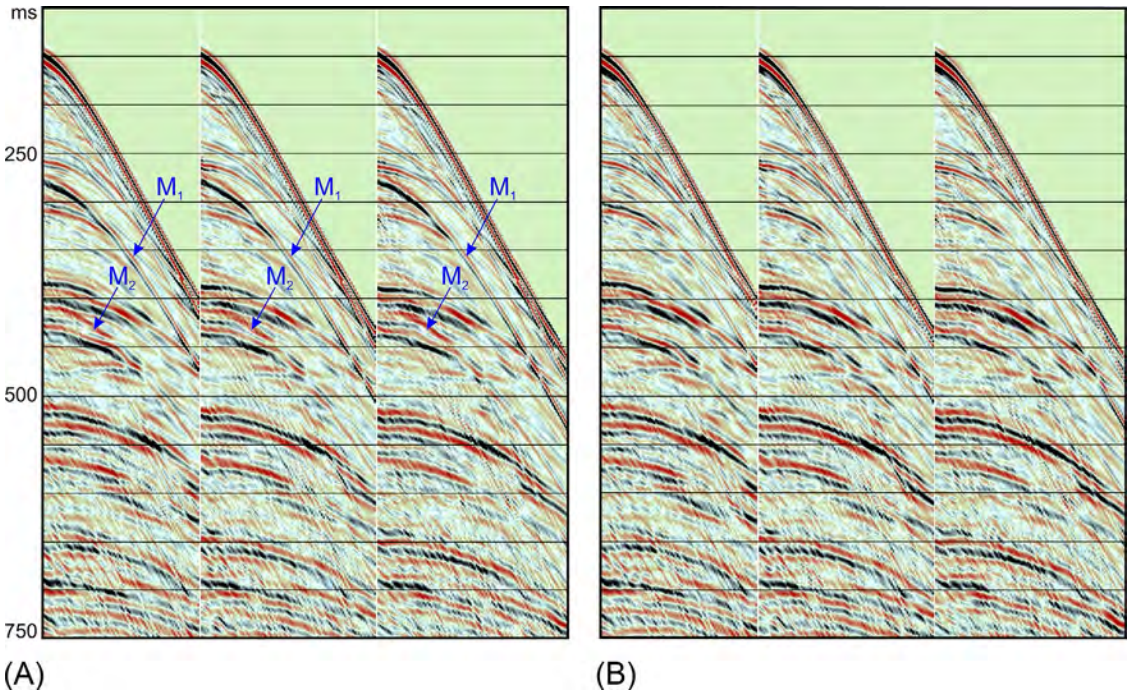


FIG. 7.30 Three successive CDPs (A) before and (B) after *f-k* filtering for multiple removal. Most of the first-order (M_1) and all of the second-order (M_2) multiples are eliminated.

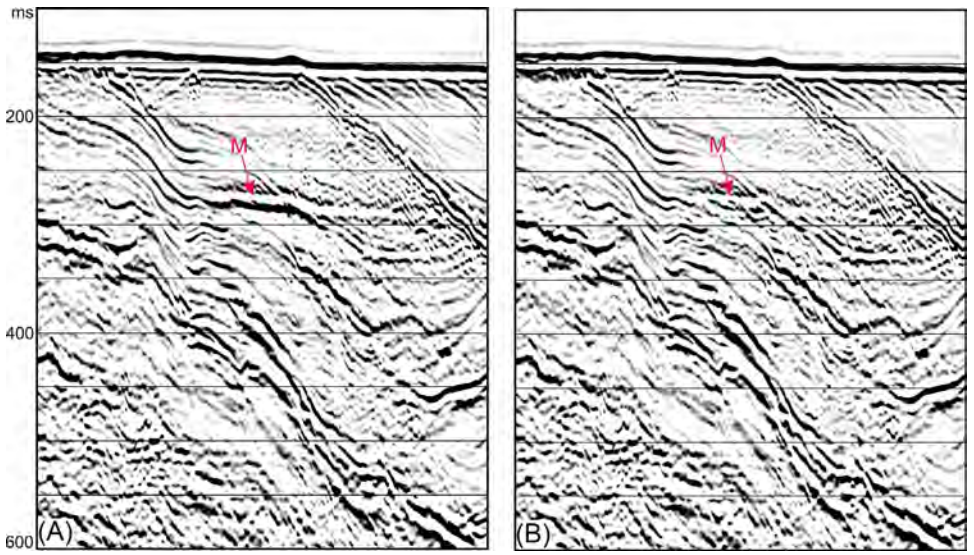


FIG. 7.31 A stack section (A) before and (B) after *f-k* filtering for multiple removal. The first-order long period multiple (*M*) is significantly suppressed by *f-k* filtering.

operator. Multiple free seismic data at the sea surface z_0 in the frequency domain can be expressed as (Verschuur et al., 1992)

$$\mathbf{S}_0(z_0) = \mathbf{S}(z_0) - A(\omega)[\mathbf{S}(z_0)]^2 + A^2(\omega)[\mathbf{S}(z_0)]^3 - \cdots \tag{7.4}$$

where $\mathbf{S}(z_0)$ is the matrix consisting of all input seismic shots with multiples, $\mathbf{S}_0(z_0)$ is the matrix of all shots without multiples, and $A(\omega)$ is the surface operator. The summation of second, third, etc. terms in the righthand side of Eq. (7.4) constitute surface-related multiples, which are subtracted from recorded seismic data. In the SRME technique, these multiples are predicted by the convolution of source and receiver gathers: When we consider that the increasing order of multiples consists of primary events as shown in Fig. 7.32A, a surface-related multiple can be predicted by convolving these primary events and multiplying the result by the sea surface reflection coefficient. This is accomplished by convolving the input seismic data with itself both in time and space domains. While convolution in the time domain provides the arrival time of multiples, convolution in the space domain gives their offsets. This procedure enables us to obtain the multiples directly from primaries, and higher-order multiples from lower-order multiples. Based on the geometry in Fig. 7.32A, a primary reflection originated from shot location S_L arrives at location M_L, and a surface-related multiple is recorded at location R_L. We can consider this multiple as two successive primary events: one is originated from the shot at S_L and recorded at M_L, and the other is originated from the shot at M_L and recorded at R_L. If the location of M_L is known, then we can predict the multiple by autoconvolving the already recorded events. For each shot and receiver in the input data, a shot gather at location S_L and a common receiver gather at location R_L are selected from the input data. Traces from both gathers are combined, providing that the receiver location of the former trace coincides with the source location of the later trace. Convolution of two sets of traces and summing up the results give the predicted multiple trace for that source-receiver pair. That is, the common shot gather from location S_L is convolved with the common receiver gather at location R_L in Fig. 7.32B, and the results are summed. In fact, the autoconvolution of the input data corresponds to doubling of arrivals in the time and space directions (Fig. 7.33), which is simply used

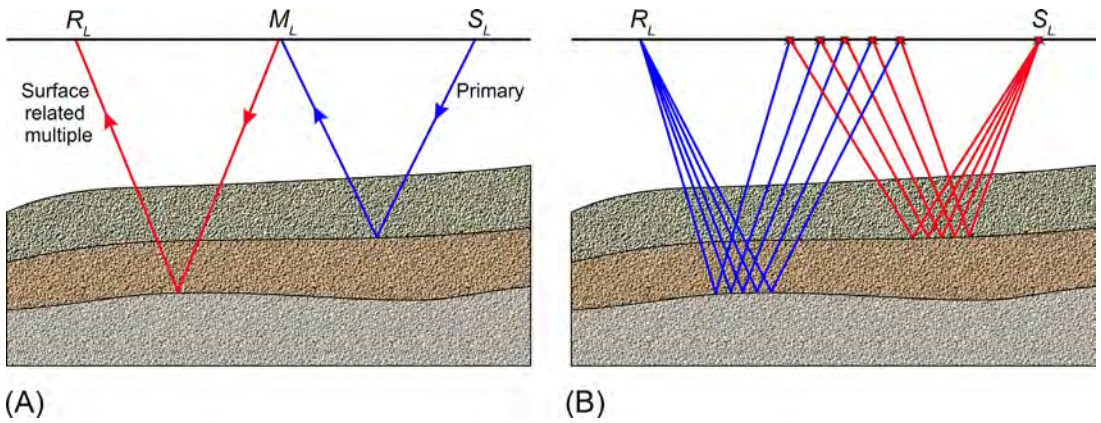


FIG. 7.32 (A) Increasing order of surface-related multiples can be regarded as successive primary events. (B) Common shot gather from location S_L is convolved with the common receiver gather at location R_L, and the results are summed to predict the multiples.

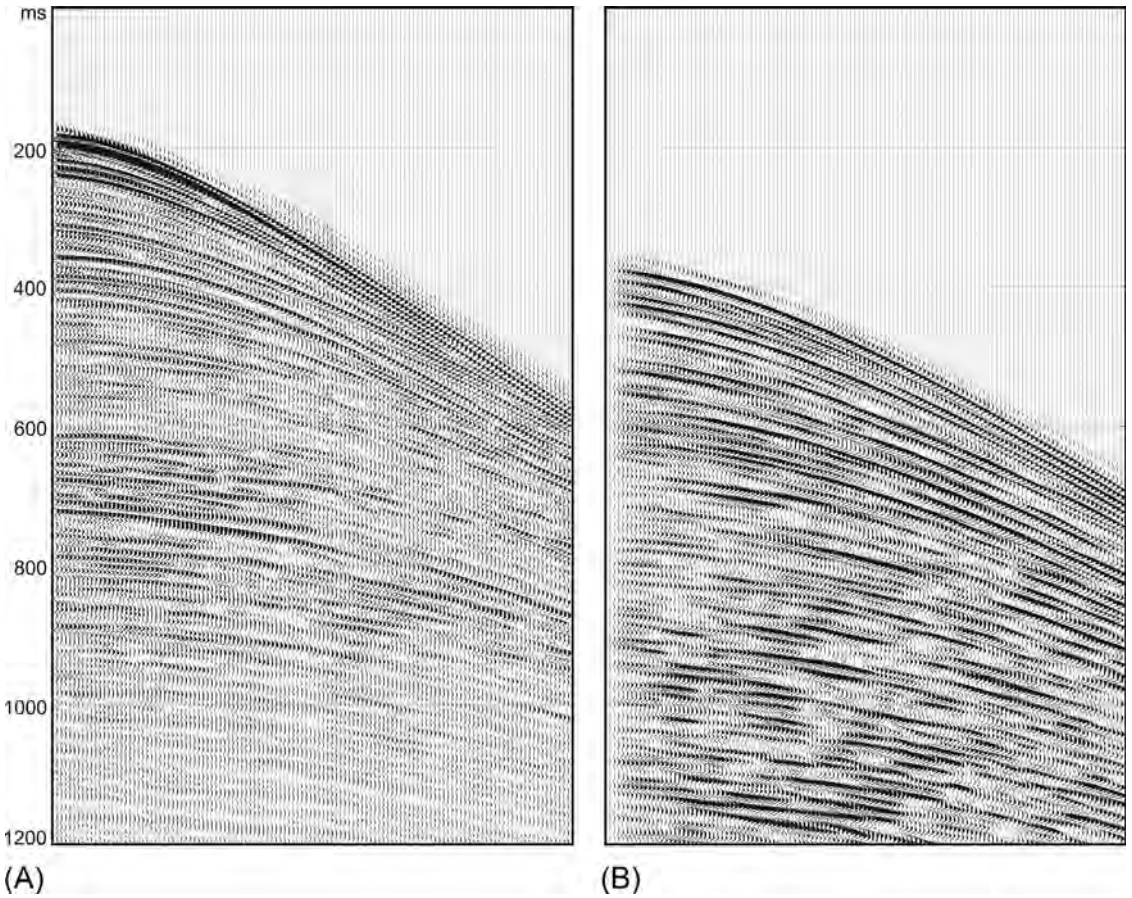


FIG. 7.33 (A) Preconditioned shot gather, and (B) its autoconvolution which doubles the arrivals in time and space directions.

to estimate the surface-related multiples. Fig. 7.34 shows an example stack section before and after SRME. SRME removes the entire surface-related multiple energy from the data, which is also evident in the autocorrelograms.

SRME is generally applied to preconditioned shot gathers, which include geometry definition, band-pass filter, trace edit, muting, *f-k* filtering, and *f-x* denoising, if necessary. Deconvolution and gain applications must be avoided before SRME since they modify the amplitude and phase relationship between primaries and multiples. Application of SRME consists of the following steps:

i. Regularization: Traces in the input data are interpolated at regular intervals resulting in a constant trace interval from zero to maximum offset of the input, particularly to compensate for the missing near-offset traces.
ii. Prediction: Predicts the multiples by 2D autoconvolution.
iii. Unregularization: Input data is transformed into its original trace locations.
iv. Match filter: Since the predicted multiples are generally not consistent with the recorded multiples regarding amplitude and wavelet shape characteristics, a

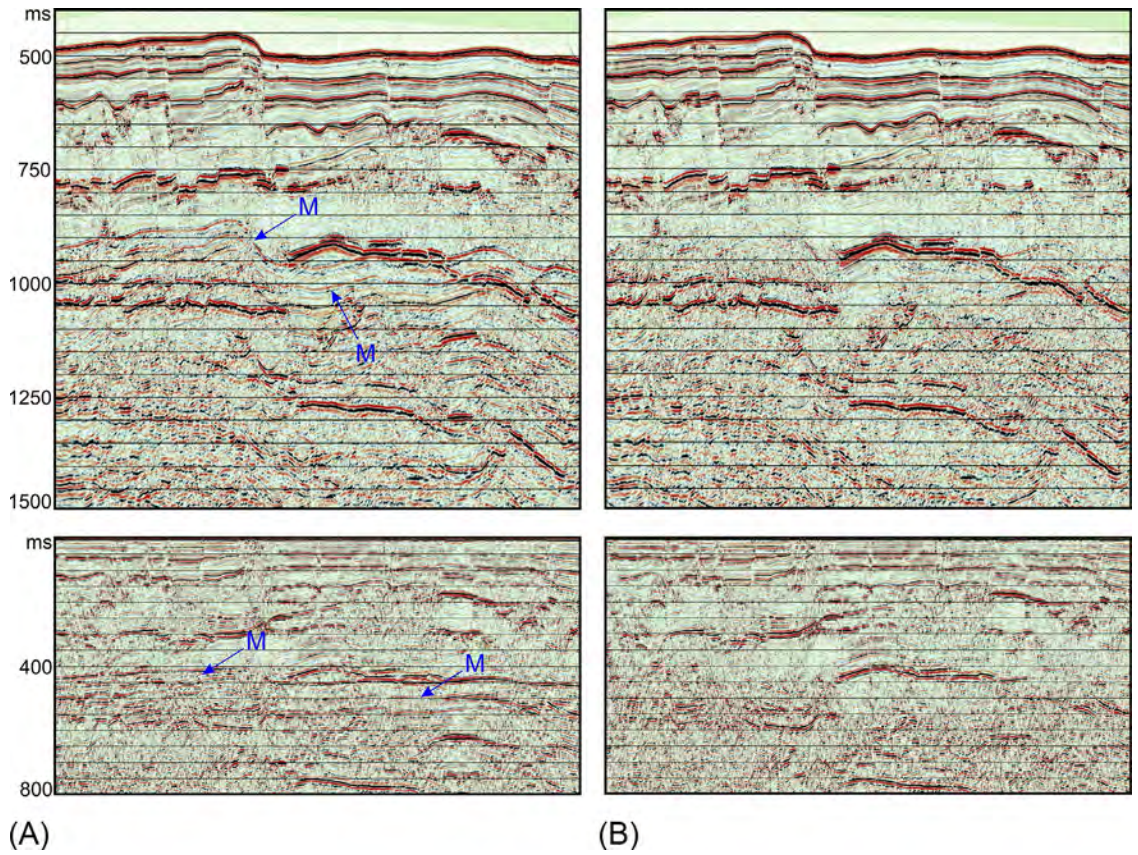


FIG. 7.34 A stack section (A) before and (B) after SRME (top) and their corresponding autocorrelograms (bottom). *M* represents surface-related multiples.

matching filter between predicted and recorded multiples is designed and applied.

v. Adaptive subtraction: Recorded shots and predicted multiples are compared and the multiples are adaptively subtracted from the input.

Although several multiple suppression approaches exist in the marine seismic data processing industry, SRME is one of the most effective and widely used methods today. Its main advantage is that it does not require any model of the subsurface structure, such as velocity information, seafloor picking, etc. While most multiple elimination methods are applicable in 2D and unable to account for 3D effects, SRME can be formulated in 3D, although it is much more expensive and complex to apply. Application of 2D SRME to 3D data is not recommended, since the accuracy of the prediction depends on the amount of crossline dip. If the 3D survey is dense enough with no feathering, and contains large apertures for in-line and crossline directions, then the multiples are almost completely eliminated by 3D SRME. However, existence of feathering on the streamers and too narrow apertures, especially for long offsets, commonly restrict the success of 3D SRME.

7.8 QC IN MULTIPLE SUPPRESSION

The expected output of a multiple attenuation algorithm is the seismic data with all types of multiples removed, with the primary reflections unaffected. Existing multiple suppression methods try to accomplish this by considering different characteristics of the multiples, which enable us to discriminate the multiples from primaries in different domains, such as time-distance, frequency, τ-p, etc. These characteristics include their moveout difference, periodicity, velocity or dip discrimination. The efficiency and success of each approach strongly depend on the criteria used to attack the multiples via the characteristic features of the multiples. Therefore, theoretical and practical factors of each approach constituting their limitations should be properly evaluated before the application. This section discusses the advantages and mostly the limitations of the demultiple methods, to provide more insight into how to determine the suitable method for a particular multiple type in seismic data. Fig. 7.35 compares outputs of different demultiple methods on the same seismic data from a shallow continental shelf. Comparisons can be made between the output of a particular method and a stack and/or brute stack section. The brute stack in Fig. 7.35A shows that the section is highly contaminated by surface-related multiples as well as peg-legs.

The most effective solution can be determined by considering the principles behind these techniques for solving a specific multiple issue. Sometimes a number of different demultiple methods must be tried on the test data in order to cope with different multiple types. Difference sections between input and output may indicate what is removed and what is left in the data after multiple removal. Autocorrelation sections may help in analyzing the effectiveness of a particular demultiple method. In general, velocity analysis is fairly improved after a successful demultiple application, and it is recommended that a second-pass velocity analysis be performed after multiple suppression.

CDP stacking is the earliest method to suppress multiples. It exploits the residual moveout differences between the primaries and multiples in CDPs after NMO correction. Stacking can suppress a significant amount of coherent and incoherent noise and can improve the S/N ratio by up to 20 dB, depending on the number of traces involved in stacking. Its efficiency increases as the moveout differences between primaries and multiples increase, and therefore long offsets are crucial in the stacking process for an effective multiple removal. In addition, velocity distribution of the subsurface is required for NMO correction, which also controls the accuracy of the residual moveouts between the primaries and multiples, especially in shallow parts where even small changes in NMO velocity may produce a significant amount of residual moveout differences at far offsets. Therefore, a careful velocity analysis is crucial in the effective removal of multiples by stacking. Picking of the velocities corresponding to the enclosures of the multiple amplitudes in semblance plots, which appear throughout the low-velocity zones (e.g., close to 1500 m/s of water velocity axis in relatively deeper parts) should be strongly avoided (Chapter 9). In Fig. 7.35B, the efficiency of stacking on the elimination of different types of noise, including multiples, is illustrated. Although first-order seabed multiples and peg-legs deeper than approximately 700 ms remain intact in the stack section, most of the higher-order long period multiples are completely suppressed after stacking.

The *f-k* domain muting is a moderately effective approach in multiple suppression. It works on the residual moveout differences between the primaries and multiples in the CDPs after NMO correction. Its efficiency increases as the residual moveout difference increases, which requires long offsets, as in the case for CDP stacking.

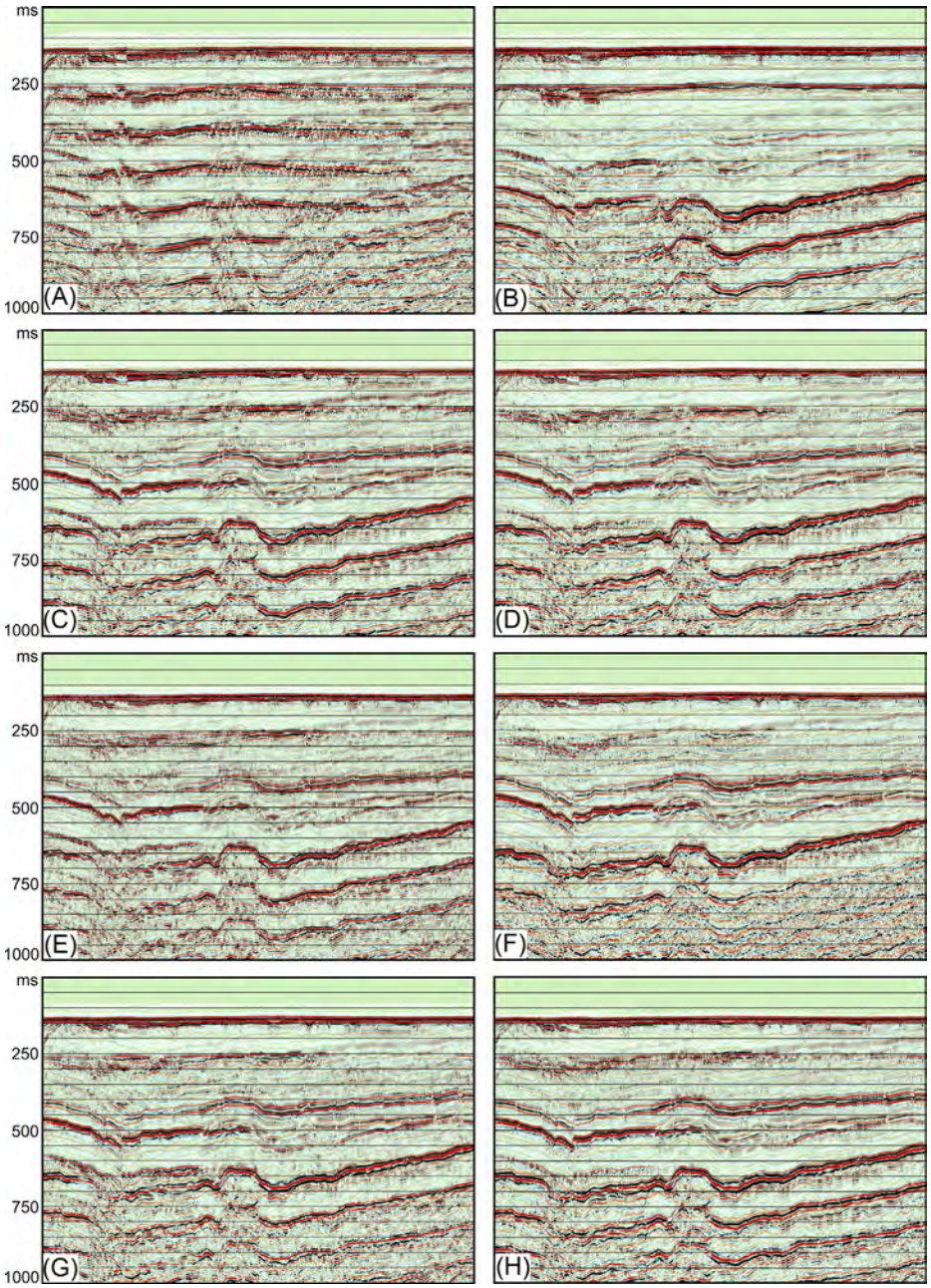


FIG. 7.35 Comparison of outputs of different demultiple methods on shallow marine seismic data. (A) Brute stack section, (B) full stack section, and outputs of (C) f-k filtering, (D) predictive deconvolution, (E) WEMR, (F) SRME, (G) predictive deconvolution in τ-p domain, and (H) Radon filtering demultiple techniques.

Its advantage is that it does not require correct subsurface velocity information obtained from primaries, but needs the velocity of the multiples, which can be assumed to be between 1480 and 1520 m/s in most cases.

Although *f-k* filtering has a simple theory and is quite straightforward to apply, practical applications indicate that the selection of the proper mute zone is important in discrimination of primary and multiple amplitudes in the *f-k* domain. It generally fails in the case of strong multiple energy due to hard seafloor conditions and leaves a significant amount of residual multiple amplitudes in the output. The most important disadvantage is that the method also removes amplitudes of primaries in near-offset traces, because the primaries also remain flattened in near offsets after NMO correction. Therefore, the performance of *f-k* filtering in multiple suppression is poor for small offset data of short streamers, even if the subsurface geology is not complex. This situation is also valid for the seafloor reflection: since its velocity is close to the multiple velocity, the seabed reflection hyperbola is also flattened after NMO correction, which results in a significant removal of the amplitudes of seabed and shallow reflections. These disadvantages generally make *f-k* filtering an unfavorable tool as compared to other techniques for multiple elimination. Fig. 7.35C shows the output of *f-k* filtering to remove the multiples. Although it works fine for first-order seabed multiples, peg-legs still exist in the output.

One of the well-known multiple suppression methods, successfully used for over 40 years, is predictive or gapped deconvolution, based on the periodicity of the multiples in the time domain to design an operator that identifies and removes the multiples (Fig. 7.35D). It is especially effective on short period multiples and fails if the multiple period is longer than approximately 200 ms, since the multiples are not perfectly periodic at far offsets on the shot records. This situation is partially tolerated by predictive deconvolution for shorter period multiples and cannot be handled for long periods. Parameter determination is an important point and autocorrelograms of the input traces are used to determine the correct prediction lag and operator length values for an efficient multiple suppression. This situation means that the success of the method depends on the experience of the processor. In general, several tests and trials are required to determine these parameters accurately. Practical applications indicate that the method also works well in the τ-p domain where the multiples are more periodic for all constant p values (Fig. 7.35E).

The SRME method is based on work done at Delft University (Verschuur et al., 1992), and therefore also is known as the Delft approximation. It is the most common and one of the most successful methods used in the seismic processing industry today. Results of SRME are generally superior as compared to the results of the other commonly used demultiple methods. It is the only technique that almost completely removes surface-related multiples as well as peg-legs (Fig. 7.35F). Like other demultiple methods, SRME has its own advantages and disadvantages. The most important advantage is that the conventional SRME technique does not require any a priori information about the subsurface, such as seafloor reflectivity, or 2D/3D velocity distribution. However, it requires a regular shooting geometry and equal shot and receiver interval, so that a shot location should exist at each receiver location, since every receiver location is also used as a source location. This prerequisite, however, is not the case for most 3D acquisition geometries. The quality of SRME output is controlled by several factors, such as wide shot spacing resulting in aliasing, narrow spread for narrow azimuth data, feathering, large crossline sampling due to the wide cable spacing in 3D acquisition, or missing near and/or far offsets. During the computations, all receiver locations from zero to maximum offset are used. The input data must

be reconstructed at missing offsets for near offset traces to obtain a regular distribution of traces for all existing offsets using data regularization and interpolation. However, interpolated data is not as good as real data, especially for a complex 3D subsurface. Although new innovations exist for 3D SRME algorithms, a regularization process for the requirement of regular shot and receiver distribution for all offsets is the main issue for 3D implementation of SRME algorithms and this makes it difficult and expensive to implement. This geometry regularization and its iterative nature can make it a time-consuming, and hence expensive, process depending on the input data volume. Although it has unique advantages, it predicts only surface-related multiples and interbed multiples are not handled. In addition, applications indicate that SRME works better for near offsets as compared to the far offset range.

Wave equation multiple rejection (WEMR) predicts multiples by extrapolation with wave equation modeling and estimation of the seafloor reflectivity (Fig. 7.35G). Its major advantage is that it works fine when the seabed is irregular, by means of dip, curvature and variable reflectivity. It requires remarkable computational time for wave field extrapolation. In addition, spatial aliasing, if it exists, and lack of near offset traces may cause issues in multiple prediction, and in ideal conditions, the WEMR technique requires data from zero to as large offsets as possible.

Radon velocity filtering has a similar theoretical basis as *f-k* filtering, which exploits the residual moveout differences between the primaries and multiples in the CDPs after NMO correction. This time, however, the velocities of primary reflections are used in NMO correction and discrimination is done in the τ-p domain after a parabolic Radon transform. Radon demultiple is successful in attenuating multiples if the subsurface is not complex (Fig. 7.35H). In complex subsurface areas, however, the NMO approximation fails and NMO velocities are generally inaccurate, which results in unflattening of the primaries after NMO. If the spatial sampling is poor, then the method may not produce satisfactory results due to the severe aliasing problems in the τ-p domain. Since the method relies on residual moveout differences, a careful and accurate velocity picking is necessary. It is effective on multiples at moderate to deep waters depending on the streamer length, since the efficiency of the Radon velocity filtering increases with increasing offsets where the residual moveouts between primary and multiples become more prominent. However, it may fail when the moveout difference decreases, such as in the case for peg-leg multiples or multiple energy in near offset traces. The remaining multiples in near offsets, however, can be removed by a subsequent inner mute, if necessary. A careful picking of the mute zone in the τ-p domain is necessary to make the primaries unaffected, which strongly makes the method operator dependent. In general, amplitudes of the primaries are also reduced to some extent after Radon filtering, as is the case in Fig. 7.35H between 150 and 400 ms.

Table 7.1 summarizes the advantages and disadvantages of the multiple suppression methods commonly used in the marine seismic industry today. In general, the most effective method in multiple suppression is CDP stacking, which removes most of the coherent noise from the data. The methods that do not require subsurface information, especially those independent from the subsurface velocity distribution and that do not require an accurate 2D/3D velocity field, such as predictive deconvolution or SRME, are preferable since they are less sensitive to operator experience. To determine the most suitable technique for a specific dataset, several tests and trials using more than one demultiple method on a small test dataset is strongly recommended.

TABLE 7.1 Major Advantages and Disadvantages of Commonly Used Multiple Suppression Methods

Demultiple Method	Advantage	Disadvantage
CDP stacking	• Can suppress coherent and incoherent noise • Improves the signal-to-noise ratio by up to 20 dB	• Requires long offset data • Requires accurate subsurface velocity information • Does not provide prestack data
Predictive deconvolution	• Computationally affordable • Quite effective on short period multiples • No subsurface velocity information is required	• Valid for 1D model • Fails on long period multiples • Correct parameter determination is crucial • Almost ineffective on long period multiples
f-k domain muting	• Computationally affordable • Suitable for simple subsurface • Practical to apply • No subsurface velocity information is required	• Requires proper selection of mute zone • Fails for strong multiple energy • Removes primary amplitudes in near offsets • Poor for short streamer data
Radon velocity filtering	• Computationally affordable • Suitable for simple subsurface • Removes multiples especially from long offsets	• Fails in complex subsurface • Requires good spatial sampling • Requires accurate subsurface velocity information • Requires long offset data
Wave equation multiple rejection (WEMR)	• Suitable for complex seafloor topography	• Requires remarkable computational time
Surface-related multiple elimination (SRME)	• Highly effective on long period multiples • Does not require any information about subsurface • Suitable for complex geology	• Requires regular shooting geometry • Predicts only surface related multiples, interbed multiples are not predicted • Requires remarkable computational time

CHAPTER

8

CDP Sort and Binning

OUTLINE

8.1 CDP Geometry 405
8.2 CDP Fold 409
8.3 Binning in 3D 411
8.4 QC in Sort and Binning 415

Seismic data consists of specific signals of earth response, generated by an acoustic source, propagated through the subsurface, and recorded at the receiver locations. Considering a pair of point source and receiver geometry, a particular time sample on a seismic trace in a seismic line can be defined by three quantities:

- Location of source
- Location of receiver
- Recording time of seismic sample

Seismic data is collected in source-receiver coordinates; however, the recorded trace is reflected from the midpoint of source and receiver, assuming a horizontal seabed and subbottom layers. The source-receiver midpoint is termed the common depth point (CDP), providing a horizontal layered earth. After assigning the geometry to the seismic data, traces from the same reflection point are collected in a group, which is termed a CDP gather and this process is known as CDP sorting, which requires trace geometry to be defined prior to the sort process. Seismic recording with the CDP method was realized in the 1950s and it significantly improved the quality or signal-to-noise ratio (S/N) of the seismic data. In the stacking, the traces in each CDP gather are linearly summed up after normal moveout (NMO) correction so that each CDP becomes a stacked trace. Each trace in a CDP contributes to increase the S/N of this trace, and the S/N is directly proportional to the square root of the number of traces in a CDP gather.

8.1 CDP GEOMETRY

For multichannel seismic acquisition, several traces reflected from the same midpoint location on the seabed as well as subbottom layers are recorded. Although these traces originate from

© 2018 Elsevier Inc. All rights reserved.

different source points and are recorded at different receivers, their common property is that they are all reflected from the same subsurface location, that is, the common depth point. Fig. 8.1 schematically shows the relationship between shot and CDP gathers using a 2D acquisition geometry displayed over a horizontal reflective surface for simplicity. During 2D data collection, both shot and receivers are moved at a certain distance along the line after each shot, defined by the shot interval. In Fig. 8.1, shot and receiver intervals are assumed to be equal. The number of recording channels is 6 and only 9 shots are displayed for simplicity in Fig. 8.1. The points where the rays are reflected along the reflective surface are indicated by small circles, which exactly coincide with the midpoint locations of specific source and receiver pairs. The ray path geometry suggests that more than one reflection is recorded from each CDP location. For instance, in Fig. 8.1, the signal reflected from the first CDP location on the reflector emanates from the first shot (black) and is recorded at the sixth receiver of the first shot gather. Similarly, the reflection from the second CDP location originates from the first shot and is recorded at the fifth receiver of the first shot gather. The third CDP location has two different reflections, and each has different pathways: the first one is from the second shot (red) to the sixth receiver, and the other one is from the first shot (black) to the fourth receiver. CDP gathers are formed by selecting (sorting) of the traces from the original locations within different shot gathers into the new trace groups of the same reflection points, determined by the midpoint locations of shots and receivers. Hence, the first and second CDP gathers have only one trace, the third and fourth gathers have two traces, and so on.

The CDP gathers are formed by grouping the traces of the same reflection point coordinate, indicated by the yellow colored trace groups in Fig. 8.1. Each trace in these groups originates from different shot-receiver pairs, which are indicated just below the CDP groups as color-coded pairs of shot/receiver numbers. The number of traces within a CDP group is known as the CDP fold and changes along the line (Section 8.2), being maximum at the central part of the line. Geometrically, the CDP sort process is to transform the data from shot records to CDP gathers (Fig. 8.2). Shot geometry ensures recording of wave fields from one specific shot at all available receiving channels, while CDP geometry assures wave fields from various shots to different receivers. If the reflective surfaces are not inclined, reflection hyperbolas both in shot and CDP gathers are similar.

The seismic vessel continuously moves along the seismic line during the acquisition and the locations of the shot points are determined by the integrated navigation system. Although the precision of the DGPS systems today is less than 1 m in the horizontal plane, the realized shot point locations may deviate from those predicted. This results in scattering of the reflecting points around the exact CDP locations on the reflecting subsurface (Fig. 8.3A). If we consider unique CDP locations on the subsurface to group the traces in construction of the CDP gathers, as for the case in Fig. 8.1, only those traces reflected exactly from that unique subsurface location will be assigned to the CDPs. To overcome this situation, all traces reflected in the proximity of a CDP location are incorporated (Fig. 8.3A), and the process is then termed binning, in which two parameters determine the number of traces involved in a specific CDP gather, that is, width of the bin (d) and distance between the bin centers (r), as shown in Fig. 8.3A. If these parameters are larger, the number of traces in the CDPs increases while the total number of CDPs along the line decreases. Normally, the same value is used for both d and r to avoid trace overlap and is taken as half of the group interval (Δx) in 2D surveys. In 3D surveys, bins are two-dimensional and their dimensions are determined by the group interval and the distance between the

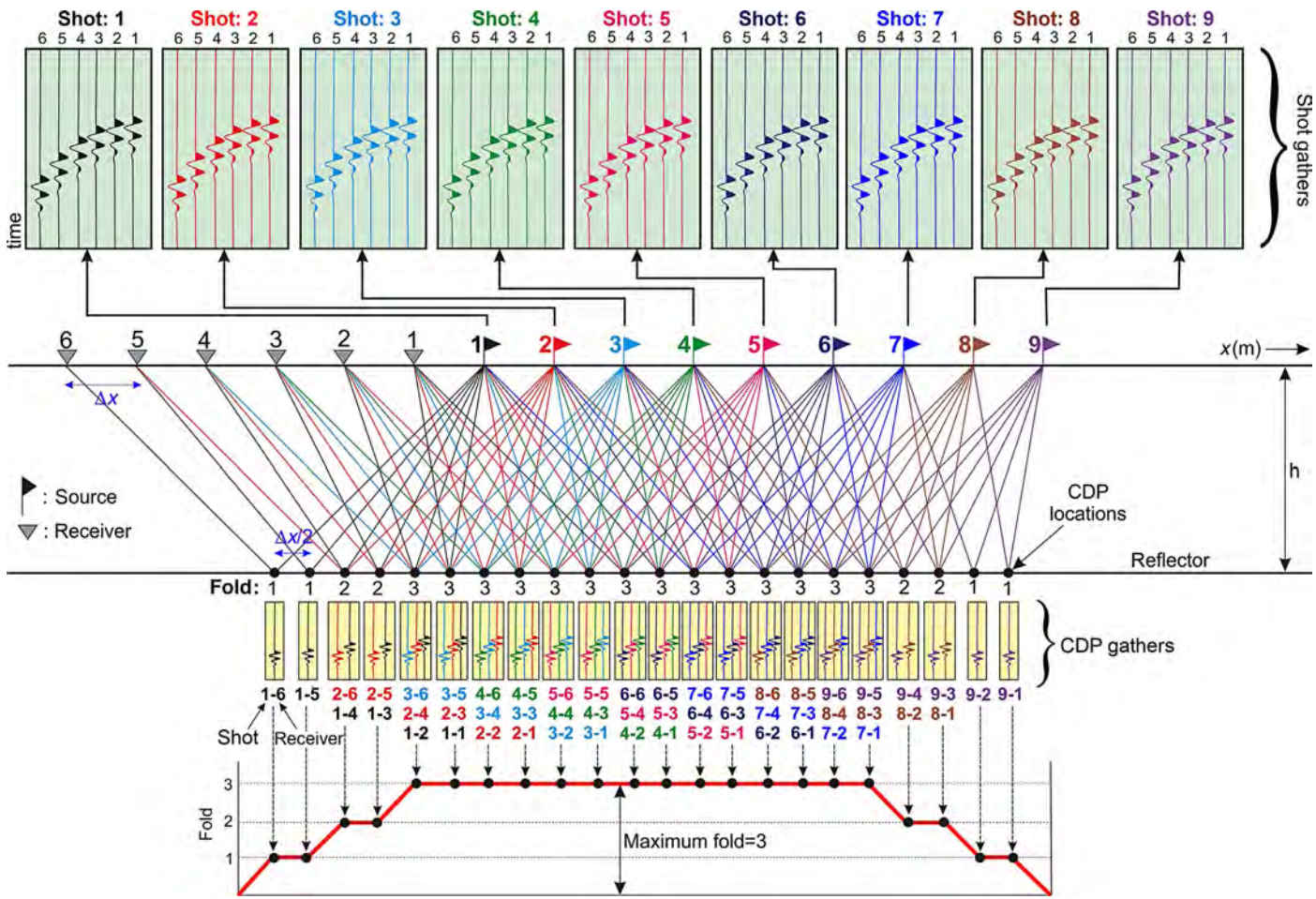


FIG. 8.1 Schematic representation of CDP gather construction from shot gathers. Traces and rays are color-coded based on the shots they belong to. Δx represents group interval.

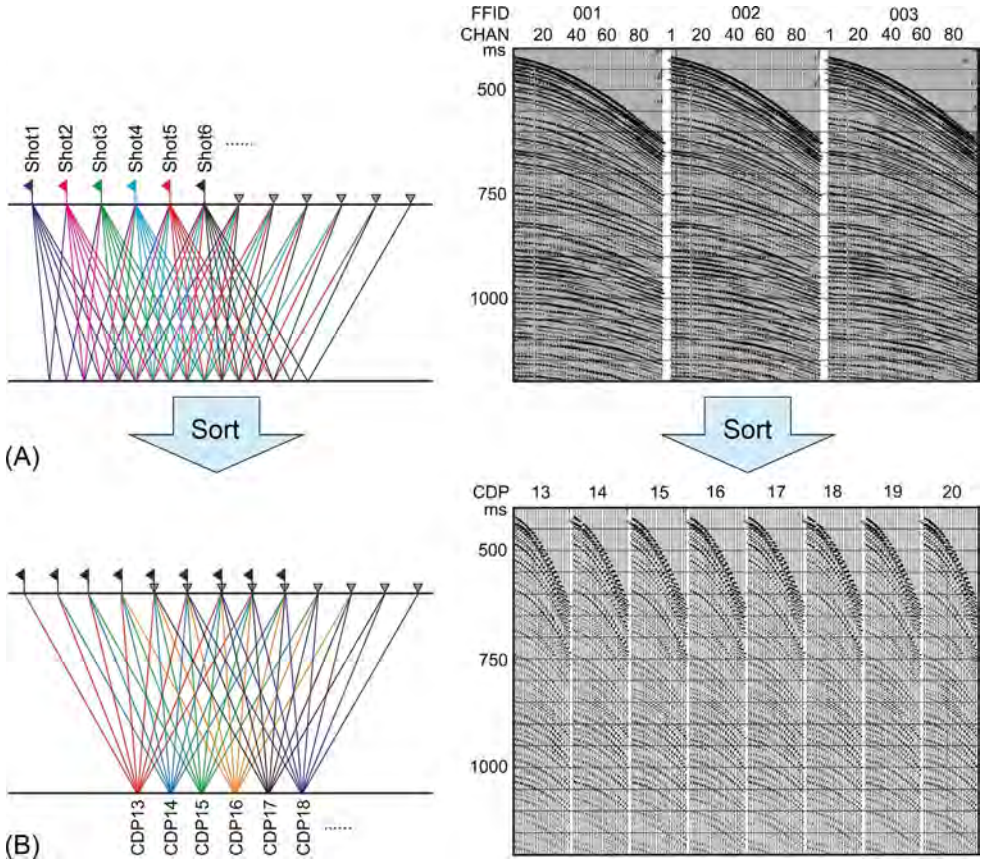


FIG. 8.2 (A) Ray paths for a shot gather (left) and example shot records (right), (B) ray paths for a CDP gather (left) and example CDP gathers (right). Transforming the trace geometry from (A) to (B) is achieved by the CDP sort process.

sources and streamers for inline and crossline directions, respectively. Fig. 8.3B and C show these parameters for 2D and 3D acquisition.

Fig. 8.4 shows a schematic representation of CDP gathers along a 2D seismic line. In a 2D line, the distance between CDPs is always half of the group interval ($\Delta x/2$), while the distance between successive traces within a CDP gather is twice the shot interval (2 s) as shown in Fig. 8.4. Fold is maximum at the central part of the 2D line, but it may not be constant because of the binning, missed shots, or killed traces.

For a certain source-receiver pair, the midpoint of source and receiver on the earth's surface is termed the common midpoint (CMP). For only horizontal interfaces, projection of a CDP point on the earth's surface coincides with this source-receiver midpoint location. The CDP and CMP terms are sometimes used synonymously in the seismic industry. These two terms are, however, identical only if the seabed and subsurface layers are horizontal and no lateral velocity changes exist. In a realistic world, this situation is almost never encountered and the earth is composed of interfaces with arbitrary dips in all directions. In this case, the traces in a CDP gather are not reflected from exactly the same depth point along the reflecting interface, and reflection points shift upslope along the dipping interface, which is known as CDP smearing (Fig. 8.5).

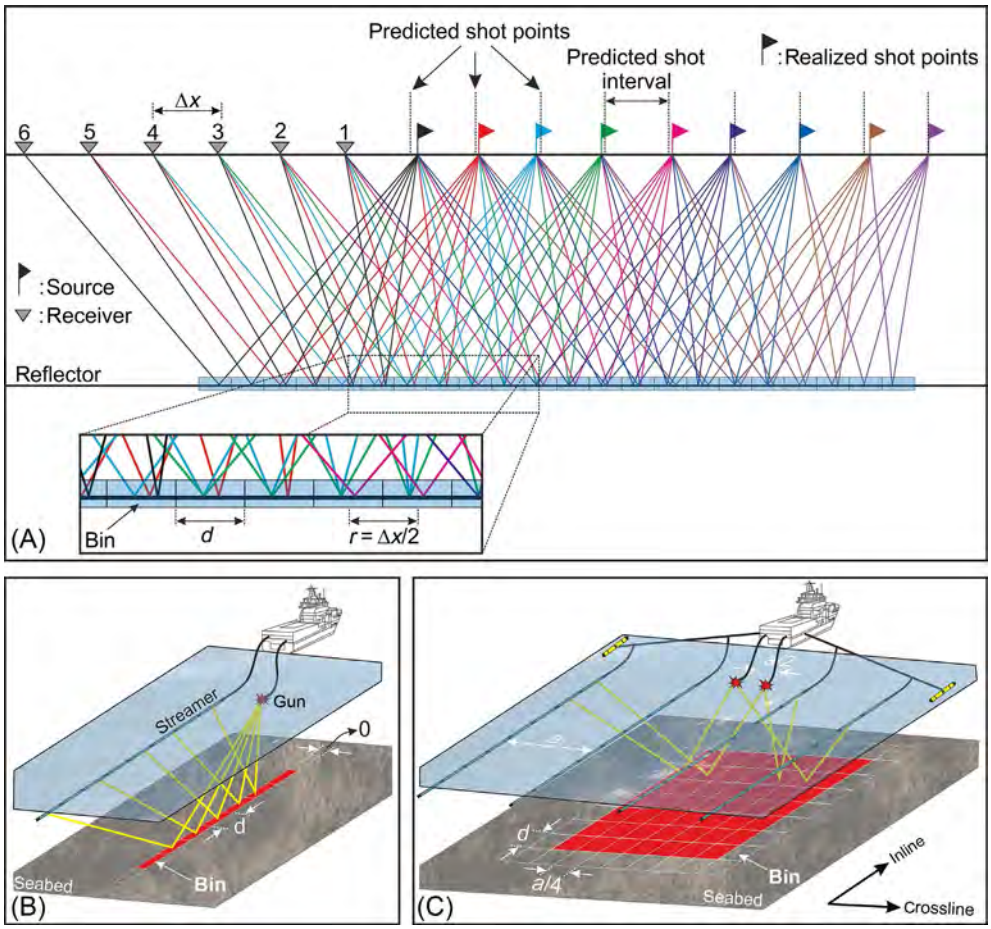


FIG. 8.3 Schematic illustration of the binning concept for 2D and 3D seismic surveys. (A) Scattering of reflection points around the exact CDP locations along the reflecting surface because of the small variations between predicted and realized shot point locations along the line. In this case, all the rays reflected from a specific reflector are not simply reflected from a single reflection point, and therefore a binning is necessary. Schematic display of bins for (B) 2D (one gun array and one inline streamer), and (C) 3D (two gun arrays and four streamers) seismic surveys. Δx is group interval, d is inline bin size, r is distance between bin centers, and a is distance between the streamers for 3D surveys.

8.2 CDP FOLD

The number of reflections received from a particular common depth point for 2D surveys, or within a rectangular bin for 3D surveys, on a reflector is termed fold and equals the number of traces in a CDP gather. Fold is always maximum along the central part of the 2D and 3D seismic data; this area is known as the full-fold (FF) coverage zone, and it decreases at both ends of 2D lines and at the borders of inline directions of 3D surveys. Fig. 8.6 shows a fold map of a 2D line and a 3D survey. In Fig. 8.6A, the fold changes from 28 to 32 in the full-fold coverage zone, and the nominal fold of this line is 30. In 3D surveys, a coverage map showing the fold

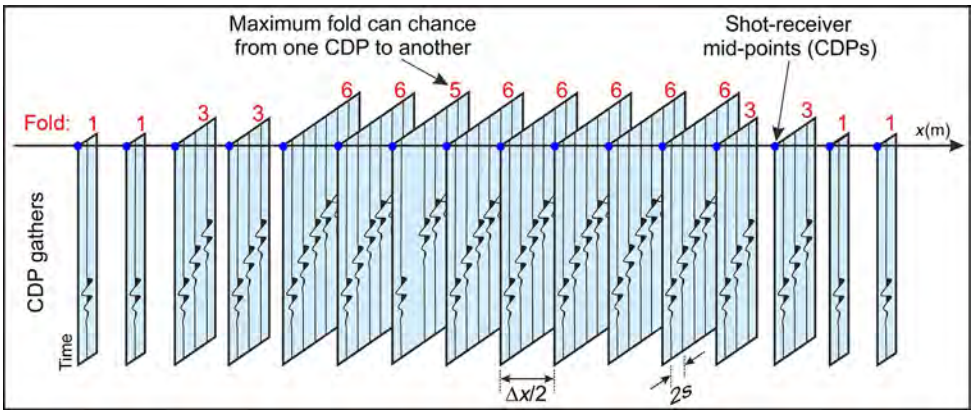


FIG. 8.4 Schematic representation of traces forming the CDP gathers using reflections from only one horizontal reflector along a 2D seismic line. Δx is group interval, s is shot interval.

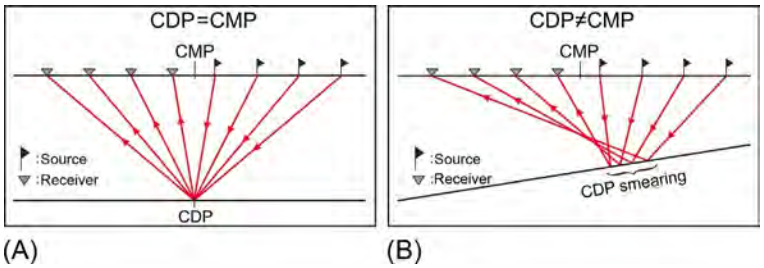


FIG. 8.5 (A) CDP and CMP terms are identical providing that the earth is composed of horizontal reflecting interfaces. (B) If the interface is inclined, these two terms are no longer equivalent to each other.

distribution for the whole survey area is prepared (Fig. 8.6B).

Maximum fold value is controlled by the survey geometry and acquisition parameters. For 2D lines, only the inline fold F_I is pronounced and is calculated by

$$F_I = \frac{\text{number of channels} \times \text{group interval}}{2 \times \text{shot interval}} \quad (8.1)$$

For 3D surveys, maximum or nominal fold of the survey is obtained by multiplying the inline and crossline folds:

$$F_N = F_I \times F_C \quad (8.2)$$

where F_I and F_C are the inline and crossline fold numbers, respectively. For 3D, the inline fold is calculated as the case in 2D surveys given by Eq. (8.1), and the crossline fold depends on the number of streamers and the distance between them. If only one vessel tows several streamers, as is the case for conventional 3D acquisition, no overlap in midpoint coverage occurs. Therefore, in narrow azimuth marine acquisitions, crossline fold is generally 1.

For instance, the nominal inline fold is $F_I = 80$ for the following parameters in a conventional 3D flip-flop acquisition:

Number of recording channels: 640.
Group interval: 12.5 m.
Shot interval: 25 m (flip-flop).
Source separation: 50 m.
Streamer separation: 100 m.

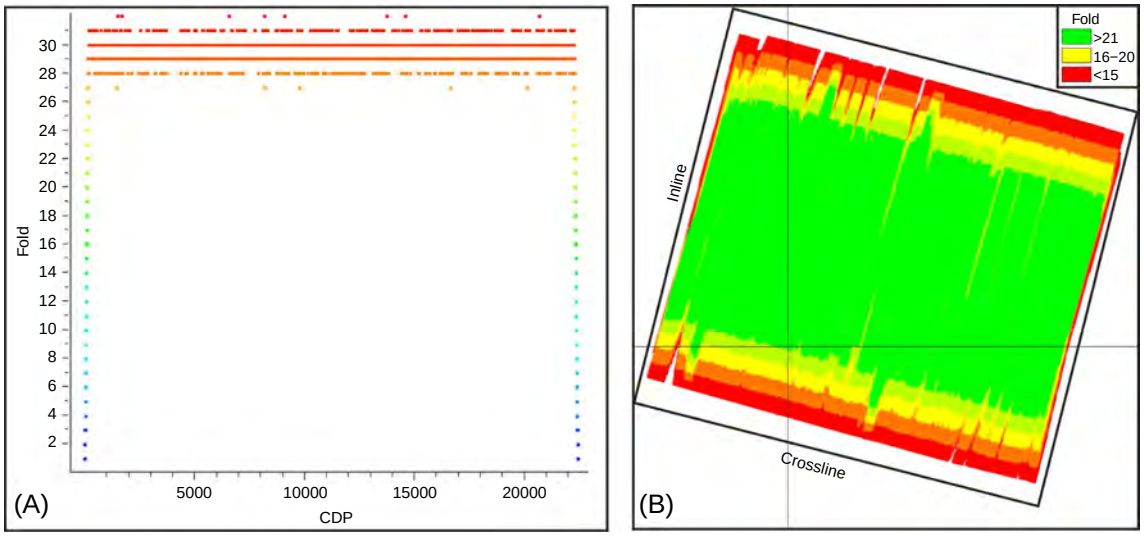


FIG. 8.6 (A) Fold distribution along a 2D seismic line with an optimum fold of 30. (B) A fold coverage map of a 3D survey with an optimum fold of 21.

Number of streamers: 8.

Note that shot interval should be doubled since a flip-flop shooting is performed, which means that the distance between successive shots for each individual CMP line is $2 \times 25 = 50$ m. Since this is a narrow azimuth (NAZ) configuration, the crossline fold $F_C = 1$.

In marine seismic systems, group interval is fixed. During the seismic survey design, the required optimum fold is obtained either by modifying the number of channels or the shot interval. Increasing the number of recording channels requires additional active streamer sections and induces additional project costs, and therefore, according to Eq. (8.1), the only way to increase the fold is to decrease the shot interval. Shot interval is a function of vessel speed and recording length (Section 2.5.1.1), and there is a trade-off between shot interval and total operation time for the survey, such that smaller shot intervals require smaller vessel speeds assuming a fixed record length, which increases the overall acquisition time.

8.3 BINNING IN 3D

In 3D surveys, binning is done in real time by integrated navigation software during the acquisition to ensure a comprehensive acquisition of the data. Additional seismic lines for the infill areas are determined by a binning process to assure a regular fold distribution in the overall 3D area. Optimal design of the infill or reshoot lines is important for the survey, since the data quality is reduced for too few infill lines, and the overall survey time significantly increases if too much infill is considered.

In 3D acquisition, seismic data covers a surficial area, or bin grid, divided into several cells, termed bins, which are generally rectangular in shape (Fig. 8.7). Inline and crossline sizes of the bins generally equal half of the group interval (d) and half of the streamer separation ($a/2$) for one single source array, and one quarter of the streamer separation ($a/4$) for two identical source arrays in flip-flop acquisition (Section 2.3.5), respectively. The latter is the

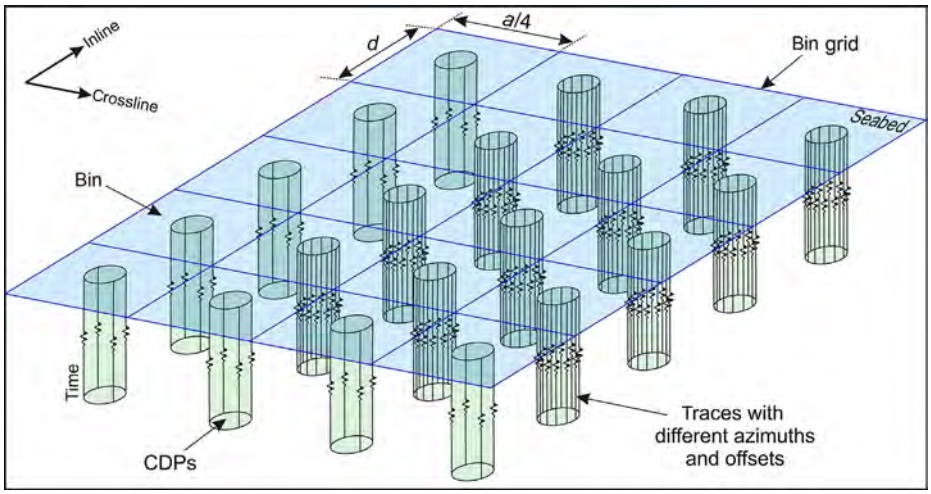


FIG. 8.7 Schematic representation of traces forming the CDP gathers using reflections from only one horizontal reflector along a 3D seismic bin grid, which is divided into several cells, termed bins. Here, *d* is inline bin size, and *a* is distance between the streamers for 3D surveys.

standard acquisition technique for conventional 3D surveys today. Each bin has several reflections from different gun arrays to various channels of different streamers, which results in groups of traces with different azimuths and different offsets. These traces are schematically illustrated as circular trace groups for each bin in Fig. 8.7. Although each individual trace is reflected from a different point within a CDP bin, and hence normally has a random reflection point distribution within the bins, all of these traces are assigned to the bin centers. Similarly to the 2D case, fold decreases towards the edges of the 3D bin grid.

As the vessel shoots along the predefined sail lines, bins within the bin grid are filled by the traces reflected from the subsurface areas defined by individual bins. Each bin then has several traces from different shots and recorded at different receivers, and the number of traces within a bin defines the fold of that particular bin. In ideal conditions, each bin should have an equal number of traces reflected exactly at the center of the bins. However, this cannot be achieved since there are several factors that negatively affect the acquisition geometry, including the streamer feathering, sail line obstructions, navigation errors, etc., and the subsurface midpoint locations of the traces deviate from their preplanned positions. Therefore, the number of traces within each bin is not constant and fold distribution is not regular. Fig. 8.8 shows a small portion of a bin grid with the midpoints of the recorded traces from eight streamers slightly feathering to the left. Each trace falling into a bin is assigned to the center of that specific bin.

In 3D exploration, it is preferred that all bins have traces with all offsets, near and far channel traces together, in ideal conditions. However, feathering of the streamers due to rough weather conditions during the surveys may cause irregular fold distributions at the end of the survey, which results in degradation of subsequent processing steps, such as migration, DMO or velocity analysis. If there are large gaps in the fold coverage, reshooting is generally applied in these areas to fill in the data gaps, which ultimately affects the total cost of the survey.

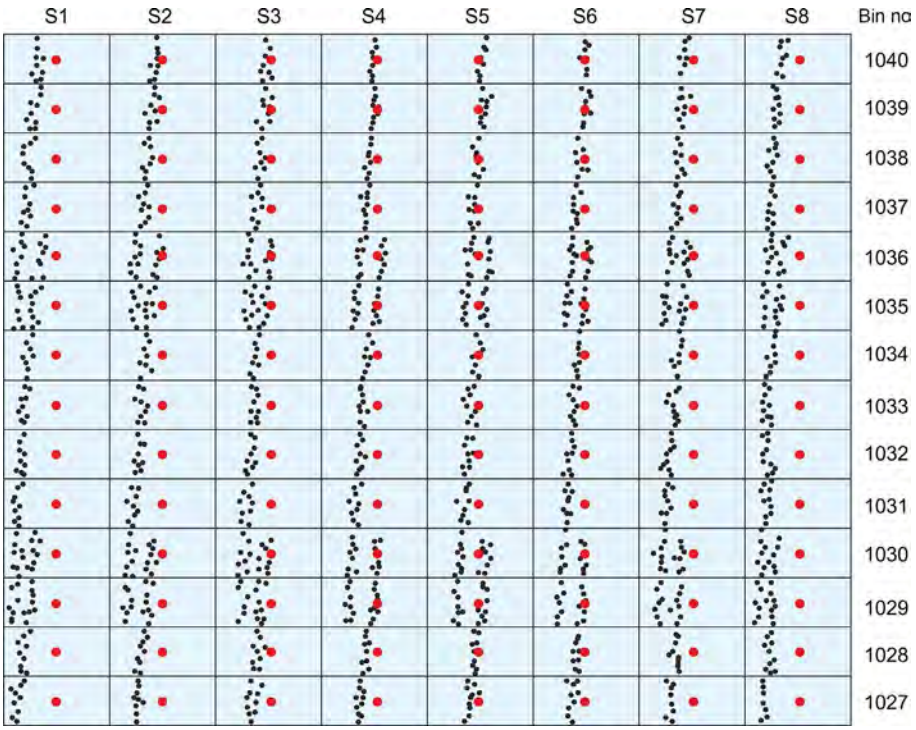


FIG. 8.8 A small portion of a bin grid with one pass of the vessel towing eight streamers (S1 to S8). The midpoints of the recorded traces are shown by black dots, while bin centers are indicated by *red circles*.

A special method known as flex binning or fixed binning is generally applied to marine 3D seismic data at the end of the survey, to obtain a more uniform fold and offset distribution along the bin grid and to reduce the total area of infill for 3D acquisition. Flex binning, or simply flexing, is a specific process that recovers the missing offsets in a particular bin from adjacent crossline bins. The process is normally constrained to prevent incorporating the traces from bins located too far from the processed bin. This is normally achieved by expanding the local bin size in the crossline direction, typically up to 200% with a criteria suggesting just one trace in each offset range be incorporated. This restriction prevents excessive use of the offsets in more than one bin, although the same midpoint is used in different adjacent bins. During flex binning, inline and crossline bin sizes are multiplied by a stretch factor and each bin is extended in both directions so that missing offsets are recovered by using the traces from adjacent bins. Fig. 8.9 schematically shows the application of flex binning for different flexing percentages of the adjacent bins. For instance, only the traces within the specific bin of a central CMP line (Line0) is used for 0% flexing (Fig. 8.9A), which is termed static binning. A 50% flex binning for Line0 incorporates half of the traces from adjacent bins of Line−1 and Line+1 (Fig. 8.9B). Similarly, 100% flex binning incorporates all of the traces from adjacent bins of Line−1 and Line+1 (Fig. 8.9C), and all traces from Line−1 and Line+1 and half of the traces from Line−2 and Line+2 are flexed for 150% flex binning (Fig. 8.9D). Finally, all traces from

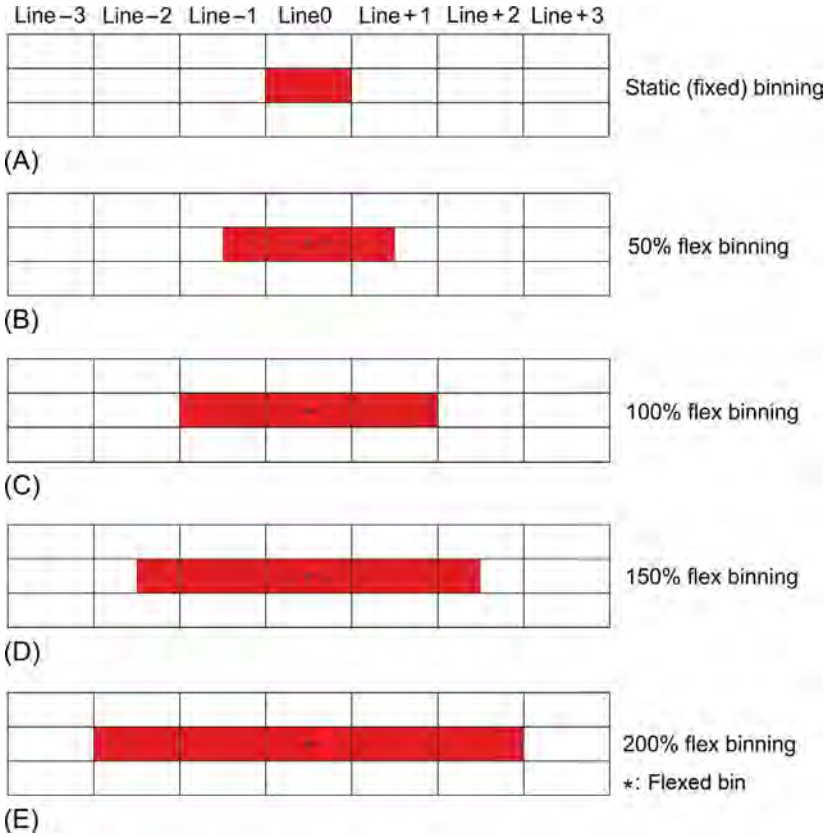


FIG. 8.9 Schematic illustration of the application of flex binning for the central bin of CMP line, Line0, to obtain a more regular fold distribution. (A) No flexing applied and only traces within the central bin are used to map the fold distribution, termed static binning. Traces from neighboring bins at both sides are used for flexing: (B) 50% flex binning incorporates half of the adjacent bins, (C) 100% flex binning incorporates all the traces of both adjacent bins, (D) 150% flex binning incorporates the traces of one and a half adjacent bins, (E) all traces from Line−1, Line−2, Line+1, and Line+2 are flexed for 200% flex binning.

Line−1, Line−2, Line+1, and Line+2 are flexed for 200% flex binning for the central bin of Line0 (Fig. 8.9E). After flex binning, each bin is expected to have the same number of traces and constant fold distribution depending on the dimension of the gap and the stretch factor used.

Fig. 8.10 shows static or fixed bin (no flexing is applied) and flexed bin fold distribution from a 3D survey for full offset range. Bin size is 6.25 m × 37.5 m for inline and crossline directions, respectively. Bin flexing is 50% at near offsets and 150% at far offsets with a linear taper in between. Although large gaps could not be harmonized completely, the flexed bin output shows much more regular fold distribution over the bin grid with a smaller number of data gaps to infill.

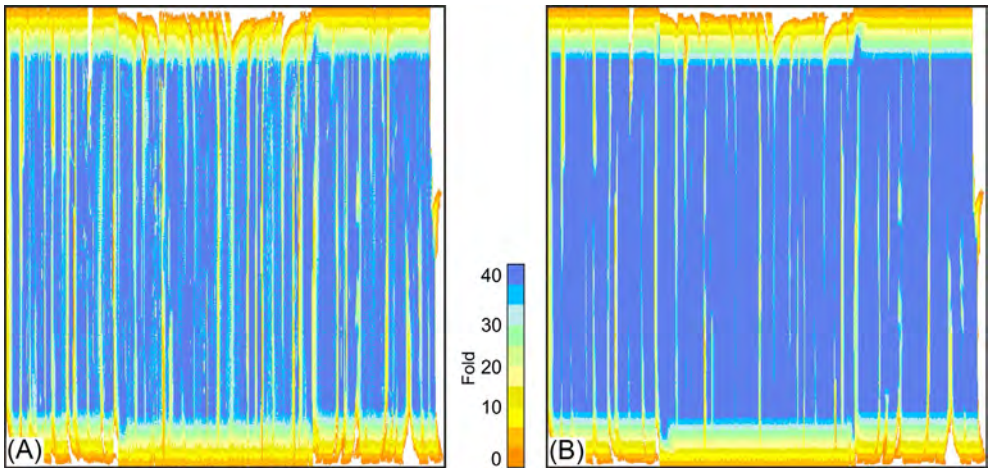


FIG. 8.10 Fold distribution for (A) no flex binning (static bin) and (B) flexed bin for 50% at near offsets and 150% at far offsets. Bin size is 6.25 m × 37.5 m for inline and crossline directions, respectively. *After Mutter, J.C., Carbotte, S.M., Canales, J.P., Nedimovic, M., 2008. A 3D MCS investigation of the magmatic-hydrothermal system at the East Pacific Rise 9° 50′N, MGL0812 Cruise Report. http://www.marine-geo.org/link/data/field/Langseth/MGL0812/docs/MGL0812SciCruiseReport-102008.pdf.*

8.4 QC IN SORT AND BINNING

Quality control (QC) in the CDP sort and binning process is done by checking the database parameters and CDP data. In the database, the most important parameter to check is the fold distribution along the line for 2D and the binning map over the whole bin grid for 3D (Fig. 8.6). CDPs can be displayed and the number of traces in the ensembles is controlled to ensure that the trace numbers within the CDPs decrease at both ends of the line. In the example illustration in Fig. 8.11, the first and last 100 CDPs of a 2D seismic line are displayed with the fold distribution graph along the line. The number of traces in the CDPs slightly increases at the beginning of the line from 1 to the optimum fold value of 48. However, the opposite situation occurs at the end of the line: the fold decreases slightly from the optimum value of 48 to 1.

Trace kill or missed shots result in variations in the optimum fold value. Especially the areas of missed shots must be carefully examined, since the fold number may dramatically decrease in these areas. Fig. 8.12 shows the effect of missed shots on the fold of 2D seismic data. Fig. 8.12A illustrates the shot points between shots 665 and 690 with several successive missed shots along a distance of 203 m, which has arisen from a time break signal issue in the gun controller during the acquisition; there were no shots between shot points 676 and 677 for a distance of 203 m. The lack of seismic data in this zone resulted in a data gap in the final stack section after NMO stretch mute due to the lack of far offsets around CDP 2400 (Fig. 8.12B) where the optimum fold decreases from 24 to 6 (Fig. 8.12C and D). In seismic operations, decreasing the fold number under a certain threshold requires filling in the data gaps by reshooting the areas of successive missed shots.

After application of flex binning to 3D data, some QC tests are needed to ensure that the binning is performed properly. The objective of flex binning is to obtain a fold distribution as uniform as possible. After flexing, a more regular distribution of the fold value indicates that the

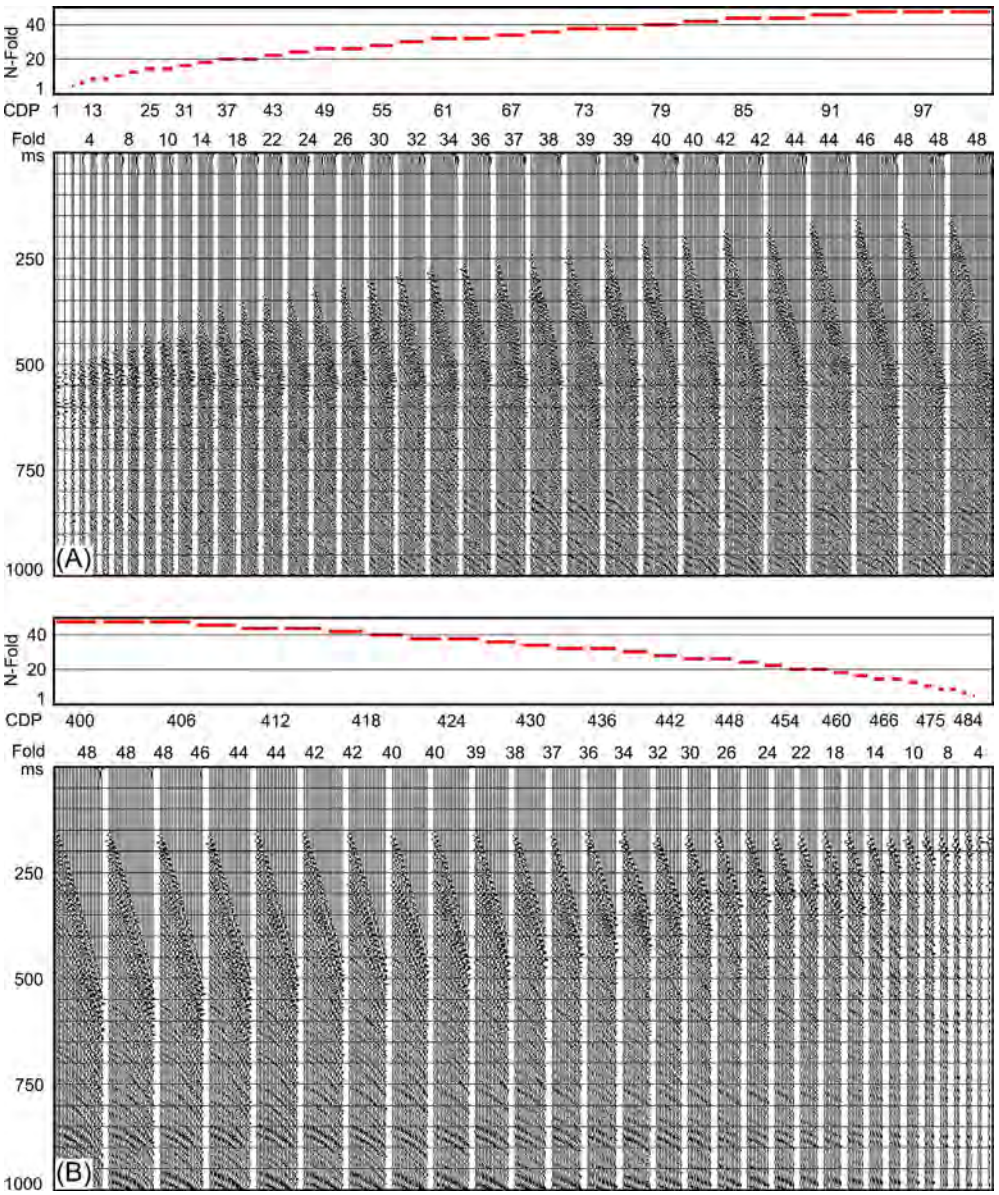


FIG. 8.11 (A) First and (B) last 100 CDPs of a 2D seismic line. Every three CDPs are displayed for simplicity (bottom) with the fold distribution graph (top). The number of traces in the CDPs slightly increases at the beginning from 1 to its optimum value of 48, and vice versa for the end of the line.

flex binning works fine. Because the other goal of flex binning is to provide a uniform offset distribution along the survey area, it is also worth checking the percent of offset bins filled by the flex binning, as well as the range of the offset values in the bins.

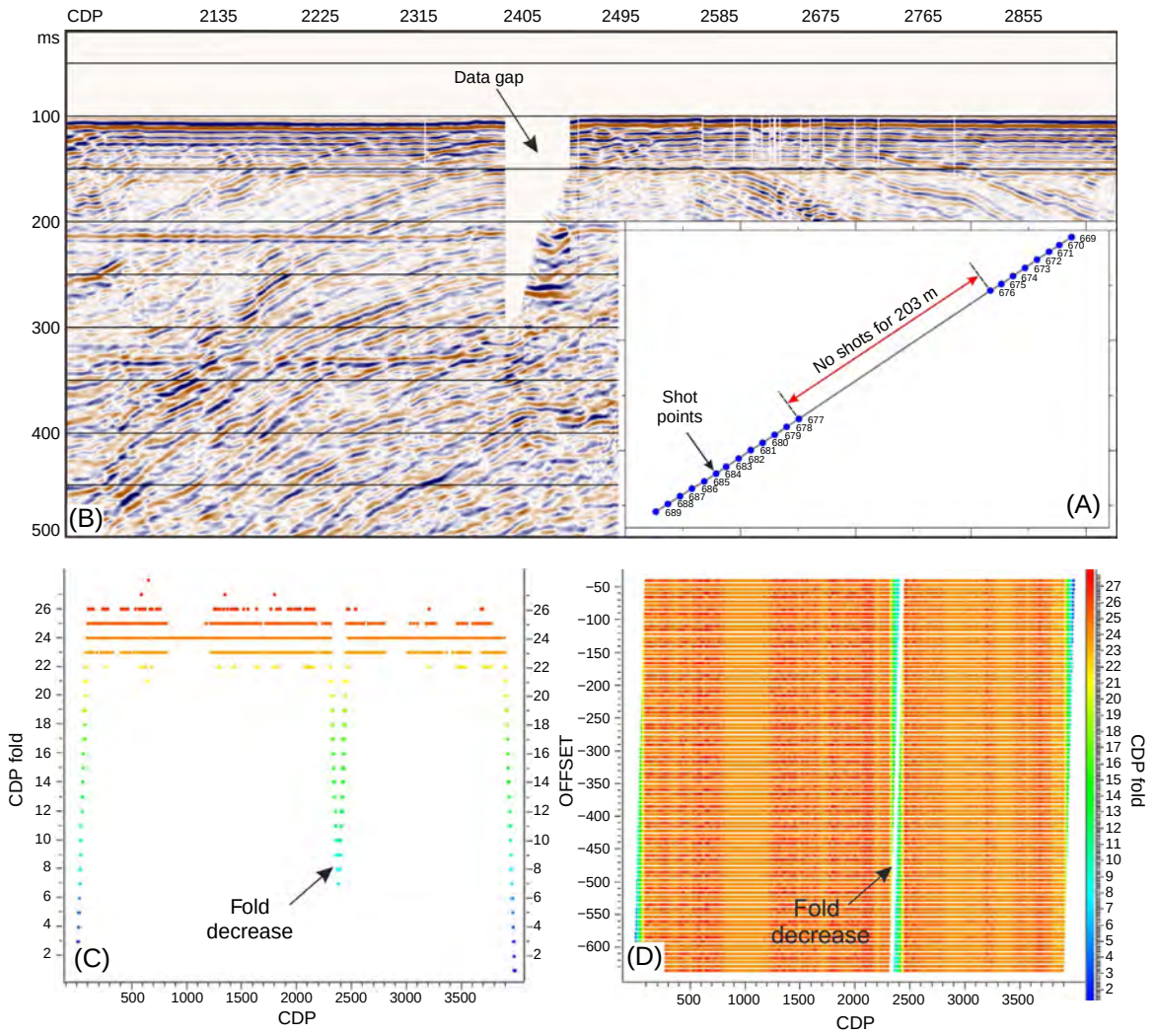


FIG. 8.12 Effect of missed shots on the fold of the 2D seismic data. (A) Shot points between shots 669 and 689 with a number of successive missed shots for 203 m along the line. (B) The final stack section of this line has a data gap due to the severe missed shots. (C) Fold map and (D) stacking chart of the seismic line indicate the fold decrease due to the missed shots.

QC implications of flex binning typically comprise analyzing the data from different offset ranges. For 3D seismic data, fold maps are prepared for near, middle and far offset segments separately and 3D binning is performed over these different ranges for QC purposes. Fig. 8.13 shows 3D fold distribution maps for near (200–1662 m), near-mid (1662–3125 m), far-mid (3125–4587 m) and far (4587–6050 m) offset ranges. Separate displaying of near, near-mid, far-mid and far offset fold maps enables us to analyze the gaps occurring due to the streamer feathering for near to far offset traces individually, and provides the design and application of suitable flex binning for different offsets of the 3D data separately.

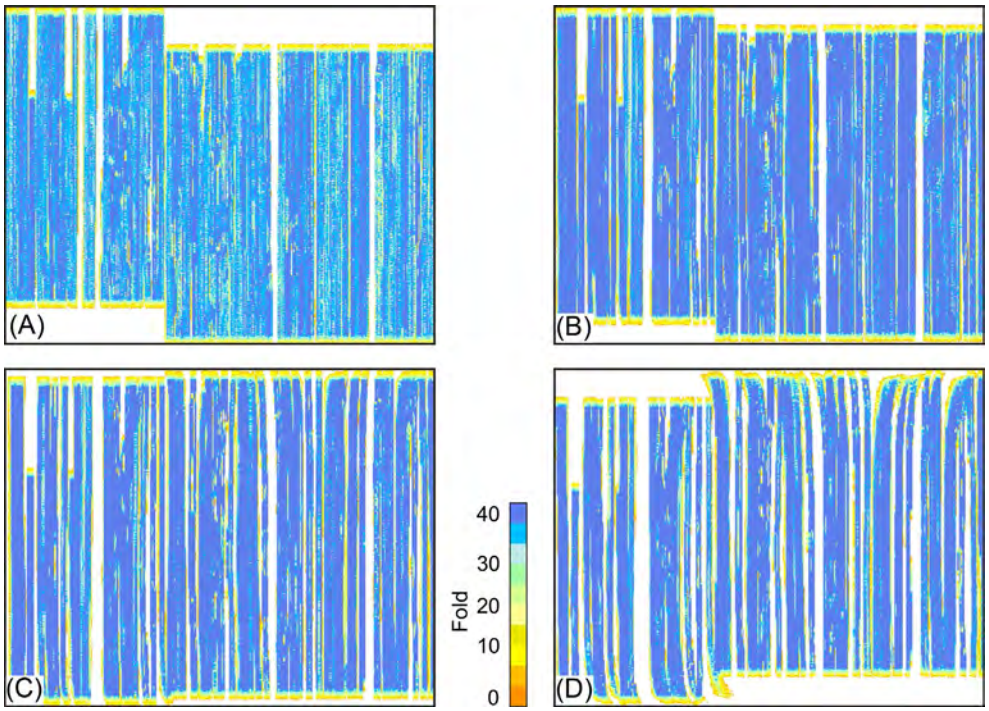


FIG. 8.13 3D fold distributions for (A) 200–1662 m, (B) 1662–3125 m, (C) 3125–4587 m, and (D) 4587–6050 m offset ranges. Data gaps with no traces *(white areas)* and low-fold areas occur due to the streamer feathering. No flex binning is applied. *After Mutter, J.C., Carbotte, S.M., Canales, J.P., Nedimovic, M., 2008. A 3D MCS investigation of the magmatic-hydrothermal system at the East Pacific Rise 9° 50′N, MGL0812 Cruise Report. http://www.marine-geo.org/link/data/field/Langseth/MGL0812/docs/MGL0812SciCruiseReport-102008.pdf.*

Generally, feathering is much more pronounced for far offsets of the streamers, and therefore it is expected that the larger data gaps arise in the fold maps of middle to far offsets, as is the case in Fig. 8.13C and D. Fig. 8.14 shows the flex binned versions of the same data. Although flexed data has much more uniform fold distribution all over the 3D area, large data gaps still exist in the output, which needs additional infill lines.

The lack of some individual offset traces in the CDP bins causes gaps in sea bottom and shallow subsurface reflections. Flex binning is typically applied in the crossline direction and such gaps for missing offsets are greatly recovered. Fig. 8.15 shows an example crossline data with a data gap in the shallow parts of the section. For QC analyses of flex binning, a similar analysis should be performed on crossline data to determine the suitable binning percentages separately for near, mid and far offset ranges. Generally, 100% or even 150% flexing for near offsets and 200% for far offsets produce satisfactory results.

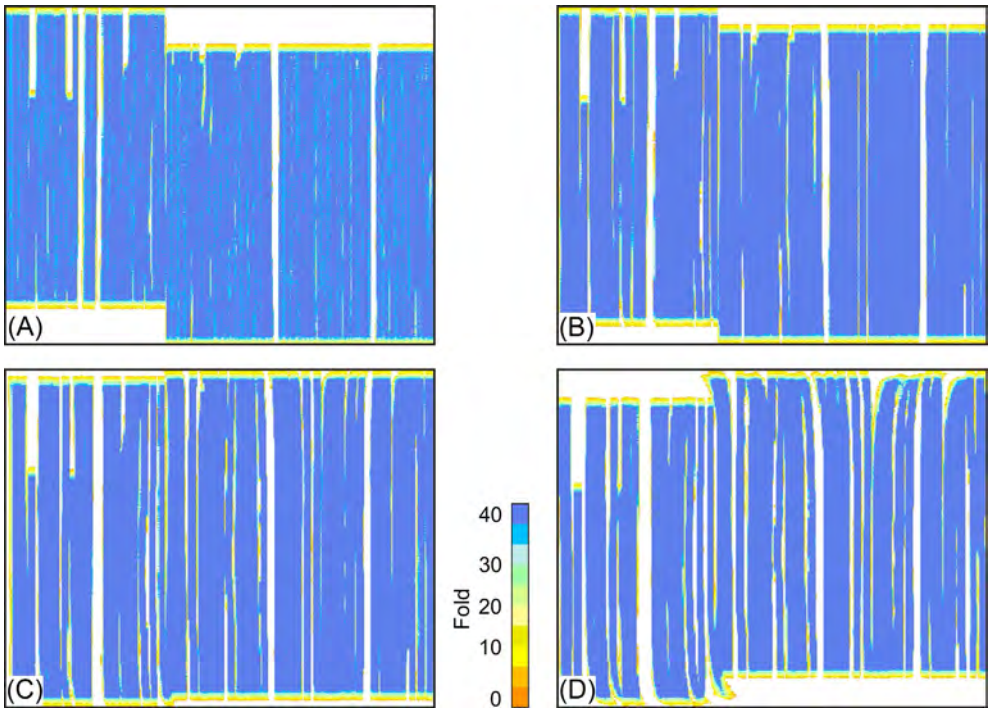


FIG. 8.14 3D fold distributions of the same data as in Fig. 8.13 after flex binning for (A) 200–1662 m, (B) 1662–3125 m, (C) 3125–4587 m, and (D) 4587–6050 m offset ranges. Bin flexing is 50% at near offsets and 150% at far offsets. *After Mutter, J.C., Carbotte, S.M., Canales, J.P., Nedimovic, M., 2008. A 3D MCS investigation of the magmatic-hydrothermal system at the East Pacific Rise 9° 50′N, MGL0812 Cruise Report.* http://www.marine-geo.org/link/data/field/Langseth/MGL0812/docs/MGL0812SciCruiseReport-102008.pdf.

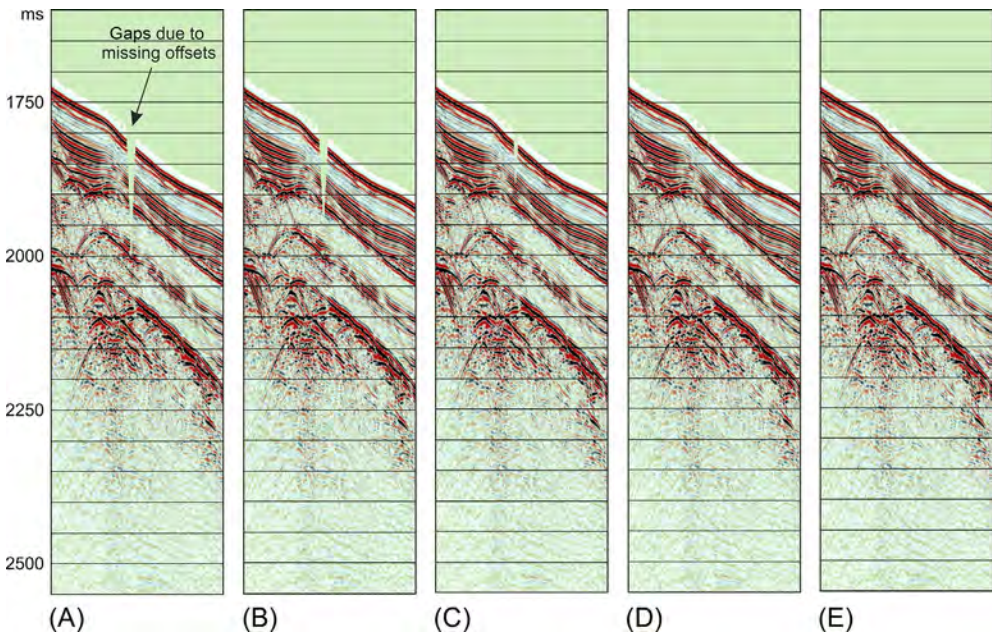


FIG. 8.15 An example of crossline data with (A) no flexing, and after (B) 50%, (C) 100%, (D) 150%, and (E) 200% flex binning.

CHAPTER

9

Velocity Analysis

OUTLINE

9.1 Types of Seismic Velocity 424
- *9.1.1 Interval Velocity (V_{int})* 424
- *9.1.2 Average Velocity (V_{ave})* 424
- *9.1.3 Instantaneous Velocity (V_{ins})* 424
- *9.1.4 Root-Mean-Square Velocity (V_{RMS})* 424
- *9.1.5 NMO or Stacking Velocity (V_{NMO})* 425
- *9.1.6 Dix Interval Velocity (V_{DIX})* 425

9.2 Velocity Determination From Seismic Data 426
- *9.2.1 Constant Velocity Scan* 427
- *9.2.2 Constant Velocity Stack* 428
- *9.2.3 Velocity Spectra* 428

9.3 Velocity Analysis in Practice 436
- *9.3.1 Supergather* 436
- *9.3.2 Effect of Reflection Depth* 440
- *9.3.3 Effect of Streamer Length* 441
- *9.3.4 Effect of Fold Number* 443
- *9.3.5 Effect of Multiple Reflections* 443
- *9.3.6 Effect of Time Gate* 444
- *9.3.7 Effect of Velocity Increment* 446
- *9.3.8 Effect of Semblance Sample Rate* 446
- *9.3.9 Effect of Noise* 447
- *9.3.10 Effect of Muting* 449

9.4 QC in Velocity Analysis 453

Seismic reflections are generated at interfaces characterized by impedance contrasts separating rock units with different velocity and density values. However, in seismic data processing, the density term is generally omitted since the variations in density are generally quite small, as compared to the variations in rock velocity. Therefore, it is supposed that the main argument of the seismic method is seismic wave velocity of the medium, and recorded reflections are assumed to originate from the interfaces that separate two layers with different velocities. Velocity information is the main parameter to define the depth, dip, and the lateral locations of the reflectors in the seismic data. It is also crucial information for some of the processing methods, such as normal moveout (NMO) correction and migration. In this section, the factors

https://doi.org/10.1016/B978-0-12-811490-2.00009-8

© 2018 Elsevier Inc. All rights reserved.

affecting the velocity, different velocity types widely used in seismic data processing, and common methods used to obtain velocity information from seismic data are explained. The acquisition and processing parameters affecting the quality and accuracy of velocity analysis are also discussed.

Seismic wave velocities change over a wide range in nature, even for the same rock type (Fig. 9.1A), since several factors control the velocity of a specified medium. This phenomenon generally prevents defining the subsurface lithology by seismic velocities only. For instance, measured P wave velocities of sandstones range from 1.8 to 4.8 km/s (Sheriff and Geldart, 1995) depending on several factors, including

- Lithology
- Saturation and fluid type
- Porosity
- Cementation, grain size and pore shape
- Age of the rock
- Pressure/compaction or depth
- Density of the medium
- Temperature

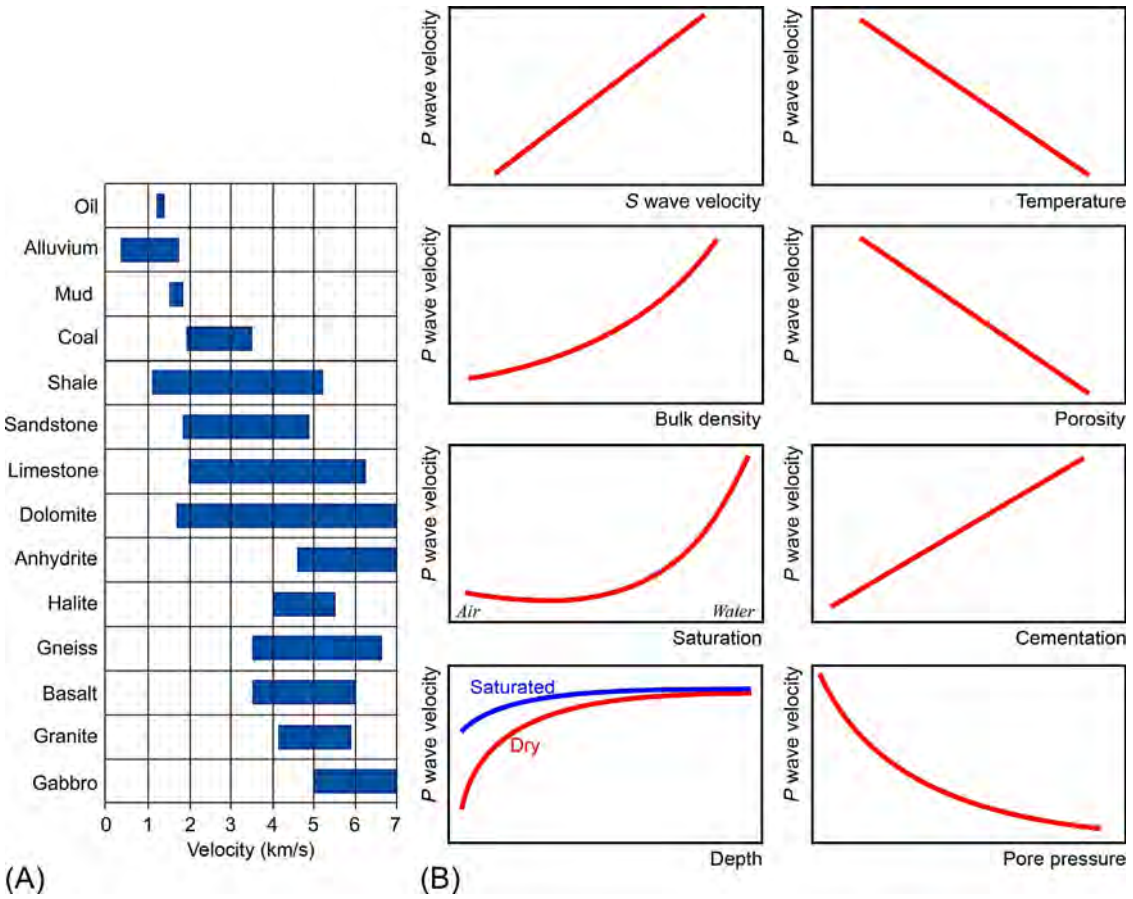


FIG. 9.1 (A) *P* wave velocity range of some specific rock types, and (B) effect of different factors on *P* wave velocity. *Compiled from Telford, W.M., Geldart, L.P., Sheriff, R.E., 1990. Applied Geophysics. Cambridge University Press; Jones, E.J.W., 1999. Marine Geophysics. John Wiley.*

- Frequency of the seismic signal
- Anisotropy and fractures
- Clay content
- Consolidation

The influences of these factors on seismic velocities and attenuation of P and S waves in sedimentary rocks are the major exploration field of rock physics research (King, 2005). The seismic velocity of the subsurface layers is not constant for most cases and varies along both time and space directions, even within a specific medium. This is because the local variations in several factors, including compaction, overburden pressure, cementation, saturation, etc., play an important role in the velocity of a subsurface layer. Wang (2001) suggests that dolomite has the highest P wave velocity in reservoir rocks, followed by limestone and sandstone, while the S wave velocity decreases, with a possible order of sandstone, dolomite and limestone. Because S wave velocity is normally not sensitive to the change of fluids in the pore spaces, while P wave velocities are strongly affected by fluid type and saturation, P to S wave velocity (V_P/V_S) ratio variations may also provide valuable information for lithology discrimination, which is particularly important in amplitude vs. offset (AVO) analysis. For instance, shales are of higher V_P/V_S ratios than sands within a reservoir. The V_P/V_S ratio is also sensitive to pore fluids and is lower in the case of gas saturation.

Although the most important factor controlling the rock velocity is lithology, experimental studies indicate that the other factors listed here also strongly affect the velocity distribution through the subsurface in 3D. Fig. 9.1B summarizes these effects in schematic illustrations. There are a number of empirical relationships between bulk density and rock velocity, which suggest that the seismic velocity increases with increasing bulk density, although it is not necessary for velocity to increase with the bulk density of the rocks. The most common one is known as Gardner's equation, given by

$$\rho = 0.23 V_P^{0.25} \tag{9.1}$$

where V_P and ρ are P wave velocity and bulk density, respectively.

Shapes and sizes of the grains also affect the velocity in sedimentary rocks. For instance, seismic velocity decreases in the case of poor grain contact, while cementation results in a significant increase in the velocity. Shape of the pores also influences the seismic velocity, and the rocks with flat pores are of lower velocities Wang (2001). Effects of anisotropy are more pronounced for the shales, which are generally considered as cap rocks for the reservoirs. Sometimes fracturing causes anisotropic effects, especially on the P wave velocity.

V_P does change with the porosity and fluid saturation of the sedimentary rocks. Increasing porosity decreases the seismic velocities; however, the V_P/V_S ratio is not strongly affected by porosity change. As the fluid saturation increases, P wave velocity slightly decreases first, then starts to increase sharply, while S wave velocity decreases, which ultimately causes an increase in the V_P/V_S ratio. Incorporating gas into the saturated liquid, however, V_P significantly decreases while V_S slightly increases, resulting in a lower V_P/V_S ratio. Increasing the viscosity and density of the pore fluids increases the velocity of the saturated rock.

In addition, velocity increases with increasing depth (or overburden pressure), thus the seismic velocities are generally higher for deeper reflections on the seismic data because the pores of the rocks are closed as the overburden pressure increases. This increase in the velocity is much more pronounced for shallow sediments since the number of pore spaces to close progressively decreases towards the deeper sediments; thus, increasing pressure does not excessively influence the velocity in deeper sediments (Fig.9.1B). Depth or pressure also results in compaction of the rocks, causing higher seismic velocities because of the better contact among the grains. An older rock has a higher velocity

for the same reason. Under pressure, velocity changes with the saturation in such a way that, under low pressures, saturated rocks have higher velocities as compared to dry rocks. In addition, dry rocks are more sensitive to pressure increase because the pore fluids in the matrix of the saturated rocks cannot be compressed.

Signal frequency also affects the velocity obtained at sonic and ultrasonic frequencies. Frequency dependence of medium velocity is known as dispersion. If the velocity decreases with the signal frequency, then it is termed normal dispersion. In marine seismics, guided waves show dispersive behavior (Section 3.8).

9.1 TYPES OF SEISMIC VELOCITY

Seismic wave velocity can be directly obtained from sonic log measurements in the wells as a function of depth. Velocity in two and three dimensions can also be obtained indirectly from multichannel seismic data. Based on the area of application, there are different velocity definitions in seismic exploration, such as interval, NMO, or root-mean-square (RMS) velocities, etc. However, the most convenient velocity type extracted from analyzing the seismic data is the one that provides the best stack section, which is directly related to the NMO and RMS velocities. Using velocity analysis tools, the only velocity that we can obtain from seismic data is the RMS velocity, yet it is possible to compute interval velocities from RMS velocities via empirical relationships.

9.1.1 Interval Velocity (V_{int})

Interval velocity is the average velocity between two reflective interfaces. If two reflectors located at depths h_2 and h_1 give one-way travel times t_2 and t_1, respectively, then the interval velocity of the layer between the depths h_2 and h_1 is given by

$$V_{int} = \frac{h_2 - h_1}{t_2 - t_1} \tag{9.2}$$

Interval velocity is an intrinsic characteristic of the subsurface rocks. Some of the migration algorithms require interval velocities to be known, and they can be obtained from RMS velocities using the Dix equation in the seismic processing stage.

9.1.2 Average Velocity (V_{ave})

Average velocity is the average of the seismic velocity between sea surface and a specific reflector, and is used for the conversion of seismic data from time to depth. If there are n number of layers down to the target reflector, the total thickness of these layers is divided by the summation of one-way travel time of the signal for each layer, that is

$$V_{ave} = \frac{h_1 + h_2 + \cdots + h_n}{t_1 + t_2 + \cdots + t_n} = \frac{\sum h_i}{\sum t_i} \tag{9.3}$$

9.1.3 Instantaneous Velocity (V_{ins})

If the wave velocity varies continuously with depth, then the $h_2 - h_1$ difference becomes ∂h while the $t_2 - t_1$ difference turns into ∂t. Instantaneous velocity is the differentiation of the depth with respect to time, and its time integral gives the average velocity between source and reflector. Instantaneous velocity can be defined as

$$V_{ins} = \frac{\partial h}{\partial t} \tag{9.4}$$

$$V_{ave} = \int_0^T V_{ins}(t)\,dt \tag{9.5}$$

9.1.4 Root-Mean-Square Velocity (V_{RMS})

If the subsurface consists of n number of layers, and if their corresponding interval velocities

are V_1, V_2, …,V_n, the RMS velocity can be defined as

$$V_{RMS}^2 = \frac{V_1^2 t_1 + V_2^2 t_2 + \cdots + V_n^2 t_n}{t_1 + t_2 + \cdots + t_n} = \frac{\sum V_i^2 t_i}{\sum t_i} \quad (9.6)$$

where t_1, t_2, …, t_n are the one-way travel times of the signal for each individual layer. This is the velocity obtained during the velocity analysis of seismic data and is used in NMO correction for the layered subsurface.

9.1.5 NMO or Stacking Velocity (V_{NMO})

For a specific reflection, the time difference between the recording time of that reflection at any offset from the shot and zero-offset time is defined as normal moveout (Chapter 10), which arises only due to the offset between source and recording channel. NMO velocity is used to remove normal moveout times from CDPs before stacking, and therefore accurate determination of NMO velocity is extremely important for the quality of final stack sections. It is defined as

$$t^2(x) = t^2(0) + \frac{x^2}{V_{NMO}^2} \quad (9.7)$$

$$V_{NMO} = \sqrt{\frac{x^2}{t(x)^2 - t(0)^2}} \quad (9.8)$$

where $t(x)$ is the arrival time of a reflection signal at offset x, and $t(0)$ is the zero-offset time of that specific reflection.

NMO velocity varies with the morphology of the seafloor and structure of the subsurface: while it equals the velocity of the upperlying medium for the horizontal single reflector case, it is proportional to the cosine of the inclination angle in the case of a dipping interface. For short offsets at a horizontally layered media, NMO and RMS velocities are identical. The same approach may also be valid for the cable lengths shorter than the reflector depths in the case of layers with arbitrary dips, providing that the inclination angles are small enough.

These assumptions can be summarized as follows (Yılmaz, 2001):

(i) Single horizontal layer: NMO velocity equals the velocity of the upperlying medium.
(ii) Horizontally stratified earth: RMS velocity is used as NMO velocity provided that the length of the seismic spread is small.
(iii) Single dipping layer: NMO velocity is the velocity of the upperlying medium divided by the cosine of the inclination angle, according to the Levin equation.
(iv) Several layers with arbitrary dips: RMS velocity is used as NMO velocity provided that the length of the seismic spread and inclination angles of the reflectors are small.

There is a small difference between NMO and stacking velocities, which is generally omitted in practice: While NMO velocity is obtained from the reflections recorded using small spreads, stacking velocity is derived from the best-fit hyperbola for the reflections from full spreads (Taner and Koehler, 1969; Al-Chalabi, 1973). This difference is known as spread-length bias, and it generally arises from the heterogenic velocity structure of the upperlying medium. Although the difference is prominent for large offsets (Fig. 9.2), stacking and NMO velocities are assumed to be equal in practice. Since this time difference between observed and theoretical arrival times at increasing offsets causes issues during NMO corrections for long offset data, several corrections for long offsets may be required during the velocity analysis using one of the proposed correction approaches to Eq. (9.7), such as Al-Chalabi's third term approach (Al-Chalabi, 1973), or Castle's shifted hyperbola (Castle, 1994).

9.1.6 Dix Interval Velocity (V_{DIX})

Using the empirical Dix equation, it is possible to calculate interval velocities from RMS velocity distribution of the subsurface. It is used

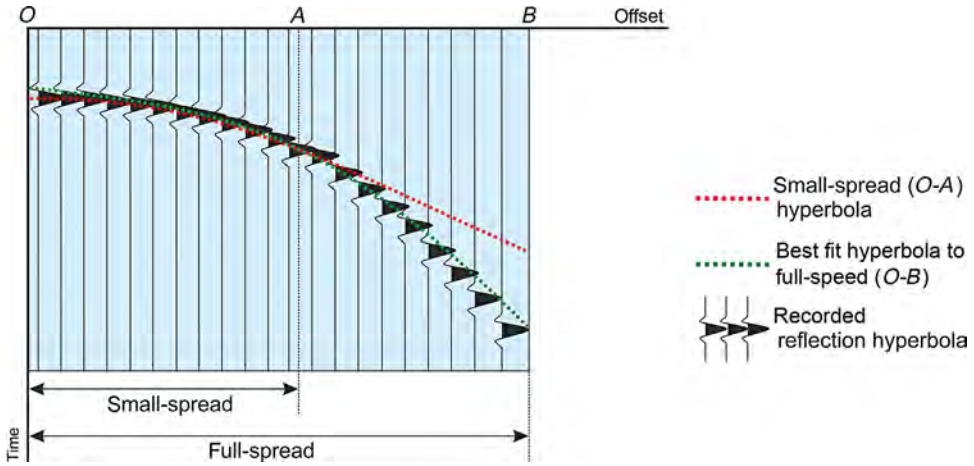


FIG. 9.2 Schematic display of difference between the hyperbolas used to calculate NMO and stacking velocities. NMO velocity is obtained from the reflections of small spread hyperbola (*O-A*), whereas stacking velocity is derived from the best-fit hyperbola to full spread (*O-B*). *Modified from Hubral, P., Krey, T., 1980. Interval velocities from reflection time measurements, SEG Monograph.*

to convert RMS velocity into interval velocity, which is used by some of the migration algorithms such as prestack Kirchhoff depth migration. If RMS velocities of two reflections with arrival times of t_2 and t_1 are V_2 and V_1, the Dix interval velocity can be expressed as (Dix, 1955)

$$V_{DIX}^2 = \frac{V_2^2 t_2 - V_1^2 t_1}{t_2 - t_1} \tag{9.9}$$

9.2 VELOCITY DETERMINATION FROM SEISMIC DATA

Basically, seismic velocity is obtained from sonic logs of the nearby wells and from the velocity analysis of multichannel seismic data. Velocity functions from sonic logs are much more detailed, and only a smoothed version of sonic log velocity can be derived from seismic surveys. Obtaining velocity from seismic data is a regular process, because the velocity distribution in 2D and 3D is required for subsequent NMO correction, migration, and some of the demultiple methods. One of the most important points about the velocity used in seismic processing is that the velocity required for stacking and migration is not necessarily the same. The stacking velocity for dipping layers is given by the Levin equation in which the stacking velocity is obtained by dividing the velocity of the upperlying medium by the cosine of inclination angle of the interface, whereas the velocity of the upperlying medium itself is used in the migration process. That is, stacking velocities are dip dependent, while the migration velocities are not.

The basis for the velocity estimation from seismic data depends on the NMOs of the reflection hyperbolas. For a given hyperbola, the higher the maximum NMO time, the higher the accuracy of the velocity estimated from the data for that specific reflection. The point here is that the NMO time decreases as the depth of reflections increases (Section 1.3.4). The same issue also arises for short cable lengths: maximum NMO time is relatively small for the data collected with short streamers. Therefore, seismic velocity of the deeper reflections generally has low resolution as compared to that in the shallow parts. Similarly, the velocity obtained from

small-spread data always has lower resolution and accuracy than the data from longer streamer acquisitions, especially for deeper parts.

The basic assumption in velocity analysis of the seismic data is that the reflections are hyperbolic on CDP gathers. However, the existence of complex seafloor morphology, anisotropy or extreme dips in the subsurface such as salt flanks can result in nonhyperbolic reflections (Fig. 1.24). In such cases, the theory behind the velocity analysis fails and it may become quite difficult to find out the accurate velocity function at the desired resolution. In practice, there are a number of velocity analysis methods in the seismic processing industry, and efficiency and accuracy of the analysis can be significantly increased by a simultaneous application of more than one method.

9.2.1 Constant Velocity Scan

Constant velocity scan is a simple method based on the flattening of the reflection hyperbolas on a particular CDP gather after NMO correction applied with a range of velocities. NMO correction is applied to a selected CDP gather using different velocities and the results are plotted. The procedure is schematically shown in Fig. 9.3.

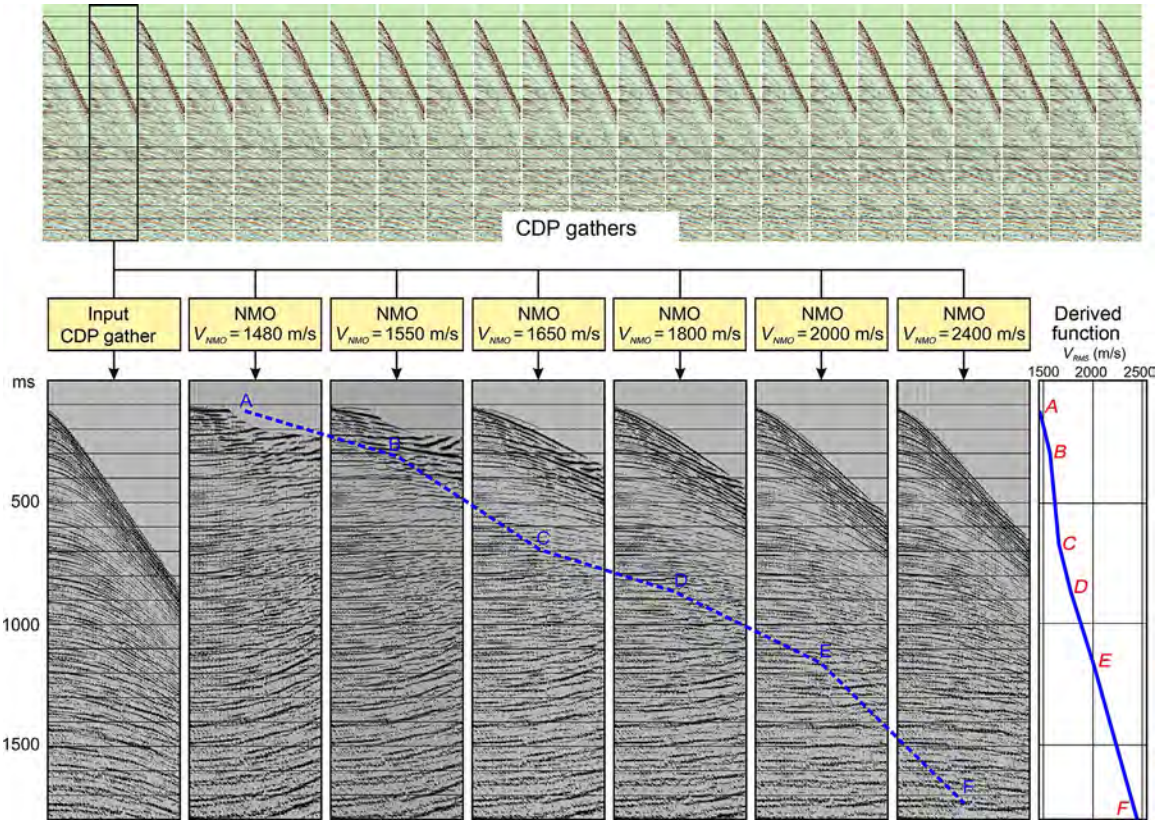


FIG. 9.3 Schematic derivation of velocity function *(dashed blue line)* for a CDP gather using constant velocity scan. NMO correction is applied to the input CDP for a range of constant velocities (here, from 1480 to 2400 m/s). The suitable velocity for a specific reflection hyperbola is the one that perfectly flattens the hyperbola.

The suitable velocity for a primary reflection is the one that perfectly flattens the hyperbola of that specific reflection. For instance, NMO correction is applied to the input CDP for different velocities ranging from 1480 to 2400 m/s. A reflection hyperbola indicated by A is flattened for 1480 m/s RMS velocity, while reflections B and C are flattened for 1550 and 1650 m/s, respectively. Therefore, the estimated velocities for events A, B and C are 1480, 1550 and 1650 m/s, respectively. If the suitable velocities are picked for each distinctive reflection hyperbola on the CDP gather, then a velocity function can be obtained for that specific CDP, indicated by the dashed blue line in Fig. 9.3.

Each reflection hyperbola is perfectly flattened if an NMO correction is applied with that reflection's dedicated seismic velocity, providing that the reflections are hyperbolic on CDP gathers. The hyperbola is overcorrected if the velocity is low and is undercorrected if the velocity is high after NMO correction. A velocity function for the whole recording time on the CDP can be derived for that specific ensemble by testing several different velocity values, as shown by the solid blue line in Fig. 9.3. If this velocity scanning procedure for constant velocities is repeated for several CDPs along the line, a 2D velocity field can be obtained for the whole seismic line.

9.2.2 Constant Velocity Stack

The theoretical basis of the velocity estimation by the constant velocity stack (CVS) method is that an optimal velocity function derived from the velocity analysis is the one that yields the best stack section. Therefore, stack sections consisting of 8–24 CDPs, stacked after NMO corrections for different constant velocities, can be used to pick the optimal velocity values. Fig. 9.4 schematically shows the constant velocity stack (CVS) procedure. A number of successive CDPs are stacked after NMO correction with a range of constant velocity values. These stack stripes are plotted to pick the velocities that produce the best stack sections. In Fig. 9.4, NMO correction is applied to 24 successive CDPs for different velocities ranging from 1480 to 2500 m/s, and prepared stack sections for each velocity are plotted side by side. The most suitable velocities are those that produce the stacks with highest amplitudes. For instance, 1480 m/s velocity produces the highest amplitudes around A in the first stack stripe, while the highest amplitudes in the second stripe are obtained for 1550 m/s velocity around B. Therefore, the suitable velocities for reflections at zero offset times A and B are 1480 and 1550 m/s, respectively.

If the suitable velocities are picked for each distinctive high-amplitude zone on the stack stripes, then a velocity function can be obtained as indicated by the dashed blue line in Fig. 9.4 and is assigned to the location of the central CDP gather. This function can be derived for a range of CDP gathers by testing several different velocity values as shown by the solid blue line in Fig. 9.4. If this constant velocity stacking procedure is repeated for several successive sets of CDPs along the line, a 2D velocity field can be obtained for the whole seismic line.

Determination of velocity range and increment is important in CVS calculations and must be selected carefully depending on the requirements of the input seismic dataset. Dipping events and sideswipes require abnormally high stacking velocity values. If such high velocities are observed in relatively shallow parts of the data, side effects may be suspected. Practical applications indicate that the CVS method is particularly useful in geologically complex areas.

9.2.3 Velocity Spectra

Velocity spectra are the most common method in deriving 2D and 3D velocity functions from multichannel seismic data. This method is based on the variations in the curvature of the reflection hyperbolas due to the

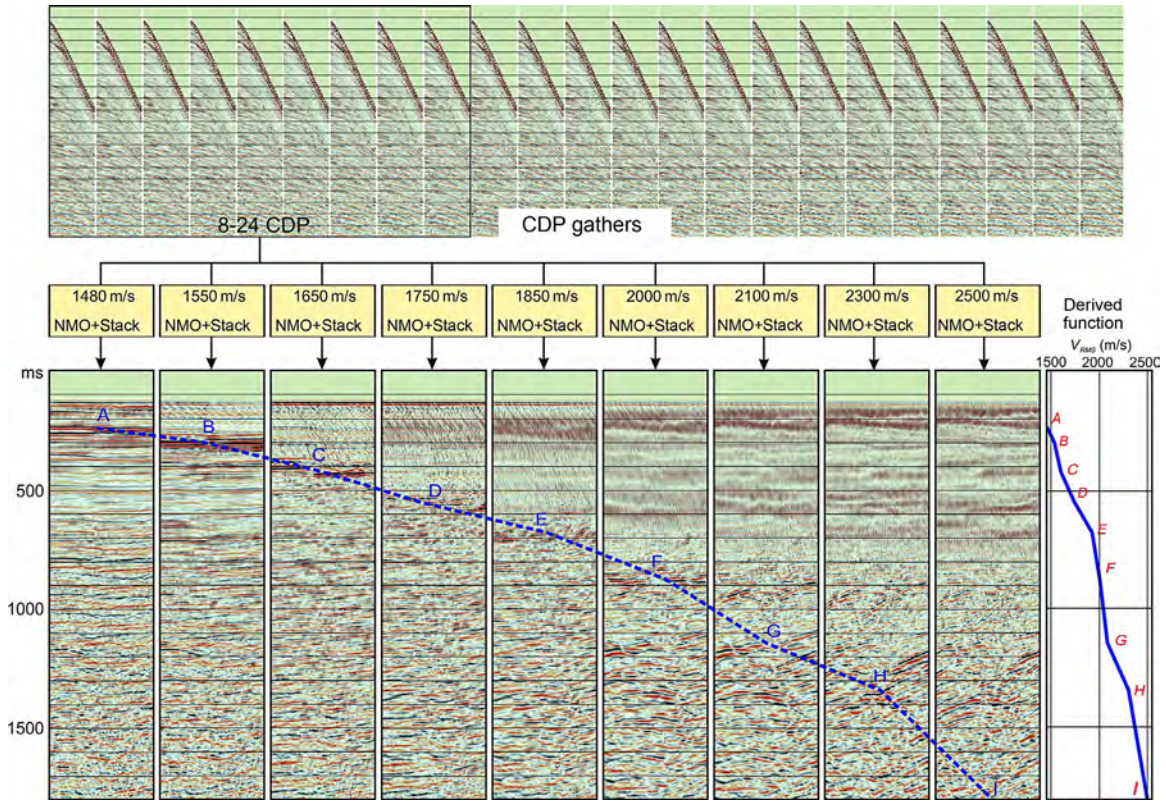


FIG. 9.4 Schematic derivation of velocity function *(dashed blue line)* for a set of CDP gathers using constant velocity stacks (CVS). The suitable velocity for a specific reflection is the one that produces the best stack section with the highest stacked amplitudes.

changes in the velocity of the upperlying medium. Indeed, for a given $t(0)$ zero-offset time, curvature of a reflection hyperbola from an interface is controlled by the velocity of the upperlying medium. Fig. 9.5 shows a number of synthetic CDPs consisting of a single reflection with different upperlying medium velocities. Variations in the velocity both affect $t(0)$ time and the curvature of the hyperbolas, which enables us to derive the velocity of a given reflection hyperbola based on its $t(0)$ time and curvature. Velocity derivation by computing the velocity spectra was first proposed by Taner and Koehler (1969), and is accomplished by an automatic scanning of all possible hyperbolas from zero to maximum recording time, using a range of velocity values on the selected CDPs.

The theoretical basis depends on automatically finding out the velocity of the best fitting theoretical hyperbola to the observed one on the CDPs. For instance, let's consider a simple synthetic CDP with one reflection hyperbola calculated using 1500 m/s velocity in Fig. 9.6A. Fig. 9.6B–G show the same CDP gather after NMO correction for a range of velocities from 1000 to 2000 m/s along with the stacked traces obtained by stacking the traces of the CDP after NMO correction. Fig. 9.6H illustrates stacked traces from several different velocities from 1000 to 2000 m/s juxtaposed by their

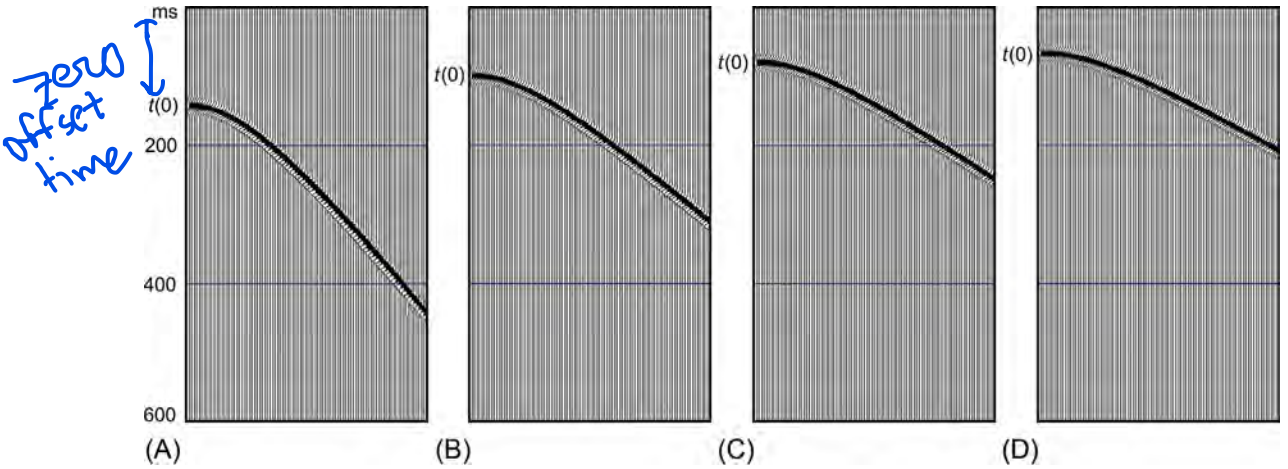


FIG. 9.5 A number of synthetic CDP gathers with a single reflection hyperbola calculated with different upperlying medium velocities of (A) 1400 m/s, (B) 2000 m/s, (C) 2500 m/s, and (D) 3000 m/s. Variations in the velocity change the zero-offset time $t(0)$ and the curvature of the hyperbolas.

corresponding stacking velocities. Thus, the horizontal axis in Fig. 9.6H represents the stacking velocity used to obtain the stacked traces, and the vertical axis is the $t(0)$ time of the reflection hyperbola(s). This process moves the seismic data from the offset two-way travel time domain into the stacking velocity-zero offset time domain.

The analysis in Fig. 9.6 indicates that the maximum amplitude in the stacked trace is obtained for 1500 m/s velocity, which is the optimal velocity to stack this reflection in the input CDP. The reflection hyperbola becomes perfectly flattened after NMO correction with this optimal velocity, resulting in the highest stacking amplitude due to the in-phase summation of the reflected signals. Small amplitudes on the stacked traces in Fig. 9.6H for the remaining velocity values are mainly the contributions of the amplitudes at near offset traces in the CDP gather. When we contour the amplitudes of the stacked traces in Fig. 9.6H, we get a distinctive enclosure at the $t(0) = 640$ ms and $V = 1500$ m/s intersection, which clearly suggests that the velocity of the reflection at 640 ms zero-offset time is 1500 m/s. This contour plot is basically the velocity spectrum of the input CDP. If we repeat this analysis automatically using several velocity values for all zero-offset times within the CDP, then we can obtain the velocities for all reflection hyperbolas along the input CDP gather.

The velocity obtained from the analysis described in Fig. 9.6 represents the stacking velocity for that hyperbola since there is only one reflection in the CDP associated with one subsurface reflector. However, in the case of an arbitrarily stratified earth, we can only derive RMS velocities from seismic data. If this velocity scanning procedure is repeated for several successive CDPs along the line for 2D surveys, or the locations suitably distributed in a 3D survey area, a 2D or 3D velocity field can be obtained.

The procedure for automatically computing the velocity versus zero offset time plots is quite simple: the arrival time of a reflection signal at a receiver located at offset x over a single horizontal reflector is given by

$$t^2(x) = t^2(0) + \frac{x^2}{V^2} \tag{9.10}$$

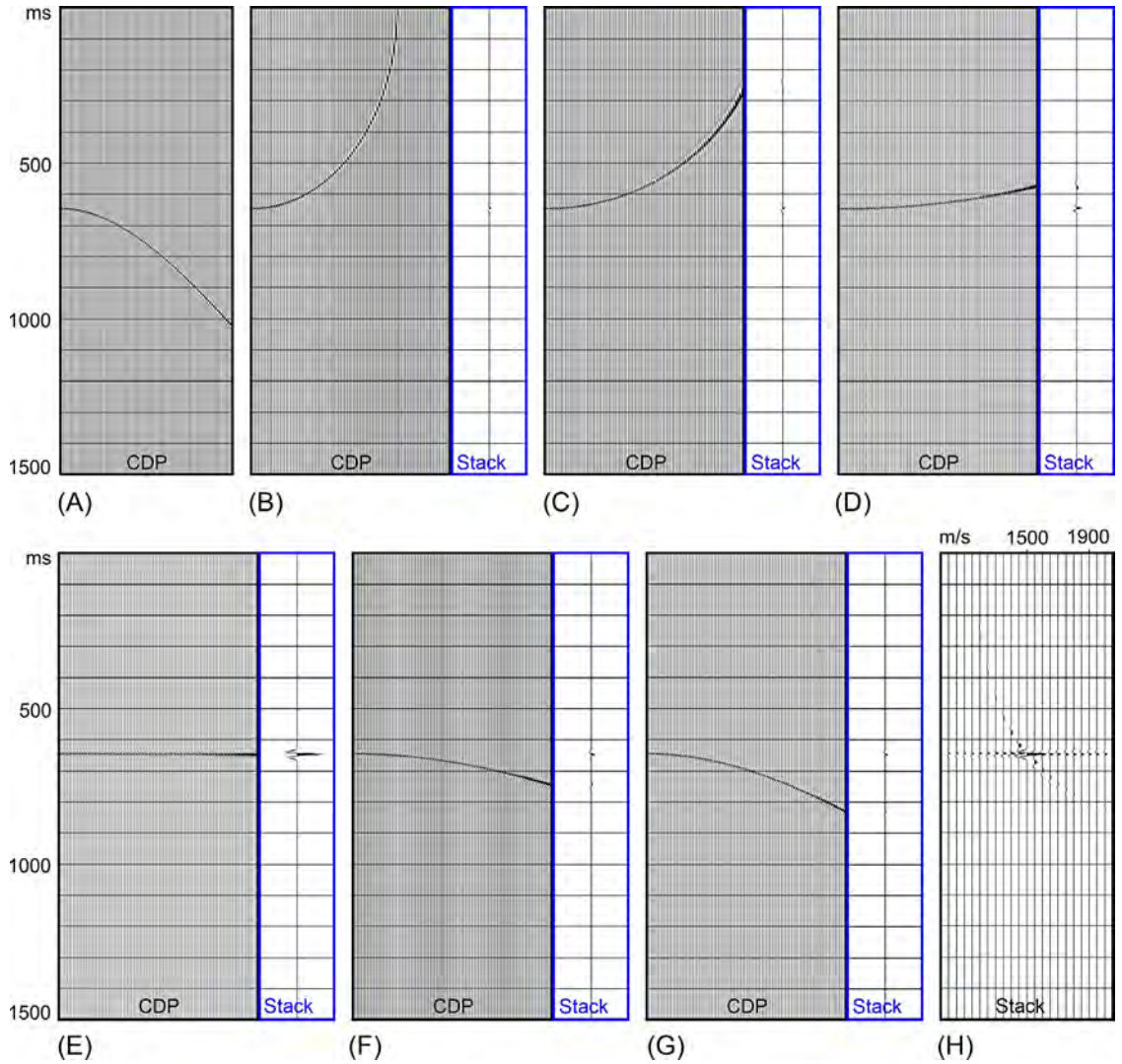


FIG. 9.6 Simple explanation of the theory behind the velocity spectra. (A) A synthetic CDP with only one reflection of 1500 m/s velocity, and its NMO corrected versions for different velocities (B) 1000 m/s, (C) 1200 m/s, (D) 1400 m/s, (E) 1500 m/s, (F) 1700 m/s, (G) 2000 m/s. Corresponding stacked traces are also provided (traces with *blue borderlines*) next to the NMO corrected gathers. (H) Stacked traces obtained from several different velocities from 1000 to 2000 m/s. A stacked trace with the highest amplitude obtained for 1500 m/s velocity in (E) represents the optimal velocity to stack the reflection in (A). If the amplitudes in (H) are contoured, a maximum enclosure is obtained at $t(0) = 640$ ms and $V = 1500$ m/s, which is the stacking velocity of the reflection at 640 ms zero-offset time.

where V is the velocity of the upperlying medium and $t(0)$ is the zero offset time of the reflection. According to Eq. (9.10), we can compute the velocity of a given reflection if x, $t(0)$, and $t(x)$ are known. Since we do not know whether an amplitude at time $t(x)$ resides to a specific reflection hyperbola with a zero-offset time $t(0)$, we must compute a number of theoretical hyperbolas with a range of velocity values using Eq. (9.10), and determine the best-fit curve with the observed hyperbola in an automatic way. To achieve this, a minimum and a maximum velocity, with an increment value, are selected. Using Eq. (9.10), a number of theoretical arrival time hyperbolas are computed for each zero-offset time on a specified CDP, each calculated by using different velocities between the minimum and maximum velocity values. That is, several hyperbolas are computed for each velocity increment from minimum to maximum velocity for $t(0) = 0$ ms; then $t(0)$ is increased a few milliseconds (e.g., 20 ms), and all the hyperbolas are computed again for the same velocity range, and the computations go on for all zero-offset times along the time axis until a maximum trace time is achieved. These theoretical hyperbolas are then matched with the real hyperbolas on the recorded CDP, and the amplitudes concurring with the arrival times of theoretical hyperbolas on the recorded CDP are summed up. Unless one of the theoretical hyperbolas completely coincides with a real observed one on the recorded CDP, the summation will produce a small value. When the theoretical and observed hyperbolas match, a large sum is obtained. A maximum can only be obtained in case of the summation along the theoretical hyperbola calculated with the velocity of that specific reflection. Thus, we can prepare a specific contour plot consisting of these summed amplitudes, horizontal and vertical axes, which represent the velocity used to calculate the theoretical reflection hyperbolas and zero-offset times, respectively. Each enclosure of a maximum value on this plot corresponds to the RMS velocity of the reflection hyperbola at its dedicated zero-offset time $t(0)$.

The specific value used to calculate a contour plot of velocity versus $t(0)$ time so far is the stacking amplitude. The most suitable representation quantity, however, may not be the reflection amplitude, depending on the S/N ratio of the input CDP. In practice, the semblance value calculated from the reflection amplitudes coinciding with the theoretical hyperbolas is calculated and used to prepare the contour plots. Hence, velocity spectrum plots are also known as semblance plots. Semblance is a statistical parameter varying from 0 to 1, and can be calculated as

$$S = \frac{1}{M} \frac{\sum_{t} \left[\sum_{i=1}^{M} |f_i| \right]^2}{\sum_{i=1}^{M} f_i^2} \tag{9.11}$$

where f_i represents the amplitude at two-way time t (i) of the ith trace in the input CDP, and M is the number of traces in the CDP gather.

All these processes are schematically illustrated in Fig. 9.7. A synthetic input CDP gather with two reflection hyperbolas of 2500 and 3500 m/s RMS velocity is shown in the upper panel. For $t(0) = 0$ ms zero offset time, six theoretical reflection hyperbolas are computed (red curves) by Eq. (9.10) for 1500, 2000, 2500, 3000, 3500, and 4000 m/s velocities, and are numbered from 1 to 6 (panel A). The recorded amplitudes on the CDP gather coinciding with these theoretical hyperbolas are used to calculate a semblance value for each hyperbola by Eq. (9.11). The calculated semblance values are placed in their relevant places in a time-velocity panel in the bottom left of Fig. 9.7, whose horizontal and vertical axes are velocity and $t(0)$ time, respectively. For instance, the semblance value for $t(0) = 0$ ms calculated using the amplitudes along the theoretical hyperbola for 1500 m/s velocity (red hyperbola of number 1

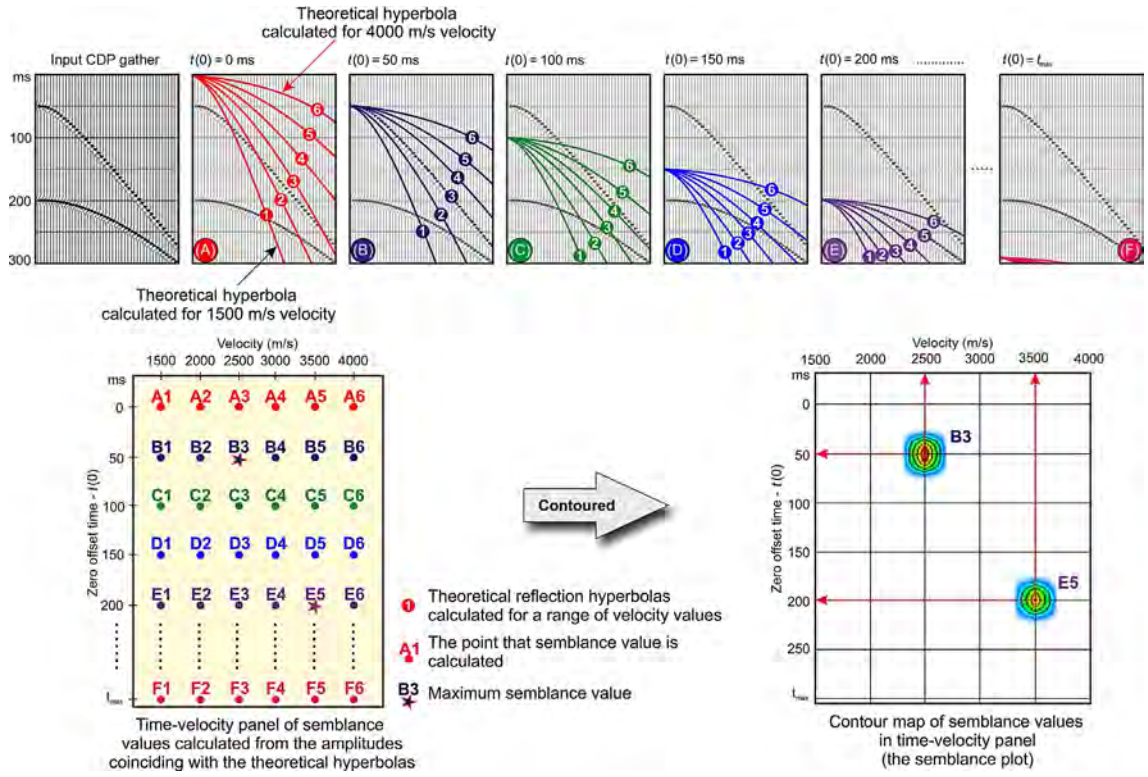


FIG. 9.7 Schematic representation of velocity spectrum calculation. See text for details.

in panel A) is assigned to the location indicated by A1 in the time-velocity panel, which is the point where 1500 m/s velocity and $t(0) = 0$ ms zero-offset time intersect. Similarly, the other semblance values calculated for the rest of the velocity values for $t(0) = 0$ ms are placed at the points marked from A2 to A6. Then, $t(0)$ time is increased by a certain amount, e.g., 50 ms (panel B), and a new set of theoretical reflection hyperbolas is obtained (dark blue curves) with the same range of velocities. Six different semblance values are calculated using the amplitudes coinciding with these hyperbolas on the recorded CDP, and are assigned to the relevant points (from B1 to B6) on the time-velocity panel. The process goes on in this fashion: the semblances are calculated for each hyperbola until $t(0)$ reaches the maximum trace time (t_{max}) of the input CDP, and the calculated values are placed at the specific location in the time-velocity panel determined by the velocity and $t(0)$ time they pertain to. Thus, the time-velocity panel is completed by the semblance values, each representing a different velocity-zero offset time pair.

The key point here is that the semblance value will be maximum only if one of these theoretical reflection hyperbolas exactly coincides with an observed reflection hyperbola in the recorded CDP gather. For instance, in the schematic illustration in Fig. 9.7, two theoretical hyperbolas in panel B number 3 and panel E number 5 (hyperbolas with dotted curves in the upper panels) exactly coincide with two reflection hyperbolas of the input CDP. Therefore, summation (and hence, their semblance value) through these two specific hyperbolas will be much higher than the summations along the remaining theoretical hyperbolas. If we prepare a contour map of the time-velocity panel of semblance values, we get the semblance plot displayed in the bottom right of Fig. 9.7, which schematically shows two enclosures at points B3 and E5. The velocities associated with these two points (2500 and 3500 m/s, respectively) are the RMS velocities for two reflection hyperbolas in the input CDP gather, and can be used to flatten these two reflections during NMO correction. In this way, we hopefully get an individual enclosure in the semblance plot for each reflection hyperbola in a recorded CDP, emanating exactly at the hyperbola's $t(0)$ time and RMS velocity. Selecting the velocity values from the horizontal axis against the zero-offset times from the vertical axis of these maximum enclosures provides the RMS velocity function of the input CDP from zero to maximum trace time.

This procedure of selecting time-velocity pairs from semblance plots is known as velocity picking and is the standard procedure today in deriving the 2D and 3D velocity fields from multichannel seismic data. If this process is repeated for several CDPs with a certain CDP increment along the seismic lines in the survey, a 2D or 3D velocity field can be obtained for the whole survey. Fig. 9.8A shows an example semblance plot from a shallow 2D seismic line, and Fig. 9.8B illustrates picked RMS velocity (dashed white line) and interval velocity functions (solid black line) calculated by the Dix equation given by Eq. (9.9). If the velocity functions picked from semblance plots of several CDPs along the seismic line are mapped, a velocity field can be constituted, in which the variations in the RMS velocity both in time and space directions are observed, as in Fig. 9.8C. This 2D or 3D RMS velocity field can be transformed into 2D or 3D interval velocity using the Dix equation (Fig. 9.8D).

Furthermore, in practice, not only amplitudes that exactly coincide with the theoretical hyperbolas are involved in semblance calculations, but also all the amplitudes within a narrow time gate along the theoretical hyperbola are included in the calculations (Fig. 9.9). This is because the reflection signal is not a spike and consists of a wavelet with a certain time length, or period. Therefore, the width of the time gate must be selected as close as possible to the dominant period of the seismic wavelet. Once the dominant frequency is calculated from the spectral analysis

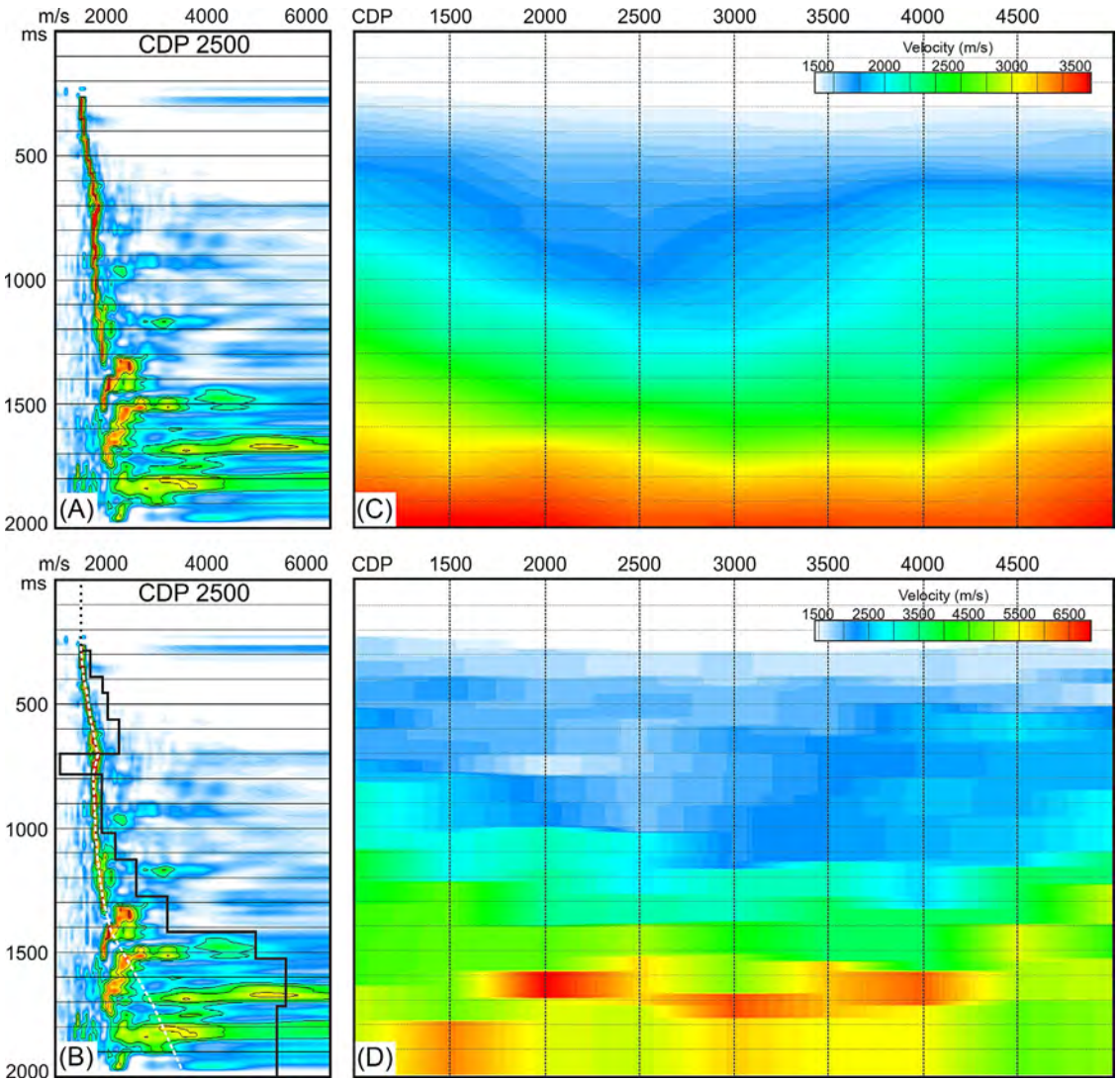


FIG. 9.8 (A) An example semblance plot from a supergather of a 2D seismic line, (B) RMS velocity *(dashed white line)* and interval velocity *(solid black line)* functions picked from the semblance plot. (C) A 2D RMS velocity field can be obtained by mapping several velocity functions along the line, and (D) the interval velocity field can be computed from (C) using Eq. (9.9).

of the data, then the effective period of the seismic signal can be found as the inverse of the dominant frequency. Since the absolute value of the amplitudes is used in the summation in Eq. (9.11), incorporating all the positive and negative amplitudes associated with reflection hyperbolas in summation results in a better resolution in semblance plots. The effect of the proper selection of time gate on the quality of semblance plots is explained in Section 9.3.6.

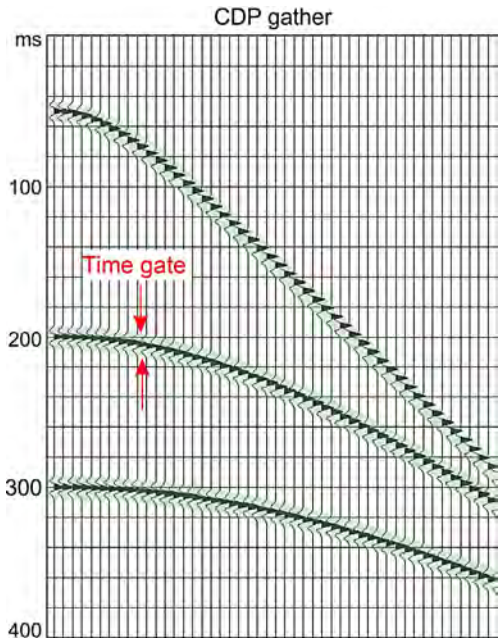


FIG. 9.9 Schematic illustration of time gate used to calculate semblance. All amplitudes within the time gates *(green shaded areas)* are incorporated in the semblance calculations.

9.3 VELOCITY ANALYSIS IN PRACTICE

There are several factors that affect the resolution and accuracy of velocity estimates from seismic data. These factors include

- Streamer length or availability of long offsets
- S/N ratio of the data
- Semblance sample rate
- Use of supergathers
- Velocity increment in semblance calculations
- Length of semblance time gate
- Nonhyperbolic reflections
- Maximum fold
- Accuracy of muting
- Anisotropy effects
- Existence of multiples
- Time length of the input data
- Seismic signal frequency

Signal-to-noise ratio (S/N) of the marine seismic data is generally much higher than that of land data, and therefore velocity analysis of offshore seismic datasets is more straightforward and velocity picking is more accurate. However, there are important points to consider during the velocity analysis, such as the noise content of the data. Furthermore, the limitations arising from the nature of data collection may decrease the efficiency and accuracy of velocity analysis. For instance, the accuracy is relatively poor for late arrivals of the data collected with a short streamer cable.

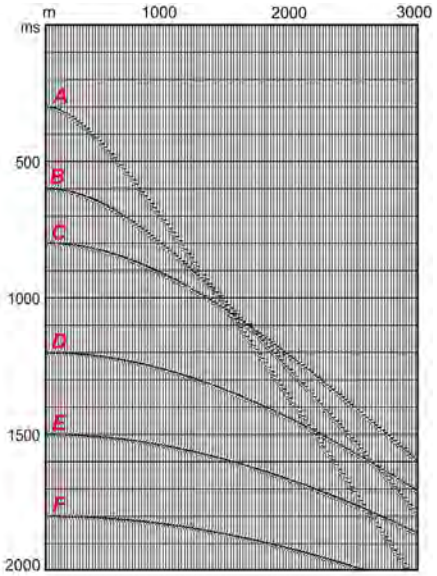
In this section, some of the factors listed are evaluated on synthetic and real CDPs and their effects on velocity analysis is discussed. The synthetic data is calculated by a simple 1D convolutional model approach to obtain the arrival times of six individual reflections at 120 traces. The parameters used in travel time computations are shown in Fig. 9.10A. A 120-fold synthetic CDP is calculated using an 80-Hz Ricker wavelet with a total recording length of 2 s. Trace intervals used are 12.5 and 25 m, which result in a CDP with an offset range from 0 to 1500, and 0 to 3000 m, respectively (Fig. 9.10B).

9.3.1 Supergather

Supergathers are basically the collection of several consecutive CDPs into a single large (super) gather. They are obtained by combining a certain number of successive CDPs in 2D lines and a certain number of traces in adjacent bins in 3D surveys, and therefore they have many more traces than ordinary CDP gathers, which ensures that much better and higher resolution semblance plots are achieved when a semblance analysis is applied to supergathers. They are generally used as the input data to semblance calculations instead of using only one specific CDP for each analysis location. Fig. 9.11 schematically shows preparing a supergather from five neighboring CDPs for a 2D seismic line:

Reflection	$t(0)$ time (ms)	Velocity (m/s)
A	300	1500
B	600	1800
C	800	2200
D	1200	2500
E	1500	2750
F	1800	3000

(A)



(B)

FIG. 9.10 (A) Parameters used in travel time computations of six reflections to obtain a synthetic CDP with 120 traces given in (B). This synthetic CDP is used to analyze some of the parameters affecting the velocity analysis.

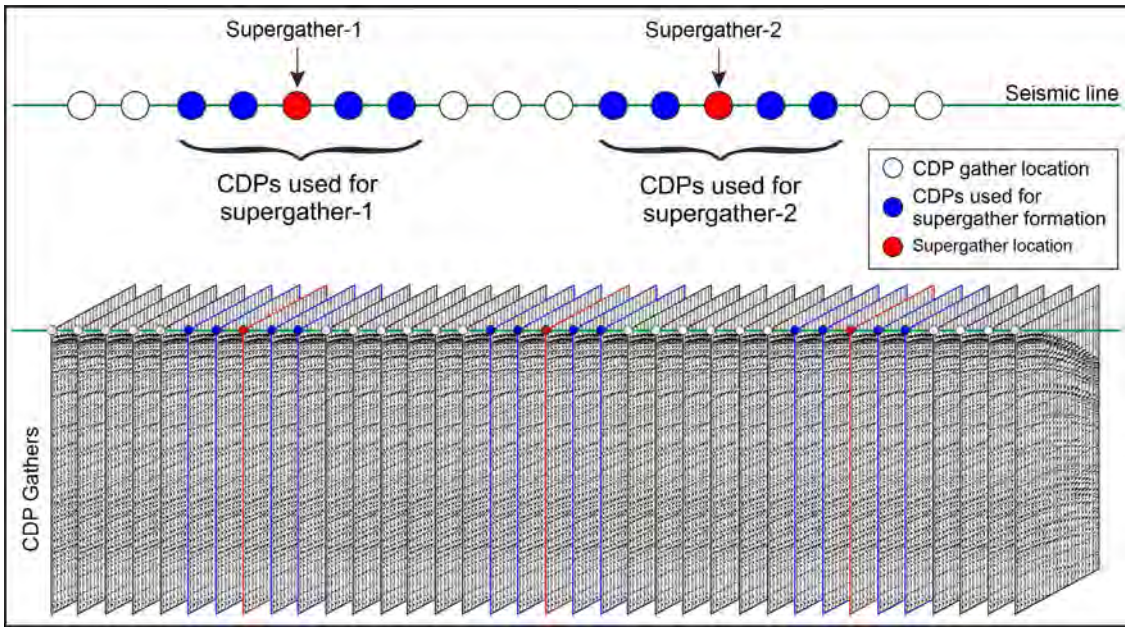


FIG. 9.11 Schematic illustration of 2D supergather formation using five neighboring CDPs *(blue circles)*. The resultant supergather is assigned to the location of the CDP at the center *(red circles)*.

traces of five successive CDPs are combined, and the resultant supergather is assigned to the location of the central CDP.

In 3D surveys, the traces of adjacent bins along inline and crossline directions are combined. In the schematic illustration in Fig. 9.12, 15 ensembles are combined (blue circles and squares) to form a single supergather (red circles and squares), 5 for crossline and 3 for inline directions, corresponding to crossline and inline ensemble sizes. The crossline and inline increments, which are the number of CDPs between supergather locations, are 9 and 6, respectively. After forming the supergathers throughout the whole 3D survey coverage with certain crossline and inline increments, a regular supergather grid can be generated (Fig. 9.12C), along which the velocity functions are obtained to form a 3D RMS velocity field. A finer grid with smaller crossline and inline increments ensures a more accurate velocity field.

The offsets of traces within each CDP gather are different from each other; that is, each CDP includes traces with different offsets from the traces located at its neighboring CDPs. This is illustrated in close-ups of five consecutive CDPs in Fig. 9.13A. For instance, in close-up I, trace offsets of CDP 45 are 62.5 m, 112.5 m, 162.5 m, etc., while the offsets of traces in CDP 46 are 68.75 m, 118.75 m, 168.75 m, etc. Note that the offset increment of the traces within the CDPs is 50 m since the shot interval is 25 m. This does not mean that there is no trace between offsets 68.75 and 118.75 m in the collected dataset: since

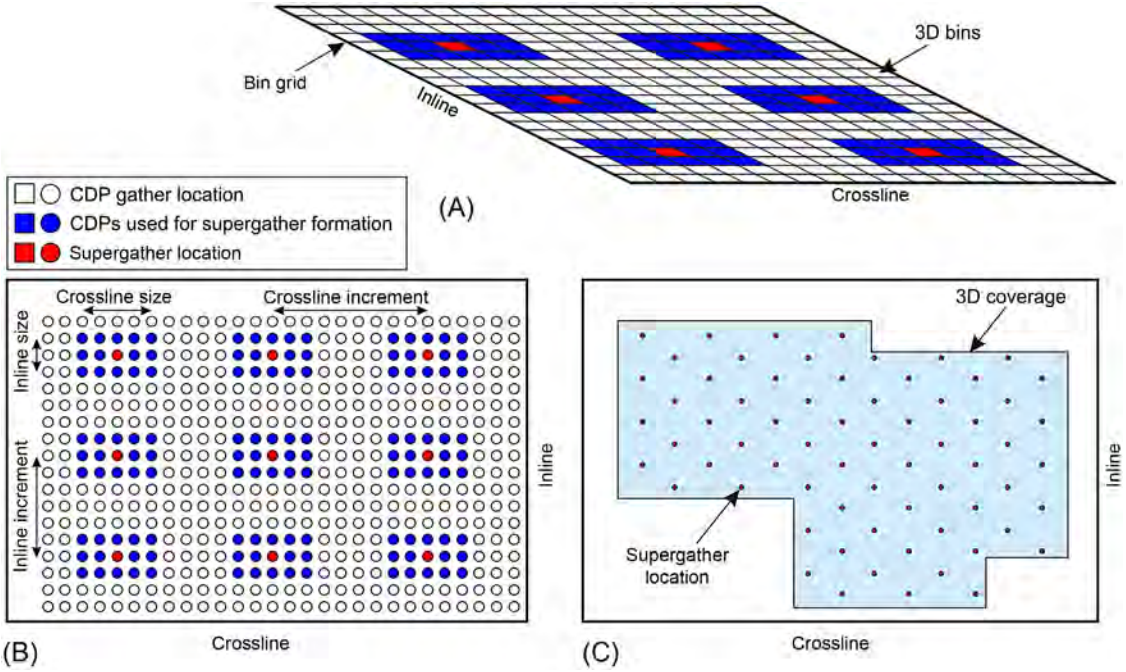


FIG. 9.12 Schematic illustration of 3D supergather formation using 15 neighboring CDPs (*blue circles* and *squares*) to form a single supergather (*red circles* and *squares*) at the center. (A) Schematic 3D bin distribution on the seafloor coverage display, and (B) schematic plan view of 3D CDP distributions *(circles)*. Ensemble sizes in *x* line and inline directions are 5 and 3, respectively. The number of CDPs between supergather locations (ensemble increment for supergather formation) are 9 and 6 for crossline and inline directions, respectively. (C) A supergather grid is obtained throughout the 3D survey area to form the 3D RMS velocity field.

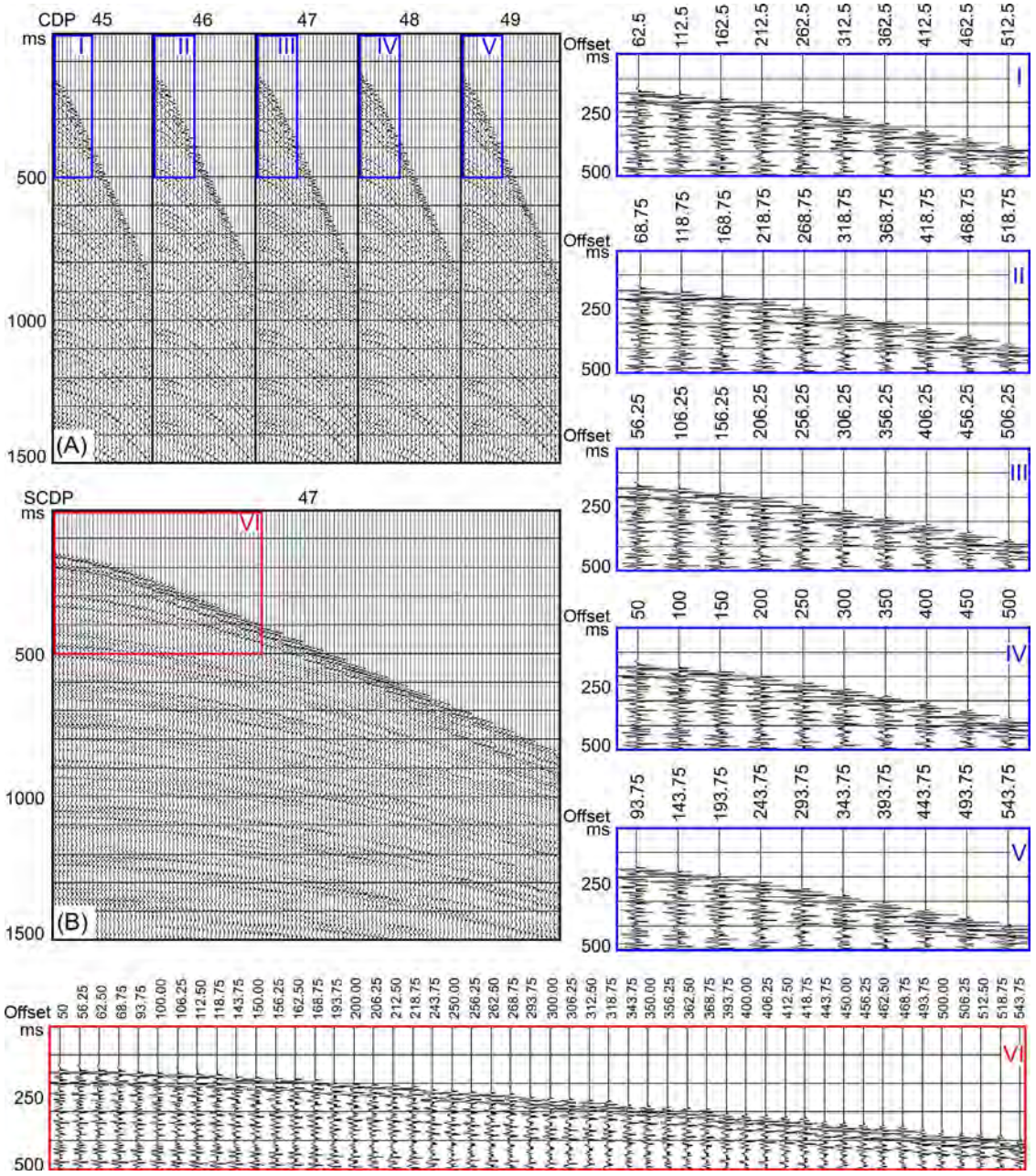


FIG. 9.13 (A) Five successive CDPs between CDPs 45 and 49. (B) Supergather at the location of CDP-47 formed by combining the five CDPs in (A). Close-ups from I to V with blue borderlines show the first 10 traces of the CDPs in (A) with associated trace offset values. Close-up VI with red borderline illustrates the first 50 traces of the supergather in (B) with its associated trace offset values. Missing offsets between consecutive traces within a specific CDP are incorporated from the traces of adjacent CDPs in the supergather.

the group interval of this dataset was 6.25 m, the subsurface was actually sampled at every 3.125 m, which means that there are traces in the data with 3.125 m offset increment. What is the reason for 50-m offset increment in the CDPs, and where are the missing offsets in a specified CDP? In fact, they are located within the adjacent CDPs. For instance, the trace with offset 106.25 m is in CDP 47, 100-m offset is in CDP 48 etc. (Fig. 9.13).

Based on the theory of the supergather formation, the traces of different offsets in the neighboring CDPs are combined to form a multioffset CDP gather, which includes as many offsets as possible. Therefore, the number of traces in a supergather is much higher than the optimum fold of the line. For the example supergather in Fig. 9.13B, it is formed by combining five adjacent CDP gathers of Fig. 9.13A, and according to the offsets of this supergather (close-up number VI with red borderline), four additional traces with different offsets are inserted among the successive traces from the input CDP gathers. For instance, there are no traces between offsets 50 and 100 m in close-up IV in Fig. 9.13; however, in close-up VI of the supergather, the traces with offsets 56.25, 62.5, 68.75, and 93.75 m are incorporated between the traces with 50- and 100-m offsets as the contributions of neighboring CDPs.

9.3.2 Effect of Reflection Depth

As the depth of a reflection from the seafloor increases, the resolution in the velocity of that reflection obtained from the semblance plots is significantly reduced. Basically, there are two reasons for this:

- The curvature of reflection hyperbolas (namely, the normal moveout) decreases as the velocity of the medium increases, and the velocity generally increases with depth (Fig. 9.10).
- The curvature of reflection hyperbolas also decreases as the depth (namely, zero offset time) of the reflection increases (Fig. 9.5).

Thus, the normal moveout times of the reflections decrease as the depth of the reflection increases. Velocity estimation using semblance analysis depends on the curvature of the hyperbolas, and since the curvature decreases with depth, the resolution in velocity estimation is significantly reduced in the deeper parts of a semblance plot. The example in Fig. 9.14 shows this degradation. The upper and lower limits from which a velocity value can be picked from the semblance enclosures are indicated with white dotted curves. For instance, the velocity of an arbitrary reflection from the shallow parts, e.g., the hyperbola indicated by I in the supergather in Fig. 9.14, can be precisely picked from point A in the semblance plot as $V_A = 1472$ m/s, since the enclosures in the region are relatively tight which prevents picking an incorrectly high or low velocity value for this reflection. On the other hand, for deeper parts of the semblance, the enclosures become much wider along the velocity (horizontal) axis, which prevents picking the precise velocity values for the reflections. For instance, the velocity of a deep reflection, such as the one indicated by II in the supergather in Fig. 9.14, can be picked either from points B, C, or D in the semblance plot as $V_B = 1843$, $V_C = 1914$, and $V_D = 1984$ m/s, respectively, since the enclosures in this area are relatively wide. This situation indicates that any velocity value between 1843 and 1984 m/s can be used to flatten this hyperbola during NMO correction, and therefore the stack section will be fine even if we cannot determine the velocity of this reflection precisely, because the reflection will be flattened for any velocity value in this range. Anyway, we cannot know the exact velocity value of this deep reflection, which denotes that we lose the resolution in velocity determination as the depth of the reflections increases, and the velocities can be estimated much more precisely in the shallow parts of the seismic data.

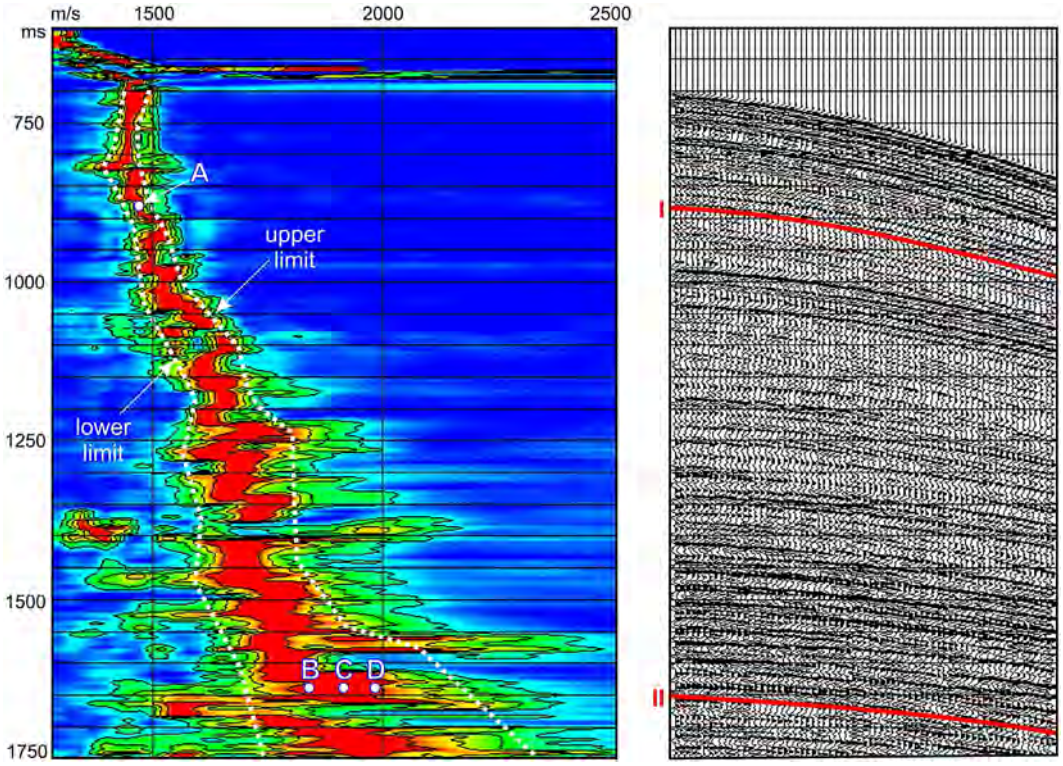


FIG. 9.14 An example semblance plot (left) and its supergather (right) indicating the degradation of resolution in velocity determination in deeper parts. A shallow reflection's velocity, such as the reflection indicated by I on the supergather, can be precisely picked at point A in the semblance plot as $V_A = 1472$ m/s since the enclosures in the shallow parts are relatively narrow. For a deeper reflection, such as the one indicated by II in the supergather, any velocity in the semblance plot at points B (1843 m/s), C (1914 m/s), or D (1984 m/s) can be used in NMO correction since the enclosures in the region are relatively wide along the velocity axis. White dotted curves on the semblance contours confine the upper and lower limits of the enclosures from which a velocity value can be picked.

9.3.3 Effect of Streamer Length

The higher the normal moveout time of the input supergather, the higher the resolution and hence the accuracy of the velocity determination from semblance calculations. The only way to increase the normal moveout time of a particular reflection for a specified zero-offset time is to use longer streamer cables, which enables us to record long offset data. Fig. 9.15 compares the semblance plots of two synthetic CDPs (parameters of the synthetic model are given in Fig. 9.10) with longer (3000 m length, Fig. 9.15A) and relatively shorter (600 m length, Fig. 9.15B) cables. Although the semblance contours correctly locate the zero-offset times of all the six reflection hyperbolas both for short and long streamers, the resolution is lost in deeper reflections later than approximately 750-ms zero-offset time: The semblance contours of longer cable data in Fig. 9.15A are relatively tight

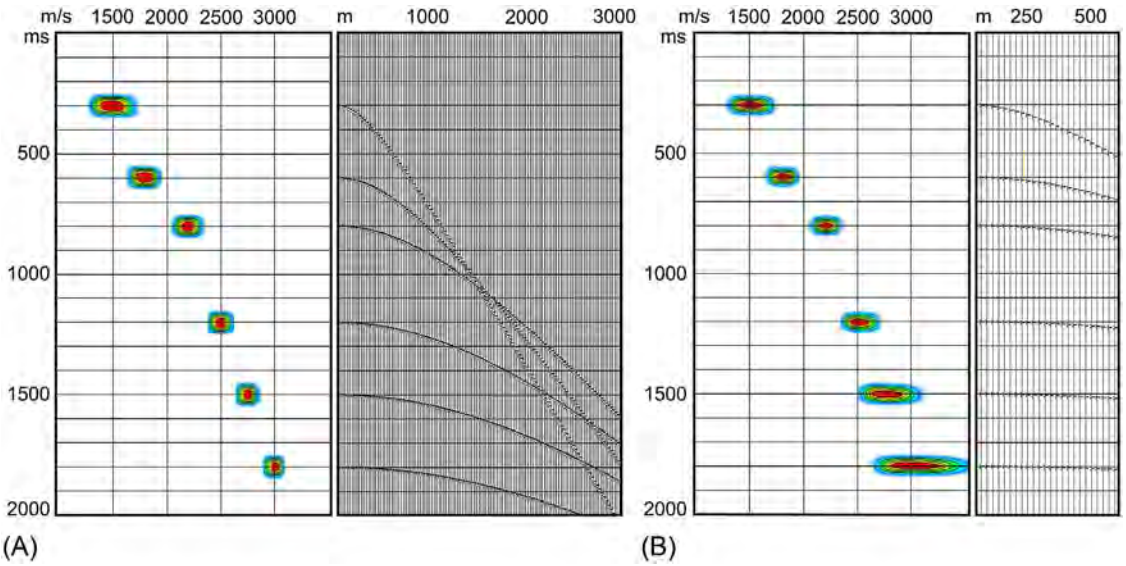


FIG. 9.15 A comparison of semblance plots of two synthetic CDPs (parameters of the synthetic data are given in Fig. 9.10) with (A) longer (3000 m length), and (B) shorter (600 m length) streamer cables. The semblance contours in (A) allow a precise velocity determination for each reflection, while the enclosures in (B) suggest a range of velocities for deeper reflections, indicating a resolution loss in velocity estimation.

and compact, allowing a precise velocity picking for each reflection, whereas the enclosures of shorter cable data in Fig. 9.15B are wide and prolate for deeper reflections, indicating a range of possible velocities for each reflection instead of a single precise velocity value. That is because the moveouts of the reflection hyperbolas are considerably reduced at the deeper parts, which is especially evident for the deepest event in Fig. 9.15B.

Lack of long offset data means the absence of sufficient normal moveout to obtain the accurate velocity function, resulting in the enclosures in the semblance plots being much wider for the short offset data. Fig. 9.16 compares the semblance plots of two marine supergathers with longer (1500 m length, Fig. 9.16A) and relatively shorter (600 m length, Fig. 9.16B) cables. The short offset data is obtained by regarding only the first 600-m offset of the long offset data; hence, both supergathers represent the same reflections. Resolution is primarily lost for deeper reflections due to their smaller moveouts for short cables.

Widening of the contours in the semblance plots, especially in the deeper parts, suggests that a range of velocity values can produce a reflection hyperbola which almost exactly fits to the real observed one, indicating that the resolution in estimation is not fine. For instance, let's consider two reflections indicated by A and B on long offset data in Fig. 9.16A and their counterparts A' and B' on short offset data in Fig. 9.16B. The corresponding velocities can be precisely picked from the semblance plot in Fig. 9.16A as 2180 and 2386 m/s for the reflections A and B (indicated by blue arrows), respectively. However, the velocities of the same reflection range from 1910 to 2490 m/s for reflection A', and from 2080 to 2800 m/s for reflection B' (indicated by white horizontal bars) from the semblance plot in Fig. 9.16B. In practice, the appropriate resolution can be obtained by using both near and far offsets together.

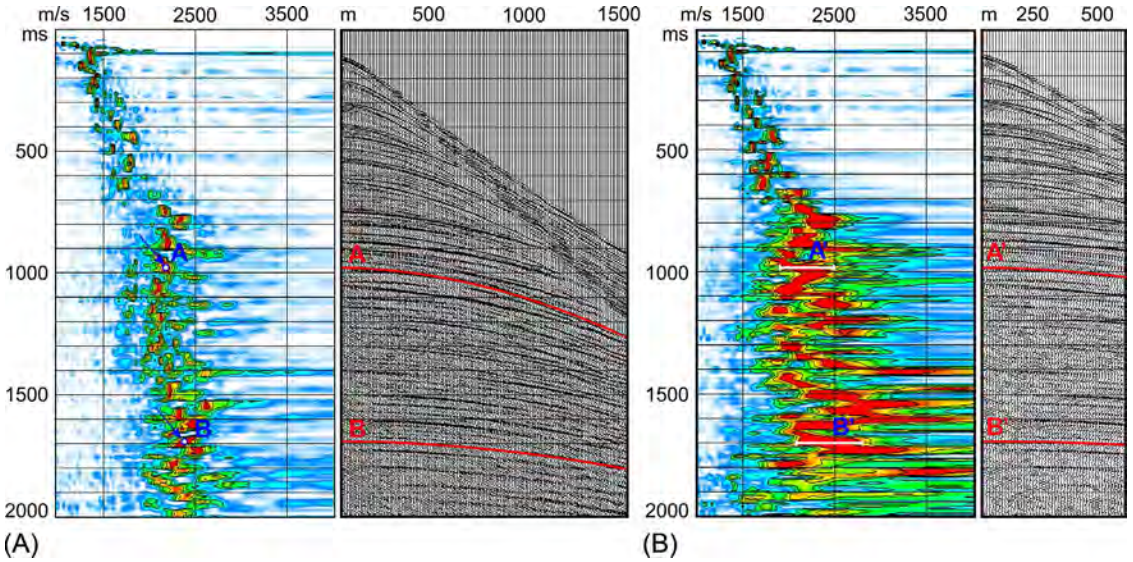


FIG. 9.16 A comparison of the semblance plots of two marine supergathers with (A) longer (1500 m length), and (B) shorter (600 m length) streamer cables. Considering two reflections indicated by *A* and *B* in (A) and their counterparts *A′* and *B′* in (B), a precise reflection velocity for *A* and *B* can be derived whereas only a range of velocity values can be estimated for *A′* and *B′* using short offset data from the areas indicated by *white horizontal bars on the semblance plot in (B)*.

9.3.4 Effect of Fold Number

Increasing the fold number of a specified CDP gather simply results in extra traces involved in the semblance calculation, and therefore increases the quality of semblance plots. Fig. 9.17 shows two semblance plots calculated from two synthetic CDP gathers (parameters of the synthetic data are given in Fig. 9.10) with different fold numbers. A 20% random noise is also included in the synthetic data to demonstrate the effect of fold on the semblance plots in the case of random noise. Fig. 9.17A and B show the semblance plots calculated from a 120-fold CDP with a 12.5-m trace interval and a 30-fold CDP with a 50-m trace interval, respectively. The semblance plot of the higher fold data in Fig. 9.17A is of higher quality, with no degradation due to the random noise. The semblance plot quality, however, is poor for the lower fold data in Fig. 9.17B which has artificial enclosures, especially in the shallow parts, arising from the noise amplitudes. Fig. 9.18 shows the effect of fold number on the quality of semblance plots on a real marine supergather. Although the major enclosures on the semblance plots are preserved, several artificial enclosures appear as the fold number decreases. This situation may become an issue when picking the velocities at the deeper parts of the semblance plots of low-fold seismic data, where the amplitudes of the primary reflections are relatively weak.

9.3.5 Effect of Multiple Reflections

One of the most important agents that complicate the semblance plots, even making the precise velocity picking quite difficult in relatively deeper parts of the data, is the existence of multiple reflections. In general, reflections from the seabed as well as shallow subsurface reflectors repeat themselves, which sometimes makes it impossible to discriminate primary reflections underneath the multiple reflections.

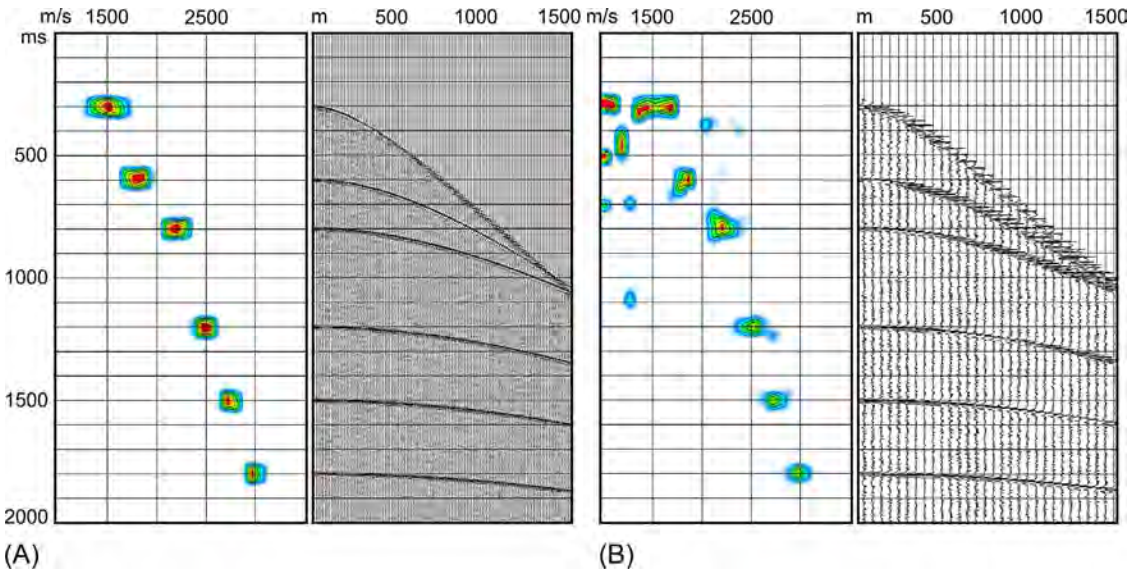


FIG. 9.17 Two semblance plots calculated from two synthetic CDP gathers with different folds including a 20% random noise. Semblance plots from (A) 120-fold CDP with a 12.5-m trace interval, and (B) 30-fold CDP with a 50-m trace interval.

The effect of multiples on semblance plots is quite dramatic: the enclosures of primary reflections on the semblance plots generally indicate a velocity trend increasing with depth until the multiple amplitudes arrive. After that, the enclosures representing the multiple amplitudes become rather distinct on the semblance plots, producing concordant velocity trends almost parallel to each other for every multiple bounce (Fig. 9.19). In such cases, the processors must be careful to pick velocities of only primary reflections.

Particularly in shallow continental shelves, seismic data may contain several orders of multiple reflections, which makes the semblance plots rather complex. For instance, there are five bounces of multiples visible on the CDP gather in Fig. 9.20. The enclosures from the amplitudes of these multiples are so dominant on the semblance plot that the enclosures corresponding to the primary reflections are restricted only between 300 and 600 ms zero-offset time. The rest of the enclosures in the semblance plot completely represent the amplitudes of the multiples. Applying a suitable demultiple method may significantly improve the quality of the semblance plots (Fig. 7.25).

9.3.6 Effect of Time Gate

Velocity spectra are calculated over theoretical trial reflection hyperbolas computed using a series of constant velocities. The semblance values are obtained from the amplitudes on the recorded CDP within a time gate along this theoretical curve (Fig. 9.9). The time length of the gate influences the quality of the resultant semblance plot. If it is selected too short, it increases the computational time of the semblance plot, whereas the resolution along the time axis decreases when it is too large.

Fig. 9.21 shows semblance plots calculated using different time gate lengths. As the gate length increases, semblance enclosures become

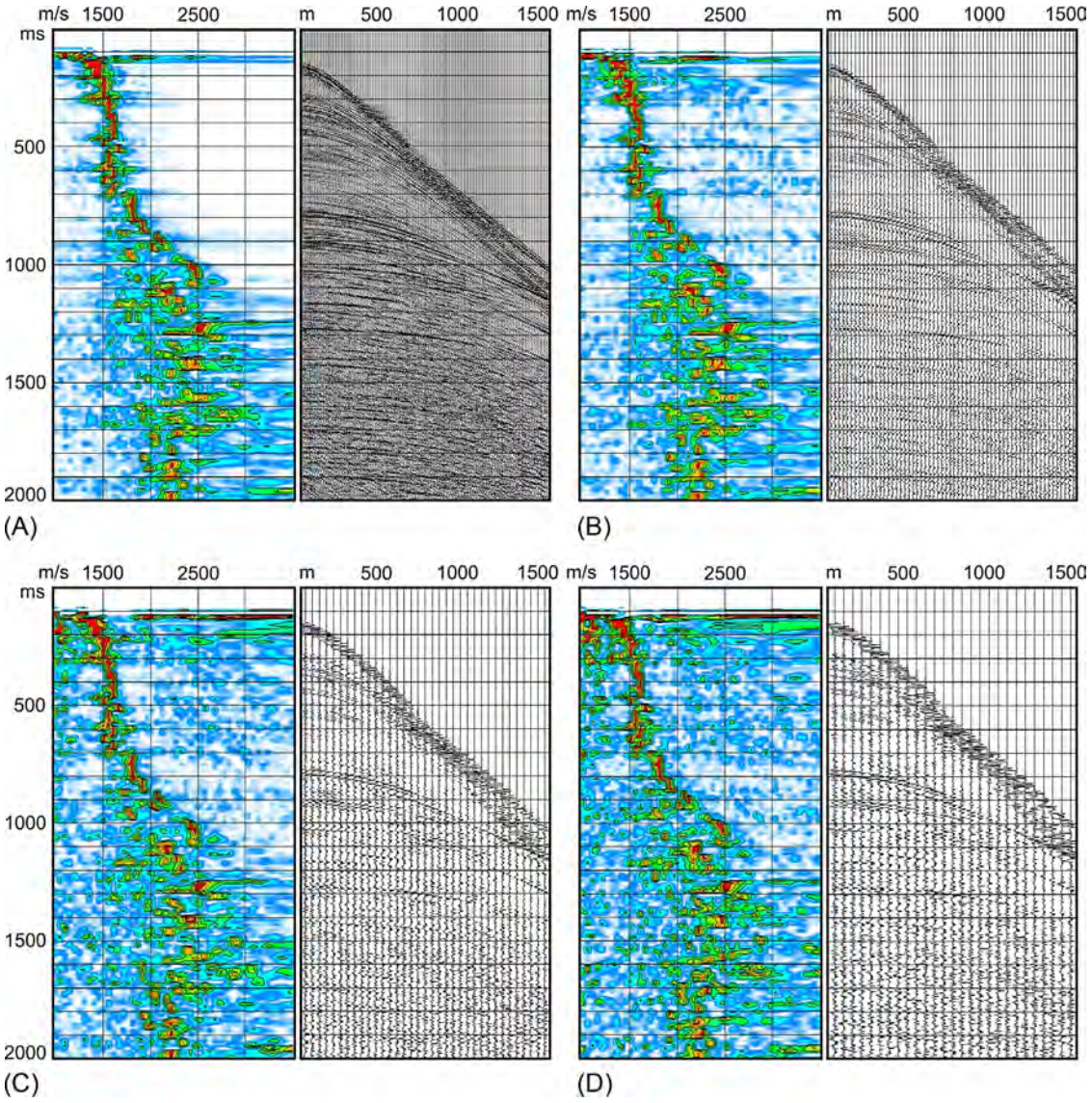


FIG. 9.18 Effect of fold number on the semblance plots on a real marine supergather. Semblance plots calculated from (A) 126-, (B) 60-, (C) 40-, and (D) 27-fold CDPs.

smoother and smoother, and the details are lost. For the example semblances in Fig. 9.21, a time gate of 30 ms seems to be suitable. In practice, the time length of the gate must be determined as close as the dominant period of the input dataset (generally 10–40 ms) to include all the absolute amplitudes of a full cycle of the seismic wavelet. During selection, it must be taken into consideration that the dominant period is time dependent, that is, it is small for early arrivals but large for deep reflections, because of the absorption effects.

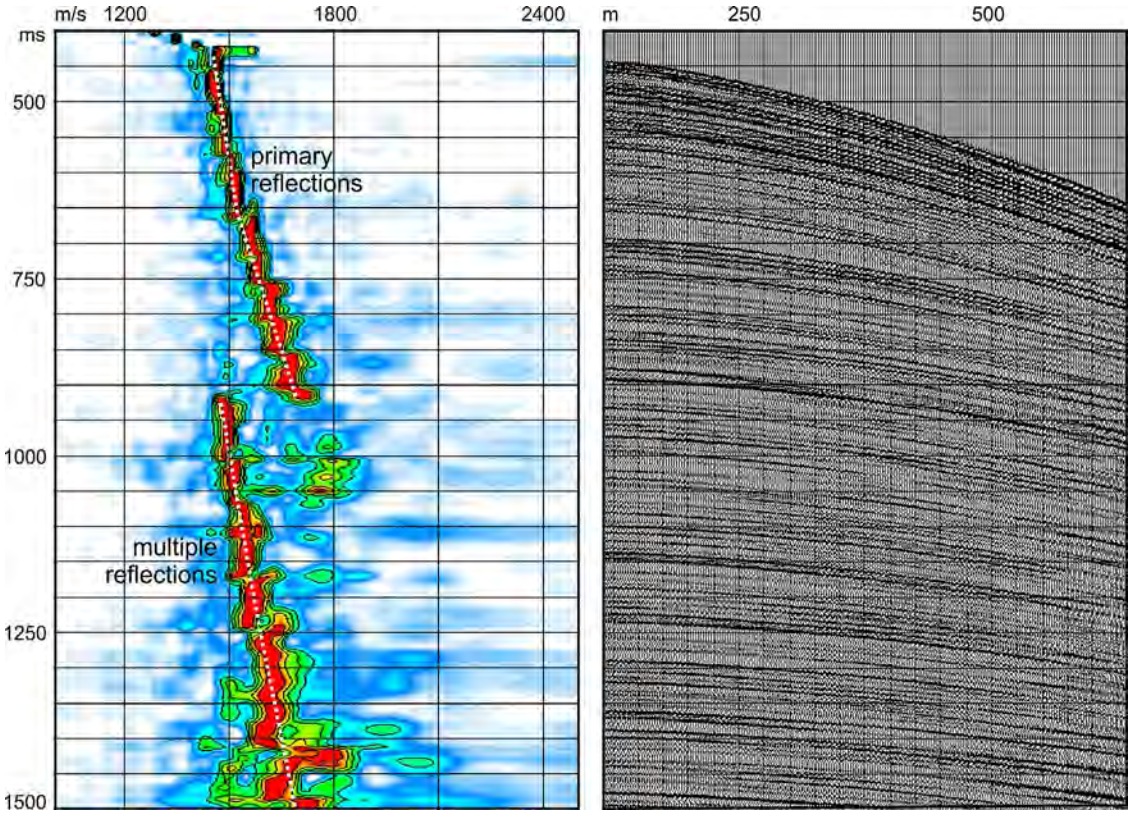


FIG. 9.19 Semblance plot (left) consisting of primary (between 450 and 900 ms) and multiple (between 900 and 1500 ms) reflection enclosures, and its corresponding supergather (right).

9.3.7 Effect of Velocity Increment

Semblance calculations are done within a minimum and maximum velocity range, and these limits must cover the velocity range expected for the survey area. Velocity increment represents the number of theoretical reflection hyperbolas, each calculated for a different velocity value within this velocity range. For instance, if the semblance velocity limits are 1000 and 6000 m/s, and if 100 different hyperbolas are used in semblance calculations within this velocity range, then this means that a 50 m/s velocity increment is used from 1000 to 6000 m/s range.

Fig. 9.22 shows semblance plots calculated using different velocity increments. If the increment is too large, the semblance enclosures become more and more smooth and the details are lost, resulting in a loss of resolution due to the sparse velocity sampling. If a too-small increment is selected, the total computational time of the semblance plot significantly increases. For the example analysis in Fig. 9.22, a velocity increment of 50–75 m/s is suitable.

9.3.8 Effect of Semblance Sample Rate

Theoretical trial reflection hyperbolas with different constant velocities are computed for the whole time axis, that is, several theoretical hyperbolas are calculated for a range of velocity

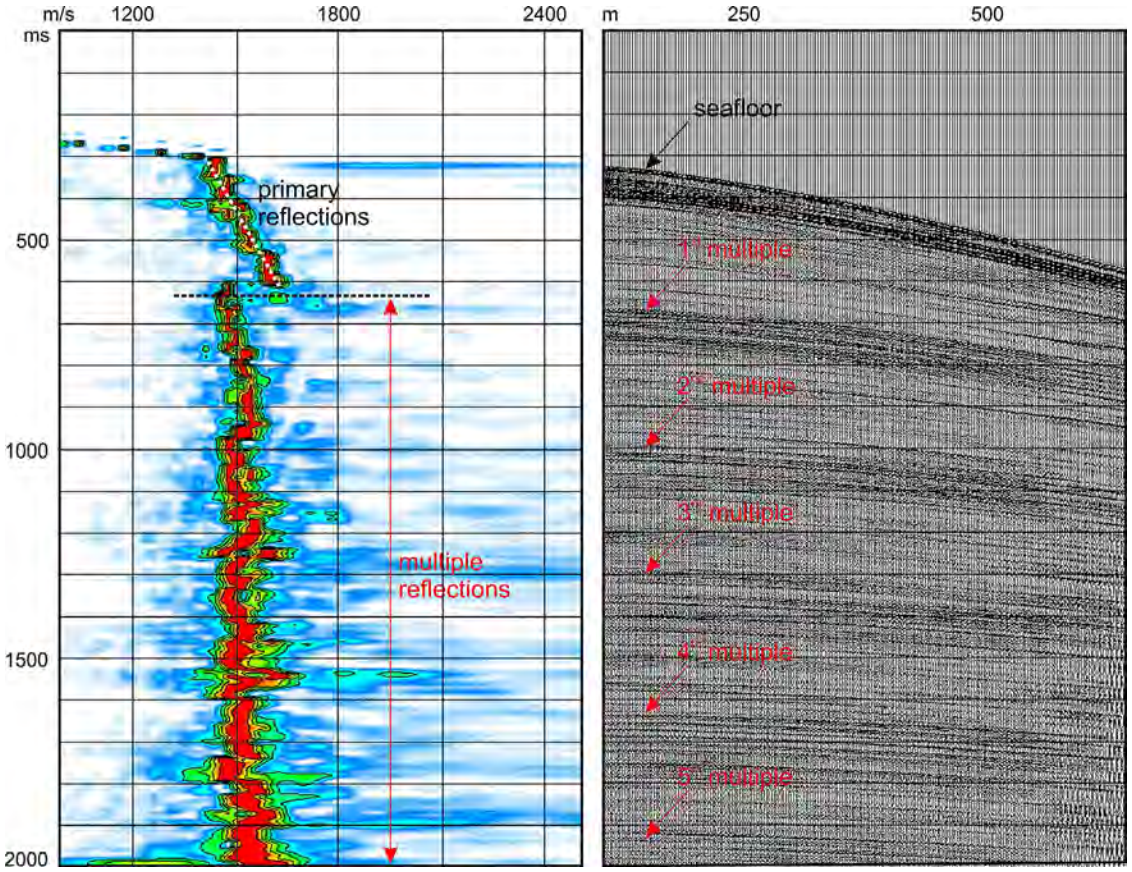


FIG. 9.20 An example semblance plot (left) consisting of primary reflection enclosures only between 300 and 600 ms, and its corresponding supergather (right). The enclosures between 600 and 2000 ms on the semblance completely represent the amplitudes of multiples, which completely prevents the picking of primary reflection velocities.

values along the zero-offset time axis. In practice, it is not necessary to calculate these trial hyperbolas for every single zero-offset time sample. The semblance sample rate stands for how densely these theoretical hyperbolas are computed along the time axis. For instance, calculations are done for every 50 ms in the schematic representation in Fig. 9.7.

Fig. 9.23 shows semblance plots calculated using different semblance sample rates. If the increment is too large, the semblance enclosures become more and more smooth, and the details are lost, resulting in a loss of resolution, especially at the deeper parts due to the sparse time sampling of the semblance. If a too-small semblance sample rate is selected, the computational time of the semblance plot increases. For the example analysis in Fig. 9.23, a semblance sample rate of 20 ms is suitable.

9.3.9 Effect of Noise

Semblance is calculated from the amplitudes in the input CDP. Even if the amplitudes of the genuine reflections are of primary importance on the accuracy of the semblance plot, any kind

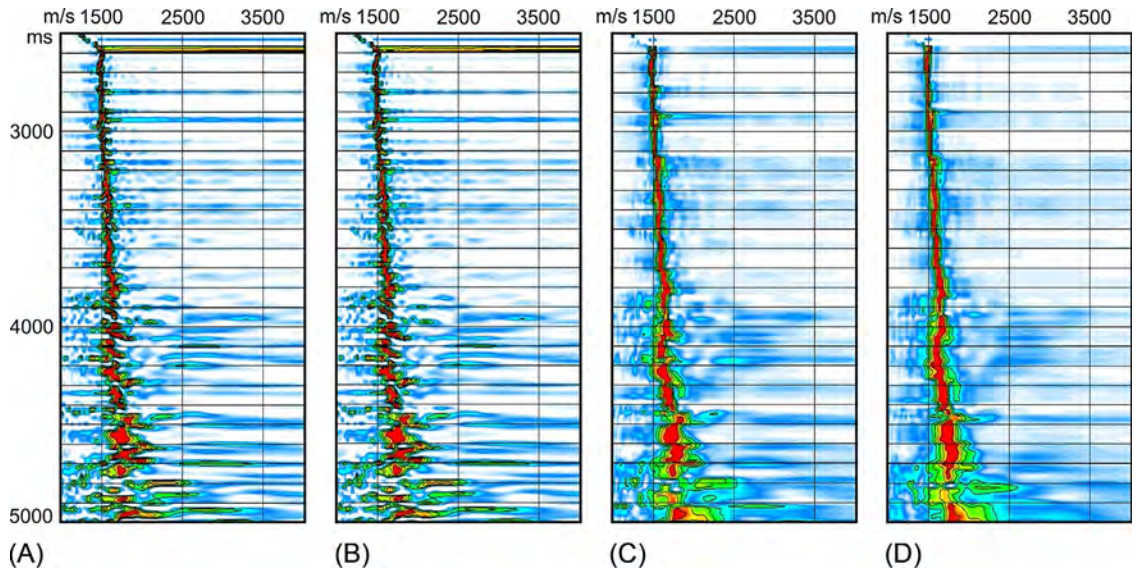


FIG. 9.21 Semblance plots calculated by using different time gate lengths of (A) 10, (B) 30, (C) 50, and (D) 80 ms. For large gate lengths, the details of semblance enclosures are lost.

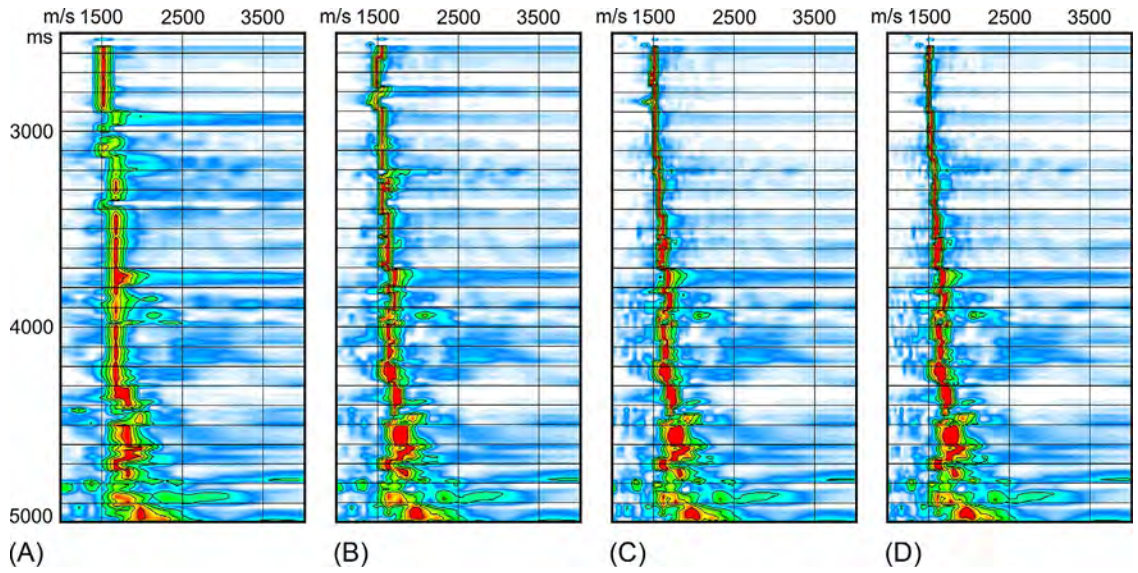


FIG. 9.22 Semblance plots calculated within 1000 to 4000 m/s minimum and maximum velocity limits with the increments of (A) 150, (B) 75, (C) 50, and (D) 30 m/s. For large velocity increments, the details of semblance enclosures are lost.

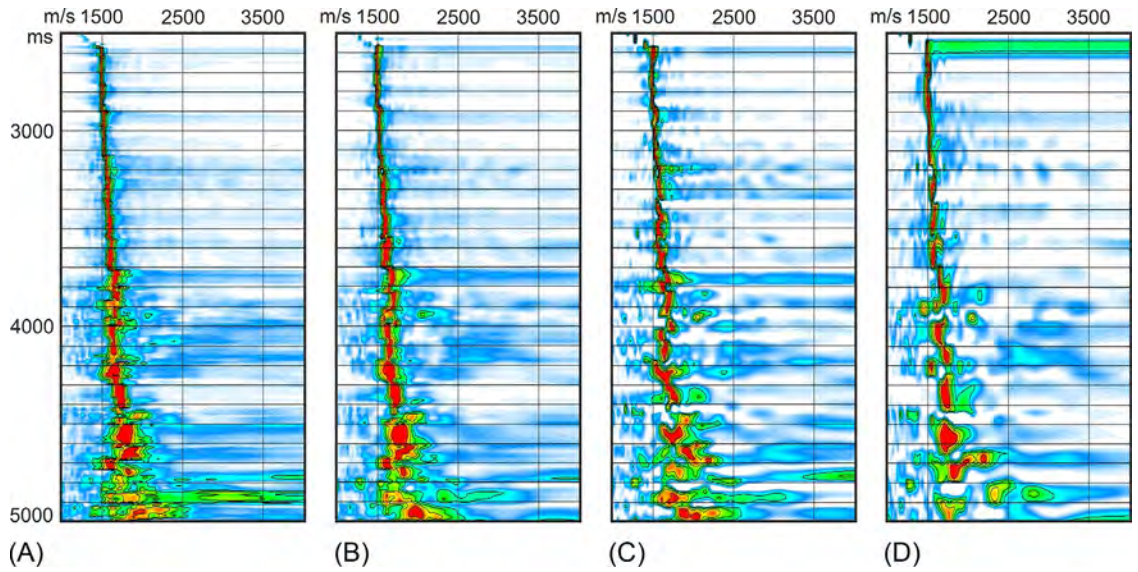


FIG. 9.23 Semblance plots calculated for different semblance sample rates of (A) 10, (B) 20, (C) 40, and (D) 60 ms. For large sample rates, the details of semblance enclosures are lost.

of amplitudes, including coherent and incoherent noise, are also involved in the calculation. Semblance is sensitive to the noise in the input data and the quality of semblance plots is affected by the amount of noise embedded in the data. Therefore, it is strongly recommended that the data be suitably preconditioned by applying necessary noise suppression techniques before the velocity analysis.

The effect of noise on the quality of semblance plots is analyzed both on synthetic and real CDPs. Fig. 9.24 shows four semblance plots of a synthetic CDP gather with different random noise levels ranging from 0% to 30% with respect to the maximum reflection amplitude. As the noise increases, the shape of the enclosures degrades and the semblance amplitudes decrease, especially for deeper reflections. Similar implications can be deduced for the semblance plots of real seismic data. A certain amount of random noise is incorporated in the supergather as a function of mean amplitude of the input data in Fig. 9.25A. As the noise ratio increases, the resolution of the semblance plot significantly decreases, especially for deeper parts, and the amplitudes of the enclosures gradually die. Furthermore, several artificial enclosures randomly distributed throughout the whole semblance plot arise with increasing noise, which degrades the enclosures of primary reflections and prevents the precise picking of the accurate velocity values.

9.3.10 Effect of Muting

As depicted in the previous section, semblance plots are sensitive to the noise in the data, which creates false enclosures. Noise in the water column such as direct wave and refractions as well as random noise recorded before the seafloor reflection also produces artificial high amplitudes and enclosures on the semblance plots. This is particularly important for shallow water data, since these false enclosures may prevent picking the correct velocity of shallow reflections. Fig. 9.26 compares two

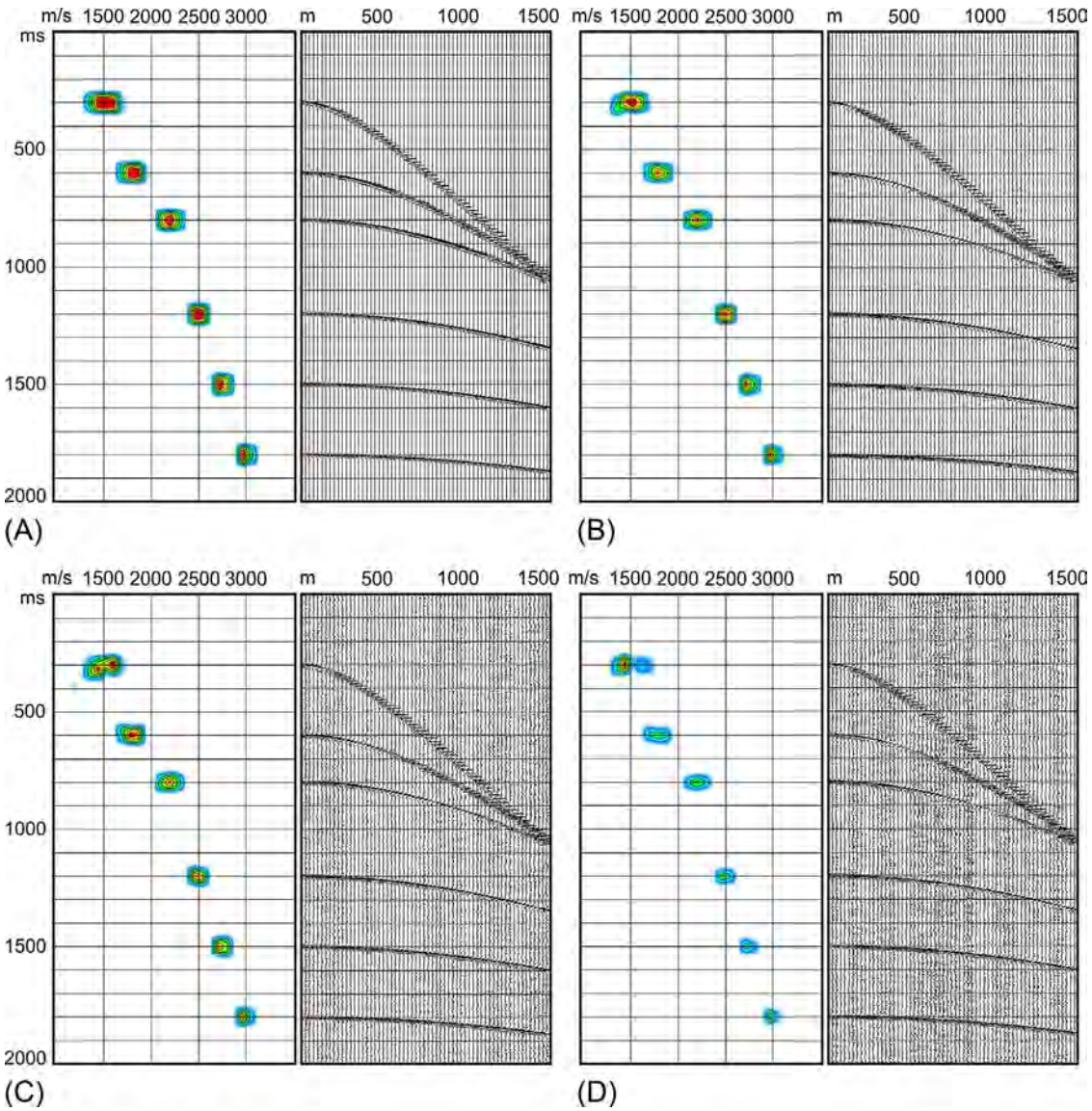


FIG. 9.24 Semblance plots calculated from a synthetic CDP gather with different random noise levels of (A) 0%, (B) 10%, (C) 20%, and (D) 30% with respect to the maximum reflection amplitude in the synthetic data. Increasing noise results in degradation of enclosures, especially for deeper reflections.

semblance plots of a synthetic CDP gather with and without top mute. A direct arrival and 20% random noise is included in the synthetic data. Several artificial enclosures just above the seafloor reflection appear in the semblance plot, which may ultimately complicate the picking of the velocity of the seabed and shallow subsurface reflections. This situation causes much more drastic results in the real supergather example in Fig. 9.27. The negative effect of

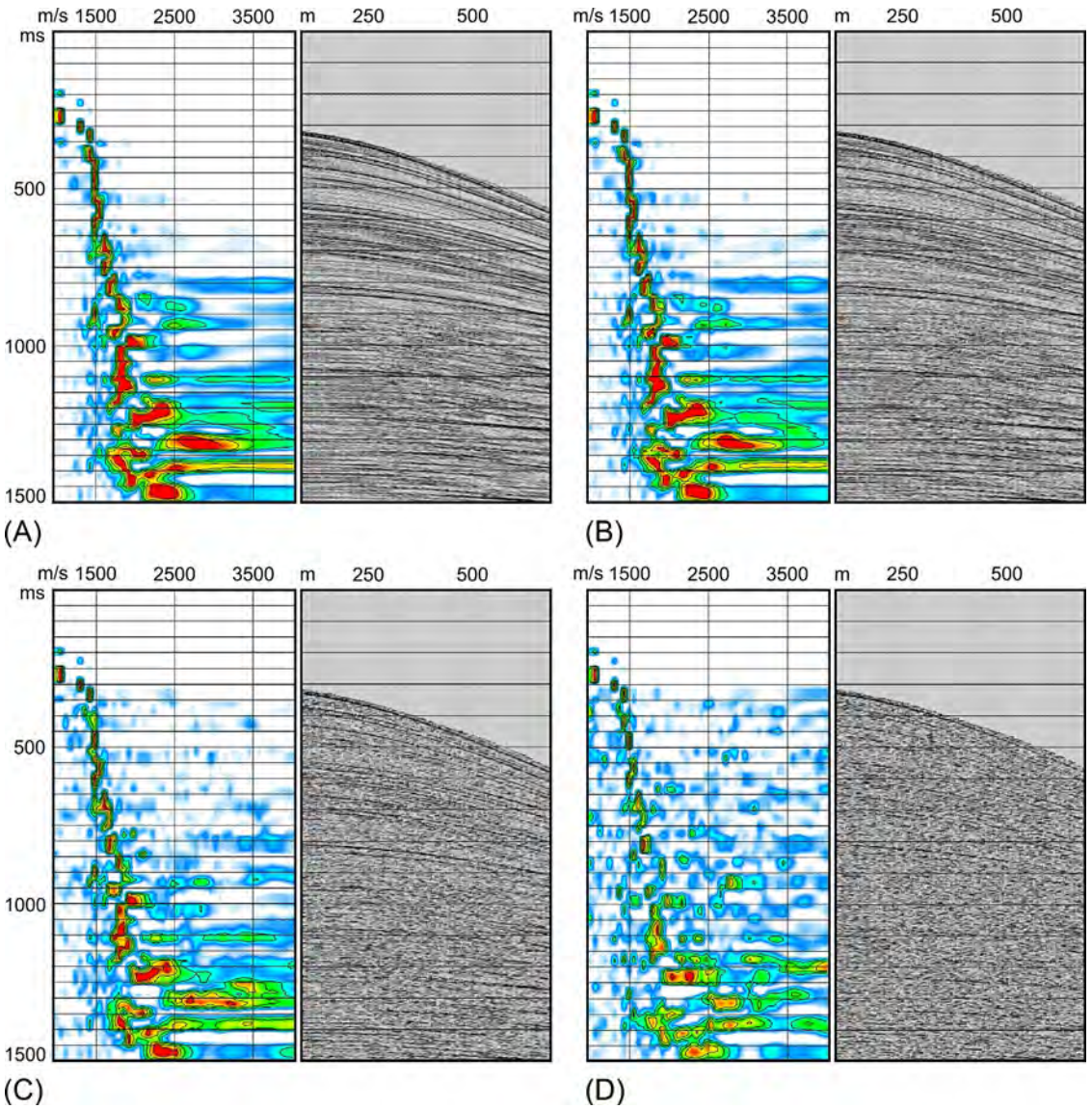


FIG. 9.25 Semblance plots calculated from a real supergather with different random noise levels added with respect to the mean reflection amplitude in the supergather: (A) 0%, (B) 20%, (C) 40%, and (D) 60% random noise. Increasing the noise ratio results in the degradation of enclosures in the semblance plots, especially for deeper reflections.

coherent and random noise in the water column may become more and more prominent as the seafloor shallows.

In addition, the theoretical hyperbolas used to compute semblance plots are incomplete for late arrivals at the end of the zero-offset time axis. This is obvious at panel F in Fig. 9.7, where the semblances can be computed using the amplitudes only for small portions of near offsets of the theoretical reflection hyperbolas. This situation may produce false enclosures at the end of the semblance plots.

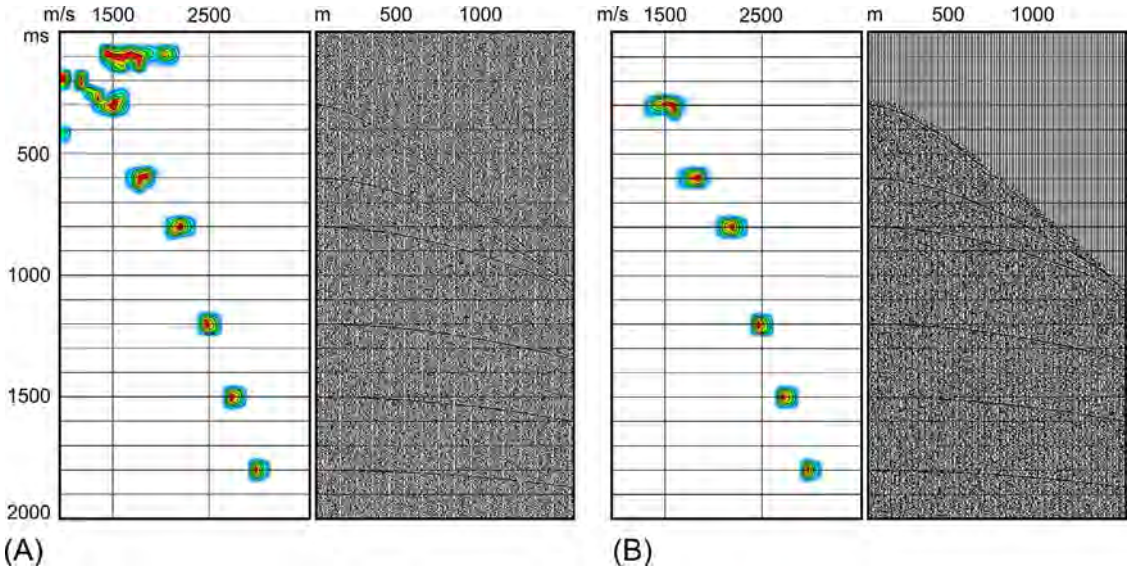


FIG. 9.26 A comparison of two semblance plots of a synthetic CDP gather (A) without and (B) with top mute. A direct wave and 20% random noise is included in the synthetic data to demonstrate the effect of top mute.

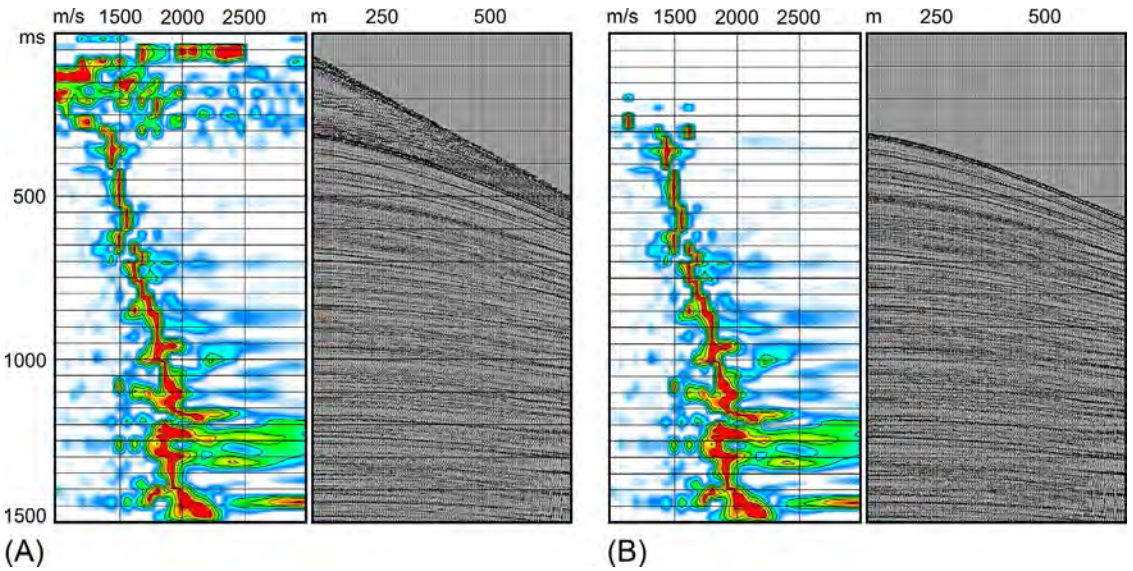


FIG. 9.27 A comparison of two semblance plots of a real marine supergather (A) without and (B) with top mute.

9.4 QC IN VELOCITY ANALYSIS

The important points that must be considered during the computation of semblance plots have been explained so far. In this section, some of the substantial issues that may occur during the picking of velocity functions on the semblance plots and their QC analyses are explained. Although not a certain rule, the velocity generally increases with depth (or with the zero-offset time) mainly because of the compaction due to the increasing overburden pressure. Therefore, the enclosures on the semblance plots generally indicate an increasing velocity trend with the depth, and a velocity function that ensures the general trend of the enclosures must be preferred. In general, if the geology is not complex, the proper velocity value of a reflection hyperbola coincides with approximately the central point of an enclosure occurring at the same zero-offset time of that specific reflection.

Modern seismic processing software systems allow us to incorporate different velocity determination approaches at the same time during velocity picking, which provides a more accurate picking of the velocity. For instance, constant velocity stack panels for different predetermined velocity functions can be displayed along with the semblance plot of a supergather, and a picked velocity value can be double-checked if it corresponds to an enclosure on the semblance plot and a high-amplitude stack stripe on a constant velocity stack panel simultaneously. Furthermore, a real-time NMO correction may be applied to the supergather using the picked velocity value to ensure that the primary reflection hyperbolas are perfectly flattened after NMO correction.

The locations of supergathers both in 2D and 3D surveys must be carefully selected based on the shapes and locations of geological structures. On 2D lines, velocity analysis locations can be selected on brute stack sections regarding the structural trend of the seafloor morphology as well as the target geological structures, that is, from the oil industry approach, the prospect. A denser distribution of supergather locations along a 2D line must be selected over the target structure. For instance, there are two regional highs on the 2D seismic line in Fig. 9.28A. It is recommended that denser analysis locations over these structures be considered as compared to the rest of the seismic line, so that the velocity structure of these highs can suitably be represented in the final 2D velocity field.

A similar approach must also be considered for complex seafloor morphology such that, if a regional or morphological trend exists in the seismic data, it almost always requires a denser velocity picking to obtain a correct 2D velocity distribution. In 3D surveys, the analysis locations must also be selected by regarding the 3D structural perspective of the subsurface geology. Fig. 9.28B shows the structural map of a regional anticline. A much denser 3D velocity grid around this anticline, as in Fig. 9.28C, may result in a better representation of the velocity distribution of this structure in the final 3D velocity cube.

During velocity picking, it is crucial to avoid the picking velocities of multiples from the enclosures appearing at relatively lower velocity values on the semblance plots. In some cases, the amplitudes of the multiples are so high that they produce their own enclosures on the semblance plots, which almost completely mask the enclosures of primary reflections (Figs. 9.19 and 9.20). If selected, the amplitudes of the multiples on the stack data become more prominent, since the efficiency of the stacking on the suppression of multiples is bypassed, which strongly depends on the hyperbolic moveout behavior of the multiple reflections after NMO correction.

During velocity picking, it is recommended to take advantage of the real-time NMO correction option for quality control purposes. Fig. 9.29

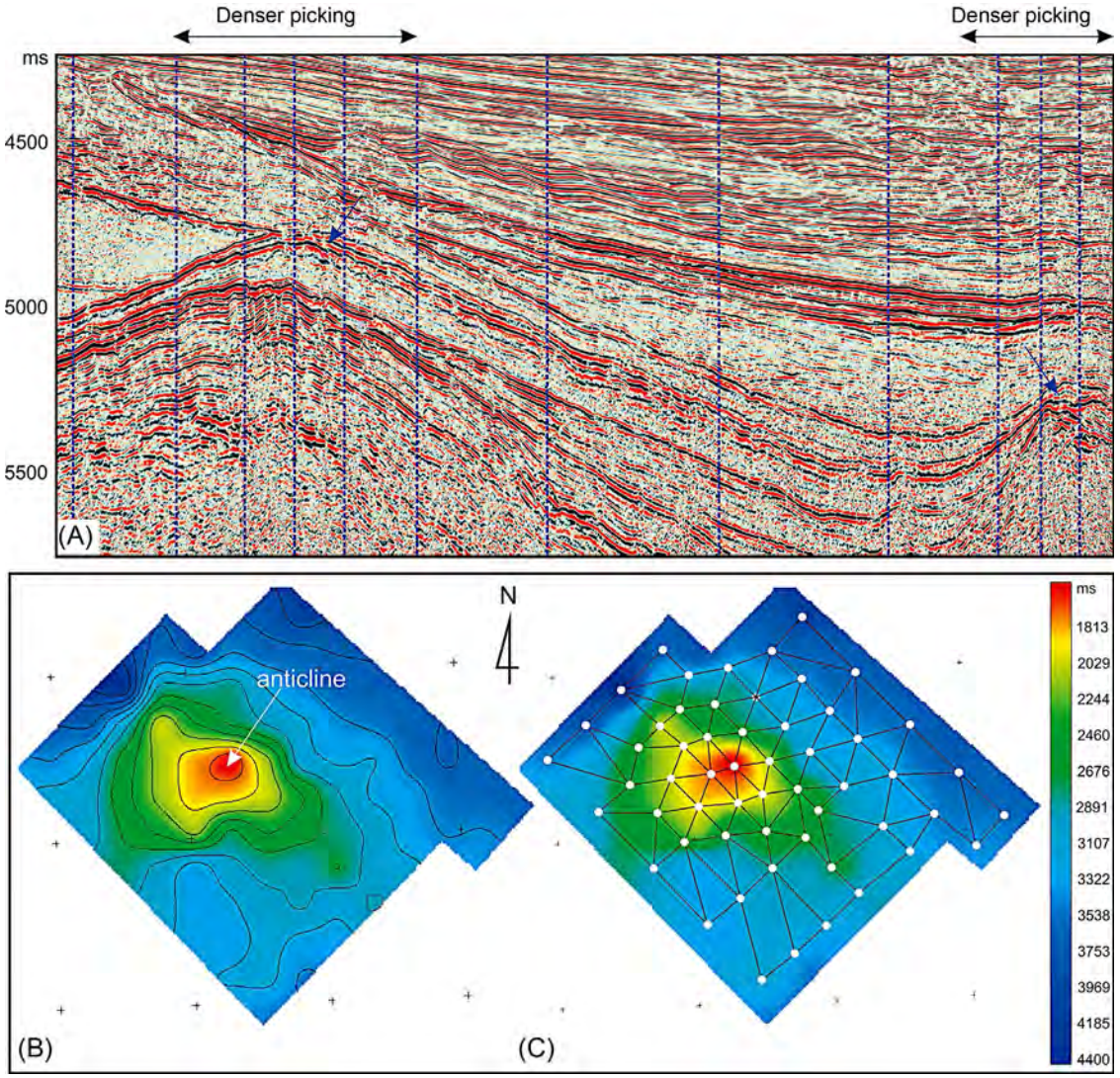


FIG. 9.28 Suitable selection of supergather locations based on the target structures in 2D and 3D cases. (A) Two regional highs *(blue arrows)* on a 2D seismic line require a denser distribution of velocity analysis locations *(blue dashed lines)* in the vicinity. (B) Structural map of a regional anticline from a 3D survey, and (C) 3D supergather locations *(white dots)* and velocity interpolation grid among these locations *(solid lines)*. A denser 2D and 3D velocity grid around these target structures will provide a better representation of their velocity structure in the final 2D and 3D velocity fields.

shows these two cases during picking with an NMO correction option: reflections of primaries are flattened while the multiples are undercorrected (e.g., they are still hyperbolic, Fig. 9.29A) when primary reflection enclosures are picked, and vice versa for the multiple reflections in which the primaries are overcorrected after NMO correction (Fig. 9.29B). This is particularly important in shallow water surveys where the primary and multiple reflections are

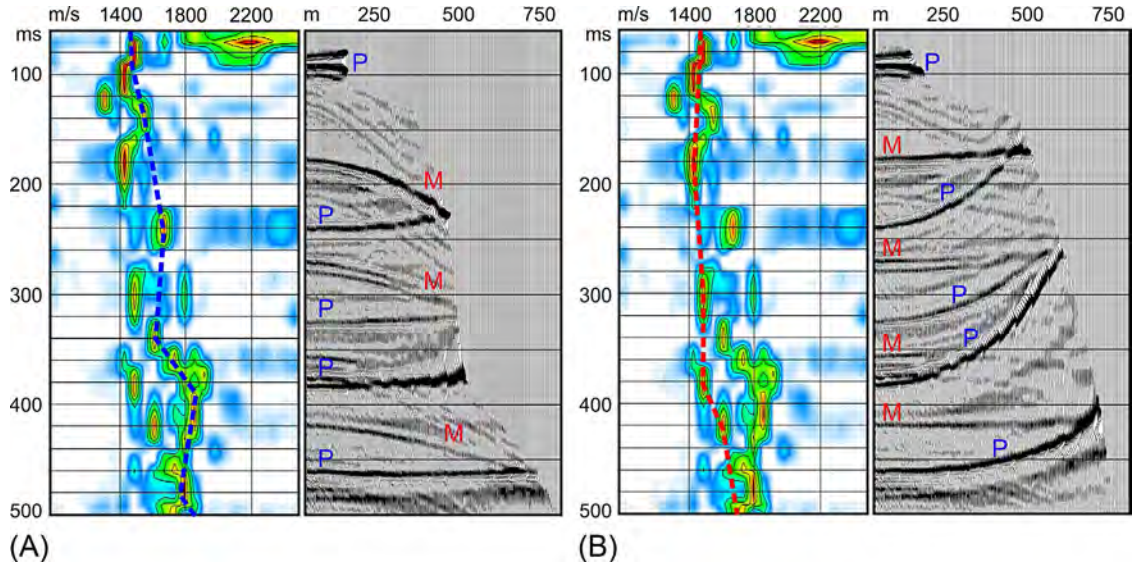


FIG. 9.29 Utilizing NMO correction during velocity picking to discriminate the primary and multiple velocities, especially in shallow water areas. (A) If the primary reflection velocities are picked (e.g., velocity function of *dashed blue line*), primaries (*P*) are completely flattened after NMO correction while the multiples (*M*) are still hyperbolic and undercorrected. (B) If velocities of multiples are picked (e.g., velocity function of *dashed red line*), then the multiples are flattened whereas the primaries are overcorrected.

not easy to discriminate, since they may strongly interfere. In shallow parts of the supergathers, even small variations in the picked velocities result in erratic changes on the flattening of the events, and therefore the processors must be extra careful when picking the velocities in shallow areas where primaries and multiples interfere.

In a complete seismic processing, generally more than one velocity analysis is necessary. After sorting the data into CDP gathers, a first-pass velocity analysis is applied. Then, this velocity field is used in multiple suppression since some of the multiple removal methods require 2D or 3D velocity field to be known, such as a Radon velocity filter. After removing the multiples, it is expected that the semblance plots will be greatly improved, and therefore a second-pass velocity analysis is applied to obtain a more appropriate velocity field. Furthermore, a third-pass velocity analysis may be applied after the dip moveout (DMO) process, which removes multiple enclosures appearing at the same zero-offset times in the semblance plots by solving the conflicting dip issues on the seismic data (Section 11.10).

The same RMS velocity field, or interval velocity field derived from RMS velocities using the Dix equation, is also used to migrate the seismic data. Some of the migration algorithms are quite sensitive to lateral velocity variations and may produce artifacts in different shapes and sizes if there are issues or erratic lateral variations in the derived velocity field. Fig. 9.30 shows an example velocity issue on a migrated section. There are two apparent normal faults on the migration section in Fig. 9.30A forming a small-scale graben, which occurs due to a gap in the RMS velocity field (Fig. 9.30B) because of an incorrectly picked velocity function at the location of the graben. Fig. 9.30C shows a migrated section obtained by the correct 2D

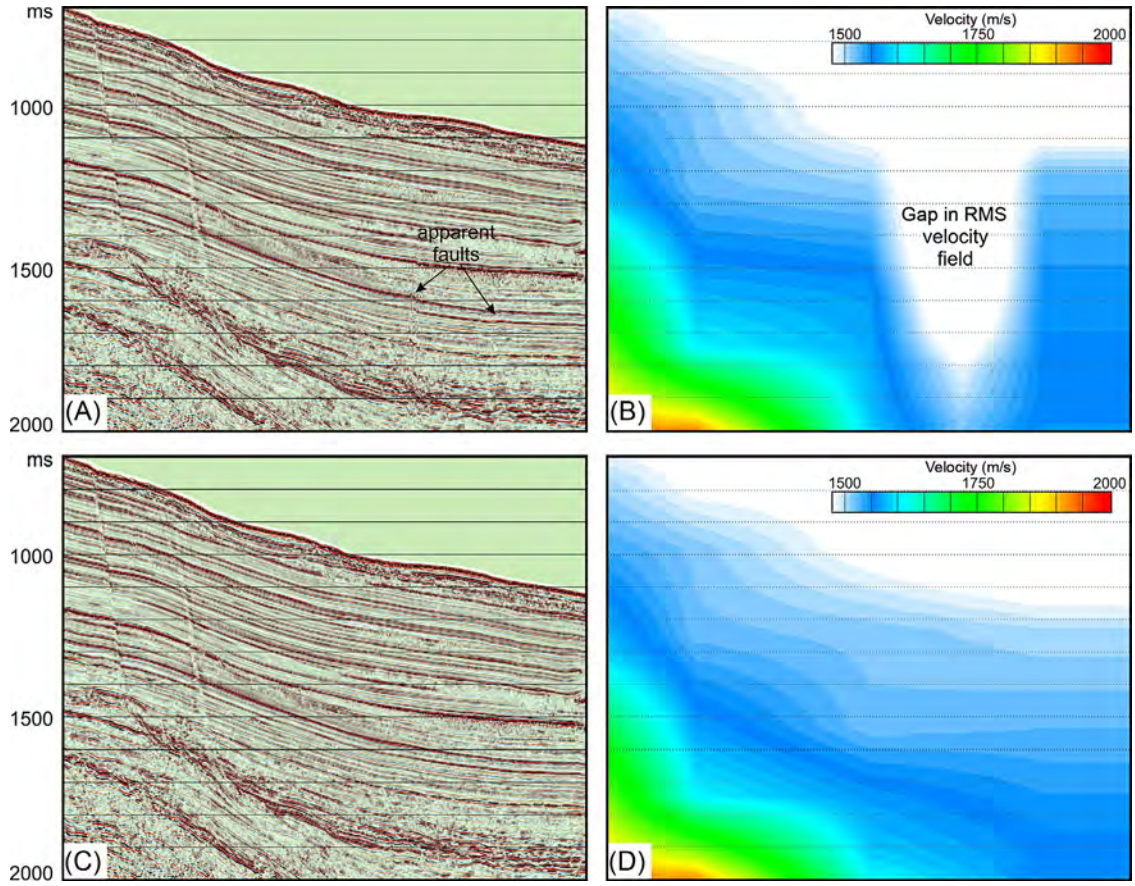


FIG. 9.30 An example of migration artifact due to a velocity picking issue. (A) A migration section with two apparent normal faults because of an incorrectly picked velocity function, resulting in a slow zone in the RMS velocity field in (B). (C) Migrated section using a correct 2D velocity field in (D).

velocity field in Fig. 9.30D for the migration process. In general, incorrectly slow velocities cause apparent fault type artifacts, whereas improperly fast velocities result in upward concave "smiles" after migration.

To overcome velocity issues, a 2D or 3D final RMS velocity field is displayed to analyze if there are problematic velocity functions because of incorrect velocity picking during the QC analyses (Fig. 9.31A). Inaccurate functions are either deleted or corrected (Fig. 9.31B) regarding the neighboring functions, to prevent improper stacking after an unfavorable NMO correction. Most of the migration algorithms are sensitive to lateral velocity variations, and rapid variations in the velocity in the space dimension produce artifacts in the migration output. Therefore, it is generally recommended to smooth over the corrected velocity field, especially along the space dimension (Fig. 9.31C), to use as an input to the migration process. However, it must be taken into consideration that the velocities required for stacking and migration are basically different: stacking velocities are dependent on the dip of the reflecting interface, while the migration velocities are not. After the DMO process, these two types of velocities become identical (Section 11.10).

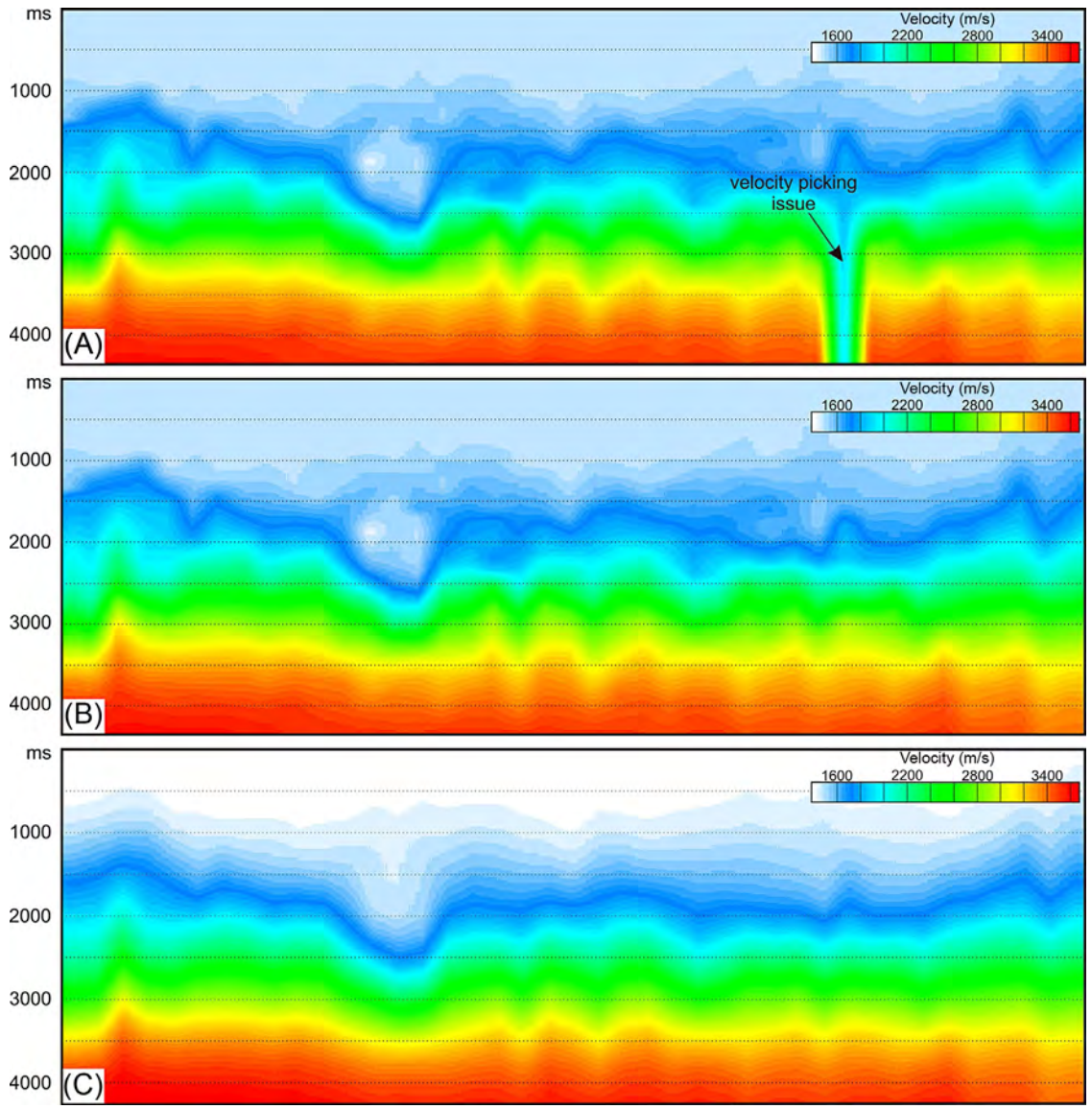


FIG. 9.31 (A) An RMS velocity field with a problematic velocity function. (B) Incorrect functions are either deleted or corrected after analyzing the resultant velocity field. (C) A smooth version of the RMS velocity field is sometimes used as an input to the migration process, since rapid lateral velocity variations may produce artifacts in the migration output.

CHAPTER

10

Normal Moveout Correction and Stacking

OUTLINE

10.1 Normal Moveout Time 461
- *10.1.1* NMO Time for Single Horizontal Interface 462
- *10.1.2* NMO Time for Several Horizontal Interfaces 463
- *10.1.3* NMO Time for Dipping Interfaces 465
- *10.1.4* NMO Corrections for Long Offsets 465
- *10.1.5* NMO Velocity in Azimuthally Anisotropic Medium 467

10.2 NMO Stretching 469

10.3 Stacking 472

10.4 Specific Stacking Methods 475
- *10.4.1* Partial Stack 475
- *10.4.2* Median Stack 477
- *10.4.3* Trimmed Stack 480
- *10.4.4* Common Reflection Surface Stack 481

10.5 QC in NMO Correction and Stacking 486

In a shot or common depth point (CDP) gather, reflection signals arrive earlier at the receivers close to the source point (near offsets) than the reflections recorded at distal locations (far offsets). The time difference between the arrival time of a reflection at a specified offset and the zero-offset time of that reflection is defined as the normal moveout (NMO) time of that reflection event. The NMO time varies for each receiver for a particular reflection hyperbola, and equals the difference of arrival time $t(x)$ at offset x for a specific reflection and zero-offset arrival time $t(0)$. NMO correction removes the normal moveout times of each reflection hyperbola on every CDP gather, using the root-mean-square (RMS) velocities obtained from velocity analysis. After NMO correction, all primary reflection hyperbolas in the CDPs are expected to be flattened so that all reflection events are repositioned at their zero-offset

© 2018 Elsevier Inc. All rights reserved.

arrival time, providing a correct velocity field is used. Fig. 10.1 shows example CDP gathers before and after NMO correction, and the velocity function used. Practically, NMO correction is a process that removes the offset distance between source and receivers so that all the reflection arrivals are reduced to $t(0)$ vertical two-way zero-offset time on a CDP gather. Fig. 10.2 shows the geometrical sense of the correction both on ray paths and on a synthetic CDP gather.

The success of the NMO correction in flattening of a primary reflection depends on a number of factors, including the accuracy of the velocity used, anisotropic effects of the subsurface, spread length, structural dip of the reflector, nonhyperbolic reflections, existence of some specific noise types such as side effects, strong multiples, etc. Fig. 10.3 shows the effect of NMO velocity on the flattening of a reflection hyperbola on a synthetic CDP gather. After a successful NMO correction, all of the primary reflection hyperbolas on the CDP gathers along the whole seismic line must be perfectly flattened (Fig. 10.3B), providing an isotropic subsurface composed of horizontal layers. If we use a slower velocity, reflection hyperbola is overcorrected (Fig. 10.3C) whereas it is undercorrected if a faster NMO velocity is used (Fig. 10.3D). The most suitable velocity is the one that flattens the primary reflection hyperbolas after NMO correction, which equals the true velocity of the upperlying medium for a single horizontal reflector case.

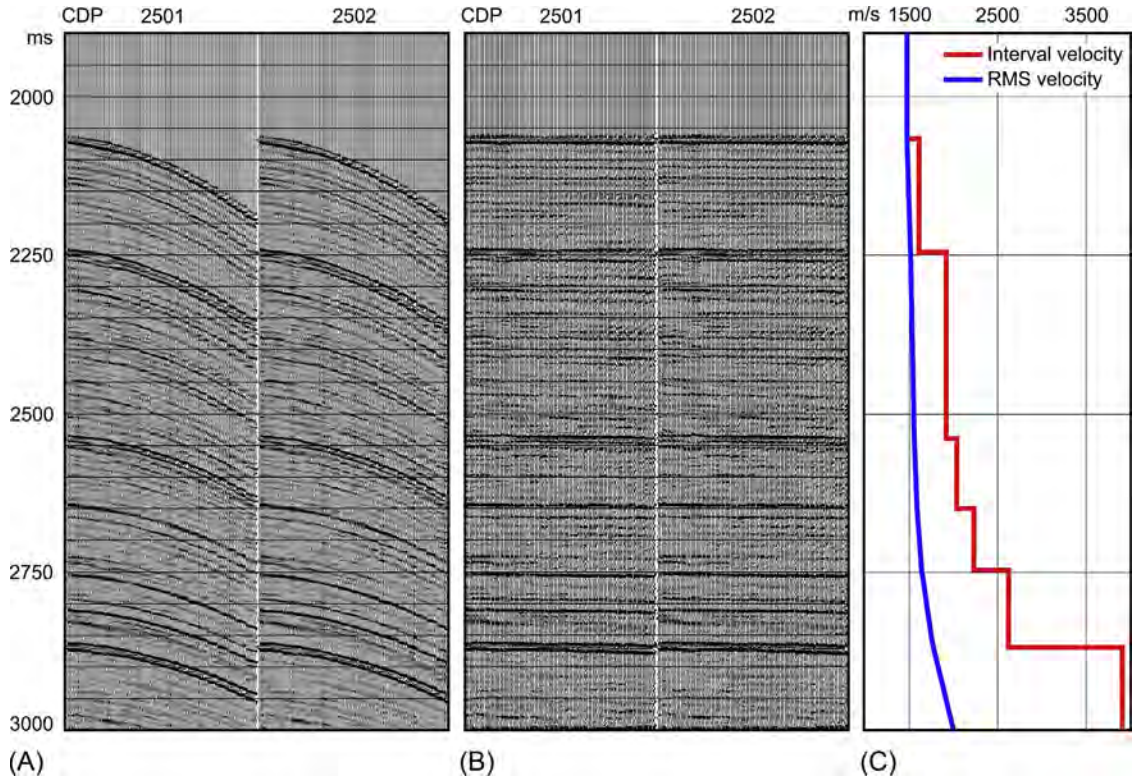


FIG. 10.1 Two successive CDP gathers (A) before, and (B) after NMO correction. (C) RMS velocity function *(blue line)* used for NMO correction as well as interval velocity function *(red line)* calculated from the Dix equation (Eq. 9.9).

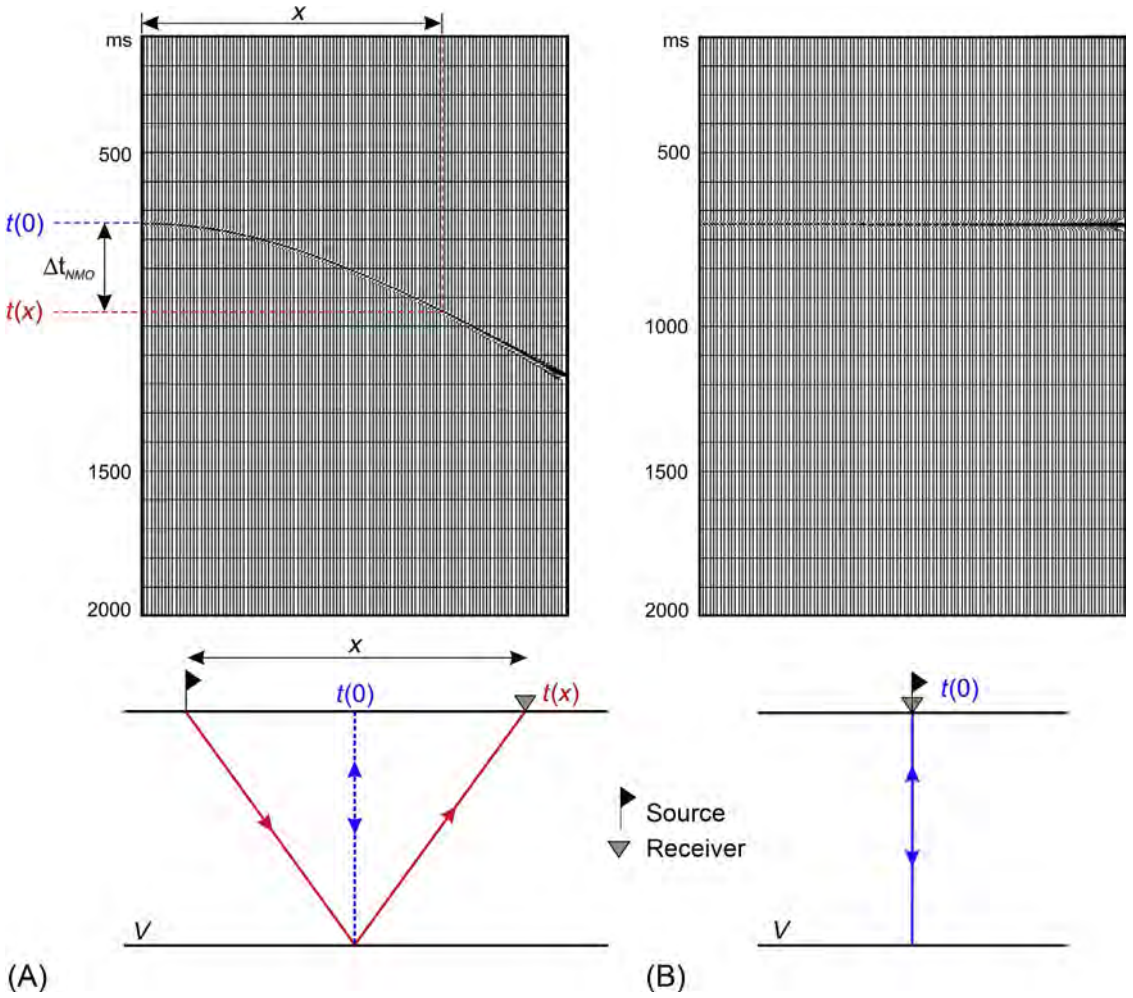


FIG. 10.2 (A) A synthetic CDP gather with a reflection hyperbola obtained from a single horizontal layer model, and (B) its NMO corrected version (upper panel). The ray paths for a reflection recorded at offset x before and after NMO correction are given in the lower panel. NMO correction removes the offset distances between the source and receivers and reduces all the arrival times to their corresponding zero-offset time $t(0)$.

Following the NMO correction, all of the traces within a CDP gather are summed up to produce a single stacked trace, and the process is known as stacking. In this section, mathematical approaches to the expressions of NMO correction are depicted, and the effects of different agents on the process as well as different stacking techniques are discussed.

10.1 NORMAL MOVEOUT TIME

Several expressions have been developed to achieve the mathematical expression of normal moveout times of the reflections for earth models consisting of horizontally stratified or dipping layers. These expressions and their constraints can be found in Castle (1994). Here,

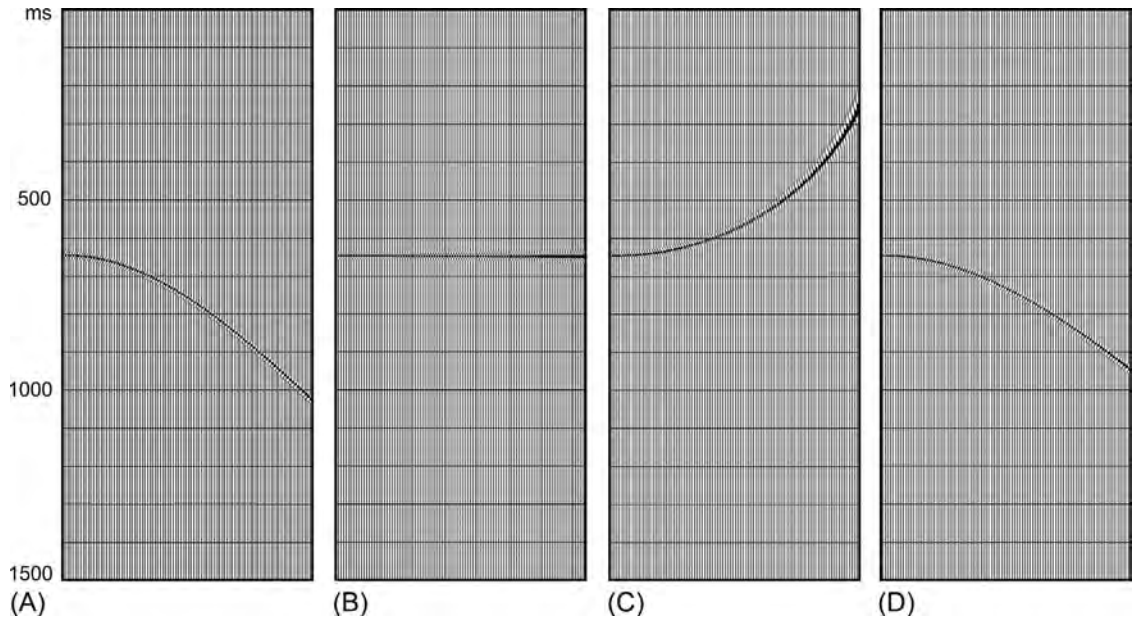


FIG. 10.3 Effect of velocity on the NMO correction during the flattening of a reflection event. (A) A synthetic CDP with a reflection hyperbola obtained from a single horizontal layer model, and its NMO corrected versions for (B) suitable, (C) slower, and (D) faster NMO velocities. The hyperbola is overcorrected for slower velocities, while it is undercorrected for faster velocities.

simple NMO approaches for single horizontal layer, several horizontal layers, dipping interface, and azimuthally anisotropic medium cases are introduced. Among these, the simple horizontal layer model, with a long offset correction option whenever required, is still commonly used in the seismic processing industry.

10.1.1 NMO Time for Single Horizontal Interface

The travel time equation for a single horizontal reflector case is given by

$$t^2(x) = t^2(0) + \frac{x^2}{V^2} \tag{10.1}$$

where $t(x)$ is the travel time from source to reflecting interface and back to the receiver located at offset x, $t(0)$ is the zero-offset time (or two-way vertical travel time) of the reflection event, and V is the NMO velocity, which equals RMS velocity in the case of a small-spread approximation (Dix, 1955). Eq. (10.1) is also known as the two-term NMO equation, and indicates a hyperbola symmetrical about the time axis. In marine seismics, only half of this hyperbola along the positive x axis can be recorded due to the acquisition geometry. Fig. 10.4 schematically compares the result of Eq. (10.1) with a real recorded reflection hyperbola, which indicates that the NMO equation of Dix (1955) is only valid for small offsets (between O and A) and deviates from the observed arrival times at far offsets (between A and B).

Using Eq. (10.1), the NMO correction time for an arrival $t(x)$ at an offset x over a single horizontal reflector model is given by

$$\begin{aligned}\Delta t_{NMO} &= t(x) - t(0) \\ &= t(0)\left\{\left[1 + \left(\frac{x}{V_{NMO}t(0)}\right)^2\right]^{1/2} - 1\right\}\end{aligned} \tag{10.2}$$

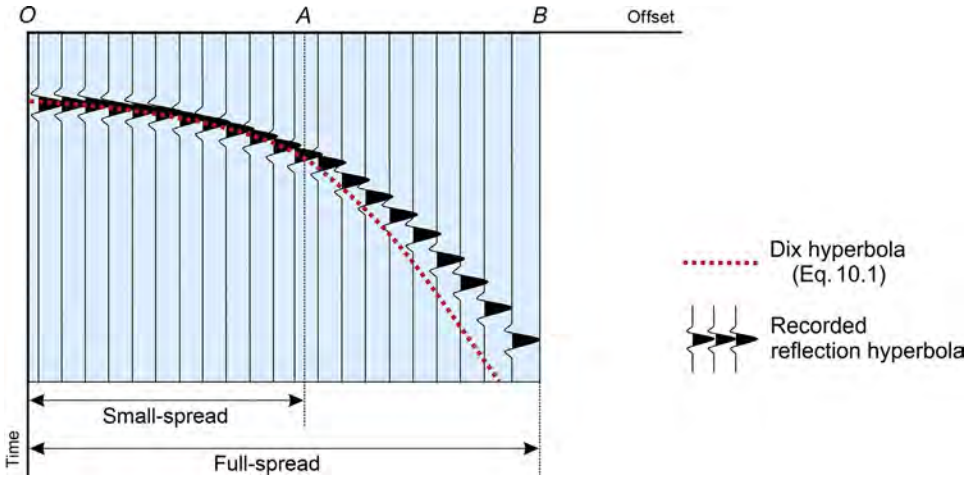


FIG. 10.4 Schematic comparison of the Dix NMO equation given by Eq. (10.1) with a real observed reflection hyperbola for a single horizontal interface model. The Dix equation is valid for small offsets (e.g., between offsets O and A) and is inaccurate for far offsets (e.g., between offsets A and B).

In practice, NMO correction using Eq. (10.2) is accomplished in the following fashion: for a given $t(0)$, x and V_{NMO} parameters, the time $t(x)$ is calculated, since V_{NMO} (in fact, V_{RMS} for small spreads) is known from velocity analysis. The seismic amplitude value at time $t(x)$ is then moved to the zero-offset time $t(0)$ at its offset distance x. For every time sample on every trace of a particular CDP gather of the seismic line, Δt_{NMO} is calculated from Eq. (10.2) and subtracted from the arrival time of that time sample to obtain NMO corrected CDP gathers.

NMO time given by Eq. (10.2) decreases as the NMO velocity increases. This decrease is much more drastic for far offsets. Therefore, NMO is known as dynamic correction, in which the amplitude samples of a specified trace are shifted to earlier times with a different number of time samples depending on their offset distances and NMO velocities. This situation results in an artificial increase of the seismic wavelength for larger offsets, especially in early arrivals. Fig. 10.5A and B show this phenomenon. For near offsets, the time shift after NMO correction is relatively small as compared to that for far offset traces. The NMO time for the reflection hyperbola on the CDPs increases with offset, and decreases with depth (or with zero-offset time and/or velocity). Fig. 10.5C shows this variation with the velocity and offset of a reflection for a constant zero offset time of $t(0) = 1.0$ s. Increasing NMO time with increasing offset, especially for early arrivals, results in a specific distortion in the NMO corrected gather, known as NMO stretching (Section 10.2). Due to the NMO stretch effect, the period of the reflected signal t_A increases to t_B after NMO correction, which is much more prominent for far offset traces (Fig. 10.5A and B).

10.1.2 NMO Time for Several Horizontal Interfaces

A complete travel time equation for the horizontally stratified earth model is given by Taner and Koehler (1969) as

$$t^2(x) = c_1 + c_2x^2 + c_3x^4 + c_4x^6 + \cdots\cdots \qquad (10.3)$$

where c_i coefficients are defined as

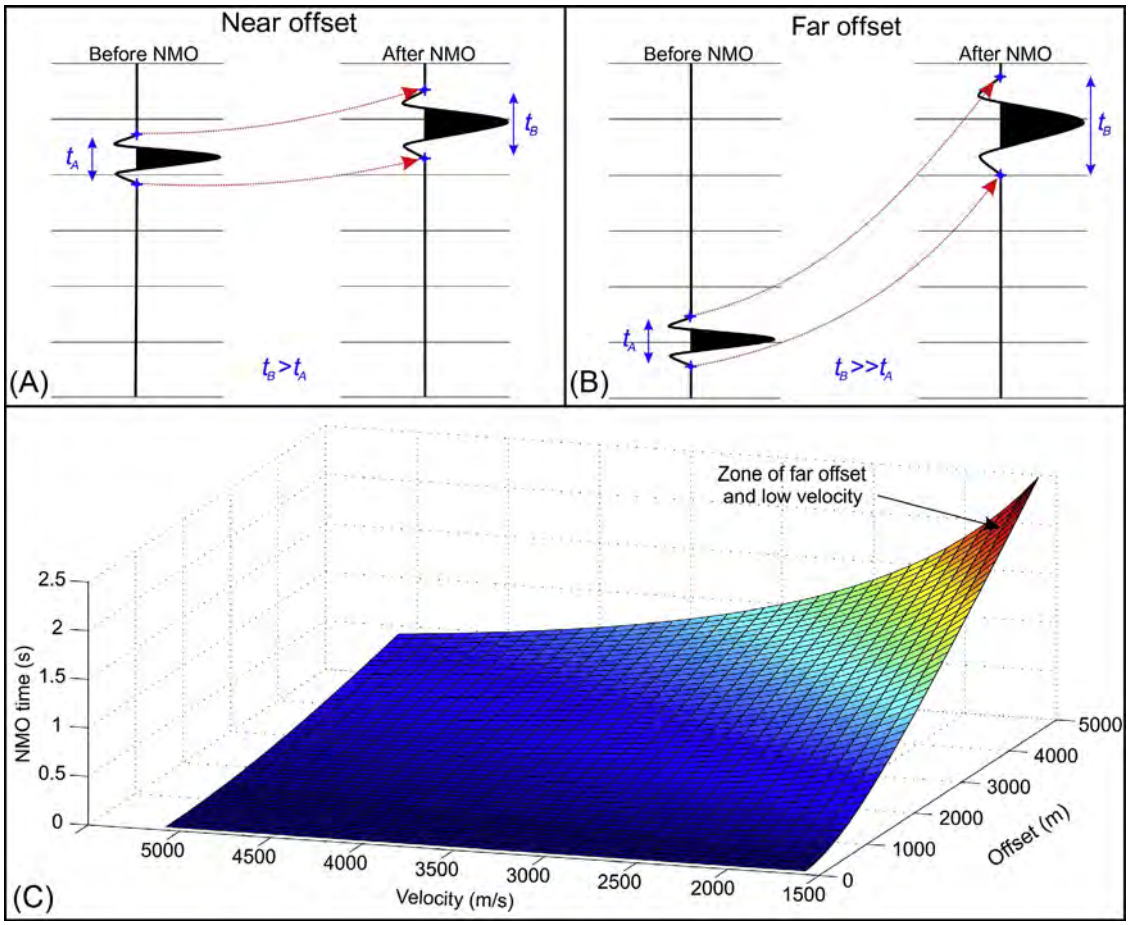


FIG. 10.5 Schematic illustration of relative time shift after NMO correction for (A) near offset, and (B) far offset traces. (C) Variation of NMO time with velocity and offset for a specific reflection at $t(0) = 1.0$ s zero-offset time calculated by Eq. (10.2).

$$
\begin{aligned}
c_1 &= t^2(0) \\
c_2 &= \frac{1}{V_{RMS}^2} \\
c_3 &= \frac{1}{4}\frac{V_{RMS}^4 - \mu_4}{t^2(0)V_{RMS}^8} \\
c_4 &= \frac{2\mu_4^2 - V_{RMS}^2\mu_6 - V_{RMS}^4\mu_4}{t^4(0)V_{RMS}^{14}}
\end{aligned}
\tag{10.4}
$$

Here, the term μ_i is given by

$$
\mu_i = \frac{\sum_{k=1}^{N} V_k^i \Delta t_k(0)}{\sum_{k=1}^{N} \Delta t_k(0)} \tag{10.5}
$$

where $\Delta t_k(0)$ is the vertical two-way time through the kth layer. Higher order c_i coefficients

are quite complicated functions of time $t(0)$ and RMS velocity. Taner and Koehler (1969) give the first five c_i coefficients, and suggest a recursion relation to calculate the higher-order terms. However, if the spread length is small enough compared to the reflector depth, by omitting the higher-order terms, the travel time equation then becomes

$$t^2(x) = t^2(0) + \frac{x^2}{V_{RMS}^2} \tag{10.6}$$

According to Eq. (10.6), the velocity for NMO correction in a horizontally stratified earth model is the RMS velocity, providing that the spread is sufficiently small as compared to the reflector depth. This assumption is of key importance in the velocity analysis today, and it enables us to use the RMS velocity obtained from velocity analysis of the seismic data in NMO correction.

10.1.3 NMO Time for Dipping Interfaces

In the case of a dipping reflector, common depth point gathers do not equal common midpoint (CMP) gathers, due to the CDP smearing effect (Fig. 8.5). Travel time expression for a single dipping layer model is given by the Levin equation (Levin, 1971)

$$t^2(x) = t^2(0) + \frac{x^2 \cos^2\phi}{V^2} \tag{10.7}$$

where ϕ is the inclination angle of the interface and V is the velocity of the upperlying medium. Eq. (10.7) also represents a hyperbola equation for primary reflections; however, the NMO velocity in the Levin equation depends on the inclination of the reflecting interface, given by

$$V_{NMO} = \frac{V}{\cos\phi} \tag{10.8}$$

Perfect flattening of a dipping event after NMO correction requires a velocity that is faster than the actual velocity of the medium above the reflector, which indicates that a horizontal layer with a higher velocity may produce the same reflection hyperbola as the reflection from a dipping layer with a lower velocity. The dip moveout (DMO) process is generally applied to the data to overcome this effect, which makes the velocities independent of reflector dips. V_{NMO} in Eq. (10.8) depends on the relative direction of the survey profile with respect to the dip direction of the planar reflector.

Following the classical paper of Levin (1971), Yılmaz (2001) gives the 3D equivalent of Eq. (10.7) as

$$t^2(x) = t^2(0) + \frac{4h^2\left(1 - \sin^2\phi\cos^2\theta\right)}{V^2} \tag{10.9}$$

and Eq. (10.8) can be rewritten by means of inclination angle ϕ, and the azimuth between dip and profile directions θ, as

$$\frac{V_{NMO}}{V} = \frac{1}{\sqrt{1 - \sin^2\phi\cos^2\theta}} \tag{10.10}$$

For the profiles in the strike direction, the ratio of NMO velocity to true velocity of the medium, V_{NMO}/V, equals to 1. If the inclination does not exceed 15 degrees, V_{NMO}/V ratio is close to 1 for all azimuthal directions. For higher inclinations, on the other hand, the ratio deviates from 1 considerably, and for 40-degree inclination, for instance, the difference is around 50% for a profile in the dip direction (Levin, 1971).

10.1.4 NMO Corrections for Long Offsets

The industry standard NMO equation of Dix (1955) in Eq. (10.1) is valid for small spreads only, and it deviates from real observed reflection hyperbolas as the offset increases. For long offset data, a proper correction can be applied to flatten the events that are overcorrected by the

two-term NMO equation in Eq. (10.1). This correction may be particularly effective if the reflections can only be flattened to an offset approximately equal to the reflector depth. There are a number of long offset correction methods, all of which incorporate a third term in the standard two-term NMO equation, which depends on the higher powers of velocity and offset to the fourth power, and hence they are also known as fourth-order corrections. The most common long offset correction approaches are Al-Chalabi's third-term approach (Al-Chalabi, 1973) and Castle's shifted hyperbola (Castle, 1994).

Al-Chalabi's third-term approach simply includes a third term given in Eq. (10.4) into Eq. (10.1) and it is the most efficient long offset correction method. Castle's shifted hyperbola also provides a better approach to the observed reflection hyperbolas than the two-term approximation, and it is given by

$$t(x)=t(0)\left[1-\frac{1}{S(x)}\right]+\sqrt{\left(\frac{t(0)}{S(x)}\right)^2+\frac{x^2}{S(x)V_{RMS}^2}} \tag{10.11}$$

$$S(x)=\frac{\mu_4}{V_{RMS}^4} \tag{10.12}$$

where term μ_4 can be calculated by Eq. (10.5). Fig. 10.6 schematically compares the result of the shifted hyperbola in Eq. (10.11) with a real recorded reflection hyperbola. Although the shifted hyperbola NMO equation shows a better fit to the observed hyperbola than the NMO equation of Dix (1955), it is also a small-spread approximation like the two-term NMO equation. However, the small-spread zone defined by *O-A* in Fig. 10.6 is improved by Castle's shifted hyperbola equation as compared to the one for the two-term approximation in Fig. 10.4.

Fig. 10.7 compares two long offset correction methods on a marine CDP gather. Hyperbolas in the dashed rectangle in Fig. 10.7A are overcorrected at their far offsets by the two-term NMO equation. These overcorrected parts of the hyperbolas are better flattened after long offset corrections of Al-Chalabi's third-term (Fig. 10.7B) and Castle's shifted hyperbola (Fig. 10.7C) approaches. The analysis in Fig. 10.7 also indicates that Al-Chalabi's long offset correction produces better results.

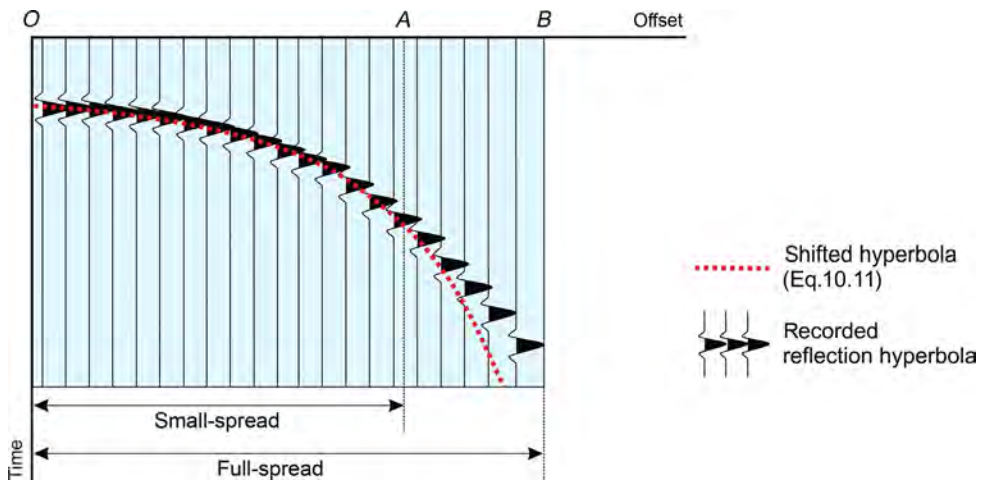


FIG. 10.6 Schematic comparison of Castle's shifted hyperbola approximation given by Eq. (10.11) with a real observed reflection hyperbola for a single horizontal layer model. It is also a small-spread approximation like the two-term NMO equation, but the small-spread zone defined by *O-A* is improved.

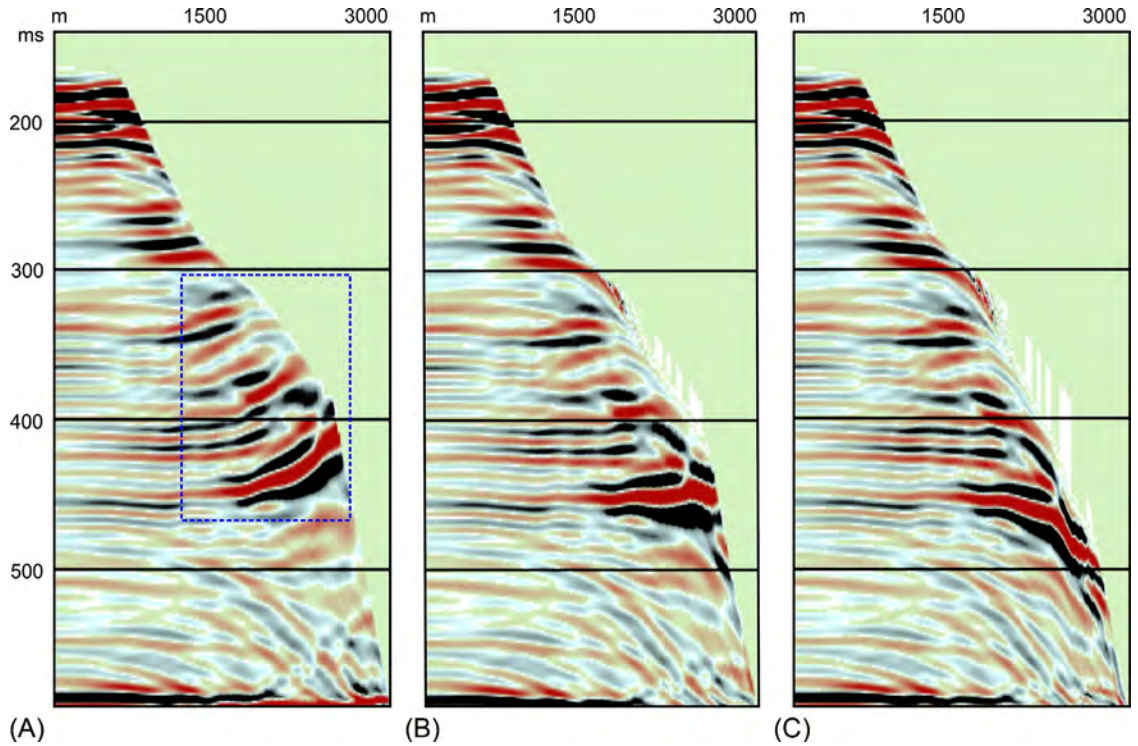


FIG. 10.7 An example NMO corrected CDP gather for long offset correction. (A) Two-term NMO equation (no long offset correction), (B) Al-Chalabi's third-term approach, and (C) Castle's shifted hyperbola. Overcorrected hyperbolas by the two-term equation in the dashed rectangle in (A) are flattened in (B) and (C).

10.1.5 NMO Velocity in Azimuthally Anisotropic Medium

Seismic anisotropy is the dependence of velocity on propagation direction or angle of the seismic signal within the geological medium. It is generally ascribed either to complex fracturing under differential horizontal stresses or gravitational effects that make the media stiffer in one direction than another. In an azimuthally anisotropic medium, seismic velocities are slower along the directions of the symmetry axis than perpendicular directions (Fig. 10.8), resulting in an azimuthally varying velocity field. Azimuthal anisotropy affects the wavelet signature, including the hyperbolic moveout as well as the amplitude versus offset (AVO) analysis.

There are three types of simple anisotropy models in the literature to define the anisotropic structure of the subsurface, classified by their axis of symmetry:

- Vertical transverse isotropy (VTI): Axis of symmetry is vertical, and is associated with thin horizontal layering generally found in shale overburdens. The stiffening in the horizontal direction due to gravity increases the velocity in the horizontal direction (Fig. 10.8A). The medium is isotropic along thin horizontal planes perpendicular to the symmetry axis.
- Horizontal transverse isotropy (HTI): Axis of symmetry is horizontal, and is related to the vertical fracturing due to the regional stress

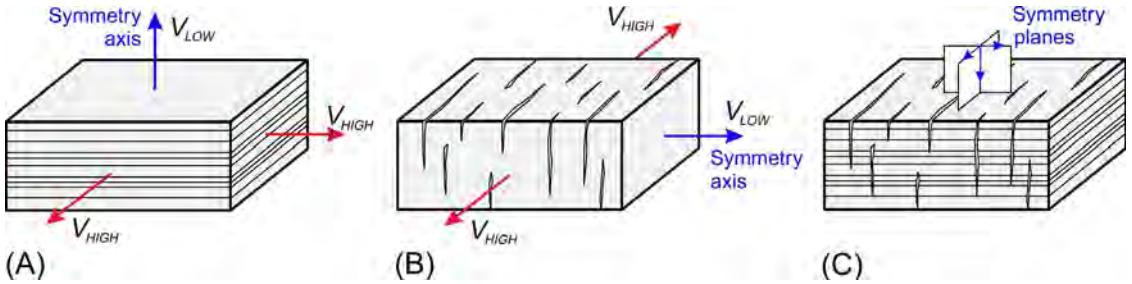


FIG. 10.8 Various types of anisotropy models. (A) Vertical transverse isotropy (VTI), (B) horizontal transverse isotropy (HTI), and (C) orthorhombic symmetry (ORT). VTI and HTI are called transverse isotropy, since the material is essentially isotropic in its horizontal or vertical plane.

regime. The medium is stiffer along the fracture directions, resulting in a higher propagation velocity along the cracks (Fig. 10.8B). The medium is isotropic along thin vertical planes perpendicular to the symmetry axis.

- Orthorhombic symmetry (ORT): This can be considered to be the combination of the two preceding types with three mutually orthogonal planes of mirror symmetry. It is caused by parallel vertical cracks within a medium of thin horizontal layering (Fig. 10.8C).

The existence of anisotropy may distort the normal moveout velocity for a small-spread approximation in a horizontally stratified subsurface and results in nonhyperbolic moveouts (Tsvankin, 1995), where two-term NMO approximations in Eqs. (10.1) and (10.7) become inaccurate with increasing offset, and therefore NMO velocities accounting for the anisotropic effects of the subsurface may be considered even for the case of a single homogenous azimuthally anisotropic medium. Wallace et al. (2007) showed that degradation of the reflections in the supergathers after isotropic NMO correction is apparent in the far offset traces resorted by their azimuths, which is associated with velocity variations of the azimuth of propagation.

Although the reflections produce hyperboloids with circular cross-sections for an isotropic medium, they create hyperboloids with elliptical cross-sections for an HTI medium, indicating high- and low-velocity directions, which results in an inaccurate velocity analysis performed, assuming an isotropic subsurface. However, it is generally not a straightforward process to obtain the anisotropic NMO velocities from the surface seismic data, which require several elastic parameters to define the anisotropic velocity. Grechka and Tsvankin (1998) showed that variations in NMO velocity depending on the azimuth are characterized by an ellipse in the horizontal plane, and the axis orientations of this ellipse are controlled by the rock properties and the direction of the reflector normal. They have also indicated that at least three azimuthal measurements are essential to obtain the NMO velocity in all azimuthal directions. Therefore, wide azimuth 3D seismic data is necessary for a complete measurement of azimuthal anisotropy to construct the azimuthal NMO velocity field. These factors make the anisotropy studies much more complex compared to the conventional processing steps, such as velocity analysis for isotropic media, especially because of the limited azimuths in data recording (Alkhalifah and Tsvankin, 1995).

Several different approaches have been suggested so far to mathematically describe the type and degree of the subsurface anisotropy. Thomsen (1986) defined three parameters, ε, γ, and δ, to describe the amount of anisotropy of

the rocks using Lame constants λ and μ as well as bulk modulus k, and he denoted a "weak anisotropy" if these parameters are small enough (e.g., $\ll 1$). For specific cases, $\varepsilon = \delta$ is known as elliptical anisotropy, and $\delta < \varepsilon$ indicates isotropic layers. Thomsen (1986) also proposed that most elastic media can be considered weakly anisotropic, which can be mathematically expressed by a certain anisotropy parameter δ. Tsvankin (1995) suggested an NMO velocity equation for a small-spread approximation depending on the phase velocity in a homogenous anisotropic VTI medium. Following this approximation, Alkhalifah and Tsvankin (1995) replaced dip angle with ray parameter p (horizontal slowness) corresponding to the zero-offset reflection to get

$$V_{NMO}(p) = \frac{V_{NMO}(0)}{\sqrt{1 - p^2 V_{NMO}^2(0)}} \tag{10.13}$$

where $V_{NMO}(0)$ is the NMO velocity in case of a horizontal (zero dip) reflector. Using anisotropy parameters defined by Thomsen (1986), Tsvankin and Thomsen (1994) suggested a long offset travel time equation which depends only on two parameters, $V_{NMO}(0)$ and η, for any orientation of the CMP line with respect to the dip plane of the reflector,

$$t^2(x) = t^2(0) + \frac{x^2}{V_{NMO}^2(0)} - \frac{2\eta x^4}{V_{NMO}^2(0)\left(t^2(0)V_{NMO}^2(0) + (1+2\eta)x^2\right)} \tag{10.14}$$

In Eq. (10.14), the anisotropic coefficient η defines the degree of deviation from hyperbolic moveout for a given $V_{NMO}(0)$ and $t(0)$. $\eta = 0$ represents an elliptical medium and the moveout is hyperbolic. In practice, anisotropic NMO correction can be applied to long offset seismic data, where only η is needed to describe the anisotropy, which can be defined in terms of Thomsen (1986)'s anisotropic parameters as

$$\eta = \frac{(\varepsilon - \delta)}{(1 + 2\delta)} \tag{10.15}$$

In general, η is positive, and larger values result in a decrease in NMO correction time.

10.2 NMO STRETCHING

As a result of the dynamic nature of NMO correction, a frequency distortion occurs in far offsets along the shallow parts of NMO corrected CDP gathers, known as NMO stretching. As schematically indicated in Fig. 10.5A and B, the waveform with a dominant period of t_A will be stretched into a larger period of t_B after NMO correction. Therefore, the amplitude spectrum of an NMO corrected wavelet has lower frequency content since the time length of the wavelet is longer than that in the zero-offset trace. This is clear in the synthetic data example in Fig. 10.9. The close-ups of NMO corrected gather in Fig. 10.9C and D compare the difference of dominant periods of the wavelets for near and far offset traces after correction. According to their corresponding mean amplitude spectra in Fig. 10.9E and F, the dominant frequency of the seismic wavelet is reduced from 60 to 30 Hz for far offset traces. This situation also lowers the resolution of the final stack sections. Shatilo and Aminzadeh (2000) propose that this low-pass filtering effect of the NMO correction is analogous to the effect of frequency dependent attenuation, which therefore adversely affects the attenuation calculations from the surface seismic data.

When two reflection hyperbolas intersect due to the increase in velocity with depth, the stretching leads to much more drastic results: for the intersecting events on the CDP gathers, conventional NMO correction completely fails since it assigns a unique time position to every time sample in the input traces (Shatilo and Aminzadeh, 2000). However, for the area of intersection, an uncorrected time sample may

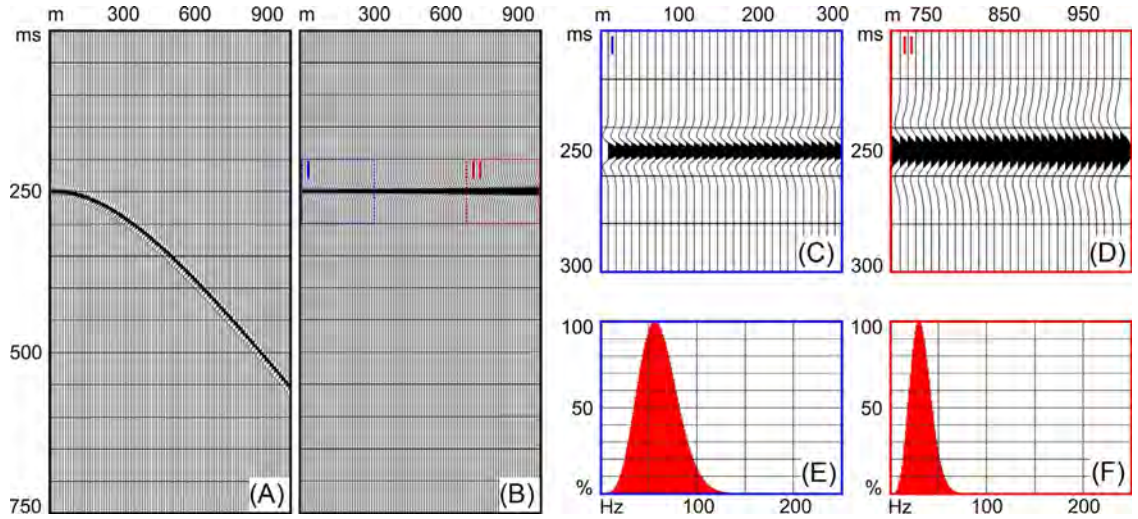


FIG. 10.9 A synthetic CDP gather with a single reflection hyperbola (A) before, and (B) after NMO correction. The close-ups of NMO corrected gather for (C) near and (D) far offset traces, are indicated by I and II, enclosed by *blue* and *red dashed rectangles*, respectively. (E) and (F) are corresponding mean amplitude spectra of the close-ups in (C) and (D).

point to multiple time locations on the corrected trace because of their interference nature through more than one individual reflection event. That is, a specific time sample of an uncorrected trace may represent more than one reflection hyperbola at the same recording time, which ultimately results in a complete degradation of early arrivals at far offset traces in a CDP gather. As an example, a synthetic CDP with two intersecting reflection hyperbolas are illustrated in Fig. 10.10A, with a close-up to emphasize the interference effect of two independent events in the intersection zone. A strong degradation arises after NMO correction due to the interference along the early arrivals for offsets larger than approximately 300 m for shallower reflection, which even influences the deeper reflection hyperbola for offsets larger than approximately 750 m (Fig. 10.10B). If two hyperbolas did not intersect as in Fig. 10.10C, depending on their velocities, the degradation would occur for the offsets greater than approximately 600 m for shallower reflection, and there would be no degradation for deeper reflection at all (Fig. 10.10D).

NMO stretch is a frequency distortion in which the dominant frequencies of the reflection events shift to the lower frequencies, and it is expressed by

$$\frac{\Delta f}{f} = \frac{\Delta t_{NMO}}{t(0)} \tag{10.16}$$

where f is the dominant frequency and Δf is the amount of shift in the frequency. NMO stretch occurs in the early arrivals of the far offset traces, which severely distorts the shallow parts of the CDPs. The stretched parts of the far offset traces are muted out and this process is known as NMO stretch mute. Muting is performed automatically using the expression given by Eq. (10.16), and the mute zone is determined by a percentage value termed the NMO stretch limit. Fig. 10.11 shows a synthetic CDP and its NMO corrected versions for different stretch limit percentages. The limit can exceed 100%, and it does not mean that the entire NMO stretch zone is successfully muted out when a 100% limit is used. The smaller the percentage mute limit, the larger the stretch mute zone. For higher

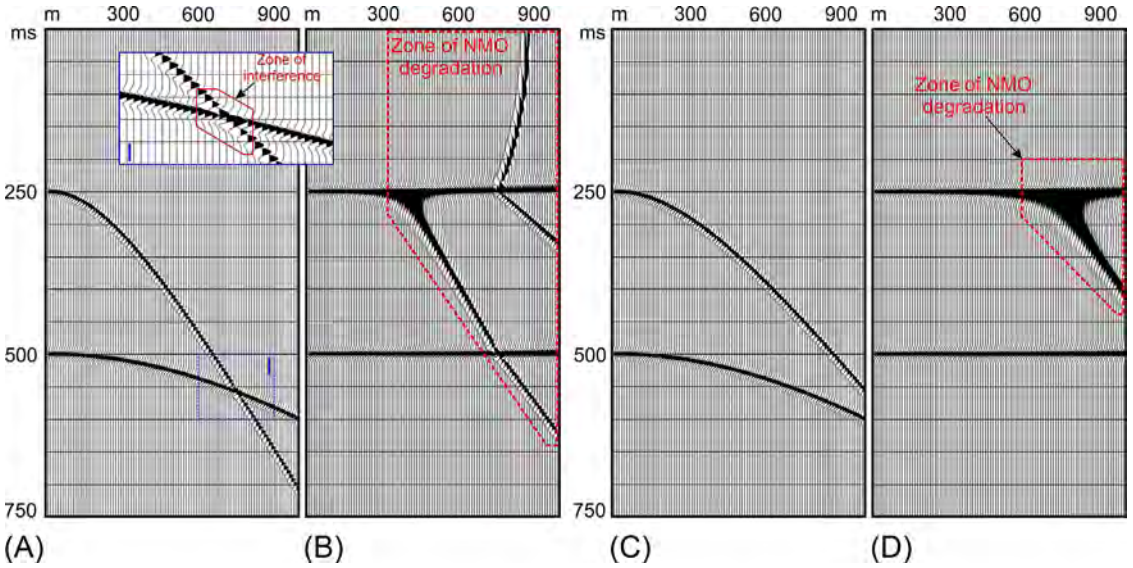


FIG. 10.10 A synthetic CDP gather with two intersecting reflection hyperbolas (A) before, and (B) after NMO correction. The inset indicates the interference effect within the intersection zone, which results in a complete degradation of early arrivals for offsets larger than 300 m for shallower reflection. (C) If two hyperbolas do not intersect, then similar degradation arises for offsets only larger than 600 m for the same reflection as in (D).

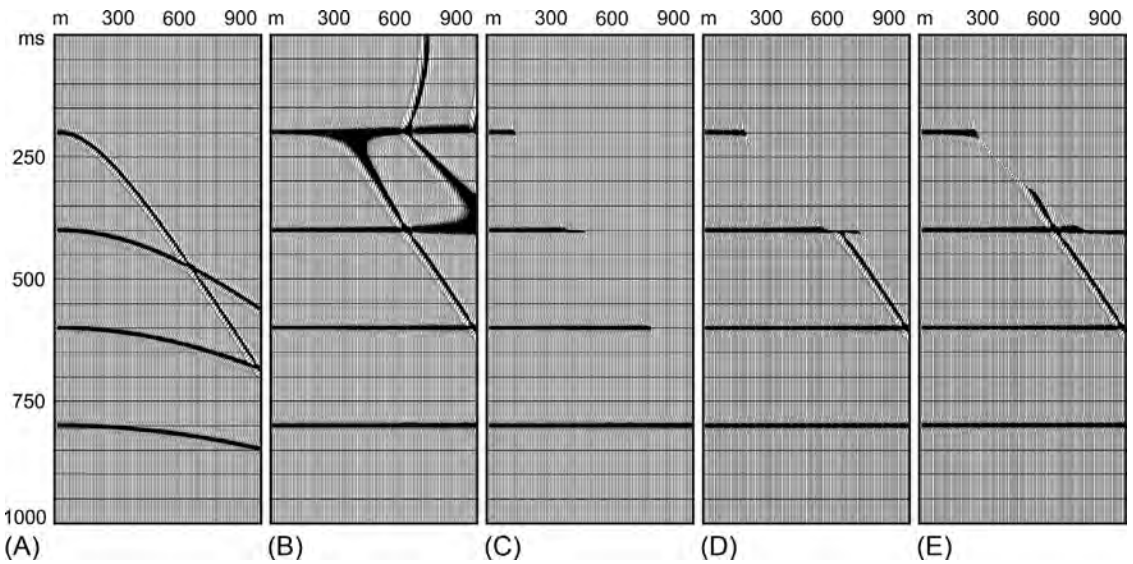


FIG. 10.11 (A) A synthetic CDP gather and its NMO corrected versions with an automated NMO stretch mute for stretch limit percentages of (B) 0%, (C) 20%, (D) 60%, and (E) 150%. A stretch limit of 20% seems to be suitable for this synthetic CDP gather.

limit values, a higher number of traces in early arrivals is involved in the stacking process.

Fig. 10.12 shows a marine CDP gather and its NMO corrected versions for different stretch limit percentages. A limit of 50% seems to be appropriate for this ensemble. Water depth is an important parameter on the selection of stretch limits for marine CDPs. In relatively deeper water data, there are no reflection hyperbolas in early arrivals, where there is no need to select a small stretch limit percentage for deep water data. However, the limit should be carefully selected in shallow waters, and generally several tests with different percentage values must be required to determine the most suitable stretch limit.

10.3 STACKING

During the stacking process, all the traces in 2D or 3D CDPs are simply summed up and averaged to obtain one single stacked trace for each CDP gather. This is known as "mean stack" and is schematically illustrated in the upper right panel of Fig. 10.13. Displaying all the stacked traces side by side for an entire seismic line constitutes the stack section of that line.

For a certain time sample k, the mean stack is mathematically defined as

$$S(t) = \frac{1}{N}\sum_{i=1}^{N} A_i(t) \tag{10.17}$$

where N is the number of traces involved in stacking, that is, the fold number of the CDP being stacked, and A_i is the amplitude value of the ith trace in the CDP gather. Each CDP gather turns into a single stacked trace after stacking, and therefore the number of CDPs in a 2D line or in a 3D volume exactly equals to the number of traces in the stack section.

Geometry of the ray paths for each specific type of ensemble from raw shot gathers to a stacked trace, and their corresponding example trace gathers are given in Fig. 10.14. The seismic

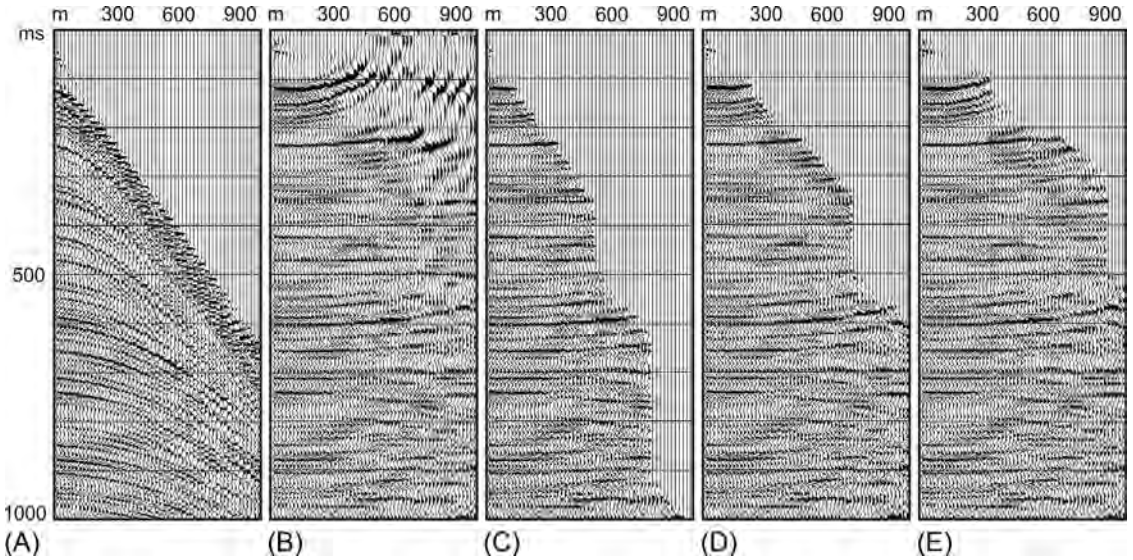


FIG. 10.12 (A) A marine CDP gather and its NMO corrected versions with an automated NMO stretch mute for stretch limit percentages of (B) 0%, (C) 50%, (D) 100%, and (E) 200%. A stretch limit of 50% seems to be suitable for this real marine CDP gather.

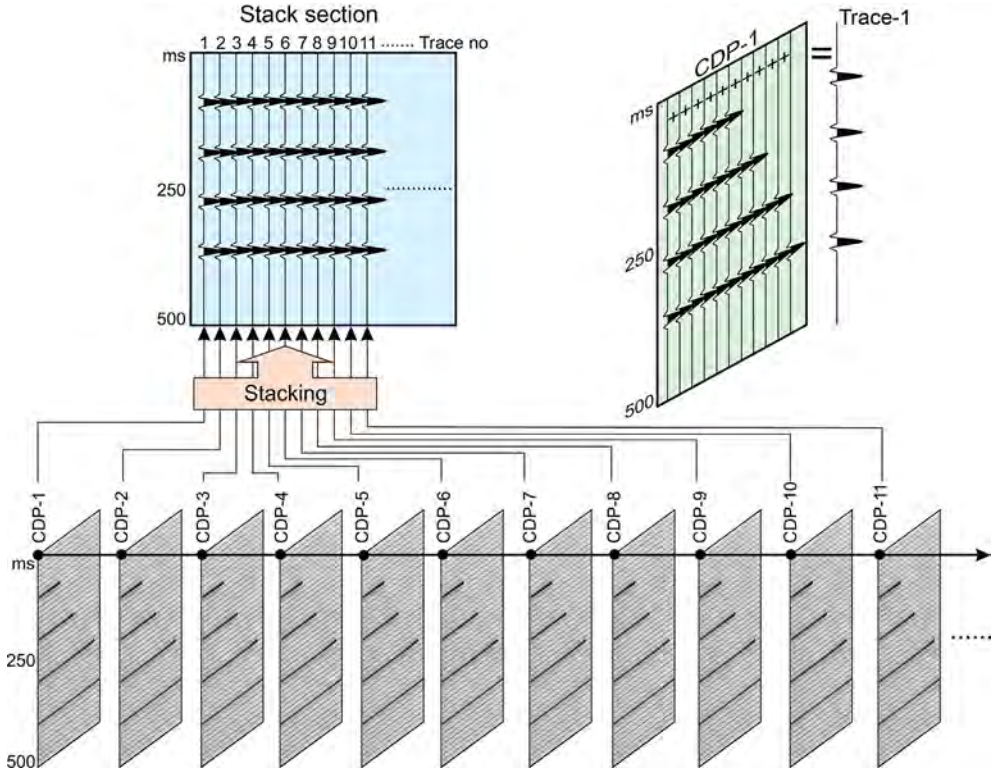


FIG. 10.13 Schematic representation of 2D stacking. After applying NMO correction to CDPs (bottom), the traces they contain are summed up to produce a stacked trace (upper right). The stack section of the seismic line is obtained by displaying these stacked traces from each individual CDP side by side (upper left). Each CDP provides only one single trace to stack section after summation.

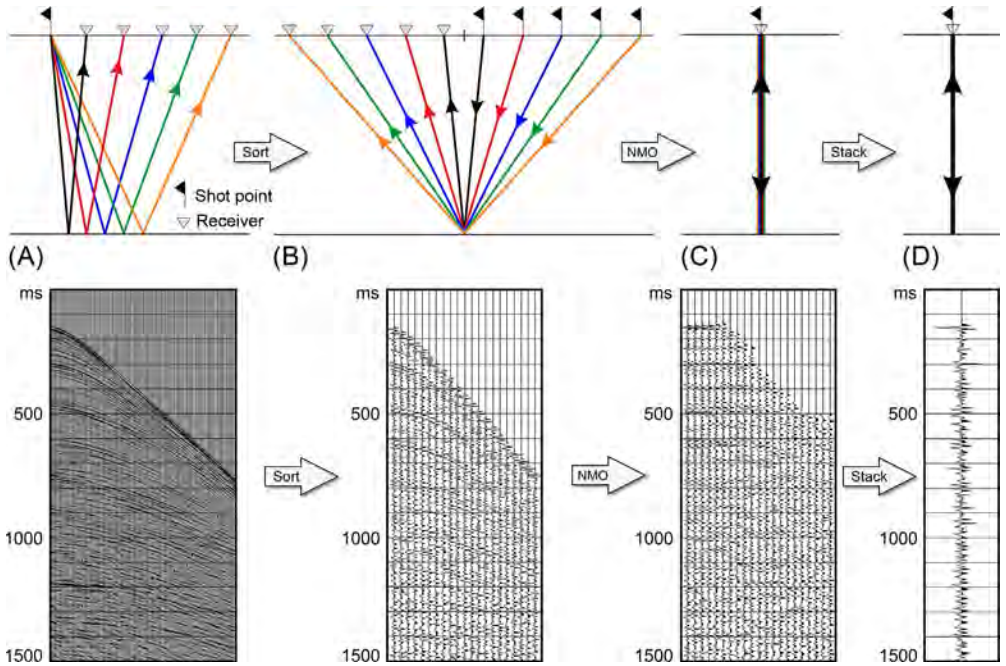


FIG. 10.14 Ray geometries (top) and real data examples (bottom) for (A) shot gather, (B) CDP gather after CDP sorting, (C) CDP gather after NMO correction, and (D) zero offset stacked trace for the CDP in (C) after stacking.

data is collected as shot gathers in shot and receiver coordinates (Fig. 10.14A), and then transformed into shot and receiver midpoint coordinates by CDP sorting (Fig. 10.14B), and the offset distance is removed by NMO correction to reduce all the traces into zero-offset arrival times (Fig. 10.14C). Finally, the traces in the CDPs are summed up to produce a stacked trace (Fig. 10.14D).

Stacking yields an interpretable seismic section for 2D surveys, and a seismic cube for 3D surveys. While a 2D stack section provides a vertical section along the survey line only (Fig. 10.15A), a seismic cube allows us to extract several, even irregular, 2D lines in any direction throughout the cube (Fig. 10.15B). In addition, a horizontal slice of amplitudes at a given time sample, known as a time slice, can be extracted from the cube, which exposes the 3D extension of the target structure.

Stacking has two considerable effects on the data: First, providing an accurate velocity analysis for primary reflections, multiples are still hyperbolic and out-of-phase while primaries are flattened and in-phase on the CDPs after NMO correction, which results in a considerable suppression of the multiples after stacking (Section 7.1). Second, if the number of traces involved in stacking is N, then the S/N ratio is improved proportional to $\sqrt{N}$ because in-phase primary reflection amplitudes strengthen each other after stacking. Random noise components, however, are trace-by-trace inconsistent and are out-of-phase in the NMO corrected CDPs. After summing up the traces during stacking, random noise is drastically suppressed, leading to an improved S/N ratio. Fig. 10.16 shows an example to emphasize the effect of stacking on the random noise suppression. An NMO corrected synthetic CDP gather consisting of 120 traces with two reflections of zero phase wavelets contaminated by a 50% random noise is shown in Fig. 10.16A. Fig. 10.16B illustrates stacked traces obtained using an increased number of traces involved in stacking: 4, 12, 24, 36, 48, 60, 72, 96, and 120 traces, respectively. As the number of traces in stacking increases, the amount of random noise in the stacked trace is significantly reduced.

Offset distance between source and receivers is removed by NMO correction, and the traces in an NMO corrected CDP as well as within the stack section are thought to be a zero offset. Due to several practical reasons, a stack section is not fully equivalent to a zero-offset section, but is an approximation. Poststack migration algorithms assume that the incoming data is zero offset. Normally, acquisition with CDP

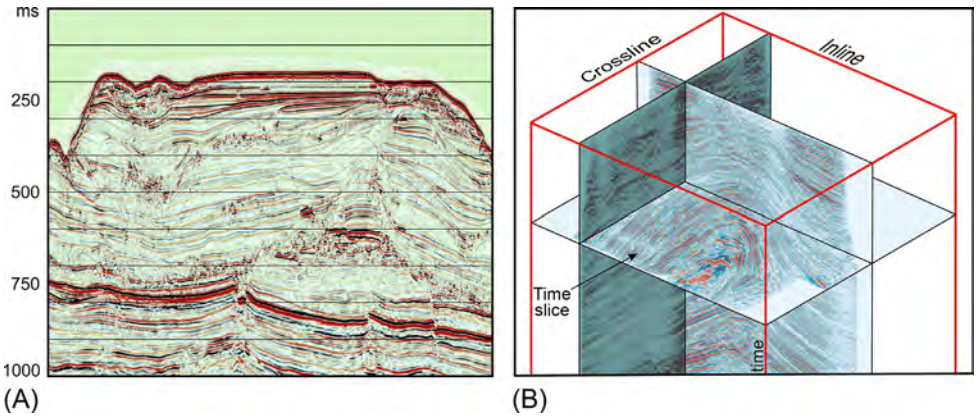


FIG. 10.15 (A) An example stack section from a 2D survey, and (B) a seismic cube from a 3D survey.

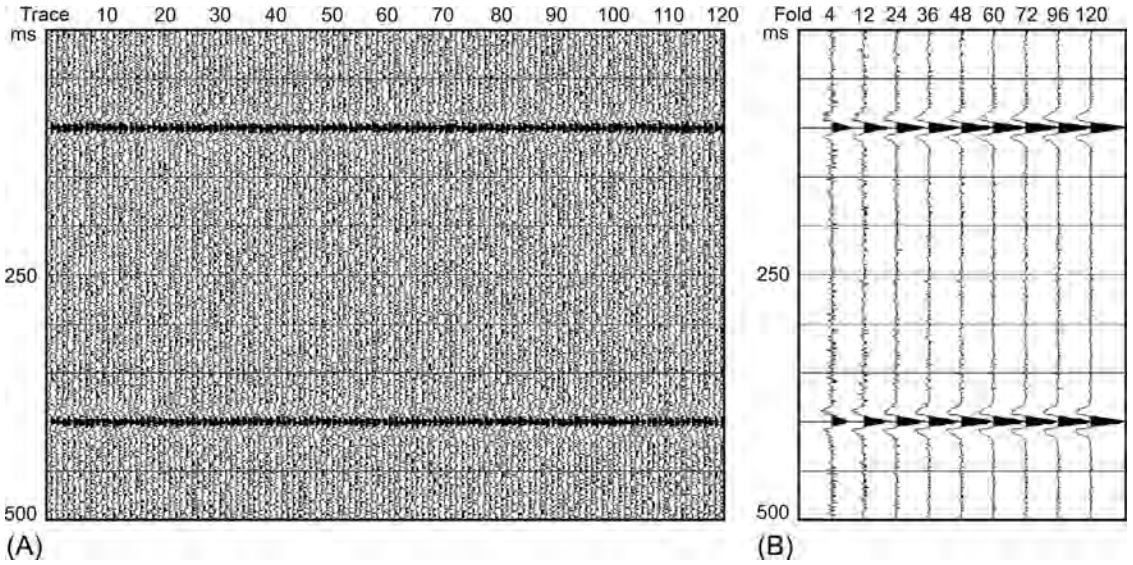


FIG. 10.16 Effect of stacking on the random noise suppression. (A) An NMO corrected synthetic CDP with 120 traces contaminated by 50% random noise. (B) Stacked traces obtained using first 4, 12, 24, 36, 48, 60, 72, 96, and 120 traces of CDP gather in (A), respectively. Increasing number of traces in stacking improves S/N ratio significantly.

geometry requires nonzero offset data recording. During the processing, source-receiver offset is removed by NMO correction based on the assumption that the reflections are of perfectly hyperbolic moveout. However, in some areas with irregular seafloor morphology and complex subsurface geology as well as lateral velocity variations, reflections may not display hyperbolic behavior. In addition, due to the multiple reflections and conflicting dips, stack sections and zero-offset sections are commonly not equivalent.

10.4 SPECIFIC STACKING METHODS

10.4.1 Partial Stack

Classical stacking of traces in a CDP gather into the zero offset destroys the amplitude variations of the reflections with respect to the source-receiver offset or incidence angle. This is because both near and far offset traces are treated similarly and stacked all together. Amplitude variations depending on the offset or incidence angle of reflections in CDP traces are, however, considered to be a significant hydrocarbon indicator and may incorporate important information for the oil and gas industry. Estimation of pore fluids in the possible subsurface reservoirs from surface seismics requires knowledge of how the pore fluid saturation affects the signal amplitudes. The variation of reflection amplitude with angle of incidence is known as amplitude versus offset (AVO) and is explained in Section 12.6. Possible AVO effects on seismic data can quickly be analyzed by partial stacking of different offset ranges independently. A common method to obtain AVO information from surface seismic data is to stack near and far offset traces in CDP gathers separately, which generates angle dependent stack sections. This method is known as partial stack or near/far offset stack, and if computed in terms of the incidence angle, then it is termed angle stack.

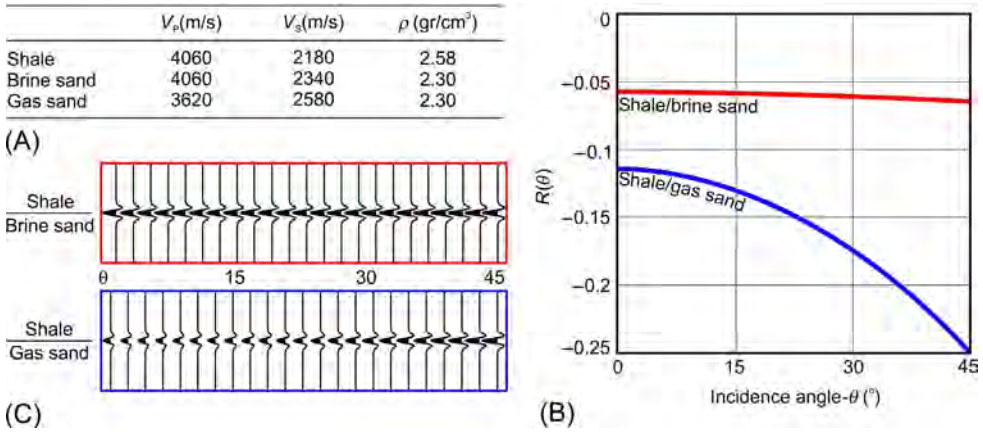


FIG. 10.17 Variation of reflection amplitude with incidence angle. (A) A shale/brine sand and shale/gas sand model parameters. (B) Variation of reflected P wave amplitude with incidence angle computed by the Aki and Richards (1980) approximation in Eq. (12.10) for the models in (A). (C) Synthetic seismograms computed from amplitude curves in (B) for shale/brine sand and shale/gas sand models. *A: From Ramos, A.C.B., Castagna, J.P., 2001. Useful approximations for converted-wave AVO. Geophysics 66, 1721–1734.*

Fig. 10.17 shows an example for variation of reflection amplitude with incidence angle. Fig. 10.17A shows two simple subsurface models for shale/brine sand and shale/gas sand interfaces, based on the velocity and density parameters given by Ramos and Castagna (2001). Using these subsurface models, variations of P wave reflection amplitudes $R(\theta)$ with incidence angle computed by the Aki and Richards (1980) approximation in Eq. (12.10) are shown in Fig. 10.17B. The curves show that the amplitudes of the reflection from shale/brine sand contact almost do not vary with the incidence angle. On the other hand, amplitudes drastically increase in the negative direction for the shale/gas sand case. Synthetic seismograms computed from these curves using a simple convolution calculation are illustrated in Fig. 10.17C, which denotes the increment in the reflection amplitude with increasing incidence angle (or offset) for the shale/gas sand case, whereas the amplitudes of the reflections are almost constant for the shale/brine sand model. If we simply stack the traces of far offsets of these CDPs, for instance, between their 30- and 45-degree incidence angles in the shale/gas sand model in Fig. 10.17C, we can obtain a distinctive bright spot anomaly on the stack section around this gas reservoir, while the stack section with near offset traces exhibits more regular amplitude distribution.

Fig. 10.18A shows an example NMO corrected CDP gather with three different offset ranges for partial stacks, that is, near, mid and far offsets. In the far offset range, reflections indicated by white arrows exhibit AVO anomalies, where the amplitudes increase as the offset increases. Fig. 10.18B shows a stacked trace composed of near offset traces while Fig. 10.18D illustrates the stack using only far offset traces. If the reflection amplitudes show variations in different offset ranges, as in the case in Fig. 10.18A, the variation can be easily distinguished by partial stacking of these different offset ranges. If there is an AVO effect in the data, it will generally produce a high amplitude "bright" reflection on the far offset stack section, whereas there is almost no indication in the near offset stack. Partial stacking is actually one of the

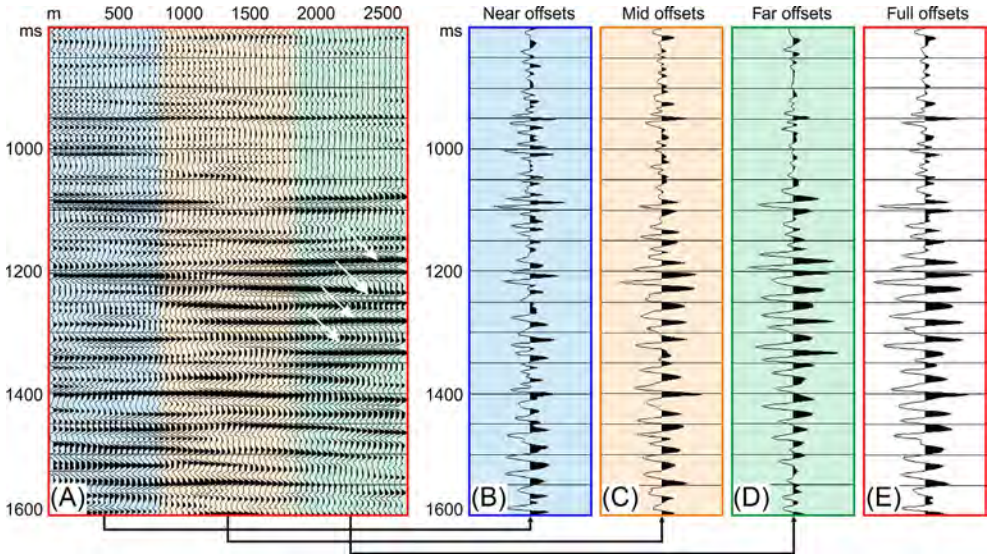


FIG. 10.18 (A) An example NMO corrected CDP gather. Different color shaded zones represent near *(blue)*, mid *(orange)*, and far *(green)* offset ranges. *White arrows* represent reflections with AVO anomalies in far offset range. Stacked traces composed of (B) near offset, (C) mid offset, (D) far offset, and (E) full offset traces of CDP in (A) show amplitude variations along the offset range. The AVO anomaly zone constitutes relatively high amplitudes in far offset stacked traces as compared to near offset stack. Location of CDP in (A) is given in Fig. 10.19C.

most common methods for AVO reconnaissance in seismic data.

In seismic surveys for hydrocarbon exploration, near and far offset stack sections are prepared and compared to prove the possible AVO effects in the seismic data. Hydrocarbon accumulations may compose different types of AVO anomalies (or AVO classes) on the prestack data (Section 12.6.3). As a general approximation for gas sands of Class III AVO anomalies, where the absolute reflection amplitude increases with the increasing offset, high-amplitude zones may exist in the far offset stack constituting improved reflections, or "bright spots." Partial stacks may indicate the clues of hydrocarbon existence as well as their lateral extent within the reservoir. Fig. 10.19 shows an excellent example for AVO reconnaissance analysis using partial stacks. In Fig. 10.19A, the full stack section shows an anticline structure related with an inverse faulting with a quite regular amplitude distribution. Although there is almost no indication of high-amplitude reflections in the near offset stack in Fig. 10.19B just below the anticline, several bright spots exist in the far offset stack in Fig. 10.19C, indicating a strong AVO effect in the prestack data.

10.4.2 Median Stack

Median is a statistical parameter defined as the central value of a series after sorting its elements in an ascending order. For instance, if the input series is $f_1 = \{10, 45, 24, 87, 36, 56, 21, 66, 61\}$, after sorting the series in the ascending order, we get $f_2 = \{10, 21, 24, 36, 45, 56, 61, 66, 87\}$. The central value, that is, 45, represents the median value of f_1. An alternative stacking technique termed a median stack uses median values of the reflection amplitudes in the CDPs after NMO correction. In median stack, only the median value of the amplitudes, or a number of

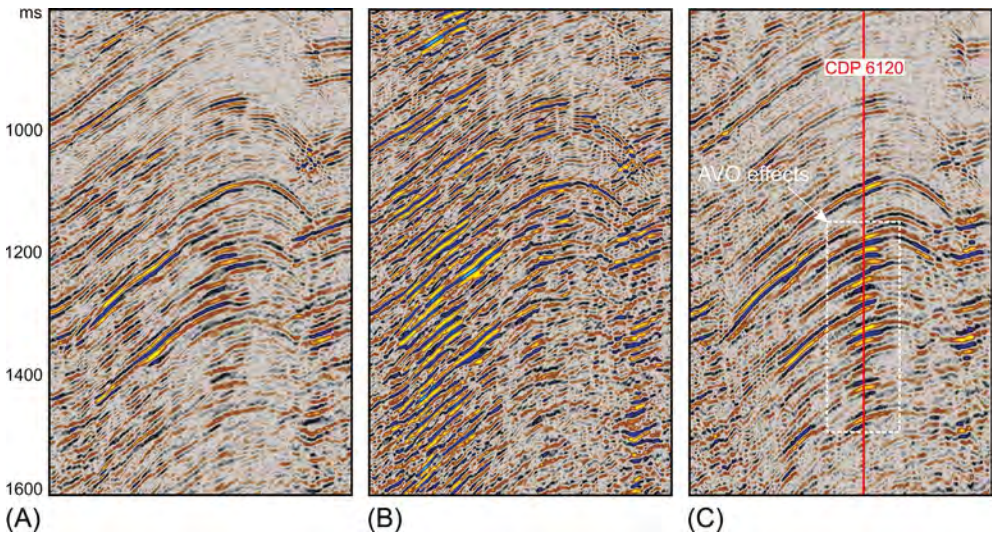


FIG. 10.19 (A) Full stack section indicating an anticline structure, (B) near offset stack with an offset range from 0 to 300 m, and (C) far offset stack with an offset range from 2000 to 2800 m. The far offset stack indicates several bright spots below the anticline (area in the dashed rectangle). Only true amplitude recovery was applied as gain correction for all three sections. CDP 6120 locates the CDP gather shown in Fig. 10.18A.

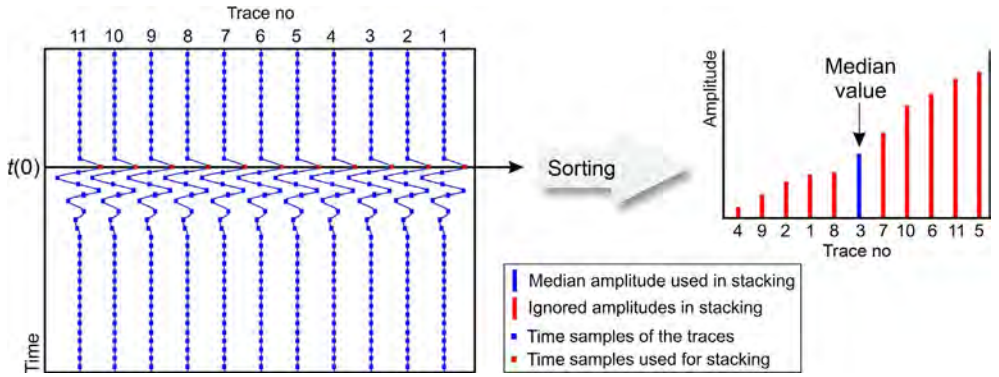


FIG. 10.20 Schematic illustration of the median value of seismic amplitudes of the same $t(0)$ time. In a classical mean stack, the amplitudes of the *red squares* are simply averaged to give the stack amplitude value at time $t(0)$. For a median stack, the amplitudes of the *red squares* are sorted in ascending order, and the central value is selected as the stacked amplitude (*blue amplitude bar* from trace 3 in the amplitude plot), while the remaining amplitudes are ignored (*the red amplitude bars* in the amplitude plot).

amplitude values around the median value, is incorporated in the stacking process.

Fig. 10.20 schematically shows the median value of the amplitudes with a certain $t(0)$ zero offset time in a CDP gather. Normally, a classical median stack does not sum the samples: before the amplitudes of the same $t(0)$ time (the *red squares* on the NMO corrected CDP in Fig. 10.20) are stacked, they are simply sorted in ascending order and the central value is selected as the stacked amplitude value for that $t(0)$ time, while remaining amplitudes are ignored. For the

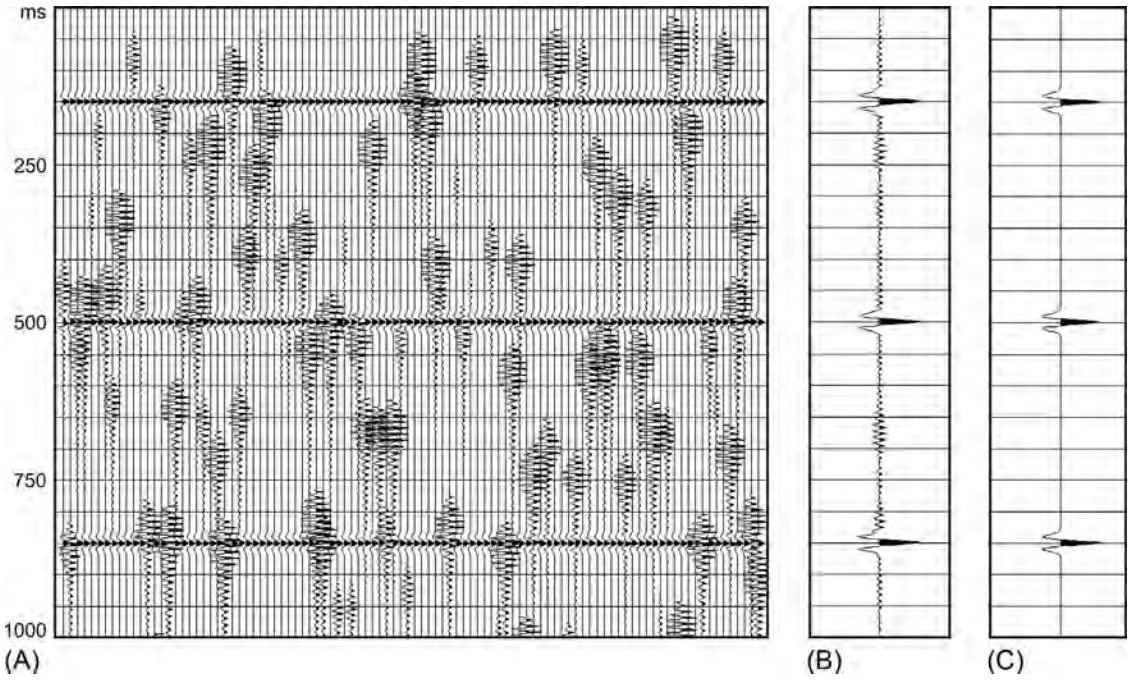


FIG. 10.21 Comparison of mean and median stack. (A) An NMO corrected synthetic CDP gather with three genuine reflections at 150, 500, and 850 ms along with high-amplitude noise bursts. (B) Mean stack, and (C) median stack traces of (A).

schematic illustration in Fig. 10.20, the amplitude value at trace number 3, indicated with a *blue bar*, is the median.

Fig. 10.21 compares mean stack and median stack on an NMO corrected synthetic CDP gather. The input CDP contains three reflections at 150, 500, and 850 ms along with high-amplitude noise bursts. The mean stack trace in Fig. 10.21B suffers from noise amplitudes, whereas the median stack trace is almost free of noise bursts. Fig. 10.22 compares mean stack and median stack on a real marine data example. There are extreme spike noise bursts distributed randomly on the traces of the stack section in Fig. 10.22A. The median stack of the same seismic data results in a stack section with much higher S/N ratio with no high-amplitude noise bursts (Fig. 10.22B).

Applications show that the median stack may be successful in the case of the noisy seismic data, especially for higher amplitude spike-like noise bursts. It is especially useful in the case of extreme strong noise amplitudes in low fold seismic data, and it produces nice results when the noise amplitudes appear at less than half of the total number of traces involved in the stacking. However, since it reserves only the median value for the stacking and ignores all other amplitude values, the median stack may reduce the quality of the stack sections in the case of low-amplitude noise.

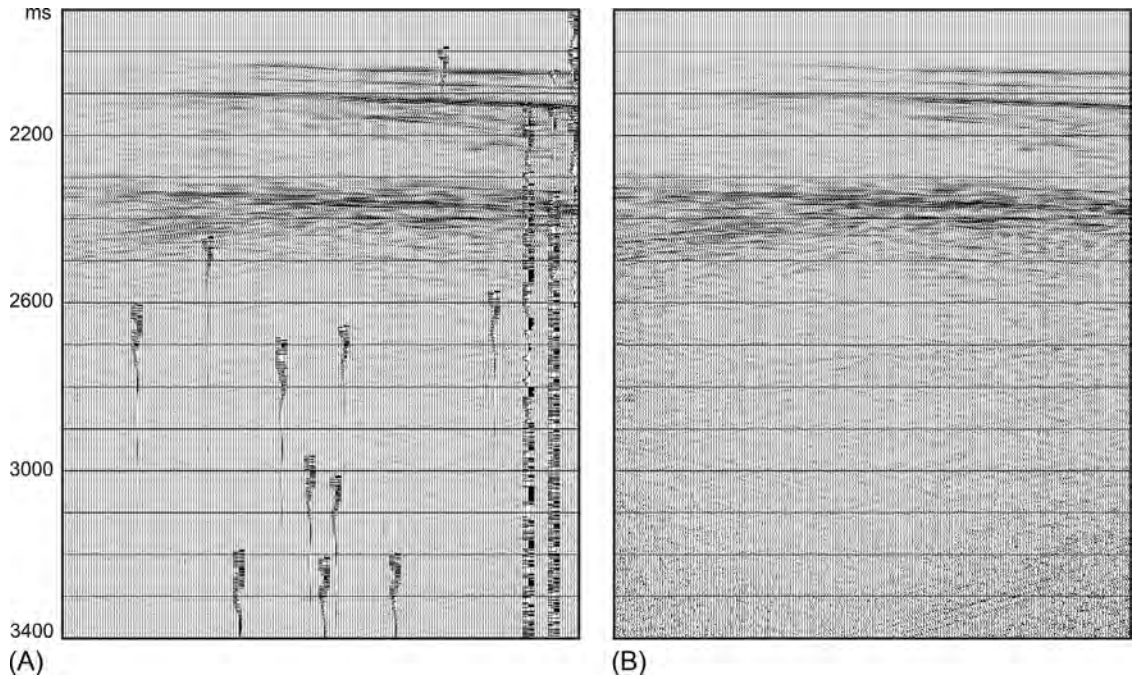


FIG. 10.22 Application of median stack to marine seismic data. (A) Mean stack of the data with extreme spike noise bursts, and (B) median stack of the same data in (A).

10.4.3 Trimmed Stack

Trimmed stack is also known as trimmed mean stack, in which the amplitudes involved in the stacking process are sorted in ascending order as for the median stack, and before taking the average of the amplitudes, a certain percentage of the high- and low-amplitude values of the sorted series is ignored. In practice, mean stack and median stack can be considered the special cases of trimmed stack (Haldorsen and Farmer, 1989). While all of the amplitude samples are incorporated and no amplitude values are ignored in a conventional mean stack, only the median amplitude is used and the highest number of amplitude values is ignored in the median stack.

After sorting of n number of amplitude samples before stacking, the sample number 1 will have the minimum amplitude value while sample number n will have the maximum amplitude value. If these two values are ignored in the averaging, the mean value of any given series with a normal distribution will not significantly change. Normally, when the same number of values is ignored from both ends of the normal distribution curve, the mean value of a series also does not change excessively. The averaging procedure of such a delimited amplitude series is termed a trimmed mean, and the stacking process using this approach is known as trimmed stack. It is mathematically expressed by

$$S(t) = \frac{1}{(n-m)} \sum_{i=m/2+1}^{n-m/2} A(t) \qquad (10.18)$$

where $S(t)$ is trimmed stack amplitude, m is the total number of ignored amplitudes ($m/2$ values for each side of the distribution), and $A(t)$ is the

series of amplitude values sorted in ascending order. In practice, a percentage value of $p = m/(n-1)$ is used instead of the number of neglected amplitudes. In practice, as the p increases from 0% to 100%, trimmed stack changes from mean stack to median stack.

Fig. 10.23 schematically shows the amplitudes used for the trimmed mean value from the amplitudes with a certain $t(0)$ zero offset time in a CDP gather. After they are simply sorted in ascending order, a number of amplitudes around the central value are selected for the stacking process to obtain the stacked amplitude value for that $t(0)$ time, while remaining amplitudes are neglected. The number of ignored amplitudes is represented by a percentage value. Fig. 10.24 shows the effect of this percentage value on the trimmed stack output. The synthetic noisy CDP gather given in Fig. 10.21A is considered the input gather, and trim stack traces are obtained by using different p values. As the percentage of the ignored amplitudes increases, the output approaches to the median stack and produces better results with a smaller number of noisy amplitudes.

Fig. 10.25 shows an application of trimmed stack on the same marine seismic data used in Fig. 10.22A. A 10% trimmed stack leaves some residual noise on the final stack; however, a 20% value seems to be appropriate for this dataset. The trimmed stack excludes the extreme amplitude values of a given percentage from the stack. It may reduce the noise amplitudes, especially from seismic interference or spike-like noise bursts. Trimmed stack, however, may reduce the S/N ratio of the input data when the data has no significant high-amplitude noise (Rückemann, 2012), as is the case for median stack.

10.4.4 Common Reflection Surface Stack

In conventional NMO correction/stacking procedure, an accurate velocity model of the subsurface is required. In most cases, however, setting up an accurate velocity model is a very time-consuming process, even impossible in areas of complex geology, especially for low fold data. Jäger et al. (2001) suggested the common reflection surface (CRS) stack method to obtain

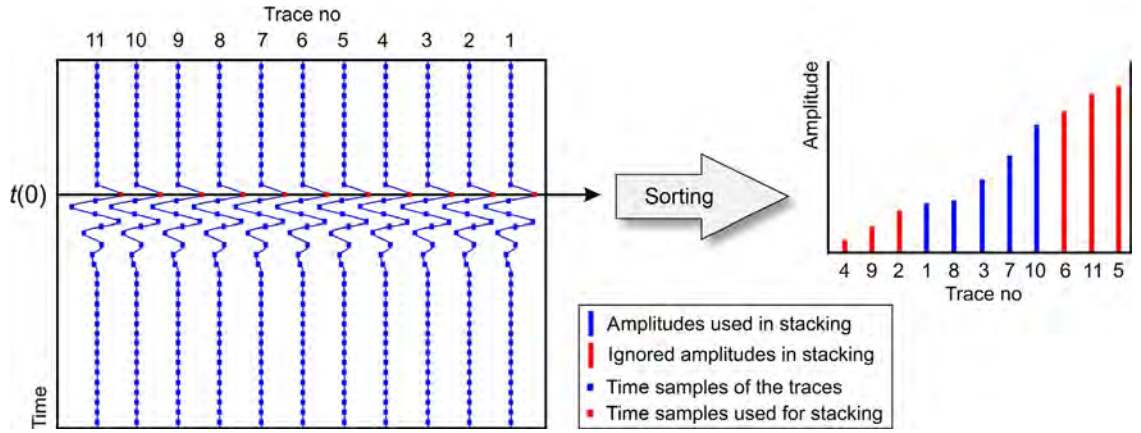


FIG. 10.23 Schematic illustration of the trimmed mean value of seismic amplitudes of the same $t(0)$ time. In a classical mean stack, the amplitudes of the *red squares* are simply averaged to calculate the stack amplitude value at time $t(0)$. For a trimmed stack, the amplitudes of the *red squares* are sorted in ascending order, and a number of amplitudes around the central value are incorporated in the stacking (*blue amplitude bars* from traces 1, 8, 3, 7, and 10 in the amplitude plot), while the remaining amplitudes are ignored (*the red amplitude bars* in the amplitude plot).

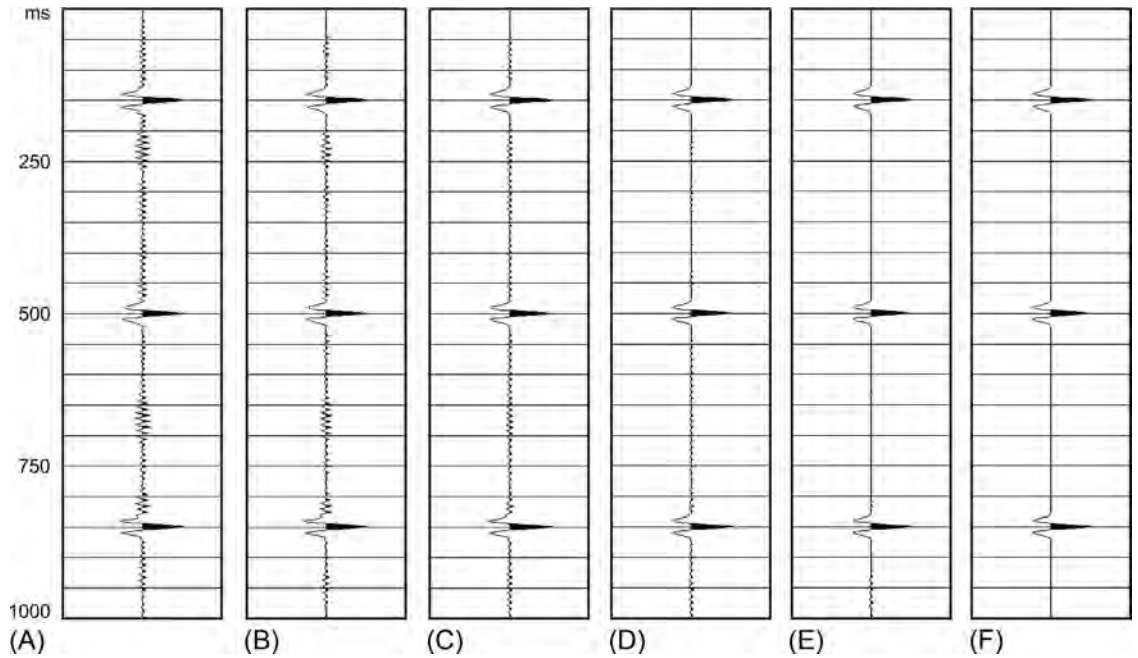


FIG. 10.24 Effect of percentage value on the trimmed stack on the synthetic CDP gather given in Fig. 10.21A. Trimmed stack outputs for (A) 0%, (B) 5%, (C) 10%, (D) 20%, (E) 30%, and (F) 50%.

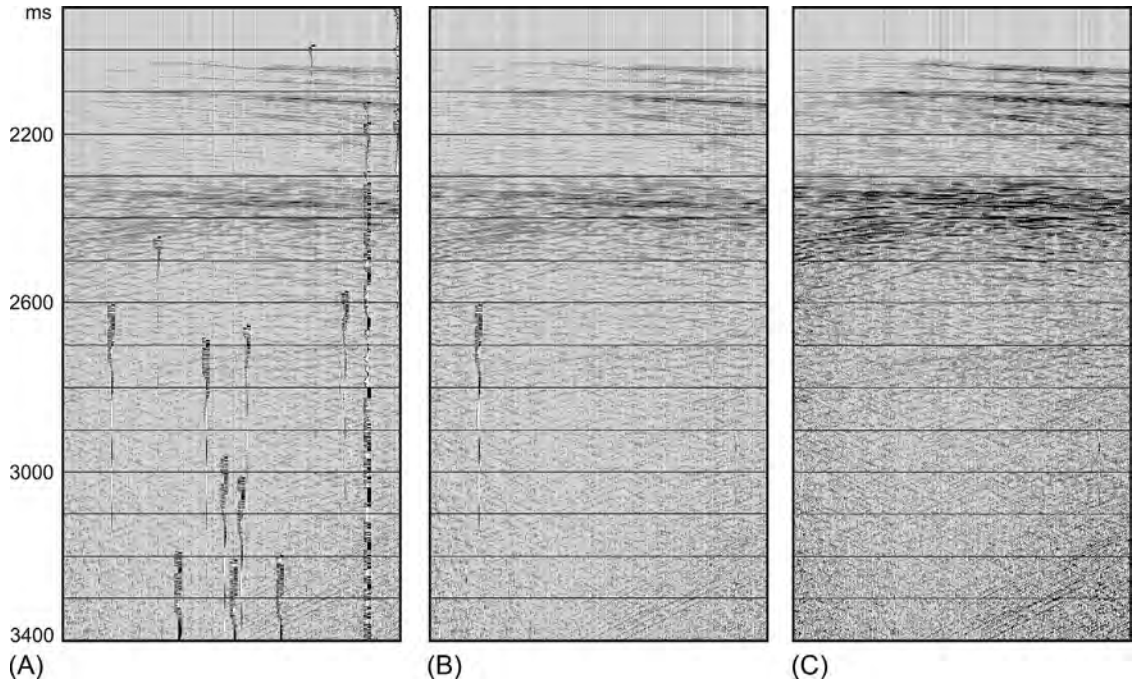


FIG. 10.25 Application of trimmed stack to the same marine data used in Fig. 10.22A. Trimmed stack outputs for (A) 5%, (B) 10%, (C) 20%.

a zero-offset stack section to compensate for the imaging problems in the low fold areas. A conventional CDP stack assumes a subsurface of homogeneous horizontal layers. The CRS stack, however, accounts for lateral variations in the subsurface model with arbitrarily curved reflectors. It is a data-driven method that is velocity-model independent, and it also provides a number of additional kinematic parameters.

The CRS method estimates the reflectors based on their dips and curvatures with a suitable CRS stack operator, which does not rely on a single CDP gather at the subsurface imaging location; it also incorporates the reflections from the contributing traces at neighboring CDPs associated from the same subsurface element of the reflector. Therefore, a CRS stack has higher fold, which significantly improves the stack quality.

In conventional NMO processing, a stack section is obtained by averaging the amplitudes over a hyperbolic curve along the offset axis using Eq. (10.1), which is defined by only one parameter, the RMS velocity. In the CRS stack method, however, the summation along a structurally consistent reflector segment significantly improves the quality of stack sections. The major advantages of the CRS stack procedure are as follows:

- The most important advantage of the CRS stack is that it does not require a macro velocity model of the subsurface, and the velocity of the uppermost layer is sufficient to obtain a CRS stack section.
- The reflections from steeply dipping reflectors, such as salt flanks, are significantly enhanced by CRS stack.
- The S/N ratio of the stack section is improved, especially for low fold data and around the deeper targets where the S/N ratio is relatively poor.
- Since the fold is increased, AVO responses are much clearer in areas contaminated by high-amplitude noise.
- It may provide clearer prestack gathers, which can be later used for residual moveout analysis or prestack migration.

In the 2D case, the CRS stack can be expressed by three parameters, termed kinematic wave field attributes: α is emergence angle of the ray normal to the reflector or the dip angle, R_N is the radius of curvature of the exploding reflector wave field, and R_{NIP} is the radius of curvature of the wave field from a point source located at the normal incidence point (NIP). These two hypothetical waves, shown in Fig. 10.26, are known as an NIP wave (or central ray) and a normal wave, respectively (Hubral, 1999). An NIP wave can be produced by a point source located at point R on the reflector, and a normal wave is generated by an exploding reflectors modeling approach (Fig. 10.26).

Wave field attributes for each zero-offset location are determined by a coherence analysis in the prestack data using a stacking operator, which yields the sections of the wave field attributes α, R_{NIP}, R_N, and a semblance section. The CRS stack is a data-driven method, and in practice these attributes are determined automatically from the prestack data.

The travel time approximation of the CRS stack method used to obtain the CRS stack operator for the paraxial ray in the vicinity of a normal ray along the SPG trajectory in Fig. 10.26 is given by (Jäger et al., 2001)

$$t^2(x_m,h)=\left(t(0)+\frac{2\sin\alpha}{V_0}\Delta x\right)^2+\frac{2t(0)\cos^2\alpha}{V_0}\left(\frac{\Delta x^2}{R_N}+\frac{h^2}{R_{NIP}}\right) \tag{10.19}$$

where $\Delta x=(x_m-x_0)$, that is, the distance between midpoint coordinate x_m and zero offset coordinate x_0, h is the half offset, $t(0)$ is the zero-offset time, and V_0 is the velocity of the uppermost medium. The CRS stack utilizes Eq. (10.19) as a stacking operator on each

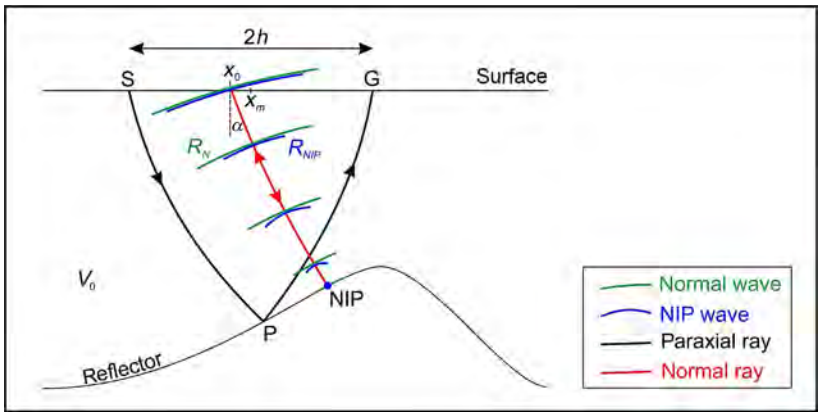


FIG. 10.26 Ray diagram for a paraxial ray *(black)* from source S to receiver G in the vicinity of a normal ray *(red)* in a 2D laterally inhomogeneous medium. An NIP wave *(blue wave front)* is produced by a point source located at point NIP on the reflector, while a normal wave *(green wave front)* is generated by an exploding reflectors experiment at point NIP. Here, x_0 and x_m represent the zero-offset and midpoint coordinates, respectively.

zero-offset sample to stack the coherent reflection amplitudes. Fig. 10.27 schematically shows the CRS surface, also known as the CRS operator, and its relation to the NMO stacking curve over the common offset sections. Conventional NMO/stacking for a reflection from a curved reflector segment is performed along a curve (the red curve at the top of Fig. 10.27A) throughout the common offset arrival times, which finally produces a stacked amplitude at zero-offset point P_0 for $h = 0$, located at (x_0, t_0). This zero-offset point is represented by a zero-offset ray reflected at point NIP on the reflector and recorded at point x_0 at the earth's surface (the red ray path at the bottom of Fig. 10.27A). Therefore, only the amplitudes along the red NMO curve contribute to the stack for a conventional NMO/stack. For the CRS stack, however, all the amplitudes along the CRS operator (green surface at the top of Fig. 10.27A) contribute to the CRS stacking amplitude.

Fig. 10.27B schematically shows the data volume that the CRS operator works on. The seismic data is represented in half offset (h)-midpoint (x_m) coordinates, and the green surface demonstrates the CRS operator. During the CRS stacking process, determination of optimum stacking values for α, R_N, and R_{NIP} parameters is the main problem to be solved during a CRS application. An objective function is defined to measure the fit between the green CRS stacking operator in Fig. 10.27B and the recorded reflection event in the prestack data, which allows the CRS algorithm to determine three parameters automatically for each time sample in the zero-offset stack section (t_0, x_0) in (x_m, h, t) space. This is done by an automatic search accounting for all possible dips available in the zero-offset data. The three-parameter search is achieved by a perturbation of the parameters, which ultimately changes the operator shape calculated from Eq. (10.19) at each perturbation, and by calculating the coherence along the operator in the multichannel seismic data. The optimum values are established by a maximum semblance value associated with that parameter along the calculated stacking surface. When the correct parameters are selected during the search, the amplitudes of any specific reflector segment are summed up constructively, which yields an enhanced coherence value, making the CRS stacking method entirely data driven (Heilmann, 2007).

Fig. 10.28 compares conventional NMO/stack and CRS stack sections for a low fold 2D

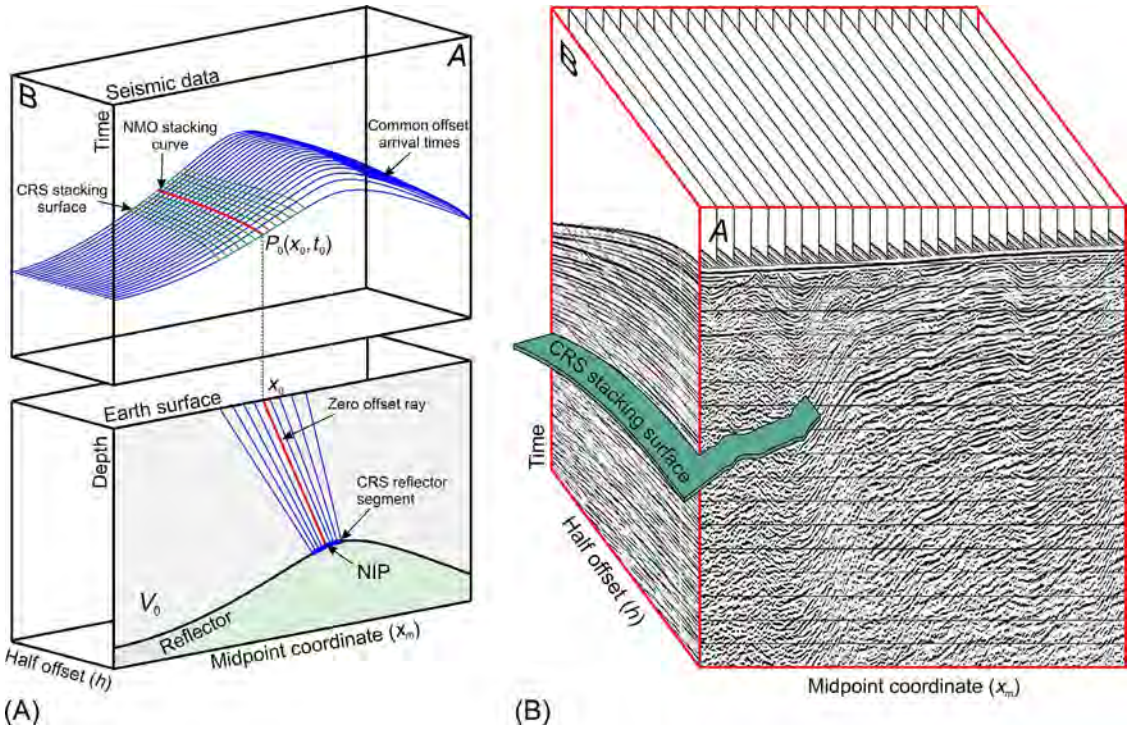


FIG. 10.27 Schematic illustration of CRS stack surface. (A) A 2D earth model of a curved reflector (bottom), and hypothetical travel time curves *(blue curves)* from the reflector on common offset gathers (top). NMO stacking is done along the *red curve* to obtain a zero-offset stacked amplitude represented by a zero-offset ray *(red line)* at point P_0 where $h = 0$ and $x_m = x_0$, whereas all the amplitudes on the CRS stack operator *(green surface)* consisting of the reflections originated from a curved segment on the reflector (*blue segment* on the reflector) are summed up to obtain a CRS stack amplitude. (B) Schematic display of seismic data at half offset (h)-midpoint (x_m) coordinates. The CRS stacking surface, or CRS operator, is indicated by the *green* surface. The frontal plane indicated by A is a zero-offset section, like a conventional stack, and the side plane indicated by B is the gathers sorted according to their half offsets.

seismic line with a low S/N ratio. In a CRS stack, stack quality is widely improved, especially for the areas of the thrust fault where the data quality is poor and high-amplitude random noise dominates. In the 3D case, the CRS stack can be expressed by eight parameters: emergence or dip angle α, emergence azimuth β, and three independent radius values for R_N and R_{NIP}. However, only α, β, and R_{NIP} are considered since an eight-parameter search is extremely expensive. It not only improves the S/N ratio of the stack data, but also widely enhances the quality of time slices from 3D cubes (Trappe et al., 2015).

No specific process is necessary for a CRS stacking procedure and a conventional processing sequence is applied to the data prior to the CRS stack algorithm. CRS processing produces four optimized sections: simulated zero-offset, α, R_N, and R_{NIP} sections, and a coherency section. Using the CRS parameters, a poststack time migration can also be applied to the simulated zero-offset section without a preliminary velocity model, since the CRS stack parameters provide the background velocity. In addition, the preliminary velocity field from a conventional velocity analysis can be used as a confinement during a CRS search to avoid stacking of the multiples (Kumar, 2008).

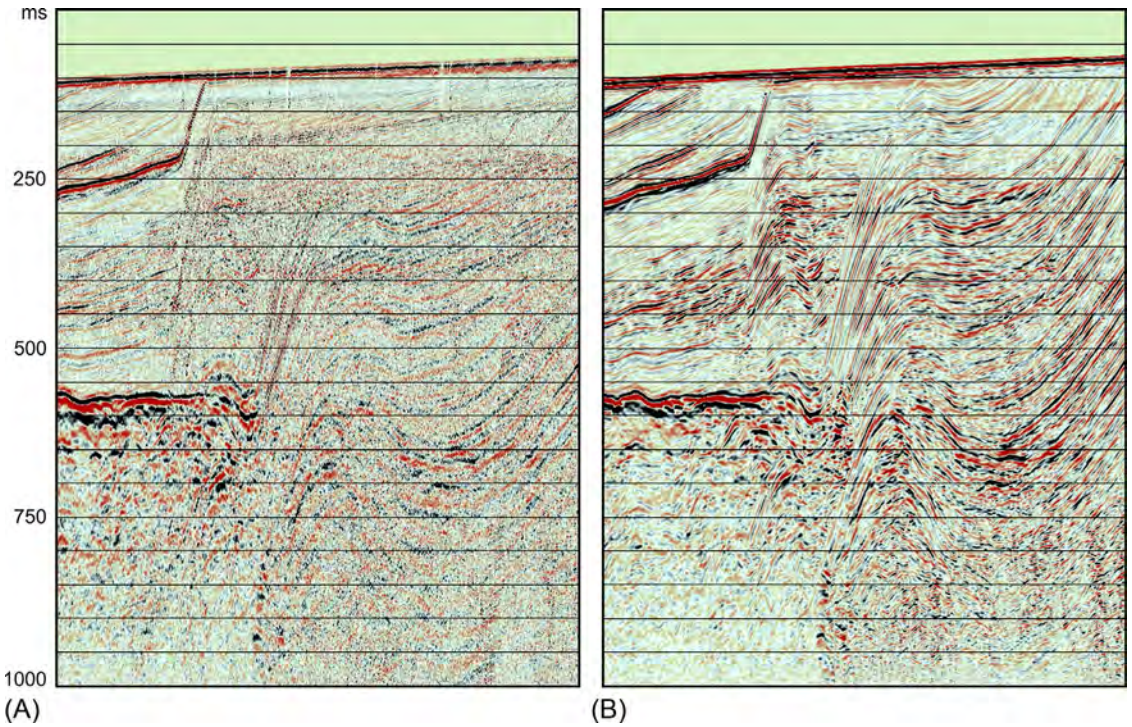


FIG. 10.28 A comparison of (A) conventional NMO/stack, and (B) CRS stack sections. Data quality is significantly improved in the CRS stack, especially for the reflections at the central part where a thrust fault is observed.

10.5 QC IN NMO CORRECTION AND STACKING

One of the most important QC applications for NMO correction is to display and check the NMO corrected CDPs to ensure that all of the primary events are flattened, which is the ultimate goal of the NMO correction. Since the success of the correction directly depends on the correctness of the velocity function used, velocity picks around the problematic CDPs after NMO correction must be edited to obtain a more accurate velocity function, which flattens the primary reflections. Apart from improper velocity functions used, unflattening frequently occurs in areas of steep dip and complex seafloor morphology, where the reflections may not be hyperbolic.

In Fig. 10.29A, a number of NMO corrected consecutive CDPs are displayed for QC purposes. In areas indicated by blue polygons, the reflections are not flattened at all, due to the fact that the velocities used for NMO correction are too fast for polygon A, while they are too slow for polygon B. Turning back to the velocity analysis, the velocity picks for the CDPs in the polygonal areas must be corrected and updated, as shown in Fig. 10.29B. If not, the reflections that are not perfectly flattened cause severe degradations on the stacked trace. Fig. 10.30 shows this effect on a synthetic CDP with two reflection hyperbolas. If we use accurate velocities for both reflections in NMO correction (e.g., $V_1 = 1500$ m/s and $V_2 = 1800$ m/s for shallow and deep reflections, respectively), we get perfectly flattened hyperbolas with a favorable

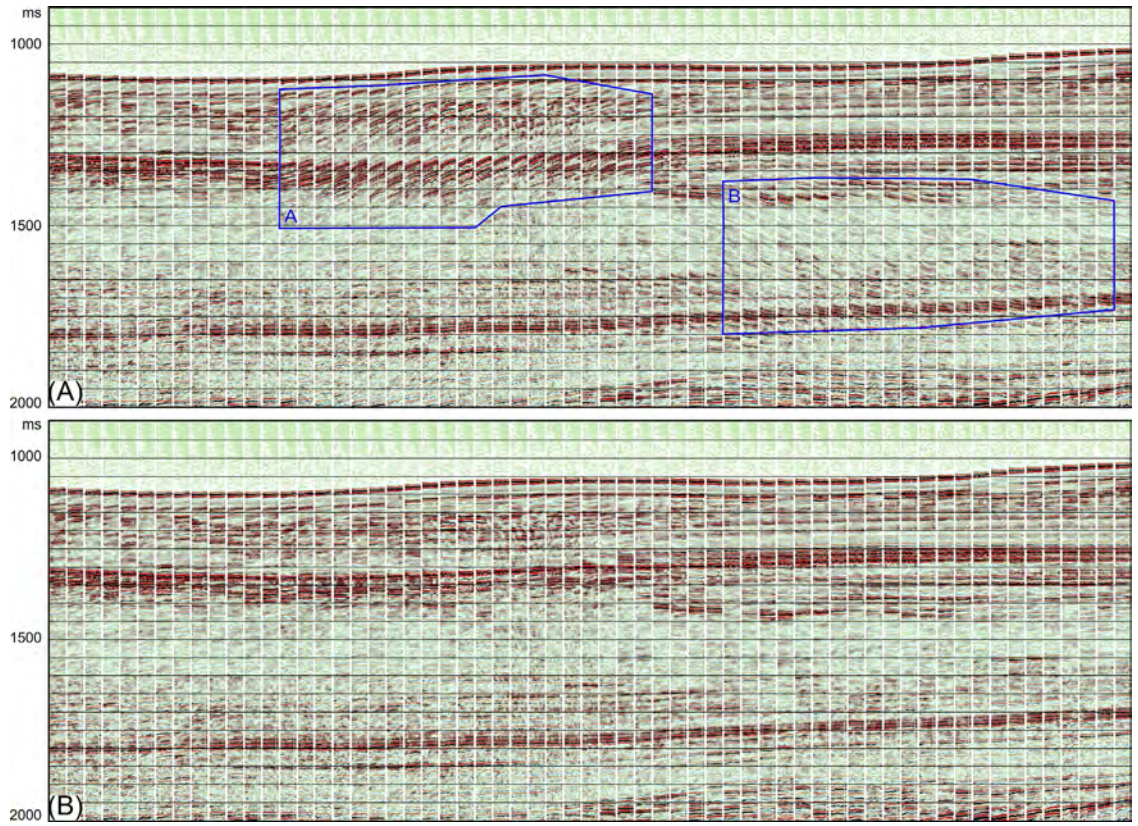


FIG. 10.29 (A) A number of successive NMO corrected CDPs. The reflections in *blue* polygons are not flattened because of the fast velocities for polygon *A*, and slow velocities for polygon *B* used in NMO correction. (B) Same CDPs after NMO correction with the corrected velocity functions.

stacked trace (Fig. 10.30B). However, if we use lower ($V_1 = 1450$ m/s and $V_2 = 1600$ m/s, Fig. 10.30C) or higher ($V_1 = 1550$ m/s and $V_2 = 2000$ m/s, Fig. 10.30D) velocities, then the hyperbolas cannot be flattened, which induces deformations on the stacked traces after summing up all of the amplitudes during stacking. Improper flattening generally moves the dominant periods of the stacked wavelets to relatively higher periods and shifts the frequency bandwidth of the data to lower frequencies, reducing the overall temporal resolution. Furthermore, the analysis in Fig. 10.30 indicates that unflattening also affects the phase and amplitude relationship of the resultant stacked wavelet. This degradation is much more pronounced for shallow parts of the seismic data where early arrivals are much more sensitive to the small velocity errors arising when the velocities are picked.

Fig. 10.31 shows three possibilities on CDPs after NMO correction and corresponding stack sections, depending on the velocity functions used. If an accurate stacking velocity field is used in NMO correction, all of the primary reflections are flattened (Fig. 10.31A) and a suitable stack section can be achieved (Fig. 10.31D). If the velocity is higher, primaries are undercorrected (Fig. 10.31B), resulting in a degraded stack section with low S/N ratio and resolution (Fig. 10.31E). Degradation of the stack section is

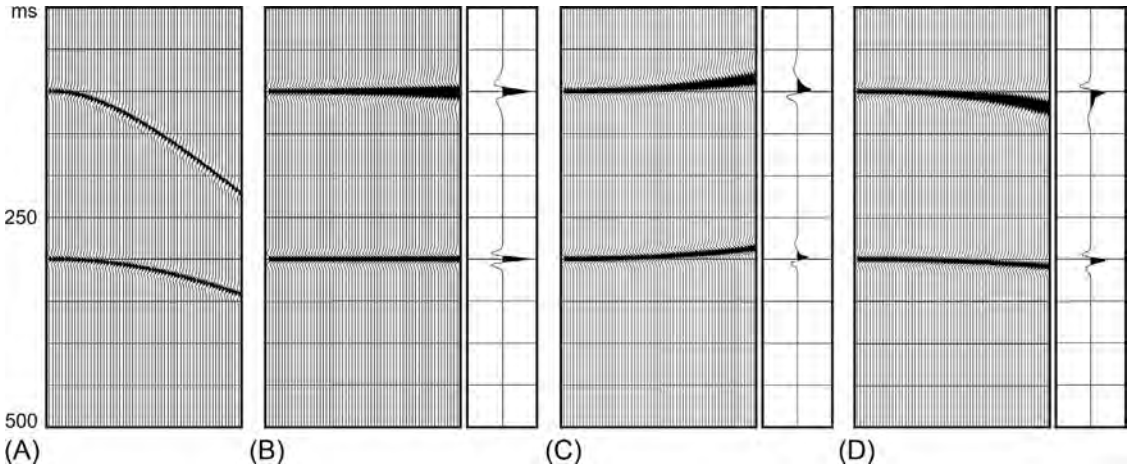


FIG. 10.30 Effect of unflattening on the stacked traces. (A) A synthetic CDP gather with two reflection events at 100 and 300 ms zero-offset time with $V_1 = 1500$ m/s and $V_2 = 1800$ m/s velocities, respectively. NMO corrected CDPs (left) and their respective stacked traces (right) with (B) correct velocities of $V_1 = 1500$ m/s and $V_2 = 1800$ m/s, (C) lower velocities of $V_1 = 1450$ m/s and $V_2 = 1600$ m/s, and (D) higher velocities of $V_1 = 1550$ m/s and $V_2 = 2000$ m/s. If the reflection hyperbolas are not perfectly flattened after NMO correction, this results in degradations in the phase, frequency and amplitudes of the stacked wavelets.

even more drastic (Fig. 10.31F) in the case of the lower velocities, resulting in overcorrection of the reflection hyperbolas (Fig. 10.31C).

Another important factor affecting the performance of the stacking and hence the quality and S/N ratio of the stack sections is NMO stretch mute percentage. Especially for shallow water data, stretch limit must be determined carefully. For a proper selection, this parameter must be tested on the selected CDPs along the line. Fig. 10.32 shows a test for the optimum NMO stretch limit on an NMO corrected CDP gather. If the limit is too high, then the quality of the stack is reduced, since degraded amplitudes of extreme low frequencies at the far offsets are incorporated in the stacking (Fig. 10.32B). If it is unnecessarily low, on the other hand, the amount of the data contributing to the stack from far offsets to enhance the S/N ratio is reduced (Fig. 10.32C). For this CDP gather, a 150% mute percentage is suitable (Fig. 10.32D).

If the S/N ratio of the data is high, a lower NMO stretch limit may be selected. For the low S/N case, however, the limit must be higher in order to incorporate more traces in the stack. To avoid data loss in far offsets of early arrivals in shallow waters, the highest possible stretch limit should be considered. The percentage of stretch limit also affects AVO analysis since it limits the maximum offset in shallow waters, shortening the effective spread length. Lack of long offsets after NMO correction causes issues during the AVO analysis, which restricts the maximum available incidence angle, and therefore a full offset of AVO response curve may not be realized. Furthermore, loss of far offsets also reduces the effectiveness of the stack in the suppression of multiples.

A considerably small stretch limit also causes data gaps as vertical strips in the stack section in the shallowest parts because the stretch mute percentage is so small that the seafloor and shallow subsurface reflections are also muted out by NMO stretch muting (Fig. 10.33). If there are vertical data gaps around the seafloor, as is the case in Fig. 10.33A, then one should consider increasing the NMO stretch limit, which causes more traces from far offsets to be involved in stacking

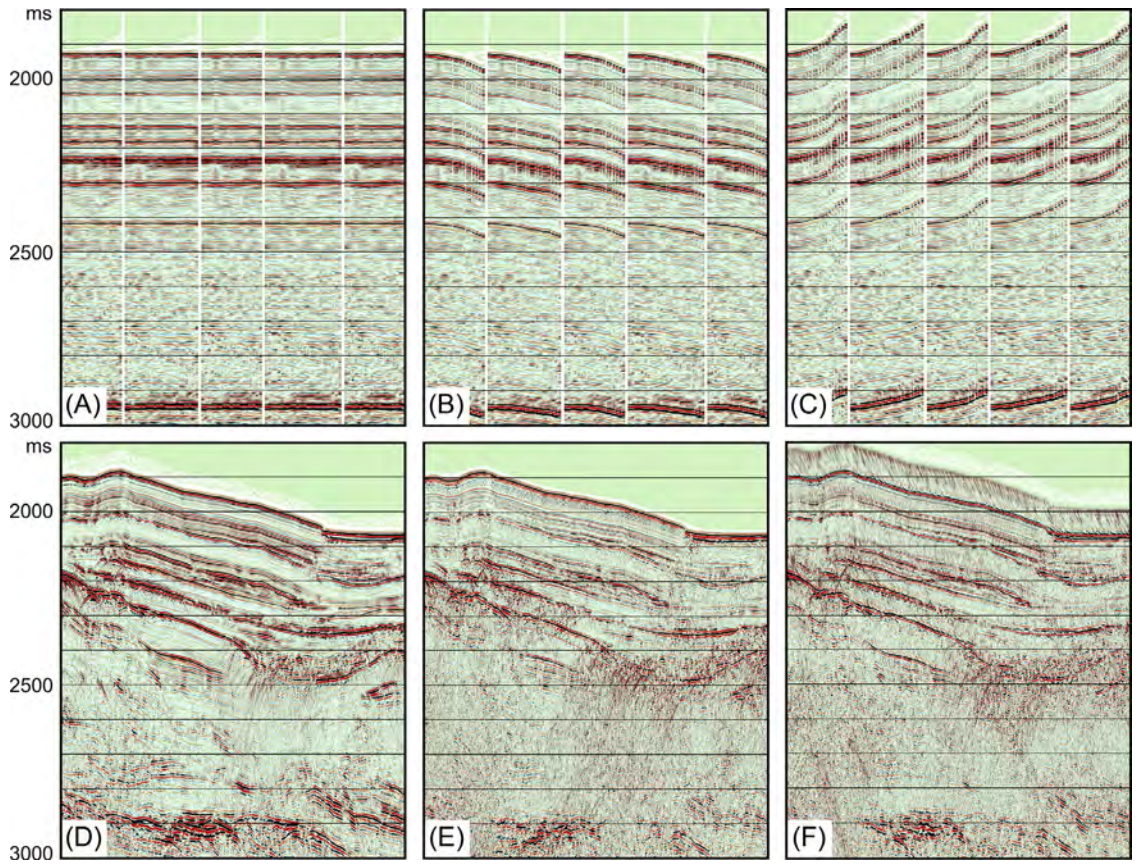


FIG. 10.31 CDP and stack examples for three possibilities after NMO correction. Five successive CDPs after NMO correction for (A) accurate, (B) 10% higher, (C) 10% lower stacking velocities, and their corresponding stack sections obtained with (D) accurate, (E) 10% higher, (F) 10% lower stacking velocities used in NMO correction.

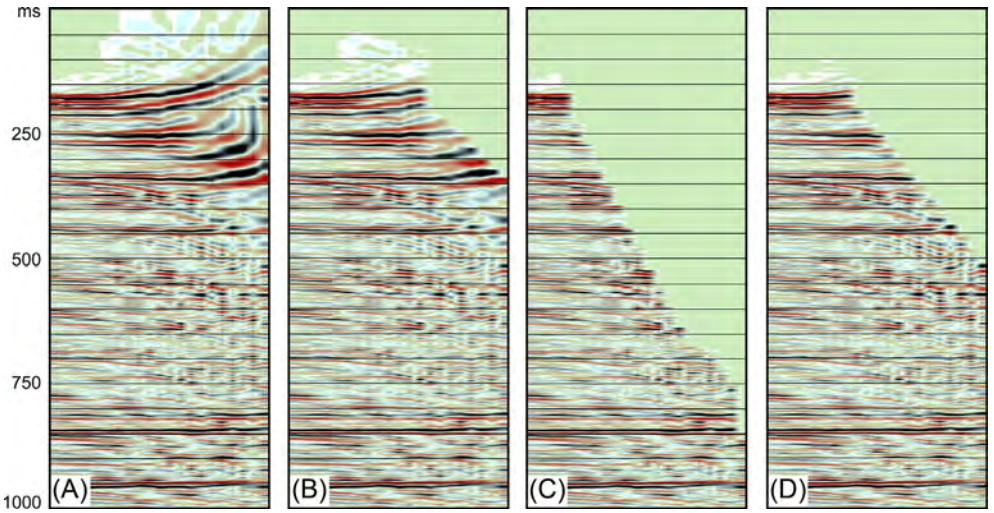


FIG. 10.32 Effect of NMO stretch mute percentage. (A) No mute, (B) high mute percentage (500%), (C) unnecessarily low mute percentage (40%), and (D) suitable mute (150%).

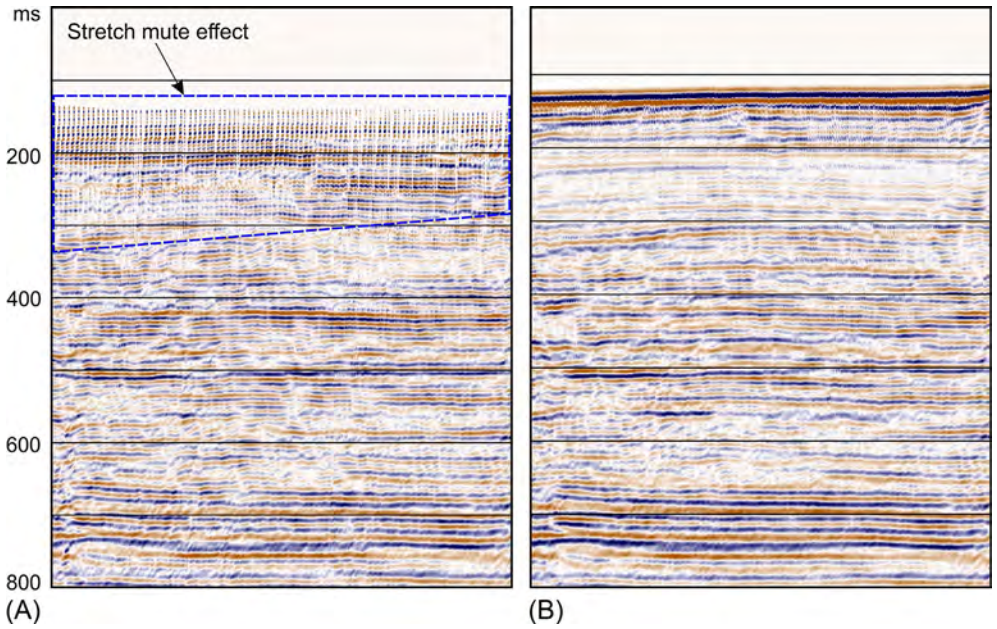


FIG. 10.33 Stack sections with NMO stretch limit percentage of (A) 20%, and (B) 60%. Small stretch limits may cause vertical gaps in the stack section around the seafloor.

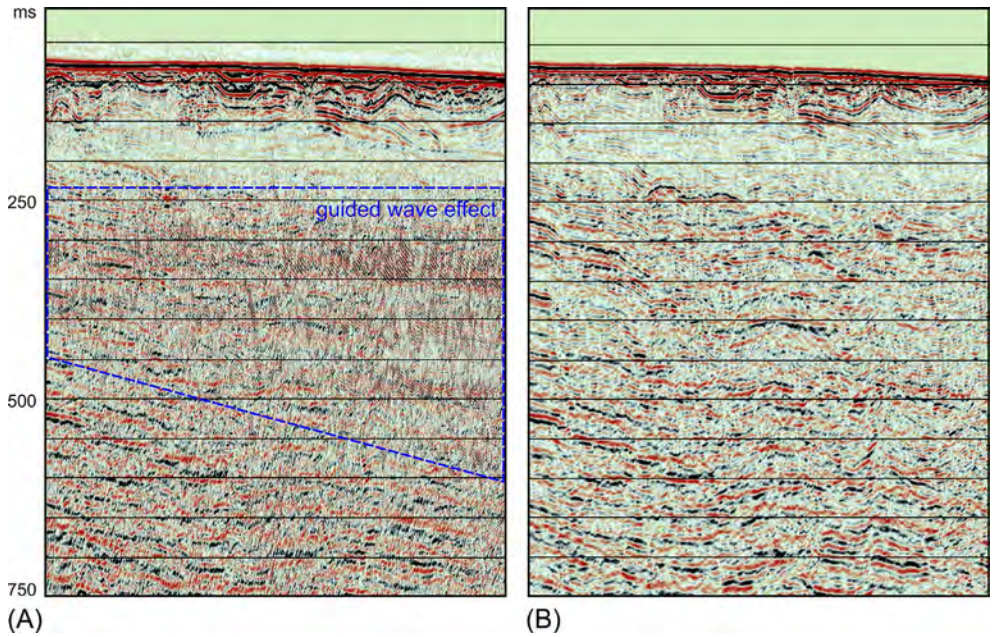


FIG. 10.34 Stack sections with NMO stretch limit percentage of (A) 90%, and (B) 40%. For higher limits, guided wave amplitudes may emanate in the stack section.

to get an acceptable stack (Fig. 10.33B). However, the increment must be determined carefully because the far offsets of shallow waters contain guided wave amplitudes in most cases. If the stretch limit is too high, then the amplitudes of these waves emanate in the stack section, as in the example data in Fig. 10.34A. Considering a stretch mute with a lower stretch

limit percentage reduces, even removes, these amplitudes (Fig. 10.34B). Consequently, there may be a trade-off between the data loss and stack quality by means of the NMO stretch mute percentage. Too-small values result in the loss of far (even near) offsets, whereas too-high limits incorporate noise amplitudes in the stack.

In shallow water data, there is a triangular data gap located at one border of the seismic line due to the NMO stretch mute. The size of this area is inversely proportional to the NMO stretch mute percentage. The gap always occurs only at the start-of-line side (Fig. 10.35A). This is because the traces in the very first CDP gathers located at the start-of-line side are always far offset traces, whereas the traces in the very last CDP gathers located at the end-of-line side are all near offset traces. Since the early arrivals of far offset traces are automatically muted out by NMO stretch mute, the early arrivals of the traces at the very first CDPs of the lines, which consist of only far offsets, are removed. This is

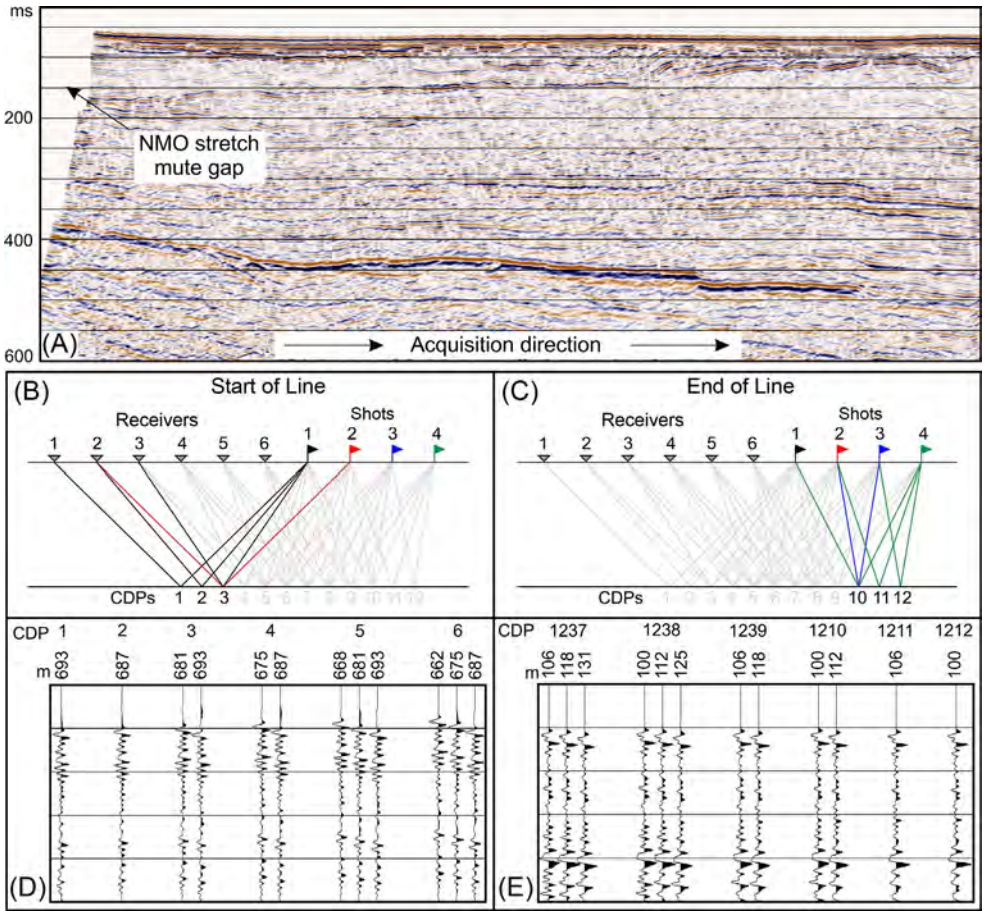


FIG. 10.35 (A) In shallow waters, NMO stretch mute results in a triangular data gap located at the start-of-line side. Schematic representation of the ray paths of the traces for (B) the very first CDPs at the start-of-line, and (C) the very last CDPs at the end-of-line. The traces in CDPs 1, 2, and 3 in (B) are composed of only far offset traces, whereas the traces in CDPs 10, 11, and 12 in (C) are composed of only near offset traces. Because NMO stretch mute removes early arrivals of far offsets, this part in the very first CDPs is completely muted out. That is why the gap in (A) always occurs only at the start-of-line side. Here, (D) and (E) show real data examples from the first and last CDPs of a small-spread marine seismic line with a 693-m maximum offset, where the trace offsets range from 662 to 693 m in the first six CDPs, while they are between 100 and 131 m in the last six CDPs.

not the case for the last CDPs, since they are composed of only near offset traces, which do not stretch after NMO correction.

This situation is schematically illustrated in Fig. 10.35. Let's consider a seismic line with only four shots recorded at six receivers. At the start-of-line in Fig. 10.35B, the first three CDPs consist of traces shown by the black and red ray paths. All traces in CDP numbers 1, 2, and 3 are recorded at the farthest three receivers, and are composed of only far offset traces. On the other hand, at the end-of-line in Fig. 10.35C, the last three CDPs consist of traces shown by the green and blue ray paths. All traces in CDP numbers 10, 11, and 12 are recorded at the nearest three receivers, and are composed of only near offset traces. Fig. 10.35D and E show real data examples from the very first and very last CDPs of a small-spread marine seismic line with a 693-m maximum offset, which indicates that trace offsets change between 662 and 693 m for the first six CDPs, while they vary from 100 to 131 m for the last six CDPs.

CHAPTER

11

Seismic Migration

OUTLINE

11.1 Migration Concept 494
11.1.1 Effects of Migration 496
11.1.2 Types of Migration 499

11.2 Kirchhoff Migration 502
11.2.1 Migration Aperture 503
11.2.2 Maximum Dip Restriction 506
11.2.3 Effect of Velocity on Kirchhoff Migration 507

11.3 Finite-Difference Migration 508
11.3.1 Depth Step Size 509
11.3.2 Effect of Velocity on Finite-Difference Migration 511

11.4 Frequency-Wavenumber (*f-k*) Migration 512
11.4.1 Stolt Stretch Factor (W) 514
11.4.2 Effect of Velocity on f-k Migration 515

11.5 Reverse Time Migration 516

11.6 Poststack Migration 519

11.7 Prestack Migration 521

11.8 Depth Migration 524

11.9 3D Migration 526

11.10 Dip Moveout 529

11.11 Which Migration to Use? 532

11.12 QC in Migration 535

Seismic migration is a process that moves the reflection events in the seismic data to their true subsurface locations both in space and time. It moves dipping reflections to their correct positions and suppresses the diffracted energy on the seismic sections based on the different approaches to wave equation solution. The main purpose is to make the seismic section similar to the geological cross-section beneath the seismic line in terms of the lateral positions, depths and structural inclinations of the reflecting layers. Migration tries to remove the effect of wave propagation in order to obtain the true image of the subsurface, and therefore it is generally

https://doi.org/10.1016/B978-0-12-811490-2.00011-6

© 2018 Elsevier Inc. All rights reserved.

RTM - Full two-wave equation
Rest - one way wave equation

expressed by the term imaging. It can be regarded as a process to improve spatial resolution of the seismic data.

Digital implementation of different migration algorithms has been used as a routine seismic processing tool since the late 1960s. Before supercomputers were involved in the processing industry, migration was applied by hand using a method known as semicircular construction, which considers the seismic amplitudes as spikes and converts them into several semicircles in a constant velocity medium (Hagedoorn, 1954). The migrated reflections were then obtained by constructively interfering semicircles. Today, several migration schemes and implementations, each using different algorithms and approaches, commercially exist on the market. In this chapter, the mathematical foundations of the migration algorithms are not addressed, and instead the practical aspects of the most common migration techniques are explained and discussed. Mathematical background can be found in Sheriff and Geldart (1995) and Yılmaz (2001), and the references therein.

It is possible to apply the migration before (prestack) or after stacking (poststack). The theory of poststack migration is applicable to stack data with identical source and receiver pairs (e.g., for zero-offset data), since stack sections are approximations to zero-offset sections. The quality and accuracy of the output image from a migration algorithm depend on

- algorithm used
- quality of the stack section for poststack migration
- *S/N* ratio of the input data, especially coherent noise and spikes
- accuracy of the velocity field used in the migration
- type of the migration (prestack or poststack, depth or time, 2D or 3D)
- spatial sampling (in case of steep dips, spatial aliasing may occur)

Most migration algorithms, excluding reverse time migration, which utilizes a full two-wave equation, are based on the solutions of the one-way wave equation, which does not handle multiples, converted waves, surface waves or noise. General assumptions for the migration process are as follows:

- All events in the seismic data are primary reflections. The data is free of multiple energy, noise components, and S waves.
- Seismic velocity is known at every sample location of the input data.
- For 2D implementation, there are no out-of-plane reflections (side-sweeps).

We definitely need to know the seismic velocity to apply the migration. Normally, the RMS velocity field obtained from regular velocity analysis primarily to use for normal moveout (NMO) correction is used to implement the migration. However, there is one significant difference between NMO and migration velocities: NMO velocity is sensitive to the dip of the reflectors, whereas the migration requires true subsurface velocity independent from the reflector inclination.

11.1 MIGRATION CONCEPT

Basically, migration is a process to replace the reflection events to their true subsurface locations on the seismic section, and it can be regarded as a process of spatial deconvolution, which tries to improve lateral resolution. This process can be explained best by an inclined reflector case, as schematically illustrated in Fig. 11.1: the zero-offset section containing the subsurface reflector segment C-D can be obtained by shooting/recording between the surface locations A and B with a zero-offset source-receiver pair (Fig. 11.1A). Then the reflector segment C-D in the subsurface is represented by the reflection C′-D′ in the zero-offset section (Fig. 11.1B).

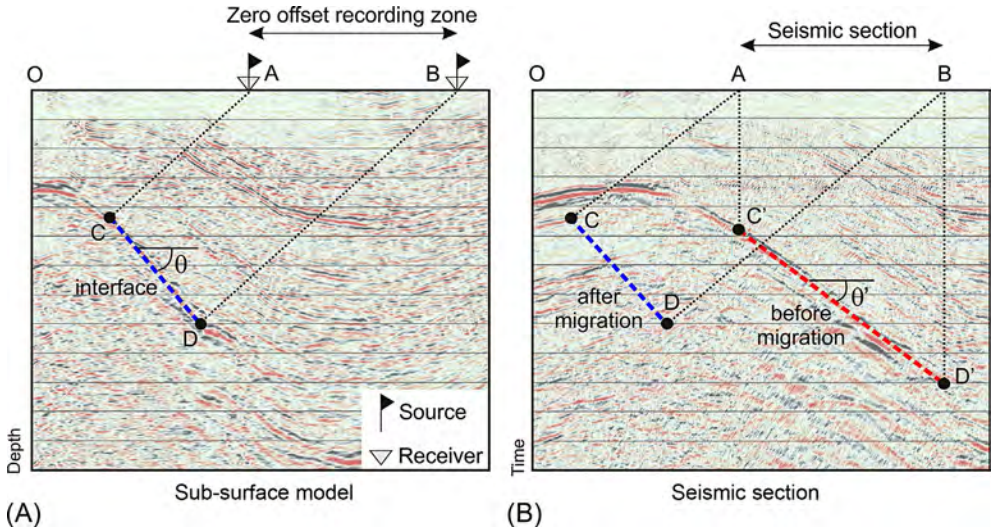


FIG. 11.1 (A) Zero-offset reflections from an interface between points C and D in the subsurface are recorded between surface locations A and B. (B) These reflections appear on the seismic section between points C′ and D′ directly beneath the surface locations A and B, and are moved to their correct subsurface locations C and D by migration.

Point C appears at point C′ below the recording location A, and point D occurs at point D′ below the recording location B. As a consequence, the reflector lying between C and D in the subsurface shows up between C′ and D′ on the zero-offset section and must be migrated to its true subsurface location C-D. Seismic data is recorded between surface locations A and B. After migration, however, reflector C-D is migrated to a location between O and A, that is, an area out of the zero-offset recording zone (the seismic line). This situation indicates that the reflections appearing on the stack sections are not restricted to involve the structures directly located on the seismic line plane. The opposite is even more important: the structure on the stack section may no longer exist on the section after migration (Yılmaz, 2001).

If the target is a reflector, such as the one between C and D in Fig. 11.1A, then the seismic line should be extended along the recording surface from A-B to O-B in order to successfully image the dipping structures after migration. If a structural dip exists in the subsurface reflectors, the seismic line must be long enough to consider the lateral displacement of the events after migration. The amount of lateral displacement increases with the recording time and is a function of the square root of the migration velocity. The extra area that must be covered due to the lateral movement of dipping reflections during the migration is referred to as migration fringe, or migration halo.

In order to replace the reflections to their correct subsurface positions, the migration algorithm swings arcs for each time sample of each trace based on the velocity of the processed time sample, in order to determine possible locations from which a reflection event has possibly originated. Let's consider a single arrival in Fig. 11.2A. This event may originate from a reflector positioned at any location on an ellipse in the subsurface between source and receiver positions, such as the ones indicated by numbers from I to IV in Fig. 11.2B as example possibilities. To find out which location is the correct one, we rely on the interference process of the amplitudes during the migration over the amplitudes

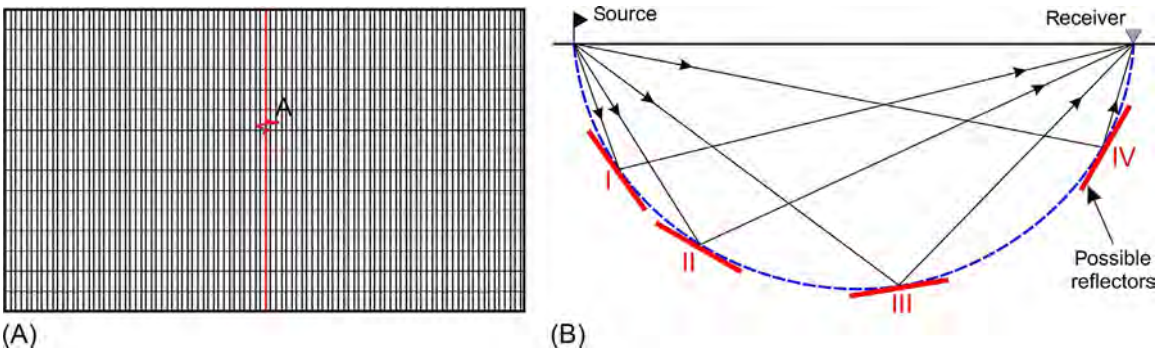


FIG. 11.2 (A) A single arrival (A) on an input data for migration. (B) The event A in (A) may originate from a reflector with an arbitrary dip and location along an ellipse (indicated by a *dashed blue curve*). Four different possibilities for reflector positions are indicated by I–IV as examples.

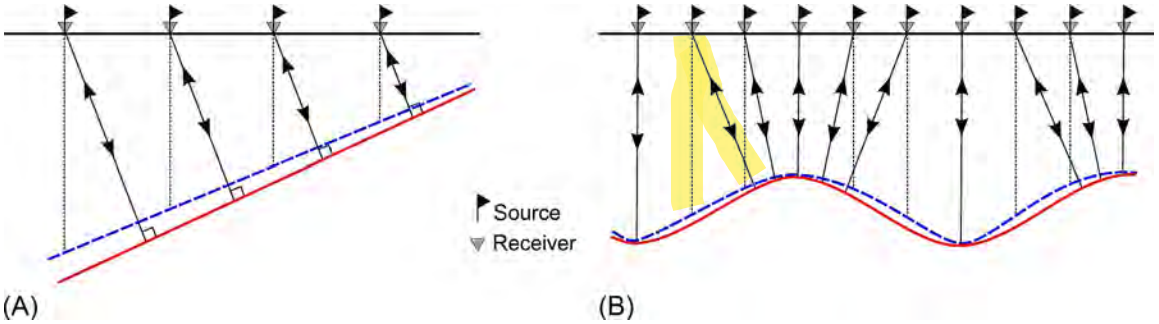


FIG. 11.3 Zero-offset ray paths on (A) inclined, and (B) undulated reflectors *(red curves)* and their incorrect representation on zero-offset seismic sections *(dashed blue curves)*. True reflection points are actually located in an updip direction for dipping reflectors, since the reflected signal is assigned to a location directly beneath the receiver location shown by the *dotted black lines*.

from several closely spaced traces. If a subsurface position is a true location of a reflection event, then constructive interference occurs among the consecutive amplitudes along the ellipse incorporating the migration process. On the other hand, amplitude degradation occurs by destructive interference if the position of the event does not correspond to the true location of a reflection, and in the ideal case, no migrated amplitude is formed in the output. As a result, the true subsurface positions of the events are preserved with a correct wave shape and amplitude by constructive interference during the migration, while the other locations are removed by destructive interference from the data.

11.1.1 Effects of Migration

The reflection from a dipping reflector is not located at its true subsurface location on the stack sections. This is because the seismic signal is not reflected back from the point exactly located beneath the receivers, but from the closest point to the source-receiver pairs and normal to the reflector in zero-offset case. This situation is schematically illustrated in the zero-offset geometry in Fig. 11.3. The zero-offset rays are

always reflected from the points perpendicular to the reflector as in Fig. 11.3A. These perpendicular reflection points move in an updip direction for dipping reflectors. During recording, however, the reflected signal from these points is assigned to a location beneath the receiver location on the seismic section shown by the black dotted lines. This situation results in a reflection with a smaller dip value (blue dashed reflector in Fig. 11.3A) than it normally should have (red reflector in Fig. 11.3A). Migration moves the reflection events to their correct reflection points in a slightly updip direction in the case of dipping reflectors.

Similar degradations occur when there is an undulating reflector in the subsurface forming syncline or anticline structures. While the tips of the anticlines are hit by denser rays, the synclines have been illuminated by a smaller number of zero-offset rays (Fig. 11.3B). Reflected signals always have a tendency to reflect back from updip directions of the dipping reflectors, but again are mapped directly beneath the receiver locations on zero-offset sections. Therefore, flanks of the anticlines and synclines are not located correctly and the anticlines appear wider while synclines are narrower on the stack sections.

The existence of synclines sometimes complicates the stack sections because of the multivalued reflections from different reflection points recorded at the same receiver. For instance, Fig. 11.4A shows a syncline model and zero-offset ray paths for five identical source-receiver pairs located on the surface. Each receiver records the signals reflected from different reflection points perpendicular to the syncline model. Because the ray paths of each reflection differ from each other, their arrival times to the same receiver also vary. Consequently, more than one reflection signal is recorded at the same receiver, each propagates different ray paths, and hence each has different arrival times, which ultimately produces a specific reflection type, termed a bow-tie on the stack sections (Fig. 11.4B). Bow ties are commonly observed in areas of rough seafloor topography and are resolved by migration.

Major effects of the migration on the seismic data can be listed as

- Synclines are broader and anticlines are narrower after migration (Fig. 11.5).
- Migration shortens the dipping reflectors, and moves them in an updip direction, resulting in a steepening (Fig. 11.6).

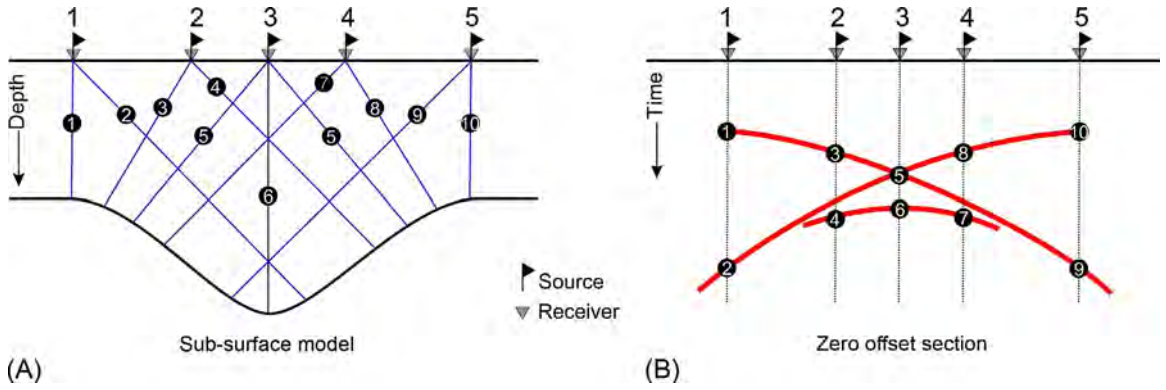


FIG. 11.4 (A) Zero-offset ray paths for identical five source and receiver pairs over a syncline model, and (B) specific reflection type called a bow-tie, formed by zero-offset rays over subsurface synclines. Numbers schematically represent the reflection arrivals of the ray numbers in (A).

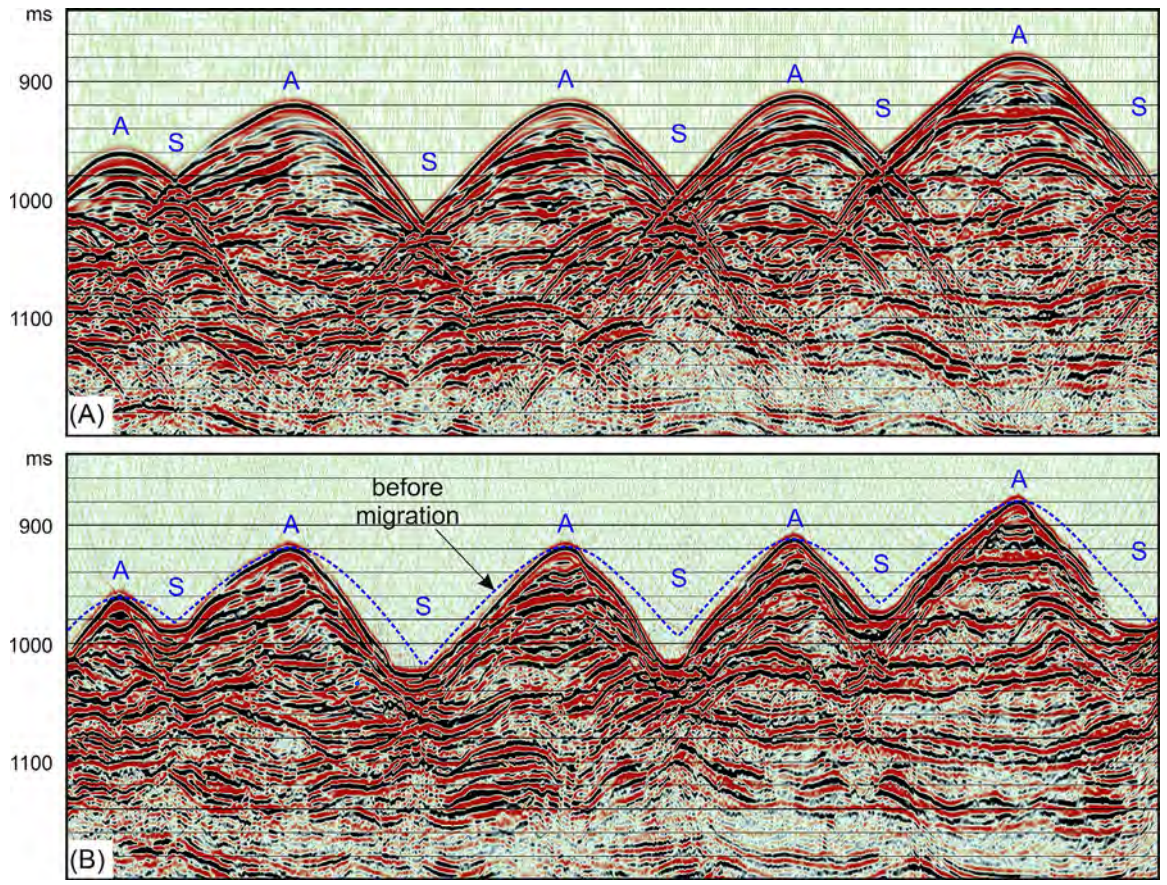


FIG. 11.5 Successive anticline A and syncline S structures (A) before and (B) after migration. The seafloor before the migration is indicated by the *dashed blue curve* in (B).

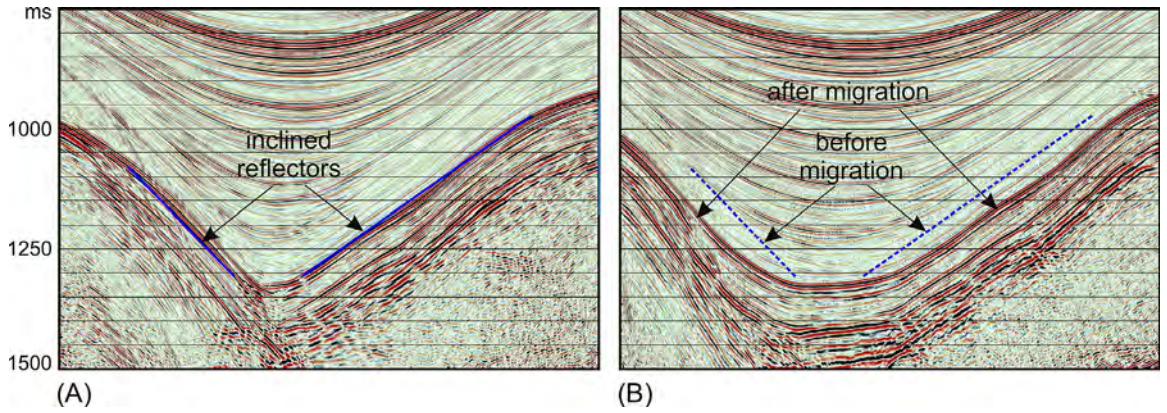


FIG. 11.6 Inclined reflectors from the flanks of a buried minibasin (A) before and (B) after migration. Reflectors are moved updip and their inclinations increase after migration.

- Migration velocities affect the apparent widths of the structures. Higher velocities result in overmigration, which makes the anticlines narrower and synclines wider (Figs. 11.5 and 11.6). The opposite occurs for slower velocities.
- Migration collapses diffractions, focusing the energy to their apex points, and fault planes become much clearer. Horizontal reflectors are not affected by migration (Fig. 11.7).
- Migration solves bow-tie effects, converting them into successive synclines and anticlines (Fig. 11.8).
- The impulse responses of 2D and 3D migrations are a semicircle and a hemisphere, respectively (Fig. 11.9). Thus, if there are high-amplitude bursts or spikes in the data, they will turn into semicircles after migration.

11.1.2 Types of Migration

Today there are several different migration types implemented in time or depth domains applied to the input data in different processing stages, such as before or after stacking. Actually, migration algorithms can be implemented in the time or depth domain for poststack or prestack seismic data, using different algorithms. For instance, the migration types that use RMS velocities and do not consider the ray bending across the layer boundaries are known as time migrations, whereas those use interval velocities and consider the ray bending are termed depth migrations. Despite the fact that time migration has been widely used as an imaging algorithm in the industry until the last two decades, depth imaging has become more attractive in recent years with the latest developments in computer technology and capacity of new-generation computers.

Before the introduction of computers to seismic data processing, migration was performed graphically. Today, several different algorithms exist, which can be grouped as three main categories, each solving the scalar wave equation using different approaches:

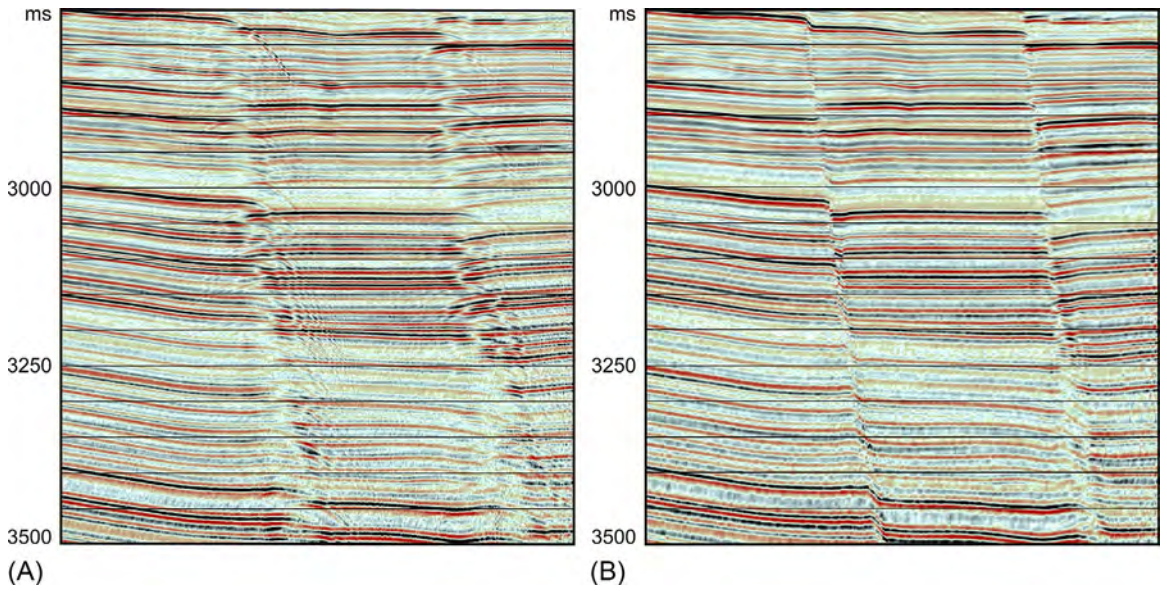


FIG. 11.7 A zero-offset section with steeply dipping normal faults (A) before and (B) after migration. Diffractions along the fault planes are collapsed by migration while horizontal reflectors are not affected.

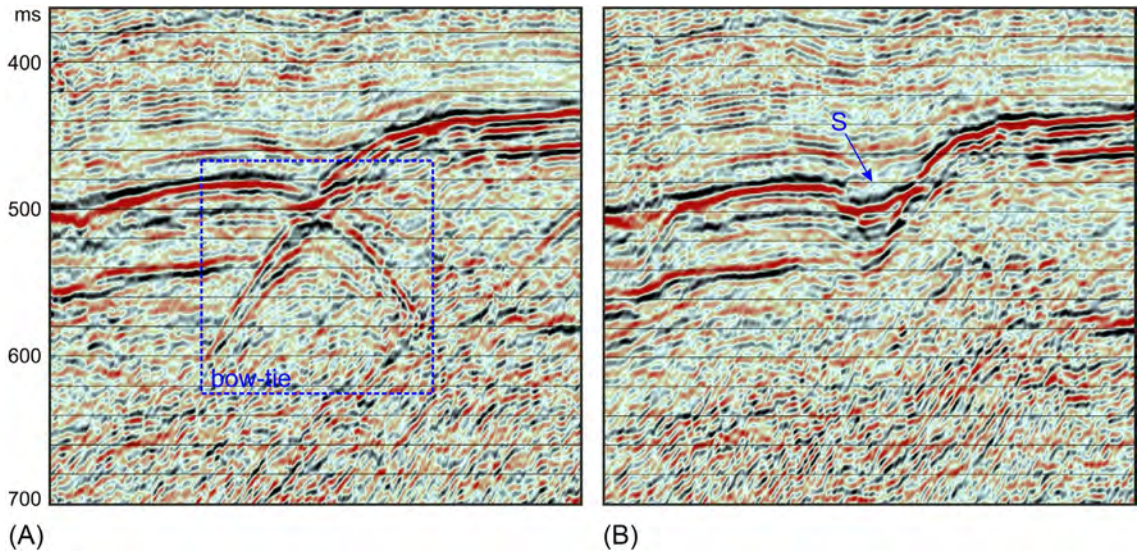


FIG. 11.8 A zero-offset section with a bow-tie effect (A) before and (B) after migration. Migration solves the bow-tie and converts it into a syncline S.

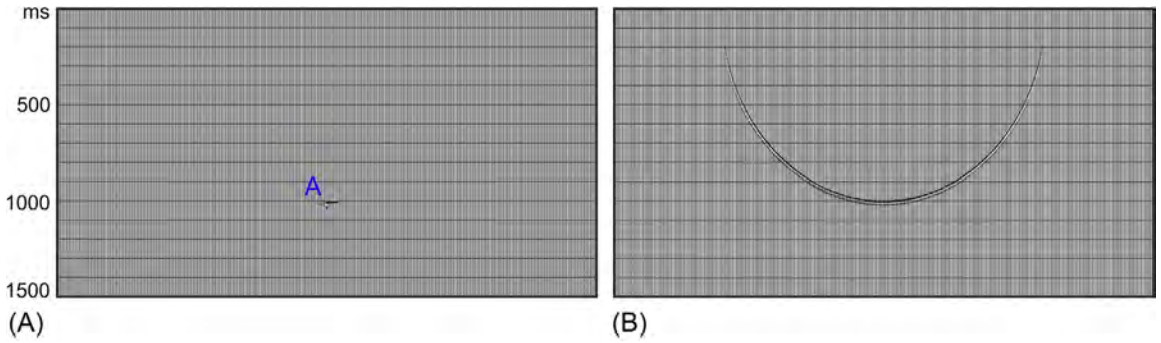


FIG. 11.9 (A) A constant velocity zero offset section consisting of a spike A. (B) Migration impulse response obtained after a Kirchhoff poststack time migration.

- Methods based on the finite-differences solution
- Integral or diffraction summation methods
- Fourier transform methods.

Migration algorithms utilizing these three approaches often take their names from their authors (Stolt, Gazdag) or the type of solution they apply (integral, finite-difference, reverse time, omega-x, etc.). Following the computer implementations, the diffraction summation method to solve the wave equation in the digital domain was developed. The basis of this method is to sum the amplitudes along a diffraction hyperbola whose curvature is controlled by the velocity of the medium. Following this approach, Schneider (1978) implemented the Kirchhoff summation method based on the integral solution of the scalar wave equation, which is one of the most common algorithms used by

both the industry and academia today. Another well-known migration algorithm, suggested by Claerbout and Doherty (1972), is based on the downward continuation of the seismic wave field and is known as finite-differences migration, which is based on the numerical solution of the scalar wave equation by the finite-differences method. Stolt (1978) introduced migration by Fourier transform as the fastest migration algorithm used today, which is known as the Stolt migration or the frequency-wavenumber (*f-k*) migration. Another *f-k* migration is the phase shift migration, or Gazdag migration, implemented by Gazdag (1978). Today, one of the most common and robust migration algorithms used by the seismic industry to image structurally complex areas, such as zones with salt intrusions, is reverse time migration (RTM), introduced by Baysal et al. (1983), in which the wave field is extrapolated backwards in time, employing an exploding reflector model for poststack migration. In the last decade, the application of RTM to 3D seismic surveys has become possible in conjunction with a rapid increase in computer hardware power.

The most common migration algorithms used in the oil and gas industry and academic environments today based on these approaches are listed in Table 11.1. Each of these algorithms has its own advantages and shortcomings. For instance, Kirchhoff migration produces good results even for 90-degree structural dips, yet it has restrictions regarding the lateral velocity variations. Finite-difference migrations produce acceptable results only up to 35-degree structural dips; however, they are not affected by lateral velocity variations (Yılmaz, 2001). Although *f-k* migrations such as the Stolt algorithm are faster than other methods, they cannot handle both vertical and horizontal velocity variations (Table 11.1). A practitioner must select the most appropriate migration type based on the requirements and complexity, as well as *S/N* ratio, of his input data.

TABLE 11.1 Different Migration Algorithms and Their Specifications, Advantages, and Shortcomings (0, Bad; 1, Average; 2, Good; 3, Superior)

Algorithm	Method	Domain	Velocity Type	$V(x)$	$V(z)$	Steep Dip
Stolt	Frequency-wavenumber	Time	V_{RMS} (x,t)	0	0	1
Phase shift (Gazdag)	Frequency-wavenumber	Time	V_{RMS} (x,t)	None	2	2
Omega-*x*	Finite difference	Time	V_{INT} (x,t)	1	2	2
Explicit finite difference-time	Finite difference	Time	V_{INT} (x,t)	1	2	1
Explicit finite difference-depth	Finite difference	Depth	V_{INT} (x,z)	2	2	2
Kirchhoff-time	Diffraction summation	Time	V_{RMS} (x,t)	1	2	2
Kirchhoff-depth	Diffraction summation	Depth	V_{INT} (x,z)	2	3	3
Prestack Kirchhoff-time	Diffraction summation	Time	V_{RMS} (x,t)	2	2	2
Prestack Kirchhoff-depth	Diffraction summation	Depth	V_{INT} (x,z)	2/3	3	3
Reverse time	Finite difference	Time	V_{INT} (x,z)	2	3	3
Reverse time TK	Finite difference	Time	V_{INT} (x,z)	None	3	3

V_{INT} (x,z) is interval velocity in depth, V_{RMS} (x,t) is RMS velocity in time, and $V(x)$ and $V(z)$ are lateral and vertical velocity variations, respectively.

11.2 KIRCHHOFF MIGRATION

Kirchhoff migration is based on the integral solution of the scalar wave equation and can handle both horizontal and vertical velocity variations. It is one of the most common migration algorithms used in the processing industry today and can be implemented in 2D and 3D data for prestack and poststack processing stages, either in the time or depth domains. Most of the prestack depth migration applications use the Kirchhoff migration.

In general, the Huygens principle is used to define the basis of Kirchhoff migration, where the reflectors in the subsurface can be regarded as consisting of several contiguous point sources, each generating a diffraction hyperbola recorded at several receivers on the earth surface. It is assumed that recorded zero offset sections are the summation of these hyperbolas after constructive or destructive interference between amplitudes of each specific hyperbola originating from a different point source on the reflector. Kirchhoff migration sums the amplitudes over the diffraction hyperbolas and assigns this summed amplitude to the apex of the hyperbola. This is the search of the energy in the output field if it originates from a diffraction in the input field. Curvature of the diffraction hyperbolas is controlled by RMS velocity at the apex and can be calculated by Eq. (9.10). This process is schematically illustrated in Fig. 11.10, where the amplitudes along the flanks of the hyperbola (B) are summed up to assign the apex point (A), and this process is repeated for all samples of all traces in the input section. The amplitude and phase relationship in the migrated output is calculated by the integral solution of the wave equation.

The most important parameter to be properly predetermined before Kirchhoff migration is the

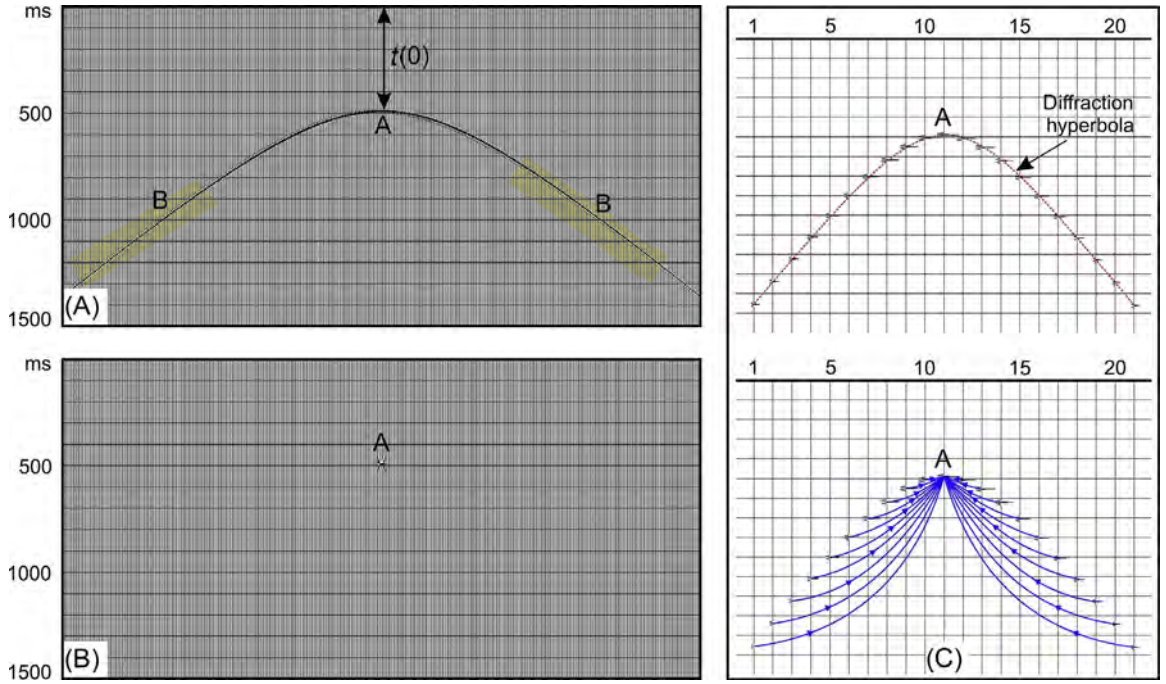


FIG. 11.10 Schematic representation of collapsing a diffraction hyperbola by Kirchhoff migration. (A) A diffraction hyperbola in a constant velocity zero-offset section. Apex and flanks of the hyperbola are indicated by A and B, respectively. (B) Migration result of (A). (C) Amplitudes along the flanks B are moved to the apex point A after migration.

migration aperture, which directly controls the quality and accuracy of the migrated output as well as the run time of the diffraction summation algorithm. Although Kirchhoff migration can handle steep dips up to 90 degrees, it is also possible to restrict the algorithm by means of the maximum structural dip to migrate, which may reduce the computational cost. Kirchhoff migration is sensitive to velocity errors and the velocity analysis must be performed carefully to obtain an accurate 2D or 3D velocity field before the migration. If a Kirchhoff depth migration is run, then the RMS velocity field must be converted into an interval velocity field by the Dix equation, using Eq. (9.9), and several tests must be performed before the migration to ensure that the velocity model used as an input to the depth migration algorithm is accurate.

11.2.1 Migration Aperture

Kirchhoff migration performs a summation over the theoretical diffraction hyperbolas along the seismic data. However, diffraction hyperbolas theoretically extend to infinite time lengths and distances. Since it is impossible to work on such infinite theoretical hyperbolas, they are truncated in the space dimension in practice. The spatial extent of the diffraction hyperbola that the actual summation path spans is termed the migration aperture or the aperture width, and is defined as the number of traces involved in the computation or the maximum horizontal distance that the diffraction hyperbola extends (Fig. 11.11A). The shape of the hyperbola is governed by the velocity at the apex. For a simple medium with vertically increasing velocity, a diffraction hyperbola with a slower velocity also has a smaller aperture width than the hyperbola with a faster velocity (Fig. 11.11B). This means that if the velocity simply increases with depth, wider apertures are required to collapse the deeper diffraction hyperbolas by Kirchhoff migration.

In practice, the velocity varies at least in the vertical direction, which makes the aperture widths time dependent (Fig. 11.11B). In this case, the shallower parts of a seismic section

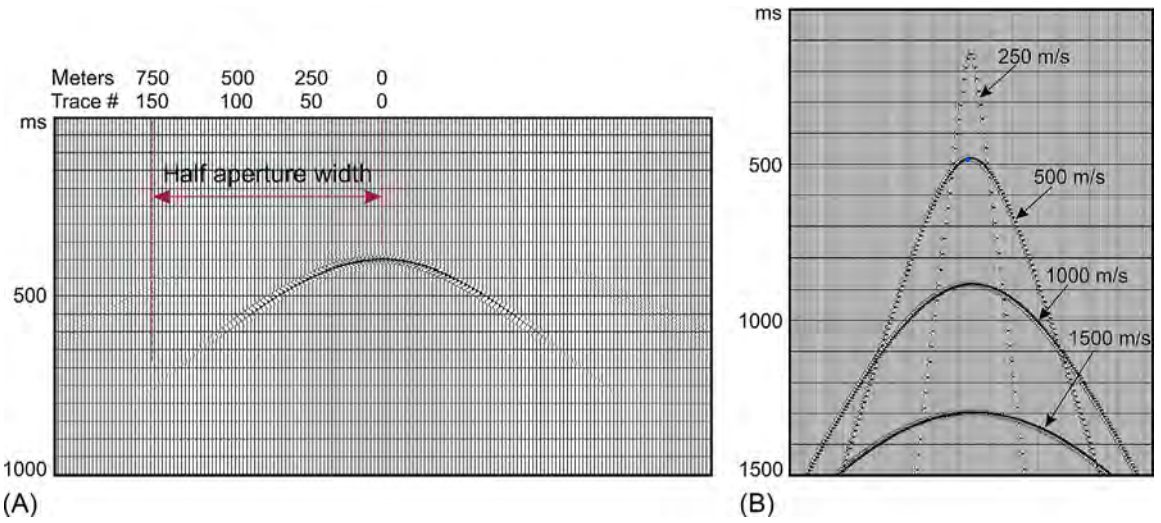


FIG. 11.11 (A) Migration aperture is the number of traces, or maximum lateral distance, that a diffraction hyperbola involved in the migration computation extends. (B) Curvature of the hyperbola is controlled by the velocity of the medium. In a vertically increasing velocity field, apertures of the hyperbolas for slower velocities in relatively shallow subsurface depths are much narrower.

require relatively narrow apertures, whereas much wider aperture widths are necessary for deeper parts. Since wider aperture, or higher velocity, denotes more migration, deeper events are migrated more than shallower events, providing a constant dip. This situation results in the Kirchhoff migration being effective in a conical area termed the migration cone (Fig. 11.12). In some cases, degradations may arise in areas close to the edges of the migrated section outside of the migration cone. Since the effective area gets narrow towards the deeper parts of the seismic sections, relatively short lines are avoided to apply Kirchhoff migration, since its effective area in deeper parts will be extremely narrow.

The effectiveness of Kirchhoff migration is directly proportional to the aperture width: wider apertures lead to better lateral resolution in the migration output. On the other hand, the run time of the algorithm also significantly increases as the aperture width increases. Unnecessarily high apertures require too much computational time and hence may not be economical. Therefore, an optimum migration aperture, which is sufficiently large for an effective migration but small enough to prevent unnecessarily long computational time, must be used. It must be approximately twice the migration halo distance. To determine the optimum aperture value, average widths of the diffraction hyperbolas on the stack sections can be computed to use as an initial aperture width for tests on a small portion of the input dataset. For a specific reflection event with a dip of θ and a depth of h, the aperture width d can be computed from

$$d = h/\tan\theta \tag{11.1}$$

Migration aperture is also important in collapsing the diffraction hyperbolas. Fig. 11.13 shows applications of Kirchhoff migration with different aperture widths to collapse of a theoretical diffraction hyperbola in a constant velocity medium. For small aperture widths, migration is ineffective to suppress the diffraction hyperbola. A migration with a small aperture, however, acts as a dip filter and removes steeply dipping events from the data, because the steep flanks of the hyperbolas are ignored in the diffraction summation process for small apertures.

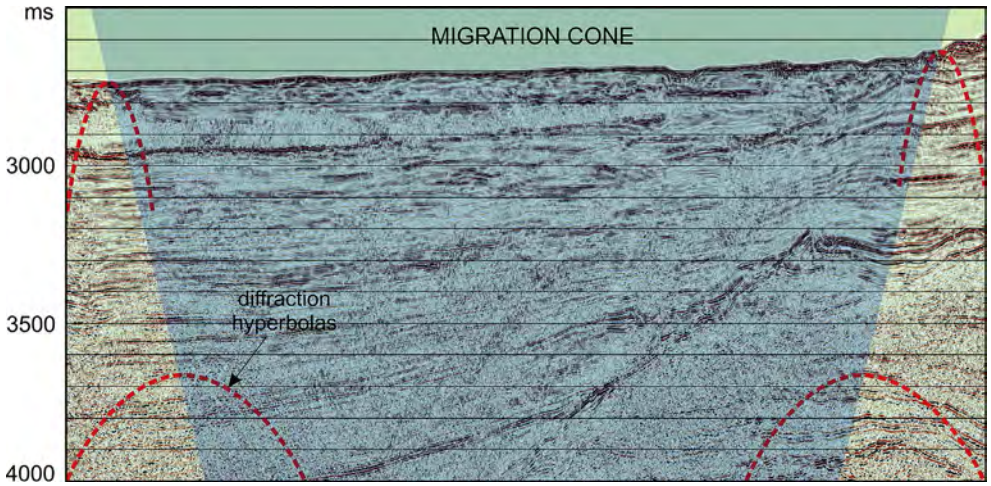


FIG. 11.12 Kirchhoff migration is effective in a conical area on the input data (*shaded zone*) because the theoretical diffraction hyperbolas, along which the summation is performed, widen towards the deeper parts of the section due to the vertically increasing velocity.

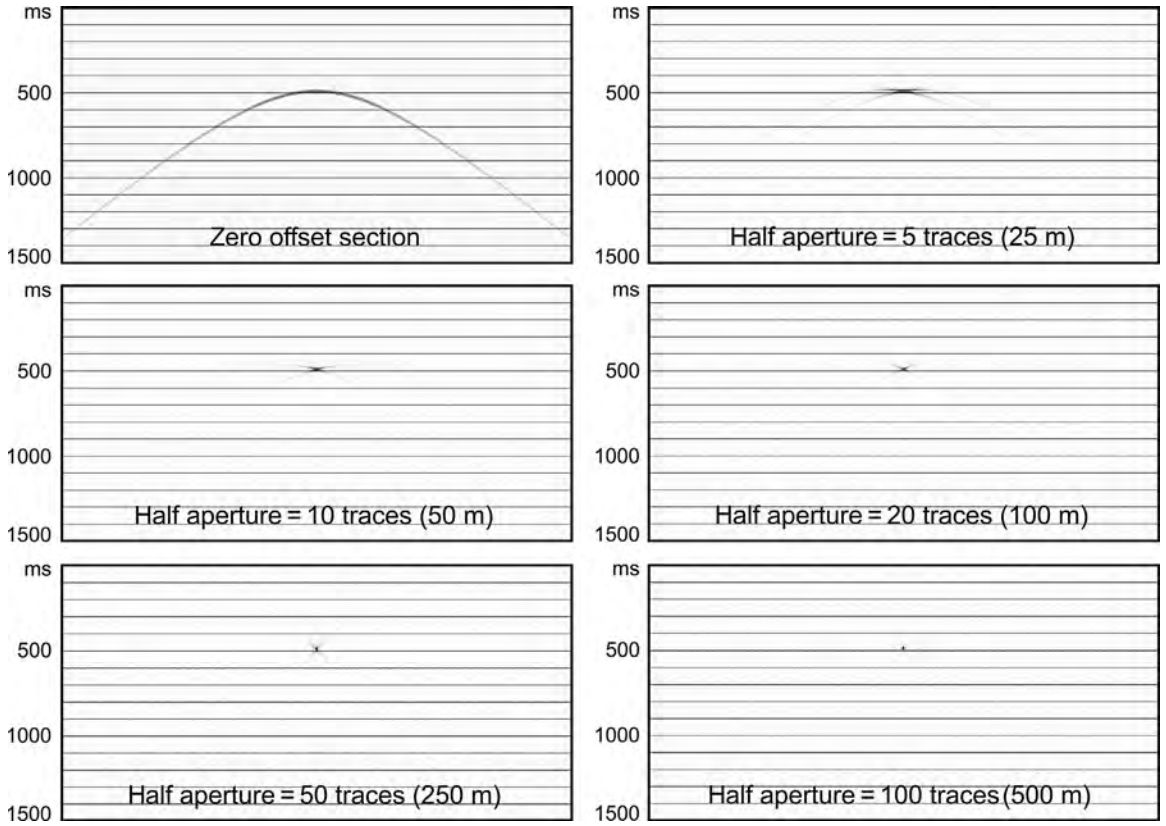


FIG. 11.13 Effect of migration aperture on the collapse of diffraction hyperbolas by Kirchhoff migration.

Fig. 11.14 shows the effect of migration aperture on the collapse of diffractions on real seismic data using a poststack Kirchhoff time migration. Too-small apertures cause total loss of steep dips, like the flanks of the diapiric structure, and random noise, especially at the deeper parts of the data, is converted into spurious horizontal events. Too-large apertures simply cause too much computational time. Therefore, an optimal aperture width must be selected to ensure the quality of the output image, which generally requires several tests before the production processing. In addition, it is recommended that the aperture width is kept similar for whole surveys in a particular area to keep the amplitude specifications of all surveys similar for a possible comparison of different seismic sections.

Migration with a small aperture causes spurious subhorizontal events at the deeper parts of the sections, known as smearing. These are especially significant at late arrivals of a section where the primary reflection amplitudes diminish and random noise becomes dominant. This situation is illustrated in Fig. 11.15, where a zero-offset section consisting of only random noise is migrated using poststack Kirchhoff time migration. For an aperture width of 50 m in Fig. 11.15B, distinct horizontal events appear in some areas, especially those deeper than 1000 ms, whereas there is no smearing in the migration output with the 500-m aperture in

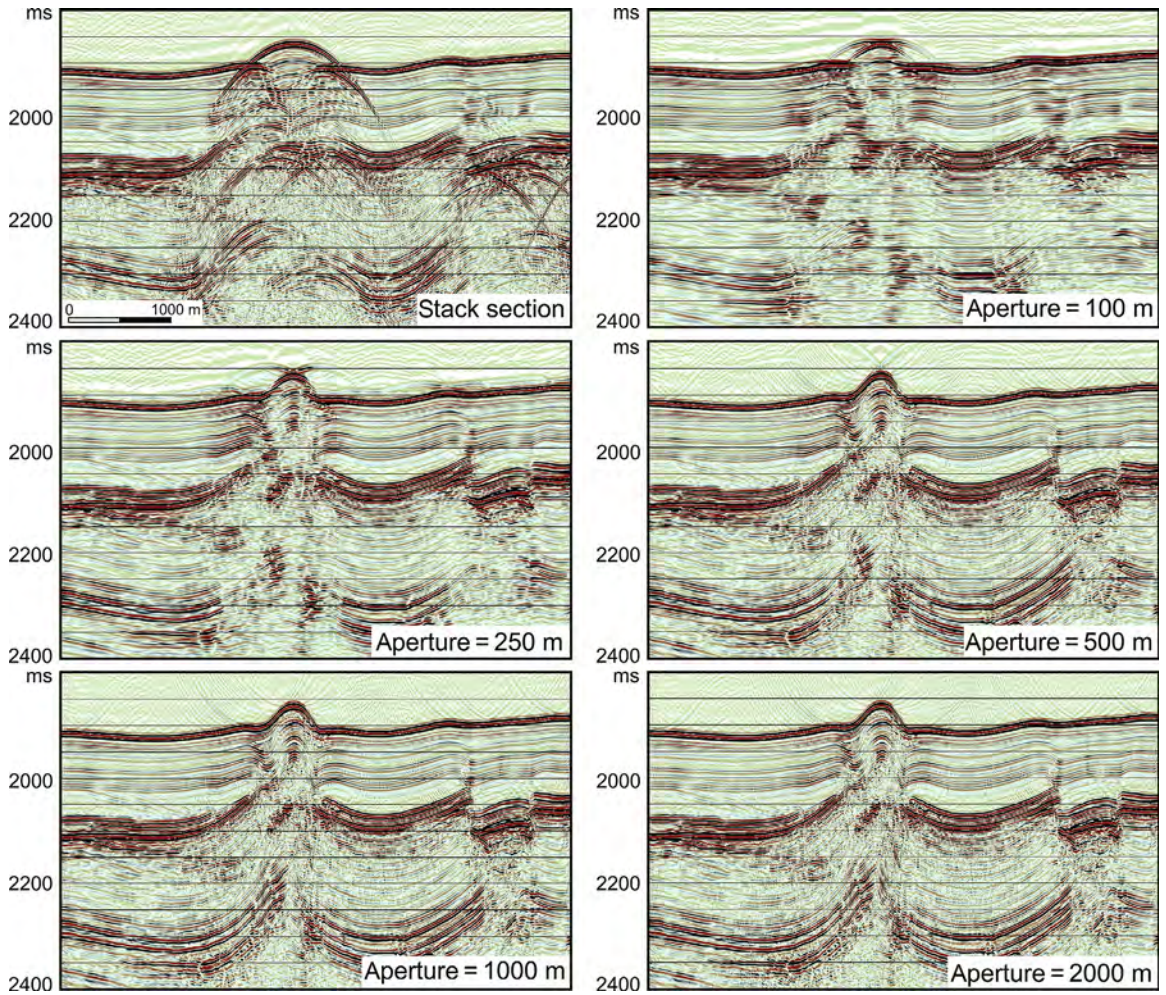


FIG. 11.14 The effect of migration aperture on the output of a poststack Kirchhoff time migration. Unnecessarily small apertures cause loss of steeply dipping events, such as the flanks of the diapiric structure at the center.

Fig. 11.15C. In conclusion, small apertures cause suppression of steeply dipping events and results in fake subhorizontal events, especially in the deeper parts of the section. In addition, an unnecessarily large aperture significantly increases the computational time of the migration and may degrade the output image quality in the shallower region of the data, when the S/N ratio of the input is low.

11.2.2 Maximum Dip Restriction

The maximum dip desired in the migration output can be defined during the Kirchhoff migration process, which can be used to suppress steeply dipping coherent noise. Restriction of the dip is a method to reduce the run time of the migration, since the dip parameter is related to the migration aperture. The smaller the maximum allowed dip, the narrower the migration

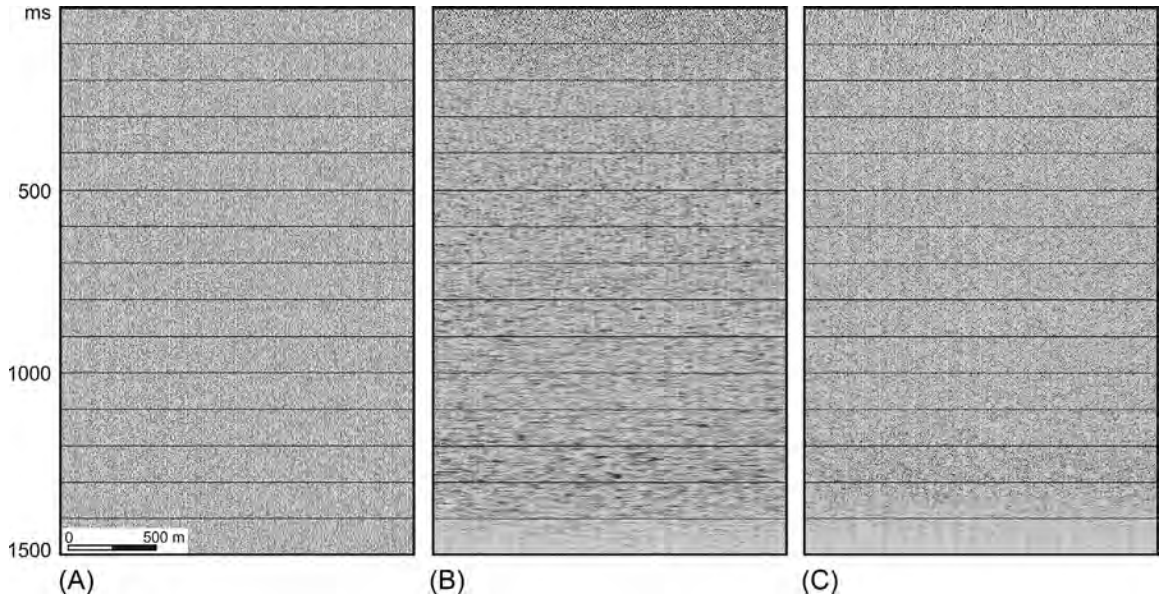


FIG. 11.15 Small apertures induce spurious horizontal events, termed smearing, at the deeper parts where the random noise is dominant. (A) A zero-offset section consisting of only random noise and its Kirchhoff poststack migration results for aperture widths of (B) 50 m, and (C) 500 m.

aperture. The flanks of the theoretical diffraction hyperbolas used for the summation during Kirchhoff migration are truncated beyond the maximum dip value.

An example 2D seismic line with different maximum dip restrictions is shown in Fig. 11.16. The effect of dip restriction is especially significant in areas of steep dips, such as the events located at the rightmost part of the section. For 10- and 20-degree dip limit, these dipping reflections are completely filtered by the migration. Migration output with 40-degree dip limit, however, produces almost the same result as the migration with no dip restriction. If the maximum structural inclination in the data is 40 degrees, then it is computationally effective to apply a 40-degree dip limit migration. Maximum allowable dip tests can be carried out for the areas of steep dips in the seismic data to determine the suitable maximum dip value.

11.2.3 Effect of Velocity on Kirchhoff Migration

Effectiveness and accuracy of all migration algorithms depend on the accuracy of the velocity field used. A slower velocity causes undermigration, where the diffraction hyperbolas are not collapsed properly and "frowns" occur in the final image. The inclined events are not relocated to their accurate lateral positions and bow-tie effects cannot be perfectly solved. Inversely, a faster velocity results in overmigration, where the diffraction hyperbolas turn into "smiles" and the inclined events are migrated too much in an updip direction. Fig. 11.17 shows the collapse of a diffraction hyperbola in a constant-velocity medium using Kirchhoff migration, and Fig. 11.18 illustrates the effect of 10% lower and 10% higher velocity on the migration output of marine seismic data.

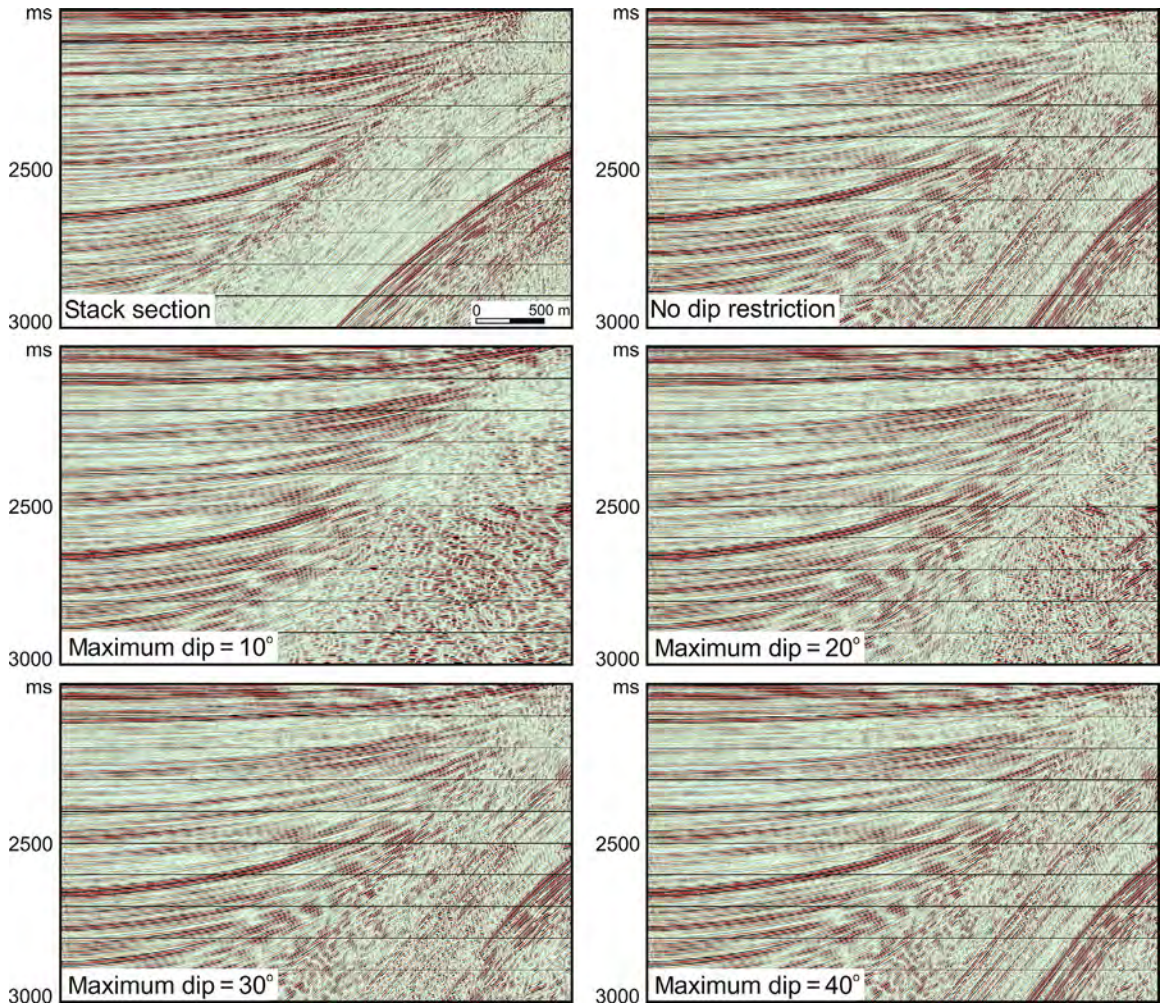


FIG. 11.16 The effect of maximum dip restriction on the output of poststack Kirchhoff time migration. For 10- and 20-degree dip limit, steeply dipping events are completely filtered out.

11.3 FINITE-DIFFERENCE MIGRATION

Finite-difference migration, based on the numerical solution of the scalar wave equation by the finite-difference method, either using an explicit or implicit finite-difference approach, was introduced by Claerbout and Doherty (1972). It can handle both vertical and horizontal velocity variations and produces good results up to a 35-degree structural dip. Its theoretical basis consists of the downward continuation of the recorded wave field, which is equivalent to the downward movement of the receivers into the subsurface (Claerbout, 1985). A point source at depth produces signals recorded as diffraction hyperbolas at the receivers along the surface. If we move the receivers downwards in finite depth steps, and shorten the spread length during the downward movement, the

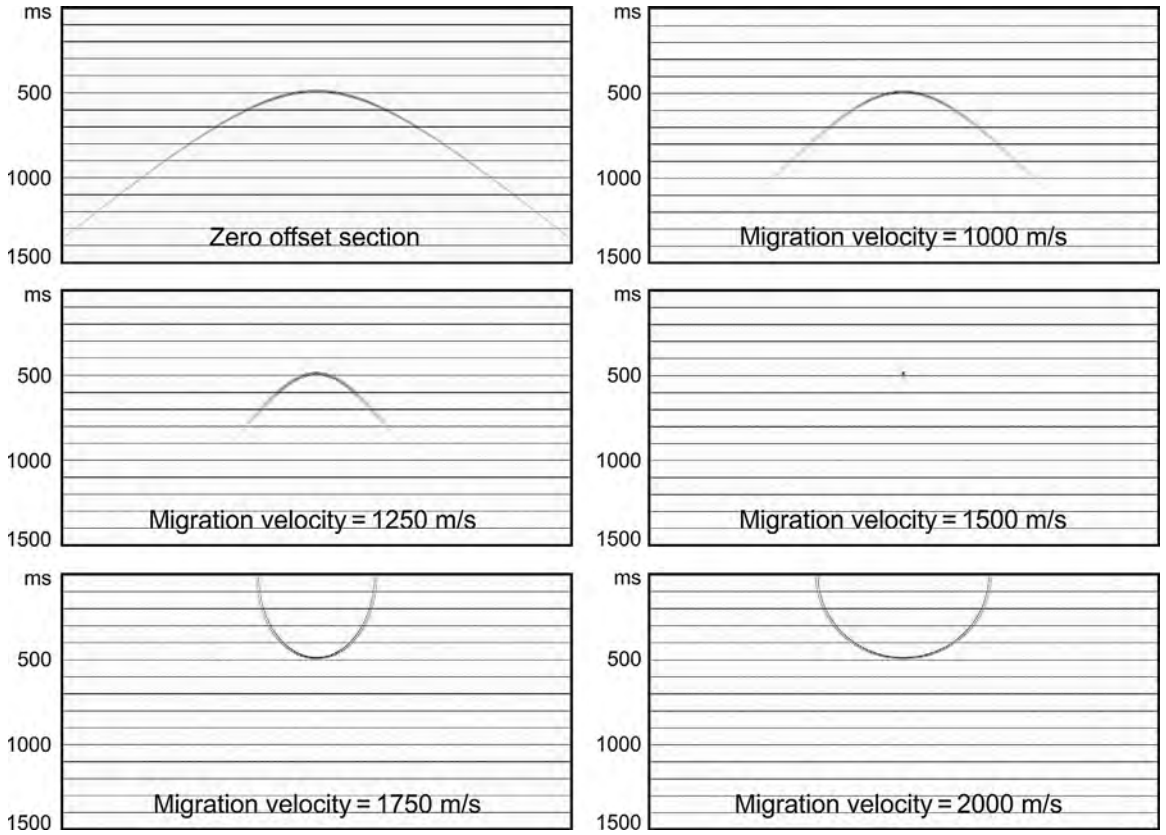


FIG. 11.17 The effect of migration velocity errors on the collapse of a diffraction hyperbola in a constant velocity medium by poststack Kirchhoff time migration. Velocity of the zero-offset section is 1500 m/s. Over- and undermigration occur when the migration velocity is faster or slower than the actual velocity of the medium, respectively.

diffraction hyperbolas shorten and arrive earlier (Fig. 11.19). When the receivers arrive at the apex, the hyperbola is completely collapsed to a single point at $t = 0$ ms (Fig. 11.19C). An undermigration occurs and the hyperbola cannot be collapsed perfectly if the downward continuation is completed before the source depth is reached (Fig. 11.19B). The same situation also occurs when a slower velocity for the migration is used. Inversely, if the downward continuation is continued after the source depth is reached, then a mirror image of the diffraction hyperbola is obtained and an overmigration occurs (Fig. 11.19D and E), such as occurs in the case when a faster velocity for the migration is used.

11.3.1 Depth Step Size

Computation of the wave field towards the depth is achieved by discrete depth steps, which determine the performance and effectiveness of the finite-difference migration algorithm. Fig. 11.20 shows the effect of depth step size on the collapse of a theoretical diffraction hyperbola. The minimum depth step size is the sampling rate of the input. Higher depth step sizes result in undermigration and the diffraction hyperbolas cannot be collapsed. Yılmaz (2001) suggests that this situation also results in kinks and a specific noise called dispersion along the flanks of the diffraction hyperbola.

due to higher depth step size

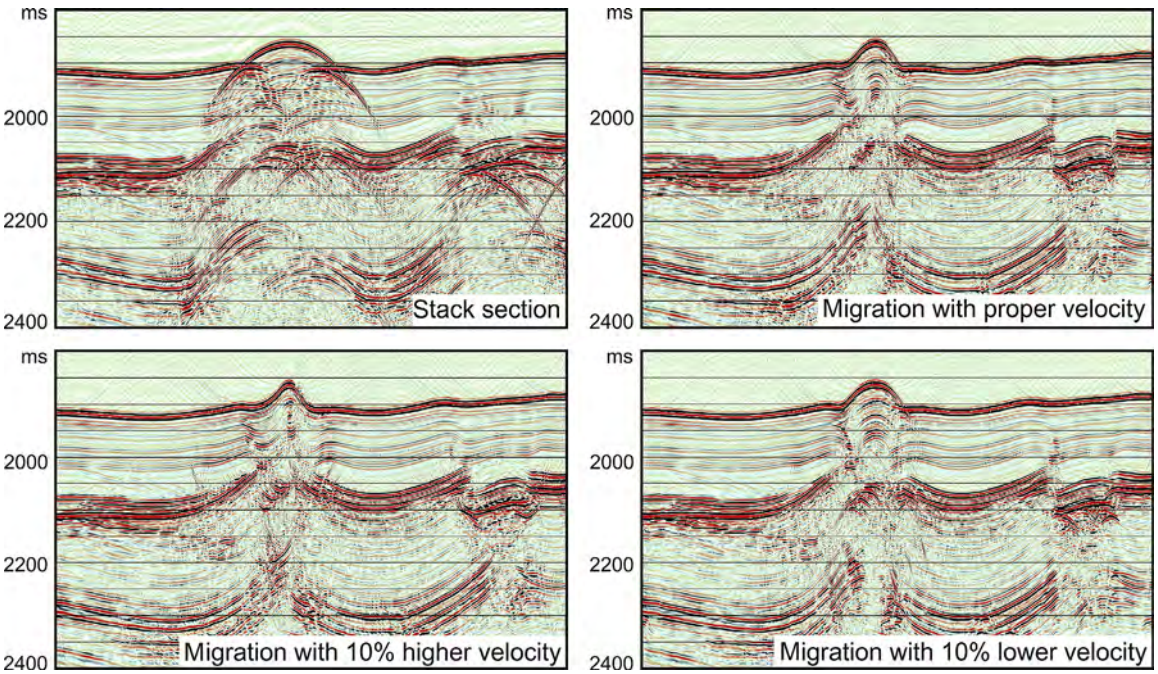


FIG. 11.18 The effect of 10% lower and 10% higher velocity on the output of poststack Kirchhoff time migration. Over- and undermigration occur when the migration velocity is faster or slower than the actual velocity of the medium, respectively.

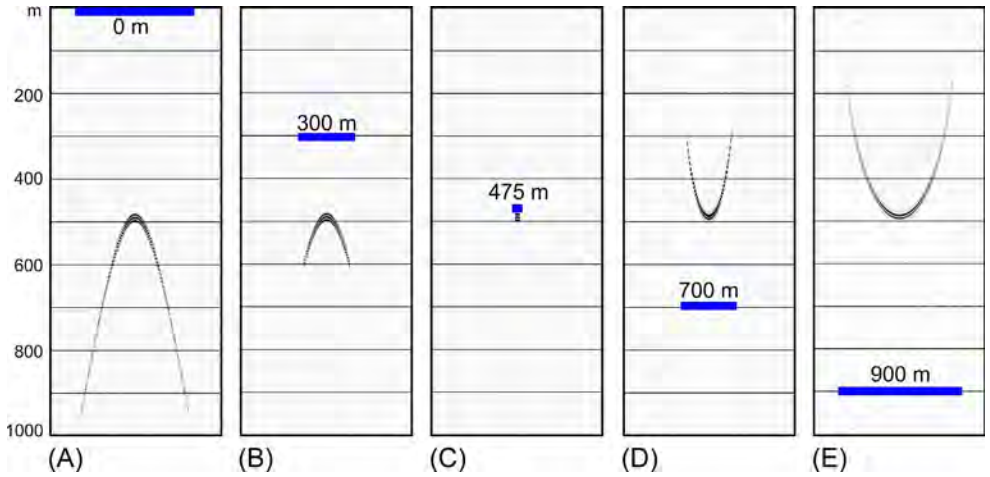


FIG. 11.19 Collapse of the diffraction hyperbola by downward continuation of the zero-offset wave field. (A) A diffraction hyperbola is recorded with the receivers at the surface. The thick *blue line* shows the total spread length. (B) If the receivers are moved downwards and the spread length is shortened accordingly, the hyperbola gets narrower. (C) When the receiver is at the apex, the hyperbola is completely collapsed. If the downward continuation proceeds, then a mirror image of the hyperbola occurs, as in (D) and (E).

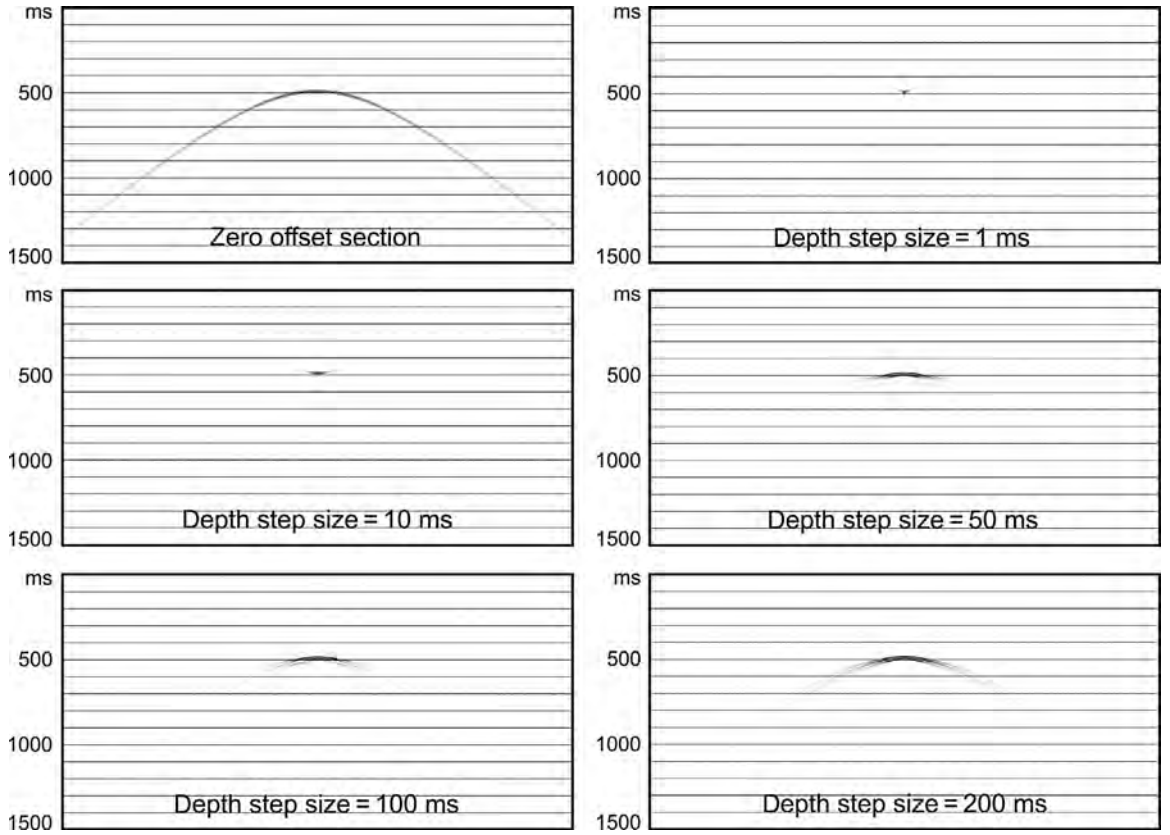


FIG. 11.20 The effect of depth step size on the collapse of a theoretical diffraction hyperbola in a constant velocity medium by finite-difference time migration. 1 ms is the sampling rate of the zero-offset section.

Higher depth step sizes also cause undermigration of steep dips, dispersions along the reflections increase, and kinks arise at regular time intervals corresponding to the depth step size. Kinks become more and more evident as the dip increases. Fig. 11.21 shows the effect of depth step size on real marine seismic data. For large step sizes, the diffractions cannot be collapsed, and the dipping events cannot be moved updip to their correct lateral positions. Although smaller depth steps produce better results, a step size typically as large as possible is preferred due to economical concerns. Steeply dipping events always require smaller depth steps. In practice, the value for the depth step size is between T_S and $0.5T_S$, where T_S is the dominant period of the input dataset.

11.3.2 Effect of Velocity on Finite-Difference Migration

Finite-difference migration is also sensitive to the velocity errors. Similar to the Kirchhoff migration, slower and faster velocities cause under- and overmigration, which results in frowns and smiles in the output image, respectively. In the case of overmigration, however,

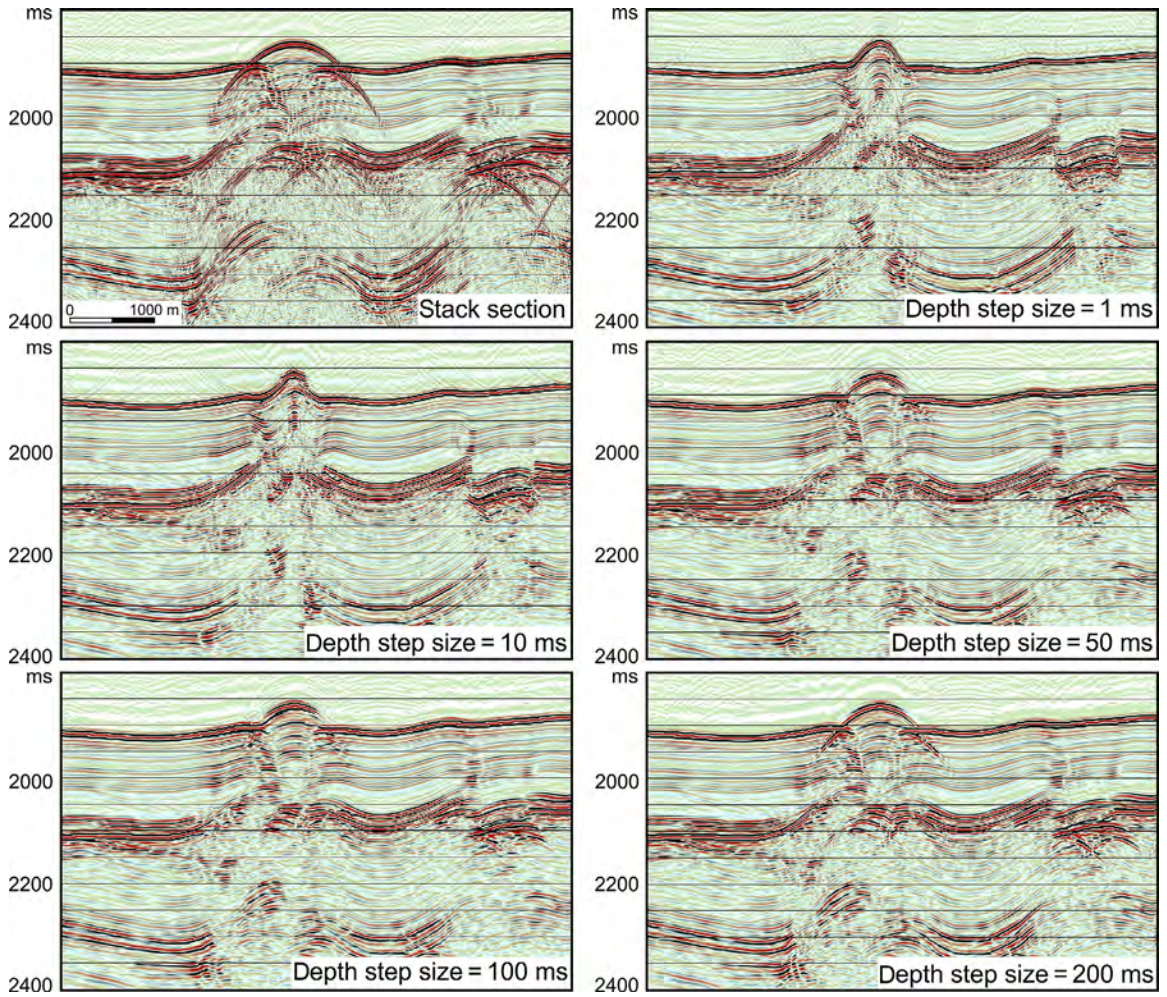


FIG. 11.21 Effect of depth step size on the output of finite-difference time migration. 1 ms is the sampling rate of the stack section. Higher depth step sizes simply cause undermigration.

the frowns are not as intensive as those for Kirchhoff migration (Fig. 11.22). The inclined events are not relocated to their true lateral positions, and the diffractions cannot be collapsed for slower velocities. Yılmaz (2001) indicates that higher velocities cause excessive dispersion since they lead to overmigration.

11.4 FREQUENCY-WAVENUMBER (f-k) MIGRATION

At the end of the 1970s, Stolt (1978) suggested that migration can be implemented using the Fourier transform, and then Gazdag (1978) proposed the migration algorithm using the phase

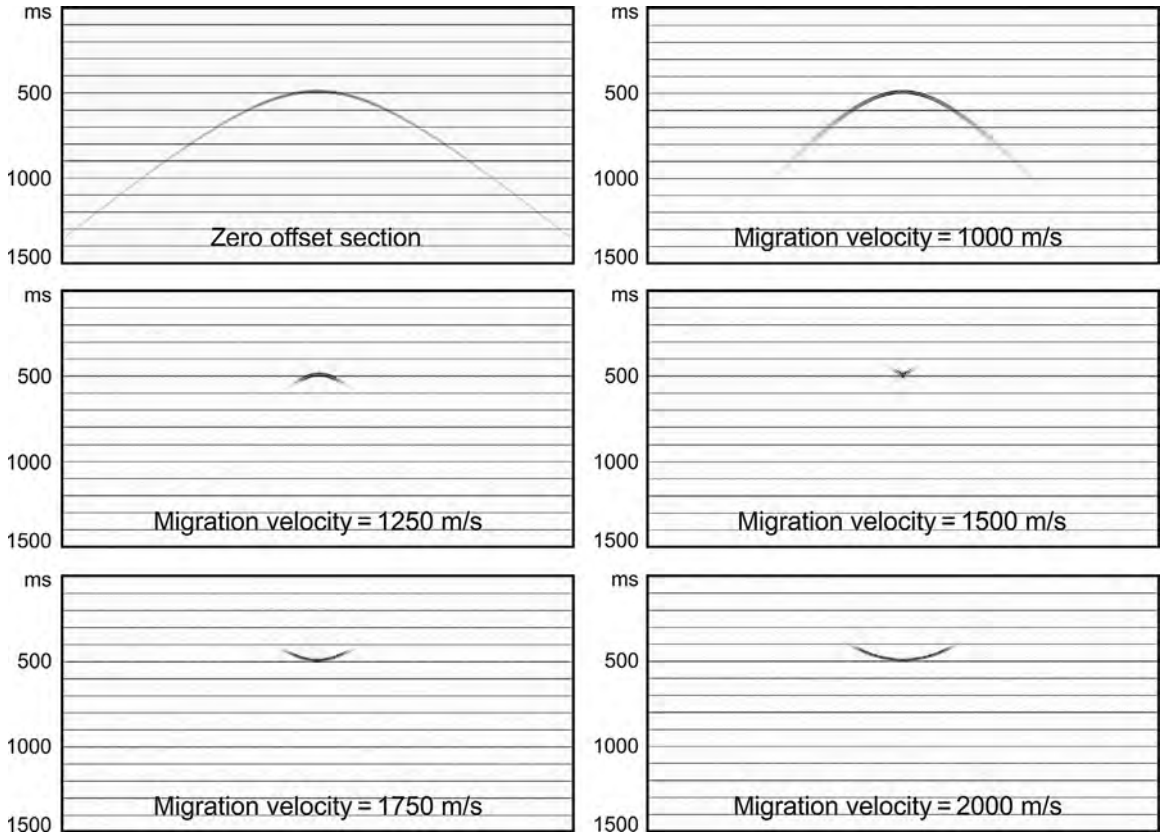


FIG. 11.22 Effect of migration velocity errors on the collapse of a diffraction hyperbola in a constant velocity medium by finite-difference time migration. Velocity of the zero-offset section is 1500 m/s.

shift method in the Fourier domain. Today, there are two types of frequency-wavenumber (*f-k*) migration: *f-k* and phase shift migrations, which are known as the Stolt and Gazdag migrations, respectively.

Stolt migration normally does not handle velocity variations in both horizontal and vertical directions and requires a constant velocity medium. On the other hand, Stolt (1978) suggested a coordinate transform where wave equation and boundary conditions are velocity independent using a constant termed the Stolt stretch factor, in order to apply the algorithm in areas with relatively complex geology where the velocity varies in both the horizontal and vertical directions. Gazdag migration, however, can handle vertical velocity variations and can be restricted for maximum structural dip in the input data.

Fig. 11.23 schematically shows the basis of the migration in the *f-k* domain. A dipping event in the time domain and its *f-k* domain representation are illustrated in Fig. 11.23A. Before the migration, the vertical axis in the *f-k* domain is frequency, which is then transformed into vertical wavenumber (k_z) after migration (Fig. 11.23B). An amplitude value in the *f-k* domain before migration, such as X in Fig. 11.23A, is moved to a point X′ after migration (Fig. 11.23B).

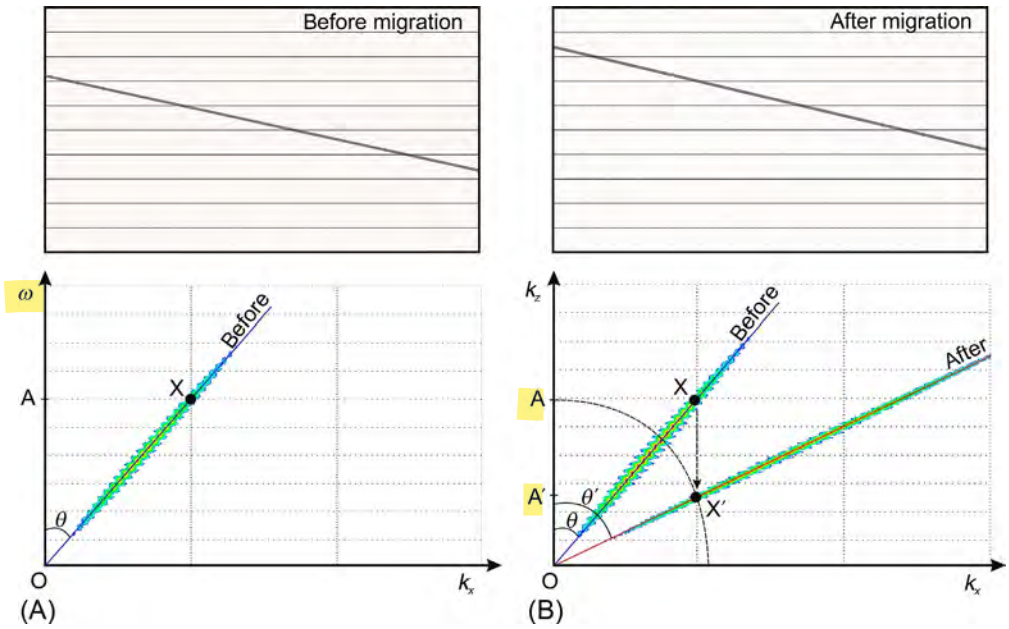


FIG. 11.23 Schematic illustration of the *f-k* domain migration. (A) A dipping event in the time domain (top) and its *f-k* domain representation (bottom) before the migration. (B) The amplitude value X in the *f-k* domain is replaced to a point X′ after migration, while its corresponding frequency value A is moved to a lower frequency of A′.

The displacement is along the vertical axis, and the horizontal wavenumber (k_x) is not affected. The frequency value A of amplitude X before migration moves to a relatively lower frequency A′. In the *f-k* domain, the inclined event OX is relocated to an event OX′, and the inclination angle θ increases to θ' after migration.

Today, Stolt migration is the fastest and hence the most computationally efficient algorithm among all available migration algorithms. It can produce acceptable results up to 90-degree structural dips when a constant velocity medium is realized. Although the Stolt stretch factor is used to obtain more correct results in a variable velocity medium, the correction is applicable only for the apex point and is invalid for the flanks of the diffraction hyperbolas. The Stolt migration can be used for a fast production or QC purposes to analyze if the input data has unexpected specific noise, such as high-amplitude noise bursts or spikes, which then become distinctive smiles after migration. Essentially Gazdag migration also works using the principle of downward continuation of the recorded wave field, like the finite-difference method, but this process corresponds to a phase shift in the *f-k* domain. It can also produce correct results up to 90-degree structural dips, providing that the velocity does not vary laterally.

11.4.1 Stolt Stretch Factor (W)

Stolt migration is valid for constant velocity media. For media with vertical and lateral velocity variations, the Stolt algorithm transforms the input data into a constant velocity section, and then the Stolt migration is applied. This transform induces a stretch to the seismic data along the vertical (temporal) axis. An inverse stretch is then performed to obtain the final migrated section after the inverse Fourier transform.

Stretch changes between 0 and 2 and it partially controls the aperture of the Stolt migration.

Constant Velocity Section - Coordinate Transformation in where the wave equation and the boundary conditions are velocity independent.

The amount of stretch depends on the ratio between the V_{RMS} of the time sample and the smallest RMS velocity of the whole dataset. For constant velocity media, W equals 1.0, and if the velocity varies with depth, $W = 1$ is not a valid value any more. In general, $W < 1$ implies undermigration while $W > 1$ indicates overmigration. The *f-k* migration results for different Stolt stretch factor values are shown in Fig. 11.24 for real marine seismic data. Migration outputs indicate undermigration for $0 < W < 1$, and overmigration for $1 > W > 2$. For most marine seismic data, $W = 0.5$ or 0.6 generally produces acceptable results for recent sediments.

11.4.2 Effect of Velocity on *f-k* Migration

Both Stolt and Gazdag migrations are sensitive to migration velocity errors, like Kirchhoff migration, and both display similar responses.

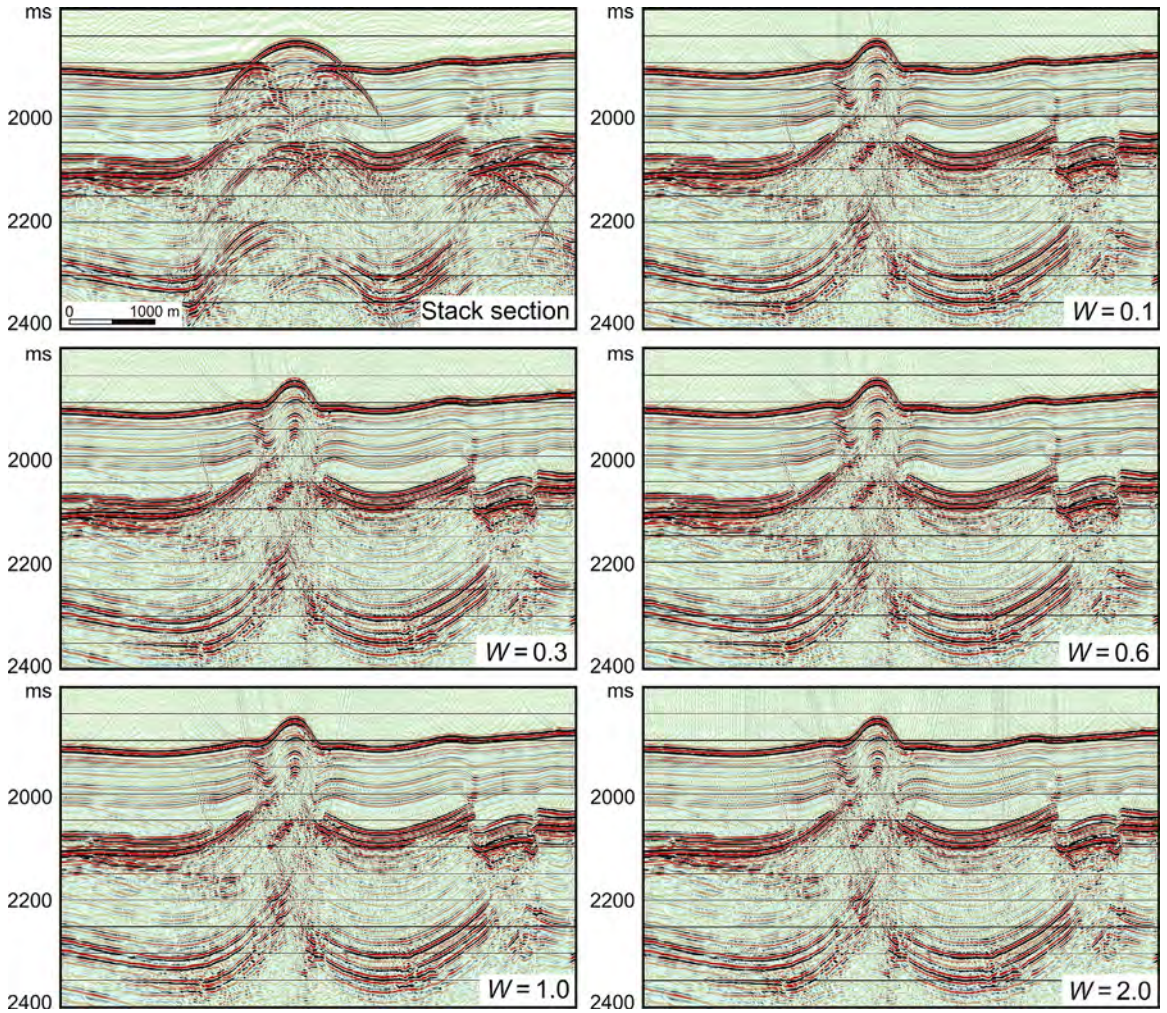


FIG. 11.24 Effect of Stolt stretch factor on the output of Stolt migration.

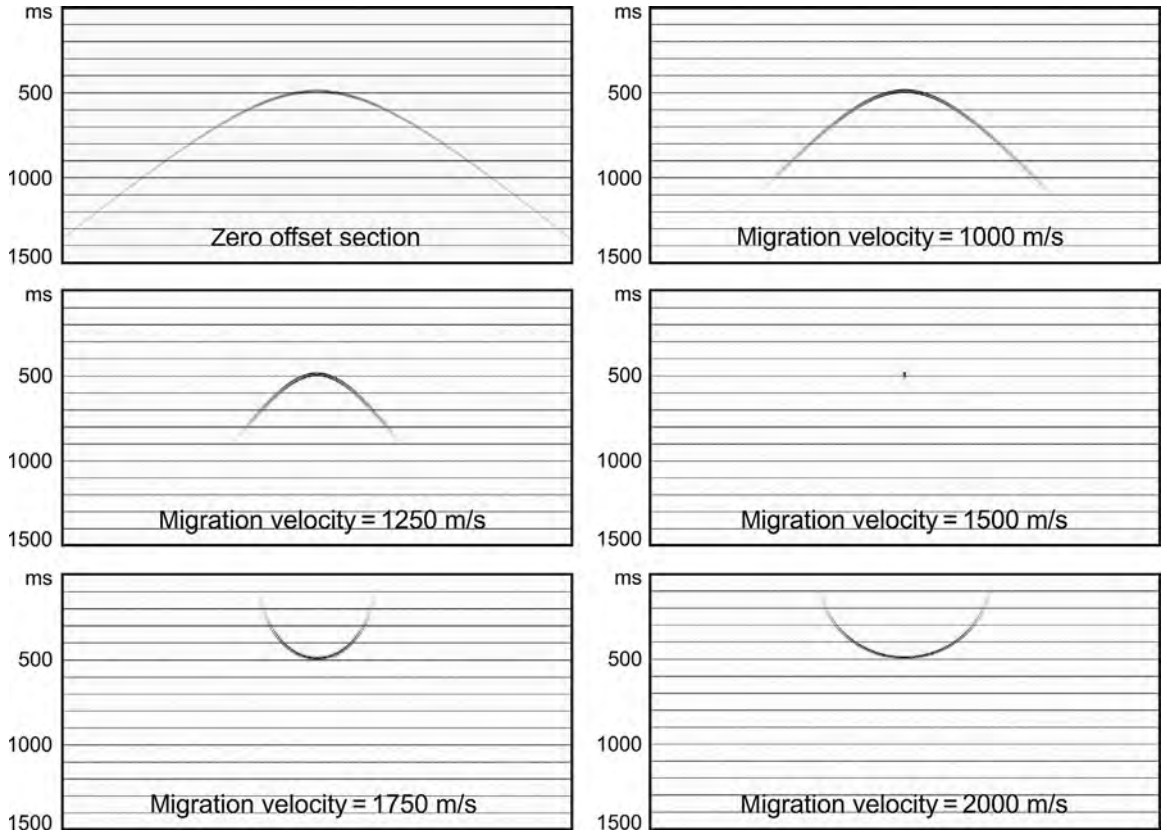


FIG. 11.25 Effect of migration velocity errors on the collapse of a theoretical diffraction hyperbola in a constant velocity medium by Stolt *f-k* migration. Velocity of the zero-offset section is 1500 m/s.

Fig. 11.25 shows the collapse of a theoretical diffraction hyperbola in a constant velocity medium by Stolt migration using different velocities. The effect of velocity errors on the migration outputs is quite similar to that for Kirchhoff migration outputs: frowns with undermigration occur for slower velocities, and strong smiles with overmigration arise for faster velocities. Fig. 11.26 illustrates the effect of 10% lower and 10% higher velocity on the Stolt migration output of marine seismic data. The response of Gazdag migration to systematic slow and fast velocities is quite similar to that of Stolt migration.

11.5 REVERSE TIME MIGRATION

Reverse time migration (RTM) is a prestack or poststack two-way wave equation migration that can handle steep dips up to and beyond 90 degrees. It also produces superior results in the case of strong velocity contrasts in both the vertical and lateral directions in areas of complex geological settings, such as salt tectonics (Baysal et al., 1983). Although its name indicates a migration in time, RTM is actually implemented either as a time or depth migration using the reverse time algorithm in 2D or 3D.

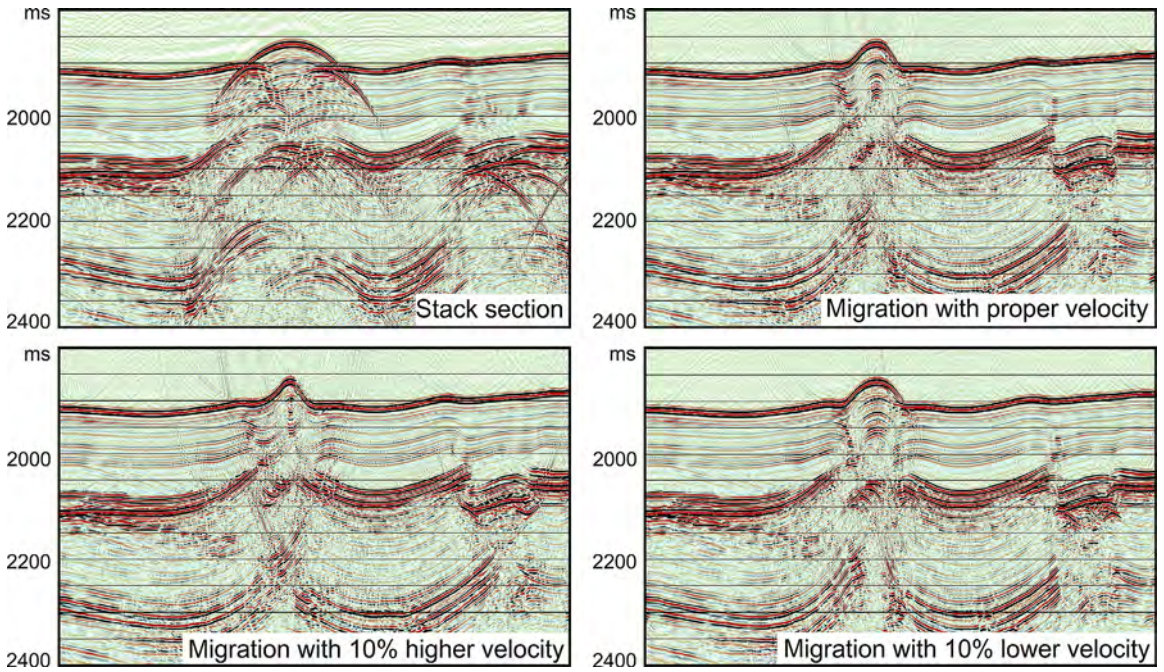


FIG. 11.26 Effect of 10% lower and 10% higher velocity on the output of poststack *f-k* Stolt migration. For slower velocities, undermigration results in frowns, while overmigration results in strong smiles in the case of faster velocities.

Conventional migration methods are applied by propagating data downward into the subsurface, whereas RTM propagates events both downward and upward in time. RTM utilizes the two-way acoustic wave equation for an inverse modeling of the seismic data. In contrast to the conventional downward continuation in depth, it reconstructs the source and receiver wave fields forward and backward in time, respectively, which actually denotes the reversing of the forward modeling. Then an imaging condition is applied to obtain the reflectivity from the reconstructed wave fields. In principle, RTM utilizes the wave field recorded at the surface as the input, and emplaces the reflections to their correct subsurface locations by stepping backwards in time.

The theory behind RTM was first developed for poststack seismic data by McMechan (1983) and Baysal et al. (1983). The principle of poststack RTM is based on the exploding reflectors model, where an approximation to the stack section is obtained by initiating explosive sources at the reflectors after replacing the subsurface velocities with half of the real earth velocities (Baysal et al., 1983). Then the wave equation is used to extrapolate the data forward and backward in time after reversing the time axis, in which the propagation is initiated from maximum time to zero time where the reflections are at their exact subsurface locations.

The poststack RTM methodology is as following:

- Reversing the zero-offset data in time so that maximum recording time becomes time zero.
- Considering the reversed zero-offset data as sources along the recording surface to propagate the wave fields in the subsurface.
- Extracting the image at time zero by applying the imaging condition.

For poststack RTM, both source and receivers are extrapolated together since the data is zero offset and the ray paths and recording times for upgoing and downgoing waves are identical. For the prestack case, however, RTM reconstructs source and receiver wave fields individually, and both extrapolations must be performed separately. The source and receiver wave fields are reconstructed forward and backward in time, respectively (Fig. 11.27). RTM was first applied to prestack data by Chang and McMechan (1986), who used ray tracing for the source extrapolation and the acoustic finite-difference algorithm for the extrapolation of the recorded wave field. At each time step, the migrated image is achieved by cross-correlating the two extrapolated wave fields. During the computations, a sufficiently small time step must be selected for numerical stability.

The prestack RTM methodology is as follows:

- Simulating the source wave front from the source location using a suitable method, such as ray tracing.
- Extrapolation of the recorded wave fronts downward from the recording surface to the subsurface.
- Cross-correlating the simulated wave field with the downward extrapolated wave field for each time step.

RTM is especially effective in areas of complex geology with steep dips, such as salt flanks, which are usually not illuminated by primary reflections, and therefore conventional migration algorithms generally cannot image the correct salt flank structures. In such cases, the waves reflected from subhorizontal reflectors at both sides of the salt bodies can reflect from the vertical salt flanks, and are recorded on the surface. These doubly scattered waves from vertical reflectors are known as prism waves (Fig. 11.28) and can successfully be used to illuminate the steep salt flanks by RTM. In salt flank imaging, to delineate the lateral extension of a salt body, RTM produces superior outputs as compared to other migration algorithms. Today, RTM is the most promising migration method for both 2D and 3D implementation to accurately migrate seismic data.

The most important advantage of RTM is to image complex areas of steep dips and complex overburdens, as well as better illumination of salt flanks and subsalt reflections. It can also

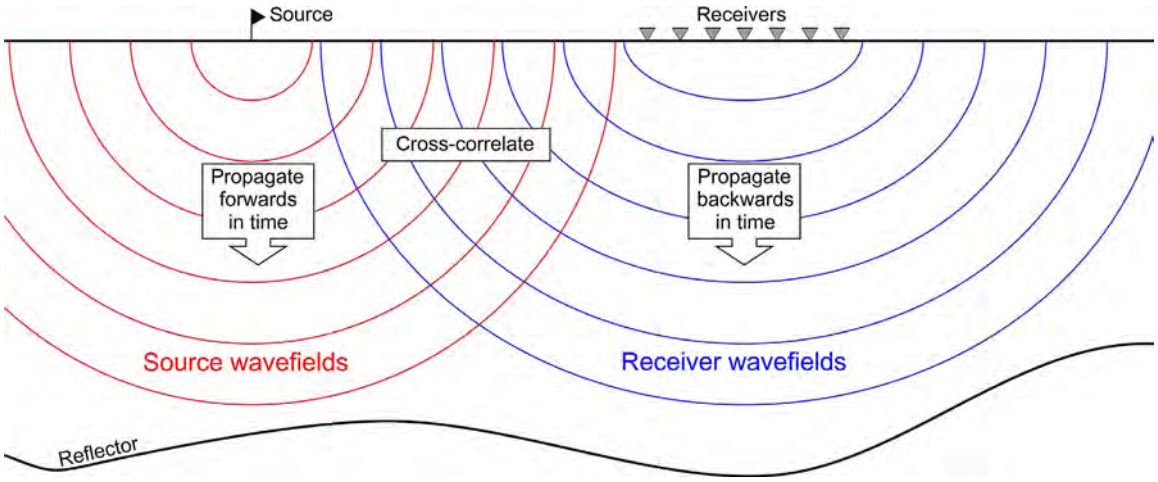


FIG. 11.27 The source and receiver wave fields are reconstructed forward and backward in time during reverse time migration, respectively. To obtain the migrated image, extrapolated wave fields are cross-correlated at each time step.

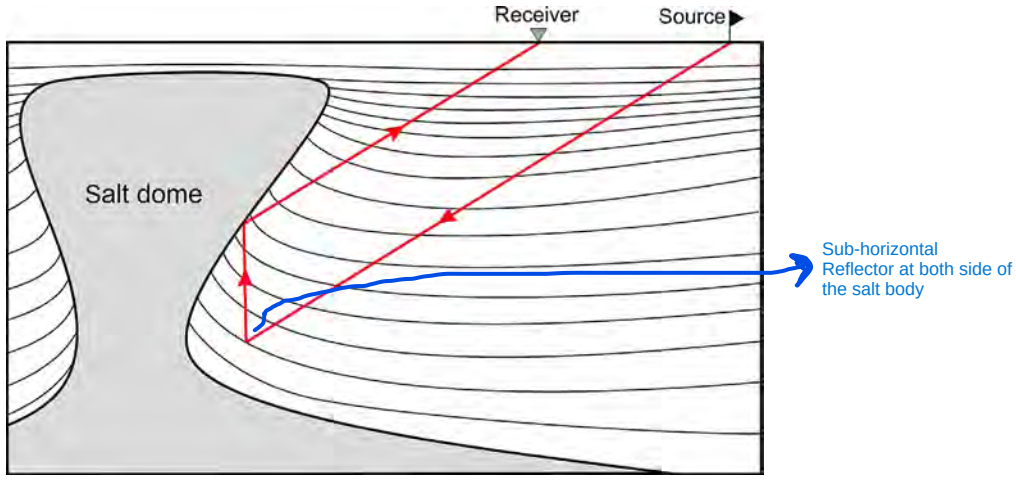


FIG. 11.28 Ray path of a prism wave reflected from the flank of a salt dome.

account for extreme lateral velocity variations and provide excellent amplitude-preserving results with a higher S/N compared to other migration algorithms. It is also suitable to use with wide azimuth (WAZ) seismic data. The most important disadvantage of RTM, however, is its extremely high computational cost; it takes several times longer to run the RTM algorithm than a conventional finite-difference algorithm, which has prevented RTM from being used widely by the seismic industry until recent years. To overcome the high computational cost, RTM can also be implemented in the time-wavenumber (T-K) domain, known as reverse time TK migration, which is relatively faster and more economical, but accounts for only vertical velocity variations.

Accuracy of the RTM output also depends on the accuracy of the interval velocity field used for the migration. A slower velocity causes frowns and the inclined events are not relocated to their true lateral positions, while a faster velocity results in overmigration, resulting in smiles. Fig. 11.29 shows the collapse of a theoretical diffraction hyperbola in a 1500-m/s constant velocity medium using RTM. Fig. 11.30 shows a poststack reverse time migration output of a marine stack section.

11.6 POSTSTACK MIGRATION

In poststack migration, the seismic data is migrated after it has been stacked. It can be implemented in the time or depth domains for 2D and 3D seismic data. The most important advantage of the poststack migration originates from stacking: removal of significant amounts of coherent and random noise embedded in the prestack data, suppression of multiple reflections, increased S/N ratio before migration, and inexpensive processing due to the reduced data volume after stacking.

During the migration process, what we have is only the seismic traces and RMS velocity field associated with the input data. The correct reflection point of a reflection from a dipping reflector in a 2D earth model can be found by using the arrival times and propagation velocities of the reflected events, as schematically illustrated in Fig. 11.31. Considering the reflection event with an arrival time of $t(x)$ at trace number 7, for instance, we can conclude that this event is originated from a reflection point in the subsurface along a semicircle of radius $Vt/2$ (red dashed curve), centered at the zero-offset location of that trace indicated by X, where V is the propagation velocity of the reflection event. This implies that

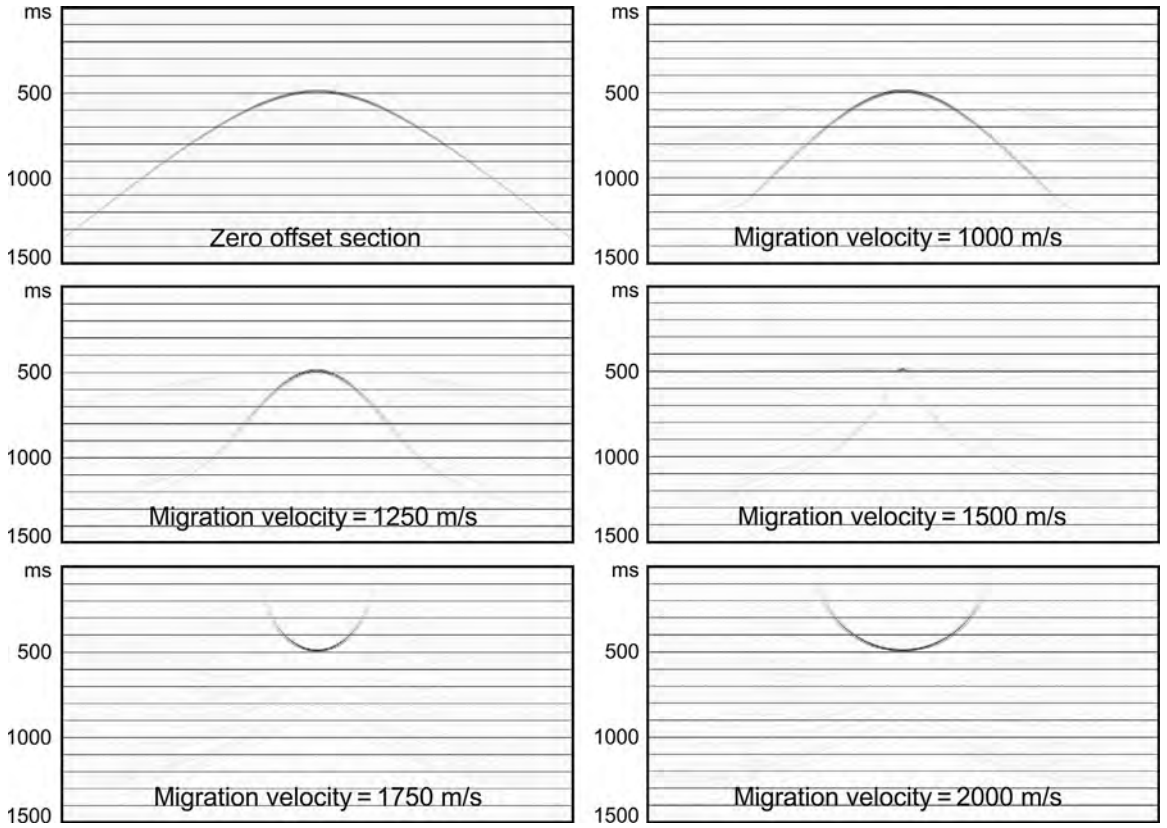


FIG. 11.29 Effect of migration velocity errors on the collapse of a theoretical diffraction hyperbola in a constant velocity medium by reverse time migration. Velocity of the zero-offset section is 1500 m/s.

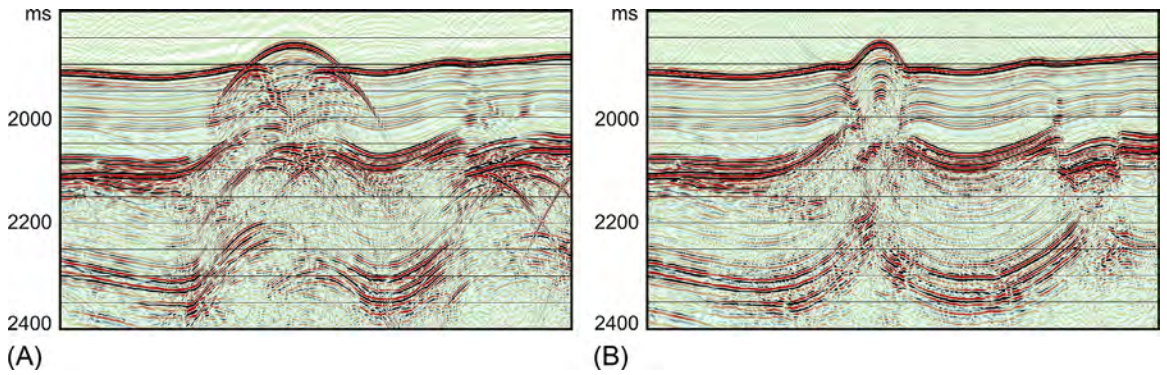


FIG. 11.30 (A) An example zero-offset section, and (B) its poststack reverse time migration output.

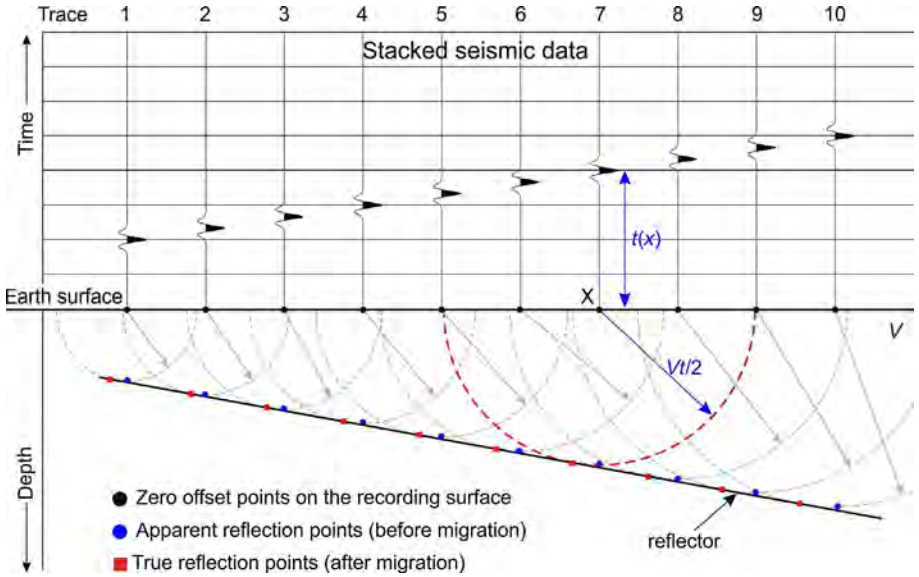


FIG. 11.31 Schematic illustration of 2D poststack migration over an inclined reflector in the subsurface (bottom) and its stack section (top). The reflection at time $t(x)$ at trace number 7 may be originated from any reflector segment tangent to a semicircle with a radius of $Vt/2$ *(red dashed curve)*, centered at zero-offset location X. To obtain the true subsurface location of the dipping reflector, the tangents of all the semicircles calculated for the entire zero-offset traces are obtained.

any subsurface reflector tangent to this semicircle can produce this reflection, since all possible contributions along the semicircle arrive at time $t(x)$ to the trace number 7. To positively locate the reflections of a dipping event in the subsurface, we can apply similar semicircle analysis to all of the traces in the data (grey dashed curves) using the arrival times of that specific reflection event at each specific trace. The final reflector can be obtained from a common tangent to all of these semicircles (Fig. 11.31).

Although it does not produce a perfectly clear and exactly accurate image of the subsurface, it is still used by processors, since it is computationally efficient and hence economical as compared to the prestack migration methods. The poststack migration assumes that the input data is zero offset, and it yields reasonable results if the data has small (poststack time migration) or moderate (poststack depth migration) structural dips, and if there are only smooth lateral velocity variations. One of the major disadvantages of poststack migration is that it removes relative amplitude information existing in the prestack data, which prevents the application of prestack amplitude analysis, such as amplitude versus offset (AVO) studies on the migrated data.

11.7 PRESTACK MIGRATION

Reasonable result for small to medium dip and only smooth velocity variation allowed

Although it produces acceptable results for most cases, the poststack migration procedure is only correct for horizontally layered subsurface geology, where there is no lateral velocity variation. However, in the case of dipping reflectors, the stacking velocity also depends on the inclination angle of the reflector (Levin, 1971). The poststack migration also assumes that the stack section is identical with the zero-offset section, which is not valid in particular for complex subsurface settings where reflections with conflicting dips exist in the data. In such cases,

NMO and stacking procedures are skipped and a prestack migration can be preferred to obtain a more correct subsurface image.

If there are intersecting reflectors with different inclination angles in the subsurface (indicated by I and II in Fig. 11.32A), that is, conflicting dips, these structures cannot be resolved by applying a conventional poststack migration followed by NMO correction-stacking flow. These reflectors form two individual reflection hyperbolas with different moveout curvatures in CDP gathers, and hence different apparent velocities since the NMO velocity of a reflection is dip dependent. The issue here is that both hyperbolas have the same zero-offset time t(0), as schematically shown in Fig. 11.32B. In this case, two enclosures at different velocities but exactly at the same zero-offset time arise in the semblance plots during the velocity analysis (Fig. 11.32C). In the example semblance plot in Fig. 11.32C, the reflection hyperbolas indicated by A and B have velocities of 1500 and 2000 m/s, respectively, even though both reflection signals propagate in the same constant velocity layer (V_1 in Fig. 11.32A).

If conflicting dips exist in the data, it may not be possible to pick an individual velocity for each particular reflection event. In velocity analysis of conflicting dips, generally the velocity is picked at the point consistent with the overall trend of the semblance contours, which means that only one reflection hyperbola of the same zero-offset time will be perfectly flattened. Fig. 11.33 schematically shows this situation. If the velocity at point A (1500 m/s) is picked, the event A is flattened and B is overcorrected

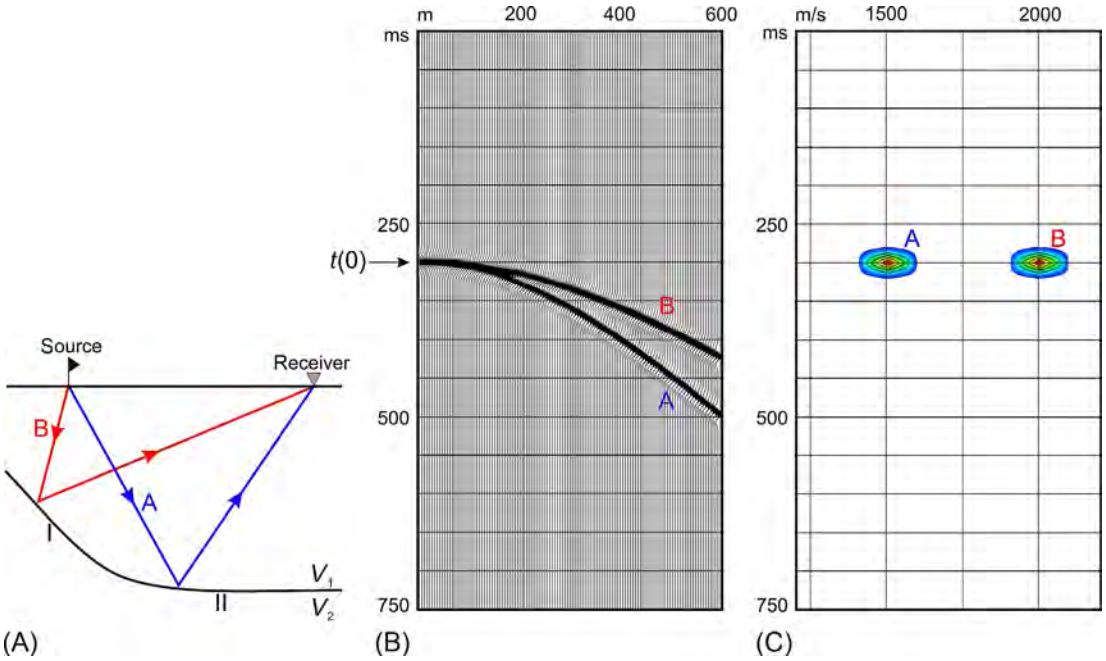


FIG. 11.32 (A) Ray paths of the signal from source to receiver in the case of subsurface reflectors with conflicting dips (reflector pieces indicated by I and II). (B) In such cases, two individual reflection hyperbolas with different curvatures but the same $t(0)$ time are obtained in CDP gathers. (C) Since the stacking velocities are dip dependent, two enclosures indicating two different velocities corresponding to the same $t(0)$ time occur in the semblance plots, preventing the picking of only one velocity value for time $t(0)$.

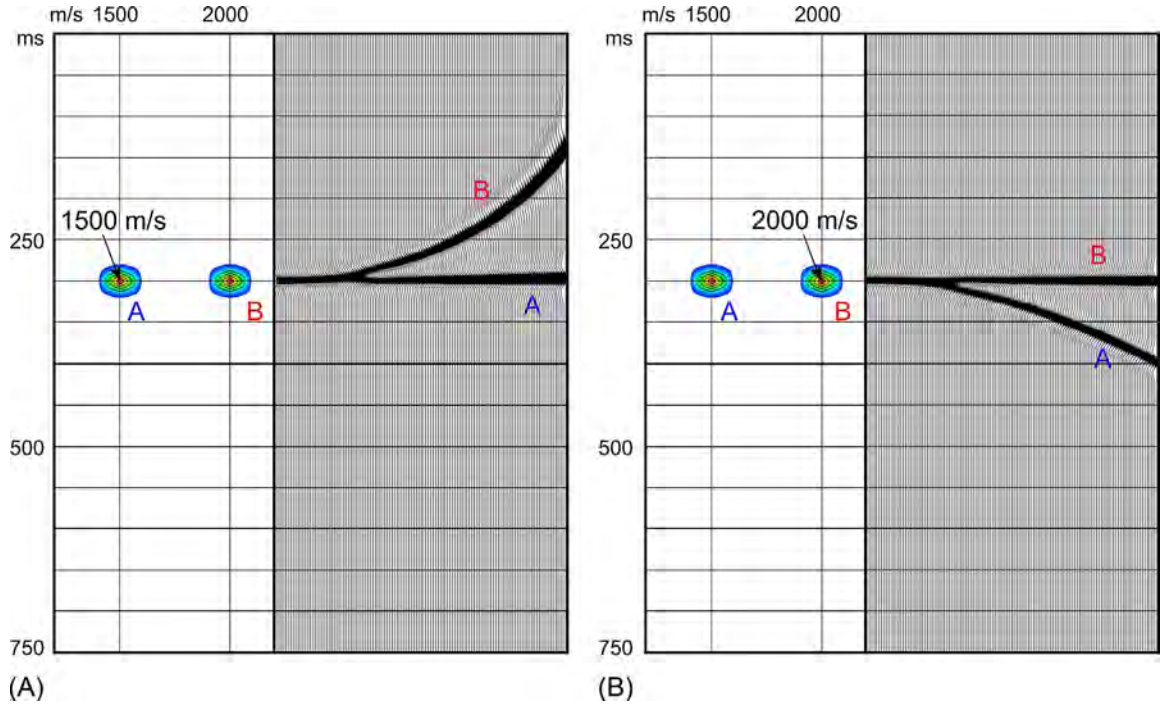


FIG. 11.33 Schematic illustration of velocity analysis in the case of conflicting dips. (A) If the velocity of A (1500 m/s) is picked (left), the event A is flattened and B is overcorrected after NMO correction (right). (B) If the velocity of B (2000 m/s) is picked (left), the event B is flattened and A is undercorrected after NMO correction (right). In both cases, only one of the reflections can be represented in the stack section with its proper amplitude value.

after NMO correction, since 1500 m/s is too slow to flatten the event B (Fig. 11.33A). On the contrary, if the velocity at point B (2000 m/s) is picked in favor of event B, this time the event B is flattened and A is undercorrected after NMO correction, since 2000 m/s is too fast to flatten the event A (Fig. 11.33B). In any case, either event A or event B is represented by lower amplitude than what it actually has in the final stack section, since only one of them can be flattened after NMO correction.

In case of conflicting dips and strong lateral velocity variations, prestack migration should be used to obtain an accurate subsurface image. In addition, in order to solve the conflicting dips issue, dip moveout (DMO), explained in Section 11.10, can also be implemented, since dip moveout is much more computationally efficient than a conventional prestack migration algorithm.

In the presence of conflicting dips, stack sections are no longer identical to zero-offset sections. Because all of the poststack migration algorithms assume a zero-offset section as an input, poststack migrations do not provide correct subsurface images, and simply prestack migration is required. Prestack migration is done by summing the amplitudes along the nonzero offset diffraction times. As in the zero-offset case, seismic velocities determine the shape of the hyperbola (the migration operator) along which the summation is performed. Prestack migration is applied to the common offset sections, and all common offsets are processed in this manner and finally summed up to obtain the migrated image.

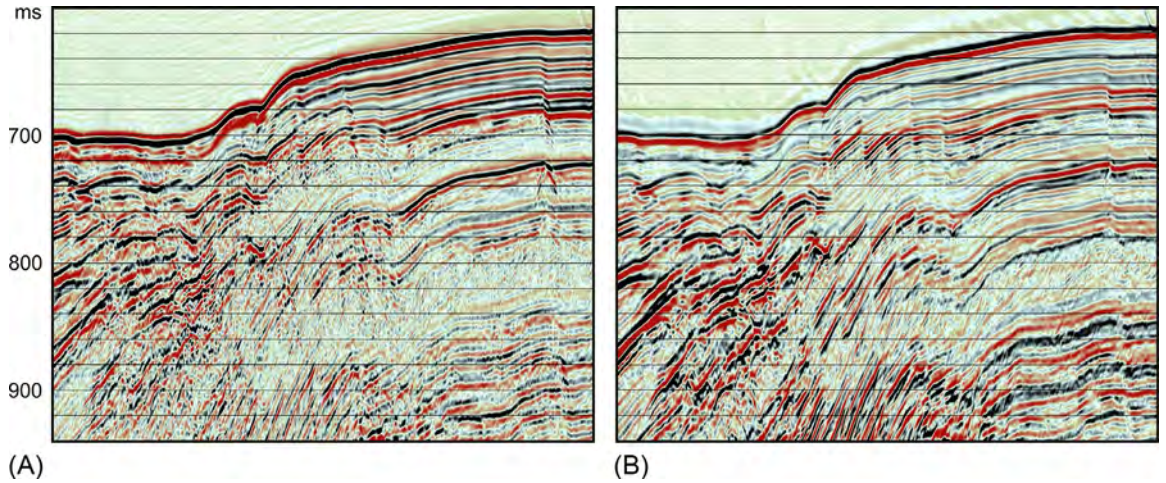


FIG. 11.34 Comparison of the results from (A) poststack and (B) prestack time migrations applied to a shallow marine survey.

Poststack and prestack time migration results of a marine survey are compared in Fig. 11.34. Prestack migration produces superior results: fault planes are much clearer and steeply dipping events like the sediments at the central part of the section are more distinct in the prestack time migration image. However, the method is expensive since, for instance, in order to migrate 120-fold seismic data, 120 successive migration applications are required and the results are summed, that is, it takes 120 times longer than a conventional poststack imaging. However, it retains the information of amplitude versus offset (AVO) and phase variations in the prestack data for a possible hydrocarbon analysis after migration.

11.8 DEPTH MIGRATION

Most of the migration algorithms produce the image of the subsurface with a vertical axis in time, while the others provide final images with a vertical axis in depth. These migration algorithms are referred to as time and depth migrations, respectively. Time migration algorithms require a simple RMS velocity field of the subsurface as the input, and they do not allow ray bending at a reflecting surface. Lateral positioning errors arising from time migrations are expressed by image ray, which is normal to the recording surfaces and bends across the subsurface layers. Although time migration methods produce a migrated image very fast, in principle, their results must be considered as imperfect, and they can supply an image of the subsurface for an initial interpretation or testing purposes for the parameters, which can be utilized later in more complicated migration algorithms, such as prestack depth migration applications.

Depth migration algorithms are, however, much more complicated and require a more accurate interval velocity field of the subsurface in the depth domain. RMS velocity fields are therefore converted into interval velocities in depth using the Dix equation. However, the Dix equation sometimes produces inaccurate and unreliable interval velocities since it is an empirical approach. When converted into interval velocities using the Dix equation, even an erroneous RMS velocity pick results in a complete degradation of the whole depth migration process. Therefore, a number of approaches to invert the interval velocity field from RMS

velocities have been developed utilizing a least-squares approximation using a vertically varying velocity field, termed constrained velocity inversion. Unlike time migrations, velocity errors in shallow areas of the seismic data induce migration errors also in deeper parts of the data in depth migrations, which require building the interval velocity-depth model very carefully, even iteratively from shallow to deep.

Depth migration can be achieved using different implementations, such as wave-equation, Kirchhoff, Beam, finite-difference or reverse time algorithms, all of which allow ray bending at the reflecting surface and are significantly slow to run, but produce more accurate images in depth. Depth migrations account for lateral velocity variations and can be achieved using different implementations, which can be classified by regarding how they propagate the wave field in the model. While reverse time and wave equation migrations utilize the numerical solution of the acoustic wave equation, Kirchhoff and Beam migrations employ ray approximations. Even though Kirchhoff depth migrations have been preferred by the seismic industry until the last decade, reverse time migration is becoming more and more popular, since it provides more accurate solutions in complex subsurface settings, though it is relatively more expensive compared to the ray-based depth migration algorithms.

Although the time migration results can easily be compared to the stack sections, since they are both in the time domain, this is not possible for depth migration results. In addition, time migration algorithms generally compensate for the minor, even moderate, errors in the input velocity model; depth migration algorithms are much more sensitive to the errors in the interval velocity field. Fig. 11.35 compares

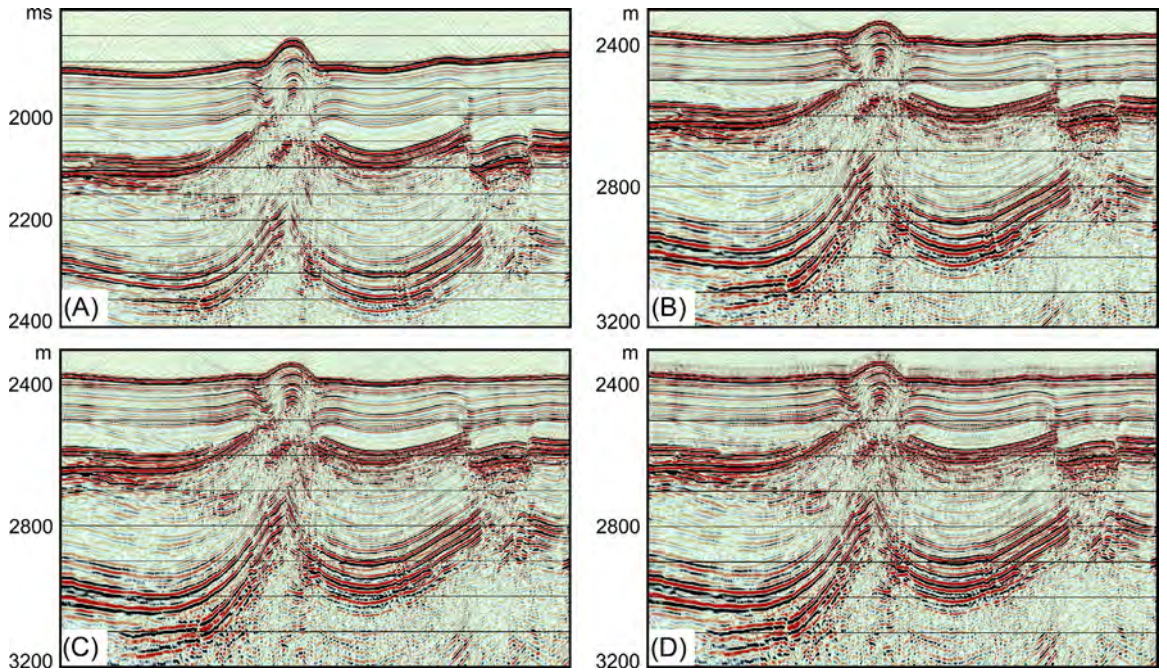


FIG. 11.35 (A) Kirchhoff time migration result of the stack section given in Fig. 11.30A, (B) depth converted version of (A) using RMS velocities, (C) Kirchhoff poststack depth migration result, and (D) finite-difference poststack depth migration result.

Kirchhoff poststack time migration results, its depth converted version, and outputs of two different depth migration algorithms of Kirchhoff and finite-difference poststack depth migrations.

11.9 3D MIGRATION

Migration can also be implemented in 3D. In 2D lines, out-of-plane reflections (side-sweeps) may exist in the seismic data even if 2D data is collected in ideal dip strike directions. Using 2D migration, it is impossible to locate side-sweeps to their correct subsurface positions, since they are originated from the outside of the seismic acquisition plane. In the 3D case, however, side-sweeps are actually the data itself and can successfully be migrated to their true locations after 3D migration. Today, 3D Kirchhoff prestack depth/time migrations have become standard for time or depth imaging in the seismic processing industry.

In the 2D case, a point source at a subsurface depth generates a diffraction hyperbola in a constant velocity medium, and only the energy reflected in the vertical plane of the seismic section is correctly imaged by 2D migration (Fig. 11.36A). In the 3D case, such a point source produces a diffraction hyperboloid, which gives a hyperbola when cut in any vertical slice of inline or crossline directions (Fig. 11.36B). Kirchhoff migration simply sums up the amplitudes along the hyperbolas and over the surface of hyperboloids in the 2D and 3D cases to their apex points, respectively.

During earlier times, before implementing 3D migration algorithms using supercomputers with adequate memory and power in the last two decades, pseudo 3D (or two-pass) migration was used to image 3D data, which migrates the data in the inline direction first and then the crossline direction, using 2D time domain algorithms. Use of different 2D migration algorithms is possible for each pass. In the first pass, the diffraction hyperbolas along the inline direction are

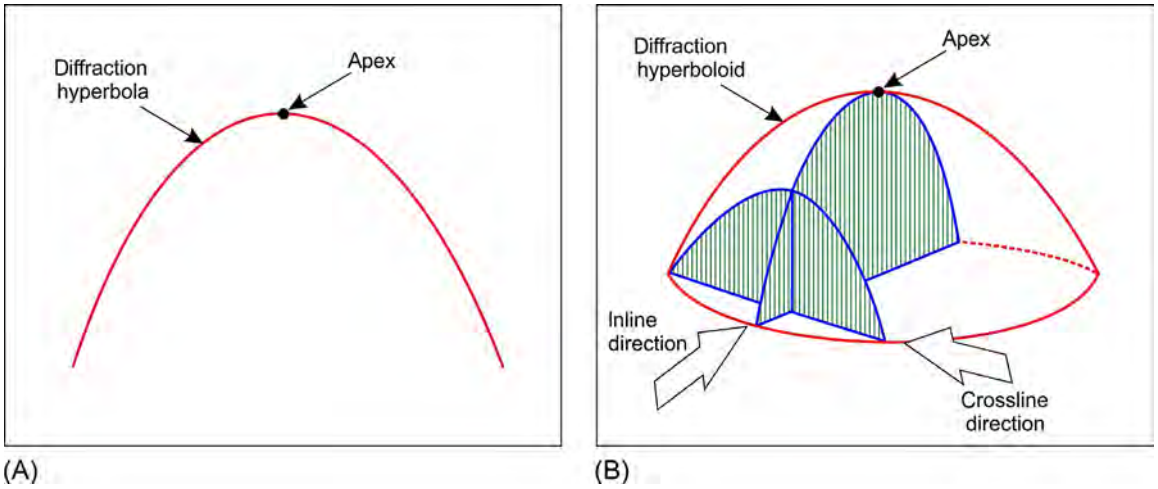


FIG. 11.36 (A) A diffraction hyperbola is produced by a point source at depth in a 2D constant velocity medium, and only the energy reflected in the vertical plane of the seismic section is correctly imaged by 2D migration. (B) A diffraction hyperboloid is produced by a point source in a 3D constant velocity medium. When vertically cut in the inline or crossline directions, 2D diffraction hyperbolas are obtained.

collapsed and repositioned at the apex locations so that the hyperboloid becomes a hyperbola in the crossline direction. In the second pass, the output of first-pass migration is used as input, and another 2D migration is applied in the crossline direction to collapse the whole hyperboloid to the apex. The one-pass 3D migration method, however, treats the hyperboloid in the crossline and inline directions simultaneously and is an industry-standard imaging method today. It can be formulated in both the time and depth domains.

In 2D processing, it is assumed that the geology changes only along the seismic line direction and subsurface structures do not vary along the orthogonal or crossline directions to the survey line, which suggests that there are no out-of-plane reflections in the data (Fig. 11.37A), although they do exist. If the earth varies in the crossline direction, then we simply

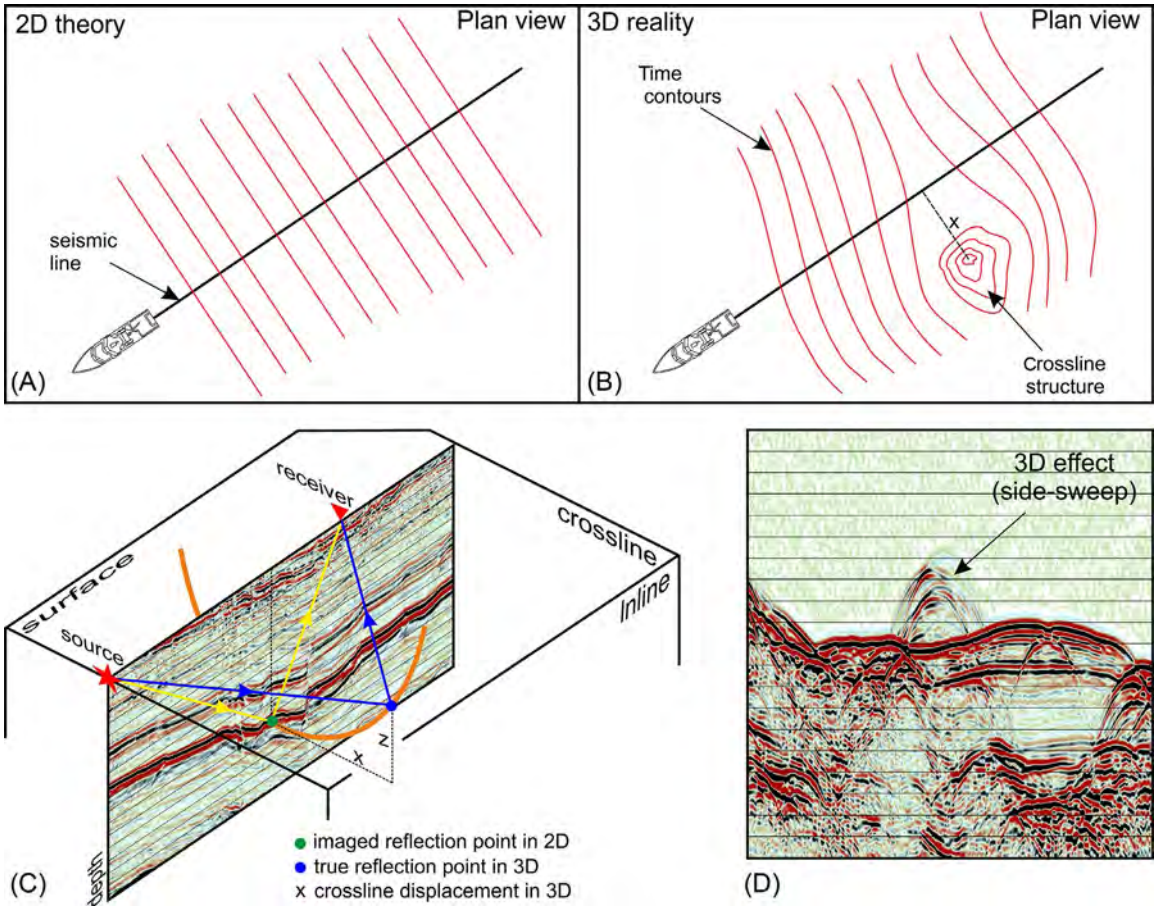


FIG. 11.37 (A) 2D processing assumes that the structures do not vary along the crossline direction. (B) Structures at crossline offsets sometimes have strong influences on the data. (C) Out-of-plane reflections are recorded and treated as ordinary 2D reflections and cannot replace to their correct subsurface locations by 2D processing. (D) As a result, it is common for 2D lines to include side-sweeps as steep linear or curved reflections remaining in the 2D image even after 2D migration.

obtain a distorted image of the subsurface using our 2D seismic data. Even though we cannot solve any structures at some crossline offset to the survey line with 2D datasets (e.g., the one at x distance away from the sail line in Fig. 11.37B), they sometimes have strong influences on the data. Out-of-plane reflections can only be properly focused after 3D migration.

The out-of-plane reflections are recorded as if they are reflected from the 2D sail line plane at the time they arrive at the receivers (green dot in Fig. 11.37C), and during 2D migration, these amplitudes are treated as ordinary 2D reflections recorded from directly beneath the seismic line. Since the process is 2D, it is not possible to move these reflections to their true reflected positions, which are actually not located in the survey line plane. In order to image the event at its true subsurface location (blue dot in Fig. 11.37C), it is necessary to back-propagate the event using 3D imaging along an oblique plane, which moves the event along the orange semicircular curve in Fig. 11.37C, where the amount of displacement (x) is indicated by crossline displacement. This ambiguity can only be solved by recording 3D data and applying 3D imaging.

As a result, 2D lines frequently involve sidesweeps as steep linear or curved reflections as well as noncollapsed diffraction hyperbolas, even after 2D migration (Fig. 11.37D). 3D migration revokes the assumption of 2D migration that "all recorded data is reflected from the survey line plane," and it displaces the events to their true subsurface locations in both inline and crossline directions. In Fig. 11.38, a 2D line (inline #150) from a 3D marine survey is processed by 2D poststack time migration (Fig. 11.38A) to compare the image quality with a 3D migration output (Fig. 11.38B) of the same dataset. In the 3D migrated section, diffraction hyperbolas are better collapsed, the events from the crossline

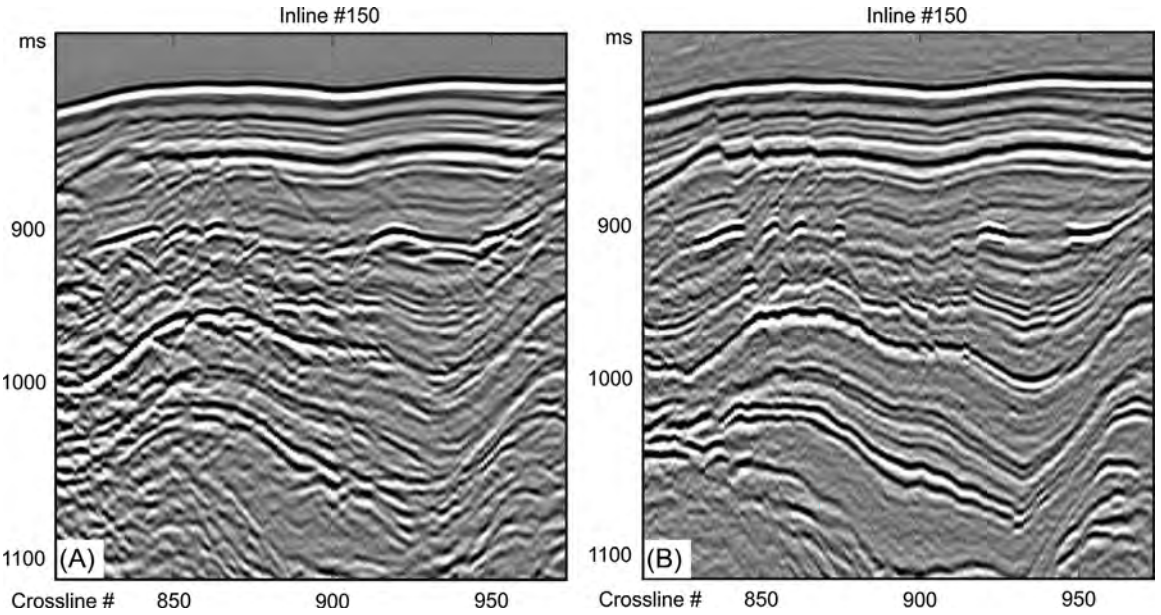


FIG. 11.38 (A) A 2D line (inline #150) from a 3D survey processed by 2D poststack time migration. (B) The same line after 3D migration. In the 3D migrated image, out-of-plane reflections are removed, fault planes are much clearer, and trace-by-trace consistency of the reflections is much better.

dimension (the side-sweeps) are completely removed, resulting in a significantly improved illumination with sharp fault planes, and the reflections have better trace-by-trace consistency.

11.10 DIP MOVEOUT

Poststack migrations generally do not yield correct results since stack sections are not perfectly equivalent to zero-offset sections, due to the conflicting dip issues and in the case of lateral velocity variations, which leads to use of costly prestack algorithms. Prestack partial migration, or the DMO approach, provides a better stack section that is almost identical to the zero-offset section, so that one can apply a more economical poststack migration to the DMO output to obtain an image very similar to that from prestack migration. The issue to be solved with the DMO process is conflicting dips, which originate from the dip dependent stacking velocities. NMO correction becomes a dip filter in areas of structurally dipping reflectors (Liner, 1999), and the processor picks the velocities in favor of only one dipping event (Fig. 11.33).

Recalling the Levin equation, given by Eq. (10.7)

$$t^2(x) = t^2(0) + \frac{x^2\cos^2\phi}{V^2} \tag{11.2}$$

where ϕ is the inclination of the reflector, V is the velocity of the upperlying medium, and x is the source-receiver offset. Considering the equality $\sin^2\phi + \cos^2\phi = 1$, we can divide Eq. (11.2) into two parts to get

$$t^2(x) = \underbrace{t^2(0) + \frac{x^2}{V^2}}_{\text{NMO}} \underbrace{- \frac{x^2\sin^2\phi}{V^2}}_{\text{DMO}} \tag{11.3}$$

The first part of Eq. (11.3) is the NMO term, while the second part is known as the DMO term. According to Eq. (11.3), we can first apply an NMO correction using the velocity of the upperlying medium, and then a DMO correction is applied. Although NMO is valid in the CDP domain, the DMO term must be defined in the common offset domain, which allows us to discriminate the dipping events.

Consecutive applications of NMO and DMO processes remove the offset and provide a more accurate NMO correction for all available dips in the data. The poststack migration followed by the NMO and DMO processing sequence will provide almost identical results with a prestack migration (Fig. 11.39) and with a considerably low cost, since the processing flow given in Fig. 11.39 is much more computationally effective as compared to conventional prestack time migration. Furthermore, in contrast to NMO correction, which is rather sensitive to velocity errors, constant velocity DMO is almost independent from the velocities picked during the velocity analysis (Liner, 1999).

For the zero-offset case of identical source-receiver pairs on the earth's surface, the reflector may be found at any depth and may have any inclination in the subsurface. For instance, if the recorded zero-offset time is 1.0 s and the propagation velocity is 1000 m/s, we only have the information that the total distance traveled will be 1000 m for all of the source-receiver pairs. Based on this information, one can conclude that there may be several possibilities to determine the correct location of the reflector, since it may be located at any position on an ellipse 1000 m away from all available source-receiver pairs. The NMO term gives only the possibility of the horizontal reflector case just below the

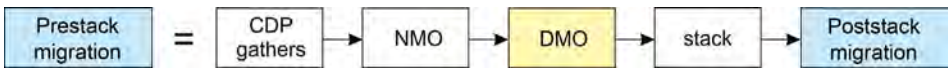


FIG. 11.39 Dip moveout (DMO) flow followed by a poststack migration can be used instead of costly prestack migration flow.

source-receiver pair at the center, while the DMO term provides all other possibilities (Liner, 1999). If the NMO result of this one trace is input to a DMO process, then it produces several DMO traces, which form another ellipse termed the DMO ellipse.

DMO processing consists of four main stages, indicated by numbers I to IV in the schematic illustration in Fig. 11.40:

I. It is assumed that the reflection point in prestack CDPs is located in the midpoint position between source and receiver (point O) and the reflection is recorded at time $t(x)$.

II. After NMO correction, arrival time $t(x)$ is moved to zero-offset time $t(0)$, but the reflection is still located below the midpoint position (point O).

III. DMO moves this reflection to true zero offset distance, which is the location between source and receiver where the true zero-offset ray normal to the reflector is recorded at the surface (point S). This process eliminates CDP smearing, shown in Fig. 8.5.

IV. After poststack migration, the reflection is moved to its correct subsurface location below the surface position M, and to its accurate recording time.

All these processes are actually done by conventional prestack migration algorithms as a single processing step (Fig. 11.40). Following the DMO process, stack data quality can be increased if the velocity analysis is repeated after an inverse NMO correction using the processing flow given in Fig. 11.41.

DMO significantly increases the quality of semblance plots and provides a better and more accurate velocity picking. Fig. 11.42 compares

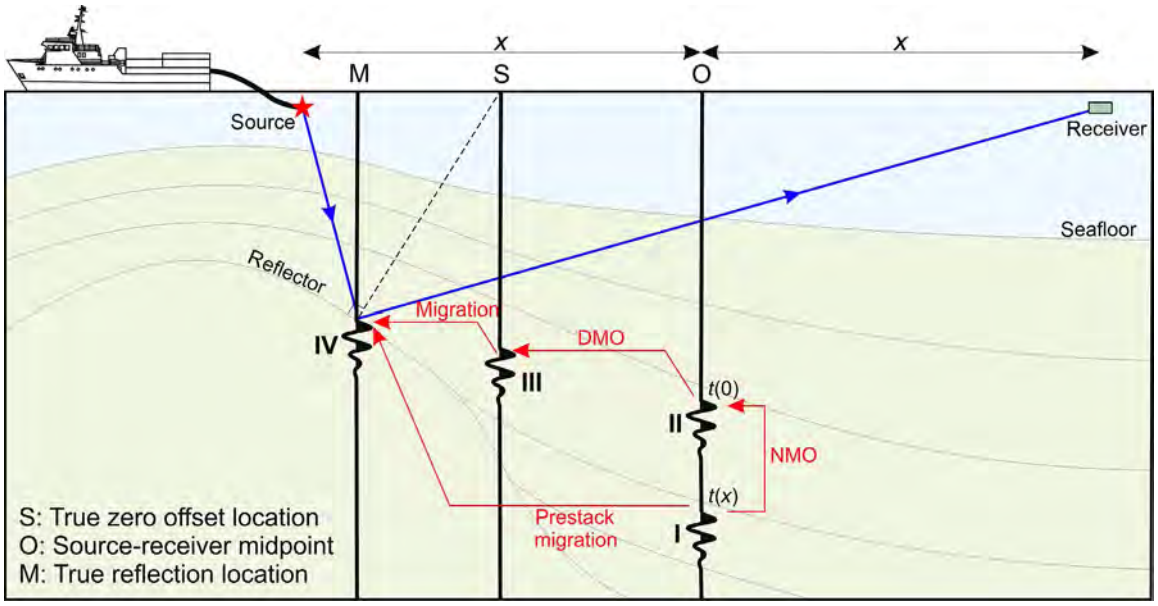


FIG. 11.40 Schematic illustration of NMO, DMO and poststack migration sequential processes and their relationship with prestack migration. A reflection event in the prestack data is assigned to the midpoint (O) between source and receiver at time $t(x)$. Arrival time $t(x)$ is moved to zero-offset time $t(0)$ after conventional NMO correction, but the reflection is still below the midpoint location O. DMO moves the event to its true zero offset distance (S), and after subsequent poststack migration, the event is moved to its correct subsurface location (M). Prestack migration fulfills all these processes at once as a single step.

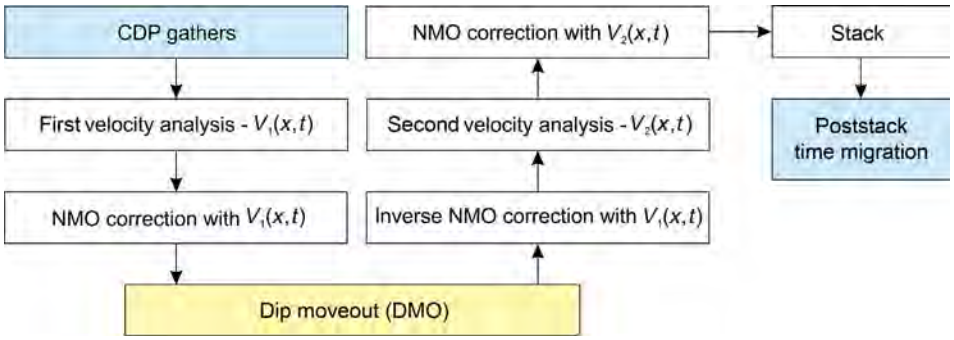


FIG. 11.41 Processing flow to improve stack quality using DMO. Since DMO removes the conflicting dips issue, quality of the semblance plots, and hence, accuracy of the velocity analysis after DMO processing is significantly improved.

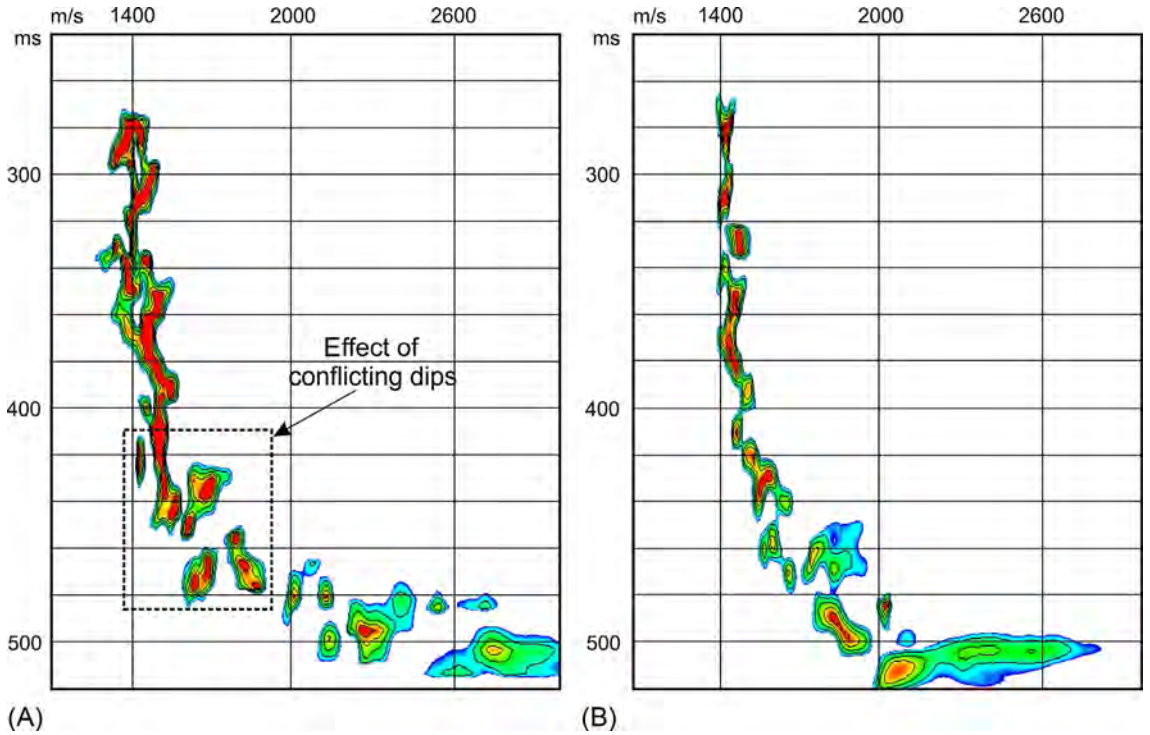


FIG. 11.42 Velocity spectra (A) before, and (B) after DMO. Accuracy of the velocity picks after DMO is enhanced since DMO removes the multiple enclosures shown by the dashed rectangle in (A) arising from the conflicting dips.

velocity spectra before and after DMO processing. After DMO processing, semblance contours generally become clearer and better velocity functions are obtained. Removal of dip dependence of the velocities allows processors to pick the correct velocity both for flat and dipping events at the same time. In Fig. 11.42A, for instance, there are several multiple enclosures approximately coinciding, with the same zero-offset time of the semblance plot

indicated by a dashed rectangle. In these zones, it is not possible to pick velocity values characterized by both enclosures with the same zero-offset time, and the processor picks a velocity value that conforms to the common trend of the semblance contours. After DMO processing, however, the conflicting dips issue is solved and a more accurate velocity picking is possible, as in Fig. 11.42B, which provides that the amplitudes of the conflicting events are better preserved in the stack section.

Fig. 11.43 compares the results of poststack time migration (Fig. 11.43A) and DMO processing (Fig. 11.43B) utilizing the flow shown in Fig. 11.41. The differences between the conventional poststack time migration and DMO outputs are distinctive, especially along the fault planes, which are much sharper and more distinct in the DMO output. Horizontal layers are not affected by DMO processing. Fig. 11.43C shows the Kirchhoff prestack time migration image to compare the output of poststack migration followed by DMO processing. One can conclude that the DMO with a poststack migration output is almost identical with the prestack migration image shown in Fig. 11.43C.

Deregowski (1986) summarizes the effects of DMO processing on input seismic data:

- DMO moves each trace to its correct zero offset location; hence each common offset section becomes identical to a zero-offset section.
- Crossline ties between the seismic data in a particular survey area are improved in the case of 2D acquisition.
- CDP smearing is eliminated and all CDPs have reflections from the same common reflection points.
- Poststack time migration becomes almost identical to prestack time migration.
- Stacking velocities become dip independent, and the events with conflicting dips are stacked correctly.
- Velocity analysis is improved, and the velocity field used for stacking becomes usable for migration.
- Abnormally steep coherent noise is eliminated and fault planes become much clearer.
- DMO has no effect on horizontal events.

11.11 WHICH MIGRATION TO USE?

Different migration implementations applied to prestack or poststack data, utilizing different theoretical basis and algorithms, exist on the market today, and each migration type has its own advantages and solution capabilities as well as shortcomings. Table 11.2 compares general characteristics of these different methods. Although cost and data characteristics (such as the quality of the input data, lateral velocity variations, structural complexity, maximum dip, etc.) are the most effective parameters on the selection of the suitable algorithm to apply prestack or poststack migration, the selection of optimal migration type appropriate for the input data commonly depends on the experience of the processor.

Farmer et al. (1993) proposes the characteristics of an ideal migration method; no algorithm could do all of them in practice. That is, an outstanding migration must

- handle full range of dips.
- compensate for large velocity changes such as >40%.
- relocate all of the reflection events to their true subsurface locations.
- preserve amplitude and phase information of the input data.
- generate no artifacts, spurious events or noise.
- be computationally efficient and fast.

Fig. 11.44 schematically summarizes the proper application of different migration

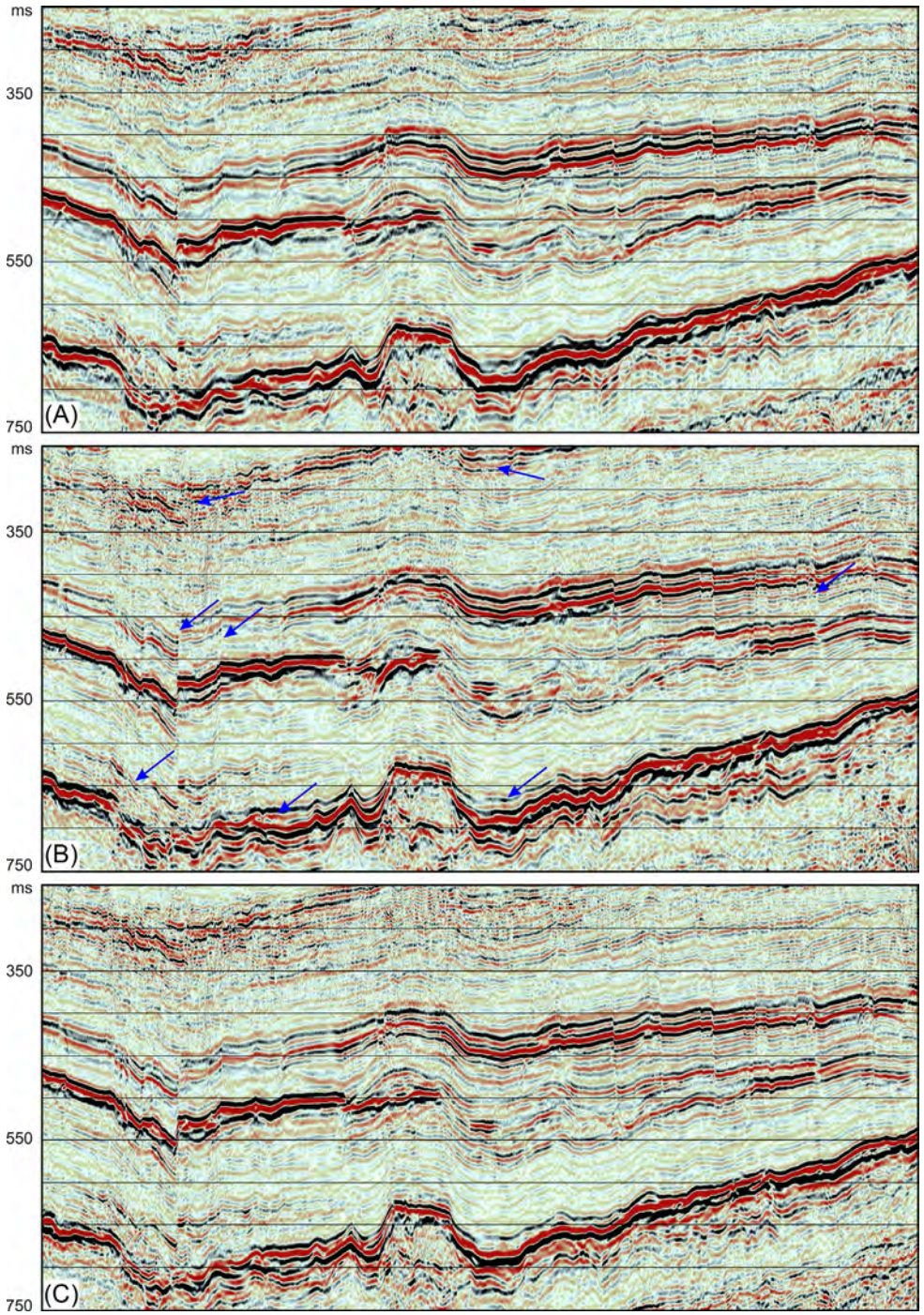


FIG. 11.43 Example seismic sections (A) after Kirchhoff poststack time migration, (B) after DMO processing, and (C) prestack Kirchhoff time migration output to compare the DMO output in (B). Improvements in the DMO image are indicated by *blue arrows*.

TABLE 11.2 Different Types of Migrations and Their Basic Specifications

Migration Type	Specification
Poststack time migration	• Valid if stack section equals to zero-offset section • Adequate in case of diffractions and structural dip • Handles vertical velocity variations • Handles smooth lateral velocity variations • The most computationally efficient migration type
Poststack depth migration	• Adequate for excess structural dip • Handles strong lateral velocity variations • Less economical than poststack time migration • Requires an accurate interval velocity-depth model
Prestack time migration (PSTM)	• Applied to CDP gathers or common offset sections • Adequate in case of strong structural complexity • Solves conflicting dips issue • Produces image gathers for velocity analysis and AVO • Less economical than poststack time or depth migrations
Prestack depth migration (PSDM)	• Applied to CDP gathers or common offset sections • Adequate in case of strong structural complexity • Adequate for excess structural dip • Handles strong lateral velocity variations • Less economical than any other migration type • Requires very accurate interval velocity-depth model
Dip moveout (DMO)	• Simplified version of PSTM • Solves conflicting dips issue • Followed by a poststack migration • Velocity analysis is significantly improved • Assumes a constant velocity model, which induces issues in areas of structural complexity

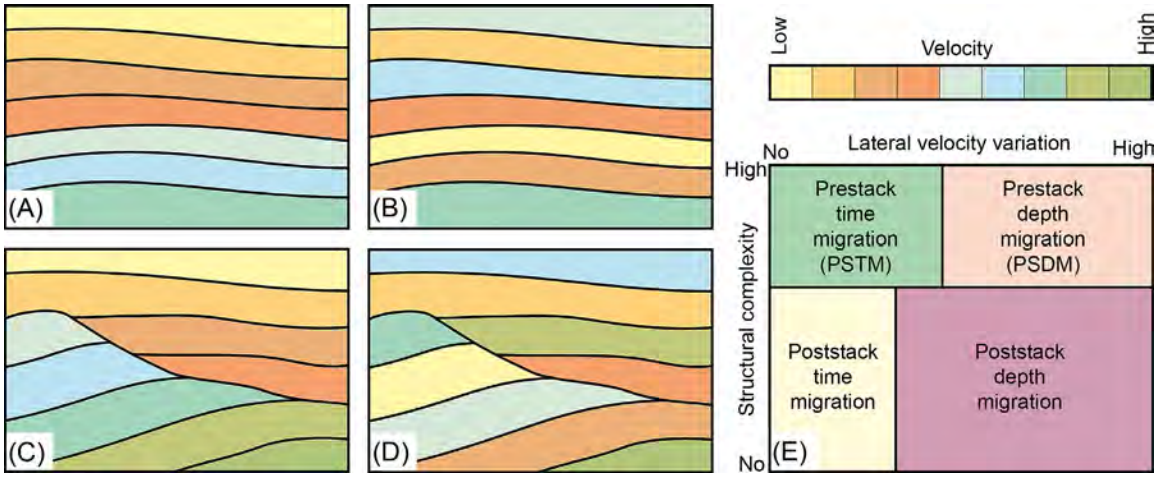


FIG. 11.44 Schematic illustration of proper migration algorithm in different geological settings. The suitable migration types are (A) poststack time migration (smooth geology, simple velocity gradient), (B) poststack depth migration (smooth geology, complex velocity gradient), (C) prestack time migration (complex geology, simple velocity gradient), (D) prestack depth migration (complex geology, complex velocity gradient). (E) A generalization of different migration types suitable for different geological situations.

algorithms in different geological settings. Poststack time migration is the simplest one, which can be applied in areas of low geological complexity and of predominantly vertical velocity gradient. If high lateral velocity variations and structural dip exist, then poststack depth migration can be preferred. In geologically complex areas and strong lateral velocity variations, prestack time or prestack depth migration should be considered. Although depth migrations yield superior results, they are very sensitive to velocity errors, and this situation, in fact, still remains as the most important and fundamental imaging problem related to all available migration types and algorithms. The accuracy of a depth migration imaging unfortunately strongly depends on the accuracy of the interval velocity versus depth model. In some cases of strong lateral velocity variations, anisotropic depth migration, which accounts for vertical transverse isotropy (VTI) or orthorhombic symmetry (ORT) (Section 10.1.5) using Kirchhoff or Beam migration algorithms, may be required to image the subsurface correctly.

Over the last few decades, time domain images of the subsurface have become acceptable by interpreters in the oil and gas industry. In recent years, however, exploration has been extended into the geologically complex areas where the velocity of the subsurface varies in all three dimensions, especially in areas of salt intrusions. In such challenging settings, depth imaging must be used to define the subsurface geology correctly, since time domain processing commonly produces misleading results (Albertin et al., 2002). As an excellent example, Fig. 11.45 compares the results of different migration types on a well-known Marmousi-II synthetic dataset (Martin et al., 2006). Among these, the best result is achieved from Kirchhoff prestack depth migration, since both the geology and velocity distribution are quite complex. Today, prestack Kirchhoff depth migration in 2D and 3D is considered to be one of the leading imaging processes in the hydrocarbon industry.

Fig. 11.46 shows the relationship between cost and computational efficiency of the available migration algorithms. Normally, prestack algorithms require more computational time than poststack algorithms, and depth migrations need more time than time migrations (time migrations are approximately 10 times faster than depth migrations). To overcome excess run times of the prestack algorithms, partial migration or DMO algorithms may be preferred.

Different algorithms utilizing the migration types in Fig. 11.46 can be used to migrate the seismic data. Table 11.3 summarizes the most common algorithms used by the seismic exploration industry and academia today. Although the cost of the migration algorithm is one of the most important parameters in selecting the suitable algorithm, the accuracy and quality of the output image, especially in complex geological environments such as the zones of salt tectonics or velocity inversions, are also deterministic factors today. Hence, despite its higher cost, the most promising algorithm used widely by the industry is reverse time migration due to its accuracy in complex geological settings, although the most common algorithm still used in the industry today is the variants of Kirchhoff diffraction summation method. The reason for this is that the Kirchhoff migration algorithms and their restrictions, advantages, and shortcomings are well known. Furthermore, the suitable selection of the parameters of Kirchhoff migration algorithms is relatively well established by seismic data processors, which results in reliable migration results over the years.

11.12 QC IN MIGRATION

In practice, a number of agents affect the performance of the migration and quality of the output images. Some of these specific factors may produce typical noise or migration artifacts, such as smiles from spikes or fake events such

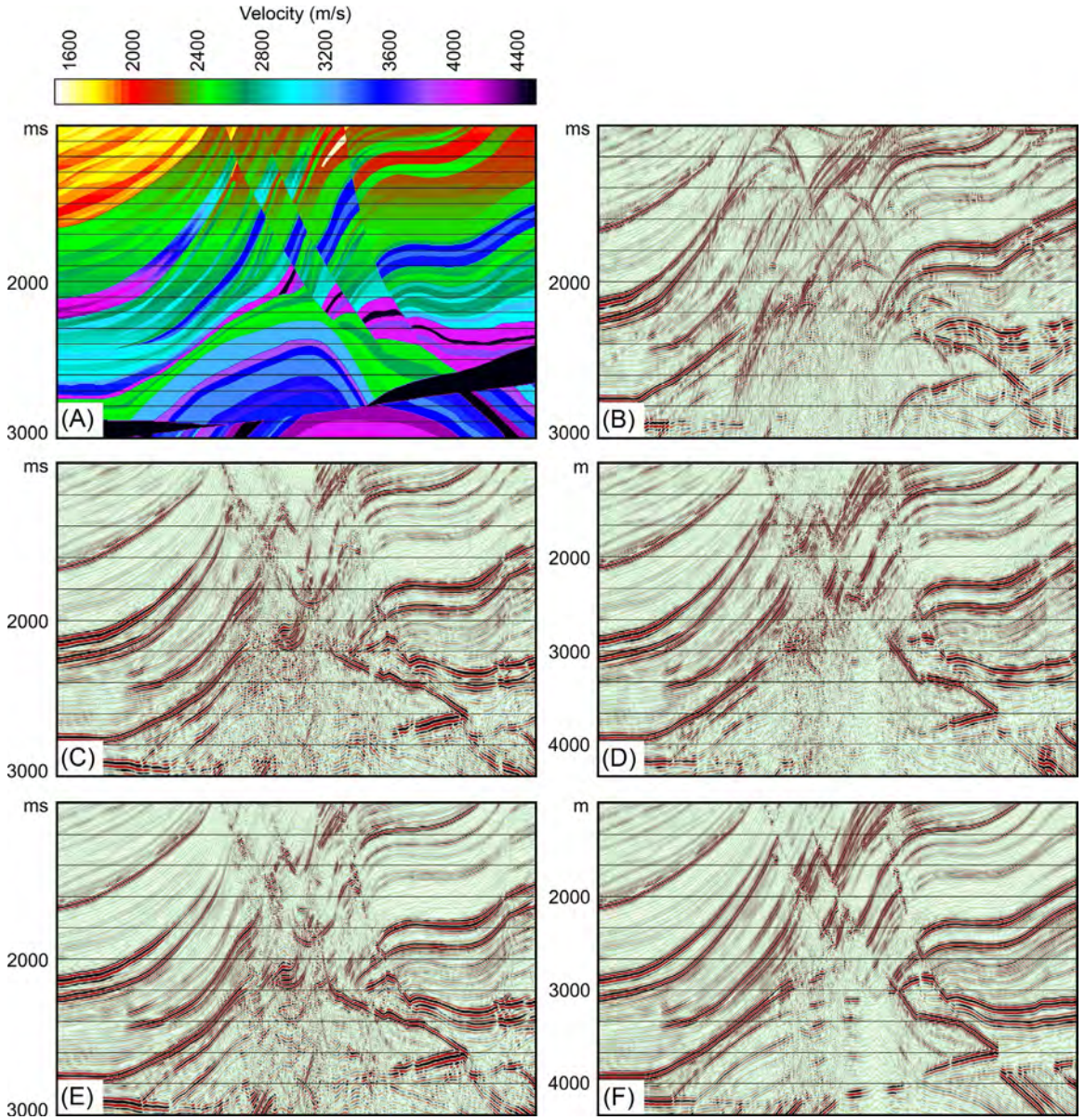


FIG. 11.45 Comparison of the results from different migration types on the Marmousi-II synthetic dataset. (A) P wave velocity model, (B) stack section, (C) Kirchhoff poststack time migration result, (D) Kirchhoff poststack depth migration result, (E) Kirchhoff prestack time migration result, and (F) Kirchhoff prestack depth migration result. Prestack depth migration produces the best image since the geological setting and subsurface velocity distribution of the model is quite complex.

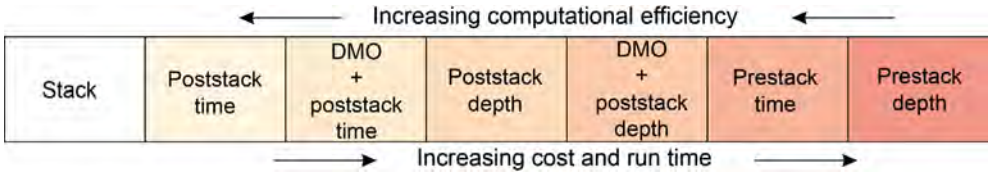


FIG. 11.46 Relationship between relative cost and computational efficiency of most common migration types. Depth migrations are more costly than time migrations, and prestack migrations are more costly than poststack migrations.

TABLE 11.3 Different Migration Algorithms and Their Specifications, as well as Their Relative Costs (0, the Most Expensive; 1, Expensive; 2, Moderate; 3, the Cheapest)

Migration Algorithm	Specifications	Cost
Stolt	• The most computationally efficient algorithm available • Valid for constant velocity medium • Handles steep dips up to 90 degrees • Available only for poststack applications • Can be used to obtain quick reference output images	3
Phase shift (Gazdag)	• Handles steep dips up to 90 degrees • Valid for vertical velocity variations • Available only for poststack applications • Low noise in the output images	2
Finite difference	• Relatively faster and hence economical • Suitable for dips up to 35 degrees • Large depth steps cause kinks, dispersion and undermigration • Less sensitive to velocity errors	2
Omega-*x*	• Uses finite-difference approach • Handles steep dips up to 70 degrees • Good at vertical and horizontal velocity variations	1
Kirchhoff	• The most widely used algorithm today • Valid for vertical and horizontal velocity variations • Handles steep dips up to 90 degrees • Can be used for prestack or poststack implementations • Can be implemented in time or depth domains • May produce false horizontal events at deep	1
Reverse time	• The most promising algorithm for the near future • Can be used for prestack or poststack implementations • Handles steep dips up to 90 degrees and beyond • Can be implemented in time or depth domains • Best algorithm for complex geology • Suitable for wide azimuth (WAZ) seismic data • Valid for vertical and horizontal velocity variations • The most costly algorithm on the market	0

as smears. To prevent artifacts, input seismic data must be preconditioned properly before the migration, which involves removing erroneous amplitudes, such as spikes, and any type of coherent and random noise. Missing traces and irregular fold distribution, data gaps or inappropriate muting of the amplitudes may induce artifacts into the migration output, since it is a process based on the principle of constructive and destructive interference of the seismic amplitudes. In such cases, input seismic data must be properly interpolated and regularized before the migration, using a suitable interpolation technique. In this chapter, some of these specific agents that cause noise or migration artifacts in the output image will be explained briefly so that the processor notices the issues directly arising from the migration process itself or its inputs, such as the input data or velocity model.

Spatial aliasing is an important problem for migration and is considered to originate from two causes:

- coarse trace spacing in the input data, known as data aliasing
- coarse sampling of the hyperbola (in 2D) or hyperboloid (in 3D) shape migration operator, known as operator aliasing.

Data aliasing is directly related to the input trace interval and is more pronounced for steeply dipping events. Aliased energy is located at the negative panel in the *f-k* spectrum, and migration supposes these events to be reverse dipping energy. After migrating the aliased amplitudes, dispersion noise or a coherent spurious event occur in the migrated image. The effect of data aliasing on migration is quite similar for the Kirchhoff, finite-difference, *f-k* and reverse time migration algorithms.

Acquisition parameters are quite important for the quality of the migration output as well as to prevent data aliasing. Input data to the migration must have trace spacing as fine as possible to prevent aliasing before the migration. The distance between the CDPs in the migration input directly affects the quality of the migration output. Fig. 11.47 shows poststack Kirchhoff migration images of the same dataset with 3.125, 6.25, and 12.5 m trace intervals. Finer trace intervals result in much higher resolution in migration and sharper images of the subsurface. Today, an inline group interval of 6.25 m is typical in the petroleum industry for seismic acquisition, which leads to a CDP interval of 3.125 m. In 3D surveys, however, crossline trace spacing is commonly higher than inline trace spacing and data interpolation in the crossline direction is generally required before the 3D migration.

Operator aliasing may occur even when the input data has a sufficiently fine spatial sampling interval and even if it is actually not spatially aliased (Biondi, 2001). Unlike data aliasing, operator aliasing also induces extra noise into the final image. Data aliasing can be solved either by data interpolation, to get a finer trace interval, or by using an antialiasing filter option of the migration operator (Zhang et al., 2003). Operator aliasing, however, is commonly avoided by removing the high-frequency components during the summation process in Kirchhoff migration, which ultimately degrades the overall image resolution (Biondi, 2001). Fig. 11.48 shows an example for operator aliasing in Kirchhoff migration. Fig. 11.48A shows the Kirchhoff poststack time migration output of zero-offset data with a 3.125-m trace interval with a suitable (unaliased) migration operator, while Fig. 11.48B illustrates the migration output of the decimated version of the section in Fig. 11.48A into a 6.25-m trace interval. It is clear that the image in Fig. 11.48B is much noisier due to the operator aliasing during the Kirchhoff migration.

The amount of aliasing in the data can be controlled in Kirchhoff migration algorithms that apply an antialiasing filter during the migration. Fig. 11.49A shows a synthetic constant velocity zero-offset section with a diffraction hyperbola

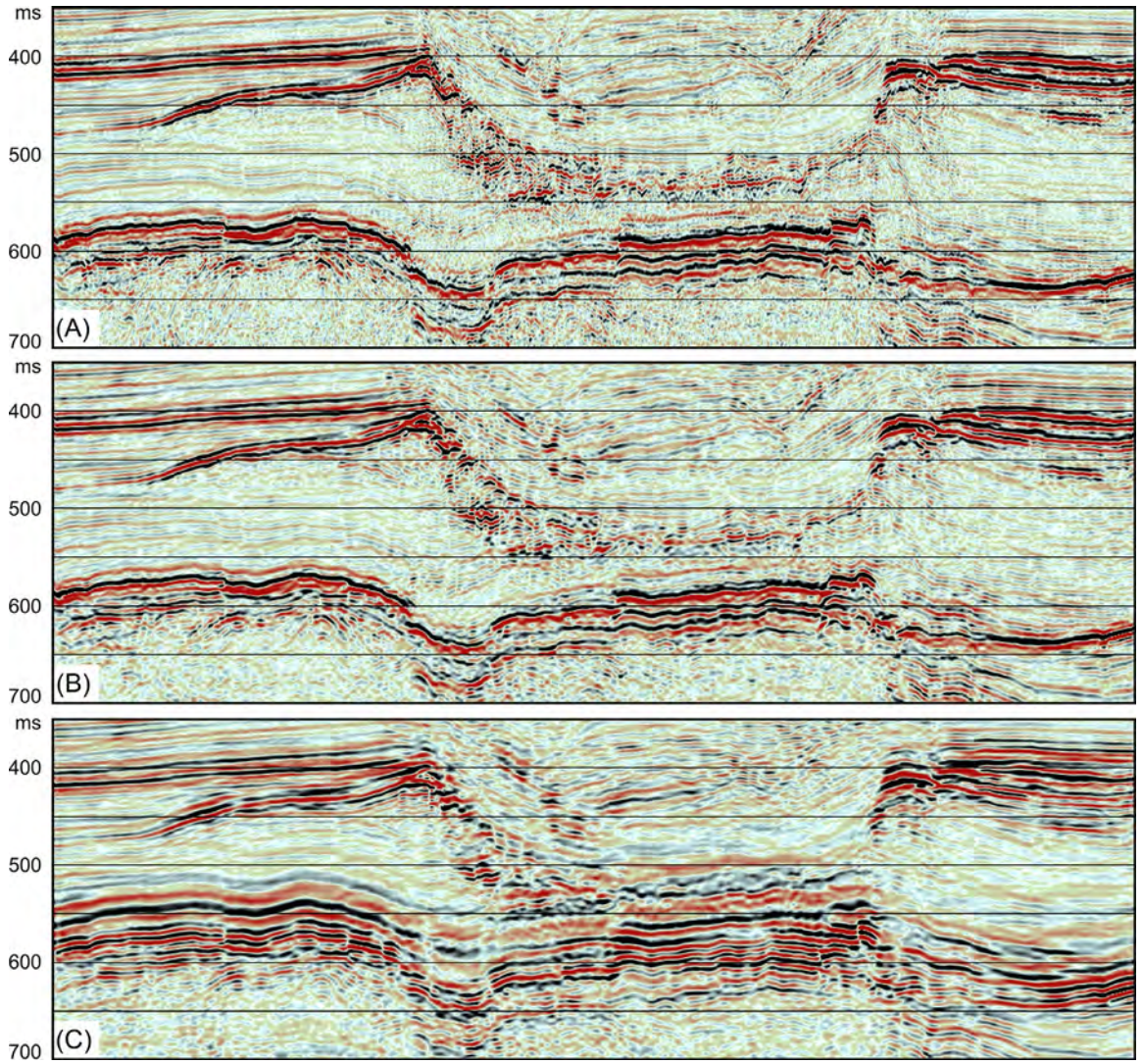


FIG. 11.47 Poststack Kirchhoff time migration results of an input dataset with (A) 3.125 m, (B) 6.25 m, and (C) 12.5 m CDP intervals. Finer trace intervals result in much higher resolution and sharper images after migration.

and a steeply dipping event. The Kirchhoff migration result with and without an antialiasing filter is given in Fig. 11.49B and C, respectively. In the case where the spatial sampling is not small enough, high-frequency components are spatially aliased, which causes artifacts in the output image, especially close to the surface where the velocities are relatively low. One must suspect data aliasing if such systematic noise exists near the surface after migration.

Aliasing also occurs in prestack migration if the data consists of steeply dipping events. Apart from Kirchhoff migration, which suffers from operator aliasing, Zhang et al. (2003)

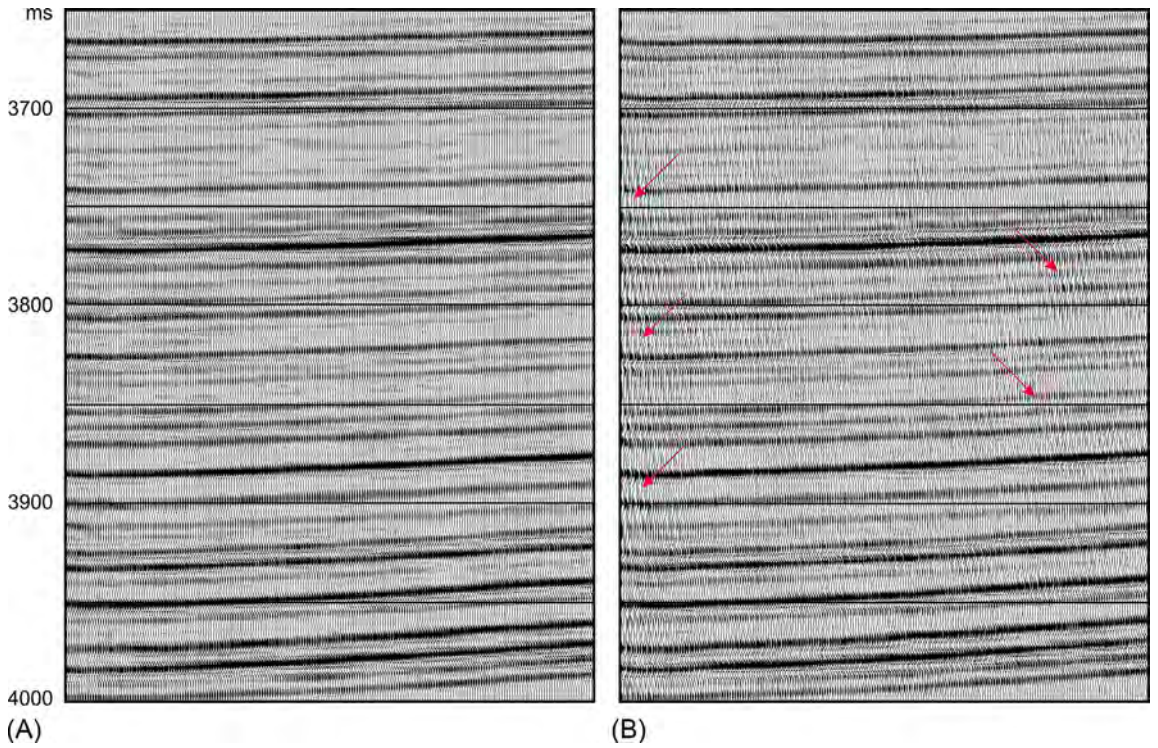


FIG. 11.48 (A) Migration result of a stack section with 3.125-m trace interval using an unaliased migration operator. (B) Migration result of decimated version of the same stack section used in (A) into 6.25-m trace interval. A Kirchhoff poststack time migration is used as the imaging algorithm. Operator aliasing causes noisy migration images *(red arrows)*.

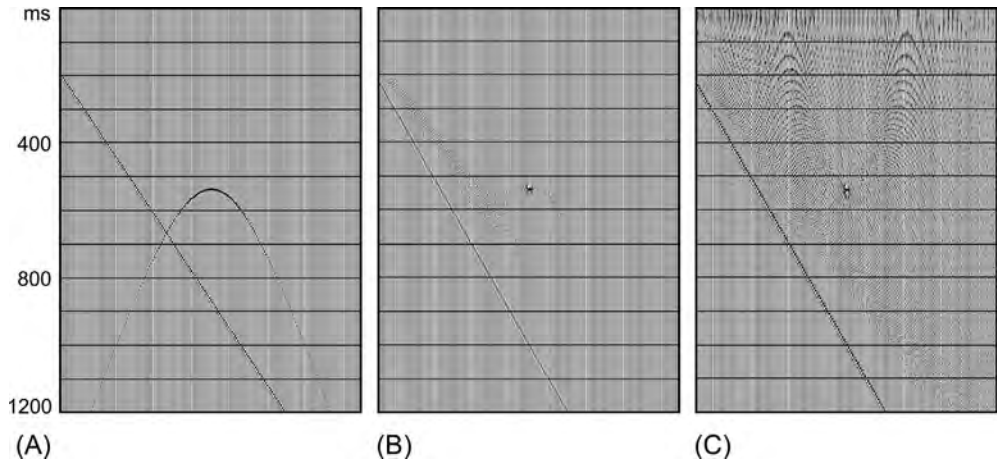


FIG. 11.49 (A) A synthetic zero offset section with a diffraction hyperbola and a steeply dipping event, and its Kirchhoff migration results (B) with and (C) without antialiasing filter option during the migration. Aliasing causes systematic noise close to the surface.

suggest that frequency domain and finite-difference prestack migration algorithms also have aliasing issues, even for unaliased input data, which is a specific type of aliasing termed imaging-condition aliasing. They also suggest that the solution is spatially interpolating the downward-continued wave fields.

The deeper parts of a seismic section are generally problematic zones for migration, where the random noise amplitudes dominate, velocity is relatively high and primary reflection amplitudes are low or even absent. Spurious horizontal events (smearing) may frequently occur after migration in these parts of the data, which is particularly visible in the outputs of small-aperture Kirchhoff migration (e.g., between approximately 4400 and 5000 ms in the Kirchhoff migration output in Fig. 11.50B). The reason for smearing in the deepest parts of a migrated section is that the summation is terminated at the end of the section where the diffraction hyperbolas are incomplete (Fig. 11.11B), and therefore the effective aperture width is indispensably smaller than that for the shallower parts. This means that only amplitudes close to the apex of the hyperbolas can be incorporated into the summation in Kirchhoff migration, which results in the migration acting as a dip filter passing only horizontal events.

Borders of the input seismic line must be treated carefully during the migration, since there would be no place to updip replacement of the dipping events located close to the edges of the input seismic line. To prevent complications, the section is expanded in both directions by incorporating zero-amplitude traces and by adding zero samples to the end of the traces in a zone, like the blue area in Fig. 11.51A. This process is accomplished during the migration and is known as zero padding.

In addition, tapering is applied to the data before migration to avoid edge effects due to the migration aperture. Generally, amplitudes within a narrow zone along the borders of the

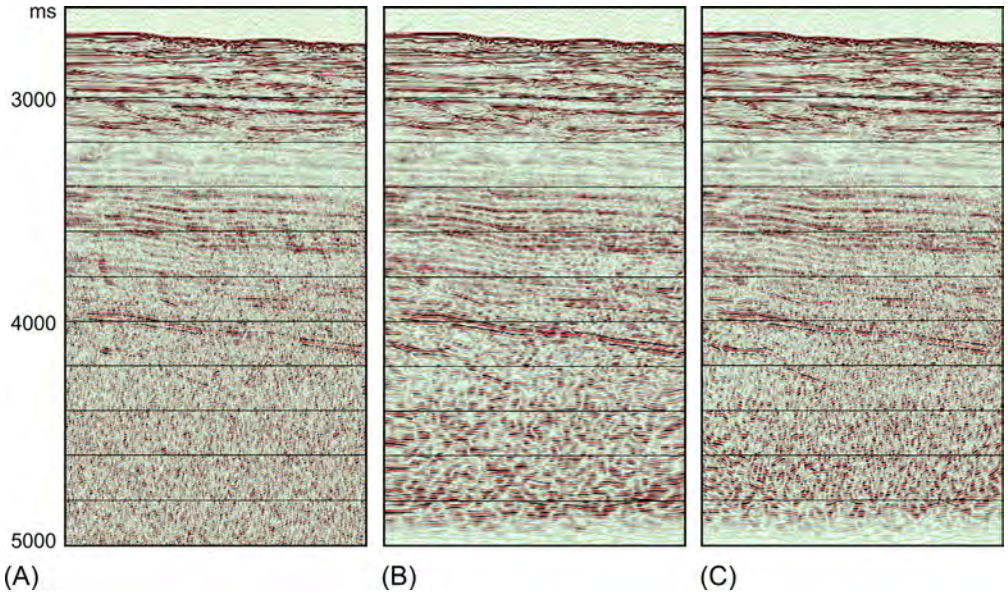


FIG. 11.50 (A) Stack section, and its Kirchhoff poststack time migration outputs for (B) 500-m and (C) 2000-m aperture width. Narrow apertures cause fake horizontal events (smears) in the deeper parts of the data (approximately between 4400 and 5000 ms) where there are almost no reflection amplitudes.

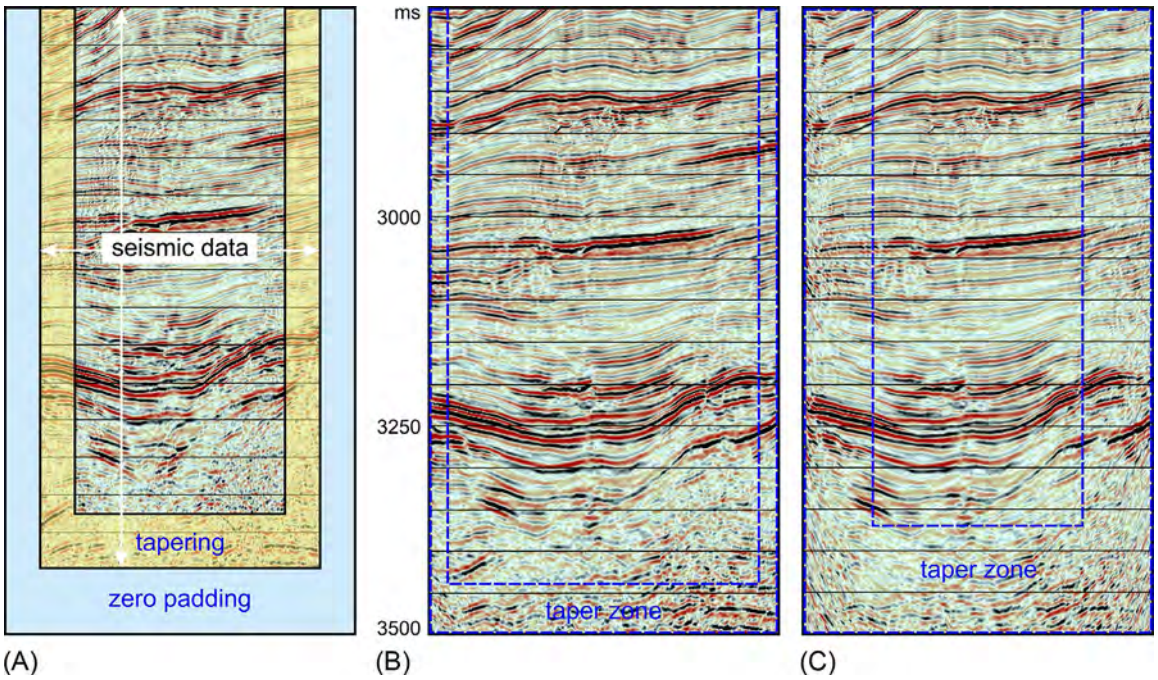


FIG. 11.51 (A) Schematic illustration of zero padding *(blue)* and tapering *(yellow)* zones applied to the input section before the migration. Migration results with (B) a suitable taper zone, and (C) an unnecessarily wide taper zone. Taper zones are enclosed with *dashed blue lines*.

seismic data, like the yellow area in Fig. 11.51A, are tapered to zero. The bottom height of the tapered zone is usually 200 ms and the width of the zone at the edges is generally 50–100 traces, depending on the trace lengths and number of traces involved in the input data. In some cases, a conical taper zone for the edges is preferred, which is narrow for time zero (e.g., 20 traces) and widens towards the end of trace length (e.g., 100 traces) since the diffraction hyperbolas, and hence the migration apertures, get wider as the depth or recording time increases. Unnecessarily wide taper zones, however, induce noise in the migration output. Fig. 11.51B shows a migration result with a suitable taper zone. If the taper zone is too wide, higher frequency, upwards-curved coherent noise appears along the sides and bottom of the section (Fig. 11.51C).

Migration artifacts at the start and end of the seismic lines are not limited to the edge effects or the inappropriate selection of the taper zone widths. We commonly have mute zones due to NMO stretching at the beginning of each seismic line where the early arrivals of the traces from far offsets are muted out, especially for shallow water surveys (Fig. 10.35). These mute zones have zero amplitudes (Fig. 11.52A) and cause very characteristic noise in the migrated image, termed swings (Fig. 11.52B). Swings occur because there are no nonzero amplitude values within the mute zone to wipe out the unnecessary amplitudes by destructive interference during the migration. Although they are observed at the start of the line, similar effects may also arise at the end of the line, or where there are any gaps in the data possibly due to trace kill, surgical mute, or irregular acquisition of the data. It is

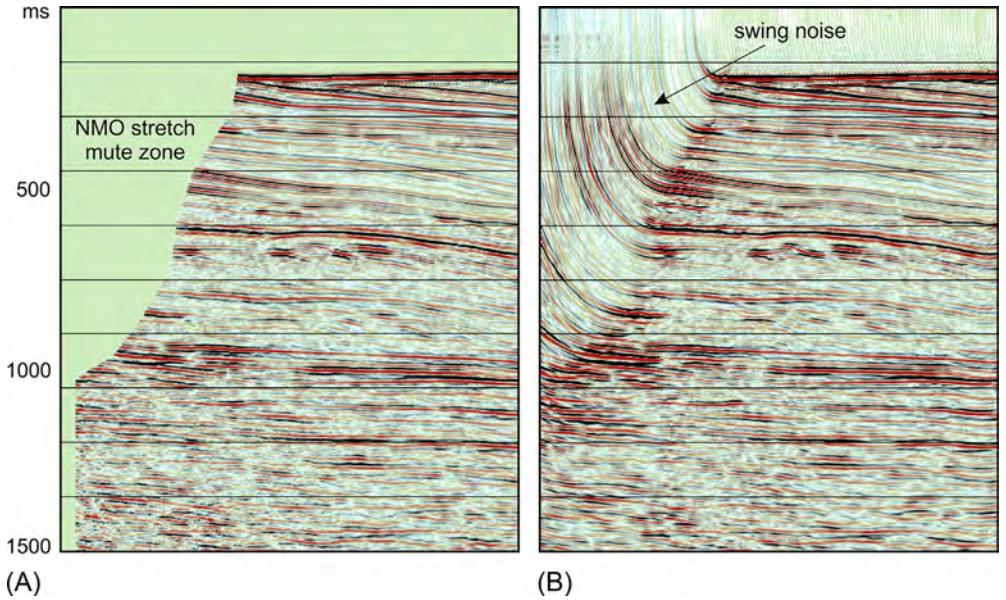


FIG. 11.52 (A) Start of the line side of a stack section from relatively shallow waters (line direction is left to right) with a relatively large NMO stretch mute zone of zero amplitude values, and (B) its migration result. Zero amplitudes within the mute zone cause swings after migration.

important to reapply trace mutes after migration to avoid swings.

As discussed in Section 11.2.1, Kirchhoff migration is effective in a conical zone on the data (Fig. 11.12). Outside of this conical zone, after migration a triangular area can form that is generally not usable, since it almost completely comprises curved fake events (Fig. 11.53) formed by the Kirchhoff migration operator, due to insufficient data for a complete diffraction summation along the edges. If the seismic line length is too short, then these edge effects may cover most of the seismic line. The most convenient solution is to collect the data along the seismic lines as long as possible, since too-short seismic lines are not appropriate for migration.

In some specific cases, discussed in Section 3.10.2, the seismic data may contain extremely high-amplitude transient noise bursts called spikes, which are of amplitudes commonly several orders of those of primary reflections. If they are severe and randomly distributed all over the line, then the data after migration becomes completely degraded (Fig. 3.38). In some cases, it may not be easy to distinguish the isolated spikes in the stack data until migration. Fig. 11.54 shows an example of an isolated spike on the stack section and its migration response. Every single spike in the input data causes a migration impulse response (Fig. 11.9) and induces distinctive smiles after migration, and it is generally required to turn back to the preprocessing to remove the spikes by a suitable process, such as surgical mute. It is recommended to apply a faster migration algorithm such as a Stolt migration before costly prestack migrations, to check if the data has spike issues.

The migration algorithms used in the oil and gas industry today are very robust and accurate. However, they do need accurate input velocity fields to produce good images of the subsurface, which is still the blind side of all migration algorithms. Although poststack time migrations are

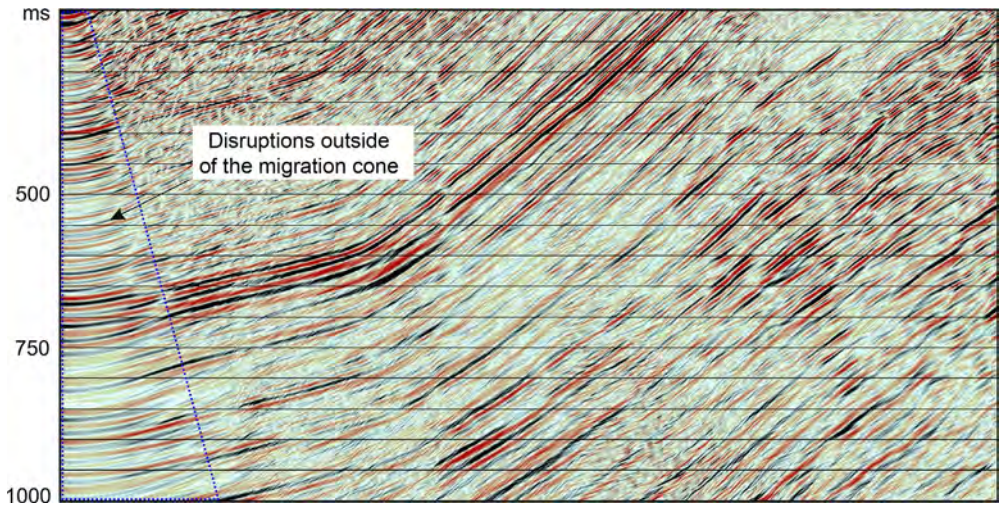


FIG. 11.53 Disruptions within a triangular area outside of the migration cone after Kirchhoff poststack time migration.

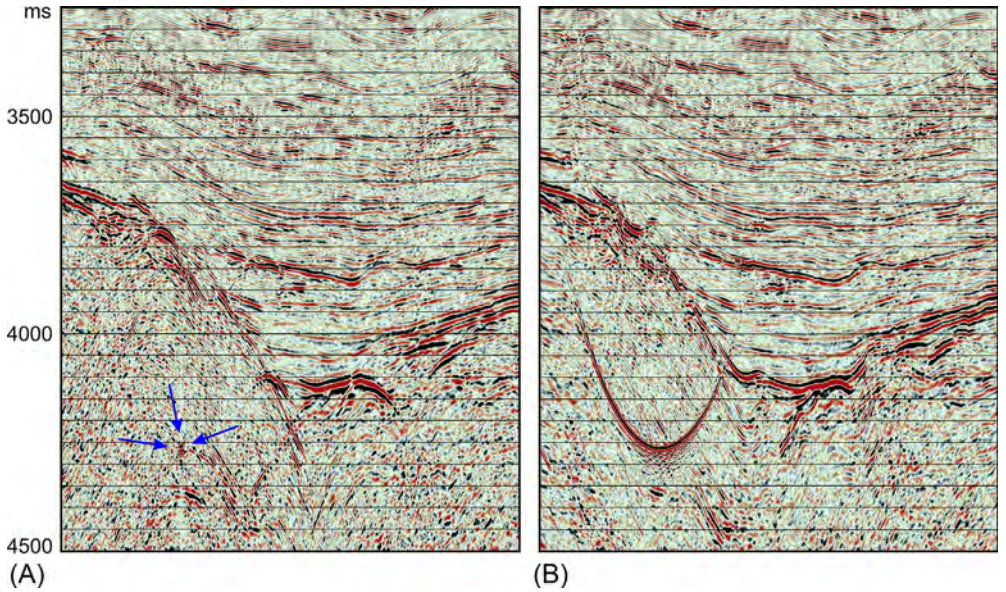


FIG. 11.54 (A) An isolated spike *(arrows)* on a stack section and (B) its Kirchhoff poststack migration result. Migration transforms the high-amplitude spikes into the migration impulse response of a semicircle.

less sensitive to velocity errors, depth migration algorithms in particular need very accurate and carefully constructed velocity models, since the whole image may be degraded due to a simple localized error in the velocity field. On the other hand, obtaining the true velocity model of the subsurface is sometimes quite a difficult process in structurally complex areas where velocity

inversion or salt tectonism exists. A processor should always keep in mind that the final image after migration strongly depends on the quality and accuracy of the velocity model as input to the migration, no matter how good the quality of input data or how robust the implemented migration algorithm is.

The effects of incorrect migration velocity on the final image can be classified into two groups:

- Systematic velocity errors appearing as a certain percent fast or slow velocities for the whole velocity model.
- Localized velocity errors arising at specific locations along the line, where the velocities are picked.

Effects of systematic velocity errors on the migration output affect the whole seismic line and show up in different ways. In the case of a few percent slower velocities, the sharpness of some specific structures such as fault planes is lost (Fig. 11.55A), since the diffractions along the fault cuts are not perfectly collapsed. Syncline structures are not imaged correctly since the bow-tie effect cannot be untied, and the inclined events are undermigrated. If the velocity field is a few percent faster, then the anticlines get too narrow while the synclines become wider than what they actually are. Inclined events are overmigrated so that they commonly overlap onto the adjacent subhorizontal events (Fig. 11.55B), creating a complicated structure consisting of subparallel reflections with relatively higher amplitudes due to the interference between the amplitudes of horizontal and overmigrated reflections. Poststack time migration algorithms can tolerate systematic velocity errors to a certain extent.

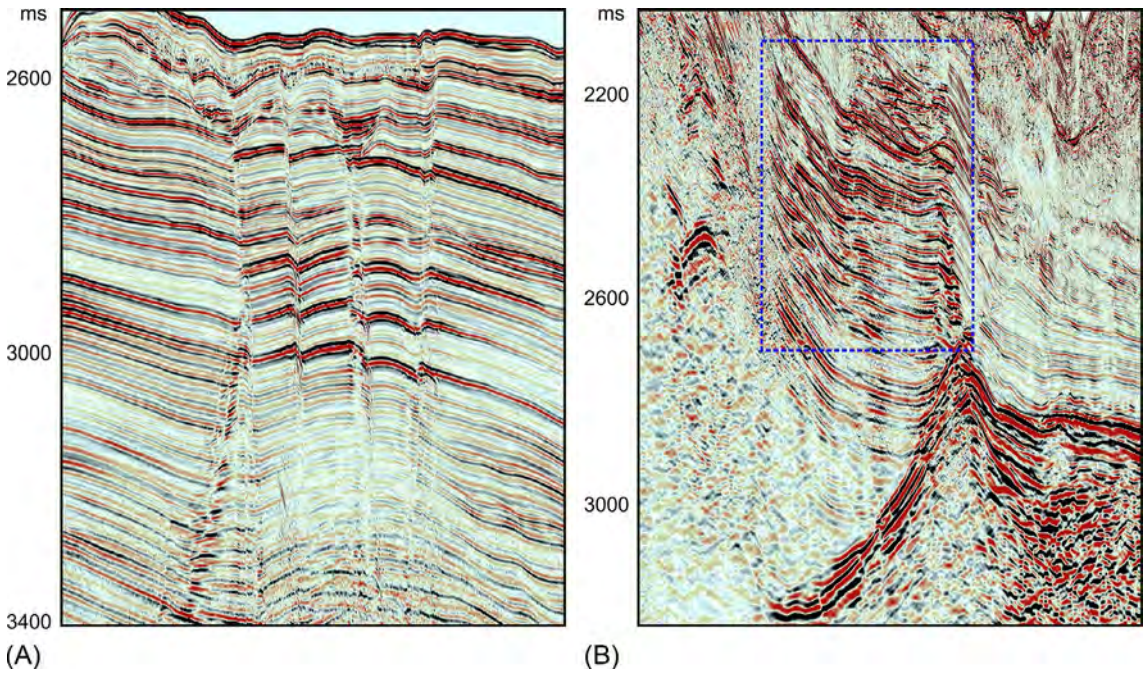


FIG. 11.55 Effects of systematic velocity errors on the image quality. (A) Sharpness along the fault planes is lost in case of slower migration velocities. (B) Faster velocities result in inclined events being overmigrated and overlapping onto the horizontal events *(blue dashed rectangle)*.

Effects of localized velocity errors on the migration output generally result in local disruptions in the final image. These types of errors are the more common velocity issues encountered during migration. As a common phenomenon, a vertical disturbance, such as a blurry fault plane as shown in Fig. 11.56, appears after migration. If such disturbances do not change their forms from top to bottom of the section, then one should suspect a localized velocity error, corresponding to a problematic velocity pick at or around the location of the disruption.

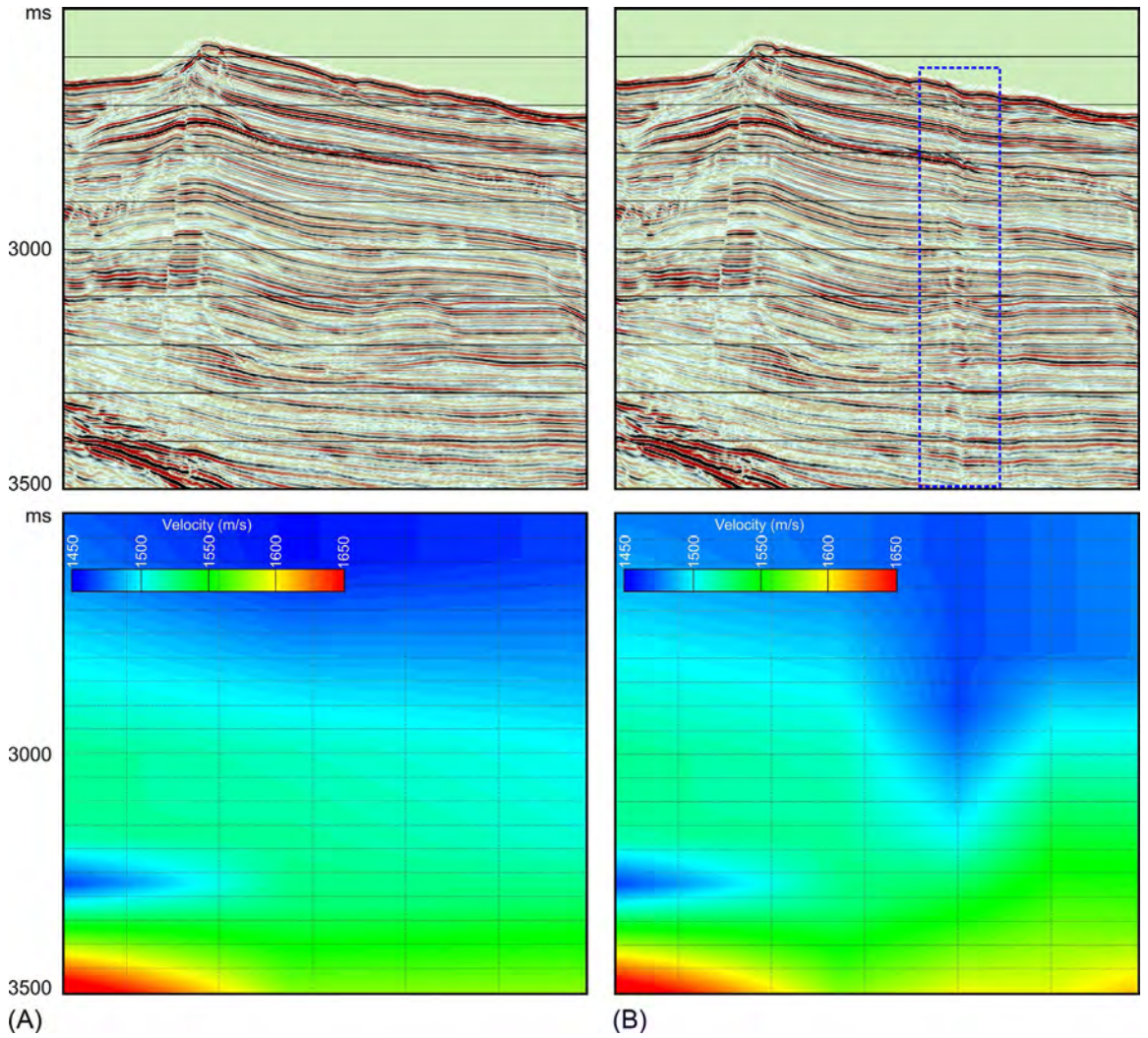


FIG. 11.56 Effect of localized velocity errors on the image quality. (A) Migrated image (top) using a proper velocity field (bottom). (B) Vertical disturbance such as a blurry fault plane *(dashed rectangle)* after migration (top) due to an improper velocity field (bottom).

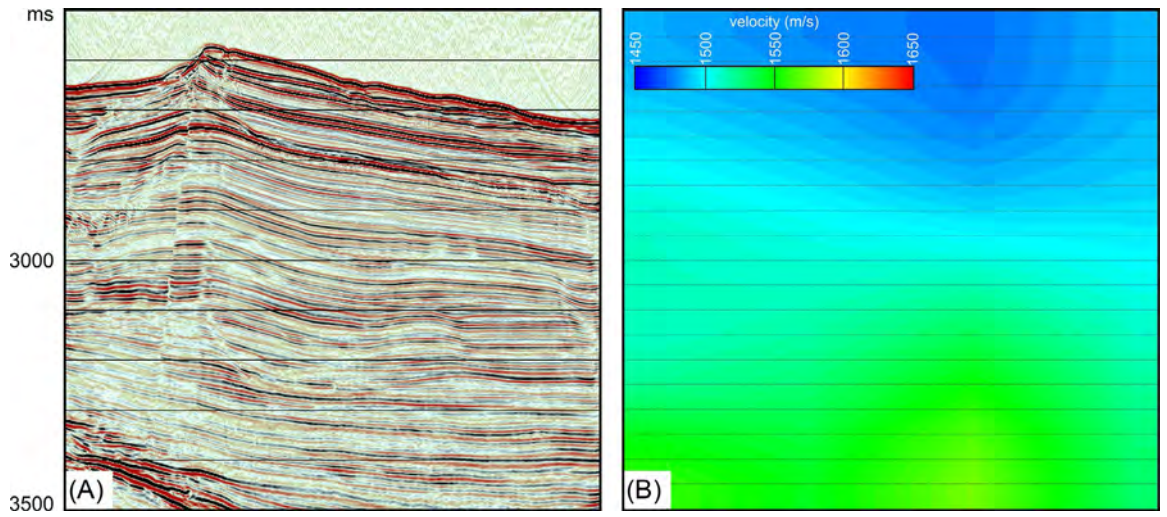


FIG. 11.57 (A) Migration result using (B) smoothed velocity field to minimize the effects of localized velocity errors. The same stack section as in Fig. 11.56 is used to obtain (A).

To minimize the effects of localized velocity errors, it is sometimes preferred to smooth the RMS velocity field both in time and space directions before the migration (Fig. 11.57), which removes abrupt lateral changes in the velocity field and hence eliminates the disruptions.

In addition to the velocity effects given previously, negative effects of near-surface structures or the effects of localized geological structures in shallower depths may result in velocity issues in the deeper parts of the data. For instance, mass transport deposits in the shallow subsurface or a near surface channel filled with high or low velocity sediment infill result in vertical disturbances in the deeper parts, such as velocity pull-up or push-down effects overspreading along the line comprising an area with a horizontal width of the structure plus recording spread length. In these cases, tomographic velocity inversion may be needed to better resolve the velocity distribution in the shallow areas, especially when reconstructing the velocity model for prestack depth migration algorithms.

CHAPTER

12

Specific Methods

OUTLINE

12.1 *f-x* Prediction Filter (*f-x* Decon) 549
12.2 Median Filter 553
12.3 Trace Mixing 556
12.4 Time-Variant Spectral Whitening 558
12.5 Instantaneous Attributes 562
12.6 Amplitude vs. Offset 567
12.6.1 AVO Equations 569
12.6.2 Intercept and Gradient 571
12.6.3 AVO Classes 572
12.6.4 Processing Considerations for AVO 576
12.6.5 AVO Analysis 577

In general, the seismic migration process is the final stage of seismic data processing, since it provides an interpretable seismic section that resembles the structural display of the subsurface geology. However, it is sometimes preferred to apply some additional steps for data quality enhancement, generally for residual noise suppression and temporal resolution improvement. Most of these additional methods are applied to poststack or migrated seismic data. In this section, some of the common methods for further signal-to-noise (S/N) ratio and temporal resolution enhancement, such as f-x deconvolution, trace mixing, or time-variant spectral whitening are provided. In addition, complex trace attributes and amplitude vs. offset (AVO) analysis as subsidiary tools for hydrocarbon indicators are briefly discussed, to describe their theoretical basis with some basic practical aspects and examples from real marine seismic datasets.

12.1 *f-x* PREDICTION FILTER (*f-x* DECON)

The *f-x* prediction filter, also known as *f-x* decon, was introduced by Canales (1984) and further developed by Gülünay (1986) based on the complex series prediction method of Treitel (1974). It is actually a simple and quite effective random noise suppression technique that predicts linear events in the frequency-space domain. The prediction is applied to small temporal and spatial windows on the input seismic data (Fig. 12.1A)

https://doi.org/10.1016/B978-0-12-811490-2.00012-8

© 2018 Elsevier Inc. All rights reserved.

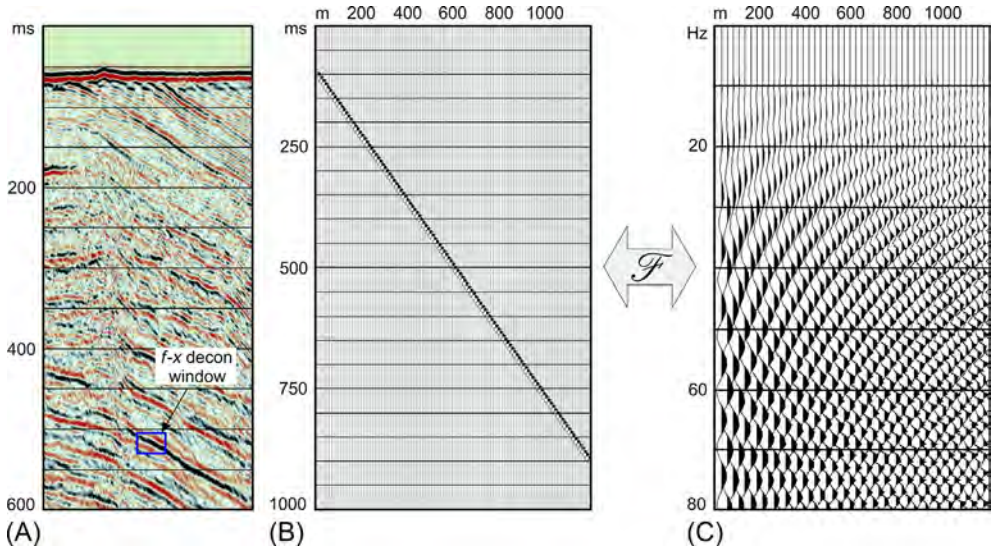


FIG. 12.1 (A) An *f-x* prediction filter is applied within small windows on the input data, such as the blue window, in which the events are locally linear. A single dipping event in the time-distance (*t-x*) domain in (B) becomes periodic in the frequency-distance (*f-x*) domain along the space dimension as in (C), and therefore, it is predictable. Only the real part of the Fourier transform is shown in (C).

so that the events in the windows are locally linear. Then each window is transformed from the time-distance (*t-x*) domain into the frequency-distance (*f-x*) domain by a Fourier transform. A Wiener prediction operator is designed along the space dimension for each constant frequency to predict the coherent parts of the signal. Each calculated filter is first applied forward and then reversed in the space dimension, and the results are averaged.

A linear event in the time domain can be expressed as

$$f(x,t) = \delta(a + bx - t) \tag{12.1}$$

where δ is the Dirac delta or unit impulse function, and x and t represent distance and time, respectively. Taking the Fourier transform of Eq. (12.1), we get (Bracewell, 1965; Abma and Claerbout, 1995)

$$F(x,\omega) = e^{i\omega(a+bx)} = e^{i\omega a}[\cos(\omega bx) + i\sin(\omega bx)] \tag{12.2}$$

For a simple linear event in the *t-x* domain (Fig. 12.1B), this function is periodic in the space dimension for each constant frequency value and, hence, it is predictable. This periodicity is shown along any constant frequency line in the *f-x* domain in Fig. 12.1C. In *f-x* decon, a complex Wiener prediction filter is applied to a given constant frequency series along the x direction in the *f-x* domain to predict the next primary reflection amplitude sample. Any difference between the predicted and real waveform are assigned as noise and removed from the data.

In the 2D case, a least-squares prediction filter in order to predict linear events in the $F(x, \omega)$ domain is suggested by Gülünay (1986) as

$$Xf = d \tag{12.3}$$

where d is the vector of desired output obtained by shifting one sample of the input, X is a matrix composed of the input data, and f is the

prediction error filter to be solved. Input to an *f-x* filter is the complex data series corresponding to the amplitudes over the distance axis for a constant frequency value in the *f-x* domain. The desired output *d* is one sample shifted version of the input. The *f-x* decon is also successfully applied to 3D poststack data by Chase (1992), referred to as *f-x-y* prediction filtering. Using the same prediction algorithm, it is also possible to interpolate the missing traces, known as the *f-x* trace interpolation method, which can be used to revive the dead traces, especially useful in compensating for the missed shots for single channel marine seismic surveys.

The time length of the prediction filter is important. If long filters are applied to shorter time series, every sample in the input series is predicted and no filtering occurs. Furthermore, long filters may produce phantom events that do not exist in the data. Another important parameter affecting the performance of an *f-x* prediction filter is the prediction trace length. Fig. 12.2 shows *f-x* decon outputs of a simple synthetic zero-offset section with 20% random noise for different prediction trace length values. It is observed that the output of the *f-x* filter is less noisy as the prediction trace length increases. This value must be less than the horizontal window length determined before the data is transformed into the *f-x* domain. Fig. 12.3 shows a similar analysis on a real marine stack section. Applications indicate that

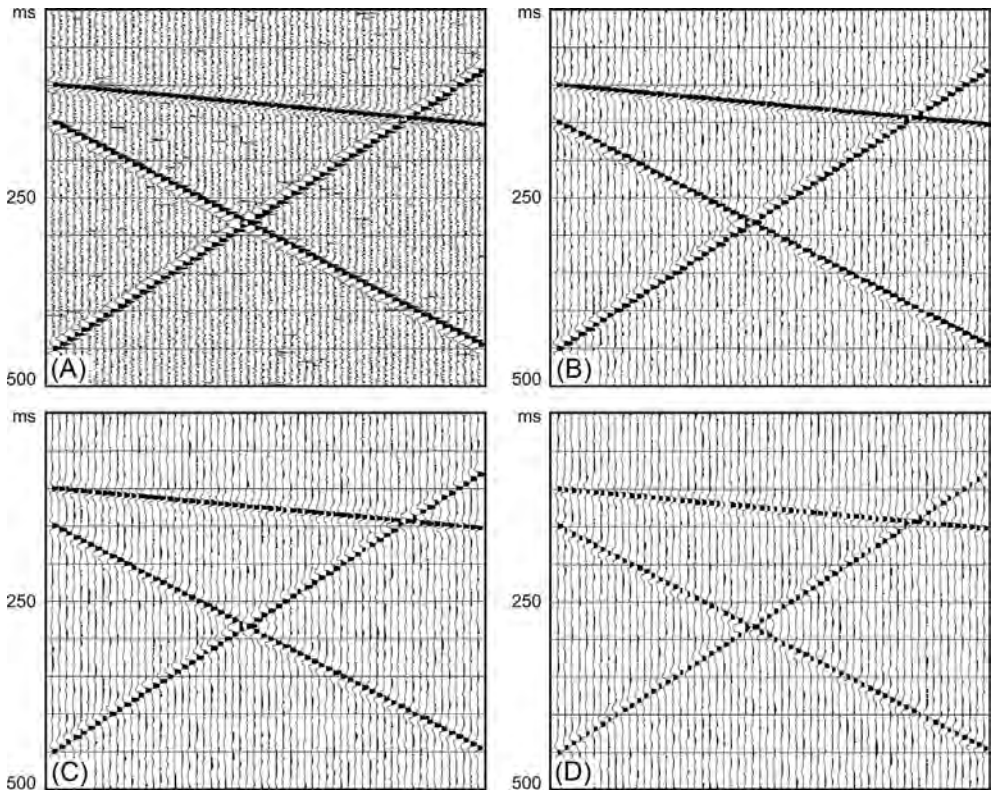


FIG. 12.2 (A) A synthetic zero-offset section consisting of dipping linear events with 20% random noise, and its *f-x* prediction filter results using prediction trace lengths of (B) 5, (C) 20, (D) 50 traces.

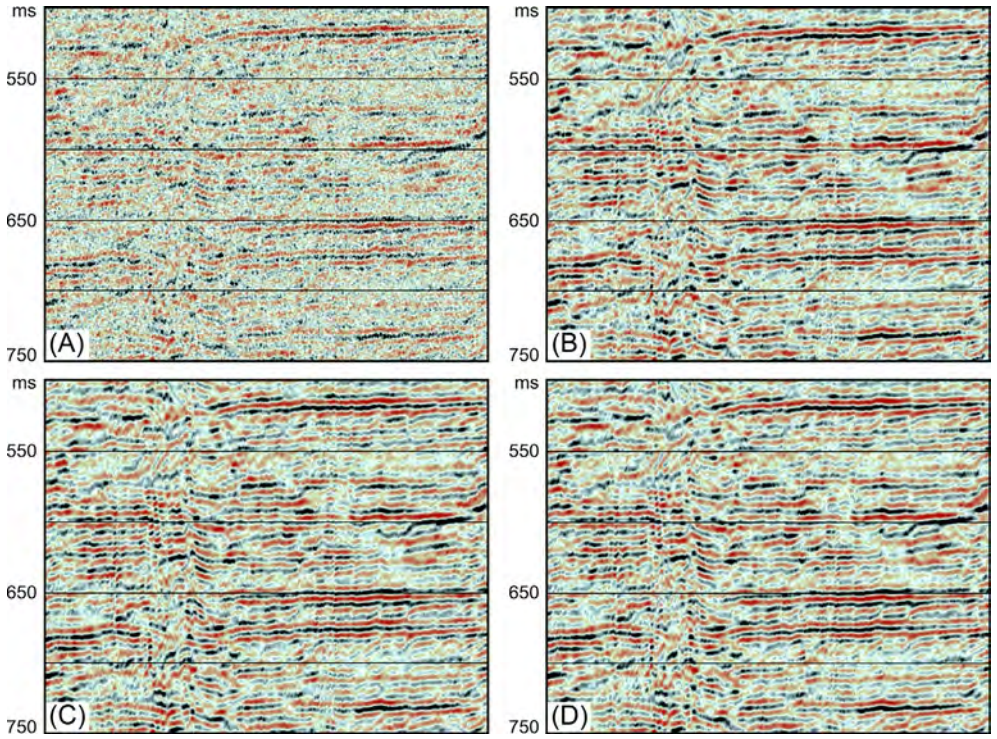


FIG. 12.3 (A) A real zero-offset section with poor S/N ratio, and its f-x prediction filter results using prediction trace lengths of (B) 5, (C) 20, (D) 50 traces.

longer trace lengths do not provide further improvement in the S/N ratio, yet they lead to too much computational time.

In practice, the f-x filter generally improves the S/N ratio of the single channel or low fold marine seismic data. In the case of low random noise when the S/N ratio of the input data is high, the f-x filter may induce sharp discontinuities in the data. Fig. 12.4A shows a 24-fold stack section with a relatively poor S/N ratio. The mean amplitude spectrum indicates that the data has amplitudes between 10 and 120 Hz with a dominant frequency of approximately 70 Hz. Random noise is especially significant towards the right side of the section, which appears as amplitudes above 120 Hz in the amplitude spectrum. The f-x decon output with a prediction trace length of 50 traces is illustrated in Fig. 12.4B. The mean amplitude spectra of the input and output data show that the f-x decon does not affect the spectral content of the input seismic section, except that it removes most of the high-frequency random noise amplitudes. Furthermore, the difference section in Fig. 12.4C indicates that the filter removes almost no primary energy from the section. The relatively higher amplitudes in the difference section correspond to the random noise components in specific locations where they are prominent in the data.

Although the f-x prediction filter also produces nice results on the prestack data, the method is generally applied to poststack data to remove the residual random noise component, since the stacking itself actually eliminates a significant part of the random noise amplitudes.

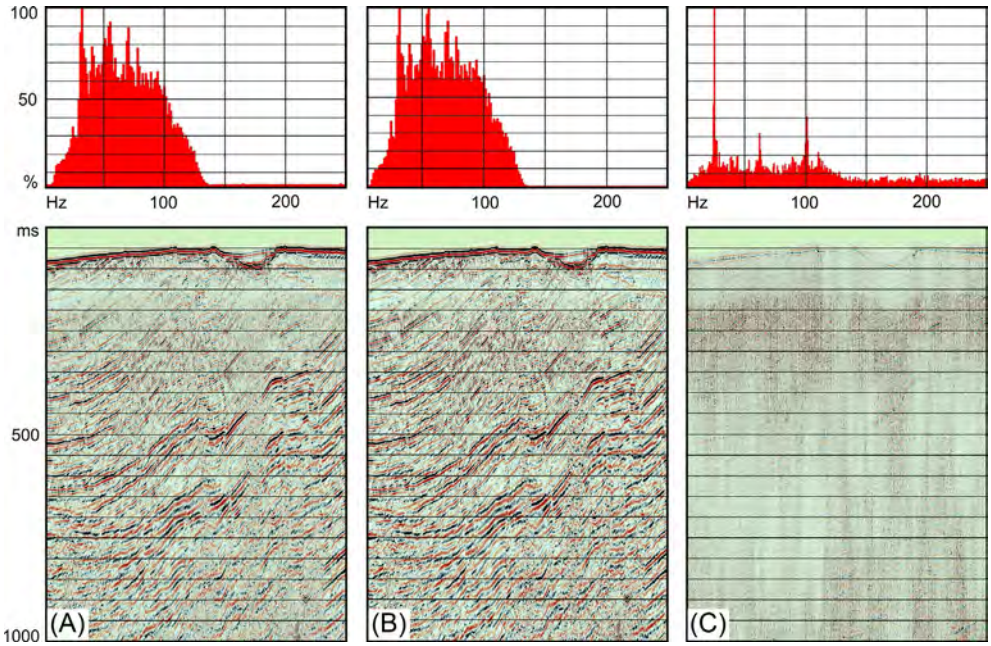


FIG. 12.4 (A) A low fold zero-offset section, (B) its *f-x* prediction filter results using a prediction trace length of 50 traces, and (C) difference between (A) and (B). Corresponding mean amplitude spectra of each section are given in the upper panels.

In the case of coherent dipping noise on the stacked data, such as cable noise or seismic interference, the *f-x* decon simply fails, since this kind of noise shows trace-by-trace consistency and is regarded as coherent reflections by the prediction filter.

12.2 MEDIAN FILTER

A median filter uses the median value of a time series to filter the random noise or very high-amplitude noise bursts. The median value of a time series is defined as the central value of the series after sorting its elements in an ascending order. For instance, let the time series $f(t)$ and its sorted version $g(t)$ be

$$f(t) = (9, 1, 6, 0, 4).$$

$$g(t) = (0, 1, 4, 6, 9).$$

Here, the median of $g(t)$ is 4. A median filter passes the central value of the input time series after sorting in ascending order. In practice, this sorting process is achieved within the defined time gates along the time axes of the seismic traces. The length of this window, in number of time samples, is the only parameter that must be suitably selected. In median filter applications, the time sample at the center of the window is replaced by the median value of the series within the window. All these processes are schematically illustrated in Fig. 12.5.

A median filter is also known as median smoothing, and is similar to the smoothing process of a moving average operator. A median filter applied to a random time series using different window lengths is given in Fig. 12.6. For a comparison, moving averages for 3 and 5 samples are also computed from the input time series (Fig. 12.6D and E). In general, as the

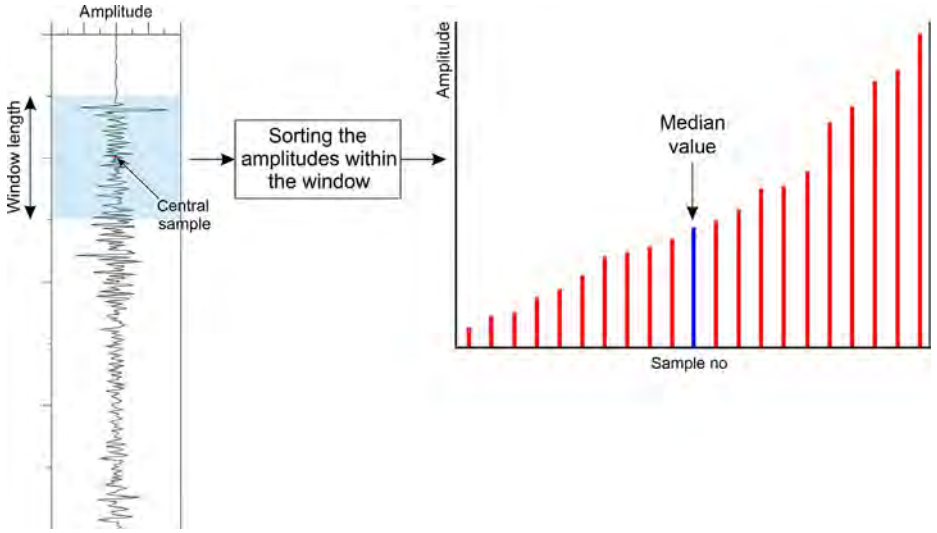


FIG. 12.5 Schematic illustration of the application of a median filter. The amplitudes of the input trace within a time window *(blue shaded area)* are sorted in an ascending order and the median value of the amplitudes within the time window *(blue bar)* is obtained. The time sample at the center of the window *(red square)* is then replaced by the median value of the time window.

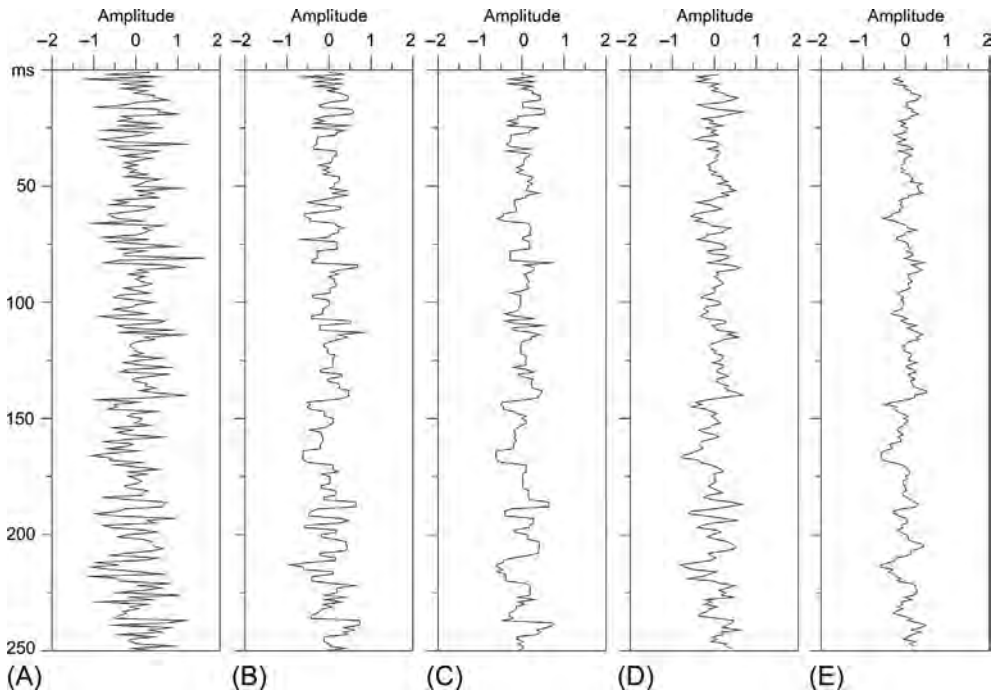


FIG. 12.6 (A) A random time series and its median filter outputs for (B) 3 and (C) 5 sample window lengths. For comparison, the moving average outputs of (A) are also calculated for (D) 3 and (E) 5 sample moving average operators.

window length increases, the output of the median filter is smoothed more and more.

The most important advantage of the method is that it can remove erratic amplitudes from the seismic data, such as spikelike noise. The median filter is used to discriminate rapidly fluctuating portions from slowly varying parts of the time series (Bednar, 1983). It can be applied to the input series several times successively in an iterative manner. When the outputs of two consecutive applications are the same, the process is terminated and the obtained final product is termed the root signal, which cannot be modified further by the median filter. If the root signal is obtained from a time series composed of the summation of both signal and noise amplitudes, then root signal corresponds to either the signal or the noise component embedded in the input series. That is, the root signal is composed of either the smoothed signal or the noise in the data.

A median filter is commonly used to eliminate random noise from the seismic data. Fig. 12.7 shows a synthetic zero-offset section with a 20% random noise and spikelike high-amplitude noise bursts, and its median filter outputs for different window lengths of 5, 7, and 9 samples. It is observed that the trace-by-trace consistency and phase of the coherent events in the input section are preserved in the median filter outputs, while the amplitudes of the random noise are suppressed. However,

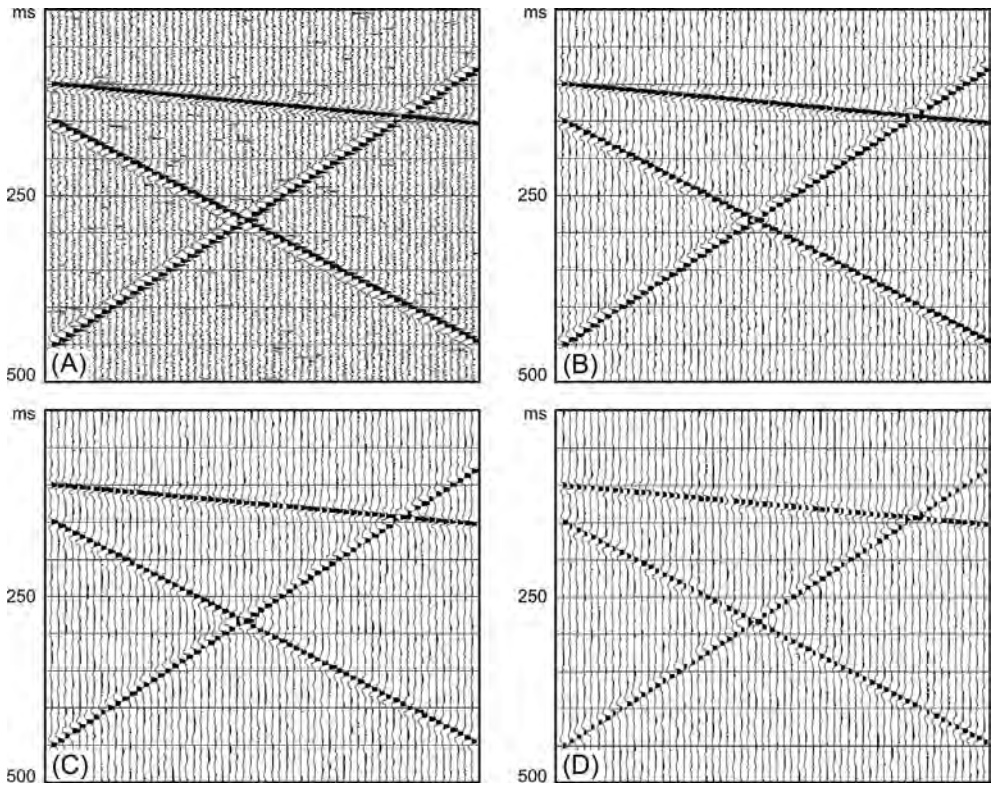


FIG. 12.7 (A) A synthetic zero offset section with 20% random noise and high-amplitude spikelike noise bursts, and its median filter results using window lengths of (B) 5, (C) 7, (D) 9 samples.

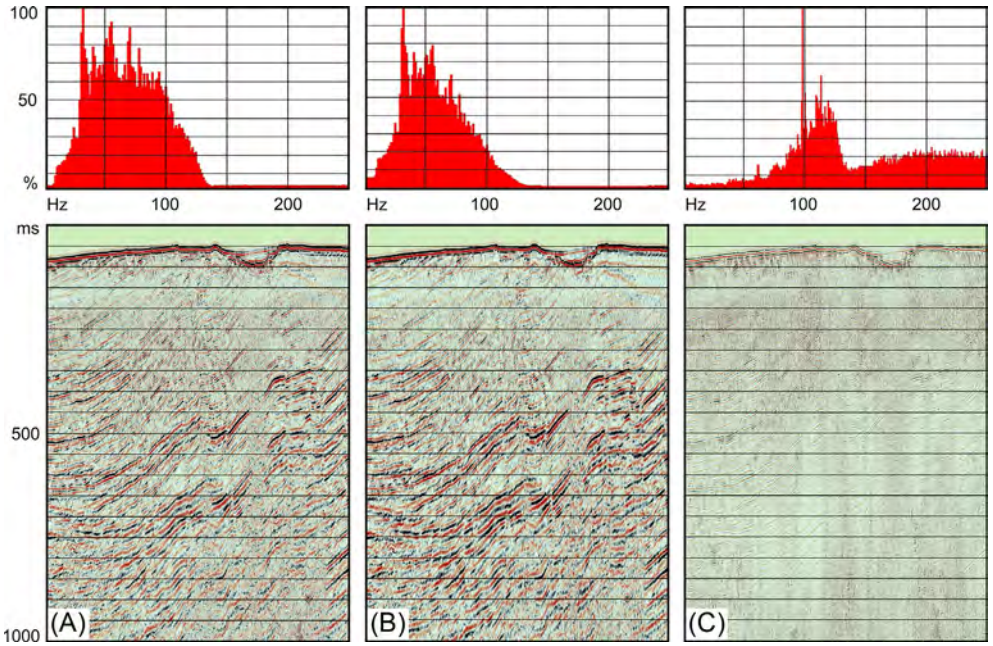


FIG. 12.8 (A) A low fold zero-offset section, (B) its median filter output using a window length of 5 samples, and (C) difference between (A) and (B). The corresponding mean amplitude spectra of each section are given in the upper panels.

when the window length increases, the amplitudes of the coherent events, such as primary reflections, are also reduced (Fig. 12.7C and D).

Fig. 12.8A shows a 24-fold stack section with a relatively poor S/N ratio, which is also used for the analysis of f-x decon performance in Fig. 12.4. The median filter output with a window length of 5 samples is illustrated in Fig. 12.8B. Unlike the f-x prediction filter, the mean amplitude spectra of the input and output data show that the median filter slightly modifies the amplitude spectrum of the input. While it removes mostly the high-frequency random noise components (Fig. 12.8C), it also suppresses amplitudes at the higher frequency end of the spectral bandwidth, leading to a clearer view of especially deeper reflection events. However, the difference section in Fig. 12.8C indicates that the median filter removes almost no primary energy from the input section.

12.3 TRACE MIXING

Trace mixing is a noise suppression method generally applied to zero-offset stack sections, in which a specified number of adjacent traces are summed and simply averaged to obtain one mixed output trace. It can be performed either as a weighted mix or trimmed mean mix. The former is more common in the seismic industry.

In a trimmed mean mix, the amplitudes are sorted in ascending order before summation, and a certain percentage of the high and low amplitudes at both ends of the sorted series are discarded and excluded from the mixing process. In weighted mix, a fixed window containing a certain number of traces is determined, and then specific weighting coefficients are assigned for each individual trace. All of the samples of the traces are multiplied by their

assigned weighting coefficients. The resultant amplitudes are horizontally summed and the summations are divided by the sum of weighting coefficients to obtain one single trace, which is then assigned as the central trace of the window. Then the window is moved to the next trace along the section, and the process is repeated. The weighted mix procedure can be expressed by

$$S(t) = \frac{\sum_{i=1}^{N} C_i A_i(t)}{\sum_{i=1}^{N} C_i} \tag{12.4}$$

where N is the number of traces in the trace mix window, C_i are their corresponding weighting coefficients, and $A_i(t)$ are the amplitude values of each trace. The weighted mix process is schematically illustrated in Fig. 12.9 for three traces with weighting coefficients of 1, 2, 1, respectively. First, all samples of the first three traces (in the window with the red dashed borderline) are multiplied by 1, 2, 1, and divided by 4 (the sum of the weighting coefficients) to obtain the first mixed trace in the bottom panel (trace number 2). Then the window is moved one trace and the process is repeated for the next three traces (in the window with the blue dashed borderline) to obtain the second mixed trace in the bottom panel (trace number 3). The window is moved from the first to last trace in this fashion along the line, and each time the weighted averaging process is repeated. The total number of traces

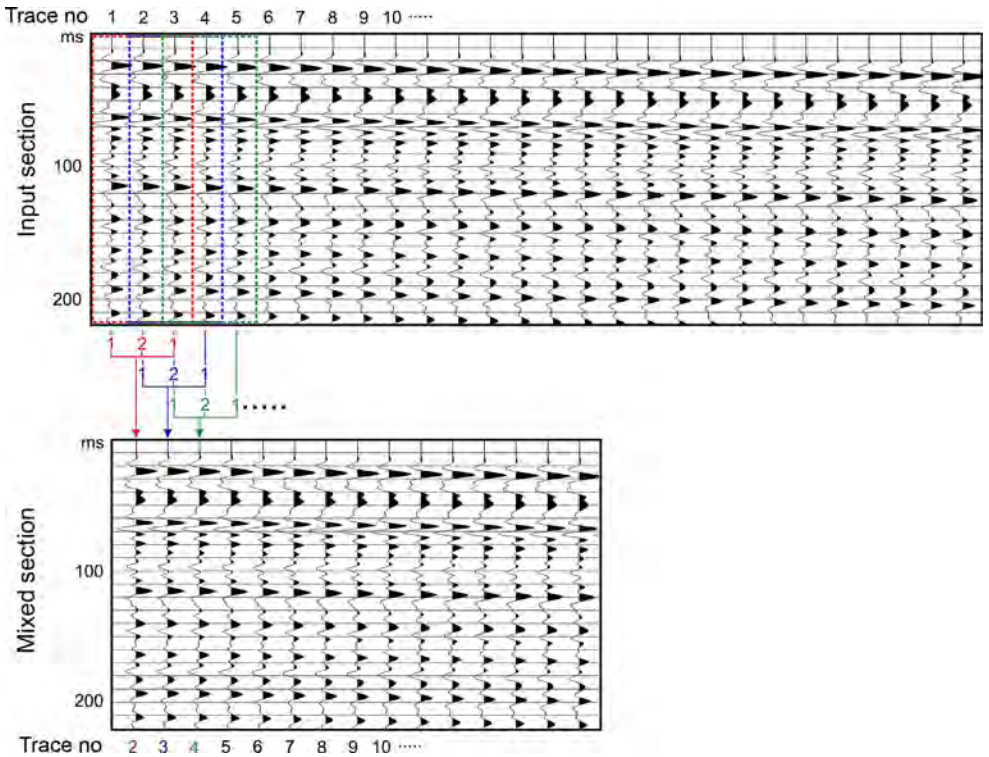


FIG. 12.9 Schematic illustration of weighted trace mix for three traces with weighting coefficients of $C_i = 1, 2, 1$. Input and mixed seismic traces are shown in the upper and lower panels, respectively.

in a window (N) must be an odd number, and the resultant mixed trace is assigned to the central trace in the window. For the schematic representation in Fig. 12.9, the first output trace for $N = 3$ will be assigned to trace number 2 in the mixed section. In the weighted mixing, generally the central trace has the largest weighting coefficient value, and the weighting coefficients decrease for each trace towards both ends of the window. Fig. 12.10 shows an example for weighted trace mixing, where the data becomes smoother for larger trace mix windows.

Trace mixing can be regarded as a method of horizontal stacking and may be effective in suppressing some incoherent and even coherent noise on the stack sections, such as remnants of guided waves in shallow waters. Fig. 12.11 shows an example application of the weighted mix to improve the S/N ratio using five traces with weighting coefficients of $C_i = 1, 2, 3, 2, 1$. Trace mixing may be especially effective on high-resolution marine seismic sections, such as single channel sparker datasets, where the advantage of stacking for random noise suppression cannot be taken. The method can also interpolate the missed shots of single channel seismic data.

12.4 TIME-VARIANT SPECTRAL WHITENING

Time-variant spectral whitening (TVSW) is a method to enhance the spectral bandwidth and hence the vertical (temporal) resolution of the seismic data. When we compose filter scans with different pass bands as in Fig. 5.28, we observe that the high-frequency components exist only in the shallow parts of the seismic data because the seismic wavelet is not stationary with time and its higher frequencies are dramatically absorbed as it propagates in the subsurface sediments, mainly due to the absorption effects of the earth.

TVSW is a method to compensate for the absorption effects of the subsurface. Its

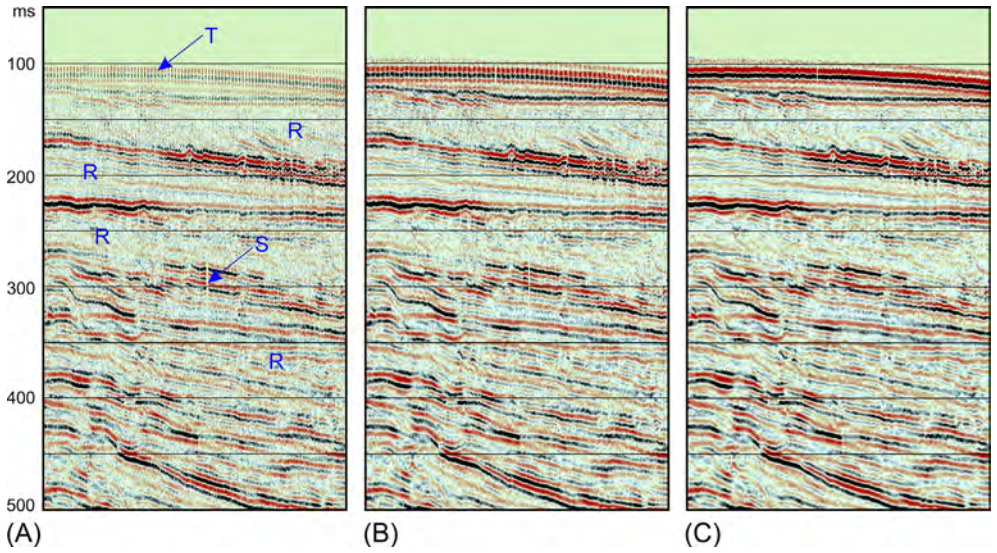


FIG. 12.10 (A) Input zero-offset section and its weighted mix outputs for (B) 5 traces with $C_i = 1, 2, 3, 2, 1$ and (C) 11 traces with $C_i = 1, 2, 3, 4, 5, 6, 5, 4, 3, 2, 1$ weighting coefficients. T is NMO stretch mute effect, S is surgical mute and R is random noise.

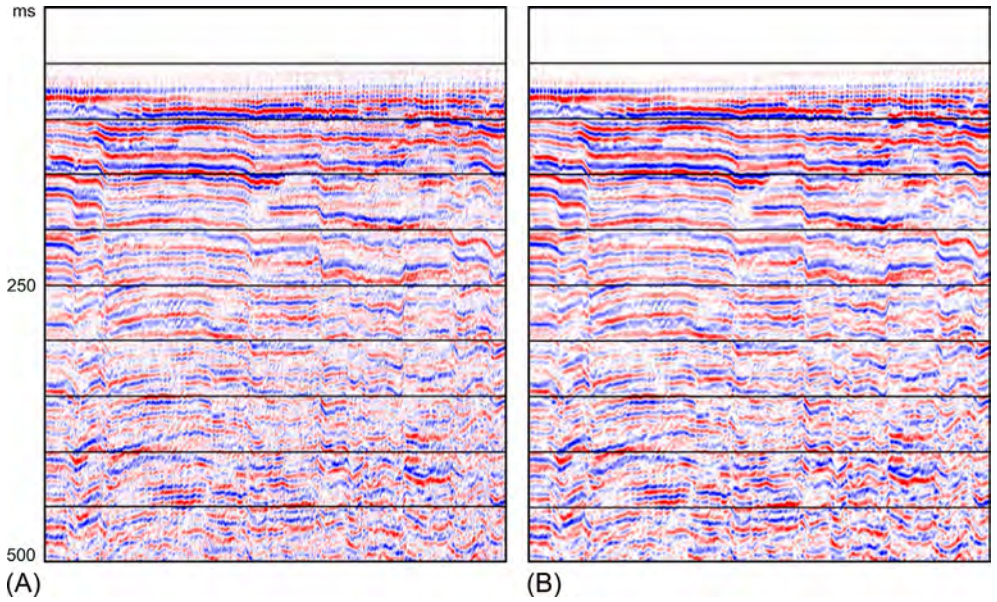


FIG. 12.11 An application of the weighted mix to improve *S/N* ratio. (A) Input zero-offset section, and (B) its weighted mix output for five traces with $C_i = 1, 2, 3, 2, 1$ weighting coefficients.

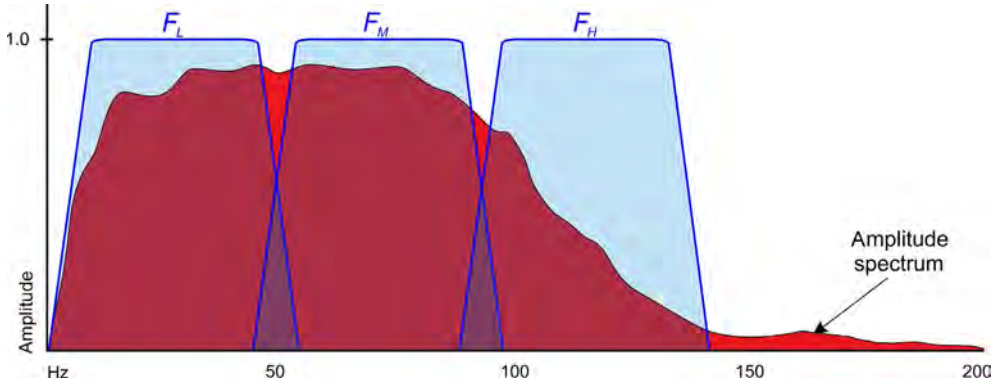


FIG. 12.12 Schematic illustration of amplitude spectra of three example narrow band-pass filter operators *(blue shaded bands)* superimposed on a schematic amplitude spectrum of an input seismic trace *(red filled curve)*. F_L, F_M, and F_H represent low-, medium- and high-frequency bands of the band-pass filter, respectively.

theoretical basis is to decompose the input signal into different frequency components by applying a number of band-pass filters with different narrow pass bands. Fig. 12.12 schematically shows the operators of three narrow band-pass filters in the frequency domain superimposed on a schematic amplitude spectrum of an input seismic trace. Using these filter panels, application of the TVSW method to seismic traces is schematically illustrated in Fig. 12.13. The input

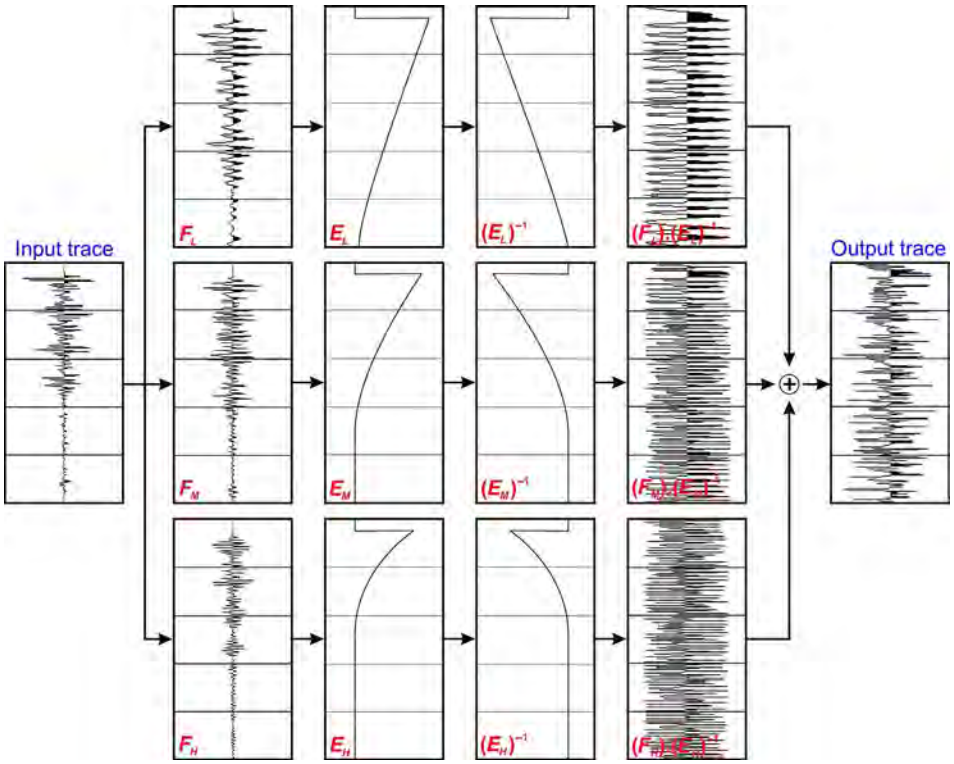


FIG. 12.13 Schematic illustration of the application of the TVSW method to seismic traces for three spectral bands. The input trace is decomposed into low (F_L), medium (F_M), and high (F_H) frequency components by applying a series of band-pass filters. Trace envelopes indicated by E_L, E_M, E_H for low-, medium- and high-frequency traces are calculated, and their corresponding inverses, shown by $(E_L)^{-1}$, $(E_M)^{-1}$, $(E_H)^{-1}$, can be used as gain functions for each filtered trace. The gain functions are multiplied by the filtered traces F_L, F_M, and F_H and the results are summed to obtain the output TVSW trace.

trace is decomposed into low (F_L), medium (F_M) and high (F_H) frequency bands by applying a band-pass filter. Since the higher frequency components are absorbed more quickly, attenuation rates for low-frequency components are smaller than those for medium- and high-frequency components. Hence, we can define different gain functions for different frequency bands of the input signal after decomposition. These gain functions actually equal to the inverse of the amplitude envelopes of the traces within each frequency bandwidth. In Fig. 12.13, the schematic envelope curves for the traces of low-, medium- and high-frequency bands are indicated by E_L, E_M, and E_H, while their corresponding inverses are shown by $(E_L)^{-1}$, $(E_M)^{-1}$, $(E_H)^{-1}$, respectively. Then these gain functions are multiplied by the filtered traces F_L, F_M, and F_H and the results are summed to obtain the output TVSW trace (Fig. 12.13). In practice, the number of filter panels is not restricted to three, and the panels can be designed with respect to the available bandwidth of the input data.

TVSW is generally applied to migrated sections as a final process to improve the temporal resolution. Fig. 12.14 shows a migration section before and after TVSW along with the mean amplitude spectra. Four filter panels are used to obtain TVSW output and the temporal

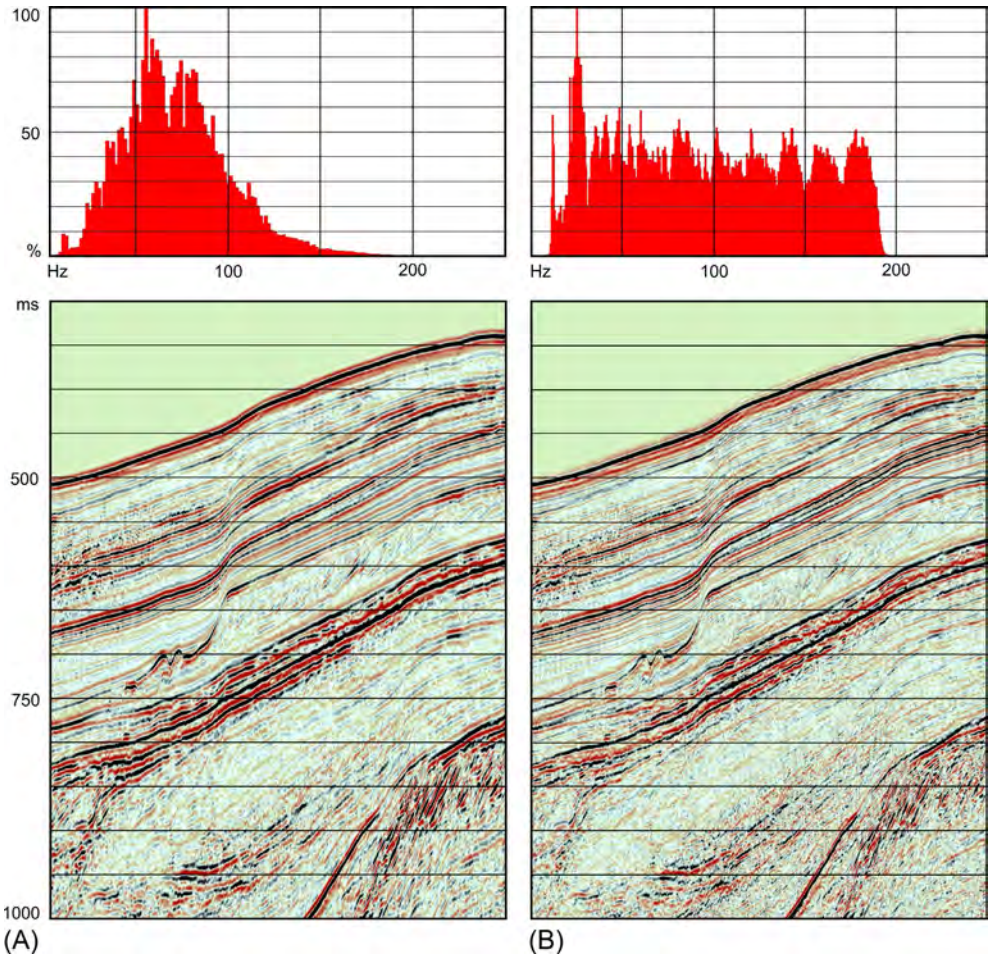


FIG. 12.14 (A) Input migration section, and (B) after TVSW application. Four filter panels are used to obtain the TVSW output. The corner frequencies of the panels are $f_1 = 10$–40 Hz, $f_2 = 40$–90 Hz, $f_3 = 90$–140 Hz, and $f_4 = 140$–190 Hz. The corresponding mean amplitude spectra of each section are given in the upper panels.

resolution of the input data is significantly improved. The amplitude spectrum of the TVSW output indicates that the amplitudes of both low- and high-frequency components are increased to obtain a flat amplitude spectrum.

TVSW can be regarded as a process that tries to remove attenuation effects and partly compresses the basic seismic wavelet embedded in the data at the same time. Its difference from conventional Wiener deconvolution is that deconvolution not only compresses the seismic wavelet, but also removes the multiple reflections as well as the ringy character of the wavelet. TVSW, however, compresses the wavelet and does not have any influence on the oscillating character and the phase of the input data. Applications show that it is much more successful in compressing the wavelet and whitening the amplitude spectrum than is the spiking deconvolution.

12.5 INSTANTANEOUS ATTRIBUTES

Seismic attributes can be defined as all available information deduced from the seismic data, either by direct measurements or by logical or experience-based reasoning, such as seismic velocity, frequency content, dip and continuity of events, seismic wavelet specifications, amplitude and phase relationships, attenuation effects, etc. Instantaneous attributes do not represent the variations within a specified time window, but characterize instantaneous changes in the seismic traces.

There are several different types of seismic attributes widely used in the seismic processing industry today. A specific attribute type is known as a complex trace attribute, introduced by Taner et al. (1979), which provides additional information about the phase, amplitude and frequency characteristics of the recorded signal. Complex trace attributes are commonly used as secondary tools for direct hydrocarbon indicator (DHI) analysis, especially in the case of high-amplitude bright reflections and frequency anomalies. In order to obtain suitable and reliable information, true amplitude processing of the data must be required, which preserves relative amplitude information and frequency content of the reflected signal.

Complex trace attributes are calculated by using the Hilbert transform (Section 4.8). Although the total energy in a dynamic system consists of the summation of kinetic and potential energy, seismic receivers (geophones or hydrophones) measure only the kinetic energy component (Fig. 12.15). The analytical signal $u(t)$ expressed by Eq. (4.29) represents the total energy in wave propagation. Considering the seismic data as an analytic signal with real and imaginary components, kinetic and potential energy are proportional to the real and the imaginary component, respectively. In complex trace attribute calculations, the recorded seismic signal represents the kinetic energy, whereas the imaginary component corresponds to potential energy (Fig. 12.15).

Considering the recorded trace as the real component of the analytical signal, its imaginary component is calculated by the Hilbert transform, and the recorded trace and its Hilbert transform constitute a Hilbert transform pair, which can be used to achieve some additional parameters in terms of instantaneous attributes. Using the definition of analytical signal in Eq. (4.29), these new parameters can be calculated by

$$g(t) = \sqrt{x(t)^2 + y(t)^2} \tag{12.5}$$

$$\phi(t) = \operatorname{atan}\left(\frac{y(t)}{x(t)}\right) \tag{12.6}$$

$$\omega(t) = \frac{\partial \phi(t)}{\partial t} \tag{12.7}$$

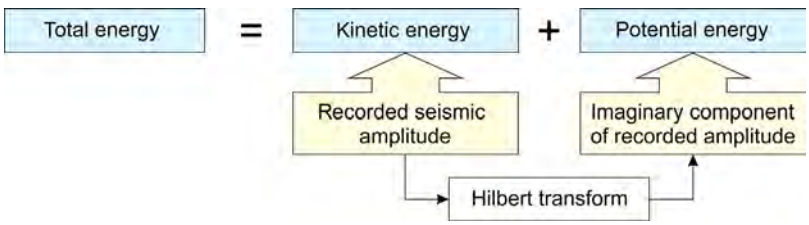


FIG. 12.15 Total energy in a dynamic system consists of the summation of kinetic and potential energy. Seismic receivers measure only the kinetic energy (real) component, and the potential energy (imaginary) component is calculated by the Hilbert transform.

where $x(t)$ is the real component of the analytical signal (the recorded trace), $y(t)$ is the imaginary component (Hilbert transform of $x(t)$), $g(t)$ is the instantaneous amplitude or envelope, $\phi(t)$ is the instantaneous phase, and $\omega(t)$ is the instantaneous frequency. An additional parameter called apparent polarity can be obtained from the envelope trace, which equals the polarity at the trace envelope peaks, and is generally weighted by the envelope peak value.

Complex trace attribute analysis is the essential tool enabling us to process amplitude and phase information in the seismic data separately (Barnes, 2007). This separation provides two fundamental attributes: instantaneous amplitude and instantaneous phase. All the other attributes are derived from these two basic attributes. Fig. 12.16 shows all of these parameters computed from a real seismic trace.

These three parameters, along with the apparent polarity, are known as the fundamental parameters of complex trace attribute analysis. Instantaneous amplitude is the envelope of the seismic signal and is independent from phase. It shows the basic lithologic changes and represents the acoustic impedance contrast, and it is particularly effective in analyzing high-amplitude zones such as bright spots from gas-water saturated sediment contacts, unconformities and sequence boundaries. Instantaneous phase is independent of trace amplitudes and both low- and high-amplitude events are at the same amplitude level in the phase sections. Therefore, it can be used to analyze the lateral event continuity in low S/N conditions where trace-by-trace consistency is poor. Instantaneous frequency is the variation rate of the signal phase and it corresponds to the center frequency

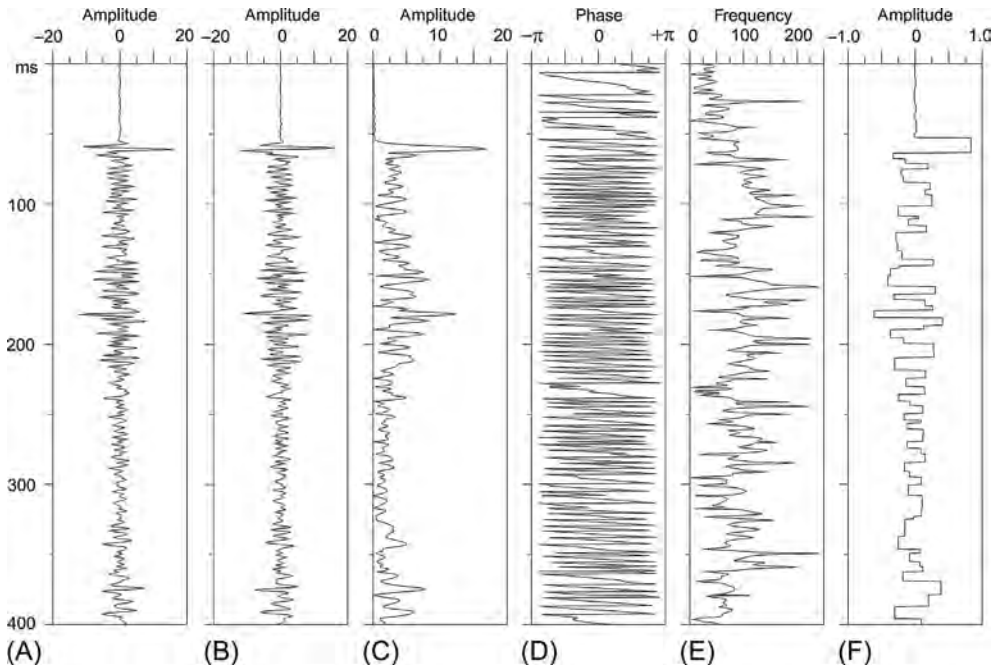


FIG. 12.16 The attributes obtained from complex trace attribute analysis. (A) Recorded seismic trace (real component of analytical signal), (B) imaginary component of analytical signal computed from (A) using Hilbert transform, (C) instantaneous amplitude (envelope) trace, (D) instantaneous phase trace, (E) instantaneous frequency trace, and (F) apparent polarity.

of the amplitude spectrum. Due to the high amount of absorption in gassy sediments, low-frequency zones in instantaneous frequency sections may indicate hydrocarbon accumulation areas. It may also reflect the fracture and chaotic reflection zones. Apparent polarity sections indicate the areas where the polarity reversals exist on the seismic data. It can be used to define low-velocity zones of brine-gas saturated sediment interfaces.

In addition to these fundamental instantaneous attributes, several other attributes are also defined, some of which use instantaneous phase and frequency traces as well as trace envelopes. For instance, the cosine of the phase section, also known as normalized phase, shows lateral continuity of the events better than the instantaneous phase section itself. Since envelope sections do not contain phase information and instantaneous phase sections do not have amplitude information, multiplying them yields a new attribute section, which indicates high-amplitude zones with correct phase information. Another common attribute is known as instantaneous acceleration, which equals the time derivative of instantaneous frequency and is an excellent event continuity indicator with a much higher resolution. Apart from these common attributes, there are several other physical, geometrical, and wavelet attributes used in the seismic processing industry today, such as integration or derivative of the input trace, first and second derivative of the envelope, instantaneous dominant frequency, instantaneous lateral continuity, etc. While integration of the input seismic traces highlights the low-frequency zones that may indicate hydrocarbons, higher frequency zones are more distinctive in time-derivative sections. A comprehensive review on the historical development and most popular attributes used by processors today can be found in the works of Chopra and Marfurt (2005).

In the presence of shallow gas accumulations, complex trace attributes yield valuable results. Existence of gassy sediments in the subsurface induces some specific anomalous effects on the seismic data, as follows:

- Low frequencies in the seismic data due to the high absorption of the seismic amplitudes in gassy sediments
- A distinct decrease in the velocity of the gassy sediments
- Negative polarity reflections with respect to the seafloor reflection along the upper boundary of gassy sediments due to the velocity reversal
- High amplitudes from upper boundary of gassy sediments due to the high impedance contrast between brine and gas saturated sediments
- Degradation in the reflections at the bottom of gassy sediments
- Velocity pull-down below the gas accumulation zone due to the low seismic velocity of gassy sediments.

These effects are schematically illustrated in Fig. 12.17. Complex trace attributes can be successfully used to reveal or to highlight all of these effects. For instance, higher absorption rates of the seismic signal propagating in the gassy sediments result in a decrease of the effective frequency bandwidth of the signal received from gassy zones, which can be discriminated by distinctive low-frequency zones in the instantaneous frequency sections (e.g., for the reflection *S* in Fig. 12.17). Reflections from the upper boundary of the gas accumulation zones are always of reverse polarity (reflection *P* in Fig. 12.17); therefore, they produce negative polarity reflections on apparent polarity sections with respect to the seafloor reflection. The amplitude of this reflection is generally several times higher than reflection amplitudes from surrounding reflectors, because of the large velocity contrast between gas and brine saturated sediments (reflection *Y* in Fig. 12.17). This contrast forms extreme amplitudes in the reflection strength or amplitude envelope sections. Reflections within the gassy zones and from

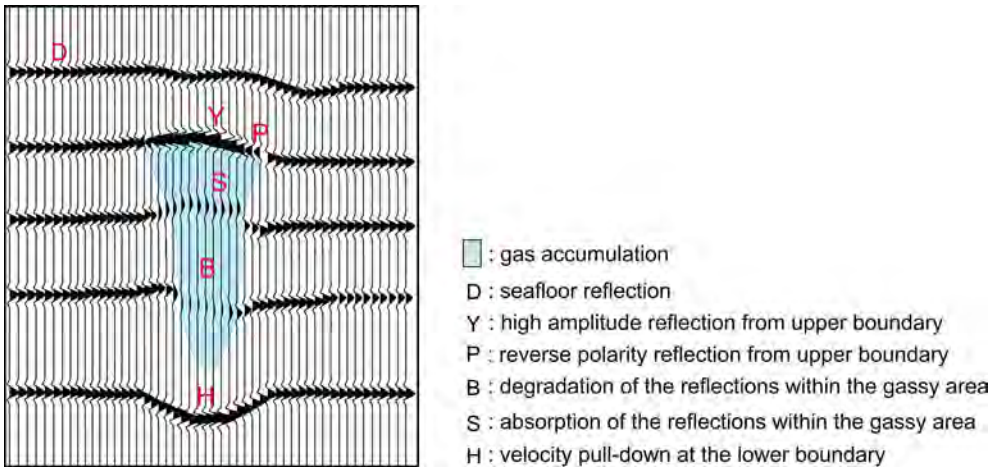


FIG. 12.17 Schematic illustration of the effects of shallow gas on the seismic data.

the bottom of the gas accumulation zones are severely degraded, and even disappear (e.g., zone B in Fig. 12.17), which can be analyzed by instantaneous phase sections.

As an application of complex trace attribute analysis, we can define a gas accumulation zone if we simultaneously observe

- High-amplitude bright reflections on the amplitude envelope sections
- Low-frequency zones on the instantaneous frequency sections just below these bright reflections
- Reverse polarity along the bright reflections on apparent polarity sections
- Discontinuities or degraded reflections below the bright reflections on the instantaneous phase sections.

If all of these anomalies are observed for the same zone on the seismic data, then it may be concluded that the zone may indicate gassy sediments. An example seismic section with a shallow gas accumulation is illustrated in Fig. 12.18, which shows all of the preceding anomalies at the same time. A migrated true amplitude section is given in Fig. 12.18A. The purpose is to analyze the bright reflections lying approximately 1050 ms below the small-scale ridge, using complex trace attribute analysis. Fig. 12.18B shows the Hilbert transform pair of the input section; both are used to obtain other instantaneous attribute sections. The envelope section in Fig. 12.18C shows that the bright reflection has amplitudes several times higher than those of the background reflections. The instantaneous frequency section is illustrated in Fig. 12.18D, which shows a columnar low-frequency zone (blue areas) below the bright reflections, possibly due to the high absorption of the signal. The envelope weighted instantaneous phase section shows the phase variations along the bright reflections (Fig. 12.18E), which may indicate the lateral continuation of the gassy zones. The apparent polarity section in Fig. 12.18F indicates that all of the bright reflections are of reverse polarity (red) with respect to the seafloor reflection (blue), suggesting a velocity inversion below the high-amplitude reflections. Fig. 12.18G, H, and I show instantaneous phase, instantaneous acceleration and cosine of the phase or normalized phase sections, all of which are prepared to analyze the lateral event continuity. A vertical column shaped zone consisting of degraded and discontinuous reflections is distinctive on all

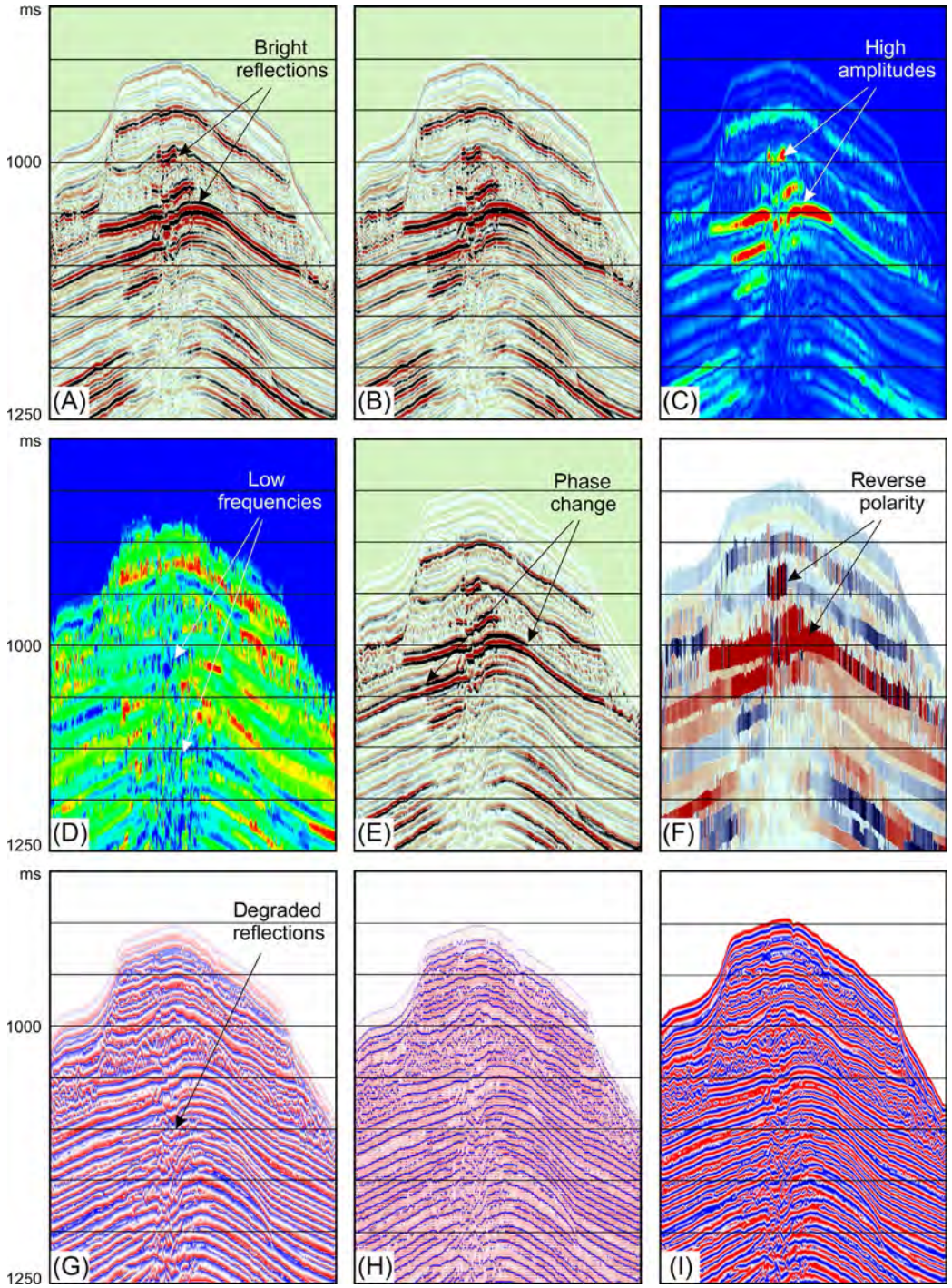


FIG. 12.18 Complex trace attribute analysis of a migrated seismic section. (A) Input seismic section, and (B) its Hilbert transform pair, (C) instantaneous amplitude (envelope) section, (D) instantaneous frequency section, (E) envelope weighted instantaneous phase section, (F) apparent polarity section, (G) instantaneous phase section, (H) instantaneous acceleration section, and (I) cosine of phase or normalized phase section.

three sections. All this evidence indicates that these high-amplitude reflections may originate from the upper boundary of a possible shallow gas accumulation zone, which is fed from deeper sediments resulting in a column-shaped vertical disruption zone just below the bright reflections.

12.6 AMPLITUDE VS. OFFSET

Amplitude vs. offset (AVO) is a specific analysis technique based on the variation of reflected signal amplitude with respect to the reflection angle, or offset, between source and receivers. If the variation is analyzed by means of offset, then the operation is termed amplitude vs. offset, and if the incidence angle is used as the parameter for amplitude variation, then it is known as amplitude vs. angle (AVA). The former is more widely used in the hydrocarbon industry.

AVO is one of the fundamental tools for reservoir geophysics and has been widely used in hydrocarbon exploration for over 30 years. The theory of variations in reflection amplitudes with incidence angles was introduced by Zoeppritz (1919), who obtained nonlinear equations of reflected and transmitted wave amplitudes at an interface with an incidence angle greater than zero. His equations are known as Zoeppritz equations and are controlled by P and S wave velocities and densities of both media. Gassmann (1951) established the theoretical connection between seismics and rock physics, and later the link between nonnormal incidence amplitudes and Poisson's ratio was developed by Koefoed (1955). Since Zoeppritz equations are not linear and are not easy to analyze, simplified versions were required for more comprehensive analyses, and the first linear approximation to Zoeppritz equations was given by Bortfeld (1961). In the early 1980s, the success of AVO analysis was verified by Ostrander (1982), who showed that the reflections from sand-shale interfaces represent different amplitude variations with offset because the Poisson's ratio of gas sands is lower than that of brine sands, and therefore this variation can be used to discriminate gas sands from brine sands via surface seismic data. Today, AVO has broad applications in the oil and gas industry, and there are several comprehensive and detailed studies, especially on the analyses of hydrocarbon zones on the seismic data, integration of rock physics with seismic data, and reducing the risks in new prospect areas, as well as characterization of existing reservoirs using AVO techniques. In this section, only the basics and fundamentals of a regular AVO analysis are explained.

In areas of regular amplitude distribution in the seismic data, we normally do not expect any variation in the amplitudes along the offset in prestack data. However, if we observe a bright reflection on the stack section, there may be two possibilities for this enhanced reflection on the prestack data, based on the theory of AVO analysis: either the amplitudes in far offsets are larger than those in near offsets, or vice versa. According to the NMO corrected real CDP gather in Fig. 12.19A, the reflection at 740-ms zero-offset time shows a strong AVO effect such that the absolute amplitudes of the reflection significantly increase with the offset. AVO analysis aims to detect such anomalous reflections from NMO corrected CDP gathers and tries to understand the reasons causing AVO effects, in order to evaluate if they are directly related to a possible hydrocarbon accumulation or not. Fig. 12.19B schematically shows the relationship between half offsets and incidence angles on a simple single horizontal reflector model, along with a synthetic CDP gather. In this schematic illustration, only five receivers exist on the surface, and the maximum offset available for the synthetic CDP gather is 6000 m, which corresponds to a maximum incidence angle of 50 degrees. As the offset increases, the angle of incidence also increases accordingly, depending on the reflector depth.

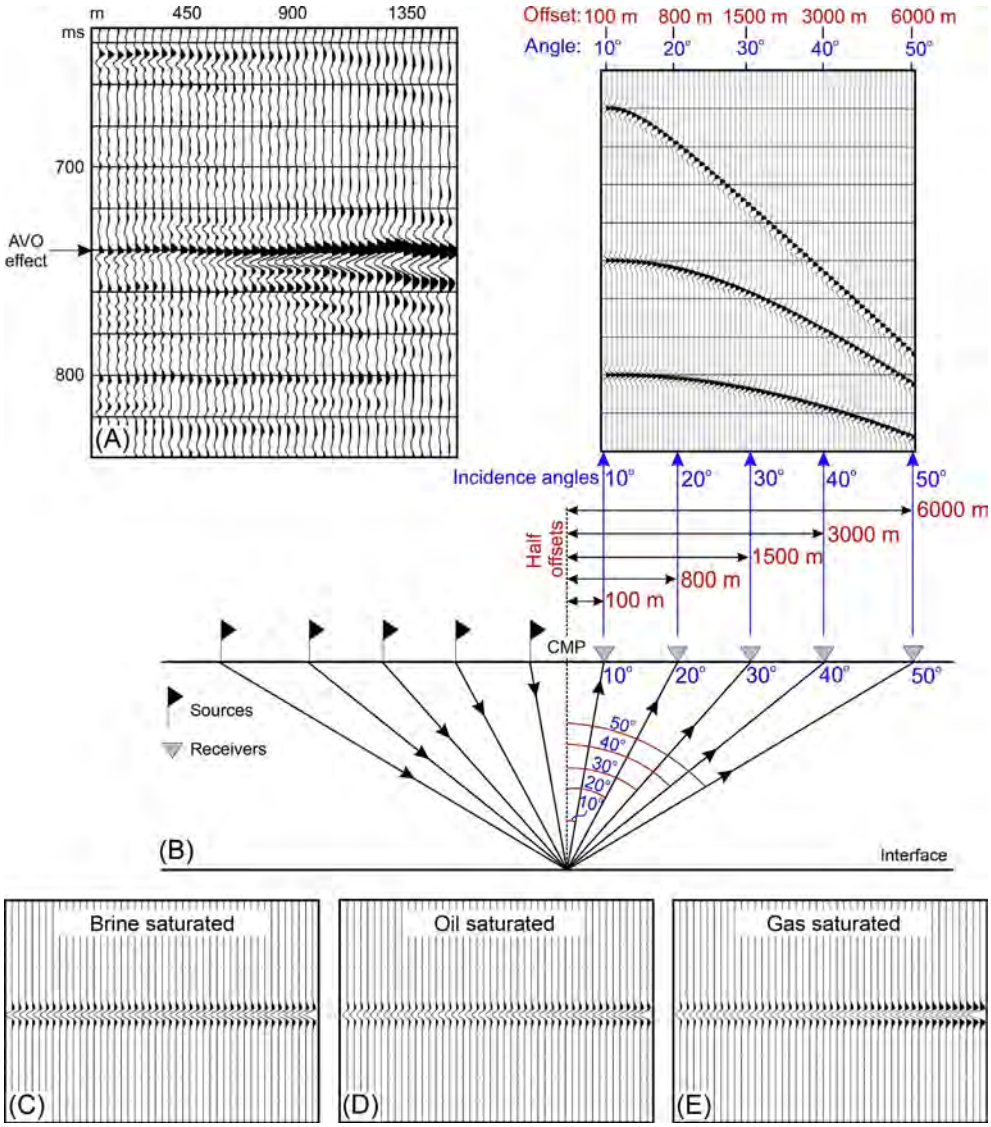


FIG. 12.19 (A) An example NMO corrected real CDP gather with a distinctive AVO effect at 740 ms. (B) Schematic illustration of the relationship between offsets and incidence angles on a model of single horizontal reflector. Theoretical AVO responses of (C) brine, (D) oil, and (E) gas saturated sediments on NMO corrected CDPs.

If the underlying medium is brine saturated, then there will be no AVO effect on the NMO corrected CDP gather for the reflection associated with that specific interface (Fig. 12.19C). If the underlying medium is oil or gas saturated, however, this may result in a typical AVO anomaly (Fig. 12.19D and E). In general, the AVO effect arising from gas saturation is much more distinctive than oil saturation. On the other hand, in some cases, lithologic peculiarities

can also produce AVO effects, which restricts the success of AVO analyses in determining the subsurface hydrocarbons.

12.6.1 AVO Equations

In order to analyze the amplitude variations of the reflection events with incidence angles, we need to know the mathematical expression of angle-dependent reflection amplitudes. Although the Zoeppritz equations provide the exact solution of the reflection coefficients, hence the reflection amplitudes at nonnormal incidence angles, a number of linear approximations to the Zoeppritz equations have also been developed. Here, only the Aki and Richards (1980) and Shuey (1985) approximations are discussed.

12.6.1.1 Zoeppritz Equations

When the seismic signal arrives at an interface between two media with different elastic properties, a certain amount of incident signal amplitudes are reflected back into the upperlying medium, while remaining parts are transmitted into the lower medium. An incident P wave with a nonnormal incidence angle also generates reflected and transmitted S waves (Fig. 12.20) due to the phase conversion during the reflection on the interface. The Zoeppritz equations represent amplitudes of the reflected signal with an arbitrary incidence angle at an interface separating two media for a given elastic properties. They can be expressed as

$$\begin{bmatrix} \sin\theta_i & \cos\phi_r & -\sin\theta_t & \cos\phi_r \\ -\cos\theta_i & \sin\phi_r & -\cos\theta_t & -\sin\phi_t \\ \sin 2\theta_i & \frac{\alpha_1}{\beta_1}\cos 2\phi_r & \frac{\rho_2\beta_2^2\alpha_1}{\rho_1\beta_1^2\alpha_2}\sin 2\theta_t & -\frac{\rho_2\beta_2\alpha_1}{\rho_1\beta_1^2}\cos 2\phi_t \\ \cos 2\phi_r & -\frac{\beta_1}{\alpha_1}\sin 2\phi_r & -\frac{\rho_2\alpha_2}{\rho_1\alpha_1}\cos 2\phi_t & -\frac{\rho_2\beta_2}{\rho_1\alpha_1}\sin 2\phi_t \end{bmatrix} \begin{bmatrix} R_P \\ R_S \\ T_P \\ T_S \end{bmatrix} = \begin{bmatrix} -\sin\theta_i \\ -\cos\theta_i \\ \sin 2\theta_i \\ -\cos 2\phi_r \end{bmatrix} \tag{12.8}$$

where θ_i is the incidence angle of the incident P wave, θ_r is the reflection angle of the P wave, θ_t

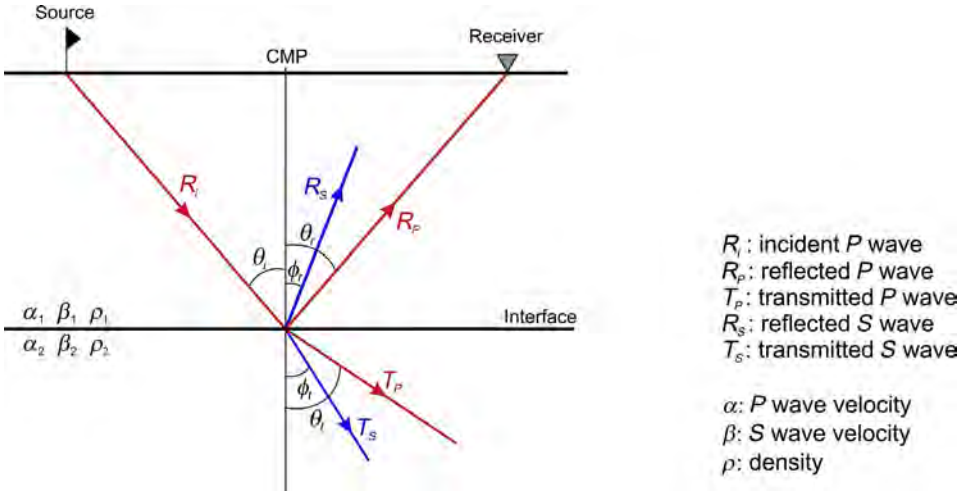


FIG. 12.20 An incident P wave at a nonnormal incidence angle generates reflected and transmitted P waves *(red rays)* as well as phase converted S waves *(blue rays)*. Here, θ_i is the incidence angle of the P wave, θ_r and ϕ_r are reflection angles, and θ_t and ϕ_t are transmission angles for P and S waves, respectively.

is the transmission angle of the P wave, ϕ_r is the reflection angle of the S wave, ϕ_t is the transmission angle of the S wave, R_p is amplitude of reflected P wave, R_s is amplitude of reflected S wave, T_p is amplitude of transmitted P wave, T_s is the amplitude of the transmitted S wave, α_1 and α_2 are P wave velocities, ρ_1 and ρ_2 are the densities, and β_1 and β_2 are S wave velocities of upperlying and underlying media, respectively (Fig. 12.20). For given α, β, and ρ parameters for both upperlying and underlying media, Eq. (12.8) can be solved to obtain the amplitudes for reflected and transmitted P and S waves (R_p, R_s, T_p, T_s) for any given angle of incidence (θ_i). As a specific case, amplitudes of the reflected waves rapidly increase beyond the critical angle, where a total reflection occurs and no transmitted P or S wave to the underlying medium is generated.

When the incidence angle θ_i is zero, the reflected signal amplitude is represented by P wave velocity and density of both media in a simple form as

$$R_P(0) = R_0 = \frac{\alpha_2\rho_2 - \alpha_1\rho_1}{\alpha_2\rho_2 + \alpha_1\rho_1} \tag{12.9}$$

where $\alpha_1\rho_1$ and $\alpha_2\rho_2$ are known as acoustic impedances of the upperlying and underlying media, respectively.

For given parameters of P and S wave velocities, densities and reflection/transmission angles of both medias, Eq. (12.8) can be used to compute theoretical AVO curves. The Zoeppritz equations are not linear and do not directly demonstrate how the reflected signal amplitude changes as a function of a specific parameter of the subsurface. For instance, they do not provide a direct analysis of amplitude variations as a function of incidence angle. This situation has led to a number of linearized approximations to the Zoeppritz equations in the form of $R(\theta) = f(\alpha, \beta, \rho)$. The most common approximations are given by Aki and Richards (1980) and Shuey (1985).

12.6.1.2 Aki-Richards Approximation

One of the most common approximations to the Zoeppritz equations was proposed by Aki and Richards (1980) as

$$R(\theta) \cong A + B\sin^2\theta + C\sin^2\theta\tan^2\theta \tag{12.10}$$

where θ is the incidence angle, and $R(\theta)$ is the reflected signal amplitude with respect to θ. Here, A, B, and C coefficients are known as AVO intercept, AVO gradient, and AVO curvature, respectively, and are expressed as

$$A = \frac{1}{2}(\Delta\alpha + \Delta\rho)$$
$$B = \frac{1}{2}\Delta\alpha - 4\gamma\Delta\beta - 2\gamma\Delta\rho$$
$$C = \frac{1}{2}\Delta\alpha$$

where

$$\Delta\alpha = 2\frac{(\alpha_2 - \alpha_1)}{(\alpha_2 + \alpha_1)} \quad \Delta\beta = 2\frac{(\beta_2 - \beta_1)}{(\beta_2 + \beta_1)}$$
$$\Delta\rho = 2\frac{(\rho_2 - \rho_1)}{(\rho_2 + \rho_1)} \quad \gamma = \frac{(\beta_2 + \beta_1)}{2(\alpha_2 + \alpha_1)}$$

where α_1 and α_2 are P wave velocities, ρ_1 and ρ_2 are the densities, and β_1 and β_2 are S wave velocities of the upperlying and underlying media, respectively.

12.6.1.3 Shuey Approximation

Another well-known simplification to the Zoeppritz equations was suggested by Shuey (1985), who replaced the S wave velocity term β with Poisson's ratio σ in the Aki-Richards approximation as

$$R(\theta) \cong A + B\sin^2\theta + C\left(\tan^2\theta - \sin^2\theta\right) \tag{12.11}$$

where θ is the incidence angle, and $R(\theta)$ is the reflected signal amplitude with respect to θ. Here, A is the reflection coefficient at normal incidence for $\theta = 0$, B is known as the AVO gradient to describe $R(\theta)$ at intermediate angles, and C is the term to explain $R(\theta)$ approaching to the critical angle, respectively. These coefficients are expressed by

$$A = R_0 = \frac{\rho_2\alpha_2 - \rho_1\alpha_1}{\rho_2\alpha_2 + \rho_1\alpha_1}$$

$$B = \left[\frac{(\Delta\alpha/\alpha)}{(\Delta\alpha/\alpha)+(\Delta\rho/\rho)} - 2\left(1 + \frac{(\Delta\alpha/\alpha)}{(\Delta\alpha/\alpha)+(\Delta\rho/\rho)}\right)\frac{1-2\sigma}{1-\sigma}\right]R_0 + \frac{\Delta\sigma}{(1-\sigma)^2}$$

$$C = \frac{1}{2}\frac{\Delta\alpha}{\alpha}$$

where

$$\Delta\alpha = (\alpha_2 - \alpha_1) \quad \Delta\rho = (\rho_2 - \rho_1) \quad \alpha = \frac{1}{2}(\alpha_2 + \alpha_1)$$

$$\rho = \frac{1}{2}(\rho_2 + \rho_1) \quad \sigma = \frac{1}{2}(\sigma_2 + \sigma_1) \quad \Delta\sigma = (\sigma_2 - \sigma_1)$$

where α_1 and α_2 are P wave velocities, ρ_1 and ρ_2 are densities, and σ_1 and σ_2 are Poisson's ratio of the upperlying and underlying media, respectively. Although both approximations produce very close amplitude values to those obtained by the Zoeppritz equations for relatively small incidence angles, the discrepancy between the Zoeppritz equations and linear approximations significantly increases for higher incidence angles. Modeling results show that the Aki-Richards approximation produces better results than the Shuey approximation when compared to the exact reflection coefficients calculated by the Zoeppritz equations, and yields acceptable results up to the critical angles.

12.6.2 Intercept and Gradient

Considering the first two terms of the Aki-Richards and Shuey approximations, we can further simplify the AVO equation in the form of

$$R(\theta) \cong A + B\sin^2\theta \tag{12.12}$$

where θ is the incidence angle, $R(\theta)$ is the reflected signal amplitude with respect to θ, and A and B are termed the AVO intercept and AVO gradient attributes, respectively. Eq. (12.12) indicates that $R(\theta)$ is linear as a function of $\sin^2(\theta)$, which enables us to calculate the AVO intercept and gradient parameters. Fig. 12.21 schematically shows the relationship between the AVO curve and these two attributes. When we pick the maximum amplitudes of the wavelets along a reflection event containing an AVO effect (e.g., the blue squares on the NMO corrected reflection in the upper panel of Fig. 12.21A) and plot them against their incidence angle θ, we can get the corresponding AVO curve, which illustrates the type or "class" of the AVO effect of that specific event (lower panel of Fig. 12.21A). On the other hand, if we plot the picked amplitudes with respect to $\sin^2(\theta)$, we can obtain a straight line as in Fig. 12.21B. The value of this line at $\theta = 0$ (i.e., amplitude at zero offset) is the AVO intercept (A in Eq. (12.12)), while the slope of the line provides the AVO gradient value (B in Eq. (12.12)), which is commonly obtained from a linear regression of the best-fitting line using a least-squares approximation.

Intercept and gradient parameters are often symbolized by I and G, and are termed the I and G attributes, respectively. In an AVO analysis, NMO corrected CDP gathers are used to compute the intercept and gradient values. Every CDP in a seismic line is scanned from zero to maximum recording time, incorporating the full time samples to obtain an intercept and a gradient trace. In AVO analysis, the accuracy of NMO correction, and hence an accurate velocity analysis, is crucial since any remaining residual NMO on the CDPs causes incorrect I and G attribute computation. In computing I and G sections, each CDP gather constitutes one single I and G trace. Then these traces are plotted side by side to display the intercept and gradient sections of the seismic line.

Intercept attribute reflects the normal incidence amplitudes, that is, the first trace in every CDP gather after NMO correction is plotted to prepare the intercept section. Fig. 12.22 shows example intercept and gradient sections of a seismic line that has a bottom simulating reflection (BSR), defined as the base of gas hydrate accumulations, which commonly yields bright

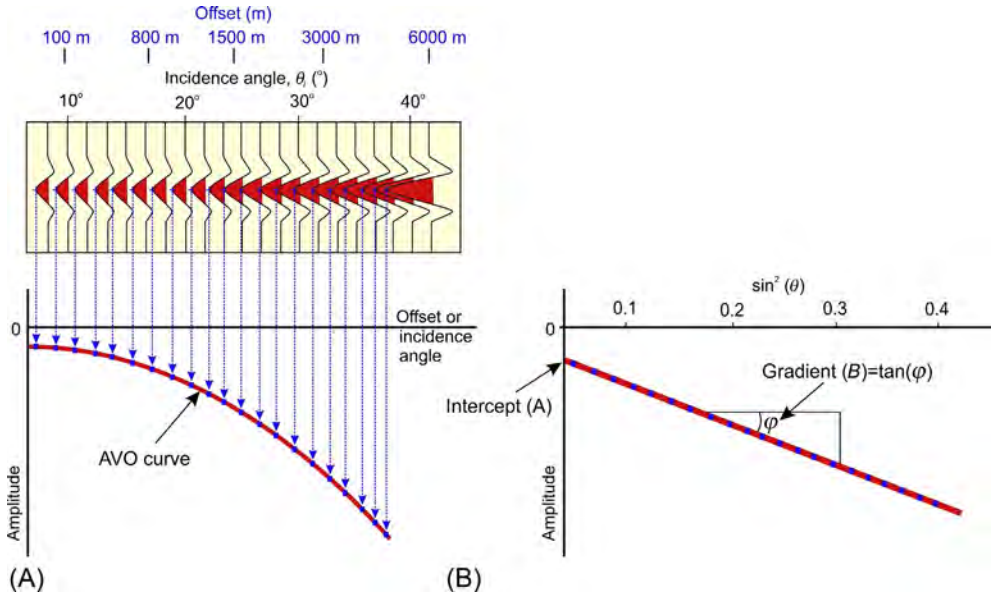


FIG. 12.21 Schematic display of reflection amplitudes with an AVO effect and obtaining intercept and gradient attributes. (A) Absolute amplitudes increase with offset on an NMO corrected reflection event (*blue squares* represent the maximum amplitudes of each wavelet of the reflection in the upper panel). When these amplitudes are plotted against their offsets or incidence angles, the AVO curve of this reflection event is obtained (lower panel). (B) If the amplitudes on the AVO curve are plotted as a function of $\sin^2\theta$, then the curve becomes linear, and the amplitude value at zero offset or $\theta = 0$ corresponds to the intercept (A) attribute, and the slope of this line is the gradient (B) attribute for this reflection event.

reverse polarity reflections, generally with a distinctive free gas accumulation below along with a prominent AVO effect on the prestack gathers. Using intercept and gradient attributes, several additional attributes or crossplots, such as *I*G*, Sign (*I*G*), and fluid factor can be computed.

12.6.3 AVO Classes

The shape of AVO curves may change depending on the physical parameters of the subsurface. In hydrocarbon exploration, shale-sand interfaces are generally target zones to analyze using AVO techniques. For instance, the amplitudes for a specific reflection change from a small negative value at zero offset and further increase in a negative direction, or start with a positive value and decrease with offset. Such different types of AVO curves are known as AVO classes, and they are classified into four groups by Rutherford and Williams (1989) as Class I, Class II, Class III, and Class IV. In the first three AVO class anomalies, the reflection coefficient curve is negative and the amplitudes decrease with increasing offset. However, Castagna et al. (1998) showed that the amplitudes for Class II and III anomalies may increase with offset, and designated them as Class IV AVO anomalies. In the seismic industry, the most common AVO class is Class III.

12.6.3.1 Class I (Dim Out) AVO Anomalies

Class I anomalies are represented by dim spots on the stack sections, and amplitudes of a specific reflection fade with increasing offset on the NMO corrected CDP gathers. They have the same polarity as seafloor reflection and never exhibit negative polarity. Fig. 12.23 shows

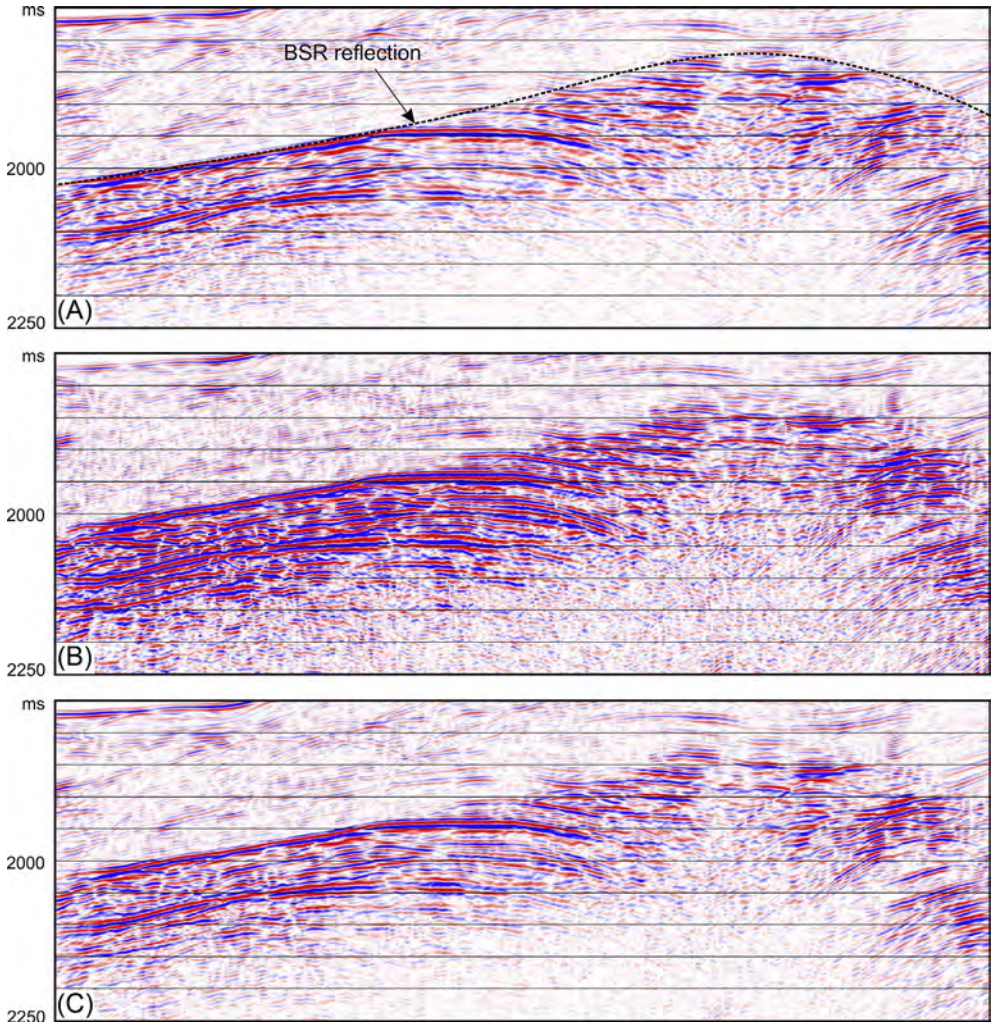


FIG. 12.22 An example (A) stack, (B) intercept (*I*), and (C) gradient (*G*) section of a BSR, from the base of subsurface gas hydrates, which generally produces a distinctive AVO effect on the prestack seismic data.

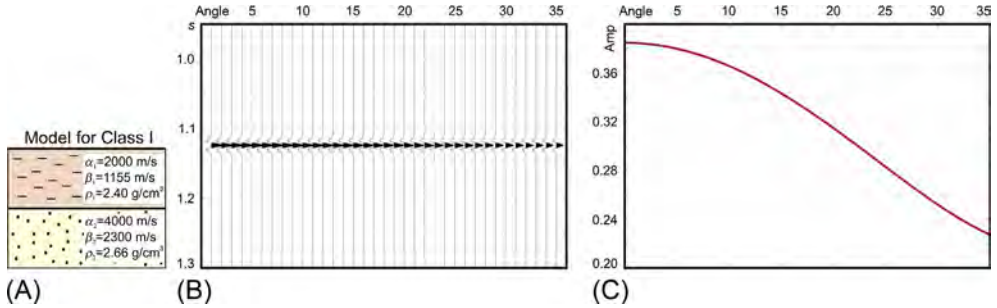


FIG. 12.23 (A) Subsurface model suitable for Class I type AVO anomaly, (B) synthetic traces calculated using the Aki-Richards approximation, and (C) plot of the maximum reflection amplitudes as a function of incidence angle.

a simple subsurface model suitable for a Class I AVO anomaly, its seismic record on an NMO corrected CDP gather and AVO curve obtained from the maximum amplitudes of the reflection in a CDP gather. For the hydrocarbon zone, full stack amplitude is generally smaller than for the brine saturated zone in Class I AVO. This is the rarest AVO type encountered in hydrocarbon exploration.

12.6.3.2 Class II (Phase Reversal) AVO Anomalies

Class II anomalies cause phase reversals on the NMO corrected CDP gathers, which is particularly prominent on the long offset prestack gathers, and therefore there is little indication of hydrocarbon accumulation on the near offset stack. Amplitudes at zero offsets are positive and close to zero, and are replaced by negative amplitudes that increase with increasing offset. They are frequently represented by bright spots on the stack sections, or rarely appear as dim spots due to the polarity reversal on the prestack data. Gas indication may not be evident on the full stack, depending on the high-amplitude contribution from far offsets. Fig. 12.24 shows a simple subsurface model suitable for a Class II AVO anomaly, its seismic record on an NMO corrected CDP gather and the AVO curve obtained from the maximum amplitudes of the reflection in the CDP gather.

12.6.3.3 Class III (Bright Spot) AVO Anomalies

Class III anomalies are represented by distinctive bright spots on the stack sections. Amplitudes of a specific reflection at zero offsets are negative and relatively large, and they significantly decrease in the negative direction with increasing offset on the NMO corrected CDP gathers. This is the most common AVO type encountered in hydrocarbon exploration, and are easy to identify on both full stack and prestack seismic data. Class III type AVO anomaly zones can easily be distinguished from the comparison of near and far offset stacks. Fig. 12.25 shows a simple subsurface model suitable for a Class III AVO anomaly, its seismic record on an NMO corrected CDP gather and the AVO curve obtained from the maximum amplitudes of the reflection in the CDP gather.

12.6.3.4 Class IV AVO Anomalies

Class IV anomalies are very rare in hydrocarbon exploration, like Class I anomalies. This type of AVO anomaly was suggested by Castagna et al. (1998), and then included in the AVO types as a specific AVO class. Amplitudes of a specific reflection at zero offsets are negative and they increase in a positive direction with increasing offset on the NMO corrected CDP gathers. Although the amplitudes increase at far offsets, no positive amplitudes occur at higher incidence

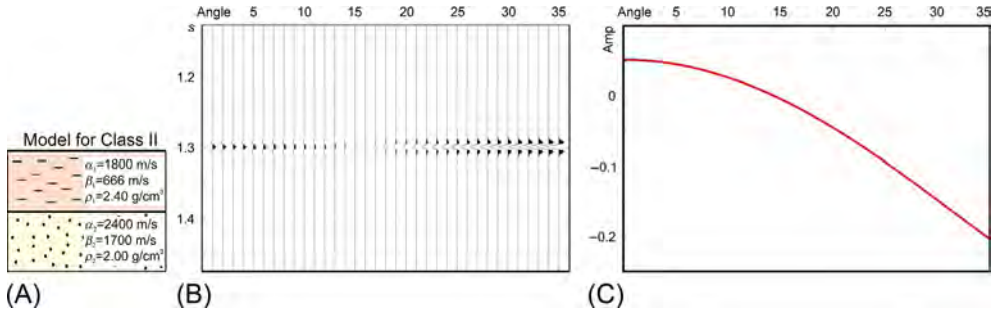


FIG. 12.24 (A) Subsurface model suitable for Class II type AVO anomaly, (B) synthetic traces calculated using the Aki-Richards approximation, and (C) plot of the maximum reflection amplitudes as a function of incidence angle.

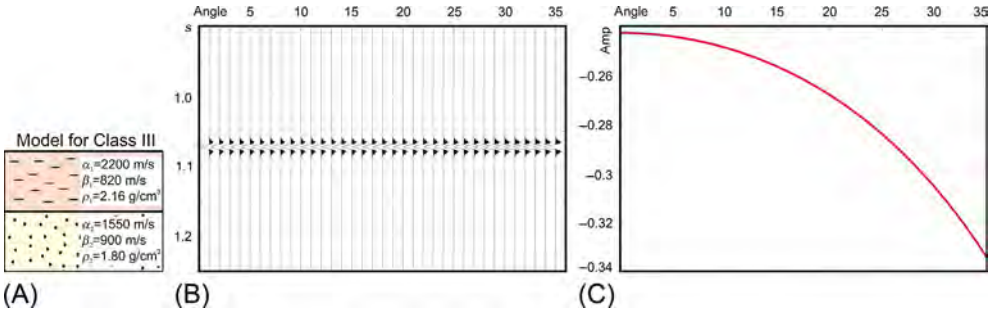


FIG. 12.25 (A) Subsurface model suitable for Class III type AVO anomalies, (B) synthetic traces calculated using the Aki-Richards approximation, and (C) plot of the maximum reflection amplitudes as a function of incidence angle.

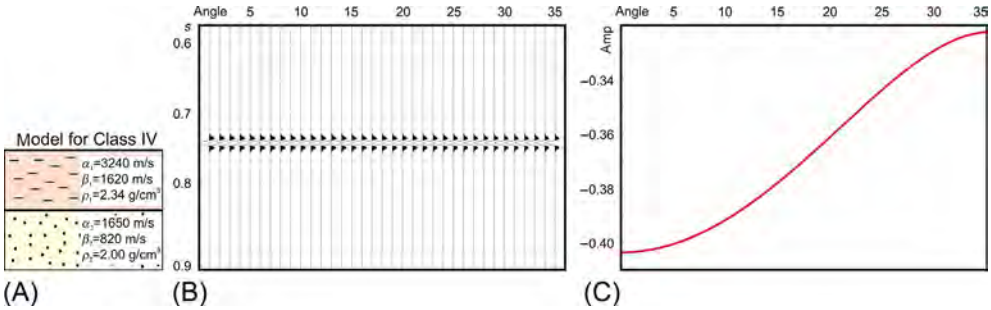
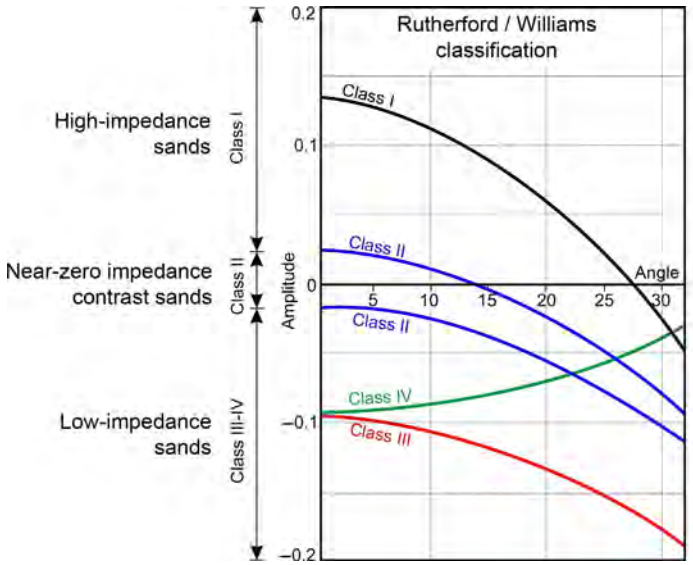


FIG. 12.26 (A) Subsurface model suitable for Class IV type AVO anomalies, (B) synthetic traces calculated using the Aki-Richards approximation, and (C) plot of the maximum reflection amplitudes as a function of the incidence angle.

angles. Fig. 12.26 shows a simple subsurface model suitable for a Class IV AVO anomaly, its seismic record on an NMO corrected CDP gather and the AVO curve obtained from the maximum amplitudes of the reflection in the CDP gather.

Different AVO classes are categorized to display their relative behavior with increasing incidence angle (Fig. 12.27), which is known as Rutherford-Williams classification and which indicates that AVO curves for different AVO classes exhibit almost a similar style: the absolute amplitudes increase in a negative direction with increasing offset, except Class IV which displays exactly the opposite behavior. The parameter distinguishing the AVO classes is the amplitude value at zero offset, which is positive for Class I, either a positive or negative small value for Class II, and prominently negative for Classes III and IV. According to their classification depending upon the gas-sand reservoir responses, Rutherford and Williams (1989) suggest that Class I anomalies arise from high-impedance sands, Class II anomalies show up from near-zero impedance contrast sands, and Class III anomalies refer to low-impedance sands. Intercept (I) and gradient (G) as well as $I*G$ attributes also change polarities with respect to the AVO classes they occur in (Fig. 12.27). In general, the G attribute is of reverse polarity with respect to the I attribute. Therefore, the $I*G$ attribute is negative for Class I and IV, while it is positive for Class III anomalies. For Class II, the polarities of I, G and $I*G$ attributes are determined by their zero-offset values.



	I	*G*	*I*G*
Class I	+	−	−
Class II	+/−	−	+/−
Class III	−	−	+
Class IV	−	+	−

FIG. 12.27 Different AVO classes on the amplitude vs. incidence angle plot, and variation of *I* and *G* attribute signs depending on the AVO class.

12.6.4 Processing Considerations for AVO

AVO analysis is normally applied to NMO corrected CDP gathers. Prior to AVO analysis, seismic data must be properly preprocessed to remove coherent and incoherent noise components as far as possible. Common preprocessing steps before AVO analysis include data loading, geometry definition, band-pass filter, true amplitude recovery and spherical divergence correction, trace kill, muting, f-k filter, array correction, multiple attenuation, surface consistent deconvolution, CDP sorting, velocity analysis and NMO correction. A prestack migration to obtain image gathers is preferred before the AVO analysis, especially in areas of complex subsurface geology.

The most important rule in preconditioning of seismic data for AVO analysis is to preserve the relative amplitude information during each individual processing step. Among these processing applications, gain correction and velocity analysis are of primary importance and must be performed carefully. Automatic gain control (AGC) should be avoided, since it completely destroys the relative amplitude relationship in the data. Therefore, true amplitude recovery or spherical divergence correction must be used, in order to restore the amplitudes. A sufficiently dense grid of velocity analysis must be done along the target area to obtain perfectly flattened events after NMO correction. A careful quality control (QC) analysis must be performed after NMO correction around the target area, to ensure that the primary reflections are perfectly flattened. If not, velocity analysis must be revised to obtain a better velocity field that flattens the primaries, especially in the target zone after NMO correction.

AVO processing also requires a specific correction known as array correction to compensate for the filtering effects of the receiver array due to the nonnormal incidence angles of the reflected signal. In seismic data acquisition, a certain number of adjacent hydrophones with a specific distance in between are grouped to form a receiving array for each recording

channel. Reflected signals are detected by these hydrophone groups, and the amplitudes at each hydrophone are linearly summed up together to increase the S/N ratio. As the incidence angle of the reflection signal increases, each hydrophone receives the signal with a certain time delay because of the spherical wave front divergence (Section 2.5.1.4). This is known as the directivity effect, which ultimately results in a reduction of the recorded reflection signal amplitude with increasing incidence angles.

If we assume that the signal is composed of a single frequency and the amplitude is filtered by N number of receiver components, we can compute the directivity effect as

$$R(\theta,f)=\frac{1}{N}\frac{\sin\left(\frac{N\pi fd}{V}\right)}{\sin\left(\frac{\pi fd}{V}\right)} \tag{12.13}$$

where N is the number of hydrophones in a group, f is the signal frequency, d is the distance between the hydrophones within the group, and V is the velocity.

12.6.5 AVO Analysis

AVO analysis is basically performed for the direct detection of hydrocarbon bearing sands from surface seismic data, or understanding and monitoring of an existing reservoir as well as the reservoir quality. In combination with the well log data, AVO analysis can provide a link between surface seismics and rock physical properties of the possible and existing reservoirs. It comprises different applications deduced from the reflection amplitudes on the NMO corrected CDP gathers (Fig. 12.28).

Although the success of AVO analysis in hydrocarbon exploration has been proven worldwide over the last two decades, there are several restrictions due to which an AVO anomaly may not directly indicate hydrocarbons. Castagna et al. (1998) suggest a number of factors affecting the success of AVO analyses, which include

- near surface effects
- S/N ratio of the input data
- geological complexity of the subsurface
- amplitude issues of the seismic wavelet, such as geometrical spreading and absorption
- array filtering
- NMO correction errors
- weathering layer effects
- processing issues.

In addition to these factors, the following assumptions are also made in AVO analysis:

- The medium is isotropic and homogeneous.
- Incidence angles never exceed the critical angle.
- $\alpha/\beta=2$.
- The third term in Eqs. (12.10) and (12.11) is ignored since $\sin\theta\cong\tan\theta$ for incidence angles approximately between 0 and 30 degrees.

The most important issues with AVO analysis are fizz water and thin bed tuning effects, both of which produce good AVO anomalies commonly indistinguishable from the AVO responses of

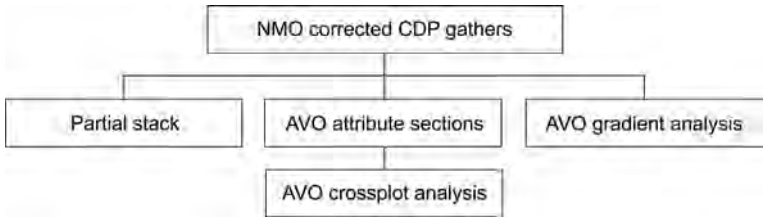


FIG. 12.28 Basic applications flow for AVO analysis.

pay zones. Fizz water, or fizz gas, can be defined as partial gas saturation, generally in a bubble phase from a few percent to 20%. Even small amounts of low saturation gas (e.g., <5%) is sufficient to reduce the interval velocity significantly, which results in a seismic anomaly very similar to that of a commercial gas reservoir. Using only seismic techniques, including amplitude analysis, direct hydrocarbon indicators (DHI) and AVO analysis, it is generally not possible to differentiate a gas saturated reservoir and a fizz water reservoir. Fizz water is often responsible for the false hydrocarbon indicators on seismic data, and hence it is often considered as a scapegoat for dry wells.

Thin bed tuning is another issue that can lead to a misinterpretation of AVO anomalies, and has a significant impact on seismic resolution. Widess (1973) defines the thin bed as a layer whose thickness is less than about $\lambda/8$, where λ is the dominant wavelength of the seismic wavelet. The reflections from the top and bottom of a thin bed interfere constructively or destructively, depending on the thickness and the wavelength of the signal, which causes significant changes in the shape and amplitude of the wavelet. In AVO analysis, an offset-dependent tuning due to the amplitude variation with offset is considered. It may mask an existing AVO effect, and even corrupt the type of AVO class, or create a phantom AVO anomaly on prestack seismic data. For instance, as the layer thickness is reduced, a trough at near offsets becomes a peak at far offsets for a Class I AVO anomaly.

12.6.5.1 Partial Stack

AVO anomalies indicate the amplitude variations of a specific reflection from a target interface in the prestack data. When all the traces in a CDP are simply stacked, the AVO information that the CDP contains may be destroyed completely, since near and far offsets are stacked all together (Section 10.3). AVO effects on the prestack seismic data can quickly be recognized by partial stacking of different offset ranges independently from each other, commonly near and far offset traces in a CDP separately, to obtain angle dependent stacks. This method is known as partial stack and is used to distinguish AVO effects on the angle-dependent stack sections as a quick AVO reconnaissance tool (Section 10.4.1).

A possible AVO effect in the prestack data generally produces an enhanced high-amplitude reflection or amplitude dimming on the far offset stack, depending on the AVO class, whereas a regular amplitude distribution is obtained in the near offset stack (Fig. 10.19). Partial stacking is normally the starting point for an AVO analysis to find out the possible AVO anomalies in the seismic lines. Partial stacks are computed for different offset ranges and are compared to each other to bring out the differences between the stack sections. If such anomalous zones are identified on the partial stacks, then it is recommended to go back to the prestack data around these anomalous zones to analyze the NMO corrected CDP gathers by means of possible AVO effects.

12.6.5.2 Gradient Analysis

Gradient analysis is performed to determine the AVO class of the specified AVO anomaly from the amplitude-offset or amplitude-incidence angle plots. The amplitudes of the reflection event with an AVO anomaly are picked on the NMO corrected CDP gathers and then displayed as a function of offset or incidence angle. In the example gradient analysis in Fig. 12.29, the red and blue curves represent the top and base of a Class III type AVO anomaly, respectively. Determination of AVO classes may provide general information on the structure of the subsurface hydrocarbon accumulations, as shown in the Rutherford-Williams classification in Fig. 12.27.

12.6.5.3 AVO Attributes

One of the most important consequences of AVO analysis is the computation of different AVO attribute sections. AVO attributes are

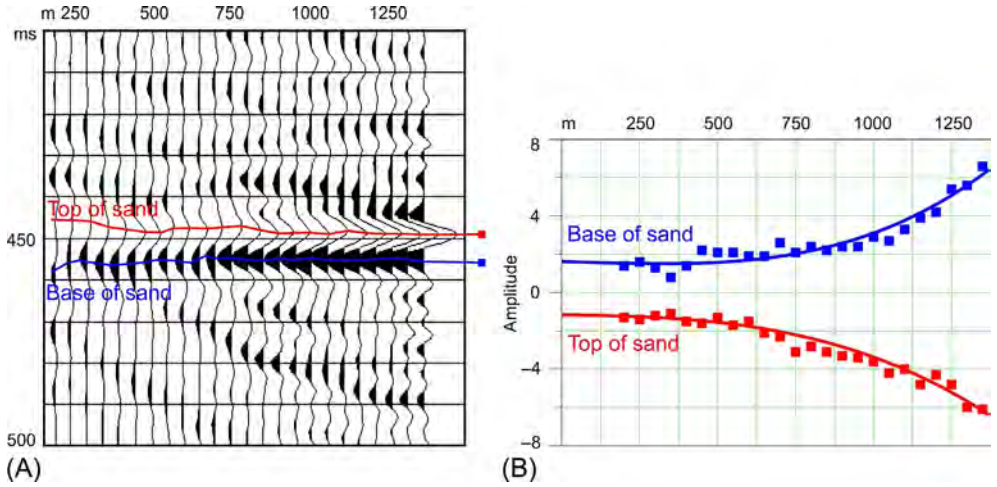


FIG. 12.29 A sample gradient analysis for a real marine CDP. (A) An NMO corrected CDP gather with an AVO anomaly approximately at 450 ms. The top and bottom of sand reflections are indicated by red and blue curves, respectively. (B) Amplitude vs. offset plot of the top and bottom of sand reflections indicating a Class III type AVO anomaly.

generally performed by considering the first two terms of Eqs. (12.10) or (12.11), that is, $A + B\sin^2\theta$. To compute the different attributes, amplitudes of the reflection with an AVO effect are plotted against $\sin^2\theta$, where θ is the corresponding incidence angle of each specific amplitude value. After the determination of intercept (I) and gradient (G) attributes, as in Fig. 12.21B, it is possible to obtain several other useful AVO attributes. The most common attributes used in the seismic industry today are

- Gradient (G) section
- Intercept (I) section
- I*G section
- Sign(I)*G section
- Fluid factor section
- $I - G$ section
- $I + G$ section
- AVO curvature

Fig. 12.30 shows several examples of AVO attributes computed for a seismic line with a distinctive bright reflection on the stack section (Fig. 12.30A), possibly from a shallow gas front. The intercept (I) and gradient (G) sections are the fundamental attributes for AVO analysis (Fig. 12.30B and C), which represent the zero-offset (or zero-angle) amplitude, and the slope of the best-fit line to the amplitude vs. $\sin^2\theta$ plot, respectively. The gradient attribute corresponds to a relative change in reflection amplitude with offset (or incidence angle). The I*G attribute is a favorable tool in AVO analysis, especially to delineate Class III gas sands, and it emphasizes high zero-offset reflection coefficients and clearly shows the possible AVO effects in the data. Peaks indicate an increase, and troughs represent a decrease of absolute amplitude with offset on I*G attribute sections (Fig. 12.30D). The sign(I)*G attribute preserves the gradient value, but the polarity of this attribute is determined by the combined polarities of the I and G attributes (Fig. 12.30E). $I - G$ and $I + G$ attributes (Fig. 12.30F and G) are not common in AVO attribute analysis, but they can provide additional information about the anomalous reflections in conjunction with other attribute sections.

An effective AVO attribute is known as a fluid factor (Fig. 12.30H), which is defined as the deviation from Castagna's mudrock line

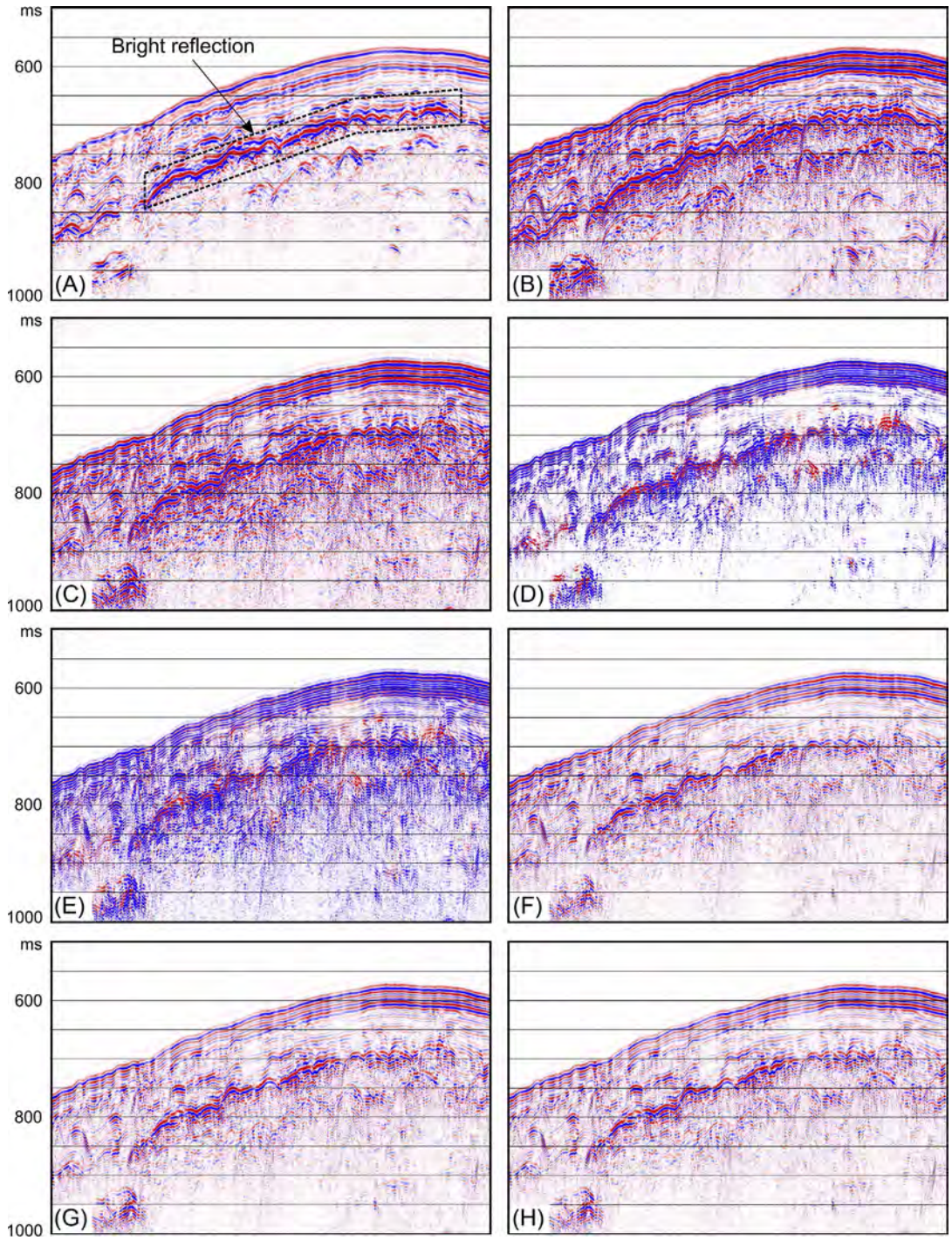


FIG. 12.30 Different AVO attributes calculated from a marine seismic line. (A) True amplitude stack section with an enhanced bright reflection possibly obtained from a shallow gas front, and its (B) intercept (I), (C) gradient (G), (D) I*G, (E) sign(I)*G, (F) $I - G$, (G) $I + G$, and (H) fluid factor sections.

(Castagna et al., 1985) on which the water saturated sands and shales approximately fall. Fatti et al. (1994) defined the fluid factor as

$$\Delta F = R_P - 1.16(\beta/\alpha)R_S \tag{12.14}$$

where R_P and R_S are P and S wave reflection amplitudes at zero offsets, respectively. Using I and G attributes, they can be approximated as

$$R_P = 1.6 \times \text{intercept}$$

and

$$R_S = \text{intercept} - \text{gradient}$$

The velocity relationship between P and S waves for water saturated sands is computed from the mudrock line trend of Castagna et al. (1985) as

$$\alpha = 1.36 + 1.16\beta \tag{12.15}$$

In ideal cases, the fluid factor values for nonpay zones on the seismic line are zero, whereas shale/gas sand interfaces produce negative and gas-sand/brine-sand interfaces yield positive fluid factor values. Carbonate and igneous rocks may also represent fluid factor anomalies of opposite polarity with respect to the gas sands. It is generally difficult to determine the high-impedance gas sands overlaid by low-impedance shale using the gradient trace. Fluid factor traces, however, may contain high-amplitude anomalies regardless of the gas sand impedance (Fatti et al., 1994).

12.6.5.4 AVO Crossplots

AVO crossplots are prepared by plotting intercept (horizontal axis) vs. gradient (vertical axis) attributes to discriminate the gas sands from brine sands. In general, gas sands can be determined much more accurately from AVO crossplot analysis, whereas oil-related amplitude anomalies are hidden in the noise of the crossplot. Each CDP gather from the target reflection provides one pair of I and G attribute values associated with that target reflection, and each I and G pair constitutes a point on the crossplot. All of the I and G amplitudes are crossplotted around the anomalous bright reflection to prepare a crossplot consisting of several I-G pairs.

For a particular reflection, there is generally a well-defined trend between I and G values for brine saturated sands: the values on the crossplot generally fall onto a linear trend which approximately passes through the origin. This linear trend is known as the background trend or wet rock trend, which indicates the amplitudes from nonhydrocarbon-bearing sediments such as brine sands (blue line in Fig. 12.31A). However, deviations from the background trend are indicative of the hydrocarbon-saturated sediments, especially the gas sands. In addition, amplitudes from different AVO classes locate in different quadrants of the crossplot: Class IV anomaly amplitudes are located in the top left, Class III amplitudes are lower left, and Class I amplitudes are lower right quadrants. Class II type amplitudes are located both at the lower left and right quadrants close to the vertical gradient attribute axis (Fig. 12.31A).

I and G crossplot values from the top of gas sand reflections arise below the background trend while the base of sand reflections appears above (Fig. 12.31B). Therefore, amplitudes on the crossplots from top and base sand reflections of an AVO anomaly show up as an approximately symmetrical distribution relative to the background trend. An increasing α/β ratio moves the base of sand amplitudes further up and a decreasing α/β ratio moves the top of sand amplitudes further down, to the locations away from the background trend. Fig. 12.31C shows a real crossplot from a Class III type AVO anomaly. The amplitudes in the blue and yellow ellipses correspond to the base and top of gas sand reflections, respectively, while the ones in the grey ellipse represent the background amplitudes from brine-saturated sands. By picking the amplitudes in blue and yellow ellipses in the crossplot, we can determine their corresponding locations on the seismic line.

Crossplots are generally used to separate brine and gas saturated sands. The fluid factor

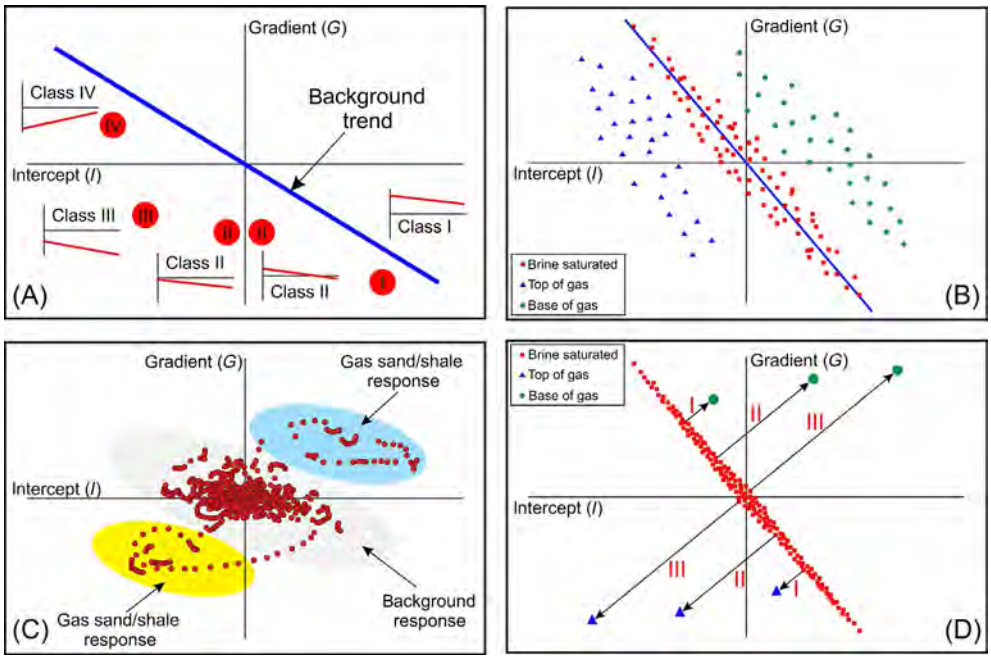


FIG. 12.31 Specifications of intercept-gradient crossplots. (A) For brine-saturated sands, the values on the crossplot generally fall onto a linear trend passing through the origin of the crossplot, termed the background trend. Amplitudes from different AVO classes locate in different quadrants of the crossplots. (B) Crossplot amplitudes from the top and base of gas sand reflections appear below and above the background trend, respectively. (C) A crossplot from a Class III type AVO anomaly. The top and base of the gas sand reflections fall into yellow and blue ellipses, respectively. Amplitudes from brine-saturated sands constitute the background trend and are located in the grey ellipse. (D) Effect of fluid substitution on the crossplots of Class I, II and III type AVO anomalies. When the brine-saturated sand becomes gas saturated, its amplitude on the crossplot replaces to a new point away from the background trend, which is termed fluid substitution.

defined by Eq. (12.14) can be considered as the distance between the I and G crossplot value to the background trend (Foster et al., 2010). The higher the distance of a crossplot point from the background trend, the higher the possibility of I and G pair (and hence, the CDP that produces a corresponding I and G pair) for that crossplot point represents hydrocarbon existence. Fig. 12.31D illustrates this phenomenon schematically for Class I, II and III type AVO anomalies. If brine-saturated sand becomes gas saturated, then its corresponding amplitude on the I-G crossplot displaces to a new point away from the background trend, which is known as fluid substitution. The amount of this variation changes according to the class of AVO anomaly.

In practice, every single point on an intercept-gradient crossplot corresponds to a reflection event on a different CDP gather. If we pick the base and top of gas sand zones on the crossplots, we can analyze the corresponding amplitudes on the stack section. Fig. 12.32 shows such a crossplot analysis. Fig. 12.32A and B show intercept and gradient sections of a zone with an anomalous bright reflection (green polygon), and Fig. 12.32C shows the crossplots prepared using these sections, which indicates that the bright reflection has a Class III type AVO anomaly. When we pick the base of gas sand

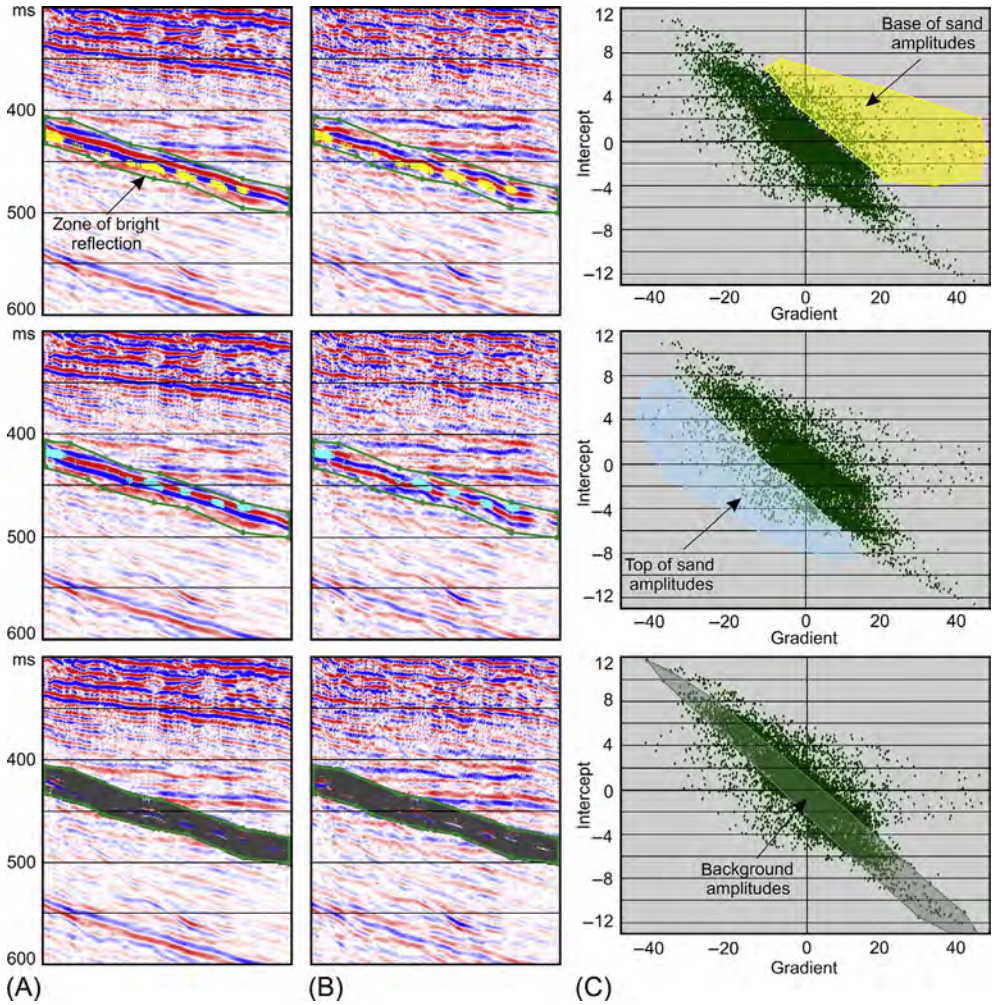


FIG. 12.32 An example AVO crossplot analysis. (A) Intercept, (B) gradient sections of a bright reflection enclosed by a *green polygon*, and (C) crossplots computed using intercept and gradient sections given in (A) and (B). Upper panel: If the base of gas sand amplitudes on the crossplot *(yellow polygon)* are picked, corresponding amplitudes can be located on the intercept and gradient sections (marked by small yellow squares on intercept and gradient sections). Middle panel: If the top of gas sand amplitudes on the crossplot *(blue polygon)* are picked, then their corresponding amplitudes can be determined on the intercept and gradient sections (marked by small *blue squares* on intercept and gradient sections). Lower panel: If the remaining amplitudes along the background line on the crossplot *(grey polygon)* are picked, brine-saturated zones can be placed on the intercept and gradient sections (marked by small *grey squares* on intercept and gradient sections).

amplitudes on the crossplot (yellow polygon on top of Fig. 12.32), we can locate the corresponding amplitudes on the intercept and gradient sections (marked by small yellow squares). Similarly, if we pick the top of gas sand amplitudes on the crossplot (blue polygon in the middle of Fig. 12.32), we can place the related amplitudes on the intercept and gradient sections (marked by small blue squares). The remaining amplitudes on the crossplot (grey polygon at the

bottom of Fig. 12.32), which directly fall onto the background line, represent the brine-saturated zones (marked by small grey squares on the intercept and gradient sections). Here, the top and base gas sand zones, indicated by yellow and blue markers on the intercept and gradient sections, represent the possible pay zones based on their AVO effects along the anomalous reflection. Note that these pay zones for the top and base of the gas sands are quite consistent with each other in the top and middle panels of Fig. 12.32A and B. That is, AVO analysis indicates the same zones for possible gas accumulations along the target reflection. In addition, the pay zones are also isolated from the brine-saturated zones in the bottom panel of Fig. 12.32A and B.

References

Abma, R., Claerbout, J., 1995. Lateral prediction for noise attenuation by t-x and f-x techniques. Geophysics 60, 1887–1896.

Akalin, M.F., Muhamad, A.A., Tan, Y.C., Yusoff, Y.B.M., Radzi, N.A.M., Zohdi, S.F.M., Hashim, M.H., Ghazali, M., Maitra, S., Wardoyo, A., Ghazali, M.L., Murthy, J.V. S., Wang, G., Miao, X.G., 2014. 3D-PS converted waves—solving 3D-imaging challenges under gas clouds—offshore Malaysia. In: 76th EAGE Conference and Exhibition, Amsterdam.

Aki, K.I., Richards, P.G., 1980. Quantitative Seismology: Theory and Methods. WH Freeman Co., San Francisco, CA.

Albertin, U., Kapoor, J., Randall, R., Smith, M., Brown, G., Soufleris, C., et al., 2002. The time for depth imaging. Oilfield Rev. 14, 2–15.

Al-Chalabi, M., 1973. Series approximations in velocity and traveltime computations. Geophys. Prospect. 21, 783–795.

Alkhalifah, T., Tsvankin, I., 1995. Velocity analysis for transversely isotropic media. Geophysics 60, 1550–1566.

Allouche, N., Drijkoningen, G.G., Versteeg, W., Ghose, R., 2011. Converted waves in a shallow marine environment: experimental and modeling studies. Geophysics 76, T1–T11.

Ashton, C.P., Bacon, B., Mann, A., Moldoveanu, N., Déplanté, C., Dickilreson, et al., 1994. 3D seismic survey design. Oilfield Rev. 6, 19–32.

Barkved, O., Bartman, B., Gaiser, J., Van Dok, R., Johns, T., Kristiansen, P., et al., 2004. The many facets of multicomponent seismic data. Schlumberger Oilfield Rev. 42–56.

Barnes, A.E., 2007. A tutorial on complex seismic trace analysis. Geophysics 72, W33–W43.

Baysal, E., Kosloff, D.D., Sherwood, J.W.C., 1983. Reverse time migration. Geophysics 48, 1514–1524.

Bednar, J.B., 1983. Applications of median filtering to deconvolution, pulse estimation, and statistical editing of seismic data. Geophysics 48, 1598–1610.

Berdenbender, J.W., Johnston, R.C., Neitzel, E.B., 1970. Electroacoustic characteristics of marine seismic streamers. Geophysics 35, 1054–1072.

Biondi, B., 2001. Kirchhoff imaging beyond aliasing. Geophysics 66, 654–666.

Bortfeld, R., 1961. Approximation to the reflection and transmission coefficients of plane longitudinal and transverse waves. Geophys. Prospect. 9, 485–503.

Bracewell, R.N., 1965. The Fourier Transform and Its Applications. McGraw-Hill Book Co, New York.

Breistøl, A.H., 2015. Broadband processing of conventional 3D seismic data for near surface geohazard investigation: a North Sea case study. MSc thesis, Norwegian University of Science and Technology, Department of Petroleum Engineering and Applied Geophysics.

Bunting, T., Watterson, P., Vassallo, M., 2013. IsoMetrix: isometrically sampled towed-streamer marine seismic data.13th International Congress of the Brazilian Geophysical Society Expanded Abstracts, pp. 1177–1180.

Burg, J.P., 1967. Maximum entropy spectral analysis.SEG 37th Meeting, Oklahoma.

Canales, L., 1984. Random noise reduction. 54th SEG Meeting Expanded Abstracts, pp. 525–527.

Carlson, D., Long, A., Söllner, W., Tabti, H., Tenghamn, R., Lunde, N., 2007. Increased resolution and penetration from a towed dual-sensor streamer. First Break 25, 71–77.

Castagna, J.P., Bazle, M.L., Eastwood, R.L., 1985. Relationships between compressional-wave and shear-wave velocities in elastic silicate rocks. Geophysics 50, 571–581.

Castagna, J.P., Swan, H.W., Foster, D.J., 1998. Framework for AVO gradient and intercept interpretation. Geopyhsics 63, 948–956.

Castle, R.J., 1994. A theory of normal moveout. Geophysics 59, 983–999.

Chang, W., McMechan, G., 1986. Reverse-time migration of offset vertical seismic profiling data using the excitation-time imaging condition. Geophysics 51, 67–84.

Chase, M.K., 1992. Random noise reduction by 3-D spatial prediction filtering.SEG Technical Program Expanded Abstracts, pp. 1152–1153.

Chen, C.T., Millero, F.J., 1977. Speed of sound in seawater at high pressures. J. Acoust. Soc. Am. 62, 1129–1135.

Chopra, S., 2004. Expert answers. Theatr. Rec. 29, 1–20.

Chopra, S., Marfurt, K.J., 2005. Seismic attributes—a historical perspective. Geophysics 70, 3SO–28SO.

Claerbout, J.F., 1976. Fundamentals of Geophysical Data Processing. McGraw-Hill Book Co, New York.

Claerbout, J.F., 1985. Imaging the Earth's Interior. Blackwell Sci. Pub, Boston.

Claerbout, J.F., Doherty, S.M., 1972. Downward continuation of moveout-corrected seismograms. Geophysics 37, 741–768.

Deregowski, S.M., 1986. What is DMO? First Break 4, 7–24.

Dix, C.H., 1955. Seismic velocities from surface measurements. Geophysics 20, 68–86.

Dondurur, D., Karslı, H., 2012. Swell noise suppression by Wiener prediction filter. J. Appl. Geophys. 80, 91–100.

Dowle, R., 2006. Solid streamer noise reduction principles.SEG Technical Program Expanded Abstracts 2006, pp. 85–89.

Dragoset, B., 2000. Introduction to air guns and air-gun arrays. Lead. Edge 19, 892–897.

Dragoset, W.H., Jeričević, Z., 1998. Some remarks on surface multiple attenuation. Geophysics 63, 772–789.
Elboth, T., Pettersson, B.A., Andreassen, Ø., 2009. Flow and swell noise in marine seismic data. Geophysics 74, Q17–Q25.
Eriksrud, M., 2014. Seabed permanent reservoir monitoring (PRM)—a valid 4D seismic technology for fields in the North Sea. First Break 32, 67–73.
Farmer, P., Gray, S., Whitmore, D., Hodgkiss, G., Pieprzak, A., Ratcliff, D., et al., 1993. Structural imaging: toward a sharper subsurface view. Oilfield Rev. 5, 28–41.
Fatti, J.L., Smith, G.C., Vail, P.J., Strauss, P.J., Levitt, P.R., 1994. Detection of gas in sandstone reservoirs using AVO analysis: a 3-D seismic case history using the Geostack technique. Geophysics 59, 1362–1376.
Fisher, W.R., 1991. Future supply potential of U.S. oil and natural gas. Lead. Edge 11, 15–21.
Flinn, E.A., Robinson, E.A., Treitel, S., 1967. Special issue on the MIT Geophysical Analysis Group reports. Geophysics 32, 411–535.
Foster, D.J., Keys, R.G., Lane, F.D., 2010. Interpretation of AVO anomalies. Geophysics 75, 75A3 75A13.
Gassmann, F., 1951. Elastic waves through a packing of spheres. Geophysics 16, 673–685.
Gazdag, J., 1978. Wave equation migration by phase shift. Geophysics 43, 1342–1351.
Grechka, V., Tsvankin, I., 1998. 3-D description of normal moveout in anisotropic inhomogeneous media. Geophysics 63, 1079–1092.
Gülünay, N., 1986. f-x decon and complex Wiener prediction filter. SEG 56th Annual International Meeting, POS2.10.
Hagedoorn, J.G., 1954. A process of seismic reflection interpretation. Geophys. Prospect. 2, 85–127.
Haldorsen, J.B.U., Farmer, P.A., 1989. Suppression of high-energy noise using an alternative stacking procedure. Geophysics 54, 181–190.
Hall, S.A., MacBeth, C., Barkved, O.I., Wild, P., 2005. Cross-matching with interpreted warping of 3D streamer and 3D ocean-bottom-cable data at Valhall for time-lapse assessment. Geophys. Prospect. 53, 283–297.
Hampson, D., 1986. Inverse velocity stacking for multiple elimination. J. Can. Soc. Explor. Geophys. 22, 44–55.
Haumonté, L., 2017. The future of marine seismic acquisition? GEO ExPro 14, 30–33.
Heilmann, Z., 2007. CRS-stack-based seismic reflection imaging for land data in time and depth domains. PhD thesis-University of Karlsruhe, Germany.
Hubral, P., 1999. Seismic illumination. Lead. Edge 18, 1268–1271.
Hubral, P., Krey, T., 1980. Interval velocities from reflection time measurements. SEG Monograph Series No. 3, Society of Exploration Geophysicists, Tulsa, OK.
Jäger, R., Mann, J., Höcht, G., Hubral, P., 2001. Common reflection surface stack: image and attributes. Geophysics 66, 97–109.
Jones, E.J.W., 1999. Marine Geophysics. John Wiley, Chichester.
King, M.S., 2005. Rock-physics developments in seismic exploration: a personal 50-year perspective. Geophysics 70, 3ND–8ND.
Koefoed, O., 1955. On the effect of Poisson's ratios of rock strata on the reflection coefficients of plane waves. Geophys. Prospect. 3, 381–387.
Kumar, L., 2008. From CMP to CRS—an overview of stacking techniques of seismic data. 7th Biennial International Conference & Exposition on Petroleum Geophysics, Hyderabad.
Landa, E., Belfer, I., Keydar, S., 1999. Multiple attenuation in the parabolic τ-p domain using wavefront characteristics of multiple generating primaries. Geophysics 64, 1806–1815.
Landrø, M., Strønen, L.K., Digranes, P., Solheim, O.A., Hilde, E., 2001. Time-lapse seismic as a complementary tool for in-fill drilling. J. Pet. Sci. Eng. 31, 81–92.
Lansley, R.M., 2006. Quality control in modern recording systems, benefits beyond contract compliance. 6th International Conference & Exposition on Petroleum Geophysics.
Larner, K., Hale, D., Zinkham, S.M., Hewlitt, C., 1982. Desired seismic characteristics of an air gun source. Geophysics 47, 1273–1284.
Larner, K., Chambers, R., Yang, M., Lynn, W., Willon, W., 1983. Coherent noise in marine seismic data. Geophysics 48, 854–886.
Lee, M.W., Hart, P.E., Agena, W.F., 2000. Processing Strategy for water-gun seismic data from the Gulf of Mexico. U.S. Geological Survey Bulletin 2181.
Levin, F.K., 1971. Apparent velocity from dipping interface reflections. Geophysics 36, 510–516.
Lin, D., Sablon, R., Gao, Y., Russier, D., Hardouin, D., Gratacos, B., et al., 2011. Optimizing the processing flow for variable-depth streamer data. First Break 29, 89–95.
Liner, C.L., 1999. Concepts of normal and dip moveout. Geophysics 64, 1637–1647.
Long, A., 2009. Evolutions in seismic azimuth: past, present and future. Geohorizons July 2009, 4–13.
Long, A., Campbell, S., Fishburn, S., Brandsberg-Dahl, S., Chemingui, N., Dirks, V., 2014. No-compromise marine seismic: a full-azimuth survey design for total-wavefield velocity model building and imaging in the deep-water Gulf of Mexico.SEG 84th Annual Meeting.
Lu, G., Ursin, B., Lutro, J., 1999. Model-based removal of water-layer multiple reflections. Geophysics 64, 1816–1827.
Lumley, D.E., 2001. Time-lapse seismic reservoir monitoring. Geophysics 66, 50–53.
Martin, G.S., Wiley, R., Marfurt, K.J., 2006. Marmousi2: an elastic upgrade for Marmousi. Lead. Edge 25, 156–166.
McMechan, G.A., 1983. Migration by extrapolation of time-dependent boundary values. Geophys. Prospect. 31, 413–420.

Mellier, G., Maples, M., Hepp, J., LeBoeuf, S., Lansley, M., 2014. A new multisensor solid streamer. SEG Technical Program Expanded Abstracts, pp. 228–232.
Moldoveanu, N., 2006. Recent and future developments in marine acquisition technology: an unbiased opinion. Theatr. Rec. 31, 1–17.
Mutter, J.C., Carbotte, S.M., Canales, J.P., Nedimovic, M., 2008. A 3D MCS investigation of the magmatic-hydrothermal system at the East Pacific Rise 9° 50′N. MGL0812 Cruise Report.
Nunes, B.I.C., Medeiros, W.E., Nascimento, A.F., Moreira, J.A.M., 2011. Estimating quality factor from surface seismic data: a comparison of current approaches. J. Appl. Geophys. 75, 161–170.
Ostrander, W.J., 1982. Plane-wave reflection coefficients for gas sands at nonnormal angles of incidence. 52nd SEG Meeting Expanded Abstracts, pp. 216–220.
Özdaş, H., Kızıldağ, N., Baydan, C., 2016. Shipwreck Inventory Project of Turkey (SHIPT). Special Project Supported by Ministry of Development of Turkey.
Özdemir, A.K., Caprioli, P., Özebek, A., Kragh, E., Robertson, J.A., 2008. Optimized deghosting of over/under towed-streamer data in the presence of noise. Lead. Edge 27, 190–199.
Pascouet, A., 1991. Something new under the water: the bubbleless air gun. Lead. Edge 10, 79–81.
Peacock, K.L., Treitel, S., 1969. Predictive deconvolution: theory and practice. Geophysics 34, 155–169.
Ramos, A.C.B., Castagna, J.P., 2001. Useful approximations for converted-wave AVO. Geophysics 66, 1721–1734.
Roberts, D., Fitzpatrick, J.P., 2016. Planning and operating a transition zone 2D seismic survey on Lake Tanganyika. Search Discov. 41765.
Robertsson, J.O.A., Moore, I., Vassallo, M., Özdemir, K., van Manen, D., Özbek, A., 2008. On the use of multicomponent streamer recordings for reconstruction of pressure wavefields in the crossline direction. Geophysics 73, A45–A49.
Robinson, E.A., Treitel, S., 1967. Principles of digital Wiener filtering. Geophys. Prospect. 15, 311–333.
Rückemann, C.P., 2012. Comparison of stacking methods regarding processing and computing of geoscientific depth data. The 4th International Conference on Advanced Geographic Information Systems, Applications and Services.
Rutherford, S.R., Williams, R.H., 1989. Amplitude-versus-offset in gas sands. Geophysics 54, 680–688.
Schneider, W., 1978. Integral formulation for migration in two and three dimensions. Geophysics 43, 49–76.
Schoenberger, M., 1996. Optimum weighted stack for multiple suppression. Geophysics 61, 891–901.
Schoenberger, M., Mifsud, F., 1974. Hydrophone streamer noise. Geophysics 39, 781–793.
Shatilo, A., Aminzadeh, F., 2000. Constant normal-moveout (CNMO) correction: a technique and test results. Geophys. Prospect. 48, 473–488.
Sheriff, R.E., Geldart, L.P., 1995. Exploration Seismology. Cambridge University Press, New York.
Shirley, T.E., Linville, A.F., Hadidi, M.T., Davis, A.J., May, C.J., Jurkevics, A., 1985. A systems analysis of dynamic range in seismic exploration. SEG Technical Program Expanded Abstracts, pp. 528–530.
Shuey, R.T., 1985. A simplification of the Zoeppritz Equations. Geophysics 50, 609–614.
Soubaras, R., 2010. Deghosting by joint deconvolution of a migration and a mirror migration. 80th SEG Annual Meeting, Expanded Abstracts 29, 3406–3410.
Soubaras, R., Lafet, Y., 2011. Variable-depth streamer acquisition: broadband data for imaging and inversion. Geophysics 78, WA27–WA39.
Stolt, R.H., 1978. Migration by Fourier transform. Geophysics 43, 23–48.
Taner, M.T., 1980. Long-period sea-floor multiples and their suppression. Geophys. Prospect. 28, 30–48.
Taner, M.T., Koehler, F., 1969. Velocity spectra-digital computer derivation and applications of velocity functions. Geophysics 39, 859–881.
Taner, M.T., Koehler, F., Sheriff, R.E., 1979. Complex seismic trace analysis. Geophysics 44, 1041–1063.
Telford, W.M., Geldart, L.P., Sheriff, R.E., 1990. Applied Geophysics. Cambridge University Press, New York.
Tenghamn, R., Vaage, S., Borresen, C., 2007. A dual-sensor, towed marine streamer; its viable implementation and initial results.Annual Meeting Expanded Abstracts, SEG, 989–993.
Thomsen, L., 1986. Weak elastic anisotropy. Geophysics 51, 1954–1966.
Trappe, H., Schuenemann, E., Pruessmann, J., Suckro, S., Linzer, H.G., Schachinger, M., 2015. CRS azimuth gathers and CRS shot gathers for improved fault imaging in Alpine 3D seismic data. Theatr. Rec. 40, 38–42.
Treitel, S., 1974. The complex Wiener filter. Geophysics 39, 169–173.
Treitel, S., Gutowski, P.R., Wagner, D.E., 1982. Plane-wave decomposition of seismograms. Geophysics 47, 1375–1401.
Tsvankin, I., 1995. Normal moveout from dipping reflectors in anisotropic media. Geophysics 60, 268–284.
Tsvankin, I., Thomsen, L., 1994. Nonhyperbolic reflection moveout in anisotropic media. Geophysics 59, 1290–1304.
Ulrych, T.J., 1972. Maximum entropy power spectrum of truncated sinusoids. J. Geophys. Res. 77, 1396–1400.
Verschuur, D.J., Berkhout, A.J., Wapenaar, C.P.A., 1992. Adaptive surface-related multiple elimination. Geophysics 57, 1166–1177.
Wallace, M., Maher, J., Schapper, S., Taylor, B., Tod, S.R., 2007. Seismic velocity anisotropy in the Illizi Basin of eastern Algeria. EAGE 69th Conference & Exhibition, London.
Wang, Z., 2001. Fundamentals of seismic rock physics. Geophysics 66, 398–412.

Wang, Y., 2002. A stable and efficient approach to inverse Q filtering. Geophysics 67, 657–663.

Whaley, J., 2017. TopSeis: imaging shallow reservoirs through innovation. GEO ExPro 14, 26–29.

Widess, M.B., 1973. How thin is a thin bed? Geophysics 38, 1176–1180.

Wiggins, J.W., 1988. Attenuation of complex water-bottom multiples by wave equation-based prediction and subtraction. Geophysics 53, 1527–1539.

Wong, G.S.K., Zhu, S., 1995. Speed of sound in seawater as a function of salinity, temperature and pressure. J. Acoust. Soc. Am. 97, 1732–1736.

Yılmaz, Ö., 1987. Seismic Data Processing. SEG, Tulsa, OK.

Yılmaz, Ö., 2001. Seismic Data Analysis: Processing, Inversion and Interpretation of Seismic Data. SEG, Tulsa, OK.

Zhang, Y., Sun, J.C., Gray, S.H., 2003. Aliasing in wavefield extrapolation prestack migration. Geophysics 68, 629–633.

Zhao, M., Qiu, X., Xia, S., Xu, H., Wang, P., Wang, T.K., et al., 2010. Seismic structure in the northeastern South China Sea: S-wave velocity and Vp/Vs ratios derived from three-component OBS data. Tectonophysics 480, 183–197.

Zoeppritz, K., 1919. On the reflection and propagation of seismic waves. Gottinger Nachrichten 1, 66–84.

Index

Note: Page numbers followed by *f* indicate figures, and *t* indicate tables.

A

Acceleration canceling hydrophone, 44–45
Acoustic Doppler current profiler (ADCP), 60, 151
Acoustic impedance
  convolutional model, 316–317
  defined, 27
Acoustic networks, 88–91, 147–148
  streamers for, 89*f*
Acoustic wave equation modeling, 388–389
Acquisition
  marine seismic data, 40
  ocean bottom seismic acquisition, 100–108
  patterns, 82–84
  P-cable, 110–111
  time lapse seismic surveys, 108–109
  transition zone, 109–110
AGC. *See* Automatic gain control (AGC)
Air gun arrays
  advantages, 63
  bubble effect, 65–68, 175–176, 177*f*
  cluster/string/array, 72–76
  defined, 62–63
  far-field source signatures, 69–72
  ghost reflection, 68–69
  near-field source signatures, 69–72
  parameters, 126–127
  principles, 63–65
  schematic diagram, 64*f*
  start-up tests, 139
  tuning and array performance, 76–81
Aki-Richards approximation, 570–571, 574–575*f*
Al-Chalabi's third-term approach, 425, 466, 467*f*
Aliasing, 226–227, 237
Ambient noise, 171–173
Amplitude spectrum, 77, 219, 324*f*
  recorded seismogram, 325
  spiking deconvolution, 334
Amplitude versus offset (AVO), 3–4, 284, 467, 475, 521, 524
  analysis, 577–584
    applications flow, 577, 577*f*
    assumptions, 577
    AVO attributes, 578–581
    AVO crossplots, 581–584
    factors affecting, 577
    gradient analysis, 578
    issues, 577–578
    partial stack, 578
  classes, 572–575
    Class I (dim out) AVO anomalies, 572–574, 573*f*
    Class II (phase reversal) AVO anomalies, 574, 574*f*
    Class III (bright spot) AVO anomalies, 574, 575*f*
    Class IV AVO anomalies, 574–575, 575–576*f*
  defined, 567
  equations, 569–571
    Aki-Richards approximation, 570
    Shuey approximation, 570–571
    Zoeppritz equations, 567, 569–570
  hydrocarbon exploration, 567
  intercept and gradient, 571–572, 572–573*f*
  NMO corrected real CDP, 567–569, 568*f*
  Poisson's ratio of gas sands, 567
  prestack data, 567–569
  processing considerations, 576–577
    array correction, 576–577
    automatic gain control, 576
    directivity effect, 576–577
    preprocessing steps, 576
    quality control, 576
Angle stack, 475
Angular frequency, 212–213
Array leakage test, 137, 139
Array tuning
  bubble effect, 76
  defined, 53–54, 76
Autocorrelation, 213–215, 215*f*
  functions, 323, 324*f*
  time gate, 339–340, 339–340*f*
Autocorrelograms, 374–375, 374*f*, 377–381, 380*f*
Automatic gain control (AGC), 275–276, 279–284, 280–281*f*, 391, 576
Average velocity, 424
AVO. *See* Amplitude versus offset (AVO)
AVO attributes
  examples, 579, 580*f*
  fluid factor, 579–581
  gas sand impedance, 581
  in seismic industry, 578–579
AVO crossplots
  amplitudes on crossplots, 581
  AVO classes, 581
  background trend or wet rock trend, 581
  brine and gas saturated sands, 581–582
  brine-saturated zones, 582–584, 583*f*
  intercept *vs.* gradient, 581–584, 582–583*f*

B

Backscatter, 16–17
Band-pass filter
  filter operator, 256–260
  frequency filtering, 253
  marine seismic data, 260–264
  mean amplitude spectrum, 256*f*
  pass-band, 253–256, 255*f*
  quality control, 268–272
  schematic representation, 259*f*
  time varying filtering, 264–268
Bathymetric systems, 12–14
Binning in 3D
  bin grid, 412, 413*f*
  CDP bin, 411–412, 412*f*
  flex binning or simply flexing, 413–414, 414*f*
  integrated navigation software, 411
  reshooting, 412
  static or fixed bin, 413–414, 415*f*
Bird noise
  amplitude spectrum, 185, 188*f*
  defined, 183
  filtered shot gather, 185, 189*f*
  mechanism of, 183–185, 187*f*
  RMS noise, 183–185, 186*f*
Boomers, 19
Broadband seismic data, 50–51, 69
Brute stacks
  vs. common offset and full stack, 311–312, 311*f*
  defined, 310
  processing steps, 310–311, 310*f*
Bubble effect
  air gun, 65–68, 66–67*f*
  of air gun, 175–176, 177*f*
  array tuning, 76
  defined, 64
Burg deconvolution, 349–350, 351–352*f*
Butterworth filter operators, 263, 263*f*

C

Cable noise, 305, 305*f*
Castle's shifted hyperbola, 425, 466, 466–467*f*
CDP fold
  defined, 409–410
  distribution and coverage map, 409–410, 411*f*
  flip-flop shooting, 411
  fold value, 410
  full-fold (FF) coverage zone, 409–410
  inline and crossline folds, 410
  in marine seismic systems, 411
  shot intervals, 411
  3D flip-flop acquisition, 410
CDP geometry
  binning, 406–408, 409*f*
  CDP gathers, 405–406, 407–408*f*, 408, 410*f*
  CDP location, 405–408
  CDP smearing, 408, 410*f*
  and common midpoint, 408, 410*f*
  integrated navigation system, 406–408
CDP smearing, 408, 410*f*
Clusters, 72–76, 74*f*
CMP. *See* Common midpoint (CMP)
Coherent noise, 171–172
Coil shooting, 98–100, 99*f*
Common depth point (CDP), 3–4, 21, 60, 121, 314–315, 459–460
  binning in 3D, 411–414
  brute and full stack section, 369, 370*f*
  CDP fold, 409–411
  CDP geometry, 405–408
  conventional stacking process
    mean stack, 371–372
    weighted stack, 371–372
  definition, 405
  first- and second-order multiples, 369–371, 373*f*
  fold stack sections, 369, 371*f*
  inner mute applications, 369–371, 373*f*
  multiple amplitudes, 369–371, 372*f*
  NMO correction, 368–371, 368–370*f*, 372*f*
  prestack data, 367, 372
  primary and seabed multiple reflection, 368, 368*f*
  primary reflection hyperbolas, 368–369, 369*f*
  quality control in, 415–419
  seismic data, 405
  source-receiver midpoint, 405
  τ-p transform, 233–234, 233*f*
Common midpoint (CMP), 60, 121, 408, 410*f*
  acquisition technique, 1
Common reflection surface (CRS) stack
  advantages, 483
  CDP gather, 483
  conventional NMO/stack, comparison, 484–485, 486*f*
  data-driven method, 481–483
  defined, 481–483
  kinematic wave field attributes, 483
  normal incidence point, 483
  Ray path, 483–484, 484*f*
  stack parameters, 485
  stack surface, 483–484, 485*f*
  travel time approximation, 483–484
  zero-offset data, 484, 485*f*
Complex trace attribute
  DHI analysis, 562
  effects on seismic data, 564–565, 565*f*
  fundamental parameters, 563–564
  gas accumulation zone, 565
  Hilbert transform, 562, 565–567
  instantaneous amplitude and phase, 563–564, 563*f*
  shallow gas accumulation, 565–567, 566*f*
Compressed High Intensity Radar Pulse (Chirp), 18, 19*f*
Conductivity-transmission-depth (CTD), 9, 10*f*
Constant velocity stack (CVS) method, 428, 429*f*
Conventional 3D seismic acquisition, 91–92
  applications, advantages and shortcomings, 23*t*
  flip-flop acquisition, 91–92
  vs. P-cable data, 110, 112*f*
  schematic illustration, 86*f*
Conventional 3D surveys, 82–83, 84*f*
Conventional 3D towed streamer acquisition, 93–94, 149–151
Conventional flat streamer acquisition, 94–95*f*
Conventional marine seismic surveys, 53
Conventional seismic data-processing flow, marine seismic data, 4, 5*f*
Convolution, 215–216, 216*t*, 217*f*
Convolutional model
  acoustic impedance, 316–317
  components for, 322–323*f*
  mathematical expression, 319, 319*f*
  1D, 316–317
  synthetic seismogram, 317, 318*f*
Correlation, 211
Crosscorrelation, 215, 216*f*
CRS. *See* Common reflection surface (CRS) stack
CVS. *See* Constant velocity stack (CVS) method

D

Daily progress reports, 160–162, 161*f*, 161*t*, 166*f*

Data acquisition
parameters, 113–114*t*, 114*f*, 139, 159*t*
data recording, 127–131
processing flows, 2–3
survey geometry, sources, and receivers, 114–127
quality control
navigation data analysis, 146–154
preacquisition instrument tests, 134–140
reporting, 158–169
seismic data analysis, 140–146
seismic source analysis, 154–157
Data aliasing, 538
Data loading, 243–244, 244*f*
Data preconditioning, 241–242
Data processing
autocorrelation, 213–215
convolution, 215–216
crosscorrelation, 215
Fourier series, 216–219
Hilbert transform, 231–232
1D Fourier transform, 219–222
processing flow and parameters, 2*f*
sampling theory, 235–239
slant stack (*see* τ-p transform)
2D Fourier transform, 222–230
Z transform, 230–231
Data recording parameters, 84
dynamic range, 128–130
optimum fold, 130–131
recording filter cut-off frequencies, 128
record length, 127
sampling rate, 127–128
seismic sample format, 128–130
Deck cables, 62, 63*f*
Deconvolution
assumptions for
noise component, 320
random reflectivity, 321–324
simple earth model, 320
source waveform, 320
stationary wavelet, 320
wavelet causality, 320–321
convolutional model, 316–319
defined, 313–314
maximum entropy (Burg), 349–350
parameter determination
autocorrelation time gate, 339–340
deconvolution design gate, 340–341
operator length, 341, 345*f*
prediction lag, 341–349
poststack, 349
predictive, 335–337
quality control, 357–361
shaping filters, 350–355
spiking
inverse filtering, 325–330
optimum Wiener filters, 330–333
prewhitening, 334–335
surface consistent, 356–357
in τ–p domain
periodicity of multiples, 382–383
plane wave decomposition, 382
predictive deconvolution, 383, 384*f*
time curves of shot, 382, 382*f*
Deconvolution after stack (DAS), 314–315, 349
Demultiplexing, 242, 242*f*
Dephasing, 353–354, 355*f*
Depth migration, 524–526, 525*f*
Depth step size, 509–511, 511*f*
finite-difference time migration, 512*f*
Design gate, deconvolution, 340–341, 342*f*
DHI. *See* Direct hydrocarbon indicator (DHI) analysis
Differential GPS (DGPS), 40–41, 44, 84, 138*t*
Diffractions, 193, 195*f*
Digital streamers, 45, 48, 49*f*, 202
Dilt floats, 60–62, 61*f*
Dip filtering, 232, 299
Dip moveout (DMO), 455, 465
input seismic data, 532
poststack/prestack migration, 529*f*
processing flow, 531*f*
schematic illustration, 530, 530*f*
velocity spectra, 531*f*
Dip restriction, maximum, 506–507, 508*f*
Direct hydrocarbon indicator (DHI) analysis, 562, 577–578
Direct waves, 190–191, 194*f*
Dirichlet conditions, 217
Dix equation, 455–456, 524–525
Dix interval velocity, 425–426
Double-sided hydrophones, 172
Drop-out tests, 137
Dual-sensor (2C) streamers, 52–53, 69
Dynamic range, 128–130, 129*f*

E

Echosounders, 12, 12*t*, 84, 138*t*
Entropy. *See also* Burg deconvolution, 349
Expendable bathythermograph (XBT), 9

F

Fan mode acquisition, 93–94, 96*f*
Far-field source signatures, 73*f*
air gun array, 78*f*
amplitude spectra, 78, 79*f*
defined, 69–70
gun array, 71
superposition, 76–77, 77*f*
Fast Fourier transform (FFT), 219–220, 220*t*
Field File ID Number (FFID), 30*f*, 31
Filter operators, 256–260, 272
time domain length, 270
Final survey reports, 163–165, 168*t*
Finite-difference migration, 500–501
depth step size, 509–511
scalar wave equation, 508–509
velocity effect, 511–512
Fizz water/fizz gas, 577–578
f-k migration. *See* Frequency-wavenumber *(f-k)* migration
Flex binning/simply flexing, 413–414, 414*f*
Flip-flop acquisition, 91–92, 93*f*, 126
CMP lines, 123*f*
3D surveys, 92*f*
Fluid-filled streamers, 48–49, 49*f*, 202
Fold number, effect of, 443, 444–445*f*
4D seismic surveys, 104, 108
Fourier series, 216–219, 218*f*
Fourier transform theory, 211, 256–257
Frequency-wavenumber *(f-k)* filtering, 302*f*
cable noise, 305, 305*f*
marine seismic data, 302–307
multiple elimination, 393–394, 393–395*f*
mute zone, 394, 396*f*
negative and positive panels, 301, 301*f*
NMO correction, CDP gathers, 393–394, 393*f*, 395*f*
primary reflections, 391–393
quality control, 307–310
2D Fourier transform, 299, 300*f*, 301–302
Frequency-wavenumber *(f-k)* migration, 224, 225*f*
Fourier transform, 512–513
Gazdag migration, 513
Stolt migration, 513
Stolt stretch factor, 514–515
velocity effect, 515–516
Full-azimuth (FAZ) survey, 98–100

f-x prediction filter (*f-x* Decon)
cable noise/seismic interference, 552–553
Fourier transform, 549–550, 550*f*
f-x trace interpolation method, 550–551
f-x-y prediction filtering, 550–551
least-squares prediction filter, 550–551
marine stack section, 551–552, 552*f*
random noise suppression technique, 549–550, 550*f*
signal-to-noise ratio, 552
synthetic zero-offset section, 551–552, 551*f*
time domain, 550, 550*f*
Wiener prediction filter, 550, 550*f*
zero-offset section, 552, 553*f*

G

Gain recovery
AGC, 275–276
attenuation effect, 274*f*
automatic gain control, 279–284
defined, 272
power correction, 277–279
quality control, 284–286
seismic signal amplitude, 273*f*
spherical divergence correction, 276–277
spherical divergence effect, 275
TAR, 275–276
Gardner's equation, 423
Gazdag migration, 500–501, 515–516
Gel-filled streamers, 48–50
Generator/injector (GI) guns, 55, 66–68, 67*f*, 175–176
Geometry, 248*f*
defined, 246–253
loading, 255*f*
propagation velocities, 251, 252*f*
quality control, 251–253
ray paths, 249–251, 250*f*
2D multichannel seismic surveys, 246–247, 247*f*
2D seismic line, 254*f*
UTM, 249
GeoRes system, 104, 104*f*
GeoStreamer, 51–52
Ghost reflection, 68–69, 69*f*
Gibbs effect, 257–258, 298
Gradient analysis, 578, 579*f*
Group interval, 118–119, 119*f*
Guided waves, 193–196, 196–198*f*
Gun arrays
in seismic surveys, 74
source directivity, 80*f*
towing depth, 78
Gun controllers, 55–56, 56*f*
Gun line integrity and triggering tests, 136
Gun signature tests, 137, 139
Gun strings, 74, 75*f*
Gyro calibration, 84, 137*t*

H

Harmonic noise, powerline, 200–201
Health, Safety and Environment (HSE), 38–39, 140, 165–168, 169*t*
High-resolution marine geophysical techniques, 10
signal frequency, 12
Hilbert transform, 231–232, 231–232*f*, 354–355, 562–563, 565–567
Horizontal transverse isotropy (HTI), 467, 468*f*
Hydrodynamic noise, 174
Hydrophones, 44–53, 44*f*, 47*f*, 206
A/D tests, 114
double-sided, 172

I

Illumination, 22*f*, 96–98
Imaging-condition aliasing, 539–541
Impulse response, 316–317, 499, 543
Inline waves
direct waves, 190–191
mechanical cable noise, 188–190
refracted waves, 191–193
tail buoy noise, 185–187
Instantaneous attributes
complex trace attribute, 562–563, 562*f*
effects on seismic data, 564–565, 565*f*
Hilbert transform, 562–563
instantaneous acceleration, 564
seismic attributes, 562
trace envelopes, 564
Instantaneous velocity, 424
Integrated navigation system (INS), 56*f*
components and peripheral systems, 59*f*
differential GPS, 59
preacquisition assessments, 134
relative GPS, 59–60
2D/3D seismic acquisition systems, 59
UKOAA files, 60
vessel reference position, 60
Interval velocity, 424
Intrinsic Ranging by Modulated Acoustics (IRMA), 88–91
Inverse filtering, 324–325
with least squares, 328–330
predictive deconvolution, 365–366
source wavelet, 325, 328*f*
spiking deconvolution, 326*f*
IsoMetrix system, 52

K

Kirchhoff diffraction summation method, 500–501, 535
Kirchhoff time migration, 501
diffraction hyperbola, 502*f*
Huygens principle, 502
maximum dip restriction, 506–507
migration aperture, 502–506
operator aliasing, 538
prestack depth migration, 502
velocity effect, 507
Kolmogorov spectral factorization, 354–355

L

Lead-in cables, 62, 63*f*
Levin equation, 426
Levinson algorithm, 331
Life of Field Seismic (LoFS), 104
Linear operational noise, 174, 175*f*
Localized velocity errors, 545–547, 546–547*f*
Long Life (LL) gun, 53, 55
Love (L) waves, 26–27, 26*f*

M

MacLaurin series expansion, 231, 326–327
Marine acoustic methods
bathymetric systems, 12–14
frequency ranges, 11–12, 11*t*
high-resolution marine geophysical techniques, 10
multichannel seismics, 19–22

seismic exploration, 22–25
side-scan sonar, 14–17
single channel seismics, 19–22
subbottom profiler, 17–19
transducers, 11–12
Marine mammals, 208
noise from, 210*f*
Marine seismic data acquisition, 40*f*
acquisition techniques
ocean bottom seismic acquisition, 100–108
P-cable, 110–111
time lapse seismic surveys, 108–109
transition zone, 109–110
air gun arrays
bubble effect, 65–68
cluster/string/array, 72–76
far-field source signatures, 69–72
ghost reflection, 68–69
near-field source signatures, 69–72
principles, 63–65
tuning and array performance, 76–81
band-pass filters, 260–264, 263*f*
coherent and random noise, 38, 172*f*
data acquisition parameters
data recording, 127–131
survey geometry, sources, and receivers, 114–127
deck cables, 62
3D techniques
acoustic network, 88–91
acquisition patterns, 82–84
fan mode acquisition, 93–94
flip-flop shooting, 91–92
multiazimuth surveys, 94–100
slant streamer acquisition, 92–93
streamer layout, 85–88
streamer steering, 84–85
f-k dip filters, 302–307, 304*f*
geophones, 38
gun control systems, 55–56
hydrophones, 44–53
INS, 59–60
lead-in cables, 62
offshore seismic surveys, 38–39
onboard generators, 200–201
quality control
navigation data analysis, 146–154
preacquisition instrument tests, 134–140
reporting, 158–169
seismic data analysis, 140–146
seismic source analysis, 154–157
seismic energy sources, 53–55
seismic recorder, 58
seismic vessels, 41–44
streamers, 38, 44–53
depth controllers, 57–58
tail buoys, dilt floats and paravanes, 60–62
Marine seismics
conventional seismic data-processing flow, 4, 5*f*
reflection
from an interface, 27–29
exploration, 24
hyperbolas, 31–35
seismic waves, 25–27
shot gathers, 29–31
Marmousi-II synthetic dataset, 535, 536*f*
Maximum dip restriction, 506–507, 508*f*
Maximum entropy (BURG) deconvolution, 349–350
Mean amplitude spectrum
marine shot gather, 197, 256*f*
raw shot gather, 268*f*
selected shot gathers, 363*f*
Mean stack, 472, 473*f*
Mechanical cable noise, 188–190, 192–193*f*
Median filter
applications, 553, 554*f*
defined, 553
f-x decon performance, 556, 556*f*
median smoothing, 553–555
random time series, 553–555, 554*f*
root signal, 555
spikelike noise, 555
zero-offset section, 555–556, 555–556*f*
Median stack
defined, 477–478
vs. mean stack, 479, 479–480*f*
noise amplitudes, 479
value of seismic amplitudes, 478–479, 478*f*
Microelectromechanical systems (MEMS), 69, 104
Migration, 496*f*
algorithms and specifications, 501, 501*t*
defined, 494–495
effects, 496–499, 498–500*f*
inclined reflector case, 494–495, 495*f*
quality control in, 535–547
types, 499–501, 534*t*, 534*f*
Migration aperture, 502–503, 503*f*
aperture width, 504
defined, 503
Kirchhoff migration, 503–504, 505*f*
poststack Kirchhoff time migration, 505, 506*f*
Mobilization report, 158–160, 168
Modern 3D survey vessels, 80*t*
Modern seismic recording systems, 114
Monthly reports, 162–163
Multiazimuth surveys (MAZ), 94–100, 97*f*, 99*f*
Multibeam echosounders, 12–13, 13*f*
side-scan sonar system, 17
vertical (depth) resolution, 13–14
Multichannel seismics, 19–22, 20*f*, 20*t*, 22*f*
Multicomponent (4C) streamers, 69
Multiple reflections
CDP stack, 368–372
characteristics, 367
deconvolution in τ–p domain, 382–383
defined, 177–178
demultiple methods, 367
effect of, 443–444, 446–447*f*
f-k filtering, 391–394
hyperbolas on shot gathers, 178*f*
inclinations, 179*f*
in marine surveys
long period or surface-related multiples, 365–366, 366*f*
short period or interbed multiples, 365–366, 366*f*
peg-leg multiples, 365–366
peg-leg reflections, 178, 179*f*
predictive deconvolution, 372–382
quality control in, 400–403
Radon velocity filter, 383–388
seabed multiples, 366–367, 367*f*
SRME, 394–399
WEMR, 388–391
Multisensor recording systems, 50–51
Muting
defined, 294–295
effect of, 449–452, 452*f*
NMO stretch mute, 294, 294*f*
quality control, 295–299
surgical mute, 294, 294*f*, 296*f*
top mute, 294–295, 294–299*f*

N

Narrow-azimuth (NAZ) surveys, 95–96, 97–99*f*
  optimum fold, 128
Navigation data analysis
  acoustic networks, 147–148
  DGPS receiver, 146, 147*f*
  shot interval, 146
  vessel speed, 146, 148*f*
  water depth profile, 153*f*
Navigation system, 136–138
Near-field source signatures
  defined, 69–70
  marine seismic source, 70*f*
  real-time quality control applications, 71
NIP. *See* Normal incidence point (NIP)
NMO correction
  CDP gathers, 459–461, 460–461*f*
  for long offsets, 465–466
    Al-Chalabi's third-term approach, 466, 467*f*
    Castle's shifted hyperbola, 466, 466–467*f*
    fourth-order corrections, 465–466
    two-term NMO equation, 466, 467*f*
  NMO velocity, 460, 462*f*
NMO stretching
  defined, 469
  marine CDP, 472, 472*f*
  synthetic CDP
    NMO correction, 469–472, 470–471*f*
    reflection hyperbolas, 469–470, 471*f*
NMO time
  for dipping interfaces, 465
    dip moveout process, 465
    Levin equation, 465
    NMO velocity, 465
  for several horizontal interfaces, 463–465
    for NMO correction, 465
    travel time equation, 463–465
  for single horizontal interface, 462–463
    Dix NMO equation, 462, 463*f*
    NMO correction, 463
    NMO velocity, 463, 464*f*
    reflector model, 462
    travel time equation, 462
    two-term NMO equation, 462
Noise
  air gun, bubble effect of, 175–176
  ambient noise, 171
  bird noise, 183–185
  coherent noise, 171–172
  component, deconvolution, 320
  defined, 171
  diffractions, 193
  double-sided hydrophones, 172
  effect of, 447–449, 450–451*f*
  guided waves, 193–196
  inline waves, 185–193
  mean amplitude spectra, 173*f*
  multiple reflections, 177–180
  operational noise, 174–175
  random noise, 171–172
  seismic interference, 196–199
  source-generated noise, 171
  swell noise, 180–183
  types, 200–210
Normal incidence point (NIP), 483
Normal moveout (NMO), 21, 32–33, 34*f*, 251, 368–371, 368–370*f*, 372*f*, 494, 530*f*
  azimuthally anisotropic medium
    anisotropic velocity, 468
    anisotropy parameters, 468–469
    horizontal transverse isotropy, 467, 468*f*
    orthorhombic symmetry, 468, 468*f*
    seismic anisotropy, 467
    two-term NMO approximations, 468
    vertical transverse isotropy, 467, 468*f*
Nyquist frequency, 127–128, 239

O

Ocean bottom cable (OBC), 27, 39–40, 101, 103–105, 104*f*
Ocean bottom nodes (OBN), 39–40, 101, 107–108, 107*f*
Ocean bottom seismic acquisition
  advantages, 101
  amplitude versus offset, 101
  OBC, 103–105
  OBN, 107–108
  OBS, 105–107
  P and PS wave seismic data, 102, 103*f*
  schematic illustration, 101*f*
Ocean bottom seismometer (OBS), 27, 101, 105–107, 105*f*
Offset-dependent tuning, 578
Offset distance, 119–120, 120*f*
Offshore seismic surveys, 38–39
  crew structure, 38*f*
1D convolutional model, 316–317
1D Fourier transform, 219–222, 221–222*f*
1D seismic modeling, 316–317
Operational noise, 174–175, 175–176*f*
Operator aliasing, 538–541, 540*f*
Optimum fold, 130–131
Optimum Wiener filters, 324–325
  autocorrelation of input wavelet, 331*t*
  cross-correlation of desired output, 331*t*
  deconvolution, 332*f*
Ormsby filter operators, 263
Orthorhombic symmetry (ORT), 468, 468*f*
Over-under streamers, 68

P

Parameter determination, deconvolution
  autocorrelation time gate, 339–340
  deconvolution design gate, 340–341
  operator length, 341, 345*f*
  prediction lag, 341–349
Paravanes, 60–62, 61–62*f*
Partial stack, 578
  amplitude versus offset, 475, 477, 478*f*
  angle stack, 475
  NMO corrected CDP gather, 476–477, 477*f*
  reflection amplitude, 476, 476*f*
  shale/gas sand model, 476, 476*f*
P-cable acquisition, 110–111, 111*f*
Peak-to-bubble ratio (PBR), 77, 125–126
Peak-to-peak *(P-P)* amplitude, 71, 77, 212–213
Periodic signal, 212–213
Per-line QC, 160
Phase shift migration, 500–501
Poststack Burg deconvolution, 353*f*
Poststack deconvolution, 349, 350*f*
Poststack Kirchhoff time migration, 508*f*, 539*f*, 541*f*, 544*f*
Poststack RTM, 517–518
Poststack time migration, 519–521, 521*f*
Powerline harmonic noise, 200–201

Preacquisition instrument tests, 134–140
gun array and components, 139–140
navigation system and components, 136–138
seismic system and streamer, 138–139
Prediction lag, 341–349, 347*f*
Predictive deconvolution, 335–337, 338*f*
attenuation rates of multiple amplitudes, 374–375, 375*f*
autocorrelation trace, 378–381, 380*f*
defined, 315–316
gapped deconvolution, 402
inverse filtering, 365–366
multiples in seismic data, 372–374
multiple suppression, 375–377, 376*f*
operator lengths and prediction lags, 374–375, 375*f*, 377–381, 379–380*f*
periodicity of multiples, 374, 374*f*, 381–382
seismic line, 381, 381*f*
spiking deconvolution, 377, 378*f*
synthetic seismic trace, 374–375, 375*f*
Preprocessing
band-pass filter
filter operator, 256–260
marine seismic data, 260–264
quality control, 268–272
time varying filtering, 264–268
brute stacks, 310–312
data loading, 243–244
demultiplexing, 242
f-k dip filters
marine seismic data, 302–307
quality control, 307–310
gain recovery
automatic gain control, 279–284
power correction, 277–279
quality control, 284–286
spherical divergence correction, 276–277
geometry
defined, 246–253
quality control, 251–253
muting, 294–299
prestack seismic data conditioning, 241–242, 242*f*
single trace section, 244–245
trace edit, 287–294
Prestack deconvolution, 337
Prestack Kirchhoff depth migration, 425–426
Prestack time migration
conflicting dips, 523, 523*f*
NMO correction-stacking low, 522
vs. poststack, 524*f*
stack section, 521–522
velocity analysis, 523*f*
Prewhitening, 334–335, 335*f*
Primary reflections, 366
and multiples, specifications, 367
Primary (P) waves, 25–27, 26*f*

Q

Q-Marine system, 81–82, 104
Q-Seabed system, 104
Quality assurance (QA), 38–39
Quality control (QC), 3*f*, 4, 38–39
auxiliary channels, 155
band-pass filtering, 268–272
data acquisition
applications, 131*f*
navigation data analysis, 146–154
preacquisition instrument tests, 134–140
seismic data analysis, 140–146
seismic source analysis, 154–157
deconvolution
autocorrelograms, 357, 360*f*
noise analysis, 357–358, 361*f*
shots gathers, 359, 361*f*, 363*f*
defined, 130
f-k dip filters, 307–310
gain recovery, 284–286
geometry loading, 251–253
marine seismic surveys, 132*f*, 133*t*
migration, 535–547
multiple suppression
advantages, 403, 404*t*
CDP stacking, 400
characteristic features, 400
disadvantages, 403, 404*t*
f-k domain muting, 400–402
f-k filtering, 402
outputs of demultiple methods, comparison, 400, 401*f*
predictive or gapped deconvolution, 402
Radon velocity filtering, 403
SRME method, Delft approximation, 402–403
WEMR technique, 403
muting, 295–299
NMO correction and stacking
AVO analysis, 488
NMO corrected CDPs, 486–487, 487*f*
NMO stretch muting, 488–492, 489–491*f*
reflection hyperbolas, 486–487, 488*f*
seismic line, 491–492, 491*f*
velocity functions, 487–488, 489*f*
reporting
daily progress reports, 160–162
final deliverables, 168–169
final survey report, 163–165
HSE report, 165–168
mobilization report, 158–160
per-line QC, 160
weekly and monthly reports, 162–163
sort and binning
CDPs, traces in, 415, 416*f*
crossline data, 418, 419*f*
flex binning, 415–416
3D fold distributions, 417–418, 418–419*f*
trace kill or missed shots, 415, 417*f*
velocity analysis
dip moveout process, 455
Dix equation, 455–456
improper stacking, 456, 457*f*
NMO correction, 453–455, 455*f*
primary reflections, 453
Radon velocity filter, 455
RMS velocity field, 455–456, 456*f*
semblance plots, 453
2D and 3D surveys, 453, 454*f*
velocity picking, 453
zero-offset time, 453

R

Radon velocity filter, 455
brute stack section, 387, 390*f*
CDP gather, 387–388, 391*f*
first-pass velocity analysis, 388
long period multiples, 383
multiple hyperbolas, 387, 389*f*
muting out
of multiple reflection amplitudes, 386–387, 387*f*
of primary reflection amplitudes, 386–387, 388*f*
NMO correction, 383–387, 386–388*f*

Radon velocity filter *(Continued)*
primaries and multiples, amplitudes of, 383
reflection hyperbolas, 383–386, 386*f*
Random noise, 171–172, 172*f*
Random reflectivity, 321–324
Rarefaction, 65–66
Rayleigh (R) waves, 26–27, 26*f*
Record length, 127
Redundancy, 90, 147–148
Reflection, 27–29, 27*f*
depth effect, 440, 441*f*
hyperbolas, 31–35, 33*f*
Reflectivity map, 14
Reflectivity series. *See* Impulse response
Refracted waves, 191–193, 195*f*
Relative GPS (rGPS), 40–41, 59–62, 138*t*, 152*f*, 185
minimum offset plot, 150*f*
Remotely operated vehicles (ROVs), 105–107
Reverse time migration (RTM), 500–501, 517
advantage, 518–519
migration velocity, 520*f*
poststack RTM, 517–518
prestack RTM, 518
reverse time TK migration, 518–519
2D/3D, 516
wide azimuth, 518–519
zero-offset, 520*f*
Reverse time TK migration, 518–519
Rich-azimuth surveys (RAZ), 98, 99*f*
Root-mean-square (RMS) velocities, 424–425, 459–460
Run-in and run-out distances, 125–126, 126*f*, 181–182

S

Sail line azimuths, 120–121
Sampling rate, 127–128
Sampling theory, 235–239, 236–238*f*
Seafloor topography, 388, 497
SeaRay system, 104, 104*f*
Secondary (S) waves, 25–26, 26*f*
SegD seismic data format structures, 243, 244*f*
SegY seismic data format structures, 243, 244*f*
Seismic acquisition, 38–39, 118
Seismic amplitude inversion, 284
Seismic attributes, 562
Seismic data processing, 1–2, 174, 211–212, 214*t*
acceptance tolerances for, 142
bad records and misfires, 141*t*
characteristics, 111
CMP acquisition technique, 1
dead and noisy traces, 141*t*
in deconvolution, 313–314, 315*f*
linear moveout correction, 147
onboard processing, 140–142
processing flow, 2, 2*f*
processing parameters, 211
RMS noise plots, 144, 144–145*f*
shaping filters, 332–333
signal-to-noise ratio, 1–2
temporal resolution, 314*f*
Seismic exploration, 22–25
Seismic interference
dead channel, 200–201, 205*f*
onboard generators, 200–201
seawater, 196
single-frequency harmonic noise, 201, 206*f*
spectral analysis, 197, 202*f*
streamer, 198–200, 204*f*
successive shot gathers, 196, 200*f*
3D shot record group, 196, 201*f*
Seismic migration
defined, 493–494
depth migration, 524–526
dip moveout, 529–532
finite-difference migration, 508–512
f-k migration, 512–516
Kirchhoff migration, 502–507
migration concept, 494–501
quality control in, 535–547
poststack migration, 519–521
prestack migration, 521–524
reverse time migration, 516–519
RMS velocity, 494
semicircular construction, 494
3D migration, 526–529
Seismic recorder, 58
Seismic reflection method, 22–24
Seismic sample format, 128–130, 129*f*, 129*t*
Seismic source analysis
near-field hydrophone outputs, 157*f*
offline source QC applications, 154
port and starboard arrays, 155, 155*f*
P-P signal strength, 155*f*
Seismic surveys, 38
offshore, 38–39, 38*f*
2D and 3D, 59, 175
Seismic velocity
average velocity, 424
Dix interval velocity, 425–426
instantaneous velocity, 424
interval velocity, 424
NMO or stacking velocity, 425
root-mean-square velocity, 424–425
Seismic vessels, 43*f*
dynamic positioning system, 44
gun deck, 43
streamer deck, 43
2D/3D seismic data acquisition, 41–42
Seismic waves
body waves, 25
defined, 25
Love waves, 26–27, 26*f*
primary waves, 25–27, 26*f*
Rayleigh waves, 26–27, 26*f*
secondary waves, 25–26, 26*f*
Seismogram, 372–374
amplitude spectrum, 335*f*
autocorrelation, 321–322
Semblance sample rate, effect of, 446–447, 449*f*
SentinelMS, 51–52
Shaping filters, 332–333, 350–355
Shot gathers, 29–31, 30*f*, 32*f*
Shot intervals, 114–116, 115*t*, 146, 147*f*
Shuey approximation, 570–571
Side-scan sonar systems, 14–17, 14*t*, 15*f*
Side-sweep reflection, 204–205, 209*f*
Signal frequency, 41–42, 212–213, 424
Signal/noise ratio (S/N), 174, 436, 552
Signature processing, 354–355, 355*f*
Simple earth model, 316–317, 318*f*, 320
Single-beam echosounders, 12, 13*f*
Single channel seismics, 19–22, 20*f*, 20*t*, 22*f*
Single frequency subbottom profilers, 18
Single trace section, 244, 245–246*f*
Slant streamer acquisition, 92–93, 94*f*
Sleeve guns, 55
Society of Exploration Geophysicists (SEG), 243
Solid streamers, 48, 49*f*
Sound Fixing and Ranging (SOFAR) channel, 8
Source directivity, of array, 79
Source-generated noise, 112, 171
Source waveform, 320, 324–325

Sparkers, 53
Spatial aliasing, 112, 538
Spectral analysis, 144–145, 197, 202*f*
Spherical divergence correction, 276–277, 277*f*
Spikelike noise, 202–204, 207–208*f*
Spike noise, 307*f*
Spiking deconvolution
  deconvolution operator, 324–325
  defined, 315–316, 324–325
  inverse filtering, 325–328, 326*f*
    with least squares, 328–330
  optimum Wiener filters, 330–333
  prewhitening, 334–335
  time domain, 325*f*
SRME. *See* Surface-related multiple rejection (SRME)
Stacking velocity
  common reflection surface stack, 481–485
  data effects, 474, 475*f*
  defined, 425
  mean stack, 472, 473*f*
  median stack, 477–479
  NMO corrected CDP, 474–475
  partial stack, 475–477
  ray paths, 472–474, 473*f*
  seafloor and subsurface structure, 425
  spread-length bias, 425, 426*f*
  trimmed stack, 480–481
  2D stack section, 474, 474*f*
Static/fixed bin, 413–414, 415*f*
Stationary wavelet, 320
Stolt migration, 500–501, 515–516
Stolt stretch factor, 514–515, 515*f*
Streamer(s), 44–53, 46–47*f*
  acoustic devices, 84
  acquisition, 94*f*
  ballasts, 208–210
  depth controllers, 57–58, 57*f*
  dual-sensor (2C), 69
  instrument mobilization checklist, 132, 134–135*t*
  layout, 84–88, 86*f*
  lead-in cables, 62
  length, effect of, 441–442, 442–443*f*
  multicomponent (4C), 69
  offset distance, 147
  over-under, 68
  source depth, 116–118
  steering, 84–85
  tail buoy, 185
  trimming, 208–209
  variable-depth/slant, 68
Strings, 72–76, 74*f*
Strum noise, 172–173, 188
Subbottom profilers, 17–19, 18*t*
Supergathers
  CDP, offsets of traces, 438–440, 439*f*
  multioffset CDP gather, 439*f*, 440
  neighboring CDPs, 436–438, 437*f*
  3D bin and CDP distribution, 438, 438*f*
Surface consistent deconvolution, 356–357
Surface-related multiple rejection (SRME), 367
  advantages, 399
  application of, 398–399
  autoconvolution, 395–398, 398*f*
  multiple elimination methods, 394–395
  primary reflection, 395–398, 397*f*
  seismic data, 395–398
  stack section, 395–398, 399*f*
Survey geometry parameters
  air gun and array, 126–127
  bin size, 122–124
  group interval, 118–119
  line interval and infill, 124–125
  offset distance, 119–120
  run-in and run-out distances, 125–126
  sail line azimuth, 120–121
  shot interval, 114–116
  streamer/source depth, 116–118
  tow distance, 127
  2D and 3D coverage, 121–122
  vessel speed, 127
Swell noise, 181*f*
  amplitude spectrum, 180, 182*f*
  characteristics, 180
  high-resolution seismic surveys, 181–182
  raw shot gathers, 180, 182–183, 183–184*f*
  streamer, turbulence effect, 180–181, 184*f*
Synthetic seismogram, 317, 318*f*
Systematic velocity errors, 545, 545*f*

T

Tail buoy noise, 60–62, 61*f*, 185–187, 191*f*
TAR. *See* True amplitude recovery (TAR)
Taylor's series expansion, 230–231
Thin bed tuning, 578
3D acoustic network, 90, 90*f*
3D conventional multichannel seismic surveys, 10–11, 23*t*
3D coverage, 121–122, 122*f*
3D data volume, 23*f*
3D Kirchhoff prestack depth/time migrations, 526
3D marine seismic data acquisition
  acoustic network, 88–91
  acquisition patterns, 82–84
  conventional 3D source, 82*f*
  fan mode acquisition, 93–94
  flip-flop shooting, 91–92
  marine seismic contractors, 81–82
  multiazimuth surveys, 94–100
  slant streamer acquisition, 92–93
  streamer layouts, 82*f*, 85–88
  streamer steering, 84–85
3D migration, 526–529, 526–527*f*
3D seismic surveys, 8–9, 41, 42*f*, 130*f*
  preplot maps, 136*f*
  RTM, 500–501
3D streamer steering devices, 85*f*
3D towed seismic acquisition, 84–85
Time gate, effect of, 444–445, 448*f*
Time lapse (4D) seismic surveys, 108–109
Time-variant spectral whitening (TVSW)
  defined, 558
  migrated sections, 560–561, 561*f*
  narrow band-pass filters, 558–560, 559*f*
  seismic traces, 558–560, 560*f*
  seismic wavelet, 561
Time varying filtering (TVF), 264–268, 267*f*
Toeplitz matrix, 331
Tow distance, 127
τ–p transform, 232–235, 233–235*f*
Trace balancing, 391
Trace edit, 287–294
  harmonic noise interference, 288*f*
Trace mixing
  horizontal stacking, 558
  weighting coefficients, 556–558, 557–559*f*
  zero-offset stack sections, 556
Trace summing, 48

Transition zone acquisition, 109–110, 109–110*f*
Trimmed stack
  amplitude values, 481, 481*f*
  defined, 480–481
  on marine seismic data, 481, 482*f*
  mean stack and median stack, 480
  on synthetic CDP gather, 481, 482*f*
True amplitude recovery (TAR), 275–276, 391
Tug noise, 172–173
TVSW. *See* Time-variant spectral whitening (TVSW)
2D conventional multichannel seismic surveys, 10–11, 23*t*
2D coverage, 121–122, 121*f*
2D earth model, 519–521
2D Fourier transform, 222–230, 224–227*f*
  f-k dip filters, 299
2D migration, 526, 526*f*, 528
2D poststack migration, 519–521, 521*f*
2D seismic dataset, 5–6, 6*f*
2D seismic surveys, 41, 42*f*
  preplot maps, 136*f*
  side-sweeps, 204–205
Two-term NMO equation, 466, 467*f*

U

Underwater acoustics
  physical properties, 7
  physical zones/clines, 8*f*
  sound velocity, 7–9, 7*t*
  warm water, 7–8
UNESCO algorithm, 9
Universal Transverse Mercator (UTM), 249

V

Variable depth, 94–95*f*
  and slant streamers, 68
VectorSeis system, 104, 104*f*
Velocity analysis
  anisotropic effects, 423
  deeper sediments, 423–424
  factors controlling, 422–423, 422*f*
  factors influencing, 423, 436
  Gardner's equation, 423
  porosity and fluid saturation, 423
  in practice, 436–452
  quality control in, 453–456
  rock velocity, 423
  seismic data processing, 421–422
  seismic velocity types, 424–426
  signal frequency, 424
  signal-to-noise ratio, 436
  supergathers, 436–440
  synthetic and real CDPs, 436, 437*f*
Velocity determination, seismic data
  constant velocity scan, 427–428, 427*f*
  constant velocity stack, 428, 429*f*
  hyperbolic and nonhyperbolic reflections, 427
  NMO time, 426–427
  stacking and migration, 426
  velocity spectra, 428–435
Velocity effect
  finite-difference migration, 511–512, 513*f*
  f-k migration, 515–516, 516–517*f*
  Kirchhoff migration, 507, 509–510*f*
Velocity increment effect, 446, 448*f*
Velocity picking, 434, 453
Velocity spectrum
  reflection hyperbolas, 428–430, 432–435, 436*f*
  RMS velocities, 430
  semblance value, 434, 435*f*
  stacking velocity, 429–430, 431*f*
  synthetic CDP, 428–429, 430*f*, 433*f*
  2D and 3D velocity functions, 428–429
  velocity picking, 434
  velocity versus zero offset time, 430–432
Vertical transverse isotropy (VTI), 467, 468*f*
Vessel speed, 127, 167*f*

W

Wave equation multiple rejection (WEMR) method, 367
  long period multiples, 388
  multiple removal technique, 391
  seabed reflection, 390
  signal propagation geometry, 389–390
  stack section, 390–391, 392*f*
  streamer and seafloor geometry, 389
  theoretical basis, 389–390
Wavelet causality, 320–321
Wavelet shaping, 332–333
Wavenumber, 213
Weekly reports, statistical information, 162–163, 164*t*
Wide-azimuth surveys (WAZ), 98, 99*f*
Wiener filter theory, 331
Wiener-Khintchine Theorem, 213–215
Wiener-Levinson algorithms, 331
Wiener spiking deconvolution, 331–332, 333–334*f*
  nonminimum phase wavelet, 354*f*

Z

Zero-offset rays, 496–497, 496–497*f*
Zero padding, 219–220, 541, 542*f*
Zero phase frequency domain deconvolution, 333
Zero phase wavelets, 320–321
Zero-to-peak (0-*p*) amplitude, 212–213
Zoeppritz equations, 569–570, 569*f*
Z transform, 230–231

Acquisition and Processing of Marine Seismic Data

Derman Dondurur

Demonstrates the main principles, equipment, and suitable selection of parameters as well as quality control (QC) analyses in 2D and 3D marine seismic data acquisition and processing.

- Contains simple step-by-step diagrams of the methodology used in the processing of seismic data to demonstrate the theory behind the applications
- Combines theory and practice, including extensive noise, QC, and velocity analyses, as well as examples for beginners in the seismic operations market
- Includes simple illustrations to provide to the audience an easy understanding of the theoretical background
- Contains enhanced field data examples and applications

Acquisition and Processing of Marine Seismic Data demonstrates the main principles, required equipment, and suitable selection of parameters in 2D/3D marine seismic data acquisition, as well as theoretical principles of marine seismic data processing and their practical implications. Featuring detailed datasets and examples, the book helps to relate theoretical background to real seismic data. This reference also contains important QC analysis methods and results both for data acquisition and marine seismic data processing.

Acquisition and Processing of Marine Seismic Data is a valuable tool for researchers and students involved in geophysics, marine seismic surveys, seismic data analysis, and oil and gas exploration.

Derman Dondurur is a research professor at the Institute of Marine Sciences and Technology at Dokuz Eylül University, Turkey. He has been working in single and multichannel seismic data acquisition for more than 15 years onboard the research vessel RV K. *Piri Reis*, where he leads the collection and processing of marine seismic data, QC processes, and parameter determination and testing applications during the acquisition and processing. He was the coordinator of several research and investigation projects, both scientific and private, working with private oil companies and research institutions, which included offshore seismic data acquisition and processing applications, for several years.



elsevier.com/books-and-journals

ISBN 978-0-12-811490-2

